The Tenth US–Japan Seminar

on

Dielectric and Piezoelectric Ceramics

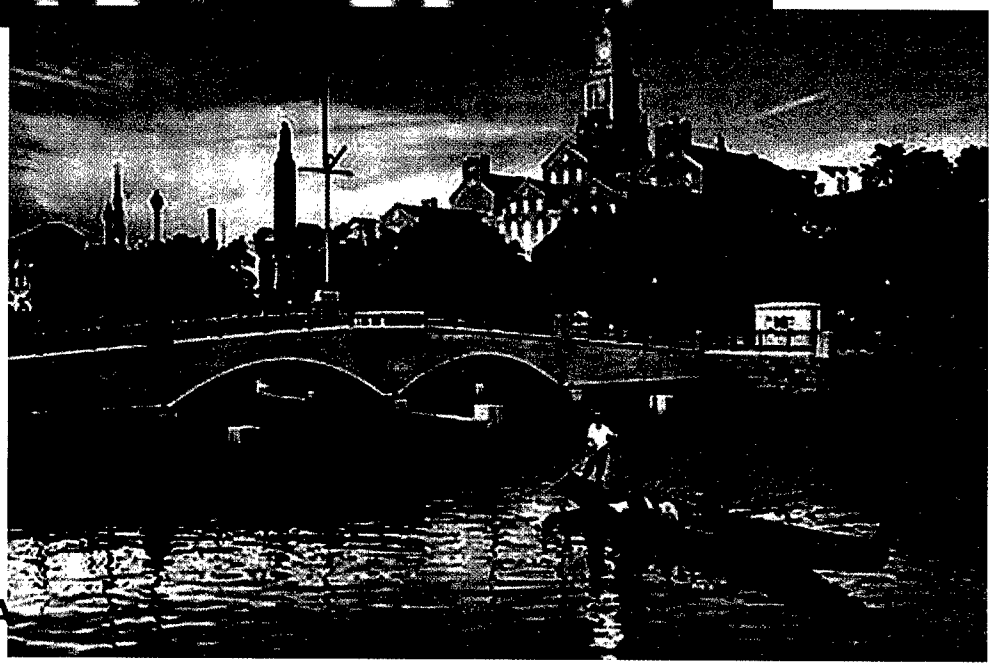

PROGRAM
SUMMARY
and
EXTENDED
ABSTRACTS

DISTRIBUTION STATEMENT A
Approved for Public Release
Distribution Unlimited

September 26–29, 2001

Providence Biltmore, Providence,
Rhode Island, USA

20020722 254

FRONT COVER:

WaterFire Providence®/Providence Skyline. The award-winning sculpture by Barnaby Evans, installed on the three rivers of downtown Providence, has enchanted many thousands of residents and visitors to Providence since its creation in 1994. Black-clad firetenders in boats silently gliding along the water tend up to 100 fires during the 20–25 lightings scheduled each year. More than thirty sponsors and the work of hundreds of volunteers help keep the bonfires burning for the enjoyment of the public.

Gondola with the Crawford Street Bridge and Courthouse. Two gondolas grace the Woonasquatucket and Providence Rivers. One is believed to be the first authentic Venetian gondola built in the United States; the other was constructed and shipped from Venice, Italy. Each is adorned with hand-sculpted ornaments and over 250 feet of solid brass trim. Italian music completes the experience, providing romantic excursions for Providence residents and visitors alike.

BACK COVER:

The Providence Biltmore Hotel. The Providence Biltmore, site of the 10th US-Japan Seminar on Dielectric and Piezoelectric Ceramics, first opened its doors in 1922. A state-of-the-art luxury hotel, over 1,000 people attended the official opening, for which the building was illuminated from top to bottom with over 25,000 lights. The hotel has played host to a number of celebrities and entertainers over the years, and it has survived some of the worst storms of the 20th Century. A plaque high up on the lobby columns commemorates the high water mark that occurred when the building flooded during a hurricane in 1954. The hotel has been placed on the National Preservation Register as one of the country's cherished architectural treasures.

- Photos are courtesy of Richard Benjamin. More of Mr. Benjamin's work can be seen at www.picturethisgalleries.com. To learn more about the artist, and the city of Providence, please visit www.providenceRI.com.

The 10th US-Japan Seminar on
Dielectric and Piezoelectric Ceramics

PROGRAM SUMMARY
and
EXTENDED ABSTRACTS

General Chairs: Shoko Yoshikawa, Active Control eXperts, Inc./Div. of Cymer, USA
Yukio Sakabe, Murata Manufacturing Co., Ltd., Japan

Program Chairs: Susan Trolier-McKinstry, Penn State University, USA
Masatoshi Adachi, Toyama Prefectural University, Japan

Sponsored by:
Office of Naval Research
Shoei Chemical Co.

Additional Support from:
Asian Office of Aerospace Research and Development
(US Air Force Office of Scientific Research)
Ferro Corporation

September 26–29, 2001
The Providence Biltmore Hotel
Providence, Rhode Island, USA

REPORT DOCUMENTATION PAGE

Form Approved OMB No. 0704-0188

Public reporting burden for this collection of information is estimated to average 1 hour per response, including the time for reviewing instructions, searching existing data sources, gathering and maintaining the data needed, and completing and reviewing this collection of information. Send comments regarding this burden estimate or any other aspect of this collection of information, including suggestions for reducing this burden to Department of Defense, Washington Headquarters Services, Directorate for Information Operations and Reports (0704-0188), 1215 Jefferson Davis Highway, Suite 1204, Arlington, VA 22202-4302. Respondents should be aware that notwithstanding any other provision of law, no person shall be subject to any penalty for failing to comply with a collection of information if it does not display a currently valid OMB control number. **PLEASE DO NOT RETURN YOUR FORM TO THE ABOVE ADDRESS.**

1. REPORT DATE *(DD-MM-YYYY)*	2. REPORT TYPE	3. DATES COVERED *(From - To)*
15-07-2002	Final	01-09-2000 to 30-11-2002

4. TITLE AND SUBTITLE

10th US-Japan Workshop on Dielectric and Piezoelectric Materials

5a. CONTRACT NUMBER

5b. GRANT NUMBER
N00014-00-1-0911

5c. PROGRAM ELEMENT NUMBER

6. AUTHOR(S)
Susan Trolier McKinstry

5d. PROJECT NUMBER

5e. TASK NUMBER

5f. WORK UNIT NUMBER

7. PERFORMING ORGANIZATION NAME(S) AND ADDRESS(ES)

Penn State University
Office of Sponsored Programs
110 Technology Center Bldg.
University Park, PA 16802-7000

8. PERFORMING ORGANIZATION REPORT NUMBER

9. SPONSORING / MONITORING AGENCY NAME(S) AND ADDRESS(ES)
Dr. Wallace A. Smith
Office of Naval Research
Ballston Centre Tower one
800 North Quincy Street
Arlington VA 22217-5660

10. SPONSOR/MONITOR'S ACRONYM(S)
ONR 332

11. SPONSOR/MONITOR'S REPORT NUMBER(S)

12. DISTRIBUTION / AVAILABILITY STATEMENT

APPROVED FOR PUBLIC RELEASE

13. SUPPLEMENTARY NOTES

14. ABSTRACT

The award partially supported the technical workshop entitled "10th U.S.-Japan Workshop on Dielectric and Piezoelectric Materials." This included the organization, mailing, abstract preparation, secretarial, travel, and related costs to hold a workshop.

Held every two years, alternating from the U.S. and Japan, the workshop is a closed meeting, by "invitation only", offering a highly interactive environment for technical exchange. The workshop took place September 27-29, 2001 in the Biltmore Hotel, Providence, Rhode Island. Topics covered included piezoelectric and dielectric materials and devices (including bulk, particulate, and thin film), and their processing technology. A proceedings of extended abstracts from the conference was distributed to participants.

15. SUBJECT TERMS
Dielectric, Piezoelectric, Ceramic

16. SECURITY CLASSIFICATION OF:			17. LIMITATION OF ABSTRACT	18. NUMBER OF PAGES	19a. NAME OF RESPONSIBLE PERSON
a. REPORT	b. ABSTRACT	c. THIS PAGE			Robert Killoren
U	U	U	UU	5	19b. TELEPHONE NUMBER *(include area code)* 814-865-3396

15. SUBJECT TERMS

Contract Information

Contract Number	N00014-00-1-0911
Title of Research	"10th U.S. – Japan Workshop on Dielectric and Piezoelectric Materials"
Principal Investigator	Susan Trolier-McKinstry
Organization	Penn State University

Technical Section

Technical Objectives

Introduction

The purpose of this award was partial support from the Office of Naval Research for the technical workshop entitled "10th U.S.-Japan Workshop on Dielectric and Piezoelectric Materials." This included the organization, mailing, abstract preparation, secretarial, travel, and related costs to hold a workshop.

Held every two years, alternating from the U.S. and Japan, the workshop is a closed meeting, by "invitation only", offering a highly interactive environment for technical exchange.

Timing and Content of Workshop

The workshop took place September 27-29, 2001 in the Biltmore Hotel, Providence, Rhode Island. Topics covered included piezoelectric and dielectric materials and devices (including bulk, particulate, and thin film), and their processing technology.

Invited talks were used to introduce each topic area. The majority of the papers, however, were given in poster sessions preceded by three-minute oral presentations.

Deliveries

At the workshop, an abstract book containing four-page extended abstracts of all the presentations was delivered to each participant.

Organization

The workshop was organized by Ms. Shoko Yoshikawa (Active Control eXperts (ACX), Inc.) and Mr. Yukio Sakabe (Murata). The program chairs were Dr. Susan Trolier-McKinstry (Penn State University) and Dr. Masatoshi Adachi (Toyama Pref. Univ). Attendance is by invitation, with all delegates participating in the presentation of their work. To maximize discussion time, the format of the meeting comprised only 2 or 3 plenary papers per morning or afternoon session, followed by 3-minute summaries of the contributed items, which were then

displayed and discussed as posters. The format was designed to foster interaction between the participants, with the preponderance of papers being offered as posters.

The conference was divided into five sessions and several sub-sessions, the topics of which are shown below with the number of contributions in each case:

I – Dielectrics for capacitor and high frequency applications

multilayer capacitors (7); MLC reliability (5); new dielectrics (3); thin film capacitors (3); high frequency and tunable dielectrics (6)

II – Memory Applications and Fundamentals

memory related materials (10); MEMS (4); basic science (9)

III – Piezoelectrics materials and devices (including single crystals)

single crystals (13); lead-free materials (4); PZT-related materials (5); piezoelectric devices (6)

IV – Novel processing

textured piezoelectric ceramics (8); powders and consolidation (4); net-shape forming (3)

V – Additional plenary talks

Additional Support

Additional support was provided for the conference by Shoei Chemical Company, the Asian Office of Aerospace Research and Development (US Air Force Office of Scientific Research) and Ferro Corporation.

Final Report

The preliminary program called for ~95 papers to be presented at the workshop. Unfortunately, the events of September 11, 2001 resulted in a considerable decrease in the number of participants, especially from the Japanese side. In particular, only one participant from Japanese industry was permitted to attend (Y. Sakabe). Fortunately, many of the Japanese academics were able to come. The numerous cancellations, many of which came at only the last minute, resulted in appreciable re-shuffling of the program. Drs. Y. Sakabe and M. Adachi were tremendously helpful in filling in gaps in the program, and presented many of the original participants' papers and posters. In spite of these difficulties, the meeting was a successful one. Several attendees commented on the high level of interaction promoted by the conference format. Technical highlights include:

- David Wilcox gave an overview of current research at Motorola. He discussed multilayer processing and future applications of dielectric materials, with an emphasis on using low temperature ceramic co-fire technology as a new platform for integrated systems. The need

for heterogeneous integration of ceramics, polymers, and semiconductor IC's was stressed.

- Yukio Sakabe discussed silver lithium niobium tantalum ceramics and their properties. These materials have an interesting array of ferroelectric transitions, and are potentially interesting for medium Q materials in the microwave, or as non-lead piezoelectrics. The biggest processing challenge is full oxidation of the silver. By restricting the calcination temperature to 900-1000°C in an O_2 atmosphere, it was possible to prepare single-phase materials. This talk replaced one originally scheduled for H. Kishi on site occupancy of rare earth dopants in $BaTiO_3$.

- Glen Fox discussed material requirements for FRAM, a ferroelectric non-volatile memory. Developments on predicting lifetime, process integration, and fundamentals of fatigue and imprint were discussed. Considerable progress has been made in this field, with commercial production being led by Fujitsu. It is encouraging that ferroelectric memory technology is now on the semiconductor road map.

- Tadashi Shiosaki discussed recent work on ferroelectric thin films and their applications, with a concentration on work being performed in Japan. A summary of the papers given at the Japan Society of Applied Physics was presented.

- Duane Dimos presented a paper on direct write of integrated electroceramic devices. This is an excellent means of integrating ceramic and polymeric materials. The technology is currently limited to writing features > 50 μm in lateral size. Of especial interest is the ability to deposit multiple materials on non-planar substrates.

- Uesu discussed domain analysis in lithium niobate. He developed a novel interferometry approach to map out three dimensional domain structures. The technique appears to be quite general, and should be very useful in domain characterization.

- Takaaki Tsurumi discussed intrinsic and extrinsic contributions to PZT. By investigating the frequency dependence of the electric field induced strain, they were able to identify two separate contributions to domain wall motion: shift and vibration.

- Wes Hackenburger discussed a new high temperature piezoelectric material with piezoelectric coefficients comparable to or slightly higher than PZT. The design of materials with low end member tolerance factors appears to facilitate high transition temperatures. The bismuth scandium titanate lead titanate looks very promising for higher temperature applications.

- Bob Heistand reported on integrated passive devices for wireless applications. AVX is pursuing thin film technology patterned with semiconductor processing techniques to achieve high levels of integration. Emphasis was placed on the ability to prepare 1 pF to 0.5 mF capacitors using thin film PZT. Use of resistive electrodes enabled formation of capacitors and resistors in a reduced volume.

- Bruce Tuttle described the process of "Robocasting" for rapid prototyping of monolithic ceramics with very complicated internal geometries. 3-3 PZT polymer composites with feature sizes of less than 1 mm were described.

- Andrew Bell presented an overview of electroceramics activity in Europe.

Other trends/highlights observed:

- "Ultra-thin Ni-compatible X7R dielectric based on alkoxides derived barium titanate", I. Burn et al., DMC^2, revealed how 2 nm layer, base-metal multilayer capacitors were made possible from an alkoxides-derived barium titanate. The 4000 liter batch size allows a production capacity of 300 tons p.a.
- H. Funakubo detailed progress on low deposition temperatures for MOCVD ferroelectric thin films. The extremely high quality films can be produced at temperatures as low as 415°C, 200°C lower than is typically reported.
- "Transmission electron microscopy investigations of Bi_2O_3-ZnO-Nb_2O_5 pyrochlore and related phases" & "Bi-pyrochlore materials for microwave applications", C. A. Randall et al., Penn State Univ., described work on elucidating the structure and properties of a new family of dielectrics with good high frequency properties and process conditions compatible with LTCC systems.
- "A novel fabrication process of ferroelectric capacitors with self-aligning patterning of top electrodes", S. Okamura et al., NAIST, described how electron beam radiation was used to cure selective areas of SBT sol-gel precursor layers on Pt bottom electrodes. After deposition of an unpatterned top electrode layer of Pt, the uncured gel acted as a photo-resist in a lift-off process to pattern the top electrode.
- "MEMS accelerometers using PZT thick films", L-P. Wang et al, Penn State Univ., reported the use of a novel "trampoline-style" architecture for accelerometers with sensitivities in the range 0.6 to 7.5 pC g^{-1}, employing multilayer deposited sol-gel PZT.
- "Growth and properties of 3" single crystals of piezoelectric $Pb[(Zn_{1/3}Nb_{2/3})_{0.91}Ti_{0.09}]O_3$", M. Matsushita et al, Kawatetsu Mining Company Ltd., described the optical and Laue images obtained from 1kg Bridgman grown crystals. The 75 mm diameter by 55 mm long crystals exhibit PbO inclusions at the periphery and the bottom, however regions approx 55 x 50 mm could be extracted that were inclusion free. The complexity of the domain structures was emphasized.
- There is considerable focus on the development of texture in bulk dielectric and piezoelectric ceramics. In addition to the U.S. work, largely sponsored by DARPA and ONR, there were contributions reported by T. Tani in Japan. "Templated grain growth of textured piezoelectric ceramics", G.L. Messing et al., Penn State Univ, showed that piezoelectric coefficients as high as 1200 pC N^{-1}, with strains up to 0.32% could be achieved in 0.68PMN-0.32PT [001] textured ceramics.
- "Electrical properties of morphotropic phase boundary in $(Bi_{1/2}Na_{1/2})TiO_3$ – $KNbO_3$ solid solution system", T. Takenaka et al., Science University of Tokyo, reports results for materials around the morphotropic phase boundary at $0.04((Bi_{1/2}Na_{1}/TiO_3$ – $0.96KNbO_3$. Samples are difficult to densify by conventional sintering and have rather

low remanent polarization (0.06 C m^{-2}), however it was felt that poling was incomplete due to low resistivity.

Travel Support

Travel support was provided for the following people to attend the meeting:
Joanne Aller: staff support
Deb Shay: staff support
Susan Trolier-McKinstry: meeting organizer
Shoko Yoshikawa: meeting organizer
Takeshi Yoshimura: meetings support
Michael Biegalski: meetings support
Glen Fox: Ramtron Corp.
David Cann: Iowa State University
Chris Lynch: Georgia Institute of Technology
Jon-Paul Maria: North Carolina State University
Andrew Bell: University of Leeds

Conclusions

The 10th US-Japan seminar gave a unique insight into recent developments in dielectrics and piezoelectrics on both sides of the Pacific Ocean. The intimacy of the meeting allowed participants the opportunity to talk to virtually every other delegate and exchange information on an informal basis. The format of the meeting could be recommended as the basis for other meetings of similar size in other parts of the world. The splendid surroundings provided by the Providence Biltmore Hotel and the location of the poster sessions in the 17th floor ballroom added to the charm of a very enjoyable and entirely successful meeting.

10TH US-JAPAN SEMINAR ON
DIELECTRICS AND PIEZOELECTRIC CERAMICS
September 2001

Schedule Summary

	Morning	Afternoon	Evening
September 26 Wednesday			5:00 - 7:30 pm Registration 7:30 - 9:00 pm Welcome Reception
September 27 Thursday	7:00 - 8:00 am Registration 8:00 - 8:15 am Opening Remarks **SESSION I** 8:15-9:15 am Plenary Lectures 9:30 – 12:00 Noon Poster summary and viewing	**SESSION II** 1:00 - 2:00 PM Plenary Lectures 2:15 - 5:00 pm Poster summary and viewing	7:00 - 9:00 pm Banquet
September 28 Friday	**SESSION III** 8:30-9:30 am Plenary Lectures 9:45 – 12:00 Noon Poster summary and viewing	**SESSION IV** 1:00 - 2:00 PM Plenary Lectures 2:15 - 5:00 pm Poster summary and viewing	
September 29 Saturday	**SESSION V** 9:00-11:00 Plenary Lectures	11:30 am - 1:00 pm Farewell Lunch	

Preface

The 10th US-Japan Seminar on Dielectrics and Piezoelectric Ceramics, celebrating 20-years of history of joint meetings between the two nations, will be held at Providence, Rhode Island, September 27-29, 2001.

This extended abstract booklet contains all of the papers presented at the meeting, including plenary lectures and poster presentations, in the order of presentation. Following the tradition of the US-Japan Seminar, the sessions typically consist of two plenary presentations, one from each country, and 20 to 30 3-4 minute presentations, followed by poster viewing and discussion at the poster site.

The presentations are categorized under the following groupings:

> Session I: Dielectrics for RF Application (including multilayer capacitors, film capacitors, high frequency, and tunable dielectrics).
>
> Session II: Memory Applications and Fundamentals (including films for MEMS applications).
>
> Session III: Piezoelectrics (including single crystal piezoelectrics).
>
> Session IV: Novel Processing and Piezoelectric Devices (including textured piezoelectrics and powder synthesis).
>
> Session V: Contains 4 plenary papers on various topics, including a special guest paper providing an overview of European activities.

Shoko Yoshikawa recalls her first experience at a US-Japan meeting, which was the 5th one in Kyoto, Japan. Throughout the years, the seminar has been not only a great opportunity to exchange the most recent research and development activities on dielectric and piezoelectric ceramics, but also to get to know the researchers and cultures of each country. We hope this 10th seminar will meet this objective again.

We would like to thank the Japanese organizers, Yukio Sakabe and Masatoshi Adachi for their wonderful collaboration. We are also grateful to the Asian Office of Aerospace Research and Development for travel support and DMC-2 for reception support. Above all, the seminar would not be possible without the financial support of the Office of Naval Research and Shoei Chemical Co., as well as collaboration of all the participants.

August 24, 2001

Susan Trolier-McKinstry
US Program Chair
Pennsylvania State University

Shoko Yoshikawa
US General Chair
ACX Division of Cymer Inc.

10th US-Japan Seminar on Dielectric and Piezoelectric Ceramics

September 26-29, 2001
Providence, Rhode Island, USA

PROGRAM

Wednesday, September 26

5:00 – 7:30 p.m. Registration
7:30 – 9:00 p.m. Welcome Reception

Thursday, September 27

7:00 – 8:00 a.m. Registration

8:00 – 8:15 a.m. *Introduction and Welcome:* Shoko Yoshikawa, US General Chair, and Yukio Sakabe, Japan General Chair

SESSION I. DIELECTRICS

Session Chair: *Noboru Ichinose, Waseda University*
Clive Randall, Penn State University

8:15 – 9:15 a.m. ***Plenary Lectures – Dielectrics for RF Applications***

PI.1 8:15 – 8:45 a.m. Multilayer Ceramic Integrated Materials Systems for Wireless, Energy and Life Science Micro-System Applications, David L. Wilcox, Sr. and S. Dai, Motorola Laboratories, USA. 1

PI.2 8:45 – 9:15 a.m. Progress of Dielectric Resonator Materials for Microwave and Millimeter-Wave Applications, Hiroshi Tamura, Murata Manufacturing Company, Ltd., Japan 9

9:15 – 9:30 a.m. ***Break***

9:30 a.m. – Noon ***Poster Summaries and Poster Viewing***

Multilayer Capacitors

I.1 Ultra-thin Ni-compatible X7R Dielectric Based on Alkoxide Derived Barium Titanate, P. Pinceloup, I. Burn, K. Albertsen, T. Ohba, and J. Roelofsma, DMC^2, USA. 15

I.2 Hydrothermal $BaTiO_3$ Based High K, Low Loss Dielectrics for Thin Active Layer BME MLCC Applications, S. Venigalla, D. L. Schultz, and J. A. Kerchner, Cabot Corporation, USA. 19

I.3 BME X7R and Y5V Dielectrics for Thin Layer MLC Applications, H. Park, D. McCauley, M. Megherhi, M. Chu, and E. Davis, Ferro Electronic Materials, USA. 23

Thursday, September 27

Multilayer Capacitors, continued

I.4 Physical and Electrical Properties of Low Fired K-3800 X8R Dielectric, G. H. Maher and S. C. Maher, MRA Laboratories, USA. 27

I.7 Development of 100% Silver Compatible Dielectric Compositions for High Performance Discrete and Integrated Passive Component Applications, B. Foster, W. Symes, E. Davis, M. Creedon , J. Bonistall, P. Pruna, J. Burton, and S. Witter, Ferro Electronic Materials, USA. 31

Capacitors: Reliability and Diffusion

I.8 Effect of Milling Process on Core-shell Microstructure and Electrical Properties for $BaTiO_3$-based Ni-MLCC, Y. Mizuno, T. Hagiwara, H. Chazono, and H. Kishi, Taiyo Yuden Company, Ltd., Japan. 35

I.9 Reliability of Base Metal Electrode Multilayer Ceramic Capacitors, L. A. Mann, J. J. Beeson, M. S. Randall, J. L. Paulsen, and E. K. Reed, KEMET Electronics Corporation, USA. 39

I.10 Effect of Occupational Sites of Rare-earth Elements on Dielectric Properties of $BaTiO_3$, H. Kishi, N. Kohzu, H. Chazono, J. Sugino*, H. Ohsato*, and T. Okuda*, Taiyo Yuden Company, Ltd., *Nagoya Institute of Technology, Japan. 43

I.11 Cation Diffusion in Barium Titanate, J. Itoh, I. Yashima, N. Ohashi^, I. Sakaguchi^, H. Haneda^, and J. Tanaka^, Mitsui Mining & Smelting Company, Ltd., Japan, ^National Institute for Materials Science, Japan. 47

I.12 Oxygen in Diffusion and Defect Structure in Perovskite Oxides, I. Sakaguchi, H. Haneda, S. Hishita, N. Ohashi, and M. Sekita, National Institute for Materials Science, Japan. 51

10-minute Break

Materials Development

I.13 Transmission Electron Microscopy Investigation of Bi_2O_3-ZnO-Nb_2O_5 Pyrochlore and Related Phases, J. C. Nino, I. M. Reaney*, M. T. Lanagan, and C. A. Randall, Center for Dielectric Studies, Penn State University, USA, *Dept. of Engineering Materials, University of Sheffield, U.K. 55

I.14 Bi-pyrochlore Materials for Microwave Applications, C. A. Randall, M. T. Lanagan, H-J. Youn, I. Reaney, H. Sogabe, J. Nino, A. Baker, and T. Shrout, Penn State University, USA. 59

I.15 Dielectric and Ferroelectric Properties of (Ag,Li)(Nb,Ta) Ceramics, Y. Sakabe, T. Takeda, Y. Ogiso, and N. Wada, Murata Manufacturing Company, Ltd, Japan. 63

Thursday, September 27

Film Capacitors

I.16 $Ba(Ti_xZr_{1-x})O_3$ Film as Dielectric for Capacitor Applications, B-H.Tsao, S. Heidger*, and J. A. Weimer*, University of Dayton Research Institute, *Air Force Research Laboratory, Wright-Patterson Air Force Base, USA. 67

I.17 Dielectric Properties of Perovskite Superlattices Measured Using Fine Planar Electrodes, T. Tsurumi, T. Ichikawa, T. Harigai, and S. Wada, Tokyo Institute of Technology, Japan. 71

I.18 Initial Results for MOCVD $(Ba,Sr)TiO_3$ Thin Film Capacitors on Metal Foils, D. Y. Kaufman*, S. K. Streiffer^, J. Im^†, S. Saha^, O. Auciello^, and R. Erck*, Argonne National Laboratory; *Energy Techology Division, ^Materials Science Division, †now of Agere Systems, USA. 75

High Frequency and Tunable Dielectrics

I.19 Measurement of Dielectric Properties of $BaTiO_3$-Based Materials in the 10 MHz to 1GHz Frequency Range, C. Nies, E. Deyneka, and M. T. Lanagan*, AVX Corporation, USA, *Penn State University, USA. 79

I.20 Microwave Properties of Dielectric Oxide and High T_c Superconductor System, S. Sugihara, T. Kawashima, C. Ishizuka, and N. Kimura, Shonan Institute of Technology, Japan. 83

I.21 Double-Layer Type Microwave Absorber Made of Magnetic-Dielectric Composite Material, M. Saitoh, T. Yamamoto, H. (Okino) Niori, M. Chino, and M. Kobayashi*, National Defense Academy, *Tayca Company, Japan. 87

I.22 Progress in $BaTiO_3$ Thin Films: High Frequency Applications and Property Investigations, J-P. Maria, C. B. Parker, F. Ayguavives, A. Tombak, G. Stauf*, A. Mortazawi, and A. I. Kingon, North Carolina State University, USA, *ATMI Corporation, USA. 91

I.23 Application of Ferroelectrics in Microwave Phased-Array Antennas, J. B. L. Rao, D. P. Patel, P. K. Park*, T. K. Dougherty*, J. A. Zelik*, A. Moffat^, and L. C. Research Sengupta+, Naval Laboratory, *Raytheon Systems Company, ^SFA, Inc., and +Paratek Microwave, Inc., USA. 95

I.24 Field Dependence of Dielectric Properties of $(Pb,Sr)TiO_3$ Thin Films, M. Adachi, K. Tsu, and T. Karaki, Toyama Prefectural University, Japan. 99

Noon to 1:00 p.m. ***Lunch***

SESSION II. MEMORY

Session Chair: *Takaaki Tsurumi, Tokyo Institute of Technology*
Angus Kingon, North Carolina State University

1:00 – 2:00 p.m. ***Plenary Lectures – Memory Applications***

			Page
PII.1	1:00 – 1:30 p.m.	Material Processing Requirements for Ferroelectric Non-Volatile Memory (FRAM) Technology, Glen R. Fox, R. Bailey, B. Kraus, F. Chu, S. Sun, and T. Davenport, Ramtron International Corporation, USA.	103

Thursday, September 27

PII.2	1:30 – 2:00 p.m.	Recent Study on Ferroelectric Thin Films and Their Applications, Tadashi Shiosaki and S. Okamura, Nara Institute of Science and Technology (NAIST), Japan.	109

2:00 – 2:15 p.m. ***Break***

2:15 – 5:00 p.m. ***Poster Summaries and Poster Viewing***

Memory

II.25	A Novel Fabrication Process of Ferroelectric Capacitors with the Self-align Patterning of Top Electrodes, S. Okamura, T. Kobayashi, K. Suzuki, and T. Shiosaki, Nara Institute of Science and Technology, Japan.	115
II.26	Preparation and Properties of $SrBi_2Ta_2O_9$ Ferroelectric Thin Films Using Excimer UV Irradiation, T. Hayashi, and D. Togawa, Shonan Institute of Technology, Japan.	119
II.27	Chemical Processing and Ferroelectric Properties of $MBi_4Ti_4O_{15}$ (M:Alkaline Earth Metals) Thin Films, K. Kato*†, K. Suzuki*, K. Nishizawa*, and T. Miki*, *National Institute of Advanced Industrial Science and Technology, Japan, †Frontier Collaborative Research Center, Tokyo Institute of Technology.	123
II.28	Integration and Characterization of Sub-micron MFIS FETs Transistor with $Pt/Pb_5Ge_3O_{11}$/ High-k/Si Structure, F. Zhang and S. T. Hsu, Sharp Laboratories, USA.	127
II.29	Low Temperature Deposition of Epitaxial-Grade PZT Films by MOCVD, H. Funakubo, M. Aratani, T. Oikawa, and K. Saito*, Tokyo Institute of Technology, Japan, *Philips Japan Ltd., Japan.	131
II.30	Retention Properties in Single-crystalline PLZT Thin Film Capacitors, N. Kamehara, M. Kurasawa, and K. Kurihara, Fujitsu Laboratories, Ltd., Japan.	135

Thursday, September 27

Film Deposition

II.31 Synthesis and Properties of Tungsten Bronze (Sr,Ba)(Nb,Ta)$_2O_6$ Thin Films by the Chemical Solution Deposition, W. Sakamoto, Y. Horie, T. Yogo, and S. Hirano, Nagoya University, Japan. 139

MEMS

II.33 Electrical Properties of $PbZrO_3$ Thin Films Prepared by Chemical Solution Deposition, H. Maiwa and N. Ichinose*, Shonan Institute of Technology, Japan, *Waseda University, Japan. 143

II.34 Microelectromechanical Systems (MEMS) Accelerometers Using Lead Zirconate Titanate Thick Films, L. P. Wang*, R. Wolf*, K. Deng^, L. Zou^, Y. Wang*, P. Wlodkowski^, R. J. Davis*, and S. Trolier-McKinstry*, *Penn State University, USA, ^ Wilcoxon Research, USA. 147

II.35 Piezoelectric Properties of $Pb(Yb_{1/2}Nb_{1/2})O_3$-$PbTiO_3$ Epitaxial Films with (100) and (111) Orientation, T. Yoshimura and S. Trolier-McKinstry, Penn State University, USA. 151

II.36 Preparation of Texture Controlled Lead Zirconate Titanate Diaphragm Type Film Actuator, T. Iijima, B. P. Zhang, and K. Kunii*, Tohoku National Industrial Research Institute, Japan, *NIDEC COPAL Corporation, Japan. 155

10-minute Break

Fundamentals

I1.37 Why the Atomic Structure Matters to Dielectric and Piezoelectric Performance, T. Egami, University of Pennsylvania, USA. 159

II.38 Polarization Relaxation in Piezoelectric $0.7Pb(Mg_{1/3}Nb_{2/3})O_3$–$0.3PbTiO_3$, D. Viehland, Naval Seasystems Command, USA. 161

II.39 Statistical Model for Poling Hard PZT, W. A. Schulze and M. K. Jha, Alfred University, USA. 165

II.40 Electric Field Effects on Dielectric Properties of MPB PZT Ceramics via Monoclinic Distortion at Low Temperatures, R. Guo, E. Alberta, A. Thomas, B. A. Jones, and L. E. Cross, Penn State University, USA. 169

II.41 Harmonic Analysis of the Electro-Mechanical Response of Electroactive Materials, C. B. DiAntonio, F.A. Williams, Jr., and S. M. Pilgrim, Alfred University, USA. 173

II.42 Calculation of Electrostrictive Coefficients and Their Complex Nature Through Fourier Analysis, C. B. DiAntonio, F. A. Williams, Jr., S. M. Pilgrim, Alfred University, USA. 177

Thursday, September 27

Fundamentals, continued

II.44 Visualization of the Domain Orientation in $PbTiO_3$ Single Crystals by Vertical and Lateral Piezoresponse Microscopy, H. (Okino) Niori, T. Ida, H. Ebihara, and T. Yamamoto, National Defense Academy, Japan. 181

II.45 Domains and Piezo Images of PZT Family Thin Films Observed by AFM and KFM, Y. Masuda, K. Kakimoto†, S. Fujita, and K. Watanabe*, Hachinohe Institute of Technology, Japan, †Nagoya Institute of Technology, *Seiko Instrument Company, Japan. 185

II.46 Progress in Flexoelectric Measurements, L. E. Cross and W. Ma, Penn State University, USA. 189

7:00 p.m. – 9:00 p.m. ***Dinner Banquet***

Friday, September 28

SESSION III. PIEZOELECTRICS

Session Chair: *Tadashi Shiosaki, Nara Institute of Science and Technology*
Yet-Ming Chiang, Massachusetts Institute of Technology

8:30 – 9:30 a.m. ***Plenary Lectures - Piezoelectrics***

PIII.1 8:30 – 9:00 a.m Domain Contribution to the Piezoelectric Properties of PZT Ceramics, Takaaki Tsurumi and S. Wada, Tokyo Institute of Technology, Japan. 193

PIII.2 9:00 – 9:30 a.m New High Temperature Morphotropic Phase Boundary Piezoelectrics Based on $Bi(Me)O_3$–$PbTiO_3$ Ceramics, R. Eitel°, C. A. Randall°, T. R. Shrout°, P. W. Rehrig^, Wesley Hackenberger^, and S. Park*, °Penn State University, ^TRS Ceramics, Inc., and *Fraunhofer Technology Center, USA. 201

9:30 – 9:45 a.m ***Break***

9:45 a.m–Noon ***Poster Summaries and Poster Viewing***

Single Crystal Piezoelectrics

III.47 Growth and Properties of 3" Single Crystal of Piezoelectric $Pb[(Zn_{1/3}Nb_{2/3})_{0.91}Ti_{0.09}]O_3$, M. Matsushita, Y. Tachi, S. Nagata, and K. Echizenya*, Kawatetsu Mining Company, Ltd., Japan, *Kawasaki Steel Company, Ltd., Japan. 209

III.48 Electromechanical Response of [001] Oriented Single Crystal Lead Zinc Niobate Titanate: DC Bias and Temperature Effects, A. Amin, L. C. Lim°, and T. S. Ramotowski, Naval Undersea Warfare Center, USA, ^Office of Naval Research, USA, and °National University of Singapore, Singapore. 213

Friday, September 28

Single Crystal Piezoelectrics, continued

III.49 Crystal Growth and Electrical Properties of High T_c Relaxor-based Single Crystals, N. Ichinose, Y. Saigo, Y. Hosono*, and Y. Yamashita*, Waseda University, Japan, *Toshiba Company, Japan. 217

III.51 Recent Progress of Growth of Ferroelectric Relaxor PMN-PT Single Crystals at SICCAS, W.A. Schulze, C. Feng*, and Z. Yin*, C. B. DiAntonio, F. A. Williams, Jr., and S. M. Pilgrim, *Chinese Academy of Sciences, China, Alfred University, USA. 221

III.52 Compressive Properties of Piezoelectric Single Crystals, L. Ewart and E. A. McLaughlin, Naval Undersea Warfare Center, USA. 225

III.53 Effects of Surface Condition on the Electrical and Chipping Properties of PZNT Single Crystal Vibrators for Medical Array Transducers, T. Kobayashi, Y. Hosono, M. Izumi, K. Itsumi, K. Harada, and Y. Yamashita, Toshiba Company, Japan. 229

III.54 New Orientation Cuts for Enhanced Electromechanical Properties of PMN-PT and PZN-PT Single Crystals, J. Chen, R. Panda, H. Beck, and R. Gururaja, Imaging Systems, Agilent Technologies, Inc., USA. 233

III.55 Domain Configuration and Polarization Switching in PZN-5%PT Crystals, S. E Park†, J. K. Lee*, and K. S. Hong*, *Seoul National University, Korea, †Fraunhofer-IBMT Technology Center, USA. 237

III.56 Domain Dynamics and Microstructure of $Pb(Zn_{1/3}Nb_{2/3})O_3$-$PbTiO_3$ Single Crystals, E. Furman, H. Yu, and C. A Randall, Penn State University, USA. 241

III.57 Poling Field Dependence of Ferroelectric Properties in Pb $(Zn_{1/3}Nb_{2/3})_{0.91}Ti_{0.09}O_3$ Single Crystal, T. Ogawa, M. Matsushita°, Y. Tachi°, and K. Echizenya*, Shizuoka Institute of Science and Technology, Japan, °Kawatetsu Mining Company, Ltd., Japan, *Kawasaki Steel Company, Ltd., Japan. 245

10-minute Break

III.58 Piezoelectric Properties of $KNbO_3$ Single Crystals with Various Crystallographic Orientations, S. Wada, A. Seike, H. Kakemoto, and T. Tsurumi, Tokyo Institute of Technology, Japan. 249

III.59 The Study of Fatigue Anisotropy in $Pb(Zn_{1/3}Nb/_{2/3})O_3$-$PbTiO_3$ Ferroelectric Single Crystals, M. Ozgul*, K. Takemura†, S. Trolier-McKinstry*, and C. A Randall*, †NEC Corporation, Japan, *Penn State University, USA. 253

III.60 Phase Transitional Behavior of the Morphotropic Phases in PZN-PT and PMN-PT Single Crystals, Y. Lu, D.-Y. Jeong, Z.-Y. Cheng, and Q.M. Zhang, Penn State University, USA. 257

Friday, September 28

Non-Pb Based Actuator Materials

III.61 Electrical Properties of Morphotropic Phase Boundary in $(Bi_{1/2}Na_{1/2})TiO_3$-$KNbO_3$ Solid Solution System, T. Takenaka, H. Nagata, and H. Ishii, Science University of Tokyo, Japan. 261

III.62 Shaped Growth of Oriented Single Crystal Rods and Fibers in the $(Bi_{1/2}Na_{1/2})_{1-x}Ba_xZr_yTi_{1-y}O_3$ (BNBZT) System, B.P. Nunes, J. Shen, A. N. Soukhojak, Y-M. Chiang, Massachusetts Institute of Technology, USA. 265

III.63 High Electrostrictive Strain Relaxors Based on Sodium Bismuth Titanate, S. A. Sheets, A. N. Soukhojak, N. Ohashi, and Y-M. Chiang, Massachusetts Institute of Technology, USA. 269

III.65 Weak Field Permittivity and High-Field Electromechanical Characterization of Ferroelectric Ceramics at Cryogenic Temperatures, C. J. Pagoda, M. L. Mulvihill*, and S. M. Pilgrim, Alfred University, USA, *Xinetics, USA. 273

Lead-Containing Actuator Materials

III.66 Cryogenic Characterization of Perovskite $Pb(Mg_{0.8}Ni_{0.2})_{1/3}Ta_{2/3}O_3$ and Tetragonal Tungsten Bronze $Ba_6FeNb_9O_{30}$ and $Ba_6CoNb_9O_{30}$ Relaxor Ferroelectrics, C. J. Pagoda, and S. M. Pilgrim, Alfred University, USA. 277

III.67 Piezoelectric Properties of Transparent $Pb(Ni_{1/3}Nb_{2/3})_{1-x-y}Zr_xTi_yO_3$ Ceramics, E. F. Alberta and A.S. Bhalla, Penn State University, USA. 281

III.68 Low-temperature Sintering of PZT with $LiBiO_2$ as a Sintering Aid, T. Hayashi and J. Tomizawa, Shonan Institute of Technology, Japan. 285

III.69 Fracture Behavior of Ferroelectric Ceramics, C. S. Lynch, Georgia Institute of Technology, USA. 289

Noon to 1:00 p.m. ***Lunch***

SESSION IV. PROCESSING

Session Chair: Tadashi Takenaka, Science University of Tokyo
Shoko Yoshikawa, Active Control eXperts, Inc./Div. of Cymer

1:00 – 2:00 p.m. ***Plenary Lectures – Novel Processing***

PIV.1 1:00 – 1:30 p.m. Texture Engineering and Enhanced Properties of Piezoelectric and Dielectric Bulk Ceramics, Toshihiko Tani, Toyota Central R & D Laboratories, Inc., Japan. 293

Friday, September 28

PIV.2 1:30 – 2:00 p.m Micropen Direct Write Fabrication of Integrated Electroceramic Devices, Duane Dimos, P. G. Clem, N. S. Bell, K. VanHeusden°, R. Parkhill*, and K. Church*, Sandia National Laboratories, USA, °Superior Micropowders, USA, *Sciperio, Inc., USA. 301

2:00 – 2:15 p.m ***Break***

2:15 – 5:00 p.m ***Poster Summaries and Poster Viewing***

Piezoelectric Devices

IV.71 Cymbal and BB Underwater Transducers and Arrays, R. E. Newnham, J. Zhang, S. Alkoy, R. Meyer, W. J. Hughes, A. C. Hladky-Herrion, J. Cochran, and D. Markey, Penn State University, USA. 305

IV.72 Design and Modeling of Porous FGM Piezoelectric Actuators, A. Almajid, M. Taya, K. Takagi*, J.-F. Li*, R. Watanabe*, *Tohoku University, Japan, University of Washington, USA. 309

IV.73 Piezoelectric Ceramic Transducers for Miniaturized Applications, A. I. Kingon, A. Gruverman, J. F. Mulling, D. J. Kim, J. P. Maria, J. A. Palmer, E. Grant, and P. Franzon, North Carolina State University, USA. 313

IV.74 Advanced Sonar Technologies for 21st Century Torpedoes, J. G. Kelly, G. T. Stevens, and F. Nussbaum*, Naval Undersea Warfare Center, USA, *ANTEON, USA. 317

IV.75 Active and Passive Structural Vibration Control using Piezoelectric Ceramics, S. Yoshikawa, and M. Giovanardi, Active Control eXperts, Inc., A Division of Cymer, USA. 319

IV.76 Large Displacement Piezoelectric Actuators Using Shear, M. T. Strauss, HME, USA. 323

Textured Piezoelectrics

IV.77 Templated Grain Growth of Textured Piezoelectric Ceramics, S. T. Kwon, E. M Sabolsky, G. L. Messing, and S. Trolier-McKinstry, Penn State University, USA. 327

IV.78 Single Crystal Ferroelectrics from Polycrystalline Precursors, A. M. Scotch, E. P. Gorzkowski, P. T. King, and D. J. Rockosi, S. Wu, M. P. Harmer, and H. M. Chan, Lehigh University, USA. 331

IV.79 Grain Orientation in BNKT-PZT Solid Solutions Made by RTGG Method, T. Kimura, and Y. Abe, Keio University, Japan. 335

IV.80 Processing and Application of Solid State Converted High Strain Undersea Transmitting Materials, K. McNeal, R. Gentilman, K. Ostreicher, and D. Fiore, Materials Systems, Inc., USA. 339

Friday, September 28

IV.81 Templated Grain Growth of Textured PMN-PT Utilizing Phase Compatible Seed Materials, P. W. Rehrig*, W. S. Hackenberger*, J. H. Adair, and T. R Shrout, Penn State University, USA, *TRS Ceramics, Inc., USA. 343

IV.82 Extruded Electroactive "Single Crystal" Fibers, M. R. Pascucci, H. B. Strock, and P. Bystricky CeraNova Corporation, USA. 347

IV.83 Textured Piezoelectric Materials Fabricated by Templated Grain Growth, M. M. Seabaugh, G. L. Cheney, K. Hasinska, A. M. Azad, S. L. Swartz, and W. J. Dawson, NexTech Materials, Ltd., USA. 351

10-minute Break

Powders and Consolidation

IV.84 Preparation of nm-sized $BaTiO_3$ Fine Particles Using a New 2-step Thermal Decomposition of Barium Titanyl Oxalates, S. Wada, M. Narahara, and H. Kakemoto, and T. Tsurumi, Tokyo Institute of Technology, Japan. 355

IV.85 A Highly Distorted Perovskite Phase in a PMN-PT Powder Synthesized via the Modified Columbite Method, H. Yamada, Cerone, Inc., USA. 359

IV.86 The Formation of PLZT from Oxides During Calcination, J. P. Dougherty, E. Breval, M. Klimkiewicz, and J. D. Weigner*, Penn State University, USA, *Lockheed Martin, USA. 363

IV.87 Synthesis of Nanosized $Pb(Zr_{0.7},Ti_{0.3})O_3$ Particles via Mechanical Activation, X. Liu and R. E. Riman, Rutgers University, USA. 367

Net Shape Forming

IV.88 Layered Manufacturing for Prototyping of Net Shape Grain Oriented Piezoelectric Materials, M. Allahverdi, K. Nonaka, and A. Safari, Rutgers University, USA. 371

IV.89 Robocast 3-3 PZT-5H – Polymer Composites, B. A Tuttle, J. E. Smay, J. Cesarano, III, M.F. Bourbina, E. L. Venturini, D. H. Zeuch, W. R. Olson, J. S. Wheeler, and J. A. Voigt, Sandia National Laboratories, USA. 375

Conductors

IV.91 Microstructure and Grain Boundary Effects on the High-field Electrical Properties of PTCR Barium Titanate, D. Cann, C. T. Chao, and R. B. Gall, Iowa State University, USA. 379

Saturday, September 29

SESSION V

Session Chair: Yukio Sakabe, Murata Manufacturing Company, Ltd.
Susan Trolier-McKinstry, Penn State University

9:00 – 11:00 a.m. ***Plenary Lectures***

PV.1 9:00 – 9:30 a.m. Integrated Passive Device Thin Film, Thick Film and Disruptive Technology for Wireless and High Speed Signal Processing Applications, Robert H. Heistand, II, J. L. Galvagni, A. P. Ritter, R. M. Kennedy III, and G. Korony, AVX Corporation, USA. 383

PV.2 9:30 – 10:00 a.m. Micromachined Capacitor Ultrasonic Transducers, B. T. Khuri-Yakub, M. Karaman, C.-H. Cheng, S. Ergun, G. Yaralioglu, B. Bayram, U. Demerci, S. Hansen, M. Badi, and O. Oralkan, Stanford University, USA. 391

PV.3 10:00 – 10:30 a.m. Recent Developments in Dielectrics and Piezoelectrics in Europe, Andrew J. Bell, Leeds University, UK. 401

PV.4 10:30 – 11:00 a.m. Three-Dimensional Analysis of Inverted Domain Structures in $LiNbO_3$ by SHG Interference Microscope, Y. Uesu, H. Shibata, and Y. Shindoh, Waseda University, Japan. 409

11:00 – 11:30 a.m. ***Break***

11:30 a.m. – 1:00 p.m. ***Farewell Lunch***

SESSION I. DIELECTRICS

Plenary Lectures – Dielectrics for RF Applications

PI.1 Multilayer Ceramic Integrated Materials Systems for Wireless, Energy, and Life Science Micro-System Applications, David L. Wilcox, Sr. and S. Dai, Motorola Laboratories, USA. 1

PI.2 Progress of Dielectric Resonator Materials for Microwave and Millimeter-Wave Applications, Hiroshi Tamura, Murata Manufacturing Company, Ltd., Japan 9

Multilayer Capacitors

I.1 Ultra-thin Ni-compatible X7R Dielectric Based on Alkoxide Derived Barium Titanate, P. Pinceloup, I. Burn, K. Albertsen, T. Ohba, and J. Roelofsma, DMC^2, USA. 15

I.2 Hydrothermal $BaTiO_3$ Based High K, Low Loss Dielectrics for Thin Active Layer BME MLCC Applications, S. Venigalla, D. L. Schultz, and J. A. Kerchner, Cabot Corporation, USA. 19

I.3 BME X7R and Y5V Dielectrics for Thin Layer MLC Applications, H. Park, D. McCauley, M. Megherhi, M. Chu, and E. Davis, Ferro Electronic Materials, USA. 23

I.4 Physical and Electrical Properties of Low Fired K-3800 X8R Dielectric, G. H. Maher and S. C. Maher, MRA Laboratories, USA. 27

I.7 Development of 100% Silver Compatible Dielectric Compositions for High Performance Discrete and Integrated Passive Component Applications, B. Foster, W. Symes, E. Davis, M. Creedon , J. Bonistall, P. Pruna, J. Burton, and S. Witter, Ferro Electronic Materials, USA. 31

Capacitors: Reliability and Diffusion

I.8 Effect of Milling Process on Core-shell Microstructure and Electrical Properties for $BaTiO_3$-based Ni-MLCC, Y. Mizuno, T. Hagiwara, H. Chazono, and H. Kishi, Taiyo Yuden Company, Ltd., Japan. 35

I.9 Reliability of Base Metal Electrode Multilayer Ceramic Capacitors, L. A. Mann, J. J. Beeson, M. S. Randall, J. L. Paulsen, and E. K. Reed, KEMET Electronics Corporation, USA. 39

I.10 Effect of Occupational Sites of Rare-earth Elements on Dielectric Properties of $BaTiO_3$, H. Kishi, N. Kohzu, H. Chazono, J. Sugino*, H. Ohsato*, and T. Okuda*, Taiyo Yuden Company, Ltd., *Nagoya Institute of Technology, Japan. 43

I.11 Cation Diffusion in Barium Titanate, J. Itoh, I. Yashima, N. Ohashi^, I. Sakaguchi^, H. Haneda^, and J. Tanaka^, Mitsui Mining & Smelting Company, Ltd., Japan, ^National Institute for Materials Science, Japan. 47

I.12 Oxygen in Diffusion and Defect Structure in Perovskite Oxides, I. Sakaguchi, H. Haneda, S. Hishita, N. Ohashi, and M. Sekita, National Institute for Materials Science, Japan. 51

Materials Development

I.13 Transmission Electron Microscopy Investigation of Bi_2O_3-ZnO-Nb_2O_5 Pyrochlore and Related Phases, J. C. Nino, I. M. Reaney*, M. T. Lanagan, and C. A. Randall, Center for Dielectric Studies, Penn State University, USA, *Dept. of Engineering Materials, University of Sheffield, U.K. 55

I.14 Bi-pyrochlore Materials for Microwave Applications, C. A. Randall, M. T. Lanagan, H. J. Youn, I. Reaney, H. Sogabe, J. Nino, A. Baker, and T. Shrout, Penn State University, USA. 59

I.15 Dielectric and Ferroelectric Properties of (Ag,Li)(Nb,Ta) Ceramics, Y. Sakabe, T. Takeda, Y. Ogiso, and N. Wada, Murata Manufacturing Company, Ltd, Japan. 63

Film Capacitors

I.16 $Ba(Ti_xZr_{1-x})O_3$ Film as Dielectric for Capacitor Applications, B-H.Tsao, S. Heidger*, and J. A. Weimer*, University of Dayton Research Institute, *Air Force Research Laboratory, Wright-Patterson Air Force Base, USA. 67

I.17 Dielectric Properties of Perovskite Superlattices Measured Using Fine Planar Electrodes, T. Tsurumi, T. Ichikawa, T. Harigai, and S. Wada, Tokyo Institute of Technology, Japan. 71

I.18 Initial Results for MOCVD (Ba,Sr)TiO_3 Thin Film Capacitors on Metal Foils, D. Y. Kaufman*, S. K. Streiffer^, J. Im^†, S. Saha^, O. Auciello^, and R. Erck*, Argonne National Laboratory; *Energy Techology Division, ^Materials Science Division, †now of Agere Systems, USA. 75

High Frequency and Tunable Dielectrics

I.19 Measurement of Dielectric Properties of $BaTiO_3$-Based Materials in the 10 MHz to 1GHz Frequency Range, C. Nies, E. Deyneka, and M. T. Lanagan*, AVX Corporation, USA, *Penn State University, USA. 79

I.20 Microwave Properties of Dielectric Oxide and High T_c Superconductor System, S. Sugihara, T. Kawashima, C. Ishizuka, and N. Kimura, Shonan Institute of Technology, Japan. 83

I.21 Double-Layer Type Microwave Absorber Made of Magnetic-Dielectric Composite Material, M. Saitoh, T. Yamamoto, H. (Okino) Niori, M. Chino, and M. Kobayashi*, National Defense Academy, *Tayca Company, Japan. 87

I.22 Progress in $BaTiO_3$ Thin Films: High Frequency Applications and Property Investigations, J-P. Maria, C. B. Parker, F. Ayguavives, A. Tombak, G. Stauf*, A. Mortazawi, and A. I. Kingon, North Carolina State University, USA, *ATMI Corporation, USA. 91

I.23 Application of Ferroelectrics in Microwave Phased-Array Antennas, J. B. L. Rao, D. P. Patel, P. K. Park*, T. K. Dougherty*, J. A. Zelik*, A. Moffat^, and L. C. Sengupta^+, Naval Research Laboratory, *Raytheon Systems Company, ^SFA, Inc., and ^+Paratek Microwave, Inc., USA. 95

I.24 Field Dependence of Dielectric Properties of (Pb,Sr)TiO_3 Thin Films, M. Adachi, K. Tsu, and T. Karaki, Toyama Prefectural University, Japan. 99

Multilayer Ceramic Integrated Materials System for Wireless, Energy and Life Science Micro-System Applications

David L. Wilcox, Sr. and Steve Dai
Ceramic Technologies Research Laboratory, Motorola Labs, 7700 South River Parkway, Tempe, AZ 85284
Fax: (480) 755 5350
Email: david.wilcox@motorola.com

INTRODUCTION

The increase in functionality in mobile phones and other portable wireless devices is driving the need for new technologies to integrate circuit functions and reduce the need for circuit assembly using discrete components. The low temperature co-fired (LTCC) laminated multilayer ceramics (MLC) process is emerging as a powerful component integration technology, especially for the radio frequency portion of these portable devices. And with the number of these devices being manufactured each year approaching 0.5 billion, economics of scale are having a positive impact on the development of the low temperature cofired ceramics (LTCC) infrastructure and the cost of designing with this MLC technology.

This paper discusses the important dielectric properties for these radio frequency (RF) applications and highlights the development of a LTCC dielectric with properties tailored for the RF applications in the consumer market. The development of co-fireable capacitor materials and experience with commercially available resistors will be presented. Challenges of co-firing important metal systems will also be addressed.

As the cost of designing devices with this technology decreases, other applications for this 3D integration technology are beginning to emerge. Technologies are being developed that enable the formation of internal microchannels and cavities making it possible to integrate microfluidic functions in addition to the electronic functions. These microfluidic capabilities open up many new microsystem opportunities, for example: miniature fuel cells, biotechnology analytical devices and other microreactor device applications. Examples of these devices will be described and advanced materials integration challenges and opportunities will be highlighted.

CERAMIC MICRO-SYSTEMS

Micro-systems technologies (MST) are emerging, characterized by the intelligent miniaturized monolithic and/or hybrid integrated systems comprising sensing, data processing, communication and/or actuating devices utilizing two or more of the following technologies: electronic, mechatronic, microfluidic, thermonic, and photonic. Integration of these multifunctions will require a rich pallet of 3 dimensional (3D) fabrication technologies involving ceramics, glass, plastics and semiconductor (e.g. Si) materials. Advances in these microsystem technologies are creating new unique miniaturized benchtop and portable multifunction appliances: 1)wireless – multiband and multimode phones requiring more components; 2)micro-scale energy sources for portable appliances; 3)emerging life science fluidic based devices, and 4). "Lab on a chip" and micro-reactor; etc. Fig. 1 highlights the rich pallet of technologies and devices that are forming the foundation of this emerging MicroSystems thrust.

Fig.1. Overview of microsystems technologies.

Much as the 40+ year old silicon semiconductor electronics based technology is "morphing" into a significant micro-electro-mechanical (Si-MEMS) MST technology, the "mature" multilayer ceramic technology is emerging from its component (multilayer ceramic capacitors) and multilayer interconnect "packaging" applications to take on additional functionality as a 3D microsystem integration technology...some refer to this advancement as Ceramic MEMS. In particular, the LTCC technology has demonstrated great potential of

integrating (embedded and/or hybrid) multiple functions. Other advantages of multiplayer LTCC include fast prototyping, high performance, high reliability, light weight, and a cost structure that is approaching printed circuit board (PCB), shown in Fig. 2.

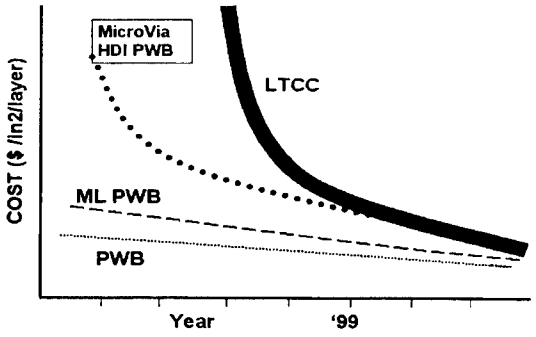

Fig. 2. Pricing trends for green sheet host dielectric layers[1].

Fig.3 shows typical process flow of LTCC. The "parallel" process versus, for example, the sequential semiconductor processing character of the multilayer ceramic technology is a key factor in its ability to achieve true 3D multilayer functional structures. In the parallel process, it is possible to inspect each "green" or unfired layer prior to the lamination enabling high yields with a many layered structure. Multilayer ceramic interconnect packages with more than 30 layers have been in manufacturing since 1979[2] and this application might be viewed as an early level of ceramic based MST integration.

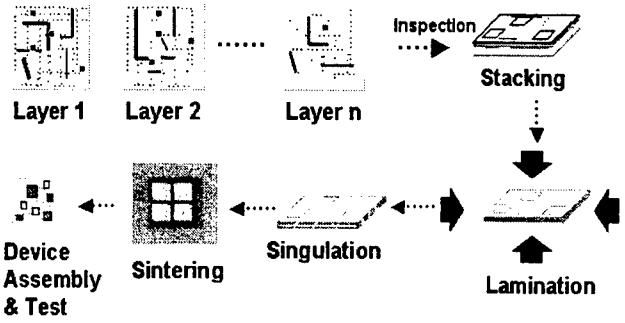

Fig.3. MLC Process Schematic

MLC MICROSYSTEM EXAMPLES

Following is a review of several examples of microsystems and devices that have been demonstrated that are showing the potential for this 3D multilayer ceramic integration technology to create microsystems incorporating the electronic, microfluidic, thermonic, photonic and mechatronic functions on a microscale.

RF Receiver Front-end for Cell Phone

Probably one of the first advances in electronic functionality of the multilayer ceramic technology beyond the interconnect role has been within the wireless industry where the technology has been used to integrate radio frequency (RF) functions. In this application, the ability to embed RF functions requiring low electrical losses, such as filtering, has been enhanced with the availability of unique ceramic materials properties and the cost effective 3D multilayer integration capability. Fig. 4 displays such a device that has integrated internally and on the surface, 41 components achieving a component density of about 40 per square centimeter. Note the ability of the technology to "package" those devices that are not integrateable, eliminating the need for additional packaging, providing further opportunity to reduce size, weight and cost. This is just one of many RF devices being enabled with this technology. Bluetooth modules being a recent application receiving serious attention. As noted earlier, these high volume applications are having a significant impact on the materials costs associated with the technology

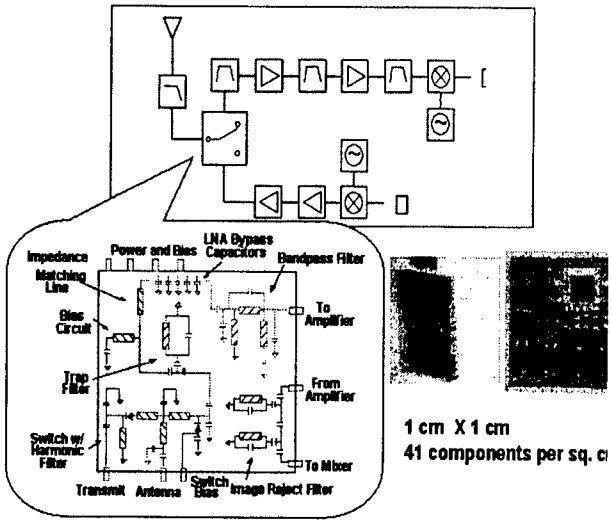

Fig. 4. RF Receiver Front End for Cell Phone

Methanol-Hydrogen Micro-Reformer

Building on these advances, recently, the ability to insert microchannels within the three dimensional multilayer ceramic structures is enabling applications associated with microscale

fuel cells and microfluidic applications associated with life science bio-devices.

Fig. 5 shows a methanol microreactor to convert methanol to H_2 as an energy source for a microscale fuel cell. Shown in the figure is a 3D multilayer ceramic monolithic prototype with the internal structure exposed to display the embedded fluid channels, microreactor cavaties, temperature sensors, heaters and catalyst. Figure 6 shows the some early results of the hydrogen formed from this micro-reactor.

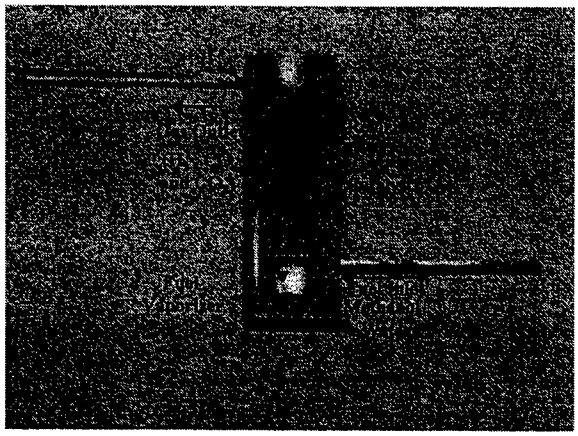

Fig. 5 Methanol-Hydrogen Micro-Reformer

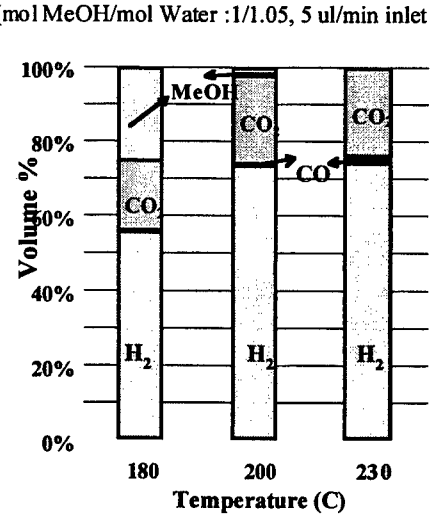

>90% MeOH Conversion @ 200C

Fig. 6 Vol% of H_2, CO_2, CO and MeOH from reactor at 180, 200 and 230 °C.

Embedded MLC Plasma Light Source

An example of a photonic element with potential to integrate this function in a microsystem is shown in Fig. 7. Displayed is a microplasma source with potential to be an integrated UV light source for fluorescing biomolecules, an element of an integrateable optical detection system. Fig. 8 shows an emission spectra from such a device, developed in collaboration with B. Vojak, et. al. at the University of Illinois[3].

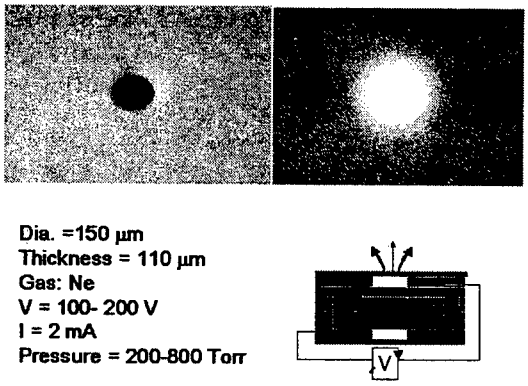

Fig. 7 Embedded Multilayer ceramic plasma light source.

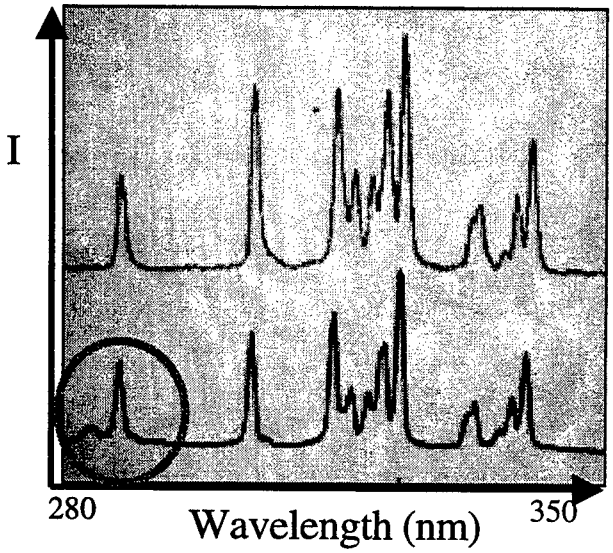

Fig. 8 Emission spectra from the ceramic micro plasma light source.

CERAMIC MICROSYSTEMS MATERIALS DEVELOPMENT AND SYSTEM INTEGRATION

Advances in the ceramic microsystems functionality are paced by the advances in the materials and fabrication technologies needed to create new functionalites, just as is the case for the semiconductor industry. For wireless communication applications, the need for host dielectrics with appropriate RF characteristics with a pallet of integrateable (embeddable) conductors, resistors, capacitors and magnetic

materials is enabling an increase in functionality of these MLC monoliths. For the integration of radio frequency (RF) functionality, the MLC host dielectric must provide low signal loss and temperature stability with the ability to integrate high conductivity metal conductors as well the materials elements to provide embedded capacitors and resistors mentioned above. These requirements drove the development of a LTCC host dielectric with low losses and a low temperature coefficient of resonant frequency (T_f), that would be able to integrate a pallet of high conductivity metals and other materials permitting the integration of the RF functions. We will highlight some examples of advances made in materials systems for RF applications and identify some opportunities for future materials and fabrication advances that will advance the integration of other functions within ceramic–MEMS/MST monoliths.

T2000 LTCC RF Host Dielectric

This RF host dielectric was developed employing a glass-ceramic material system. The system includes a specially developed lead-free glass, a ceramic filler (Al_2O_3) and a T_f adjustment material. Based upon the fact that the glass is the Q limiting phase at high frequency in the sintered dielectric, this dielectric was designed to have a minimum amount of glass after sintering. The approach was to form a glass that first helps densification of the dielectric and later reacts with Al_2O_3 to form high Q crystalline phases in a self-limiting process. For sintered T2000 the dielectric constant K is ~ 9.1 with Q>1000 at 0.5 GHz.

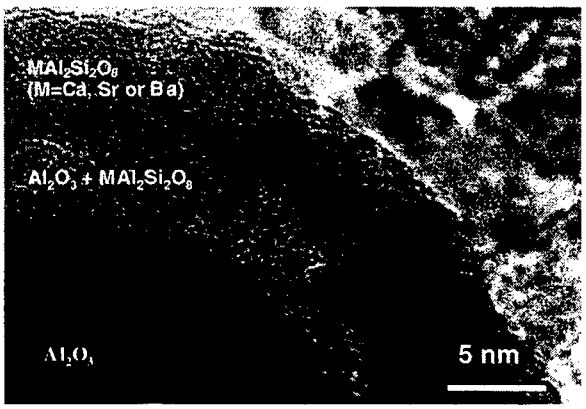

Fig. 9 HRTEM of an Al_2O_3 particle showing diffusion layer crystalline phases.

Fig. 9 is a high resolution transmission electron microscopic (HRTEM) image of the dielectric. It is clearly seen that during sintering the Al_2O_3 particles dissolved into glass and form the desired crystalline phases both at the Al_2O_3 - glass interface and within the glass matrix. Details on the chemistry of the T2000 dielectric was published elsewhere [4].

Fig. 10 shows the change of resonant frequency of a microstrip over temperature for T2000 dielectric formulations prepared with and without TiO_2. The dielectric has a T_f around –80 ppm/°C without the addition of TiO_2. The TiO_2 modified dielectric shows a T_f close to zero near 25 °C. T_f over the temperature range –40~80 °C is 4.2 ppm/°C. The T_f of T2000 can be continuously adjusted over a wide range with increasing TiO_2 content. It was also demonstrated [5] that the TiO_2 dissolved into the glass during sintering and formed Ti-rich-plate-like crystalline phases via a nucleation and growth mechanism. It is noted that this process makes the T_f modification more efficient than would be predicted by a simple mixing of TiO_2 into the composition, a phenomena not clearly understood.

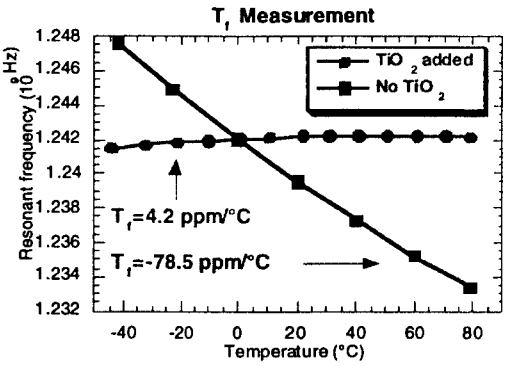

Fig. 10 Change of Resonant Frequency with and without TiO_2 Addition.

High K Dielectric for Integrated Capacitors

To expand the ability to integrate higher value capacitor elements within the ceramic microsystem, the Bi-Zn-Nb-O (BZN) pyrochlore phase based dielectrics[6] have been developed to form internal capacitors in T2000 dielectric. The BZN phases, glass additives, and particle size were key parameters in assuring cofireability of BZN with T2000 and the associated metal systems. Results of these studies were presented at the IMAPS 2001 conference [7].

The dielectric constant K and loss factor Q of BZN with appropriate sintering additives at a frequency range 10 kHz to 4 GHz are summarized in Table 1. K is typically 80 ~ 100 at RF frequencies. Temperature response of the formulated composition is of NPO capacitor characteristics.

Table 1. Dielectric properties of BZN dielectrics as a function of frequency

Freq (Hz)	K	Q	Sample type	Test method
10 K	~110	10000	tape	LCR
1 M	~106		Embedded	LCR
0.5 G	~98	~500	pellet	Boonton
2.5 G	~98	<200	tape	Split-poster
4 G	~81	~87	pellet	Haaki-coleman

Table 2 lists capacitance and variation of the embedded capacitors from size 0.75x0.75 to 1.5x1.5 mm with printed BZN based paste dielectric. Each size has a 12x12 array with a total of 144 capacitors. The estimated dielectric K was calculated from the sintered thickness of dielectric, which was ~ 20 μm from SEM cross-section measurement. Overall the embedded capacitor showed relatively good tolerance with σ in a range 3~4%.

Table 2. Average capacitance and standard deviation of the internal capacitors

Capacitor Size (mm)	Cap. (pF)	σ (%)	Estimated K
0.75x0.75	26.4	4.1	106
1.0x1.0	42.8	3.1	97
1.25x1.25	66.2	4.0	96
1.5x1.5	93.4	3.3	94

Commercial Resistor Evaluation

RuO_2 based resistor pastes from several commercial sources were tested in T2000 dielectric. Test criteria included shrinkage mismatch, interaction with T2000, resistor value and variation. Fig. 11 shows cross section of an embedded resistor that has the best fit to T2000. The resistor layer was sintered to high density. However excessive voids are seen along the interface, indicating possible reactions between the two materials.

Resistance should scale to the inverse of the thickness of the embedded resistor assuming no reaction, $R \sim 1/t$, where t is the thickness. The actual resistor can be modeled as $R \sim 1/(t-t_o)$, where t_o is the effective thickness of the reaction layer. Fig. 12 plots the resistance of a cofired 1 kΩ/sq paste as a function of thickness of the resistor layer. The t_o is estimated ~ 11 μm from curve fitting.

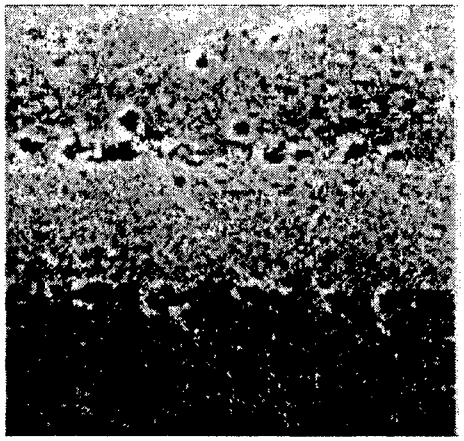

Fig 11. Embedded resistor in T2000 dielectric.

It also seen from Fig. 12 that the embedded resistors hit the 1 kΩ/sq targeted value at a thickness of 25 to 30 μm. In a study to evaluate a 16x16 array of embedded resistors using 1 kΩ/sq paste, an average value of 1026 Ω with standard deviation σ ~ 15.5% were achieved. Measurement on the same resistor set showed average thickness of 25 μm with a σ ~ 8.6%.

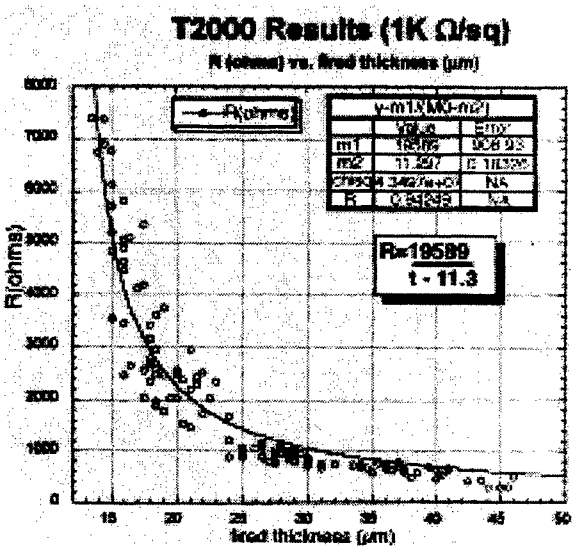

Fig 12. Resistance of a cofired 1 kΩ/sq paste as a function of thickness of the resistor layer.

LTCC Cofireable Conductors Ag and Ag/Pd

The requirements for the conductor pastes for RF applications are good screen printing quality and the ability to be co-fired with tape systems at 850-900 °C without camber or cracking problems. The materials must exhibit high conductivity (high metal Q) and the ability to be soldered when serving as an external metallization.

Good shrinkage match between the conductor paste and the tape dielectric is critical for the minimization/elimination of chamber/warping during the sintering operation. As an example of the materials issues that must be controlled, it is known that the shrinkage mismatch may be more pronounced for Ag/Pd used for surface metallization due to the oxidation/reduction of Pd during sintering[8]. Fig. 13 shows the XY shrinkage curves of T2000 dielectric tape and a Ag/Pd (designed for good solder leaching performance and reduced Ag migration) formulation formed of an alloy of Ag and Pd powder and a Ag/Pd paste formed of a mixture of Ag and Pd powders (data courtesy Dr. T. Garino, Sandia National Laboratories, Albuquerque, NM). The conductor pastes were printed on mylar and then peeled off for test after drying. The shrinkage was measured in situ via an optical system. Clearly, the influence Pd oxidation may have on the shrinkage behavior of the metal system is strongly controlled by the form it takes in the paste.

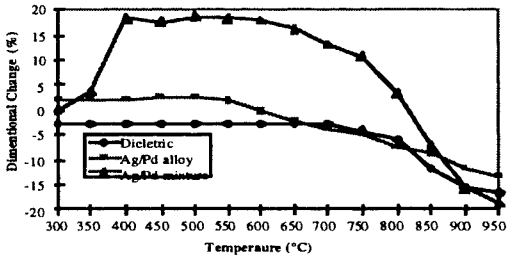

Fig. 13. Shrinkage of dielectric, Ag/Pd alloy and Ag/Pd mixture as a function of temperature.

Adhesion of the surface metallization is important. Pull test results exceeding 25 lbs are considered adequate for most lead attachment and device attachment applications. Table 3 summarized a typical stud pull test. Ag-B and Ag/Pd-A are commercially available cofired formulations. Ag-M is a specially formulated improved conductivity paste[9] with adhesion promoters for use in the tape dielectric. It is used as co-firable internal and external metallizations with good solder wetting characteristic.

Table 3, Adhesion forces of several Ag and Ag/Pd conductors on the dielectric, σ is the standard deviation.

	Ag - M	Ag - B	Ag/Pd - A
f (lb)	29.1	28.9	26.5
σ	2.3	3.5	4.2

CHALLENGES AND OPPORTUNITIES

The above material development targeted primarily wireless applications. Other materials issues are being addressed for applications like energy and life sciences. Multi-functionality of a ceramic based microsystem is ultimately reflected in the variety of materials with desired properties that may be integrated into the substrate. Equally important is the integration fabrication processes. Beyond the materials and processes, a significant develpment on the infrastructure of multi layer ceramic technologies is required to advance the MST.

Materials and Process Opportunities

Magnetic materials: Magnetic functions like high value inductors, generation of magnetic field and even magneto-actuation are desirable in many applications. To form high permeability cofireable ferrites, both in tape and paste forms, is one of the approaches. Although there are activities in developing such materials for specific applications in some areas, there is no standard material offered by major LTCC material suppliers.

Mechanical functions: Materials that could provide mechanical actuation, such as piezoelectric, electrostrictive, magnetostrictive, etc, will certainly elevate the capability of CMEMS to a next level. Microfluidic management and RF switches for wireless integrated modules are the two applications.

Chemically active functions: These materials could sense parameters such as humidity and gas species, as well as act as chemical catalysts in micro reactors and provide hydrophobic/hydrophilic surfaces.

Other desireable materials: Various cofireable metal and cermet systems will serve to provide electrical, resistive and thermally conductive paths for electronic and thermonic functions.

LTCC processes: With increasing level of integration, feature size shrinking from current 75- 100 μm to 1 – 10 μm will be important. Methods in traditional thin film processes have been explored to achieve these goals. For devices handling micro fluids, rapid and precise internal channel forming and processes that insure the integrity of the features are essential.

Infrastructure for MLC Technology

Beyond the multilayer ceramic microsystems device fabrication and design challenges there is the need to develop a strong industry infrastructure. For the wireless application, there is a plethora of LTCC

materials systems made up of host dielectrics and cofireable thick film materials to serve as capacitors, resistors and electrical interconnects, all requiring unique design rules for similar applications. Achieving appropriate standardized materials systems for the various market segments will be important to bring down costs and accelerate the application development which in turn will encourage a robust manufacturing/foundry infrastructure. Such has been the case for FR4 "standards" for multilayer organic wiring boards, alumina substrates for the hybrid circuit industry and Si for the semiconductor industry.

SUMMARY

There are tremendous opportunities in wireless, energy, life sciences and auto applications for ceramic based microsystems. Yet the opportunities represent great challenges for material and process technologists for system integration. Collaborative efforts between industry, universities and national laboratories to cover materials, processes, systems and applications and the establishment of standards will be needed to accelerate the CMEMS potential.

REFERENCES

1. Presentations by DuPont and Heraeus at the 13th International Electronics and Packaging Conference, Strasbourg, FR, May 30 – June 1, 2001.
2. A. J. Blodgett, Jr., "Microelectronics Packaging", Scientific American 249, no. 1, pp 89-96, (July 1983).
3. B.A. Vojak, S.J. Park, C.J. Wagner, J.G. Eden, R. Koripella, J. Burdon, F. Zenhausern and D. L. Wilcox, "Multistage, monolithic ceramic microdischarge device having an active length of 0.27 mm", Appl. Phy. Lett., Vol. 78, No. 10, pp1340-42, 2001.
4. S. Dai, R. F. Huang and D. Wilcox, "Temperature stable, low loss and low fire dielectric for consumer wireless applications", the 1st China International Conference on High Performance Ceramics, Oct. 31- Nov. 3, 1998, Beijing, China.
5. S. Dai, R. F. Huang and D. Wilcox, "Use of Titanates to achieve a temperature stable LTCC dielectric for wireless applications", American Ceramic Society Annual Meeting, St Louis, Apr 24-27, 2000.
6. D.P. Cann, C. A. Randall and T. R. Shrouts, Solid State Communications, Vol. 100, No. 7, pp529-534, 1996.
7. W. Zhang, J. T. Hochheimer, C. Modes, P. Barnwell and S. Dai, "Higher K low loss dielectric ceramic cofireable with a commercial LTCC tape system", IMAPS 2001, Baltimore, USA.
8. "Silver-Palladium Thick-Film Conductors", S. F. Wang, J. P. Dougherty, W. Huebner and J. G. Pepin, J. Amer. Ceram. Soc., 77[12], 3051-72 (1994).
9. J. Lombard and R.F. Huang, "High Adhesion, Solderable, Metallization Materials" U.S. patent # 5431718; July (1995).

Progress of Dielectric Resonator Materials for Microwave and Millimeter-Wave Applications

Hiroshi Tamura

Development Department II, Materials Division, Murata Manufacturing Co., Ltd.
Yasu-gun, Shiga 520-2393, Japan
FAX: +81-77-586-8523
E-mail: tamura@murata.co.jp

INTRODUCTION

Since the 1970's, dielectric resonator materials have been developed and put into practical use for filters and oscillators in microwave frequency, miniaturizing these components and saving costs [1-4]. The telecommunication systems are now expanding to higher frequency and to broader-band, and the new applications at millimeter-wave frequency are now up-and-coming for such as the Intelligent Transport System and the Wireless LAN. These new applications demand the lower dielectric loss of the dielectric resonator materials.

This paper reports the origins of dielectric loss tangent at microwave and millimeter-wave frequency. The dielectric materials suitable for the applications such as the duplexer for W-CDMA portable phones, the filters for cellular base stations with thick film high temperature superconductor, and the millimeter-wave applications are introduced with their dielectric properties.

PROPERTIES OF DIELECTRIC RESONATOR MATERIALS

Dielectric resonator materials

Table 1 shows the property of practical dielectric resonator materials. Notation εr is the dielectric constant, Q is the quality factor; Q=1/ tanδ, and τ_f is the temperature coefficient of resonant frequency. As the tanδ is proportional to frequency at microwave and millimeter-wave frequencies, the product of Q and frequency, Q×f, is often used as the material constant.

Dielectric resonator materials are required to have low dielectric loss tangent and zero-ppm temperature coefficient of resonant frequency.

Frequency dependence of tanδ

Dielectric resonator materials are generally made of the paraelectric dielectric ceramics. Their complex permittivity reasonably follows the classical dielectric dispersion equation, which is expressed as the superposition of the ionic and electronic polarization.

$$\dot{\varepsilon}(\omega) - \varepsilon(\infty) = \frac{\omega_T^2(\varepsilon(0) - \varepsilon(\infty))}{\omega_T^2 - \omega^2 - j\gamma\omega} \qquad (1)$$

Where $\dot{\varepsilon}(\omega)$ is the complex permittivity at an angular frequency ω, $\varepsilon(\infty)$ is the permittivity by the electronic polarization, ω_T and γ are the resonance frequency and damping constant of the infrared active lattice vibration modes.

At microwave and millimeter wave frequencies, following equations are derived from eq. (1) under the condition $\omega^2 << \omega_T^2$.

$$\varepsilon'(\omega) - \omega(\infty) = \varepsilon(0) - \varepsilon(\infty) \qquad (2)$$

$$\tan\delta = \frac{\varepsilon''(\omega)}{\varepsilon'(\omega)} = \frac{\gamma}{\omega_T^2}\omega \qquad (3)$$

Table 1. Property of dielectric resonator materials.

Materials	εr	Q×f (GHz)	τ_f (ppm/℃)
$MgTiO_3$-$CaTiO_3$	21	56,000	0 - 6
$Ba(Sn,Mg,Ta)O_3$	24	240,000	0 - 6
$Ba(Mg,Ta,Sb)O_3$	24	360,000	0 - 6
$Ba(Zr,Zn,Ta)O_3$	30	180,000	0 - 6
$Ba(Co,Zn,Nb)O_3$	34	130,000	0 - 6
$Ba_2Ti_9O_{20}$	38	55,000	4
$(Zr,Sn)TiO_4$	38	60,000	0 - 6
$CaTiO_3$-$NdAlO_3$	43	47,000	0 - 6
$Ba(Sm,Nd)_2Ti_4O_{12}$	80	10,000	0 - 6
$(Ba,Pb)Nd_2Ti_4O_{12}$	92	5,000	0 - 6
$(Ba,Pb)(Nd,Bi)_2Ti_4O_{12}$	110	2,500	0 - 6

These equations show that the dielectric constant is independent of frequency and the dielectric loss tangent increases proportionately to frequency. Many experimental results assist the correctness of these equations in the microwave and millimeter-wave frequency range.

Figure 1 shows the measurement result of tanδ from 1 to 35 GHz. These properties were measured by the dielectric resonator method from 1 to 10 GHz [5] and by the $TE_{01\delta}$ mode cavity method using NRD guide from 10 to 35 GHz [6]. As expected from eq. (3), tanδ increases proportionately to frequency.

Origins of dielectric loss tangent

Equation (3) shows that the tanδ is determined by the damping constant γ. If the dielectric resonators were made of the defect-free perfect crystal, the damping constant would be given by the anharmonic terms in the crystal's potential energy [7].

Practical dielectric ceramics, however, have many lattice defects such as the grain boundaries, pores, and impurities in the crystal grain. These lattice defects are the second origin that increases tanδ. Among these defects, most serious one is the substitutional ions that derive the disorder in the periodic charge arrangement in the mother crystal.

Schlömann reported that the random distribution of the deviated charges increases the tanδ at microwave frequency [8].

Figure 2 shows the experimental result that investigated the effect of oxygen vacancy and acceptor ion on the tanδ of $(Zr,Sn)TiO_4$ ceramic [9].

The monitor in the figure represents the specimen prepared to have the minimum lattice defects, and has the lowest tanδ among three specimens.

In the specimen annealing in a reduced atmosphere, the oxygen vacancies increased by 1000 ppm compared with the monitor specimen. One oxygen vacancy creates the deviated charge of +2 eV in a unit cell of $(Zr,Sn)TiO_4$ crystal, and the 1000 ppm oxygen vacancies increased the tanδ by about 0.2×10^{-4}.

The doping of 13,000 ppm Fe ions increased the tanδ drastically. A trivalent Fe ion creates the deviated charge of −1 eV by substituting a tetravalent cation. It is also assumed that the oxygen vacancies are generated in the crystal at the same time with the substitution of Fe ions into tetravalent cations. Thus, the Fe ion and oxygen vacancy, which have the deviated charge of −1 eV and +2 eV, respectively, derive unnecessary dipole moments and increase the tanδ drastically.

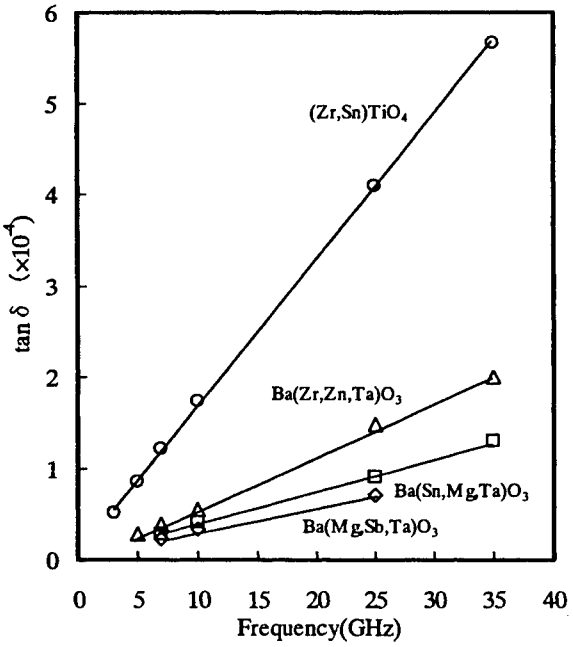

Fig.1. Frequency dependence of tanδ from 1 to 35 GHz.

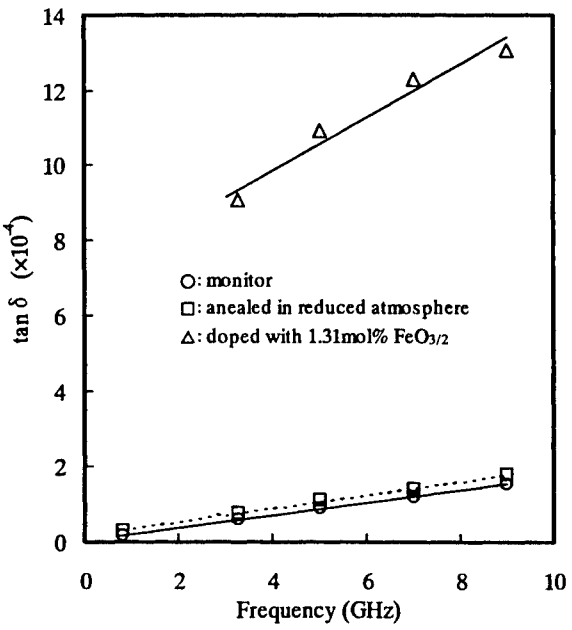

Fig.2. Effect of oxygen vacancies and Fe ions on tanδ of $(Zr,Sn)TiO_4$ ceramics.

Temperature dependence of tanδ

The temperature coefficient of resonant frequency is defined by the following equation.

$$\tau_f = -\frac{1}{2}\tau_\varepsilon - \alpha \qquad (4)$$

where τ_ε is the temperature coefficient of dielectric constant and α is the linear thermal expansion coefficient of the dielectric resonator.

Figure 3 shows the temperature dependence of resonance frequency around room temperature. Good temperature stability of resonant frequency is obtained by selecting the composition of the material.

Figure 4 shows the temperature dependence of tanδ from 20 to 300 K, which shows that the tanδ increases proportionately to temperature except for some exceptional materials.

The damping constant γ in eq. (3) is the function of anharmonic terms in the crystal's potential energy. The anharmonic terms allow the transfer of the phonon energy from infrared active modes into the other modes. Maradudin and Fein derived the equation of the temperature dependence of γ from the third anharmonic term ϕ_3 of the crystal's Hamiltonian [7].

$$\gamma \propto |\phi_3|^2 \times T \qquad (5)$$

This equation shows that the tanδ increases proportionately to temperature. The abnormal increase of tanδ occurs at the phase transition temperature or at low temperature due to the impurities such as the magnetized ions.

APPLICATIONS

Resonant mode of dielectric resonator

Figure 5 shows the most commonly utilized three dominant modes for dielectric resonators. The TEM mode dielectric resonator is characterized by a guided mode field distribution of a TEM mode with standing wave of a quarter wavelength. This mode causes significant size-reduction effect.

The TE01δ mode dielectric resonator is characterized by a dominant TE mode field distribution, the field of which leaks in the direction of wave propagation. A High unloaded quality factor can be achieved using this mode.

The TM010 mode dielectric resonator is characterized by a TM mode field distribution. This mode gives the middle level of unloaded Q and size reduction effect between the TE01δ and TEM mode resonators.

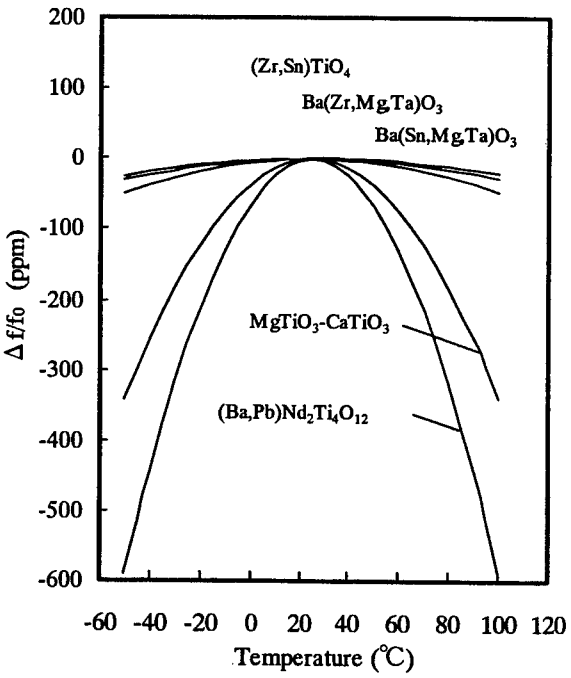

Fig.3. Temperature dependence of resonant frequency around room temperature.

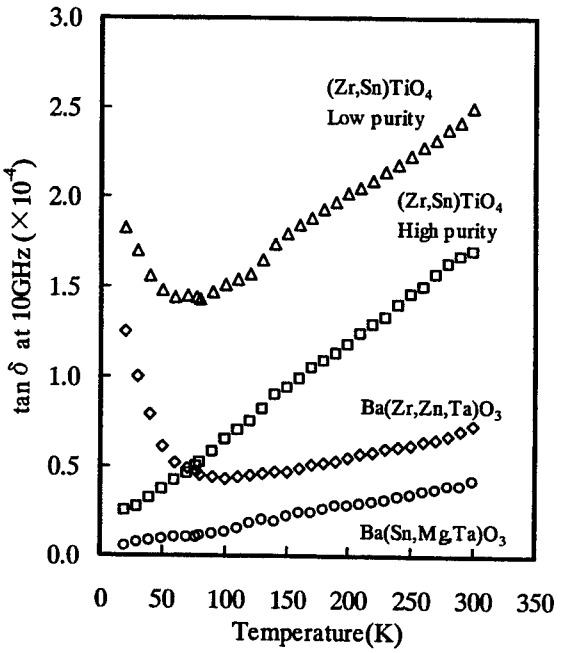

Fig.4. Temperature dependence of tanδ from 20 to 300 K.

Antenna duplexer for portable phone

Figure 6 shows the example of an antenna duplexer for portable phones. The quarter-wavelength TEM mode resonator is used for miniaturizing this duplexer.

The $BaNd_2Ti_4O_{12}$ based materials with ε r of 90 have been popularly used for the 900 MHz band antenna duplexer. But, the higher unloaded Q is needed for the new mobile phone system such as the Wideband-CDMA system at 2 GHz band.

Figure 7 shows the calculation result of unloaded Q for dielectric resonators with ε r of 20, 40 and 90, which were calculated under the conditions that the resonator has the outer diameter of 3 mm and the conductivity of the shielding conductor is 4.8×10^{-7} [$\Omega^{-1}cm^{-1}$].

The figure shows that the resonator with lower ε r has higher unloaded Q due to the longer length of the resonator.

The materials with ε r around 40 are suitable for the antenna duplexer of W-CDMA system. The miniaturized duplexer with the dimension of $12.6\times5.3\times1.9$ mm^3 are developed for this application with the low insertion loss of 1.5 and 2.4 dB in the Tx and Rx pass-band, respectively.

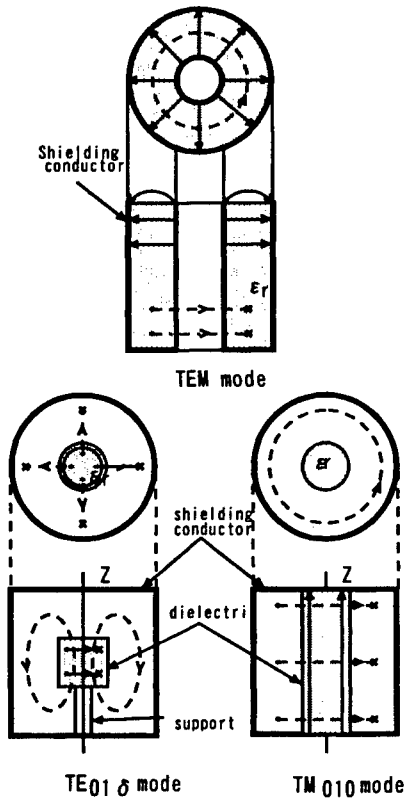

Fig.5. Three dominant modes for dielectric resonator.

Filter for cellular base station

For the high-power applications such as the channel filter and duplexer of cellular base stations, dielectric resonator material must have the low tanδ and the low third intermodulation distortion level to prevent the heat generation and the interference between signals.

The channel filter for cellular base stations generally needs the Q values higher than 50,000 at the operating frequency. The $(Zr,Sn)TiO_4$ and $CaTiO_3$-$NdAlO_3$ materials meet this condition at900 MHz, and the $Ba(Zn,Ta)O_3$ or $Ba(Zn,Nb)O_3$ meet the application at 2 GHz: their Q×f products are higher than 100, 000 GHz.

Figure 8 shows the measurement result of the third intermodulation distortion level at 800 MHz [10]. The distortion level of $(Zr,Sn)TiO_4$ material is −140 dBc at a field intensity of 60 V/mm, which is applicable to the filters of cellular base stations with an maximum input power of 500 Watts.

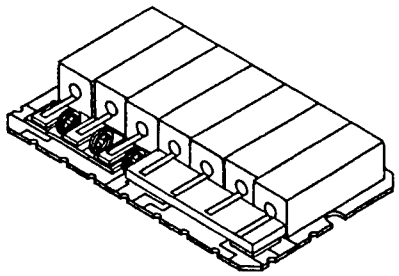

Fig.6. Antenna duplexer using TEM mode dielectric resonators.

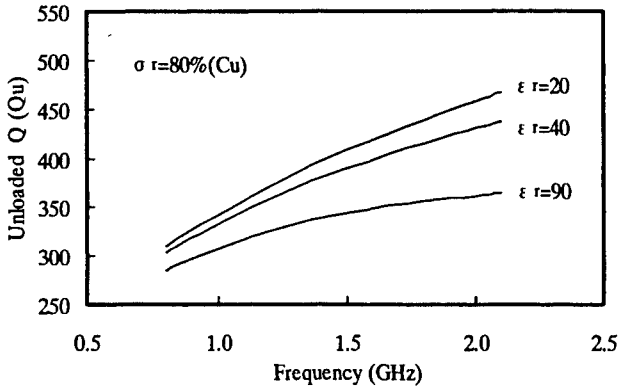

Fig.7. Unloaded Q of $\lambda/4$ TEM mode dielectric resonator with ε r of 20, 40 and 90.

Figure 9 shows an example of the antenna duplexer using the TM_{110} dual-mode dielectric resonators [11]. The TM mode dielectric resonator is suitable for the high power application due to the structure that aids in the release of heat. Dual mode resonators minimize the valume of the filter to 1/2.

Filter for cellular base stations with thick film high-temperature super conductor

The Filter for cellular base stations is one of the most expecting applications for high-temperature superconductor (HTS). For this applications, the microstripline filter made of the $YBa_2Cu_3O_{7-\delta}$ thin film on $LaAlO_3$ substrate and the TEM or TM mode dielectric resonator filter made of the $(Bi,Pb)_2Sr_2Ca_2Cu_3O_x$ thick film on $Ba(Sn,Mg,Ta)O_3$ resonator are proposed.

As Fig. 4 shows, the $Ba(Sn,Mg,Ta)O_3$ material has the extremely high $Q \times f$ value of 1,000,000 GHz at 70K and is a promising candidate for low-temperature application [12]. Figure 10 shows the configuration of the TM_{010} mode $Ba(Sn,Mg,Ta)O_3$ dielectric resonator on which the HTS thick film is fired.

Figure 11 shows the temperature dependence of unloaded Q of TM_{010} mode $Ba(Sn,Mg,Ta)O_3$ dielectric resonator with Bi2223 thick film and with conventional silver electrode. The unloaded Q increase drastically from 4,500 of silver electrode up to 30,000 of Bi2223 thick film at 70 K and at 2 GHz [13].

The surface resistance of this Bi2223 thick film is calculated to be 0.8 mΩ at 70 K and at 2 GHz, which is not sufficiently high for the application of cellular base stations. More improvement is needed.

Filter for millimeter-wave application

New applications such as the Intelligent Transport System and the Wireless-LAN are expected at millimeter-wave frequencies. The dielectric resonator material must have very high Q value for these applications. The first candidate for this application is the $Ba(Mg,Ta)O_3$ material.

Figure 12 shows the filters with the center frequency of 26 GHz and 60 GHz. The TE_{010} mode dielectric resonators were constructed using the poreless $Ba(Sn,Mg,Ta)O_3$ substrate, which has the Q value of 13,500 at 26 GHz and 5,900 at 60 GHz. Their dimensions are miniaturized to $10 \times 20 \times 4$ mm^3 for 26 GHz filter and $7 \times 7 \times 1.5$ mm^3 for 60 GHz filter [14].

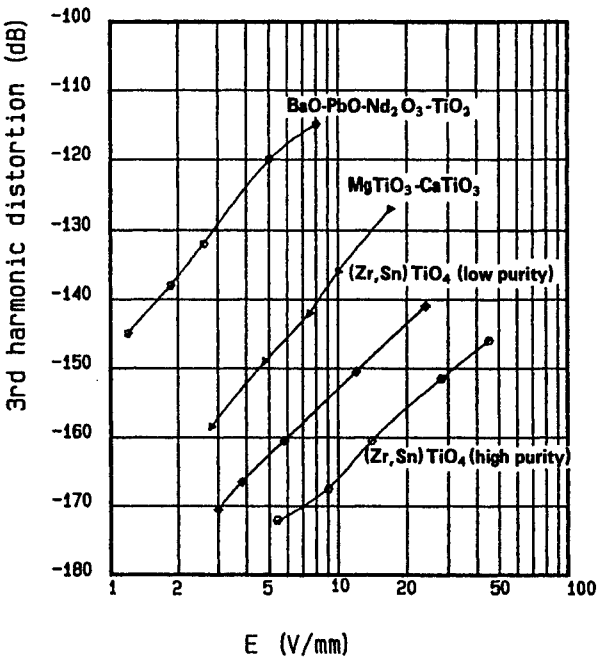

Fig.8. Third intermodulation distortion level of dielectric resonator materials at 800 MHz.

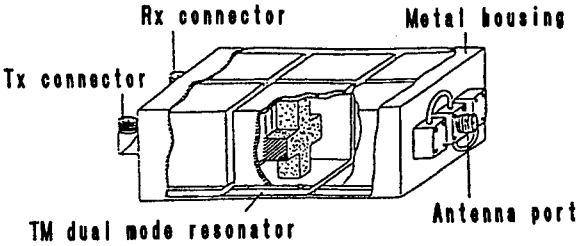

Fig.9. Antenna duplexer for cellular base station using TM_{110} dual-mode dielectric resonator

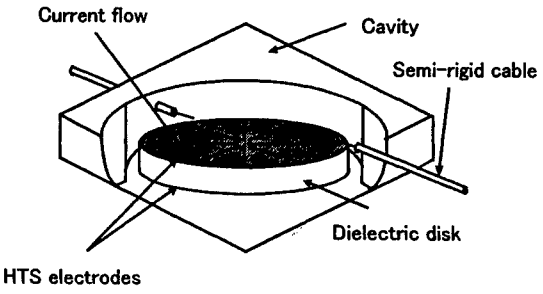

Fig.10. Configuration of TM_{010} mode dielectric resonator with $(Bi,Pb)_2Sr_2Ca_2Cu_3O_x$ HTS thick film.

CONCLUSIONS

Several kinds of filters such as the dielectric filter, the SAW filter and the chip-type LC filter are now available for the applications at microwave frequencies. Among these filters, the dielectric filter has the advantage of high Q value, high power durability and good adaptability for wide frequency range and filter designing. The applications described here utilize these advantages of the dielectric resonator materials.

The dielectric loss tangent at microwave and millimeter-wave frequency is mainly determined by the anharmonic terms in the crystal's potential energy, and increases by the additional crystal defects, especially by the disordered charge distribution in the crystal. These additional increase of tanδ must be eliminated.

The research and development are still actively performed in the world. New materials are expected for the coming new applications.

References

[1] H. M. O'Bryan,Jr., J. Thomson,Jr., and J. K. Plourde, J.Am.Ceram.Soc., 57, 450-53 (1974).

[2] S. Kawashima, M. Nishida, I. Ueda, and H. Ouchi, J.Am.Ceram.Soc., 66, 421-23 (1983).

[3] K. Wakino, K. Minai, and H. Tamura, J.Am.Ceram.Soc., 67, 278-81 (1984).

[4] H. Tamura, T. Konoike, and K. Wakino, J.Am.Ceram.Soc., 67 C-59-C-61 (1984).

[5] Y. Kobayashi and M. Katoh, IEEE Trans. on MTT, MTT-33, 586-92 (1985).

[6] Y. Ishikawa, H. Tanaka, H. Nishida and T. Nishikawa, IEICE. Jpn. Tech. Rep., MW90-13, 31-36 (1990).

[7] A. A. Maradudin and A. E. Fein, Phys.Rev., 128, 2589-608 (1962).

[8] E. Schlömann, Phys.Rev., 135, A413-19 (1964).

[9] N. Michiura, T. Tatekawa, Y. Higuchi, and H. Tamura, J. Am. Ceram. Soc., 78, 793-96 (1995)

[10] H. Tamura, J. Hattori, T. Nishikawa, and K. Wakino, Jpn. J. Appl. Phys., 28, 2528-31 (1989)

[11] Y. Ishikawa, J. Hattori, M. Andoh, and T. Nishikawa, IEEE MTT-S Dig., II-3, 11617-1620 (1992)

[12] H. Tamura, H. Matsumoto, and K. Wakino, Jpn.J.Appl.Phys., 28, Suppl., 28-2, 21-23 (1989).

[13] Hiroshi Tamura, Tsutomu Tatekawa, Yuji Kintaka and Akio Oota, 9th US-Japan Seminar on Dielectric and Piezoelectric Ceramics (1999)

[14] Y. Ishikawa, T. Hiratsuka, T. Sonoda, and S. Mikami, Topical Symposium on Millimeter Waves Proc., 93-96 (1997)

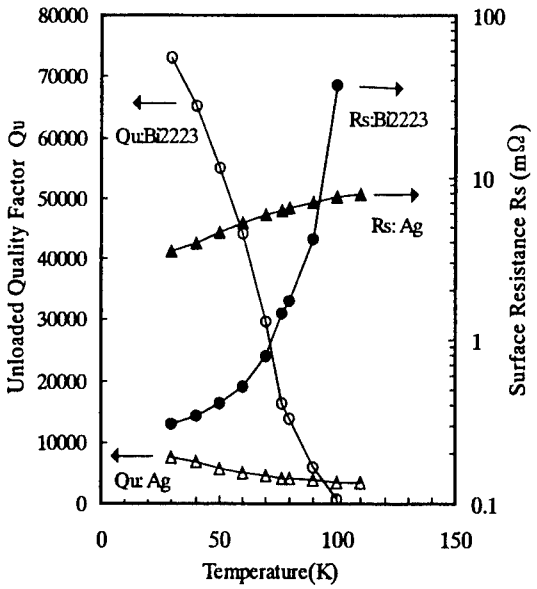

Fig.11. Temperature dependence of unloaded Q of TM_{010} mode dielectric resonator and surface resistance of Bi2223 thick film at 2 GHz.

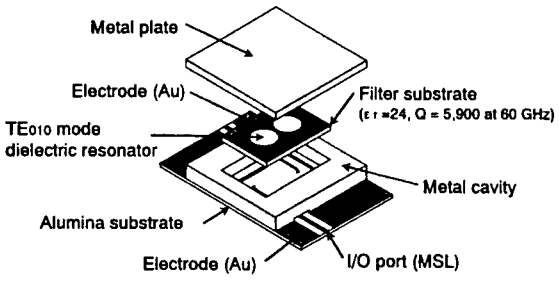

(a) Filter with f0 of 26 GHz

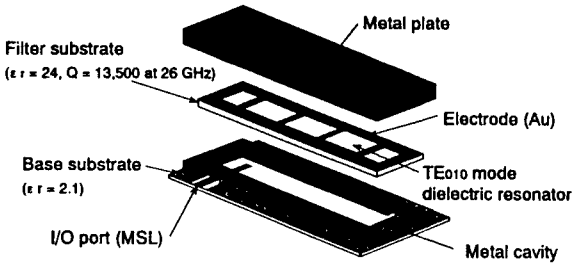

(b) Filter with f0 of 60 GHz

Fig.12. TE010 mode dielectric filters for millimeter-wave application.

Ultra-thin Ni-compatible X7R Dielectric Based on Alkoxide Derived Barium Titanate

P. Pinceloup, I. Burn
dmc[2], Electronic Materials America
South Plainfield, New Jersey, USA
Fax: 01-908-757-0411
K. Albertsen, T. Ohba and J. Roelofsma
dmc[2], Electronic Materials BV
Uden, The Netherlands
Fax: 31-413-283-369

1. INTRODUCTION

Ni electrode technology is now well established for multilayer ceramic capacitors (MLC's) but there is a continual drive to reduce the thickness of the dielectric layers. In the case of MLC's with X7R designation, a dielectric thickness of 2 μm, or less, is practicable when the fired grain size is not more than 250 nm [(1)]. However, achieving adequate dielectric characteristics, such as breakdown voltage, HALT, TCC, DF and K, at this thickness is not possible unless high performance powders are used. In this paper we will describe a high purity barium titanate made by the semi-alkoxide process that consists of 0.4 μm monosize clusters of 40-60 nm crystallites. This type of powder provides some of the benefits of nanosized particles but allows processing into a slurry by standard techniques because of its relatively low surface area. For X7R applications, the barium titanate must be modified with dopants to achieve the necessary core-shell microstructure and compositional uniformity is essential for high reliability in thin layers. Accordingly, chemical-coating technology has been employed to achieve the necessary uniform distribution of dopant ions.

2. BARIUM TITANATE POWDER

2.1 Chemistry

The semi-alkoxide process involves hydrolysis of tetrabutyl titanate by an aqueous solution of barium hydroxide. The hydrous titanium oxide precipitate is then refluxed at about 95 °C and high pH to produce a crystalline barium titanate powder which is then washed of residual barium hydroxide and dried. The process is similar to that employed for hydrothermal powders except that elevated pressures are not required to achieve crystalline product. This permits some simplification of the equipment needed.

2.1 Process

The equipment is shown schematically in Figure 1. Hydrolysis is accomplished under conditions of high turbulence using a coaxial jet mixer [(2)]. The equipment currently in place allows the manufacture of approximately 300 ton/year of product.

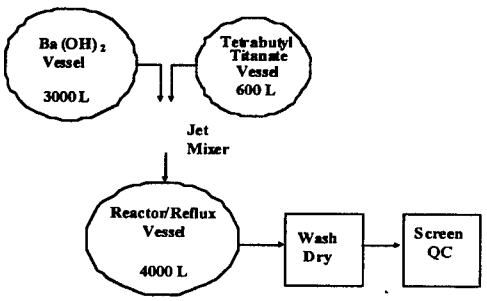

Fig. 1. Schematic of barium titanate powder process.

3. BARIUM TITANATE PROPERTIES

3.1 Particle size and morphology

Typical morphology of the dried powder with no calcination or milling is illustrated in Fig. 2. Each powder particle is composed of a cluster of fine crystallites. Particle size measurements (Microtrac X100) show that the clusters have a very monomodal size

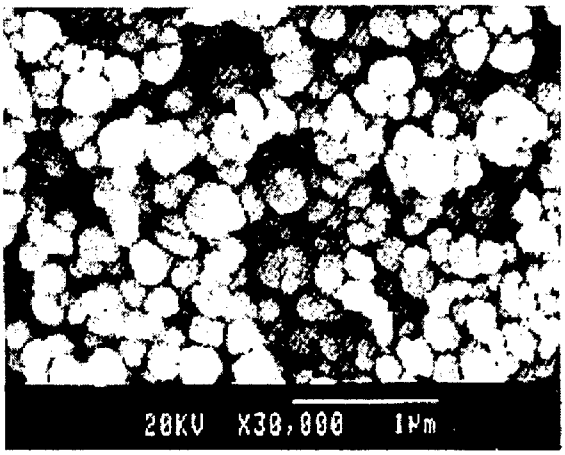

Fig.2 Precipitated powder (uncalcined)

distribution (Fig. 3). X-ray diffraction scans show that the material is crystalline as precipitated with cubic symmetry and a (111) crystallite size of 60 nm [3]. Typical properties of the uncalcined powder (ADHPBT) are summarized in Table 1.

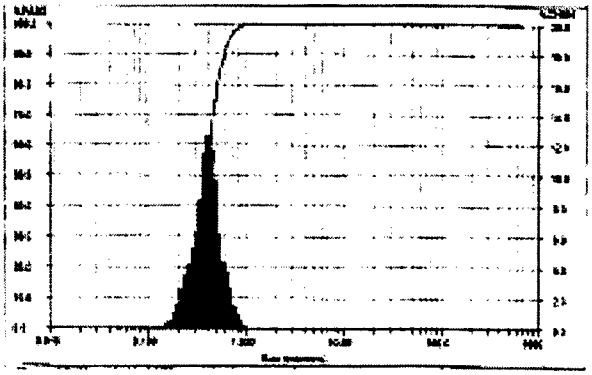

Fig. 3. Particle size distribution

Table 1. Typical Properties of ADHPBT

PSD (μm)	
D_{90}	0.50
D_{50}	0.38
D_{10}	0.25
Surface Area (m^2/g)	9.0
Ba/Ti ratio	1.000 (+/- 0.003)
Moisture Loss (110 °C)	0.10 %
Ignition Loss (538 °C)	2.0 %

The uncalcined powder was found to have very beneficial properties as an additive to MLC electrode compositions to reduce metal lay down and to control electrode shrinkage on firing. On the other hand, if the powder is subjected to low levels of calcination, the powder can be used as a base material for X7R dielectrics for very thin layers.

3.2. Influence of calcination

Calcination of the powder in the range of 850 to 1050 °C resulted in removal of hydroxyl ions [4] and some fusion of the crystallites. The morphology of calcined powder is shown in Fig. 4. It was found that some level of calcination was needed to avoid excessive reaction of the dopants with the barium titanate particles when trying to achieve a core shell structure that would produce satisfactory X7R dielectric characteristics. Some properties of the calcined powders are given in Table 2. Particle size of powder calcined at 850 °C was identical to that shown in Fig. 3 for uncalcined powder but surface area was reduced to 5.0 m^2/g, a level adequate for standard slip making techniques.

Table 2. Properties of Calcined Powders

Calc. Temp. (° C)	850	950	1050
Powder Density (g/cc)	5.65	5.73	5.90
Surface area (m^2/g)	5.0	3.5	2.6

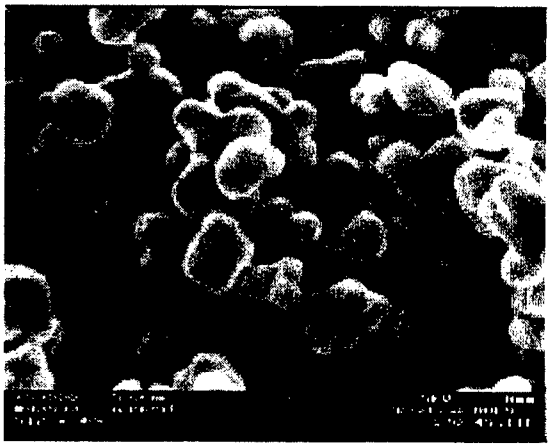

Fig. 4. Calcined powder (unmilled)

In addition to fine particle size, the particles must be chemically coated with dopant solution for optimum compositional uniformity. Coating technology for dielectric powders has been pioneered by dmc[2] and has been well proven in the industry for dielectrics compatible with Ag-Pd electrodes [5]. Coating technology is now being applied to Ni compatible compositions. Powder shown in Fig. 5 is an example of the degree of dopant dispersion obtained for coated powders.

Fig. 5. Coated barium titanate showing distribution of dopants

5. DIELECTRIC PROPERTIES

Tests were performed on coated powders in MLC's. The MLC's were made with Ni electrodes and fired at 1225 - 1255 °C in an atmosphere of low oxygen partial pressure (10^{-10} atm.) followed by an anneal at 1000 °C with an oxygen partial pressure of 10^{-9} atm. Average grain size of the fired dielectric was close to the target of 0.25 µm, as shown in Fig. 6.

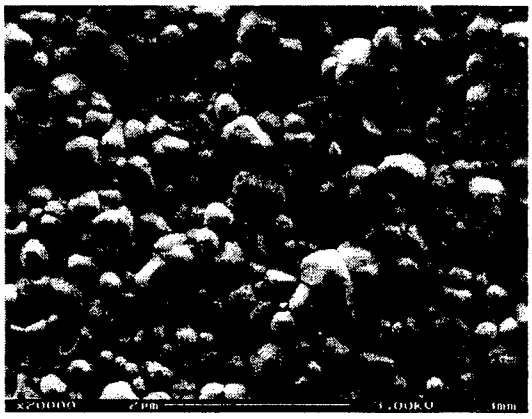

Fig. 6. Microstructure of fired dielectric

5.1. Results for 50 layers at 3 µm (fired)

The coated barium titanate produced a dielectric which met the X7R requirements for temperature dependence (+/- 15% capacitance change from -55 °C to 125 °C), as shown in Fig. 7. Maintaining the X7R specification is generally quite difficult with fine powders because of their tendency to over-react with the dopants and make the temperature dependence exceed the -15 % requirement at 125 °C. Dielectric constant was 2100 and DF was 3.7 % at 0.5 V. Lifetime under HALT exceeded 100 hours at 140 °C and 75 V (25V/µm).

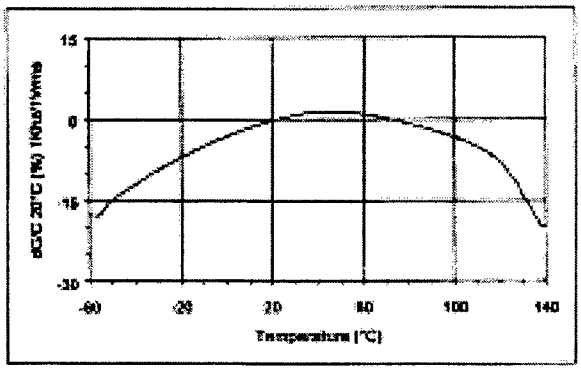

Fig. 7. Temperature dependence of capacitance

5.2. Results for 2 µm (fired) layers

Tests were also carried out on MLC's with three layers at 3 µm fired thickness and on single layer MLC's at 2 µm fired thickness. Temperature coefficient of capacitance (TCC) curves are shown in Fig. 8. It can be seen in Fig. 8 that the results for three layers at 3 µm thickness are quite similar the results for 50 layers in Fig. 7, indicating that the number of layers was not a significant factor in determining the TCC. On the other hand ,

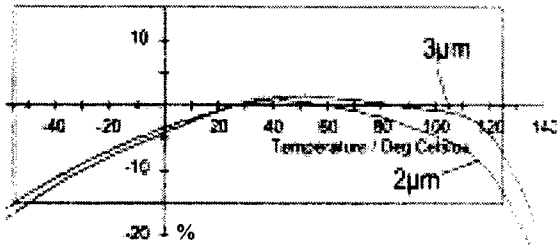

Fig. 8. TCC at 2 microns fired thickness

while the TCC for the 2 μm layer parts was still within X7R limits at 125 °C, there was progressive deterioration in TCC due the increased electric field of the measuring voltage. Measured dielectric constant was 2200 for the 2 micron layer parts, similar to that reported for 3 micron layers, and DF was < 5 % (at 0.5 V).

High breakdown strength was measured on these thin layers (Fig. 9) and lifetime under HALT (140 °C, 25 V/μm) exceeded 100 hours for the 3 micron layers (as before) and was up to 44 hours for the 2 micron layers.

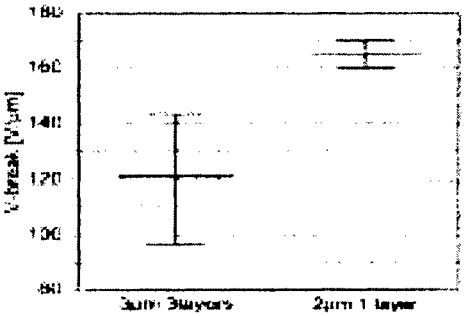

Fig. 9. Breakdown voltages for thin layers

5.3. Results for 1.5 μm (fired) layers

Initial results at 1.5 microns show further deterioration of TCC (Fig. 10) but still within X5R requirements (+/- 15 % from –55 °C to 85 °C). DF was again < 5 % at 0.5 V and K was measured at 2100. High reliability can be expected due to the fine grain size of the material (Fig. 6) but work is needed on minimizing the thickness of the Ni electrodes which are now comparable to the dielectric thickness (Fig. 11).

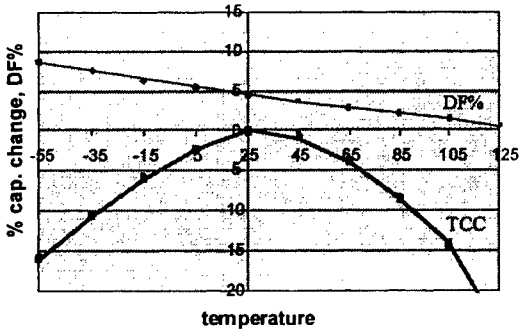

Fig. 10. TCC and DF for ca. 1.5 micron layers

Fig. 11. MLC fracture section

6. SUMMARY

Alkoxide barium titanate is an ideal base material for ultra-thin MLC dielectrics. The fine grain size provides high reliability and X7R temperature dependence down to a layer thickness of at least 2 μm. Some compromise in TCC might be required for layer thickness below 2 μm and further work is needed to achieve electrodes that are < 1 μm thick so that reliability is not degraded by internal mechanical stress.

7. REFERENCES

1. Y. Sakabe, "MLC Technologies of Today and Future", Proc. 9th US-Japan Seminar on Dielectric and Piezoelectric Ceramics, 1-6 (1999).
2. S.A. Bruno and W.L. Monson, "Process for Preparing Crystalline Mixed Metal Oxides", U.S. Patent 5,242,674 (1993).
3. E.K. Akdogan and A. Safari, "Crystallite Size and Microstrain Studies in High Purity Submicron Barium Titanate Powders", Proc. 10th IEEE Int. Symp. on Appl. of Ferroelectrics, Vol. 2, 1007-1011, (1996).
4. Y. Sakabe, N. Wada, J.Ikeda and Y. Hamaji, "Ceramics for Ultra-thin Dielectric Layer of Multilayer Ceramic Capacitors", Proc. 11th IEEE Int. Symp. on Appl. of Ferroelectrics, 565-569, (1998).
5. S.A. Bruno, D.K. Swanson and I. Burn, "High Performance Multilayer Capacitor Dielectrics from Chemically Prepared Powders", J. Am. Ceram. Soc., **76**, (5), 1233-41 (1993).

Hydrothermal $BaTiO_3$ Based High K, Low Loss Dielectrics for Thin Active Layer BME MLCC Applications

Sridhar Venigalla, Dorran L. Schultz, and Jeffrey A. Kerchner
Cabot Corporation, Countyline Road, Boyertown PA 19512
FAX: 610-369-8552
Email: sridhar_venigalla@cabot-corp.com

INTRODUCTION

Multilayer ceramic capacitors (MLCCs) offer unique combination of characteristics such as low equivalent series resistance (ESR), high insulation resistance and breakdown voltage. This makes them attractive in digital and high frequency circuit applications including DC-DC converters, switching power supplies, and power supply bypass capacitors in liquid crystal modules. High capacitance MLCCs also offer an attractive replacement to tantalum and aluminum electrolytic capacitors due to their higher permissible ripple current values, smaller case sizes relative to rated voltage, improved reliability, and lower cost. Recent strides in microelectronic and communication technologies have propelled the miniaturization of multilayer ceramic capacitors (MLCCs), while the performance requirements have tremendously increased: higher capacitance in smaller case sizes (high volumetric efficiency), higher mechanical strength and reliability. In order to meet these advanced performance features, the manufacturers need to fabricate MLCCs possessing 200-400 uniform, ultra-thin ceramic active layers (2-4 μm active thickness), with dense, defect-free microstructure and controlled grain size. In addition, recent increases in Pd price has made the MLCCs containing precious metal electrodes (Pd, Ag-Pd) cost prohibitive. While reducing the manufacturing cost, use of a base metal (nickel) as the electrode material also enhances solderability and thermal shock resistance of MLCCs, improving the overall reliability of the device. Therefore, most MLCC manufacturers are aggressively developing high volumetric efficiency MLCCs with base metal electrodes (BME). However, there are several material requirements that need to be met in order to fabricate reliable devices.

DIELECTRIC REQUIREMENTS

Several characteristics of the dielectric material are important for the manufacture of MLCCs with ultra-thin active layers. Fine, uniform, sub-micron particle size and good dispersibility of the dielectric are essential to be able to fabricate good quality thin (<5 μm) green sheets of ceramic. These features also improve surface quality of the green sheet, which is critical to minimize processing-related defects during electrode printing and multilayer (several hundred alternating layers of dielectric and electrode) lamination. A variety of dopants are added to the dielectric to obtain temperature stability of capacitance as well as reduction resistance (to withstand the reducing atmospheric conditions of sintering employed in Ni electrode MLCC fabrication). Uniform distribution of these dopants among the sub-micron dielectric particles is critical for the optimal control of grain size and microstructure to maintain high reliability. To provide these dielectric material capabilities for the manufacture of advanced MLCCs, Cabot Corporation has developed high purity, sub-micron hydrothermal barium titanate. Through unique coating and dispersion techniques, these particles are formulated to provide uniform distribution of dopants at microscopic scale.

HYDROTHERMAL BARIUM TITANATE

Cabot's patented hydrothermal process produces spherical, uniform nano-sized particles of $BaTiO_3$ using a low temperature, aqueous reaction between hydrous TiO_2 and $Ba(OH)_2$. The reaction conditions in the hydrothermal process are maintained such that the formation of crystalline, stoichiometric perovskite (ABO_3 type) compound is thermodynamically favored, thereby eliminating the need for high

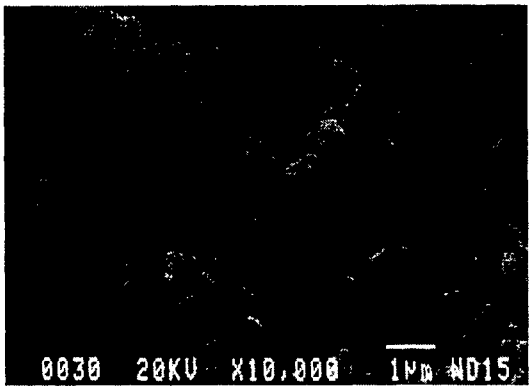

Figure 1: SEM micrograph of 450 nm average particle size Cabot hydrothermal barium titanate.

temperature calcination to achieve crystallinity and phase purity. In addition, the kinetics of hydrothermal reaction (nucleation and growth rates) as well as other processing conditions are precisely controlled to vary the primary particle size in the range 50-500 nm, yielding a wide variety of particle size grades to suit specific dielectric applications. Figure 1 shows a scanning electron micrograph of a 450 nm average particle size grade Cabot hydrothermal barium titanate.

SURFACE COATINGS OF DOPANTS

Use of nickel as internal electrode requires that the green MLCCs are sintered in a reducing atmosphere (pO_2 between 10^{-7} and 10^{-11} atm) to prevent the oxidation of nickel. However, the dielectric has to be formulated with reduction-resistant dopants (rare earth elements such as Y, Ho, and Dy) to prevent loss of insulation characteristics. Other dopants (such as Mg, Mn, V, Cr, Mo, W) are also added to the dielectric to obtain temperature stability and reliability characteristics. As mentioned earlier, uniform distribution of these dopants is critical to control the sintered microstructure of the dielectric layers (average grain size, grain size distribution, porosity and average pore size) as well as the consistency of electrical characteristics. Achieving uniform distribution of various dopants using conventional formulation methods such as ad-mixing and calcination becomes even more challenging as the primary particle size of dielectric gets smaller. To overcome this hurdle, Cabot has developed a unique aqueous coating process to incorporate a variety of dopants onto the surface of the ceramic particles, providing a uniform layer of dopant compounds. Each dopant is individually coated and varied in sequence to provide optimal performance. In addition to the dopants mentioned earlier, fluxing agents such as SiO_2 and $BaSiO_3$ can also be coated on the particle surface to provide uniform sintering behavior. Various combinations of dopant elements in a wide range of concentrations can be applied to match customer-specific dielectric formulations. Sophisticated multi-variant statistical methods are applied via experimental

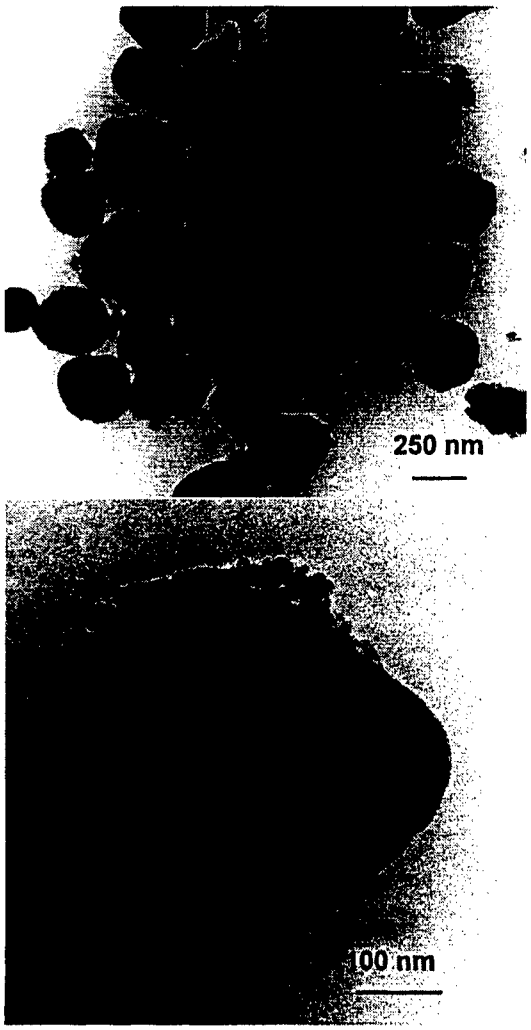

Figure 2: TEM micrographs of surface coated (with dopants) hydrothermal barium titanate particles.

design and mathematical modeling to rapidly optimize the formulation and achieve desired MLCC characteristics. Figure 2 shows the transmission electron micrograph of a group

of barium titanate particles coated with dopants.

GREEN MICROSTRUCTURE

Green ceramic sheets with good surface quality (low roughness) and dense microstructure have been fabricated in 2-8 micron thickness range, as shown in Figure 3. Suspension stability and fine, dispersed particle size allow the use of extremely fine slip filtration systems to remove foreign contaminants and minimize defect density in the green sheet, which are critical to meet stringent MLCC reliability requirements.

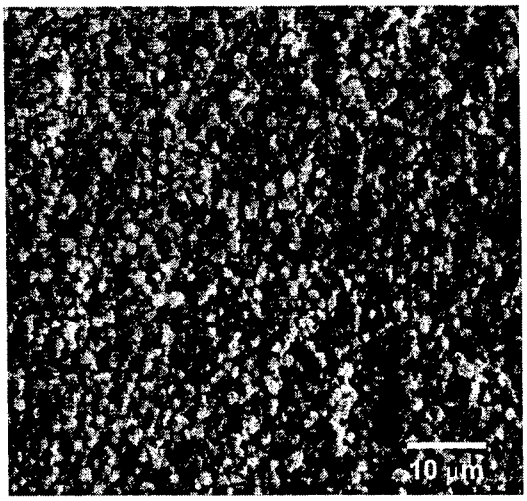

Figure 3. Scanning electron micrograph of a top surface of a 4.0 µm thick green dielectric sheet with a green density of 3.3 g/cc, fabricated by doctor blade tape casting.

MLCC PROPERTIES

A typical sintered microstructure for Cabot X5R dielectric is shown in Figure 4. Uniform thickness and high sintered density of dielectric layers were achieved through good surface quality and high green density of the green sheet. Table I shows the electrical and reliability characteristics for 4.0 micron and 6.5 micron active layer prototype MLCCs, with 25 active layers. High insulation resistance and accelerated life time (HALT) indicate good reliability of the dielectric. Figure 5 shows a chemically etched cross section of a 4 micron active layer MLCC, where the advantage of uniform distribution of dopants at microscopic levels is manifested via the uniform, controlled grain structure.

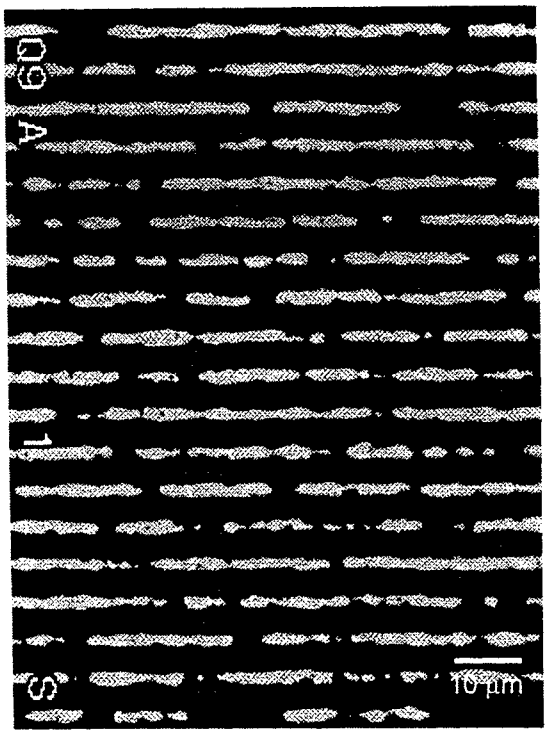

Figure 4: SEM micrograph of a polished cross section of a 4.0 micron active layer MLCC, showing uniform dielectric layers.

TABLE I. X5R MLCC Electrical Properties

Active Layer	4.0 µm	6.5 µm
# of Actives	25	25
Sinter Temp. (C)	1300	1300
Case Size	1206	1206
Capacitance (nF)	485	275
Dielectric Constant	2700	2700
D.F. @ 1.0 V (%)	4.0	2.5
TC @ 125C (%)	-22.2	-19.1
TC @ 85C (%)	-14.4	-12.9
TC@ -55C (%)	-2.33	-4.79
BDV (V)	350	550
I.R. @ 25C (GΩ)	4.4	8.5
I.R. @ 125C (GΩ)	0.72	1.2
RC Factor @ 25C	2134	2338
RC Factor @ 125C	349	330
HALT Temp. (C)	150	150
HALT Voltage	20V/µm	20V/µm
HALT Max. TTF (h)	>100	>100

Figure 5: SEM micrograph of a chemically etched cross section of a 4.0 micron active layer MLCC, showing typical grain structure of Cabot BME X7R dielectric with 0.4 μm average grain size.

SUMMARY

A hydrothermal barium titanate - based X5R dielectric designed for manufacturing high volumetric efficiency MLCCs with Ni internal electrodes is described. The dielectric has a high dielectric constant (2700) and exhibits low loss and high reliability characteristics. The dielectric particles are highly dispersible, to facilitate the fabrication of thin green sheets with good surface quality and high green density. Controlled grain structure resulting from the uniform distribution of dopants promotes higher part yields and device reliability.

ACKNOWLEDGMENTS

Authors thankfully acknowledge the contributions of Don Clancy, Sr. Process Engineer and Anne Poncheri, Quality Systems Manager, in experimental design and statistical analysis.

BME X7R and Y5V Dielectrics for Thin Layer MLC Applications

Hyun Park, Dan McCauley, Mohammed Megherhi, Mike Chu, Everette Davis
Ferro Electronic Materials
Ferro Corporation
1789 Transelco Drive
Penn Yan New York 14527, USA
Fax: 315 536 0376
E-mail:Parkh@Ferro.com

Dielectric compositions suitable for high capacitance BME multilayer ceramic capacitor (MLC) applications have been developed. The X7R dielectrics demonstrate dielectric constant > 3600 with a fired dielectric thickness less than 5 μm whereas the Y5V dielectric exhibits a dielectric constant > 17,000 at 10 μm dielectric. Both X7R and Y5V dielectrics show excellent reliability and uniform fine-grained dense microstructures. Electrical properties and microstructural development are studied as a function of sintering temperature and oxygen partial pressure. Both dielectric systems are designed to provide stable electrical properties when fired over a wide range of oxygen partial pressures and temperatures.

INTRODUCTION

Recently more multilayer ceramic capacitors (MLC's) have been made with nickel electrodes[1-7] and this trend will be continued to replace expensive Pd electrodes. Furthermore larger capacitance MLC's are fabricated with thinner dielectric and higher number of active layers to replace tantalum and aluminum electrolytic capacitors in many low voltage applications.

Ferro Electronic Materials (FEM) has developed high K X7R and Y5V dielectric material systems with excellent reliability suitable for larger capacitance MLC applications. In this paper we will discuss dielectric properties of these material systems processed in a variety of firing conditions.

PROCESS

In house and commercial $BaTiO_3$ precursors were used to develop dielectric compositions. Average particle size (D_{50}) is in the range of 0.5 to 0.9 μm, and surface area is 1.5 to 3 m^2/g (for commercial) and 5 to 6.5 m^2/g (for in-house). 1206 size MLC's were fabricated for both X7R and Y5V compositions with fired dielectric thickness 4 to 10 μm. The binder of the green chips was removed at 250°C in an air.

The MLC chips were sintered in a Tokai Konetsu Kogyo batch kiln between 1250°C and 1300°C for 2 hours in a controlled PO_2 atmosphere ranging from 10^{-8} to 10^{-12} atmospheres. Chips were reoxidized in a temperature range of 1000°C with an oxygen concentration at 6 ppm's. A typical profile is shown in Figure 1. Ni and Cu pastes prepared by FEM Vista, CA were used for internal electrodes and termination. Cu terminated chips were fired in a 9 zone belt furnace in a dry nitrogen atmosphere.

Electrical properties are measured by Hewlett Packard 4278A capacitance meter and Micro Instrument model 8201 capacitor insulation resistance tester. Aging rates are obtained by automatic capacitance measurement using Thermotron chamber. Reliability of

processed chips were tested at 140 to160°C and 10 - 30V/μm with Ingalls Engineering HALT system. Failure limit was set at 1 or 10 mΩ depending on material and layer thickness.

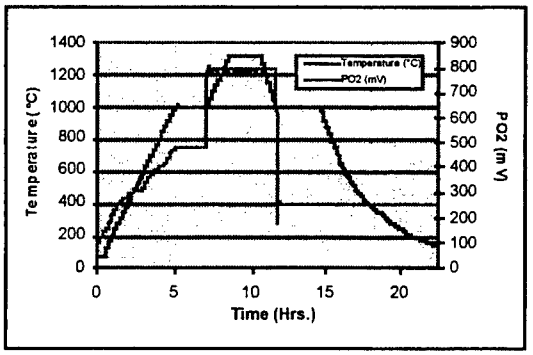

Figure 1 Sintering profile.

X7R DIELECTRIC COMPOSITIONS

Electrical properties of the second generation X7R composition sintered at 1250°C and 10^{-9} atm. pO_2 are summarized in Table 1 and TCC plot is shown in Figure 2. Dielectric constant is higher than 3500 and DF value is less than 4.0 % with fired dielectric thickness 5 μm. Dielectric breakdown voltage is 450volt and TCC is well within EIA X7R specification. The dielectric exhibits very small aging rate at 2.5% per decade. The microstructure of the X7R dielectric sintered at 1250°C with 10^{-9} atm. pO_2 is shown in Figure 2. A sub-micron dense microstructure can be seen in the fracture and thermally etched surface of the MLC chips. Grain size is very uniform with average grain size about 3 microns

Figure 3 and 4 illustrate the effect of processing conditions on the dielectric properties of X7R dielectric. Dielectric constant remains above 3500 when sintering temperature is higher than 1250°C with pO_2 in the range of 10^{-8} ~ 10^{-12} atm. DF value increases with sintering temperature and lower pO_2 as expected. However DF value remains less than 4.0% when dielectric is sintered between 1250°C and 1300°C with pO_2 in the range of 10^{-8} ~ 10^{-12} atm. TCC is within EIA X7R specification in the entire range of the sintering study.

No noticeable change is observed in microstructure when sintered in 1225 ~ 1320°C with pO_2 in the range of 10^{-8} ~ 10^{-12} atm. These results indicate that X7R composition can be processed in a wide range of processing conditions in terms of sintering temperature between 1265 ~ 1300 °C and oxygen partial pressure between 10^{-8} and 10^{-12} atmosphere. TCC meets EIA X7R specification for the X7R dielectric in entire range of processing conditions.

Table I. Electrical Properties of X7R Dielectric sintered at 1250°C, pO_2 10^{-9} atmosphere

Dielectric Constant	3577
Capacitance, nF	144.47
DF, %	3.73
IR @ 25°C	8.40E+09
IR @125°C	2.20E+08
DBV, volt	450
Aging rate, %/decade	2.5
Dielectric thickness	5.5 μm, fired

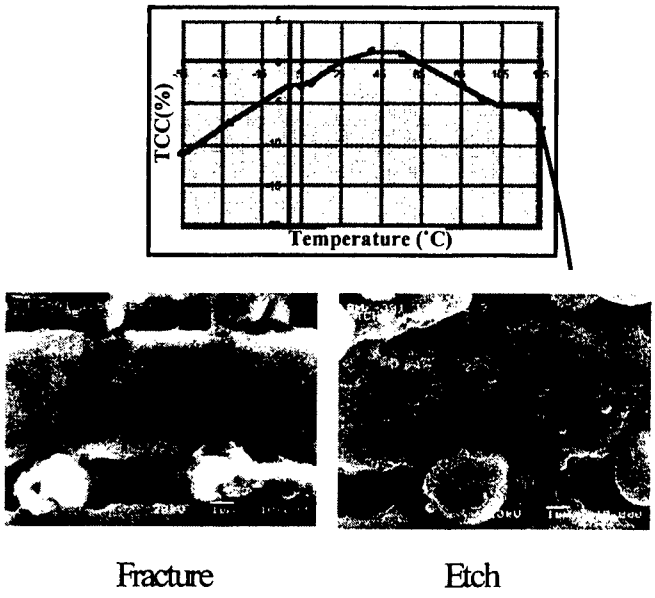

Figure 2. TCC plot and microstructure of second generation X7R dielectric sintered at 1250 °C and pO_2, 10^{-9} atm.

Mean time to failure in HALT testing exceeds 24 hours when chips are tested at 150°C and 10 volt/um.

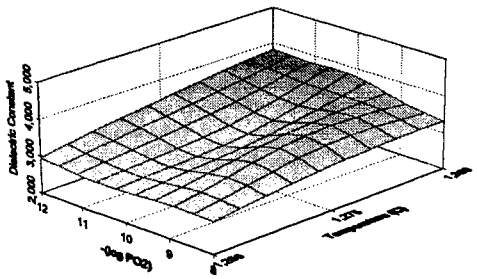

Figure 3. Dielectric constant of second generation X7R dielectric as a function of sintering temperature and pO_2

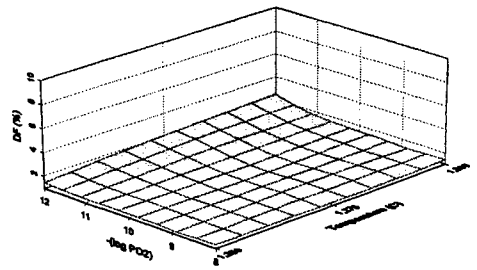

Figure 4. DF value of the second generation X7R dielectric as a function of processing conditions

The dielectric properties of the third generation X7R dielectric sintered at 1275°C and oxygen partial pressure at 10^{-9} atm. are summarized in Table 2. Dielectric constant is higher than 4,000 with DF value 2.54 % at a fired dielectric thickness 4.9 um. Aging rate is excellent with 2.5 %/decade.

TCC plot and microstructure of the third generation X7R dielectric are shown in Figure 5. TCC is within EIA X7R specification with core-shell structure. Very dense microstructure with uniform grains can be seen in the thermally etched fracture surface.

Results of firing matrix study shown for second generation X7R shown in Figures 3 and 4 indicate the electrical properties of third generation X7R dielectric are also stable in wide range of sintering process in terms of firing temperature between 1275 °C and 1325 °C and oxygen partial pressure between 10^{-8} and 10^{-12} atmosphere. Dielectric constant is 3500 –4200 with DF value less than 4.0 %. TCC meets X7R specification in entire range of study.

Mean time to failure exceeds 50 hours when tested at 30volt/um and 160°C HALT conditions at 10 um fired dielectric thickness.

The dielectric is believed to be suitable for thin layer less than 5 μm MLC application since it possesses good reliability and stable dielectric properties in the wide range of processing conditions with very small aging rate.

Table II. Dielectric properties of third generation X7R dielectrics with 5 μm fired thickness sintered at 1275°C, pO_2 at 10^{-9} atmosphere

Dielectric constant	4272
Capacitance, nF	187
IR @ 25°C, Ω	3.20E+09
IR @ 125°C, Ω	7.80E+06
DBV, volt	130
Aging rate, %/dec.	2.5
Dielectric Thickness	4.9 μm fired

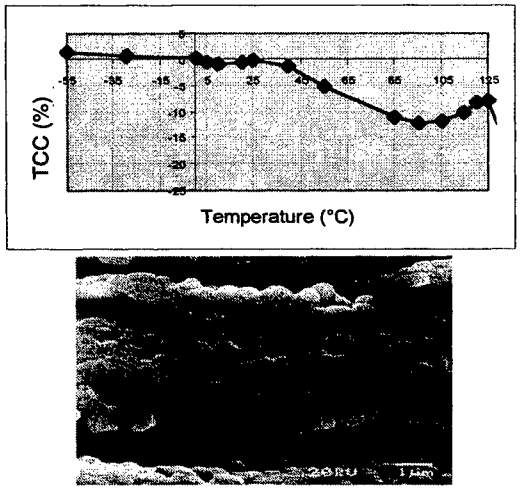

Figure 5. TCC plot and microstructure of the third generation X7R dielectric sintered at 1275°C and pO_2 at 10^{-9} atm

Y5V DIELECTRIC COMPOSITION

Electrical properties of the Y5V composition sintered at 1250°C and 10^{-10} atm. pO2 are summarized in Table 3. For an MLC with a fired dielectric thickness of 11 μm the dielectric constant is greater than 17,000 and DF value is less than 4.5%. The composition exhibits excellent 25°C and 85°C RC values and dielectric breakdown voltage is 28 V/μm.

The TCC plot is shown in Figure 6 and is well within EIA Y5V specification. Uniform microstructure with average grain size less than 5 μm can be seen in Figure 7 and microstructure remains same with sintering atmosphere from 10^{-9} to 10^{-11} atm.

Firing matrix data indicate that the Y5V dielectric can be processed in the range of 1225 ~ 1275 °C with pO_2, 10^{-9} to 10^{-11} atm. Dielectric constant varies between 12000 and 17000 and DF values are between 2.5 to 7.0 %.

Table III. Electrical Properties of Y5V Dielectric sintered at 1250°C, pO_2 10^{-10} atm.

Dielectric thickness	11.5 μm, fired
Capacitance,nF	388
K	17082
DF,%	4.5
25°C RC, ΩF	>10000
85°C RC, ΩF	>10000
UVBD,Volts/μm	28

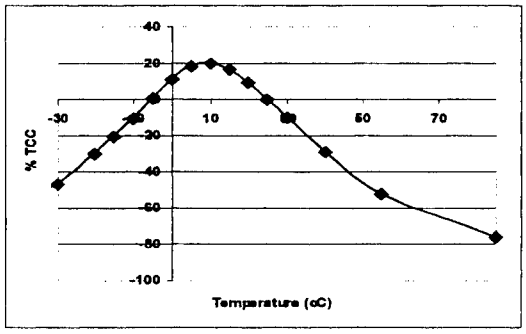

Figure 6. TCC plot of Y5V dielectric sintered at 1250°C and pO_2 10^{-10} atm.

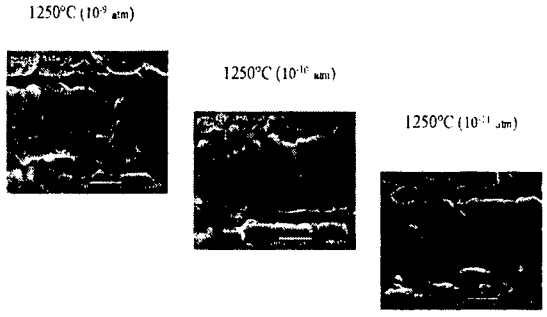

Figure 7. Microstructure of Y5V dielectric sintered at 1250 °C with different atmosphere

Reliability of Y5V dielectric is measured at 20 volt/um and 120°C. At these HALT conditions the mean time to failure is in excess of 60 hours.

CONCLUSION

The K:4,000 X7R dielectrics have been developed and are suitable for thin (<5 μm) layer MLC applications. This dielectric can be processed in wide range of sintering temperatures from 1250°C to 1325°C and oxygen partial pressures ranging from 10^{-8} to 10^{-12} atm.

A fine-grained Y5V dielectric composition has been developed which exhibits a dielectric constant >17,000 and a DF value that is less than 4.0%. The composition can be processed in wide range of oxygen partial pressures.

The grain size in the fired microstructure remained very stable when fired in a wide range of oxygen partial pressures. Average grain size in the fired MLC is <4 μm.

REFERENCES

1. T.Nomura,A.Sato and Y.Nakano J.Soc.Mater.Eng.Resour.Jpn.,5 (1992)44
2. T.Nomura,Y.Nakano,andT.Arashi, US Patent 5,335,139, Aug.2, 1994
3. H.Kishi,H.Shizuno,S.Kusumi,andH.Saito, US Patent 5,453,409, Sep. 26, 1995
4. T.Mizuno,H.Sano, Y. Hamaji, and S. Nishiyama Jap. Patent 8-171814, 7/2/1996
5. H.Park,J.Nance,M. Chu, and A.Yuval, US Patent 6,185,087 Feb 6, 2001
6. H.Park, D. McCauley,M. Chu, M. Megherhi Proceedings Carts-Europe 2000
7. D.McCauley, H.Park, M.Megherhi, M.Chu, Proceedings Carts USA 2001

Physical and Electrical Properties of a Low Fired K-3800 X8R Dielectric

By
Galeb H. Maher and Samir Maher

MRA Laboratories
96 Marshall Street
North Adams, MA 01247 U.S.A.
Fax: 413-663-5535
Email: MRAlabs@sover.net

Abstract:

A low fired K-3800 dielectric was recently developed to meet the X8R characteristic (±15% between -55°C and 150°C). This dielectric is based on fine grain $BaTiO_3$ system and is compatible with 75 Ag/25 Pd and 70 Ag/30 Pd internal electrode.

With inherent dielectric breakdown in excess of 110 volts/micron, it will also make it ideal for high voltage MLC applications. In thin layer designs, it can meet the X7R characteristics at 6 microns for 50V rated and at 4 microns for 25V rated chips.

Data on "HALT" at 500V, 155°C for chips with 12 microns fired thickness is also presented.

INTRODUCTION

At the 9th U.S.-Japan Seminar (Nov. 1999), we reported the "HALT" results on the K-4500 low fired X7R dielectric. In this paper, we will report on the recent dielectric developments designed for the X8R and for thin layer standard X7R MLC applications.

The dielectric chemistry is similar to that reported in reference 1. However, the $BaTiO_3$ used in this new dielectric has an average particle size of about 0.4 microns.

The MLC chips used for this study were produced by the "wet deposition" process and consisted of two groups, both with 0805 chip design and 15 active layers. The fired layer thickness of group A was about 6 microns while that for group B was about 12 microns.

RESULTS AND DESIGNS

A summary of the basic electrical properties generated on MLC chips, is shown in Table I. This data represents sintering at 1110°C for 3 hours for both the 6 and 12 micron chips. Sintering at 1130°C also gave excellent properties with the K and D.F. being slightly higher. Similarly, sintering at 1090°C still showed good density (5.91 g/cm^3) and TCC characteristics, which were within ± 10% between –55 and + 150°C, on the 12 micron layer chip, as shown in Figure 1.

Fig. 1
X8R Dielectric
Chip Size = 0805
Layer Thickness = 12 micron
K = 3550 D.F. = 0.8% (at 1 KHz, 1 Vrms)

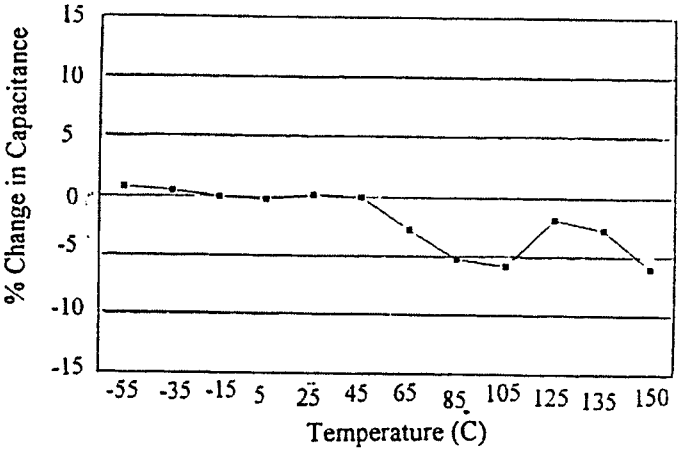

Figure 2 shows the as fired surface grain structure. The sintered grains appeared to be around 0.7 to 0.8 micron. However, examination of the TCC curve (Figure 1), clearly shows the evidence of the curie temperature of pure $BaTiO_3$ at 125°C. This observation may indicate that there was little grain growth. Therefore, the observed grain size of about 0.8 micron may represent 2 to 3 sintered grains without solid solution of $BaTiO_3$ and additives.

Fig. 2
As fired surface sintered at
1110°C/3 Hrs.

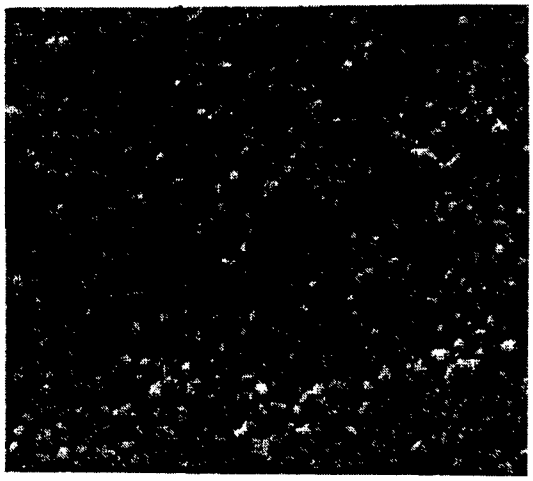

Figures 3 and 4 show SEM images of fractured chips, which were sintered at 1110°C and 1130°C, respectively. With the exception of a few trapped pores, the microstructure showed excellent densification, which is consistent with the measured fired density of the ceramic without electrode, as determined by the Archemedes'method.

HALT RESULTS

For this X8R application, we only performed HALT on the 12 micron chips, sintered at the highest temperature (1130°C). Two test conditions were done: (a) 500V, 152°C and (b) 450V, 161°C. The procedure and the test apparatus that were described in Reference 1, were also used for this evaluation. Each test consisted of 22 chips. It should be noted that the manufacturing environment for these chips was not ideal.

Figure 5 shows a Weibull plot curve for both test conditions. The early failures (below 30%) were considered to be caused by manufacturing defects. The mean time to failure at 63% failure level, for each test condition was determined from the graphs with the help of a MathCad Program and curve fit linear regression statistics, as shown in Figure 6.

Fig. 5

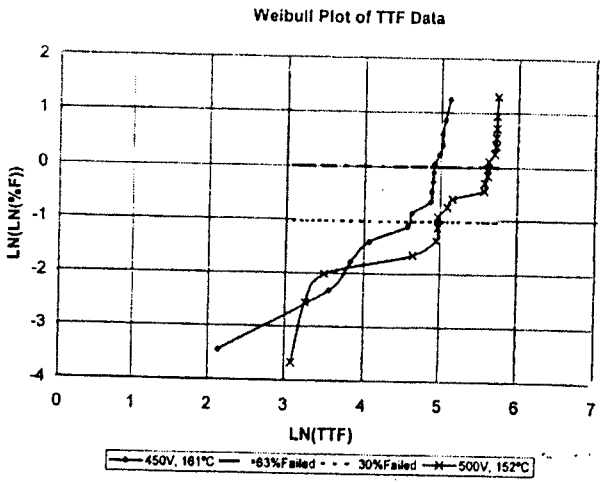

Fig. 6

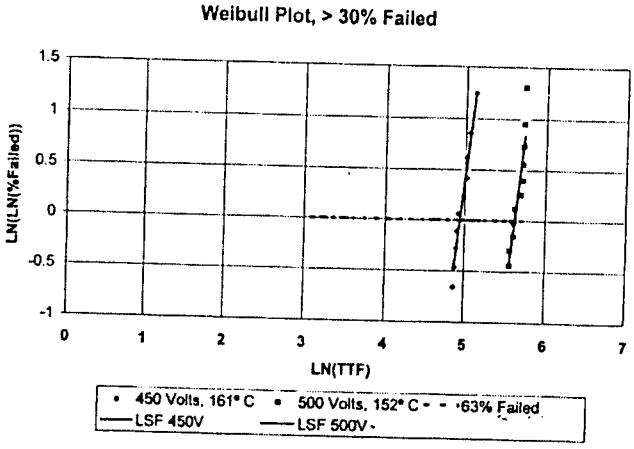

For convenience, the HALT equation described in reference 1 is also shown below.

$$\frac{t_1}{t_2} = \left(\frac{V_2}{V_1}\right)^n \exp.\frac{E_a}{K}\left(\frac{1}{T_1} - \frac{1}{T_2}\right)$$

Where:

t_1 = the mean time to failure at V_1 and T_1
t_2 = the mean time to failure at V_2 and T_2
V_1, V_2 = test voltage of the MLC, in Volts
T_1, T_2 = test temperature of the MLC, in °K
n = voltage stress exponent
Ea = activation energy (electron volt)
K = Boltzman Constant = 0.86×10^{-4}ev/°K.

Using the activation energy, Ea = 1.2 ev, and an average voltage stress exponent n = 6.5 from reference 1, we made a prediction as to the expected life time of these capacitors at various test voltages and temperatures. These results are summarized in Table II.

As can be seen from the data, the predicted time to failure at 63% failure level for the various voltages and temperatures, were nearly similar to those calculated from each of the HALT conditions. This implies that the 1.2 ev for Ea and 6.5 for n, from reference 1, are also applicable for this slightly modified X7R/X8R low fired dielectric.

ACKNOWLEDGEMENT

We wish to thank Dr. George Shirn for the analysis of the HALT data and Messrs. John Martin and Richard Zona for sample preparation and test performance.

REFERENCES

1. Maher, G.M. "Highly Accelerated Life Testing (HALT) of K-4500 Low Fired X7R Dielectric." Proceeding of the 9th U.S.-Japan Seminar on Dielectric and Pieroelectric Ceramics, pp. 357-361, 1999.

Table I
Sample Size 0805
Layers: 15
Sintering Temperature: 1110°C/3 Hrs.

Group	A	B
Fired Layer Thickness (Microns)	6	12
Fired Density (g/cm^3) (Ceramic Only)	5.93	5.93
% Theoretical	98.8	98.8
Dielectric Constant at 1KHz, 1Vrms, 24 Hrs. aging	3950	3730
D.F. %	2.3	1.3
Average Dielectric Breakdown (Volts)	520	1350
TCC % at		
- 55°C	4.4	1.8
- 15°C	2.7	1.0
25°C	0.0	0.0
85°C	-9.0	-6.5
105°C	-11	-7.5
125°C	-10	-4.0
Test Condition	75V, 125°C	150V, 125°C
Insulation Resistance (ohms)	$> 10^{10}$	$> 10^{11}$

Table II
Predicted Life Time of MLC Chips with 12 Microns Fired Layer Thickness
Using n = 6.5 and Ea = 1.2 ev

	HALT Test Conditions	
	450V, 161°C	500V, 152°C
Time to Failure at 63% Failure Level, from Figure 6	144 Hrs.	276 Hrs.
	Predicted Time to Failure at 63% Failure Level (Hrs.)	
Test Conditions		
50V, 150°C	5.1×10^8	5.3×10^8
100V, 150°C	5.7×10^6	5.8×10^6
100V, 125°C	4.5×10^7	4.6×10^7
200V, 125°C	4.9×10^5	5.1×10^5

Fig. 3
Fractured section sintered at
1110°C/3 Hrs.

⟵⟶ = 5µm

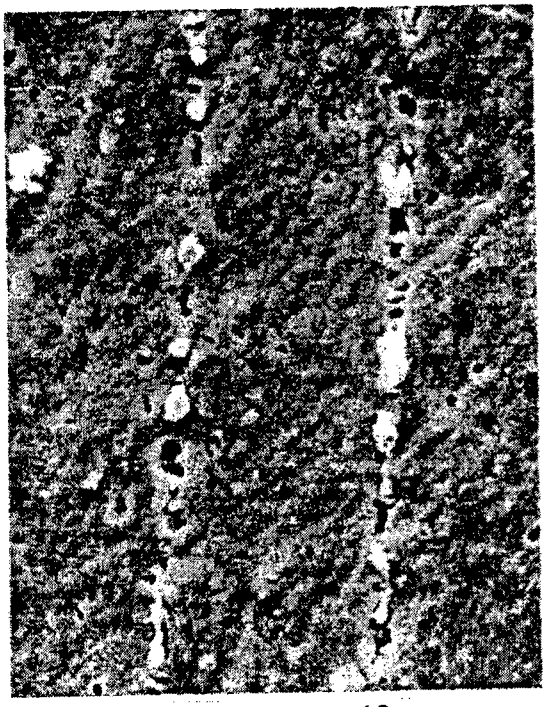

⟵⟶ = 10µm

Fig. 4
Fractured section sintered at
1130°C/3 Hrs.

⟵⟶ = 5µm

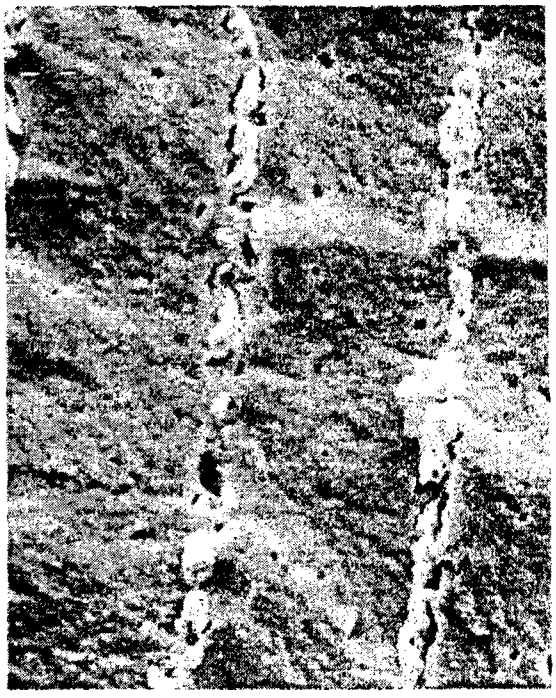

⟵⟶ = 10µm

Development of 100% Silver Compatible Dielectric Compositions For High Performance Discrete and Integrated Passive Component Applications

Brian C. Foster, Walter J. Symes, Everette A. Davis, Dr. Matthew J. Creedon, John F. Bonistall, Philip M. Pruna, Julie B. Burton, and Sandra A. Witter

Ferro Electronic Materials
1789 Transelco Drive
Penn Yan, New York, USA 14527
Tele: 001-315-536-3357
Fax: 001-315-536-0376
Email: FOSTERB@Ferro.com

ABSTRACT

Three dielectric material compositions have been developed that exhibit sintering temperatures below 930 °C. These compositions meet EIA Class I and II characteristic requirements and exhibit dielectric constant values of 14, 87 and 2400. Multilayer ceramic capacitors fabricated with these dielectric materials using 90:10, 95:5 AgPd and 100% Ag internal electrodes show comparable electrical performance. Reliability test results have shown that multilayer ceramic capacitors fabricated using 100% silver internal electrodes and these dielectric materials do not exhibit silver migration.

INTRODUCTION

During the past 4 to 5 years there has been a considerable effort to minimize or eliminate the use of precious metal conductor systems in electronic ceramic passive components. Two approaches have been taken in the development of dielectric formulations to achieve this goal, reduction resistant base metal compatible materials and lower sintering temperature materials that are compatible with reduced precious metal content conductors. In the later case a reduction in sintering temperature to below 1000 °C has allowed the commercial implementation of dielectric compositions that are compatible with 90:10 AgPd conductors.[1-4] In this paper dielectric compositions that exhibit sintering temperatures below 930 °C will be described. With this further reduction in sintering temperature compatibility with 100 % Ag conductors is now feasible. This paper will review the physical and electrical property characterization results generated from multilayer ceramic chip capacitors fabricated using EIA Class I & II characteristic dielectrics and 100% silver internal electrodes. In addition reliability data including HALT and temperature humidity/bias will be discussed.

RESULTS AND DISCUSSION

Dielectric Composition Development

The Class I temperature compensating dielectric compositions developed in this program exhibit dielectric constant values of 14 and 87. Both of these materials are intended to support low ESR, high Q applications such as remote keyless entry systems, RF ID tags, Bluetooth, etc. The lower dielectric constant material is a BaCaMgZr silicate composition. The higher dielectric constant material is a BaNdBiPb titanate material fluxed with a zinc borosilicate glass.

The Class II dielectric composition developed in this program is a Nb and Nd doped barium titanate fluxed with Bi, Pb and zinc borosilicate glass. This material is designed for the automotive, telecommunication, computer and consumer electronic chip component markets and is also suitable for high voltage, high reliability applications.

Table I gives the relevant physical and electrical properties of these dielectric compositions. Table II shows the high frequency bulk properties for the two Class I materials. A Kent resonant mode dielectrometer with a HP 8722C network analyzer was used to generate the high frequency measurement data.

Prototype Fabrication

To evaluate the compatibility of 100% silver internal electrodes with ultra low firing Class I & II dielectric materials a series of multilayer ceramic capacitors were produced. Structures using dielectric thickness from 3 to 40 microns with 7 to 50 active layers were fabricated. Capacitance value targets were 30-60 picofarads for the Class I compositions and 150-700

nanofarads for the Class II composition. A tape transfer prototype manufacturing process was used to fabricate the test structures. Dielectric tape was cast on a PET carrier film using a floating doctor blade, and internal conductors were deposited using a vision aligned screen printer. A PVB binder system, Ferro B74001 was used with binder solids loading adjusted for each dielectric composition to match green and fired shrinkage characteristics. Ferro EL43-025 and A290-3P, 100% Ag internal conductors and Ferro T33-008, 100% Ag low stress platable termination were used as the compatible metal systems.

Completed green ceramic capacitors were processed through a binder removal step in a Blue M model MP-206C mechanical convection oven. A linear ramp over 24 hours to a peak temperature of 250 °C with a 3-hour soak time was used. The capacitors were then transferred to a separate tunnel or box kiln for final sintering. Peak temperatures of 860-920 °C with linear ramps of 3-6 hours were investigated. The soak time at peak temperature was varied from 3-6 hours. The cooling rate in the box kiln was uncontrolled while the cooling rate in the tunnel kiln was identical to the ramp rate. All of the capacitors were processed on open zirconia setters.

Electrical Property Characterization

Table III summarizes the chip capacitor electrical property data for the two Class I temperature compensating dielectric materials. A 90:10 AgPd internal electrode was used as a control for comparison. All of the primary electrical properties; dielectric constant, dissipation factor, temperature coefficient and insulation resistance showed no change when the 100% Ag internal electrode was compared to the 90:10 AgPd control. Cross section analysis of the capacitors using both optical microscopy and SEM showed no adverse interaction between the dielectric materials and the internal electrodes.

Table IV summarizes the chip capacitor electrical property data for the Class II dielectric material. In this case both 90:10 and 95:5 AgPd internal electrodes were used as controls for comparison. As was observed with the Class I materials no change in primary electrical property performance was seen with the capacitors fabricated with 100% Ag internal electrodes. In addition to the AgPd ratio comparison the effect of fired dielectric thickness and the number of internal electrodes when using a 100% Ag metal system was investigated. Table V summarizes the data generated in this study. No degradation in dielectric property performance was observed when the fired dielectric thickness was reduced from 10 microns down to 3 microns. Increasing the number of internal electrodes from 10 to 50 also did not alter electrical performance.

Reliability Test Summary

A series of reliability tests that included standard dry life test, temperature/humidity/bias test (THB), and HALT were performed on capacitors fabricated with the Class II dielectric using 90:10 AgPd and 100% Ag internal electrodes. The intention of this test regime was to determine whether silver migration/diffusion could occur when 100% Ag electrodes are employed. The life test and THB test were normalized to a 5 VDC/micron field stress. In both cases the failure criteria was established at a 1 decade IR drop from pre-test measured values. The THB conditions were 85 °C and 85% RH. To date over 2,000,000 unit hours have been generated without a failure that can be attributed to silver migration.

HALT performance as a function of internal electrode silver content was also investigated. HALT test conditions were 8x rated voltage and 140 °C. No difference in mean time to failure was observed for the capacitor groups tested.

CONCLUSIONS

Three dielectric material compositions have been developed that exhibit sintering temperatures below 930 °C. These compositions meet EIA Class I and II characteristic requirements and have been demonstrated to be compatible with 100 % silver internal electrodes. Reliability test results have shown that multilayer ceramic capacitors fabricated using 100% silver internal electrodes and these dielectric materials do not exhibit silver migration. The class I compositions are considered preferred candidate dielectric materials for low ESR, high Q applications. The class II composition is considered suitable for all X7R type applications including automotive, telecommunication, computer, and consumer electronics.

REFERENCES

[1] B. Foster, W. Symes and E. Davis, "Development and Characterization of Ultra-Low Fire COG and X7R Dielectric Compositions for Multilayer Ceramic Chip Capacitors Using 90% Silver Internal Electrodes," *Proceedings of the 1998 European Capacitor and Resistor Technology Symposium*, Nice, France, pp. 445-450.

[2] B. Foster and W. Symes, "Development of Ultra-Low Fire COG and X7R Dielectric Compositions for Multilayer Ceramic Chip Capacitor and Integrated Passive Component Applications," *Proceedings of the 1998*

International Symposium on Microelectronics, San Diego, CA, pp. 445-450.
[3] B. Foster, et. al., "Characterization of Multilayer Ceramic Chip Capacitors Made with 90% Silver Internal Electrodes," *Proceedings of the 19th Capacitor and Resistor Technology Symposium*, New Orleans, LA, pp. 343-349.
[4] B.C. Foster et al., "Development of Ultra-Low Fire Dielectric Compositions for Integrated Passive Component Applications," *Proceedings of the 9th U.S.- Japan Seminar on Dielectric and Piezoelectric Ceramics,* Okinawa, Japan, pp. 341-44, Nov. 2-5, 1999

ACKNOWLEDGEMENTS

The authors would like to acknowledge Skip Quackenbush, Lori Monroe, Kelly McKay and the entire Ferro Electronic Materials R&D team for their contributions to this paper and the development of the ultra-low fire dielectric technology.

Table I. Physical property measurements

Material Type	Particle Size D10	D50	D90	Surf Area m2/g	True density g/cm3	Dielectric constant	Firing temp	Density g/cm3
COG	0.5	0.9	1.7	6.5	4.4	14	900	3.9
COG	0.4	0.7	1.1	6.2	5.7	87	880	5.4
X7R	0.5	0.8	1.3	3.7	6.1	2400	900	5.8

Table II. High frequency bulk electrical property summary

Material	Firing Temp (deg C)	Fired Density (g/cc)	ε'	tan δ	Q*f (GHz)
K14	900	3.90	12.86	1.526*e-3	5,437@ 8.3 GHz
K87	880	5.41	86.59	3.101*e-3	1,032@ 3.1 GHz

Table III. Electrical property data for the Class I dielectrics

Chip Size	1206	1206	1206	1206
Layer Count	7	7	7	7
Electrode % Ag Content	90	100	90	100
Firing Cycle	900°C/ 3 hr soak	900°C/ 3 hr soak	860°C/ 3 hr soak	860°C/ 3 hr soak
Dielectric constant	14	14	88	86
DF, 1 MHz (%)	0.005	0.004	0.137	0.152
Insulation Resistance				
RxC at 25C	921	1,094	>7662	>6662
RxC at 125C	864	944	7531	>6529
Temperature Coefficient				
-55	N006	N010	N003	N008
25	0	0	0	0
85	N003	N002	N045	N059
125	P021	P024	N060	N074

Table IV. Electrical property data for the Class II dielectric

Chip Size	1206	1206	1206
Layer Count	35	35	35
Fired Active Thickness	10.92	10.00	11.00
Electrode Type	EL 44-010	A290-D	A290-F
Electrode % Ag Content	90	95	100
Firing Cycle	900°C/ 6 hr soak	925°C/ 4 hr soak	900°C/ 4 hr soak
Capacitance (pF)	153,889	168,580	158,660
DF (%)	1.63	1.80	1.56
Insulation Resistance			
RxC at 25C	19,790	14,698	16,519
RxC at 125C	3396	3144	3363
Temperature Coefficient			
-55	-11.82	-8.82	-10.82
25	0	0	0
85	-5.08	-3.52	-4.45
125	-7.17	-3.57	-5.31

Table V. Class II dielectric thickness and active layer matrix

Chip Size	1206	1206	1206
Layer Count	10	50	35
Fired Active Thickness	3.00	3.00	10.00
Electrode Type	A290-F	A290-F	A290-F
Electrode % Ag Content	100	100	100
Firing Cycle	860°C/ 6 hr soak	860°C/ 6 hr soak	900°C/ 4 hr soak
Capacitance (pF)	120,597	649,740	157,540
DF (%)	2.65	2.59	1.61
Insulation Resistance			
RxC at 25C	22,886	22,134	17,944
RxC at 125C	1980	2099	2896
Temperature Coefficient			
-55	-9.86	-9.07	-9.41
25	0	0	0
85	-3.26	-3.81	-3.94
125	-4.02	-5.86	-4.74

EFFECT OF MILLING PROCESS ON CORE-SHELL MICROSTRUCTURE AND ELECTRICAL PROPERTIES FOR $BaTiO_3$-BASED Ni-MLCC

Y. Mizuno, T. Hagiwara, H. Chazono, and H. Kishi

Taiyo Yuden Co., Ltd., 5607-2 Nakamuroda Haruna-machi Gunma-gun Gunma 370-3347, Japan
Fax: 81-27-360-8315, Email: ymizuno@jty.yuden.co.jp

The effect of the process parameter in the milling process on the microstructural evolution and the electrical properties of multilayer ceramic capacitor (MLCC) samples were investigated in $BaTiO_3$ (BT)-Ho_2O_3-MgO system. The given damage on BT by milling process had a fatal influence on the microstructure. The mean grain size (D_{50}) decreased, judging from the statistical analysis by the field emission scanning electron microscopy (FE-SEM). The transmission electron microscopy (TEM) observation revealed that the rate of frequency for grains showing the core-shell microstructure increased as the damage increased for disk samples fired at 1320°C. Furthermore, the electrical properties were dependent on the degree of damage. The dielectric constant for MLCC samples decreased and the peak of dielectric constant at around room temperature shifted to a higher temperature as the damage increased. It was found that the MLCC sample showed the small leakage current and long mean lifetime as the degree of damage increased.

1. INTRODUCTION

In the past decade, the technology for fabricating multilayer ceramic capacitors (MLCCs) has made great strides by the need for higher volumetric efficiencies, and cost reduction. In order to meet these stringent requirements, the number of the dielectric active layers was increased, and the thickness was decreased, without compromising product reliability. Furthermore, the noble metal (Pd) is replaced by the base metal (Ni) as the internal electrode material to lower the production cost. In recent years, MLCCs with Ni internal electrodes composed of more than 400 layers of below 2μm thickness have been developed. A deliberate design of the microstructure for individual grains must be essential for such MLCCs with considerably thin dielectric layers since the microstructure has a decisive influence on the electrical properties and reliability of the MLCCs.

It was reported that the incorporation of the rare earth ion into BT lattice was dependent on the ionic radius of the rare earth ion,[1,2] and that the site occupancy of the rare earth ion affected the microstructural evolution.[3,4] On the other hand, the microstructure and the electrical properties are also dependent on the fabricating process, especially for the material with X7R characteristics. Because, it is well known that the material with flat temperature characteristics has so-called grain core-grain shell structure.[5,6]

Therefore, the influence of the degree of damage given by the milling process on the microstructure and the relationship between the microstructural evolution and the electrical properties for MLCC samples were investigated in BT-Ho_2O_3-MgO system.

2. EXPERIMENTAL

2.1. Sample Preparation

BT, reagent-grade MgO, Ho_2O_3, MnO, and $BaSiO_3$ were weighed in following composition: 1.000BT+ 0.005MgO+0.010Ho_2O_3+0.001MnO+0.015$BaSiO_3$. BT was synthesized hydrothermally with a mean particle diameter of about 0.5μm (SAKAI Chemical Industry Co., Ltd.). $BaSiO_3$was used as a sintering aid. They were mixed by ball milling for 15h. The degree of damage for BT powder was controlled by the amount of the ZrO_2 ball. The weight of medium used in a milling process was equal to that of BT for the sample-1, and was twice and four times as heavy as BT for the sample-2 and sample-3, respectively. The powder mixtures were subsequently dried and sieved. The obtained powders with an appropriate organic binder system were uniaxially pressed into disks

(10mmφ X 0.6mmt) and fired at 1320°C for 2h in a reducing atmosphere controlled by H_2, N_2, O_2, and H_2O, then cooled to room temperature in a weakly oxidizing atmosphere ($P(O_2)$=30 Pa at 1000°C).

MLCC samples were prepared by the following procedure. The obtained powders and an appropriate organic binder were dispersed into a slurry. Then green sheets with the thickness of 5μm were formed by the so-called doctor-blade method. After Ni internal electrodes were printed on these green sheets, they were laminated and pressed into a bar with 10 dielectric layers and cut into pieces. After burning out the binder, they were fired under the same condition as the disk samples.

2.2. Characterization

The samples were observed by the FE-SEM to study the particle diameter changes by milling process. The X-ray diffraction analysis was carried out for milled powders in order to evaluate the degree of damage given by milling process for BT powder.

The chemically etched surface for disk and MLCC samples were observed by the FE-SEM to investigate the microstructural changes. The grain diameter was measured for more than 500 grains by the intercept method and the mean grain size (D_{50}) was defined as the grain diameter giving 50% of the accumulated volume. In order to classify the microstructure of grain, 100 grains with not less than 0.3μm were observed by TEM. The phase transition of the sintered samples was characterized by DSC measurement in order to obtain the information only from the core region.

The capacitance and dissipation factor (tanδ) for the MLCC samples, which had been deaged thermally at 150°C for 1h, were measured using an LCR meter (HP4284A) at 1kHz 1Vrms on heating from -55°C to 150°C. A highly accelerated life test (HALT) of insulation resistance (IR) was conducted at 150°C under applied voltage of 20V/μm.

3 RESULTS AND DISCUSSIN

3.1 Powder characterization

Powder characteristics were investigated in order to compare the influence of milling damage. The powder features were summarized in Table I. The crystallinity of BT decreased as the amount of the media increased, which was determined by FWHM calculation in XRD analysis. Furthermore, the mean grain size decreased, and the frequency of chipped particles increased as the damage increased.

Table. I Powder features.

	D_{50}(μm)	BET(m^2/g)	FWHM(°)
raw BT	0.500	(2.40)	0.1036
sample-1	0.508	3.53	0.1080
sample-2	0.489	3.71	0.1113
sample-3	0.479	4.40	0.1224

3.2 Microstructural evolution

It is important to know whether the microstructure of MLCC samples is similar to that of disk samples or not. So the microstructure of MLCC samples was compared with that of disk samples. The mean grain size (D_{50}) for both samples fired at 1320°C determined from the chemically etched surface decreased as the degree of damage increased as summarized in Table II. Furthermore, D_{50} for MLCC samples were almost equal to that of the disk samples and that of the initial particle size. Therefore, little grain growth was also occurred for all MLCC and disk samples.

Table II. Comparison between the mean grain size for fired MLCC samples and for disk samples.

	D_{50}(μm) MLCC	D_{50}(μm) disk
sample-1	0.502	0.507
sample-2	0.478	0.497
sample-3	0.475	0.474

In order to obtain the information from the core region, DSC measurement was carried out since the core is composed of pure BT. The DSC profiles for MLCC samples were shown in Fig. 1 and the results of DSC measurement were summarized in Table III. The peak was broadened and the peak area decreased as the damage increased, whereas the peak temperature was

Table III. DSC peak temperature and its peak area.

	Peak temp. (°C)		Peak area (mcal/g)	
	disk	MLCC	disk	MLCC
sample-1	124.0	123.4	100.0	107.8
sample-2	124.2	123.3	86.7	69.2
sample-3	123.6	123.2	75.1	53.4

almost independent on the degree of damage. The change of the peak profile must be conjunction with the core volume and the presence of the internal stress in samples composed of the core-shell microstructure. The results of DSC measurement for MLCC samples were almost equal to that of disk samples.

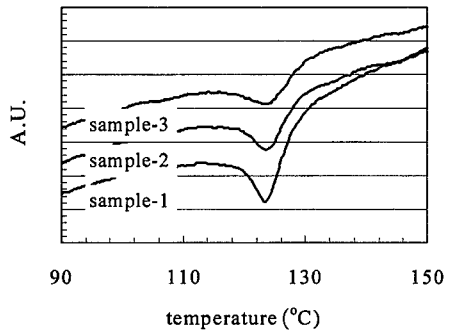

Fig.1 DSC profiles for MLCC samples fired at 1320°C.

Furthermore careful TEM observation revealed that there were grains without 90° domain pattern (named S-grain) and grains showing only 90° domain pattern (named C-grain), as well as grains showing core-shell microstructure (named CS-grain) for disk samples as shown in Fig. 2. It was reported that the grain showing core-shell microstructure (CS-grains) was formed by the reaction between the additives and BT.[7] It was noteworthy that there were C-grains and S-grains, when the careful and statistical observation by TEM was done. The rate of frequency for three kinds of grains was summarized in Table IV. Therefore, it was found that the rate of frequency for CS-grains and the shell region increased similarly as the damage increased for MLCC samples, judging from SEM observation and DSC measurement.

The given damage on BT by milling process has a fatal influence on not only the mean grain size but also the microstructure in a grain. It was suggested that the C-grain were mainly composed of the pure BT, judging from the fact that the grain showed only 90° domain, and that the S-grains were formed by the diffusion of the additives into a whole grain. The damage on BT surface accelerated the incorporation of additives like Ho, Mg, and Mn into BT. The active chipped particles reacted with the additives and formed S-grains. Therefore, the rate of frequency for CS-grains and S-grains increased as the damage increased.

Table IV. The rate of frequency for C-grains, CS-grains, and S-grains.

	C-grain (%)	CS-grain (%)	S-grain (%)
sample-1	50	46	4
sample-2	48	45	7
sample-3	23	70	7

3.3 Electrical Properties

The electrical properties, temperature characteristics of dielectric constant and tanδ were measured next. The dielectric constant for MLCC samples with 3.5μm dielectric thickness decreased monotonically with the degree of damage increased in all the measuring temperature range as shown in Fig. 3. Furthermore, the peak of dielectric constant at around room temperature shifted to a higher temperature as the damage increased. Arlt has reported that dielectric constant decreased with

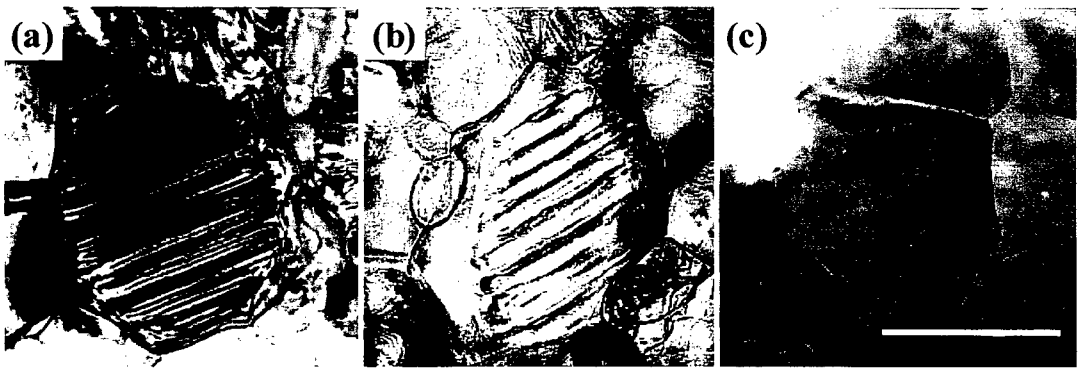

Fig. 2 The typical TEM micrographs; (a) is the C-grain, (b) is the CS-grain, and (c) is the S-grain (bar=0.5μm).

decreasing grain size for pure BT in the grain size range of below 0.7μm.[8] It was suggested that the decrease of dielectric constant with increasing damage was caused by the volumetric decrease of core region composed of pure BT. On the other hand, the tanδ increased as the damage given by milling process increased. It seemed that there was an intimate relationship between tanδ and the peak shift of dielectric constant.

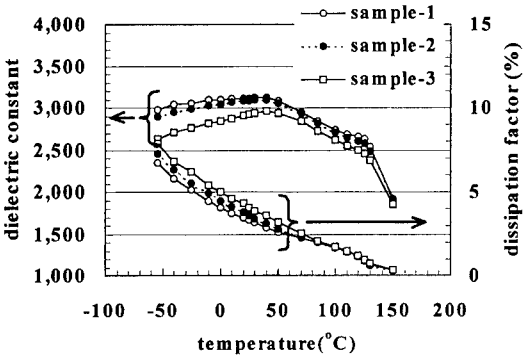

Fig. 3 The dielectric constant and the dissipation factor for MLCC samples as a function of temperature.

HALT was conducted on 20 MLCC samples and the leakage current of the samples with the mean time to failure (MTTF) were plotted in Fig. 4. The leakage current decreased and the lifetime was prolonged as the degree of damage increased. It was suggested that the volumetric ratio of shell region influenced on the load lifetime characteristics of MLCC samples.

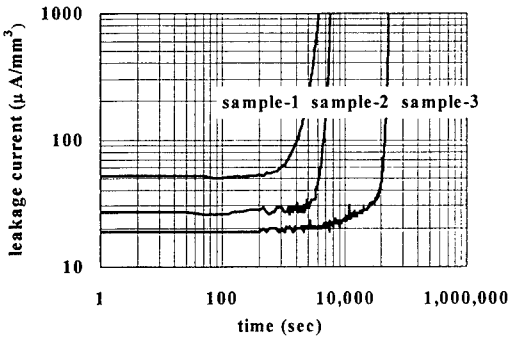

Fig. 4 Typical data of the time dependence of leakage current for MLCC samples at 150°C under 20 V/μm.

These findings indicated that electrical properties were strikingly affected by the microstructural evolution. Further investigation of the physical and chemical properties such as the compositional distribution in the shell region is necessary to elucidate the relationship between the microstructural evolution and electrical properties.

REFERENCES

1. H. Kishi, Y. Okino, M. Honda, Y. Iguchi, M. Imaeda, Y. Takahashi, H. Ohsato and T. Okuda, *Jpn. J. Appl. Phys.*, 36 5954-5957 (1997)
2. H. Kishi, N. Kohzu, Y. Mizuno, Y. Iguchi, J. Sugino, H. Ohsato and T. Okuda, *Jap. J. Appl. Phys.*, 38 5452-5456 (1999)
3. Y. Mizuno, Y. Okino, N. Kohzu, H. Chazono, and H. Kishi, *Jpn. J. Appl. Phys.*, 37, 5227-5231 (1998).
4. H. Chazono, Y. Okino, N. Kohzu and H. Kishi, "Effect Of Sm and Ho Addition on the Microstructure and Electrical Properties in MLCC with Ni Internal Electrode,"; pp.53-64 in *Ceramic Transaction*, Vol. 97, Edited by Jau-Ho Jean, T. K. Gupta, K. M. Nair, and K. Niwa, The American Ceramic Society (1999).
5. H. Saito, H. Chazono, H. Kishi, and N. Yamaoka, *Jpn. J. Appl. Phys.*, 30, 2307-2310 (1991).
6. T. R. Armstrong and R. C. Buchanan, *J. Amer. Ceram. Soc.*, 73 [5], 1268-1273 (1990).
7. H. Chazono and H. Kishi, *J. Amer. Ceram. Soc.*, 82 [10] 2689-97 (1999).
8. G. Arlt, *Ferroelectriccs,* 104, 217-227 (1990).

Reliability of Base Metal Electrode Multilayer Ceramic Capacitors

Larry A. Mann, James J. Beeson, Michael S. Randall,
Jonathan L. Paulsen, and Erik K. Reed
KEMET Electronics Corporation
PO Box 849
Fountain Inn, SC 29644-0849
FAX: 864-409-5665
e-mail: larrymann@kemet.com

INTRODUCTION

Technology for producing high capacitance value multilayer ceramic capacitors (MLCC) has advanced at a rapid rate in recent years. MLCC with capacitance values of up to 100 μF are now available from a number of manufacturers. The higher capacitance values come not from higher dielectric constant materials, but from the use of materials and processes which enable the manufacture of products with larger numbers of thinner dielectric layers.

Concurrently, the use of base metal electrode (BME) technology has become widespread. This is a consequence of the fact that larger capacitance value MLCC require increased amounts of metal electrode materials and the high cost of precious metals (most notably Pd and Ag/Pd alloys) which have traditionally been used in the manufacture of MLCC. Whereas MLCC manufactured with precious metals are fired in air, those produced with BME technology must be fired in a reducing atmosphere, thus potentially degrading the reliability of the dielectric through the formation of oxygen vacancies and other defects.

In this study, highly accelerated life testing (HALT) is used to compare the reliability of 0805 0.1 μF X7R MLCC with 50 volt ratings made with precious metal electrode (PME) technology and BME technology. These products were chosen for study because they fall on the boundary delineating MLCC products that can be economically produced using PME technology from those which can be more economically produced with BME technology. Both types of products were found to have excellent long term reliability, with expected useful lifetimes in excess of 1000 years at maximum rated temperature and voltage. The voltage acceleration factors observed were considerably larger than expected. This is believed to be due to the relatively thin dielectric layers employed in the product studied, and is consistent with other recent studies on MLCC made with thin dielectric layers.

EXPERIMENTAL PROCEDURES

The PME product tested was made with a proprietary low-fire dielectric system, and contained electrodes composed of 75% Ag/25% Pd. The PME product contained 38 dielectric layers, each approximately 12 microns thick. The BME product tested was made with a proprietary, reduction resistant dielectric and Ni electrodes. The BME product contained 23 dielectric layers, each 10 microns thick.

The products tested were all manufactured according to standard procedures, and screened for capacitance, dissipation factor, dielectric withstanding voltage, and insulation resistance using EIA limits for each characteristic prior to being placed on test. The HALT system used was purchased from Micro Instrument Co., Escondido, California. The system is capable of continuously monitoring the leakage current of each component on test, and recording the time at which the leakage current exceeds a pre-set value. In this case, a component was deemed to have "failed" when its leakage current exceeded 100 microamps.

HALT was conducted on both PME and BME products at combinations of temperatures between 155 °C - 175 °C, and voltages of 250 V to 400 V. The sample size for each test was 100 units. The median life, or time at which half the

components on test failed, was chosen as the statistic to represent the performance of each sample on test. The data were fitted to the following model, first suggested by Prokopowicz and Vaskas [1], to extract the voltage coefficient "n" and the activation energy "E_a", which represent the voltage and temperature acceleration factors, respectively.

$$\frac{t_1}{t_2} = \left(\frac{V_2}{V_1}\right)^n \exp\left[\frac{E_a}{k}\left(\frac{1}{T_1} - \frac{1}{T_2}\right)\right] \qquad (1)$$

ANALYSIS OF THE DATA

The HALT data for the BME and PME product are shown in Figures 1 and 2, respectively. The data in each case are plotted on log-normal scales, anticipating that the failures follow a normal distribution in time. While some curvature in the data is observed, especially at early times, straight lines were fitted to each population with a reasonable "fit," and were used to extract the median lifetime statistic. The median lifetimes of the PME product ranged from 800 minutes when tested at 400 V and 175 °C to 8800 minutes when tested at 325 V and 165 °C. The median lifetimes of the BME product under these same conditions were 260 minutes and 1600 minutes, respectively. (Note that the BME product was tested at up to 600 V. At 600V and 155 °C significant curvature in the data was observed, indicating that another failure mechanism was coming into play.)

The data shown in Figures 1 and 2 were used to calculate the voltage exponent "n" and activation energy "E_a" using Equation (1). The voltage exponent "n" of equation (1) was determined to be approximately 6.5 for the PME product tested, and 5.5 for the BME product tested. These values are considerably higher than the commonly accepted value of 3, which has been found to match the observed voltage acceleration of many MLCC in the past, but are in good agreement with those observed by Maher, who studied PME MLCC with dielectric thicknesses in the same range as those studied here. [2] Maher proposes that the higher than expected voltage coefficients in his study were, at least in part, due to reduced thickness of the dielectric layers. The activation energies, E_a, associated with both the PME and BME products were found to be in the range of 1.3-1.4 eV, which is also in good agreement with Maher.

The median lifetimes for the PME product predicted by the model represented in Equation (1) are shown in Table 1, using values of n = 6.5, E_a = 1.3 eV, and the observed median lifetime of 8800 minutes when tested at 325 V and 165 °C. The median lifetime predicted for this product at maximum rated voltage (50 V) and temperature (125 °C) is 100,000 years, and at 32 V and 85 °C, the predicted median lifetime is 130 million years. Similarly, the median life times for the BME product predicted by the model are shown in Table 2 using values of n = 5.5 , E_a = 1.3 eV and the observed median lifetime of 1600 minutes when tested at 325 V and 165 °C. The median lifetime predicted for this product at maximum rated voltage (50 V) and temperature (125 °C) is 3,000 years, and at 32 V and 85 °C, the predicted median lifetime is 2.3 million years.

CONCLUSIONS

The relatively large values of the voltage exponent observed in this study are believed to be due to the relatively thin dielectric layers in the products that were studied. The activation energies associated with degradation of both the PME and BME MLCC were found to be similar, indicating that similar degradation mechanisms are responsible for wearout of the products within the boundaries of the conditions studied. The BME product exhibited median lifetimes that were slightly shorter than those exhibited by the PME product studied.

The shorter predicted median lifetime of the BME product can be attributed in part to their thinner dielectric layers (10 microns vs 12 microns in the PME product), as this results in a higher dielectric field for a given applied voltage. It is likely that oxygen vacancies and other defects, consequences of the reduced atmosphere firing of the BME products, is also partially responsible for their reduced median lifetimes, relative to the PME product. Still, the expected median lifetime for both BME and PME products is certainly sufficient for even the most demanding applications, even at maximum rated conditions..

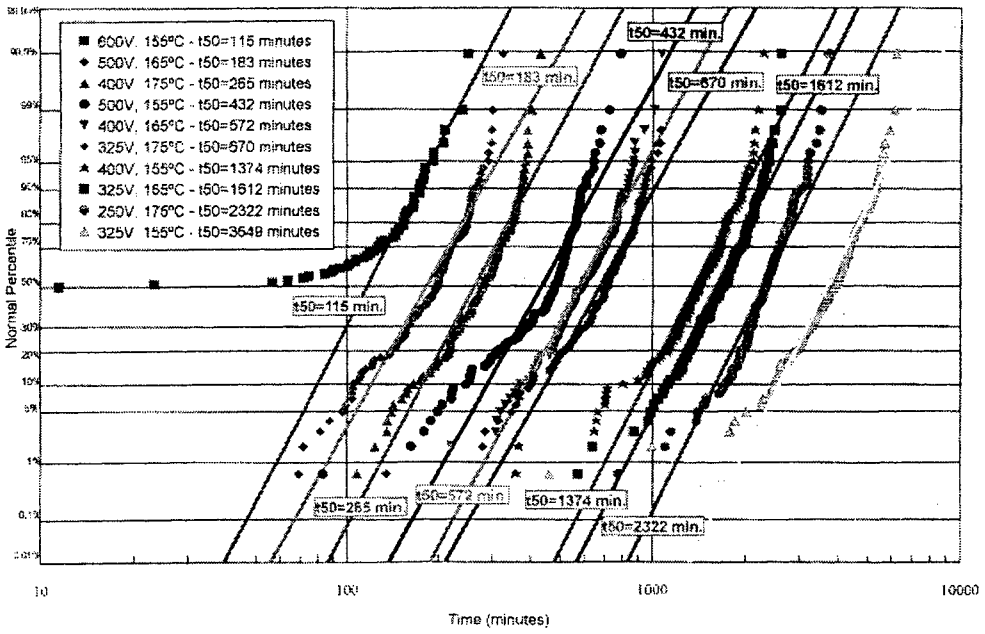

Figure 1. BME 0805 0.1 uF HALT Data

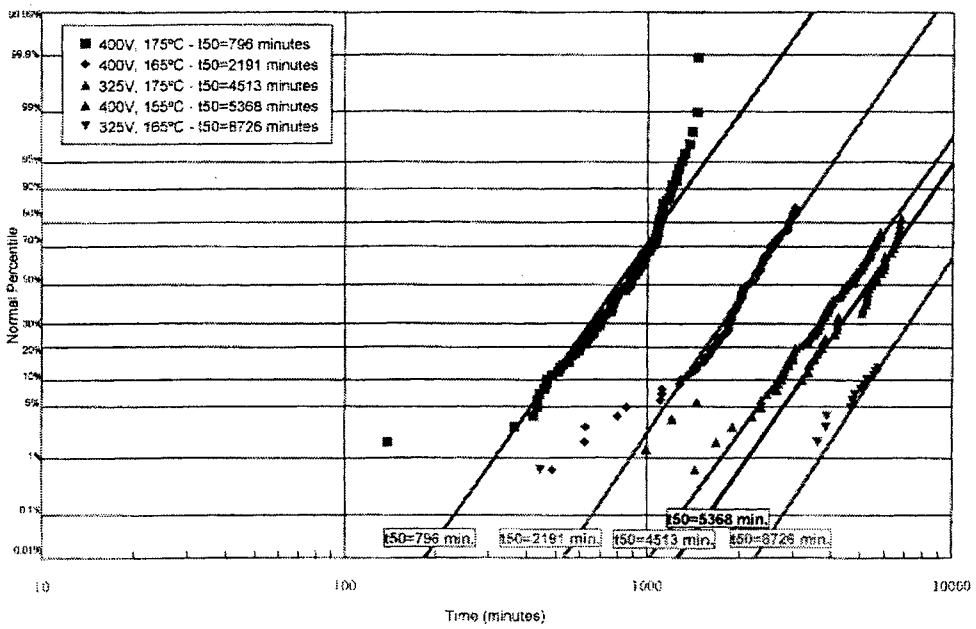

Figure 2. PME 0805 0.1 uF HALT Data

Table 1. Predicted Median Lifetimes for Precious Metal Electrode 0805 0.1 mF MLCC (from Equation (1) using observed values for "n" and "E_a")

Predicted Median Lifetimes (Years) for BME 0805 0.1 uF X7R MLCC								
		Temperature (C)						
		10	25	55	85	100	125	165
Acutal	0.5	4.9E +024	3.3E +023	3.3E +021	7.0E +019	1.3E +019	1.0E +018	3.2E +016
Use	1	5.4E +022	3.7E +021	3.6E +019	7.7E +017	1.4E +017	1.1E +016	3.6E +014
Voltage	5	1.5E +018	1.1E +017	1.0E +015	2.2E +013	4.1E +012	3.2E +011	1.0E +010
	10	1.7E +016	1.2E +015	1.1E +013	2.4E +011	4.5E +010	3.6E +009	1.1E +008
	16	8.0E +014	5.5E +013	5.4E +011	1.2E +010	2.1E +009	1.7E +008	5.3E +006
	32	8.9E +012	6.1E +011	6.0E +009	1.3E +008	2.3E +007	1.9E +006	5.9E +004
	50	4.9E +011	3.3E +010	3.3E +008	7.0E +006	1.3E +006	1.0E +005	3.2E +003
	100	5.4E +009	3.7E +008	3.6E +006	7.7E +004	1.4E +004	1.1E +003	3.6E +001

Table 2. Predicted Median Lifetimes for Base Metal Electrode 0805 0.1 mF MLCC (from Equation (1) using observed values for "n" and "E_a")

Predicted Median Lifetimes (Years) for BME 0805 0.1 uF X7R MLCC								
		Temperature (C)						
		10	25	55	85	100	125	165
Acutal	0.5	1.4E +021	9.4E +019	9.2E +017	2.0E +016	3.6E +015	2.9E +014	9.0E +012
Use	1	3.0E +019	2.1E +018	2.0E +016	4.3E +014	8.0E +013	6.3E +012	2.0E +011
Voltage	5	4.3E +015	3.0E +014	2.9E +012	6.2E +010	1.1E +010	9.0E +008	2.8E +007
	10	9.5E +013	6.5E +012	6.4E +010	1.4E +009	2.5E +008	2.0E +007	6.3E +005
	16	7.2E +012	4.9E +011	4.8E +009	1.0E +008	1.9E +007	1.5E +006	4.7E +004
	32	1.6E +011	1.1E +010	1.1E +008	2.3E +006	4.2E +005	3.3E +004	1.0E +003
	50	1.4E +010	9.4E +008	9.2E +006	2.0E +005	3.6E +004	2.9E +003	9.0E +001
	100	3.0E +008	2.1E +007	2.0E +005	4.3E +003	8.0E +002	6.3E +001	2.0E +000

REFERENCES

1. T. Prokopowicz and A. Vaskas, "Research and Development, Intrinsic Reliability, Subminiature Ceramic Capacitors," Final Report, ECOM-90705-F, 1969 NTIS AD-864068.

2. G. Maher, "Highly Accelerated Life Testing (HALT) of K-4500 Low Fired X7R Dielectric", Proceedings of the 9th US-Japan Seminar on Dielectric and Piezoelectric Ceramics, 1999, pp. 357-361.

Effect of Occupational Sites of Rare-earth Elements on Dielectric Properties of $BaTiO_3$

H. Kishi*, N. Kohzu, H. Chazono, J. Sugino[1], H. Ohsato[1], and T. Okuda[1]

General R&D laboratories, Taiyo Yuden Co. Ltd., 5607-2 Nakamuroda, Haruna-machi, Gunma-gun, Gunma 370-3347, Japan
[1]Department of Material Science and Engineering, Nagoya Institute of Technology, Gokiso-cho, Showaku, Nagoya 466-8555, Japan
*Fax: +81-27-360-8315, E-mail:hkishi@jty.yuden.co.jp

The relationship between the change in dielectric properties by re-oxidation treatment and the occupational sites of rare-earth ions in (La, Ho) and (Mg, Mn)-substituted $BaTiO_3$ was investigated. The lattice parameter result indicated that La ions occupied *A*-sites and Ho ions occupied both *A*- and *B*-sites. In the case of Ho-Mn-substituted samples, the decrease in lattice parameter and a shift of the Curie point (T_c) to higher temperatures by re-oxidation treatment were observed in the range in which Ho ions predominantly occupy *B*-sites (act as acceptors). On the other hand, the other samples showed little change. Electron spin resonance measurements revealed that these changes due to re-oxidation were based on the decrease of the ionic size of Mn due to the oxidation of Mn^{2+} to Mn^{3+} or Mn^{4+}. These results suggested that the formation of the donor-acceptor complexes prevented the valence change of Mn^{2+} in rare-earth and acceptor co-doped $BaTiO_3$ based systems. The occupational sites of Ho ions strongly affected the valence state of Mn and the dielectric properties of $BaTiO_3$.

INTRODUCTION

In recent years, multilayer ceramic capacitors (MLCs) with Ni internal electrodes composed of about 500 dielectric layers of below 2μm thickness have been developed. In nonreducible $BaTiO_3$ (ABO_3) based dielectric materials, it is well known that the resistance degradation of dielectrics strongly depends on the *A*/*B* molar ratio and the ratio of donor dopant to acceptor dopant.[1, 2] Saito *et al.* reported that highly reliable Ni-MLCs conforming to X7R specification were obtained, using $BaTiO_3$-MgO-Ho_2O_3 based dielectrics, in combination with a re-oxidation treatment at the cooling stage below 1000°C during in the firing process.[3] Resistivities of the dielectrics were increased by the addition of Ho_2O_3 when they were treated in an oxidizing atmosphere in the cooling stage. Kishi *et al.* reported the solubility of Mg and the rare-earth element into $BaTiO_3$ lattice.[4] It was confirmed that the larger ionic size rare-earth ions (La, Sm) predominantly dissolved in *A*-sites, and acted as donors, and the intermediate ionic size rare-earth ions (Dy, Ho, Er) dissolved in both the *A*-sites and *B*-sites, and acted as both donors and acceptors.

Albertsen *et al.* reported the changes in the Curie point (T_c) and the sample length under reduction and re-oxidation of $BaTiO_3$ ceramics containing Mn acceptors and various donor dopants on *B*-sites.[5] With increasing donor concentration, both the differences of the T_c and the sample length between the reduced and the re-oxidized state decreased. They deduced that the formation of donor-acceptor complexes suppressed the valence change of Mn^{2+} to Mn^{3+}. These results indicate that the change of dielectric properties between the reduced and the re-oxidized state is strongly affected by the valence change of acceptor dopant and the ratio of donor/acceptor dopant. Thus, in the case of rare-earth and acceptor co-doped $BaTiO_3$ based systems, understanding the effect of both the valence of acceptor dopant and the ratio of occupational sites of rare-earth elements on the dielectric properties is important to control the electrical properties of Ni-MLCs.

It is well known that Mn ions in $BaTiO_3$ lattice act as divalent acceptors like Mg ions on *B*-sites under the reducing condition, and Mn^{2+} is easily oxidized to Mn^{3+} or Mn^{4+} by re-oxidation treatment, while Mg maintains a constant valency of 2+. Therefore, in the present study, using two kinds of rare-earth element (La and Ho) and valence-stable Mg acceptor and valence-unstable Mn acceptor, we investigated the effect of re-oxidation treatment on the solubility of dopants and the dielectric properties of rare-earth and acceptor co-doped $BaTiO_3$ solid solutions, assuming the shell phase of $BaTiO_3$-MgO(MnO)-rare-earth based X7R dielectrics.

EXPERIMENTAL

Samples were prepared according to the formula $(Ba_{1-2x}R_{2x})(Ti_{1-x}M_x)O_3$; where *R*=La or Ho, *M*=Mg or Mn, x=0~0.10. This formula is based on a model substituting rare-earth and Mg(Mn) ions for Ba and Ti, respectively. The raw materials, $BaCO_3$, La_2O_3, Ho_2O_3, TiO_2, MgO and MnO were mixed and then calcined at 1250°C. The calcined powder containing an organic binder was pressed into disks, and then the disks were fired at 1380°C in a low oxygen atmosphere controlled by H_2, N_2, O_2 and H_2O (Po_2 of approximately 10^{-11}Pa) after the binder was burned out. Re-oxidation of the disks was carried out at 1250°C in air. The microstruc-

tures of the sintered samples were observed by scanning electron microscopy (SEM). Liquid In-Ga was applied to opposite surfaces of the disks as electrodes and dielectric properties of the samples were measured using a LCR meter. The ceramics were crushed and ground into a powder, and the identification of crystalline phases and the phase transition of the samples were characterized by powder X-ray diffraction (XRD) analysis and differential scanning calorimetry (DSC), respectively. The solubility of La, Ho, Mg and Mn into $BaTiO_3$ was determined by the behavior of the lattice parameters as a function of the doped amount x. In order to avoid the influence on the lattice parameters due to phase transition, high-temperature powder XRD analysis was carried out at 300°C which was much higher than the Curie point. The lattice parameters were determined precisely using the whole-powder-pattern decomposition method (WPPD[6]) program as described in a previous paper.[7] The valence state of Mn ions of the samples was confirmed by X band electron spin resonance (ESR) measurement.

RESULTS AND DISCUSSION

Changes of the microstructure and crystalline phases of the samples were not observed by re-oxidation treatment. No secondary phase appeared in the range up to x=0.100 for the La-Mg- and La-Mn-substituted samples. On the other hand, in the case of Ho-Mg- and Ho-Mn-substituted samples, a single phase of $BaTiO_3$ solid solution was obtained only up to x=0.010, and the pyrochlore ($Ho_2Ti_2O_7$) phase appeared as a secondary phase from x=0.015.

The effect of re-oxidation treatment on the solubility of dopants in rare-earth (La, Ho) and acceptor (Mg, Mn) co-doped $BaTiO_3$ solid solutions was investigated. The ionic radii of Ba, Ti, La, Ho, Mg and Mn are summarized as follows: *A*-site (12 coordinate): Ba^{2+}=1.610 Å, La^{3+}=1.360 Å, Ho^{3+}=1.234 Å; and *B*-site (6 coordinate): Ti^{4+}=0.605 Å, La^{3+}=1.032 Å, Ho^{3+}=0.901 Å, Mg^{2+}=0.720 Å, Mn^{2+}=0.670 Å, Mn^{3+}=0.580 Å, Mn^{4+}=0.530 Å. The ionic radii of Ho ions in a 12-coordinate system are based on the relationship between coordination number and effective ionic radii according to Shannon's table.[8] The substitution sites were determined based on the change of the lattice parameter. Fig. 1 shows the lattice parameters of the samples measured at 300°C, as determined by WPPD. Ho-Mn-substituted samples showed a large difference in the lattice parameter by re-oxidation treatment, while the other samples showed little change. In the case of La-Mg- and La-Mn-substituted samples, the lattice parameter decreased monotonously as a function x. This indicated that La ions mainly occupied the *A*-site accompanied by *B*-site occupation of Mg or Mn^{2+} ions. In the case of the reduced state Ho-Mg- and Ho-Mn-substituted samples, the change in lattice parameter behavior was as follows. Initially, the lattice parameter decreased gradually up to x=0.015 for the Ho-Mg-substituted sample and x=0.010 for the Ho-Mn-substituted sample, and then showed little change up to x=0.025 for the Ho-Mg-substituted sample and x=0.020 for the Ho-Mn-substituted sample. In the third stage, the increase in the lattice parameter was observed up to x=0.100 for both samples. Thus, the change of the lattice parameter for the reduced state samples is considered as follows. In the first stage, Ho mainly occupied the *A*-site accompanied by *B*-site occupation of Mg or Mn^{2+} ions. The occupation ratio of Ho in the *A*-site decreased during the second stage and then Ho ions mainly occupied the *B*-site along with Mg or Mn^{2+} ions in the third stage. On the other hand, in the case of the Ho-Mn substituted samples, the difference of

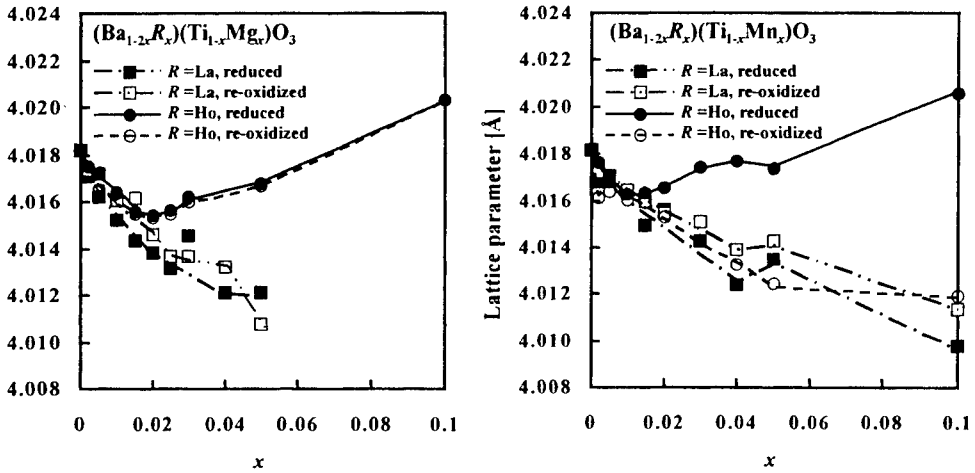

Fig. 1. Lattice parameters of $(Ba_{1-2x}R_x)(Ti_{1-x}M_x)O_3$ solid solutions measured at 300°C as a function of x.
(R=La, Ho, M=Mg, Mn)

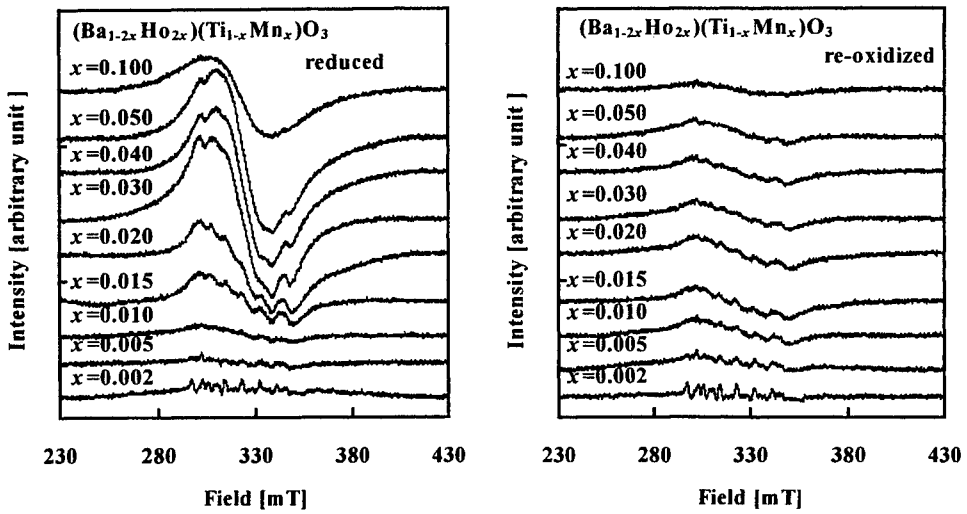

Fig. 2. ESR spectra of the reduced state and the re-oxidized state $(Ba_{1-2x}Ho_x)(Ti_{1-x}Mn_x)O_3$ solid solutions as a function of x.

lattice parameter between the reduced state and the re-oxidized state samples was observed above x=0.020. The decrease of the lattice parameter by re-oxidation treatment increased with increasing doped content.

To clarify the effect of Mn on the change of the lattice parameter by re-oxidation treatment, the valency of Mn of La-Mn- and Ho-Mn-substituted samples was examined. In the case of the reduced state samples, the intensity of ESR spectra of Mn^{2+} increased by increasing the amount doped. By re-oxidation treatment, La-Mn-substituted samples showed little change in the ESR spectra, while Ho-Mn-substituted samples showed a large difference. Fig. 2 shows ESR spectra of the reduced state and the re-oxidized state Ho-Mn-substituted samples. In the case of Ho-Mn-substituted samples, the intensity of ESR spectra of Mn^{2+} was strongly depressed in the range above x=0.015 by re-oxidation treatment. This indicated that a portion of doped Mn^{2+} ions were oxidized to Mn^{3+} or Mn^{4+}. Thus, it is considered that the decrease of the lattice parameter of Ho-Mn-substituted samples by re-oxidation treatment is based upon the decrease of the ionic size of Mn ions due to the valence change of Mn^{2+} to Mn^{3+} or Mn^{4+}.

The T_c of the reduced state and the re-oxidized state samples was determined by DSC and dielectric measurement. DSC was carried out for samples with lower electrical resistivites, for which it is impossible to measure dielectric properties. Fig. 3 shows the T_c shift of the reduced state and the re-oxidized state of the samples. In the case of La-Mg- and La-Mn-substituted samples, Tc decreased almost linearly with increasing doped content. On the other hand, the slope of the Tc shift of Ho-Mg- and Ho-Mn-substituted samples became steeper with increasing doped content. By re-oxidation treatment, the T_c of the Ho-Mn-substituted samples shifted to higher temperatures with increasing doped content above x=0.015, while the change in T_c of the other samples was not observed. These results correspond well with the results of the lattice parameters. Thus, it is considered that the smaller ionic size Mn^{3+} and Mn^{4+} ions induce the shift of Tc by re-oxidation treatment.

The lattice parameter as well as the T_c measurements indicated the effect of valence change of Mn ions by re-oxidation treatment. In the case of La-Mn-substituted samples, the changes in the lattice parameters and Tc were not observed. It is expected that La-donors compensate Mn-acceptors. On the other hand, in the case of the Ho-Mn-substituted samples with smaller doped content below x=0.010, the changes in the lattice parameters and T_c were not observed. As mentioned above, Ho ions mainly act as donor dopants up to x=0.010 and as acceptor dopants above x=0.020. Thus, in the Ho-Mn-substituted $BaTiO_3$ system, it is expected that Ho-donors compensate Mn-acceptors in the range up to x=0.010 and excess Mn-acceptors increase with increasing Ho-acceptors in the range above x=0.020. Albertsen *et al.* reported that Mn^{2+} could not be oxidized in donor-acceptor charge complexes, and the T_c of reduced and re-oxidized material coincided for equivalent concentrations of Mn-acceptor and donor.[5] The present results showed good agreement with the result of Albertsen *et al.*, and can be explained as follows. In the case of La-Mn-substituted samples, donor-acceptor complexes $[2La_{Ba}^{\cdot}\text{-}Mn_{Ti}^{''}]$ prevent valence change of Mn^{2+}, so that the differences of both the lattice parameters and the T_c between the reduced state and the re-oxidized state are negligible. On the other hand, in the case of Ho-Mn-substituted samples, for equal concentrations of Ho-donors and Mn^{2+}-acceptors, donor-

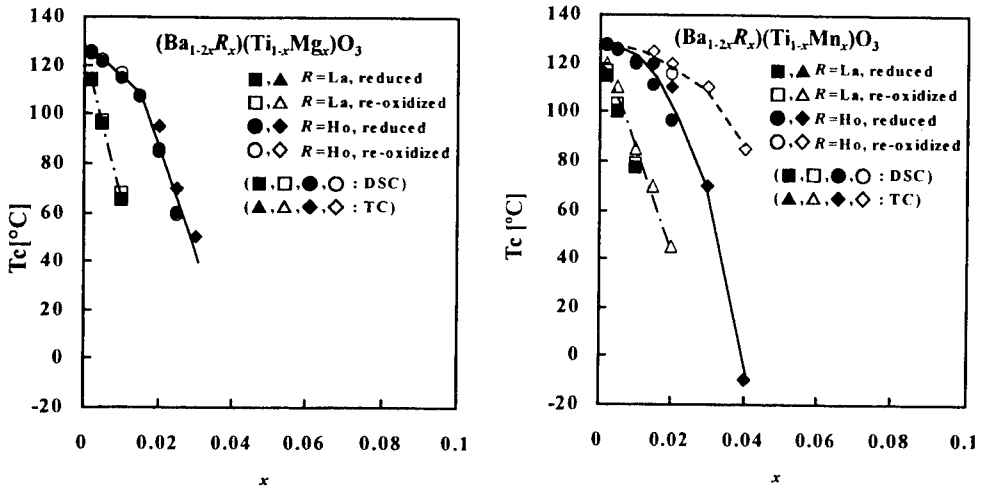

Fig. 3. Change in Tc of the reduced state and the re-oxidized state $(Ba_{1-2x}R_x)(Ti_{1-x}M_x)O_3$ solid solutions. (R=La, Ho, M=Mg, Mn)

acceptor complexes [$2Ho_{Ba}^{\cdot}$- Mn_{Ti}''] are formed in the range up to x=0.010, so that oxidation of Mn^{2+} is prevented. In the range above x=0.020, as Ho-acceptors increase, the differences of both the lattice parameters and the T_c between the reduced state and the re-oxidized state increase with increasing free Mn^{2+} which can be oxidized to Mn^{3+} or Mn^{4+}. Consequently, it was confirmed that the change of the occupational sites of Ho ions in $BaTiO_3$ lattice strongly affected the valence state of acceptor ions and resultant dielectric properties.

CONCLUSION

The effect of re-oxidation treatment on the solubility in dopants and the dielectric properties in rare-earth (La, Ho) and acceptor (Mg, Mn)-substituted $BaTiO_3$ solid solutions was investigated. High-temperature powder XRD analysis revealed that La ions occupied A-sites and Ho ions occupied both A- and B-sites. By re-oxidation treatment, Ho-Mn-substituted samples showed a decrease of the lattice parameter in the range above x=0.020, while the other samples showed no change. The intensity of ESR spectra of Mn^{2+} in Ho-Mn-substituted samples was strongly depressed in the range above x=0.015 by re-oxidation treatment. The Tc of Ho-Mn-substituted samples shifted to higher temperatures by increasing the amount doped above x=0.015 by re-oxidation treatment, while La-Mn-substituted samples showed no change. It is considered that the changes in the lattice parameter and the Tc of Ho-Mn substituted samples by re-oxidation is based upon the decrease of the ionic size of Mn due to the valence change of Mn^{2+} to Mn^{3+} or Mn^{4+}. Moreover, these results suggested that the formation of the donor-acceptor complexes prevent the valence change of Mn^{2+} in rare-earth and acceptor co-doped $BaTiO_3$ based systems. It was determined that the occupational sites of Ho in $BaTiO_3$ lattice strongly affected the valence state of acceptors and the dielectric properties. Further investigation of the physical and chemical properties such as the compositional distribution, the concentration of the additives, and the occupational sites of the rare-earth ions in the shell phase is necessary to understand the re-oxidation effect on the electrical properties of Ni-MLCs.

REFERENCES

1. Y. Sakabe, K. Minai and K. Wakino, *Jpn. J. Appl. Phys.*, Suppl. **20-4**, 147-150 (1981)
2. Y. Nakano, A. Satoh, A. Hitomi and T. Nomura, *Ceram. Trans.*, **32**,119-128 (1993)
3. H. Saito, H. Chazono, H. Kishi and N. Yamaoka, *Jpn. J. Appl. Phys.*, **30**, 2307-2310 (1991)
4. H. Kishi, N. Kohzu, J. Sugino, H. Ohsato, Y. Iguchi and T. Okuda, *J. Euro. Ceram. Soc.*, **19**, 1043-1046 (1999)
5. K. Albertsen, D. Hennings and O. Steigelmann, *J. Electroceram*, **2:3**, 193-198 (1998)
6. H.Toraya, *J. Appl. Crystallogr.*, **16**, 440-447 (1986)
7. H. Ohsato, M. Imaeda, Y. Okino, H. Kishi and T. Okuda, *Advances in X-ray Analysis*, **40** (CD-ROM: International Centre for Diffraction Data) (1997)
8. R. D. Shannon, *Acta. Crystallogr.*, **A32**, 751-767 (1976)

Cation diffusion in Barium Titanate

Jun-ichi ITOH, Isamu YASHIMA, Naoki OHASHI*,Isao SAKAGUCHI*,

Hajime HANEDA* and Junzo TANAKA*

Corporate R&D Center, Mitsui Mining & Smelting Co., Ltd. 1333-2 Haraichi, Ageo-shi, Saitama 362-0021, JAPAN

* Advanced Materials Lab., National Institute for Materials Science 1-1 Namiki, Tsukuba-shi, Ibaraki 305-0044, JAPAN

FAX : 81-298-55-1196, E-Mail : ITO.Junichi@nims.go.jp

Introduction

Multi-layer ceramic capacitors (MLCC) have been established for the production of dielectric layers thickness $\leq 3\,\mu$m and electrode thickness about 0.5 μm. To keep costs down, nickel is generally used as internal electrodes in MLCCs, and a number of workers have reported studies for Ni-MLCC. However , the problem such as ion migration and delamination which occur at the metal electrode – dielectric interface, was not still made clear.

We present the results of using secondary ion mass spectrometry to evaluate the diffusion behavior of Ni in non-doped, Ho-doped $BaTiO_3$ and Single crystal $BaTiO_3$. The effect of Ho-doping on the properties of Ni-MLCC will be discussed in relation with the defect structures.

Experimental

In this study, we evaluated the diffusion of Ni using various types of sintered BTO-based materials and single-crystal BTO. The BTO-based materials were obtained by normal sintering as follows. The starting materials — $BaTiO_3$ (BT-05; Sakai Chemical Industry Co., Ltd.) with Ho_2O_3 (Nippon Yttrium Co., Ltd.) as a dopant — were weighed according to the amounts shown in Table 1, and ball-milled for 15 hours. A metal die (approx. pressure 600 kg/cm^2) was used to form the resulting powder into tablets with a diameter of 10 mm and thickness 2 mm, which were then fired to obtain sintered ceramic samples. When firing, the temperature was increased at a rate of 300°C/hr, and held at 1360°C for 1 hour. The single-crystal BTO were used commercial samples (CASTECH) for comparing. The physical properties of these sintered and single-crystal samples are listed in Table 1.

To evaluate the Ni diffusion properties were polished to mirror surface with a diamond abrasive, cut to a size of 3×3×1 mm. The Ni films (about 200 A thick) were deposited the polished surfaces by vacuum vapor deposition at $\leq 10^{-6}$ Torr. NiO powder was used as the nickel source.

The Non-doped, Ho-doped and single-crystal BTO samples were diffusion-annealed at temperatures from 1100°C to 1400°C. Depth profiles of the Ni concentration were measured by secondary ion mass spectrometry (SIMS,CAMECA IMS-4F)in the depth direction. After these measurements, the crater depth was measured by a surface roughness gage (Dektak 3030) to obtain data in the depth direction. The diffusion coefficients were calculated from the results.

Results

Fig.1 shows the typical diffusion profiles obtained after annealing for 30 minutes at 1300°C. All the samples were found to have different diffusion profiles, from which it can be inferred that the diffusion behavior differs according to the composition and micro-structure of the samples. These profiles can be divided into two regions — a region corresponding to volume diffusion near the surface (I), and a region corresponding to high diffusivity path at deeper side (II) [1]. The high diffusivity paths correspond to grain boundaries and pores in the polycrystalline samples, and defects such

Table 1 Properties of Non-doped, Ho-doped and Single Crystal $BaTiO_3$.

	Name Composition	Non-doped $BaTiO_3$	Ho-doped $BaHo_{0.01}TiO_3$	Single-Crystal $BaTiO_3$
Chemical Analysis	A/B	1.00	1.01	< 1
	SrO (%)	0.02	0.02	< 0.001
	CaO (%)	< 0.001	< 0.001	< 0.001
	Na_2O (%)	0.001	0.001	< 0.001
	SiO_2 (%)	0.002	0.002	0.001
	Al_2O_3 (%)	0.001	0.001	< 0.001
	Fe_2O_3 (%)	< 0.001	< 0.001	< 0.001
XRD	a-axis (Å)	3.995	3.985	(4.014)
	c-axis (Å)	4.036	4.027	
	Grain size (μm)	40	2	-
	Relative density (%)	93.5	94.9	
	Permittivity / 1kHz	3000	21300	3600
	tan δ / 1kHz	0.02	0.23	0.01
	Resistivity (Ω·cm)	10^{11}	10^{6}	
				Direction <100>

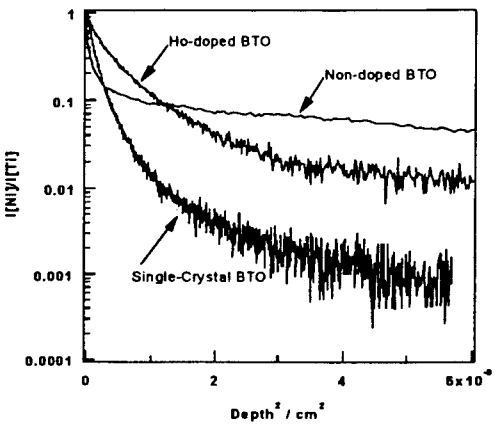

Fig.1. Diffusion profile of ^{58}Ni obtained Non-doped $BaTiO_3$, Ho-doped $BaTiO_3$ and single-crystal $BaTiO_3$ annealed at 1300℃ for 30 min.

therefore analyzed the diffusion profiles at each temperature from 1100°C to 1400°C, and calculated the volume and high diffusivity path coefficients for each.

< Volume diffusion of Ni >

To analyze the volume diffusion (in region I), we calculated the volume diffusion coefficient D_v (cm^2/s) by fitting our results to a solution of the thin film diffusion formula shown in Equation (1)[2].

$$c = \frac{\alpha}{2\sqrt{\pi D t}} \exp\left(-\frac{x^2}{4D_v t}\right) \quad (1)$$

Where, c is the concentration of Ni ions at a distance x (cm) from the surface, and t is the diffusion time (s). Fig.2 shows an Arrhenius plot of the volume diffusion coefficients D_v for non-doped, Ho-doped and single-crystal BTO. From these results, it can be shown that they roughly follow individual Arrhenius formulae as follows:

Non-doped BTO:

$D_v = 1.4\times10^{-6} \exp(-241.9\ [kJ/mol]/RT)$ (2)

Ho-doped BTO:

$D_v = 4.4\times10^{-6} \exp(-227.7\ [kJ/mol]/RT)$ (3)

Single-crystal BTO:

$D_v = 6.7\times10 \quad \exp(-473.2\ [kJ/mol]/RT)$ (4)

The Ho-doped samples have much higher diffusion coefficients, which seems to be because the activation energy of the ceramic samples is from 230–240 kJ/mol, whereas that is the single-crystal sample is much larger at about 470 kJ/mol.

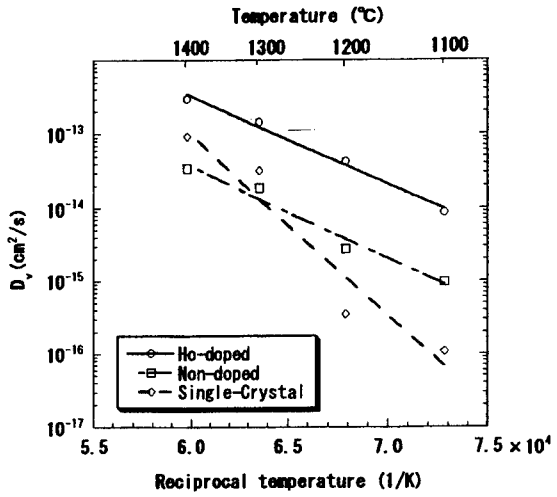

Fig.2. Arrhenius plot of volume diffusion coefficients (D_V) obtained from several $BaTiO_3$s annealed in static air.

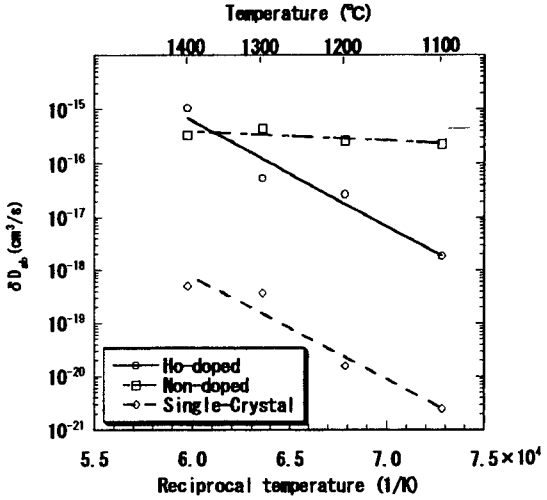

Fig.3. Arrhenius plot of $\delta \cdot D_{gb}$ obtained from several $BaTiO_3$s annealed in static air. The δ and D_{gb} are the width and the diffusion coefficients of high diffusivity path.

<High diffusivity path diffusion of Ni>

High diffusivity path diffusion can be analyzed using the following analytical formula when $D_v \cdot t < \delta$, where δ (cm) is the distance between grain boundaries (or dislocations) [3].

$$\delta D_{gb} = 0.66\left(-\frac{d \ln C}{dx^{6/5}}\right)^{-5/3}\left(\frac{4D_v}{t}\right)^{1/2} \quad (5)$$

where D_{gb} (cm²/s) is the grain boundary diffusion coefficient, and D_v is the volume diffusion coefficient obtained from Equation (1).

Fig.3 shows an Arrhenius plot of the diffusion coefficients (D_{gb}). In a similar fashion, the values of D_{gb} for each sample can be expressed as following equations:

Non-doped BTO:

$\delta D_{gb} = 4.0\times10^{-15}\exp(-32.5\ [\mathrm{kJ/mol}]/RT)$ (6)

Ho-doped BTO:

$\delta D_{gb} = 3.7\times10^{-4}\exp(-375.9\ [\mathrm{kJ/mol}]/RT)$ (7)

Single-crystal BTO:

$\delta D_{gb} = 2.5\times10^{-7}\exp(-473.2\ [\mathrm{kJ/mol}]/RT)$ (8)

Discussion

<The effects of doping with Ho>

In Fig.2, when we compared the Ho-doped and non-doped BTO, which have the same polycrystalline structure, the diffusion activation energies were found to be of the same order, but the Ho-doped sample had a higher diffusion coefficient. Thus, these samples also have activation energy that is equivalent to the migration energy at B-sites. On the other hand, the reason for the larger diffusion coefficient in the Ho-dopes sample can be explained using the following defect formula. When BTO perovskite with a cation-stoichiometric composition is doped with Ho_2O_3, it is thought that V_{Ti}'''' is produced as shown by the following formula:

$$3Ho_2O_3 + 6TiO_2 \rightarrow 6Ho_{Ba}^{\cdot} + V_{Ba}'' + 6Ti_{Ti}^{\times} + V_{Ti}'''' + 21O_O^{\times} \quad (9)$$

The radii of Ti and Ni ions are quite similar (0.605 A and 0.69 A, respectively[4]), and it is thus thought that Ni ions can easily occupy Ti sites. Accordingly, the V_{Ti}'''' produced by doping with Ho_2O_3 allows the occupancy of Ni, and is thus thought to contribute to the promotion of Ni ion diffusion.

<High diffusivity path diffusion and microstructure>

Fig.4 shows the microstructure of each sample under an optical microscope. The non-doped BTO sintered sample has a grain size of about 40 μm with a lot of pores present at triple-junctions. Fig.3 shows that the high diffusivity path diffusion of Ni in non-doped BTO is much less temperature-dependent than

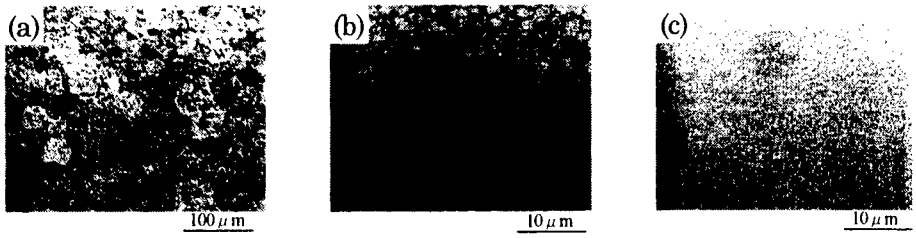

Fig.4 Photomicrographs of (a) Non-doped ,(b)Ho-doped and (c) Single-Crystal BTO annealed at 1100℃

in the other samples, and has a comparatively large value even at lower temperatures. This is thought to be because the pores observed at triple-junctions are connected together like pipes in the depth direction, and act as high diffusivity paths.

In the Ho-doped BTO, the grain size is only about 2–3 μm, which is much less than that of the non-doped sample in Fig.4. For this reason, the grain boundary surface area is much larger than non-doped BTO and the high diffusivity paths diffusion in this material is primarily grain boundary diffusion, with a small contribution made by the pores observed at triple-junctions.

As for high diffusivity path diffusion in the single-crystal sample, it is thought that dislocations in the crystal contribute to the diffusion of Ni ions. This diffusion in the single crystal is interpreted as being equivalent to grain boundary diffusion in the polycrystalline samples.

The diffusion profile (Fig.1) of Ho-doped BTO, which relies on pore diffusion and grain boundary diffusion, describes an intermediate curve that lies between the profile of non-doped BTO, which is dominated by pore diffusion, and the profile of single-crystal BTO, which is dominated by diffusion along dislocations. The high diffusivity in single-crystal BTO can thus be interpreted as being equivalent to grain boundary diffusion in a polycrystalline material.

Conclusion

We have evaluated the diffusion behavior of Ni in non-doped and Ho-doped polycrystalline BTO and single-crystal BTO.

Differences in the behavior of Ni volume diffusion are thought to be due to defect structure, and to be dependent on the quantity of $V_{Ti}^{''''}$ positive ion defects. It has also become clear that differences in the diffusion behavior along high diffusivity paths are closely related to the crystalline microstructure. In non-doped BTO, pores are distributed in large numbers at triple-junction, and diffusion along pores is predominant. Ho-doped BTO has a small grain size, which clearly contributes to pore diffusion and grain boundary diffusion. And as for single-crystal BTO, although diffusion along dislocations equivalent to grain boundaries was observed, the Ni diffusion rate is much slower than in polycrystalline BTO. Accordingly, the distribution of pores and grain boundaries is thought to dominate high diffusivity path diffusion, so suppressing the diffusion of Ni into the bulk requires the use of a compact sintered material with a low pore ratio.

Reference

1) I.Sakaguchi and H.Haneda, J. Solid State Chem. 124, 195–97 (1996).
2) J.Crank,"The Mathematics of diffusion", Chap. 3.3, Oxford Univ. Press, London (1975)
3) A.D.Le Clarie, Brit. J. Appl. Phys.14, 351–56 (1963).
4) R.D.Shannon, Acta Cryst., 32A, 751–67 (1976)

Oxygen in Diffusion and Defect Structure in Perovskite Oxides

I. Sakaguchi, H. Haneda, S. Hishita, N. Ohashi and M. Sekita

Advanced Materials Lab., National Institute for Materials Science, 1-1 Namiki, Tsukuba-shi, Ibaraki 305-0044, JAPAN

FAX: 81-298-55-1196, E-Mail : HANEDA.Hajime@nims.go.jp

INTRODUCTION

Oxygen diffusion and their defects influence many properties in various functional ceramics[1]. It is well known that the sinterability is directly controlled by the diffusion coefficients. The electrical conductivity has a close relation with oxygen vacancy concentration in perovskite compounds. Furthermore some defect decreased the photoluminescence intensity of $TbAlO_3$ perovskite single crystal[2].

We had already reported the oxygen diffusion and defect structure of oxygen sub-lattice in some perovskite oxides[3]. In these results, the oxygen metastable vacancies exist in the perovskites compounds. The relationship between grain-boundary diffusion of oxygen ions and PTCR effects had been also discussed in the 6th US-Japan seminar. In the present report we survey the oxygen diffusion properties in the perovskite compounds and focus our attention on the effects of A/B ratio on oxygen vacancy concentration in the perovskite oxides, particularly $TbAlO_3$.

Experimental

In the present study the oxygen diffusivities were evaluated in some perovskites, i.e. $BaTiO_3$ (BT), $SrTiO_3$ (ST), and $TbAlO_3$(TA). Commercial single crystals were used for SrTiO3 and $BaTiO_3$, and TA single crystals that were grown in N_2 or N_2-H_2 atmosphere were also done, respectively. Photoluminescence concerned with Tb^{3+} was observed in $TbAlO_3$ single crystal grown in N_2-H_2[2]. However the crystals grown in N_2 had not this characteristic, and were colored pale brown with Tb^{4+} ions.

To evaluate an effect of donor doping on oxygen diffusivity, Nb-doped $SrTiO_3$ single crystal and La-doped $BaTiO_3$ poly crystals were applied.

All samples were cut to desired plate form, i.e. 0.4 by 0.4 by 0.1cm, and the one side of the large faces were polished to optical flatness with diamond paste of decreasing particle size (10, 3, 1, 0.5 μm).

Diffusion coefficient was determined by a solid-gas exchange technique[4]. After being cleaned with water, ethanol, acetone, and ethanol, the samples were placed inside a platinum crucible with platinum sucseptor in a vessel of a RF furnace. The system was evacuated, and the ^{18}O-enriched oxygen gas of 5kPa pressure was introduced into vessel. For $TbAlO_3$ ^{18}O-enriched carbon dioxide gas with a few percent carbon monoxide was also used to evaluate an effect of oxygen partial pressure on oxygen diffusion coefficients. The sample crucible was firstly heated at 873K for 15 minutes to maintain the constant concentration at sample surface, and then the temperature was elevated to a desired temperature for isotope exchange. The temperature was monitored by an optical pyrometer. Although the temperature accuracy of pyrometer was in 10K, the temperature variation among samples in a same experimental cycle is believed to be less than few degrees.

After diffusion annealing, depth profiles (concentration versus depth) of ^{18}O in the samples were measured by means of a secondary ion mass spectrometer (hereafter denoted, SIMS (CAMECA; IMS4F))[5]. The negative secondary ions, $^{18}O^-$ and $^{16}O^-$ were detected as a function of sputtering time.

Results and Discussion

Typical ^{18}O concentration versus penetration

curves in TA single crystals is presented in Figure 1. If the surface is maintained at a constant concentration of ^{18}O c_g, that is the same concentration as in the gaseous phase, and if the concentration in the solid is initially uniform ($c(x,0)=c_0$, natural abundance), the following relation can be used to calculate the volume diffusion coefficients, D[6];

$$\frac{c(x,t)-c_0}{c_g-c_0} = \mathrm{erfc}\left(\frac{x}{2\cdot\sqrt{D\cdot t}}\right) \quad (1)$$

where c(x, t) is the ^{18}O concentration at the depth x from the sample surface after a diffusion duration time, t. Solid line in Fig.1 shows the result of the fitting procedure, and sets a volume diffusion coefficient, 1.86×10^{-12} cm^2/s.

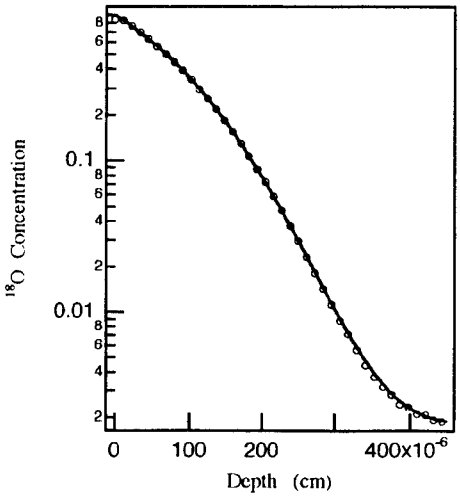

Fig. 1. Typical diffusion profile in $TbAlO_3$ single crystal grown in H_2-N_2 atmosphere. Open circles: observed data, solid line: calculated values using Eq.(1). Diffusion annealing, at 1465K for 1h. Calculated diffusion coefficient, 1.86×10^{-12} cm^2/s.

Temperature dependencies of the oxygen volume diffusion coefficients in BT and ST are shown in Figure 2. Seen in this figure, all "Pure" crystals have higher values than that of the donor doped samples, indicating that the oxygen diffusion coefficients correspond to that of extrinsic, and two kinds of "pure" perovskites have higher oxygen defects concentration than of those doped donor. The diffusion coefficients in the 100 ppm Nb-doped ST is two orders magnitude higher than 5000ppm Nb-doped. According to these results, oxygen ions diffuse through oxygen vacancy that were annihilated as following equation due to donor doping;

$$Nb_2O_5 + 2Ti_{Ti}^{\times} + V_O^{\bullet\bullet} \rightarrow TiO_2 + 2Nb_{Ti}^{\bullet} + O_O^{\times} \quad (2)$$

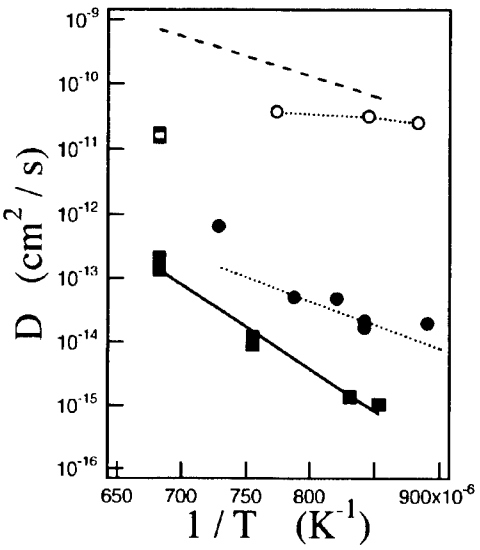

Fig.2. Oxygen Diffusion Coefficients in $SrTiO_3$ (ST) and $BaTiO_3$ (BT). Dashed line: pure, a open square: 100 ppm Nb-doped and closed squares and solid line: 5000 ppm Nb-doped ST single crystals, respectively. Dotted line and open circles: pure BT single crystal, and small dotted line and closed circles: La-3000ppm doped BT polycrystal, respectively.

We reach a following conclusion by the higher diffusion coefficients in "pure" samples; small amounts of excess titanium ions dissolved in the perovskite structure as follows;

$$TiO_2 \rightarrow Ti_{Ti}^{\times} + V_{Sr}^{''} + 2O_O^{\times} + V_O^{\bullet\bullet} \quad (3)$$

The effect of cation nonstoichiometric on the concentration of oxygen vacancy, above mentioned, more clearly appeared in $TbAlO_3$ perovskites (TA). It is described in the pages that follow in detail.

After diffusion annealing in oxygen atmosphere, the all samples were colored to pale brown, which

was same color as pre-annealed samples before diffusion annealing, believed to be due to Tb^{4+} ion creation in single crystal. This tendency is strong in the samples grown in nitrogen gas. The weight change was not observed after preannealing in 10 μg order accuracy (typical sample weight; 0.1g), which indicates the weight change for the oxidation to be less than 0.01%. We tried to measure the oxygen volume diffusion coefficients in oxidizing (O_2) and reducing (CO_2-CO mixture) atmospheres, respectively.

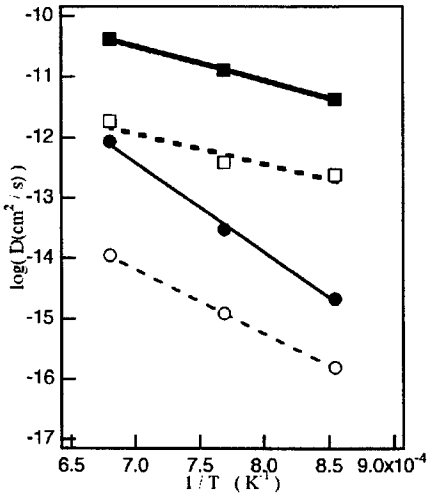

Fig.3. Arrhenius plots of oxygen diffusion coefficients of TA measured in O_2 and CO-CO_2 mixture. Closed symbols and solid lines, for TA grown in N_2. Open symbols and dashed lines, for TA grown in N_2-H_2 mixture. Circles and thin lines, measured in O2, and squares and thick lines, in CO-CO2 mixture.

Resultant values of oxygen diffusion coefficients in O_2 atmosphere are plotted as a function of a reciprocal temperature in Figure 3. The diffusion coefficients of the samples grown in nitrogen are larger than those grown in mixed gas containing hydrogen. The temperature dependencies are described by following equations, respectively:

$$D = 1.93\times10^{-7}\cdot\exp\left(\frac{-204(kJ/mol)}{RT}\right)\ cm^2/s$$

TA grown in H_2 - N_2 mixture (4)

$$D = 1.05\times10^{-2}\cdot\exp\left(\frac{-285(kJ/mol)}{RT}\right)\ cm^2/s$$

TA grown in N_2 mixture (5)

It is remarkable that the activation energy of TA grown in N_2 is slightly larger than that in H_2-N_2 atmosphere.

The Arrhenius relations are also shown in Fig.3, and expressed as following equation:

$$D = 4.08\times10^{-9}\cdot\exp\left(\frac{-96(kJ/mol)}{RT}\right)\ cm^2/s$$

TA grown in H_2 - N_2 mixture (6)

$$D = 2.79\times10^{-7}\cdot\exp\left(\frac{-108(kJ/mol)}{RT}\right)\ cm^2/s$$

TA grown in N_2 mixture (7)

The activation energy measured in reducing atmosphere is characteristically greater than for oxidizing atmosphere, the level of the oxygen diffusion coefficients is tow or four orders of magnitude lager in the reducing atmosphere than oxidizing one.

Tracer diffusion coefficient, D, generally relates to the ion migration energy, ΔH_m, as follows,

$$D = K_0\cdot N_D\cdot\exp(-\Delta H_m/RT) \quad (8)$$

where, N_D, defect ratio to host lattice concerning diffusion. If N_D can be assumed to be constant, the activation energy corresponds to ΔH_m. At the reducing condition with carbon dioxide, the activation energy corresponds to the value of ΔH_m, since it dose not depend to the atmosphere at crystal growth and is relatively small.

Because oxygen diffusion coefficients at reduced atmosphere is larger than at oxygen gas, oxygen ions is believed to diffuse through oxygen vacancy, for instance following simple mechanism;

$$O_O^{\times} \rightarrow \frac{1}{2}O_2 + O_O^{\times} \quad (9)$$

However, the activation energy depends on atmosphere of oxygen diffusion annealing, and level is different with each other, so the creation mechanism of oxygen vacancy is more complex.

In the case of double oxide, the cation ratio must be considered.

Making a model of oxygen vacancy structure, we assumed that (1) site ratio was settled in [A]:[B]:[O]=1:1:3, where [A] is site number at A-site; [B], at B-site; [O], at oxygen ion site in perovskite structure, (2) no interstitial ion existed, and (3) site change between A-site ions and B-site ions did not occur.

In the present study, it was considered that Tb/Al=y is less unity. The assumption leads to a following chemical formula;

$$Tb^{\times}_{Tb\ y}\ V^{'''}_{Tb\ 1-y}\ Al^{\times}_{Al\ 1}\ O^{\times}_{O\ 3\cdot(y+1)/2}\ V^{\cdot\cdot\cdot}_{O\ 3\cdot(1-y)} \quad (10)$$

Assuming this defect model, the partial reducing or oxidizing process can be expressed as follows;

Reducing side		oxidizing side
$1/2\,O_2 + V_O^{\cdot\cdot} + 2Tb_{Tb}^{\times}$	$\leftrightarrow$	$2Tb_{Tb}^{\cdot} + O_O^{\times}$

Electr - neutrality;

$$2[V_{Tb}^{'''}] = 3[V_O^{\cdot\cdot}] \qquad [V_{Tb}^{'''}] = 3[Tb_{Tb}^{\cdot}] \quad (11)$$

The equilibrium equation for above-mentioned process is formulated as follows;

$$[Tb_{Tb}^{\cdot}]^2 \cdot [V_O^{\cdot\cdot}]^{-1} \cdot P_{O_2}^{\ 2}$$
$$= [3 \cdot V_{Tb}^{'''} - 2 \cdot V_O^{\cdot\cdot}]^2 \cdot [V_O^{\cdot\cdot}]^{-1} \cdot P_{O_2}^{\ 2} = K \quad (12)$$

According to the above-mentioned model the defect concentrations are schematically plotted in Figure 4, in which the equilibrium constant is fixed, and Tb/Al ratio, changed. As the Tb/Al ratio is increased, both concentrations of terbium tetravalent ion, $Tb^{\cdot}$ and oxygen vacancies, $V_O^{\cdot\cdot}$ increase. The oxygen vacancy concentration continuously decreases with oxygen partial pressure.

Above mentioned, the difference of samples and oxygen partial pressure is considered to be caused by the difference of Tb/Al ratio, where the difference of activation energy between reducing atmosphere (CO-CO_2) and oxidizing atmosphere (O_2) corresponds to the vacancy formation energies, ΔH_f, that are 100kJ/mol to 180kJ/mol. The variation of ΔH_f among samples is considered to be caused by association among some kinds of defects. exist of other formation mechanism. In the present case, e.g., $[V_O$-$V_{Tb}^{'''}]$ association was created. The concentration of $[V_O$-$V_{Tb}^{'''}]$ association depends on $V_{Tb}^{'''}$ concentration, so the activation energy varied with samples.

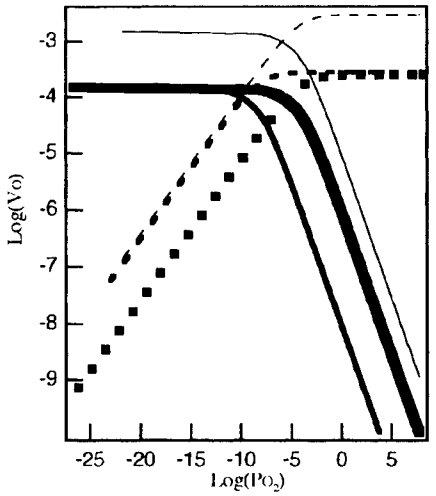

Fig.4 Schematic drawing of oxygen partial pressure dependence of V_O (solid lines) and Tb^{4+} (dashed lines), calculated under various K in Eq.(12) and V_{Tb} values. Thickest and medium lines, having the same V_{Tb}, and K of the thickest, one order higher than the medium.. Thinnest and medium lines, having the same K values, and V_{Tb} concentration of the thinnest, one order higher than the medium.

Reference

1) e.g. Y.Fukuda, H.Haneda et. al., Jpn.J.Appl.Phys. **36**, L1514-16 (1997).
2) M.Sekita, Y.Miyazawa, S.Morita, H.Seliwa, and Y.Sato, Aool.Phys.Lett., **65**, 2380-82 (1994).
3) Sakaguchi, I. and Haneda, H., J. Solid State Chem. 124, 195–97 (1996).
4) H.Haneda et. al., J.Jpn.Soc. Powder &Power Metallurgy, **46**, 28-35 (1999).
5) HHaneda and C.Monty, J.Am.Ceram.Soc., **72**, 1153-57 (1989).
6) Crank, J., "The Mathematics of diffusion", Chap. 3.3, Oxford Univ. Press, London (1975)

Transmission Electron Microscopy Investigation of Bi_2O_3-ZnO-Nb_2O_5 Pyrochlore and Related Phases

J. C. Nino, I. M. Reaney*, M. T. Lanagan and C. A. Randall

Center for Dielectric Studies, Materials Research Laboratory Bldg., The Pennsylvania State University, University Park, Pa 16802, USA

*Engineering Materials, University of Sheffield, Western Bank, Sheffield S10 2TN, UK

FAX: (814) 865 8126

E-mail: jcn125@psu.edu

Transmission Electron Microscopy (TEM) study of the main phases in the Bi_2O_3-ZnO-Nb_2O_5 system was performed. Electron diffraction patterns revealed a conventional cubic pyrochlore structure, space group Fd3m for the $Bi_{3/2}ZnNb_{3/2}O_7$ composition, and a monoclinic zirconolite-like structure, space group C2/c for the $Bi_2Zn_{2/3}Nb_{4/3}O_7$ composition. Evidence of stacking faults was detected in the monoclinic phase along the <001> direction, which is consistent with the layered nature of the phase.

INTRODUCTION

The pyrochlore family of oxides has a general formula $A_2B_2O_6O'$ and are predominantly cubic and ionic in nature. The structure allows a wide variety of chemical substitution at the A, B sites, hence exhibiting an enormous range of physical properties. Therefore uses for pyrochlore materials are manifold: from electronic materials and solid electrolytes, to heating elements, high temperature electrodes and fixation of radioactive waste[1].

Extensive research has been done since the early seventies on pyrochlore systems for electronic applications. In particular, the Bi_2O_3-ZnO-Nb_2O_5 (BZN) system has been studied consistently over the recent past years as a promising dielectric material for low fire multilayer applications and electronic devices for microwave communication[2-11]. These studies have dealt with processing, phase formation, dielectric properties, electrode interaction, cofiring, etc. Early X-ray diffraction (XRD) studies on the BZN system reported the $Bi_{3/2}ZnNb_{3/2}O_7$ phase as a conventional cubic pyrochlore, space group Fd3m, and the $Bi_2Zn_{2/3}Nb_{4/3}O_7$ phase was partially characterized as a pseudo-orthorhombic pyrochlore[5]. Recently a more complete structural refinement of the phases, based on neutron diffraction and high-resolution XRD experiments was performed[12]. The phases were characterized as follows: $Bi_{3/2}ZnNb_{3/2}O_7$, cubic, space group Fd3m (No. 227), a = 10.552 Å. $Bi_2Zn_{2/3}Nb_{4/3}O_7$, monoclinic, space group C2/c (No. 15), a = 13.104 Å, b = 7.674 Å, c = 12.158 Å and β = 101.318°.

In order to better understand similarities and differences in the physical properties of these two phases, a better knowledge of the crystallographic relationship among them is extremely important. It is essential to remember that compounds of the pyrochlore family can crystallize into orthorhombic, rhombohedral, hexagonal, monoclinic and even triclinic structures[1,13]. It has also been shown that the crystal habit is not only determined by composition via the ionic radii of the cations, but also by electronegativity and in particular by the configurations of the electron shells of the cations[14-15]. In addition, crystallographic transformations among these structures and the cubic phase have been proposed for various systems showing the close relationship among the high symmetry and distorted phases[16-21]. In the particular case of the CaO-ZrO_2-TiO_2 system, small variations in stoichiometry result in two different phases zirconolite (space group C2/c), and zirkelite (space group P312), which are indistinguishable under simple XRD experiments[18]. Even more, within the zirconolite structure, there is a possibility for two types of twinning mechanisms[20]. Typically, it is through TEM techniques that

additional information regarding polytypic behavior of such phases is obtained and analyzed. Therefore, in order to further characterize the main phases of the BZN system, Transmission Electron Microscopy (TEM) studies were performed.

EXPERIMENTAL PROCEDURE

Pellets with base composition $Bi_{3/2}ZnNb_{3/2}O_7$ and $Bi_2Zn_{2/3}Nb_{4/3}O_7$ were prepared by conventional mixed-oxide route. Samples underwent thinning by conventional ceramographic techniques followed by ion milling (Model 3000, E.A. Fischione Instruments, Inc.) to electron transparency for observation in the transmission electron microscope (TEM) (Philips 420, operated at 120 kV). Simulation of the Electron Diffraction Patterns (EPD) and crystallographic models were done using CaRIne Crystallography software[22].

RESULTS AND DISCUSSION

$Bi_{3/2}ZnNb_{3/2}O_7$ composition

Figure 1 shows the EDP from the [110] zone axis (ZA) from the sample with $Bi_{3/2}ZnNb_{3/2}O_7$ composition. The pattern was successfully indexed on the basis of a cubic pyrochlore structure, with lattice parameter a=10.55 Å consistent with previous reports[6,12]. It is important to note that symmetry constraints for the pyrochlore structure, forbids the appearance of {100}, {110} and {200} reflections. Nonetheless, the {200} reflections appear due to double diffraction as exemplified here: (111) + (1-1-1) = (200). Additional microstructural analysis using Bright and Dark Field images taken from this and other zone axes showed no unusual microstructural features. Therefore, TEM characterization of this phase reveals a conventional cubic pyrochlore structure.

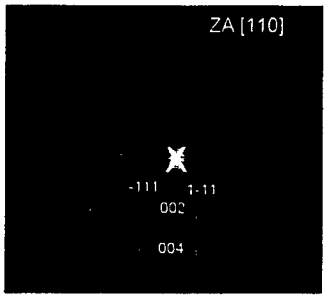

Figure 1. EDP from the [110] zone axis for the $Bi_{3/2}ZnNb_{3/2}O_7$ composition.

$Bi_2Zn_{2/3}Nb_{4/3}O_7$ composition

Figure 2 shows the EDPs from the [001], [0-10] and [1-10] zone axes for the sample with $Bi_2Zn_{2/3}Nb_{4/3}O_7$ composition. The patterns were successfully indexed on the basis of the monoclinic zirconolite-like structure reported by Levin et al.

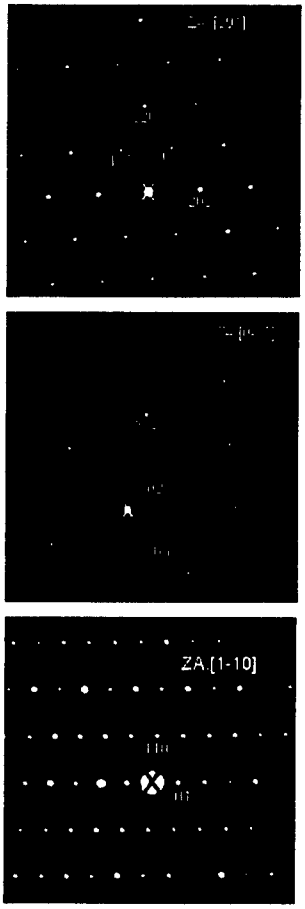

Figure 2. From top to bottom,EDP from the [001], [0-10] and [1-10] zone axis for the $Bi_2Zn_{2/3}Nb_{4/3}O_7$ composition

It is noteworthy that in order to characterize the crystal structure solely by TEM, convergent beam techniques (CBED), are required. However, the indexing of the above EDPs utilizing the lattice parameters obtained via X-ray and Neutron Diffraction experiments gives an additional confirmation to the characterization previously cited.

Planar defects: Figure 3 shows the dark field (DF) image using the 001 reflection from the [1-10] zone axis of the monoclinic BZN phase. This particular type of reflections corresponds

to the largest d-spacing (smallest R-distance) observed in the EDPs recorded. The DF image shows planar defects suggesting the presence of stacking faults.

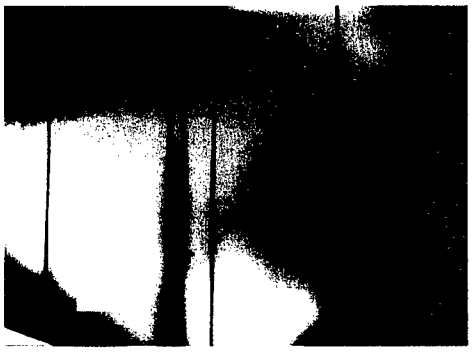

Figure 3. Dark Field image of the 001 reflection from the [1-10] zone axis of the monoclinic BZN phase.

Since the corresponding zone axis for Figure 3 is [1-10], the direction of the observed faults lies perpendicular to the (1-10) plane. Additionally, the 001 reflection, from where the image was collected, corresponds to the diffraction from the planes parallel to the c-axis of the unit cell. Stacking faults along the c-axis have been reported in distorted pyrochlore structures with $Ho_2Mn_xTa_{2-x}O_7$ composition[23,24]. Therefore it is very reasonable to suggest that the stacking faults observed lie along the (00*l*). It is important to say that in order to fully understand and characterize the stacking faults, a complete invisibility check or g•R analysis as well as high resolution TEM characterization is needed; both falling beyond the scope of this investigation.

Nonetheless, in order to further analyze this feature, it is useful to recall that the pyrochlore structure can be considered as the stacking of hexagonal tungsten bronze (HTB) layers, formed by the octahedrally coordinated smaller cations, while the larger cations occupy the interlayer positions[15]. Under this scope, the crystal habit of the distorted pyrochlores and pyrochlore related superstructures and their crystallographic relationship is then analyzed by understanding the different stacking sequences as well as the displacement between successive layers[16-21]. In addition, it was showed that the presence of stacking errors in these structures allows the incorporation of cationic impurities, atomic substitutions[19]. The study on Lead niobate pyrochlore related structures by Bernotat-Wulf and Hoffmann (1982) showed how the distortion of the unit cell and alterations in the stacking sequences provides more point positions for the larger cation, (Lead in that case)[25].

Figure 4(a) shows the [100] view of the crystallographic model for the $Bi_2Zn_{2/3}Nb_{4/3}O_7$ phase based on the lattice parameters and atomic positions presented by Levin et al., where the Oxygen atoms have been removed to emphasize the layered characteristics of this structure. Figure 4(b) shows the HTB layers formed by the octahedra with bismuth atoms occupying the interlayer positions.

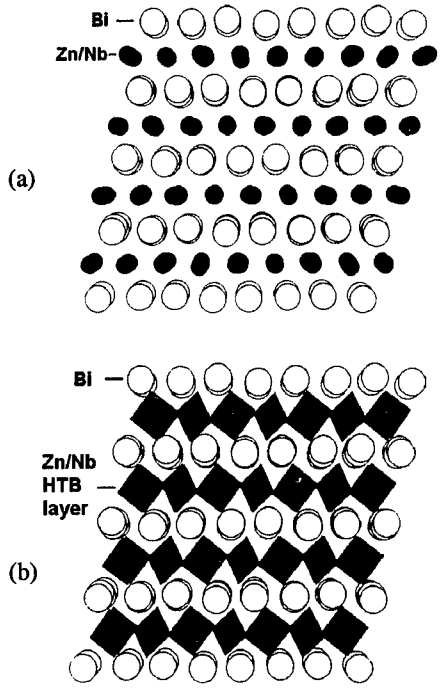

Figure 4. Crystallographic model for the $Bi_2Zn_{2/3}Nb_{4/3}O_7$ phase after Levin et al. Oxygen atoms have been removed for clarity. (a) [010] view showing sheet-like ordering of Bismuth, and Zinc and Niobium atoms; (b) [010] view showing the HTB Zinc/Niobium layers and Bismuth between layers.

From these models it is clear that a similar situation as in the Lead niobates may be the origin of the planar defects observed. As expressed before, it is matter of future investigations to perform a complete characterization of the phenomena here reported.

1. Conclusions

The TEM study performed on the main phases in the Bi_2O_3-ZnO-Nb_2O_5 system revealed a conventional cubic pyrochlore structure, space group Fd3m for the $Bi_{3/2}ZnNb_{3/2}O_7$ composition. No unusual microstructural features were observed on the cubic phase.

Based on a monoclinic zirconolite-like structure, space group C2/c, the EPDs from the $Bi_2Zn_{2/3}Nb_{4/3}O_7$ composition were successfully indexed. The crystallographic structure here characterized is consistent with the latest X-ray and Neutron Diffraction reports on the phases. In addition, evidence of stacking faults was detected in the monoclinic phase perpendicular to the {1-10} planes, most likely along the <001> direction, which can be explained by the layered nature of the phase.

Acknowledgements: Useful discussions were held with Igor Levin from the National Institute of Standards and Technology (NIST).

References

[1]M.A. Subramanian, G. Aravamudan and G.V. Subba Rao, *Prog. Solid State Chem.* **15**, 55-143 (1983).

[2]H. Kagata, T. Inoue, J. Kato and I. Kameyama, *Jpn. J. Appl. Phys.* **31** 3152-55 (1992).

[3]J. Champarnaud-Mesjard, M. Manier and B. Frit, *Journal of Alloys and Compounds* **188** 174-178 (1992).

[4]D. Liu, Y. Liu, S. Huang and X. Yao, *J. Am. Ceram. Soc.* **76** [8] 2129-32 (1993).

[5]D. Cann, C.A. Randall and T.R. Shrout, *Solid State Commun.* **100** [7] 529-34 (1996).

[6]X. Wang, H. Wang and X. Yao, *J. Am. Ceram. Soc.* **80** [10] 2745-48 (1997).

[7]S. Cho, H. Youn, D. Kim, T. Kim and K Hong, *J. Am. Ceram. Soc.* **81** [11] 3038-40 (1998).

[8]J.C. Nino, T. Sogabe, M.T. Lanagan, T.R. Shrout and C. A. Randall, *Extended Abstract 9th US-Japan Seminar on Dielectric and Piezoelectric Ceramics* (Okinawa, 1999) pp. 453-7. Edited by Tadashi Takenaka and Thomas R. Shrout.

[9]M. Valant and P. Davies, *J. Am. Ceram. Soc.* **83** [1] 147-53 (2000).

[10]J. C. Nino, M. T. Lanagan and C. A. Randall, *J. Appl. Phys.*, **89** [8] 4512-16 (2001).

[11]J.C. Nino, M.T. Lanagan and C. A. Randall, *J. Mater. Res.*,**16** [5] 1460-64 (2001).

[12]I. Levin, J. C. Nino, I. M. Reaney, M. T. Lanagan and C. A. Randall (to be published)

[13]F. Brisse, D. J. Stewart, V. Seidl and O. Knoop, *Can. J. Chem.*, **50**, 3648-3666 (1972).

[14]I. N. Belyaev, L. N. Aver'yanova and S. S. Lopatin, *Russ. J. Inorg. Chem.*, **28** [4] 517-19 (1983).

[15]S. S. Lopatin, L. N. Aver'yanova and I. N. Belyaev, *Russ. J. Inorg. Chem.*, **30** [4] 485-487 (1985).

[16]K. Yagi and R.S. Roth, *Acta Cryst.*, A**34**, 765-773 (1978).

[17]H.J.Rossell, *Nature*, **283**, 282-3 (1980).

[18]F. Mazzi and R. Munno, *American Mineralogist*, **68**, 262-276 (1983).

[19]T. J. White, R. L. Segall, J. C. Barry and J. L. Hutchison, *Proc. R. Soc. Lond.*, A**392**, 343-358 (1984).

[20]T .J. White, *American Mineralogist*, **69**, 1156-1172 (1984).

[21]J. C. Nino and C. A. Randall, (To be published).

[22]C. Boudais and D. Monceau, *CaRIne Crystallography V3.1* © 1989-1998.

[23]H. Nakano, A. Kishigami, M. Hisa and N. Kamegashira, *Mater. Res. Bull.*, **34** [12/13] 2075-2084 (1999).

[24]H. Nakano, N. Kamegashira and K. Urabe, *J. Am. Ceram. Soc.*, **83** [9] 2305-10 (2000).

[25]H. Bernotat-Wulf and W. Hoffmann, "Die Kristallstruckturen der Bleiniobate vom Pyrochlor-Typ" (Crystal structure of Lead niobates of the pyrchlore-type), *Zeitschrift für Kristallographie*, **158**, 101-117 (1982).

Bi-pyrochlore Materials for Microwave Applications

C. A. Randall, M. T. Lanagan, H. J. Yoon, I. Reaney, H. Sogabe, J. Nino, A. Baker and T. Shrout
Center for Dielectric Studies, Materials Research Laboratory Bldg., Penn State University,
University Park, PA 16802 USA; Fax: (814) 865-8126; Email: car4@psu.edu

Abstract

There is a need to develop new materials for passive component integration for wireless systems. This study reflects a series of investigations on pyrochlore-related dielectrics based on two ternary systems Bi_2O_3–ZnO–Ta_2O_5 and Bi_2O_3–ZnO–Nb_2O_5. These materials can be processed to produce dielectrics with NPO characteristics that can be cofired into LTCC packages or modules for high frequency filters and capacitors.

Introduction

With the advancement of wireless electronics, there is a major increase in the interest in integrated passive component devices, including capacitors, inductors, and resistors. This study focuses on embedded components that fulfill a large range of functions, including decoupling, filtering, and low reflection termination loads in ceramic substrates.

Most commercial low temperature cofired ceramics (LTCC) have K values between 5–10. Dielectric constant values exceeding 20 will be required to increase the volumetric efficiency of embedded capacitors and for miniaturized filters.

Ceramics based on the Bi_2O_3–ZnO–Ta_2O_5, and Bi_2O_3–ZnO–Nb_2O_5 ternary compounds are promising dielectrics for integrated passive components[1]. Understanding the process-property-structure relations for these systems is key to the development of the final dielectrics. The objective of this paper is to outline the important correlations for these relationships.

Structure and Composition

In the Bi_2O_3–ZnO–Ta_2O_5 (BZT) and Bi_2O_3–ZnO–Nb_2O_5 (BZN) ternary systems, there are several phases [2-5]. The most important for the development of a low fire dielectric is based on two primary compositions $(Bi_{3/2}Zn_{1/2})(Zn_{1/2}M_{3/2})O_7$ (where: M=Nb^{+5} and Ta^{+5}) and is to be designated as the α-phase, and $Bi_2(Zn_{1/3}M_{2/3})_2O_7$, which is designated the β-phase. The α-phase is a pyrochlore structure with a cubic symmetry with space group Fd3m. The β-phase is monoclinic with space group, C 2/c.[6,7] Figures 1 (a)–(b) shows electron diffraction data consistent with this symmetry. Pyrochlores are based upon stoichiometric compositions $A_2B_2O_7$ or non-stoichiometric forms of $A_{1.5}B_2O_{6.5}$. The general structure can be considered in terms of a defective fluorite structure, or the stacking of hexagonal tungsten bronze layers[8], with the β-phase having a pyrochlore polytype structure known as zirconolite.

Processing

Properties are highly sensitive to the mixing and milling conditions in these systems. As such, a columbite precursor was used to ensure that a single-phase zirconolite material could be obtained (β-phase). The columbite phase, e.g. $ZnNb_2O_6$ was calcined at 1000°C for 4 hours. The formation of the cubic (α-phase) can be problematic in the fact that metastable phases can be present up to high temperatures.[9] In particular, a $BiNbO_4$ phase can exist, and if this is present in the final dielectric powder, it can readily react with the silver electrode materials. So in the powder processing and calcination stages, we have ensured that $BiNbO_4$ and $BiTaO_4$ are not present in the final powders that are formulated for LTCC cofiring.[9-10]

Dielectric Characterization

Dielectric properties were determined over a frequency range of 100 Hz to 10 GHz. A variety of techniques were employed, including typical LCR (Hewlett-Packard 4284) measurements. At high frequencies, measurements were based on transmission and resonator methods. A comparison of the BZT system properties is given in

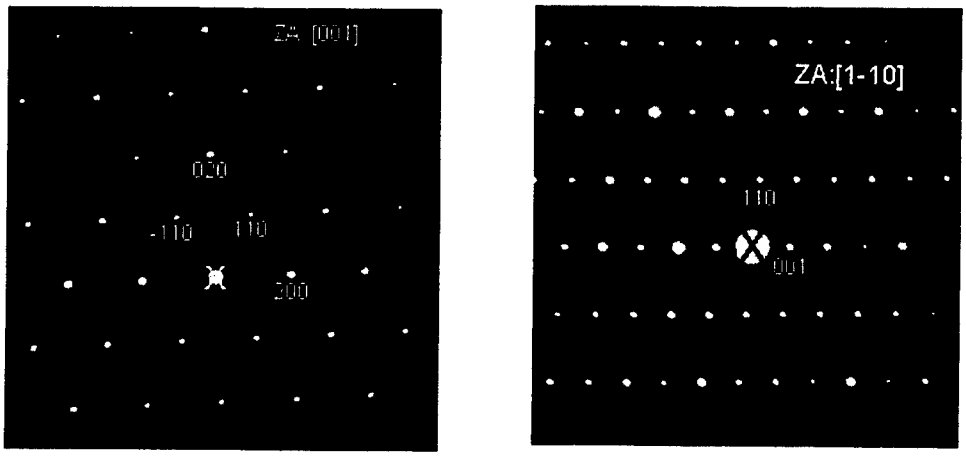

Figure 1. Electron diffraction pattern (EDP) from the [001] (a) [1-10] and (b), zone axis for the $Bi_2Zn_{2/3}Nb_{4/3}O_7$ composition (β-phase).

Table I. With these BZT materials, it is clear that to develop NPO capacitors, a composite of phases are required to establish the dielectric properties with low temperature coefficient of capacitance. To illustrate this point, we consider a compositional range between the α and β phases in BZT, such that $Bi_2(Zn_{1/3}Ta_{2/3})_2O_7$–(1-r)$(Bi_2Zn_{1/2})(Zn_{1/2}Ta_{3/2})$ O_7 ($0 \le r \le 1$). In such a study, it is important to isolate kinetic factors such as phase formation and bismuth loss. Once these are eliminated, we can determine the phase boundaries for the α and β phases. In this case, the boundaries were $r<3.0$ and $r \ge 0.74$ for α and β, respectively. These boundaries were determined by mixing the end member powders and heat treating the powders. Analysis of the solubility and phase formation was performed by x-ray powder diffraction. In addition, dielectric properties were correlated to the phase formation in the form of sintered disks. Figure 2 shows the dielectric constant and temperature coefficient of capacitance over the phase field. The solid solution boundaries are readily identified, and in the α-phase region, the properties have only one degree of freedom based on the phase rule and magnitude of K and TCC can be modeled with composite mixing laws using the solid solution limit for the properties of the mixed phases.[11]

The cubic phases in the pyrochlore are the minor phases in the composite compared to the zirconolite material. However, there is an interesting dielectric relaxation that can be found in the cubic pyrochlore materials. Measurements at cryogenic temperatures and high frequencies reveal a broad distribution of relaxation times

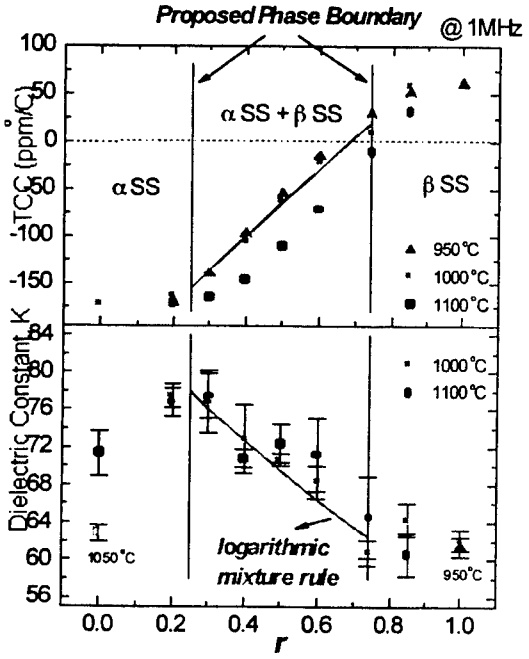

Fig. 2. Dielectric properties as a function ofcompositions r in r $Bi_2(Zn_{1/3}Ta_{2/3})_2O_7$ – (1-r)$(Bi_{3/2}Nn_{1/2})(Zn_{1/2}Ta_{3/2})O_7$ at 1 MHz. (SS = solid solution

exist, as can be seen in Figure 3. The associated dielectric loss data can be readily modeled with a function convoluting the Vogel-Fulcher law and a Gaussian distribution of relaxations. Figure 4 shows the general comparison of experimental and predicted data for the $(Bi_{1.5}Zn_{0.5})(Zn_{0.5}Nb_{1.5})O_7$ composition at 2 KHz up to 3 GHz over a temperature range of 300 K. Further details of this model can be found in Nino et al. (2001).[12]

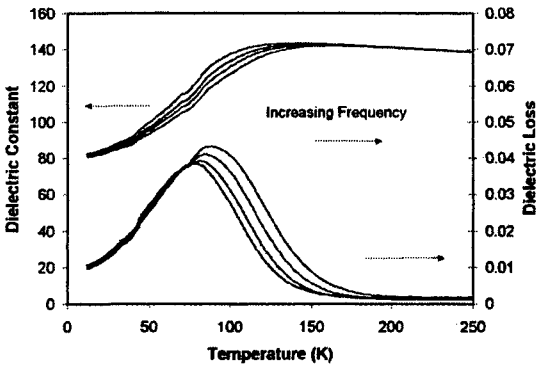

Figure 3. Dielectric constant and loss measured at 2, 10, 30, 100 KHz from left to right for BZN (α-phase).

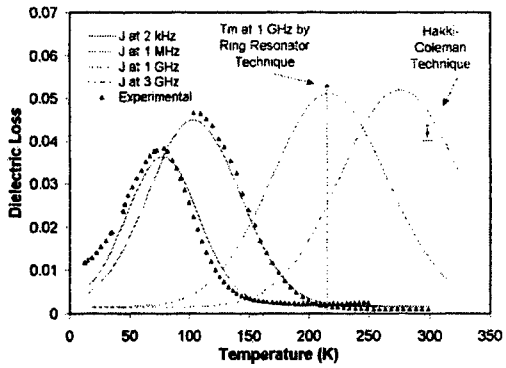

Figure 4. General comparison of experimental (triangles) and predicted data lines for BZN (a-phase) at a variety of frequencies.

Table 1: Microwave dielectric properties in the BZT system.

	α phase T.C.C. ≈ −172 ppm/°C			β phase T.C.C. ≈ 60 ppm/°C		
Technique	Frequency (GHz)	Dielectric Constant	tanδ	Frequency (GHz)	Dielectric Constant	tanδ
Resonant Post	4.9	59.3	0.021	4.8	63.2	0.0019
Dielectrometer	5.2	61.4	0.018	6.0	60.4	0.0014
Waveguide Transmission	8.6	64.4	0.050	8.8	59.4	<0.005*
Ring Resonator	1.6	66.0	†Q_T=41 †Q_d=56	1.6	57.9	†Q_T=80 †Q_d=723

*The low loss limit for the dielectric waveguide technique.
†The ring resonator Q-factor Q_T is related to the sum of conductor and dielectric loss.
Qd represents the dielectric contribution to the total Q factor.

Prototype Development

Thick film devices have been demonstrated for high frequency applications. Both thick film inks and tapes have been formulated with the BZN and BZT composite formulations. An embedded high K capacitor has been fabricated with BZN ink and a commercial LTCC tape, adjoined with silver electrodes. Multilayer LTCC structures were fabricated by stacking patterned green sheets, laminating and then sintering into a monolithic structure at 850°C for 15 minutes. Figure 5 shows a layer of BZN dielectric cofired into a silver electroded LTCC structure.

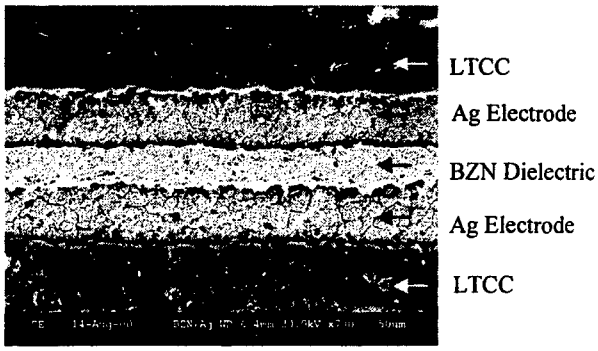

Figure 5. Scanning electron micrograph of a printed BZN dielectric, with silver electrodes embedded into a LTCC tape.

High dielectric constant materials give the possibility to miniaturize modules that are constructed around filtering functions. In order to demonstrate the utility of the new BZN and BZT dielectric materials, a low pass filter was designed, built, and tested. The filter consists of a multilayer structure with two embedded capacitors and one inductor. There are a total of 8 dielectric layers and 9 metal layers. The capacitors are located in dielectric layer number 6, and the inductor in metal layer number 2. The inductor, capacitor, and I/O pads are connected by vias through the dielectric layers.

The BZT material was mixed with a small amount of glass and was fabricated into a tape. The capacitor and transmission line conductors were screen printed and vias punched into dielectric tape and filled with silver conductors. After lamination, the green body was heat-treated and the film was marked to a printed circuit board as shown in Figure 6(a). The transmission parameter S_{21} for the low-pass filter was measured from a HP 8510 network analyzer up to 5 GHz, and the S_{21} magnitude drops significantly above 1 GHz, Figure 6(b). The filter exhibited low insertion loss in the designed transmission frequency range, below 1 GHz, which demonstrates that low loss BZT dielectrics can be cofired with silver to form a practical device.

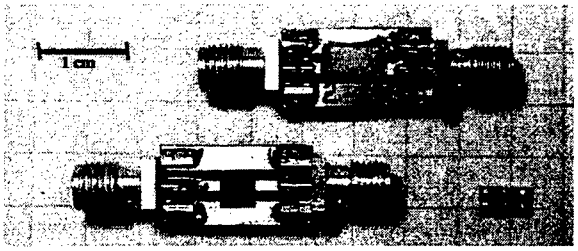

Figure 6(a). Prototype low-pass filter fabricated by cofiring BZT dielectric tapes and printed silver conductors, mounted with a coaxial SMA connector.

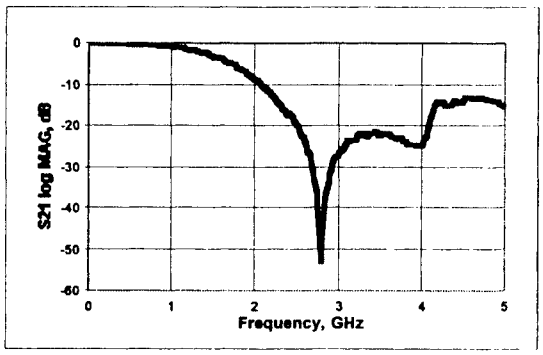

Figure 6(b). Low pass filter frequency response demonstrating high frequency rejection above 1 GHz.

Acknowledgements

The authors wish to thanks TDK and Center for Dielectric Studies for funding and Joanne Aller for typing the manuscript. Thanks to Igor Levin for sharing structural information on zirconolite (NIST).

References

[1] H. Kagata, I. Inoue, J. Kato, and I. Kameyama, Jap. J. Appl. Phys., Part 1, **31**, 3152 (1992).

[2] D. Liu, Y. Liu, S. Huang, and X. Yao, J. Am. Ceram. Soc. **76**, 2129 (1993).

[3] A. Merger and W.C. Lee, Mat. Res. Bull. **32** 175 (1997).

[4] M. Valant and P. Davies, J. Am. Ceram. Soc. **83**, 147 (2000).

[5] D. Cann, C.A. Randall, and T.R. Shrout, Solid State Communications **100**, 529 (1996).

[6] Igor Levin (private communication).

[7] J. Nino, I. Reaney, M. Lanagan, and C.A. Randall (to be published).

[8] T.J. White, R.L. Segal, J.C. Barry, and J. L. Hutchison, Proc. R. Soc. Lond. **A392**, 343–358 (1984).

[9] S. Cho, H.J.. Youn, D. Kim, and K. Hong, J. Am. Ceram. Soc. **81**, 3038 (1998).

[10] J. Nino, M.T. Lanagan, and C.A. Randall, J. Mat. Res. **16**, No. 5, 1460–1464 (2001).

[11] H.J. Youn, T. Sogabe, C.A. Randall, T.R. Shrout, and M.T. Lanagan (accepted J. Am. Ceram. Soc.)

[12] J.C. Nino, M.T. Lanagan, C.A. Randall, J. Appl. Phys. 89, 8, 4512–4516 (2001).

Dielectric and Ferroelectric Properties of (Ag,Li)(Nb,Ta) Ceramics

Y. Sakabe, T. Takeda, Y. Ogiso, and N. Wada
Murata Mfg. Co., Ltd. 2-26-10 Tenjin Nagaokakyo-shi, Kyoto, Japan
Email; sakabe@murata.co.jp

INTRODUCTION

Today's advanced telecommunication devices require further miniaturization of microwave components to have a higher performance and lighter in weight. Dielectric filter and resonator are used as principal elements of the devices. Therefore, dielectric materials of high permittivity with high quality factor Q value have been developed. BaO-PbO-Nb_2O_5-Bi_2O_3-TiO_2 ceramics are widely used as resonator materials of the highest permittivity of 110 with small temperature dependence. Recently, $Ag(Nb_{1-y}Ta_y)O_3$ (abbreviated as ANT) ceramics have been investigated as microwave dielectrics by Valant et al[1]. Permittivity of the composition $Ag(Nb_{1-x}Ta_x)O_3$, where x was from 0.48 to 0.52, was about 400. However, Q×f value of from 360 to 500 and temperature dependence of resonance frequency (τ_f) of from –400 ppm/°C to +100 ppm/°C were not good enough for microwave application such as filter and resonator. Pawełczyk reported phase diagram of the ANT ceramics, which has three monoclinic phases of M_1, M_2 and M_3[2]. Kania studied dielectric properties of the ANT solid solution in conjunction with its crystal phases and found that M_1 phase had weak ferroelectric properties at room temperature[3-4]. Spontaneous polarization Ps at room temperature was 0.04 $\mu C/cm^2$. Substitution of alkaline ion such as Na^{1+} and K^{1+} to the Ag^{1+} ion lattice site of the ANT ceramics was also studied[5-7]. Remarkable change of the characteristics was not recognized by these substituted ions. In this study, Li doped ANT ceramics was prepared to study the dielectric properties and crystal structure of the solutions.

EXPERIMENTAL

To synthesize the homogenous solid solution of the ANT ceramics modified with Li^{1+} ion, reagent grade raw materials of Nb_2O_5 and Ta_2O_5 were batched to have the composition of $(Nb_{1-x}Ta_x)_2O_5$ and milled in water with zirconia ball media. The dried mixture was calcined at 1200°C for 2h in air. The obtained $(Nb_{1-x}Ta_x)_2O_5$ powder was batched with reagent grade of Ag_2O, Li_2CO_3 and/or Na_2CO_3 to prepare the composition of $(Ag_{1-y}Li_y)(Nb_{1-x}Ta_x)O_3$ (abbreviated as ALNT) and $(Ag_{1-y}Na_y)(Nb_{1-x}Ta_x)O_3$, where x was from 0 to 0.8, and y was from 0 to 1.0, then mixed with zirconia ball media in alcohol. After drying, the mixture was calcined at from 900°C to 1000°C for 10h in oxygen atmosphere. Firing in air atmosphere cased dissociation of Ag and provided ceramics poor density. The obtained powder was mixed with organic binder in water to prepare the powder for dry pressing. Disk samples were formed into 12mm in diameter and 1mm thick. Test samples were fired at from 960°C to 1240°C for 10h in oxygen atmosphere. Silver electrode paste was screen printed on both sides of the disk surface, and fired at 800°C in air. To identify the elements in the fired ALNT ceramics, Inductively Coupled Plasma Atomic Emission Spectroscopy (ICP-AES) was used for Ag, Nb and Ta ions. Atomic Absorption Spectroscopy (AAS) was used for Li ion. The crystal phase of the sintered powder samples was analyzed by X-ray Diffraction (XRD) and High Temperature X-Ray Diffraction (HT-XRD). Microstructure of the ceramics was observed by Scanning Electron Microscope (SEM) and Wavelength Dispersive X-ray Spectrometry (WDX, JXA-8800, JEOL). Micro-domain structure was observed by transmission electron microscope (TEM). Capacitance and dissipation factor were measured at 1kHz by Broadband Dielectric Spectrometer System Analyzer (Novocontrol GmbH), which was composed of an Impedance Gain-Phase Analyzer (Solartron Inc.). D-E hysteresis curve was observed by Virtual Ground Measurement System (RT6000HVS/M, Radiant Tech. Inc.). For piezoelectric measurements, some of sintered samples were sliced rectangular plate (dimensions 0.7 × 0.7 × 3.0 mm^3). Silver electrodes were formed on both longitudinal sides of the rectangular plate, and fired at 800°C in air. Then the samples were poled under electric fields 0.55 to 0.88 kV/m in silicone oil at room temperature to 150°C for 10min. Piezoelectric constant d_{33}, electro-mechanical coupling coefficient k_{33}, and mechanical quality factor Q_m of the ALNT ceramics were measured by resonance-antiresonance method using an impedance/gain phase analyzer (HP4194A).

RESULT AND DISCUSSION

The compositions of the ALNT ceramics fired at 1240°C were analyzed. About 6% to 8% of the batched Li ion were lost during firing as Li concentration was higher than 10mol.%. Color of the ceramics changed from reddish brown of the pure $Ag(Nb_{0.5}Ta_{0.5})O_3$ to yellow with increasing the Li concentration. Density of the ALNT ceramic bodies were obtained higher than 97% of theoretical density at the most of compositions. However, the samples composed with higher Li concentration y than 0.5 did not sintered well because of the serious decomposition with Li dissociation during firing. Powder XRD patterns of

$(Ag_{1-y}Li_y)(Nb_{0.5}Ta_{0.5})O_3$ were shown in Fig.1. The secondary phase of $Li(Nb_{0.5}Ta_{0.5})O_3$ was recognized at Li concentration higher than 15mol.%. Solubility limit of the Li^{1+} ion to the ANT ceramics was estimated to be between 10mol.% to 15mol.% from XRD study. Figure 2 shows TEM image of the $(Ag_{0.8}Li_{0.2})(Nb_{0.5}Ta_{0.5})O_3$ ceramics. Bimodal phase of the main phase $(Ag_{1-y}Li_y)(Nb_{0.5}Ta_{0.5})O_3$ and secondary phase $Li(Nb_{0.5}Ta_{0.5})O_3$ were clearly observed. Ferroelectric domain like structure was found in the main phase. Crystal phase change of the compositions $(Ag_{0.9}Li_{0.1})(Nb_{0.5}Ta_{0.5})O_3$ and $(Ag_{0.9}Li_{0.1})NbO_3$ were observed with high temperature XRD and shown in Fig.3. The crystal symmetry of the $(Ag_{0.9}Li_{0.1})(Nb_{0.5}Ta_{0.5})O_3$ changed from rhombohedral to monoclinic, tetragonal and cubic with increasing temperature. The transition temperature from rhombohedral to monoclinic was at 80°C. The rhombohedral phase had lattice length a = 0.3920nm and angle α = 89.45° at room temperature. In the case of the composition $(Ag_{0.9}Li_{0.1})NbO_3$, The transition temperature from rhombohedral to monoclinic was at 295 °C. The lattice parameter a = 0.3928nm and α = 98.21° were obtained at room temperature. The phase transition temperature from rhombohedral to monoclinic increased remarkably with Li content.

Temperature dependence of permittivity of $(Ag_{0.9}Na_{0.1})(Nb_{0.5}Ta_{0.5})O_3$ and $(Ag_{0.9}Li_{0.1})(Nb_{0.5}Ta_{0.5})O_3$ were shown in Fig.4 in comparison with undoped ANT ceramics. The ANT and $(Ag_{0.9}Na_{0.1})(Nb_{0.5}Ta_{0.5})O_3$ had permittivity of in the range from 400 to 500, and fairly stable temperature characteristics. On the other hand, $(Ag_{0.9}Li_{0.1})(Nb_{0.5}Ta_{0.5})O_3$ showed a sharp permittivity peak at 80°C. This result indicated that Li^{1+} ion gave a great influence on the phase transition of the ANT ceramics. Permittivity changes with temperature for the compositions of $(Ag_{1-y}Li_y)(Nb_{0.5}Ta_{0.5})O_3$ and $(Ag_{0.9}Li_{0.1})(Nb_{1-x}Ta_x)O_3$ were shown in Fig.5. Permittivity peak shifted to higher temperature with Li concentration y in the range less than 0.125, which correspond to the phase transition from rhombohedral to monoclinic as mentioned before. The maximum permittivity of 1180 was obtained when Li was 10mol.%. Permittivity peak corresponding to the phase transition decreased with increasing the Ta ion concentration as shown in Fig.5 (b). Phase change was

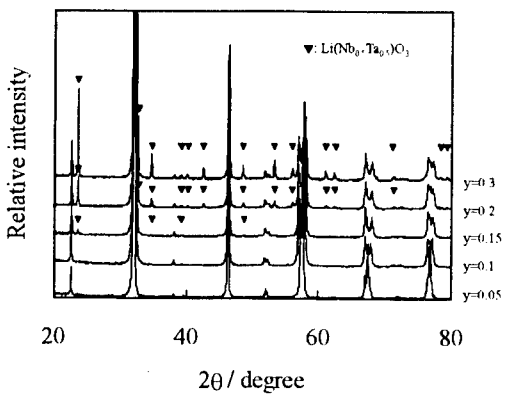

Fig. 1. X-ray diffraction patterns of $(Ag_{1-y}Li_y)(Nb_{0.5}Ta_{0.5})O_3$ ceramics at room temperature. Li concentration y is from0.05 to 0.3.

Fig. 2. TEM image of $(Ag_{0.8}Li_{0.2})(Nb_{0.5}Ta_{0.5})O_3$ ceramic.

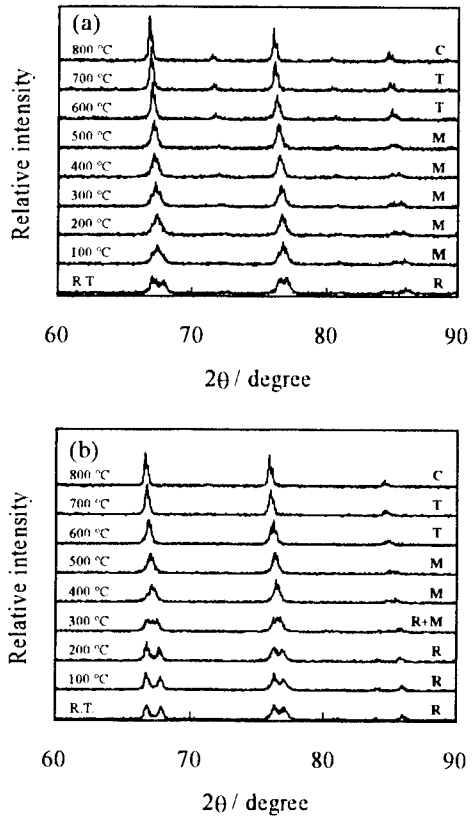

Fig. 3. High-Temperature X-ray diffraction patterns of $(Ag_{1-y}Li_y)(Nb_{1-x}Ta_x)O_3$ ceramic. The composition is (a) x=0.5, y=0.1, (b) x=0, y=0.1. Notation R is rhombohedral phase, M is monoclinic phase, R+M is mixed phase of both rhombohedral and monocolinic, T is tetragonal phase and C is cubic phase.

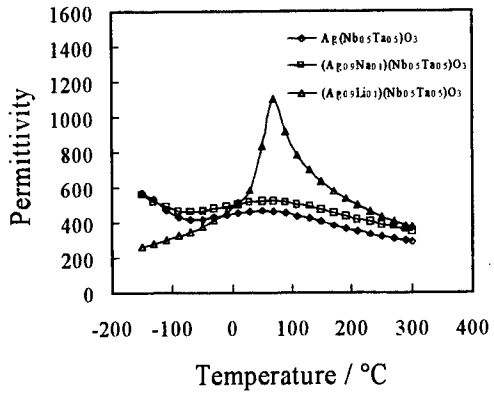

Fig. 4. Temperarure dependence of permittivity of the $Ag(Nb_{0.5}Ta_{0.5})O_3$ ceramics doped with Li and Na ions

traced with permittivity peak shift with temperature for both dielectrics and shown in Fig.6. In this figure, it considered that the phase transitions among monoclinic M_1, M_2 and M_3 are similar to the phase transitions of ANT ceramics[8]. Because the temperature dependence curves of permittivity of ALNT ceramics at low Li concentration was similar to one of ANT[3]. Existence of a morphotropic phase boundary was presumed at Li concentration of 5mol.%.

Figure 7 shows D-E hysteresis curves observed with the Li doped ANT ceramics at room temperature. Remnant polarization P_r of 23μC/cm^2 and coercive field Ec of 22kV/cm were observed at rhombohedral phase of $(Ag_{0.9}Li_{0.1})NbO_3$. P_r was changed with Li concentration as shown in Fig.8. Maximum value of P_r was obtained at Li concentration of about 5 mol.% , which may corresponds to the morphotropic phase boundary. Permittivity and dissipation factor at 1kHz was 200 and 2.1% respectively. These dielectric data were comparable with the value of $Pb(Zr,Ti)O_3$ ceramics. Ferroelectricity at room temperature was degraded with increasing Ta concentration due to the lowering of the phase transition temperature. Ferroelectric D-E hysteresis curve disappeared at monoclinic phase of all ALNT compositions. Kania reported the monoclinic M_2 and M_3 phase of the ANT ceramics has anti-ferroelectric properties[3]. His result suggests us the same anti-ferroelectric at the monoclinic phase of this ALNT ceramics. To obtain a detail phase transition temperature and a complete phase diagram, it would be necessary to perform structure analysis and differential thermal analysis throughout the whole range of possible composition and temperature.

Figure 9 shows piezoelectric constant d_{33} for $(Ag_{1-y}Li_y)NbO_3$ ceramics. Typical d_{33} value was obtained 52 pC/N at x = 0.1. In the same composition, electro-mechanical coupling coefficient k_{33} and mechanical quality factor Q_m values were obtained 44 % and 120 respectively. From these results, Li doped $Ag(Nb,Ta)O_3$ would be useful piezoelectric materials for electronics components.

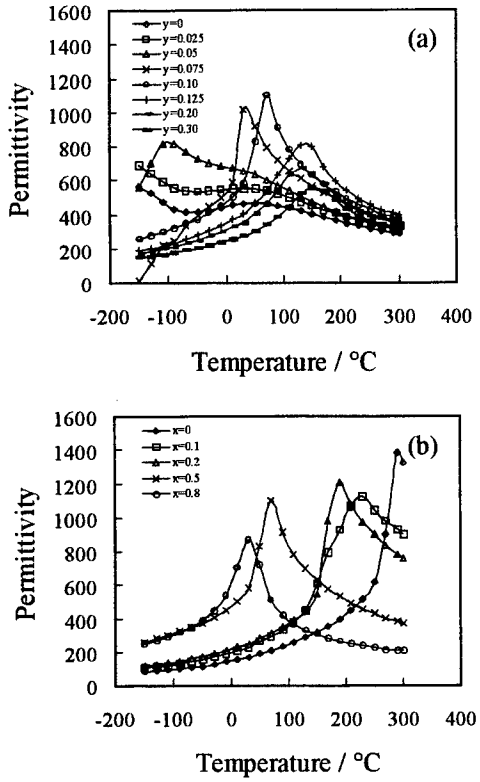

Fig. 5. Temperature dependence of permittivity of $(Ag_{1-y}Li_y)(Nb_{1-x}Ta_x)O_3$ ceramics. The composition range is (a) x = 0.5, y = 0~0.3, (b) x = 0~0.8, y = 0.1.

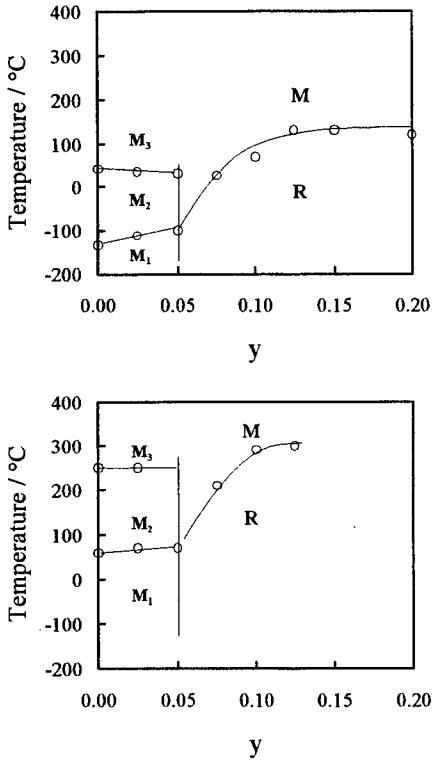

Fig. 6. Phase transition of $(Ag_{1-y}Li_y)(Nb_{1-x}Ta_x)O_3$ ceramics from rhombohedral to monoclinic. (a) $(Ag_{1-y}Li_y)(Nb_{0.5}Ta_{0.5})O_3$ ceramics and (b) $(Ag_{1-y}Li_y)NbO_3$ ceramics. Natation M_1, M_2, M_3 and M are monoclinic phase, R is rhombohedral phase.

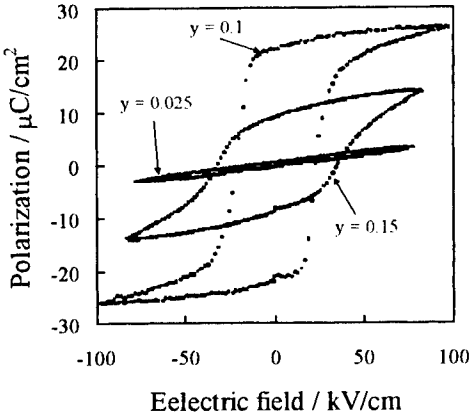

Fig. 7. D-E hysteresis curves of $(Ag_{1-y}Li_y)NbO_3$ ceramics at room temperature.

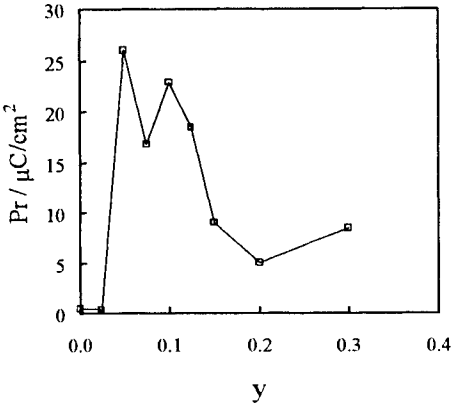

Fig. 8. Remnant polarization change with Li concentration of $(Ag_{1-y}Li_y)NbO_3$ ceramics. Li concentration y is from 0 to 0.3.

CONCLUSIONS

Lithium ion doped $Ag(Nb,Ta)O_3$ ceramics was prepared to investigate the Li ion dope effects on the crystal structure and dielectric properties. From XRD analysis and dielectric measurement, solubility limit of Li_2O to $Ag(Nb,Ta)O_3$ was estimated to be at in the range from 10 to 15mol.%. At above the solubility limit, secondary phase of $Li(Nb,Ta)O_3$ was recognized. Ferroelectric domain like structure was observed at rhombohedral phase of the $(Ag,Li)(Nb,Ta)O_3$ ceramics. The crystal phase of the $(Ag,Li)(Nb,Ta)O_3$ ceramics changed from rhombohedral to monoclinic, tetragonal and cubic with increasing temperature. The transition temperature increased remarkably with Li concentration. Permittivity peak corresponding to the phase transition from rhombohedral to monoclinic of the $(Ag_{0.9}Li_{0.1})NbO_3$ ceramics was 295°C. Strong ferroelectric response was observed at the rhombohedral phase by measuring the D-E hysteresis

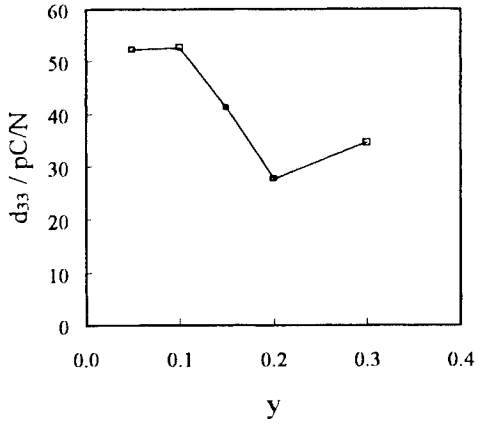

Fig. 9. Piezoelectric constants d_{33} change with Li concentration of $(Ag_{1-y}Li_y)NbO_3$ ceramics. Li concentration y is from 0.05 to 0.3.

curve. Remnant polarization P_r of 23μC/cm² and coercive field E_c of 22kV/cm was obtained for the composition of $(Ag_{0.9}Li_{0.1})NbO_3$ ceramics. Piezoelectric properties were investigated by resonance-antiresonance method. Piezoelectric constant d_{33} of 52 pC/N, electro-mechanical coupling coefficient k_{33} of 44% and mechanical quality factor Q_m of 120 were obtained in the same composition. Li doped $Ag(Nb,Ta)O_3$ would be useful piezoelectric materials for electronics components.

REFERENCES

[1] M. Valant and D. Suvorov, J. Am. Ceram. Soc., 82, 88-93 (1999).
[2] M. Pawełczyk, Phase Transitions, 8, 273-292 (1987).
[3] A. Kania, Phase Transitions, 3, 131-139 (1983).
[4] A. Kania, K. Roleder and M. Łukaszewski: Ferroelectrics, 52, 265-269 (1984).
[5] C. F. Pulvari: Physical Review, 120, 1670-1673 (1960).
[6] C. N. Darlington: Powder Diffr., 14, 253-257 (1999).
[7] D. F. Weirauch and V. J. Tennery: J. Am. Ceram. Soc., 50, 671-673 (1967).
[8] J. Petzelt, S. Kamba, E. Buixareras, V. Bovtun, Z. Zikmund, A. Kania, V. Koukal, J. Pokorný,J. Polívka, V. Pashkov, G. Komandin and A.Volkov: Ferroelectrics, 223, 235-246 (1999).

$Ba(Ti_xZr_{1-x})O_3$ FILM AS DIELECTRIC FOR CAPACITOR APPLICATIONS

Bang-Hung Tsao
University of Dayton Research Institute, 300 College Park, Dayton OH 45469-0179
bang.tsao@wpafb.af.mil
Susan Heidger and Joseph A. Weimer
Air Force Research Laboratory, 1950 Fifth Street, WPAFB, OH 45433

Abstract

Thin $Ba(Ti_xZr_{1-x})O_3$ film is being developed as a dielectric for microelectronics and electromechanical applications. Thin $Ba(Ti_xZr_{1-x})O_3$ films were produced using a dual-gun ($BaTiO_3$ and $BaZrO_3$) rf co-sputtering technique. The concept of this work is to develop a formulation of ceramic films that achieves high dielectric constants over a broad temperature and frequency range. Thin film capacitor devices were fabricated using the multiple-layer configuration of $Si/SiO_2/Ti/Pt$ as both the substrate and bottom electrode, and Pt as the top electrode. The dielectric constant of the as deposited $Ba(Ti_xZr_{1-x})O_3$ films was calculated to be in the range of 17-24 and the dissipation factors ranged from 0.004 to 0.008. The resistivity was $3.5x10^{13}$ ohm-cm. The $Ba(Ti_xZr_{1-x})O_3$ film capacitors had a parallel resistance of 1.4 $x10^7$ ohms and insulation resistance of 3.4 $x10^{10}$ ohms. The variation of the capacitance was within 3% as the frequency was increased from 400 Hz to 100 kHz at room temperature. Electrical testing was performed while thermal cycling from 25°C to 200°C. Capacitance increases slightly with increasing temperatures.

Introduction

Thin $BaTiO_3$ (BT), (BaSr) TiO_3 (BST) and Pb (ZrTi) O_3 (PZT) films are very promising high dielectric constant materials for use in capacitors, dynamic random access memories (DRAMs) [1], microsensors [2], and microwave devices [3]. The electrical properties such as low leakage current, fast dielectric response, low dielectric loss, and long lifetime are important for the high quality and reliability of these devices. Thin ceramic films, usually 0.5 to 2 μm, are being developed for use in integrated passive capacitor components. The search for electrically and thermally superior ceramic dielectric materials is an on-going task for many organizations. Present materials lack many attributes for example miniaturization, high capacitance, and high reliability desired by application engineers. The materials typically are thick, (usually greater than 10 μm), porous, and temperature limited. The dielectric properties of $Ba(Ti_xZr_{1-x})O_3$ films, produced by co-sputtering technique, were studied for potential applications as high dielectric constant material in micro-electronic components of high volumetric efficiency [4]. Films of BT, PZT, and BST[5] were previously produced with various techniques of which radio frequency (RF) sputtering appears to be the most reproducible. Depending on the substrate temperature, ratio of oxygen to argon, deposition rate, and post-deposition heat treatment, both amorphous and crystallized films can be produced by RF sputtering. Early efforts to produce thin films of $BaTiO_3$ were directed at attaining a very high dielectric constant which is characteristic of the bulk material. Films that exhibited high dielectric constants often had a high dissipation factor. The current challenge for the technology is to produce capacitors providing simultaneously high capacitance, high voltage capability, compact size, high electrical stability, low leakage current, and high temperature capability. Advances in ceramic processing and thin film technology are being applied to existing applications and to the development of new applications in electronics and optical devices. This work is aimed at studying the dielectric and electrical properties of co-sputtered $Ba(Ti_xZr_{1-x})O_3$ films for capacitor applications.

Experimental Procedures

$Ba(Ti_xZr_{1-x})O_3$ films were produced under dual-gun co-sputtering conditions. The target materials ($BaTiO_3$, and $BaZrO_3$ targets), and electrical contact material (platinum) were held constant. The variable parameter was the RF power for each gun. The deposition system used

to produce the $Ba(Ti_xZr_{1-x})O_3$ films was a dual-gun RF sputtering system, model DV502-A, manufactured by Denton Vacuum with an RFX generator from Advanced Energy Industries. The film thickness of the electrode was monitored by using an STM-100/MF Thickness/Rate Monitor from Sycon Instruments. The film thickness of the $Ba(Ti_xZr_{1-x})O_3$, was measured by using the DekTak IIIST System. The argon (99.999%) concentration was monitored using the MKS flow controller model 1179. The substrate was a multilayer configuration of Si/SiO2/Ti/Pt. The substrates went through four stages of ultrasonic cleaning: acetone, methanol, 2-propanol, and deionized water. The frequency response of the capacitance and dissipation factors was characterized on a HP LCR precision meter model 4284A with a PC controller. The insulation resistance was measured using the force voltage measure current (FVMI) technique. A Keithley model 6517 Electrometer capable of measuring 10^{17} ohms was used to measure resistance at fixed voltage. Data acquisition was conducted by using Lab Windows/CVI on a PC. Breakdown voltage was determined by I-V characteristics, which were generated by the same electrometer at various voltages. Scanning Electron Microscopy (SEM) was performed to inspect the surface morphology. Auger Electron Spectroscopy (AES) and (X-ray Photoelectron Spectroscopy (XPS) was used to determine the surface chemical composition. Thermal cycling, from room temperature to 200°C, was performed to investigate the temperature effect on the capacitance and dissipation factor of the capacitors.

Experimental Results

Energy-Dispersive Spectrum (EDS) of X-ray Spectrometer was performed on the starting targets. The peaks showed the targets had the correct chemical compositions. Films prepared under various conditions were examined using optical microscopy and SEM. No signs of cracking or peeling were observed. The adhesion of the films to the substrate was good. The morphology of as-deposited $Ba(Ti_xZr_{1-x})O_3$ films observed by optical microscopy was smooth and featureless. The color of the film changed with the thickness. SEM also revealed that before annealing a typical microstructure of $Ba(Ti_xZr_{1-x})O_3$ film was continuous and smooth.

The XPS spectrum shows the binding energy peaks of the elements present in the film as shown in the Figure1.

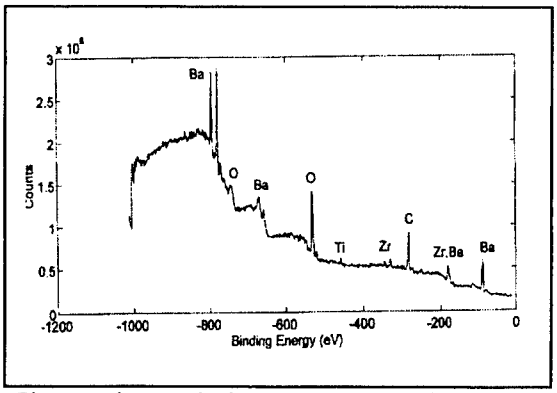

Figure 1 is a typical XPS spectrum of $Ba(Ti_xZr_{1-x})O_3$ test capacitor.

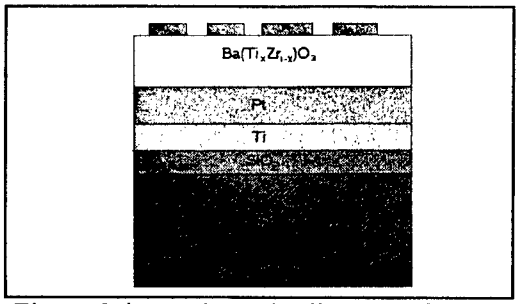

Figure 2 is a schematic diagram of the cross-sectional view of test capacitors.

Figure 2 is a schematic diagram of the cross-sectional view of the actual device. There were six layers ($Pt/Ba(Ti_xZr_{1-x})O_3/Pt/Ti/SiO_2/Si$). The thickness of the electrode is about 3,000 Å and the dielectric film is about 10,000 Å.

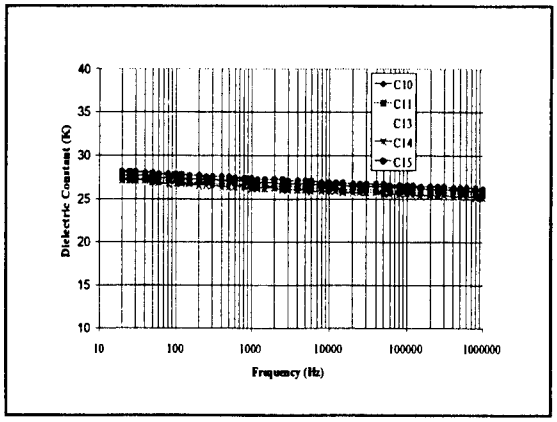

Figure 3 is the dielectric constant-frequency response for as deposited $Ba(Ti_xZr_{1-x})O_3$ film.

The average dielectric constant of as-deposited $Ba(Ti_xZr_{1-x})O_3$ film was 26. The dielectric constant had a weak dependence on frequency. Slight decreases (less than 3% over the entire frequency range) in the dielectric constant were observed with increasing frequency. The dielectric constant is expected to increase greater than 10 times with annealing.

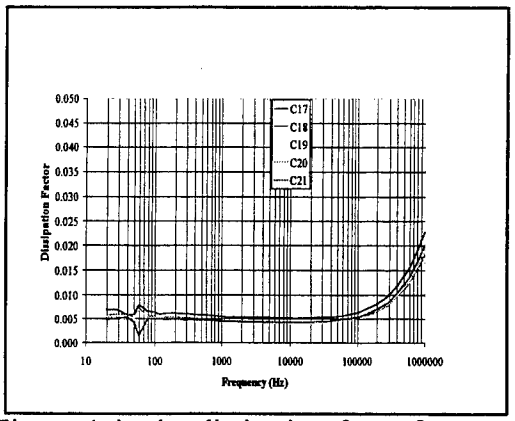

Figure 4 is the dissipation factor-frequency response for as deposited $Ba(Ti_xZr_{1-x})O_3$ film.

Figure 4 is the dissipation factor (a.k.a. DF, tangent loss, and tan δ) -frequency response for the $Ba(Ti_xZr_{1-x})O_3$ film. The dissipation factor was nearly constant up to 50 kHz, then increased dramatically up to 1 MHz. The typical dissipation factors of these $Ba(Ti_xZr_{1-x})O_3$ film capacitors were in the range of 0.004 to 0.006.

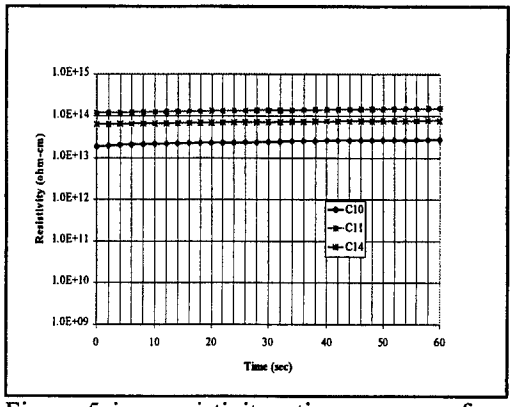

Figure 5 is a resistivity –time response for as-deposited $Ba(Ti_xZr_{1-x})O_3$ film.

The resistivity for the $Ba(Ti_xZr_{1-x})O_3$ film is in the range of 10^{13} to 10^{14} ohm-cm as shown in Figure 5. This value is satisfactory for dielectric applications.

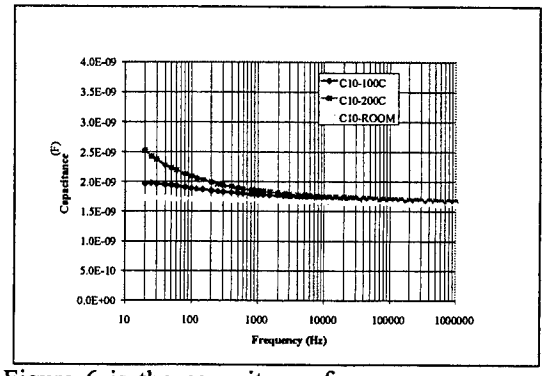

Figure 6 is the capacitance-frequency response for the as-deposited $Ba(Ti_xZr_{1-x})O_3$ film at various the temperatures.

The capacitance changes with the heating and cooling cycle, but not significantly. For frequency below 1 kHz, the capacitance increased with increasing temperature. Above 1 kHz, less than 3% change in capacitance was observed as the temperature increased to 200°C. Some of the electrodes gradually delaminated after testing at 250°C. The thermal stress may be the reason for this delamination.

The $Ba(Ti_xZr_{1-x})O_3$ film capacitors had a parallel resistance of 10^7ohm. The insulation resistance was in the range of 10^{11} to 10^{12} ohm. The product of insulation resistance and leakage current (IR) is equal to 5. The $Ba(Ti_xZr_{1-x})O_3$ film capacitors were tested at 140 volts and the corresponding leakage current was $1.84x10^{-6}$ amp/cm^2. The breakdown strength was $1.4x10^6$ V/cm.

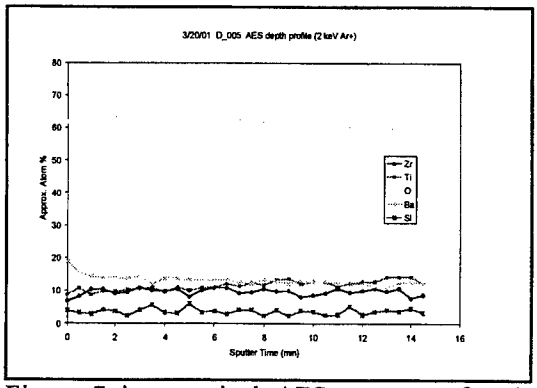

Figure 7 is a typical AES spectrum for the $Ba(Ti_xZr_{1-x})O_3$ film.

Figure 7 shows the AES spectrum for a representative $Ba(Ti_xZr_{1-x})O_3$ film. The results of AES analysis indicated that the composition of the $Ba(Ti_xZr_{1-x})O_3$ film was not stochiometric as

shown in Table I. The chemical compositions of samples were oxygen, and/or barium enriched.

Table I Chemical Composition and Electrical Properties of $Ba(Ti_xZr_{1-x})O_3$ film

Sputter Power Gun1/Gun2 (watts)	Stoichiometry	Dielectric Constant (1kHz)	DF (1kHz)
100/0	$Ba(Ti_{1.02})O_{3.57}$	24-30	0.002-0.005
100/25	$Ba(Ti_{0.44})O_{3.21}$	23-24	0.004-0.006
75/50	$Ba(Ti_{0.37}Zr_{0.22})O_{3.61}$	20-22	0.004-0.006
50/50	$Ba(Ti_{0.50}Zr_{0.49})O_{3.44}$	18-19	0.004-0.005
50/75	$Ba(Ti_{0.18}Zr_{0.40})O_{4.18}$	17-20	0.006-0.008
0/100	$Ba(Zr_{0.78})O_{4.49}$	15-18	0.006-0.009

*Gun1 strikes $BaTiO_3$ Target
Gun2 strikes $BaZrO_3$ Target

Discussion

The as-deposited $Ba(Ti_xZr_{1-x})O_3$ films produced test capacitors with stable dielectric response and low losses over a broad frequency range. The results are summarized in Table I. Dielectric constants ranged from 17 to 24. The dielectric constants are not expected to reach the level of conventional ceramic powder capacitors because these films were not annealed. External annealing experiments will be performed on these films and the results will be presented. One of the critical issues in producing high dielectric quality $Ba(Ti_xZr_{1-x})O_3$ films will be to determine the influence of the stoichiometry. The RF sputtering process does not produce an exact stochiometric $Ba(Ti_xZr_{1-x})O_3$ film as shown in Table I. The chemical compositions of samples were oxygen and/or barium enriched. Excess ion conductors and interdiffusion between the electrode and dielectric film may increase the leakage current of the $Ba(Ti_xZr_{1-x})O_3$ capacitors. Annealing experiments are necessary to fully determine the influence of the zirconate addition on the frequency and temperature response of the dielectric properties.

Summary

Capacitors using co-sputtered $Ba(Ti_xZr_{1-x})O_3$ film as the dielectric on a multilayer substrate were processed and tested. The dielectric constant of the as-deposited $Ba(Ti_xZr_{1-x})O_3$ films was in the range of 17 to 24. The capacitance of the as-deposited $Ba(Ti_xZr_{1-x})O_3$ film capacitors decreased by 3 percent with increasing frequency from 400 Hz to 100 kHz. The resistivity of the $Ba(Ti_xZr_{1-x})O_3$ films was consistently within 10^{13}-10^{14} ohm-cm. The breakdown strength of these films was $1.4x10^6$ V/cm. The typical dissipation factors (DF) of these films were in the range of 0.004 to 0.008. The dielectric constant is low compared to bulk ceramic capacitors, but is expected to increase by at least an order of magnitude with annealing. Annealing experiments have been initiated. In order to obtain the high dielectric constant of $Ba(Ti_xZr_{1-x})O_3$ film, modification of the microstructure is necessary. The cosputtering ranges and the choice of the combination of targets needs to be further studied. High temperature in-situ processing and high temperature electrodes are needed to achieve the required high temperature, high volumetric efficient capacitor devices for future applications.

Acknowledgements

Research activities were performed by University of Dayton Research Institute under Air Force contract F33615-98-D-2891. The authors would like to thank Mr. Victor McNier and Jeff Fox for their help in the electrical characterization and data acquisition.

References

[1] D.L. Polla, et al., "Applications of PZT and related thin films in piezoelectric microsensors," Mat. Res. Soc. Symp. Proc., 243, 55 (1992).

[2] H. Takasu, "Integrated ferroelectrics as a strategic device," Int. Ferro.,14, 1 (1997).

[3] H.N. Al- Shareef, D. Dimos, M. V. Raymond, R. W. Schwartz, and C. H. Mueller, "Tunability and calculation of the dielectric constant of capacitor structures with interdigitated electrodes," J. Electroceramics, (1997).

[4] S.L. Swartz, "Topics in Electronic Ceramics", IEEE Transactions On Electrical Insulation, Vol. 25, No5, Oct. 1990, pp. 935-987.

[5] B.H Tsao et al., "Barium Strontium Titanate (BST) as Dielectric for Capacitor application," 24th Aerospace Science Symposium, AIAA, April 1999 pp. 65.

Dielectric Properties of Perovskite Superlattices Measured Using Fine Planar Electrodes

T. Tsurumi, T. Ichikawa, T. Harigai, and S. Wada

Department of Metallurgy and Ceramics Science, Graduate School of Science and Engineering,
Tokyo Institute of Technology, 2-12-1 Ookayama, Meguro-ku, Tokyo 152-8552
Fax: +81-3-5734-2514, e-mail: ttsurumi@ceram.titech.ac.jp

$BaTiO_3$(BTO)/$SrTiO_3$(STO) and $BaTiO_3$(BTO)/$BaZrO_3$(BZO) artificial superlattices were fabricated by molecular beam epitaxy (MBE) process and their dielectric properties and refractive indices were measured. A large leakage current was observed in the films on Nb-doped STO substrate. Dielectric permittivity was therefore measured using planer interdigital electrodes. Fine planer electrodes were necessary to reduce the penetration of electric flux into the substrate. Interdigital electrodes were formed by electron beam lithography. Dielectric permittivity of superlattices was determined using electromagnetic field analysis. It was found that the dielectric permittivity of $[(BTO)_{10}/(STO)_{10}]_4$ and $[(BTO)_{10}/(BZO)_{10}]_4$ was ε_r = 720,000 and ε_r = 330,000, respectively. A large dielectric dispersion was observed in the latter. The refractive index of the superlattices was measured by a spectroscopic ellipsometer as a function of wavelength from 350 to 850 nm. It was found that the refractive index of the superlattices changed with the structure, and that of $[(BTO)_{10}/(STO)_{10}]_4$ and $[(BTO)_{10}/(BZO)_{10}]_4$ superlattices was larger than other superlattices.

INTRODUCTION

Artificial superlattices of oxide materials have attracted the attention of material scientists because the superlattices have the potential to drastically improve material properties [1,2]. Oxides with perovskite-type structure exhibit various properties, such as ferroelectricity, piezoelectricity and superconductivity; therefore, the artificial superlattices of perovskite structure, where different materials are stratified at an atomic level, seems to be one of the most interesting systems in the research of the oxide superlattices. Some research groups have succeeded in fabricating artificial superlattices of perovskite compounds [3-10]. An anomaly of dielectric properties in $BaTiO_3/SrTiO_3$ (BTO/STO) superlattice was pointed out by Tabata *et al.*[7] and Nam *et al.*[11]. However, the dielectric properties of BTO/STO superlattices are still not very reliable because of their high leakage currents. It is very important to understand the origin of the high leakage current and to establish the method to measure dielectric properties of oxide superlattices.

Optical properties of oxide superlattices are also attractive research topic. Ellipsometry is a powerful technique to determine the thickness and the refractive index of thin films. This technique has been applied to superlattices of semiconductors by many researchers [12-14]. However, ellipsometric measurements of oxide superlattices have not been done so far. Ellipsometry of oxide superlattices is extremely difficult because they are ultra-thin transparent films whose refractive index is very close to that of the substrate.

In this study, we have fabricated BTO/STO and $BaTiO_3/BaZrO_3$ (BTO/BZO) artificial superlattices by a computer-controlled automatic MBE apparatus. Dielectric properties of the superlattices were measured using interdigital electrodes, and their refractive indices were determined by means of a spectroscopic ellipsometer modified for the measurements of ultra-thin transparent films.

EXPERIMENTAL PROCEDURE

Growth of the superlattices

The BTO/STO and BTO/BZO superlattices were grown on (001) STO or (001) Nb-doped STO single crystals using computer-controlled automatic MBE apparatus. Growth temperature was about 650℃. In order to oxidize metal sources (Ba, Sr, Ti and Zr) in a high vacuum of about 10^{-6} Torr, electron cyclotron resonance (ECR) plasma was irradiated on the surface of the films during the growth. A negative bias voltage was also applied on the substrate to improve the crystallinity of the films.[15] The superlattices were fabricated by an atomic-layer-epitaxy where monolayer of BaO, SrO or TiO_2 was deposited alternatively to make BTO/STO superlattices. The structure of the BTO/STO superlattices is represented by a formula $[(BTO)_m/(STO)_m]_n$, where the subscript m indicates that the structure has a repeating

sequence of m monolayers of BTO and STO, and n is the period of the superlattice. The total thickness (2 x m x n) was fixed at 80 monolayers for both BTO/STO and BTO/BZO superlattices but m had different values from m = 1 to 40.

Characterization of the Superlattices

The crystal structure of the superlattices was verified by the x-ray diffraction (XRD) method.

Two kinds of electrode structure were used for dielectric measurements. In the first structure, a top electrode (0.1 mmϕ) of Pt was formed on a film surface, and a semiconductive Nb-doped STO substrate was used as a bottom electrode. In the second structure, planer interdigital electrodes were formed on a film surface. The size of the interdigital electrodes should be as small as possible because the penetration of electric flux into the substrate increases with the width between the digits. The interdigital electrodes with the size of 5μm between the digits were formed by electron beam lithography. An electromagnetic field analysis was carried out to calculate dielectric permittivity of the superlattices from admittance data. Detail of the electromagnetic field analysis is shown in the following section.

A rotating-analyzer type spectroscopic ellipsometer was used to determine the refractive indices of superlattices. Polarized light from 350 to 850 nm was provided from a Xe lamp (75W) through a computer-controlled monochrometer and an optical fiber. The incident angle was varied from 58 to 77 degree. The ellipsometric parameters (Ψ and Δ) were measured with interval of 5 nm of wavelength and 0.5 degree of incident angle. The total number of data was about 2000 for each sample. Experimental errors in the ellipsometric measurements are theoretically proportional to $(\sin \Delta)^{-1}$ [17] . Measurements on transparent materials is usually difficult because they sometimes give Δ<10 degree. In this case, a compensator (a quarter-wave retarder) was inserted after the polarizer to reduce the experimental errors [18]. The refractive indices of thin films were calculated using the three-phase model (ambient-thin films-substrate). In the analysis, the superlattices were regarded as uniform thin films along the thickness. The Marquardt method [19] was employed to determine the complex refractive index of thin films from ellipsometric parameters measured at different incident angles. The refractive indices of the films were determined at different wavelengths independently and no theoretical formula of wavelength dispersion of refractive index was assumed. Detail of the analysis was described previously [20].

Electromagnetic Field Analysis

An empirical formula is often used to calculate the dielectric permittivity of thin films from capacitance measured with an interdigital electrode. However, the accuracy of this formula markedly reduces if the film thickness is much smaller than the size of electrode. In the case of superlattices prepared in this study, the thickness is only 32 nm which is too thin to determine the dielectric permittivity from the empirical formula. Therefore, an electromagnetic field analysis becomes indispensable to characterize the dielectric properties of the superlattices.

We used commercial software (Sonnet, em) for the field analysis. A model for the analysis is shown in Fig.1. The software calculates the s-parameters and admittance between the port 1 and port 2.

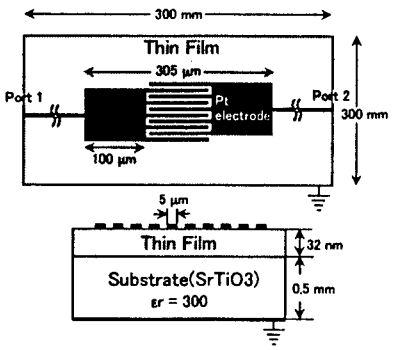

Fig.1 A model used in the electromagnetic field analysis

RESULTS AND DISCUSSION

Dielectric Properties of Superlattices

The current vs. voltage (I-V) curve was first measured using two neighboring circular electrodes (0.1 mmϕ) on the films. The distance between the centers of the two electrodes was 2.0 mm. Figure 2 shows the I-V curves of the $[(BTO)_5/(STO)_5]_8$ superlattice on Nb-doped STO and STO substrates. It was found that the leakage current of the film on the Nb-doped STO was much larger than that on the STO. Actually, the leakage current of the latter was below the measuring limit. A notable difference was observed between the currents of the two specimens in spite that the Nb-doped STO was not used as an electrode. This indicated that the film on Nb-doped STO was leaky in itself. The diffusion of Nb into the film may be the origin of

the large leakage current. We concluded that the Nb-doped STO substrate was not suitable for the measurements of dielectric properties of the superlattices. Planer electrodes on a film deposited on the STO was necessary to determined the dielectric permittivity of superlattices.

In the electromagnetic field analysis for interdigital electrodes, the admittance of a film (30nm, ε_r=1000) with substrate (Y_t) was first compared with the admittance of substrate (Y_s). The Y_t and Y_s were calculated using the field analysis. A parameter ΔY, defined as $\Delta Y = (Y_t - Y_s)/Y_s$, is shown in Fig.3 as a function of the width of the digits in an interdigital electrode. It is obvious that the ΔY increased with decreasing size of electrode. In order to reduce the penetration of electric flux into the substrate and to accurately determine the dielectric permittivity of films, we selected the width of 5μm. Figure 4 shows an optical micrograph of an interdigital Pt electrode formed by the electron beam lithography. Before the measurements The electrode was annealed at 400℃ for 10 min. to reduce the electric resistance.

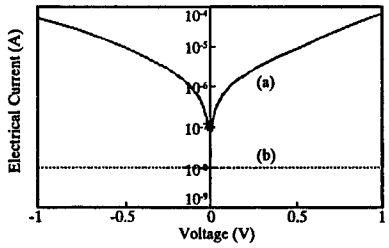

Fig.2 I-V curves measured for superlattices on Nb-doped STO (a) and pure STO (b). In the latter, current was below the detection limit.

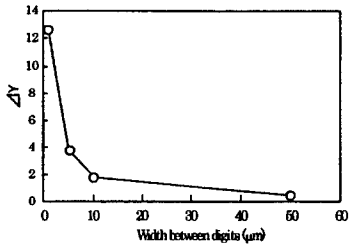

Fig.2 Relation between the change in admittance and the width between digits of electrode.

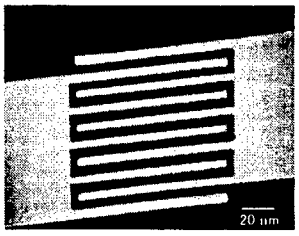

Fig.4 Interdigital electrode formed by electron beam lithography.

The capacitances of BTO/STO and BTO/BZO superlattices were measured as a function of frequency. It was found that the capacitance of $[(BTO)_{10}/(STO)_{10}]_4$ and $[(BTO)_{10}/(BZO)_{10}]_4$ superlattices were much larger than other specimens, and a large dielectric dispersion was observed for the latter. The dielectric permittivity of superlattices was calculated by the following procedure. The dielectric permittivity of the substrate was first determined by fitting calculated admittance to that observed. And, the admittance of a thin film on the substrate was calculated using a tentative dielectric permittivity of the film and the permittivity of the substrate determined above. The permittivity of the film was changed and refined to fit the observed data. The admittance of superlattices is shown in Fig.5 as a function of frequency. It was found that the dielectric permittivity of $[(BTO)_{10}/(STO)_{10}]_4$ and $[(BTO)_{10}/(BZO)_{10}]_4$ superlattices were 720,000 and 330,000, respectively. These values may be the highest in known materials.

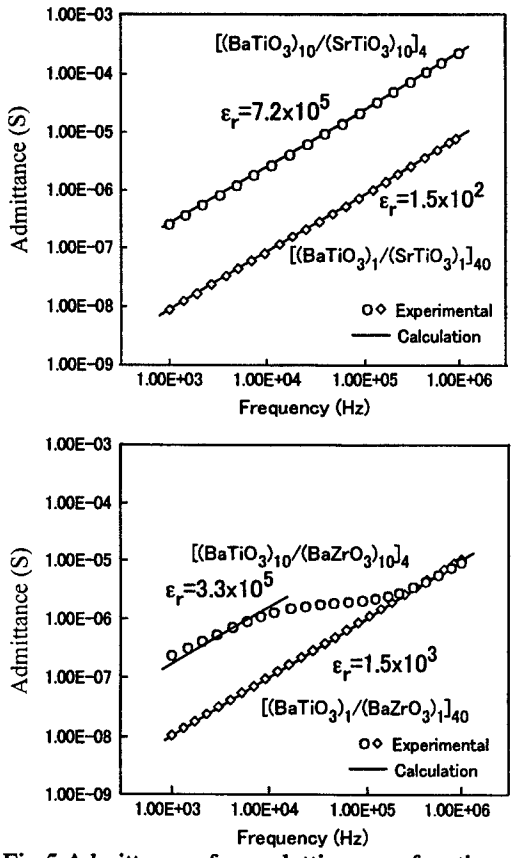

Fig.5 Admittance of superlattices as a function of frequency.

Optical Properties of Superlattices

The refractive index of the superlattices determined by the ellipsometry was shown in Fig.6 as function of light wavelength. The refractive index decreased with increasing wavelength for all specimens. It is obvious that the refractive index of $[(BTO)_{10}/(STO)_{10}]_4$ and $[(BTO)_{10}/(STO)_{10}]_4$ is higher than other specimens. This result is well consistent with that of the result of dielectric measurement. The dielectric permittivity at low frequencies may be determined by the ionic polarization while the refractive index is determined by the electric polarization. The similar behavior of the dielectric permittivity and the refractive index is very interesting phenomenon. The stacking structure in a superlattice affects not only the ionic motion but also on the electronic structure or chemical bonding nature in the superlattice. However, the detail of the origin is not known at present. Theoretical work seems to be necessary to explain the properties of oxide superlattices.

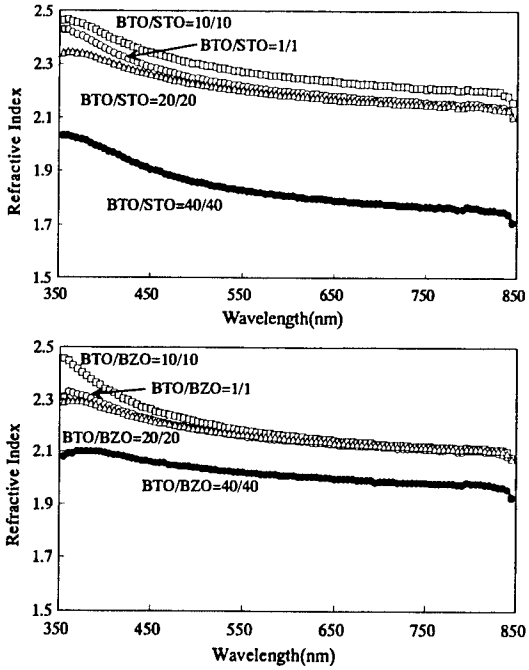

Fig.6 Refractive indices of BTO/STO and BTO/BZO superlattices

CONCLUSION

The BTO/STO and BTO/BZO artificial superlattices were fabricated by MBE process and their dielectric and optical properties were measured.

Superlattices on Nb-doped STO substrates showed large leakage currents, indicating that this substrate was not suitable for the use of bottom electrodes. Dielectric permittivity was therefore measured using planer interdigital electrodes. Fine planer electrodes were necessary to reduce the penetration of electric flux into the substrate. It was found that the dielectric permittivity of $[(BTO)_{10}/(STO)_{10}]_4$ and $[(BTO)_{10}/(BZO)_{10}]_4$ was ε_r = 720,000 and ε_r = 330,000, respectively. These values may be the highest in known materials.

The Refractive index of the superlattices was measured by a spectroscopic ellipsometer. It was found that the refractive index of the superlattices changed with the structure, and that of $[(BTO)_{10}/(STO)_{10}]_4$ and $[(BTO)_{10}/(BZO)_{10}]_4$ superlattices was larger than other specimens. This indicated that the stacking structure in a superlattice affected not only the ionic polarization but also on the electronic polarization in superlattices.

References

[1] H.Koinuma and N.Kanda, Shinku 36 (1993) 67 (in Japanese).
[2] H.Tabata and T.Kawai, Shinku, 36 (1993) 81 (in Japanese).
[3] K.Iijima, T.Terashima, Y.Bando, K.Kamigai and H.Terauchi, J.Appl.Phys., 72 (1992) 2840.
[4] T.Tsurumi, T.Suzuki, M.Yamane and M.Daimon, Jpn.J.Appl.Phys., 33 (1994) 5192.
[5] T.Tsurumi, T,Miyasou, Y.Ishibashi and N.Ohashi, Jpn.J.Appl.Phys., 37 (1998) 5104.
[6] F.Le Marrec, R.Farhi, M.El Marssi, J.L.Dellis and M.G.Karkut, Phys.rev., B61 (2000) 6447.
[7] H.Tabata, H.Tanaka and T.Kawai, Appl.Phys.Lett., 65 (1994) 1970.
[8] M.Yoshimoto, H.ohkubo, N.Kanda and H.Koinuma, Jpn.J.Appl.Phys., 31 (1992) 3664.
[9] T.Zhao, Z.-H.Chen, F.Chen, W.-S.Shi, H.-B.Lu and G.-Z. Yang, Phys. Rev. B60 (1999) 1697.
[10] D.H.Kim, D.-W.Kim, B.S.Kang, T.W.Noh, D.R.Lee, K.-B.Lee and S.J.Lee, Solid State Communications, 114 (2000) 473.
[11] S.M.Nam, S.Mitarai, Y.Ishibashi, T.Tsurumi and O.Fukunaga, J.Korea Phys.Soc., 29 (1996) S632.
[12] R.H.Hartley, M.A.Folkard, D.Carr, P.J.Orders, D.Rees, I.K.Varga, J.Cryst.Growth, 117 (1992) 166.
[13] D.Behr, J.Wagner, J.Schmitz, N.Herres, J.D.Ralston and P.Koidl, Appl.Phys.Lett., 65 (1994) 2972.
[14] L.H.Qin, Y.D.Zheng and R.Zhang, Appl.Phys., A55 (1992) 297.
[15] Y.Ishibashi, T.Tsurumi, N.Ohashi and O.Fukunaga, Solid State Ionics, 108 (1998) 91.
[16] Y.Ishibashi, N.Ohashi and T.Tsurumi, Jpn.J.Appl.Phys., 39 (2000) 186.
[17] J.M.M.de Nijs and A.van Silfhout, J.Opt.Soc.Am. A5 (1988) 773.
[18] P.Chindaudom and K.Vedam, Appl.Opt., 32 (1993) 6391.
[19] D.W.Marquardt, J.Soc.Indust.Appl.Math., 11 (1963) 431.
[20] Y.Ma, T.Tsurumi, S.Nishizawa, N,Ohashi and O,Fukunaga, J.Am.ceram.Soc., 81 (1998) 2125.

Initial Results for MOCVD (Ba,Sr)TiO_3 Thin Film Capacitors on Metal Foils

D.Y. Kaufman[1], S.K. Streiffer[2], J. Im[2,3], S. Saha[2], O. Auciello[2], and R. Erck[1]

[1]Energy Technology Division
[2]Materials Science Division
Argonne National Laboratory
9700 S. Cass Ave., Argonne, IL 60439
[3]Now at Agere Systems
FAX: (630) 252-4289
Email: streiffer@anl.gov

(Ba,Sr)TiO_3 thin films are candidates for volumetrically efficient high charge storage density and high energy density capacitors. A broader range of cost competitive applications could be met by fabricating the thin film capacitors on base-metal and alloy foils. Here we report on (Ba,Sr)TiO_3 thin films deposited by liquid delivery metalorganic chemical vapor deposition on Ni, Hastelloy, and Inconel foils. The effects of film composition and substrate on dielectric properties were studied. Little impact on the permittivity of BST synthesized on platinized silicon was found when varying the Ba:Sr ratios from 25:75 to 70:30. A 650nm thick BST film on nickel showed a permittivity of 240 and a dielectric loss of 0.8%.

INTRODUCTION

Significant achievements have been made in electronic circuit designs and module components. Considerable attention is now concentrated on improving overall performance while reducing module size, weight, and cost. While progress has been made in active components, substantial technological advances are needed in capacitors. Specific improvements desired include increased capacitance density, decreased electrical and thermal losses, improved packaging, and improved reliability and lifetimes.

Capacitor architecture plays a significant role in device performance as well. Although research and development is progressing on other fabrication techniques, multilayer ceramic capacitors are still generally tape-cast multilayer structures consisting of μm-thick ceramic dielectric layers sandwiched between interdigitated metal electrodes. In contrast to this, vapor deposited thin film dielectric layers can exhibit improved materials uniformity, higher density, and smoother electrode-dielectric interfaces, which all lead to higher breakdown strengths. Indeed, vapor deposited ($Ba_{1-x}Sr_x$)TiO_3 (BST) thin film capacitors have shown [1] breakdown fields as high as 3MV/cm, and dissipation factors of ~0.2% over several frequency decades have been reported [2]. Additionally, the extremely fine microstructure, coupled with potential mechanical clamping of the dielectric thin film by the substrate, can result in improved temperature stability for vapor phase deposited films [3], at the expense of overall permittivity. Thin film capacitor technologies can also result in smaller device footprints and the possibility of integrating capacitors directly onto semiconductor circuits.

To realize these potential improvements for discrete devices, however, the weight and cost of the substrates used for vapor deposited dielectrics should be greatly reduced. This may potentially be achieved by replacing relatively expensive noble metal bottom electrodes on a silicon substrate, with base metal or alloy foils that serve as an integrated electrode/substrate. Routine patterning methods have been established for a number of foil materials of interest that would allow straightforward fabrication of various device geometries. Additionally, BST thin films on metal foils could potentially be coiled into high volumetric capacitance structures, if the critical radius of curvature for failure of the dielectric is not exceeded. Several groups have explored this approach using chemical solution deposition to

produce the high-permittivity dielectric layer [4], [5], yielding extremely promising results. Here we explore the potential for using metalorganic chemical vapor deposition as an alternative route to fabricate the high-permittivity dielectric layer.

EXPERIMENTAL PROCEDURES

BST films were deposited using a commercial liquid precursor delivery system (ATMI LDS-300B) which allows fine compositional control with a high degree of process reproducibility [6]. Liquid solutions of the metalorganics (polyamine adducts of β-diketonate complexes) are metered to a flash evaporator and the vapor stream then directed into the reactor.

The vertical reactor was designed at Argonne National Laboratory and incorporates an oil-heated gas delivery line and injection of the reactant O_2 and N_2O gases adjacent to the substrate. BST films were deposited at 650°C to 700°C, at 0.4 to 1 Torr total pressure. The film composition was controlled by adjusting the LDS parameters to obtain Ba:Sr ratios ranging from 0:100 to 70:30, and Ti compositions of 50-55 at% as determined by RBS and XRF. Good film uniformity was obtained over a 4" diameter as observed by a uniform thickness fringe color. Growth rates as high as 120Å/min have been achieved.

RESULTS

Effect of Ba:Sr Ratio

Although the optimum Ba:Sr ratio for specific operating conditions has been intensively explored for bulk ceramics and for sputtered thin films, relatively little data exists for the temperature dependence of the dielectric properties of MOCVD BST films as a function of this ratio. Therefore, the first goal of this research was to deposit films with different Ba:Sr ratios onto standard platinized silicon substrates, in order to select a ratio to deposit onto metal foil substrates.

Three compositions were selected for investigation: Ba:Sr = 0:100, 25:75, and 45:55. These can be compared to previously published data for Ba:Sr = 70:30 [3]. Curves of permittivity vs. temperature for the three samples are shown in Figure 1. The samples had losses below 1% at room temperature, that gradually increased as measurement temperature was lowered. The BST films were all approximately 70 nm in thickness, but had slightly different Ti contents, 52% for 0:100, 53% for 25:75, and 51% for the 45:55. This variation arose primarily from LDS metering inaccuracies, as individual Ba, Sr, and Ti sources were utilized to achieve the widest accessible composition range. Note that this complicates comparison of the absolute magnitude of the permittivity, as permittivity strongly depends on Ti content for this film thickness. However, the 25:75 and 45:55 samples have room-temperature permittivities within 20% of those of 70:30 BST films of the same thickness and composition [3].

To more directly compare the samples, Figure 2 shows inverse permittivity vs. temperature, normalized to its value at 300K for each Ba:Sr ratio. This normalization should at least qualitatively remove the effect of the Ti variation. It is clear that the two Ba-containing samples show very similar temperature dependencies, whereas the pure $SrTiO_3$ sample shows a much more Curie-Weiss like behavior over most of the investigated temperature range. This intriguingly suggests that the Ba-containing samples show diffuse dielectric behavior because of compositional effects, such as Ba clustering in a compositionally-inhomogeneous matrix.

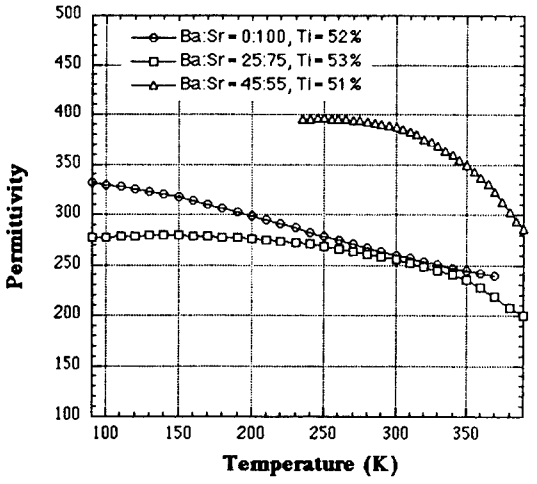

FIGURE 1: Permittivity vs. temperature for 70nm BST films with different Ba:Sr ratios. Note that the Ti contents of the films are different, thus it is difficult to compare absolute magnitudes of the permittivity.

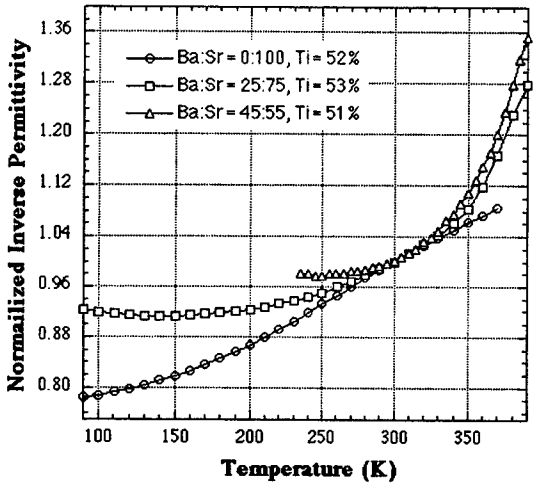

FIGURE 2: Inverse permittivity vs. temperature for 70nm BST films with different Ba:Sr ratios, normalized to inverse permittivity at 300K for each sample. Note the difference in behavior for the pure $SrTiO_3$ samples vs. the Ba-containing samples.

Deposition Onto Metal Foils

As illustrated by the results discussed above, there is no strong motivation for choosing a particular Ba:Sr ratio from among those investigated. Therefore it was decided to deposit films onto metal foils using a Ba:Sr ratio of 70:30, to most easily compare to the results achieved for deposition onto platinized silicon. The Ti content was fixed at 50%. Before deposition, foils were polished to 0.25μm using diamond paste.

Figure 3 shows the results for an 650nm BST film deposited onto a pure Ni foil. The permittivity is somewhat reduced, presumably by oxidation of the Ni at the bottom interface. Nonetheless, the dielectric loss is acceptable over the entire frequency range. Measurement of smaller devices indicates that the slow increase of the dielectric loss with increasing frequency is a measurement artifact.

Films were also deposited onto Inconel and Hastelloy foils. Properties are summarized in Table I. On these two materials, the BST showed unacceptably high losses, accompanied by a very strong dispersion in the permittivity with frequency. However, the Ni substrates appear to survive the relatively oxidizing ambient of the MOCVD deposition process, based on the reasonable dielectric properties of the BST deposited onto it.

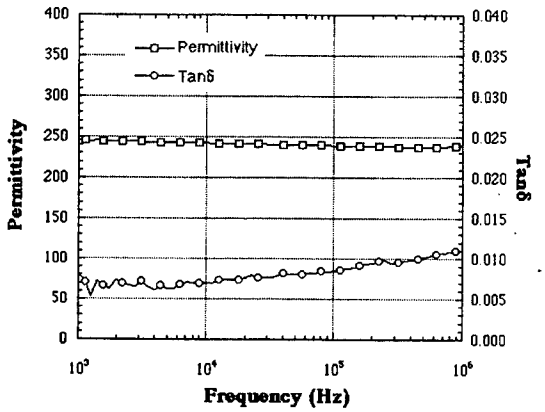

FIGURE 3: Permittivity and dielectric loss vs. frequency for an 650nm BST 70:30 film deposited on a Ni foil. The slow increase of tanδ with frequency is an artifact of the measurement.

TABLE I: Dielectric properties of 650nm BST deposited on various foils, measured at 10kHz.

Foil Material	Permittivity	Tanδ
Nickel	240	0.8%
Inconel	450	34%
Hastelloy	890	25%

The hard breakdown field of the 650nm BST film on the Ni foil was determined to be approximately 0.7MV/cm. A thinner BST film on Ni, only 130nm thick, showed a permittivity of 80, and had a hard breakdown field of approximately 1.25 MV/cm.

CONCLUSIONS

BST films were synthesized by MOCVD on nickel, Inconel, and Hastelloy metal foils. Based on BST deposited on platinized silicon substrates, it was deduced that choice of the Ba:Sr ratio in the range of 25:75 to 70:30 does not qualitatively influence the dielectric behavior as a function of temperature for room temperature application. Films deposited onto Ni showed acceptable properties, although permittivity was somewhat reduced. The permittivity and loss tangent (240 and <1%, respectively) of a 650nm MOCVD BST film on nickel compare favorably with those of PLZT films deposited by chemical solution deposition onto foils, which show permittivities and loss tangents in this same range (240 and 1.5%, respectively, for 600nm

PLZT deposited by CSD onto nickel-plated copper foils [5]). Films grown on the two other materials exhibited unacceptably high losses.

ACKNOWLEDGMENTS

This work has been supported by the United States Department of Energy, Offices of Transportation Technologies and BES-Material Sciences, under Contract W-31-109-ENG-38.

REFERENCES

[1] C.M. Foster and L.F. Wills, unpublished result.

[2] J. D. Baniecki, R. B. Laibowitz, T. M. Shaw, P. R. Duncombe, D. A. Neumayer, D. E. Kotecki, H. Shen and Q. Y. Ma, "Dielectric Relaxation of $Ba_{0.7}Sr_{0.3}TiO_3$ Thin Films from 1 mHz to 20 GHz", *Appl. Phys. Lett.* **72**, 498 (1998).

[3] S. K. Streiffer, C. Basceri, C. B. Parker, S. E. Lash and A. I. Kingon, "Ferroelectricity in Thin Films: The Dielectric Response of Fiber-Textured $(Ba_xSr_{1-x})Ti_{1+y}O_{3+z}$ Thin Films Grown by Chemical Vapor Deposition", *J. Appl. Phys.* **86**, 4565 (1999).

[4] Q. Zhou, H.E. Ruda, B.G. Yacobi, K. Segusa, and M. Farrell, "Dielectric Properties of Lead Zirconate Titanate Thin Films Deposited on Metal Foils," *App. Phys. Lett.* 77, 1038 (2000).

[5] J.-P. Maria, K. Cheek, S.K. Streiffer, S.-H. Kim, G. Dunn, and A.I. Kingon, "Lead Zirconate Titanate Thin Films on Base-Metal Foils: An Approach for Embedded High-*K* Passive Components," accepted for publication in *J. Amer. Cer. Soc.* (2001).

[6] P. C. Van Buskirk, S. M. Bilodeau, J. F. Roeder and P. S. Kirlin, "Metalorganic Chemical Vapor Deposition of Complex Metal Oxide Thin Films by Liquid Source Chemical Vapor Deposition", *Jpn. J. Appl. Phys.* **48**, 2520 (1996).

Measurement of Dielectric Properties of $BaTiO_3$-Based Materials in the 10 MHz to 1 GHz Frequency Range

C.W. Nies and E. Deyneka
Advanced Products and Technology Center, AVX Corporation, Myrtle Beach, SC
M. Lanagan
Materials Research Laboratory, The Pennsylvania State University, University Park, PA.
Email: cnies@avxus.com

INTRODUCTION

One of the largest volume applications for multilayer ceramic capacitors is in decoupling applications. Decoupling capacitors act as local energy sources for integrated circuits, providing the needed voltage to switch and refresh the logic gates. In this regard, the decoupling capacitor isolates the IC from spurious noise from the power supply and other local circuitry. $BaTiO_3$-based MLCCs, meeting either X7R or Y5V temperature ratings are usually selected for these applications, with relative permittivities ranging from 2500 to 15000.

As the switching speeds of microprocessors increase, decoupling capacitors are being used in circuits operating in the 10 MHz to 1 GHz range. In this range, ferroelectric $BaTiO_3$ is known to show a decline in dielectric constant with frequency, related to the relaxation of polarization created by domain wall motion [1]. However, this behavior has been difficult to investigate with bulk samples using popular measurement techniques. In the lower frequency range, the measurement would normally be made using a lumped impedance test such as standard impedance bridges supply. However, samples with K>100 typically show a resonance in this frequency range due to self-inductance, and the sample impedance is often too low for accurate measurement. At frequencies near 1 GHz, resonance or transmission techniques can be used, but produce values only at discrete frequencies depending on sample dimensions. The measurements are also limited to low dielectric loss specimens (tan delta< 0.01). Most $BaTiO_3$-based materials chosen for decoupling capacitors have higher losses than this.

To help simplify dielectric measurements on these materials, a combination of improved lumped impedance measurements and data analysis by numerical analysis were employed. Lumped impedance measurements were taken on either an impedance analyzer or a network analyzer, using small disc samples held in a shorted coaxial cable sample holder. This minimizes stray inductance and simplifies the measurement geometry. Permittivity and loss data were then extracted using either a Bessel function field model for nonuniform electromagnetic fields or with commercial equivalent circuit modeling software. The resulting procedures reduced the inaccuracies associated with sample resonance, and offered continuous dielectric data in the high megahertz range with a minimum number of samples prepared.

EXPERIMENTAL

Sample Preparation

Experiments performed in this study centered on a commercial capacitor material with K~4000 at room temperature and a Curie point well above 25°C. This material was chosen to emphasis the frequency variability at room temperature. Bulk samples of this materials were obtained by standard disc pressing and sintering means. The samples were then given thin sputtered electrodes of Au or Au/Pd, followed by a coating of an air-dried silver epoxy to protect the thin film surface. Smaller disc samples were then ultrasonically cut from the original discs with an outside diameter of 3 mm. This dimension was chosen to match the dimension of the center conductor of an APC7 coaxial connector, used in the sample fixture described below.

Measurement

Measurements for this experiment were taken using either a Hewlett-Packard 4921A impedance analyzer or an 8510 network analyzer, whose sample holder terminated in an APC7 connector. This connector was fitted with the "shorted coaxial cable" sample holder shown in Figure 1. Each 3 mm disc sample was placed directly on the center collet of the APC7, then enclosed in the sample holder. The sample

Figure 1: Low inductance test fixture and sample resting on APC7 connector.

holder was fitted with a movable electrode which is brought into contact with the upper disc surface by tightening a feed screw. In this configuration, the sample holder inductance is minimized.

Data Analysis

The impedance/phase data thus collected requires correction due to resonances in the sample. This resonance develops when a non-uniform electric field develops across the sample as the sample size and wavelength approach each other, producing an inductance associated with the specimen. Under these conditions, dielectric measurements are usually evaluated at frequencies at least 1 order of magnitude below a resonance point. If the inductive term can be modeled, dielectric data could be evaluated over much larger portions of the frequency spectrum. For this reason, the self-inductance effects were analyzed using two techniques.

In the first technique, the magnitude of the distributed electromagnetic field was evaluated by modeling it using a similar approach to one used by Sharpe and Brockus [2]. In the technique, a modified Bessel function was used to calculate the real and imaginary parts of the permittivity from the measured admittance. A small variation in the model was made to account for the inductance due to the sample in the test jig. This data was then translated into K values. Mathcad®-based software was developed for this purpose.

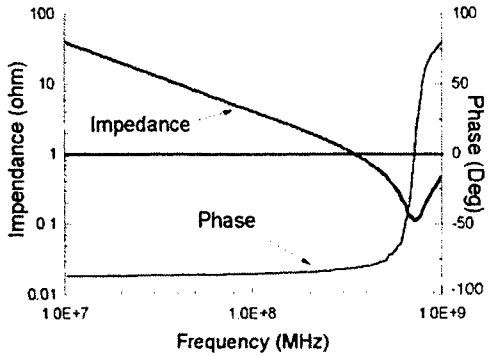

Figure 2: Typical Impedance and Phase Data for Disc Samples (taken on HP 4291A).

In the second technique, the sample inductance was approximated by measuring the inductance of small brass discs of a similar size to the sample. A simple circuit model was then constructed using RF/microwave design software (GENESYS 7, Eagleware Corporation). The model contains a variable capacitor whose value can be programmed as a function of frequency. The model was then fit to the impedance and phase data, yielding a function which approximated the disc's capacitance. This function was then used to approximate the dielectric constant.

RESULTS

Figure 2 shows an example of the impedance and phase data taken with the HP 4291A. The data shows a distinct resonance near 700 MHz, which would limit direct measurement of capacitance data to below 70 MHz. The data shown was then analyzed using either the distributed field (Bessel function) or equivalent circuit approach.

Distributed Field Approach

Figure 3 shows a plot of the K both before and after using the modified Bessel function to compensate for the distributed field. The plot shows the elimination of the resonance peak in the data and indicates that the capacitance rolls off by almost 20% at 300 MHz. Past this point, the calculated values begin to increase, and also show apparent instability above this point. The source for this instability is unknown, but it is probably the result of higher frequency resonances related to stray reactive components that have not been accounted for yet

Figure 4 shows a comparison of the distributed field data to measurements taken at lower frequencies using a standard LCR meter. The measured data again show good agreement

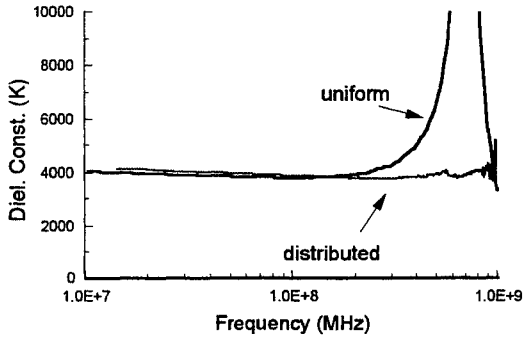

Figure 3: Comparison of K Values Calculated Assuming Uniform and Distributed Fields

with the calculated data in the crossover 1-10 MHz range up to the 300 MHz vicinity where both permittivity and loss data become unstable.

Equivalent Circuit Approach

For this study, the GENESYS software was used to calculate the impedance of given circuit model, then evaluate the difference between the model and the measured data. The program then automatically adjusts the circuit element iteratively to minimize the difference. The program requires realistic initial values or relationships to be assigned to the components as a starting point for the iterative calculations.

The well-known circuit in Figure 5 was chosen as the model for this study and assigned initial values based on previous experience and experiments. Resistors Rs and Rp were selected as 0.1 ohm and 100 Gohm, respectively. The value of inductor Ls was estimated at ~0.15

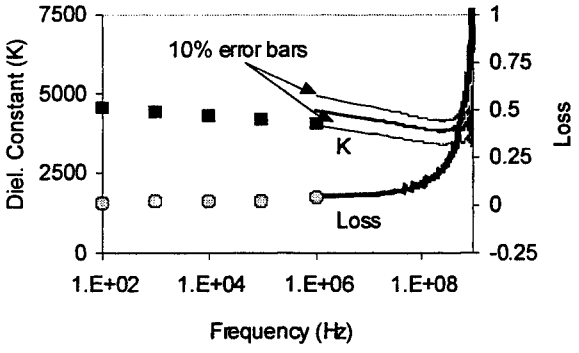

Figure 4: Comparison of K Calculated from Low Frequency Measurement and Distributed Field Model

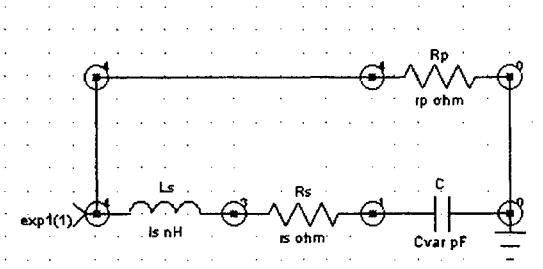

Figure 5: Equivalent Circuit Used to Model Impedance Data.

nH by measuring the inductance of a brass slug that was similar in size to the sample. The parallel capacitance Cp was modeled as a linear function of frequency using the relationship

$$Cp = Co - Af$$

where Co is the sample capacitance at 1 MHz (~430 pF), and A is the frequency coefficient (~0.3 pF/MHz). Its Q value was also estimated at 18.

After a period of iteration, the program converged on the following values:

A = 0.204 pF/MHz	Co = 425 pF
Ls = 0.178 nH	Q = 18
Rp = 270 Gohm	Rs = 0.058 ohm

Plots of the measured impedance and phase data and modeled values are shown in Figure 6. The fit is extremely close over most of the frequency spectrum evaluated; there is little visible divergence between measured and model data. Furthermore, the optimized parameters returned by the software are very close to the expected values, indicating again that the model represents actual behavior.

Figure 7 shows a comparison of the calculated K values for both treatments of the data. Both models predict values within ~5% of each other up to 300 MHz, at which point the distributed model becomes unstable. The linear model suggests the permittivity will continue to decline as is expected, but no measured values are available at this time to confirm those predicted by the model. This will require the use of resonance or transmission techniques, to be performed at a later point. The equivalent circuit model has not been altered yet to account for the changing loss values of the capacitor in this region.

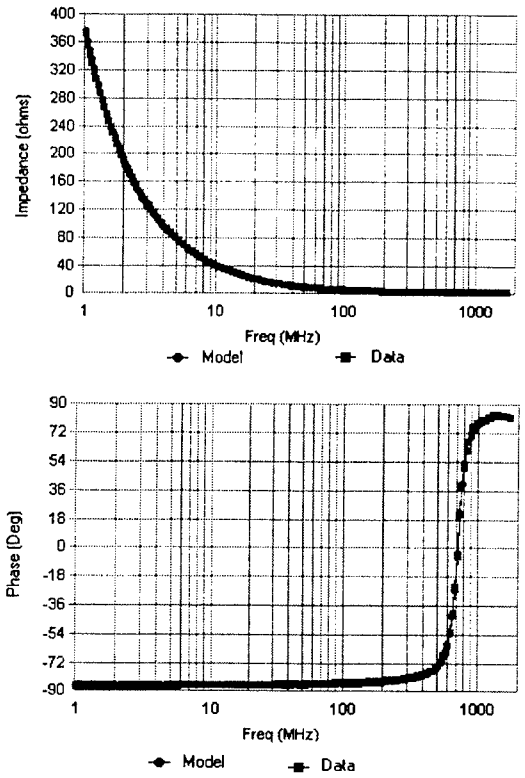

Figure 6: Impedance and Phase Model Compared to Measured Data based on Equivalent Circuit with Variable Capacitance.

DISCUSSION

Each of these techniques for modeling the frequency dependent behavior of a dielectric has advantages and disadvantages.

The distributed field modeling more accurately describes the inductance conditions of the sample and produces a technically better estimate of the permittivity. However, it is somewhat more difficult to alter the calculations for other stray impedance components.

The equivalent circuit simulation offers a simplified model of the frequency dependence of capacitance and permittivity. This model could potentially be used to construct models of actual devices to be used with SPICE or other circuit design software. This model could readily be extended to higher frequencies by including other RLC components to account for parasitic impedances or to match any observed behavior. However, any equivalent circuit model is mainly empirical and requires confirmation by actual measurements. The physical significance of additional circuit elements must be considered to keep the model in touch with reality.

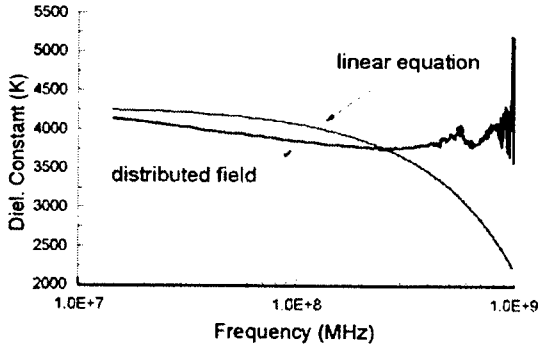

Figure 7: Comparison of Predicted K Values for Distributed Field and Equivalent Circuit (Linear Equation) Models with Frequency

SUMMARY

$BaTiO_3$-based dielectric materials exhibit frequency dependent permittivity in the 10 MHz to 1 GHz range. In this study, two techniques are proposed for estimating the permittivity of these materials from lumped impedance measurements, using disc samples in a low inductance test fixture. In the first, the field distribution in the sample is calculated using a modified Bessel function, and the permittivity then calculated using this field. In the second, the lumped impedance data was modeled using an equivalent circuit by high frequency circuit modeling software. The equivalent circuit contained a frequency variable capacitor, whose estimated value with frequency was used to calculate the permittivity. These methods produce estimated permittivity values within ~5% of each other up to about 300 MHz. Above this, the models diverge and will require refinement and experimental verification.

Acknowledgments – The authors would like to thank S. Perini, S.K. Rajab and Joseph Hock for their assistance in this study. Funding was provided by AVX Corporation and the Penn State Center for Dielectric Studies.

REFERENCES

1. M.P. McNeal, S.J. Jang, and R.E. Newnham, J. Appl. Phys., 83(6), pp. 3288-3297 (1998).
2. C.B. Sharpe and C. G. Brockus, J. Am. Ceram. Soc., 43(6), pp. 302-305 (1960).

Microwave Properties of Dielectric Oxide and High T_c Superconductor System

S. Sugihara, T.Kawashima, C.Ishizuka and N.Kimura

Department of Materials Science and Engineering, Shonan Institute of Technology,
1-1-25, Tsujido nishikaigan, Fujisawa, Japan
Tel: 81-466-30-0227, Fax: 81-466-36-1594
Email: sugihara@mate.shonan-it.ac.jp

Abstract

The high-Tc superconductor and TiO_2-sandwiched system was investigated under microwave irradiation. The change of TiO_2 length with the superconductor effected the relative permittivity with the maximum value of 42 and about 350 of Q at room temperature. Furthermore, superconductor-surrounded TiO_2 sandwiched system was also studied to result in higher Q such as 834 and over 2000 at room temperature and liquid nitrogen, respectively.

INTRODUCTION

High temperature superconductor has been developed in various points for more than the last ten years. The applications have not been prevailed yet in commercial base. However, superconductor wire is popular recently. The new systems with superconductor aimed at usage under microwave were reported in low phase noise superconducting oscillators, the coplanar resonator, band pass filter etc. We reported the bulk type high-Tc superconductor and TiO_2-sandwiched system for microwave at room temperature as well as liquid nitrogen [1] . In this report, the dependences of the microwave property on the length of TiO_2 was investigated as well as the superconductor -surrounding TiO_2 sandwiched system which is a new devise of this system.

EXPERIMENTAL

The superconducting powder of BiSrCaCuO was provided by Institute of Kusaka Rare Metal and pressed at 192 MPa followed by sintering for 24 hours at 1133 K. The dielectric powder of TiO_2 (Fuji Titanium Industry Co., Ltd) was compacted at the same pressure as the superconductor ,and sintered for 2 hours at 1613 K. A pellet of TiO_2 was sandwiched between the superconductor having different thickness of TiO_2 from 0.9 mm to 2.7 mm. The ratio of total length (L) to diameter (D) , L/D should be more than 0.4 for this resonator. The sandwiched system was set into the cavity for measurement of microwave properties using HP8510B network analyzer, then relative permittivity and tan δ were obtained with a resonant frequency. Thermal dependence of the resonant frequency was investigated at the temperature range of 100 K and 300K. Furthermore, the different type of the sandwiched system was investigated ,where the circumferences of the specimen except for the windows of the input and output of the microwave to the resonator were coated by the superconductor powder with thick film.

RESULTS AND DISCUSSION

Relative permittivity

Figure 1 shows the changes of relative

permittivity against the ratio of the total length of the TiO_2 to the superconductor, $\lambda = \lambda_t / \lambda_s$. Actually, the minimum thickness of TiO_2 was 0.940mm and the maximum of 3.604 mm. It came out that the larger λ_t showed smaller permittivity. The mode was considered to be $Te_{01\delta}$ in the net work analyzer. The top and bottom of the system were the Bi-series superconductor which functioned as semiconductor at room temperature concerning with electrical resistivity. Therefore, admittance(Y) in the equivalent circuit of capacitance(C_t) with dielectric loss and superconductor having capacitance(C_s) with resistivity of R_s is indicated under the microwave irradiation as following equation,

$$Y = j\omega C_t + \frac{1}{R_t + \frac{1}{j\omega C_s}} \quad \text{------ (1)}$$

R_t of TiO_2 increased when thickness of the dielectric was larger ($\lambda \rightarrow$larger) as shown in the equation (2), then C_s decreased, leading to the decreasing of the admittance in the system.

$$\lambda = \frac{\lambda_t}{\lambda_s} \approx \frac{R_t}{R_s} \quad \text{---------- (2)}$$

Quality factor

Figure 2 illustrates the dependence of Q value on temperature at 6.2 GHz and Q value increased with decreasing temperature around the transition temperature of the superconductor. This fact suggested that the superconductor confined the magnetic field energy into the system around superconducting state, then the loaded Q value increased as followed by the following equation;

$$Q = \omega_0 \frac{stored\ energy\ in\ dielectric}{consumed\ power\ in\ system}$$

Tamura et al. reported temperature dependence of unloaded Q at 2.1 GHz for TM_{010} mode dielectric resonator with Bi2223 thick film on MgO and silver conductors[2]. At lower temperature around 100K, unloaded Q increased abruptly, showing the Q value up to 70000 at 30K. The system of YBCO superconductor with Cu showed the unloaded Q increase with decreasing temperature[3].

Superconductor-surrounded TiO_2 specimen

The specimen surrounded by superconductor without the ports for microwave inlet- and outlet-windows was provided for measuring the change of Q value in liq. Nitrogen as shown in Table I.

Table I Effect of superconductor surrounding TiO_2 sandwiched system.
Dark line represents superconductors, and TiO_2 for white part.

	εr	△f (MHz)	Average f_0 (GHz)	Q	Temp (K)
Normal	37.9	24	6.20	258	300
	38.2	21	6.20	294	300
	38.5	7.5	6.20	834	123

The Q value (at room temperature) of the

specimen surrounded by superconductor increased by 14% as compared with normal type which had superconductor at both ends only. Furthermore, the Q increased more than three times when the specimen was measured at 123 K. It was found that dielectric loss became smaller before the transition temperature. Electric field in the radius direction for this mode ($Te_{01\delta}$)seemed to be stronger due to the surrounding of superconductor and was less diminished in the z direction, so $Te_{01\delta}$ may be closed to TM_{010} mode. We could confirm that the properties of the normal one ($\lambda = \lambda_t / \lambda_s$ =0.797) was almost same when the specimen was compared to the λ =0.72 shown in Fig.1.

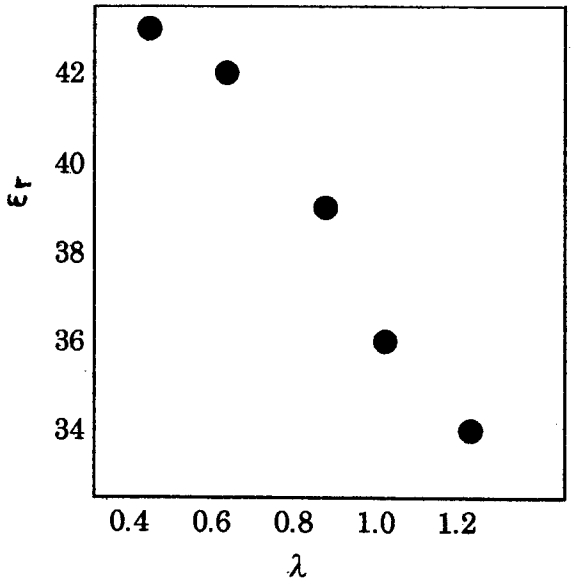

Fig. 1 Relative permittivity vs thickness ratio defined by $\lambda = t_t / t_s$;
t_t and t_s :thickness of TiO_2 and of the superconductor, respectively, T= 300K.

Furthermore, superconductor-surrounded TiO_2 sandwiched system showed the larger change of Q value in liquid nitrogen. This specimen was the same one that temperature dependence of the property was measured ,as shown in Fig.2. The results was summarized in Table II.

The value of Q×f was 12700 which was the higher than one reported in the system of Bi-series/MgO at 105 K by Tamura[2]. As shown in Table 1, superconductor-surrounded TiO_2 sandwiched system improved quality factor at the low temperatures. This system was supposed to cause the decrease of insertion loss at the resonant frequency around 6 GHz in the low temperatures.

The microwave penetration depth has a low

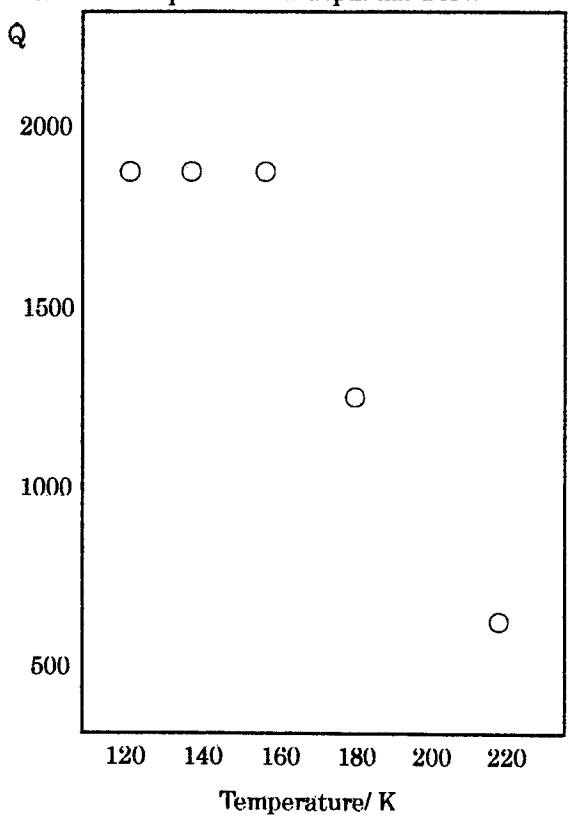

Fig. 2 Temperature changes of quality factor of the system($\lambda = t_t / t_s$ =1.91).

Table II Effect of superconductor- surrounded TiO_2 sandwiched system.

λ	εr	△f (MHz)	Average f_0 (GHz)	Q	Temp (K)
1.908	35.1	3	6.18	2060	105

temperature linear behavior followed by a faster

increase at higher temperature than Tc as reported by T.Jacobs et al [4].

The effect of TiO_2 length ($\lambda = t_t / t_s$)

Furthermore, we found the effect of TiO_2 length ($\lambda = t_t / t_s$) on the Q at the room temperature as shown in Fig.3. This system is not the superconductor-surrounded TiO_2 system. The length of TiO_2 effected Q, showing larger Q with increasing t_t. This is because of conductor loss due to the superconductor which is a semiconductor in the electrical resistivity, not perfect conductor.

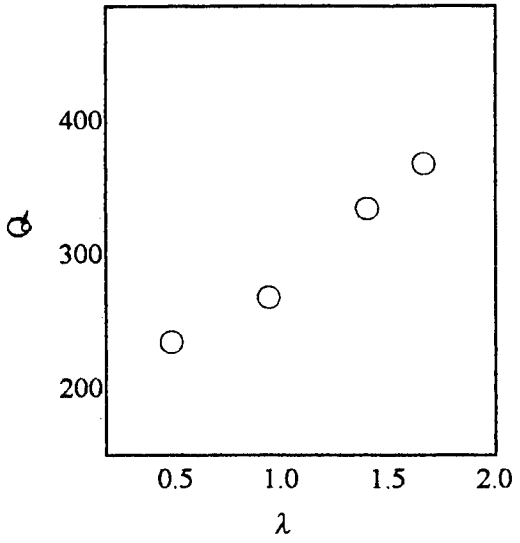

Fig.3 Dependence of Q on TiO_2 length ($\lambda = t_t / t_s$).

The temperature dependence of resonant frequency

Figure 4 illustrates the temperature dependence of the resonant frequency investigated for the same specimen as shown in Fig.1.

According to results in Fig.4, temperature coefficient between 105K and 230 K was calculated to be +7.8 ppm/K. The temperature coefficient of the superconductor-surrounded TiO_2 system was also estimated to be + 6.4 ppm/K up to 200K. We can suggest to use our system for low temperature when we apply the device to the field under superconductor.

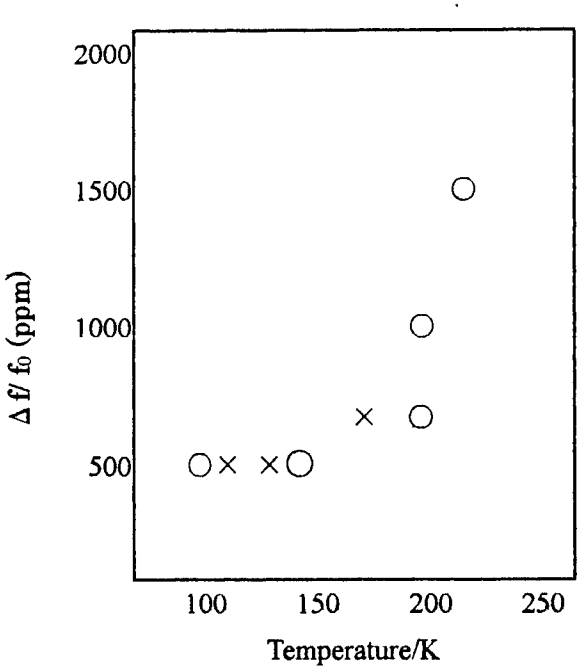

Fig.4 Temperature dependence of resonant frequency of the specimen (λ =1.91for ○ and 1.64 for×).

CONCLUSION

The superconductor-surrounded TiO_2 sandwiched system was also studied to result in higher Q such as 834 and over 2000 at room temperature and liquid nitrogen, respectively.

REFERECES

[1] S.Sugihara, Y.Yutoh and N.Kimura, to be published in Ferroelectrics.

[2] H.Tamura, T.Takekawa, Y.Kintaka and A.Oota, , Proceedings of The 9th US-Japan Seminar on Dielectric and Piezoelectric Ceramics, pp269-272, Nov.2-5, 1999, Okinawa, Japan.

[3] Y.Kobayashi, T.Imai and H.Kayano,, IEEE Transactions of Microwave Theory and Technique, 39, 1530-1538(1991).

[4] T.Jacobs, S.Sridhar, Q.LI, G.D.Gu and N.Koshizuka, Phy. Rev. Lett., 75, 4516-4519 (1995).

Double-Layer Type Microwave Absorber Made of Magnetic-Dielectric Composite Material

M. Saitoh, T. Yamamoto, H. Okino, M. Chino and M. Kobayashi*

Dept of Communications Eng., National Defense Academy, Hashirimizu 1-10-20, Yokosuka, 239-8686 Japan
FAX : +81-468-44-5911, Email : mituru@pop02.odn.ne.jp
*Tayca Co. Osaka laboratory, Funnamati 1-3-47 Taisho-ku, Osaka, 551-0022 Japan
FAX : +81-6-6555-3261, Email : m-kobayashi@tayca.co.jp

INTRODUCTION

Recent usage because of the high frequency region (GHz band) has rapidly increased by wireless LAN, personal digital assistant and other communications equipments. Many problems have been occurred along with it, which are a miss-operation of precise electronic equipment and outflow of secret information are occurred by a leakage of electromagnetic wave. We made a new microwave absorber combining magnetic with dielectric characteristics and examined microwave absorbing characteristics.[1] In this research, double-layer type microwave absorbers combining magnetic with dielectric characteristics are reported and their microwave absorption properties are evaluated.

THEORY [2], [3]

When a transverse electromagnetic wave (TEM wave) is at vertical incidence and vertically reflects from double- layer microwave absorber composed of the 1st layer as a load side and 2nd layer as a the incident wave side shown in Fig. 1 (a). It is possible to treat as an equivalent distributed constant circuit in Fig.1 (b). Using the standardized input impedance (Z_{in1}) when the only 1st layer (single layer) is composed and short-circuited, characteristic impedance (Z_{c2}) and propagation constant (γ_2) of the 2nd layer, the standardized input impedance of the double-layer (Z_{in}) is derived by the eq. (1) and the reflection loss (S_{11}) of the double-layer is obtained from the eq. (2).

$$Z_{in} = Z_{c2} \times \frac{Z_{in1} + Z_{c2} \tanh \gamma_2 d_2}{Z_{c2} + Z_{in1} \tanh \gamma_2 d_2} \quad \cdots \quad (1)$$

$$S_{11} = 20 \log \left| \frac{1 - Z_{in}}{1 + Z_{in}} \right| \quad \cdots \quad (2)$$

where, d_2 is the layer thickness of 2nd Layer.

When the terminal is shorted, the reflection loss and the matching frequency were measured by a network analyzer.

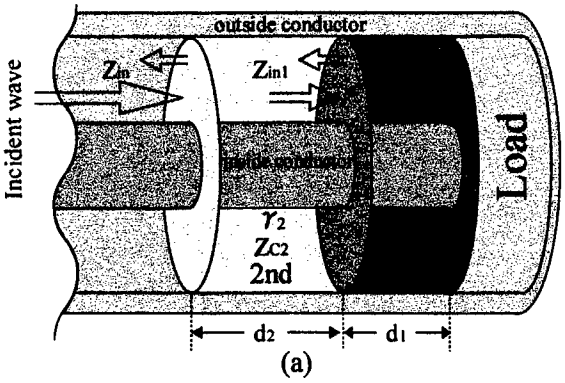

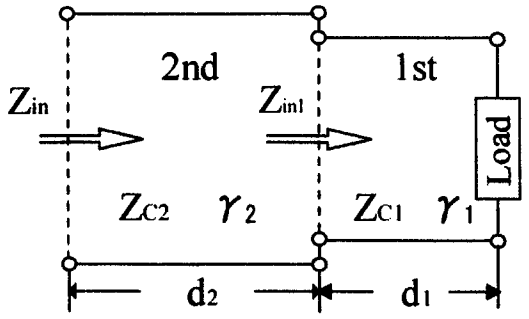

(b)

Fig.1 (a) Construction of double-layer type microwave absorber.
(b) Equivalent distributed constant circuit

SAMPLE [4]

Carbonyl iron ($Fe(CO)_5$ called "FE" for short) powder was used as a magnetic material, and titanium oxide (TiO_2 called "TI" for short) powder as a dielectric material. The grain sizes of TI and FE are 0.98μm and 0.5μm on average, respectively. They mixed with hyparon by the arbitrary weight-mixing ratio and molded in the toroidal shape, which could be inserted in 7D (7mm in outer

diameter) coaxial wave-guide. Table I shows the FE/TI weight-mixing ratio made of dielectric and magnetic composite material. A main property has changed from a dielectric to magnetism by changing the weight-mixing ratio from dielectric materials (FE/TI=50/50) to magnetic material (FE/TI=100/0). The entire filling rate is 83.3%, and the remainder of 16.7% is the hyparon.

Table I FE/TI weight-mixing ratio made of dielectric and magnetic composite material

FE/TI ratio (wt.%)	FE	TI	hypalon	packing factor	characteristics
100/0	500g	-	100g	83.3%	magnetic
95/5	475g	25g	100g	83.3%	magnetic>>dielectric
90/10	450g	50g	100g	83.3%	magnetic>>dielectric
85/15	425g	75g	100g	83.3%	magnetic>>dielectric
80/20	400g	100g	100g	83.3%	magnetic>dielectric
75/25	375g	125g	100g	83.3%	magnetic>dielectric
70/30	350g	150g	100g	83.3%	magnetic>dielectric
65/35	325g	175g	100g	83.3%	magnetic>dielectric
60/40	300g	200g	100g	83.3%	magnetic≒dielectric
55/45	275g	225g	100g	83.3%	magnetic≒dielectric
50/50	250g	250g	100g	83.3%	magnetic=dielectric

CHARACTERISTICS of REFLECTION LOSS in MATCHING FREQUENCY in SINGLE LAYER

Firstly, we measured reflection loss of single layer type composite materials in matching frequency. The maximum reflection loss of each composition (FE/TI) is below -50dB (99.996% of incident wave is absorbed). Characteristics of matching frequency, matching thickness, μ_r* and ε_r* were showed in

Table II Experimental values of matching frequency, matching thickness, ε', μ' and μ" in the FE/TI composite (single layer)

FE/TI	Matching freq.(GHz)	Matching thickness (mm)	Band width (GHz)	ε'	μ'	μ"
100/0	5.72	1.73	1.02	11.52	2.50	2.74
95/5	7.12	1.54	1.13	10.28	2.09	2.46
90/10	8.20	1.54	1.23	8.55	1.73	2.20
85/15	8.44	1.53	1.17	8.84	1.73	2.05
80/20	9.54	1.33	1.23	8.04	1.56	2.25
75/25	10.37	1.27	1.25	7.34	1.42	2.22
70/30	11.09	1.24	1.32	6.65	1.39	2.21
65/35	11.12	1.20	1.21	7.44	1.36	2.13
60/40	11.60	1.17	1.15	6.90	1.37	2.19
55/45	13.07	1.09	1.34	6.38	1.19	2.09
50/50	13.92	1.04	1.34	4.19	1.08	2.65

Table II and Fig.2 when the weight-mixing ratio was changed from FE/TI=100/0 to 50/50. The matching frequency increased from 5.72 to 13.92GHz in proportion to the content of TI. The thickness decreased from 1.73 to 1.04mmin proportion to the content of TI. We calculated the matching frequency, the reflection loss, and the matching thickness of double-layer type microwave absorber using the μ_r*, ε_r* values of single layer type given for the matching frequency listed in Table II measured by the open and short circuit method.

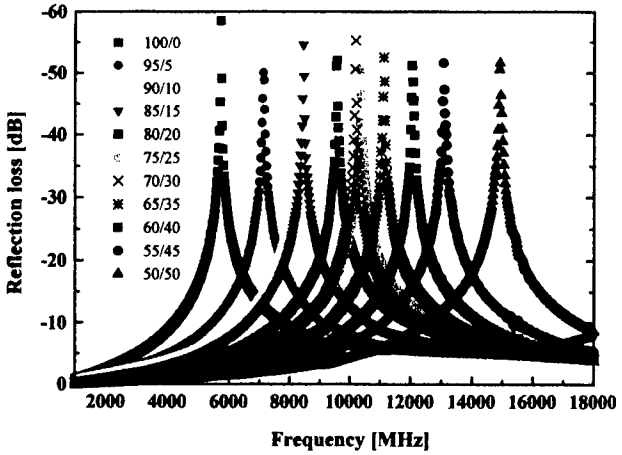

Fig.2 Reflection loss vs. frequency by FE/TI weight-mixing ratio (single layer).

For instance, when thinking about combination 75/25 (1st layer) and 80/20 (2nd layer), Figs.3 and 4 show the maximum reflection loss and the center frequency calculated by changing the thickness of 1st and 2nd layer. At first when the thickness of 1st layer is 0.72mm, we can select from 0.55 to 0.60mm as a matching thickness (thickness with a reflection below -50dB) in Fig.3. Using such thickness of 1st and 2nd layer, the matching frequency can be selected from 9.97 to10.40GHz in Fig.4.

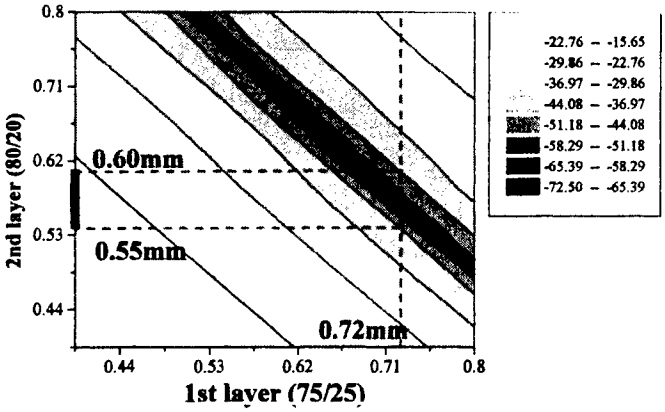

Fig.3 Calculation of maximum reflection loss vs. 1st layer (75/25) – 2nd layer (90/10)

Thus, reflection loss of double-layer microwave absorber can be controlled by changing the composition of 2nd layer from FE/TI=90/10 to50/50 maintaining FE/TI=75/25 as a 1st layer.

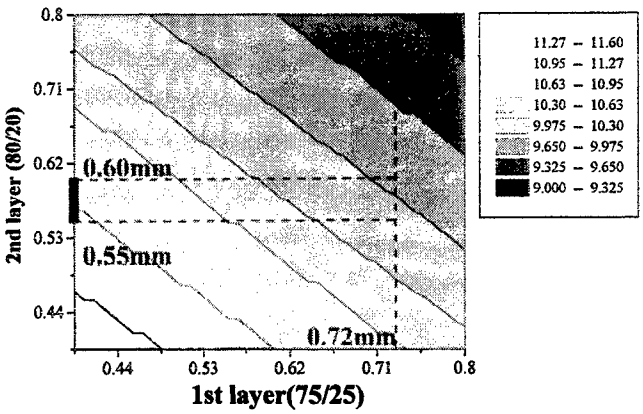

Fig.4 Calculation of matching frequency as 1st layer (75/25) – 2nd layer (90/10)

Figure5 shows experiment values of reflection loss vs. frequency by changing the weight-mixing ratio FE/TI in 2nd layer. Table III show the matching frequency and thickness, band width of the frequency below -20dB, μ_r* and ε_r* when the mixing ratio of 2nd layer was changed from FE/TI=90/10 to 50/50. Matching frequency decrease from 10.88GHz (90/10) to 8.10GHz (55/45) in proportion to increase the component ratio of TI. Matching thickness increase from 1.16mm (90/10) to 1.59mm (55/45) in proportion to increase the component ratio of TI. Band width decrease from 1.53GHz (90/10) to 0.94GHz (55/55).

Table III Experimental values of matching frequency, matching thickness, ε', μ' and μ" in the double-layer FE/TI composite (1st layer : FE/TI=75/25, 0.72mm)

FE/TI (2nd)	Matching freq.(GHz)	Matching thickness (mm)	Band width (GHz)	ε'	μ'	μ"
90/10	10.88	1.16	1.53	6.96	1.75	2.68
85/15	10.48	1.21	1.38	7.40	1.62	2.46
80/20	9.95	1.27	1.28	7.33	1.58	2.46
75/25	10.37	1.27	1.25	7.34	1.42	2.22
70/30	9.90	1.30	1.25	7.40	1.52	2.34
65/35	9.73	1.27	1.19	7.46	1.54	2.47
60/40	8.25	1.56	0.96	8.17	1.44	2.12
55/45	8.10	1.59	0.94	7.84	1.38	2.16
50/50	8.80	1.58	0.98	7.40	1.28	1.97

Figure 6 shows the matching frequency of the double-layer (FE/TI weight-mixing ratio of 1st layer is fixed 75/25 and thickness is taken by 0.72mm, that of 2nd layer is changed from 90/10 to 50/50) and the single layer (composition of FE/TI change from 90/10 to 50/50). Comparing with single and double-layer, when TI ratio of the composition in 2nd layer is less than 25% (FE/TI=75/25), matching frequency of double-layer is higher than that of single layer, where in this case 10.37GHz for FE/TI=75/25. On the contrary, when the TI ratio of the composition is more than 25%, the matching frequency of double-layer is lower than that of single layer. Moreover, the change increases in proportion to the TI content rate of the 2nd layer. Figure7 shows the matching thickness of the same double-layer shown in Fig.6 (the component of 1st layer is 75/25,0.72mm, that of 2nd layer is change from 90/10 to 50/50) and the single layer (FE/TI change from 90/10 to 50/50).

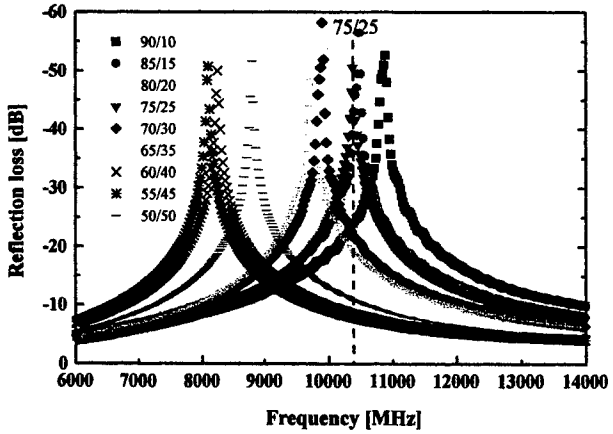

Fig.5 Reflection loss vs. frequency by FE/TI weight-mixing ratio in the double-layer FE/TI composite (1st layer : FE/TI=75/25, 0.72mm).

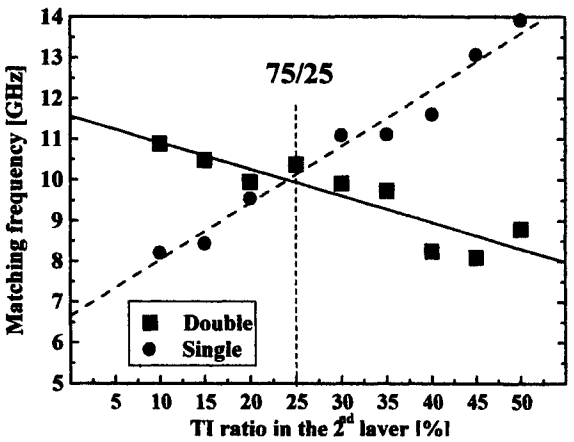

Fig.6 Matching frequency of single layer and double-layer as the component of FE/TI.

Similar with the matching frequency in the double-layer, when the TI composition of 2nd layer is less than FE/TI=75/25 matching thickness of double-layer is thinner than that of single layer. On the contrary, the matching frequency of double-layer is thicker than that of single layer in the composition over 25%. If we want to shift the matching frequency of certain FE/TI to high frequency side, we can make double-layer microwave absorber made by lower TI content for 1st layer. At that time the thickness become thinner. In oppose to, higher TI content have it shift low frequency side and thicker.

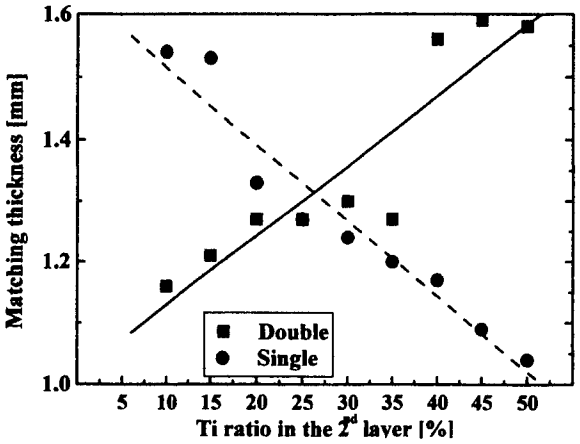

Fig.7 Matching thickness of single layer and double-layer as the component of FE/TI mixing ratio.

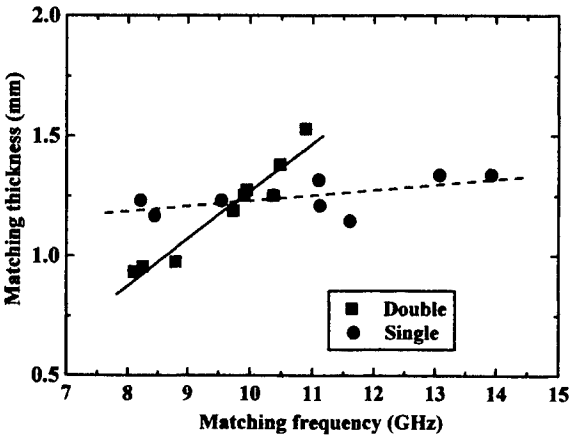

Fig.8 Relations between the matching frequency and the matching thickness

For instant, when the content of 1st layer is 75/25, relations between the matching frequency and the matching thickness are shown in the Fig.8. When there is more amount of TI than the 1st layer, the matching thickness of double-layer become thinner than single-layer in the same matching frequency as for the thickness. In the contrary, when there are a fewer TI than that of 1st layer, the double- layer becomes more thick than single-layer in the same matching frequency. If the component of 1st layer is changed, the matching frequencies of double-layer microwave absorber become wider range.

CONCLUTION

The frequency characteristic of the reflection loss of double- layer were calculated by using μr^* and εr^* of single- layer, and designed the double-layer microwave absorber. It is shown the matching frequency of double-layer was shifted from 10.88 to 8.10GHz as the central frequency of 10.37GHz by changing the mixing ratio of 2nd layer from 90/10 to 50/50. It is able to cover the frequency band of 3.36GHz in the bandwidth of -20dB from 1.53 to 0.94GHz by the same material. Moreover, double-layer microwave absorber which had higher matching frequency than that of single-layer by using 2nd layer made of less amount of TI than the 1st layer.

REFERENCES

[1] Masaru Chino, "Wave absorber which used composite material" and "Development and application of wave absorber" industrial technology academy, (1998)

[2] Yoshiyuki Naito "Wave absorber" Ohm Co. (1998) PP.55.

[3] Masaru Chino, "Measurement of complex ε_r^*, μ_r^* for ferrite wave absorber in coaxial line" EIC, EMCJ91-59, (1991)

[4] Mitsuru Saito, "Double layered electric wave absorber using magnetic $(Fe(Co)_3)$-dielectric (TiO_2) material for GHz frequency" ITE Technical Report Vol.25, No15, pp.19-22, (2001)

Progress in $BaTiO_3$ Thin Films: High Frequency Applications and Property Investigations

J-P. Maria, C. B. Parker, F. Ayguavives, A. Tombak, G. T. Stauf, A. Mortazawi, A. I. Kingon

North Carolina State University, Department of Materials Science and Engineering, Department of Electrical and Computer Engineering, 1010 Main Campus Drive, Suite 223-D, Campus Box 7920, Raleigh, NC, 27695; ATMI Corporation, 7 Commerce Drive, Danbury, CT, 06810.
FAX: (919) 515-3027
jpmaria@unity.ncsu.edu

ABSTRACT

We report on our recent efforts to produce high quality factor tunable BST capacitors defined by Pt top and bottom electrodes on 150 mm wafers by MOCVD. The technological goals include low loss tangent BST deposition, low ESR metallization, device designs appropriate for the frequencies and power of interest, an integration scheme facilitating fabrication. Scientific goals include full characterization of properties as a function of film thickness, temperature, dc and RF bias.

To date, BST films have been prepared with loss tangents of 0.003 between 100 Hz and 200 MHz. Permittivity measurements to 10 GHz reveal minimal dispersion, < 1%/decade, suggesting that loss tangents remain small to the GHz regime. At 100 MHz, tunabilities of 2:1 are commonly achieved. An analysis of the temperature and field dependence of the permittivity for films between 600 nm and 15 nm is presented. The thickness and temperature dependencies are discussed in terms of models describing ferroelectric transitions in dimensionally scaled systems. The field dependent permittivity and its relationship to the field dependence will be discussed in the context of high frequency devices and the optimal choice of a tunable high frequency dielectric.

EXPERIMENTAL PROCEDURE

All BST films in this study were prepared by metallorganic chemical vapor deposition with liquid precursor delivery.[1] The target BST composition included a Ba to Sr ratio of 70/30 and a Ti to (Ba+Sr) ratio of 55/45. These values were chosen as they are know to provide films with reasonably low losses and a room temperature tunability suitable for the high frequency of interest. Film compositions were verified by wavelength dispersive x-ray fluorescence. Films were deposited on Si substrates with 500 nm of thermal oxide followed by a dc magnetron sputtered Pt bottom electrode. The Pt electrode ranged between 100 nm and 500 nm in thickness. In select cases, thicker metallization was required in which a multilayer stacked structure comprising 250 nm Pt and 50 nm IrO_2 layers was used. This combination could achieve bottom electrodes of 2 μm total thickness.

Top electrodes were also dc magnetron sputtered Pt. These layers were prepared at thicknesses between 100 nm and 1 μm. After top electrode deposition, all films were annealed at 550 °C in air for 30 minutes.

Low frequency dielectric measurements were made using an HP 4192A impedance analyzer. High frequency measurements (> 1 MHz) were made using an HP 8510C vector network analyzer. Temperature dependent low frequency measurements were made using an MMR Industries combination hot and cold stage. This stage enabled a temperature range between 80 K and 580 K.

RESULTS AND DISCUSSION

1 Thickness dependent properties

A set of BST thin films were prepared as a function of thickness and the temperature dependence of the permittivity was compared. For these measurements, the small-signal oscillation voltage was controlled such that the field values were relatively constant. In the case of the thinnest films, the oscillation voltage could not be reduced sufficiently while maintaining sufficiently high measurement resolution and low noise. Fig. 1 shows the temperature dependent analysis.

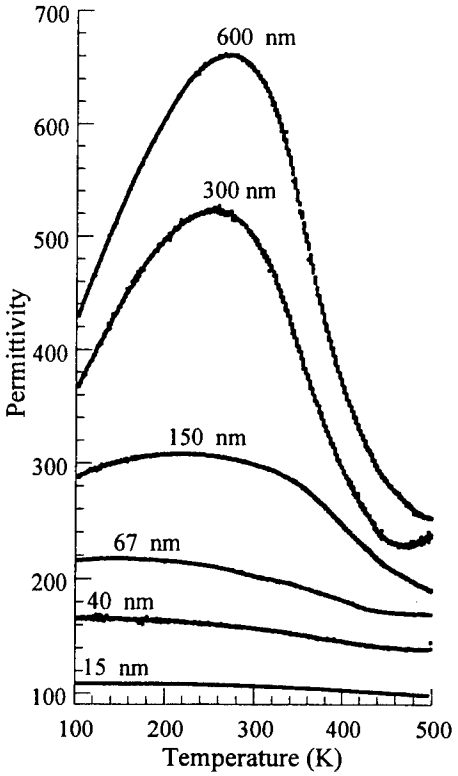

Fig. 1: The temperature dependence of the permittivity for a thickness series of BST films. The Ba/Sr ratio is 70/30 for all cases.

As seen in Fig.1, reducing the thickness of the BST film seriously impacts the dielectric properties. As expected, there is a reduction in T_{max}, a broadening of the dielectric anomaly, and a reduction of the magnitude of the permittivity. Fig. 2 shows the dielectric loss tangent of the same thickness series. The loss tangent trends are consistent with expectations from the permittivity. As has been previously observed, the loss tangent of MOCVD BST thin films at room temperature falls with decreasing thickness. Previously, this was believed to be due to changing stoichiometry or small microstructural changes. With this temperature dependent data set it is apparent that the loss tangent reduction is also due, in part, to the changing ferroelectric transition temperature. Loss tangents are expected to procede through a maxima near the temperature of maximum permittivity. As film thickness decreses, the temperature separation between T_{max} and RT increases, thus the reduction in loss tangent.

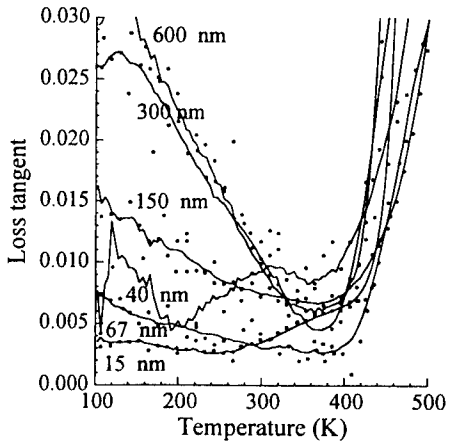

Fig. 2: The temperature dependence of the dielectric loss tangent for the BST film thickness series.

This reduction in permittivity with some critical dimension has been observed by many groups, and is often referred to as size effects or size induced transitions.[2-6] For bulk materials, the dimensionality of importance is often believed to be grain size, while for thin films, this dimensionality is most commonly referred to in the context of film thickness. In the case of our BST films, TEM analysis typically indicates a homogeneous fiber textured microstructure where grain boundaries are only present vertically through the films. Because of this, the critical dimension of the films may, to a first approximation, be considered to be the vertical length of the grains, thus the total thickness. Since the measurement direction for these films is normal to the substrate, categorizing the dimensionality by thickness is further substantiated. Note that low angle grain boundaries are likely in the plane of the film, a more correct size interpretation will take this into account via x-ray, or similar diffraction analysis.

An attractive explanation of these size induced transitions has been the presence of a dead, or non-ferroelectric layer existing at the interface between the BST and the Pt electrodes. This interpretation follows the model of Zhou.[7] In such a case, the inverse of capacitance can be plotted as a function of film thickness, and an interface capacitance density can be calculated if the y-intercept of such a plot is non-zero. This approach has also been used by many groups. Using this thickness series of BST films, this extrapolation has been made, however in this case as a function of temperature. The result is given in Fig. 3.

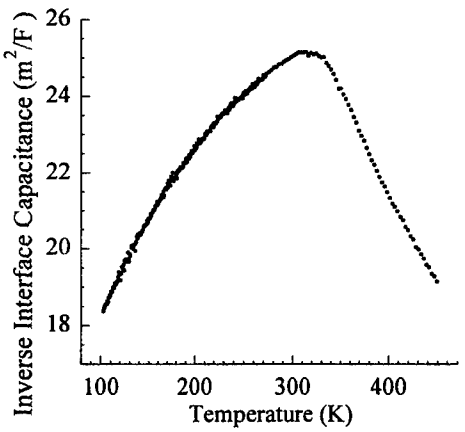

Fig. 3: The temperature dependence of the interface capacitance extrapolated from the set of BST thin films spanning 15 nm and 600 nm.

From this figure it is apparent that the extrapolated interface capacitance is strongly temperature dependent. From a relative standpoint, the interface component exhibits approximately 30% fluctuation in the temperature range investigated. In contrast, the thickness series of BST films exhibits between 60% and 10% variation for the thickest and thinnest films respectively. There are several apparent implications of this result, three important ones include: (1) The interface component of the capacitance is ferroelectric, but exhibiting supressed spontaneous polarization suggesting that a model based on Binder's approach is more appropriate.[3,8] (2) The measurements are being influenced by a transition from fully depleted films in the thinnest cases to a not-fully depleted case for the thickest films, and were this influence extracted, the interface capacitance would be temperature independent. And (3) The thickness dependent phenomena included a combination of a non-ferroelectric interface and a near interface supressed polarization component. In either case, this data clearly shows that more analysis is required to fully describe these dimension-induced electrical properties. Additional data and analysis will be presented and discussed.

2 Voltage dependent behavior

Because of current technological trends, research into the voltage dependent behavior of BST films is of greater interest than is research targeting the use of BST for embedded DRAM applications. The thickness dependent analysis is of particular use for addressing some of the tunable capacitor application issues. This interest into voltage or field dependent behavior is driven by the need for electrically tunable RF and microwave devices. The optimal BST for these devices exhibits a maximum tunability, a minimal loss tangent, and a very small temperature dependence. The analysis presented in the previous section clearly showed that the temperature dependence of the permittivity of BST is strongly thickness dependent and that very thin films exhibit a temperature dependence, which is very attractive from a device standpoint. In this section we will look at the voltage dependence of these materials as a function of thickness as well as the temperature dependence of the tunability for select cases.

Shown in Fig. 4 is the field dependence of the permittivity for the thickness series of BST films. As seen in the figure, the total tunability decreases strongly with film thickness. Though not shown, the loss tangents for all films are similar to the data shown in Fig. 2.

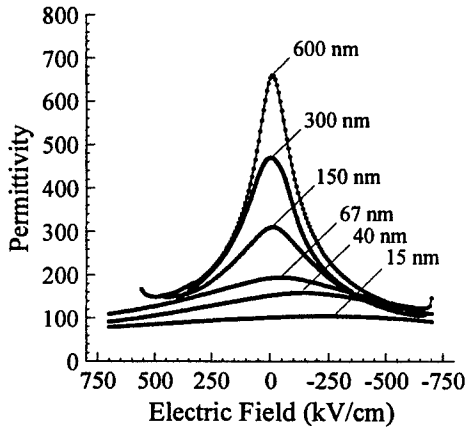

Fig. 4: Electric field dependence of the permittivity for BST films as a function of dielectric thickness. All measurements in this case taken at a frequency of 10 kHz at room temperature.

The apparent question of which BST represents the optimal combination of properties remains. Three fundamental criteria can be established. First, the maximum amount of voltage tunability is desired as to make the devices of use for envisioned circuit applications. A common metric for this tunability is 2:1, meaning that the high voltage capacitance is reduced by 50% from the zero field value.[9] The BST films in this study achieve that level of tunability at approximately 70 nm. Simultaneously, the temperature dependence of the permittivity and the permittivity's tunability should be minimized. As seen from figure 1, only the thinnest films exhibit temperature fluctuations of less than 10%. Finally, the films should have

low loss, which again corresponds to the thinnest structures. Fig. 5 shows the field tunability plotted against the temperature tunability for the range of thicknesses investigated. In this case temperature tunability corresponds to the difference in permittivity between T_{max} and 450 K divided by ε_{max}.

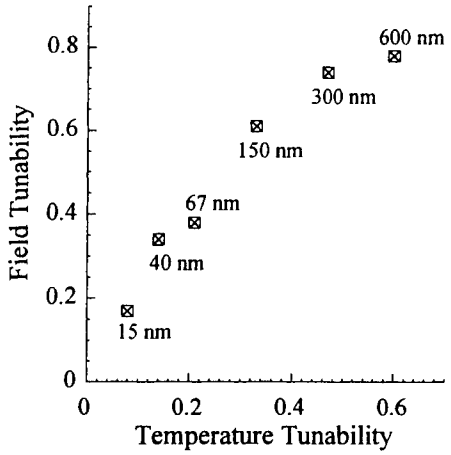

Fig. 5: Temperature tunability plotted against field tunability for BST film thickness series. In this case, the voltage tunability corresponds to $(C_{0V}-C_{HV})/C_{0V}$ and temperature tunability corresponds to $(C_{max}-C_{450})/C_{450}$

As seen in Fig. 5, no optimal composition is apparent for the maximization of field tunability with minimization of temperature tunability. Conversely, this relationship indicates that the two parameters are intimately coupled. This result is not unexpected, as fundamentally, the application of an applied electric field is in some ways similar to cooling a material to temperatures below the transition temperature. Both operations are expected to reduce the susceptibility (provided that additional transitions do not occur with additionally applied electric fields or additionally reduced temperatures).

CONCLUSIONS

1 A new data set showing the temperature dependence of the dielectric permittivity and loss tangent as a function of film thickness was presented. The observation of a temperature dependent interface capacitance was shown and the implications of this observation as they pertain to the applicability of scaling models was mentioned.

2 The temperature dependent data was combined with the electric field dependent data, both as a function of thickness. Using this treatment, a methodology for choosing the optimal BST (70/30) thin films for high frequency tunable devices was assessed. In general, the voltage tunability and temperature dependence cannot be separated. The well-known reduction of TCC for fine-grained ferroelectric materials is equally pronounced in the field dependent permittivity.

REFERENCES

[1]P. C. v. Buskirk, S. Bilodeau, J. F. Roeder, and P. Kirlin, Jpn. J. Appl. Phys. **35,** 2520 (1996).

[2]C. Basceri, S. K. Streiffer, A. I. Kingon, and R. Waser, J. Appl. Phys. **82 (5),** 2497-2504 (1997).

[3]D. McCauley, R. E. Newnham, and C. A. Randall, J. Amer. Ceram. Soc. **81 (4),** 979-987 (1998).

[4]K. Ishikawa, K. Yoshikawa, and N. Okada, Phys. Rev. B **37 (10),** 5852-5855 (1988).

[5]M. H. Frey, Z. Xu, P. Han, and D. A. Payne, Ferroelectrics **206 (4),** 337-353 (1998).

[6]S. K. Streiffer, C. Basceri, C. B. Parker, S. E. Lash, and A. I. Kingon, J. Appl. Phys. **86 (8),** 4565 (1999).

[7]C. Zhou and D. M. Newns, J. Appl. Phys. **82 (6),** 3081-3088 (1997).

[8]K. Binder, Ferroelectrics **15,** 99-104 (1981).

[9]F. D. Flavis, N. G. Alexopoulos, C. D. Cubbage, K. B. Bhasin, R. K. Singh, and S. D. Harkness, IEEE Trans. Micro. Theory and Tech. **45 (6),** 963 (1997).

Application of Ferroelectrics in Microwave Phased-Array Antennas

J. B. L. Rao[a], D. P. Patel[a], P. K. Park[b], T. K. Dougherty[c], J. A. Zelik[c], A. Moffat[d], and L. C. Sengupta[e]

[a]Naval Research Laboratory, Radar Division, 4555 Overlook Ave, SW, Washington, DC 20375
[b]Raytheon Systems Co., Tucson, AZ 85374
[c]Raytheon Systems Co., El Segundo, CA 90245
[d]SFA, Inc., 9315 Largo Drive West, Suite 200, Largo, MD 20774
[e]Paratek Microwave, Inc., 6935-N Oakland Mills Rd, Columbia, MD 21045
FAX: (202) 767-2986
Email: patel@radar.nrl.navy.mil

ABSTRACT

A phased-array antenna can scan its beam by electronic means without moving mechanical structures. This capability is desired in many defense and commercial applications. However, traditional phased-array antennas are expensive. The development of a novel, low-cost, phased-array antenna, being funded by the U. S. Defense Advanced Research Projects Agency (DARPA), is presented. The antenna uses voltage-tunable dielectrics (VTDs) to provide the phase shift that is needed to scan the beam. The VTDs are a ceramic-ceramic composite of Barium Strontium Titanate and low-loss dielectric. A prototype antenna has been built; the test results demonstrate electronic beam scanning at 10 GHz. The VTD loss is about 2 dB with the dielectric constant of approximately 100.

INTRODUCTION

One of the most versatile antennas used in radar and communications systems is the phased-array antenna. It can rapidly scan its beam without mechanical movement. Each radiating element of a phased array is usually connected to a phase shifter or a transmit/receive (T/R) module, which determines the phase of the signal at each element to form a beam at the desired angle. The most commonly used phase shifters are ferrite and diode phase shifters. The phase shifters or T/R modules with their control circuitry along with the feed network account for the major hardware cost in the phased-array antenna. A typical array may have several thousand elements and that many phase shifters or T/R modules; hence, it is very expensive. Therefore, reducing the cost and complexity of the phase shifters or T/R modules and their control circuitry is an important consideration in the design of phased arrays.

The concept of the novel antenna described in this paper has been published elsewhere [1]. Even though it does not use pure ferroelectric materials, we will call it the ferroelectric lens phased-array antenna. It uniquely incorporates bulk phase shifting using voltage-tunable dielectrics (VTDs); the array does not contain an individual phase shifter at each element. The number of phase shifters is reduced from ($n \times m$) to ($n + m$), where n is the number of columns and m is the number of rows in a phased array. The number of phase shifter drivers and phase shifter controls is also reduced by the same factor using row-column phase control. This can potentially lead to low-cost phased-array antennas.

An ideal application for the ferroelectric lens is a semiactive tactical missile seeker [2]. Rapid beam switching can advance missile seeker capability including forward looking guidance-integrated fusing and tracking in shorter range. The development of a low-cost, phased-array antenna for seeker application is being funded by DARPA's Frequency Agile Materials for Electronics (FAME) program.

In this paper, we review the ferroelectric lens concept. We describe the bulk VTD ceramics that we used. Radiation patterns of a prototype array demonstrating electronic beam scanning are also presented.

DESCRIPTION OF THE FERROELECTRIC LENS

The ferroelectric lens is shown conceptually in Fig. 1; each column of the lens is a pair of conducting parallel plates that are loaded with two pieces of bulk VTD ceramic with a center conducting plate that is used to apply the dc bias voltage. The separation between the conducting plates is about $\lambda_o/2$, where λ_o is the free space wavelength; this separation is the maximum allowed to avoid grating lobes. To propagate only the dominant transverse electromagnetic (TEM) mode and cut-

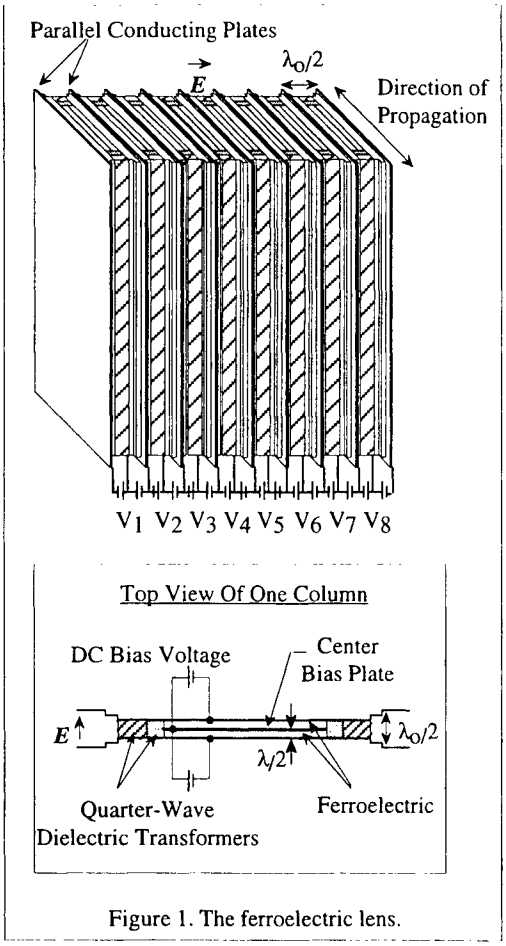

Figure 1. The ferroelectric lens.

off higher order modes in the VTD-loaded section, the separation between the center bias plate and either conducting plate is chosen to be less than $\lambda/2$, where λ is the wavelength in the VTD. Quarter-wave dielectric transformers are used to match the empty parallel-plate waveguide to the VTD-loaded parallel-plate waveguide. The dielectric constant (ε_r) of the VTD is a function of the bias voltage. Therefore, by applying a different bias voltage (V_1, V_2....V_8) to each column, a linear phase gradient can be created in the ***E***-plane. So, if a plane wave is incident on one side of the lens with the electric field ***E*** normal to the plates, the beam on the other side can be scanned in the ***E***-plane.

PHASED-ARRAY CONFIGURATIONS USING FERROELECTRIC LENS FOR 2-D SCANNING

A single ferroelectric lens provides one-dimensional (1-D) electronic beam scanning. Two-dimensional (2-D) beam scanning can be achieved by cascading two ferroelectric lenses or using one ferroelectric lens in a hybrid configuration with another phased array that can scan the beam in one plane [1].

Figure 2 shows the cascading of two spatially orthogonal ferroelectric lenses. The first lens provides an elevation scan of a vertically polarized wave. A passive 90° polarization rotator then rotates the RF electric field to become horizontally polarized. The second lens then provides the azimuth scanning of the horizontally polarized wave. In Fig. 2, a non-scanning planar array is shown as the illuminator (or feed) for the dual lenses. A horn can also be used as the feed for the dual lens configuration.

Another method of achieving 2-D beam scanning uses a hybrid technique in which a planar array with phase shifters scans the beam in one plane and the ferroelectric lens scans the beam in the other plane. For example, as shown in Fig. 3, a slotted waveguide array with phase shifters provides electronic beam scanning in azimuth plane. Electronic beam scanning in the elevation plane is obtained by placing a ferroelectric lens in front of the slotted waveguide array.

VOLTAGE-TUNABLE DIELECTRICS

The VTDs were developed at Paratek Microwave, Inc. They are bulk composite ceramics of tunable ferroelectrics in the paraelectric phase and non-tunable materials [1,3]. In addition to providing bulk phase shift, VTDs offer reciprocal phase shift. Ferroelectrics are inherently broadband. Until the development of these composites, the large ε_r and tan δ of ferroelectric materials excluded them from being used at microwave frequencies. VTDs can be manufactured in bulk, thick film and thin film forms. Only bulk ceramics are suitable for the ferroelectric lens because of the physical size requirements.

The ferroelectric in the VTD that we used was Barium Strontium Titanate (BST), specifically $Ba_{0.55}Sr_{0.45}TiO_3$. BST is the most widely used ferroelectric at microwave frequencies. We are interested in applications at X band (8-12 GHz). Experiments were conducted at X band with a VTD whose ε_r and tan δ were 81 and 0.0069, respectively at 10 GHz. Tunability was a respectable 24% at a bias of 8 V/μm. Curie temperature, T_c, was -75°C, which means that the BST is in the paraelectric phase at room temperature. T_c is controlled not only by the Ba:Sr ratio, but also by the amount of the non-tunable material that is added. Theoretically, the loss due to the VTD that we

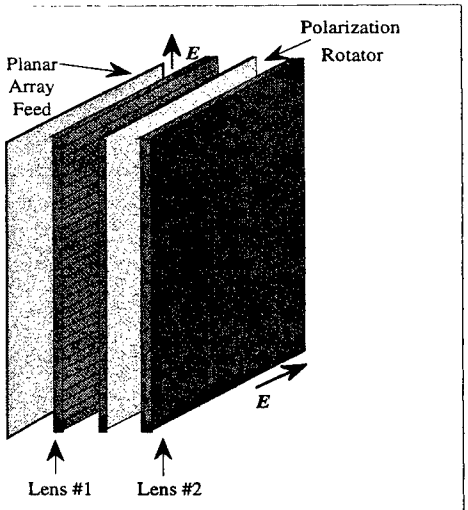

Figure 2. Dual Lens Configuration with a Planar Array Feed.

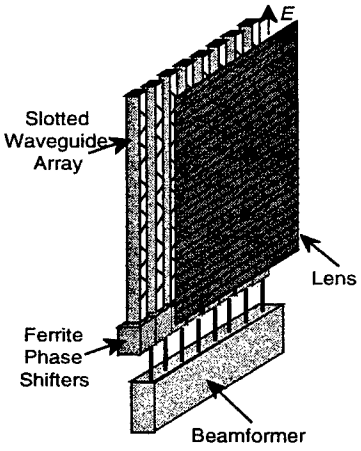

Figure 3. Hybrid Phased Array Configuration for 2-D Scanning.

used is 1.5 dB for obtaining 360° differential phase shift at 10 GHz.

EXPERIMENTAL RESULTS

First, we built and tested a single column of the ferroelectric lens at the Naval Research Lab (NRL) [1]. The experimental results agreed well with the theoretical results of the lens aperture matching. Control of the column phase shift with dc bias voltage was also demonstrated. The measured loss was about 2 dB, which also agreed well with theoretical result. We would like to reduce this loss. We are pursuing material improvements as participants in DARPA's FAME program. A two-column interferometer has also been built and tested at NRL. The pattern was measured as dc bias was applied to one column to scan the phased-array antenna pattern. Electronic beam scanning was demonstrated at 10 GHz. There was no indication of any material inhomogeneity in the patterns.

For the tactical missile seeker application, a 12-column lens was built and tested at Raytheon. The pattern was measured as dc bias was applied to each column to scan the phased-array antenna pattern. Fig. 4 shows the prototype antenna in an antenna test chamber. In Fig. 5, four of the measured patterns are plotted for 10 GHz frequency. Electronic beam scanning was again demonstrated; the beam clearly scanned to 60°.

PLANS

A ferroelectric lens phased-array antenna has been demonstrated at X band. There is strong interest to operate missile seekers at higher frequencies, especially Ka band (27-40 GHz). At these frequencies, wide frequency bandwidths and narrow antenna beamwidths can be achieved. We have started the process to develop a ferroelectric lens at Ka band.

SUMMARY

The work done so far in developing the ferroelectric lens, a low-cost, phased-array antenna, was reviewed. The VTD ceramics that we used provide 360° differential phase shift with about 2 dB loss at 10 GHz. Electronic beam scanning has been demonstrated in a prototype ferroelectric lens at 10 GHz. Work is continuing in reducing the loss in the dielectrics.

REFERENCES

1. J.B.L. Rao, D.P. Patel, and V. Krichevsky, *IEEE Trans. Antennas Propag.*, Vol. 47, No. 3, 458-468 (1999).
2. P.K. Park, S.H. Kim, J. Gandolfi, R.T. Tadaki, T.K. Dougherty, D. Patel, J. Rao, L. Sengupta, S. Wolf, and D. Treger, "Digest 2000 IEEE Antennas and Propag. Soc. Int. Symp.", IEEE, Piscataway, NJ (2000) pp. 974-977.
3. L.C. Sengupta, E. Ngo, J. Synowczynski, and S. Sengupta, "Proc. 10th Int. Symp. Applications Ferroelectrics (ISAF '96)", Ed. by B.M. Kulwicki, A. Amin, and A. Safari, IEEE, Piscataway, NJ (1996) pp. 845-849.

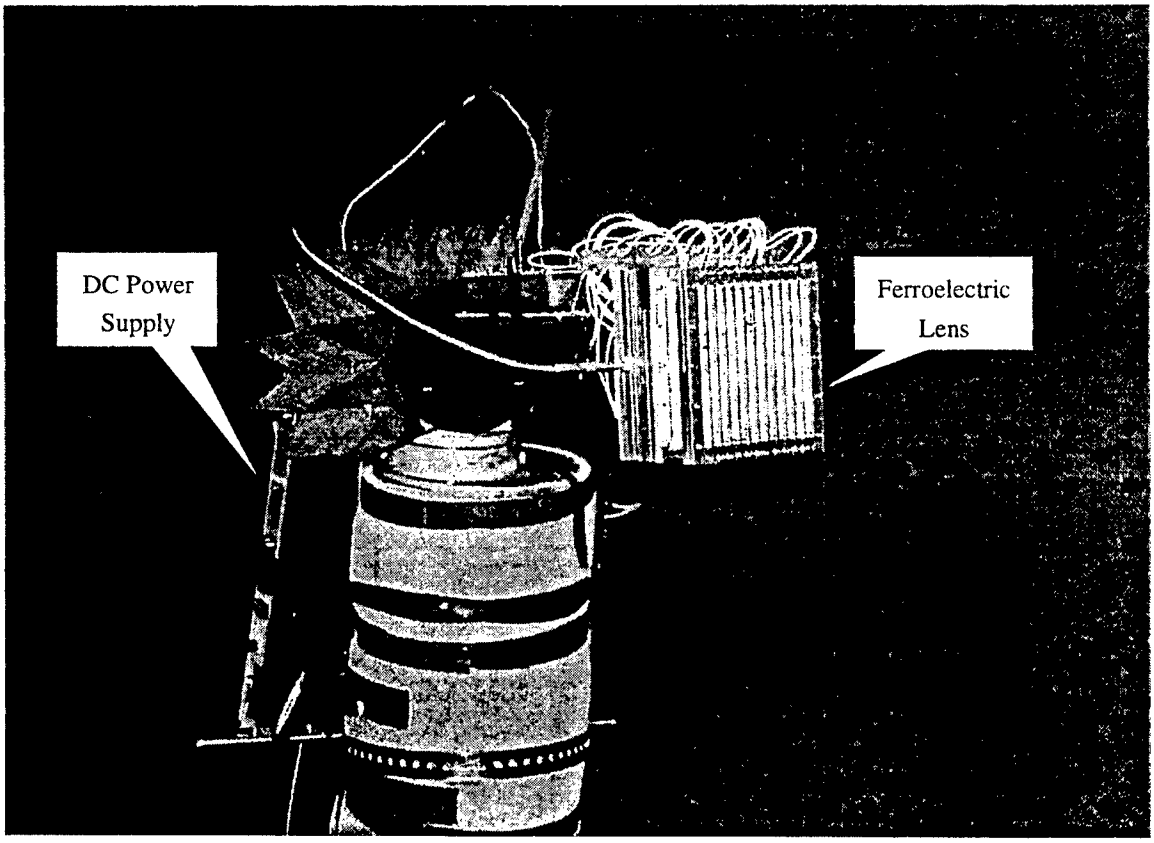

Fig. 4 - Prototype Ferroelectric Lens

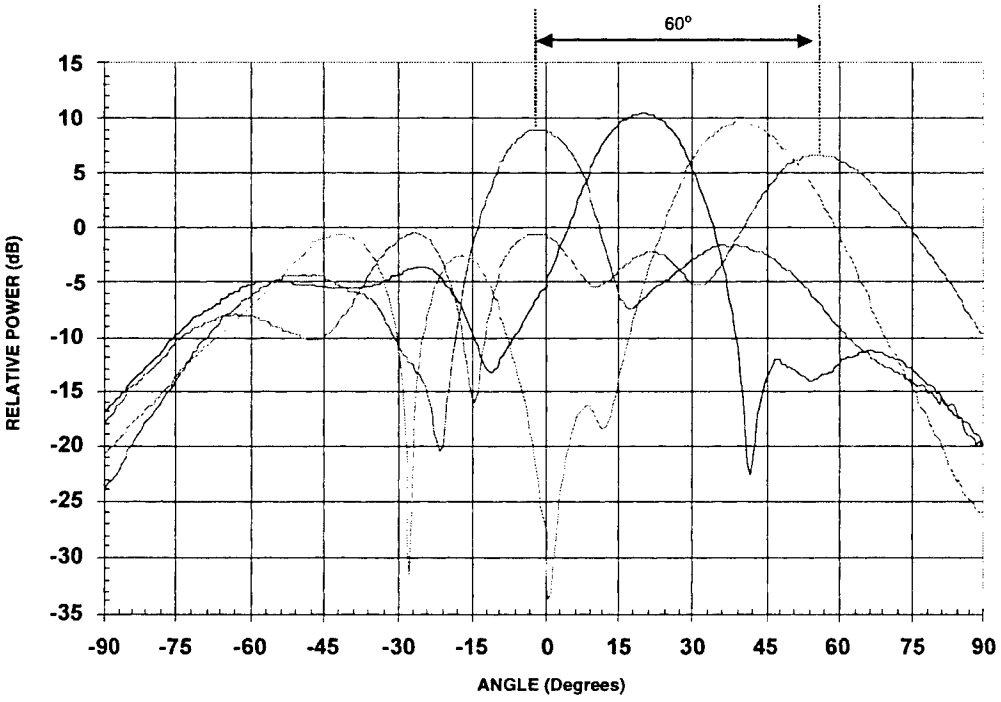

Fig. 5 - Measured Radiation Patterns of the Prototype Ferroelectric Lens at 10 GHz for Four Different Scan Angles

Field Dependence of Dielectric Properties of $(Pb,Sr)TiO_3$ Thin Films

Masatoshi Adachi, kazuhiro Tsu and Tomoaki Karaki
Department of Electronics & Informatics, Toyama Prefectural University
5180 Kurokawa, Kosugimachi, Toyama 939-0398, Japan
FAX: +81-766-56-8023
E-Mail: adachi@pu-toyama.ac.jp

$(Pb,Sr)TiO_3$ (PST) thin films have been grown on $Ir/SiO_2/Si$ substrates by RF magnetron sputtering. A multi-target comprised of a $SrTiO_3$ ceramics target, 4 PbO pellets and some Ti metal chips on it was used. PST films with the perovskite structure were obtained at the substrate temperature of around 600 to 630°C. The temperature dependence of dielectric constant showed a broad peak at 60°C. The dielectric constant was 1250 at 500kHz. The DC bias field decreased the both dielectric constant and loss of the PST films. The change of dielectric constant under the DC field is strongly accentuated around the Curie temperature. The dielectric tunability performs a high value of approaching 50% (E=15kV/mm) at room temperature for the 400nm thick film. A slender *D-E* hysteresis loop was observed. The spontaneous polarization P_r and coercive field E_c were $2\mu C/cm^2$ and 2.1kV/cm, respectively.

INTRODUCTION

Ferroelectrics are very interesting materials for various functional devices [1]. Recently, ferroelectric thin films such as $(Ba,Sr)TiO_3$, Pb-based perovskite PZT, Bi layered $SrBi_2Ta_2O_9$ and so on, have been actively studied as promising materials for capacitor dielectric films in dynamic random access memories (DRAMs), ferroelectric random-access memories (FeRAMs) and gate insulators in metal ferroelectric semiconductor (MFS) or metal ferroelectric insulator semiconductor (MFIS) gate structures [2-6].

On the other hand, Electronically tunable microwave components have become the subject of intense research efforts in recent years. Ferroelectric thin films are also being used to develop next generation, high performance microwave control components such as tunable filters, phase shifters, oscillators, etc.. So far, $Ba_{0.6}Sr_{0.4}TiO_3$ (BST) is a tunable dielectric that is being investigated for new generation of room temperature microwave devices [7, 8].

$Pb_{1-x}Sr_xTiO_3$ (PST) material is one of the old-fashioned ferroelectric systems with the perovskite structure as well as the BST [9]. By controlling Pb/Sr ratio in the PST, its Curie temperature changes from –230 to 490°C. Therefore it is possible to fabricate different temperature range devices.

EXPERIMENTAL

An RF magnetron sputtering equipment with three cathods (SH-250-TO6, Nippon Vacuum Technology Co. Ltd.) was used to fabricate Ir and PST films. PST thin films with a perovskite structure were prepared on $(111)Ir/SiO_2/Si$ substrates using a multi-target, which was comprised of PbO pellets of 12mm diameter and 2mm thickness, pure titanium metal chips positioned on a $SrTiO_3$ ceramic target of 75mm diameter and 5mm thickness produced by High Purity Chemicals Co. Ltd.. Preparation of the PbO pellets was carried out by a conventional oxide

Tab. 1 Sputtering conditions for PST films

Substrate	$Ir/SiO_2/Si$
Substrate Temperature	470-630℃
Input Power	100W
Gas Flow	Ar, 10sccm
Gas Pressure	4-8 mTorr
Sputtering Time	1-2 h
Target	$SrTiO_3+PbO+T_i$

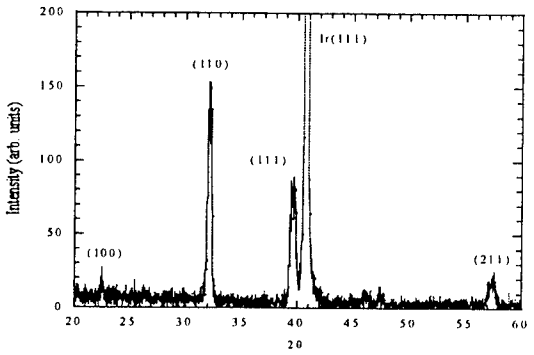

Fig. 1. X-ray diffraction pattern of the PST film

calcinations technique. PbO was used as Pb source of PST film, because PbO has a higher melting point than Pb and its sputtering rate is comparable to that of Pb. The Pb/Sr ratio of PST thin films were easily controlled by appropriately arranging the PbO pellets and Ti metal chips. Sputtering conditions are shown in Tab.I. The crystal structure and crystallographic orientation of PST films were examined by the X-ray diffraction (XRD) method. An X-ray micro analyzer (XMA) was also used to determine the composition. The capacitance and *tan δ* were measured by using the YHP4192A LF impedance analyzer at frequencies of 1, 10, 100 and 500kHz under an DC bias of 0 to 10V.

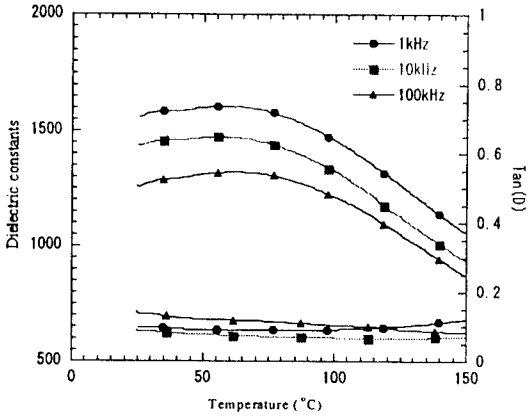

Fig. 2. Temperature dependence of Dielectric constants and *tan δ*.

RESULTS AND DISCUSSION

Fig. 1 shows an XRD pattern of a PST film sputtered on the (111) Ir/SiO/Si substrate at aubstrate temperature of 630°C. From the XRD analysis, PST thin films with the perovskite structure were obtained at the substrate temperature from 600 t0 630°C. Film thicknesses were around 400 nm. Fig. 2 shows the temperature dependence

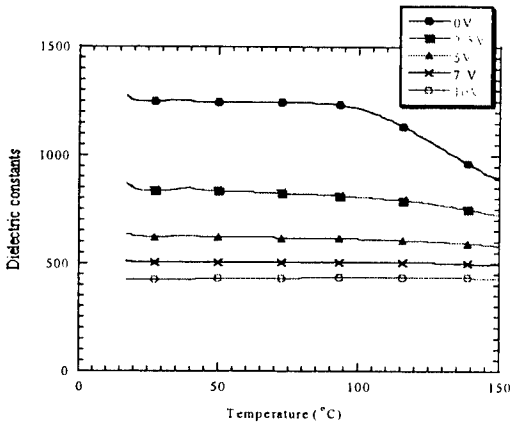

Fig. 3. Temperature dependence of dielectric constants as a function of DC-bias fields.

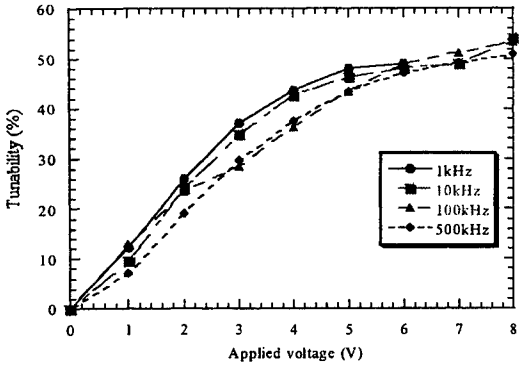

Fig. 4. DC field dependence of dielectric tunability at room temperature.

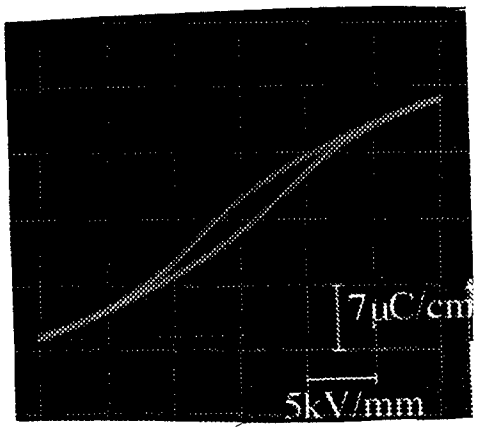

Fig. 5. D-E hysteresis loop.

of dielectric constants and *tan δ* without a bias field. The dielectric constant was 1600 at 1kHz and its maximum value (Curie temperature) was 60°C.

Fig. 3 shows the temperature dependence of dielectric constants at 500kHz as a function of DC bias fields obtained by the isothermal run experiment. The DC bias field decreased the dielectric constant and dielectric loss in the PST thin film. The change of dielectric constant was also strongly accentuated around the Curie temperature. The bias field suppresses the paraelectric-ferroelectric phase transition. The dielectric tunability at room temperature, defined as $D_t=[1-(\varepsilon(E)/\varepsilon(E=0))]\times100\%$, is shown in Fig. 4. The dielectric tunability reaches a high value at room temperature, approaching 50 % at the voltage of 6V for the 400nm thick PST film and has a tendency to saturate from 5V. A *D-E* hysteresis loop of the PST thin film is shown in Fig. 5. A slender *D-E* hysteresis loop was also observed at room temperature. The spontaneous polarization P_s and coercive field E_c were 2 μC/cm^2 and 21kV/cm, respectively.

CONCLUSIONS

$(Pb,Sr)TiO_3$ (PST) thin films have been grown on $Ir/SiO_2/Si$ substrates by RF magnetron sputtering. A multi-target comprised of a $SrTiO_3$ ceramics target, 4 PbO pellets and some Ti metal chips on it was used. PST films with the perovskite structure were obtained at the substrate temperature of around 600 to 630°C. The temperature dependence of dielectric constant showed a broad peak at 60°C. The dielectric constant was 1250 at 500kHz. The DC bias field decreased the both dielectric constant and loss of the PST films. The change of dielectric constant under the DC field is strongly accentuated around the Curie temperature. The dielectric tunability performs a high value of approaching 50% (E=15kV/mm) at room temperature for the 400nm thick film. A slender *D-E* hysteresis loop was observed. The spontaneous polarization P_r and coercive field E_c were 2μC/cm^2 and 2.1kV/cm, respectively.

REFERENCES

[1] M. Okuyama and Y. Hamakawa, Ferroelectrics, 63, 243-252 (1985).

[2] K. Abe, H. Tomita, H. Toyoda, M. Imai and Y. Yokote, Jpn. J. Appl. Phys., 30, 2152 (1991).

[3] K. Torii, H. Kawakami, H. Miki, K. Kushida and Y. Fujisaki, J. Appl. Phys., 81, 2755 (1997).

[4] K. Aoki, Y. Fukuda, K. Numata and a. Nishimura, Jpn. J. Appl. Phys., 35, 2210 (1996).

[5] T. hirai, k. teramoto, k. Nagashima, H. Koike, S. Matsuno, S. Tanimoto and y. tarui, Jpn. J. appl. Phys., 35, 4016 (1996).

[6] S. Horita, T. Kawada and Y. Abe, Jpn. J. Appl. Phys., 35, l1357 819969.

[7] J.-W. Liou and B. -S. Chioum, J. Am. Ceram. Soc., 80, 3093 (1997).

[8] d. Garcia, R. Guo and a. Bhalla, Ferroectric Letters, 27, 137-146 (2000).

[9] S. Nomura and S. Sawada, J. Phys. Soc. Jpn., 10, 108 (1955).

SESSION II. MEMORY

Plenary Lectures – Memory Applications

PII.1 Material Processing Requirements for Ferroelectric Non-Volatile Memory (FRAM) Technology, Glen R. Fox, R. Bailey, B. Kraus, F. Chu, S. Sun, and T. Davenport, Ramtron International Corporation, USA. 103

PII.2 Recent Study on Ferroelectric Thin Films and Their Applications, Tadashi Shiosaki and S. Okamura, Nara Institute of Science and Technology (NAIST), Japan. 109

Memory

II.25 A Novel Fabrication Process of Ferroelectric Capacitors with the Self-align Patterning of Top Electrodes, S. Okamura, T. Kobayashi, K. Suzuki, and T. Shiosaki, Nara Institute of Science and Technology, Japan. 115

II.26 Preparation and Properties of $SrBi_2Ta_2O_9$ Ferroelectric Thin Films Using Excimer UV Irradiation, T. Hayashi, and D. Togawa, Shonan Institute of Technology, Japan. 119

II.27 Chemical Processing and Ferroelectric Properties of $MBi_4Ti_4O_{15}$ (M:Alkaline Earth Metals) Thin Films, K. Kato*†, K. Suzuki*, K. Nishizawa*, and T. Miki*, *National Institute of Advanced Industrial Science and Technology, Japan, †Frontier Collaborative Research Center, Tokyo Institute of Technology. 123

II.28 Integration and Characterization of Sub-micron MFIS FETs Transistor with $Pt/Pb_5Ge_3O_{11}$/High-k/Si Structure, F. Zhang and S. T. Hsu, Sharp Laboratories, USA. 127

II.29 Low Temperature Deposition of Epitaxial-Grade PZT Films by MOCVD, H. Funakubo, M. Aratani, T. Oikawa, and K. Saito*, Tokyo Institute of Technology, Japan, *Philips Japan Ltd., Japan. 131

II.30 Retention Properties in Single-crystalline PLZT Thin Film Capacitors, N. Kamehara, M. Kurasawa, and K. Kurihara, Fujitsu Laboratories, Ltd., Japan. 135

Film Deposition

II.31 Synthesis and Properties of Tungsten Bronze (Sr,Ba)(Nb,Ta)$_2O_6$ Thin Films by the Chemical Solution Deposition, W. Sakamoto, Y. Horie, T. Yogo, and S. Hirano, Nagoya University, Japan. 139

MEMS

II.33 Electrical Properties of $PbZrO_3$ Thin Films Prepared by Chemical Solution Deposition, H. Maiwa and N. Ichinose*, Shonan Institute of Technology, Japan, *Waseda University, Japan. 143

II.34 Microelectromechanical Systems (MEMS) Accelerometers Using Lead Zirconate Titanate Thick Films, L. P. Wang*, R. Wolf*, K. Deng^, L. Zou^, Y. Wang*, P. Wlodkowski^, R. J. Davis*, and S. Trolier-McKinstry*, *Penn State University, USA, ^ Wilcoxon Research, USA. 147

II.35 Piezoelectric Properties of $Pb(Yb_{1/2}Nb_{1/2})O_3$-$PbTiO_3$ Epitaxial Films with (100) and (111) Orientation, T. Yoshimura and S. Trolier-McKinstry, Penn State University, USA. 151

II.36 Preparation of Texture Controlled Lead Zirconate Titanate Diaphragm Type Film Actuator, T. Iijima, B. P. Zhang, and K. Kunii*, Tohoku National Industrial Research Institute, Japan, *NIDEC COPAL Corporation, Japan. 155

Fundamentals

I1.37 Why the Atomic Structure Matters to Dielectric and Piezoelectric Performance, T. Egami, University of Pennsylvania, USA. 159

II.38 Polarization Relaxation in Piezoelectric $0.7Pb(Mg_{1/3}Nb_{2/3})O_3$–$0.3PbTiO_3$, D. Viehland,Naval Seasystems Command, USA. 161

II.39 Statistical Model for Poling Hard PZT, W. A. Schulze and M. K. Jha, Alfred University, USA. 165

II.40 Electric Field Effects on Dielectric Properties of MPB PZT Ceramics via Monoclinic Distortion at Low Temperatures, R. Guo, E. Alberta, A. Thomas, B. A. Jones, and L. E. Cross, Penn State University, USA. 169

II.41 Harmonic Analysis of the Electro-Mechanical Response of Electroactive Materials, C. B. DiAntonio, F. A. Williams, Jr., and S. M. Pilgrim, Alfred University, USA. 173

II.42 Calculation of Electrostrictive Coefficients and Their Complex Nature Through Fourier Analysis, C. B. DiAntonio, F. A. Williams, Jr., S. M. Pilgrim, Alfred University, USA. 177

II.44 Visualization of the Domain Orientation in $PbTiO_3$ Single Crystals by Vertical and Lateral Piezoresponse Microscopy, H. (Okino) Niori, T. Ida, H. Ebihara, and T. Yamamoto, National Defense Academy, Japan. 181

II.45 Domains and Piezo Images of PZT Family Thin Films Observed by AFM and KFM, Y. Masuda, K. Kakimoto[†], S. Fujita, and K. Watanabe*, Hachinohe Institute of Technology, Japan, [†]Nagoya Institute of Technology, *Seiko Instrument Company, Japan. 185

II.46 Progress in Flexoelectric Measurements, L. E. Cross and W. Ma, Penn State University, USA. 189

Material Processing Requirements for Ferroelectric Non-Volatile Memory (FRAM) Technology

G.R. Fox, R. Bailey, B. Kraus, F. Chu, S. Sun, and T. Davenport
Ramtron International Corporation, 1850 Ramtron Drive, Colorado Springs, CO 80921
FAX: (719)481-9170
Email: Glen.Fox@Ramtron.com

Ferroelectric non-volatile memories (FRAM) have been mass-produced since 1992 and densities up to 256 Kbit are currently available in a range of products. Both memory density and the market for FRAM are increasing at an exponential rate due to the demands for non-volatility, high read/write endurance, fast access speed and low power operation. Current applications include smart cards, data collection and storage (e.g. power meters), configuration storage and buffers. FRAM cell designs utilize a $PbZr_xTi_{1-x}O_3$ based bistable ferroelectric capacitor structure that is integrated with a transistor (1T1C) or a complementary capacitor and two transistors (2T2C). Small memory cell sizes under development will not only enable high density stand–alone memories but also extend the application of FRAM that is already used in embedded and system-on-chip devices. A review of ferroelectric materials performance in current memory products will be presented. Recent development has lead to capacitor performance with endurance beyond 10^{12} read/write cycles and operation at 1.8 V. A roadmap for future FRAM development will be presented.

INTRODUCTION

Over the past 15 years, nonvolatile ferroelectric random access memories (FRAM) have evolved from a concept on paper to memory products that are used in a variety of consumer products and industrial applications. FRAM is a vital component to applications including smart cards, power meters, printers, and video games. The advantage of using FRAM instead of other types of nonvolatile memories such as EEPROM and battery backed SRAM varies according to the application. FRAM exhibits a unique combination of performance features including low power consumption, high read/write endurance, fast read/write access time, and long term retention. Not only is FRAM of interest as a high performance stand-alone memory, it also provides a low cost embedded memory solution that can be scaled to high densities.

FRAM was first demonstrated in 1988 using $PbZr_xTi_{1-x}O_3$ (PZT) as the ferroelectric material for data storage (Fig. 1). The FRAM cell consisted of two transistors and two capacitors commonly referred to as a 2T2C cell. The ferroelectric capacitors were added to the underlying CMOS by applying backend ferroelectric, electrode, metallization, and interlevel dielectric processes. With a cell factor of approximately 110 and a CMOS feature size of 3 μm, these initial FRAM devices had a very large cell size of nearly 1000 μm^2.

FRAM mass production commenced in 1992 [1]. Soon after production was started, the cell size was significantly reduced by decreasing the minimum feature size to 1.0 μm. Near the same time, La doping of the PZT was also introduced in order to improve read/write cycling endurance and data retention. Access to new process lines have lead to a current feature size of 0.35 um, and steady advances in PZT processing and dopant additions have allowed production of FRAM products with a density of 256 Kbit, 10 yr retention (-45 to 85°C) and a read/write endurance as high as 10^{16} cycles. Memories fabricated and tested but that are still

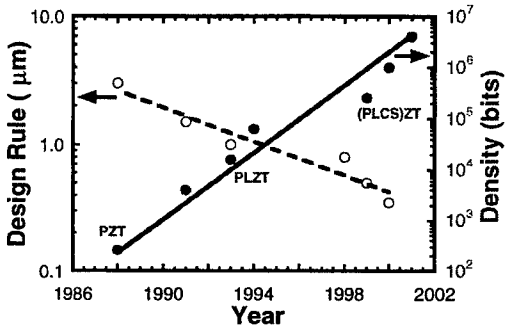

FIG. 1 – Progression of FRAM memory density and design rule in manufacturing.

under development have achieved densities as high as 4 Mbit.

A new era is emerging for FRAM development and product manufacturing. FRAM is now being manufactured in state-of-the-art facilities. In addition, advances in materials and cell design and architecture are allowing for rapid decreases in cell size, which will enable production of low cost high density memories. With a well organized development effort FRAM based products have the potential to capture a majority of the stand-alone and embedded non-volatile memory market as well as penetrate the SRAM and DRAM markets. The rest of this paper presents a roadmap that outlines the requirements for high density FRAM and describes the status of ferroelectric materials development with respect to this roadmap.

HIGH DENSITY FRAM ROADMAP

In order to achieve cost effective production of high density FRAM, both the cell factor and feature size must be reduced. Most commercial FRAM devices that are currently available utilize a 2T2C cell with a 0.5 μm minimum CMOS feature size. In these devices, the ferroelectric capacitors are formed on top of field oxide such that the capacitors are next to the accompanying transistors and each component of the cell occupies a uniquely defined area. This architecture will be referred to as the capacitor-over-field-oxide (COFO) architecture.

The large, 110, cell factor for the 2T2C devices can be reduced by changing both the cell design and architecture. Introduction of a 1T1C type cell decreases the cell factor to approximately 63, therefore, the cell area is nearly half that for a 2T2C cell. Because a 2T2C cell is self-referencing, the change to a 1T1C cell places stricter requirements on the ferroelectric capacitor performance with respect to switchable polarization, retention and cycling endurance.

An additional decrease in cell factor is achieved by building the ferroelectric capacitor on top of a plug that contacts an underlying access control transistor as shown in Fig. 2. Cell factors as small as 4 have been proposed for 1T1C designs with the capacitor-over-plug (COP) architecture [2]. The COP architecture also introduces new demands on the ferroelectric capacitor materials since the capacitor is grown on a conducting plug material (as apposed to field oxide) that must be protected from oxidation to insure low contact resistance

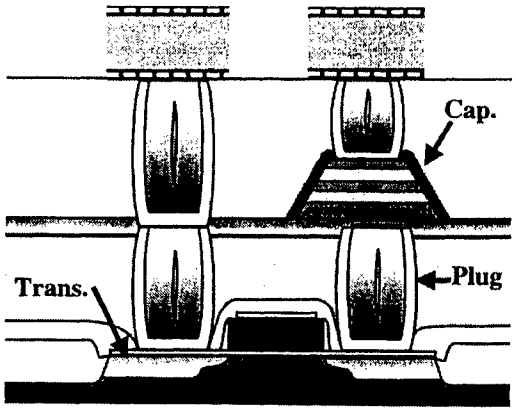

Fig. 2 – Diagram of FRAM capacitor-over-plug (COP) architecture.

between the capacitor and plug. Cell factors, architectures, and cell sizes for 1T1C based FRAM are given in Table I for existing processes based on 0.5 and 0.35 μm CMOS feature sizes. Targets for future 1T1C FRAM generations with smaller feature sizes are also shown in Table I. A range of cell factors and sizes is given for each generation because these values depend on several factors including the ferroelectric capacitor stability, reference scheme for detecting the 0 and 1 state of the cell, and the minimum ferroelectric switched charge detectable by the CMOS sensing circuitry. Although FRAM has a potentially low processing cost with a requirement for only two or three additional mask steps (making it particularly attractive for embedded applications) the current cell factor of 63 must continue to be reduced in advanced generations in order to maintain cost competition with other memory technologies.

In addition to cell size and architecture, Table I also lists the targets for memory density and performance specifications for feature sizes down to 0.1 μm. The reduction of feature size is accompanied by scaling of not only cell factor but also operating voltage, access time, and read/write endurance. FRAM memory based on all feature sizes must maintain data for a period of 10 yr over the specified operating temperature (typically –45 to 85°C) and it is desirable to keep the active current below 15 mA. Meeting all performance requirements while scaling cell size and density for each generation requires increased design efficiency and control of ferroelectric capacitor performance. Since FRAM design is outside the scope of this publication, only a discussion of ferroelectric capacitor requirements will follow.

Table I– Roadmap for 1T1C FRAM memory.

	0.5 μm	0.35 μm	0.25 μm	0.18 μm	0.13 μm	0.1 μm
Density (Mbit)	1	4	64	256	512	2000
Architecture	COFO	COFO/COP	COP	COP	COP	3D-COP
Cell Factor	63	63 - 30	30 - 15	20 – 8	16 - 8	12 - 6
Cell Size (μm^2)	15.8	8.0 – 3.7	1.9 – 0.9	0.65 – 0.26	0.27 – 0.14	0.12 – 0.06
Operating Voltage (V)	5/3.3	3.3	2.5	1.8	1.5	1.2
Data Retention (yr)	10	10	10	10	10	10
Read/Write Endurance (No. Cycles)	$10^{10}/10^{16}$	10^{16}	10^{16}	10^{16}	10^{16}	10^{17}
Access Time (ns)	70	50	30	20	15	10
Active Current (mA)	<15	<15	<15	<15	<15	<15

Table II – Ferroelectric capacitor properties for current generations and target requirements for future 1T1C FRAM.

	0.5 μm	0.35 μm	0.25 μm	0.18 μm	0.13 μm	0.1 μm
Capacitor Area (μm^2)	3.0	1.5 - 1.0	1.0 - 0.5	0.33 - 0.13	0.14 - 0.07	0.06 - 0.03
PZT Thickness (nm)	200	180	140	100	80	65
V(90%) (V)	4.0/2.8	2.2	1.8	1.5	1.2	0.9
Q_{sw} ($\mu C/cm^2$)	30	30	30	35	40	45
Q_{sw}(10yr)@150°C	20	20	10	20	35	40
Switching Endurance (No. Cycles)	$10^{10}/10^{14}$	10^{14}	10^{15}	10^{15}	10^{15}	10^{16}
Switching Time (ns)	<10	<10	<10	<10	<5	<5
Energy/Bit (pJ)	2.3/1.4	0.68	0.19	0.04	0.02	0.02

Table II provides a summary of the ferroelectric capacitor requirements at each feature size. For the 0.5 and 0.35 μm generations, which employ the COFO architecture, sufficient ferroelectric switchable charge can be generated from a planar capacitor that occupies less than 20% of the total cell size. The capacitor dimensions and performance metrics for these two generations are typical of those found for capacitors in FRAM products. The capacitor switchable charge is determined by the ferroelectric switchable polarization (Q_{sw}) multiplied by the area of the capacitor. Since mechanisms such as relaxation, imprint, and fatigue can reduce the magnitude of Q_{sw}, the capacitor must be sized such that sufficient switched charge is available for data state detection during the specified memory lifetime, e.g., 10 yr. One metric that can be used for capacitor sizing is the extrapolated Q_{sw} remaining after a 10 yr 150°C bake (Q_{sw}(10yr)@150°C). This metric gives a conservative measure of the switchable polarization remaining after 10 yr retention of a data state. For the 0.5 and 0.35 μm generations a Q_{sw} of approximately 5 $\mu C/cm^2$ is required to generate the switched charge necessary for data state detection. Since Q_{sw}(10yr)@150°C is 20 $\mu C/cm^2$ a significant switched charge margin remains even if other Q_{sw} degradation mechanisms occur. The capacitors in these FRAM products have purposely been oversized to allow a larger than required margin for switched charge in order to increase product reliability.

Because the capacitor is stacked on top of the transistor for the COP architecture, the relative cell area occupied by the capacitor increases to approximately 50%. Starting with the 0.35 μm COP generation, it can be seen that the capacitor size scales proportionally to the cell size. It is desirable to maintain the largest possible capacitor area since this increases the ferroelectric switchable charge that can be used to detect the difference between a 0 and 1 data state. Although larger capacitor areas provide a larger margin for Q_{sw} degradation over the lifetime of a memory it is not desirable to achieve this margin at the expense of an increased cell size. For this reason, it is required that Q_{sw} increases for generations with feature sizes smaller than 0.25 μm in order to maintain sufficient switched charge for data state retention. In addition, less degradation of Q_{sw} is

allowed for advanced generations as can be seen from the reduced difference between Q_{sw} and Q_{sw}(10yr)@150°C. For the 0.1 μm generation, meeting the Q_{sw} scaling requirement with a planar PZT-based capacitor becomes difficult. A Q_{sw} of at least 45 μC/cm^2 is required even with a cell factor of 12. Smaller cell factors will require even larger Q_{sw} values. In order to meet the switched charge requirement for an aggressive cell factor of 6 at the 0.1 μm generation, three-dimensional capacitor structures are expected to be required.

Since a high number of switching cycles can degrade the magnitude of Q_{sw}, Table II lists the switching endurance, i.e., number of cycles, required without appreciable loss of Q_{sw}. For the 0.5 and 0.35 μm generations, some reduction of Q_{sw} with cycling is allowable due to the margin afforded by the oversized capacitors. Modeling of reliability test data has confirmed that 3.3 V FRAM products can achieve 10^{16} read/write cycle endurance [3]. But as the feature size is decreased, less margin in Q_{sw} is available and nearly fatigue free films are required for the endurance specification. A capacitor endurance specification of at least 10^{16} cycles is required for use in a parallel FRAM to ensure a 10 yr lifetime. Taking into account differences in bit access within a FRAM memory and the continuous cycling in a capacitor test allows a capacitor with an extrapolated fatigue free 10^{15} cycles to achieve 10^{16} read/write cycles in a memory. As the memory access time decreases, a corresponding increase in read/write endurance is required. At the 0.1 μm generation, an endurance of 10^{17} read/write cycles is required for the memory indicating that the capacitor within a bit must have an endurance of at least 10^{16} cycles.

A PZT thickness reduction is introduced with each generation for two reasons. One reason is to maintain a reasonable capacitor height to width aspect ratio for minimizing difficulties with a single step capacitor stack etch process. But the primary reason for scaling the PZT thickness is to meet the operating voltage requirements for each generation. In order to insure proper data retention and data state detection, PZT must switch at voltages below the standard operating voltage of the FRAM product. Saturation of ferroelectric switching as a function of applied voltage is quantified by determining the voltage at which 90% of the maximum Q_{sw} is achieved ($V_{90\%}$). Because of the operating voltage reduction with each generation (Table I) $V_{90\%}$ must be scaled accordingly (Table II). Typically, $V_{90\%}$ should be 20 to 30% below the operating voltage to insure performance over a range of temperature and stress conditions. Since ferroelectric switching is determined by the magnitude of the electric field applied to the ferroelectric, the most direct method for reducing $V_{90\%}$ is to reduce the PZT thickness. This approach is expected to be viable even for the 0.1 μm generation where it is estimated that PZT films as thick as 65 nm can be used to achieve a $V_{90\%}$ of 0.9 V. Dopants can also be introduced to lower $V_{90\%}$, but strong effects on processing and other ferroelectric properties, such as Q_{sw}, can complicate this approach.

By combining the Q_{sw} and operating voltage requirements for each technology node, the energy per bit, i.e., energy required to change data states within a single capacitor can be calculated. This energy is extremely low even at the 0.5 um generation and it decreases with advanced generations. The energy required to switch the data state within a ferroelectric capacitor is in fact negligible in comparison with the energy required to drive the supporting circuitry; therefore, the active current for FRAM memory is primarily determined by the circuit design.

CURRENT STATUS OF PZT CAPACITOR MATERIALS

Development of the capacitor stack for the 0.5 and 0.35 μm generations is for the most part complete. The capacitor properties for both the 0.5 and 0.35 μm generations and the mass-produced memories at the 0.5 μm generation (memories for the 0.35 μm generation have not yet been qualified) meet the specifications listed in Tables I and II. For both generations, the capacitor stack consists of a Pt bottom electrode, PZT ferroelectric, and IrO_x top electrode. The Pt has a {111} texture, which seeds the growth of {111} textured PZT. It has been confirmed that the PZT and Pt have corresponding rocking curve angular widths for films that give the most efficient ferroelectric switching performance.

Because FRAM materials development is currently driven by access to production facilities, the next generation FRAM products could be introduced with 0.25, 0.18, or 0.13 μm minimum feature sizes. For this reason, basic materials studies are focused on thickness scaling to meet the reduced operating voltages for these generations. These studies also

determine whether sufficient Q_{sw} and retention can be achieved in films with reduced thickness.

Fig. 3 shows the change in $V_{90\%}$ and Q_{sw} as a function of PZT film thickness. The PZT has a Zr:Ti ratio of 40:60 and also contains dopants of La, Ca, and Sr. The PZT sputter

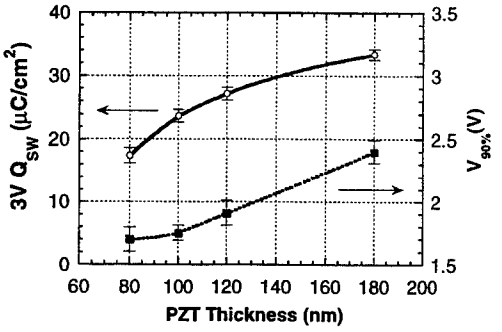

Fig. 3 – Dependence of Q_{sw} and $V_{90\%}$ on PZT film thickness.

deposition and anneal processes were established at a film thickness of 180 nm and then thinner films were produced with the same process by reducing deposition time. For all film thicknesses, greater than 90% (by volume) {111} texture was maintained. It is observed that the $V_{90\%}$ decreases linearly with thickness until 80 nm where it departs from linear behavior. With $V_{90\%}$=1.8 V, the 100 nm thick film could be used for the 0.25 μm generation. Process reoptimization for this thickness is likely to provide the 1.5 V $V_{90\%}$ needed for the 0.18 μm generation. The Q_{sw} for the 100 nm thick film is below the value required for both the 0.25 and 0.18 μm generations. In addition, the Q_{sw}(10yr)@150°C for both the same-state and opposite-state retention test is insufficient even though the absolute rate of Q_{sw} degradation with bake time remains constant with thickness scaling. As with the $V_{90\%}$ metric, it is expected that careful attention to Pb concentration gradients and anneal thermal budgets can bring the Q_{sw} and Q_{sw}(10yr)@150°C values in line with requirements for the 0.25 and 0.18 μm generations. In all cases, the thickness scaled films exhibit excellent cycling endurance when compared at equal fields. The films exhibit no fatigue when tested beyond 10^{11} cycles and voltage accelerated testing indicates that 10^{13} cycles could be achieved without fatigue. Because of testing limitations, new fatigue models and testing methodology must be established to confirm fatigue free behavior beyond 10^{13} cycles. In general, these reduced thickness films, which were deposited in a mass-production sputtering tool, provide capacitor performance that is close to that which is needed for the 0.25 and 0.18 μm FRAM memory generations even without full process optimization.

In order to achieve capacitor properties that meet the requirements for the 0.13 and 0.10 generations, changes in PZT composition will likely be required. Low voltage (1.5 V) switching has been demonstrated for capacitor sizes as small as 0.12 μm^2 with undoped 20:80 PZT grown by MOCVD. A Q_{sw} of 40 $\mu C/cm^2$ was achieved, indicating that process optimization for these films may lead to capacitor specifications that match the 0.13 and 0.1 μm generation requirements [4].

In addition to meeting the capacitor performance specifications for generations with a 0.18 μm and smaller feature size, it is believed that control of the ferroelectric PZT crystallographic texture will become a critical factor. Texture becomes important in two ways. For planar capacitors with areas below 0.5 μm^2, the capacitor size is of the same order-of-magnitude as the grain size of the PZT. Randomly oriented films are expected to show a wide capacitor-to-capacitor Q_{sw} distribution due to the random orientation of the PZT grains and corresponding angular distribution of the ferroelectric polarization. The distribution will be broadest in the case where no 90° domain

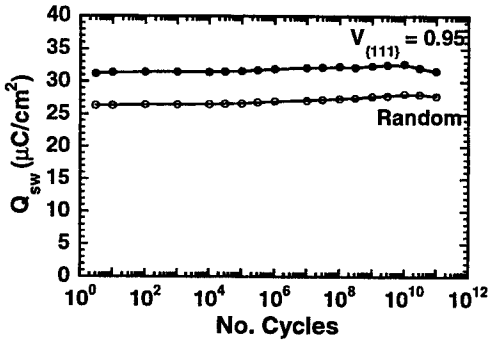

Fig. 4 – Comparison of voltage accelerated cycling endurance of {111} textured and randomly orientated 180 nm thick PZT films cycled at 5V and 1 MHz.

switching occurs, which is the commonly observed case for films with thicknesses below 300 nm. For 3D capacitor structures, better capacitor-to-capacitor uniformity may be achieved with random PZT since it is expected to

be difficult to uniformly control texture over the surface of a 3D structure, but this will depend on the physical area of the capacitor and domain switching mechanisms of the film. It has been demonstrated that both random and {111} textured PZT films can be produced with similar fatigue free performance up to more than 10^{11} switching cycles as shown in Fig 4. If the voltage acceleration is taken into account these films will continue to show fatigue free behavior to greater than 10^{12} cycles under the 3V operating voltage for which the films were designed. Although it may be less difficult to control the growth of random PZT films, this relaxation of processing constraints is gained at the expense of ferroelectric switching performance. Randomly oriented films exhibit a reduced Q_{sw} and a higher $V_{90\%}$ than films of the same thickness with {111} texture. The decreased switching performance of the random film is believed to result primarily from the absence of 90° domain switching. Both the {111} textured and randomly oriented PZT materials show potential for meeting the requirements of the 0.1 μm generation, but the trade-off between ease of manufacturing, ferroelectric anisotropy, and size effects will need to be clearly understood.

CONCLUSIONS

A roadmap and requirements for 1T1C FRAM memory was presented for generations having feature sizes between 0.5 and 0.1 μm. The corresponding roadmap for ferroelectric capacitor requirements was described in relation to the memory roadmap. The ferroelectric capacitor requirements for the 0.5 and 0.35 μm generations have been achieved with {111} textured PZT containing La, Ca, and Sr dopants. With process modifications, similar PZT films are expected to meet the requirements for the 0.25 and 0.18 μm generations. At the 0.13 and 0.1 μm generations, a PZT composition modification will be required and careful consideration of the trade-off between ease of manufacturing, crystallographic texture and cell size will be needed.

REFERENCES

1. T. Davenport and S. Mitra, *Integrated Ferroelectrics*, **31**, 213-231 (2000).
2. D. Takashima, S. Shuto, I. Kunishima, H. Takenaka, Y. Oowaki, and S. Tanaka, *IEEE J. Solid-State Circuits*, **34**, 1557-1563 (1999).
3. T.D. Hadnagy, D. Dalton, B. Thomas, S. Sun and R. Bailey, to be published in *Integrated Ferroelectrics* (2001).
4. T.S. Moise, S.R. Summerfelt, G. Xing, L. Colombo, T. Sakoda, S.R. Gilbert, A. Loke, S. Ma, R. Kavari, L.A. Wills, T. Hsu, J. Amano, S.T. Johnston, D.J. Vestyck, M.W. Russell, and S.M. Bilodeau, *IEDM Tech. Dig.*, 940 (1999).

Recent Study on Ferroelectric Thin Films and Their Applications

Tadashi SHIOSAKI and Soichiro OKAMURA
Graduate School of Materials Science, Nara Institute of Science and Technology (*NAIST*)
8916-5 Takayama-cho, Ikoma, Nara 630-0101, Japan
Fax: +81-743-72-6069
e-mail: shiosaki@ms.aist-nara.ac.jp

In this paper, the recent study on ferroelectric thin films and their applications, especially embedded memory system in Japan, is reviewed. In addition, our recent activities in NAIST, for example, liquid delivery metalorganic chemical vapor deposition (MOCVD) of PZT thin films and analysis of defects in ferroelectric thin films using thermally stimulated current (TSC) method are briefly reported.

1. INTRODUCTION

Ferroelectric random access memories (FeRAMs) with 1T-1C or 2T-2C cell architecture[1] have become reality. Ramtron put a 4 kb FeRAM product on the market in 1993 for the first time. The problem of polarization fatiuge in $Pb(Zr,Ti)O_3$ (PZT) thin films was settled by introducing metal-oxide electrodes such as IrO_2.[2] Rohm corporation mass-produced FeRAMs and embedded integrated circuits (ICs) with PZT thin films and IrO_2 electrodes. On the other hand, Araujo *et al.* proposed fatigue-free ferroelectric material $SrBi_2Ta_2O_9$ (SBT), so-called Y1.[3] Symetrix and Matsushita Electric Industrial chose SBT thin films as a storage material in FeRAMs. SBT thin films usually needed higher temperatue for crystallization than PZT thin films at the beginning of studies. Recently, they have succeeded in the lowering process temperature to 650°C.[4] Park et al. reported La-substituted bismuth titanate $(Bi_{3.25}, La_{0.75})Ti_3O_{12}$ (BLT) thin films were fatigue-free.[5] The crystallization temperature of BLT is lower than that of SBT. The BLT may become a promising candidate of storage materil in FeRAMs although its fundamental properties are not yet clear.

For the formation of ferroelectric thin films, only the chemical solution deposition (CSD) [6,7] was utilized at the beginning of production. The CSD is excellent in reproducibility and the controllability of film composition. However, the CSD is not suitable for high-density FeRAM because it is inferior in step coverage. Fujitsu has been using rf-magnetron sputtering for the deposition of PZT thin films in their mass-production process of FeRAMs. They improved the ferroelectric properties of PZT films by adjusting Pb content in the films exactly to Pb/(Zr+Ti)=1.12 $\pm$ 0.02.[8] The deposition rate of amorphous PZT films was, however, not so high. The deposition technique with higher deposition rate and higher step coverage is required for the FeRAM in next generation.

In this paper, the recent study on ferroelectric thin films and their applications, especially memory system in Japan, is reviewed. In addition, our recent activities in NAIST, liquid delivery metalorganic chemical vapor deposition (MOCVD) of PZT thin films and the analysis of trap levels in ferroelectric thin films using thermally stimulated current (TSC) method are briefly reported.

2. PRESENT AND FUTURE OF FeRAMs

Figure 1 shows an example of FeRAM application in Japan. This is a memory card used in early version of the amusement machine, SONY PlayStation2(R). It mainly consists of a EEPROM and an embedded IC with FeRAM fabricated by Fujitsu Limited. Table I shows the device features of the embedded FeRAM.[9] The capacitor structure is planar and memory size is 3 kbytes. Rohm corporation is manufacturing embedded FeRAMs for smart cards or tags. As mentioned above, FeRAMs have won small success. The market of FeRAMs is, however, still too small for its potential. Absence of an epochmaking application due to small capacity of current FeRAMs is one of the reasons for small market. In the future, increasing of capacity of FeRAMs will be strongly required.

Table II shows a road map of FeRAM technology

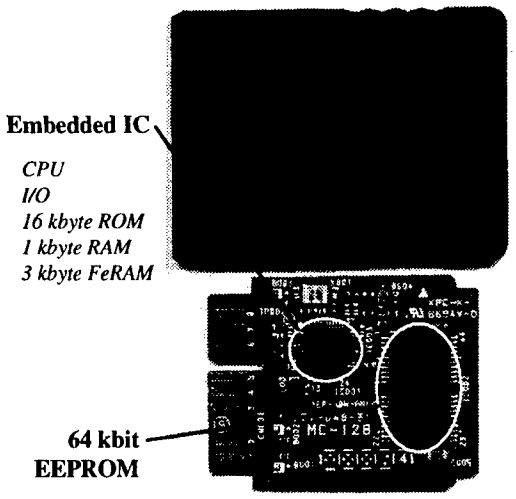

Fig.1 An example of FeRAM application, a memory card for SONY PlayStation2(R).

Table I Device features of the embedded FeRAMs.

Design rule	0.5 μm
Structure	Planar (Encapsulation)
Wiring	Triple Layer Metal (TiN, Al, Al)
Configuration	2T/2C and 1T/1C
Capacitor	Sputtered PZT
Size	1.6 x 1.9 μm^2
Top electrode	IrO_2
Bottom electrode	Pt/Ti
Cell size	27.3 μm^2 (2T/2C)
	12.5 μm^2 (1T/1C)
Operation voltage	3.3 V (Logic)
	5.0 V (FeRAM)
Retention	> 10 years @ 85°C
Fatigue	> 10^{10} cycles

forecasted by a Japanese assciation.[10] We can probably manufacture 64 Mb FeRAM by using the present technology. Actually, Fujitsu Limited has announced that they will start the mass-production of 512 kb FeRAM in the summer of 2001.[11] On the other hand, Toshiba corporation has announced that they use 8 Mb FeRAM with the chain structure[12] for celluar phones in collaboration with Infineon Technologies AG.[13] Furthermore, they have aimed to develop stand-alone 32 Mb FeRAMs by the beginning of 2003.[11] Such FeRAMs will be used in smart media instead of FLASH memories. They will make faster writing possible and certainly extend the FeRAM's market. However, there are some barriers to realize the FeRAMs with a capacity over 128 Mb as shown in Table II. I suppose that the ferroelectric society can mainly contribute to the development of deposition method and the improvement of reliability among them. We should develop the MOCVD technique for PZT thin films which make possible high-rate and uniform formation on large scale wafers. I am pessimistic for the discovery of new materials superior to PZT. It seems that the switching charge of 40 μC/cm^2 required at 2017 will be achived by using epitaxial or oriented PZT thin films. We should study the physics of PZT thin films in more detail to improve their reliability.

3. TREND OF THE STUDY ON FERROELECTRIC THIN FILMS IN JAPAN

Annual meetings of the Japan Society of Applied Physics are held twice a year, on autumn and spring. We have a session for ferroelectric thin films in the meetings. Recently, approximately 130 papers for ferroelectric thin films have been presented in each meeting. I have classified them by affiliation and topics as shown in Table III. Most of Hitachi's papers in the '01 spring meeting were not for FeRAMs while they presented eight papers. Eight papers presented by Toshiba in the spring meeting were for epitaxial $BaTiO_3$ films not PZT films. NEC, Mitsubishi and Rohm presented no paper in the '01 spring meeting. As we have seen, the number of papers for FeRAMs presented by major semiconductor manufactures obviously decreased. These facts clearly indicate that their interests have been shifted from the deposition and evaluation of ferroelectric thin films to circuit design or making products. Hitachi has drawn off from FeRAM business.

Kijima has reported new ferroelectric thin films based on BIT, SBT and PZT. He called them as K-I, K-II and K-III material, respectively. The features of them are summerized in Table IV. Unfortunately, the details are not yet open.

Many papers for the MOCVD of PZT and SBT thin films were presented. Some papers for the MOCVD of electrodes, Pt, Ir and Ru thin films, were also presented. They are for future high-density FeRAMs. Funakubo (Tokyo Inst. Tech.), Shimizu (Himeji Inst. Tech) and we are studying the MOCVD of ferroelectric thin films. Among them, only we are trying the deposition of the films on 6 inch wafers by liquid delivery MOCVD.

The study for MFIS or MFMIS is also active. Ishiwara (Tokyo Inst. Tech.) is putting his enegies

Table II Road map of FeRAM technology[10)]

Year of first product shipment	2000	2001	2002	2003	2004	2005	2008	2011	2014	2017
Technology node	180nm	130nm	130nm	130nm	100nm	100nm	70nm	50nm	35nm	25nm
1) Feature size (μm): F	0.6	0.5	0.35	0.25	0.18	0.18	0.13	0.1	0.07	0.05
2) FeRAM generation (bit) (Standard memory samples)	256 kb	1 Mb	4 Mb	16 Mb	64 Mb	128 Mb	256Mb	1 Gb	4 Gb	16 Gb
3) Access time (ns)	120	100	80	65	40	30	20	10	8	6
4) Cycle time (ns)	180	160	130	100	70	50	32	16	12	10
6) Cell area factor: a	81	60	40	24	16	10	10	8	8	8
7) Cell size (μm^2)	29.0	15.0	4.90	1.50	0.52	0.32	0.17	0.08	0.04	0.02
8) Total cell area (mm^2) for standard memory	7.60	15.73	20.55	25.17	34.79	43.49	45.37	85.90	168.36	343.60
10) Projected capacitor size (μm^2)	3.00	2.00	1.00	0.50	0.25	0.13	0.07	0.03	0.015	.0075
11) Capacitor area (μm^2)	3.00	2.00	1.00	0.50	0.25	0.13	0.088	0.069	0.055	0.044
12) Capacitor structure	planar	planar	stack	stack	stack	stack	3D	3D	3D	3D
12.5) Ferro. depo. method	sputter, CSD				sputter, CSD, MOCVD		MOCVD, new method			
13) 2T2C, 1T1C	2T2C	2T2C	2T2C	1T1C	1T1C	1T1C	1T1C	1T1C	1T1C	1T1C
14) Ferro. material	PZT, SBT					PZT, SBT	PZT, new materials			
18) Vdd: Voltage applied to ferro. capacitor (V)	5.0	3.0	3.0	2.5	1.8	1.5	1.2	1.0	0.7	0.7
19) Switching charge @Vdd ($\mu C/cm^2$)	20	20	20	20	20	30	40	40	40	40
19.5) Switching charge @Vdd (fC/cell)	600	400	200	100	50	39.0	35.4	27.8	22.0	17.5
21) Retention @85°C (Years)	10	10	10	10	10	10	10	10	10	10
22) Fatigue with assuring retention	10^{10}	10^{12}	10^{15}	10^{15}	10^{16}	10^{16}	10^{16}	10^{16}	10^{16}	10^{16}

An implementation method already exists.

An implementation method is only proposed.

An implementation method should be developed.

5), 9), 15), 16), 17), 17.5) deleted.

Table III The number of papers presented on the ferroelectric thin film session in the annual meetings of the Japan Society of Applied Physics.

(a) by affiliation	'00 Autumn	'01 Spring
Manufactures	(Total 41)	(Total 41)
Fujitsu	7	3
Hitachi	1	8
Matsushita	4	5
Mitsubishi	6	0
NEC	2	0
Sharp	1	1
Toshiba	7	8
Rohm	1	0
others	12	16
University	(Total 74)	(Total 78)
NAIST	6	4
Osaka Univ.	9	6
Tokyo Inst. Tech.	22	28
others	37	40
National Lab.	14	12
Grand total	129	131

(b) by topics	'00 Autumn	'01 Spring
MOCVD	(Total 20)	(Total 18)
PZT	6	9
SBT	3	4
BLT (BIT)	3	1
BST	7	3
Others	1	1
Deposition	(Total 55)	(Total 47)
PZT (PT, PZ)	16	14
SBT	13	4
BLT	3	2
YMO	5	2
BST (BT, ST)	10	5
Others	8	20
Electrode	(Total 13)	(Total 12)
Pt	3	3
Ir	4	1
Ru	3	5
SRO	2	0
others	1	3
MFIS, MFMIS	13	18
Evaluation	20	29
Circuits	8	7
Grand total	129	131

Table IV Features of novel ferroelectric materials proposed by Kijima.

Process	Sol-gel
Starting solution	Ferroelectrics + Dielectrics
Drying	150°C, 3 min
Calcination	400°C, 5 min
Repetition	1 ~ 8

Code name	Base	Sintering temperature	Minimum Film thickness
K-I	BIT	500°C	13 nm
K-II	SBT	550°C	25 nm
K-III	PZT	450°C	25 nm

on the develop of this type FeRAM. He has proposed a novel structure, 1T2C structure, in which retention property was improved by eliminating the depolarization field caused in a ferroelectric capacitor using two ferroelectric capacitors.[14] On the other hand, Matsushita has proposed another structure for MFMIS memory with longer retention time.[15] The ferroelectric capacitors are short-circuited by transistors during keeping data in that structure. It is very difficult to realize practical memories by using conventional MFIS or MFMIS structure due to leakage current.[16]

On the other hand, only the few studies have been made on the analysis of ferroelectric properties and their degradation. Many problems are still unsolved and new problems have come to light with the progress of the study. I suppose that we should turn our attention to them.

4. LIQUID DELIVERY MOCVD

A liquid delivery MOCVD method is a promising technique to form homogenous oxide thin films on large size wafers with high step coverage and high deposition rate. Some groups are trying to apply this technique to the formation of ferroelectric thin films for high density FeRAMs.[17,18] In this process, the selection of source materials is important for stable and high rate deposition. Usually, $Pb(DPM)_2$/THF, $Ti(O\mathit{i}Pr)_2(DPM)_2$/THF and $Zr(DPM)_4$/THF are used as source materials for the deposition of PZT thin films by liquid delivery MOCVD. However, the deposition rate of Zr component is limited by reaction and is low below the substrate temperature of 600°C when the $Zr(DPM)_4$/THF was used as a Zr source. Funakubo *et al.* have proposed that they use 1-Hexen-

3-ol as a catalystic additive to enhance the decomposition of $Zr(DPM)_4$. On the other hand, we have decided to use a novel Zr source, $Zr(DIBM)_4$/THF.[19] Figure 2 shows the deposition rates of $Zr(DPM)_4$ and $Zr(DIBM)_4$/THF. It is found that the deposition rate in case $Zr(DIBM)_4$/ THF was to be constant at 4.0 nm/min above 500°C because it was limited by the amount of supplying source.

Figure 3 shows a schematic diagram of the liquid delivery MOCVD system we used. Three kinds of liquid sources which amounts were controlled by liquid mass flow controllers were injected into the vaporizer. The liquid sources were mixed and converted into mist by an ultrasonic vibrator. The misted sources were then introduced into the chamber heated at 270°C and vaporized. The vapors were transported to the vertical cold-wall type reactor by N_2 carrier gas with a flow rate of 2 L/min. The pressures in the reactor and in the vaporizer were kept at 20 and 500 Torr, respectively, during deposition. We used a gas-

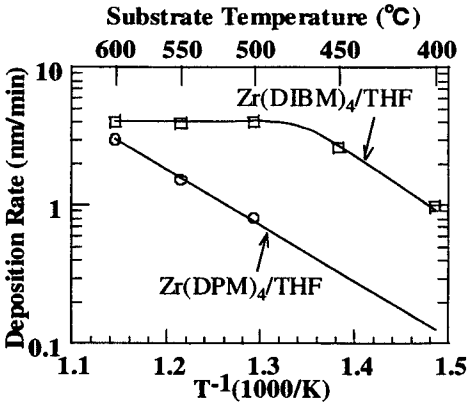

Fig.2 The substrate temperature dependence of the deposition rates of ZrO_2 thin films prepared from $Zr(DIBM)_4$/THF-O_2 and $Zr(DPM)_2$/THF-O_2 system.

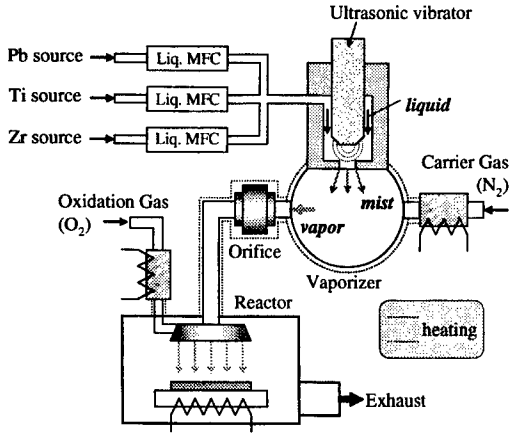

Fig.3 A schematic diagram of the liquid delivery MOCVD system.

ket with an orifice to make the difference in pressures between the reactor and the vaporizer. The selective vaporization of solvent THF in the vaporizer was successfully prevented by inserting the gasket. O_2 gas introduced into reactor with a flow rate of 1L/min was used as oxidation gas. Pt/SiO_2/Si wafers with a size of 3x3 cm^2 were used as substrates. Source materials and typical deposition conditions are summarized in Table V.

PZT thin films were deposited on Pt/SiO_2/Si substrates at the substrate temperature of 550°C. The flow rates of the Pb-, Zr- and Ti-sources were set to be 56, 50 and 51 μmol/min, respectively. The ratios Pb/(Zr+Ti) and Zr/(Zr+Ti) were estimated to be 1.05 and 0.35, respectively, by XRF analysis. The deposition rate was 12 nm/min. The deposited PZT films exhibited ferroelectric properties as shown in Fig.4. Remanent polarization and coercive field were estimated to be 35 μC/cm^2 and 90 kV/cm, respectively.

Table V Deposition conditions for PZT thin films.

Source materials		
Pb source :	$Pb(DPM)_2$/THF	(0.05 mol/L)
Ti source :	$Ti(OiPr)_2(DPM)_2$/THF	(0.1 mol/L)
Zr source :	$Zr(DIBM)_4$/THF*	(0.1 mol/L)
Carrier gas (N_2) flow rate		2 L/min
Oxidation gas (O_2) flow rate		1 L/min
Vaporizer temperature		270°C
Vaporizer pressure		500 Torr
Reactor pressure		20 Torr
Substrate temperature		550°C
Showerhead temperature		200°C
Pipe temperature		270°C
Substrate		(111)Pt/Si
Deposition time		40min

* DIBM: $C_9H_{15}O_2$ 2,6-Dimethyl 3,5-Heptanedione

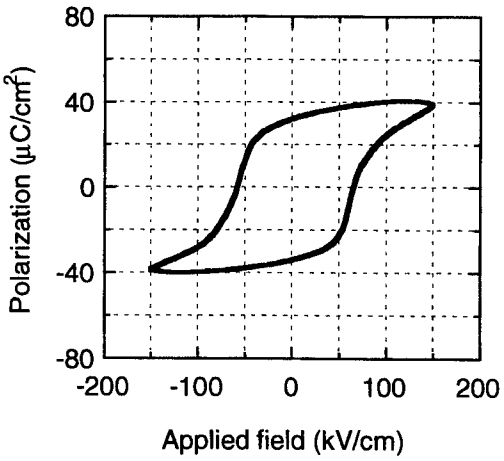

Fig.4 *D-E* hysteresis loop of the PZT(35/65) thin films fabricated by liquid delivery MOCVD at the substrate temperature 550°C.

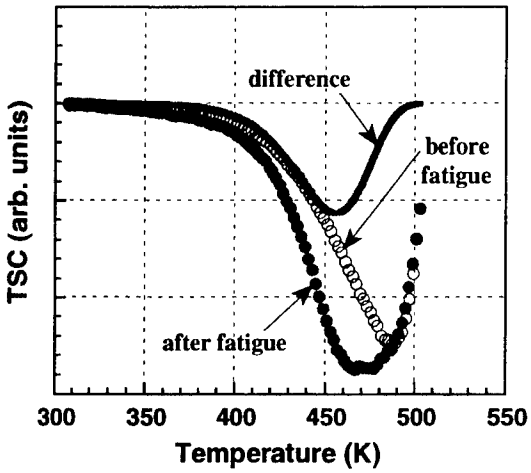

Fig.5 Thermally stimulated current (TSC) signals of PZT thin films before and after fatigue.

From these results, we have concluded that Zr $(DIBM)_4$/THF is a promising source material for the formation of PZT thin films by liquid delivery MOCVD.

5. TSC MEASUREMENT

TSC measurements were carried out for Pt/PZT/Pt capacitors in order to investigate the relationship between defects and polarization fatigue. Figure 5 shows TSC signals before and after fatigue. It is found that the peak around 450-460 K was generated by fatigue. This result suggests that defects in the film increased by fatigue. The activation energy of the defects was estimated to be 0.80 eV. The identification of the origin of the defects is in progress.

6. SUMMARY

Recent study on ferroelectric thin films and their application has been reported. FeRAMs with small density are practically used in embedded ICs. However, the market of FeRAMs is still small. Increasing the density, reducing the fabrication cost and improving the reliability are required to extend the market. Liquid delivery MOCVD is one of promising solutions for these requirements. We have succeeded in the formation of PZT thin films with high deposition rate, 12 nm/min, by using Zr$(DIBM)_4$/THF as a Zr precursor. Now, we are trying to improve the uniformity on 6 inch wafers. Furthermore, we are analyzing the defects and the origin of degradations of PZT thin films by TSC measurement. I belive that the FeRAMs have a bright future.

REFERENCES

1) S. S. Eaton, D. B. Butler, M. Parris, D. Wilson and H. McNeile, *ISSCC Digest of Technical Papers*, 130 (1988).
2) T. Nakamura, Y. Nakao, A. Kamisawa and H. Takasu, *Jpn. J. Appl. Phys.*, **33**, 5207 (1994).
3) C. A. Araujo, J. D. Cuchiaro, L. D. McMillan, M. C. Scott, and J. F. Scott, *Nature*, **374**, 627 (1995).
4) K. Uchiyama, K. Arita, Y. Shimada, S. Hayashi, E. Fujii, T. Otsui, N. Solayappan, V. Joshi and C. A. Araujo, Integrated Ferroelectrics, 30, 103 (2000).
5) B. H. Park, B. S. Kang, S. D. Bu, T. W. Noh, J. Lee and W. Jo, *Nature*, **401**, 682 (1999).
6) G. Yi, Z. Wu and M. Sayer, *J. Appl. Phys.*, **64**, 2717-2724 (1988).
7) T. Mihara, H. Watanabe, H. Yoshimori, C. A. Araujo, B. M. Melnick and L. D. McMillan, *Integrated Ferroelectrics*, **1**, 269 (1992).
8) T. Takai, T. Takamatsu, K. Matsuura, M. Shibata, S. Ozawa, H. Noshiro, Y. Horii, S. Mihara, M. Nakamura and T. Yamazaki, *Ext. Abst. 61th Autumn Meeting of Jpn. Soc. Appl. Phys.*, **No.2**, 427 (2000) [in Japanese].
9) A. Itoh, Y. Hikosaka, T. Saito, H. Naganuma, H. Miyazawa, Y. Ozaki, Y. Kato, S. Mihara, H. Iwamoto, S. Mochizuki, M. Nakamura and T. Yamazaki, *VLSI Tech. Digest Tech. Paper*, (2000).
10) The Electronics and Information Technology Industries Association, Report on Ferroelectric ME Applied technology, 116 (2001) [in Japanese].
11) THE NIKKAN KOGYO SHIMBUN, on May 10 (2001) [in Japanese].
12) D. Takashima *et al.*, *J. Solid State Circuits*, **33**, 787 (1998).
13) Toshiba Press Release, on Dec. 21 (2000) [in Japanese]
14) H. Ishiwara, *Integrated Ferroelectrics*, **34**, 11 (2001).
15) T. Otsuki *et al.*, *13th Inter. Symp. on Integrated Ferroelectrics (ISIF)*, Plenary talk on March 13, (2001).
16) M Okuyama, H. Sugiyama, T. Nakaiso and M. Noda, *Integrated Ferroelectrics*, **34**, 37 (2001).
17) S. Narayan, L. McMillan, C. A. Araujo, F. schienle, D. Burgess, J. Lindner, M. Schumacher, H. Jurgensen, K. Uchiyama and T. Otsuki, *12th Inter. Symp. on Integrated Ferroelectrics (ISIF)*, 64C on March 14, (2000).
18) B. K. Moon, K. Hironaka, C. Isobe and S. Hishikawa, *J. Appl. Phys.*, **89**, 6370 (2001).
19) M. Miyake, K. Lee, S. Okamura and T. Shiosaki, *Integrated Ferroelectrics*, to be published.

A Novel Fabrication Process of Ferroelectric Capacitors with the Self-align Patterning of Top Electrodes

Soichiro OKAMURA, Tomokazu KOBAYASHI, Kouzo SUZUKI
and Tadashi SHIOSAKI
Graduate School of Materials Science, Nara Institute of Science and Technology (*NAIST*)
8916-5 Takayama-cho, Ikoma, Nara 630-0101, Japan
Fax: +81-743-72-6069
e-mail: okamura@ms.aist-nara.ac.jp

We have fabricated ferroelectric $SrBi_2Ta_2O_9$ (SBT) capacitors by a novel patterning process based on chemical solution deposition and lift-off technique. Homogeneous precursor films (500nm) were first formed on substrates with bottom Pt electrodes and then an electron beam was irradiated on the films. Thickness of the irradiated area was reduced to be 30 % of the initial state at an electron dose of 4.0 mC/cm^2. Pt thin films (30 nm) were deposited on the precursor films by sputtering at low pressure, 0.12 Pa. Top Pt electrodes were patterned by developing the Pt films on unirradiated area with precursor films. Finally, Pt/precursor/Pt structures were heat treated at 800°C for 30 min for pyrolysis and crystallization. Final thickness of SBT layer was 100 nm. The SBT capacitors fabricated by this process exhibited excellent ferroelectric properties: a remanent polarization of 12.5 $\mu C/cm^2$ and a coercive field of 30 kV/cm.

1. INTRODUCTION

Micropatterning of ferroelectric materials is one of key technologies to realize high-density FeRAMs. In a conventional dry-etching process, the circumference of micropatterns receives some damage and does not work as ferroelectric capacitors.[1] Therefore, top electrodes are usually to be smaller than ferroelectric patterns not to use the circumference. It is also difficult to put a photo mask for top electrodes upon ferroelectric micropatterns accurately. Furthermore, ferroelectric capacitors have taper at their edges to prevent the redeposition of etched Pt or Ir atoms on side walls during the patterning of electrodes.[2,3] They are preventing to increase the density of FeRAMs. An improved micropatterning process for ferroelectric and metal electrode materials is required.

We had proposed a novel micropatterning process for composite oxides in 1992.[4] We called this process the eletron-beam-induced micropatterning process. In this process, precursor micropatterns are first formed by electron beam irradiation on precursor films and subsequent development. Then, they are crystallized into target materials by heat treatment. We had applied this process to the fabrication of ferroelectric capacitors.[5-9] Ferroelectric $Bi_4Ti_3O_{12}$ micropatterns with a linewidth of 300 nm were successfully fabricated by this process.[9] SBT and $Pb(Zr,Ti)O_3$ capacitors with good ferroelectric properties were also fabricated by this process. Alexe *et al.* reported that they fabricated 100 nm SBT micropatterns by the same process.[10,11]

In the electron-beam-induced micropatterning process, thickness of precursor films significantly decrease by electron beam irradiation. Recently, we have developed a novel fabrication process of ferroelectric capacitors with self-align patterning of top electrodes by utilizing this property. This paper describes the novel process and the properties of fabricated SBT capacitors.

2. EXPERIMENTAL

Figure 1 shows a flow diagram of the fabrication process of ferroelectric capacitors we proposed. In this process, homogeneous SBT precursor thin films with a thickness of 500 nm were first formed on Pt/SiO_2/Si substrates by spin-coating and then dried at 120°C for 10 min. Two kinds of 2-ethylhexanoate based mixed solutions were used as precursors. They contained Sr, Bi and Ta atoms at the molar ratios of 0.8:2.2:2.0 (Bi2.2 solution) and 0.8:2.1:2.0 (Bi2.1 solution), respectively. An electron beam with an accelerating voltage of 25 kV was irradiated on the pre-

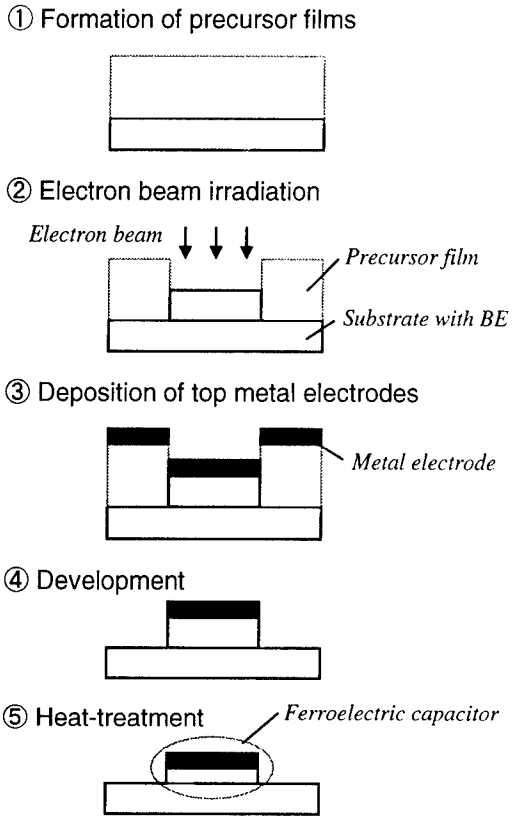

Fig.1 Fabrication process of ferroelecric capacitors with self-align patterning of top electrodes.

cursor films to form circular patterns with diameters of 100, 200 and 400 μm. Electron dose was adjusted to be 1 ~ 4 mC/cm^2. After the electron beam irradiation, Pt thin films with a thickness of 30 nm were deposited on the precursor films by rf-magnetron sputtering at 0.12 Pa. The development was carried out at room temperature in toluene with assistance of ultrasonic vibration. They were calcined at 400°C for 30 min to pyrolyze and vaporize organic components, and subsequently sintered at 800°C for 30 min to crystallize them into ferroelectric phase. The heating rate up to 400°C was set to be 2 ~ 10°C/min to prevent the damage on top electrodes due to the rapid vaporization of organic components. Figure 2 shows the heating sequence used in this study. Final thickness of SBT layer was 100 nm. Electrical properties of SBT capacitors with a diameter of 100 μm were evaluated by the ferroelectric thin film tester RT-6000 (Radiant Technologies Inc., USA).

3. RESULTS AND DISCUSSION

Figure 3 shows the aspect of the capacitors at the each point in the process. It is found that only the Pt

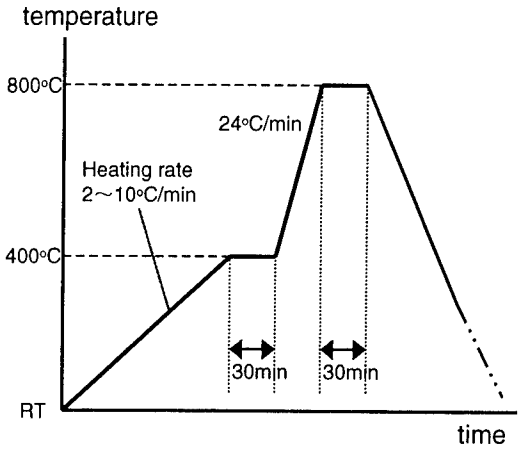

Fig.2 Sequence of heat treatment for Pt/SBT/Pt capacitors.

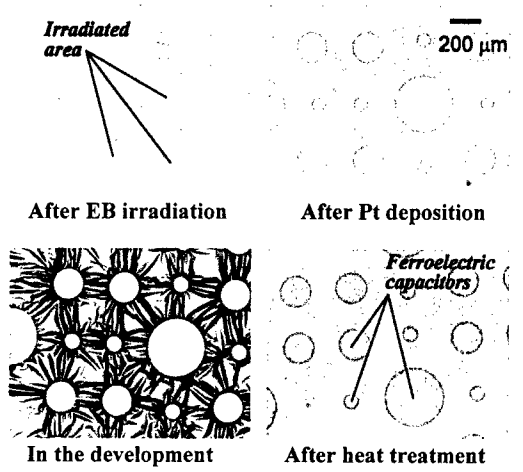

Fig.3 Aspect of the formatin process of ferroelectric capacitors.

films on unirradiated area were removed by development. Finally, circular top electrodes were successfully formed on ferroelectric patterns with self-alignment. No obvious damage on top electrodes was observed in these photographs.

Figure 4 shows the relationship between the heating rate up to 400°C and the ferroelectric properties of the SBT capacitors fabricated from the Bi2.2 solution. The electron dose was 1.5 mC/cm^2. The remanent polarization decreased with increasing heating rate. It seems that much vapor generated by heating with higher rate made worse the adhesion between the top electrodes and the SBT layer. From these results, the heating rate was fixed to 2°C/min to obtain better properties.

Figures 5(a) and 5(b) show the relationship between the electron dose and the *D-E* hysteresis loops of the SBT capacitors fabricated from the Bi2.2 and the

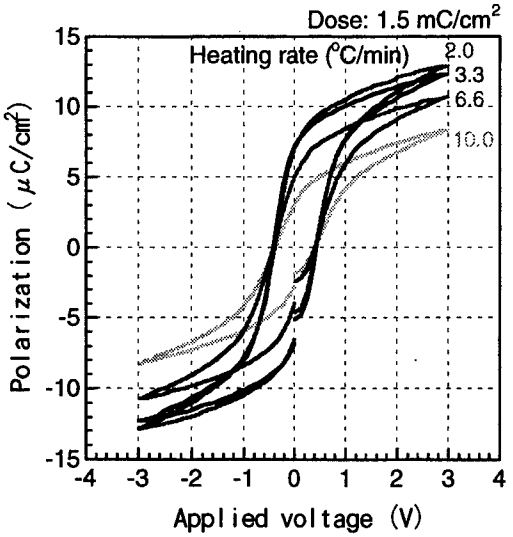

Fig.4 Relationship between the heating rate up to 400°C and the ferroelectric properties of SBT capacitors.

Bi2.1 solutions, respectively. Figure 6 shows the electron dose dependence of $2P_r$. The $2P_r$ in case of the Bi2.2 solution linearly increased with increasing electron dose and reached to approximately 18 μC/cm² at 4.0 mC/cm². It seems that the vaporization of appropriate amount of Bi atoms by electron beam irradiation caused such improvement in electrical properties.[12] On the other hand, in case of the Bi2.1 solution, the $2P_r$ also increased with increasing electron dose but almost saturated at 3.0 mC/cm² and reached to 25 μC/cm² at 4.0 mC/cm². That value was significantly larger than that in case of the Bi2.2 solution. In conventional CSD process, Sr:Bi:Ta=0.8:2.2.2:2.0 solutions were used as starting solutions to obtain largest remanent polarization.[13] Such solutions are in Bi-excess to compensate the evaporation of Bi atoms during heat treatment. However, the excess Bi atoms were not necessary in our process. It seems that the evaporation of Bi atoms was less than in the conventional process because top Pt electrodes were deposited before heat treatment and they played the role as a cap. This may be the reason why the Bi2.1 solution showed better properties than the Bi2.2 solution.

Figures 7(a) and 7(b) show the ferroelectric properties of the SBT capacitor fabricated from Bi2.1 solution with an electron dose of 4.0 mC/cm². It is found from Fig. 7(b) that the remanent polarization was almost saturated at the applied voltage of 1 V. The remanent polarization and the coercive field of the SBT capacitor were estimated to be 12.5 μC/cm² and 30 kV/cm, respectively. Figure 8 shows *I-V* characteristics of the capacitor. Leakage current density

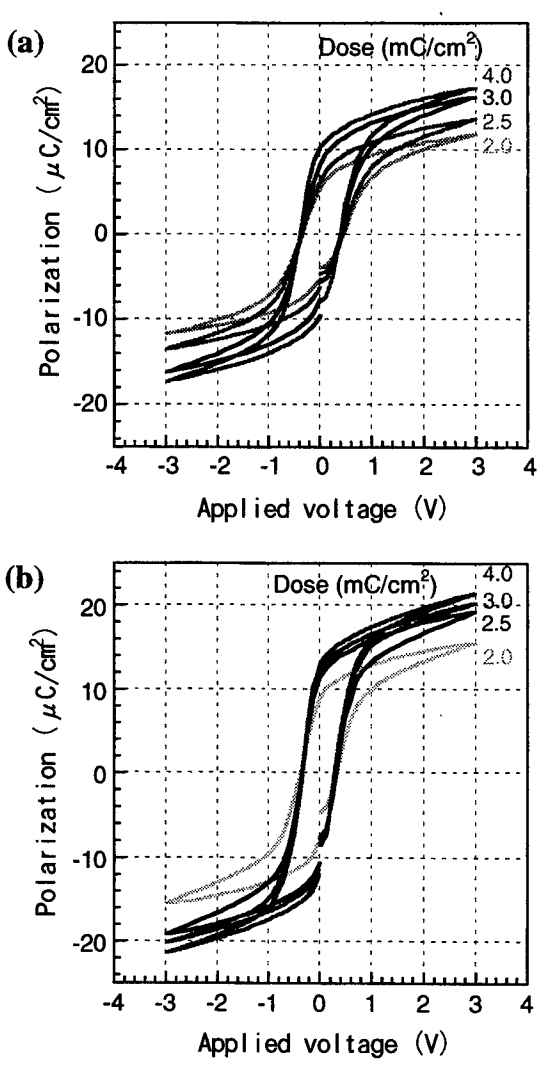

Fig.5 Relationship between the electron dose and the ferroelectric properties of SBT capacitors in cases of (a) the Bi2.2 solution and (b) the Bi2.1 solution.

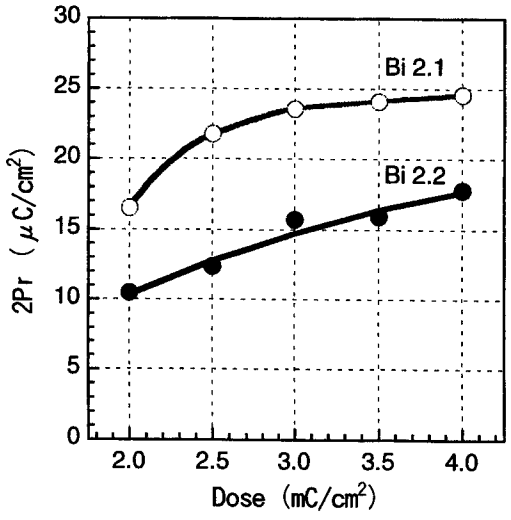

Fig.6 Electron dose dependence of switching charge $2P_r$ of SBT capacitors.

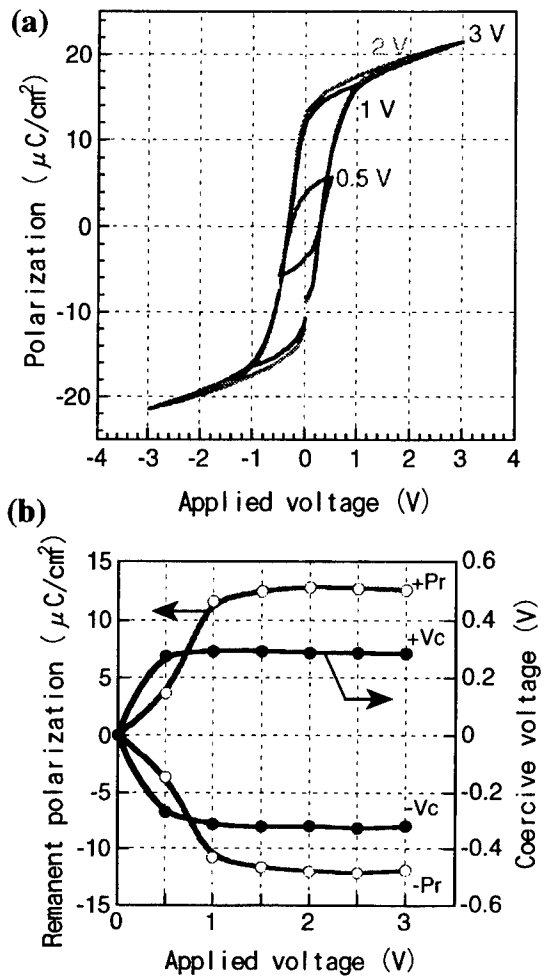

Fig.7 Ferroelectric properties of the SBT capacitors fabricated from the Bi2.1 solution. (a) *D-E* hysteresis loop and (b) the dependence of remanent polarization and coercive field on applied voltage.

was below 1.0×10^{-7} A/cm^2 at the applied voltage of 1 V. From these results, we have concluded that it is possible to fabricate ferroelectric capacitors with excellent properties by our novel patterning process with self-align patterning of top electrodes.

4. CONCLUSIONS

We have proposed a novel fabrication process of ferroelectric capacitors with self-align patterning of top electrodes. In this process, top metal electrodes were deposited on precursor films before heat treatment while they are deposited on crystallized ferroelectric thin films in conventional processes. The SBT capacitors fabricated from the Bi2.1 solution showed better properties than that from the Bi2.2 solution. Furthermore, the properties of the SBT capacitors were improved with increasing electron dose. The

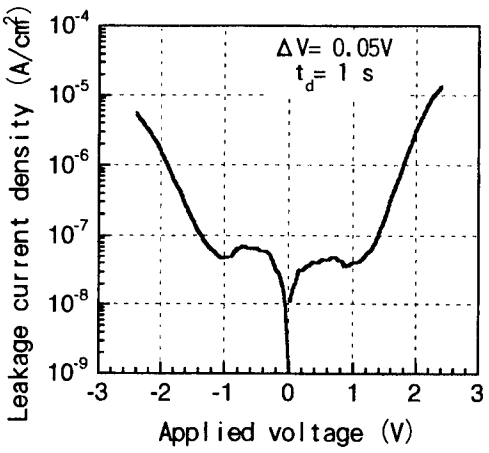

Fig.8 *I-V* characteristics of the SBT capacitors fabricated from the Bi2.1 solution with an electron dose of 4.0 mC/cm^2.

remanent polarization and the coercive field of the SBT capacitor fabricated from the Bi2.1 solution with an electron dose of 4 mC/cm^2 were estimated to be 12.5 μC/cm^2 and 30 kV/cm, respectively.

REFERENCES

1) W. Hartner, G. Schindler, V. Weinrich, M. Ahlstedt, H. Schroeder, R. Waser, C. Dehm and C. Mazure, *Integrated Ferroelectrics*, **27** 213 (1999).
2) K. Kim, *Integrated Ferroelectrics*, **25** 149 (1999).
3) Y. J. Song, H. H. Kim, S. Y. Lee, D. J. Jung, B. J. Koo, N. W. Chang, C. J. Kim and K. Kim, *Integrated Ferroelectrics*, **31** 351 (2000).
4) K. Mori and S. Okamura, *Jpn. J. Appl. Phys.*, **31** L1143 (1992).
5) A. Kakimi, S. Okamura, Y. Yagi, K. Mori and T. Tsukamoto, *Jpn. J. Appl. Phys.*, **33** 5301 (1994).
6) S. Okamura, A. Kakimi, Y. Yagi, K. Mori and T. Tsukamoto, *Proc. 9th IEEE Inter. Symp. Appl. Ferroelectrics*, **IEEE 94CH3416-5** 62 (1995).
7) S. Okamura, Y. Yagi, A. Kakimi, S. Ando, K. Mori and T. Tsukamoto, *Jpn. J. Appl. Phys.*, **35** 5224 (1996).
8) S. Okamura, Y. Yagi, S. Ando, T. Tsukamoto and K. Mori, *Jpn. J. Appl. Phys.*, **35** 6579 (1996).
9) S. Okamura, K. Mori, T. Tsukamoto and T. Shiosaki, *Integrated Ferroelectrics*, **18** 311 (1997).
10) M. Alexe, C. Harnagea, D. Hesse and U. Gosele, *Appl. Phys. Lett.*, **75** 1793 (1999).
11) M. Alexe, C. Harnagea, A. pignolet, D. Hesse and U. Gosele, *Piezoelectric Materials*, **76** 49 (2000).
12) S. Okamura, T. Kobayashi and T. Shiosaki, *Integrated Ferroelectrics*, to be published.
13) T. Atsuki, N. Soyama, T. Yonezawa and K. Ogi, *Jpn. J. Appl. Phys.*, **34** 5096 (1995).

Preparation and Properties of $SrBi_2Ta_2O_9$ Ferroelectric Thin Films Using Excimer UV Irradiation.

Takashi Hayashi and Daichi Togawa

Dept. of Materials Science, Shonan Institute of Technology.

1-1-25 Tsujido-Nishikaigan, Fujisawa, Kanagawa 251-8511, Japan.

PHONE : +81-466-30-0224, FAX : +81-466-30-0224

E-mail : hayashi@mate.shonan-it.ac.jp

Low-temperature chemical processing of $SrBi_2Ta_2O_9$ (SBT) thin films on Pt(200nm)/Ti(50nm)/SiO_2/Si substrates was investigated using excimer UV and seed layer. The excimer UV irradiation onto as-deposited SBT thin films at 200-300℃ in O_2 atmosphere and the use of Sr-Ta-O seed layer were very effective to lower the crystallization temperature for SBT thin films to 500℃. The 600℃-annealed SBT thin films of approximately 200nm thickness with the seed layer exhibited a Pr of 2.3 μ C/cm^2 and a Ec of 43kV/cm.

1. INTRODUCTION

$SrBi_2Ta_2O_9$ (SBT) has been intensively investigated as a promising ferroelectric material for nonvolatile random access memory because of its fatigue-free property and low voltage operation. However, the high temperature annealing process such as 700-800 ℃ is not suitable for high-density memory devices, bacause the silcon semiconductor is often seriously damaged during the annealing process. Recently, in order to lower the processing temperature, new process for the film preparation using an excimer laser or Hg UV lamp accompanying a photolysis reaction of organic species and crystallization has been actively investigated [1-2]. In this work, we investigated the low temperature processing of SBT thin films using an excimer UV irradiation and Sr-Ta-O seed layers, and their ferroelectric properties.

2. EXPERIMENTAL PROCEDURES

Strontium di-n-butoxide and bismuth tri-n-butoxide were refluxed in 2-methoxyethanol at 130℃ for 1h, and then the solution was added to tantalum ethoxide, and finally refluxed at 130 ℃ for 2h. The composition of SBT thin films was $Sr_{0.7}Bi_{2.2}Ta_2O_9$.

SBT thin films were prepared on Pt(200nm)/Ti(50nm)/SiO_2/Si substrates by a spin-coating technique from alkoxide precursor solutions of SBT. As-deposited thin films were irradiated using Xe excimer UV lamp (172nm) at various temperatures of 100-300 ℃ for 5-30min in O_2 atmophere. The excimer UV-processed films were annealed at 400-750℃ for 30min in an O_2 atmosphere by RTA. On the preparation of some of SBT thin films, strontium tantalum oxide ($SrTa_2O_6$: ST) layer was used as a seed. ST seed layer was spin-coated from 1wt% alkoxide precursor solution of ST onto the substrate and annealed at 500-600℃ for 5min by RTA. A typical film thickness of SBT layer and ST seed layer was approximately 200nm and 5nm, respectively.

The crystallinity and crystalline phase of SBT thin films were examined by X-ray diffraction (XRD) measurements. The chemical species in the excimer UV-processed thin films were analyzed by fourier transform infrared spectrometer (FT-IR). The surface morphology of thin films was observed using an atomic force microscope (AFM) and field-emission scanning

electron microscope (FE-SEM). P-E hysteresis loops were observed using RT-66A (RADIANT TECHNOLOGIES, Inc.) at 1kHz. The applied voltage was 5V.

3. RESULTS AND DISCUSSION

3.1 FT-IR spectra of excimer UV-irradiated SBT thin films

Figure 1 shows the FT-IR spectra of as-deposited SBT thin films irradiated with excimer UV lamp at 100-300℃ for 30min in O_2 atmosphere. The peak due to the C-H group of residual organic species disappeared at the excimer irradiation temperatures of 200 ℃ or above.

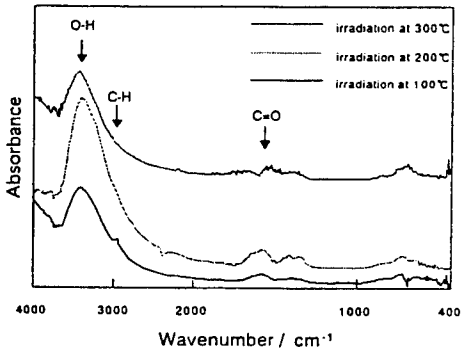

Fig.1 FT-IR spectra of as-deposited SBT thin films irradiated with excimer UV lamp at various temperatures for 30min in O_2 atmospheres.

3.2 Crystallization of SBT thin films

Figure 2 shows XRD patterns of SBT thin films irradiated by excimer UV at 200 and 300 ℃ for 30min, followed by RTA process at 400, 500 and 550 ℃ for 30min. Without excimer UV-irradiation, a higher annealing temperature of 700 ℃ was required in order to prepare SBT thin films with a high crystallinity, as shown Fig.2(a). The excimer UV-irradiation in O_2 atmosphere was effective to lower the crystallization temperature of SBT from the gel films. The irradiation in O_2 atmosphere was considered to promote the decomposition of residual organic species with the formation of O_3 as well as photolysis reaction. The SBT films excimer UV-irradiated at 300℃ crystallized at 500℃. The SBT thin films crystallized at 550 ℃ exhibited a high crystallinity and random orientation with a high (115) diffraction intensity as well as weak (008) diffraction peak, as shown in Fig.2(b).

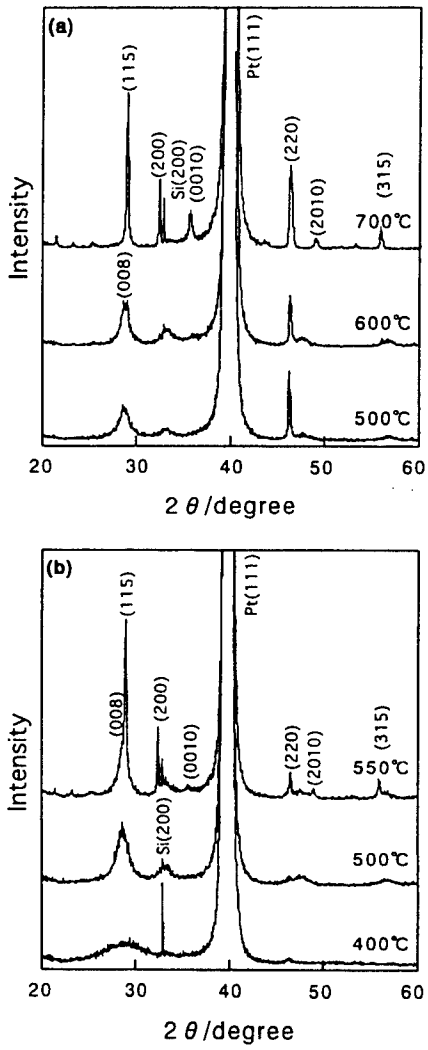

Fig.2 XRD patterns of SBT thin films using excimer UV irradiation : (a) unirradiation (b) irradiation at 300℃ in O_2 atmosphere.

3.3 Effect of strontium tantalum oxide seed layer on the crystallization of SBT

The effect of strontium tantalum oxide (ST) seed layers on the crystallization of SBT from alkoxide precursor solution was investigated to lower the processing temperature for SBT thin films. The thin film which has a similar composition with $SrTa_2O_7^{2-}$ perovskite-like layers in SBT structure was selected for a seeding layer.

Figure 3 showed XRD patterns of SBT thin films with ST seed layer prepared by excimer UV process at 300 ℃ and subsequent RTA process at various temperatures. The insertion of ST seed layer between SBT layer and the substrate decreased the crystallization temperature to 500℃, resulting in the formation of single phase SBT thin films exhibiting a random orientation with a relatively high (115) diffraction intensity. It was noted that the utilization of excimer UV lamp and seed layer for SBT film preparation was very effective to lower the crystallization temperature.

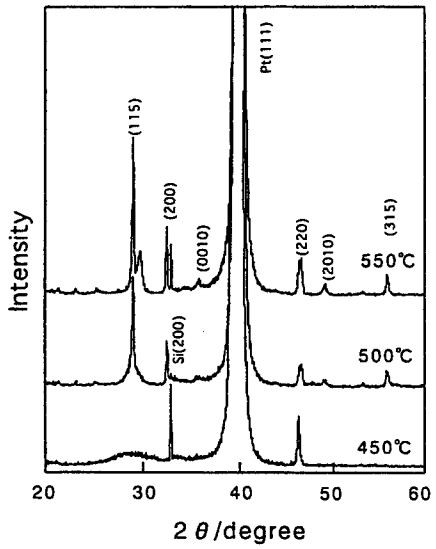

Fig.3 XRD patterns of SBT thin films prepared by excimer UV process with ST seed layer.

3.4 Surface morphology of SBT thin films

Figure 4 shows FE-SEM micrographs of the SBT films prepared with excimer UV irradiation and ST seed layer insertion. SBT thin films prepared at 700℃ by RTA without excimer UV irradiation exhibited a relatively smooth grain structure with small rod-like grains of 200-300nm, while those prepared at 550℃ with excimer UV irradiation at 300 ℃ showed somewhat porous microstructure with larger plate-like grains of 400-500nm. The excimer UV irradiation onto as-deposited SBT films promoted the grain growth of SBT during annealing. In addition, 550℃ -annealed SBT thin films with ST seed layer exhibited a homogeneous microstructure consisting of very fine grains with approximately 50nm in size, which grew to a larger grains of 200-300nm by annealing at 700℃.

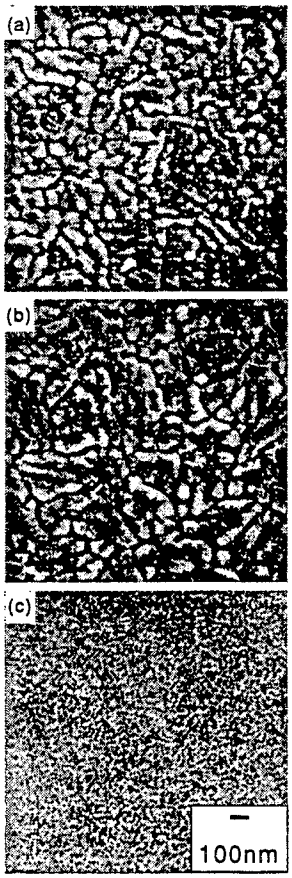

Fig.4 FE-SEM micrographs of the SBT films prepared with excimer UV irradiation and ST seed layer : (a) 700℃ by RTA without excimer UV irradiation, (b) 550℃ with excimer UV irradiation at 300℃, (c) 550℃ with excimer UV irradiation and ST seed layer.

Figure 6 shows AFM images of the surface of 550℃ -annealed SBT thin films using excimer UV irradiation without and with a ST seed layer. SBT thin films with the seed layer showed a smooth surface microstructure, compared to those without the seed layer.

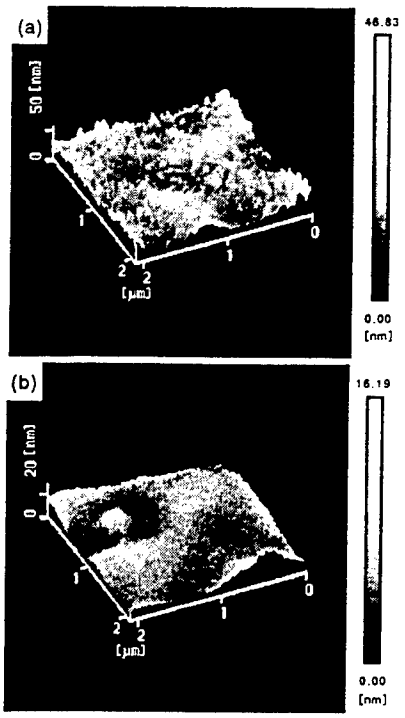

Fig.5 AFM images of the surface of 550℃ -annealed SBT thin films using excimer UV irradiation : (a) without ST seed layer, (b) with ST seed layer.

3.5 Ferroelectric properties of SBT thin films

Figure 6 shows P-E hysteresis loops of SBT thin films prepared at 600-700℃ by RTA using excimer UV irradiation at 300℃ and the seed layer. SBT thin films prepared at 750℃ for 30min without excimer UV irradiation showed a remanent polarization, Pr, of 1.3 μ C/cm^2 and a coecive electric field, Ec, of 120kV/cm. On the other hand, SBT thin films prepared at 600℃ using excimer UV irradiation and the seed layer showed a Pr of 2.3 μ C/cm^2 and a Ec of 43kV/cm.

4.CONCLUSIONS

SBT thin films were prepared by sol-gel method using excimer UV irradiation and Sr-Ta-O seed layer, and their microstructure, crystal phase and ferroelectric property were investigated. The excimer UV irradiation onto as deposited films at 200-300 ℃ in O_2 atmosphere was very effective to remove the residual organic groups in the gel films and to lower the crystallization temperature of SBT upto 550℃ . The use of the seed layer further decreased the crystallization temperature to 500 ℃. The 600℃-annealed SBT thin films using excimer UV irradiation and the seed layer showed a Pr of 2.3 μ C/cm^2 and a Ec of 43kV/cm.

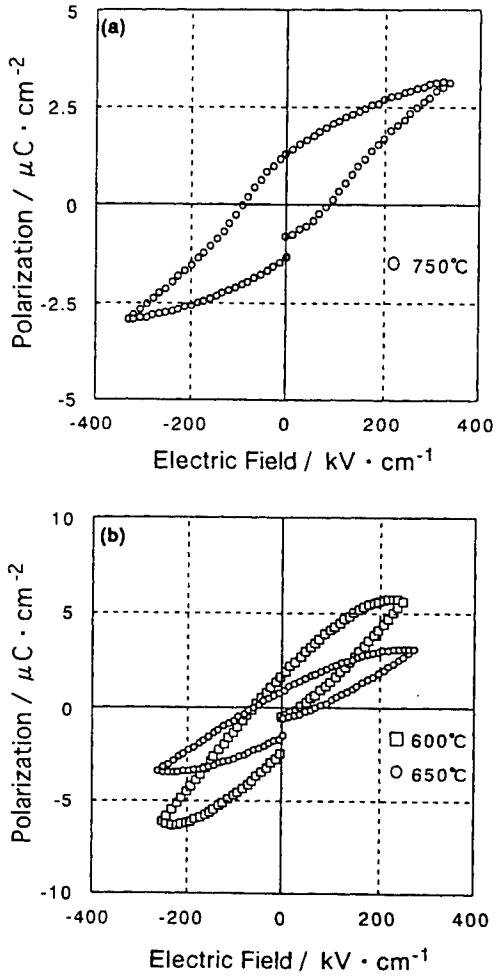

Fig.6 P-E hysteresis loops of SBT thin films prepared by RTA using excimer UV irradiation at 300℃ and the seed layer : (a) unirradiation, (b) irradiation at 300℃ with ST seed layer.

REFERENCES

1) K.Nishizawa, T.Miki, K.Suzuki and K.Kato : Abstracts of The 1st Asian Meeting on Electroceramic and The 20th Electronics Division Meeting.(2000) 48.

2) T.Tsuchiya, A.Watanabe, Y.Imai, H.Niino, I.Yamaguchi, T.Manabe, T.Kumagai and S.Mizuta : Jpn.J.Appl.Phys.**39**(2000) L866-868.

Chemical Processing and Ferroelectric Properties of $MBi_4Ti_4O_{15}$ (M:Alkaline Earth Metals) Thin Films

Kazumi Kato[1,2], Kazuyuki Suzuki[1], Kaori Nishizawa[1], Takeshi Miki[1]

[1]National Institute of Advanced Industrial Science and Technology, 1 Hirate-cho, Kita-ku, Nagoya 462-8510, Japan, FAX: 81-52-916-6992, Email: kzm.kato@aist.go.jp

[2]Frontier Collaborative Research Center, Tokyo Institute of Technology, 4259 Nagatsuda-cho, Midori-ku, Yokohama 226-8503, Japan

INTRODUCTION

The Aurivillius family, $(Bi_2O_2)^{2+}(A_{n-1}B_nO_{3n+1})^{2-}$, in which A represents mono-, di-, tri-valent ions or a mixture thereof, and B represents tetra-, penta- or hexa-valent ions, has been paid attention to because of its unique crystal structure and the resultant anisotropic electrical properties. The compounds such as $PbBi_4Ti_4O_{15}$, $BaBi_4Ti_4O_{15}$ and $SrBi_4Ti_4O_{15}$ (SBTi144), which have the n value of 4, had been studied for their anisotropic ferroelectricity [1-5]. Recently, it was reported that highly-textured $CaBi_4Ti_4O_{15}$ (CBTi144) ceramics had enhanced piezoelectric properties [6-8]. The thin films of these compounds have been synthesized via the chemical solution deposition (CSD) techniques, such as the sol-gel and metal-organic decomposition method, and characterized for application to integrated systems such as ferroelectric random access memories because of their high resistance to fatigue [4, 5, 9, 10 ,11]. Additionally, applications to the piezoelectric filters, resonators, and micro-electromechanical-systems (MEMS) would be expected especially for CBTi144 thin films. In spite of a great potentiality that the properties of the thin films are controllable by adjusting A site cations in the perovskite layer, there has been no report on the details so far.

The ferroelectric thin film processing, especially for integration on silicon semiconductor, should be conducted at low temperatures and be lined with the complementary-metal-oxide-semiconductor (CMOS) processing in order to prevent interface reactions which are often severe at high temperatures. A critical temperature for the integration of ferroelectric thin films on CMOS is considered as 650°C, because some materials used for a stack structure are refractory to the temperature. In this paper, the crystallinity, surface morphology, microstructure and ferroelectric properties of 650°C-annealed CBTi144 and SBTi144 thin films on Pt-passivated Si are comparatively investigated. Additionally, the effect of A site cations in the perovskite layer on the properties is discussed.

EXPERIMENTAL PROCEDURE

Calcium metal was dissolved in ethanol (C_2H_5OH) by reaction at 78°C. In a separated portion, bismuthtriethoxide ($Bi(OC_2H_5)_3$) and titaniumtetraisopropoxide ($Ti(Oi\text{-}C_3H_7)_4$) in the molar ratio of 1:1 were dissolved together in methoxyethanol ($CH_3OC_2H_4OH$) at 124°C. The two solutions were mixed and then heated at 78°C for 2 h. Next, deionized water, diluted in $CH_3OC_2H_4OH$ was added to the mixture solution in the molar ratio of 1:30 (H_2O:alkoxy group). The solution was stirred at room temperature for 1 h after hydrolysis. The concentration of the hydrolyzed alkoxide solution was 0.02 M. The volume ratio of C_2H_5OH to

$CH_3OC_2H_4OH$ was 1:4.5. The atomic ratio of calcium, bismuth and titanium was stoichiometric 1:4:4. For preparation of SBTi144 precursor solution, Sr metal was dissolved in methoxyethanol by reaction at 124°C. The following procedure was similar to the preparation of the CBTi144 precursor solution as mentioned above. The atomic ratio of strontium, bismuth, and titanium was stoichiometric 1:4:4.

Platinum - passivated silicon ($Pt(111)/TiO_x/SiO_2/Si(100)$) were used as substrates. CBTi144 and SBTi144 thin films were deposited on the substrates by spin coating the hydrolyzed alkoxide solutions. Each layer was deposited at 2 steps of 1000 rpm for 3 s and 3000 rpm for 30 s. As-deposited thin films were dried at 150°C, calcined at 350°C for 10 min in air, and then heated by rapid thermal annealing in an oxygen flow. The ramp rate was 100°C/s and the heating period at 650°C was 10 min. Film thickness was increased to about 200 nm by repeating the spin coating and rapid thermal annealing.

The crystal phase and crystallinity of the thin films were identified using X-ray diffraction (XRD) measurements using Cu Kα radiation. The acceleration voltage and current were 40 kV and 40 mA, respectively. Microstructure and surface morphology of the thin films were observed using a transmission electron microscopy (TEM) and an atomic force microscopy (AFM). Film thickness was determined by an ellipsometer. Prior to electrical measurements, circular Pt electrodes of 500 μm diameter were deposited by r. f. sputtering, which was followed by annealing at the same temperatures as crystallization for 10 min in oxygen flow. Dielectric and ferroelectric properties were measured using a multi frequency LCR meter (HP 4275A) and a Radiant Technologies RT6000S instrument at room temperature, respectively.

RESULTS AND DISCUSSION

XRD analysis indicated that both CBTi144 and SBTi144 thin films initiated the crystallization below 550°C. The 550°C- and 600°C-anealed CBTi144 thin films contained pyrochlore phase. The 650°C- or higher temperature-annealed CBTi144 thin film was a single phase of perovskite. In contrast, the SBTi144 thin films seems to crystallize to perovskite phase at relatively low temperatures. The crystallinity improved with annealing temperature. The diffraction profiles of the SBTi144 thin films annealed at temperatures higher than 650°C were similar to those of the CBTi144 thin films. The different crystallization behavior at lower temperature range may be related to the mobility of cations in the non-crystalline and amorphous alkoxy-derived thin films.

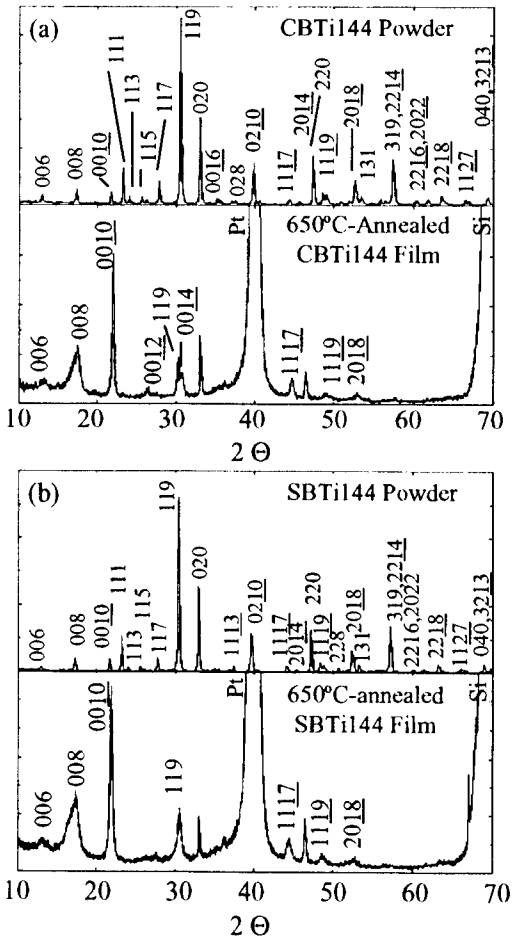

Fig. 1 XRD patterns of powders and 650°C-annealed thin films of (a) CBTi144 [9] and (b) SBTi144 .

Figures 1 (a) and 1 (b) show XRD patterns of powders and 650°C-annealed thin films of CBTi144 and SBTi144, respectively. The patterns of CBTi144 and SBTi144 powders were very similar. Compared with each powders, both thin films were found to show random orientation although (00*l*) diffraction lines had relatively high intensitites. The (0012) and (0014) diffraction lines were distinct with respect to CBTi144 thin films.

Figure 2 shows AFM images of 650°C-annealed CBTi144 and SBTi144 thin films. The uniform and isotropic grains with a diameter of about 220 nm were observed with respect to the 650°C-annealed CBTi144 thin films. Compared to the CBTi144 thin films, the grains were smaller and the uniformity was lower with respect to the SBTi144 thin films. The 650°C-annealed SBTi144 thin films consited of smaller grains with a diameter of about 140 nm, some of which were agglomerated to make colonies.

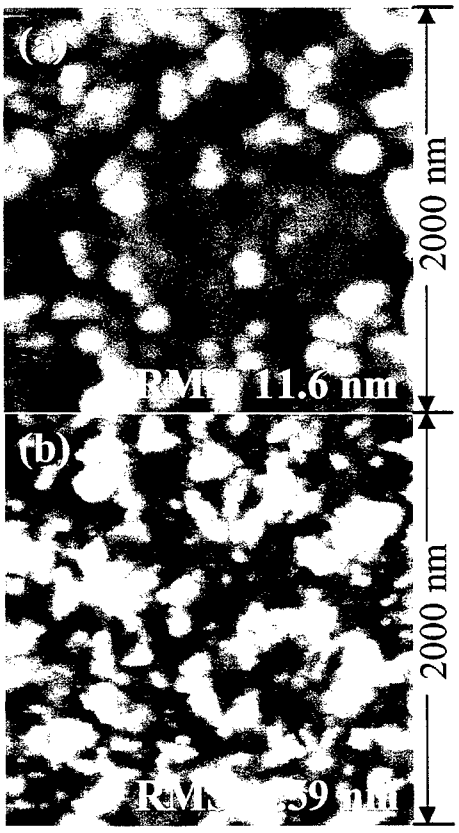

Fig. 2 AFM images of 650°C-annealed (a) CBTi144 and (b) SBTi144 thin films.

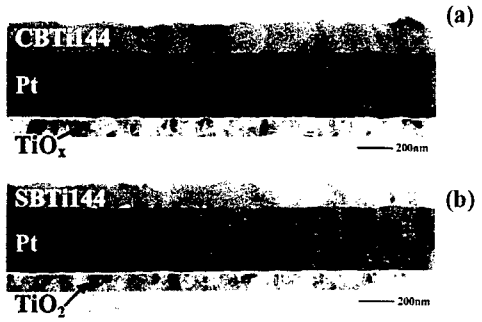

Fig. 3 TEM cross-section photographs of 650°C-annealed (a) CBTi144 [10] and (b) SBTi144 thin films.

Figure 3 shows TEM cross-section photographs of 650°C-annealed CBTi144 and SBTi144 thin films. It was confirmed that the both thin films had columnar structures and no interface layer was between the thin films and Pt layer. The grains were closely packed in the CBTi144 thin film and comparatively, there were small pores in the interface region of the SBTi144 thin films.

The dielectric constant (ε) and loss factor (tanδ) of both thin films were almost constant in the frequency range of 10 kHz to 1 MHz. The ε and tanδ of the 650°C-annealed CBTi144 and SBTi144 thin films were 300 and 0.03, 330 and 0.04, respectively, at 100 kHz. Figure 4 shows P-E hysteresis loops of the 650°C-annealed CBTi144 and SBTi144 thin films. The remanent polarization (Pr) and coercive electric field (Ec) of the 650°C-annealed CBTi144 and SBTi144 thin films were 6.0 $\mu C/cm^2$ and 79 kV/cm, 2.9 $\mu C/cm^2$ and 55 kV/cm, respectively, at 9 V. The P-E hysteresis properties of the 650°C-annealed SBTi144 thin films were inferior to those of the 650°C-annealed CBTi144 thin films. The smaller Pr must be caused by both effects of larger Sr ion size in the A site and smaller grain size with respect to the SBTi144 thin films. Figure 5 shows fatigue behaviors of the 650°C-annealed CBTi144 and SBTi144 thin films. The voltage and width of applied bipolar pulse was 5 V and 1 μs, respectively. The polarization of the 650°C-annealed CBTi144 thin film did not change after 10^{11}

switching cycles, however, the polarization began to decrease gradually after 7.2 x 10^7 switching with respect to SBTi144 thin films.

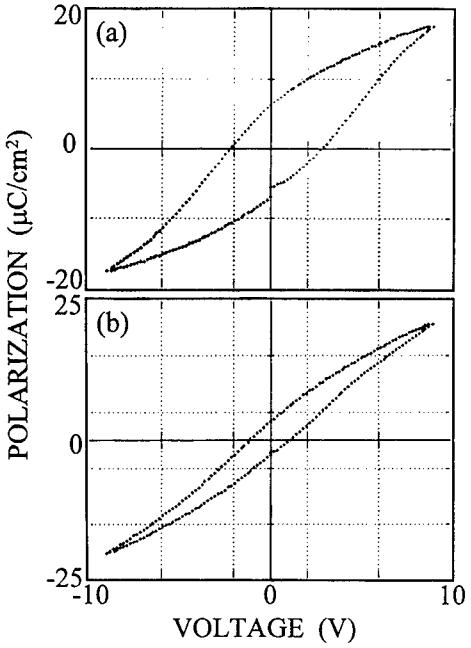

Fig. 4 P-V hysteresis loops of 650°C-annealed (a) CBTi144 and (b) SBTi144 thin films on Pt-passivated Si [11].

CONCLUSION

CBTi144 and SBTi144 thin films were prepared on Pt-passivated silicon substrate by using complex metal alkoxide solutions. The CBTi144 thin films crystallized to a single phase of perovskite at 650°C via a mixture of perovskite and pyrochlore phases. The CBTi144 thin films consisted of uniform and isotropic grains and had a closely-packed columnar structure. In contrast, the SBTi144 thin films crystallized to perovskite phase at relatively lower temperature and consisted of smaller and non-uniform grains. The ε and tanδ of the 650°C-annealed CBTi144 and SBTi144 thin films were 300 and 0.03, 330 and 0.04, respectively, at 100 kHz. The Pr and Ec were 6.0 μC/cm^2 and 79 kV/cm, 2.9 μC/cm^2 and 55 kV/cm, respectively, at 9 V. The dielectric and ferroelectric properties depended on both of the cation size in the A site and the microstructure.

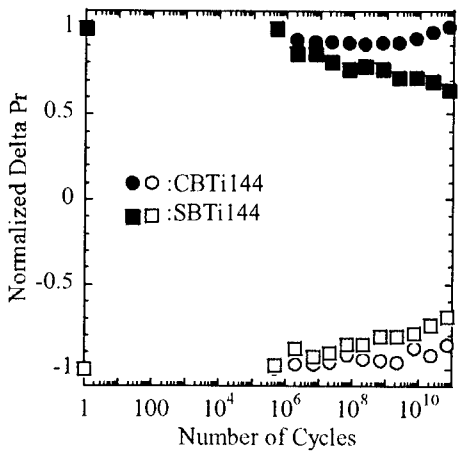

Fig. 5 Fatigue behaviors of 650°C-annealed CBTi144 and SBTi144 thin films.

ACKNOWLEDGMENT

The authors acknowledge the financial support by the Industrial Science and Technology Frontier (ISTF) Program promoted by AIST, METI, Japan.

REFERENCES

[1] S. Kim, M. Miyayama and H. Yanagida: *J. Ceram. Soc. Jpn.*, 102, 722 (1994).
[2] S. Kim, M. Miyayama and H. Yanagida: *J. Ceram. Soc. Jpn.*, 103, 315 (1995).
[3] I. Yi and M. Miyayama: *Trans. Mater. Res. Soc. Jpn.*, 20, 660 (1996).
[4] Y. Park, M. Miyayama and T. Kudo: *J. Ceram. Soc. Jpn.*, 107, 413 (1999).
[5] H. Watanabe, T. Mihara, H. Yoshimori and A-Paz de Araujo: *Jpn. J. Appl. Phys.*, 34, 5240 (1995).
[6] T. Takeuchi, T. Tani and Y. Saito: *Jpn. J. Appl. Phys.*, 38, 5553 (1999).
[7] T. Takeuchi, T. Tani and Y. Saito: *Jpn. J. Appl. Phys.*, 39, 5577 (2000).
[8] H. Yan, C. Li, J. Zhou, W. Zhu, L. He and Y. Song: *Jpn. J. Appl. Phys.*, 39, 6339 (2000).
[9] K. Kato, K. Suzuki, K. Nishizawa and T. Miki: *Appl. Phys. Lett.*, 78, 1119 (2001).
[10] K. Kato, K. Suzuki, K. Nishizawa and T. Miki: submitted to *Integr. Ferroelectr.*
[11] K. Kato, K. Suzuki, K. Nishizawa and T. Miki: submitted to *Jpn. J. Appl. Phys.*

Integration and Characterization of Sub-micron MFIS FETs Transistor with $Pt/Pb_5Ge_3O_{11}$/High-k/Si Structure

Fengyan Zhang, Sheng Teng Hsu
Sharp Laboratories of America, Inc.
5700 NW Pacific Rim Blvd
Camas, Washington, USA
Tel: •1 360 834 8654 Fax: • 1 360 834 8689 Email: Fzhang@sharplabs.com

The Metal-Ferroelectric-Insulator-Silicon (MFIS) FETs NMOS and PMOS using $Pt/Pb_5Ge_3O_{11}$/high-k/Si structure have been successfully fabricated. The PGO thin film was deposited by spin on method. Different high-k substrates were studied. It is shown that single phase PGO with strong c-axis orientation and low leakage current can be obtained on ZrO_2, HfO_2, Zr-Al-O and Hf-Al-O substrates. Pt was used as top electrode and the gate stack was dry etched using chlorine chemistry. Using CMOS compatible process, the integration of MFIS FETs is simple and reliable. V_G -I_D and V_D -I_D were characterized on 0.6x10 μm (l x w) devices with HfO_2 as the gate dielectric. The memory window obtained is about 1V with 150nm PGO and 11nm HfO_2.

INTRODUCTION

Ferroelectric Memory FETs have the potential for high speed, high density and low programming voltage nonvolatile memory device applications. One promising structure is the MFIS FETs structure that has been extensively studied using different ferroelectric materials such as $SrBi_2Ta_2O_9$ (SBT) and $Bi_{4-x}La_xTi_3O_{12}$ (BLT) with different dielectric buffer layers. The high deposition and annealing conditions required for both SBT and BLT have limited their compatibility with conventional CMOS processes. The thermal cycles will easily cause diffusion between the ferroelectric and dielectric buffer layers and degrade the device functionality.

$Pb_5Ge_3O_{11}$ (PGO) is a promising ferroelectric material for MFIS FETs device because it has moderate polarization ($2Pr=4\text{-}8\mu C/cm^2$) and relatively low dielectric constant (ε=50-100). Its spontaneous polarization exists only along one axis (c-axis). The deposition and annealing temperatures for PGO thin film are around 500-600°C.

EXPERIMENT

Pure c-axis PGO film with smooth surface, low leakage current and very well saturated hysteresis loop has been obtained on Ir substrate with a spin-on method using lead acetate trihydrate and germanium isopropoxide in di (ethylene glycol) ethyl ether solution [1]. The 2Pr is about 4~8 $\mu C/cm^2$ and the dielectric constant is about 50~100 for 100-120 nm thick PGO thin film. Since the MFIS single transistor structure requires the PGO thin film to be deposited on gate dielectric layers, crystallization of PGO on different insulating layers also has to be studied. In this study, high-k insulating layers, such as ZrO_2, HfO_2, ZrAlO and HfAlO were selected as the gate dielectric layers. It is reported that these high-k insulating layers deposited on Si substrate have low leakage current and good interface properties. They are alternative gate dielectric materials for high-density CMOS devices[2]. In our experiment, these high-k thin films were deposited by reactive DC sputtering in oxygen and argon ambient with the flow ratio of Ar/O_2=5/2. The base pressure is about $5x10^{-7}$ torr and the deposition pressure is about 7 mtorr. The power on a 4" diameter metal (Zr, Hf, etc) target is 300W. After deposition, these films were annealed in oxygen ambient at 500°C for 1min. Then the PGO thin films were deposited on these high-k layers by spin on method. The deposition and annealing conditions are similar to that of PGO thin films deposited on Ir substrate [2]. The Pt top electrode was then deposited by e-beam evaporation to a thickness of about 100nm to form MFIS capacitors.

The MFIS FETs single transistors with Pt/PGO/high-k/Si stacked gate structure were also successfully fabricated. The fabrication processes of these transistors are compatible with

conventional CMOS process. It uses convention CMOS process for the front-end process to form shallow trench isolation, replacement gate and source-drain implantation. After high-k layer, PGO and Pt top electrode deposition, the Pt/PGO/high-k gate stack was patterned by dry etching using chlorine chemistry. No ferroelectric property degradation was observed after etching and photoresist striping. The back end process also uses the conventional CMOS process to form the metal contact. TEOS and AlCu are used as ILD layer and metal interconnects receptively.

XRD was used to characterize the phases of PGO thin film. SEM was used to characterize the surface roughness and microstructure of the PGO thin film. The hysteresis loops were measured on a standard RT66 system. The CV characteristics of Pt/PGO/HfO_2 capacitor were measured at 1MHz on a HP 4284A precision LCR meter system. The device characteristics were measured on a HP 4156A Precision Semiconductor Parameter.

RESULTS AND DISCUSSION

The PGO thin films deposited on different high-k layers show similar crystal structure and phases. From the XRD spectrum as shown on figure 1, high c-axis orientation and single phase PGO thin film have been obtained on all these substrates. There is no reaction observed between PGO and these high-k layers when the annealing temperature is around 500-550°C. As thin as 3nm high-k layers show good barrier properties between PGO and Si substrate.

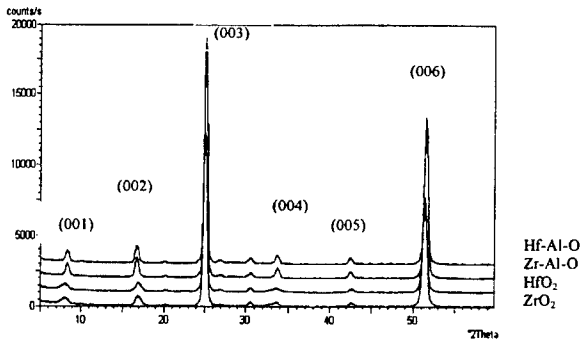

Figure 1. XRD spectrum of PGO on different high-k substrates

Figure 1 demonstrated that spin on PGO thin film is not sensitive to different high-k substrates. This has great advantages for fabricating MFIS FETs using most advanced CMOS processes. As an example, in this paper we will focus on using HfO_2 as the gate dielectric layer. The memory window for Pt/PGO/HfO_2/n-Si capacitors with a 3nm HfO_2 and different PGO thickness are shown on Figure 2. As large as 1V memory window with 150nm PGO and 3nm high-k layers were observed. Since the hysteresis loop observed on Pt/HfO_2/Si capacitors is negligible, It confirmed that the memory window obtained from the Pt/PGO/high-k/n-Si capacitors are caused by polarization switching of the ferroelectric PGO thin film.

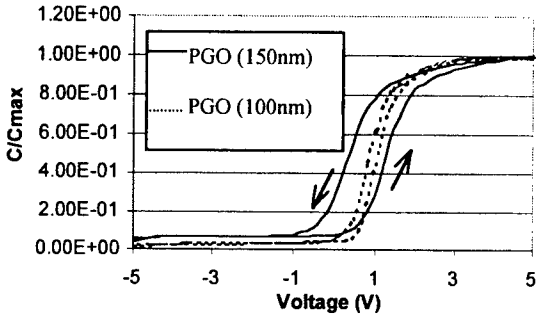

Figure 2. Memory window of MFIS capacitors with different PGO thickness

The Metal-Ferroelectric-Insulator-Silicon (MFIS) NMOS and PMOS were both fabricated using HfO_2 as the gate dielectric layer. These devices were fully characterized by measuring the V_G -I_D and V_D-I_D characteristics on 0.6μm x 10μm devices. Memory windows as large as 1V were obtained and they show less dependency on the device sizes. The smallest working device obtained is 0.3 μm x 0.5 μm (L x W). Figure 3 (a) is the V_G-I_D scan for NMOS devices by fixing V_D=0.5V. The memory window for the on and off currents is about 3 orders of magnitude. Figure 3 (b) is the V_D-I_D scans when stepping the V_G from +5V to −5V and from −5V to +5V. Similar memory windows observed.

Similar results were also obtained on PMOS devices also as shown on Figure 4. The V_D was fixed at -0.5V for V_G-I_D scan as shown on Figure 4 (a).

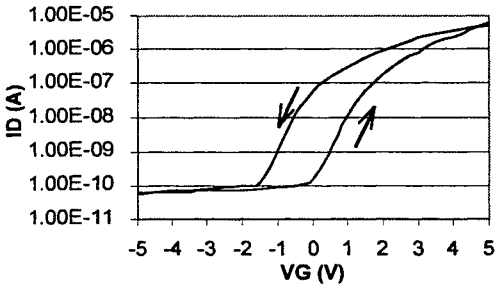

(a)

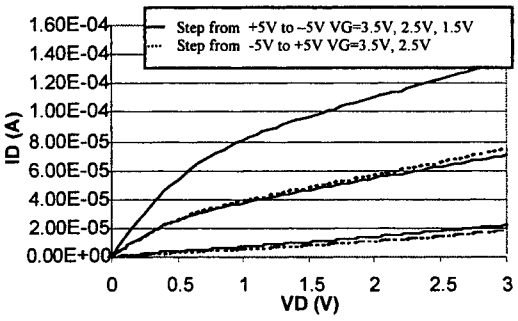

(b)

Figure 3. (a) V_G-I_D characteristics of MFIS NMOS single transistor with Pt/PGO/HfO_2/p-Si structure. (b) V_D-I_D characteristics of MFIS NMOS single transistor with Pt/PGO/HfO_2/p-Si structure.

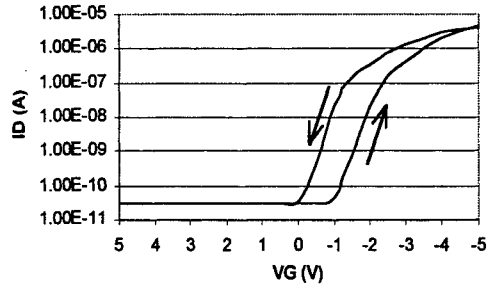

(a)

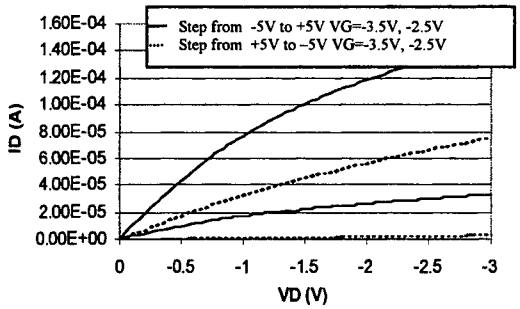

(b)

Figure 4. (a) V_G-I_D characteristics of MFIS PMOS single transistor with Pt/PGO/HfO_2/n-Si structure. (b) V_D-I_D characteristics of MFIS PMOS single transistor with Pt/PGO/HfO_2/n-Si structure.

The endurance of these devices measured at 1kHz and 10kHz are up to 10^8 switching cycles without degradation. The retention properties were measured by programming the device to either the on or off state, then setting the V_G at 0V, followed by sweeping the V_D to obtain I_D current along time. It can be seen that for NMOS the on current decreases and off current increases along time. On the other hand, for PMOS both on and off current decrease along time. In both cases, the memory window remained after 10^4 seconds retention test.

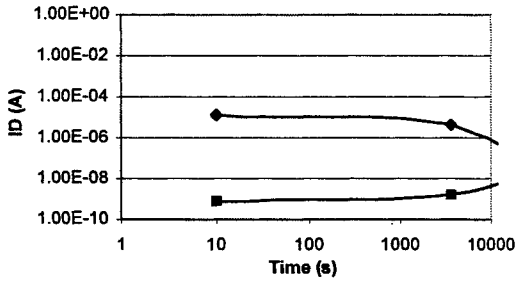

(a)

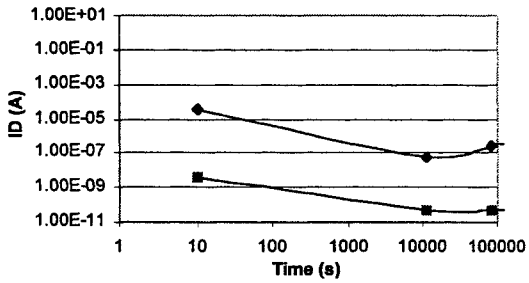

(b)

Figure 5. Retention properties of MFIS single transistors. (a) NMOS; (b) PMOS

CONCLUSION

In conclusion, The MFIS NMOS and PMOS using Pt/$Pb_5Ge_3O_{11}$/HfO_2/Si structure have been successfully fabricated. The integration process is simple and reliable, and it is fully compatible with conventional CMOS process. The devices also show large memory windows, good endurance and retention properties.

REFERENCE

1) Fengyan Zhang, Sheng Teng Hsu, Yoshi Ono, Bruce Ulrich, Weiwei Zhuang, Hong Ying, Lisa Stecker, David R. Evans, Jershen Maa, Jpn. J. Appl. Phys. Vol.40, No.6B pp.L635 - L637, 2001

2) Yanjun Ma, Yoshi Ono, Lisa Stecker, David R. Evans, and S.T. Hsu, IEDM Digest of Technical papers, p149, 1999

Low Temperature Deposition of Epitaxial-Grade PZT Films by MOCVD

Hiroshi Funakubo[1)], Masanori Aratani[1)], Takahiro Oikawa[1)] and Keisuke Saito[2)]
[1)]Department of Innovative and Engineered Materials, Tokyo Institute of Technology
G1-405, 4259, Nagatsuta-cho, Midori-ku, Yokohama, 226-8502
Fax: +81-45-924-5446, e-mail: funakubo@iem.titech.ac.jp
[2)]Analytical Department, Application Laboratory, Philips Japan Ltd.,
35-1 Sagamiono, 7-Chome, Sagamihara-shi, Kanagawa, Japan,

Epitaxial-grade polycrystalline $Pb(Zr,Ti)O_3$ [PZT] films were deposited at low deposition temperature by source-gas-pulsed-introduced metalorganic chemical vapor deposition (pulsed-MOCVD). (111) orientation changed to (100) and (001) one when the deposition temperature decreased. Well-saturated Ferroelectricity with a remanent polarization (Pr) and coercive field (Ec) of 41.4 $\mu C/cm^2$ and 78.5 kV/cm, respectively, was obtained for polycrystalline PZT film with the Zr/(Zr+Ti) ratio of 0.35 deposited at 415°C. This Pr value is almost the same as that of epitaxially grown films at 580 ℃ with the same composition and orientations taking into account of the volume fraction of (100) and (001) orientations.

1. INTRODUCTION

$Pb(Zr,Ti)O_3$ [PZT] thin films have been widely investigated for application to ferroelectric random access memory (FeRAM).[1] Various methods have been reported for PZT thin film preparation. Among them, metalorganic chemical vapor deposition (MOCVD) is one of the most important preparation methods from a practical point of view because of its high step-coverage, high deposition rate and large area uniformity of the film quality.[2,3]

Lowering the preparation temperature of crystalline PZT films is essential for high-density FeRAM applications. Low temperature deposition of the crystalline PZT films down to 450 ℃ has been reported by changing the composition of film and the suitable substrate, using a seeding layer, or optimizing preparation process.[4-7] However, the remanent polarization (*Pr*) generally decreased down to 25 $\mu C/cm^2$ with decreasing deposition temperature.

In the previous study, the pulsed introduction of a mixture of source gases into the reaction chamber (pulsed-MOCVD) was developed.[7-9] Simultaneous improvement of the crystallinity, surface smoothness and electrical properties have been reported by using this method for films deposited at 580 ℃.

In this paper, the quality of the films with (100) and (001) orientations prepared at 415 ℃ by the pulsed-MOCVD was reported compared with that of epitaxial film with the same composition. As a result, PZT films with epitaxial-grade ferroelectric properties was obtained even at 415 ℃ for the Zr/(Zr+Ti) ratio of 0.35.

2. EXPERIMENTAL

250nm-thick polycrystalline PZT thin films were prepared on (111)Pt/Ti/SiO_2/Si substrates from 390 to 580 ℃ by the pulsed-MOCVD using $Pb(C_{11}H_{19}O_2)_2$, $Zr(O\cdot t\text{-}C_4H_9)_4$, $Ti(O\cdot i\text{-}C_3H_7)_4$ and O_2 gas as the source materials.[10] Epitaxial PZT thin film was also prepared on (100)$SrRuO_3$//(100)$SrTiO_3$ substrate at 580 ℃ by the pulsed-MOCVD. A horizontal cold-wall type reactor maintained at a pressure of 667 Pa was used for the film preparation. In this process, a pulsed mixture of the source gases was introduced for 10 s with a 5 s interval time, while O_2 gas was continuously introduced into the reaction chamber. Films with Pb/(Pb+Zr+Ti) and Zr/(Zr+Ti) of 0.50, and 0.35 and 0.62, respectively,

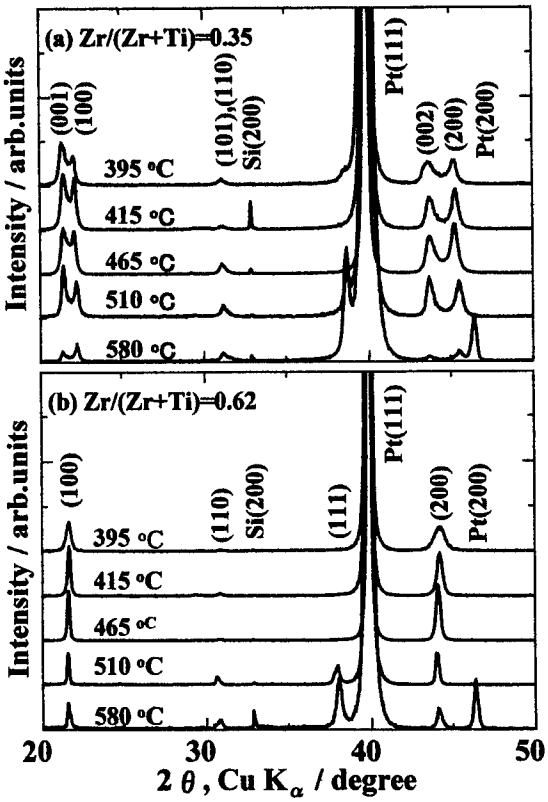

FIG. 1 XRD patterns of the polycrystalline PZT films deposited at various temperatures on (111)Pt/Ti/SiO_2/Si substrates.
Zr/(Zr+Ti) : (a) 0.35, (b) 0.62

were prepared by adjusting the input source gas composition. This composition corresponded to the tetragonal PZT phase.

The orientation of the film was measured by X -ray diffractometer (XRD). The volume fraction of the (001) orientation of (100) and (001) preferred-oriented film, $V(001)/[V(100)+V(001)]$, was calculated from the integrated areas of XRD peaks of PZT(001) and PZT(100).

Electrical properties were measured using a 100 μmϕ Pt top electrode.

3. RESULTS AND DISCUSSION

Fig.1 shows the change in the XRD patterns of the films for the deposition temperature from 395 to 580 ℃. The *(h00)* and *(00l)* peak intensities were found to increase when the deposition temperature decreased irrespective of the Zr/(Zr+Ti) ratio. Fig.2 shows the XRD patterns of the polycrystalline film and the epitaxial film deposited at 415 ℃ and 580 ℃, respectively. All films showed strong (100) and/or (001) orientations, but the volume fractions of (100) and (001) were not found to be the same from the enlarged XRD pattern shown in Fig. 2(b) for the Zr/(Zr+Ti) ratio

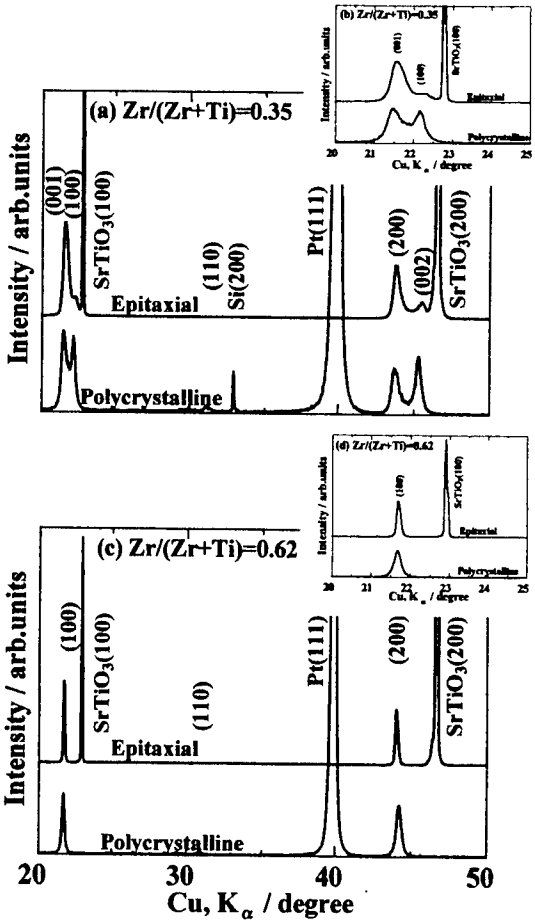

Fig.2 XRD patterns of the polycrystalline and epitaxial PZT films deposited at 415°C on (111)Pt/Ti/SiO_2/Si substrate and at 580°C on (100)$SrRuO_3$//(100)$SrTiO_3$ substrate, respectively.
Zr/(Zr+Ti) : (a) 0.35, (b) 0,62

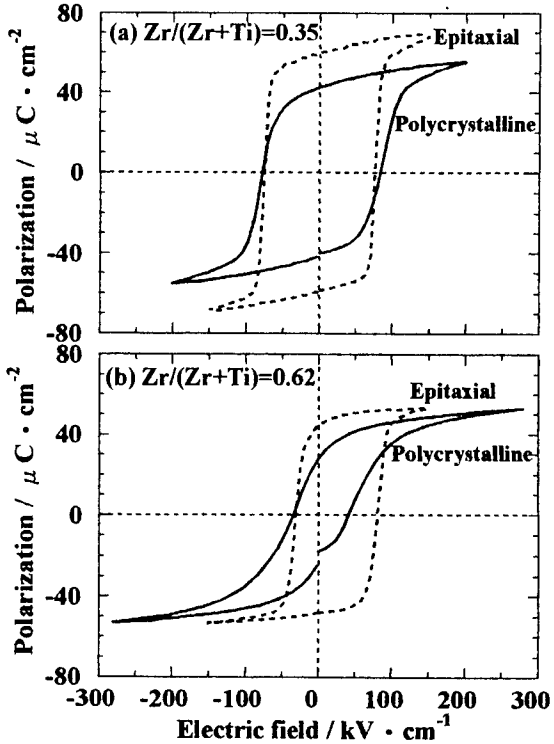

Fig. 3 P-E hysteresis loops of the polycrystalline and epitaxial PZT films deposited at 415°C on (111)Pt/Ti/SiO_2/Si substrate and at 580°C on (100)$SrRuO_3$//(100)$SrTiO_3$ substrate, respectively.
Zr/(Zr+Ti) : (a) 0.35, (b) 0,62

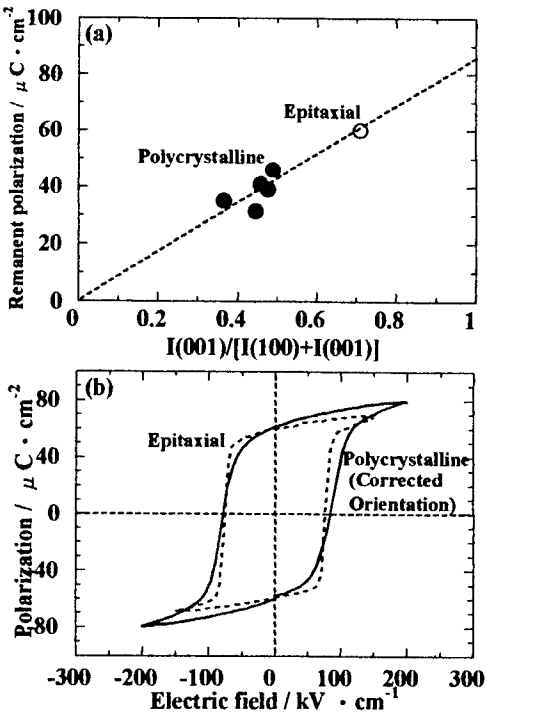

Fig.5 (a) The relationship between the volume fraction of the (001) orientation, $V(001)/[V(1001)+V(001)]$, and the remanent polarization.
(b) Estimated P-E hysteresis loops corrected orientation

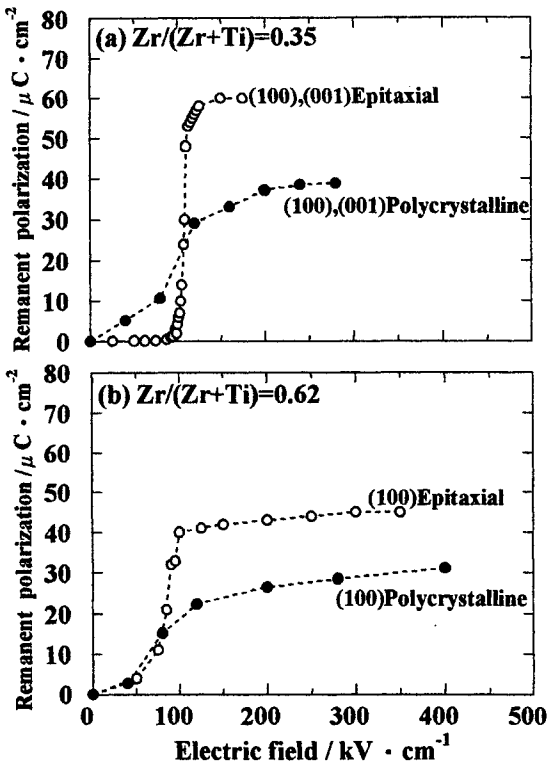

Fig.4 Saturation properties of the polycrystalline and epitaxial PZT films deposited at 415°C on (111)Pt/Ti/SiO_2/Si substrate and at 580°C on (100)$SrRuO_3$//(100$SrTiO_3$ substrate, respectively. Zr/(Zr+Ti) : (a) 0.35, (b) 0,62

of 0.35.

Fig.3 shows the *P-E* hysteresis loops of the same films shown in Figs.2. Well-saturated hysteresis loops were obtained for both films. Fig.4 shows the saturation properties of the *Pr* values of the same films shown in Fig.3. Epitaxial films showed abrupt increase of Pr value at about 100 and 80 kV/cm for the Zr/(Zr+Ti) ratio of 0.35 and 0.62, suggesting the saturation at fixed electric field, while polycrystalline one gradually saturated against the electric field compared with the epitaxial one. The almost constant *Pr* value observed at high electrical fields suggest the good saturation character of all films. Pr value of the epitaxially grown film was larger than that of polycrystalline ones for both Zr/(Zr+Ti) ratio. The lower *Pr* value of the polycrystalline PZT film could be due to either a decrease in the crystallinity or a change in the orientation. For the films with the Zr/(Zr+Ti) ratio of 0.62 the orientation of the film was the same so that the Pr difference is mainly originated to the difference of the film quality. Note that the value of the saturation polarization (Ps) was almost the same for these films as shown in Fig.3(b). On the other hand, for the film with the Zr/(Zr+Ti) ratio of 0.35, the volume fraction of the (100) and the (001) orientations was not the same for both films as shown in Fig. 1(c), The $V(001)/[V(100)+V(001)]$ ratio was 52 % and 85 % for the polycrystalline and epitaxial films, respectively. This difference affects the *Pr* value of the film because the polar axis of tetragonal PZT is [001] and (100)-oriented grains do not display ferroelectricity.

Figure 5(a) shows the relationship between the volume fraction of the (001) orientation and the Pr. The polycrystalline and epitaxial films data were on the same straight line. This result suggests that the Pr difference in Fig.3(a) is due to the volume fraction of the (100) and the (001) orientations but not the crystallinity of the film. The estimated P-E physteresis loops of the polycrystalline film with the same volume fraction as the epitaxial film is shown in Fig. 5(b). This shows that the Pr value of the polycrystalline and epitaxial films were basically the same if the orientation of both films is the same. As a result, the polycrystalline PZT film prepared by pulsed-MOCVD had the epitaxial-grade ferroelectric property even though the deposition temperature was as low as 415 ℃; Pr value was 41.4 μC/cm^2

4. CONCLUSION

250nm-thick polycrystalline PZT thin film prepared at 415 ℃ by pulsed-MOCVD was compared with an epitaxial film prepared at 580 ℃ from the viewpoint of ferroelectric properties. Well-saturated hysteresis loop of the polycrystalline PZT film with a Pr value of 41.4 μC/cm^2 was obtained even at 415 ℃, but the Pr value was smaller than that of the epitaxial film. This difference was explained by the larger volume fraction of non-poled (100)-oriented grains in the polycrystalline film with the Zr/(Zr+Ti) ratio of 0.35. This suggests that the Pr value of the polycrystalline film was almost the same as that of the epitaxial film if the orientation of both films was the same. As a result, the polycrystalline PZT film prepared at 415℃ by pulse-MOCVD showed an epitaxial-grade ferroelectric property.

References

1) A. Mannish, Ferroelectrics **102**, 69 (1990).
2) T. Li, P. Zawadzki, and R. Stall, Integ. Ferro. **18**, 155 (1997).
3) C. M. Foster, G. R. Bai, R. Csencsits, J. Vetrone, R. Jammy, L. A. Wills, and J. Amano, J. Appl. Phys. **8**, 2349 (1997).
4) H. Suzuki, T. Koizumi, Y. Kondo, and S. Kaneko, J. Eur. Ceram. Soc. **19**, 1397 (1999).
5) H. Suzuki, M. B. Othman, K. Murakami, K. Kaneko, and T. Hayashi, Jpn. J. Appl. Phys. **35**, 4896 (1996).
6) S. Hirano, T. Yogo, K. Kikuta, Y. Araki, M. Saitou, and S. Ogasawara, J. Am. Ceram. Soc. **75**, 2785 (1992).
7) K. Maki, N. Soyama, S. Mori, and K. Ogi, Proc. Int. Soc. Int. Ferro. (unpublished).
8) K. Nagashima, M. Aratani, and H. Funakubo, Jpn. J. Appl. Phys. **39**, L996 (2000).
9) M. Aratani, T. Ozeki, and H. Funakubo, Jpn. J. Appl. Phys. **40**, L343 (2001).
10) M. Aratani, K. Nagashima, and H. Funakubo, Jpn. J. Appl. Phys. **40**, 4126 (2001).
11) K. Nagashima and H. Funakubo, Jpn. J. Appl. Phys. **39**, 212 (2000).

Retention properties in Single-crystalline PLZT Thin Film Capacitors

N. Kamehara, M. Kurasawa and K. Kurihara

Fujitsu Laboratories LTD.

10-1 Morinosato-Wakamiya, Atsugi 243-0197, Japan

FAX:81-46-248-8812

Email:kamehara.nobuo@jp.fujitsu.com

ABSTRACT

Retention and imprint properties of single-crystalline (Pb,La)(Zr,Ti)O_3 (PLZT) thin film capacitors were investigated. The capacitors showed a good retention property and an asymmetric voltage shift in P-V hysteresis loop depending on poling direction. These imply that the retention is attributed to the bulk thin film quality and the imprint is dominantly affected by the interface effect. In current-voltage measurements for initial and imprinted capacitors, the space charge distribution change was observed at the interface. The charge accumulation is considered to associate with the imprint failure.

INTRODUCTION

Retention and imprint failures is the most prominent issue for ferroelectic random access memory (FeRAM) capacitors. Many reports have been done in these failures, especially imprint, in terms of bulk thin film effect and/or electrode interface effect such as aligned defect dipoles through a bulk thin film and charge trapping at domain walls or at interfaces [1-7]. In polycrystalline thin film capacitors, which have been generally used for FeRAM, it is not easy to investigate the bulk and interface effects apart due to grain boundaries.

In this study, retention and imprint properties are investigated by comparing those properties between polycrystalline and single-crystalline thin film capacitors in order to clarify the origins of these failures.

EXPERIMENT

PLZT thin films with 300nm thick were prepared by chemical solution deposition method with PLZT (113/1.5/45/55) solution on Pt (200nm) /MgO single-crystalline substrates and on Pt(100nm)/SiO_2/Si substrates. Top 100nm thick Pt electrodes were deposited through a metal mask and post-annealed in O_2 gas flow.

We characterized the PLZT capacitors with use of X-ray diffraction and SIMS measurement. Hysteresis and pulse measurements were carried out using Radiant RT6000HVS ferroelectric tester and current-voltage (J-V) measurements were carried out using a HP 4140B pA meter. We performed a thermally induced test for the evaluation of the retention and imprint properties. The test was performed that initially the capacitors were poled to negative or positive polarized state. And then the capacitors were stored at 150 °C. After storage for a specified period, hysteresis and pulse measurements were carried out at room temperature.

RESULTS

Figure 1 shows X-ray diffraction patterns for (a) PLZT thin film on Pt/MgO and (b) on Pt/SiO_2/Si substrates, respectively. The *c*-axis of PLZT is grown perpendicular to the MgO substrate surface. PLZT thin film on Pt/SiO_2/Si has a dominant (111) diffraction peak and other peaks as shown in Fig.1 (b). The result of pole-figure measurement indicates that the PLZT film on Pt/MgO is also oriented in plane. It is confirmed that the PLZT film is epitaxially grown on Pt/MgO.

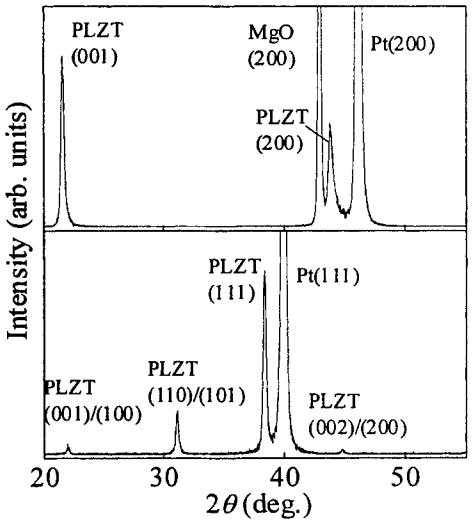

Fig. 1 X-ray diffraction θ-2θ scan profile for (a) PLZT/Pt/MgO and (b) PLZT/Pt/SiO_2/Si

Figure 2 shows P-V hysteresis loops for single-crystalline and polycrystalline PLZT thin film capacitors. About two times larger remnant polarization

was observed in single-crystalline PLZT comparing to the polycrystalline PLZT.

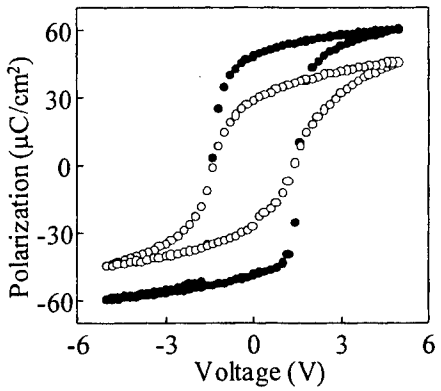

Fig.2 Hysteresis loops for single-crystalline (closed circles) and polycrystalline PLZT thin film capacitors (open circles).

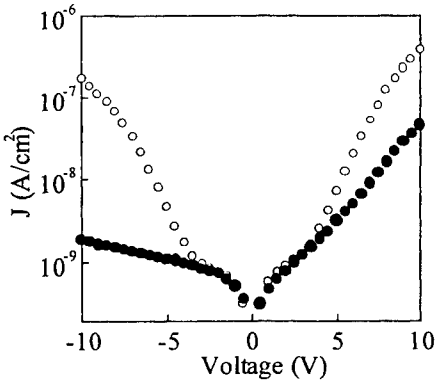

Fig.3 J-V curves for single-crystalline (closed circles) and polycrystalline (open circles) PLZT thin film capacitors.

Figure 3 shows the J-V curves for single and polycrystalline PLZT thin films. Smaller leakage current was observed in single-crystalline PLZT films. This is considered to be due to reduction of grain boundary effect. Furthermore, an asymmetric J-V curve was obtained in single-crystalline PLZT thin film capacitors.

The retention properties for single-crystalline and polycrystalline thin film capacitors are shown in Fig. 4 (a). The single-crystalline shows the excellent retention characteristics. Reduction of polarization was hardly observed. The thermally induced voltage shifts are shown in Fig. 4 (b). Symmetric voltage shift was observed in polycrystalline PLZT thin films. On the other hand, an asymmetric voltage shift was observed in single-crystalline PLZT capacitors depending on poling direction. Large voltage shift was observed in positive poled state. The values are almost the same as these in polycrystalline. On the other hand, smaller voltage shift was observed in negative poled state.

Figure 5 shows the J-V curves for single-crystalline thin film capacitor before and after thermally induced test. After thermal stress with negative poled state, in which the voltage shift was smaller, J-V curves were almost the same as that in the initial capacitor. On the other hand, after thermal stress with positive poled state, in which the large voltage shift was observed, an increase of current was observed in the negative polarity of applied voltage.

DISCUSSIONS

Single-crystalline PLZT thin film capacitors showed excellent retention properties as shown in Fig. 4 (a). This indicates that the retention was largely influenced by the bulk thin film quality. However, Asymmetric imprint property was observed depending on the poling direction in single-crystalline thin film capacitor as shown in Fig. 4(b). Because the large

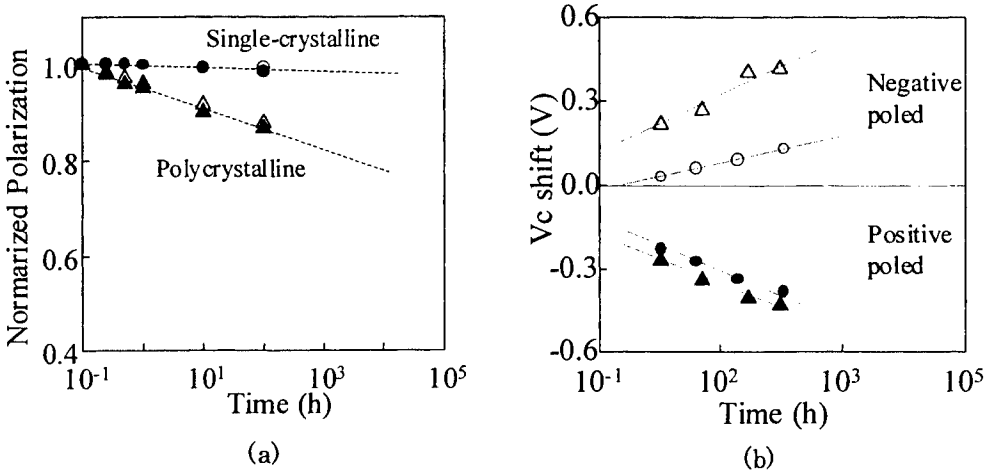

Fig.4 (a) retention and (b) imprint properties for single-crystalline (circles) and polycrystalline (triangles) PLZT thin film capacitors.

voltage shift, which was observed in positive poled state, is almost the same as that in polycrystalline thin film capacitor, it is considered that the imprint failure is largely related to the interface effect, such as charge trapping at interface.

Asymmetric J-V characteristics were observed as shown in Fig. 3 in the initial state of the capacitors. This indicates that the conduction current is controlled by the interface-limited mechanism. Hence, we can explain the J-V curves in the high electric field region fitted with the curves based on interface-limited mechanisms. Figure 6(a) shows the log(J)-$V^{1/2}$ plot, which is called as Schottky plot, and Fig. 6(b) shows log(J/V^2)-1/Vplot, which is called as Fowler-Nordheim (F-N) plot of J-V curves for the initial capacitor, respectively. In the Shottky plot, a linear relation was obtained when the negative polarity of voltage applied to the bottom electrode. In the F-N plot, a linear relation with the negative slope was obtained when the positive voltage was applied to the bottom electrode.

When we assume the injected carriers are holes, as some researchers have reported for Pt/PZT interface [8, 9], it is considered that the Schottky emission current is the dominant mechanism at top electrode interface and the tunneling current is the dominant mechanism at the bottom electrode interface. This difference of the carrier injection mechanism indicates that the potential barrier structures are different between the top and the bottom electrode interfaces. Fig. 6(c) shows the F-N plots of J-V curves for the initial and the thermally stressed capacitor under the positive poled state, in which the large voltage shift was observed in the hysteresis loop. An increase of current density at high electric field region seems to be the transition from the Schottky current to tunneling current at the top electrode interface. This is considered to be due to the space charge distribution change by the thermal stress under positive poled state.

Figure 7 shows the SIM depth profiles of the single-crystalline PLZT film capacitor. Pb diffusion were observed in both top and bottom electrodes. There seems to be Pb deficient layers at the both top and bottom electrodes interfaces. On the other hands, O deficient layer was clearly observed near the top electrode interface.

From the asymmetric J-V characteristics and the SIMS depth profiles, the potential barrier structures and the space charge distributions at top and bottom electrode interfaces are considered, as shown in Fig. 8(a). At the bottom electrode interface where the tunneling current was dominant, the downward bending of energy band was formed by ionized acceptors such as Pb vacancies. Since the Schottky emission current was dominant at top electrode interface, the band bending was smaller at the top electrode interface. Therefore, the negative charge concentration in the space charge region is lower at the top electrode interface than the bottom electrode interface. It seems that ionized acceptors are compensated by the ionized donors such as O vacancies.

As a result of J-V measurements for thermal stressed capacitors, we observed the change of conduction mechanism from Schottky current to tunneling current at the top electrode interface. This indicates that the potential barrier width became thinner due to the

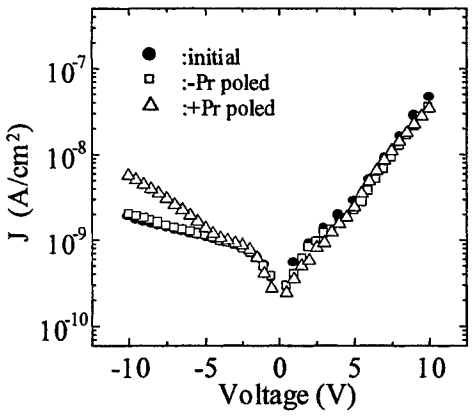

Fig.5 J-V curves for the single-crystalline PLZT capacitors.

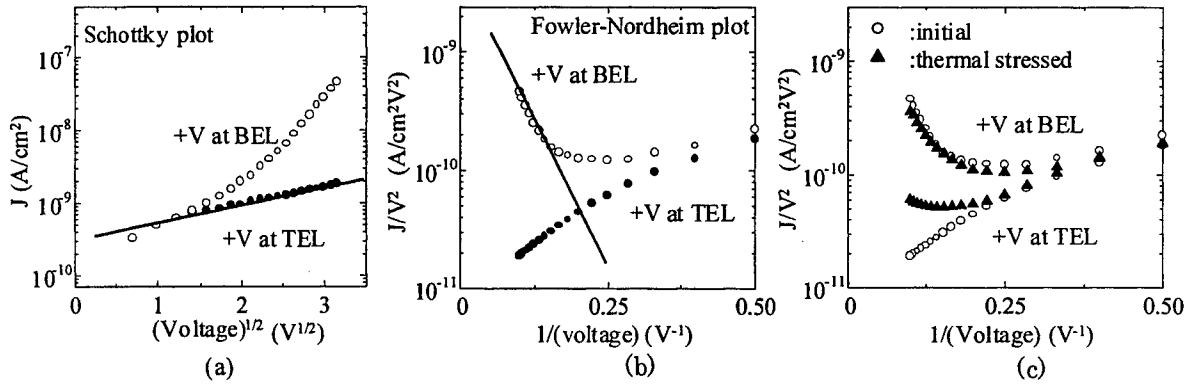

Fig. 6. (a) Schottky plot and (b) Fowler-Nordheim (F-N) plot of J-V curves of initial states. F-N plots of J-V curves before and after thermal stressed under positive poled capacitor.

accumulation of negative charges at top electrode interface by the thermal stress as shown in Fig. 7(b). Because the ionized acceptors can not trap the negative charges, it is reasonable to conclude that the ionized donors are related to the trapping of negative charges such as electrons.

CONCLUSION

We investigated the retention and imprint properties in single-crystalline PLZT thin film capacitor.

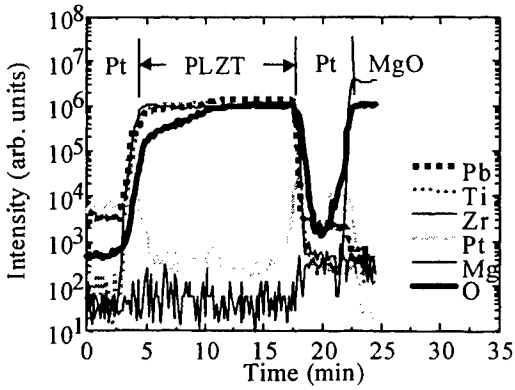

Fig. 7 SIMS depth profiles of PLZT capacitor

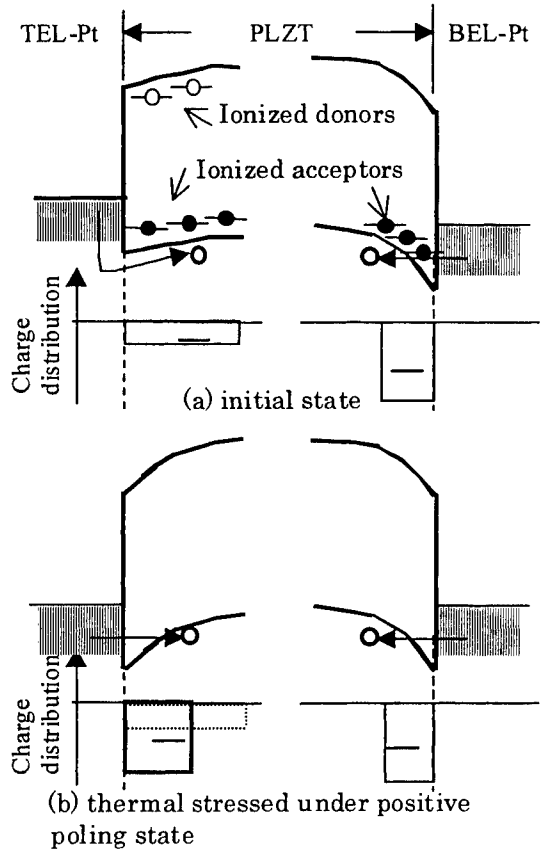

Fig. 8. Potential barriers at interfaces (a) in the initial capacitor and (b) in the thermal stressed capacitor under positive poled state

The single-crystalline PLZT thin film capacitors showed excellent retention property comparing to the polycrystalline thin film capacitor. On the contrary, large thermally induced voltage shift as well as that in polycrystalline thin film was observed in the positive poled state. These results indicate that the retention failure is largely influenced by the bulk thin film quality and the imprint failure is dominantly affected by the electrode interface effect.

Smaller voltage shift was observed under the negative poled state. The asymmetric voltage shift depending on the poling direction was considered to be due to the difference between the top and bottom electrode interface qualities. As a result of J-V measurements, asymmetric J-V characteristic was observed between the positive and negative bias. The asymmetric characteristic was considered to be due to the difference between the space charge distribution at the top and the bottom electrode interfaces. Furthermore, we observed the negative charge accumulation in the top electrode interface after thermally stressed capacitors under the positive poled state. The imprint is considered to be due to the charge accumulation at interface.

REFERENCES

[1] J. Lee et al., "Imprint and oxgen deficiency in (Pb, La)(Zr, Ti)O_3 thin-film capacitors with La-Sr-Co-O electordes," Appl. Phys. Lett. Vol. 66 pp. 1337~1339, March 1995.

[2] W. L. Warren et al., "Voltage shifts and imprint in ferroelectric capacitors," Appl. Phys. Lett. Vol 67, pp. 866~868, August 1995.

[3] G. E. Pike et al., "Voltage offsets in (Pb, La)(Zr, Ti)O_3 thin films," Appl. Phys. Lett. Vol. 66, pp. 484~486, January 1995.

[4] W. L. Warren et al., " Driving force behind voltage shifts in ferroelectric materials," Appl. Phys. Lett. Vol. 68, pp. 1681, March 1996.

[5] W. L. Warren et al., "Imprint in Ferroelectric Capacitors," Jpn. J. Appl. Phys. Vol. 35, pp. 1521~1524, February 1996.

[6] S. Sadashivan et al., " Evaluation of imprint in fully integrated (La, Sr)CoO_3/Pb(Nb, Zr, Ti)O_3/(La, Sr)CoO_3 ferroelectric capacitors," J. Appl. Phys. Vol. 83, pp. 2165~2171, February 1998.

[7] S-H. Kim et al., "Imprint and fatigue properties of chemical solution derived $Pb_{1-x}La_x(Zr_yTi_{1-y})_{1-x/4}O_3$ thin films," J. Mater. Res. Vol. 14, pp. 1371~1377, April 1999.

[8] I. Stolichinov and A. Tagantsev, "Space-charge influenced-injection mode for conduction in $Pb(Zr_xTi_{1-x})O_3$ thin films," J. Appl. Phys., vol. 84, pp. 3216~3225, September 1998.

[9] T. Mihara and H. Watanabe, "Electronic conduction characteristcs of sol-gel ferroelectric $Pb(Zr_{0.4}Ti_{0.6})O_3$ thin film capacitors:part 1," Jpn. J. Appl. Phys., vol. 34, pp. 5664~5673, October 1995.

SYNTHESIS AND PROPERTIES OF TUNGSTEN BRONZE $(Sr,Ba)(Nb,Ta)_2O_6$ THIN FILMS BY THE CHEMICAL SOLUTION DEPOSITION

Wataru Sakamoto, Yu-saku Horie, Toshinobu Yogo and Shin-ichi Hirano

Dept. of Applied Chem., Graduate School of Engineering,

Nagoya University, Furo-cho, Chikusa-ku, Nagoya, 464-8603 JAPAN
Fax: 81-52-789-3182, e-mail: sakamoto@apchem.nagoya-u.ac.jp

Tungsten bronze $(Sr,Ba)(Nb,Ta)_2O_6$ thin films have been prepared by the chemical solution deposition process. Highly oriented tungsten bronze $(Sr,Ba)(Nb,Ta)_2O_6$ thin films were successfully fabricated on MgO(100) and Pt(100)/MgO(100) substrates at around 700°C. The synthesized films have excellent c-axis preferred orientation and exhibit the characteristic behavior as a relaxor dielectrics. The Curie temperature (T_c) of the $(Sr,Ba)(Nb,Ta)_2O_6$ film shifted to a low temperature region with increasing the amount of tantalum substitution. Also, the T_c showed the remarkable compositional dependence.

1. Introduction

Strontium barium niobate ($Sr_{1-x}Ba_xNb_2O_6$, SBN) is a ferroelectric solid solution of $SrNb_2O_6$ and $BaNb_2O_6$ with a tetragonal tungsten bronze structure.[1,2] SBN based materials are known to have excellent electrical and optical properties.

The chemical solution process which is one of the most common methods for film fabrication has characterized by advantages such as high purity, good homogeneity, lower processing temperature, feasibility of composition control.[3-5] The crystallization of tungsten bronze films at lower temperatures is indispensable for the fabrication of high-quality films. The substitution with potassium ion is found to be very effective in reducing the crystallization temperature of the tungsten bronze phase.[4] On the other hand, both $SrTa_2O_6$ and $BaTa_2O_6$ have the tungsten bronze structure, and its tungsten bronze phase is considered to exhibit high structural stability.[6] Increase in the stability of the tungsten bronze phase in SBN is expected by the formation of a solid solution with $(Sr,Ba)Ta_2O_6$.

This paper focuses on the chemical processing of tantalum substituted $(Sr_{0.5}Ba_{0.5})(Nb,Ta)_2O_6$ (SBNT) thin films from metal-organic substances. The crystallization and microstructure of tungsten bronze SBNT films were investigated. The optical and electrical properties of the films were also evaluated.

2. Experimental Procedure

The precursor solution was prepared by the reaction of Sr metal, Ba metal, $Nb(OEt)_5$, $Ta(OEt)_5$ in ethanol with a 12 equiv. of 2-ethoxyethanol as a stabilizing agent.

Films were fabricated using the precursor solution by dip coating on MgO(100) and Pt(100)/MgO(100) substrates.

The prepared films were analyzed by X-ray diffraction (XRD), Raman microprobe spectroscopy, UV-visible spectroscopy and scanning electron microscopy (SEM). The electrical properties of the films were measured using Au as the top electrode and Pt(100) layer on MgO(100) as the bottom electrode. The dielectric and ferroelectric properties were measured using a LCZ meter and a ferroelectric test system, respectively.

3. Results and Discussion

3.1 Fabrication of Tungsten Bronze SBNT Thin Films

Tantalum substituted SBN ($(Sr,Ba)(Nb,Ta)_2O_6$, SBNT) precursor solutions were prepared by controlling the reaction of metal alkoxides using a mixture solvent of ethanol and 2-ethoxyethanol. The SBNT precursor solutions were used for the preparation of films by dip coating.

In order to synthesize highly oriented tungsten bronze SBNT thin films, MgO(100) and Pt(100)/MgO(100) were selected as substrates, because the oxygen alignment of a-plane of MgO can match to that of c-plane of tungsten bronze SBNT. From the results of the crystallization behavior of SBNT precursor powders, tantalum substitution more than 20 mol% was necessary to stabilize the tungsten bronze phase. Thin film fabrication was performed on $(Sr_{0.5}Ba_{0.5})(Nb_{0.8}Ta_{0.2})_2O_6$ (SBNT50/80), $(Sr_{0.5}Ba_{0.5})(Nb_{0.7}Ta_{0.3})_2O_6$ (SBNT50/70), $(Sr_{0.5}Ba_{0.5})(Nb_{0.5}Ta_{0.5})_2O_6$ (SBNT50/50) and $(Sr_{0.5}Ba_{0.5})Ta_2O_6$ (SBT50), compositions. Figure 1 shows the XRD profiles of SBNT50/80 thin films on MgO(100) and MgO(100)/Pt(100) substrates crystallized at 700°C. The SBNT50/80 films on MgO(100) and MgO(100)/Pt(100) substrates have strong 001 and 002 reflections as shown in Fig.1, although the 002 reflection of SBNT50/80 might be superimposed on 200 reflection of Pt.

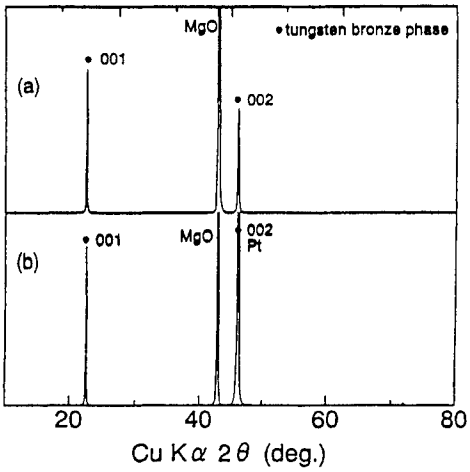

Fig.1 XRD profiles of $(Sr_{0.5}Ba_{0.5})(Nb_{0.8}Ta_{0.2})_2O_6$ (SBNT50/80) thin films on (a) MgO(100) and (b) Pt(100)/MgO(100) substrates heat-treated at 700°C.

SBNT50/70, SBNT50/50 and SBT50 films on MgO(100) and Pt(100)/MgO(100) crystallized at 700°C also showed an excellent c-axis preferred orientation. The SBNT thin films on MgO(100) substrates were examined further by Raman microprobe spectroscopy as for the cases of the SBN and K-substituted SBN films.[3,4] The SBNT film showed the characteristic Raman scatterings of tungsten bronze niobate, such as the Nb-O-Nb bending modes (200-300 cm^{-1}) and the symmetric stretching mode of the NbO_6 octahedron (550-700 cm^{-1}). The Raman scattering profile was in good agreement with that of the tetragonal tungsten bronze SBN50 ($Sr_{0.5}Ba_{0.5}Nb_2O_6$),[7] although the scattering positions are slightly shifted to each other. The SBNT thin films crystallized on MgO(100) substrates were thus determined to consist of a single-phase tungsten bronze.

The formation of tetragonal tungsten bronze phase on MgO(100) and Pt(100)/MgO(100) is attributed to the assistance of nucleation sites with oxygen alignment of substrates. The calculated lattice mismatch between SBNT(001) and MgO(100) is 6-7 %. Deposited Pt layers on MgO(100) had a (100) orientation with a three dimensional alignment.[6] The lattice mismatch between SBNT(001) and Pt(100) is calculated to be about 1 %. The crystallization of SBNT films with c-axis preferred orientation results from the crystallographic matching of SBNT(001) to Pt(100)/MgO(100).

3.2 Properties of Synthesized SBNT Thin Films

The SBNT50/80, SBNT50/70, SBTN50/50 and SBT50 thin films on transparent MgO(100) substrates crystallized at 700°C showed high transparency over wide wavelength region. If these films have appropriate dielectric properties, these films are expected for applications in optical thin film devices.

Figure 2 shows the SEM photograph of the SBNT50/80 thin film on Pt(100)/MgO(100) substrates crystallized at 700°C. The film thickness is about 0.6 μm after 20 cycles of dipping. In the case of SBN50 film on MgO(100), a heat-treatment at 1000°C was required for complete transformation to tetragonal tungsten bronze.[3] However, the SBNT50/80 thin film of

tungsten bronze was crystallized at much lower temperatures compared with the SBN50 thin film. The surface smoothness of the SBNT50/80 film was much superior to that of the tungsten bronze SBN50 film crystallized at 1000°C. In addition, synthesized SBNT50/80, SBNT50/70, SBNT50/50 and SBT50 films have a uniform thickness, with no voids and cracks, which enables the characterization of dielectric properties.

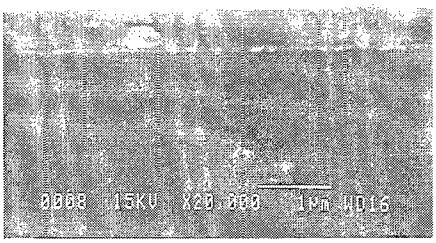

Fig.2 SEM photograph of SBNT50/80 thin film on Pt(100)/MgO(100) substrate crystallized at 700°C.

Figure 3 shows the temperature dependence of the dielectric constant and loss tangent for SBNT50/80 thin film on Pt(100)/MgO(100) substrate crystallized at 700°C. The dielectric maximum of the 0.6 μm thick SBNT50/80 film about 2200 was observed at −80°C at 1 kHz. Also, the temperatures of the dielectric maxima depend upon the frequency of measurement. Since the peaks of ε-T curves were broadened, the SBNT50/80 film was found to show the diffuse phase transition as shown in Fig.3. This result indicates that the SBNT50/80 film seemed to have a relaxor type character. This behavior is characteristic for the property along the c-axis of tungsten bronze SBN single crystal.[8] A similar behavior was observed for the SBNT50/70, SBNT50/50 and SBT50 thin films on Pt(100)/MgO(100). Figure 4 shows temperature and compositional dependences of dielectric constant and loss tangent for SBNT50/80, SBNT50/70, SBNT50/50 and SBT50 thin films crystallized at 700°C on Pt(100)/MgO(100) substrates. It turns out from Fig.4 that the Curie temperature (Tc) was decreased with an increase of tantalum in amount, because, in general, the Curie temperature of SBN shifts to lower temperature side by the substitution of Ta. Tsurumi et al. reported a similar dielectric behavior for $(Sr,Ba)(Nb,Ta)_2O_6$ bulk ceramics.[9] The Curie temperatures of the SBNT thin films were lower than that for reported SBNT bulk ceramics.[9] The small grain size of SBNT film is considered to be one of the reasons for the shift of the Curie temperature.

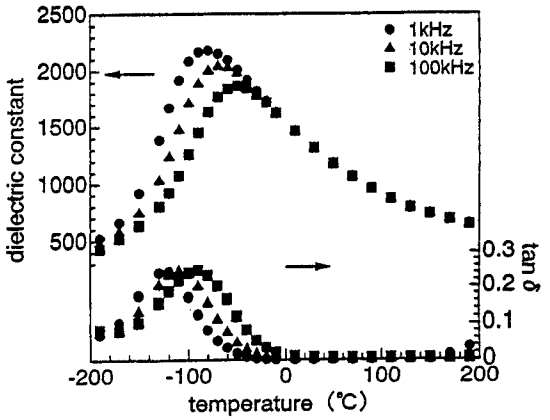

Fig.3 Temperature dependence of dielectric constant and loss tangent of SBNT50/80 thin film on Pt(100)/MgO(100) substrate crystallized at 700°C.

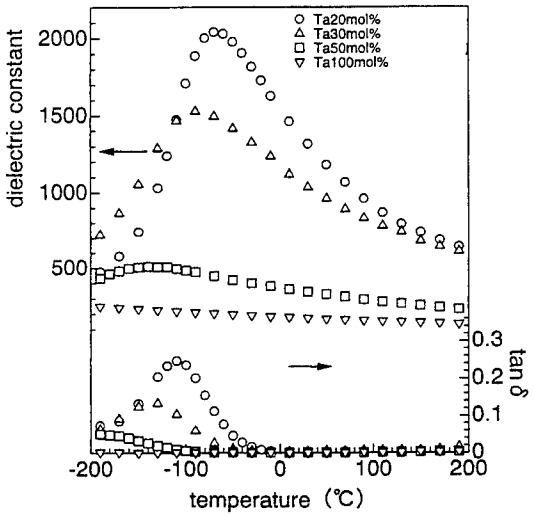

Fig.4 Temperature and compositional dependences of dielectric constant and loss tangent for SBT50, SBNT50/50, SBNT50/70 and SBNT50/80 thin films crystallized at 700°C on Pt(100)/MgO(100).

Also, a typical slim P-E hysteresis loop was observed in low temperature region for the SBNT50/80 and SBNT50/70 films. Therefore, the SBNT50/80 and SBNT50/70 thin films were ferroelectric in low temperature region. However, the present SBNT films were paraelectric at room temperature. The study on the effects of the Sr/Ba ratio and doping of other ions on the properties of SBNT films are now in progress. Since the current SBTN films have good dielectric properties and high transparency, they can be proposed as a transparent dielectric layer for electroluminescence device, etc. On the other hand, the SBNT films are also expected for application as an insulator layer of MFIS or MFMIS type ferroelectric memory devices via the further optimization of several processing conditions.

4. Conclusions

Highly oriented $(Sr,Ba)(Ta,Nb)_2O_6$ (SBNT) films with tungsten bronze structure were successfully synthesized on MgO(100) and Pt(100)/MgO(100) substrates from metallo-organic precursor solutions. The substitution of Nb by Ta in SBN promoted the direct crystallization of the SBNT precursor to tungsten bronze SBNT at 700°C. The tungsten bronze SBNT50/80, SBNT50/70, SBNT50/50 and SBT50 films on MgO(100) and Pt(100)/MgO(100) showed a prominent c-axis preferred orientation. The dielectric constant of the SBNT50/80 thin film was about 1200 at 25°C and 1 kHz, and showed the Curie temperature at around − 80°C at 1 kHz. Synthesized SBNT films exhibited the characteristic behavior of relaxor dielectrics and the remarkable compositional dependence.

Acknowledgement

This work is supported by Grant-in-Aid for Scientific Research, The Ministry of Education, Science and Culture, Japan.

References

1. M.H.Francombe: Acta Cryst. 13 (1960) 131.
2. B.Jaffe, W.R.Cook Jr and H.Jaffe: Piezoelectric ceramics (Academic Press Limited, New York, 1971) pp213-35.
3. W.Sakamoto, T.Yogo, K.Kikuta, K.Ogiso, A.Kawase and S.Hirano: J. Am. Ceram. Soc. 79 (1996) 2283.
4. W.Sakamoto, T.Yogo, A.Kawase and S.Hirano: J. Am. Ceram. Soc. 81 (1998) 2692.
5. T.Yogo, K.Kikuta, Y.Ito and S.Hirano: J. Am. Ceram. Soc. 78 (1995) 2175.
6. F.Galasso, G.Layden and G.Ganung: Mat. Res. Bull. 3 (1968) 397.
7. G.Burns, F.H.Dacol, R.R.Neurgaonkar, A.S.Bhalla and R.Guo: Ferroelectrics, 108 (1990) 189.
8. W-H.Huang, D.Viehland and R.R.Neurgaonkar: J. Appl. Phys. 76 (1994) 490.
9. T.Tsurumi, and Y.Hoshino: J. Am. Ceram. Soc. 72 (1989) 278.

Electrical Properties of $PbZrO_3$ Thin Films Prepared by Chemical Solution Deposition

H. Maiwa and N. Ichinose[1]

Department of Materials Science and Engineering, Shonan Institute of Technology, 1-1-25Tsujido-Nishikaigan, Fujisawa, Kanagawa 251-8511, Japan

FAX: 81-466-36-1594

Email: maiwa@mate.shonan-it.ac.jp

[1]Department of Materials Science and Engineering,Waseda University, 3-12-5 Okubo, Shinjuku, Tokyo 169-8555, Japan

INTRODUCTION

Recently, electric field induced-strains in thin films have been extensively studied due to their potential applications in microelectromechanical systems (MEMS). The origin of the field induced strain is roughly divided into three mechanisms. The first is the inverse piezoelectric effect, the second is the electrostrictive effect, and the third is phase-change-related strains. Since the strain jump at the phase transition is much larger than that in either the antiferroelectric or the ferroelectric state, a rectangular field-strain hysteresis loop appears. This feature can be applied to a digital displacement transducer because of the two on/off strain state.[1)] So far, in the field of thin films, the research efforts have concentrated to the materials using the inverse piezoelectric effects, such as PZT. On the other hand, the phase-change-related strains in antiferroelectric thin films have not been investigated in detail.

Lead zirconate ($PbZrO_3$, PZ) is a typical antiferroelectric material. For bulk PZ ceramics, field-induced antiferroelectric (AFE)-to-ferroelectric (FE) phase transformation is observed only near the Curie Point (~230°C).[2)] A modified composition system, such as $Pb_{0.97}La_{0.02}(Zr_{0.66}Sn_{0.25}Ti_{0.09})O_3$, is used usually for bulk ceramics, and the induced strain reaches up to 0.85%.[3)] In the case of thin films, some recent papers have reported that field-induced AFE-FE switching occurred in non-doped PZ films [4,5)] and in doped PZ films [6,7)] at room temperature.

We recently confirmed that the polycrystalline PZ thin films prepared by chemical solution deposition exhibited the signs of the double hysteresis loop in polarization-field measurement.[8)] In the present paper, we report the electrical and electromechanical properties of the optimized PZ thin films in detail. The non-doped PZ thin films deposited on $Pt/Ti/SiO_2/Si$ substrate exhibited a double hysteresis loop in field-polarization measurement, and a rectangular hysteresis loop in field-displacement measurement, indicating that the electric field-induced AFE to FE phase transformation occurred at room temperature.

EXPERIMENTAL

PZ films were fabricated from two sol-gel type solutions. The starting Pb/Zr ratio of the solutions was 1.1/1. The solutions were spin-coated onto a $Pt/Ti/SiO_2/Si$ substrate. The films were then dried in air at 400°C for 10 min. This process was repeated 3 times, and the films were crystallized in air at various temperatures (600 – 700°C) for 1h.[8)] The obtained film was (111) oriented, the thickness was 500nm. Thin film Pt top electrodes were deposited by magnetron sputtering. Depth profile of the films were measured by secondary ion mass spectroscopy (CAMECA, IMS-6F). The polarization hysteresis loops and the dielectric constants were measured by means of a Radiant Technology Ferroelectric tester, RT66A and Agilent Technology impedance analyzer, 4192A, respectively. The dielectric constants were computed from the capacitance measured in a small signal oscillation voltage of 100mV and frequency of 100kHz. Measurements of the electric-field-induced displacements in PZ films were performed using a combination of scanning probe microscopy (SPM, SEIKO SPI3800N) and a ferroelectric tester (aixACCT TF2000).[9)] The period of one measurement cycle was 200ms.

RESULTS AND DISCUSSION

Figure 1 shows the depth profiles of PZ films on $Pt/Ti/SiO_2/Si$ annealed at (a) 600°C and (b) 700°C, respectively. Judging from the profile of Zr, Pt electrodes appear after about 500s etching. Compared to Zr, Pb is distributed not only in the PZ film but also in the electrode region. It is considered that Pb has the tendency to diffuse into Pt and SiO_2 regions, probably due to the restrained reactivity between Pb and Zr. In this experiment, 10mol % excess Pb was added in the initial solution. It is estimated that the excess Pb compensates for the loss both by the evaporation from the film surface and by the diffusion into electrode and substrate to form $PbZrO_3$ film. Comparing the two figures, Pb diffusion into the electrode and surface regions, and Pt, Ti, and Si diffusion into PZ films, are accelerated by higher temperature annealing.

The polarization hysteresis loops of the PZ films are shown in Figure 2. In the films annealed at 600°C, the field-induced phase transformation was not recognized at the field applications up to 400kV/cm. The films annealed at 650°C and 700°C exhibited double hysteresis loops, indicating AFE to FE phase transformation. The field in which phase switching occurs decreases slightly with increases in annealing temperature. This is probably due to the increase of the PZ grain size. On the other hand, the films annealed at 650°C exhibited more square loop than the film annealed at and 700°C. The reason for this would be explained as follows. As shown in Fig.1, higher temperature annealing accelerated Pb diffusion into the electrode and surface regions, and Pt, Ti, and Si diffusion into PZ films. These interdiffusions might lead to the increase of leakage components and the distribution of the film chemical composition, resulting the deterioration of the squareness of the polarization hysteresis loop.

Although pure PZ bulk does not show a double hysteresis loop at room temperature, the PZ film studied here did exhibit a double hysteresis loop. Two possible reasons for this can be proposed. One reason is that the higher breakdown field of the thin films enables a field application which exceeds the switching field. The other reason is that the film has the defect structure similar to the one in the Sn-doped ceramics. At any rate, in terms of control of the manufacturing process, PZ film has an advantage in that it contains only two metal components.

As far as we know, temperature-dependent polarization hysteresis loops in the PZ films have not reported so far, we measured those for the films annealed at 650°C. The results in the temperature range from 23°C to 220°C are shown in Figure 3. The switching field decreased with increases in measuring temperature; for example, 300KV/cm is required to exhibit AFE to FE phase transformation in the forward direction at 23°C, while the phase transformation occurs under 210-220kV/cm at 100°C. The sign of the neck in the loop is barely recognized at 200°C, the loop shape at 220°C were judged to be that of a ferroelectrics. Through the temperature range from 23°C to 220°C, the saturated polarization values were almost identical.

The temperature-dependent dielectric constant is shown in Figure 4. Dielectric anomaly was observed at 224°C on heating. This value is close to the reported value of 230°C in the bulk [2] and corresponds well to the result of the temperature dependent polarization loops.

Polarization hysteresis change after cycling was also investigated. The load was a rectangular 20V unipolar or ±20V bipolar pulse. 20V is equivalent to 400kV/cm, and the frequency was 100Hz in each measurement. Polarization decrease was recognized in both samples, with the degradation more severe in the sample after bipolar pulse switching. The degradation have been observed in the doped PZ ceramics [3] and in the non-doped PZ thin films [4]. The mechanism of these degradations is not clear at present; however, the prescription to overcome the polarization fatigue problem in a thin ferroelectric capacitor might help to solve the reliability problem of the antiferroelectric PZ thin film capacitor.

The field-induced displacement for the PZ films annealed at 650°C were measured by scanning probe microscopy is given in Figure 5. A typical rectangular field-strain hysteresis loop appears. Tani *et al.* reported the field-strain loop of the sol-gel deposited PZ films measured by interferometer and the loop were asymmetric with the applied field direction. The observed strain loop in this study is almost symmetric and well corresponds to the polarization hyseresis loop. The obtained displacement values of 3.2-3.4 are equivalent to strains of 6.4-6.8 x 10^{-3}. These are comparable to the Sn-doped PZ ceramics strain of 8.5 x 10^{-3}.

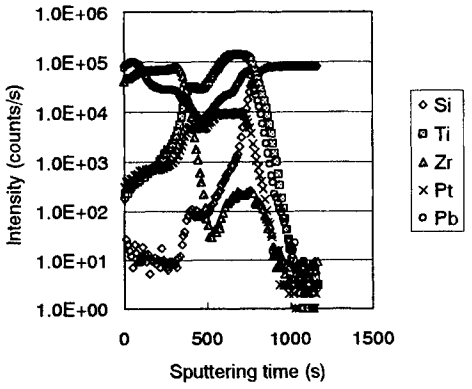

(a)

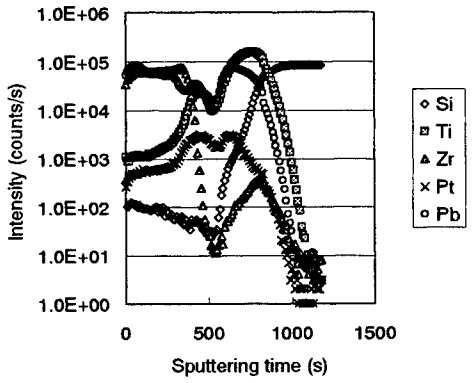

(b)

Fig.1 Depth profile of the PZ films on $Pt/Ti/SiO_2/Si$ annealed at (a) 600°C and (b) 700°C.

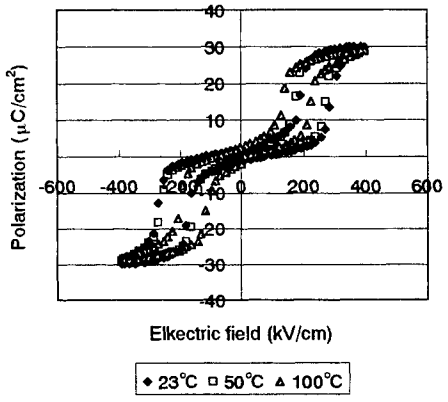

(a)

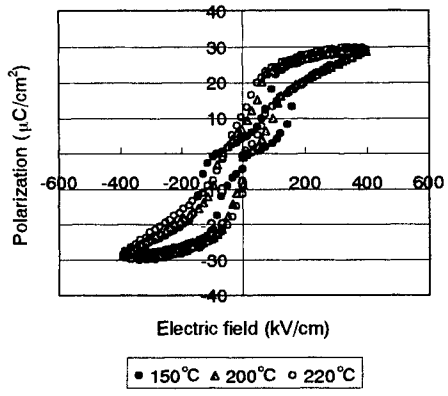

(b)

Fig.3. Polarization hysteresis loops were measured at various temperatures in the PZ films annealed at 650°C.

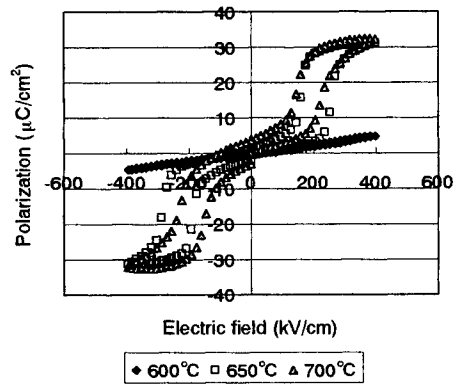

Fig.2 Polarization hysteresis loops of the PZ films annealed at 600°C , 650°C, and 700°C.

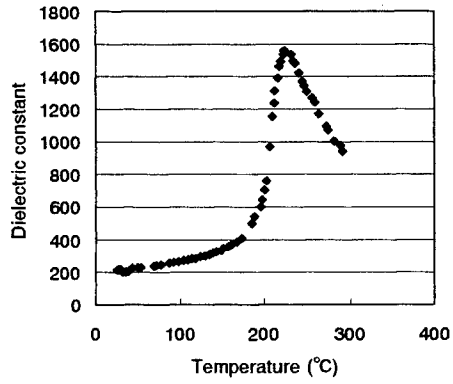

Fig.4. Temperature-dependent dielectric constant for the PZ films annealed at 650°C.

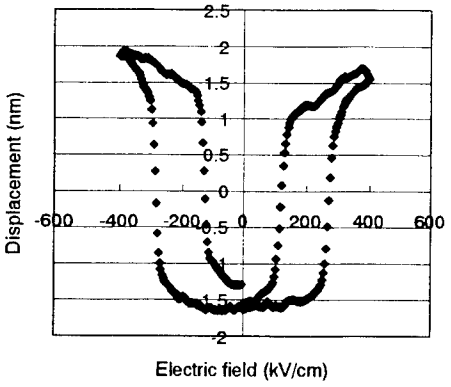

Fig.5. Field-induced displacement of the PZ films annealed at 650°C.

CONCLUSION

Properties of PZ films on Pt/Ti/SiO_2/Si prepared by chemical solution deposition were investigated. Without doping, the electric-field-induced antiferroelectric to ferroelectric phase transformation was observed at room temperature. The switching fields were 300kV/cm in the forward direction and 190kV/cm in the backward direction at room temperature. The switching field decreased with increases in measuring temperature, and at 220°C polarization hysteresis loop took the shape of that of a ferroelectrics. While, the saturation polarization were almost identical up to 220°C. In small signal measurement, dielectric anomaly was observed at 224°C.

The strain accompanied by the phase transformation was observed by means of scanning probe microscopy. Symmetric rectangular field-strain hysteresis loops, peculiar to the antiferroelectrics, exhibited. The observed maximum strain values were 6.4-6.8 x 10^{-3} and comparable to those of Sn-doped PZ ceramics.

In summary, we demonstrated that the PZ thin films possess both electrical and electromechanical on/off states in the unipolar field direction. The results obtained in this study indicate that PZ thin films have great potential applications in digital displacement actuator, transducer and electrical and mechanical memory devices in miniaturized and integrated systems.

ACKNOWLEDGEMENTS

The authors thank Mr. Shibata of Ya-man Ltd. for SPM measurements and Mr. Iinuma and Mr. Ishiwata for sample preparation.

REFERENCES

1 K. Uchino, "Piezoelectric actuators and ultrasonic motors", Kluwer Academic Publishers, (1996).
2 G. Shirane, E. Sawaguchi, and Y. Takagi, Phys. Rev. **84**, 476, (1951).
3 W. Pan, Q. Zhang, A. Bhalla, and L.E. Cross, J. Am. Ceram. Soc., **72** 571, (1989).
4 T. Tani, J-F. Li, D. Viehland, and D. A. Payne, J. Appl. Phys. **75**, 3022, (1994).
5 K. Yamakawa, S.Trolier-Mckinstry, and J. P. Dougherty, Proc. 10th Int. Symp. Appl. Ferroelectrics, p.405 (1996)
6 Y. Akiyama, S. Kimura, and I. Fujimura, Jpn. J. Appl. Phys., **32** 4154, (1993).
7 J. H. Jang, and K.H. Toon, Jpn. J. Appl. Phys., **38** 5162, (1998).
8 H. Maiwa and N. Ichinose, Ferroelectrics, in press.
9 H. Maiwa and N. Ichinose, Jpn. J. Appl. Phys., **39** 5403, (2000).

Microelectromechanical Systems (MEMS) Accelerometers Using Lead Zirconate Titanate Thick Films

L-P. Wang*, R. Wolf*, K. Deng†, L. Zou†, Y. Wang*, P. Wlodkowski†, R. J. Davis*, and S. Trolier-McKinstry*

*Penn State University, University Park, PA 16802
†Wilcoxon Research, Gaithersburg, MD 20878
FAX: 814-865-2326
STMcKinstry@psu.edu

ABSTRACT

MEMS (micro-electro-mechanical system) accelerometers using lead zirconate titanate (PZT) 52/48 films as the active sensing element were designed and fabricated. 6 mm square MEMS accelerometers in trampoline and annular diaphragm configurations were designed with thick (1.5 – 7 μm) PZT films on Si flexing elements, with a heavy Si proof mass to increase the sensitivity. The PZT films were deposited from an acetylacetonate modified sol-gel solution, using multiple spin coating, pyrolysis, and crystallization steps. The resulting films show good dielectric and piezoelectric properties, with P_r values > 20 $\mu C/cm^2$, ε_r > 800, tanδ < 3%, and $|e_{31(eff)}|$ values > 4 C/m^2. The proof mass fabrication, as well as the accelerometer beam definition step, was accomplished via deep reactive ion etching of the Si substrate. The resulting accelerometers show sensitivities ranging from 0.1 to 7.6 pC/g with resonance frequencies from 44.3 to 3.7 kHz. These accelerometers are being incorporated into packages including ASIC electronics and an rf telemetry system to facilitate wireless monitoring of industrial equipment.

INTRODUCTION

Micromachined piezoelectric accelerometers offer the possibility of higher sensitivities than are currently available using capacitive or piezoresistive devices. Typically, the sensitivities of MEMS accelerometers using ZnO films are relatively small [1-4] since the electromechanical coupling coefficients and the piezoelectric constants of ZnO are an order of magnitude smaller than those of PZT films. Consequently, this work concentrated on the use of PZT films. There are previous reports on MEMS piezoelectric accelerometers utilizing PZT [5-8]. The novelty of this work results from the combination of a new sensor design with thick film PZT and deep-trench reactive ion etching (DRIE).

DEVICE DESIGN AND FABRICATION

Two main sensing structures were investigated, a trampoline – style sensor, in which the proof mass is suspended at the juncture of crossed beams, and a circular diaphragm sensing structure [9] with an annular membrane with a suspended proof mass (See Fig. 1). The thickness of the Si layer supporting the PZT film/electrode stack is between 6 and 45 microns. The piezoelectric film is deposited on a bottom electrode so that it can be poled through its thickness, and the top electrodes are adjusted

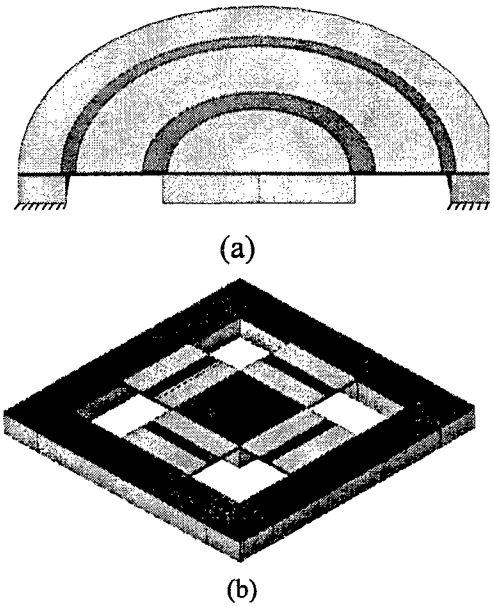

Figure 1. Schematics showing the cross sections of (a) an annular diaphragm and (b) a trampoline –style MEMS accelerometer.

so that the areas are identical. Compared with beam-type sensing structures, the annular design uses area efficiently, has a high resonant frequency and wide bandwidth, and low sensitivity to transverse acceleration. From a fabrication standpoint the design does not require through-etching the silicon to release the membrane, therefore, the fabrication process is simplified and yield can be enhanced. Consequently, most of the results are reported for the annular design. Details on the sensor design and modeling are given elsewhere [10].

For both designs, the stresses are of opposite signs for the outer (i.e. close to the frame) and inner sides of the diaphragm; therefore, the top electrodes are separated in order to pole the two sections in opposite directions. When the outputs of the electrodes are connected in parallel, the pyroelectric output of the sensor should be cancelled. To lower the overall sensor capacitance (to ~6 nF), the top electrodes are placed only over highly stressed areas. The die size was 6 mm x 6 mm.

The MEMS accelerometers reported here were fabricated on 4-inch diameter, double-side-polished, n-type <100> silicon wafer. 0.8μm of wet silicon oxide was grown on both sides of the wafer, and the bottom Ti/Pt electrode (200Å Ti, 1500Å Pt) was then sputtered (NOVA Electronic Materials Inc.). Thick PZT films were then deposited using a chemical solution deposition approach. In brief, films were prepared from 2 – methoxyethanol based solutions using lead acetate trihydrate, zirconium n-propoxide, and titanium isopropoxide as precursors. 0.7 to 0.8 Molar solutions were prepared and modified with 22.5 vol% acetylacetonate (Aldrich Chemical Co.). The solution was batched to produce the morphotropic phase boundary composition, $Pb(Zr_{0.52}Ti_{0.48})O_3$, with 20 mole% excess lead.

The sol was deposited by spin-coating at 1500 rpm for 30 sec on a photoresist spinner (Headway Research, Inc., Garland, TX). After deposition, each layer was subjected to a two-stage pyrolysis sequence. A 1 - minute 300°C heat treatment was immediately followed by one at 450 - 500°C. Thelayer was then crystallized to a phase-pure perovskite at 700°C for 30 sec in an RTA furnace (A. G. Associates, San Jose, CA). A multilayering scheme was employed to achieve the desired film thickness (~1 – 7 μm). The resulting PZT films had relative permittivities in the range of 800 to 100, a tan δ < 0.03, P_r ~ 20 $\mu C/cm^2$, and a product of d_{31} x Young's modulus of ~ – 4 to –5 C/m^2. Fig. X shows the piezoelectric properties of the films as a function of thickness and composition. All devices were made using the 52/48 Zr/Ti ratio in order to maximize the piezoelectric response.

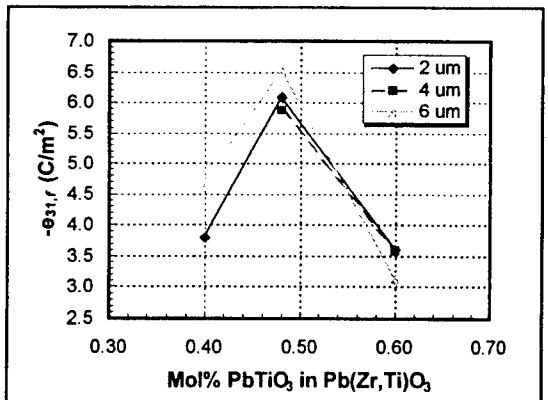

Figure 2: Piezoelectric response of the PZT films as a function of the Zr/Ti ratio and the film thickness. $e_{31,f}$ = surface charge developed/(sum of in-plane strain)

Following the PZT deposition, the top Cr (8nm) and Au (80 nm) electrode was deposited via thermal and electron – gun evaporation, respectively. Photoresist was then coated on both sides of the wafer and front-to-back side alignment was done using a mechanical jig in a Karl Suss MA6 aligner. After development, the top electrode was wet-etched, and the backside oxide was reactive ion etched in CF_4/O_2. The resist was then stripped from both sides. After recoating the back with a blanket layer of photoresist, the PZT was etched using a 2 step process [11]. The bottom electrode was then patterned using reactive ion etching. To complete the back-side of the wafer, 13 μm thick AZ 4620 photoresist was used to define the die frames, diaphragms, and proof masses. After defining the beam and diaphragm thicknesses with a short DRIE step, a buffered oxide etch was used to remove the patterned oxide on the beam areas. After this a second DRIE step was used to etch through the wafers (for the trampoline design). The sidewall of the proof mass had an angle of ~83°. After stripping the remaining front-side oxide, and stripping the resist, the dies were separated. An example of a completed annular accelerometer is shown in Fig. 3.

MEASUREMENTS

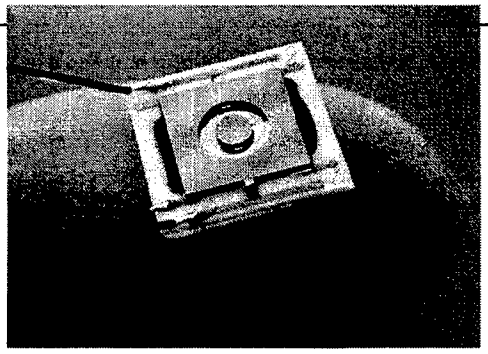

Figure 3: Backside of an annular MEMS accelerometer flip-chip bonded to a carrier.

Dynamic frequency response measurements were performed to evaluate the accelerometers. The devices were attached to ceramic substrates with screen-printed contact pads and wire-bonded contacts were made. Wires were soldered to the ceramic substrates for signal output. The MEMS accelerometer was connected to a charge amplifier with an amplification of 10 mV/pC. The reference accelerometer (Wilcoxon Research 05238) was connected to a charge amplifier (Wilcoxon Research CC701). The outputs of both accelerometers were connected to a two-channel dynamic signal analyzer for a comparative transfer function measurement. A swept-sine signal, generated by the analyzer and enhanced by a power amplifier was used to drive an electromagnetic shaker (Wilcoxon Research AV50) to mechanically excite both accelerometers. Fig. 4 shows the measured frequency response of one fabricated MEMS accelerometer.

RESULTS AND DISCUSSION

Good sensitivities and broad usable frequency ranges (see Table I) were obtained; the sensitivities of the annular accelerometer range from 0.77 to 7.6 pC/g with resonant frequencies from 35.3 to 3.7 kHz. The sensor-to-sensor variations were caused largely by variations of the silicon membrane thickness because of non-uniformity in the Si DRIE etching. The measured sensitivities were, for thick (> 30 μm) supporting Si membranes, ~36% lower than the sensitivity calculated from finite element analysis using a $d_{31(eff)}$ x Young's modulus for the PZT film of –4.5 C/m^2 which was measured on a test die on the same wafer [16]. The transverse sensitivity was found to be <2% of the sensitivity along the principal axis. The discrepancy between the measured sensitivity and the FEA calculations is believed to be due to the ~20μm tolerance in the mechanical front & backside alignment, residual stress in the membrane, and piezoelectric film variations. Fewer measurements were made for the sensitivity of the trampoline accelerometer. Fig. 4 shows the result of one such measurement, in which a sensitivity of 0.1 pC/g was obtained with a resonant frequency of 44 kHz.

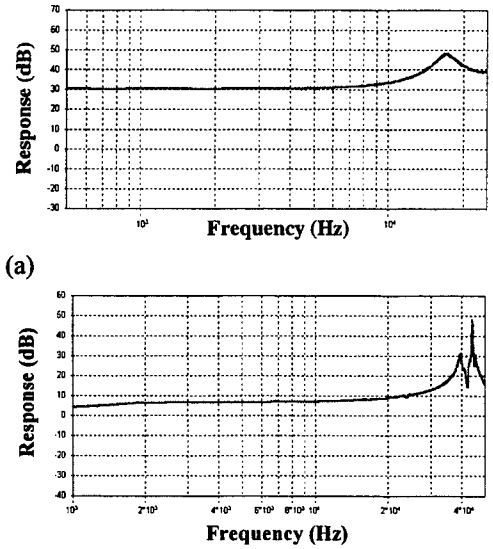

Figure 4. (a) Typical frequency response of an annular MEMS accelerometer; the resonant frequency is 17.4 kHz and the sub-resonance sensitivity is 1.4 pC/g. (b) Sensitivity of a trampoline – style accelerometer. In both cases, the response is flat below the first resonant frequency.

ACCELEROMETER INTEGRATION

Wilcoxon Research has developed a low power ASIC for amplifying the piezoelectric signal, filtering and processing the signal and performing analog to digital signal conversion. The MEMS accelerometer connected to the ASIC is managed by a DSP which also controls a Bluetooth rf system for wireless transmission of the accelerometer signal. Battery power management is achieved by a combination of the ASIC and the DSP. The MEMS contributes to both the minimization of the size of the instrument and to the low power requirements of

the circuitry thus enabling the integration of a low-profile, high sensitivity, wireless accelerometer.

CONCLUSIONS

Piezoelectric MEMS accelerometers using an annular diaphragm and 5.6 μm thick PZT films demonstrate high sensitivities (0.1 to 7.6 pC/g) and broad usable frequency ranges (44 to 3.7 kHz). The annular piezoelectric inertial sensing structure is an efficient design and is compatible with the piezoelectric film and IC fabrication processes.

TABLE I: Measured results in comparison with the simulated results

Measured Results		**FEA Calculation**	
Resonant Frequency (kHz)	Sensitivity (pC/g)	Sensitivity (pC/g)*	Silicon membrane thickness[1] (μm)
3.7	*7.60*	*15.0*	6.1
17.4	*1.45*	*2.10*	21.2
27.5	*1.06*	*1.18*	36.8
35.3	*0.77*	*0.84*	44.4

* The sensitivity was calculated using d_{31}*Young's modulus = – 4.5 C/m^2, which was measured on a test die on the same wafer

[1] The silicon thickness was calculated from the measured resonance frequency

ACKNOWLEDGEMENTS

The authors thank the National Institute of Standards and Technology for supporting this research under WR-ATP-0001, and the Penn State and Cornell Nanofabrication Facilities.

REFERENCES

[1] P. L. Chen, R. S. Muller, R. D. Jolly, G. L. Halac, R. D. White, A. P. Andrews, T. C. Lim, and M. E. Motamedi, *IEEE Trans. Electron. Dev.*, vol. ED-29, no. 1, pp. 27-33, 1982.

[2] P. L. Chen and R. S. Muller, *Sens. Actuators*, vol. 5, pp. 119-126, 1984.

[3] D. L. DeVoe, and A. P. Pisano, *IEEE Int. Conf. Solid-State Sens. Actuators*, vol. 2, pp. 1025-1028, 1997.

[4] R. de Reus, J. O. Gullov, and P. R. Scheeper, *J. Micromech. Microeng.*, vol. 9, pp. 123-126, 1999.

[5] J. H. Kim, L. Wang, S. M. Zurn, L. Li, Y. S. Yoon, and D. L. Polla, *Int. Ferroelec.*, vol. 15, pp. 325-332, 1997.

[6] D. Eichner, M. Giousouf, and W. von Munch, *Sens. Actuators*, vol. A76, pp. 247-252, 1999.

[7] S. P. Beeby, N. Ross, and N. M. White, *IEEE Electron. Lett.*, vol. 35, no. 23, pp. 2060-2062, 1999.

[8] S. P. Beeby, N. Ross, and N. M. White, *J. Micromech. Microeng.*, vol. 10, p. 322-328, 2000.

[9] Patent pending, The Pennsylvania State University and Wilcoxon Research.

[10] L.-P. Wang, K. Deng, L. Zou, R. Wolf, R. J. Davis, and S. Trolier-McKinstry, submitted to IEEE Elec. Dev. Lett.

[11] L.-P. Wang, Ph.D. Thesis, Penn State University, 2001.

[12] J. F. Shepard, Jr., P. J. Moses, and S. Trolier-McKinstry, *Sens. Actuators A,* vol. 71, pp. 133-138, 1998.

Piezoelectric Properties of $Pb(Yb_{1/2}Nb_{1/2})O_3$-$PbTiO_3$ Epitaxial Films with (100) and (111) Orientation

Takeshi Yoshimura and Susan Trolier-McKinstry
Materials Research Institute, The Pennsylvania State University
University Park, PA 16802, USA
Email: txy7@psu.edu

The orientation dependence of the piezoelectric and ferroelectric properties for $(1-x)Pb(Yb_{1/2}Nb_{1/2})O_3$-$xPbTiO_3$ (PYbN-PT, x=0.4, 0.5) epitaxial films was investigated. (001) and (111) PYbN-PT films with $SrRuO_3$ bottom electrodes were grown epitaxially on (001)$LaAlO_3$, (001)$SrTiO_3$, and (111)$SrTiO_3$ substrates by pulsed laser deposition. In the (001)PYbN-PT (50/50) film, the highest remanent polarization (29 $\mu C/cm^2$) and effective piezoelectric coefficient $e_{31,f}$ (-14 C/m^2) were observed. The transition temperature of the (001)PYbN-PT (50/50) film was around 380 °C.

INTRODUCTION

Microelectromechanical systems (MEMS) have shown significant promise for miniaturized devices.[1-3] Piezoelectric thin films are one of the key elements to enhance the sensing and actuation function of such devices. Relaxor ferroelectric films are especially attractive, since relaxor based ferroelectric single crystals exhibit very large piezoelectric responses.[4] Although there are several reports on the deposition and properties of relaxor-$PbTiO_3$ films, most of materials on these studies such as $Pb(Mg_{1/3}Nb_{2/3})O_3$-$PbTiO_3$ have relatively low transition temperature (typically <200 °C).[5-7] For MEMS applications, since temperature stability of the piezoelectric properties is also important, ferroelectrics with high transition temperature are attractive. Of the known relaxor ferroelectric-$PbTiO_3$ solid solutions, $(1-x)$ $Pb(Yb_{1/2}Nb_{1/2})O_3$-$xPbTiO_3$ (PYbN-PT) has the highest transition temperature (~360 °C) near the morphotropic phase boundary (x~0.5).[8-12] In this study, the orientation dependence of the ferroelectric and piezoelectric properties of PYbN-PT epitaxial films with compositions of x=0.5 and 0.4 were investigated.

EXPERIMENTAL PROCEDURE

(001)$LaAlO_3$, (001)$SrTiO_3$, and (111)$SrTiO_3$ single crystal wafers were used as the substrates. (Note that in this paper, the Miller indexes of all material are given in terms of a pseudocubic unit cell.) PYbN-PT films and $SrRuO_3$ bottom electrodes were prepared by pulsed laser deposition (PLD) using a KrF excimer laser (Lambda Physik Compex 102) with a 248 nm wavelength. Details on the epitaxial growth of $SrRuO_3$ films are given elsewhere.[10,13] $SrRuO_3$ bottom electrodes were deposited using stoichiometric $SrRuO_3$ ceramic targets (Target Materials Inc.), while PYbN-PT films were deposited using sintered ceramics of PYbN-PT with 50:50 and 60:40 compositions, including 25 wt% excess PbO to compensate lead loss during growth.[5,10-12] Oxygen and ozone gases were introduced to the deposition chamber using a commercial ozone generator (PCI). The specific deposition conditions of the $SrRuO_3$ bottom electrodes and PYbN-PT films are given in Table I.

The structure and crystallinity of the films were characterized by x-ray diffraction (XRD) using Cu-Kα radiation. θ-2θ scans and ω scans were performed using a Scintag Pad V diffractmeter. For texture analyses, ϕ scans were performed using an X'PERT Phillips four circle diffractometer. To characterize electrical properties, Ar/Cr dot electrodes (area= 0.040-0.128 mm^2) were fabricated by thermal evaporation and photolithographic processing. Low and high-field dielectric properties were

Table I. Deposition conditions for $SrRuO_3$ and PYbN-PT films.

	$SrRuO_3$	PYbN-PT
Temperature	730-760°C	620-680°C
Atmosphere	100% O_2	10% O_3 90% O_2
Pressure	200 mTorr	400 mTorr
Laser energy density	1.2 J/cm^2	1.5 J/cm^2
Laser frequency	10 Hz	2-5 Hz
Number of laser shots	15000	3000
Target to substrate distance	8 cm	4.5 cm
Thickness	300 nm	1000 nm

measured using an impedance analyzer (HP4192A) or a Radiant Technologies RT66A standard ferroelectrics tester. The effective piezoelectric transverse coefficient ($e_{31,f}$) were measured using a modification of the wafer flexure method described previously.[14,15] $e_{31,f}$ is defined for a thin film clamped on a substrate as

$$e_{31,f} = \frac{d_{31}}{s_{11}^E + s_{12}^E} \quad (1)$$

where d_{31} is the transverse piezoelectric coefficient (C/N) and s_{ij}^E are the elastic compliance coefficients (N/m^2) under steady electric field.[1,2,16,17] $e_{31,f}$ is determined by bending the substrate and collecting the developed charges as

$$D_3 = e_{31,f}(x_1 + x_2), \quad (2)$$

where x_1 and x_2 are the strain components in plane and D_3 is the induced dielectric displacement (C/m^2). Thus, Young's modulus and Poisson's ratio of the film material are not required to calculate $e_{31,f}$. Prior to each test, samples were poled with a DC electric field (typically two or three times their coercive field) for 20 min. On all measurements of ferroelectric and piezoelectric properties, the electric field was applied to the top electrode.

RESULTS AND DISCUSSION

Optimization of the growth conditions for PYbN-PT epitaxial films was carried out on (001)$SrRuO_3$/(001)$LaAlO_3$ substrates using the 50:50 composition target. PYbN-PT films were deposited at various substrate temperatures and laser frequencies. Although (001)PYbN-PT epitaxial films with good phase purity were obtained for a wide range of deposition rates (60-90 nm/min) and temperatures (620-680 °C), it was found that the best temperature to grow PYbN-PT epitaxial films was from 650 °C to 660 °C. Figure 1 shows the XRD θ-2θ pattern for the PYbN-PT film deposited at 650 °C and a laser frequency of 3 Hz. A strong diffraction peak corresponding to PYbN-PT (002) was obtained. Although small peaks were present at 31° and 34.7°, which were corresponded to PYbN-PT (110) and pyrochlore respectively, the intensity ratio of the small peaks to PYbN-PT (002) peak was <0.1%. The full width at half maximum (FWHM) of the θ-2θ profile and

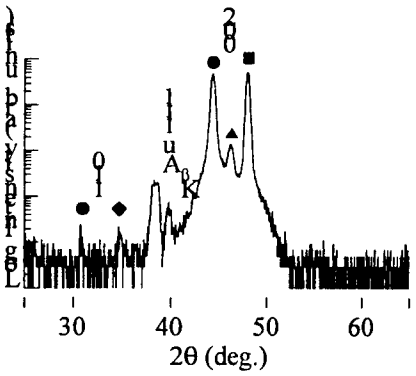

Fig. 1. XRD θ-2θ pattern for the PYbN-PT film deposited on a (001)$SrRuO_3$/(001)$LaAlO_3$ substrate. (_) perovskite PYbN-PT, (_) $LaAlO_3$, (_) $SrRuO_3$, (_) pyrochlore.

rocking curve (ω scan) for the PYbN-PT 002 reflection were 0.23° and 0.59°, respectively. Figure 2 shows φ scans of the PYbN-PT 101 and $LaAlO_3$ 101 reflections for the PYbN-PT film shown in Fig. 1. Although a small amount (<0.1%) of grains were misoriented by 45° in-plane, cube-on-cube epitaxial growth of PYbN-PT films was confirmed. The FWHM of the φ scan profile for PYbN-PT 101 reflection was 1°.

The ferroelectric properties of the (001) PYbN-PT (50/50) epitaxial films on (001) $SrRuO_3$/(001)$LaAlO_3$ were also characterized. Figure 3 shows the temperature dependence of the dielectric constant and loss. This measurement was performed during cooling. The dielectric constant exhibits a peak near 380 °C; this temperature is consistent with the value obtained in bulk ceramics with the same composition. At room temperature, the dielectric

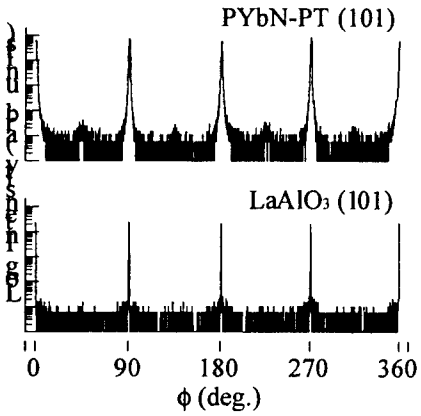

Fig. 2. φ scans of PYbN-PT 101 and $LaAlO_3$ 101 reflections for the PYbN-PT film shown in Fig. 1.

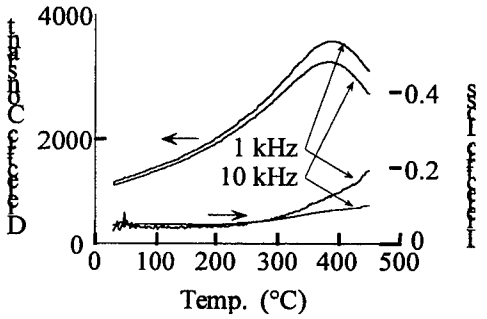

Fig. 3. The temperature dependence of the dielectric constant and loss for a (001) PYbN-PT (50/50) film on (001)$SrRuO_3$/(001) $LaAlO_3$.

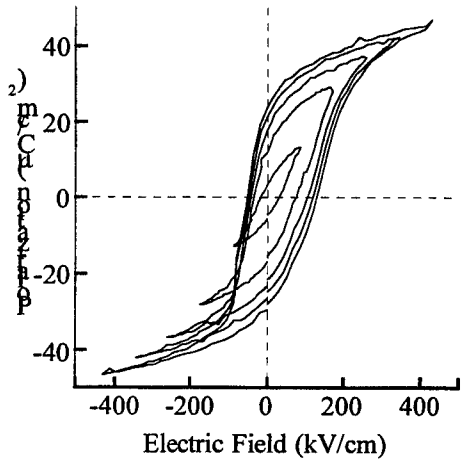

Fig. 4. Polarization hysteresis loops for a (001) PYbN-PT (50/50) film on (001)$SrRuO_3$/(001) $LaAlO_3$.

constant and loss were 900 and 0.05, respectively. As shown in Fig. 4, well-developed polarization hysteresis loops were also obtained in the (001) PYbN-PT (50/50) film. The remanent polarization was 29 $\mu C/cm^2$.

(001)PYbN-PT (60/40) epitaxial films were grown on (001)$SrRuO_3$/(001)$LaAlO_3$ substrates at 650 °C, which was the same deposition condition as (001)PYbN-PT (50/50) films. In terms of the crystalline quality, there were no significant differences between the PYbN-PT (50/50) films and the PYbN-PT (60/40) films. Details of the crystalline quality and the electrical properties for (001)PYbN-PT (60/40) epitaxial films are summarized in Table II.

To obtain (111)PYbN-PT epitaxial films, films were deposited on (111)$SrRuO_3$/(111)$SrTiO_3$ substrates. Since it is reported that the piezoelectric properties of films depend on the substrate due to the difference of the thermal expansion rate or the lattice mismatch,[18] PYbN-PT films were also deposited on (001)$SrRuO_3$/(001)$SrTiO_3$ substrates. At 650 °C, (001)PYbN-PT epitaxial films with good crystalline quality were obtained on (001) $SrRuO_3$/(001)$SrTiO_3$ substrates. However, PYbN-PT films deposited on (111)$SrRuO_3$/(111)$SrTiO_3$ substrates were not crystallized. To optimize the growth conditions on (111)$SrRuO_3$/(111)$SrTiO_3$ substrates, PYbN-PT (50/50) films were deposited at various substrate temperatures. Figure 5 shows XRD patterns of these films. It was found that the optimum growth temperature to grow epitaxial films depended on the orientation of the substrates. (111)PYbN-PT (50/50) epitaxial films with good phase purity were obtained at 600-620 °C. In the same way, the optimum growth temperature for (111)PYbN-PT (60/40) epitaxial films was 620 °C.

Thus, in both 50:50 and 60:40 compositions, PYbN-PT epitaxial films were obtained on (001)$LaAlO_3$, (001)$SrTiO_3$, and (111)$SrTiO_3$ substrates. Although in some cases misoriented grains of perovskite PYbN-PT or pyrochlore phase were observed by XRD, the amount estimated from the intensity ratio of the diffraction peaks was less than 1%. The piezoelectric coefficients $e_{31,f}$, electrical properties, and crystalline quality for these films are listed in Table II.

In both 50:50 and 60:40 compositions, (001) epitaxial films showed lower dielectric constants

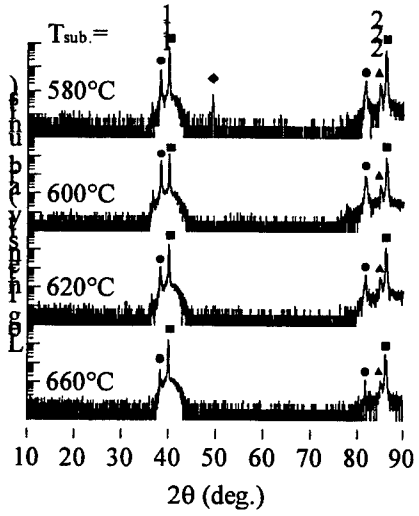

Fig. 5. XRD θ-2θ patterns of PYbN-PT (50/50) films deposited at various substrate temperatures on the (111)$SrRuO_3$/(111)$SrTiO_3$ substrates. ○ perovskite PYbN-PT, ◯ $SrTiO_3$, ◯ $SrRuO_3$, ◯ pyrochlore.

Table II. The crystalline quality, electrical properties, and piezoelectric coefficient $e_{31,f}$ for the (1-x)PYbN-xPT epitaxial films.

Substrate	Orientation	x	FWHM $\Delta 2\theta$, $\Delta\omega$, $\Delta\phi$	ε_r at 1kHz, R.T.	$T\varepsilon_{Max}$ (°C)	Pr ($\mu C/cm^2$)	$e_{31,f}$ (C/m^2)
$LaAlO_3$	001	0.5	0.23°, 0.59°, 0.99°	900	380	29	-14
$SrTiO_3$	001	0.5	0.25°, 0.52°, 0.74°	1000		30	-12
$SrTiO_3$	111	0.5	0.26°, 0.89°, 1.76°	1300		25	-3.3
$LaAlO_3$	001	0.4	0.21°, 0.53°, 0.96°	950	320	27	-10
$SrTiO_3$	001	0.4	0.24°, 0.56°, 0.91°	1000		26	-9
$SrTiO_3$	111	0.4	0.18°, 0.71°, 1.48°	1300		24	-2.5

and higher remanent polarizations than (111) epitaxial films. It seems that in (111) epitaxial films, the polarization in some regions of the film is largely in-plane and is not switched by the applied electric field due to the limited non-180° domain wall motion.[11] (001) epitaxial films also showed larger $e_{31,f}$ coefficients. This result is comparable to that previously reported for relaxor-PT single crystal.[4] In both (001) and (111) epitaxial films, PYbN-PT (50/50) films exhibited higher remanent polarizations and $e_{31,f}$ coefficients than PYbN-PT (60/40) films. Thus, the highest $e_{31,f}$ coefficients were obtained on (001)PYbN-PT (50/50) epitaxial films.

CONCLUSION

The ferroelectric and piezoelectric properties of PYbN-PT epitaxial films were investigated. In both 50:50 and 60:40 compositions, well crystallized (001) and (111) PYbN-PT films were obtained. An $e_{31,f}$ coefficient (-14 C/m^2) was observed on (001)PYbN-PT (50/50) epitaxial films deposited on (001)$SrRuO_3$/(001)$LaAlO_3$ substrates.

ACKNOWLEDGMENTS

The authors are grateful to B. Jones and M. Angelone for their cooperation in the ceramic target synthesis and texture analyses, respectively. Support for this work was provided by the Office of Naval Research (U.S.) under Contract No. N00014-98-1-0527.

REFERENCES

1. P. Muralt, J. Micromech. Microeng., **10**, 136 (2000).
2. P. Muralt, IEEE Trans. Ultrason. Ferro. Freq. Control, **47**, 903 (2000).
3. T. Tuchiya, T. Itoh, G. Sakai, and T. Suga, J. Ceram. Soci. Jpn., **104**, 159 (1996).
4. S. E. Park and T. R. Shrout, J. Appl. Phys., **82**, 1804 (1997).
5. J. P. Maria, W. Hackenberger, and S. Trolier-McKinstry, J. Appl. Phys., **84**, 5147 (1998).
6. J. H. Park, F. Xu, and S. Trolier-McKinstry, J. Appl. Phys., **89**, 568 (2001).
7. Z. Kighelman, D. Damjanovic, and N. Setter, J. Appl. Phys., **89**, 1393 (2001).
8. T. Yamamoto and S. Ohashi, Jpn. J. Appl. Phys., **34**, 5349 (1995).
9. H. Lim, H. J. Kim, and W. K. Choo, Jpn. J. Appl. Phys., **34**, 5449 (1995).
10. V. Bornand and S. Trolier-McKinstry, Thin Solid Films, **370**, 70 (2000).
11. V. Bornand and S. Trolier-McKinstry, J. Appl. Phys., **87**, 3958 (2000).
12. V. Bornand, S. Trolier-McKinstry, K. Takemura, and C. A. Randall, J. Appl. Phys., **87**, 3958 (2000).
13. J. P. Maria, S. Trolier-McKinstry, D. G. Schlom, M. E. Hawley, and G. W. Brown, J. Appl. Phys., **83**, 4373 (1998).
14. J. F. Shepard Jr., P. J. Moses, and S. Trolier-McKinstry, Sens. Actuators A **71**, 133 (1998).
15. J. F. Shepard Jr., F. Chu, I. Kanno, and S. Trolier-McKinstry, J. Appl. Phys., **85**, 6711 (1999).
16. P. Muralt, A. Kholkin, M. Kohli, and T. Maeder, Sens. Actuators A **53**, 398 (1996).
17. M-A Dubois, and P. Muralt, Sens. Actuators A **77**, 106 (1999).
18. V. Nagarajan S. P. Alpay, C. S. Ganpule, B. K. Nagarai, S. Aggarwal, E. D. Williams, A. L. Roytburd, and R. Ramesh, Appl. Phys. Lett., **77**, 438 (2000).

Preparation of Texture Controlled Lead Zirconate Titanate Diaphragm Type Film Actuator

Takashi Iijima*, Bo-Ping Zhang and Kouki Kunii[1]

Tohoku national Industrial Research Institute, AIST, MITI, 4-2-1 Nigatake, Miyagino-ku, Sendai 983-8551, JAPAN
Fax: +81-22-236-6839
E-mail: Iijima-t@aist.go.jp
[1]Technical Development Dept., NIDEC COPAL CORPORATION, 37 Suwanai, Tomita, 963-8637 Koriyama, JAPAN

ABSTRACT

A diaphragm type (100) dominant oriented tetragonal phase lead zirconate titanate (PZT) film actuator is fabricated to achieve the micro actuators and acoustic transducers system. The ferroelectric properties of the texture controlled PZT film is relatively good compared with other reported data and is comparable to those of bulk PZT ceramics. The displacement of the PZT film actuator driven at ± 20 V shows a butterfly like hysteresis. However, this butterfly shape shows opposite direction compared with the typical displacement curve of bulk PZT ceramics. This depressed displacement property of the PZT film appears to indicate bend motion in the vertical direction on the film surface since the film is not clamped, and it does not reflect the genuine piezoelectric property. For unipolar drive, the value of the displacement was about 220 nm at 20 V. The deflection amplitude of the diaphragm actuator showed a peak at 77.5 kHz. Therefore, it can be seen that the texture controlled PZT films is applicable to the film micro actuator.

INTRODUCTION

Ferroelectric thin films including lead zirconate titanate (PZT) are in demand for applications in many fields like sensors, memories and actuators. Combination of the preparation technique for the ferroelectric films and the micro machining technique of Si is effective way to fabricate micro actuators for electric devices and acoustic transducers for medical devices called microelectromechanical systems (MEMS) [1-4]. One of the techniques to increase the ferroelectric and piezoelectric properties is supposed to be arrangement of the polarization direction using a texture control process. We reported the preparation process of the (100) and (111) dominant oriented $Pb(Zr_{1-x}Ti_x)O_3$ thin film system using a chemical solution deposition (CSD) process [5]. In this work, the preparation process of the texture controlled PZT film and the diaphragm type micro actuator fabrication process are described. Moreover, the ferroelectric properties of the PZT film are examined, and the displacement property of the diaphragm type PZT micro actuator is measured.

* Present address; Smart Structure Research Center, AIST, 1-1-1 Umezono, Tsukuba 305-8568, Japan
E-mail: Iijima-t@aist.go.jp

EXPERIMENTAL PROCEDURE

To prepare the CSD precursor solutions, we used trihydrated lead acetate (99.9%, Nakarai tesque), titanium iso-propoxide (97%, Kanto chemical) and zirconium iso-propoxide (98%, Kojyundo chemical) as starting materials and 2-methoxyethanol (99.7%, Aldrich) as the solvent. The rate of Zr/Ti was 45/55, which was tetragonal phase, and excess Pb (10 mol%) was added to the solution, so that the nominal compositions of the precursor solutions were equivalent to those of $Pb_{1.1}(Zr_{0.45}Ti_{0.55})O_3$. Details of the preparation of the precursor solutions are described elsewhere [6]. The concentration of the Pb-Zr-Ti precursor solution was controlled at 0.5 M. The precursor solution was deposited onto (111) oriented Pt on $Ti/SiO_2/Si$ substrates using a spin coater operated at 3000 rpm. Before the coating process, a buck side of the $Pt/Ti/SiO_2/Si$ substrate was etched to form a diaphragm shape. A sequence of spin coating and pyrolysis treatment between 400°C and 500°C for 1- 3 min was performed five times, and the samples were fired at 700°C for 10 min in oxygen flow atmosphere. This process was repeated several times to increase the film thickness at 1 μm. A flow diagram of coating process is shown in Fig. 1.

Figure 2 shows the structure of the PZT film actuator. The actuator has a 2.6 mm square

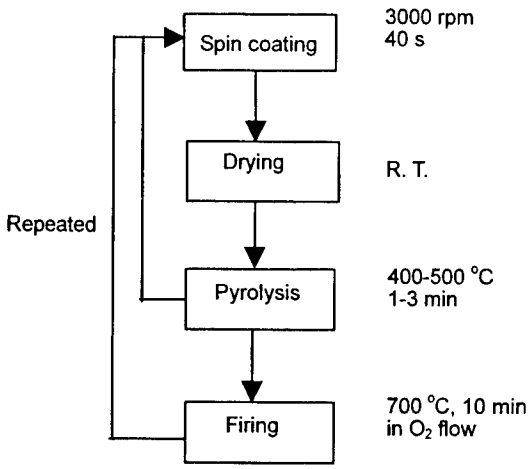

Fig. 1. Flow diagram of thin film preparation process.

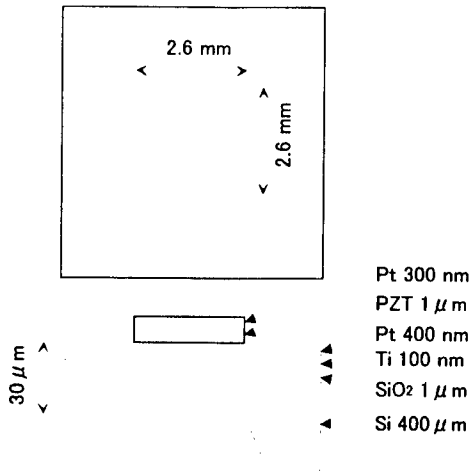

Fig. 2. Schematic diagram of diaphragm type PZT film actuator.

diaphragm. To fabricate the diaphragm thermal oxidized Si wafers were etched using an anisotropic wet etching technique. After etching, Ti and Pt layer for a bottom electrode were sputter deposited onto the surfaces of the SiO_2/Si substrate. PZT thin film was formed as mentioned above, and Pt layer for a top electrode was sputtered on the surfaces of the PZT film. Finally, the top electrode and the PZT layer were patterned using a wet etching process.

The crystal structure of the films was examined by an X-ray diffractometer. The *P-E* hysteresis curves were examined using a ferroelectric test system (RT-6000, Radiant Technologies). To measure the displacement property of the actuator, a heterodyne type laser interferometer (MLD-102, Nihonkagaku Engineering) was connected with the ferroelectric test system or multifunction synthesizer (NF 1945, NF electronic instruments).

RESULTS AND DISCUSSION

Figure 3 shows X-ray diffraction (XRD) patterns of the PZT films. All patterns show a well-defined perovskite structure except for the Pt peak. When the pyrolysis temperature is 400 °C, the PZT film shows (100) dominant orientation. On the other hand, the PZT film pyrolyzed at 500 °C shows (111) preferred orientation. These results are consistent with former experimental results [5]. The degree of the orientation of (100) and (111) plane, α_{100} and α_{111}, is calculated from the formula as follows using the peak intensity (I) of XRD.

$$\alpha_{hkl} = I(hkl) / \{I(100) + I(110) + I(111)\}$$

In the case of the PZT film pyrolyzed at 400 °C, α_{100} is 0.75, whereas α_{111} is 0.69 for the PZT film pyrolyzed at 500 °C.

Figure 4 shows the *P-E* hysteresis curves of the (100) dominant oriented PZT film measured at ± 5 and ± 20 V. It can be seen that the shape of the hysteresis curve is saturated in spite of relatively low applied field (200kV/cm). The values of the remanent polarization (Pr) and the coercive field (Ec) are 11 μC/cm^2 and 45 kV/cm, respectively. It can be seen that the amount of Pr is not so high compared with randomly oriented PZT films [4, 7]. The reason of the relatively low rectangularity is considered to be the difference of the polarization direction from the texture-oriented direction. On the other

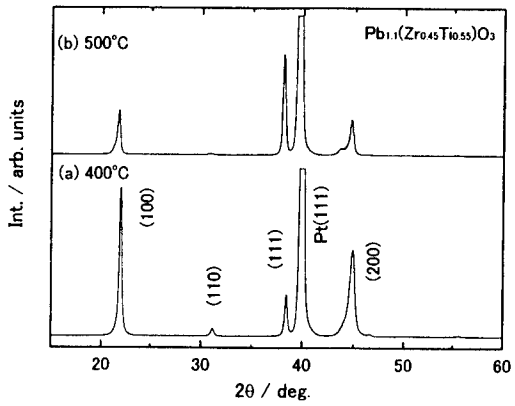

Fig. 3. XRD result of $Pb_{1.1}(Zr_{0.45}Ti_{0.55})O_3$ film. (a) Pyrolyzed at 400 °C, (b) Pyrolyzed at 500 °C.

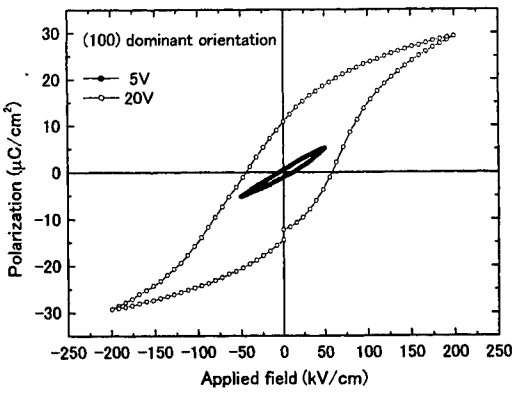

Fig.4. Ferroelectric properties of (100) dominant oriented PZT film measured at ± 5 and ± 20 V.

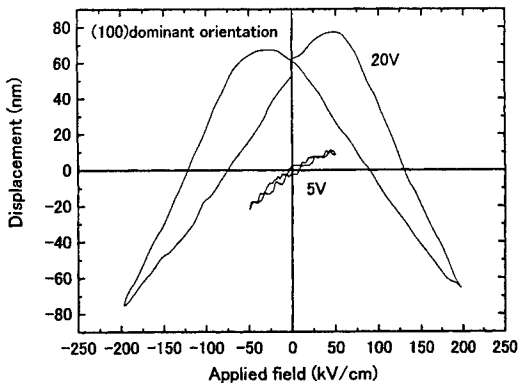

Fig. 5. Displacement property of (100) dominant oriented PZT film measured at ± 5 and ± 20 V.

hand, the *Ec* is comparable to the value of bulk PZT ceramics, and it is relatively low compared with that of reported PZT film actuator [3, 4].

Figure 5 shows the displacement property of the (100) dominant oriented PZT film actuator applied at bipolar field. When the applied voltage is ± 5 V, which is lower than *Ec*, the displacement property seems to vary with the applied field. However, value of the displacement is small and it is amounted to 30 nm. The reason of the small and linear displacement seems to be the contribution of the piezoelectric effect. On the other hand, for ± 20 V, which is higher than *Ec*, the displacement curve is large and shows hysteresis like a butterfly shape that is typical characteristics of piezoelectric materials, since domain orientation of the PZT film occur. The value of the maximum displacement is about 160 nm. However, this butterfly shape shows opposite direction compared with the typical displacement curve of a bulk PZT ceramics. This displacement property of the PZT film appears to indicate bend motion in the vertical direction on the film surface and does not reflect the genuine piezoelectric property. In the case of piezoelectric thin film deposited on Si substrate, ratio of the film thickness to the film surface is too low, so that magnitude of shrinkage in the surface direction is larger than that of elongation in the film thickness direction when the electric field is applied in the film thickness direction. Consequently, the thin film bends like bimorph actuator because Si back side layer does not shrink. Moreover, the reason whey direction of the bending motion is negative, which means depression, is that the displacement property was measured without clamping the sample. If the PZT diaphragm actuator sample is free and the field is applied in the film thickness direction, the PZT surface layer shrink and center of the diaphragm bend downward. Therefore, the displacement in the film thickness direction is depressed [8] and the displacement curve shows opposite shape [2] compared with usual piezoelectricity. From these results, the (100) preferred PZT film actuator shows bending displacement property.

Figure 6 shows the relationship between deflection displacement and applied voltage at unipolar drive operation. With increasing applied voltage to 20 V, displacement increases to about 220 nm to the depression direction. When the applied voltage was higher than 10 V, which was over the *Ec*, displacement increased linearly with increasing applied voltage. Therefore, the diaphragm actuator can achieve large displacement by unipolar drive operation. This result suggests that linear deflection

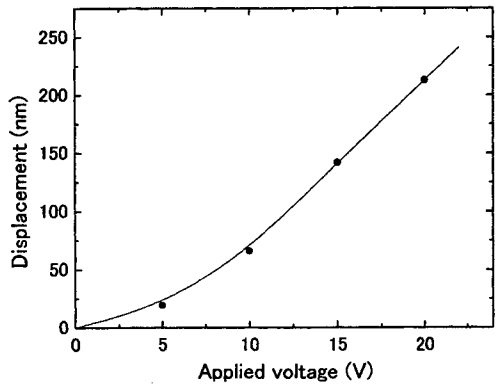

Fig. 6 Relationship between displacement and applied voltage at uni-polar drive.

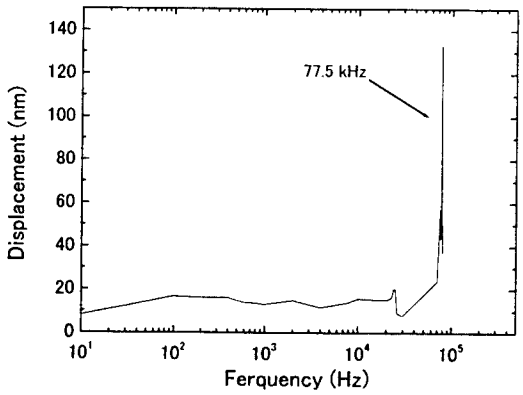

Fig. 7 Relationship between the amplitude of bend displacement and applied frequency of sine wave at 2 V p-p.

displacement control of positive and negative direction is possible if the DC bias voltage is applied to the actuator more than 10V.

Figure 7 shows the relationship between the amplitude of deflection and applied frequency of sine wave by bipolar drive at 2 V p-p. Peak amplitude of deflection was observed at 77.5 kHz. This peak seems to correspond to the resonance frequency of bend motion for the Pt/PZT/Pt/Ti/SiO_2/Si diaphragm structure, of which total thickness was about 30 μm. Therefore, this device can adapt up to 77.5 kHz for bend actuator like micro pomp. When the thickness of the Si back layer of the PZT diaphragm decreases and the thickness of the PZT layer increases successfully in the future, the resonance frequency of the device will increase.

CONCLUSION

Texture controlled 1μm- thick PZT film was deposited onto Pt/Ti/SiO_2/Si substrate, and a diaphragm type film actuator was fabricated. The ferroelectric properties of the (100) dominant oriented PZT film were comparable to those of the bulk PZT ceramics. The *Pr* and the *Ec* at a applied voltage of ± 20 V are 11 μC/cm^2 and 45 kV/cm, respectively. The (100) dominant oriented PZT film showed depressed displacement property caused by bending motion.

The value of displacement was about 220 nm by a unipolar drive at 20V. For bipolar drive, the resonance frequency of deflection for the PZT diaphragm was about 77.5 kHz. It can be seen that the texture controlled PZT films is applicable to the film micro actuator. However, further investigation must be undertaken to calculate the piezoelectric coefficient like d_{31} and to clear the physical properties of the PZT diaphragm actuator.

AKNOWRILEDGEMENTS

This work was partially supported by Researches on Artificial Materials for the Next Generation (RFTF96P00105) from the Japan Society for the Promotion of Science and Regional Consortium Project (NEDO). The authors would like to thank Mr. Y. Hayashi for experimental assistance in this work.

REFERENCES

[1] H. D. Chen, K. R. Udayakumar, L. E. Cross, J. J. Bernstein and L. C. Niles, *J. Appl. Phys,.* 77, 3349-3353 (1995).

[2] S. Wakabayashi, M. Sakata, H. Goto, M. Takeuchi and T. Yada, *Jpn. J. Appl. Phys.*, 35, 5012-5014 (1996).

[3] I. Kanno, S. Fujii, T. Kamada and R. Takayama, *Appl. Phys. Lett.*, 70, 1378-1380 (1997).

[4] M. lebedev, J. Akedo and Y. Akiyama, *Jpn. J. Appl. Phys.*, 39, 5600-5603 (2000).

[5] Takashi Iijima, Toshihiko Abe and Norio Sanada, *Proc. of The 9th US-Japan Seminar on Dielectric and Piezoelectric Ceramics*, pp. 215-218 (1999).

[6] T. Iijima, N. Sanada, K. Hiyama, H. Tsuboi and M. Okada, " *Mat. Res. Soc. Symp. Proc.*, 596, pp. 223-228 (1999).

[7] T. Tsurumi, S. Ozawa, G. Abe, N. Ohashi, S. Wada and M. Yamane, *Jpn. J. Appl. Phys.*, 39, 5604-5608 (2000).

[8] A. L. Kholkin, Ch. Wuetchrich, D. V. Taylor and N. Setter, *Rev. Sci. Instrum.*, 67, 1935-1941 (1996).

Why the Atomic Structure Matters to Dielectric and Piezoelectric Performance

T. Egami
Department of Materials Science and Engineering
and Laboratory for Research on the Structure of Matter,
University of Pennsylvania, Philadelphia, PA 19104
FAX: 215-573-2128
Email: egami@seas.upenn.edu

INTRODUCTION

Atomic structure may not be the first thing that comes to mind when one considers application of ferroelectric or piezoelectric materials. In most cases it is sufficient to consider the material as a continuum body, and not to think of tiny atoms that make up the material. However, the atomic structure does matter in some applications, such as the nano-structures and relaxor ferroelectrics [1] including $Pb(Zn,Nb)O_3$-$PbTiO_3$ (PZN-PT) that exhibits excellent piezoelectric performance [2]. Here we discuss how disorder in the atomic structure influences the relaxor ferroelectric behavior. When local disorder in the atomic structure is important its knowledge may lead to opportunities of manipulating the local disorder, and designing better compositions or processing conditions.

RELAXOR FERROELECTRICS

The relaxor ferroelectrics are characterized by the diffuse ferroelectric transition. They are widely used in various applications because of their high dielectric or piezoelectric response above the freezing temperature. Recently giant piezoelectric strain was demonstrated for single crystals of PZN-PT, in which PZN is a relaxor ferroelectric compound.

It is well known that for the relaxor phenomenon to occur the randomness in the atomic structure is required. For instance in a widely used relaxor ferroelectric, $(Pb,La)(Zr,Ti)O_3$ (PLZT), Pb and La occupy the same crystallographic site (A-site of the pseudo-perovskite structure) and Zr and Ti the B-site, both randomly. The situation is a slightly more complex in the case of another well-known relaxor ferroelectric compound, $Pb(Mg_{1/3}Nb_{2/3})O_3$ (PMN), but disorder still is the primary characteristic. In PMN Mg^{+2} and Nb^{+5} occupy the B-site. Because of electrostatic repulsion between Mg^{+2} and Nb^{+5} short-range positional correlation develops up to about 50 - 100 Å [3]. This local ordering creates two sublattices, β' and β" on the B-site. Once it was assumed that these sublattices are each occupied by Nb and Mg, resulting in charge segregation due to excess Nb and superparaelectric behavior [4]. However, it is now well established that such charge segregation does not exist [5,6], and the two sublattices are each occupied with Nb and $Mg_{2/3}Nb_{1/3}$, with the second sublattice remaining compositionally disordered for the kinetic reason [7].

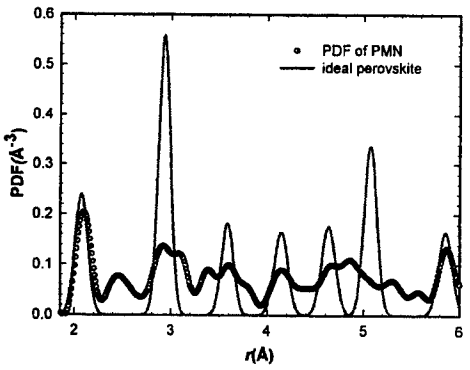

Fig. 1. Pulsed neutron PDF of PMN (circles) and the PDF expected for the ideal perovskite (solid line) [8].

LOCAL ATOMIC STRUCTURE

Before explaining how local atomic disorder affects the relaxor behavior and the piezoelectric performance, it is useful to demonstrate that chemical disorder actually causes very extensive displacive disorder in the crystal. This was discovered by the use of a pulsed neutron source and the atomic pair-density function (PDF) analysis. The crystal structure of PMN is

a very slightly distorted perovskite. However, the pulsed neutron PDF shown in Fig. 1 revealed that the local structure is far from what is expected for perovskite. The PDF describes the distribution of distances between all atoms in the sample. Since it is obtained by the Fourier-transformation of the total scattering intensity including Bragg peaks and diffuse scattering, aperiodic as well as periodic structure can be described [9]. It has been used widely for the study of liquids and glasses, but because of advances in the tools of structural analysis, such as pulsed neutron sources and synchrotron radiation sources, its application on crystalline materials became feasible.

What became clear by analyzing the PDF via atomistic modeling is that locally Pb ions are strongly polarized (Fig. 2), but the direction of polarization varies in the space, resulting in a non-collinear structure (Fig. 3). As a result polarization rotation occurs not only through the motion of the domain walls but through local rotation of polarization as well [11]. Such local rotation occurs over some correlated atoms, resulting in the so-called polarization nano-domains [12]. This ease of polarization rotation is crucially important for high piezoelectric response [11].

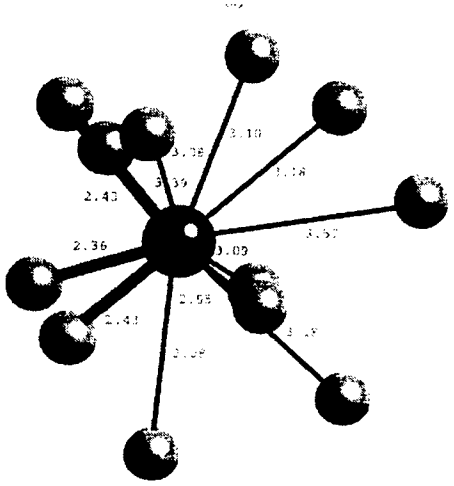

Fig. 2 Local oxygen environment of Pb in $PbZrO_3$ [10]. The local Pb environment is very similar in PMN and PZN, except that the directions of polarization are not collinear.

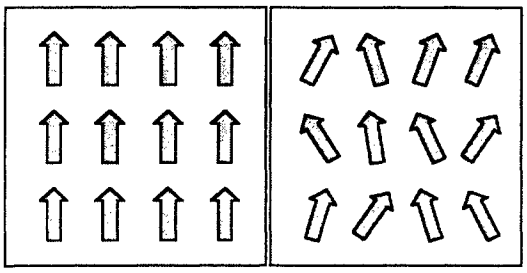

Fig. 3 Collinear state (left) and non-colinear state (right) of polarization.

The study of the local atomic structure of relaxor ferroelectric materials revealed wide variation in the local structure. Controlling and designing such variation is the key in improving the performance of relaxor-based ferroelectric and piezoelectric materials.

ACKNOWLEDGMENT

This work was supported by the DARPA-ONR through N00014-01-10860.

REFERENCES

1. G. A. Smolensky *et al.*, "*Ferroelectrics and Related Materials*" (Gordon and Breach, New York, 1981).
2. S.-E. Park and T. R. Shrout, *J. Appl. Phys.*, **82**, 1804 (1997).
3. E. Husson, M. Chubb, and A. Morell, *Mat. Res. Bull.*, **23**, 357 (1988).
4. L. E. Cross, *Ferroelectrics*, **76**, 241 (1987).
5. M. Akbas and P. K. Davies, *Commun. Amer. Ceram. Soc.*, **80**, 2933 (1997).
6. T. Egami, W. Dmowski, S. Teslic, P. K. Davies, I.-W. Chen and H. Chen, *Ferroelectrics*, **206-207**, 231 (1998).
7. W. Dmowski, M. K. Akbas, P. K. Davies and T. Egami, *J. Phys. Chem. Solids*, in press.
8. T. Egami, H. D. Rosenfeld, B. H. Toby and A. Bhalla, *Ferroelectrics*, **120**, 11 (1991).
9. T. Egami and S. J. L. Billinge, "*Underneath the Bragg Peaks: Structural Analysis of Complex Materials*" (Elsevier, Oxford, to be published).
10. S. Teslic and T. Egami, *Acta Cryst. B* **54**, 750 (1998).
11. T. Egami, *Proc. 12th IEEE Int. Symp. Appl. Ferroelectrics*, 273 (2001).
12. V. Westphal, W. Kleemann and M. D. Glinchuk, *Phys. Rev. Lett.* **68**, 847 (1992).

POLARIZATION RELAXATION IN PIEZOELECTRIC $0.7Pb(Mg_{1/3}Nb_{2/3})O_3$-$0.3PbTiO_3$

D. Viehland, Naval Seasystems Command, Newport, RI 02841

INTRODUCTION

Defects and substituents are known to significantly influence the electromechanical properties of ferroelectrics in both poled and unpoled conditions[8-10]. Various classifications of piezoelectric behaviors have been categorized in lead zirconate titanate (PZT) ceramics (grain sizes greater than several microns). The basic two types of classifications are commonly called "soft" and "hard"[8]. In general, higher valent substituents induce "soft" piezoelectric behavior, where as lower valent ones induce "hard"[8-10]. "Soft" ferroelectrics have lower coercive fields, higher hysteretic losses, higher dielectric and mechanical loss factors, and lower remanent polarizations and strains, relative to "hard" ones. "Soft" ferroelectrics also de-pole more easily, and have higher susceptibilities and piezoelectric constants, relative to "hard" varieties. Furthermore, the electromechanical properties of "soft" materials are much higher than that predicted by Landau-Devonshire theory[1]. The extra contribution is designated as extrinsic, as it can not be accounted for solely by considerations of nonlinear polarization behavior in a homogeneously ordered state. Rather, the extrinsic contributions are believed to be due to domain dynamics[1,11,12]. Thus, in a soft ferroelectric, even in a poled condition, some form of excess contribution is induced under weak and moderate AC field excitations. The nature of the extrinsic contributions, although often attributed to domains, remains unclear.

The purpose of this investigation was to study the polarization dynamics of "soft" ferroelectrics. Investigations have been performed on a lead magnesium niobate lead titanate (PMN-PT) composition close to the morphotropic phase boundary. In this compositional range, a remanent polarization state can be sustained and piezoelectric behavior is observed. The electromechanical performance characteristics of this system are close to that of commercially available "soft" PZTs. Systematic P-E investigations have been performed for various frequencies and maximum fields. It was hoped that such investigations would provide a better understanding of the domain dynamics and polarization reversal in "soft" ferroelectrics.

EXPERIMENTAL PROCEDURE

The composition chosen for study was $0.7Pb(Mg_{1/3}Nb_{2/3})O_3$-$0.3PbTiO_3$ (PMN-PT 70/30). Processing details can be found in previous publications[13]. P-E (polarization vs. field) measurements were made using a modified Sawyer-Tower bridge. This system was computer controlled and capable of automatic determinations of standard P-E measurement parameters. The system was capable of precise measurement of the P-E behavior over the frequency range of 10^{-2} to 10^2 Hz using a sinusoidal driving field.

RESULTS AND DISCUSSION

Figure 1(a)-(d) illustrates P-E curves taken at various maximum AC drive amplitudes. Each figure contains data taken at frequencies of 10^{-2}, 10^{-1}, 1, and 10^2 Hz. These figures clearly demonstrate a strong frequency dependence of the P-E response for E<2.5 kV/cm. At E~1 kV/cm (Figure 1(a)), a strong frequency relaxation of P is clearly observable. However, the induced polarization is less than 0.005 C/m^2 at 10^{-2} Hz, and decreased to less than 0.0025 C/m^2 with increasing frequency to 10^2 Hz. These results demonstrate the presence of a relaxational polarization within the previously believed linear range of the polarization response, for E significantly less than E_c. At E~2 kV/cm (Figure 1(b)), the degree of frequency relaxation in P and the hysteretic losses (δPE) were significantly increased. For example, P was decreased from ~0.04 C/m^2 to ~0.01 C/m^2, and

δPE was decreased from ~$2x10^4$ J/m^3 to ~$2x10^3$ J/m^3 with increasing frequency between 10^{-2} and 10^2 Hz. The frequency relaxation in P and δPE were most pronounced for E~2.5 kV/cm, as shown in Figure 1(c). At 10^{-2} Hz, a P-E curve typical of that of a ferroelectric was observed, however upon increasing frequency to 10^2 Hz, only a near-linear polarization was observed. Upon increasing the maximum AC field to 5 kV/cm (Figure 1(d)), the degree of relaxational polarization was dramatically reduced. A true remanent polarization was sustained which was nearly constant for all measurement frequencies investigated. Polarization relaxation was only observed near E_c. In addition, E_c was found to be frequency dependent, decreasing with decreasing measurement frequency.

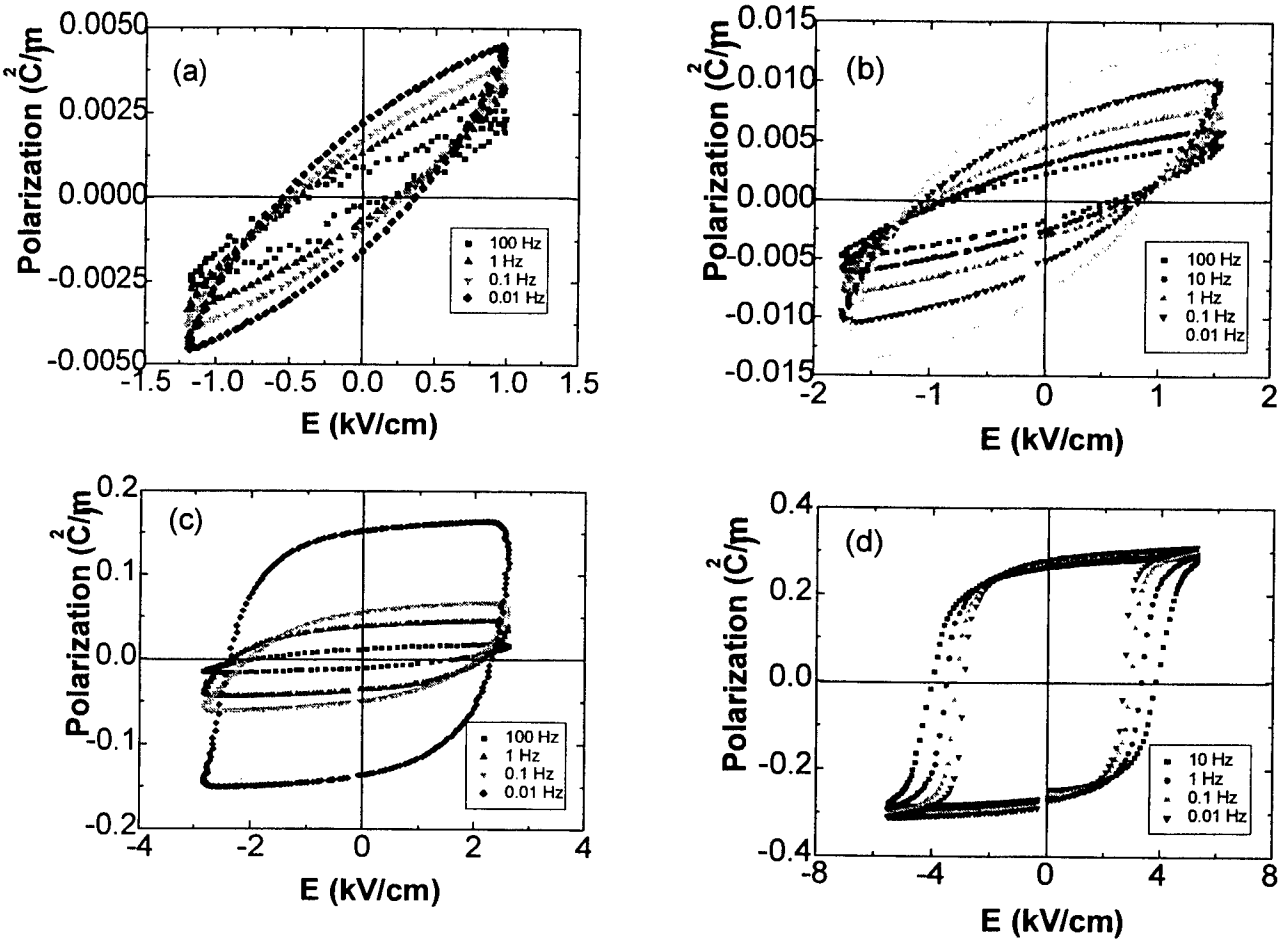

Figure 1. P-E curves for PMN-PT 70/30 taken at maximum AC drive amplitudes of: (a) 1 kV/cm, (b) 2 kV/cm, (c) 2.5 kV/cm, and (d) 5 kV/cm. Arrows are shown in the Figure to illustrate the direction of changing frequency. Data are shown for measurement frequencies of 10^{-2} to 10^2 Hz.

These results are in disagreement to those expected from conventional ferroelectric concepts[2,3]. According to conventional ferroelectric concepts, polarization reversal does not occur until $E>E_c$. For $E<E_c$, a near linear P-E response is expected that is frequency independent. However, for $E>E_c$, it has been known for many years that E_c is frequency dependent in many ferroelectrics, including unmodified crystals and thin layers[14-20].

The nature of the polarization relaxation in "soft" ferroelectrics can be understood by comparing the results presented in this paper with previous transmission electron microscopy (TEM) investigations of "soft" La-modified PZT (PLZT) for specimens of varying electrical histories[21]. Ex-situ TEM investigations revealed domain breakdown with increasing AC electrical drive for $E<E_c$, rather than domain movement or growth. These results for "soft" PLZT are consistent with the P-E data presented here for "soft" PMN-PT 70/30. We believe that the origin of "soft" behavior can be attributed to the presence of quenched random fields[22-24] associated with an underlying compositional and/or structural disorder. The magnitude of the quenched random field is insufficient to overcome the long-range ferroelectric interactions, as in the case of a relaxor ferroelectric. However, upon excitation with an electric field, polar clusters are nucleated in the vicinity of quenched random fields. At $E<E_c$, this results in a hierarchy of domain features, i.e., subdomain irregularities of a reversed polarization within normal micron-sized domains. Upon removal of the AC electric field, the original polarized state is recovered as twin boundary elimination/motion has not occurred. However, for $E>E_c$, twin boundary elimination/motion occurs, resulting in complete switching of the remanent polarization. The fundamentals of these concepts are consistent with the theoretical random-field model previously developed by Imry and Ma[24].

According to random-field theory, nucleation of domain boundaries under field occurs in the vicinity of quenched defects that are conjugate to the applied ordering field. Thus, application of field results in the breakdown of long-range order and the creation of fine-scale domain states in the vicinity of the quenched disorder (i.e., the activation of the random-field). Interestingly, the dynamics of ferroelectric domain nucleation-growth process have previously been investigated using I-t methods[14-16]. These investigations have revealed that the process can be treated as a continuous re-nucleation process, i.e., growth of domain nuclei is not an important step to the overall nucleation-growth process. However, these investigations have been void of physical understanding of the nucleation-growth process.

Thermodynamically, nucleation barriers are well-known to be lowered by impurities in many types of transitional states. However, in ferroelectric domain theory, this point has never been considered as important. It may have been assumed that the interaction between a phonon process involving time scales on the order of 10^{-12} sec and quenched disorder involving times on geological scales can not significantly alter the barrier height between two polar states, and consequently the kinetics of domain nucleation-growth. In the case of a ferroelectric, quenched defects and/or substituents that are charged couple strongly to the polarization, controlling polarization reversal and domain dynamics.

In fact, relatively small concentrations of randomly quenched point defects that are charged could play a significant role in polarization reversal and domain dynamics. For example, assume a concentration of one such defect per thousand lattice sites (i.e., 0.1 at.%). The average distance in one dimension (λ) that will be defect free can be estimated as $(10^{-3})^{1/3}a_o$, where a_o is the unit cell parameter (~4 angstroms). Thus, λ can be estimated as 40 angstroms, which is on the length scale of polar clusters. This indicates that polarization reversal and domain dynamics in many ferroelectrics may occur by a random field mechanism. Clearly, further investigations are required for both the theory and applications of modified ferroelectrics.

SUMMARY

The results of this paper have demonstrated that polarization reversal in "soft" ferroelectrics occurs by nucleation of polar clusters with a reversed polarization within normal micron-sized ferroelectric domains in the vicinity of quenched random fields.

References

1. M. J. Haun, PhD Dissertation, The Pennsylvania State University (1988).
2. M.E. Lines, and A.M. Glass, "Principles and Applications of Ferroelectrics and Related Materials", Clarendon Press, Oxford (1977).
3. F. Jona and G. Shirane, "Ferroelectric Crystals", Pergamon Press, New York, (1962).
4. W. Cao and J. Krumhansl, Phys. Rev. B 42, 4334 (1990).
5. N. Pertsev and G. Arlt, Ferroelectrics 132, 27 (1992).
6. G. Arlt, Journal of Materials Science 25, 2655 (1990).
7. R. Herbiet, U. Robels, H. Ederichs and G. Arlt, Ferroelectrics 98, 107 (1989).
8. D. Berlincourt, H. Krueger, and B. Jaffe, J. Phys. Chem. Solids 25, 659 (1964).
9. Q. Tan, PhD Dissertation, The University of Illinois (1998).
10. X.H. Dai, PhD Dissertation, The University of Illinois (1995).
11. W. Cao, S. Tavener, and S. Xie, J. Appl. Phys. 86, 5739 (1999).
12. Q. Zhang, H. Wang, N. Kim, and L.E. Cross, J. Appl. Phys. 75, 454 (1994).
13. S. Swartz and T. Shrout, Mat. Res. Bull. 17, 1245 (1982).
14. W.J. Merz, Physical Review, 95, 690 (1954).
15. R.C. Miller and G. Weinreich, Phys. Rev. 117, 1460 (1960).
16. M. Hayashi, J. Phys. Soc. Japan, 33, 616 (1972).
17. Y. Ishibashi and Y. Takagi, J. Phys. Soc. Japan 31, 506 (1971).
18. Y. Ishibashi, Integrated Ferroelectrics 2, 41 (1992).
19. Y. Ishibashi and H. Orihara, Integrated Ferroelectrics 9, 57 (1995).
20. T. Song, S. Aggarwal, Y. Gallais, B. Nagaraj, R. Ramesh, and J. Evans, Appl. Phys. Lett. 73, 3366 (1998).
21. Q. Tan and D. Viehland, Phys. Rev. B 53, 14103 (1996).
22. W. Kleemann, Inter. J. Mod. Phys. 7, 2469 (1993).
23. T. Nattermann and J. Villain, Phase Transitions 11, 5 (1988).
24. Y. Imry and S. Ma, Phys. Rev. Lett. 35, 1399 (1975).

Acknowledgments:
This work was supported by the Office of Naval Research.

Statistical Model for Poling Hard PZT

W. A. Schulze and M. K. Jha

Alfred University, School of Ceramic Engineering and Material Science
2 Pine Street, Alfred, NY 14802 USA
FAX: 607-871-2354 Email: schulze@alfred.edu

A statistical model was developed for poling a hard PZT. The model successfully predicts the resultant planar coupling coefficient for times from near zero to 30 minutes, with fields of 1 to 4 MV/m and temperatures from 25 to 120C. To achieve a good fit with time it was necessary to combine two building exponentials, one sensitive to field and temperature and the other affected by temperature and the square root of time.

INTRODUCTION

Most of the work done in the field of poling ferroelectric ceramics has suggested that the process of poling for a particular material is mainly a function of electric field, temperature at which the poling field is applied and the time duration of poling. Theories proposed by various authors seem to explain this process, and some empirical equations have also been proposed. Merz and Little[1-4] have done extensive work on the polarization, electric field and switching currents. Wieder[5] proposed an equation relating polarization with electric field for barium titanate as:

$$P=2P_s\exp(-\alpha'/t)$$

where

$$\alpha'=\alpha'_0\exp(\Delta F/k\theta')$$

here ΔF is energy, which is proportional to 1/E, θ' is the absolute temperature and α'_0 is a constant having the dimension of time and k is the Boltzmann's constant. An exponential type if relationship for polarization and internal bias field have been also suggested by Takahasi.[6]

Sayer[7] and others performed a more comprehensive study on different aspects of poling including a variation of temperature and time of poling at varying field. An empirical formula correlating electromechanical coefficients with different parameter has been suggested as:

$$k_p=k_{p\,max}\,[1-\exp(-Bt)]$$

where B is a function of temperature which decreases with increasing temperature whereas k_{pmax} is a function of electric field and temperature only.

However, these empirical equations are appropriate within certain regions of the variables (electric field, temperature and time) and have not been probed in the continuous spectrum of these three variables,). This paper deals with this aspect of poling.

Statistical methods have been used successfully to model potentially complicated processes in various fields. Using D-optimal design an experimental design was made and then is was successfully solved with various statistical software packages for various models to explain and optimize poling process.[8]

A statistical experimental design is made to define and accurately quantify the effects of one or more variables on the response (or responses) with the smallest number of experiments. Some of the essential characteristics of a good experimental design are:

1) Important effects and interactions are accurately quantified and effects of uncontrollables are minimized
2) The number of experiments is held to a minimum by minimizing the number of low information experiments.
3) Data are easily analyzed and the conclusions are valid.
4) Existing theories and mechanisms are tested and new theories and mechanisms are suggested if the existing ones are unsatisfactory.
5) Many variables are screened effectively and the optimum combinations or areas for further study are clearly indicated.

A D-Optimal design was used for making the experimental design because of the following advantages:

(a) Many variables can be simultaneously analyzed.
(b) The number of experiment required to quantify effects greater than or equal to the experimental error are minimized.

(c) Effects due to uncontrolled variables are minimized.

(d) In addition to the main effects it allows for modeling of complicated non-linear effects and high order interactions. Specific relationship can also be studied, so the design can fit the unique features of process/product being studied.

(e) Undesirable combinations can be excluded and the design can build on any existing experiments, so it is very good for explaining the complicated effects in which stepwise procedure is necessary.

The efficiency of D-Optimal design is expressed in terms of error of prediction ratio (EOPR), which is written in matrix notation as: EOPR (at any point in the design space) = Standard error of prediction/experimental error $=\{x_0'(X'X)^{-1}x_0\}^{1/2}$, where x_0 is any point in the design space, x_0' is the transpose of x_0, X is the whole design matrix and X' is the transpose of X. Hence, the average error of prediction ratio for any experimental design is given by Average EOPR $=\Sigma(EOPR)/N$ Where N is the total number of experiments. Maximizing the X'X term minimizes the average EOPR, which is done by iterative computer calculations.

EXPERIMENTAL

The purpose of poling is to get the maximum polarization in a material without dielectric breakdown, hence determination of the breakdown voltage is very important so that the maximum poling can be achieved while working with the constraint of electric field, temperature, and time of poling. Breakdown voltage was determined at 25 °C. Electroded pellets of a commercial PZT-4 like material of size 0.01905 m (19.05 mm diameter) x 0.001 m (1 mm thickness) were chosen. The sample was placed between two gold-plated copper electrodes and the whole assembly was immersed in a vegetable oil maintained at a temperature of 25 °C. A gradually increasing dc field was applied at a rate of 0.1 kV every 5 seconds. The limiting current setting was kept at 2 mA. An average breakdown field of 5 samples was 4.9 ± 0.2 Mv/m.

Resistivity as a function of temperature was measured on a unpoled sample at 2C/min. Activation energy was calculated as 0.99eV.

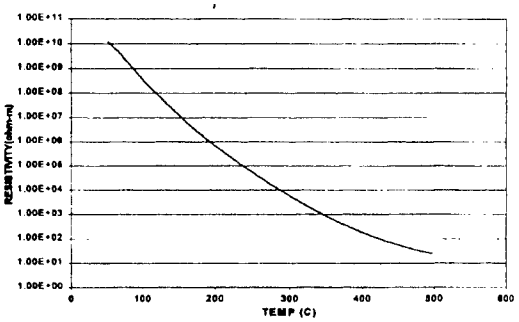

Resistivity as a function of temperature.

Dielectric constant recorded at 2C/min on heating and cooling showed typical Curie-Weiss response with the Curie temperature at about 320C.

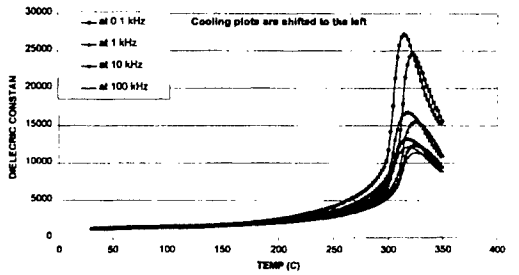

Dielectric constant as a function of temperature

While making this design, it was considered that the polarization and hence the electrical and electromechanical properties of the poled samples are dependent on the independent variables such as type of material, poling field (dc), temperature of poling and the time of poling. However the interactions between these variables are not well understood, so the linear, two-factor and three-factor interactions were considered only. The following variable levels were considered.

Levels of Variables Used for Making Design

Type of Variable	Levels
Type of Material	Soft PZT(0), Hard PZT (1)
DC Field (in MV/m)	1, 2, 3, 4
Temperature of Poling (in °C)	25, 80, 100, 120
Time of Poling (in minutes)	5, 10, 20, 30

Extremes (experiments with highest and lowest values of variables) for both the materials were avoided to have the optimum poling conditions. Various authors have reported that exponential equations are more appropriate in describing the poling behavior. Moreover, on plotting any of the poled properties (for example k_p) as a function of any of the independent variables, an exponential curve is obtained. This curve can be described by an equation of type:

$$Y=H*[1-\exp(-x)] \quad (1)$$

Where H is a constant and the dependent variable y can attain a maximum value of H at higher values of the independent variable x. The value of y approaches H asymptotically. Sayer and others did an extensive study of the poling behavior and reported a similar type of curve.[43] On comparing the curve obtained by Sayer and others with the above equation 1, it can be seen that the only difference is in the number of independent variables as there are 3 independent variables (x_1=E, x_2 =θ, x_3=t) that affect the poling mechanism. The maximum value of y (k_p in the case of poling) is H ($k_{p\,sat}$ in the case of poling), so the poling curve can be represented with a similar equation of type:

$$Y=H*[1-\exp\{f(-(x_1, x_2, x_3))\}] \quad (2)$$

where $H = f(x_1, x_2)$

$$k_p = k_{p\,sat}*[1-\exp\{f(-(E, \theta, t))\}] \quad (3)$$

where $k_{p\,sat}$ is assumed proportional to saturation polarization (maximum polarization achievable at a particular electric field and temperature of poling). Therefore $k_{p\,sat}$ is a function of electric field and temperature of poling, so it can be written as:

$$k_{p\,sat} = f(E, \theta) \quad (4)$$

To solve equation 3 for E, θ and t, the value of k_{psat} needs to be known. Additional groups of data were obtained for hard PZT, so that the value of $k_{p\,sat}$ could be determined at a specific field (E) and temperature (θ). Temperature and electric field were kept at a specific level and only the poling time was varied to obtain the saturation polarization.

Data collected for the above experiments for hard PZT showed the saturation polarization ($k_{p\,sat}$) to be:

$k_{p\,sat}$ = 0.596 at E = 3 MV/m and θ' = 373 K
$k_{p\,sat}$ = 0.568 at E = 2 MV/m and θ' = 393 K
$k_{p\,sat}$ = 0.510 at E = 3 MV/m and θ' = 353 K

Where θ' is the temperature in Kelvin.

In this study the extrinsic contribution to the poling properties have been considered. This extrinsic contribution is probably by domain reorientation and reversal by the nucleation and growth mechanism. At absolute temperature 0 K, all thermal fluctuations and excitations are frozen out including the freezing of the domain boundary motion, which is an extrinsic contribution and freezing of lattice phonons take place which is regarded as an intrinsic contribution. Therefore, k_{psat} is assumed to be 0 at absolute temperature. At the same time k_p can be considered to be 0 at the start of the poling process (in the unpoled samples). Therefore, while making separate models for these two sets of data, these two boundary conditions were taken into account:

$k_p = 0$ at θ = 0 K(Kelvin) and
$k_p = 0$ at t = 0

It was observed during this research work that the maximum value of k_p that can be obtained for a particular PZT at any field and temperature of poling is a fixed number. The same behavior has been reported in various journals. This number is a constant and can be called as the $k_{p\,max}$ for that particular material. k_{pmax} found during this work is:

$k_{p\,max}$ = 0.61 for hard PZT

Therefore $k_{p\,sat}$ can be written as:

$$k_{p\,sat} = k_{p\,max}*[1-\exp\{f(-E*\theta')\}] \quad (5)$$

After a number of simpler equations, an exponential based model was chosen for $k_{p\,sat}$. This model is very good in explaining the variability of the data set as its R-sq is very high (0.996) and residuals are small and are normally distributed.

$$\mathbf{k_{p\,sat} = k_{p\,max}*[1-\exp(-0.011671*E*\theta')]} \quad (6)$$

Where $k_{p\,max}$ for hard PZT has been considered as 0.61 (which was the maximum value obtained and reported in various journals).

The final equation relating k_p with E, θ' and t (for a hard PZT 4H) can be written as:

$$k_{p\ sat} = k_{p\ max}*[1 - \exp(-0.011671*E*\theta')]* [1-\exp(-J*t^{1/2})] \quad (7)$$

Where $k_{p\ max}$ = 0.61 and J is a variable which depends on only temperature (θ'). A relation J and θ' is shown below in equation 8.

$$J = -1.846 + 0.07825*\theta' \quad (8)$$

The actual experimental values and the Equation 7 predicted values for hard PZT's are shown in the figure.

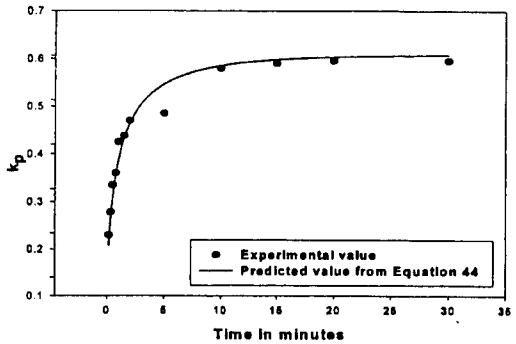

Experimental data and predicted values using the model shown by equation 7 as modified by equation 8.

DISCUSSION

Exponential models were made to explain the poling behavior in Hard PZT. First the saturation polarization value at E = 3 MV/m and θ' = 373 K was obtained by varying the poling time (between 0.167 to 30 minutes). At first an increase in k_p was observed with increasing poling time, but after about 10 minutes, k_p reached to a peak. This peak value of 0.596 was considered as the saturation k_p (k_{psat}). Using the regression technique a model relating k_p with θ' and t was developed. This model was not found adequate because of the large differences in the predicted and experimentally obtained values in the lower region of time in the curve. Therefore, variables were transformed and another model was obtained. This model (shown in equation 7) is excellent in terms of predicting the data in the whole design space. Residuals (difference between the actual and [predicted value from the model) were found to be low with no outliers.

Therefore, the poling process in hard PZT can be well predicted by the product of two exponential terms along with a constant (equation 7 and 8). One of the exponential terms controls the rise time behavior where as the second exponential term controls the maximum achievable polarization.

SUMMARY

Comparison with Sayer's model for the rise time curve of k_p with the current work shows a subtle change in the incorporation of a temperature factor and a significant change in the time factor.

Sayer's model:

$k_{p\ max} * \{1 - \exp(-B*t)\}$
where B is a function of temperature

Current model:

$k_{p\ sat} * \{1 - \exp(-J*t^{1/2})\}$
where $J = -1.846 + 0.07825*\theta'$

The most significant differences are the power of time and the more complex incorporation of temperature in the exponential. The significance of the difference in the power of time is found in the need to model the steep rise in k_p at low values of time. At large values of time the equations saturate in a similar manner.

REFERENCES

1. W. J. Merz, Phys. Rev., **88**[2] 421-422(1952)
2. W. J. Merz, Phys. Rev., **95**[3] 690-698(1954)
3. W. J. Merz, J. Appl. Phys., **27**[8] 938-943(1956)
4. E. A. Little, Phys. Rev., **98**[4] 978-984(1955)
5. H. H. Wieder J. Appl. Phys., **27**[4] 413-416(1956)
6. S. Takahashi, Ferroelectrics, **41** 143-156 (1982)
7. M. Sayer, B. Judd, K. El-Assal and E. Pressad, J. Can. Ceram. Soc., **50** 23-28 (1981)
8. D. Montgomery, "Design and Analysis of Experiments", John Wiley and Sons, New York, 1997.

ELECTRIC FIELD EFFECTS ON DIELECTRIC PROPERTIES OF MPB PZT CERAMICS VIA MONOCLINIC DISTORTION AT LOW TEMPERATURES

Ruyan Guo, Edward Alberta, A. Thomas, Beth A. Jones, L. Eric Cross
Materials Research Institute
The Pennsylvania State University, University Park, PA 16802, USA

Fax: 814-863-7846 (RG)
Email: ryguo@psu.edu (RG)

ABSTRACT
This paper reports the latest studies on the dc biased complex dielectric properties of PZT ceramics with compositions in the vicinity of the morphotropic phase boundary (x=0.48), when subjected to various dc bias fields, measured under small ac signal conditions. E-field dependent dielectric permittivity is shown to have decreasing trend with field in monoclinic phase; but increasing trend with field in tetragonal phase accompanied by the induced monoclinic distortion. Temperature dependence of the dc biased dielectric property allows possible distinction of dielectric anomalies associated with domain switching or crystallographic phase transition.

INTRODUCTION
The complex dielectric permittivity of ferroelectric material is one of the most sensitive material parameters dependent on domain configuration, poling or electric/mechanical field treatment and boundary conditions, in addition to its dependencies on temperature and frequency. Previous studies on bias dependence of the dielectric properties of PZT ceramics can be found in literature,[1,2] among them primary understanding of the separate contributions of 180 and 90 degree domains has been established. Bias electric field dependence of dielectric permittivity at the vicinity of the rhombohedral-tetragonal morphotropic phase boundary, however, has not been fully studied. In the light of recent discovery[3] of the low temperature monoclinic phase in the PZT system and structural dependence on E-field[4], bias electric field dependency study of the dielectric permittivity has been carried out, in an attempt to further clarify the monoclinic phase transition and the interplay of domain switch process.

In this paper, dielectric properties as function of both dc electric field (up to ±20 kV/cm) and temperature (300K to 12K) performed on three PZT ceramic compositions (PZT54:46, PZT52:48, and PZT49:51) are reported.

EXPERIMENTAL DESCRIPTION
$Pb(Zr_{1-x}Ti_x)O_3$ ceramic samples of well controlled crystallographic phase purity and composition uniformity with x ranging from 0.42 to 0.52 were prepared by conventional solid-state reaction technique using high purity (better than 3N) lead carbonate, zirconium oxide and titanium oxide as starting compounds. Powders were calcined at 900°C for six hours and recalcined as needed. After milling, sieve, and adding binder, the pellets were formed by uniaxial cold pressing. The pellets after binder burnout were sintered at 1250°C in a covered crucible for 2 hours, and furnace-cooled. During sintering, $PbZrO_3$ was used as a lead source in the crucible to minimize volatilization of lead. Sintered ceramic samples were ground into parallel plates and polished with 1 μm diamond paste to a smooth surface finish.

For temperature dependence of DC biased dielectric measurement, all ceramic samples were annealed in order to be free from strains caused by sintering, handling and previous treatment. Gold electrodes were sputtered on sample surfaces to which silver wires were then attached.

Temperature dependent dc biased dielectric measurements were carried out in a cryostat system in temperature range 10 to 300K, using a HP 4284A LCR meter. An interfacing computer program was developed for this measurement which allows continued measurement with full control of temperature, dc bias setting, frequency setting, and data acquisition. Each sample at initial starting temperature was held for longer than an hour in vacuum chamber (~10^{-5} torr.) to allow complete thermal equilibrium. At each desired temperature setting, the specimen was again held for 5 min for temperature to equilibrate.

The dc bias voltage was applied in steps of 2 kV/cm, from 0 up to +20 to –20 to 0 kV/cm, switched physically (within dV/dt limit of the

power supply) via the computer control system. Following each changing in dc field, a delay time of several seconds was used to allow the voltage supply, sample, and blocking circuit to stabilize before next measurement. The capacitance and loss were measured at 10kHz and 100kHz at each bias and temperature setting. After the heating cycle was complete, the experiment was repeated while cooling from 300K back to 12K.

The ac signal used in dielectric measurement was equivalent to 2V/mm to satisfy small signal conditions, thus the dielectric properties measured under different bias conditions were independent of domain boundary movements caused by ac field.

A large amount of data were obtained for each sample using the designed experimental configuration. Representative results reported in this paper include three compositions: PZT 46, PZT 48, and PZT 51. At ~300K, PZT46 is of monoclinic phase, PZT 48 is on the border of its monoclinic phase, PZT 51 is of tetragonal phase and obtain monoclinic symmetry at near 50K. The structural relations of these compositions can be found in the modified phase diagram,[3] Fig. 1, in which cubic (C), tetragonal (T), rhombohedral (R) and monoclinic (M_A) are labeled.

RESULTS AND DISCUSSION

Figures 2, 3, and 4 present the dielectric constant and dielectric loss measured as function of temperature and dc bias electric field. All samples show weak frequency dependency (up to 100kHz) and only 10 kHz results are shown in these figures.

Temperature dependencies: In general, dielectric constant decreases monotonically with decreasing temperature, evidently due to slowing down of the dipolar reorientation and the domain movement contributions. In PZT46 and PZT48, the dielectric constants at 12K are both approaching their intrinsic values (260 for PZT46 and 360 for PZT48). For PZT51 however, a inflection point on the dielectric constant curve and a maxima on the dielectric loss curve indicate an anomaly around 45-50K, which may be attributed to the low temperature monoclinic phase reported. Additional anomalies are also seen for low temperature dielectric properties of PZT48 (110K and 224K) and PZT46 (285K), though the nature of which is yet to be determined. Indications of these anomalies have been observed by low temperature strain measurement [Guo et al., to be published].

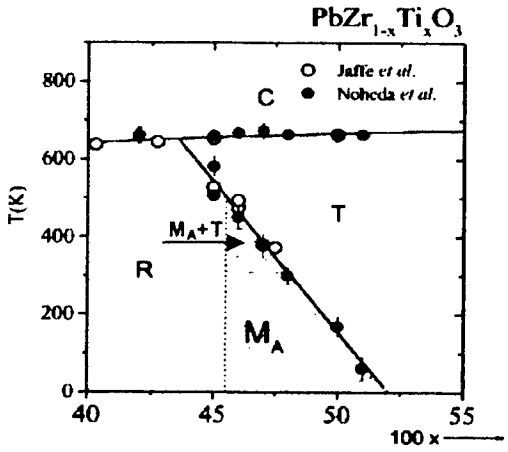

Fig. 1. Modified PZT phase diagram for compositions near the MPB with monoclinic phase indicated.

DC bias dependencies: Dependencies of dielectric properties on the applied bias field become weaker at lower temperature. One obvious reason is that as the temperature decreases, the coercive field increases therefore the applied dc bias (20 kV/cm) become insufficient in domain switching. Dielectric loss in all three samples showed the same increasing trend as the bias field increased.

Further examination however reveals subtle difference for electric field dependencies obtained for three compositions. In PZT46, dielectric permittivity decreases monotonically with increasing bias field, as shown in Fig. 2(a). In PZT51, however, the dielectric permittivity increases with increasing bias field, as shown in Fig. 3(a). PZT48, Fig. 4(a), represents a situation in between that of PZT46 and PZT51 that at near 300K dielectric constant increases with increasing bias field, yet the trend reverses at a lower temperature(<235K).

The theoretical model dealing with the electric field dependencies of the dielectric permittivity can be derived from the electric field dependence of polarization that contains a nonlinear term composed of the Langevin functions. By taking first two terms of series expansion of the Langevin function into consideration, one gets for polarization:

$$P = N\left(\bar{\alpha}E + \frac{\mu^2 E}{3k_B T} - (1 - 4u - 2u^2)\frac{\mu^4 E^3}{45k_B^3 T^3} + \cdots\right)$$

where N is the number of dipoles in unit volume, $\bar{\alpha}$ the average polarizability, $u=\Delta\alpha k_B T/\mu^2$, $\Delta\alpha$ is the anisotropy of the polarizability, μ the dipole moment, k_B the Boltzmann constant, T the absolute temperature, and E the field strength.

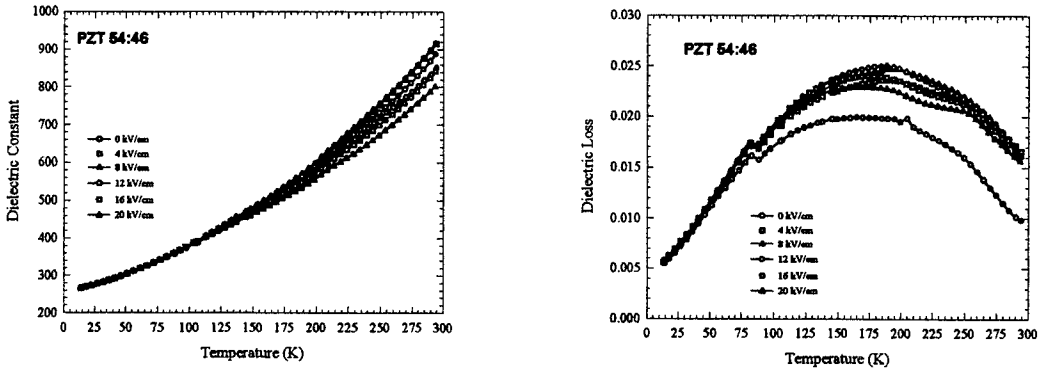

Fig. 2. (a) Dielectric permittivity and (b) loss of PZT 54:46 ceramic samples as function of temperature, under dc bias condition from 0 to 20 kV/cm.

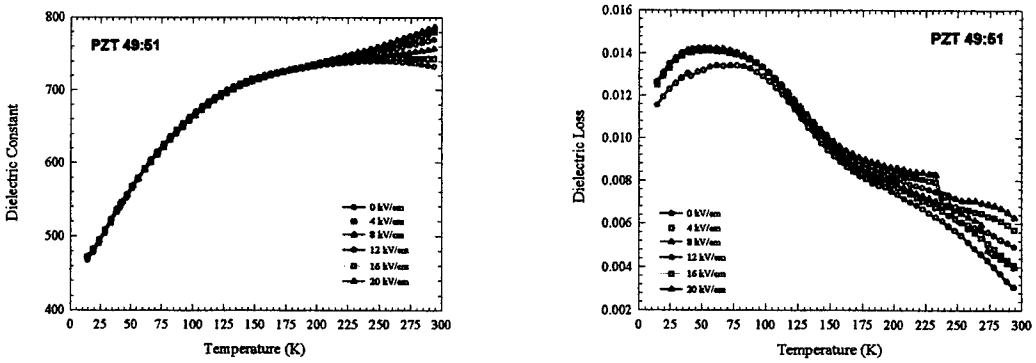

Fig. 3. (a) Dielectric permittivity and (b) loss of PZT 49:51 ceramic samples as function of temperature, under dc bias condition from 0 to 20 kV/cm.

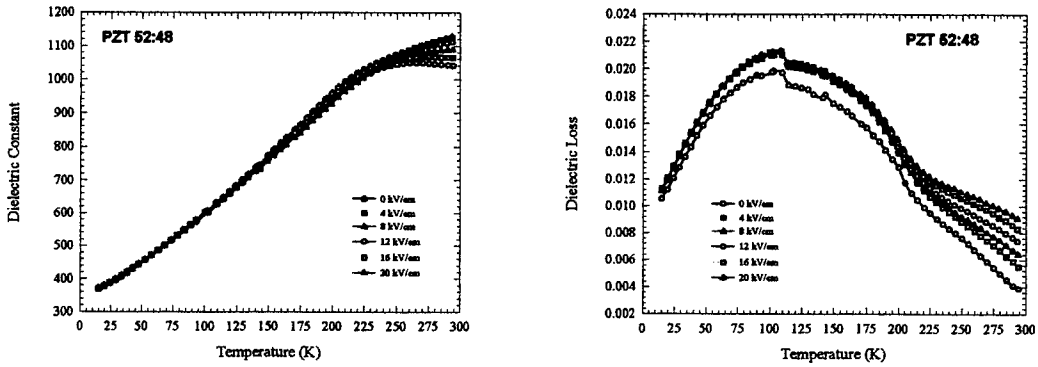

Fig. 4. (a) Dielectric permittivity and (b) loss of PZT 52:48 ceramic samples as function of temperature, under dc bias condition from 0 to 20 kV/cm.

Thus the dielectric permittivity has an approximately quadratic relation with E-field:

$$\varepsilon = \varepsilon_0 + N\left(\overline{\alpha} + \frac{\mu^2}{3k_BT} - (1-4u-2u^2)\frac{\mu^4E^2}{45k_B^3T^3} + \cdots\right)$$

For all known ferroelectrics and dielectrics, u<<1, hence $(1-4u-2u^2)$ is positive which leads to the conclusion that the dielectric permittivity decreases with the increasing bias. Therefore the polarization of un-reversed domain is only weakly field dependent and behaves like a regular dielectric with negative quadratic E-field dependence.

This formalism holds generally true so long the behavior of the material can be modeled as a polarizable but **uniform** medium. When domain reversal is involved, however, dielectric

permittivity shows positive dependencies on dc bias, such as in the case of anti-ferroelectric species[5] and as observed in rhombohedral PZTs near threshold field where domain switching takes place.[4]

Restricted by the page limit of this paper, only the basic trend is briefly discussed here. As seen in Fig. 5, [shown are the dielectric constant (solid symbol) and loss (hollow symbol) at 10 kHz as function of dc bias at 300 K], for dc bias below ±6 kV/cm, positive dc bias dependent permittivity is found for PZT46, which can be attributed to 180° domain reversal, combined with average 90° (or 109° and 71°) domain switch. Strong but negative dc bias field dependence for higher dc bias was observed for PZT46 sample throughout the temperature range measured.

As to the PZT51 (Fig. 6) and PZT48 (Fig. 7) samples, at near room temperature, PZT51 and PZT48 both show anomalous positive dc bias dependent dielectric permittivity upto ±20 kV/cm. Dielectric loss curves reveal further details of the polarization process at different bias levels. The large positive dielectric permittivity dependencies on dc bias found in both PZT48 and PZT51 near their tetragonal to monoclinic phase transition or in their tetragonal phases, gave strong evidence that electric field not only cause domain reversal which usually show dependence on E_C, but also induce phase transition which is accompanied by continued polarization rotation establishing the monoclinic phase. PZT48 showed "regular" negative bias field dependency at a lower temperature, e.g., as seen in Fig. 7 (bottom) for 200K.

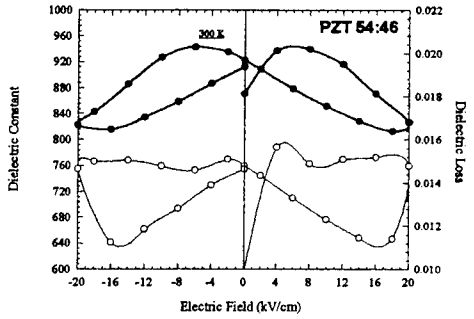

Figure 5. PZT 54:46.

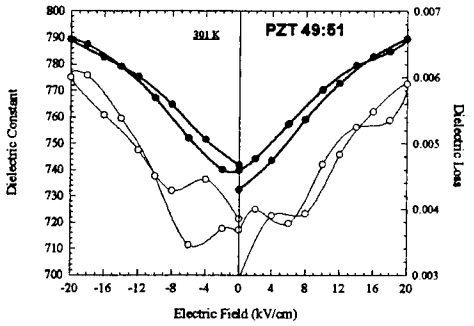

Figure 6. PZT 49:51.

SUMMARY

Anomalous behavior of the dielectric permittivity with bias electric field is found in PZT48 and PZT51 in their tetragonal phase and at temperatures near the on-set of the monoclinic phase transitions. Although the phase transition and domain switching activities are intricately related, no threshold domain reversal field can be unambiguously assigned; rather, a continuous induced phase transition process combined with domain switching is found to accompany the increasing dc bias field.

ACKNOWLEDGEMENT

Collaborative effort leading to this study with Drs. G. Shirane, B. Noheda, and D.E. Cox, at Brookhaven National Lab and partial financial support from ONR under MURI project N00014-96-1-1173 are gratefully acknowledged.

REFERENCES:

[1]N. Uchida & T. Ikeda, *Jpn, J. Appl. Phys.* **4**(1965)867.
[2]N. Bar-Chaim, M. Brunstern, J. Grunberg, A. Seidman, *Ferroelectrics*, **6**(1974)299.
[3]B. Noheda *et al. Appl Phys. Lett.* **74**(1999)2059.
[4]R. Guo et al., *Phys. Rev. Letters*, **84**(2000)5423.
[5]Yutake Takagi, *Phys. Rev.* **85**(1952)315

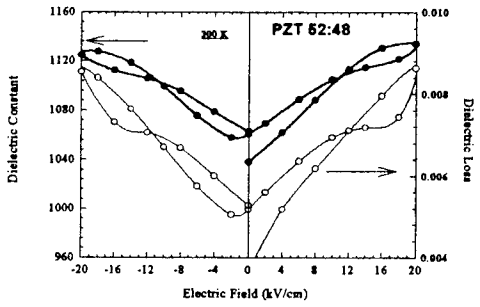

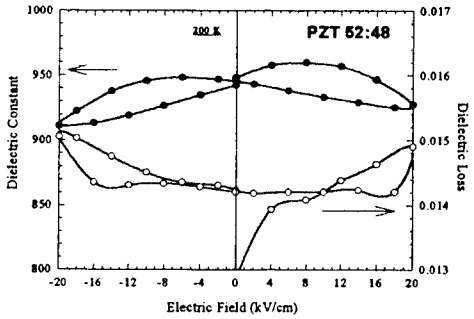

Figure 7. Dielec. constant (solid) and loss (hollow) at 10 kHz as function of dc bias at 300K(top) and 200K(bottom), for PZT52:48.

Harmonic Analysis of the Electro-Mechanical Response of Electroactive Materials

C. B. DiAntonio, F. A. Williams Jr., and S. M. Pilgrim
Laboratory for Electronic Ceramics
New York State College of Ceramics at Alfred University
2 Pine Street, Alfred, New York, 14802
Phone: 607-871-2576
Fax: 607-871-2354
Email: pilgrim@alfred.edu

ABSTRACT

The main thrust of this examination is the incorporation of signal decomposition through Fourier analysis to aid quantification of electro-mechanical and aging properties. Fourier analysis is not a novel technique to the electrical engineering community; however, the application presented here allows a fresh look at some old phenomena. The analysis has not been applied to a materials response and linked to materials coefficients. This work attempts to build a bridge that connects the theory of phenomenology, developed by Devonshire and others, to Fourier signal analysis of the electro-mechanical response of an electro-active material. An extensive literature search and review did not reveal any previous work involving this type of analysis.

INTRODUCTION

Since their discovery in the 1950's, the relaxor electrostrictors (specifically those based on $Pb(Mg_{1/3}\ Nb_{2/3})O_3$ (PMN)) have been of scientific interest.[1] Continuing progress on basic research has been increasing as a parallel to the application of PMN-based electrostrictors. Electrostrictive ceramics possess large field-induced strain (>0.1%), low electromechanical hysteresis (<5%), high (>600 pC/N) effective d_{33}, and high energy density.[2] This makes them an excellent choice for use in projector materials, transducers and actuators.[3] Studies of relaxor materials often focus on the properties of greatest interest like induced strain, hysteresis, and polarization.[4] The effect of these properties on electromechanical performance is often examined as a function of composition, frequency, temperature, and magnitude of the applied electric field.

Signal Theory and Fourier Analysis

One of the most important and often overlooked aspects of scientific research is the ability to collect and integrate information in a proper and concise manner. The manipulation of this data, post-collection, can also influence the interpretation of the information and subsequent conclusions that are drawn. Strain and polarization measurements of an electroactive device can often be complicated and difficult to collect. The procedure and setup detailed here attempt to minimize collection errors and noise through the implementation of a digital collection and filtering technique. The ability to digitize the applied and signal responses allows the use of Fourier spectrum analysis and filtering techniques. These techniques, long established in the electrical engineering community, provide a very detailed look at the strain, polarization and aging response of electroactive materials.

EXPERIMENTAL PROCEDURE

Previously fabricated and well-aged $Pb(Mg_{1/3}Nb_{2/3})O_3$-$PbTiO_3$-$BaTiO_3$ [PMN-PT-BT] based materials were tested for their strain and polarization response to an applied electric field.[5] An HP8904A Multifunction Waveform synthesizer (DC-600 kHz) and a Trek high voltage amplifier (model #609D-6) were used to apply an AC, 1 Hz sinusoidal waveform with an amplitude of 1 MV/m to all samples tested. Longitudinal strain measurements were collected using a Fotonic™ sensor (MTI Instruments – 2000 Fotonic™ Sensor model #MTI-2125R). The sensor has a resolution of ≈1.0 μm and a sensitivity of ≈0.92 μm/mV. The polarization was measured using a typical Sawyer-Tower circuit[6] with the variable integrating capacitor set at 10 μF. The tests were run at room temperature (≈25°C) inside a Delta Design 9023 furnace using a 9010 temperature control unit.

At this point, the collected data would be mathematically ready to be transformed using a commercial spectrum analyzer. However, a number of practical considerations preclude such

an approach. The primary ones arise from the large electric fields (~10,000 V_{rms}), the energy stored in the test sample (~50 mJ), and the amplifier power and current needed to drive the highly capacitative load (~10 nF). In the unlikely event of a sample failure, all three considerations lead to dangerous and/or failure situations at the analyzer. (Note that monolithic ceramic failures are rare, but lead to rapid catastrophic shorts—making the analyzer the path to ground).

While it is possible to build suitable protective circuitry for the analyzer, this superimposes substantial parasitic and harmonic distortion on the response signal. An alternative is to use a robust, inexpensive, high impedance digital converter (~1 GΩ) that can survive sample failure and a computer. Specifically, the data were collected using a 16-bit analog-to-digital converter (IO Tech – ADC488/8SA) connected to a Dell Workstation 400 (Windows NT and IEEE 488 bus) running a Labview™ data acquisition program (Labview™ version 5.0.1 – National Instruments). The harmonic analyses of the applied electric field and the strain signals were performed using a Diffuse Fourier Transform in Autosignal™ Select (Version 1.0 for Windows, ©1999 AISN Software Inc.). In order to transform the time domain signals into the frequency domain a Best Exact N, Fast Fourier Transform algorithm was used. The sampling frequency was set at 500 Hz and 2000 samples were collected for each waveform. This provided a frequency resolution of 0.25 Hz over 4 complete periods of the signal. The strain signals used for analysis purposes were digitally low-pass filtered prior to examination to remove residual 60 Hz components.[7]

RESULTS AND DISCUSSION

The applied electric field (MV/m), as a function of time (seconds), is shown in Figure 1. The Fourier spectrum analysis of this signal is shown in Figure 2. This spectral analysis confirms the applied field settings of a 1 MV/m sinusoidal wave driven at a 1 Hz frequency. Note the main component of the applied field at the drive frequency of 1 Hz and the smaller but significant peak at 60 Hz. The 60 Hz peak can be attributed to "noise" components (line voltage) that have leaked into the drive voltage or sensing circuits. The as-collected data strings are initially represented in terms of the time-domain (data as a function of time). Figure 3 shows the as-collected microstrain response (typical response of a PMN-PT-BT electroceramic above its temperature of maximum permittivity, T_{max}) as a function of time. Figure 4 shows these values plotted as a function of applied electric field.

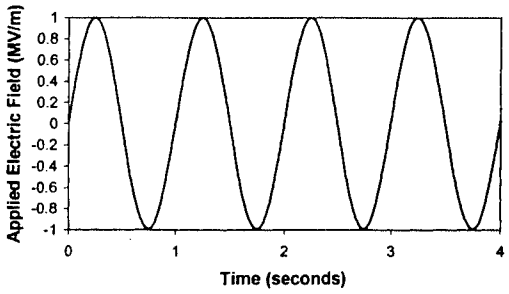

Fig. 1. Applied electric field (MV/m), $E = E_o \sin\theta$, as a function of time (seconds) (1 MV/m and 1 Hz).

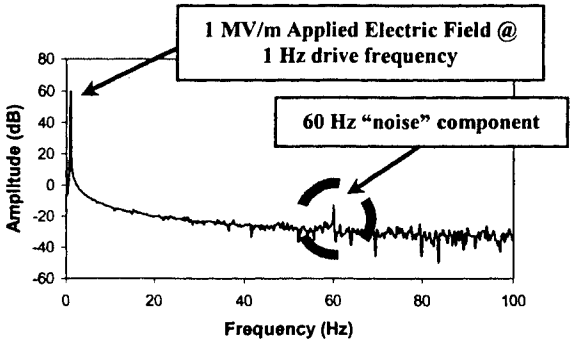

Fig. 2. Fourier spectral analysis of the 1 MV/m applied electric field. Note the 60 Hz "noise" component.

The time domain signal is initially considered to be a raw signal that contains, not only the material response, but also any "noise" components that are part of the signal. The "noise" components frequently are due to 60 Hz or 120 Hz AC electric fields from external/internal testing equipment and power lines.

In terms of the strain measurement, it is also possible to obtain "noise" components from low-level mechanical vibrations from the testing apparatus. Although it is desirable to electrically shield and mechanically isolate the system, some residual noise may still be present.

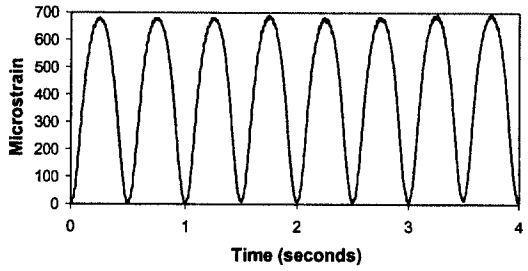

Fig. 3. Time domain representation of a typical microstrain response of an PMN-PT-BT electroactive material (1 MV/m, 1 Hz).

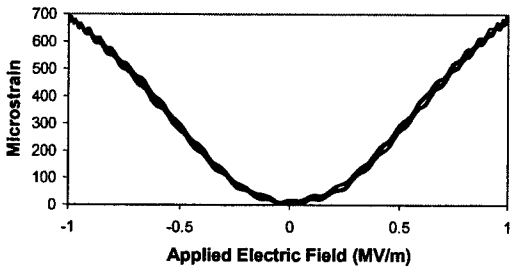

Fig. 4. Typical microstrain response of an PMN-PT-BT electroactive material as a function of applied electric field (1 MV/m, 1 Hz).

It is obvious from Figure 4 (microstrain vs. applied electric field) that any of these "noise" components can severely complicate and degrade the actual response from the material and any subsequent interpretation. It is for these reasons that the analog response is digitized and manipulated using a Fourier analysis technique.[7]

Following collection of data using best practices for electrical shielding and mechanical isolation, the filtering and manipulating process can involve several digital filtering steps. A forward fast Fourier transform (FFT) is performed on the data string using a Best Exact N algorithm. This transforms the time-domain signal into the frequency domain and provides a frequency spectrum. This particular algorithm is used because of its overall flexibility in being able to handle data strings of varying sizes. Figure 5 is the frequency spectrum of the time domain strain signal previously shown in Figure 3. It is obvious from this spectrum that a number of "noise" components have become integrated as part of the strain response. The true strain response of an electrostrictive material, above T_{max} (temperature of maximum permittivity), should be limited to the even harmonics. As expected, the zero, 2nd and 4th harmonic components are evident in the frequency spectrum. Also apparent are several large signals that are attributable to "noise" from the test apparatus.

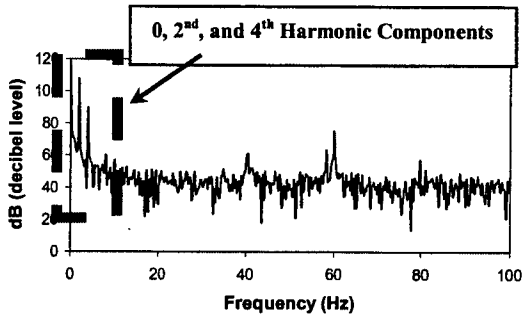

Fig. 5. Fourier frequency spectrum (function of frequency) of the time domain strain signal, previously shown in Figure 3.

The signal components around 60 Hz and 80 Hz (and others) are a particular problem and need to be removed from the spectrum to assure the results are indicative of only the true strain response of the sample. In order to accomplish this, first, a digital low pass filter is applied to the spectrum to remove spectral components above a preset cut-off frequency level, f_c.[7] Typically this cut-off frequency is taken as 15 Hz. The low pass filter allows all the frequency components lower than its pre-chosen value to pass and remain as part of the original signal. Figure 6 shows the frequency spectrum after applying a 15 Hz digital low pass filter. It is obvious in this figure that the low pass filter has driven all extraneous frequency components, which were originally part of the collected signal, to extremely small decibel levels.

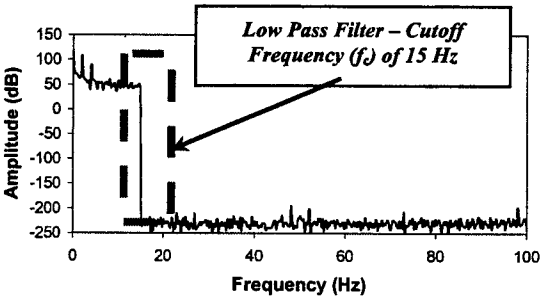

Fig. 6. Fourier spectral analysis with the applied low pass filter at a cut-off frequency of 15 Hz.

An anharmonic filter is then performed on the spectrum to remove any components that do not contribute to the harmonic strain response of the material. In this particular case

(electrostrictive response above T_{max} with an applied field frequency of 1 Hz) all even harmonics (0, 2, 4, etc..), up to and including 14 Hz, are filtered into one clean signal. This low pass and anharmonically filtered frequency spectrum is shown in Figure 7. The true frequency components that make up the strain response are dependent on the frequency of the voltage drive signal and the nature of the response.

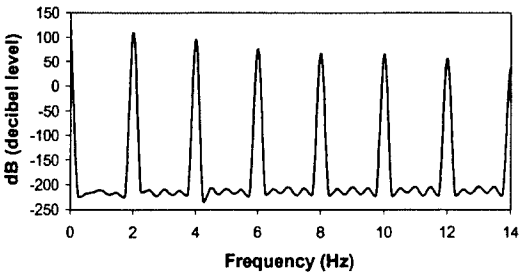

Fig. 7. Anharmonic filter removes additional frequency components considered to be contamination of the signal.

Once a clean filtered signal is obtained, an inverse fast Fourier transform is used to reconstruct the original time domain representation of the strain response from the filtered frequency spectrum. This filtered reconstruction only contains the appropriate harmonic components. The signal is now free of any undesired ("noise") components that may have been part of the harmonic response of the signal. Figure 8 shows the filtered strain response as a function of time (time-domain) and applied electric field.

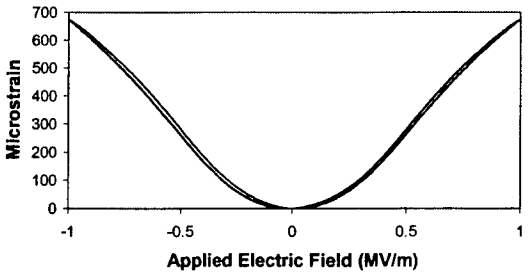

Fig. 8. Filtered strain response (microstrain) of a typical PMN-PT-BT electroactive material as a function of applied electric field (MV/m). Note compare to Figure 4.

Another important point to note about the digital collection and filtering process involves phase relationships among all the signals collected. When the data are digitized, the analog signals (applied electric field, displacement and polarization voltage) are collected simultaneously. This is an extremely important condition because any subsequent digital manipulation of one signal affects all three signals (applied electric field, polarization, and microstrain) when they are recombined or plotted against one another (ex: microstrain vs. applied electric field). The signals are collected as a set and are considered "phase-locked" with each other. For this reason, digital manipulation of the signals needs to be identical between each of them or the filtering procedure will result in a phase mismatch.

REFERENCES

[1] V. A. Bokov and I. E. Myl'nikova, "Electrical and Optical Properties of Single Crystals of Ferroelectrics with a Diffused Phase Transition," *Sov. Phys. – Solid State (Engl. Transl.)*, **3**, 613 (1961).

[2] K. Uchino, "Electrostrictive Actuators: Materials and Applications," *Am. Ceram. Soc. Bull.*, **65** [4] 647-56 (1986).

[3] S. R. Winzer, N. Shankar, and A. P. Ritter, "Designing Cofired Multilayer Electrostrictive Actuators for Reliability," *J. Am. Ceram. Soc.*, **72** [12] 2246-57 (1989).

[4] E. Bailey, S. R. Winzer, A. E. Sutherland, and A. P. Ritter, "Electrostrictive Ceramic Materials Including a Process for the Preparation Thereof and Application Therefore," U.S. Pat. No. 5023032, June 11, 1991.

[5] S. M. Pilgrim, M. Massuda, J. D. Prodey, and A. P. Ritter, "Electromechanical Properties of Some $Pb(Mg_{1/3}Nb_{2/3})O_3$ - $PbTiO_3$ - (Ba, Sr)TiO_3 Ceramics: I," *J. Am. Ceram. Soc.*, vol. 75, no. 7, pp. 1964-1969, 1992.

[6] C. B. Sawyer and C. H. Tower, "Rochelle salt as a dielectric," *Phys. Rev.*, vol. 35, pp. 269-273, 1930.

[7] S. P. Leary and S. M. Pilgrim, "Harmonic Analysis of the Polarization Response in PMN-based Ceramics–A Study in Aging", *IEEE Trans. Ultrasonics, Ferroelectrics, and Frequency Control*, vol. 45, no. 1, pp. 163-169, 1998.

Calculation of Electrostrictive Coefficients and Their Complex Nature Through Fourier Analysis

C. B. DiAntonio, F. A. Williams Jr., and S. M. Pilgrim
Laboratory for Electronic Ceramics
New York State College of Ceramics at Alfred University
2 Pine Street, Alfred, New York, 14802
Phone: 607-871-2576
Fax: 607-871-2354
Email: pilgrim@alfred.edu

ABSTRACT

Implementation of a discrete Fourier transform in conjunction with Devonshire phenomenology allows the electromechanical response of an electroactive material to be fully characterized. The calculated Fourier series from the strain and/or polarization response results in the necessary spectral components to quantitatively determine the electrostrictive coefficients without the use of least squares curve fitting techniques. In addition, the Fourier analysis provides an equation, in the form of a Fourier series, that exactly models the electromechanical response of the material. The spectral components contain the necessary amplitude information used to calculate the electrostrictive coefficients. The spectral analysis also provides the phase information (imaginary part) for these response signals. This allows for the determination of complex electrostrictive coefficients that maintain the phase relationships necessary to reproduce the hysteretic nature of these signals.

INTRODUCTION

The strain response of a dielectric material is often expressed as a polynomial expansion of the applied electric field, following Devonshire methodology.[1,2] The response follows a Taylor series expansion and contains a series of tensor coefficients. The strain (S_{ij}) is:

$$S_{ij} = d_{kij} E_k + M_{ijkl} E_k E_l + A_{ijklm} E_k E_l E_m + B_{ijklmn} E_k E_l E_m E_n + \bullet\bullet\bullet\bullet\bullet \quad (1)$$

In these expressions, E_k is the applied electric field, d_{kij} is the piezoelectric coefficient, M_{ijkl} is the second order electrostrictive coefficient, A_{ijklm} is the third order piezoelectric voltage coefficient, and B_{ijklmn} the fourth order electrostrictive coefficient. For a PMN-based material operating in the electrostrictive regime and operated with a bipolar excitation, symmetry can be used to simplify equation 1; all odd-order tensors in a centrosymmetric material are null properties.[3]

$$S_{ij} = M_{ijkl} E^2 + B_{ijklmn} E^4 + D_{ijklmnop} E^6 + \bullet\bullet\bullet\bullet\bullet \quad (2)$$

Therefore, an unbiased electrostrictor will not display a linear dependence of the strain on the applied electric field, but should show a sequence of even power responses.[4,5] This has been confirmed by a number of studies using polynomial fitting of the strain-field data. Since the electric field is sinusoidal, $E=E_o \sin(\omega t \pm \phi)$, equations 3-4 can be easily derived from Eqn. 2..

$$S_{ij} = M_{ijkl}(E_o \sin(\omega t + \phi))^2 + B_{ijklmn}(E_o \sin(\omega t + \phi))^4 + D_{ijklmnop}(E_o \sin(\omega t + \phi))^6 + \bullet\bullet \quad (3)$$

where E_o is the maximum amplitude of the applied field over the time interval, ω is the angular frequency ($\omega=2\pi\nu$), t is the time, and ϕ represents the phase angle of the wave (referenced to zero radians).

When an electric field, with a sufficiently large amplitude is applied, the higher harmonics predicted by equation 1 are more apparent after expansion (use of trigonometric identities) and rearrangement of the electric field components:

$$E^2 = (E_o \sin(\omega t \pm \phi))^2 = E_o^2(\sin(\omega t \pm \phi))^2 = E_o^2/2 - (E_o^2/2)(\cos 2(\omega t \pm \phi)) = E_o^2/2 - (E_o^2/2)(\cos(2\omega t \pm 2\phi)) \quad (4)$$

Notice that the second harmonic, in addition to the fundamental, is produced. Equation 4 can now be manipulated to match the form of the Devonshire phenomenology:

$$S_{ij} = M_{ijkl}[E_o^2/2 - (E_o^2/2)(\cos(2\omega t \pm 2\phi))] + B_{ijklmn}[3E_o^4/8 - E_o^4/2\,[\cos(2\omega t \pm 2\phi)] + + E_o^4/8[\cos(4\omega t \pm 4\phi)]\,] + \bullet\bullet\bullet\bullet \quad (5)$$

Notice that the second and fourth harmonics, in addition to a term independent of frequency (zero frequency component), are produced.

In general it can be seen that the term with $E^{(2n-1)}$, where n = 1, 2, 3,..., generates the $(2n-1)^{th}$ harmonic and contributes to all odd harmonics below the $(2n-1)^{th}$.[6] By continuing with the expansions (E^5, E^6, E^7, etc.) it is clear that the harmonic components of the signal each contain a contribution to the lower harmonic amplitudes. This concept holds for both the strain and polarization polynomial expansions. For example, the E^4 term contributes to the amplitude at both the second and zero frequency responses. It is possible to derive the Devonshire coefficients from the harmonic response. Note that the phase information for each component must be preserved since it provides the necessary information to model the hysteretic response of the material. Harmonic analysis also suggests two quantitative checks for the necessary depth of the expansion. The zero frequency response is an algebraic sum that depends on the even coefficients (providing a 'goodness of fit' parameter). In addition, a minimum important level of a harmonic amplitude can be defined to truncate the expansion, e.g., the expansion can be truncated when the harmonic amplitude becomes 60 dB less than that of the primary (this level has been chosen arbitrarily based on signal strength and underlying noise components).

The strain response of the material as a function of time is determined through the implementation of the Fourier transform of a measured strain response. The strain and/or polarization, as a function of time, is set equal to the strain and/or polarization as a function of applied electric field. This relation provides an indirect way of obtaining an equation of the strain response of the material as a function of the applied electric field.

The Fourier analysis of the measured time domain signal results in a Fourier series of sine components (this could also be cosine components or a combination of sine and cosine components based on phase manipulation) that model the strain or polarization response signal of the material. The Fourier series takes the following shape:

Measured Waveform (time) =

$$A_0 + \Sigma\, A_n \sin(\omega_n t + \phi_n) \quad (6)$$

Where;
A_0 = zero frequency amplitude, DC or average value
A_n = specific harmonic component amplitude
$\omega_n = 2\pi\nu$ = radial frequency
t = time (seconds)
ϕ_n = phase angle (radians)

The Fourier series is equated with the polynomial expansion of the strain (S_{ij}) response, as a function of applied electric field (E) or as a function of the polarization (P_i). The components of the expansion are then grouped based upon the frequency component they contribute to:

$$S_{ij}(E) = d_{ijk}E + M_{ijkl}E^2 + \ldots = FS \quad (7)$$

$$S_{ij}(P) = g_{ijk}P + Q_{ijkl}P^2 + \ldots = FS \quad (8)$$

Where;
$S_{ij}(E)$ = strain as a function of electric field
$S_{ij}(P)$ = strain as a function of polarization
FS = Fourier series as a function of frequency

The Fourier series of the strain response can be used to calculate the electrostrictive coefficients as a function of the applied electric field. If the series is truncated to only consider the M_{ijkl} coefficients (truncated after the 2^{nd} order contributions) then the expansion takes the following form (M_{ijkl} is a 2^{nd} order component but a 4^{th} rank tensor):

$$FS = A_0 + \Sigma\, A_n \sin(\omega t + \phi) = = d_{ijk}E_o \sin\theta + M_{ijkl}E_o^2 \sin^2\theta = = A_0 + \Sigma\, A_n \sin(\omega t + \phi) = = (d_{ijk}E_o \sin\theta) + ((M_{ijkl}E_o^2/2) - (M_{ijkl}E_o^2/2 \cos 2\theta)) \quad (9)$$

(Note: phase relationships have intentionally been neglected-- the polynomial expansion cannot account for phase relationships) After rearrangement of equation 9, the contributions are apparent:

$$\text{Zero Frequency contribution} = M_{ijkl}E_o^2/2 \quad (10)$$

$$\text{First Order Contribution} = d_{ijk}E_o \sin\theta \quad (11)$$

Second Order Contribution
$$= (M_{ijkl}E_o^2/2)\cos 2\theta \quad (12)$$

this can then be set equal to the Fourier analysis results in order to calculate the zero frequency, d_{ijk} and M_{ijkl} coefficients:

$$A_0 = M_{ijkl}E_o^2/2 \quad (13)$$

$$A_1 = d_{ijk}E_o \quad (14)$$

$$A_2 = M_{ijkl}E_o^2/2 \quad (15)$$

Where;
A_0 = Amplitude of the Zeroth Harmonic
A_1 = Amplitude of the First Harmonic
A_2 = Amplitude of the Second Harmonic

therefore,

$$\text{Zero or Y-intercept} = A_0 - (ME_o^2/2) \quad (16)$$

$$d_{ijk} = A_1/E_o \quad (17)$$

$$M_{ijkl} = 2A_2/E_o^2 \quad (18)$$

The expansion can be continued to include higher order harmonics.

EXPERIMENTAL PROCEDURE

In order to demonstrate how the Fourier series can be used to obtain the strain coefficients (function of applied electric field) an "un-aged" PMN-PT-BT sample (B125650 composition – [0.9875(0.935PMN-0.065PT)-0.0125BT or 0.9233PMN-0.06419PT-0.0125BT]) was measured for its strain response to an applied electric field.[7] An HP8904A Multifunction Waveform synthesizer (DC-600 kHz) and a Trek high voltage amplifier (model #609D-6) were used to apply an AC, 1 Hz sinusoidal waveform with an amplitude of 1 MV/m to all samples tested. Longitudinal strain measurements were collected using a Fotonic™ sensor (MTI Instruments – 2000 Fotonic™ Sensor model #MTI-2125R). The sensor has a resolution of ≈1.0 μm and a sensitivity of ≈0.92 μm/mV. The polarization was measured using a typical Sawyer-Tower circuit with the variable integrating capacitor set at 10 μF. The tests were run at room temperature (≈25°C) inside a Delta Design 9023 furnace using a 9010 temperature control unit.

RESULTS AND DISCUSSION

The measured microstrain as a function of applied electric field is shown in Figure 1 (1 MV/m, 1 Hz applied sinusoidal electric field at 25°C). From the spectral analysis of the strain response, the coefficients of the temporal Fourier series can be used to directly model the material response (microstrain as a function of time or applied electric field). The specific microstrain spectral information (using equation 9 and data from Figure 1) is shown in Table I for each of the noted signal components. The first two columns (real and imaginary components) are the direct result of the DFT. The subsequent derived columns present these data in the alternative forms needed for calculations. Additional harmonics exist, but they were neglected since they are more than 60 dB below the primary.

Therefore the Fourier series has the following form:

$S_{ij}(t) =$ 395.23 [0^{th} frequency component]
+ 331.49 sin(2*2πt + 4.75) [2^{nd} Harmonic]
+ 62.16 sin(4*2πt + 4.82) [4^{th} Harmonic]
+ 6.24 sin(6*2πt + 4.91) [6^{th} Harmonic]
+ 2.26 sin(8*2πt + 1.92) [8^{th} Harmonic]
+ 1.92 sin(10*2πt + 2.10) [10^{th} Harmonic]
+ 0.67 sin(12*2πt + 2.49) [12^{th} Harmonic]
+ 0.08 sin(14*2πt + 0.81) [14^{th} Harmonic]

This single equation precisely models the strain signal in both magnitude and hysteretic behavior as a function of time and/or applied electric field.

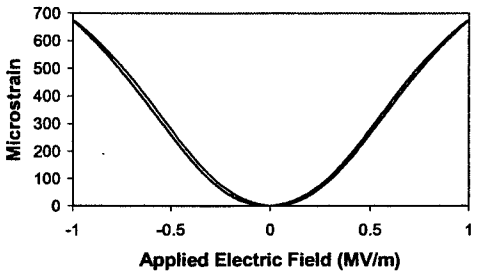

Fig. 1. Electrically induced microstrain (anharmonically and low pass filtered to 15 Hz) for a typical B125650 response.

The real strength of this Fourier series approach lies in its ability to accommodate hysteresis and provide a distinct quantification of a given strain response while faithfully describing the true harmonic content. Each of these advantages aids engineering and device application of electromechanical materials by

providing the inputs for nonlinear controls and a comparative basis for different materials[8].

Table I. Spectral Representation Information.[∀]

Freq. [ν_n] (Hz)	Real	Imaginary	dB*	Phase[⊗] [ϕ_n] (Rad.)	Amplitude# [A_n] (μstrain)
0	7.90 x 10^5	0.00	117.96	1.57	395.23
2	-3.31 x10^5	-13670.01	110.41	4.75	331.49
4	-61829.96	-6423.97	95.87	4.82	62.16
6	-6113.02	-1244.24	75.90	4.91	6.24
8	2124.39	763.70	67.07	1.92	2.26
10	1657.87	974.23	65.68	2.10	1.92
12	406.30	537.87	56.57	2.49	0.67
14	57.31	-54.60	37.97	0.81	0.08

∀ The DFT results (Real, Imaginary, Frequency [Hz]) and ancillary data that are derived from these values: decibel level (dB), amplitude (μstrain), phase (radians).
* dB has been referenced to 1 μstrain; *dB = $(10)\log_{10}(\text{Real}^2 + \text{Imaginary}^2)$
⊗ Phase (sine-based) = $(\pi/2)$ + atan(Imaginary/Real); referenced to zero radians.
Amplitude (normalized) = $(2/n)(\sqrt{(\text{Real}^2 + \text{Imaginary}^2)})$ [where n = # of data points collected].

Table II. Calculated Electrostrictive Coefficients.*

Method of Determining Electrostrictive Coefficients	M_{3333} (m^2/V^2)	B_{333333} (m^4/V^4)	R^2
FFT (Fourier Series of Microstrain)	**$1288.09e^{-18}$**	**$-816.30e^{-30}$**	—
Even and Odd Polynomial Fit	**$1291.27e^{-18}$**	**$-826.13e^{-30}$**	**0.99**
Even Polynomial Fit Only	**$1291.26e^{-18}$**	**$-826.12e^{-30}$**	**0.99**

*Electrostrictive coefficients calculated using the DFT, polynomial least squares, and polynomial even order least squares, at 25°C, all values determined from the same base data set. Note that the odd coefficients from a polynomial expansion fit (1st order = 0.177 m/V, 3rd order = -0.289 m^3/V^3, and 5th order = 0.104 m^5/V^5) conflict with the physics.

A benefit of the FFT approach is the direct calculation of electrostrictive coefficients (and piezoelectric coefficients) with quantitative criterion for truncation and a 'goodness of fit' criterion related to the zero frequency component. These results can be directly compared to those obtained from the more conventional polynomial fit, but include the benefits noted above. In order to directly compare the two approaches, it is convenient to truncate both expansions at the 4th order. Most least squares curve-fitting programs do not extend their fit past the 6th or 8th order, therefore it is prudent to show that FFT analysis can be used to calculate the values to at least the 4th order. The results of this comparison are listed in Table II. Overall, this approach provides data consistent with previous approaches, but it also provides additional insight.

REFERENCES

[1] A. F. Devonshire, "Theory of Ferroelectrics," *Adv. Phys.*, **3** [10] 85-130 (1954).

[2] H. Beige and G. Schmidt, "Electromechanical Resonances for Investigating Linear and Nonlinear Properties of Dielectrics," *Ferroelectrics,* **41**, 39-49 (1982).

[3] J. F. Nye, *Physical Properties of Crystals: Their Representation by Tensors and Matrices*; pp. 473-786. Oxford University Press, Oxford, 1993.

[4] R. Newnham and G. Ruschau, "Electromechanical Properties of Smart Materials," *J. Intell. Mater. Syst. Struct.*, **4** [3] 289-294 (1993).

[5] S. M. Pilgrim, "Electrostrictive Ceramics for Low Frequency Transducers," *IEEE Trans. Ultrason., Ferroelectr., Freq. Control*, **47** [4] 861-876 (2000).

[6] S. P. Leary and S. M. Pilgrim, "Harmonic Analysis of the Polarization Response in PMN-based Ceramics–A Study in Aging," *IEEE Trans. Ultrason., Ferroelectr., Freq. Control*, **45** [1] 163-169 (1998).

[7] S. M. Pilgrim, M. Massuda, J. D. Prodey, and A. P. Ritter, "Electromechanical Properties of Some $Pb(Mg_{1/3}Nb_{2/3})O_3$ - $PbTiO_3$ - (Ba, Sr)TiO_3 Ceramics: I," *J. Am. Ceram. Soc.*, **75** [7] 1964-1969 (1992).

[8] C.B. DiAntonio, F.A. Williams Jr., and S.M. Pilgrim, "The Use of Harmonic Analysis of the Strain Response in $Pb(Mg_{1/3}Nb_{2/3})O_3$-based Ceramics to Calculate Electrostrictive Coefficients," in press, *IEEE Trans. Ultrasonics, Ferroelectrics, and Frequency Control*, November 2001.

Visualization of the Domain Orientation in $PbTiO_3$ Single Crystals by Vertical and Lateral Piezoresponse Microscopy

H. Okino, T. Ida, H. Ebihara, and T. Yamamoto

Department of Communications Engineering, National Defense Academy,
1-10-20 Hashirimizu, Yokosuka, Kanagawa 239-8686, Japan
Fax: +81-468-41-3810 (Ext. 3330), E-mail: hokino@nda.ac.jp

Four kinds of domain structures (180° *c*-*c*, 180° *a*-*a*, 90° *a*-*a* and 90° *a*-*c* domains) on grown surface of $PbTiO_3$ (PTO) single crystals were imaged successfully using vertical and lateral piezoresponse force microscopy (PFM). Domain orientations (i.e. polarization vector distributions) at the surface of each domain structures are presented. These domain images will be compared with simultaneously observed surface topographic images decorated by an acid etching treatment.

INTRODUCTION

Studies on ferroelectric domains are required to understand various characteristics of ferroelectric materials.

Piezoresponse force microscopy (PFM)[1,2] is most effective technique for domain observations. This is because PFM has enough sensitivity to reveal the polarization on a ferroelectric sample and can be easily employed for visualizing domains on various ferroelectric samples (single crystals, ceramics and thin films). In addition, as Abplanalp *et al.*[3] recently demonstrated, both vertical and lateral component of polarization can be imaged simultaneously by PFM.

Nevertheless, the results of vertical and lateral PFM observations were not verified by other established domain observation techniques yet. Moreover, a few studies[3–6] on domain visualization by these vertical and lateral PFM have been reported up to now.

In this paper, four kinds of domain structures (see Fig. 1) on grown surface of pure $PbTiO_3$ (PTO) and Mn-doped PTO single crystals were visualized using PFM. The purpose of the present paper is to establish vertical and lateral PFM as a domain imaging technique. To this end, the result of PFM observation will be compared with surface topographic images[7] decorated by an acid etching treatment.

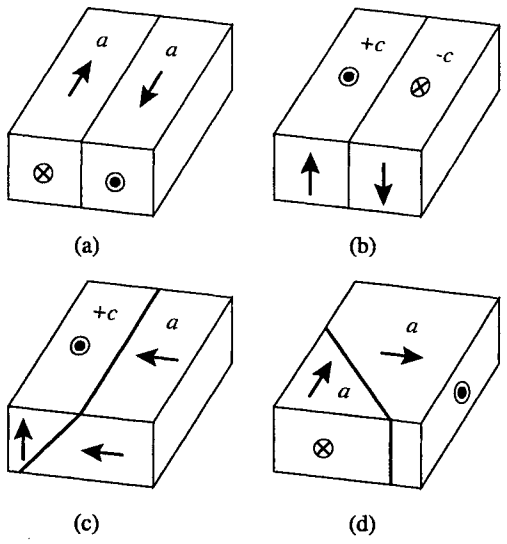

Fig. 1 Domain structures formed in tetragonal crystals; (a) 180° *a*-*a* domain, (b) 180° *c*-*c* domain, (c) 90° *a*-*c* domain, and (d) 90° *a*-*a* domain. The arrows and the signs represent the directions of the polarizations.

EXPERIMENTAL

During PFM observations, domains are visualized by detecting the inverse piezoelectric oscillations caused by the modulation a.c. voltage $U(t) = U_0 \sin(\omega t)$ applied between the conducting tip and an electrode on the backside of the sample.[1] These local oscillations on the sample surface consist of vertical and lateral vibrations originating from out-of-plane (z) and in-plane (x–y) components of polarization under the tip, respectively. Here, x, y and z correspond to a coordinate system fixed in space with the z-axis perpendicular to the inspected surface and the x-axis along the cantilever. Then, owing to the tip in contact with the ferroelectric sample surface, these vertical and lateral vibrations result in the cantilever bending in z direction and torsion along y direction. Figure 2 shows that the cantilever bending and torsion can be measured using commercial SFM based on the principle of laser deflection onto a four-quadrant photodetector. These normal and torsional cantilever oscillation can be demodulated individually with a lock-in amplifier using modulation signal U(t) as the reference signal. Consequently, it is possible to determine the projection of the polarization vector onto z and y direction (P_z and P_y). It must be noted that the low-pass cutoff of the SFM feedback loop is

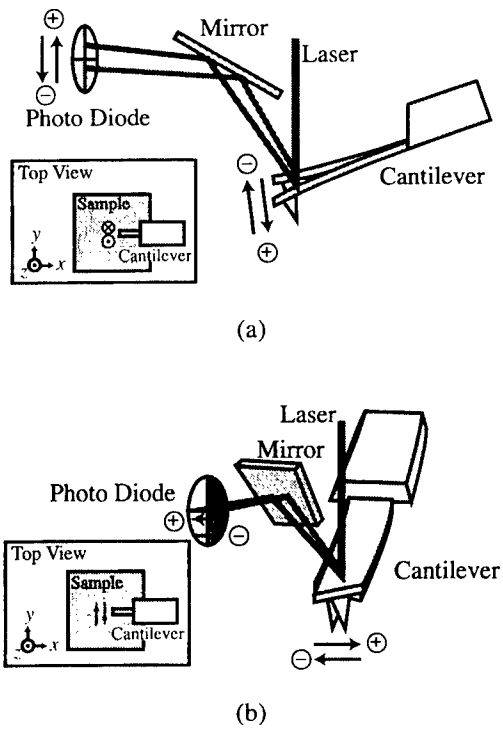

Fig. 2 Schematics showing laser beam detection of (a) cantilever bending and (b) cantilever torsion. The cantilever bending and torsion can be measured through the principle of laser deflection onto a four-quadrant photodetector.

limited to frequencies lower than the frequency ω of the modulation voltage to avoid the cantilever vibration signal attenuation.

The experimental setup consisted of a commercial atomic force microscope (Seiko Instruments, SPA300 and SPI3700) connected to a lock-in amplifier (NF Electronic Instruments, LI-575). A conductive gold coated Si cantilever (Seiko Instruments, SI-DF3) was used for domain visualization. The force constant and the resonance frequency of the cantilever were 1.8 N/m and 28 kHz, respectively. The domains were imaged by scanning the single crystals with an applied ac 4 V voltage (peak-to-peak) oscillating at 5 kHz.

Pure PTO and Mn-doped PTO single crystals were prepared to investigate four kinds of domain structures. This is because the dominant domain structures are 90° *a*-*c* and 90° *a*-*a* for pure PTO and 180° *a*-*a* and 180° *c*-*c* for Mn-doped PTO. Pure PTO and 0.5 mol% Mn-doped PTO single crystals were grown by the flux technique in air. Details of crystal growth procedures were already reported elsewhere.[7)]

As-grown PTO crystals were washed in a hot thin HNO_3 water solution for removing the excess PbO flux. During this process, domains on the PTO surface were etched at different speeds depending on the polarization directions on each domain surface.[8)]

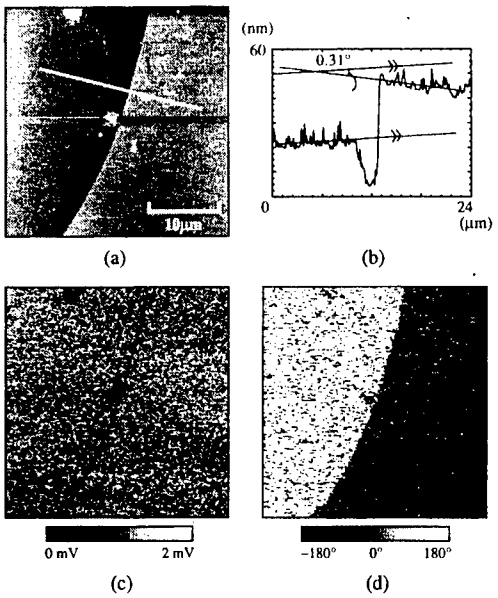

Fig. 3 Topographic image and vertical PFM images observed near 180° *c*-*c* domain boundary on Mn-doped PTO single crystal. (a) 31μm×31μm topographic image. (b) Crosssectional plot of the white line in (a). (c) Amplitude image and (d) phase image of vertical piezoresponse simultaneously recorded with (a).

RESULTS AND DISCUSSIONS

180° *c*-*c* domains

180° *c*-*c* domain boundary come to be visible by the acid etching treatment, since the etching rate on $-c$ domain is greater than that on $+c$ domain.[8)] Here, polarizations of $+c$ and $-c$domains goes out of and comes into the sample, respectively. Polarizing light microscopy and TEM are not available to observe 180° *c*-*c* domain boundary, because crystal anisotropy along *c*-axis between $+c$ and $-c$ domains are nearly zero.

Figure 3 (a) shows surface topographic image of Mn-doped PTO near 180° *c*-*c* domain boundary. A step existed at the center of the image and flat surfaces at the right and left side met at the step with a negligible gradient angle of 0.31° (see Fig. 3 (b)). This negligible gradient angle is not attributable to 90° *a*-*c* domain boundary, because the calculated gradient angle on 90° *a*-*c* domain boundary of Mn-doped PTO is 3.54°. The detail of gradient angle on 90° *a*-*c* domain boundary will be described later. Consequently, this step arisen from the etching rate difference and the right and left side area in Fig. 3 (a) were $+c$ and $-c$ domain, respectively.

The vertical PFM images were simultaneously recorded with Fig. 3 (a). Figure 3 (c) illustrates piezoresponse amplitude A mapped image, which shows that the quantity of the vertical polarization vector $|P_z|$ in the right side domain was equal to that in the left side domain. Figure 3 (d) illustrates the spatial distribution of phase shift ϕ be-

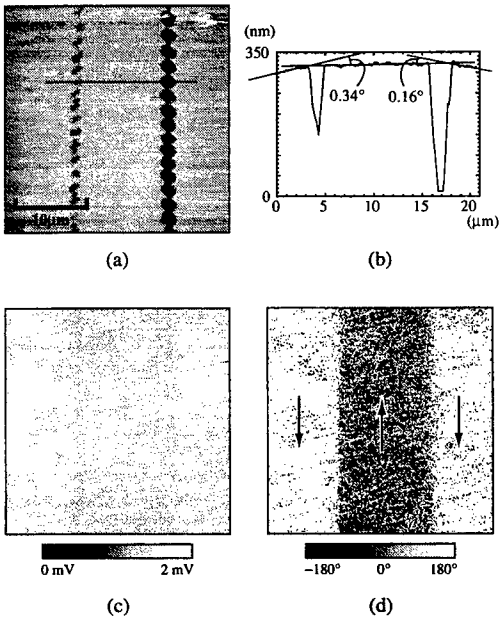

Fig. 4 Topographic image and lateral PFM images observed near 180° a-a domain boundaries on Mn-doped PTO single crystal. (a) 31μm×31μm topographic image. (b) Crosssectional plot of the white line in (a). (c) Amplitude image and (d) phase image of lateral piezoresponse simultaneously recorded with (a).

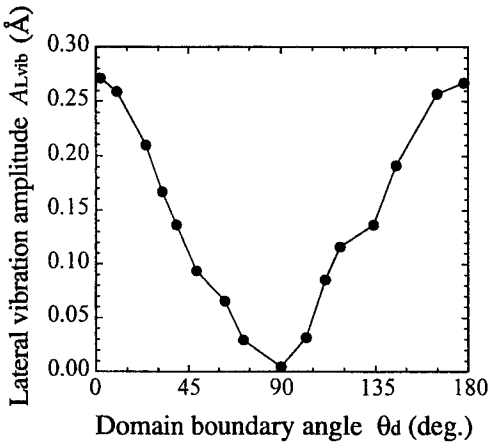

Fig. 5 The dependence of the detected lateral vibration amplitude (A_{Lvib}) on the domain boundary (the etched pits line) angles with y-axis (θ_{d}). A_{Lvib} increased as the domain boundary came to be parallel with y-axis ($\theta_{\mathrm{d}} = 0°$ or 180°).

tween the modulation voltage and piezoresponse signal. The phase shift correspond to the direction of the vertical polarization vector ($\mathrm{sgn}(P_z)$ = $\cos\phi$). Under the present experimental conditions this phase shift in $+c$ domains is 0°, while that in $-c$ domains is 180°. Hence, these amplitude and phase PFM images indicates that the right and left side domains were ascribed to the antiparallel vertical polarization, i.e. $+c$ and $-c$ domains, respectively. This is consistent with the result of the AFM topographic image analysis.

180° a-a domains

As a result of the acid etching treatment, 180° a-a domain boundaries emerged with etched pits as shown in Fig. 4 (a). Figure 4 (b) is the crosssectional plot of black line in Fig. 4, showing that there was no step across the etched pits line and the gradient angle on the etched pits line was negligible. However, the polarization directions in each a domains cannot be determined by the topographic image.

The lateral PFM amplitude and phase images simultaneously recorded with Fig. 4 (a) are shown in Fig. 4 (c) and (d), respectively. The amplitude image (Fig. 4 (c)) shows that the quantity of the lateral polarization vector $|P_y|$ was almost equal in the whole scanning region. Besides, the phase image (Fig. 4 (d)) represented the direction of the lateral polarization vector along the y-axis ($\mathrm{sgn}(P_y)$) in a similar manner to vertical PFM. Under the present experimental conditions the phase shift in a domains with polarization vector oriented toward the up side is 0°, while that in the antiparallel domains is 180°. Thus, the polarization vectors in these a domains can be illustrated as shown in Fig. 4 (d).

Figure 5 shows the dependence of the detected lateral vibration amplitude (A_{Lvib}) on the domain boundary (the etched pits line) angles with y-axis (θ_{d}). θ_{d} was changed by rotating the sample. A_{Lvib} is calculated by the following equation.

$$A_{\mathrm{Lvib}} = S_{\mathrm{torsion}} \times A_{\mathrm{Llockin}} \qquad (1)$$

where S_{torsion} is sensitivity of cantilever torsion detection estimated from friction curve measurement, and A_{Llockin} is torsional signal amplitude demodulated by lock-in amplifier. A_{Lvib} increased as the domain boundary came to be parallel with y-axis ($\theta_{\mathrm{d}} = 0°$ or 180°). This dependence of lateral piezoresponse amplitude indicates that the polarization directions in the a domains were parallel with the 180° a-a domain boundaries. This result is consistent with the condition of polarization continuity at domain boundaries.

90° a-a domains and 90° a-c domains

Figure 6 (a) shows the topographic image on the grown surface of pure PTO single crystal observed near a 90° a-a domain boundary with each a domains consisting of 90° a-c domain structures. The straight groove running through the middle of the image is the 90° a-a domain boundary. This groove was also caused by the acid etching treatment. Figure 6 (b) shows the crosssectional plot of black line in Fig. 6 (a). The convex-concave shape with gradient angles ranging from 2.92° to 4.08° was observed. The gradient angle θ_{g} on 90° a-c domain structure is dominated by the crystal tetragonality (ratio of c- and a-axis lattice constants in the crystal, c/a) and obeys

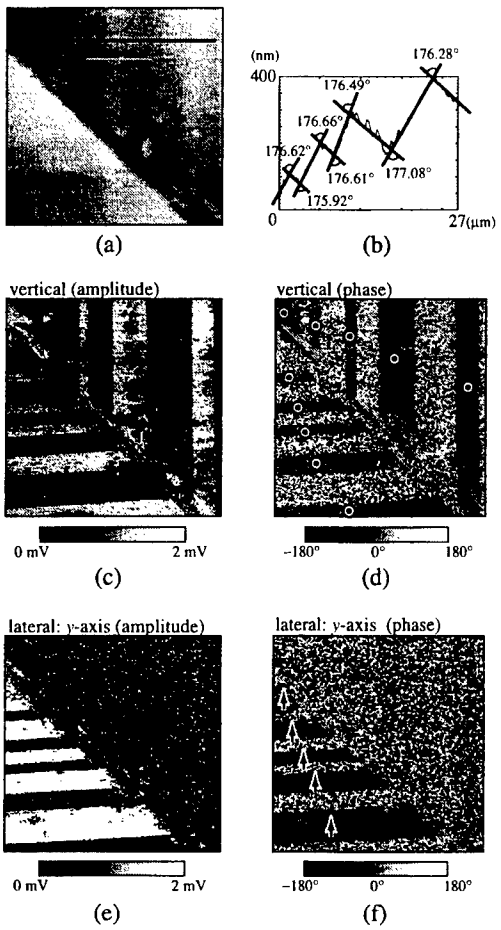

Fig. 6 Topographic image and vertical and lateral PFM images observed near 90° *a-a* domain boundary on pure PTO single crystal. (a) 31μm×31μm topographic image. (b) Crosssectional plot of the black line in (a). (c) Amplitude image and (d) phase image of vertical piezoresponse, and (e) amplitude image and (f) phase image of lateral piezoresponse observed at the same position with (a).

the following equation.

$$\theta_g(\text{deg.}) = 2\tan^{-1}(c/a) - 90 \qquad (2)$$

For our pure PTO single crystal lattice constants a and c measured by conventional XRD method were 3.904 $\AA$ and 4.150 $\AA$, respectively. According to equation (1), the theoretical gradient angle θ_{th} was found to be 3.64°, which coincided with the measured gradient angles. Thus, the observed convex-concave shape was ascribed to 90° *a-c* domain structure, and the crests and the troughs were 90° *a-c* domain boundaries. Nevertheless, it is impossible to determine the polarization orientation of each domains by the topographic image.

Vertical piezoresponse amplitude and phase images (Fig. 6 (c) and (d)), and lateral piezoresponse amplitude and phase images (Fig. 6 (e) and (f)) observed at the same position with Fig. 6 (a). The bright areas in Fig. 6 (c) and (e) corresponded to c domains and a domains, respectively. The phase image (Fig. 6 (d) and (f)) implies that the polarizations of these c and a domains went out of the sample surface along z-axis and oriented toward the up side along y-axis, respectively. The arrows illustrated in Fig. 6 (d) and (f) represent the direction of the polarization vector in these domains.

The dark areas in both the vertical and lateral piezoresponse amplitude images existed in upper right region of the etched groove. These areas were attributed to a domains with the polarizations oriented toward the right side due to the condition of polarization continuity at domain boundaries. This was able to be confirmed by lateral PFM observation with sample rotations.

CONCLUSIONS

Four kinds of domain structures (180° *c-c*, 180° *a-a*, 90° *a-a* and 90° *a-c*) on grown surface of PTO single crystals were visualized successfully using vertical and lateral PFM. The determined domain structures using PFM were consistent with simultaneously observed surface topography decorated by the acid etching treatment. In addition, polarization orientations in a domains could be determined using lateral PFM.

ACKNOWLEDGEMENTS

This work was partly supported by Foundation for Promotion of Material Science and Technology of Japan (MST Foundation).

References

1) K. Takata, K. Kushida, K. Torii, and H. Miki, Jpn. J. Appl. Phys. **33**, 3193 (1994).

2) R. Luthi, H. Haefke, K. P. Meyer, L. Howald, and H. J. Guntherodt, J. Appl. Phys. **74**, 7461 (1993).

3) M. Abplanalp, L. M. Eng, and P. Guenter, Appl. Phys. **A66**, S231 (1998).

4) L. M. Eng, H. J. Guntherodt, G. A. Schneider, U. Kopke, and J. M. Saldana, Appl. Phys. Lett. **74**, 233 (1999).

5) L. M. Eng et al., Ferroelectrics **222**, 153 (1999).

6) A. Roelofs et al., Appl. Phys. Lett. **77**, 3444 (2000).

7) T. Yamamoto, K. Kawano, M. Saito, and S. Omika, Jpn. J. Appl. Phys. **36**, 6145 (1997).

8) J. A. Hooton and W. J. Merz, Phys. Rev. **98**, 409 (1955).

Domains and Piezo Images of PZT Family Thin Films Observed by AFM and KFM

Y.Masuda , [1]K.Kakimoto , S.Fujita , and [2]K.Watanabe.

Department of Electrical Engineering, Faculty of Engineering,
Hachinohe Institute of Technology,

88-1 . Ohbiraki , Myo , Hachinohe , Aomori 031-8501 , Japan.

1:Department of Materials Science and Engineering ,
Nagoya Institute of Technology ,
Gokiso-cho,Showa-ku,Nagoya 466-8555 , Japan.

2:Seiko Instrument Company. Nakase 1-8 Mihama-ku, Chiba 261-0023 , Japan

Fax: +81-178-25-8047, Email: ymasuda@hi-tech.ac.jp

1. Introduction

Ferroelectric materials are very interesting functional materials which have piezoelectric, pyroelectric, nonlinear- optic and polarization switching phenomena for the dependence of applied electric field, temperature, stress and light beam irradiation, respectively.

$PbZr_{1-x}Ti_xO_3$(PZT) thin film has been actively studied for it's potential application in ferroelectric nonvolatile random access memories (NVRAMs) and micro electro mechanical systems (MEMS). It is expected the micro actuators to be applied piezoelectric properties, such as a precision optical axis control of optical apparatus, a precisions position control of micro robot and a blood control in a blood vessel, respectively. PZT thin films with repeated polarization switching endurance and voltage are desirable for these applications, respectively.

In the present study, PZT thin films with composition n ear the MPB were prepared by YAG: PLD technique using bulk target source for control of the Pb content of the thin films.

The domain, piezo-images and piezoelectric properties were investigated using by AFM, KFM and laser Doppler equipment.

2. Experimental

PZT bulk targets were made from metal oxides PbO (98.0% purity), ZrO_2 (99.9% purity) and TiO_2 (99.9% purity). The PbO and ZrO_2 enriched mixed powders to the MPB composition were ball-milled for 24h in methanol. The dried material was crushed and sieved, followed by uniaxial pressing at 100MPa into cylindrical forms (*d*: 20mm, *h*:5mm). The green tablets were calcined at 850℃ for 3h, then sintered at a max. of 1200℃ for 3h after repeating the above treatments.

The composition of the sintered PZT bulk target was checked by XRF analysis and controlled so as to contain 20% excess Pb and 7% excess Zr to MPB composition, which was an optimum target composition for PZT films with composition corresponding to the MPB (Pb/Zr/Ti=100/53/47) under our PLD conditions.

For film deposition, a YAG laser beam with a wavelength λ of 266nm (the fourth harmonic generation, FHG) and a repetition rate of 10Hz was focused onto a rotating, sintered PZT bulk target. The fluency of the incident laser beam was 1.5J/cm^2 and the base pressure of the vacuum chamber was of the 10^{-5} Pa order.

The vaporized material was deposited on a substrate heated at 700℃ under oxygen partial pressure ambient of 5 Pa. The distance between the bulk target and the substrate was 46mm. After the film growth, the

sample was cooled to room temperature (5℃/min) in 0.1MPa of oxygen. The substrate used for PZT film deposition was Pt(111)/Ti/SiO_2/Si substrates.

The thickness of the deposited PZT thin films was 1 μ m for all the cases. For electrical measurement, Pt top electrode was sputtered on the PZT thin film using a contacting metal mask (Φ:200 μ m). The films were analyzed by X-ray diffraction (XRD, Rigaku RAD-3C) using CuKα radiation, X-ray fluorescence spectroscopy(XRF, Rigaku3030), and atomic force microscopy (AFM: Seiko Instruments SPM400). Dielectric constant was measured at room temperature in the frequency range of 1-1000kHz using an LCR meter (HP4284A). Polarization versus applied electric field (P-E) hysteresis loops were recorded using a modified Sawyer-Tower circuit. The thickness of the PZT thin films are approximately 500 nm as measured from a cross-sectional scanning electron micrograph. The PZT thin films display a granular structure with a grain size of 200-500 nm. The surface of those grains is fairly flat, while the films include some valleys that prevent us from measuring remanent polarization, (Pr). the coercive field(Ec), dielectric constant(ε_r) and dielectric loss tangent(tan δ) are measured at room temperature, these values are 20.3 μ C/cm^2, 93 kV/cm, 400 and 0.03, respectively.

Polarization and observation of domains are performed in room temperature using a Seiko Instrument SPI-3800N atomic force microscope (AFM) system equipped with a conductive tip. The tip is made of Si covered with Au. The repeated polarization switching endurance ("fatigue") test was performed at 1 kHz up to 10^8 cycles with a bipolar square pulse of 10 V_{P-P} using a ferroelectric evaluation system (Randiant Technologies RT-6000HVS) under virtual ground mode. The response of electric-field-induced displacement at the center of the top electrode was measured using a laser-Doppler-displacement measuring system (Graphtec AT7211) under a bipolar drive up to 20 V_{P-P} at 1 kHz using a function generator. The piezo-response method is based on the detection of the film vibration caused by the external ac field applied to the film through the SPM tip. A schematic diagram of the SPM piezoelectric measurement is shown in Fig.1 using Seiko Instrumental SPI-3800N atomic microscope (AFM) system.

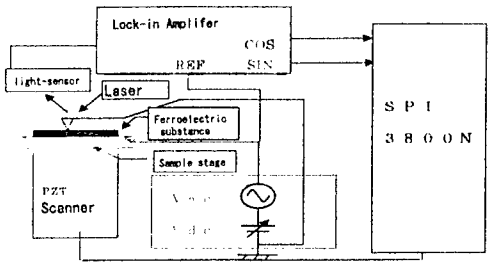

Figure 1. A schematic diagram of SPI-3800N. (Seiko-Instrument co.)

An ac modulation and dc bias voltage apply to the sample through the Au coated tip and the sample base plate. The output of the photo-detector is fed to a lock-in amplifier and, through a low-pass filter, to the *z*-control feedback circuit of the AFM system. The lock-in amplifier detects the first harmonic signal. The low-pass filter prevents the modulation induced tip vibration signal from going to the *z*-control feedback circuit. Signals from the *z*-control feedback circuit and from the lock-in amplifier.

A cos ϕ are recorded and imaged simultaneously as a topography image and a tip vibration image, respectively. Here, A is amplitude of the first harmonic signal and ϕ is the phase difference between the ac modulation signal and the first harmonic signal. The phase difference ϕ contains the phase shift arising within the AFM system and phase off-set in the lock-in amplifier.

The phase off-set is adjusted to give a maximum value of A cos ϕ . The amplitude and phase offset in the lock-in amplifier. The phase offset is adjusted to give a maximum value of

A $\cos\phi$. The amplitude and frequency of the modulation are $\pm$2.5V and 5 kHz, respectively. The amplitude is lower than the coercive voltage of the PZT film.

3. Results and Discussion

The 20%Pb excess PZT thin film exhibits a similar XRD pattern to the stoichiometric PZT thin film. PbO or Pb-related compounds are not detected in the XRD pattern. AFM image of the surface morphology of the 20% Pb deficient and excess PZT thin films present both the films are composed of granular grains with a diameter of about 100 nm, and show dense morphology and fairly smooth surface with small vertical roughness less than 40nm corresponding to the 1/3 diameters of a single grain. A unimorph type cantilever with piezoelectric PZT films are formed by YAG-PLD deposition on Si(001) wafer for the piezoelectric measurement. The cantilever was oscillated at 50kHz frequency by a PZT plate. The displacement of PZT films was measured by Doppler interferometer, the signal was the voltage and displacement after current-voltage conversion.

Figure 2 shows the poling voltage dependence of the voltage and displacement amplitude. The Curve showed similar to a shape of D-E hysteresis loop and the property corresponds to polarization reversal of ferroelectric PZT film.

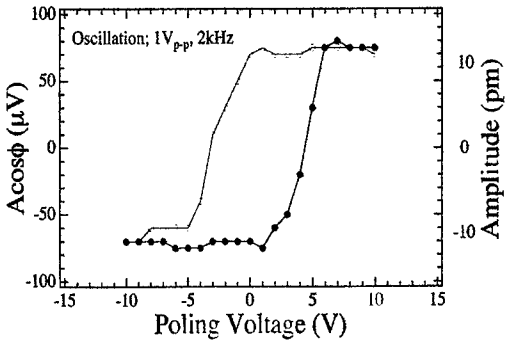

Figure 2. Bias dependence of voltag e(μ V) and displacement amplitude (nm) of PZT films.

Piezoelectric modulus d_{33} is obtained about 30pm/V from this curve. This value is about 10% less than that of PZT ceramics.

It seems so that a small d_{33} in estimated PZT films may be composed to nano-structure and the PZT films are inhomogeneous composition.

Voltage (A $\cos\phi$) and piezoelectric stain display approximate to $V=Vo(1-e^{-t/CR})$, the formula shows the time dependence of current changed characteristic of PZT thin film capacitor. The polarized domain images are observed by SPM piezo-response method.

Figure 3 shows (a) topographic image and (b) polarization reversal response image in the region $2\times2\,um^2$ film. Each storage space are yellow color (negative DC bias) and dark brown (positive DC bias), so that memoried information can be seen visibly.

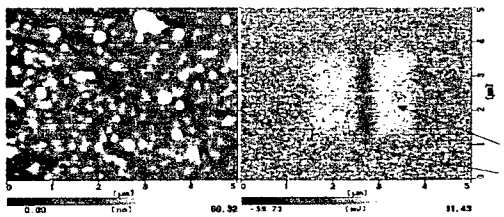

(a) (b)

Figure 3. (a) Topographic image and (b) Ferroelectric memory image of PZT thin films.

Figure 4 shows the DC bias dependence of strain(χ) of the PZT film. This curve display $\chi=dE+ME^2$, here, d, M, E are piezoelectric, electrostrictive moduli and electric field, respectively. Piezoelectric modulus is estimated about 100Pm/V from this curve.

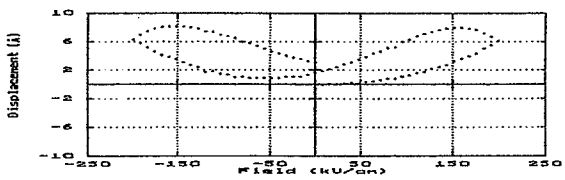

Figure 4. Electrostractive properties of PZT thin films.

The voltage images of plane and cross section of PZT film in shown in Fig.5. Electric field in focused to the center of the film and the electric field decrease with correspond to out side.

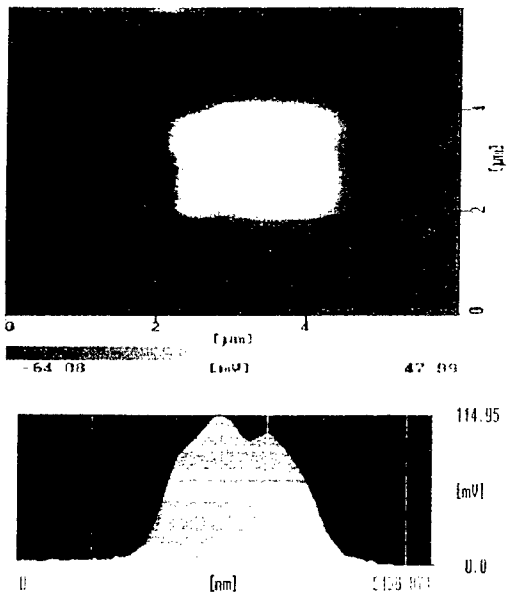

Figure 5. The KFM electro potential image of plane and cross section of PZT thin film.

4. Conclusion

PZT film was epitaxial grown on Pt/Ti/SiO_2/Si substrate by YAG: PLD method.

Topographic, piezoelectric response images (AFM) and voltage image (KFM) of PZT film are observed by SPM method. This results are available knowledge to application of a precision position control of micro actuator and a blood control in blood vessel.

Acknowledgements

This work was supported in part of New generation for the Future, Japan Society for the Promotion of Science (JSPS-RFTF- 96P00105). The anthers would like to thank Dr. S. Watanabe of Nikon Corporation for many useful discussions.

References

1. S. Watanabe and T. Fujii: Rev. Sci. Instrum.67(11),Nov.(1996) pp3898-3901
2. T. Hidaka, T. Maruyama, M. Sai toh, N. Mikoshiba, M. Shimizu, T. Shiosaki, L.A.Wills, R.H.Skes, S.A.Dicarolis and J. Amano: Appl. Phys.68, 17 (1996) pp2359-2359
3. C. Yoshida, M. Ikeda, A.Yoshida and N.Yokoyama: Tran. of The Mater. Res. Soc. of Japan: 24(1) (1998) pp7-11
4. Y.Masuda,S.Fujita,T.Nishida, H.Masumoto and T.Hirai: Proc. of IEEE Intern. Symp. on Appl. Ferro.(1999) pp23-26

PROGRESS IN FLEXOELECTRIC MEASUREMENTS

L. Eric Cross and Wenhui Ma
Materials Research Laboratory,
Pennsylvania State University
University Park,
Pennsylvania 16802
Fax: 814-863-7846
Email: Lec3@psu.edu

ABSTRACT

Flexoelectricity concerns the separation of electric charges (polarization in an insulating solid) produced by an elastic strain gradient. It can be described by an equation of the form

$$P_l = \mu_{ijkl} \frac{\partial S_{ij}}{\partial x_k}$$

Where μ_{ijkl} is the ferroelectric coefficient a fourth rank polar tensor, S_{ij} the electric strain component, x_k the length coordinate in the system and P_l the resulting polarization component.

Earlier measurements on soft elastomers show μ_{ijkl} values of order 10^{-10} to 10^{-11} C/m in agreement with general theory for homogeneous dielectrics. Our recent measurements on the relaxor ferroelectric lead magnesium niobate (PMN) give a value for $\mu_{1122} \sim 6.10^{-6}$ C/m some 4 orders larger.

It has been suggested that it may be much easier for the strain gradient to re-orient the pre-existing micro-polar regions in the relaxor.

Measurements of the temperature dependence of μ_{1122} show a strong peak near the low frequency dielectric permittivity maximum, with a rapid exponential decay at higher temperature going to near zero at the Burns temperature of PMN where micro-polar regions disappear. The μ_{1122} does not scale with ε_{33} again supporting the key role of micro-polar regions. From the values measured in PMN it appears that the possibility of fabricating a useful piezoelectric composite from completely non piezoelectric components may be realizable.

INTRODUCTION

Flexoelectricity describes the generation of electric polarization in an insulating solid by an elastic strain gradient. Phenomenological analysis of the effect was first made by Kogan (1). The flexoelectric coefficient μ_{ijkl} is a fourth rank polar tensor, so that for a cubic crystal the non-zero components are μ_{1111} μ_{1122} and μ_{1212}, or in matrix notation μ_{11} μ_{12} μ_{44}. For homogeneous solids all earlier investigators agree that the effect is very small in simple low permittivity dielectrics, and the μ_{ijkl} coefficient are of order 10^{-10} to 10^{-11}C/m (2-4).

For ceramic lead magnesium niobate ($PbMg_{1/3}Nb_{2/3}O_3$) (PMN) we have used a simple flexing beam to generate a uniaxial gradient in the elastic strain S_{zz} along the normal to the bar surface x_1 and measured the resulting alternating voltage V_1 from which we can calculate the induced polarization P_1. (5). Measurements from spot electrodes along the bar track well with the expected strain gradient to reveal a massive $\mu_{12} \sim 6.10^{-6}$C/m

EXPERIMENT

Temperature dependent flexoelectric measurement was performed by using an experimental setup schematically shown in Fig.1.

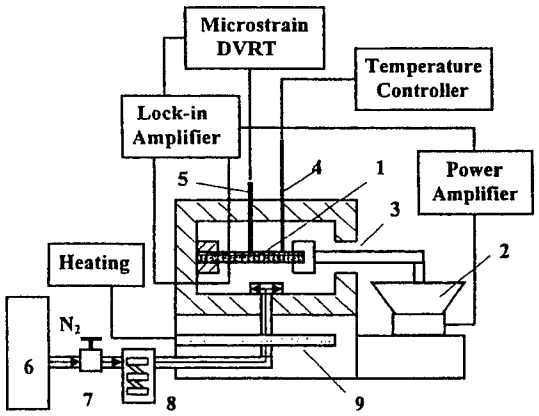

Fig. 1 Experimental setup for the temperature dependent flexoelectric measurement: 1. PMN bar, 2. loudspeaker, 3. driving arm, 4. thermocouple, 5. microstrain transducer core, 6. high purity nitrogen, 7. gas flow meter, 8. copper coils immersed in liquid nitrogen, 9. heating elements.

The measurement configuration, sample dimension and electrode geometry are the same as those used before [5]. As shown in Fig.1, one end of the sample was fixed to form a cantilevered beam. Temperature is uniform all over the sample bar. A loudspeaker was used to drive the beam at a frequency of 1 Hz, so a natural vibration was generated at the fundamental mode. By measuring the mode shape, we can calculate the strain all over the sample bar. Because the top and bottom surfaces are subjected to strain of opposite sign, there is a strain gradient along the thickness direction. Our former measurements [5] show that the flexoelectric polarization is proportional to the applied strain gradient and the μ_{12} coefficients obtained from measurements at different positions along the beam are close.

Fig. 2 shows the experimental result of flexoelectric polarization as a function of temperature obtained in the PMN ceramic.

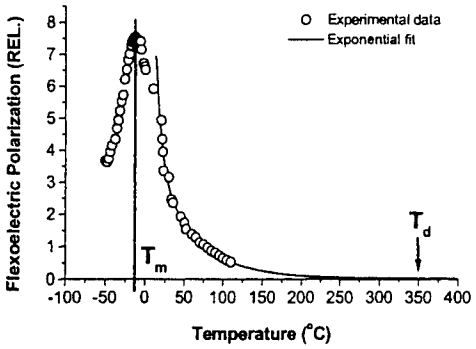

Fig.2 Flexoelectric polarization as a function of temperature in the PMN ceramic.

There is a maximum around the dielectric maximum temperature, T_m. Above T_m, the flexoelectric polarization decreases rapidly with increasing temperature. As shown in Fig.2, an exponential decay function fits the experimental data well. By extrapolation, it is found that the flexoelectric polarization becomes near to zero around T_d, the so-called Burns temperature [6]. At this temperature, the polar micro-regions disappear and the relaxor reverts to classical Curie-Weiss behavior. Our result indicates that there is a close relation between the flexoelectric polarization and the already existing polar micro-regions in PMN, suggesting that the pre-existing polar micro-regions might play a dominant role in the polarization mechanism.

In order to understand the origin of the greatly enhanced μ_{12} coefficients in relaxor PMN, let us make a simple analysis of the contributors to the flexoelectric effect. In the mid 1980s, Tagantsev developed the theory for flexoelectric effect in single crystals [2, 3]. In a crystal whose bulk symmetry does not allow the piezoelectric interaction the appearance of a polarization proportional to a strain gradient can be comprised of four components: a bulk static flexoelectric effect; a bulk dynamic flexoelectric effect; a surface flexoelectric effect and a surface piezoelectric effect. As shown in the discussion by Tagantsev, for a simple homogeneous ionic solid of cubic centric symmetry based on the rigid ion model, all the four components of the flexoelectric response are of the order of 10^{-10} C/m, although the magnitude of surface piezoelectric effect depends markedly on the nature of the surface. For a soft-mode ferroelectric dielectric above T_c in the cubic phase the flexoelectric behavior is much simplified, both static and dynamic bulk coefficients become larger in proportion to the enhanced dielectric susceptibility, and the surface flexoelectric coefficient becomes unimportant as it does not scale with the susceptibility. The surface piezoelectric effect might also be enlarged in proportion to the dielectric susceptibility, but again depends on details of the surface characteristics. For the current measurement configuration, the piezoelectric polarization from the upper and lower halves neutralize, so there should be no net effect even in the low temperature ferroelectric phase. We have also performed the flexoelectric measurements with the sample bar turned over, i.e., with the upper and lower surfaces interchanged, the results obtained for the two opposite orientations are found to be in-phase, evidencing the absence of a piezoelectric effect due to unbalanced inhomogeneous surface layers.

Fig. 3 displays the dielectric response of the PMN ceramic sample.

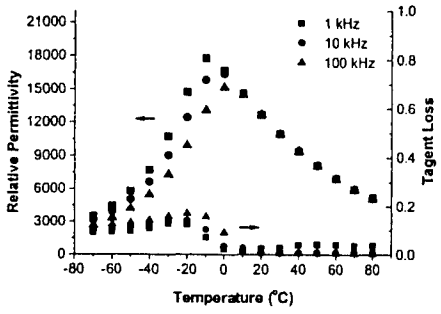

Fig. 3 Dielectric permittivity and loss tangent versus temperature for the PMN ceramic.

As shown in the dielectric spectrum, the dielectric maximum temperature increases with frequency, which is typical for a relaxor ferroelectric dielectric. Permittivity of PMN at room temperature is of the order of 15,000, while the dielectric permittivity for a simple ionic solid on the point charge model is about 5, so an enhancement of 3×10^3 can be expected from the high dielectric permittivity. However, the flexoelectric coefficient μ_{12} of PMN is of the order of 5 $\times10^{-6}$ C/m, some 5×10^4 times larger than that of the simple ionic solid. It is clear that the high dielectric permittivity is inadequate to explain the observed larger μ_{12} value.

Fig. 4 shows the curve of measured μ_{12} coefficient versus dielectric susceptibility χ, and the solid line is from the phenomenological analysis ($\mu_{ijkl} = \chi \frac{e}{a}$, where e is the elementary charge and a is the dimension of lattice cell).

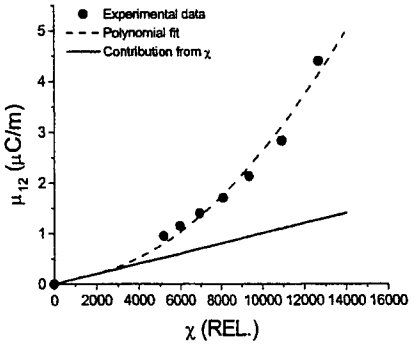

Fig. 4 Flexoelectric coefficient μ_{12} versus dielectric susceptibility χ in the PMN ceramic, where the solid circles are the experimental data, the dashed curve is the polynomial fit, and the solid line is the estimated μ_{12} values by phenomenological analysis.

It is found that there is discrepancy between the experimentally observed μ_{12} values and the linear estimations, which increases with the increase of dielectric susceptibility or decrease of temperature below T_d. It may be noted that similar deviations from linear extrapolation of high temperature properties have been found during the temperature-dependent measurements of optic index of refraction [6] and thermal expansion [7] in PMN, which were unanimously attributed to the appearance of localized polarization.

Relaxor ferroelectrics are inhomogeneous media containing micro-polar regions even at temperatures well above T_m, and the existence of nanoscale B-site order has been directly confirmed by the TEM investigations [8]. The dielectric behavior in relaxor ferroelectrics can be understood by the combination of compositional heterogeneity model [9] and superparaelectric model [7]. Above T_d, PMN is cubic both globally and locally without any polar regions.

Fig. 5(a) shows a lattice cell of cubic paraelectric phase of perovskite structure displaying eight equivalent <111> orientations.

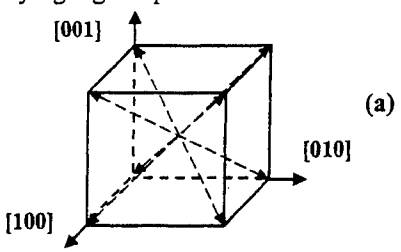

Fig. 5 (a) Schematic illustrations of eight equivalent <111> polarization orientations in a cubic lattice cell,

With temperature going down below T_d, localized polarization appears. According to the superparaelectric model, it is expected that the nanopolar regions are dynamically disordered in the thermal field and the chance of appearance of a polar vector along any of the eight <111> directions is equivalent.

Fig. 5(b) shows the Gibbs free energy for four of the eight <111> polarization for a low temperature ferroelectric phase, it is clear that all energy minima are of the same depth in the infinite perfect crystal.

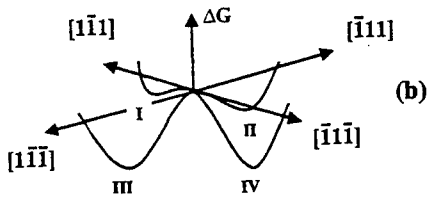

Fig. 5(b) Gibbs free energy ΔG versus polarization for four of the eight equivalent <111> orientations in a rhombohedral ferroelectric phase, and cross sections of the PMN bar showing the arrangement of orientation of the nanopolar regions in a [001]-oriented grain (defined by the dotted line)

However, in the relaxor ferroelectrics, due to composition fluctuation it is expected that the local symmetry will be lower than the global symmetry so that the eight <111> polarization orientations are now inequivalent in the local

polar micro-regions. Under zero strain condition, possible arrangement for the orientations of the nano-sized domains in a [001]-oriented grain in the PMN bar is schematically shown in Fig. 5(c), the sum of all those polar vectors is zero.

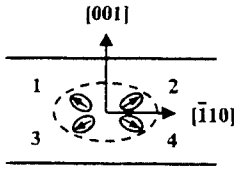

(c) $\sum \vec{P} = 0$

Fig. 5 (c) before

In Fig. 5(d), the sample bar is subject to an elastic strain gradient whose direction is defined as pointing from contraction to expansion and is parallel to the normal direction of sample surface.

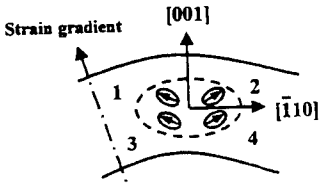

(d) $\sum \vec{P} \neq 0$

Fig. 5 (d) after being subject to an elastic strain gradient.

When the PMN bar is bent, some polarization orientations become free energy unfavorable and it is suggested that the inhomogeneously deformed nano-sized polar regions reorient themselves towards the direction of strain gradient by polarization rotation between adjoining <111> directions, e.g., from $[1\bar{1}\bar{1}]$ to $[1\bar{1}1]$, so as to reach the Gibbs free energy minima and there will be net polarization in the strain gradient direction.

In summary, flexoelectric coefficient μ_{12} has been measured as a function of temperature and the results suggest that the observed large flexoelectric polarization might be caused by reorientation of the pre-existing polar clusters in the relaxor ferroelectrics by the elastic strain gradient.

We thank M. Marvan from Charles University, Czech Republic for his suggestion of the importance of pre-existing polar micro-regions in the PMN ceramics.

References

[1] Sh. M. Kogan, *Soviet Physics-Solid State* **5**, 2069 (1964).
[2] A. K. Tagantsev, *Sov. Phys. JETP* **61**, 1246 (1985).
[3] A. K. Tagantsev, *Phys. Rev.* **B 34**, 5883 (1986).
[4] M. Marvan and A. Havránek, *Progr. Colloid Polym. Sci.* **78**, 33 (1988).
[5] Wenhui Ma and L. Eric Cross, *Appl. Phys. Lett.* **78**, 2920 (2001).
[6] Gerald Burns and F. H. Dacol, *Solid State Communications* **48**, 853 (1983).
[7] L. Eric Cross, *Ferroelectrics* **76**, 241 (1987).
[8] C. A. Randall and A. S. Bhalla, *Jpn. J. Appl. Phys.* **29**, 327 (1990).
[9] G. A. Smolensky, *J. Phys. Soc. Jpn.* Suppl. **28**, 26 (1970).

SESSION III. PIEZOELECTRICS

Plenary Lectures - Piezoelectrics

PIII.1 Domain Contribution to the Piezoelectric Properties of PZT Ceramics, Takaaki Tsurumi and S. Wada, Tokyo Institute of Technology, Japan. 193

PIII.2 New High Temperature Morphotropic Phase Boundary Piezoelectrics Based on $Bi(Me)O_3$–$PbTiO_3$ Ceramics, R. Eitel°, C. A. Randall°, T. R. Shrout°, P. W. Rehrig^, Wesley Hackenberger^, and S. Park*, °Penn State University, ^TRS Ceramics, Inc., and *Fraunhofer Technology Center, USA. 201

Single Crystal Piezoelectrics

III.47 Growth and Properties of 3" Single Crystal of Piezoelectric $Pb[(Zn_{1/3}Nb_{2/3})_{0.91}Ti_{0.09}]O_3$, M. Matsushita, Y. Tachi, S. Nagata, and K. Echizenya*,Kawatetsu Mining Company, Ltd., Japan, *Kawasaki Steel Company, Ltd., Japan. 209

III.48 Electromechanical Response of [001] Oriented Single Crystal Lead Zinc Niobate Titanate: DC Bias and Temperature Effects, A. Amin, L. C. Lim°, and T. S. Ramotowski, °National University of Singapore, Singapore, Naval Undersea Warfare Center, USA. 213

III.49 Crystal Growth and Electrical Properties of High T_c Relaxor-based Single Crystals, N. Ichinose, Y. Saigo, Y. Hosono*, and Y. Yamashita*, Waseda University, Japan, *Toshiba Company, Japan. 217

III.51 Recent Progress of Growth of Ferroelectric Relaxor PMN-PT Single Crystals at SICCAS, W.A. Schulze, C. Feng*, and Z. Yin*, C. B. DiAntonio, F. A. Williams, Jr., and S. M. Pilgrim, *Chinese Academy of Sciences, China, Alfred University, USA. 221

III.52 Compressive Properties of Piezoelectric Single Crystals, L. Ewart and E. A. McLaughlin, Naval Undersea Warfare Center, USA. 225

III.53 Effects of Surface Condition on the Electrical and Chipping Properties of PZNT Single Crystal Vibrators for Medical Array Transducers, T. Kobayashi, Y. Hosono, M. Izumi, K. Itsumi, K. Harada, and Y. Yamashita, Toshiba Company, Japan. 229

III.54 New Orientation Cuts for Enhanced Electromechanical Properties of PMN-PT and PZN-PT Single Crystals, J. Chen, R. Panda, H. Beck, and R. Gururaja, Systems, Agilent Technologies, Inc., USA. 233

III.55 Domain Configuration and Polarization Switching in PZN-5%PT Crystals, S. E. Park†, J. K. Lee*, and K. S. Hong*, *Seoul National University, Korea, †Fraunhofer-IBMT Technology Center, USA. 237

III.56 Domain Dynamics and Microstructure of $Pb(Zn_{1/3}Nb_{2/3})O_3$-$PbTiO_3$ Single Crystals, E. Furman, H. Yu, and C. A Randall, Penn State University, USA. 241

III.57 Poling Field Dependence of Ferroelectric Properties in $Pb(Zn_{1/3}Nb_{2/3})_{0.91}Ti_{0.09}O_3$ Single Crystal, T. Ogawa, M. Matsushita°, Y. Tachi°, and K. Echizenya*, Shizuoka Institute of Science and Technology, Japan, °Kawatetsu Mining Company, Ltd., Japan, *Kawasaki Steel Company, Ltd., Japan. 245

III.58 Piezoelectric Properties of $KNbO_3$ Single Crystals with Various Crystallographic Orientations, S. Wada, A. Seike, H. Kakemoto, and T. Tsurumi, Tokyo Institute of Technology, Japan. 249

III.59 The Study of Fatigue Anisotropy in $Pb(Zn_{1/3}Nb/_{2/3})O_3$-$PbTiO_3$ Ferroelectric Single Crystals, M. Ozgul*, K. Takemura†, S. Trolier-McKinstry*, and C. A Randall*, †NEC Corporation, Japan, *Penn State University, USA. 253

III.60 Phase Transitional Behavior of the Morphotropic Phases in PZN-PT and PMN-PT Single Crystals, Y. Lu, D.-Y. Jeong, Z.-Y. Cheng, and Q. M. Zhang, Penn State University, USA. 257

Non-Pb Based Actuator Materials

III.61 Electrical Properties of Morphotropic Phase Boundary in $(Bi_{1/2}Na_{1/2})TiO_3$-$KNbO_3$ Solid Solution System, T. Takenaka, H. Nagata, and H. Ishii, Science University of Tokyo, Japan. 261

III.62 Shaped Growth of Oriented Single Crystal Rods and Fibers in the $(Bi_{1/2}Na_{1/2})_{1-x}Ba_xZr_yTi_{1-y}O_3$ (BNBZT) System, B.P. Nunes, J. Shen, A. N. Soukhojak, Y-M. Chiang, Massachusetts Institute of Technology, USA. 265

III.63 High Electrostrictive Strain Relaxors Based on Sodium Bismuth Titanate, S. A. Sheets, A. N. Soukhojak, N. Ohashi, and Y-M. Chiang, Massachusetts Institute of Technology, USA. 269

III.65 Weak-Field Permittivity and High-Field Electromechanical Characterization of Ferroelectric Ceramics at Cryogenic Temperatures, C. J. Pagoda, M. L. Mulvihill*, and S. M. Pilgrim, Alfred University, USA, *Xinetics, USA. 273

Lead-Containing Actuator Materials

III.66 Cryogenic Characterization of Perovskite $Pb(Mg_{0.8}Ni_{0.2})_{1/3}Ta_{2/3}O_3$ and Tetragonal Tungsten Bronze $Ba_6FeNb_9O_{30}$ and $Ba_6CoNb_9O_{30}$ Relaxor Ferroelectrics, C. J. Pagoda, and S. M. Pilgrim, Alfred University, USA. 277

III.67 Piezoelectric Properties of Transparent $Pb(Ni_{1/3}Nb_{2/3})_{1-x-y}Zr_xTi_yO_3$ Ceramics, E. F. Alberta and A.S. Bhalla, Penn State University, USA. 281

III.68 Low-temperature Sintering of PZT with $LiBiO_2$ as a Sintering Aid, T. Hayashi and J. Tomizawa, Shonan Institute of Technology, Japan. 285

III.69 Fracture Behavior of Ferroelectric Ceramics, C. S. Lynch, Georgia Institute of Technology, USA. 289

Domain Contribution to the Piezoelectric Properties of PZT Ceramics

T.Tsurumi and S.Wada

Department of Metallurgy and Ceramics Science, Graduate School of Science and Engineering,
Tokyo Institute of Technology, 2-12-1 Ookayama, Meguro-ku, Tokyo 152-8552
Fax: +81-3-5734-2514, e-mail: ttsurumi@ceram.titech.ac.jp

The non-180° domain contribution to the piezoelectric properties of PZT ceramics was discussed. The domain contribution to the electric-field (E-field) induced strain of tetragonal PZT ceramics was estimated by XRD method. The degree of the 90° domain switching increased with decreasing tetragonality (*c/a* ratio) of the crystal lattice, while the strain due to the switching decreased with c/a ratio. The non-180° domain contribution was also estimated from the measurement of frequency dependence of E-field-induced strain. At high frequencies, the apparent piezoelectric *d* constant decreased because the domain contribution decreased with increasing frequency. The domain contribution to the piezoelectric properties of PZT ceramics in resonant mode was discussed. Elastic, dielectric and piezoelectric constants were determined as complex values for hard PZT and soft PZT by a nonlinear least-squares fitting of complex admittance and impedance data. The procedure to estimate intrinsic elastic, dielectric and piezoelectric losses were proposed. The piezoelectric loss dominantly derived from the elastic and dielectric losses but imaginary part remained even in the intrinsic piezoelectric *h* constant. The domain-wall-clamping in hard PZT markedly reduced the elastic loss rather than dielectric or piezoelectric losses. The displacement in resonant mode was measured using a newly developed double beam laser Doppler interferometer. The displacement of hard PZT is larger than the soft PZT around the resonance frequency because the displacement was determined not only by the piezoelectric *d* constant by also by the elastic loss.

INTRODUCTION

Perovskite ferroelectrics have 180° domain and non-180° domain structures. The domain switching of non-180° domains is ferroelastic and affects the various properties of piezoelectric ceramics, such as dielectric constant,[1-5] electric field (E-field) induced strain,[3-6] and durability during high power applications.[7] In piezoelectric actuators, it is known that the E-field-induced strains of PZT ceramics observed under strong E-fields are usually larger than that expected from piezoelectric *d*-constant determined by the resonance technique.[8] The unexpected large strains observed under strong E-fields are regarded as the contribution of the non-180° domain switching[3]. This paper reviews our work on the non-180° domain contribution to the piezoelectric properties of PZT ceramics in off-resonant mode and in resonant mode.

In the case of tetragonal PZT, the non-180° domain means the 90° domain. The 90° domain switching can be detected by x-ray diffraction (XRD) method. To establish the domain contribution in the E-field-induced strains, it is necessary to analyze the domain switching under the E-field. For this purpose, *in situ* XRD data was monitored as a function of the E-field. The relation between the domain contribution and anisotropy of crystal lattice of tetragonal PZT will be shown in the first section.

The velocity of non-180° domain-wall-motion is restricted because the domain-wall-motion is accompanied with the strains. Therefore, the non-180° domain contribution is possibly separated from the total piezoelectric strain by measuring frequency dependence of the E-field-induced strain. For this purpose, we used a double-beam laser interferometer. The domain contribution to the apparent piezoelectric *d* constant and E-field *vs.* strain curve will be discussed in the second section

Piezoelectric ceramics often used in resonant mode. In order to estimate the domain contribution in resonant mode, elastic, dielectric and piezoelectric constants should be accurately determined as complex values. This was done using a nonlinear least-squares fitting of complex admittance and impedance data. Elastic, dielectric and piezoelectric losses determined by the least-squares fitting are not intrinsic losses. Procedure to estimate intrinsic losses will be proposed in the third section.

In the off-resonant mode, the E-field-induced strain of soft PZT is larger than that of hard PZT because the domain-wall-motion is clamped in the latter. However, in resonant mode, the situation is totally different. The E-field-induced strain in resonant mode was measured using a

newly developed double beam laser Doppler interferometer. The experimental results will be shown in the last section.

DOMAIN CONTRIBUTION TO THE E-FIELD-INDUCED STRAIN IN OFF-RESONANT MODE

Evaluation of the Domain Contribution by XRD Method

PZT ceramics were prepared by a conventional solid sintering technique. The compositions in Table I were selected to form tetragonal phases of PZT.

Table I Chemical compositions of PZT ceramics

Sample name	Chemical composition
PZT	$Pb(Zr_{0.5}Ti_{0.5})O_3$ + 0.5mol%Nb_2O_5
PS5ZT	$(Pb_{0.95}Sr_{0.05})(Zr_{0.5}Ti_{0.5})O_3$ + 0.5mol%Nb_2O_5
PS10ZT	$(Pb_{0.90}Sr_{0.10})(Zr_{0.5}Ti_{0.5})O_3$ + 0.5mol%Nb_2O_5
PL3ZT	$(Pb_{0.97}La_{0.03})(Zr_{0.5}Ti_{0.5})O_3$ + 0.5mol%Nb_2O_5
PL8ZT	$(Pb_{0.92}La_{0.08})(Zr_{0.5}Ti_{0.5})O_3$ + 0.5mol%Nb_2O_5

XRD intensities of the 002 and 200 peaks of PZT ceramics were measured as a function of the E-field using an x-ray diffractometer. Au-sputtering electrodes were formed on the both sides of ceramic plate (15mmϕ). The electrode was made as thin as possible (~10 nm) on the x-ray irradiating surface to avoid x-ray absorption by Au. A bipolar power supply was used to apply voltages from -1 to 1 kV between the electrodes. Before measurements, samples were annealed at 700℃ for 3 h in air in order to remove the residual strains.

Figure 1 shows a schematic representation of the 90° domain structure in a representative cubic grain in tetragonal PZT ceramics. Small arrows indicate the direction of spontaneous polarization in each domain. By applying an E-field as shown in Fig.1, the switching of polarization occurs and the domain wall o-p in the figure moves to o'-p'. In the XRD measurement, the change in the ratio of area A and area B with domain-wall-motion could be measured as the change in the intensity ratio of the 200 and 002 diffraction peaks.

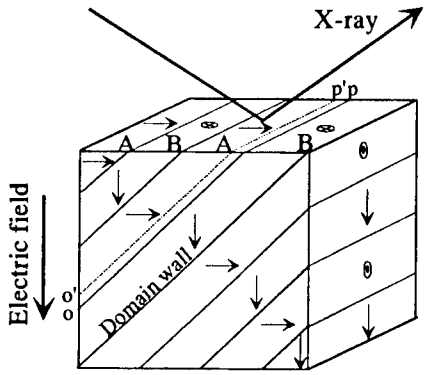

Fig.1 90° domain structure of a representative cubic grain in tetragonal PZT ceramics

Figure 2 shows the change in the XRD pattern of poled PZT by the application of an external E-field. It is seen that the intensity of the 002 peak slightly increases but that of the 200 peak slightly decreases as a result of applying a positive E-field to the X-ray irradiating surface. This change is caused by the 90° domain switching. The strain due to the domain switching (S_d) was approximately estimated by the following equation;

$$S_d = \frac{(R(E)-R(0))(c-a)}{(1-R(0))a+R(0)c)}, \quad R(E) = \frac{I(002)}{I(200)+I(002)} \qquad (1)$$

where $I(002)$ and $I(200)$ are XRD intensities of the 002 and 200 diffraction peaks, a and c are lattice parameters, and $R(E)$ is an XRD intensity ratio at the E-field E in MV/m. The denominator of S_d in eq.(1) denotes the averaged lattice constant along the E-field in a hypothetical grain shown in Fig.1, and the numerator denotes the change of the average lattice constant by the E-field: $[(1-R(E))a+R(E)c]-[(1-R(0))a+R(0)c]$. In actual ceramics, the 90° domain switching in a grain is not independent but is restricted by the stress and the deformation of the grains

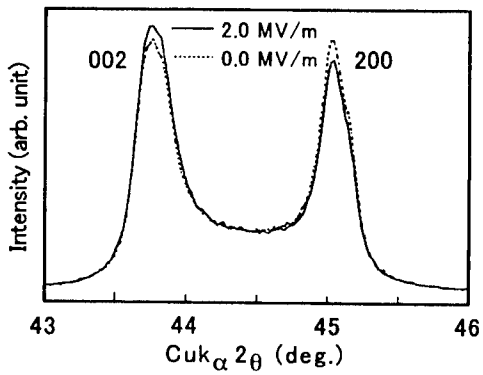

Fig.2 Change in XRD pattern of PZT by the E-field.

surrounding the grain under consideration. The observed $R(E)$ involves these effects, therefore, the strain derived from eq.(1) is a roughly approximated value.

Figure 3 shows changes in S_{obs}, S_p and $S_p + S_d$ for PL8ZT as a function of the E-field, where S_{obs} is the actual strain measured with a displacement meter, S_p is the strain due to the 'intrinsic' piezoelectric effect calculated from $S_p = d_{33} \times E$, and S_d is the strain due to the 90° domain switching calculated from eq.(1). (Here, we used the term of 'intrinsic' for S_p but it is not truly intrinsic. This will be discussed in a later section.) The curves of $S_p + S_d$ plotted in Fig.3 were those obtained during the increase in E-field. The piezoelectric d_{33} constants were determined by a resonance technique. In Fig.3, the $S_p + S_d$ curve is approximately consistent with that of S_{obs}. Similar results were obtained for other specimens. From these experiments, it is confirmed that the E-field-induced strain (S_{obs}) of PZT ceramics is composed of the strain due to the 'intrinsic' piezoelectric effect (S_p) and that due to the 90° domain switching (S_d).

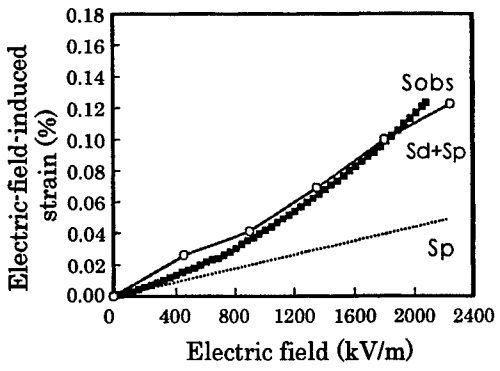

Fig.3 Changes in S_{obs}, S_p+S_d and S_p of PL3ZT as a function of the E-field.

The XRD intensity ratio $R(0)$ was about 0.33 before the poling treatment, and it increased to 0.5 - 0.6 after poling, which indicates that the remnant degree of the 90° domain alignment (γ_{90}) is from 0.26 to 0.42, where γ_{90} = $(R(0)-0.33)/(1.0-0.33)$ is the ratio of the remnant domain alignment with respect to the perfect switching. These results indicate that the amount of domain switching in the poling treatment is relatively small in soft PZT ceramics. After the poling treatment, some 90° domains relax and gradually change their polarization directions to the initial state. These 90° domains can switch reversibly by the subsequent application of the E-field, and contribute to the E-field-induced strains.

In Fig.4 the XRD intensity ratio $R(0)$ after the poling treatment and the change of the intensity ratio ($R(2.2)-R(0)$) by the application of the E-field up to 2.2MV/m are plotted as a function of the tetragonality (c/a) of the crystal lattice. A linear correlation was found between $R(0)$,$R(2.2)-R(0)$ and the c/a ratio. We could not find a good relation between $R(0)$, $R(2.2)-R(0)$ and the coercive field. This means that the degree 90° domain switching under the E-field was determined by the tetragonality rather than the coercive field of PZT ceramics. A small c/a ratio gives a large degree of domain switching. However, from eq.(1), it is obvious that the additional strain due to the domain switching is determined not only by the degree of the domain switching but also by the difference of c and a parameters.

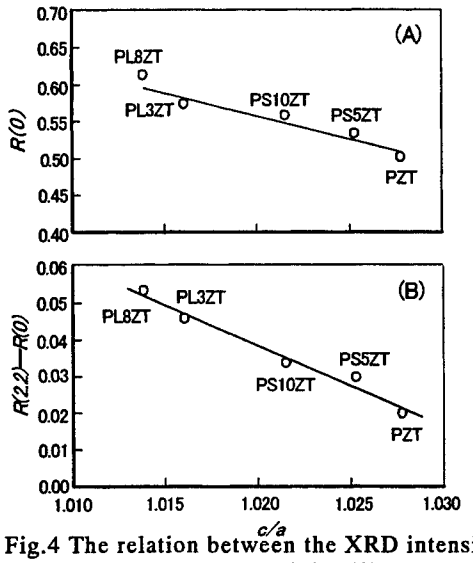

Fig.4 The relation between the XRD intensity ratio and c/a ratio. (A) $R(0)$ after poling treatment, and (B) $R(2.2)-R(0)$.

Evaluation of Domain Contribution from Frequency Dependence of E-field-induced Strain

As mentioned above, we could estimate the degree 90 ° domain switching and its contribution to the E-field-induced strain from XRD measurements. However, this method can be used only for 90° domains. A new method is necessary to universally determine the non-180° domain contribution to the E-field-induced strain.

The velocity of non-180 ° domain-wall-motion may be restricted because of its ferroelastic nature. Therefore, it seemed to be possible to separate the non-180 ° domain

contribution in the E-field-induced strains by measuring strains as a function of frequency. We have made a Mach-Zehnder type interferometer (double beam interferometer) and measured E-field-induced strains and strain *vs.* E-field curves of PZT ceramics in order to separate the non-180° domain contribution in the E-field-induced strains.

A sample used for the measurement was PZT ceramics with the composition of $Pb(Zr_{0.53}Ti_{0.47})O_3$+0.5mol%$Nb_2O_5$. The piezoelectric d_{33} constant of the sample was determined to be 370 pm/V by a resonance technique. For the interferometric measurements, a PZT ceramic sample with 2x2x2 mm^3 in size was prepared. Two small mirrors, which were made by Pt-sputtering cover glasses used for optical microscope, were attached on the ceramic surfaces with an epoxy resin after the electric poling procedure.

A schematic diagram of the Mach-Zehnder interferometer constructed in our lab. is shown in Fig.5. The basic structure is the same as that reported by Khohlkin *et al.*[9] The samples were suspended by thin Cu-wires. Two kinds of electric setups (setup 1 and 2) were used: the setup 1 was for measuring very small displacements, where the signal of the photo-detector was amplified by a current amplifier and its *dc* and *ac*-component were measured by a digital voltmeter and a lock-in amplifier, respectively. The voltage applied to the sample was 1-6V. The setup 2 was for measuring strain *vs.* E-field curves. In this case, the signal of the photo-detector was first amplified with the current amplifier and successively with a low noise amplifier to store in a digital oscilloscope. High voltages of 400V-1kV were applied to the sample to increase the displacement.

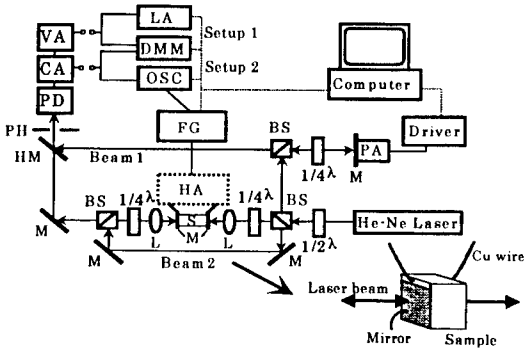

Fig.5 Schematic diagram of Mach-Zehnder interferometer. BS: Beam splitter, 1/4λ: 1/4λ plate, L: Lens, S: Sample, 1/2λ: 1/2λ plate, PH: Pin hole, HM: Half mirror, M:Mirror, PA: Piezoelectric actuator, PD: Photo-detector, VA: Voltage amp., CA: Current amp., LA:Lock-in amp., OSC: Digital oscilloscope, DMM: Digital multi meter, FG: Function generator, HA: High voltage amp.

The piezoelectric constant (d_{33}) measured using the setup 1 is shown in Fig.6 as a function of frequency. The d_{33} values were about 370 pm/V which was well consistent with that determined by the resonance technique. The d_{33} value tends to increase with frequency above 70kHz. This seemed to be experimental errors due to the bandwidth of the current amplifier or mechanical resonance.

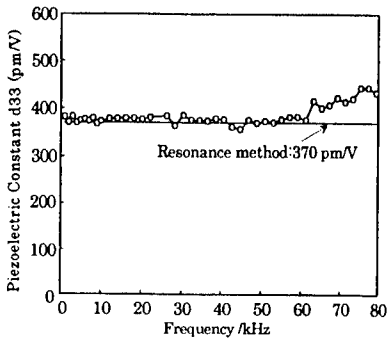

Fig.6 Piezoelectric d_{33} constant of PZT ceramics determined by the interferometer as a function of frequency. The E-field applied to the sample was 1V/mm.

The strain *vs.* E-field curves of PZT ceramics are shown in Fig.7. The curves were almost linear when the applied E-field was relatively low (<600V/mm) and the frequency was relatively high (>5kHz). The piezoelectric constant determined from the slope of line was about 370 pm/V, which was consistent with the piezoelectric constant determined by the resonance method. On the other hand, the strain curve showed a hysteresis when the applied voltage was high and the frequency was low. Both the hysteresis and slope of curves increased with increasing maximum E-field. These are the effect of non-180° domain reorientation. It was

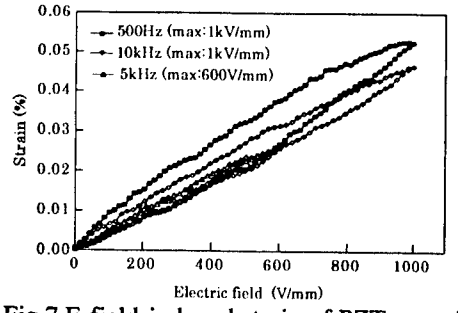

Fig.7 E-field-induced strain of PZT ceramics as a function of applied E-field.

found that the non-180° domain reorientation gave the hysteresis to the strain *vs.* E-field curves and increased the apparent E-field-induce strains. The apparent piezoelectric constant calculated from the E-field-induced strain at maximum E-field is shown in Fig.8 as a function of frequency. At high frequencies, the apparent piezoelectric constant was consistent with d_{33} determined by the resonance method (370 pm/V), but it increased with decreasing frequency. This behavior became notable when the applied field is high. The deviation of apparent piezoelectric constant from 370pm/V was due to the contribution of non-180° domains. It was indicated that the domain contribution was possibly separated by measuring strains as a function of frequency. The separation was possible because the velocity of non-180° domain-wall-motion was restricted. The non-180° domain switching could not follow the E-field at high frequencies and gave a piezoelectric relaxation at a certain frequency. This relaxation behavior may change with materials, E-field strength, temperature and so on.

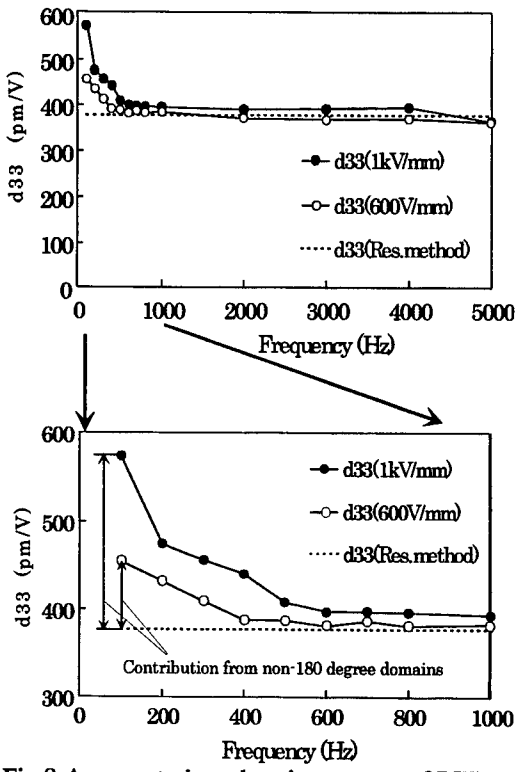

Fig.8 Apparent piezoelectric constant of PZT ceramics as a function of frequency. Apparent piezoelectric constant was determined from the E-field induced strain at the maximum E-field (600 V/mm or 1kv/mm).

DOMAIN CONTRIBUTION TO THE PIEZOELECTRIC PROPERTIES IN RESONANT MODE

Evaluation of elastic, dielectric and piezoelectric losses

In the previous section, we have demonstrated that the non-180° domain contribution to the E-field-induced strain could be estimated by measuring the frequency dependence of the E-field-induced strain. With increasing frequency, the apparent d constant approached to that determined by the resonance technique. However, we cannot say that the piezoelectric constant determined by the resonance technique is intrinsic to the crystal lattice. There should be the domain contribution in the d constant determined by the resonance technique because we know that the piezoelectric resonators of hard PZT and soft PZT shows different properties. The difference of hard and soft PZT are only clamping of domain-wall-motion or domain-wall-vibration. Therefore, their difference in properties should be attributed to the domain contribution. In this section, we tried to find the non-180° domain contribution to the piezoelectric properties in resonant mode using non-linear least-squares fitting of complex admittance and impedance.

The admittance of Z cut X plate of piezoelectric ceramics poled along Z-axis is given by the following equation,

$$Y = \frac{j\omega a\ell}{t}\left(\varepsilon_{33}^{T} - \frac{d_{31}^2}{s_{11}^{E}} + \frac{d_{31}^2}{s_{11}^{E}}\frac{\tan(\omega l/2v)}{\omega l/2v}\right) \qquad (2)$$

where ω is an angular frequency, $(a \times \ell \times t)$ is (width x length x thickness) of the specimen, d is a piezoelectric constant, ε is a dielectric constant, s is a elastic compliance and $v = \sqrt{1/\rho s_{11}^{E}}$ (ρ:density) is a sound velocity. The d, ε, s constants should be represented as complex values,

$$d^* = d' - id'', \quad \varepsilon^* = \varepsilon' - i\varepsilon'', \quad s^* = s' - is''$$

In the least-squares calculation, these complex parameters were substituted into the eq.(2) and the following function F was minimized,

$$F = |G_c - G_o| / |G_o| + |B_c - B_o| / |B_o| + |R_c - R_o| / |R_o| + |X_c - X_o| / |X_o|$$

where G, B, R and X are respectively conductance, susceptance, resistance and reactance, and suffixes "c" and "o" represent calculated and observed values. The complex

impedance term was indispensable to accurately determine the imaginary part of d constant.

Samples used for the analysis were soft PZT with the composition of $(Pb(Zr_{0.52}Ti_{0.48})O_3$ + 0.5mol% $Nb_2O_5)$ and hard PZT with the composition of $(0.95Pb(Zr_{0.45}Ti_{0.55})O_3$ + 0.05Pb $(Sb_{0.5}Nb_{0.5})O_3$ + 1.5mol%MnO). The complex admittance data was measured as a function of frequency using an impedance analyzer.

Figure 9 shows a result of the least-squares fitting of soft PZT. At first, the imaginary part of the d constant was fixed at zero and the least-squares fitting was performed. A relatively good fitting was obtained for the conductance and susceptance but large deviations were observed in the resistance and reactance as shown in Fig.9. These deviations were markedly improved by incorporating imaginary part of d constant (d'') into the calculation. This indicates that the piezoelectric d constant of soft PZT is complex number and it seems to be necessary to modify the analysis in the resonance technique in order to determine the parameters accurately. Material constants determined by the least-squares fitting are listed in Table II. The elastic compliance, dielectric constant and piezoelectric constant of hard PZT are smaller than those of soft PZT. Most notable difference between soft PZT and hard PZT was observed in $(s^E)''$ and d''.

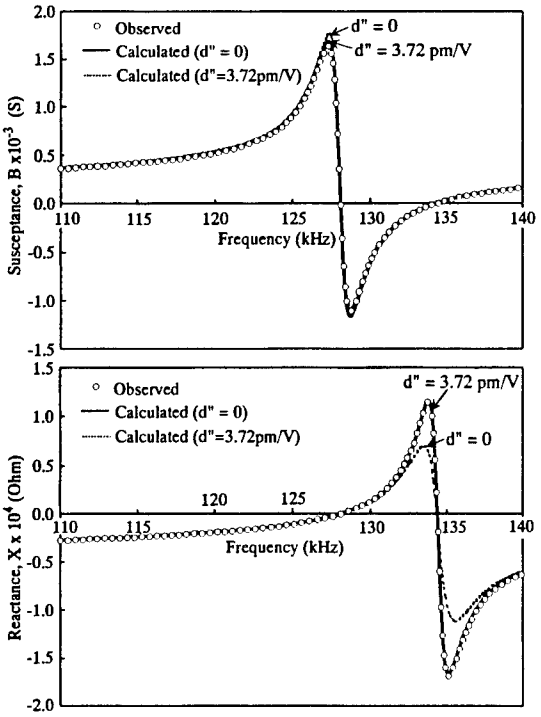

Fig.9 Calculated and observed susceptance and reactance of soft PZT around the resonance frequency.

Table II Material constants of hard PZT and soft PZT

Materials constants	Hard PZT	Soft PZT
$(s_{11}^E)'$ x10^{-12} [m^2/N]	9.72	13.49
$(s_{11}^E)''$ x10^{-12} [m^2/N]	0.011	0.15
$(\varepsilon_{33}^T)'/\varepsilon_0$	815	1337
$(\varepsilon_{33}^T)''/\varepsilon_0$	9.2	43.7
$(d_{31})'$ x10^{-12} [m/V]	65.2	135
$(d_{31})''$ x10^{-12} [m/V]	0.53	3.72

The elastic, dielectric and piezoelectric losses are defined as follows[10,11],

$$\left(s_{11}^E\right)^* = \left(s_{11}^E\right)' - i\left(s_{11}^E\right)'' = \left(s_{11}^E\right)'\times\left(1 - i\psi\left(s^E\right)\right)$$

$$\left(\varepsilon_{33}^T\right)^* = \left(\varepsilon_{33}^T\right)' - i\left(\varepsilon_{33}^T\right)'' = \left(\varepsilon_{33}^T\right)'\times\left(1 - i\phi\left(\varepsilon^T\right)\right)$$

$$\left(d_{31}\right)^* = \left(d_{31}\right)' - i\left(d_{31}\right)'' = \left(d_{31}\right)'\times\left(1 - i\eta(d)\right)$$

where $\psi(s^E)$ is the elastic loss, $\phi(\varepsilon^T)$ is the dielectric loss and $\eta(d)$ is the piezoelectric loss. However, it is very important to point out that the $\psi(s^E)$, $\phi(\varepsilon^T)$ and $\eta(d)$ defined above are not intrinsic elastic, dielectric and piezoelectric losses because these losses are coupled with each other. It is known that $\psi(s^E)$ includes both the mechanically derived and the electrically derived losses. The intrinsic losses can be defined as follows,[10]

$$\left(s_{11}^D\right)^* = \left(s_{11}^D\right)'\times\left(1 - i\psi\right)$$

$$\left(\varepsilon_{33}^S\right)^* = \left(\varepsilon_{33}^S\right)'\times\left(1 - i\phi\right)$$

$$\left(h_{31}\right)^* = \left(h_{31}\right)'\times\left(1 + i\eta\right)$$

where ψ is the intrinsic elastic loss, ϕ is the intrinsic dielectric loss and h_{31} is a piezoelectric constant in (S, D) form, and η is the intrinsic piezoelectric loss. The relation between these intrinsic losses and $\psi(s^E)$, $\phi(\varepsilon^T)$ is given by

$$\psi\left(s_{11}^E\right) = \left[\psi + k^2(\phi - 2\eta)\right]/\left(1 - k^2\right) \quad (3)$$

$$\phi\left(\varepsilon_{33}^T\right) = \left[\phi + k^2(\psi - 2\eta)\right]/\left(1 - k^2\right) \quad (4)$$

where k is an electromechanical coupling factor in 31 mode.[10]

We tried to determine the intrinsic losses of hard PZT and soft PZT by the following procedure. The s_{11}^D constant was first calculated as a complex value using the relation, $s_{11}^D=(1-k^2)s_{11}^E$ and the intrinsic elastic loss (ψ) was determined from $\psi = (s_{11}^D)''/(s_{11}^D)'$, where the coupling constant k should be a complex number. The quasi-intrinsic dielectric loss $\phi(\varepsilon^{LS})$, where LS means the length of the specimen is fixed, was calculated using the relations,

$\varepsilon_{33}^{LS}=\varepsilon_{33}^{T}(1-k^2)$ and $\phi(\varepsilon^{LS})=(\varepsilon_{33}^{LS})''/(\varepsilon_{33}^{LS})'$. In the strict sense, $\phi(\varepsilon^{LS})$ is not equal to the intrinsic dielectric loss (ϕ). Both losses have the following interrelation,

$$\phi(\varepsilon^{LS})=[\phi+f(\psi-2\eta)]/(1-f)$$

where f is a coupling factor which is not equal to k^2 because the type of coupling is different. As f is unknown, we used an approximation of $\phi(\varepsilon^{LS}) \fallingdotseq \phi$. The same approximation was used by Takahashi *et al.*,[10] and the validity of this approximation seems to be confirmed in the following procedure. As the piezoelectric h_{31} constant could not determined directly, only loss of h_{31} was estimated. Three routes were used to estimate the loss (η), i.e., it was calculated from eq.(3) or eq.(4) by substituting constants determined above. As an another route, a new relation was derived by eliminating unknown parameter ϕ from eqs.(3) and (4), and known constants were substituted for the parameters in the relation to calculate η. The difference in η derived from the three routes was negligible for both hard PZT and soft PZT, which may be indicating the reliability of the procedure to estimate η as well as the validity of the approximation of $\phi(\varepsilon^{LS}) \fallingdotseq \phi$. The elastic, dielectric and piezoelectric losses are listed in Table III. All intrinsic losses are smaller than the corresponding extrinsic losses ($\psi(s^E)$, $\phi(\varepsilon^T)$, and $\eta(d)$), which is fairly reasonable. The difference between the intrinsic and the extrinsic losses is smaller in the elastic and dielectric losses than in the piezoelectric loss. This means that the piezoelectric loss ($\eta(d)$) is dominantly derived from the elastic and dielectric losses. Takahashi *et al.*[10] reported that the η of PZT was very small and negligible. The analysis of this study was based on their paper and the theory established by Ikeda.[11] However, the η determined in this study seems to be somewhat larger than their estimation. From our analysis, it is difficult to say that the piezoelectric h constant is a real number. Considerable value remains in η even taking into account errors in it. The intrinsic piezoelectric loss is definitely much smaller than the loss of d constant, but we can not answer whether h constant is real or complex number at present. Further study and discussion should be necessary to solve this problem.

Table III Elastic, dielectric and piezoelectric losses of hard PZT and soft PZT

Parameters	Hard PZT	Soft PZT
$\psi(s^E)$	1.15×10^{-3}	1.11×10^{-2}
ψ	9.20×10^{-4}	9.66×10^{-3}
$\phi(\varepsilon^T)$	1.13×10^{-2}	3.27×10^{-2}
$\phi(\varepsilon^{LS}) \fallingdotseq \phi$	1.11×10^{-2}	3.12×10^{-2}
$\eta(d)$	8.2×10^{-3}	2.7×10^{-2}
η	4.2×10^{-3}	1.5×10^{-2}

The difference of hard and soft PZT is considered to be the degree of domain-wall-clamping. Domain walls in hard PZT were clamped by oxygen vacancies. The result in Table III indicates that the domain-wall-clamping markedly reduces the elastic loss but its effects to the dielectric and piezoelectric losses are relatively small. The domain-wall-clamping also reduced the real parts of material constants (Table II) because domain-wall-vibration may contribute to these constants.

E-Field-Induced Strain in Resonant Mode

The E-field induced strain of a vibrating piezoelectric resonator cannot be calculated only from the piezoelectric d constant and the E-field applied to the resonator. It seems to be important to know the displacement of a resonator because of the followings: the motional current through PZT ceramics is determined by $du(\ell/2)/dt$ where u is the displacement. The current is an important parameter to design piezoelectric transformers. Moreover. the ultrasonic power generated from piezoelectric ceramics is also determined by the displacement in resonance mode.

For this purpose, we used a newly developed double beam laser Doppler interferometer (DB-LDI). A schematic diagram of the interferometer is shown in Fig.10. Two LDIs measured the velocities of two opposite surfaces of PZT plate at the same time. Signals from the interferometers were amplified with lock-in amplifiers and analyzed by a computer. The advantage of the DB-LDI over the double beam laser interferometer in Fig.5 is that 1) optical

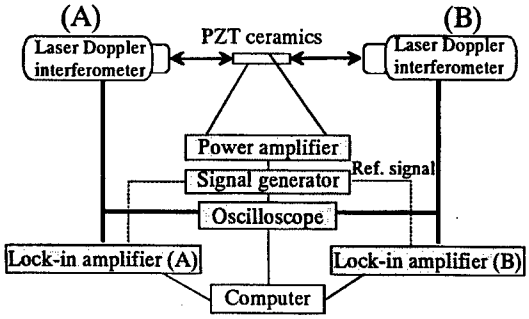

Fig.10 Schematic diagram of double beam laser Doppler interferometer.

alignment is very easy, and 2) displacements of the two opposite surfaces can be measured independently. The latter point is very important to characterize piezoelectric thick films on a substrate because piezoelectric d_{33} and d_{31} constants can be determined at the same time by analyzing signals from two LDIs.

Figure 11 shows the experimental results (k_{31} mode) of soft and hard PZT. The displacements show maximum around the resonance frequency. Total displacement of ceramics plate can be obtained by adding the displacements of surface (A) and (B). As shown in Fig.11, the displacements of surface (A) and (B) are not consistent because of asymmetry in sample holding. This indicates that the DB-LDI is necessary to measure the displacement even for ceramic sample as far as the two surfaces are not mechanically clamped.

In Fig.11, it should be noted that the displacement of hard PZT is larger than that of soft PZT in spite that the piezoelectric d constant of hard PZT is smaller than soft PZT (Table II). This is because the sharpness of the resonance is mainly determined by the elastic loss. A small elastic loss gives sharp resonance to give a large displacement. In the off-resonant mode, the

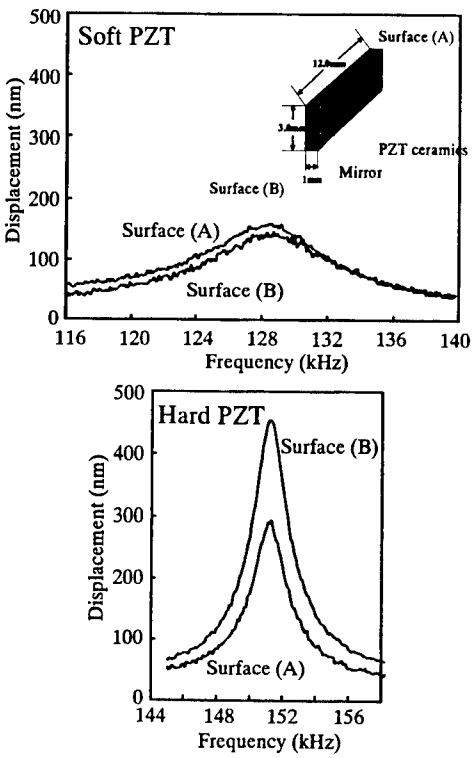

Fig.11 Displacements (k_{31} mode) of soft and hard PZT. Driving voltage was 10V for 1mm thick sample.

displacement of soft PZT is larger than that of hard PZT because of the domain contribution. However, in the resonance mode, the domain contribution increased the elastic loss to reduce the displacement.

CONCLUSION

In this paper, we have demonstrated the non-180 ° domain contribution to the piezoelectric properties of PZT. It was obvious that the domain contribution derived from domain-wall-motion. As a conclusion, we like propose that there are two kinds of domain-wall-motion, shift and vibration. The shift of domain-wall affects the E-field induced strain measured under high E-fields and at low frequencies (off-resonant mode), while the vibration is possible under low E-fields and affects the properties at high frequencies (resonant mode).

Acknowledgements

The works reviewed in this paper was financially supported by the Research Development Program of the University-Industry Alliance - A Matching Funds Approach from the Japan Society for the Promotion of Science (JSPS), a Grant-in-Aid for Scientific Research from the Ministry of Education, Science, Sports and Culture, Japan and the TDK Corporation.

The authors deeply express their thanks to many students in Tsurumi-Wada laboratory in T.I.Tech. for their cooperation and efforts in experiments.

References

1) N.Bar-Chaim, *et al.*: J. Appl.Phys. 45 (1974) 6.
2) E.I.Bondarenko *et al.*: Ferroelectrics 110 (1990) 53.
3) N.Uchida *et al.*: Jpn. J. Appl. Phys. 4 (1965) 867.
4) Y. Masuda: Jpn. J. Appl. Phys. 33 (1994) 5549.
5) S.Li, *et al.*: Ferroelectrics 139 (1993) 25.
6) Y.Masuda and A.Baba: Proc. FMA-6, Jpn. J. Appl. Phys. 26 (1987) Suppl. 26; p.132.
7) T. Sakai, M. Ishikiriyama and R. Shimazaki: Jpn. J. Appl. Phys. 31 (1994) 3051.
8) K.Furuta and K.Uchino:Adv. Ceram. Mater. 1 (1986) 61.
9) A.L.Kholkin *et al.*:Rev.Sci.Instrum. 67(1996) 1935.
10) Y.Sasaki, S.Takahashi and S.Hirose : Jpn. J. Appl. Phys. 36 (1997) 6058.
11) T.Ikeda: Fundamentals of Piezoelectricity (Oxford Science Pub., Oxford, New York, Tokyo, 1996).

New High Temperature Morphotropic Phase Boundary Piezoelectrics Based on $Bi(Me)O_3$–$PbTiO_3$ Ceramics

Richard Eitel*, Clive A. Randall*, Thomas R. Shrout*, Paul W. Rehrig†, Wes Hackenberger†, and Seung-Eek Park#

*Materials Research Laboratory, The Pennsylvania State University, University Park, PA 16802,

†TRS Ceramics, Inc, 2820 East College Avenue, State College, PA 16801,

#Fraunhofer-IMBT Technology Center Hialeah, 601 West 20th Street, Hialeah, FL 33010

INTRODUCTION

Since the development of $Pb(Zr_{1-x}Ti_x)O_3$ [PZT] in the 1950s, these polycrystalline ceramics have been the mainstay of transducer and actuator applications.[1,2] Compositionally, PZT ceramics lie near the morphotropic phase boundary (MPB) between tetragonal and rhombohedral phases. MPB compositions exhibit anomolously high dielectric and piezoelectric properties as a result of enhanced polarizability arising from the coupling between two equivalent energy states, i.e. the tetragonal and rhombohedral phases, allowing optimum domain reorientation during the poling process for polycrystalline materials. Guided primarily by an empirical crystallographic approach, systematic compositional engineering has led to the discovery of alternative MPB systems, primarily found in the Relaxor–$PbTiO_3$ systems, where relaxors are complex perovskites with the general formula $Pb(B_1B_2)O_3$, ($B_1 = Mg^{+2}$, Zn^{+2}, Ni^{+2}, Sc^{+3}..., $B_2 = Nb^{+5}$, Ta^{+5}, W^{+6}...).[3] To achieve yet higher dielectric and piezoelectric activity, MPB-based ceramics are further engineered by compositionally adjusting the Curie temperature (T_c) downward relative to room temperature. This enhanced effect comes with the expense of more temperature dependent properties, and less polarization stability, leading to aging and loss of piezoelectric activity. It is also important to point out that to date, no Relaxor-PT MPB system exhibits a higher T_c than that for PZT (~ 386°C), nor does any one type of MPB piezoelectric material offer significant advantages in overall performance.[4] Although MPB systems outside of the perovskite family are found in the tungsten bronze family and high T_c piezoelectrics, including modified $PbTiO_3$ (~ 470°C), $Na_{0.5}Bi_{4.5}Ti_4O_{15}$ (600°C), and $Pb,BaNb_2O_6$ (400°C), are well known, their level of piezoelectric activity is far inferior to that of PZTs.[5,6]

It was the intent of this work to explore the possibility of predicting new MPB systems with significantly higher T_cs than that of PZT. In the following sections, we will demonstrate the utilization of a crystallographic relationship between the perovskite tolerance factor and transition temperature, allowing us to project and experimentally confirm new high temperature MPB systems.

PEROVSKITE TOLERANCE FACTOR

Since the discovery of piezoelectricity in polycrystalline $BaTiO_3$ in the 1940s, the nature and search for new perovskite ferroelectrics has been guided by traditional crystal chemistry concepts, with limited success. The perovskite structure has the general formula: $A^{XII}B^{VI}O_3{}^{VI}$, where the Roman numerals represent the corresponding cation:anion coordination number. Based on their geometrical packing, Goldschmidt proposed the concept of a tolerance factor 't', given in equation 1.

$$t = \frac{r_A + r_o}{\sqrt{2}(r_B + r_o)} \qquad (1)$$

where r_A, r_B, and r_o are the respective ionic radii.[7] It was concluded that the stability of the

perovskite structure may be expected within the limits t=0.77 to 0.99, using ionic radii based on octahedral coordination, with t=0.88 to 1.09 if the radii for the A-site cation are corrected for the coordination number 12. This is typified by $SrTiO_3$ where t=1, while $LiNbO_3$ with a 't' of 0.86 has the ilmenite structure and for t>1 a hexagonal structure generally occurs.[8] In conjunction with ionic electronegativity, tolerance factor has been used as a guideline for a number of difficult-to-prepare Pb-based relaxor systems, such as $Pb(Mg_{1/3}Nb_{2/3})O_3$ (t=0.89) and $Pb(Zn_{1/3}Nb_{2/3})O_3$ (t=0.986) whereby the substitution of the small Pb^{+2} cation with a few mole% Ba^{+2} significantly enhanced the stability of the perovskite phase.[9-11]

Although the existence of ferroelectricity cannot be predicted based on tolerance factor, general observations of a low symmetry distortion of the unit cell for ferroelectric perovskites with $t < 1$, being rhombohedral or monoclinic while those with $t > 1$ are tetragonal, depending on whether the ferroelectric active ions are on the A- or B-site (e.g., A=Pb^{+2}, Bi^{+3}, Cd^{+2}; B=Ti^{+4}, Nb^{+5}, Ta^{+5}) have been reported.[12] It has also been noted that there is a general trend of higher transition temperature in ferroelectric perovskites with decreasing 't'.[8,13]

From the observations presented above, a relationship between tolerance factor and transition temperature for MPB systems was proposed. Using ionic radii suggested by Shannon,[14], the tolerance factor for the end members in PZ-PT (PZT), Relaxor-PTs, and related MPB systems were calculated from equation (1) and plotted as a function of the MPB transition temperature (T_c) and presented in Table I and Fig. 1. Although there is significant scatter in the data, it is evident that as the tolerance factor decreases below t=1, the corresponding T_c of the morphotropic phase boundary composition increases. Causes of the scatter may arise from the complexity of ferroelectric perovskite solid solutions with limited solubility of components, varying levels of cation order, and diffuseness of the phase transition.[15] Structural irregularities have also been noted, particularly for systems with multiple valence changing cations, such as Fe, Co, W, and Ni, being exemplified for the $BiFeO_3$–$PbTiO_3$ systems which exhibit a T_c of ~850°C for the MPB composition.[16] Regardless of the relationship inconsistencies and scatter, it was projected that perovskites with "t" less than that for $PbZrO_3$ (t=0.96), with ferroelectrically active cations, would meet the necessary requirements of a low symmetry distortion (rhombohedral or monoclinic), resulting in a MPB with $PbTiO_3$, while exhibiting a corresponding increase in T_c.

From the empirical analysis presented, $Bi(Me)O_3$-based perovskites with decreasing values of 't' were suggested to confirm the premise. From Figure 1, it is evident that solid solutions of $BiScO_3$ (t=0.907), $BiInO_3$ (t=0.884), and $BiYbO_3$ (t=0.857) with $PbTiO_3$ would exhibit MPBs with T_c's significantly greater than PZT and $PbTiO_3$ (T_c=490°C) itself. Experimental confirmation of the proposed tolerance factor relationship and its implication and impact on transducer and actuator performance and prediction of yet higher T_c MPBs is presented in the following sections.

EXPERIMENTAL

Solid solutions of (1-x) $BiScO_3$–(x)$PbTiO_3$ (BS-PT), (1-x) $BiInO_3$–(x)$PbTiO_3$ (BI-PT), and (1-x) $BiYbO_3$–(x)$PbTiO_3$ (PY-PN) were prepared using conventional ceramic processing. Reagent grade oxides of Bi_2O_3, Sc_2O_3, Yb_2O_3, PbO, TiO_2, and In_2O_3 were used as the starting materials. The powders were vibratory mixed/milled and subsequently calcined. As expected from their low tolerance factors, bismuth-based perovskites exhibited poor perovskite stability and have been prepared only under high pressure conditions[17]. For the system (1-x)$BiScO_3$–(x)$PbTiO_3$, the addition of $PbTiO_3$ with a substantially larger tolerance factor (t=1.019) resulted in phase pure perovskites with $x \geq 0.5$, as determined by XRD. For (1-x)$BiInO_3$–(x)$PbTiO_3$, however, phase pure perovskites could not be achieved even for $x \geq 0.9$, thus the addition of 1–3 mole% Ba for Pb was employed, analogous to perovskite stabilization in PZN.[10] The issue of perovskite stability was further compounded for the BY-PT system; hence, emphasis was directed on the BS-PT system accordingly. After calcination, vibratory milled powders were pressed into disks 10 mm in diameter and 1–2 mm in thickness. The disks were fired at 1000–1250°C for 2 hrs. in closed crucibles. To minimize weight loss due to PbO and Bi_2O_3 volatility, a source of powder of the same composition was used.

Electrical measurements were made on disks with densities greater than 92% of the theoretical value. Prior to measurement, the disks were ground parallel and gold electrode applied by

sputtering. Dielectric properties were obtained by measuring the capacitance and loss using an LCR meter (HP model 4172). To determine T_c, capacitance measurements were made as a function of temperature in automated temperature controlled furnace interfaced with a computer for data acquisition. The polarization E-field behavior was determined using a modified Sawyer-Tower system, described in reference. Piezoelectric coefficients and electromechanical coupling were determined from samples poled under a field of 30–50 kV/cm for 10–60 min. at 120°C. The piezoelectric coefficient d_{33} was recorded from one-day aged samples using a d_{33} meter (Berlincourt). The electromechanical coupling factor k_p was measured using an impedance analyzer (Model HP 4194) based on IEEE standards.[18]

RESULTS AND DISCUSSION

Guided by the proposed tolerance factor relationships, a morphotropic phase boundary (MPB), separately tetragonal and rhombohedral phases was observed in the (1-x)$BiScO_3$–(x)$PbTiO_3$ system at x~0.64, as shown in Fig. 2. For simplicity, the MPB is given as a single composition, though the phase boundary defined where the two phases are present in equal quantity.[2] Similar to Relaxor-PT and $PbZrO_3$–$PbTiO_3$ MPB systems, the degree of tetragonally decreased with decreasing $PbTiO_3$ with a c/a ratio near the MPB of ~ 1.023, slightly larger than PZT (c/a =1.02).

The temperature dependence of the dielectric constant for the MPB composition is given in Fig. 3. A transition temperature T_c of 450°C for x=0.64 was found, being significantly higher than that for PZT as projected from the tolerance factor relationship presented in Fig. 2.

Enhanced polarizability associated with a MPB is evident in Fig. 4, as the level of remnant polarization (P_r) was found to be highest at x=0.64. This enhancement is further translated into ease of which the samples could be poled as evident by the compositional dependence of both the piezoelectric coefficient d_{33} and electromechanical coupling coefficient k_p, shown in Figs. 5 and 6, respectively. Though not shown, k_p was found to be nearly temperature independent as necessitated by an MPB. In the (1-x)$BiInO_3$–(x)$PbTiO_3$ system, perovskite stability was enhanced with the addition of 1–3 mole% $BaTiO_3$, for compositions with $x \geq 0.7$. Though the existence of a MPB was not found, the dielectric temperature behavior for a tetragonal composition (x=0.7) revealed a $T_c \geq$ 570°C, as shown in Fig. 7, being significantly higher than $PbTiO_3$ itself and a correspondingly higher c/a ratio (1.08). The transition temperature tolerance factor relationship was further substantiated in the (x)$BiYbO_3$–(x)$PbTiO_3$ system with a T_c of >620°C, determined from DSC for a tetragonal composition (c/a=1.10) x=0.7, though mixed phase.

SUMMARY

A relationship between perovskite tolerance factor (t) and transition temperature of morphotropic phase boundary (MPB) compositions was established. With decreasing tolerance factor ($t \leq 1$), T_c was found to increase for various MPB end members with solid solutions with $PbTiO_3$. New MPB systems were projected for perovskite end members with t<0.96, corresponding to $PbZrO_3$ PZT MPB systems. As projected, a MPB was confirmed in the $BiScO_3$–$PbTiO_3$ system (x=0.64), exhibiting a T_c>450°C and corresponding enhanced piezoelectric and electromechanical properties. Evidence of yet higher T_c MPB systems ≥ 600°C were noted for $BiInO_3$–$PbTiO_3$ and $BiYbO_3$–$PbTiO_3$ systems, though issue of perovskite stability remains.

ACKNOWLEDGEMENTS

The authors would like to thank Kate Schultz, Beth Jones, and Blanche DeArmitt for their technical assistance. The work was supported by ONR and DARPA.

REFERENCES

1) B. Jaffe : J. Res. Nat. Bus. Stand. **55**, (1955) 239–240.

2) B. Jaffe : W.R. Cook, and H. Jaffe, Piezoelectric Ceramics, Academic Press Ltd. Reported by R.A.N. Publishers, Marietta, Ohio (1971).

3) Y. Yamashita : Jpn. J. Appl. Phys. **33** [1] 9B (1994) 5328–5336.

4) S.E. Park and T.R. Shrout : IEEE Trans. on UFFC **44** [5] (1997) 1–8.

5) R.C. Turner, P.A. Fuierer, R.E. Newnham, and T.R. Shrout : Applied Acoustics **41**, (1994) 299–324.

6) Landolt–Börnstein : Ferroelectrics and Related Substances, Vol. 16 New Series, Group III, Springer Verlag, Berlin (1981): Supplement Vol. 28 (1990).

7) V.M. Goldschmidt : Shrifter Norske Videnskop-Adad. Oslo: Matemot. Naturuid Klasse, (Nov. 1926).

8) O. Muller and R. Roy : Springer Verlag, Berlin, Heidelberg, and New York (1974) 221–224.

9) O. Furukawa, Y. Yamashita, M. Harata, T. Takahashi, and K. Inagaki : Jpn. J. Appl. Phys. **24** (1985) 96–99.

10) A. Halliyal, T.R. Gururaja, U. Kumar, and A. Safari : IEEE (1986) 437–441.

11) T.R. Shrout and A. Halliyal : Amer. Cer. Soc. Bull. **66** [4], (1987) 704–711.

12) V.A. Isupov : Izvestiya Akademic Nouk SSR Seriga Fizichokayo **47** [3] (1983) 559–565.

13) N. Yu and V. Venutsev : Proc. JSSF-2, Kyoto, J. Phys. Soc. Jpn. **49**, Suppl. B, (1980) 49–52.

14) R.D. Shannon : Acta Cryst. **A32**, (1976) 751–767.

15) V.A. Isupov : Phys. Stat. Sol. **181** (2000) 211.

16) A.N. Salak, A.D. Shilin, M.V. Bushinski, N.P. Vyshatka, and N.M. Olekhnovich : Mats. Res. Bull. **35** (2000) 1429.

17) Y. Tomashpol'skii, E.V. Zubova, K.P. Bordino, and Y.N. Venutsev : Soviet Physics–Crystallography **13** [6] (1969) 859–861.

18) IEEE Standard on Piezoelectricity, ANSI/IEEE Std. **176** (1987).

Table I.

Abbreviation	S.S. End Member (1-x)ABO_3 + x$PbTiO_3$	End Member tolerance	MPB Curie Temp (°C)
PMW	$Pb(Mg,W)O_3$	0.993	60
PMT	$Pb(Mg,Ta)O_3$	0.989	80
PNN	$Pb(Ni,Nb)O_3$	0.994	130
PFN	$Pb(Fe,Nb)O_3$	1.001	140
PMN	$Pb(Mg,Nb)O_3$	0.989	160
PMnN	$Pb(Mn,Nb)O_3$	0.973	187
PZnN	$Pb(Zn,Nb)O_3$	0.986	190
PST	$Pb(Sc,Ta)O_3$	0.977	205
PSn	$PbSnO_3$	0.978	220
PCN	$Pb(Co,Nb)O_3$	0.985	250
PSN	$Pb(Sc,Nb)O_3$	0.977	260
PCW	$Pb(Co,W)O_3$	0.987	310
PIN	$Pb(In,Nb)O_3$	0.965	320
PH	$PbHfO_3$	0.969	340
NBT	$(Na,Bi)TiO_3$	0.977	350
PYN	$Pb(Yb,Nb)O_3$	0.951	360
PZ	$PZrO_3$	0.964	385
BS	$BiScO_3$	0.907	450
BI	$BiInO_3$	0.884	560
BY	$BiYbO_3$	0.857	613

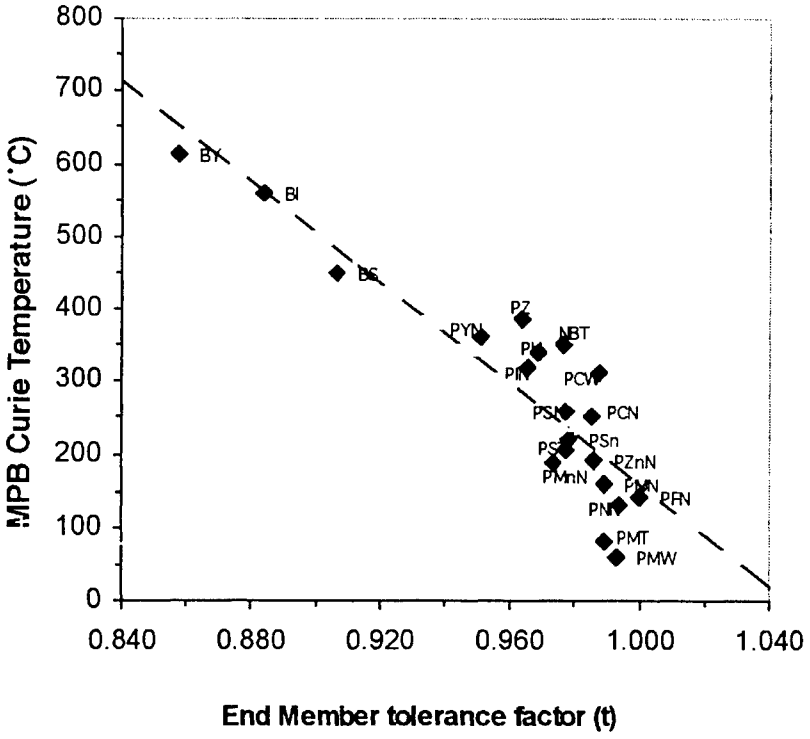

Figure 1. Curie Temperature (Tc) of $PbTiO_3$-based MPBs versus end member tolerance factor (dashed line drawn as a visual aid), refer to Table I. The perovskite tolerance factor was calculated from tables of ionic radii given by Shannon(14). An ionic radii for Bi^{3+} (CN: XII) of 1.34Å was extrapolated from Figure 2-C, Ref. 14.

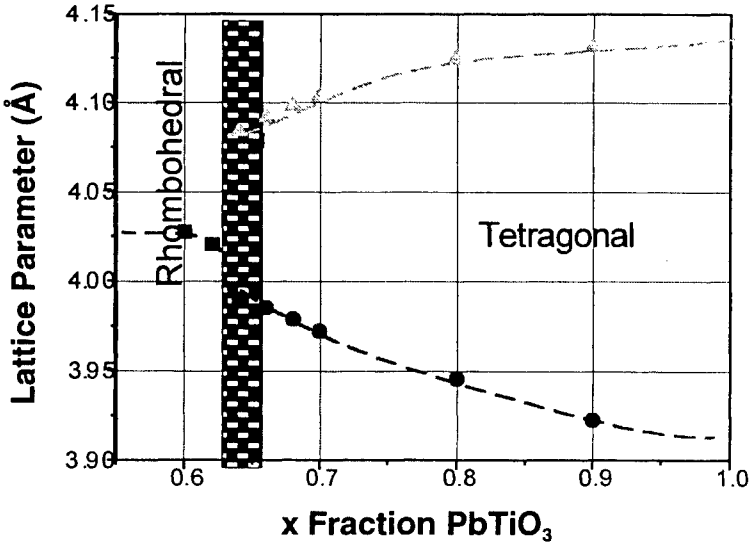

Figure 3. Phase diagram for $BiScO_3$-x$PbTiO_3$ showing perovskite lattice parameters as a function of %PT, revealing and rhombohedral–tetragonal MPB in the region 64-66 %mol PT.

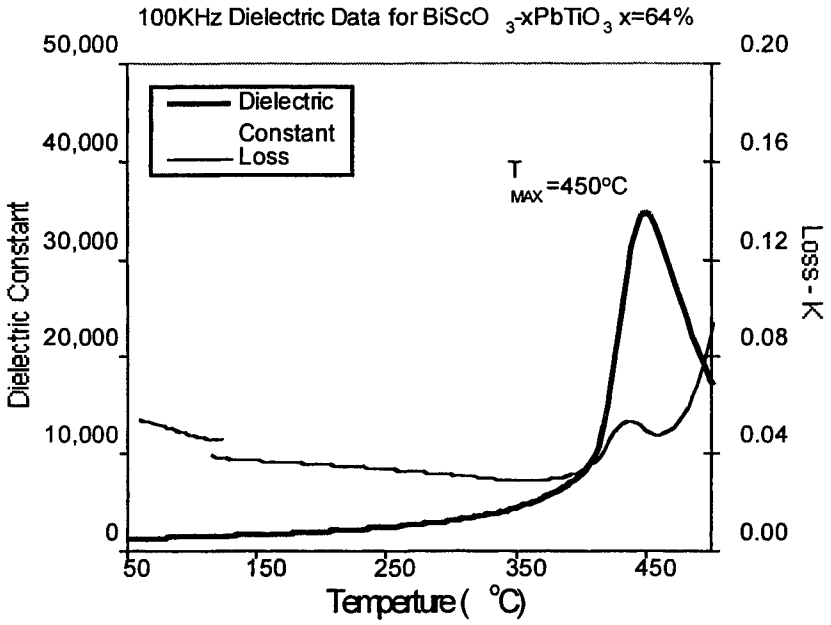

Figure 3. Dielectric constant (100 KHz) versus temperature for (1-x)$BiScO_3$–(x)$PbTiO_3$ x=64%PT, showing a dielectric maximum at T~450°C.

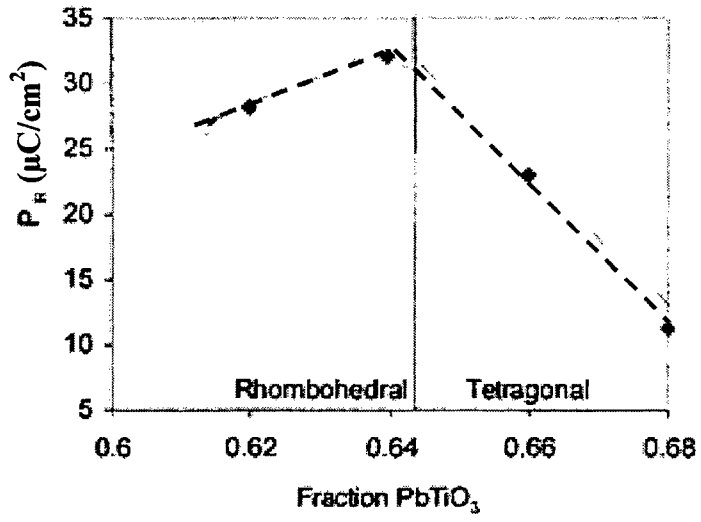

Figure 4. Remnant polarization P_r as a function of lead titanate content showing enhanced polarizability in the MPB region for (1-x)$BiScO_3$-(x)$PbTiO_3$.

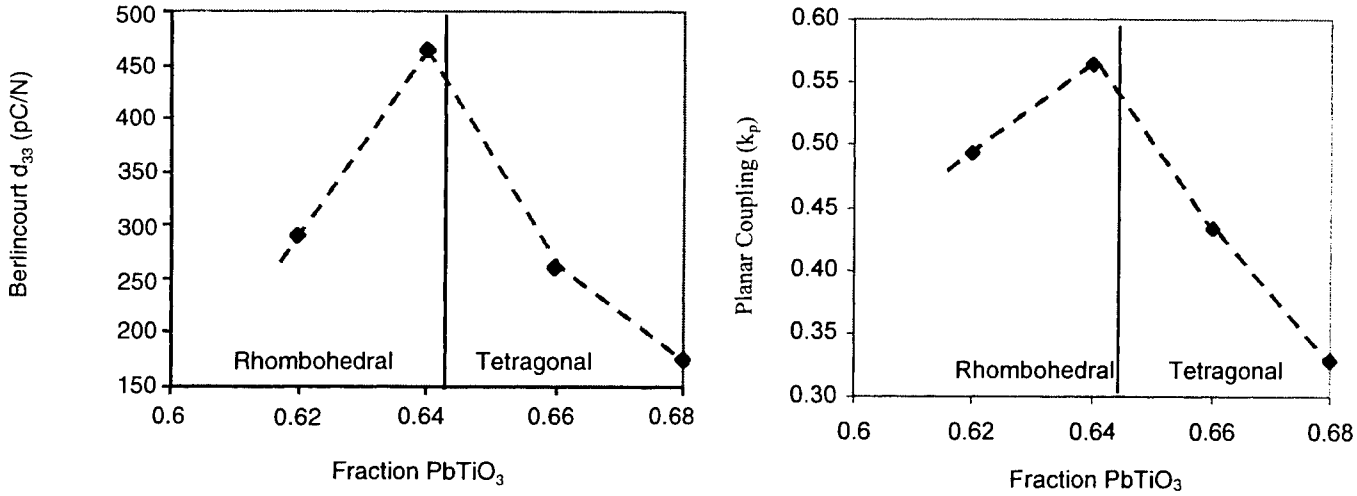

Figures 5-6 (left to right). Piezoelectric properties in the region 60–68% PT for (1-x)$BiScO_3$-(x)$PbTiO_3$, showing enhanced piezoelectric properties associated with the MPB. Figure 6 (left) shows the piezoelectric coefficient d_{33} obtained using a Berlincourt meter.

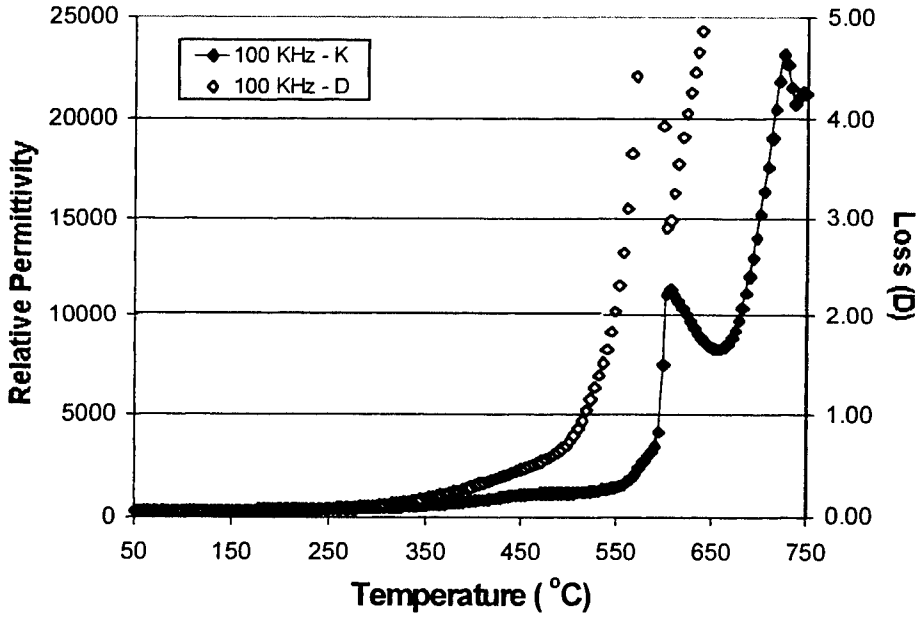

Figure 7. Dielectric constant (100 KHz) versus temperature for 0.27$BiInO_3$–0.7$PbTiO_3$–0.03$BaTiO_3$ showing a dielectric maximum ≥ 570°C.

Growth and Properties of 3" Single Crystal of Piezoelectric Pb[(Zn1/3Nb2/3)0.91Ti0.09]O3

M. Matsushita, Y. Tachi, S. Nagata and K. Echizenya*

Research Laboratory, Kawatetsu Mining Company Ltd., 1, Niihama-cho, Chuo-ku, Chiba, Chiba, Japan

FAX: 81-43-262-4259

*Technical Research Laboratories, Kawasaki Steel Co., Ltd., 1, Kawasaki-cho, Chuo-ku, Chiba, Chiba, Japan

FAX: 81-262-2467

E-mail: mi-matsushita@kawako.kawatetsu.ne.jp

Abstract: Piezoelectric single crystals of $Pb[(Zn_{1/3}Nb_{2/3})_{0.91}Ti_{0.09}]O_3$ (PZNT91/09) were grown by one batch supported solution Bridgman method. Average diameter and height of the crystals are approximately 75 mm and 55 mm respectively. Total weight is approximately 1000 g. Though there were PbO inclusions at the bottom and at the peripheral of the crystals, 55 mm x 50 mm inclusion free region was obtained. Rectangular rods and wafers with (100) surfaces were cut from these crystals. There exist three types of straight stripe patterns. Two of them are parallel to <100> axis and perpendicular each other. Residual one is approximately 45 degree inclined against formers. The interval of two stripes was approximately 200 μ m. This means the existence of the domain structure in the crystal. Relation between the domain structure and the crystal defects and the strains were investigated by optical microscopic images and by Laue topography using synchrotron radiation.

I. INTRODUCTION

$Pb[(Zn_{1/3}Nb_{2/3})_{0.91}Ti_{0.09}]O_3$ (PZNT91/09) piezo-electric single crystals are interested because of their large electromechanical coupling constant k_{33}. For 2-inch crystals of PZNT91/09, growth of high quality single crystals by one batch supported solution Bridgman method was reported.[1]. The authors therefore investigated to grow larger PZNT91/09 single crystals by this method and successfully grew 3-inch single crystals, though small sub-crystals were present at the bottom. Inclusions of PbO flux were also observed at the bottom and at the peripheral of the crystal. Average diameter and height of the crystals are approximately 75 mm and 55 mm respectively. Total weight is approximately 1000 g. As growing conditions and the analysis on the variation of the Ti^{4+} along with the growth direction and in the wafer were presented elsewhere[2] , analysis on the domain structure using optical microscopic images and Laue topographic diffraction images are presented.

II. EXPERIMENTAL RESULTS

II.1 Optical microscopic images

Though there were PbO inclusions in the ingot of the crystal, 55 mm x 45 mm inclusion free region of 25mm in thickness was obtained. Rectangular rods of 4 mm x 4mm x 12 mm with six (100) surfaces and 30 mm x 30 mm x 0.3 mmt wafers with wide (100) surfaces were cut from these crystals. Optical microscopic images with polarized light is shown in Fig.1 and Fig.2. A schematic explanation of the observed straight stripes on the 4 mm x 4 mm x 12 mm rod is shown in Fig.3.

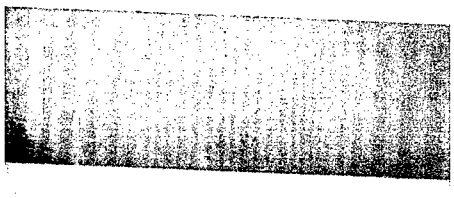

Fig.1 Straight stripes on the 4 mm x 4 mm x 12 mm rod. Direction of the stripes is parallel to <100> axis.

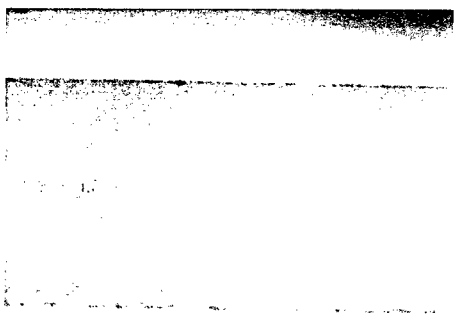

Fig.2 Stripes of 45 degree inclined against <100> axis.

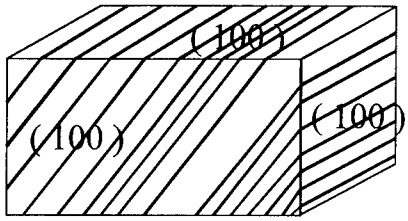

Fig.3 A schematic explanation of the observed straight stripes on the 4 mm x 4 mm x 12 mm rod

From the observation, all rod samples show the configuration of Fig.3 on three independent (100) crystal planes. The interval between two stripes varies periodically, and the average interval of the stripes is approximately 200 μ m.

The straight stripes were also observed on the (100) wafer surface. Figure 4 shows one of the wafers with stripes parallel to <100> axis. The interval of stripes were also approximately 200 μ m.

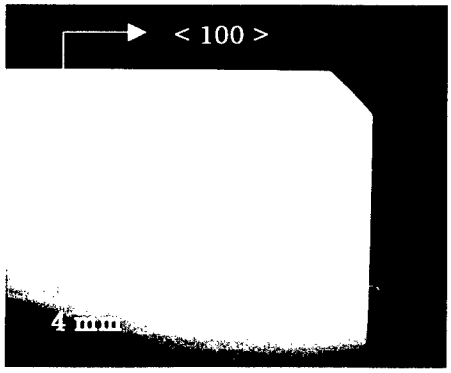

Fig.4 Straight stripes on the wafer. Direction of the stripes is parallel to one of < 100 > axis. The interval of the stripes was approximately 200 μ m.

The color changes from place to place in one stripe regardless of a dark or a bright stripe.

Crystal defects and the strains are thought to be one of the causes of these features

So, to investigate the effects of the crystal defects and the strains, Laue topographies using synchrotron radiation were conducted and the diffraction images were analyzed.

II. 2 Laue topographic analysis

The Laue topographies were conducted on beam line BL-28 B2 at the SPring8 of JASRI, Harima Science Garden City. The camera length was 85mm and a water filter, 30mm thick, was used as a filter of long wave length radiation[3]. Laue photographs were recorded on Agfa D2 and D4 films with an exposure time of 0.5 to 1.5 second with beam dimension of 3mm x 5mm.

Two wafers of 0.3mm thick PZNT91/09 single crystal were used for the analysis. Point A was a horizontal stripe region and point B was a 90 -degree crossing region of two stripes.

Fig.5 PZNT91/09 single crystal wafer for Laue Topography. A: horizontal stripe region. B: 90-degree crossing region of two stripes. (Black spots are markers.)

A whole transmission Laue diffraction pattern is shown in Fig.6. (010) plane of the crystal was set to be perpendicular to the beam, and [001] axis was set

to be vertical. Four-fold symmetry of the diffraction pattern is clearly observed. As the camera length is 85mm, these diffraction spots have high indices, and so were sensitive to the strains.

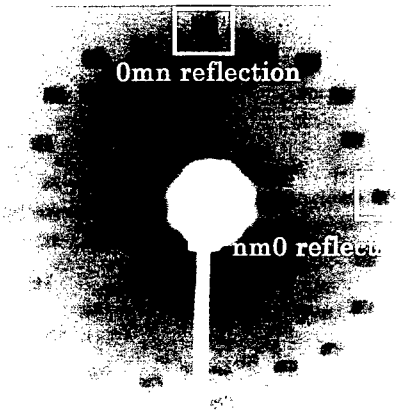

Fig.6 Transmission Laue pattern of a PZNT91/09 single crystal wafer.

Using 0mn and nm0 reflections, crystal defects and the distortions were investigated. Figure 7 shows 0mn reflection (a) and nm0 reflection (b) of position A of Fig.5 respectively.

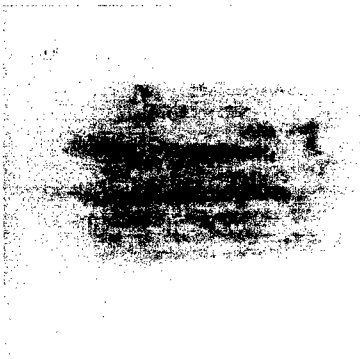

Fig.7 Diffraction images of A: horizontal stripe region. (a) 0mn, (b) nm0 reflections. The dimension of the image corresponds to 3mm x 5mm.

Comparing these diffraction contrasts to the optical microscopic images, the dark band of the diffraction corresponds to the dark stripe of the optical image.

From the contrast of Fig.7 (a) and (b), no crystal defects such as dislocations or stacking faults are clearly observed. However strains are observed, and they show the contrasts of the spikes. The spikes are little inclined against the vertical axis in (a), and are spreading horizontally in (b). The components of Burgers vector of these strains are thought to be <100>, which is parallel to the horizontal stripes. These strains are not distributed uniformly, but seem to have smaller structures in the band. So, the domain structures of the PZNT91/09 single crystals are complex one. To investigate the boundary of two domain structure, 0mn reflection (a) and nm0 reflection (b) of position B of Fig.5 are shown in Fig.8

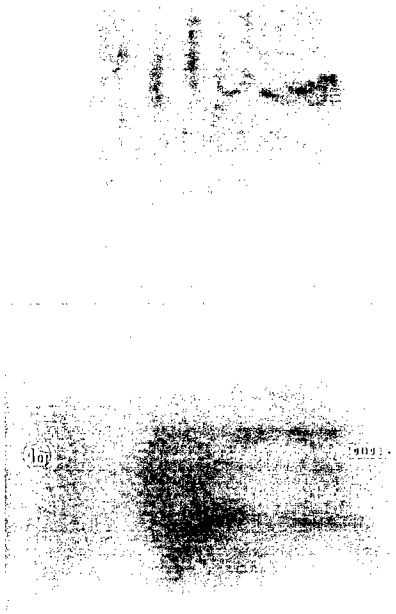

Fig.8 Diffraction images of B: 90-degree crossing region of two stripes. . (a) 0mn, (b) nm0. The dimension of the image corresponds to 3mm x 5mm.

The vertical stripes of (a) disappear in the diffraction image of (b). But the horizontal stripes still remain in (b) though somewhat fading. In the case of B, vertical

stripes correspond to those of horizontal stripes of A. So Burgers vector of the distortions in vertical stripes of B near the boundary where two straight stripes are crossing seems to have large component of <100> like the horizontal stripes in A. Crystal defects like dislocations or stacking faults are not clearly observed in the case of B similar to the case of A.

As mentioned before, the domain structure of the PZNT91/09 is so complicated, detailed investigation on the domain structure is needed. It is also worth to recognize the electric properties of this crystal.

III. CONCLUSIONS

[1] PZNT91/09 single crystals of 75mm in diameter and 55mm in height was grown by one batch solution Bridgman method. 4mm x 4 mm x 12mm rods with (100) planes and (100) wafers are cut out from these crystals.

[2] Straight stripes on the (100) surface of the rods and wafers were observed by the optical microscope. The configuration of the stripes on the rods is two parallel stripes and one 45 degree inclined stripe.

[3] Laue topographies using synchrotron radiation are conducted. Crystal defects like dislocations or stacking faults are not clearly observed. But the strains in the stripes were observed. The Burgers vector of the distortions seem to have large <100> components either in the isolated stripes or the boundary of crossing two stripes.

ACKNOWLEDGMENTS

The authors wish to express their sincere thanks to Dr. M. Tachibana of Yokohama City University and the members of Miyaji Labs. of Kyoto University for their collaboration at Spring8 of JASRI. The authors also express their sincere thanks to Dr. K. Izumi of Kyoto University for his useful advises on analyzing the Laue topographic images. He also collaborated with us at the SPring8 of JASRI.

REFERENCES

[1] K. Harada et al., J. Cryst. Growth (2001) in press.

[2] M. Matsushita et al., J. Cryst. Growth (2001) submitted

[3] K. Izumi et al., J. Cryst. Growth **168** (1996) pp106

Electromechanical Response of [001] Oriented Single Crystal Lead Zinc Niobate-Titanate: DC Bias and Temperature Effects

A. Amin*, L. C. Lim+, and T. S. Ramotowski*

*Naval Undersea Warfare Center, Newport, RI, USA
FAX: 401-832-6401
+Department of Mechanical Engineering, National University of Singapore, Kent Ridge, Singapore
FAX: 65-779-1459
*Email: aminah@npt.nuwc.navy.mil

ABSTRACT

The electromechanical properties of [001] oriented 0.9 lead zinc niobate - 0.1 lead titanate single crystals have been measured as a function of temperature and dc bias field using a resonance method. The measurements were conducted on two length extensional bars cut from a flux grown boule measuring 20 x 14x 5 mm. The temperature and field dependencies of the length extensional coupling coefficient k_{33}, the dielectric K_{33}, piezoelectric d_{33}, and short circuit elastic compliance s_{33} will be presented and discussed in terms of crystal homogeneity.

INTRODUCTION

Because of their extremely large electromechanical coupling coefficient (k_{33}> 0.90), a new generation of relaxor ferroelectric single crystal compositions in the lead zinc niobate/lead titanate (PZN/PT), lead magnesium niobate/lead titanate (PMN/PT), and lead scandium tantalate/lead titanate (PSN/PT) systems [1-3] show great promise as a future underwater sonar projectors and receiving arrays. They offer the potential for both broadband and high acoustic energy density capabilities when compared to standard PZT8 ceramic transducers. Their potential application in medical ultrasound arrays has already been discussed in several publications, see for instance [4].

Over the past five years many researchers have devoted significant effort on growing large single crystals with high electromechanical properties and optimizing crystal orientation to achieve best performance. Impressive progress has occurred towards achieving these goals. However, there are still many issues of the single crystal compositions to be investigated and to identify their impact on device performance. Some of these issues are chemical homogeneity (e.g., inclusions, defects, stoichiometry), mechanical strength, and stability of the electromechanical properties under uniaxial stress (~ 40 MPa), dc bias field (~ 0.8 MV/m), and large signal drive (~ 0.4 MV/m) as demanded by many underwater projector applications. We have evaluated many of the single crystal compositions in our laboratories for naval applications [5] in sound projectors and sound receivers (hydrophones). Both small signal (resonance) and large signal methods are being used to characterize the electromechanical response of the single crystals. In some cases, we encounter instabilities. Their excellent electromechanical properties do not sustain the thermal, electrical, and or mechanical loads of interest to the application engineer. Crystal inhomogeneity, for instance, is a culprit. It will have a significant impact on the mechanical and dielectric strength. This will adversely affect the device stability under mechanical and electrical stresses. Besides, non-uniformity of the electromechanical properties from pixel-to-pixel in an imaging array will result in undesirable fixed pattern noise.

EXPERIMENTAL AND RESULTS

The PZN/PT crystal used in the present work was grown by the slow-cooling technique using PbO flux [6].

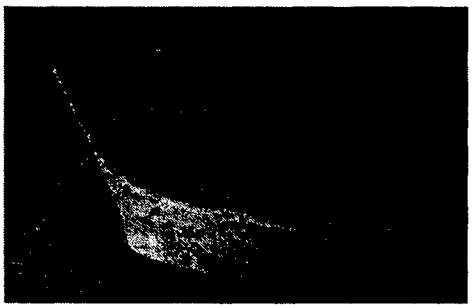

Figure 1. A single crystal PZN/PT 91/09 measuring 20 x 14x 5 mm. All rectangular faces are {001}.

The starting materials used were PbO (99.99%, Alfa), ZnO (99.99%, Alfa), Nb_2O_5 (99.99%, Alfa), and TiO_2 (99.95%, Aldrich) powders. The chemiclas were weighed for a $Pb[(Zn_{1/3}Nb_{2/3})_{0.91}Ti_{0.9}]O_3$:PbO ratio of 55:45 mol%. After thoroughly mixed in a jar, the powder mixture was loaded into a 250 c.c. platinum crucible with lid and then placed in a lid-covered, sealed alumina crucible to minimize PbO loss during the crystal growth run. The crucible assembly was then placed in a specially designed furnace with bottom gas cooling facilities.

The temperature distribution of the furnace was engineered such that after an initial period, during which a single crystal had nucleated at the center of the crucible bottom, nucleation of new crystals was effectively suppressed throughout the subsequent phase of the growth run including sidewall nucleation.

A typical crystal growth run consisted of the following. Firstly, the temperature in the furnace was raised to above 1250°C and maintained for about 3h to homogenize the solution. Then, the solution was rapidly cooled at a rate of 30°C/h to about 1200°C, at which point slow cooling was implemented at the rate of about 0.7 to 1.2 °C/h to commence the growth run. The growth run was stopped after the temperature dropped to about 900°C and the solution was again cooled rapidly to room temperature. Then, the crystal was separated from the solidified flux by leaching in boiling concentrated nitric acid. With the said arrangement, one large-size PZN-PT crystal (typically >25 mm in edge length) was consistently grown in each run. The quality of the crystals grown by the above technique was found to depend on the actual growth conditions notably the growth rate.

The crystal used in the present work was grown at a relatively high rate (i.e. at a cooling rate of about 1°C/h with the entire growth run lasted for about 3 weeks). The crystal appeared translucent to transparent when viewed against the light and was pale yellow to light brown in color. The bulk of the crystal was relatively free from flux inclusions except the surface region of the bottom half of the crystal.

The analysis, which follows, was obtained from the bulk interior of the crystal, which was inclusion-free and pale yellow in color. Four 3 x 3 x 9 mm crystals were cut, polished and electroded on the3 x3 mm faces. We used a Cr (500 A) and Au (2000 A) sputtered on electrode system. The crystals were poled along the [001] -9 mm axis at room temperature using a 20 kV/cm continuous on, poling field for 10 minutes.

Finite element results clearly demonstrated that a 3:1 (l/w) aspect ration is sufficiently close for an accurate determination (less than 1%) of the length extension (33- mode) electromechanical properties [7]. Resonance measurements as function temperature and dc bias fields were performed on the two crystals. Data acquisition and reduction were performed under PRAP environment [8]. The derived material properties include the 33-mode length extensional coupling coefficient k_{33}, the piezoelectric d_{33}, the free K^T_{33} and clamped K^s_{33} dielectric constant, and the short s^E_{33} and open circuit s^D_{33}elastic compliance in complex notation.

Figures 2 to 5 depict the field and temperature dependencies of the isothermal electromechanical properties of the two crystals. The electromechanical properties Crystal 1 were measured under 0 and 0.44 MV/m dc bias. It exhibits a coupling coefficient >0.90 near room temperature (Fig.2). Solid circles in Figs. 2 to 5 illustrate the electromechanical properties of crystal 4 under 0 dc bias.

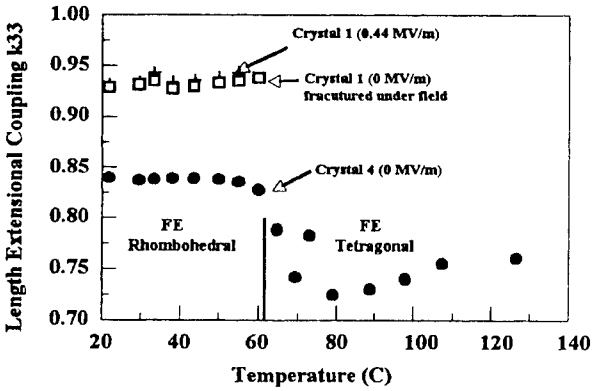

Figure 2. Length extensional coupling coefficient k_{33} of two PZN/PT 91/09 single crystals. Data points are labeled and + for the 0 bias and 0.44 MV/m bias (crystal 1) and • for 0 bias (crystal 4).

The coupling coefficient is nearly field independent up to 55 °C, a temperature close to the ferroelectric rhombohedral-ferroelectric tetragonal phase transition. k_{33} is weakly temperature dependent over this temperature range with a temperature coefficient ~ 1400 ppm/°C, assuming a linear behavior.

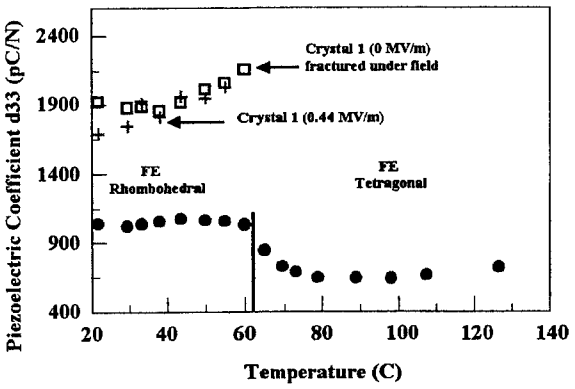

Figure 3. Piezoelectric coefficient d_{33} of two PZN/PT 91/09 single crystals. Data points are labeled and + for the 0 bias and 0.44 MV/m bias (crystal 1) and • for 0 bias (crystal 4).

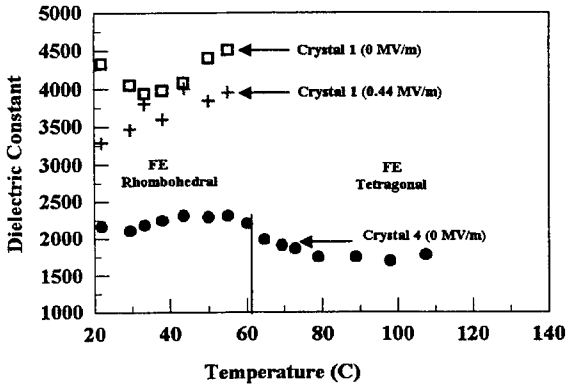

Figure 4. Dielectric constant K^T_{33} of two PZN/PT 91/09 single crystals. Data points are labeled and + for the 0 bias and 0.44 MV/m bias (crystal 1) and • for 0 bias (crystal 4).

Unfortunately, crystal 1 collapsed in the vicinity of 60 °C upon the application of the dc bias field (0.44 MV/m). The field and temperature dependencies of the piezoelectric, dielectric, and short circuit Young's modulus are illustrated in Figures 3, 4, and 5 respectively.

The value for k_{33} of crystal 4 is much lower than that of crystal 1 with a much lower temperature dependency ~ 200 ppm/ °C over ferroelectric rhombohedral phase field. The onset of the ferroelectric rhombohedral-ferroelectric tetragonal phase transitions occurs at ~ 62 °C (Fig.2). This transition is associated with a sharp drop in the electromechanical coupling k_{33} in the tetragonal state and its subsequent increase as a function of temperature.

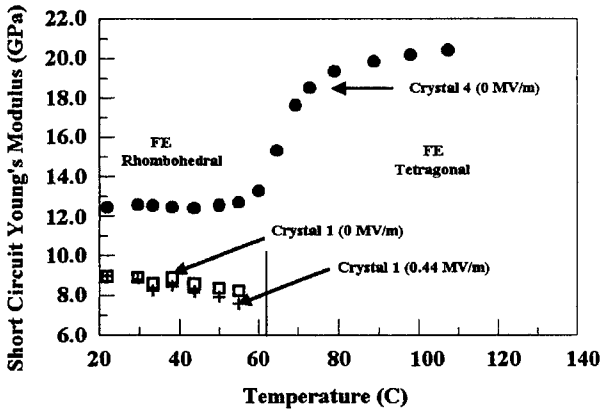

Figure 5. Short circuit Young's modulus Y^E_{33} of two PZN/PT 91/09 single crystals. Data points are labeled and + for the 0 bias and 0.44 MV/m bias (crystal 1) and • for 0 bias (crystal 4).

Qualitatively this behavior has been found in other single crystal compositions [9-11]. Besides lower k_{33} ($=d_{33}/\sqrt{\varepsilon_0 s^E_{33} K^T_{33}}$), crystal 4 has a much lower piezoelectric and dielectric properties (Figs. 3 and 4). Young's modulus, on the other hand, is about 50% higher than that of crystal 1, Fig.5. A coexisting rhombohedral and tetragonal ferroelectric phases in crystal 4 is a likely possibility. To test for compositional gradient that would be associated with Curie temperature distribution, crystal 4 has been sliced into 5 parts as schematically illustrated in Fig.6. We have used a differential scanning calorimeter (DSC) to analyze for heat of transition of samples taken from the 5 slices. Approximately a 10-milligram sample from each slice was crimped into aluminum sample pans

Poling direction

Figure 6. Single crystal PZN/PT 91/09, original orientarion of crystal 4 is shown and the resulting 5 slices for DSC analysis. Slices were numbered consecutively 1 to 5 from left to right.

and placed into the DSC sample holder. Nitrogen flowing at 50 milliliters/minute served as a purge gas. The samples were heated from room temperature to 250 °C at a rate of 10 °C /minute. The DSC scan of a sample from slice 4 of Crystal 4 is shown in Fig.7. The two partially overlapped endothermic peaks in the temperature range 170 °C to 174 °C can be associated with a tetragonal – cubic transition (lower temperature endotherm) while the

higher temperature corresponds to a rhombohedral-cubic transition (main phase).

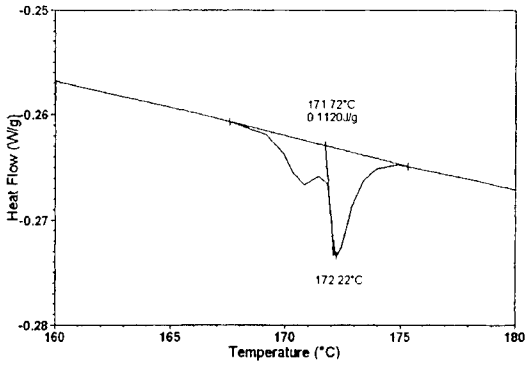

Figure 7. DSC scan of a sample from slice 4 of Crystal 4. Note the two partially overlapped endotherms in the temperature range 167 to 175. The higher temperature endotherm can be associated with a tetragonal – cubic transition ($T_C \sim 171°C$) while the higher temperature corresponds to rhombohedral-cubic transition.

TABLE I
Heat of Transition and Curie Temperature As Determined from DSC Analysis

Slice number	Curie Temperature T_C (°C)	*Heat of Transition Jgm^{-1}	Comments
1	171.89	.1017	Single endotherm
2	171.19	.0890	Single endotherm
3	170.92	.1197	Double endotherm
4	172.22	.1121	Double endotherm
5	171.42	.1097	Single endotherm

*Heats of transition are based on single peak numerical integration where the heat flow is maximum. The software is incapable of de-convoluting partially overlapped endotherms. The temperature of maximum heat flow is taken as T_C .

SUMMARY

Impressive progress has occurred over the past few years in growing novel single crystals with electromechanical coupling coefficient k_{33} >0.90 in the relaxor ferroelectric $Pb(Zn_{1/3}\ Nb_{2/3})O_3$ - $PbTiO_3$ (PZN/PT), $Pb(Mg_{1/3}Nb_{2/3})O_3$- $PbTiO_3$ (PMN/PT), and $Pb(Sc_{1/3}\ Nb_{2/3})O_3$ - $PbTiO_3$ (PSN/PT) systems. These crystals will have a significant impact in broadband underwater acoustics and medical ultrasound imaging. Researchers have successfully grown large crystals, optimized composition, and determined best cut for maximal properties. There are still some issues to be investigated such as mechanical integrity and compositional homogeneity and their implication on device performance.

In this brief study we have attempted to identify the effect of chemical inhomogeneity on the electromechanical response of [001] oriented single crystal $Pb(Zn_{1/3}\ Nb_{2/3})O_3$ - $PbTiO_3$ (PZN/PT ~ 91/09) composition. Further work will be required to improve homogeneity, stability under electrical and mechanical loading, and reproducibility of the single crystal compositions.

ACKNOWLEDGMENT

This work is supported by grants from ONR, DARPA, and the NUWC science and technology ILIR program.

REFERENCES

[1]. Y. Yamashita, and N. Ichinose, Proc. 10th IEEE Inter'l Sympo. Appl. Ferroelectr., 71-77 (1996).
[2]. S.E. Park, M. L. Mulvihill, P. D. Lopath, M. Zipparo, and T. R. Shrout, Proc. 10th IEEE Inter'l Sympo. Appl. Ferroelectr., 79-82 (1996).
[3]. S.E. Park and T. R. Shrout, IEEE Trans UFFC, vol. 44, No. 5, 1140-1147 (1997).
[4]. C. G. Oakley and M.J. Zipparo, Proc. IEEE Ultrasonics Symposium, 1157-1167 (2000).
[5]. J. M. Powers, M. B. Moffett, and F. Nussbaum, Proc. 12th IEEE Inter'l Sympo. Appl. Ferroelectr., 351-354 (2000).
[6]. F.J. Kumar, L.C. Lim, C. Chilong and M.J. Tan, Journal of Crystal Growth, 216, 311-316 (2000).
[7]. R. Janus, Private Communication.
[8]. PRAP, Piezoelectric Resonance Analysis Program, TASI Technical Software, Kingdton, Ontario, Canada.
[9]. D. Viehland, A. Amin, and J. F. Li, Appl. Phys. Lett. (in press).
[10]. A. Amin and J. Powers, The 2001 U.S. Navy Workshop on Acoustic Transduction Materials & Devices, May 14-16, 2001, Baltimore, Maryland.
[11]. A. Amin (unpublished).

CRYSTAL GROWTH AND ELECTRICAL PROPERTIES OF HIGH-Tc RELAXOR-BASED SINGLE CRYSTALS

N.Ichinose, Y.Saigo, Y.Hosono[2] and Y.Yamashita[2],
School of Science and Engineering, Waseda Univ.
3-4-1 Ohkubo, Shinjuku-ku, Tokyo 169-8555, Japan
[2]Toshiba Corp., Kawasaki 212-8582, Japan,
ichinose@mn.waseda.ac.jp

Single crystals of the $xPb(Sc_{1/2}Nb_{1/2})O_3$-$yPb(Zn_{1/3}Nb_{2/3})O_3$-$zPbTiO_3$(PSZNT) and $Pb(In_{1/2}Nb_{1/2})O_3$-$Pb(Zn_{1/3}Nb_{2/3})O_3$ – $PbTiO_3$ (PIZNT)ternary systems have been synthesized by a flux method using PbO flux. The single crystals were grown in a Pt crucible by a mass crystallization, achieved by slow cooling of the 55PbO-45 PSZNT 10/75/15 or PIZNT 10/77/13 (mol%) molten solution with 1.5-3°C/h from1,230-1,250°C to 850°C. The resulting crystals are 2-5 mm in length and dark brown perovskite. For the PSZNT system, the (001) single crystal near the morphotropic phase boundary, showed a room temperature dielectric constant after poling of 2,700 and a very low dielectric loss of 0.5%. A maximum dielectric constant leached to 22,000 at 216°C. On the other hand, the PIZNT system showed Tc=222°C, ε_r=3,900 at 20 C and ε_r=14,000 at Tc.

1. INTRODUCTION

Relaxor materials have the general formula $Pb(B_1B_2)O_3$ where B_1 is a low-valence cation (such as Mg^{2+},Zn^{2+},Ni^{2+},In^{3+},or Sc^{3+}) and B_2 is a high-valence cation (Nb^{5+},Ta^{5+} or W^{6+}). The solid solutions between a relaxor and lead titanate $PbTiO_3$(PT) have a morphotropic phase boundary (MPB) separating the rhombohedral and tetragonal phases as in the case of PZT. One of the principal advantages of the relaxor-PT systems over the conventional PZT ceramics is the ease in growing single crystals of the MPB composition. Single crystals generally have superior properties compared with ceramics if the appropriate crystallographic axis is utilized. Exceptionally good piezoelectric properties were reported for $Pb[(Zn_{1/3}Nb_{2/3})_{0.91}Ti_{0.09}]O_3$ (PZNT 91/9)[1] ,$Pb[(Mg_{1/3}Nb_{2/3})_{0.67}Ti_{0.33}]O_3$ (PMNT 67/33)[2] and $Pb[(Sc_{1/2}Nb_{1/2})_{1-x}Ti_x]O_3$ (PSNT)[3] as binary system single crystals. Various applications have been proposed which would make use of these excellent properties.[4][5] However, these binary system single crystals have some shortcomings which must be overcome. Although the PZNT 91/9 crystals are relatively easy to grow by the solution Bridgman process up to 40 mm in diameter,[6][7] the material shows poor perovskite stability. But a low Curie temperature (Tc<190°C) restrains the PZNT 91/9 crystals in more general applications. PSNT 58/42 has a relatively high Tc(Tc>260°C); however, it has two major shortcomings: a high melting point of 1,420°C[8] and a high raw-material cost.

The ternary systems such as $xPb(Sc_{1/2}Nb_{1/2})O_3$-$yPb(Zn_{1/3}Nb_{2/3})O_3$-$zPbTiO_3$(PSZNT 100x/100y/100z) and $aPb(In_{1/2}Nb_{1/2})O_3$-$bPb(Zn_{1/3}Nb_{2/3})O_3$-$cPbTiO_3$(PIZNT 100a/100b/100c) will have great potential provided single crystals of good quality and sufficient size can be grown. Excellent electromechanical coupling factors, a relative high Tc and good perovskite stability for these systems have been reported.[9]

The purpose of this work is to investigate the possibility of growing PSZNT and PIZNT ternary single crystals near the MPB and to characterize their properties.

2. EXPERIMENTAL

The selected composition for single crystals were PSZNT 10/75/15 and PIZNT 10/77/13. The high-purity chemicals (better than 99.99%), PbO,TiO_2 (Kojundo Chemical Lab., Co., Ltd. Saitama, Japan), Sc_2O_3(Boulder Scientific Co,.USA), In_2O_3, ZnO, and Nb_2O_5(Soekawa Chemical Co., Tokyo, Japan) were used as starting materials. The flux PbO was selected for single crystal synthesis. The flux and the precalcined PSZNT or PIZNT powder were lightly mixed in a plastic bag without any solvent. The selected ratio is 55PbO: 45PSMNT 10/75/15 or PIZNT 10/77/13(mol%). A mixture of 80g was placed in 100cm^3 and 500cm^3 Al_2O_3 double crucibles with lids to prevent the evaporation of lead oxide and possible damage to the electric furnace.[10] The crucibles were placed in a computer-controlled electric furnace. The temperature was increased to 1,230~1,250 °C and maintained for 5h before being slowly decreased to 850 °C at 1.5~3 °C/h. After cooling to room temperature at a rate of 100°C/h, the crucibles were weighed to determine the weight loss of contents during heat treatment. The Pt crucibles were stripped off using a pair of nippers to allow observation of the features of the solidified contents. The contents were rinsed crystals from the residual flux. The crystal

structure was studied by X-ray diffraction after pulverizing the single crystals.

The chemical composition of the crystals was confirmed by the inductive charge plasma (ICP) analysis method. Obtained crystals were used for dielectric measurements. The test specimen are sputtered using Au electrodes. The dielectric properties were measured using a computer controlled LCR meter(HP4194A) within a temperature range of 20°C to 300°C.

3. RESULTS AND DISCUSSION

PSZNT and PIZNT single crystals were obtained. The PbO flux caused negligible damage to the Pt crucible and the weight losses due to PbO evaporation were more than 6.0% within the temperature profile describer above PSZNT crystals in the crucibles were visible to the naked eye. Several transparent crystals ranging 2-5 mm in edge length are visible near the Pt crucible wall and top surface around the center of the crucible. Crystals are dark brown in color. Some of the crystals are agglomerated.

On the other hand, reddish crystals were obtained for PIZNT system. They were found to be mostly pyrochlore phase. Perovskite phase crystals in the PIZNT system were small and brown color. Figure 1 shows XRD patterns of single crystals, the PSZNT 10/75/15 and PIZNT ceramics. The single crystals had a perovskite structure as in the case of the PSZNT and PIZNT ceramics. The high angle peaks in the XRD pattern are split up, indicating a tetragonal symmetry for the PSZNT and PIZNT crystals.

Table I lists the results of ICP chemical analysis of the PSZNT and PIZNT crystals. The chemical composition of the pulverized powder of some PSZNT single crystals is considerably different from that of the charged composition. The single crystals showed a lower Zn content and higher Sc. It appears that the Sc ion is primarily incorporated into the perovskite structure before the Zn ion. The composition of the PSZNT crystals is calculated to $Pb(Sc_{0.23}Zn_{0.16}Nb_{0.55}Ti_{0.15})O_3$ on the basis of the results of the ICP analysis. For the PIZNT system, the very close values were obtained. Figure 2 shows the dielectric properties of one of the PSZNT and PIZNT single crystals compared with PZNT 91/9. Their Tc are higher than that of PZNT 91/9 single crystals. A small peak of the dielectric considered to be the transition point from the rhombohedral to the tetragonal phase. This indicates that the single crystal is in the rhombohedral phase at room temperature. However, the splitting of high angle peaks in the XRD pattern of the PSZNT crystals(Fig.1) would indicate a tetragonal phase. This inconsistency can be attributed to the MPB effects which result in the coexistence of the rhombohedral and tetragonal phases with the proportion of the two phases varying from one crystal to another. The room-temperature dielectric constant was found to be 2,700 for the PSZNT and 3,900 for PIZNT crystals, respectively. These values are slightly bigger than of ceramics.

4. CONCLUSIONS

1) The single crystals of the perovskite-type $xPb(Sc_{1/2}Nb_{1/2})O_3$-$yPb(Zn_{1/3}Nb_{2/3})O_3$-$zPbTiO_3$ (PSZNT 100x/100y/100z) and $aPb(In_{1/2}Nb_{1/2})O_3$-$bPb(Zn_{1/3}Nb_{2/3})O_3$-$cPbTiO_3$ (PIZNT 100a/100b/100c) ternary system have successfully been grown by a flux method with cooling from 1,230~1,250°C to 850°C at a rate of 1.5~3°C/h. The perovskite single crystals were obtainded from the melt with a composition of 55PbO:45PSZNT 10/75/15 and 55PbO:45PIZNT 10/77/13(mol%).

2) Chemical analysis showed that there was a difference in chemical composition between the original charged compositions and the grown PSZNT single crystal; the PSZNT single crystals had a lower Zn and higher Sc content.

3) The PSZNT and PIZNT single crystals with a composition close to that of the MPB exhibit a dielectric constant of 2,700 and 3,900 at room temperature and a Tc=216 °C and 222 °C respectively, which are higher than that of PZNT 91/9 crystals.

5. REFERENCES

[1] J. Kuwata, K. Uchino, and S. Nomura: Jpn. J. Appl. Phys. 21 (1982) 1298.

[2] T. R. Shrout, Z. P. Chang, N. Kim and S. Markgraf: Ferroelectrics Lett. 12 (1990) 63.

[3] Y. Yamashita and S. Shimanuki: Mater. Res. Bull. 31 (1996) 887.

[4] S. E. Park and T. R. Shrout: *1996 Proc. IEEE Ultrasonic Sympo.* (1996) p.935.

[5] S. Saitoh, M. Izumi, S. Shimanuki, S. Hashimoto and Y. Yamashita: U. S. Patent 5,295,487,1994.

[6] S. Shimanuki, Y.Yamashita and S. Saitoh: Jpn. J. Appl. Phys. 37 (1998) 3382.

[7] K. Harada, S. Shimanuki and Y. Yamashita: J. Am. Ceram. Soc. 81 (1998) 2785.

[8] K. Yanagisawa and J. C. Rendon-Angeles: J. Mater. Sci. Lett. 17 (1998) 2105.

[9] Y. Yamashita, Y. Hosono and N. Ichinose:Jpn. J. Appl. Phys. 36 (1997) 1141.

[10]Y. Yamashita and K. Harada: Jpn. J. Appl. Phys. 36 (1997) 6039.

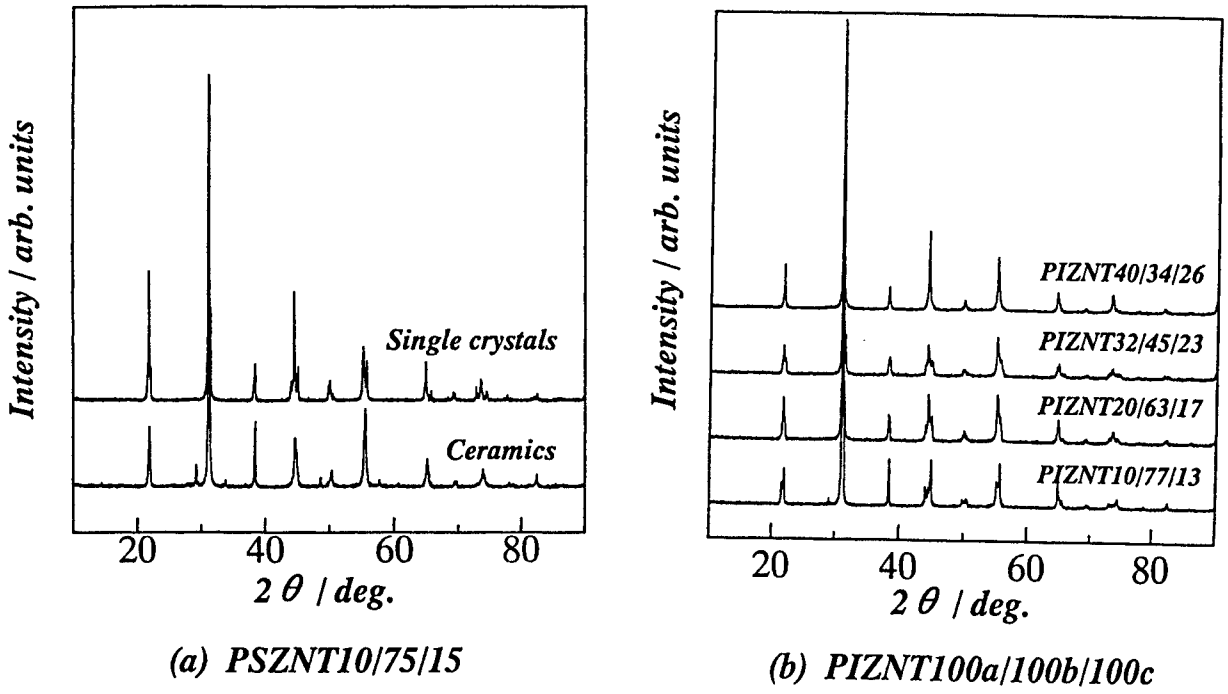

Fig.1 XRD patterns of single crystals, PSZNT 10/75/15 and PIZNT ceramics.

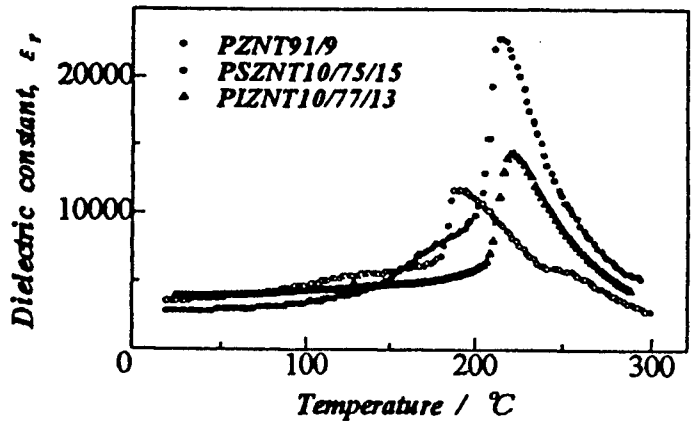

Fig.2 Dielectric properties of the PSZNT, PIZNT and PZNT91/9 single crystals.

Table 1 ICP chemical analysis of crystals.

(a) PSZNT10/75/15

Nominal	$Pb(Sc_{0.05}Zn_{0.25}Nb_{0.55}Ti_{0.15})O_3$
Obtained crystals	$Pb(Sc_{0.23}Zn_{0.16}Nb_{0.55}Ti_{0.15})O_3$

(b) PIZNT10/77/13

Nominal	$Pb(In_{0.05}Zn_{0.26}Nb_{0.56}Ti_{0.13})O_3$
Obtained Dark brown crystals	$Pb(In_{0.05}Zn_{0.23}Nb_{0.56}Ti_{0.16})O_3$
Obtained red crystals	$Pb(In_{0.14}Zn_{0.08}Nb_{0.80}Ti_{0.09})O_3$

Recent Progress of Growth of Ferroelectric Relaxor PMN-PT Single Crystals at SICCAS

Chude Feng and Zhiwen Yin
Shanghai Institute of Ceramics, Chinese Academy of Sciences
1295 Dingxi Road, Shanghai 200050, China

C. B. DiAntonio, F. A. Williams Jr., and S. M. Pilgrim
Laboratory for Electronic Ceramics
New York State College of Ceramics at Alfred University
2 Pine Street, Alfred, New York, 14802
Phone: 607-871-2576
Fax: 607-871-2354
Email: pilgrim@alfred.edu

ABSTRACT

Growth of ferroelectric relaxor PMN-PT single crystals has been conducted at Shanghai Institute of Ceramics, Chinese Academy of Sciences (SICCAS) since 1996 through a modified Bridgman approach. During these years, a series of technological barriers on the growth of ferroelectric relaxor PMN-PT single crystals, such as making seeds, seeded-orientation control, size-enlargement, uniformity of the grown single crystals, and crucible leakage, have been progressively broken down and solved. As a result, ferroelectric relaxor PMN-PT single crystals of ≈45 x 80 mm^3 in size have been successfully grown in SICCAS and produced in a small mass scale. After poling, the electromechanical properties of the grown PMN-PT single crystals are; weak-field permittivity max (ε_{max}) ~ 27,000 at 165°C, 1 kHz and 1 Vrms, dielectric loss (tan δ) < 0.9%; piezoelectric coefficient d_{33} > 2,000 pC/N; mechanical-electric coupling factors, k_{33} ~ 0.92-0.94 and k_t ~ 0.61-0.62, respectively.

INTRODUCTION

Some of the interesting piezoelectric properties of ferroelectric relaxor PMN-PT and PZN-PT single crystals were published by Science journal in 1997.[1] They possess an extremely high piezoelectric constant (d_{33} >2,000 pC/N), mechanical-electric coupling factors (k_{33}>0.90 and k_t> 0.62), low mechanical factor of merit (Q_m~70-80) and high dielectric constant (ε~4,000-5,000) and dielectric loss (tan δ<1%). These single crystals have wide potential applications in medical and military areas, such as in SONAR system, B-ultrasound imaging, micro-positioners, deformable mirrors, micro strip antennas and optical-electric devices. This makes them an important topic worldwide for studies examining crystal growth, characterization and applications.

There are a few differences that exist when comparing between Bridgman and solvent growth techniques to produce these kinds of single crystals.[2,3,4,5] For the solvent method, it is difficult to; (1) control compositions of the grown single crystals, (2) separation from the solvent due to growth among the phases, and (3) it is difficult to control the seeded orientation of the grown single crystals. As for the Bridgman method, it has the following advantages; (1) it is easy to grow the single crystals in large sizes, (2) it is easy to control the seeded orientation of the growth of the single crystals, (3) it is easy to conduct the mass production. Based on these considerations, ferroelectric relaxor PMN-PT single crystals, grown by a modified Bridgman method, have been produced at Shanghai Institute of Ceramics, Chinese Academy of Sciences (SICCAS) since September of 1996.

RESULTS AND DISCUSSION

Bridgman Growth Method

A schematic diagram of a modified Bridgman furnace is shown in Fig. 1. A series of single crystals, including oxide single crystals, such as mica, BGO, $PbWO_4$ and TeO_2; and non-oxide single crystals, such as BaF_2, CsI(Tl), PbF_2 and CsF_3 were successfully grown in atmosphere and conducted in mass production over the past few decades. The modified Bridgman growth approach has been developed and a number of technological barriers overcome.

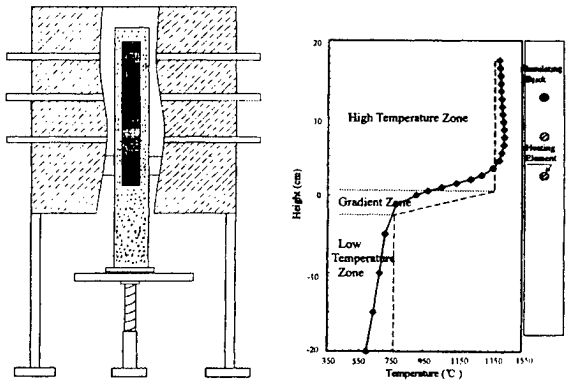

Fig. 1. (a) Schematic diagram of the Bridgeman furnace; (b) Longitudinal temperature gradient of the Bridgeman furnace (—Actual temperature field, ---Ideal temperature field).

Producing Seeds

It is well known that if you intend to grow single crystals with (001) orientation by the modified Bridgman method, you must obtain a seed with (001) orientation. The growth rate of the crystals on (001) is faster than that on (111), therefore initially single crystals with (111) orientation have been grown by the solvent method. Then the seeded orientation of the single crystals grown by the solvent method has to be progressively optimized from (111) to (001) as a seed during the growth by the modified Bridgman method. Figure 1 shows the schematic diagram of the Bridgeman furnace and the longitudinal temperature gradient.

Size Enlargement of the Grown Single Crystals

The size of the grown single crystals has progressively been enlarged to satisfy requirements of different applications. The ability for size enlargement of these single crystals has followed a growth pattern:

(1) Single crystals (65PMN-35PT and 76PMN-24PT) with ≈4 x 20 mm^3 in size and (111) and (001) seeded orientation as well as ≈10 x 20 mm^3 in size and (001) seeded-orientation were grown by the modified Bridgman approach (1997)

(2) ≈(15-20) x (25-30) mm^3 in size and (.001) seeded-orientation (1998).

(3) ≈(25-35) x (40-50) mm^3 in size and (001) seeded-orientation (1998).

(4) ≈(45-55) x (60-80) mm^3 in size and (001) seeded-orientation have been grown and produced in a small scale (2000).

Characterization of the Grown PMN-PT Single Crystals

The size of the as-grown PMN-PT single crystal boles and (001) cut crystal plates are ≈50 x 65 mm^3 and 40 x 30 x 1 mm^3, respectively, as shown in Figure 2.

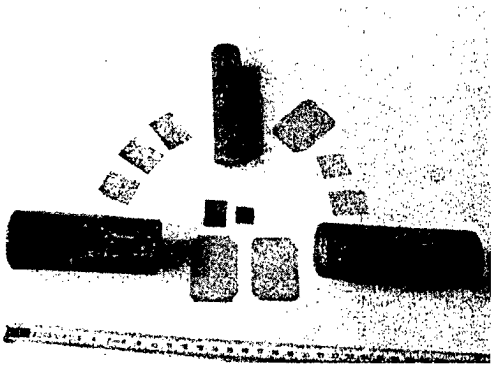

Fig. 2. As-grown PMN-PT single crystal boles and (001) cut crystal plates.

Non-uniformity or non-homogeneity can exist in the grown single crystals and subsequent cut crystal plates. This is attributed to the segregation of compositions in the system during the growth process and structural non-uniformity. The segregation of compositions is due to the differing mobilities of species in the melt. This is induced by; high viscosity and poor convection, volatility of PbO and the other components, and the reaction of PbO with impurities in the Pt crucible, resulting in diffusion of these species into the melt during the growth process. The structural non-uniformity is due to the order-disorder transformation and micro-domains that exist in the grown single crystals and the multiple phases that coexist in the system because of the growth near the MPB (multiphase boundaries). The polarization and piezoelectric properties of the grown single crystals can be affected by the thermal strain structure.

Weak-field permittivity measurements were performed as a function of frequency (1, 10, 100 kHz) and temperature (50°C to 200°C). Frequency and temperature measurements were conducted to examine the relaxor nature of these materials. The capacitance and dielectric loss values of the materials were measured using an HP4284A precision LCR meter (1 V_{rms} level) that was attached to an HP3488A automatic switch scanner and a Delta Design 9039 temperature control chamber. Figure 3 shows the weak-field permittivity and dielectric loss

results as a function of temperature and frequency.

An HP8904A Multifunction Waveform synthesizer (DC-600 kHz) and a Trek high voltage amplifier (model #609D-6) were used to apply an AC, 1 Hz sinusoidal waveform with an amplitude of 1 MV/m to all samples tested. Longitudinal strain measurements were collected using a Fotonic™ sensor (MTI Instruments – 2000 Fotonic™ Sensor model #MTI-2125R). The sensor has a resolution of ≈1.0 μm and a sensitivity of ≈0.92 μm/mV. The polarization was measured using a typical Sawyer-Tower circuit with the variable integrating capacitor set at 10 μF. The strain and polarization tests were run at 100°C inside a Delta Design 9023 furnace using a 9010 temperature control unit. Figure 4 shows the typical longitudinal and transverse strain results as a function of electric field. A typical polarization response, as a function of electric field, is shown in Figure 5. Testing procedures followed previously established protocol.[6,7,8,9,10,11]

The dielectric and piezoelectric properties of (001) cut plates of the grown PMN-PT single crystals were characterized. In general, properties of (001) cut crystal plates of the grown single crystals after poling are as follows: dielectric constant (ε) ~ 4,000-5,000, dielectric loss (tan δ) < 0.9%; piezoelectric coefficient (d_{33}) > 2,000 pC/N; mechanical-electric coupling factors, (k_{33})~ 0.92-0.94 and (k_t) ~ 0.61-0.62, respectively.

Application and Mass Production

As to applications and mass production of PMN-PT single crystals, there still exist a few challenges for growth and characterization. For applications, challenges are non-uniformity or non-homogeneity of properties and multi-domains existing in the grown crystals. It is difficult to maintain homogeneity and mono-domains in different positions of the same crystal plates and in the different crystals plates of the same bole and in different boles grown in the different batches.

For mass production of the growth of PMN-PT single crystals, the challenges are reproducibility or repeatability and consistency. Presently the inability to maintain reproducibility of different growth times and in different growth batches can produce spurious results.

CONCLUSIONS

A series of technological barriers on the growth of PMNT single crystals, such as seed production, seeded-orientation control, size-enlargement, crucible leakage and non-uniformity of the grown single crystals, have been broken down and solved. PMNT single crystals of ≈45 x 80 mm^3 in size have been grown at SICCAS and produced in a small scale. After poling, properties of the grown single crystals are; dielectric constant (ε) ~ 4,000 - 5,000; dielectric loss (tan δ) < 0.9%; piezoelectric coefficient (d_{33}) > 2,000 pC/N, mechanical electric coupling factors (k_{33}) ~ 0.92-0.94 and (k_t) ~ 0.61-0.62, respectively.

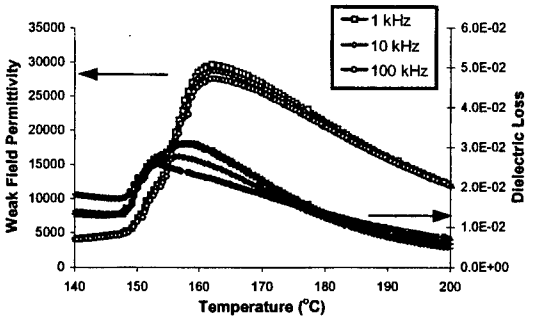

Fig. 3. Typical weak-field permittivity and dielectric loss as a function of temperature and frequency for PMN-PT single crystal.

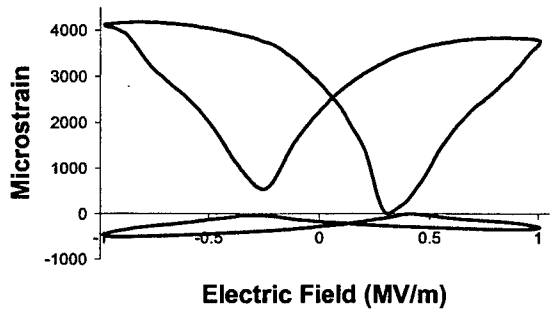

Fig. 4. Typical longitudinal and transverse microstrain response as a function of electric field at 100°C (1 MV/m, 1 Hz).

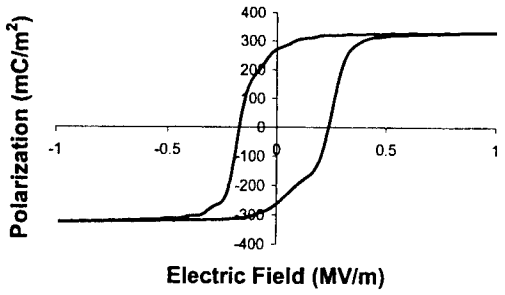

Fig. 5. Typical polarization (mC/m^2) response of PMN-PT single crystal as a function of electric field at 100°C (1 MV/m, 1 Hz).

REFERENCES

[1] R. Service. Shape-changing crystals get shiftier. *Science*, 28 March 1997, 275: 1878.

[2] H. Luo, G. Shen, P. Wang, X. Le, Z. Yin, Study of new piezoelectric material – relaxor ferroelectric single crystals, *J. Inorganic Mater.* 1997 (12) 767 (in Chinese).

[3] Z. Yin, H. Luo, P. Wang, G. Xu, *Ferroelectrics*, 1999 (299) 207-216.

[4] Haosu Luo, Guangshun Shen, Pingchu Wang and Zhiwen Yin, *Ferroelectrics* 1999 (231)97-102

[5] Xu Guisheng, Luo Haosu, Zhong Weizhuo, Yin Zhiwen, *Science in China (Series E)*, 1999,42(5):541-549.

[6] A. F. Devonshire, "Theory of Ferroelectrics," *Adv. Phys.*, **3** [10] 85-130 (1954).

[7] H. Beige and G. Schmidt, "Electromechanical Resonances for Investigating Linear and Nonlinear Properties of Dielectrics," *Ferroelectrics,* **41**, 39-49 (1982).

[8] J. F. Nye, *Physical Properties of Crystals: Their Representation by Tensors and Matrices*; pp. 473-786. Oxford University Press, Oxford, 1993.

[9] R. Newnham and G. Ruschau, "Electromechanical Properties of Smart Materials," *J. Intell. Mater. Syst. Struct.*, **4** [3] 289-294 (1993).

[10] S. M. Pilgrim, "Electrostrictive Ceramics for Low Frequency Transducers," *IEEE Trans. Ultrason., Ferroelectr., Freq. Control*, **47** [4] 861-876 (2000).

[11] S. P. Leary and S. M. Pilgrim, "Harmonic Analysis of the Polarization Response in PMN-based Ceramics–A Study in Aging," *IEEE Trans. Ultrason., Ferroelectr., Freq. Control*, **45** [1] 163-169 (1998).

Compressive Properties of Piezoelectric Single Crystals

Lynn Ewart and Elizabeth A. McLaughlin
Naval Undersea Warfare Center
Code 2132, Building 1170
1176 Howell Street
Newport, RI 02841-1708
(401)-832-5103
mclaughlinea@npt.nuwc.navy.mil

Abstract – This research focuses on the development of a new compression strength test employing right circular cylinders and the results obtained from applying it to specimens of single crystal lead magnesium niobate in solid solution with lead titanate (PMN-PT). Preliminary testing was performed on alumina and ceramic PMN-PT to determine the accuracy of the material property values measured with the cylinders. Comparison of the material property values measured with cylinders to results from measurements on standard dumbbell specimens of alumina and ceramic PMN-PT confirm that the new test is accurate and repeatable. The compressive strength, compressive instantaneous modulus and Poisson's ratio of single crystal PMN-32%PT are reported.

INTRODUCTION

The electromechanical properties of piezoelectric single crystals (piezocrystals) provide significant advantages for sonar transducer applications compared to contemporary polycrystalline ceramics. In particular, the electromechanical coupling factor of piezocrystals is typically greater than 0.90, which is significantly larger than typical values for polycrystalline ceramics. For sonar projector applications this large electromechanical coupling factor creates the possibility of achieving considerably greater bandwidth than is possible with current polycrystalline ceramics. This potential gain in transducer bandwidth is being realized in current programs that are designing prototype piezocrystal sonar projectors. For hydrophone applications the superior properties of the piezocrystals can be employed either to achieve large performance improvements in the signal to noise ratio or to reduce the ship impact of the sonar system.

Naval sonar transducers employed as projectors either at the water surface or at depth are subject to large mechanical stresses during sonification and, for submerged applications, from the water pressure. These stresses are transferred to the stack of active elements inside a transducer. Since piezocrystals are expected to be mechanically similar to other brittle materials, in that they are expected to be considerably stronger in compression than in tension, the transducers are designed to maintain compressive stresses on the piezocrystal elements during the entire lifetime of the transducer. This is achieved through the application of a static compressive stress to the stack of piezocrystal elements during manufacturing. This static stress, which is termed the "prestress", is sufficiently large in magnitude to avoid the development of tensile stresses during operation of the transducer. In designing a transducer which will be subject to large compressive mechanical stresses it is important to know the compressive strength of the active material.

In this research a test method is developed to measure the mechanical properties of single crystals in compression. The accuracy and repeatability of the test is determined by comparing the compressive strength, Young's modulus and Poisson's ratio measured with the new test to these values measured on standard dumbbell specimens in a standard test. The test was then used to measure the compressive properties of piezocrystal PMN-PT.

EXPERIMENTAL PROCEDURE

The mechanical behavior in compression of single crystal lead magnesium niobate in solid solution with 32 mol% lead titanate (PMN-32%PT) from H.C. Materials in Urbana, IL has been studied using a newly developed compression test setup and methodology. The accuracy and repeatability of the test set up and methodology were verified by measuring the compressive properties of two model materials: Grade AD94 alumina from Coors Ceramics in Golden, CO and lead magnesium niobate polycrystalline ceramic in solid solution with 10 mol% lead titanate and doped with 1 wt% lanthanum manufactured by TRS Ceramics in State College, PA. The compressive properties

obtained from the new test were compared to property values measured from standard dumbbell specimens of the same materials [1-3].

In the newly developed compression test specimens are small right cylinders measuring 9.53mm in height by 6.35mm in diameter. The test specimen is shown in Figure 1 along with several other components of the load train. On either side of the specimen are short disks termed inserts. Contacting the other face of the inserts are components termed load blocks. The diameter of the inserts and the small diameter of the load blocks is the same as that of the specimen. The insert and load block materials are chosen to insure that the specimen is the failure point in the load train. The insert material is also chosen to minimize the development of a complex stress state in the specimen, especially at the specimen loading faces.

The development of a complex stress state is minimized by choosing an insert material whose Young's modulus and Poisson's ratio are close to those of the material being tested. It is also important to avoid the development of tensile stresses at the interface, which can lead to premature failure. There are two other requirements for the insert material: 1) it must not yield before the piezocrystal specimen breaks, and 2) it must be conducive in order to maintain short circuit electrical conditions on the specimen during testing.

For the alumina specimens the insert material was tungsten carbide cobalt with alumina load blocks. For the ceramic PMN-PT the insert material was a high strength titanium alloy with alumina load blocks. For the piezocrystal specimens two insert materials were evaluated, ytterbium and high strength titanium. The load blocks were alumina.

On all specimens the end faces that were in contact with the inserts were electroded. A wire connected the two inserts to establish an electrical short. The application of three biaxial strain gages spaced 120° apart in the same cross sectional plane in the middle of the gage section allowed the measurement of both the Young's modulus and, for isotropic materials, the Poisson's ratio. The gaged specimens, inserts and load blocks were aligned in a specially designed fixture and then encapsulated with Composite Polymer Design 9130 polyurethane. The encapsulant served two main functions. First, it retained the broken pieces of the test specimens during the explosive failure. Second, the encapsulant held the specimen, inserts and load blocks together in proper alignment as one composite specimen for testing. The specimens were tested in a servo hydraulic test machine with a double ball-joint loading fixture. (Instron load frame model 1332 and control system 8500). The testing rate was 6 kN/min.

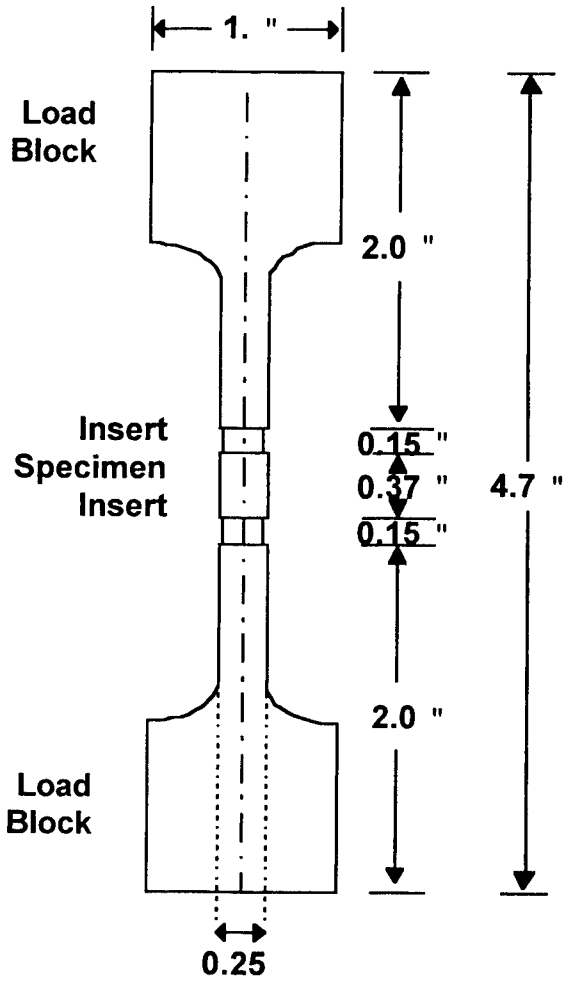

Fig. 1. The specimen, insert and load block dimensions and position in the load train.

RESULTS

The first series of tests examined issues of alignment and test accuracy. The alignment of the load train components was determined through measurements of the percent bending at failure of alumina specimens. The average percent bending of fourteen alumina cylindrical specimens was 3.1 ± 2.8. The average percent bending of six alumina dumbbell specimens was 2.0 ± 1.5.

The accuracy of the test was examined by comparing material property values measured from cylindrical and dumbbell specimens. In alumina the values for cylindrical and dumbbell specimens, respectively, were: a compressive

strength of 2813 ± 295 MPa and 2986 ± 143 MPa, a Young's modulus of 298 ± 5 GPa and 294 ± 9 GPa, and a Poisson's ratio of 0.24 ± 0.01 and 0.25 ± 0.02. In PMN the values for cylindrical and dumbbell specimens, respectively, were: a compressive strength of 697 ± 53 MPa and 896 ± 47 MPa, a Young's modulus of 131 ± 3 GPa and 132 ± 2 GPa, and a Poisson's ratio of 0.31 ± 0.03 and 0.30 ± 0.00.

Two piezocrystal PMN-32%PT specimens were tested first with ytterbium inserts. The compressive strengths were 170 MPa and 157 MPa. However, these stress levels are beyond the yield strength of Ytterbium, which is 66 MPa. Post-test examination of the ytterbium inserts revealed evidence of yielding. Examination of the piezocrystal stress-strain data revealed non-linear behavior with the instantaneous modulus (instantaneous slope of the stress-strain curve) stiffening from 8 GPa at the start of the test to 50 GPa by failure. Based on these results the insert material was changed to a high strength titanium alloy with a yield strength of 1350 MPa. One piezocrystal specimen, which appeared to have a pre-existing crack, was tested with the titanium inserts. The compressive strength was 697 MPa.

DISCUSSION

Good alignment of the load train components is essential to obtaining accurate and repeatable results. The average percent bending in the alumina cylindrical specimens was slightly higher than in the dumbbell specimens, however the target for an acceptable test is to be below five percent. Thus, the alignment procedure developed for the cylindrical specimens yielded very good results.

For both the alumina and the ceramic PMN-PT the cylindrical specimens measured compressive strengths that were somewhat lower that the dumbbell specimens. In the alumina the strength values were only 6% lower, however in the ceramic PMN-PT the strength numbers were 22% lower. While the compressive strength values measured by the cylinders are not as accurate as the strength values measured from dumbbells, the values are conservative in that they underestimate the strength. Also, the PMN cylindrical samples and dumbbell samples did not originate from the same plate.

The values of Young's modulus and Poisson's ratio measured for alumina and ceramic PMN-PT with cylinders and dumbbells are within the standard deviation. Given this result and the conservative measure of compressive strength obtained with the cylindrical specimens, the new test setup and methodology, including the use of cylindrical specimens, was deemed acceptable for measuring the compressive properties of piezocrystals.

The strength results and post-test analysis from the testing of the piezocrystal PMN-32%PT specimens reveal that Ytterbium is not a good insert material for piezocrystal testing. The titanium inserts produced a successful test. The compressive strength, which was measured as 697 MPa, is quite good for naval sonar applications. Since this specimen appeared to have a pre-existing crack, further testing is expected to raise the compressive strength value of piezocrystal PMN-32%PT.

CONCLUSIONS

A new test set-up and methodology have been developed for performing mechanical tests in which the specimen is loaded in uniaxial compression to failure. One key feature of the new test is that the specimen geometry is a small cylinder. The test was determined to be accurate and repeat by comparing material property values measured from cylindrical specimens of alumina and ceramic PMN-PT to values measured for the same materials from standard dumbbell specimens. The test was then applied to piezocrystals of PMN-32%PT. It was found that titanium is the preferred insert material for testing PMN-32%PT. A cracked piezocrystal specimen yielded a strength of 697 MPa.

ACKNOWLEDGMENT

This work was sponsored by the Defense Advanced Research Projects Agency. The author wishes to thank Mr. Chris Bull for assistance with the mechanical testing.

REFERENCES

[1] C.A. Tracy, "A Compression Test for High Strength Ceramics," Journal of Testing & Evaluation, vol.15, no.1, pp 14-19 (1987).
[2] W.A. Dunlay, C.A Tracy, and P.J. Perrone, A Proposed Uniaxial compression Test fof High Strength Ceramics, MTL Technical Report 89-89, U.S. Army Materials Technology Laboratory, Watertown , MA, Sep. 1989.
[3] Lynn Ewart, Elizabeth A. McLaughlin, and Kim D. Gittings, "Mechanical Properties of New Electrostrictive Ceramics," Technical Digest: Transduction Materials, Naval Undersea Warfare Center Division Newport, 45-57 September 2000.

Effects of Surface Condition on the Electrical and Chipping Properties of PZNT Single Crystal Vibrators for Medical Array Transducers.

Tsuyoshi KOBAYASHI, Yasuharu HOSONO, Mamoru IZUMI, Kazuhiro ITSUMI, Koichi HARADA and Yohachi YAMASHITA

Power Supply Materials and Devices Laboratory, Corporate R.& D. Center, Toshiba Co.

1, Komukai Toshiba-cho, Saiwai-ku, Kawasaki 212-8582, JAPAN

Phone_+81-44-549-2134, Fax_+81-44-520-1286, Tuyosi.kobayashi@toshiba.co.jp

Abstract. Effects of different surface conditions on the electrical and mechanical properties of lead zinc niobate titanate ($Pb0.91(Zn_{1/3}Nb_{2/3})0.09TiO_3$ (PZNT 91/9)) piezoelectric single crystal (PSC) have been investigated. The PZNT PSC wafers manufactured by different surface conditions, such as lapped by #2,000, #4,000, #6,000 Al_2O_3 powders and by diamond paste to mirror, were cut into many slivers elements by pitch of 180 μm with 30μm thick diamond blade for fabricating array medical transducer. The amounts of chippings were increased of the surface conditions of #6,000 and mirror. lapped wafers. In addition, a weak bonding strength of Au electrode on the PSC was seen of the mirror lapped wafers after dicing. Damaged PSC sliver showed many spurious modes on the piezoelectric impedance response. It is important to control the surface roughness of PSC to prevent chipping and to realize a good electrode bonding strength on the PSC after dicing.

1. Introduction

Recent reports indicate that some single crystals of the relaxor $(Pb(B1,B2)O_3)$-lead titanate $PbTiO_3$ (PT) binary system have excellent piezoelectric properties near the MPB[1-2]. The authors have conducted an investigation with a view to improving a high sensitivity and a broad bandwidth of ultrasonic transducers of echo ultrasound (Fig. 1) by using $Pb[(Zn_{1/3}Nb_{2/3})_{0.91}Ti_{0.09}]O_3$ (PZNT 91/9) single crystal[3-4] instead of the conventional $Pb(Zr_{1-x}Ti_x)O_3$ ceramics that have mainly been used for present transducers. Single crystals between $Pb(Zn_{1/3}Nb_{2/3})O_3$ and $PbTiO_3$ can be grown by a flux method over the whole composition range. Kuwata et al. reported an extremely large electromechanical coupling factor in the longitudinal bar-mode (k_{33} = 0.92) and piezoelectric strain constant $d33$>1,500 pC/N for PZNT 91/9 PSC. The authors reported that large size PZNT 91/9 single crystals have been successfully obtained using a novel flux method[5] and solution Bridgman process[6] with a suitable ratio of 45mol% PZN-PT 91/9 : 55mol% PbO flux[5]. The largest crystal had dimensions of 43 x 42 x 40 mm and weighed 420 g. The transducer obtained from the ingot has an enough size (>15x25x0.3mm) and quality level for cardiac medical transducers.

In order to fabricate array type transducer, the PSC vibrator is cut into tiny slivers ranging from 100-200 microns pitch by diamond blade saw. In the dicing process, many chippings are occurred due to its low mechanical brittleness of the PSC compared to that of PZT ceramics. However, no reports on the effects of different surface conditions on the electrical and mechanical properties of PZNT PSC have been reported. The purpose of this report is to investigate chipping, mechanical strength and electrical properties of PZNT PSC with different surface controlled vibrators.

2. Experimental Procedure

The PZNT 91/9 single crystal was grown by solution Bridgman method using a PbO flux. A detail process of PSC growth has been reported. [6] Obtained PZNT ingot was sliced into 0.5mm thick (001) wafers. These wafers were lapped with different white Al2O3 powders, #2,000, #4,000 and #6,000. In addition, mirror lapped wafers were prepared by lapping of #6,000 wafers by using diamond paste. Thickness of 0.05 and 0.2 μm-Cr/Au electrodes were deposited on both sides of PSC by sputtering.

For the investigation of electrical and mechanical properties, the 10 pieces of 1mm width x 0.3 mm thick x 10 mm Length rectangular bars and 10 pieces of 0.15 mm width x 0.3 mm thick x 10 mm length sliver vibrator were formed from the each surface roughness (100) wafer. The sliver vibrator's size is a similar to that of the medical array ultrasonic transducers of 2.5 MHz center frequency. In order to measure the piezoelectric properties, the specimens were poled at 0.3 kV/mm in a silicone oil bath. The electric field was applied at a temperature of 200°C for 10 min, and the specimens were cooled to 25°C in the same field. The electromechanical coupling factor rectangular bar mode, k_{33}' was measured by the resonance-and anti-resonance method using the sliver vibrator.

The bending strength σ max was measured by 3-point bending test by using 1x10x0.3mm rectangular bar and 0.15x10x0.3mm sliver samples. The average value of 10 pieces of 1 mm width rectangular plates and 0.15 mm width sliver of each four kinds of surface roughness vibrators were measured.

3. Result and Discussions

Table I shows the summarized results.

Figure 3 shows a typical frequency response and an impedance of a damage-free PSC sliver (A) and a damaged PSC sliver. Many spurious modes are seen if the sliver has many chipping or cracks after the dicing.

Figure 4 shows a surface condition of #2,000 sample view from the top. There are many scratches and small bumps caused by Al_2O_3 polishing powder. These small mechanical damages may cause a origin of the chippings or cracks of the sliver in dicing process. However, the sliver vibrators rapped by #2,000 or #4,000 showed a few amounts of chippings or cracks. In comparison mirror lapped sliver vibrators showed many chippings or cracks after dicing as seen in Fig. 5. Therefore, hidden cracks below the surface strongly affect the chipping and cracks of PSC sliver during the dicing.

In addition, samples of #6,000 and mirror showed a weak electrode bonding strength.

The chipping-less vibrators that of #2,000 and #4,000 showed high electro-mechanical coupling factor; $k_{33}' = 85\%$. However, the lower value of 79% and 75% were obtained and many spurious modes were seen in the #6,000 and mirror samples, respectively. These degradations of electro-mechanical coupling factor k_{33}' caused by the defects of surface may affects the sensitivity scattering between channels of array type transducer. Three point bending strength of PSC 1mm bar sample increase with decreasing surface roughness, Rmax. up to 0.05 μm. Surprisingly, the mirror lapped samples showed the lowest bending strength of the 1mm bar and 0.15 mm slivers samples. The cause is estimated that there are many hidden small cracks under the surface.

4. Conclusion

The relation between surface roughness, bending strength and its electrical properties of the PZNT 91/9 piezoelectric single crystal (PSC) were investigated. The results are as follows:

1) The bending strength increased with decreasing surface-roughness of the PZNT PSC vibrator if no chipping were seen.
2) The amount of chippings in the PZNT vibrator increased markedly in the vibrator lapped #6,000 and mirror.
3) The increasing of the chipping amounts affects a decreasing of the bending strength, deteriorated electromechanical coupling factors and boding strength of the electrodes on the sliver vibrators.
4) In the view point of the fine pitch dicing process for fabricating the array type ultrasonic transducers, the #4,000 lapping which has approximately the Rmax=0.1μm surface roughness is the best for the PZNT 91/9 PSC vibrators.

References:

1) J. Kuwata, K. Uchino and S. Nomura: Jpn. J. Appl. Phys. 21(1982)1298.
2) T. R. Shrout, Z. P. Chang, N. Kim and S. Markgraf: Ferroelectr. Lett. 12(1990)63.
3) S.Saitoh, M.Izumi, S.Shimanuki, S.Hashimoto and Y.Yamashita, U.S. Patent 5,295,487,(1994).
4) S.Saitoh, T.Takeuchi, T Kobayashi, K.Harada, S.Shimanuki and Y.Yamashita, Jpn. J. Appl. Phys.,Vol.38,No.5B,pp.3380-3384(1999).
5) T. Kobayashi, S. Shimanuki, S. Saitoh and Y. Yamashita: Jpn. J. Appl. Phys. 36(1997)6035.
6) K.Harada, S.Shimanuki, S.Saitoh, and Y.Yamashita, J.Am. Ceram. Soc., Vol.81,[11], pp.2785-2788(1998).

Table I Physical and electrical properties of PZNT 91/09 PSC vibrators with different surface conditions.

Surface condition		#2,000	#4,000	#6,000	Mirror
Al_2O_3 Powder particle size	(μm)	12.7	6.4	4.2	<1.0
Surface roughness Rmax.	(μm)	0.16	0.08	<0.05	<0.02
Bending strength (W=1.0mm)	(kg/mm3)	43	44	45	38
Bending strength (W=0.15mm)	(kg/mm3)	51	63		48
E/M coupling factor k_{33}'	(%)	85	85	79	76
Spurious mode		few	few	few	many
Chipping		few	few	some	many
Electrode peeling off		none	none	few	many

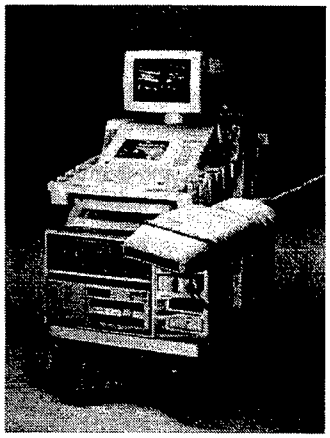

Figure 1. Echo ultrasound and medical prove

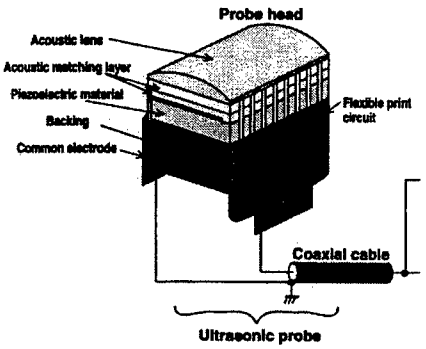

Figure 2. Structure of medical proves. Note: Piezoelectric material and matching layers are cut into small slivers by dicing.

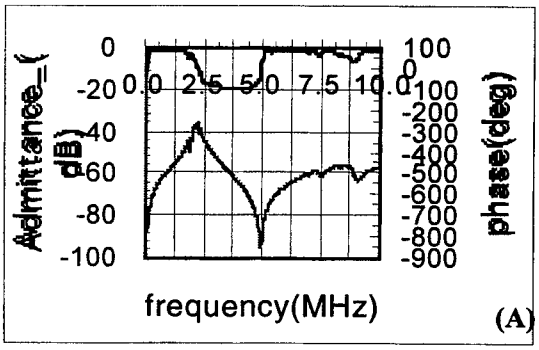

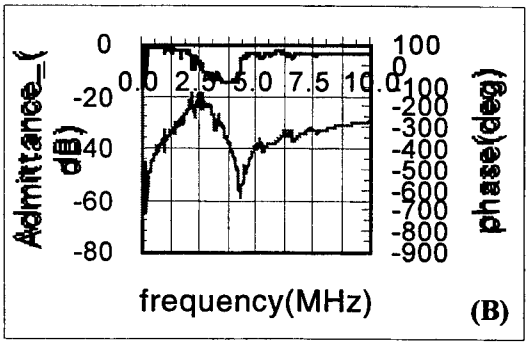

Figure 3. Typical frequency response and impedance of good PSC sliver(A) and damaged PSC sliver(B). The damaged PSC sliver shows many spurious modes.

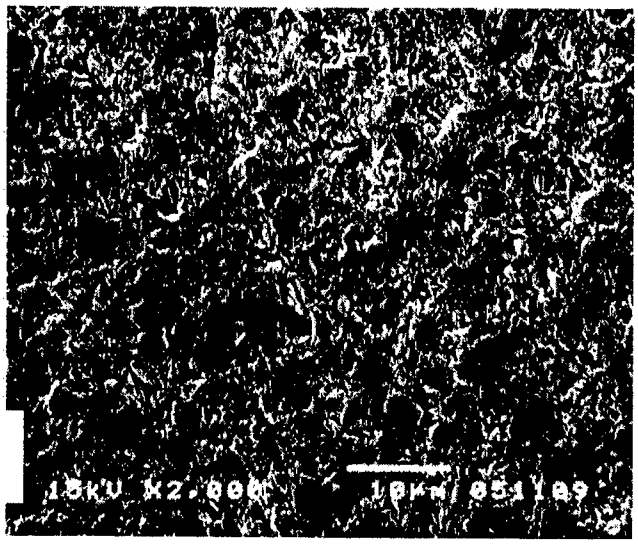

Figure 4. PZNT PSC surface lapped by #2,000 Al_2O_3 powder. Note: There are many scratches on the surface of the PSC.

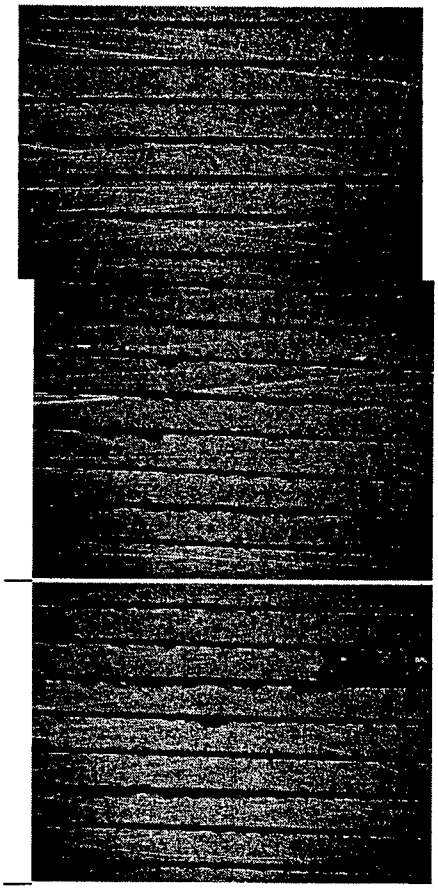

Figure 5. Diced PSC surfaces of different surface conditions, #2,000, #6,000 and mirror lapping (View from the top). Note: Mirror lapping and #6,000 lapped PSC show electrode peeling off and many chipping after dicing. Dicing pitch is 180 micron with 30 micron blade.

New Orientation Cuts for Enhanced Electromechanical Properties of PMN-PT and PZN-PT Single Crystals

Jie Chen, Rajesh Panda, Heather Beck, and Raj Gururaja

Imaging Systems, Agilent Technologies, Inc.
3000 Minuteman Road, Andover, MA 01810
Fax: 978-687-7265 Email: jie_chen2@hsgmed.com

INTRODUTION

The high piezoelectric constants (k_{33} of $\geq$0.92 and d_{33} of $\geq$2000pC/N) of <001> oriented lead-based single crystals of $Pb(Mg_{1/3}Nb_{2/3}O_3$-$PbTiO_3$ (PMN-PT) and $Pb(Zn_{1/3}Nb_{2/3}O_3$-$PbTiO_3$ (PZN-PT) make them attractive for medical imaging and actuator applications[1-6]. The previous work has focused primarily on the <001> orientation. Although the (001) wafer offers the best orientation for electromechanical properties, it is difficult to grow crystals along the <001> orientation due to cleavage parallel the (001) plane which causes cracks within the crystals. The crystals grown along other orientations are relatively easier, such as <011> and <111> orientations. But the compositional gradient along the growth direction of the crystals dramatically reduces the yield for (001) oriented wafers. Very little work has been done to explore the electromechanical properties of other orientations, such as the <011> and <111>. The electromechanical properties of <111> cuts appear to be low (k_{33} of 0.35-0.65 only compared to k_{33} of 0.92 for <001> orientation) and sensitive to the chemical composition of the crystals [7].

Most of the ultrasound transducers for medical imaging utilize a sliver geometry, where the length >> thickness > width (1 and 1.5D arrays). The resonance is laterally clamped in the length direction that tends to reduce the coupling coefficient from the ideal longitudinal k_{33}. In order to obtain high effective coupling constants (k_{33}'), researchers have traditionally cut slivers with <001> thickness orientation and width along the <010>.

For sliver-shaped resonators, not only the thickness orientation, but also the width orientation affects the resonance behavior. This work studies the effects of both thickness and width orientations for one-dimensional transducer arrays. New thickness and width orientation cuts with excellent electromechanical properties (similar to the <001> orientation cuts) have been found over a broad orientation range for ultrasonic transducer applications.

EXPERIMENTAL

Chemical grade PbO, MgO, Nb_2O_5, and TiO_2 were used to form PMN-PT compositions. The PMN-PT contained 26% to 40% of PT. Bridgman technique was used to grow PMN-PT single crystals. The single crystals were oriented using the Laue back reflection method and sliced using an ID saw parallel to the (001) and (011) planes to approximately 1 to1.5 mm in thickness. After the wafers were lapped and polished, gold coating was deposited on opposite surfaces to form the electrodes.

The single crystal wafers with <001> and <011> thickness orientations were then diced using a dicing saw typically into 10 - 15 mm x 0.3 - 0.5 mm x 0.15 - 0.3 mm slivers having various width orientation cuts. Longitudinal oriented rods with <001> and <011> orientations were also tested. The length to width aspect ratio of these rods were in the range of about 7:1. Figure 1 shows two <001> thickness oriented slivers with the width along the <010> and <011> orientations respectively (the $<001>_t/<010>_w$ and $<001>_t/<011>_w$ slivers). A <001> oriented rod is also shown in Figure 1. The slivers and rods were poled at room temperature in air or in oil and the electromechanical and dielectric properties were measured using a HP 4194A impedance gain phase analyzer.

RESULTS AND DISCUSSION

(1) <001> and <011> Oriented Rods

The rods, having a PMN-31%PT composition and a length-to-width aspect ratio of 7:1, were oriented longitudinally along the <001> and <011> orientations. Coupling constants of k_{33}' higher than 0.90 were obtained on both oriented rods (See Table-1). This data indicates that not only the <001> orientation offer excellent coupling constants, but also the <011> orientation.

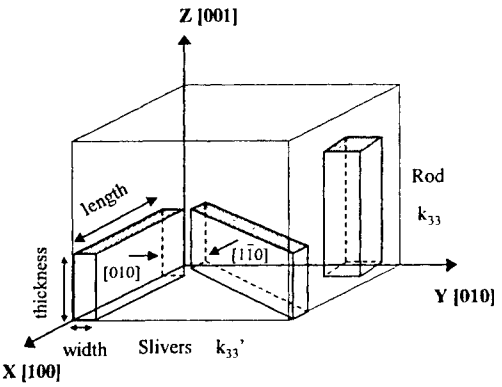

Figure 1: A schematic drawing shows two slivers with thickness oriented along the [001] and width along the [010] and [1$\underline{1}$0] directions, respectively. A [001] longitudinal oriented rod is also shown in the graph.

Table-1. The effective coupling constants of PMN-31%PT rods along <001> and <011> orientations.

PMN-PT 31% (rod, L:W=7:1)	Effective Coupling Constant k_{33}'
<001>	0.93
<011>	0.91

(2) <001> Thickness Oriented Slivers

PMN-PT slivers with rhombohedral phase composition (32% PT) were tested at thickness orientation of <001> and width orientation from <010> to <011> orientations. Figure 2(a) shows the experimental impedance (Z-θ) spectrum of a $<001>_t/<010>_w$ oriented sliver. As expected, the spectrum was clean without spurious modes (Additional width resonance mode can be seen at 9-10MHz) and a high coupling of k_{33}'=0.85~0.87. Figure 2(b) shows the spectrum of a sliver, 32° off the <010> width orientation, showing the presence of undesirable spurious modes. In addition to the low frequency resonance peak, a high frequency resonance peak appears.

As shown in Figure 2(c), the impedance plot of $<001>_t/<011>_w$ oriented slivers, 45° off the <010> width orientation, had a clean resonance mode with an effective coupling constant of 0.76~0.78. This result is different compared to Park's data [3 and 7] who have shown the existence of spurious modes on cutting at a width angle 45° away from the <010> direction for <001> thickness oriented slivers.

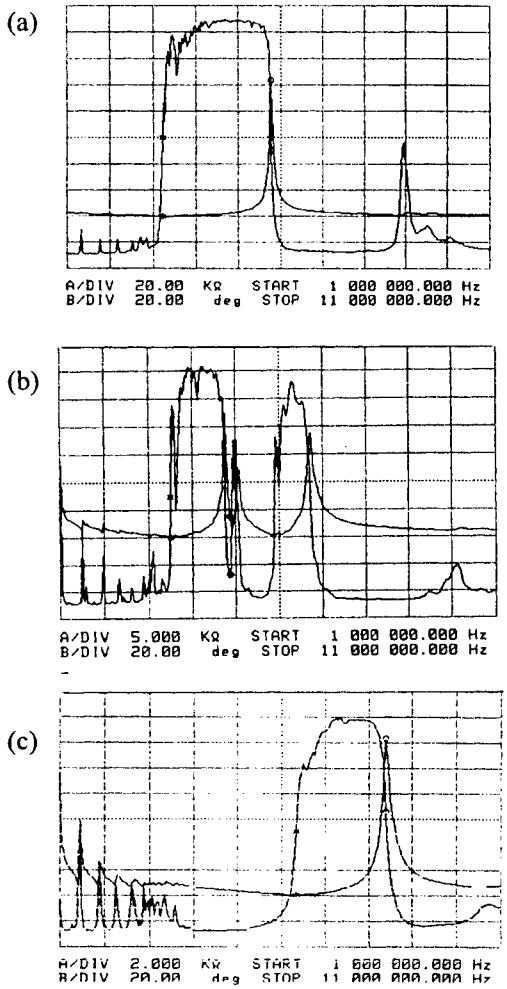

Figure 2: The Z-θ impedance plot for <001> thickness oriented sliver with (a) the width oriented along the <010> direction; (b) the width oriented –32° away from the <010> direction; and (c) the width oriented –45° away from the <010> direction.

We have found that unlike the $<001>_t/<010>_w$ orientation cuts, the resonance mode for the $<001>_t/<011>_w$ cuts is very sensitive to the width orientation. A slight misorientation in width orientation will show the spurious modes in the impedance plot. Apart from the high sensitivity of the width orientation, the impedance plot of $<001>_t/<011>_w$ slivers had one major difference compared to the $<001>_t/<010>_w$ slivers. The $<001>_t/<011>_w$ oriented sliver resonates at a higher frequency, hence it has a higher velocity than the $<001>_t/<010>_w$ sliver.

The different resonance behavior of <001> oriented slivers are possibly related to the lateral clamping effects of the polarization dipoles. The orientation relationship of sliver shaped resonators can be seen easily from the stereographic projection. When four preferred <111> polarization directions in rhombohedral phase are not clamped along the length direction of $<001>_t/<010>_w$ slivers (see Figure 3(a)), the coupling constant at this orientation is high (k_{33}' =0.86) and it is less sensitive to the width orientation. When the width orientation is along the <011> orientation (the $<001>_t/<011>_w$ slivers), the original main resonance peak disappears and the high resonance peak becomes the main peak. Because two of the four <111> polarization directions are clamped along the sliver length direction as shown in Figure 3(b) (54.7° away from the poling orientation), this cut has a lower coupling constant (k_{33}'=0.77 vs. 0.86) and it is more sensitive to the width orientation. Also due to the clamping effect, the velocity of $<001>_t/<011>_w$ oriented sliver is higher compared to the unclamped condition of $<001>_t/<010>_w$ oriented sliver.

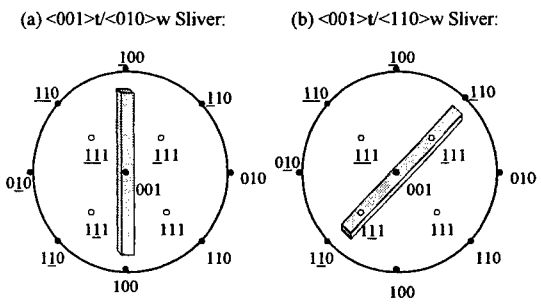

Figure 3: Showing the stereographic projections of (a) $<001>_t/<010>_w$ sliver and (b) $<001>_t/<011>_w$ sliver. The open cycles indicate the four possible <111> polarization directions.

(3) <011> Thickness Oriented Slivers

PMN-PT single crystals with thickness orientation along <011> were investigated for the existence of orientation cuts having favorable electromechanical properties. As shown in the <011> stereographic projection of Figure 4(a-d), there are two preferred <111> polarization directions (for rhombohedral phase) and two preferred <001> polarization directions (for tetragonal phase) within the (011) plane. Each of them is 35.3° and 45° away from the <011> poling direction (also the thickness orientation).

For PMN-32%PT, the primary phase for this composition is within the rhombohedral phase. It is expected that when the sliver is cut with <011> width orientation (Figure 4(a)), the effective coupling will be lower since the two primary <111> polarization directions are clamped in the sliver length direction. The sliver data shows that k_{33}' as low as 0.46 was obtained in this orientation. On the other hand, for $<011>_t/<100>_w$ sliver as shown in Figure 4(b), the dominant <111> polarization directions are free from the length clamping effect, the k_{33}' is much higher (k_{33}'=0.82). Due to the possible coexistence of both rhombohedral and tetragonal phases near the MPB compositions[8], the clamping effect of <010> polarization directions (small contribution from tetragonal phase) still limits the sliver to resonate freely. Therefore, it has a lower k_{33}' value than $<001>_t/<010>_w$ slivers.

Table-2 shows the effective coupling constants of <011> oriented PMN-PT slivers with width orientations between the <110> and <010>. When both <111> and <001> polarization directions are free of clamping along the length direction (see Figure 4(c) and (d)), high coupling constants can be obtained from these slivers. As shown in Table-2, k_{33}' as high as 0.90 can be obtained for slivers with width orientations from 50 to 70 degrees away from $<110>_w$. These $<011>_t/<110>_{w\ 50\text{-}70\ degree}$ cuts include the $<011>_t/<211>_w$ (55.4°), $<011>_t/<522>_w$ (60.4°), and $<011>_t/<311>_w$ (65.4°) cuts. Not only do the $<011>_t/<110>_{w\ 50\text{-}70\ degree}$ cuts exhibit very high values of k_{33}', but their properties also show little sensitivity to the width orientation over a wide range of angles, which enables easier transducer fabrication. These results demonstrate that the <011> thickness orientation offers a range of useful cuts with excellent coupling properties for transducer applications.

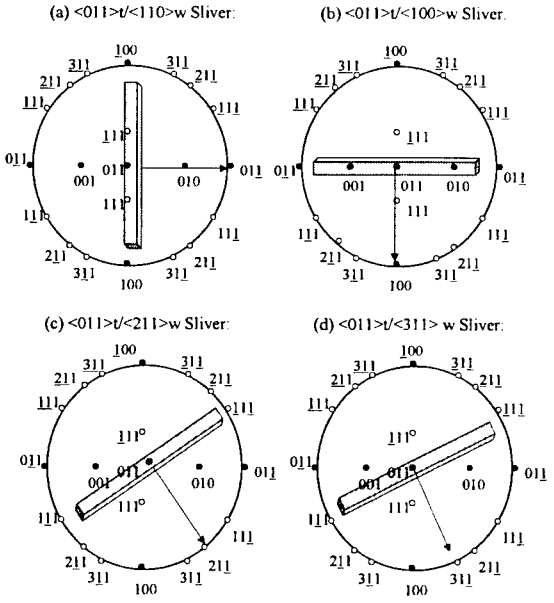

Figure 4: Stereographic projections of <011> orientation showing the orientation projections of (a) $<011>_t/<110>_w$ sliver, (b) $<011>_t/<100>_w$ sliver, (c) $<011>_t/<211>_w$ sliver, and (d) $<011>_t/<311>_w$ sliver. The arrows indicate the width orientations of the slivers.

Table-2. The effective coupling constant of PMN-PT slivers with $<011>_t/<110>_{w\ 0\text{-}90\ degree}$ orientation cuts.

PMN-PT 32%	Effective Coupling k_{33}' (sliver)
$<011>_t/<110>_{w\ 0\ degree}$	0.46
$<011>_t/<110>_{w\ 35\ degree}$	0.72
$<011>_t/<110>_{w\ 40\ degree}$	0.79
$<011>_t/<110>_{w\ 50\ degree}$	0.88
$<011>_t/<110>_{w\ 55\ degree}$ ($<011>_t/<211>_w$ sliver)	0.90
$<011>_t/<110>_{w\ 60\ degree}$ $<011>_t/<522>_w$ sliver)	0.90
$<011>_t/<110>_{w\ 65\ degree}$ ($<011>_t/<311>_w$ sliver)	0.90
$<011>_t/<110>_{w\ 70\ degree}$	0.88
$<011>_t/<110>_{w\ 75\ degree}$	0.86
$<011>_t/<110>_{w\ 80\ degree}$	0.85
$<011>_t/<110>_{w\ 90\ degree}$ $<011>_t/<100>_w$ sliver)	0.82

CONCLUSIONS

This work studied the effects of both thickness and width orientations on the resonance behavior of sliver-shaped resonators. The data indicates that not only the <001> orientation, but also the <011> orientation offers excellent coupling constants for electromechanical applications. The coupling constant of k_{33}' as high as 0.90 (similar to <001> orientation) can be obtained in <011> thickness oriented slivers ($<011>_t/<110>_{w\ 50\text{-}70\ degree}$ cuts include $<011>_t/<211>_w$, $<011>_t/<522>_w$, and $<011>_t/<311>_w$ oriented slivers). Another advantage of <011> oriented slivers is that the coupling constant is less sensitive to the width orientation over a range of angles which enables easy transducer manufacture.

REFERENCES

[1] J. Kuwata, K. Uchino, S. Nomura, Jpn. J. Appl. Phys., Part1 21, 1298-1302 (1982)

[2] S. Saitoh, M. Izumi, S. Shimanuki, S. Hashimoto, and Y. Yamashia, U.S. Patent 5,295,487, 1994

[3] S. Park and T. Shrout, IEEE Trans. Ultrason. Freeoelectr. Freq. Control, Vol.44, 1140-1147 (1997)

[4] S. Saitoh, T. Takeuchi, T. Kobayashi, K. Harada, S. Shimanuki, and Y. Yamashia, IEEE Trans. Ultrason, Freeoelectr. Freq. Control, Vol.46, 414-421 (1999)

[5] R. Panda, J. Chen, H. Beck, and T. Gururaja The 9th US-Japan Seminar on Dielectric and Piezoelectric Ceramics, Okinawa, Japan, Nov.2-5, 1999 pp143-146

[6] C. Okaley and M. Zipparo, IEEE Ultrasonics Symposium Proceedings, pp1157-1167 2000

[7] S. Park, P. Lopath, K. Shung, and T. Shrout, Proc. SPIE Vol.3037, 140-147, Medical Imaging 1997

[8] Z. Ye and M Dong, J. Appl. Phys. Vol.87, No.5, 2312-2319, 2000

Domain Configuration and Polarization Switching in PZN–5% PT Crystals

S.-E. Park*, J.-K. Kee, and K. S. Hong

*Fraunhofer-IBMT Technology Center Hialeah, Hialeah, FL, 33010, USA

School of Materials Science and Engineering, Seoul National University, Seoul, 151-742, Korea

epark@ftech.org

INTRODUCTION

Since the discovery of the stable "averaged" domain configuration in <001> oriented rhombohedral $Pb(Zn_{1/3}Nb_{2/3})O_3$-$PbTiO_3$ (PZN-PT) crystals, resulting in the hysteresis-minimized strain behavior, [1,2] additional discoveries related to the domain configuration and its dynamic switching behaviors have been reported, - i.e. the charged domain walls [3] and dendritic domain patterns generated by the dynamic pulse poling. [4] Interestingly, the random dendritic domain configurations in ref. 4 imply that, once the dynamic pulse generates non-equilibrium state, the rhombohedral crystals may possess a symmetry lower than rhombohedral, i.e., monoclinic or even triclinic, probably in association of their chemical and electrical characteristics of relaxor ferroelectrics. These findings in mesoscopic structure in PZN-PT crystals are quite intriguing, whereas the intrinsic contribution contributed by the monoclinic shear deformation, associated with <001> E-field, is more than enough to explain the ultrahigh piezoelectric activity of <001> oriented PZN-PT crystals. [5]

These new insights gained upon the crystallographic engineering triggered an additional interest on the polarization switching behavior of ferroelectric single crystals. The fatigue anisotropy, another key discovery in relaxor-PT single crystals, is also related to the crystallographic engineering. [6,7] The pinning of the domain walls by entrapped space charges was suggested as a fatigue mechanism because the initial charge value was fully restored upon heating the crystal at temperatures higher than T_{max}. Its correlation with the domain configuration and switching behavior, however, is not clearly understood.

Rhombohedral PZN-PT crystals with low PT content such as PZN-5%PT exhibit the macroscopic domain structure only after the crystal is exposed to E-field. Therefore, the domain configuration must be constructed complying to the crystallographic relationship, based upon the crystal structure of the first emerged ferroelectric under E-field, which is c-axis unique monoclinic for <001> oriented crystals.[8]

In this work, we report our investigation of the domain configuration and the polarization switching behavior as a function of crystallographic orientation, in rhombohedral PZN-5%PT crystals. The polarization switching anisotropy will be discussed using the traditional crystallography and domain configurations with respect to the E-field direction.

EXERIMENTAL PROCEDURE

PZN-5%PT crystals were prepared using the flux method. After the crystals are oriented along <111> and <001> directions using Laue back reflection Laue method, the final polished single crystals with 4×4×0.3 mm plates and 2x2x2 mm cubes were prepared for the domain observation and X-ray analysis, respectively. The transverse directions of the <111> plates and <111> cubes were controlled to be $<01\bar{1}>$ or $<2\bar{1}\bar{1}>$. Two (001) cubes with the transverse faces of {100} and {110} were fabricated for the detection of ferroic distortions using XRD. For *in-situ* domain observation with polarized light along the E-field direction, transparent indium-tin-oxide (ITO) electrodes were sputtered onto the faces of plate samples. In addition, air dry silver, which was removed after E-field application, was pasted as an electrode and thin gauge wires were attached on the faces of cubes for transverse domain observation.

For switching current measurements, the polished crystals plates (3x3x0.2mm) were prepared. For electrical analysis, gold electrodes were sputtered onto both polished sides. Bipolar hysteresis loops were measured as a function of crystallographic orientation, using modified Sawyer-Tower circuit, at 0.2 Hz. Square pulses with alternating polarity were applied to poled samples connected to a resistor (10 ohm) in series, to measure the transient electric current. AC function was produced and amplified using arbitrary wave function generator (Model AWG 2010, Tektronix, USA) and high voltage amplifier (Model 609E-6, Trek, USA), respectively. The voltage applied to a resistor (10W) in series, was measured with the aid of an oscilloscope (Model TDS 420A, Tektronix, USA). Amplitudes of pulses

Figure 1 Domain configuration of <111> PZN-5%PT after E-field exposure.

were in the range of 150 (7.5 kV/cm) to 450V (22.5 kV/cm), greater than coercive fields of crystals. The pulse width was 0.1 ~ 5μsec, respectively.

RESULT AND DISCUSSION

Domain Configuration

As previously mentioned, no ferroelectric domain pattern was detected in virgin PZN-5PT crystals. In <111> oriented crystals, the macroscopic ferroelectric domain configurations were first generated under bias and domain boundary density decreased upon increasing E-field to ultimately become a single domain at E-fields > 30kV/cm. Upon the removal of E-field, as reported in ref. [1], the multi-domain state was reappeared, as presented in Fig. 1. The crystal consisted of large domains and stripes of narrow domain bands (depoled part), with all domain boundaries being indexed as (110). This domain boundary is the most favorable state of rhombohedral ferroelectrics.

In <001> oriented crystals, normal ferroelectric domain boundaries appeared at E~5kV/cm, and did

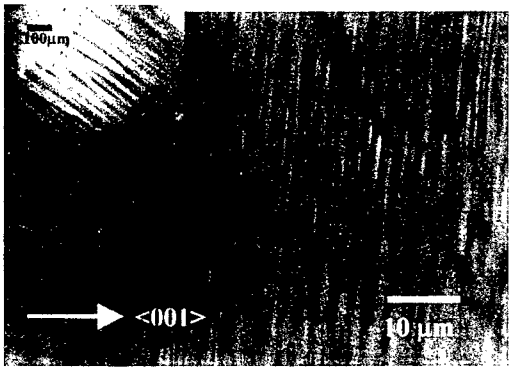

Figure 2 Domain configuration of <001> PZN-5%PT crystals after E-field exposure (inserted is the moiré stripes at low magnification).

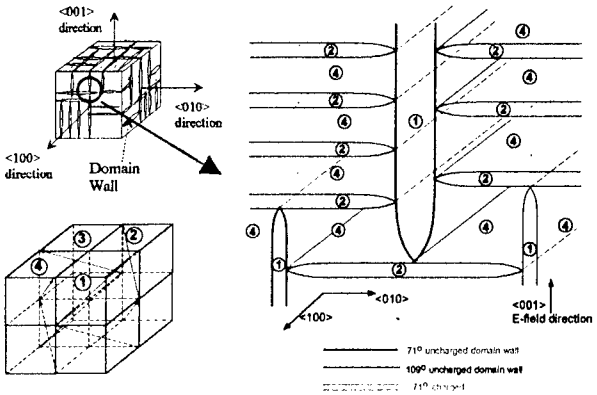

Figure 3 Schematic of domain configuration in E-field exposed <001> cube sample.

not change their configuration with increasing E-fields, again similar to the observation by Wada et al. [1]. The width of domains in <001> crystals was equal to or less than 1 μm, as shown in Fig.2. It is noted that the authors often misinterpreted 50 to 100 μm thick stripes as ferroelectric domains as shown in the figure put in the Fig. 2. These thick stripes were generated by the moiré interference, commonly observed in <001> oriented thick samples. Crystallographic orientation of almost all domain boundaries in <001> oriented crystals was indexed to be {100}, which was not minimum energy walls in rhombohedral ferroelectric crystals. To confirm the crystallographic indices of domain boundaries, cubes with six {100} planes were prepared and all planes were investigated. It revealed that most boundaries on three {100} surfaces were parallel to <100>. A pair of four transverse faces exhibited boundary density significantly lower than the others. Domains in [001] oriented crystals taper with forming wedge shapes, especially when a domain confronts the boundary of another domain, or the crystal surface. The schematic domain configurations in <001> oriented crystals are presented in Fig. 3. Curved domain boundaries in Fig. 3 are the result of the reduced ratio of domain width to the crystal size. In actual crystals, the domain width was significantly smaller compared with the crystal and all boundaries were straight obeying the crystallographic requirement. Under this condition, where all domains boundaries are encountering another one at each tip, domain boundaries can satisfy "head-to-tail" condition and form the electrically uncharged domains.

As <111> is the polar direction, the application of E-field along <111> direction should enhance rhombic lattice distortion (i.e., decreased interaxial angle α). If an E-field is applied precisely along

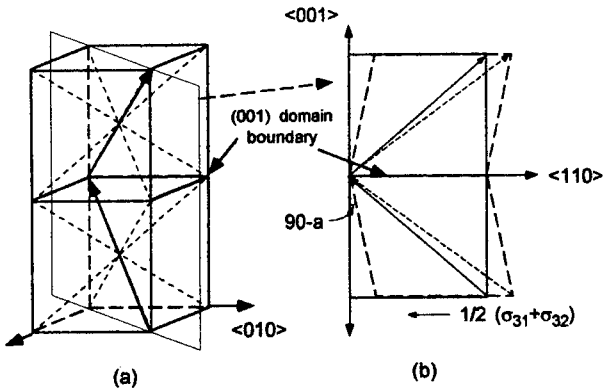

Figure 4 (a) Schematic of "averaged" domain configuration - a set of 109° domain boundary is demonstrated. (b) Cross-section onto (-110) plane

<001>, the perovskite crystals are expected to possess c-axis unique pseudo-monoclinic structure with $P_x \approx P_y \neq P_z$. It is noted that the monoclinic point group, m, is a subgroup of rhombohedral 3m, obeying the Aizu's criteria.[9] In <001> oriented PZN-5PT crystals, the first ferroelectric domain configuration is constructed under bias where the crystal structure is deviated from its original rhombohedral symmetry. According to the calculations in ref. 10 and 11, both electrical and elastic energy of the (100) boundary is higher than those of the (110) boundaries for rhombohedral crystals when interaxial angle, α, of the rhombohedral structure is smaller than 90°, which is the case for (111) oriented PZN-5%PT crystals. In contrast, when the crystal was biased along <001> direction, the crystal structure deviated from rhombohedral and became (c-axis unique) pseudo-monoclinic. According to ref. 11, this transition causes {110} domain boundaries to become unstable. Therefore, <001> crystals, monoclinic ferroelectrics under bias, favor the {100}domain boundary.

The XRD patterns of <001> crystals (not shown in this article) presented that the PZN-PT crystal retains c-axis elongation even upon the removal of E-field, indicating that the crystal preserves c-axis unique monoclinic (point group m) symmetry, a subgroup of rhombohedral 3m, even upon the removal of E-field. Fig. 4 is the schematic diagram of averaged domain structure, and its projection on (011) plane, schematizing the elastic constraint causing the local ionic displacements to be fossilized in the "averaged domain configuration.

Polarization Switching

The switching currents *i(t)* measured through the external resistance are shown in Fig. 5. Peak currents

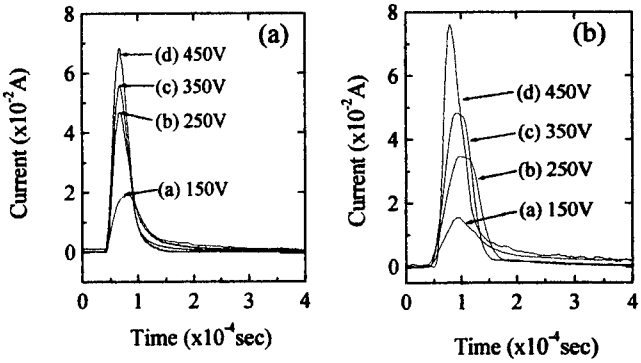

Figure 5 Switching characteristics of PZN-5%PT crystals as a function of field ; (a) when E-field was applied along <001> direction, (b) when E-field was applied along <111> direction.

(i_{max}) ranged from 0.2 - 0.7 A and switching times were ~ 10 μsec. Fig. 6 shows log (i_{max}) vs. reciprocal of pulse voltage curves as a function of crystallographic orientation when the square pulse width was 3μsec. The switching rate, characterized by the maximum switching current (i_{max}), or switching time (t_s), can be written [13] such as,

$$i_{max} = i_0 \exp(-\alpha / E) \text{ or } t_s = t_0 \exp(-\alpha / E) \quad (1)$$

where α is the activation field. Note that the minimum E-field in this study was 7.5 kV/cm, higher than E_C of both crystallographic orientations, to observe overall domain switching behavior. As presented in Fig. 6, α (~ 2.5kV/cm) for <111> crystals was greater than that of <001> oriented crystals (~1.5kV/cm). Since the switching rate, dP/dt (or = i_{max}) is proportional to the value of $\exp(-\alpha / E)$, the overall domain switching occurs

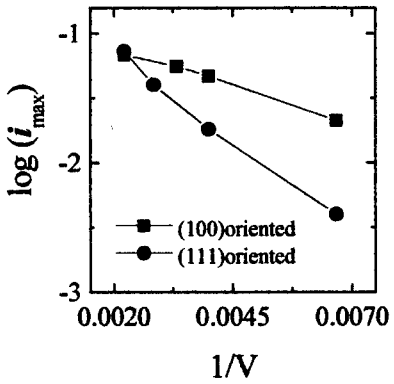

Figure 6 log(i_{max}) vs. 1/V curve for PZN-5%PT crystals.

more rapidly in <001> crystals than in <111> crystals. In ferroelectrics switching, two types of switching processes represent the polarization switching kinetics, - (1) nucleation and forward growth process, and (2) sideway growth process. Although most ferroelectric crystals involve the combination of both processes, the variation in crystal quality or boundary condition can promote either one of these two processes. The dominant mechanism in the crystal can also be interpreted from the switching current and pulse, which can be written as;

$$i_s = 4P_s Rk^2\{-1+(\tau+k^{-1})+e^{-\tau}(1-k^{-1})+\frac{1}{2}k^{-2}\}\cdot \qquad (2)$$
$$\exp\{-2k^2[1-(\tau+k^{-1})+\frac{1}{2}(\tau+k^{-1})^2-e^{-\tau}(1-k^{-1})-\frac{1}{2}k^{-2}(1-\tau)]\}$$

where, P_s: the spontaneous polarization, R: the probability of nucleus formation per unit time, and $k = 1/Rt_0$, $t = Rt$. In equation (2), the parameter k is the measure of switching characteristics. If the switching behavior is dominated by sideway growth, k value becomes large (k>>1), whereas k nears zero when the nucleation and forward growth dominates during domain switching. When the domain switching involves both characteristics, k values in the range of 1 to 5 still exhibit the trend of dominant switching mechanism. The switching current of PZN-PT crystals at 450V was fitted and calculated. k values were 1.2 and 3.2 for <001> and <111> oriented crystals, respectively. From these results, it is found that the contribution of nucleation and forward growth (sideway growth) is more dominant when E-field is applied along <001> (<111>), respectively.

The activation energy required for the nucleation of reverse domains is proportional to the polarization value (along E-field direction) of ferroelectric crystals. [14] Therefore, orienting rhombohedral crystals along <001>, with lower (projected) polarization value of $1/\sqrt{3}$ of $P_{<111>}$, will foster the dominance of nucleation and growth characteristics. Combined with higher activation energy for nucleation, the lower domain wall energy in <111> crystals should prefer the sideward growth during polarization switching. In addition, defective and heterogeneous parts in crystals, including surfaces, point defects [4], and boundaries such as domain walls, are the most favorable sites of the nucleation for the reverse domain switching. In <001> crystals, the poling results in a stable multi-domain state averaged by E-field, with domain width ~ 1μm. Therefore, the possible nucleation sites (domain walls) are much more abundantly distributed in the entire specimen of <001> crystals, another factor promoting the contribution of nucleation for the domain switching in [001] crystals. This domain switching anisotropy may be one of the origins for the fatigue anisotropy observed in PZN-PT crystals. The domain wall pinning in domain averaged <001> crystals must be minimized due to its minimum domain wall motion, as a result of its nucleation dominated domain switching process. In contrast, the entrapment of space charges and subsequent domain wall pinning must be maximized in <111> crystals due to the enhanced domain wall motion during sideward growth.

CONCLUSION

In <111> oriented PZN-5PT crystals, {110} domain boundaries were dominant and the contribution of side way growth increased. E-field application along the <001> direction stabilized domain boundaries on the {100} plane, being attributed to the structural modification into monoclinic under <001> bias. The different mechanism in domain switching behavior, nucleation and forward growth vs. sideward growth, may be one of the origins for fatigue anisotropy.

REFERENCES

[1] S. Wada, S. -E. Park, L. E. Cross, and T. R. Shrout, Ferroelectrics **221**, 147 (1999).

[2] S.-E. Park and T. R. Shrout, J. Appl. Phys. **82**, 1804 (1997).

[3] J. Yin and W. Cao, J. Appl. Phys. **87**, 7438 (2000).

[4] H. Yu and C. A. Randall, J. Appl. Phys. **86**, 5733 (1999).

[5] L. E. Cross, SPIE's 6th Annual International Symmposium on Smart Structures and Materials, Newport Beach, CA, March 2001.

[6] K. Takemura, M. Ozgul, V. Bornand, S. T-McKinstry, and C. Randall, J. Appl. Phys. 88, 7272 (2000).

[7] M. Ozgul, K. Takemura, S. T-McKinstry, and C. Randall, J. Appl. Phys. 89, 5100 (2000).

[8] S.-E. Park, S. Wada, L. E. Cross, and T. R. Shrout, J. Appl. Phys. **86**, 2746 (1999).

[9] K. Aizu, J. Phys. Soc. Jpn. **27**, 387 (1969).

[10] V. A. Zhirnov, Sov. Phys. JETP **35**, 822 (1959).

[11] J. Sapriel, Phys. Rev. B **12**, 5128 (1975).

[12] K. Aizu, J. Phys. Soc. Jpn. **28**, 706 (1970).

[13] E. Fatuzzo, Phys. Rev. 127, **1999 (1962).**

[14] T. K. Song, S. Aggarwal, A. S. Prakash, B. Yang, and R. Ramesh, Appl. Phys. Lett. **71**, 2211 (1997).

Domain Dynamics and Microstructure of $Pb(Zn_{1/3}Nb_{2/3})O_3 - PbTiO_3$ Single Crystals

E. Furman, H. Yu, and C. A. Randall

Materials Research Institute, The Pennsylvania State University
Fax: 814-865-8126; Email: euf1@psu.edu

PZN-PT crystals are of considerable scientific and technological interest because of their excellent piezoelectric and dielectric properties. Phase instability near morphotropic boundaries can lead to enhanced properties. Investigation of the microstructure and kinetics of domain switching in PZN-PT crystals shows that these crystals have an additional degree of instability: competition between the long-range dipolar forces leading to the ferroelectricity and random field frustrating interactions leading to dipolar glass behavior. Gross features of the domain switching can be described by phenomenological models developed for classical ferroelectrics. The random field effects are manifested in fractal, dendritic domain structure; random orientation of the domains; and a long tail in switching current.

INTRODUCTION

Currently there is considerable interest in Lead Zinc Niobate – Lead Titanate (PZN-PT) single crystals due to their unusually high field-induced strain and piezoelectric coupling coefficients [1]. It is not clear to what extent these excellent properties are due to the intrinsic vs. the extrinsic contributions. To differentiate between these contributions, it is desirable to investigate properties of the crystals in the single or stable domains in which intrinsic properties are more likely to control crystal behavior [2]. In parallel, it is useful to study kinetics and morphology of domains under a wide variety of conditions.

PZN is a classical relaxor, and the addition of PT gradually transforms it to a normal ferroelectric. The PZN-PT system is characterized by the morphotropic phase boundary (MPB) between the rhombohedral (on PZN side) and tetragonal phases. This, boundary, however, has appreciable curvature towards the PZN at elevated temperatures. Near room temperature, the MPB is at about 9% PT. On the rhombohedral side, excellent piezoelectric properties with low hysteresis exist for all the compositions for the 001 oriented crystals. In comparison, the 111 oriented crystals have much lower piezoelectric response and considerable hysteresis in strain vs. field. Because of the large difference in the electromechanical behavior for 001 and 111 oriented crystals, it is informative to study domain switching for these crystals.

This paper extends earlier work of Yu et. al. [3,4] in which the domain morphology and switching kinetics for PZN-PT crystals were investigated. The goals of this paper are:

1). To model switching behavior of single crystals using alternative models of domain switching. It will be shown that the phenomenological models developed for classical ferroelectrics can be successfully applied to describe gross features of the domain switching kinetics in PZN-PT crystals.

2) To demonstrate that the unusual dendritic domains on the surfaces of these crystals are fractals, and to show that the results of this study are consistent with the importance of random fields on properties of PZN-PT crystals.

EXPERIMENTAL PROCEDURE

Crystals of PZN and their solid solutions with PT were grown using a high temperature flux technique described elsewhere [5]. Compositions of (1-x)PZN-xPT, where x=0%, 4.5%, and 8% were studied, designated PZN-0%PT, PZN-4.5%PT, and PZN-8%PT. Typical crystal sizes ranged from 5 to 20 mm. As-grown crystals were oriented along one of the 001 directions using a back reflection Laue camera before being cut into square plates. The final crystal dimensions were 5 mm × 5 mm with a thickness of 200–300 μm.

To study the dynamic behavior of domains in an electric field, electric transient currents were

measured by pulsing experiments. Square pulses were applied through liquid mercury electrodes to a crystal in series with a resistor. We applied 1–100 pulses of 10 μs in length with a rise time of about 100 ns (IRCO C12K-20). The resulting switching currents were monitored by an oscilloscope (Tektronix TDS 340). The system setup is illustrated in Fig.1.

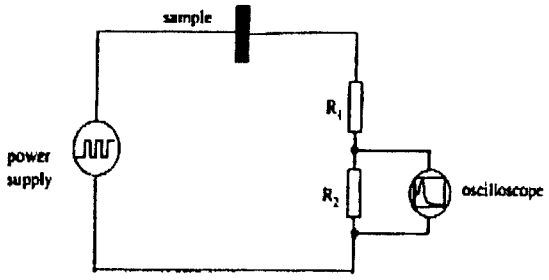

Fig. 1. Schematic system setup of switching current measurement.

Following the pulsing experiments, the samples were chemically etched at room temperature using a solution made of HNO_3 and HF. The etched surfaces were investigated with an optical reflection microscope and additionally probed by an atomic force microscope (AFM), which was operated in contact mode (Multi Mode, Digital Instruments Inc., Santa Barbara, CA).

RESULTS AND DISCUSSION

The switching behavior of PZN-4.5%PT <001> crystal is shown in Figure 2.

At first glance, the switching current (Figure 2A) is similar to classical ferroelectric switching: the initial capacitive charging current is followed by a switching current peak. However, a long tail of slowly decaying current is unexpected from the classical models, and suggests that there is a wide distribution in relaxation times. Similar observation of the extended relaxation range was previously observed in magnetic random field systems and in PMN-PT crystals [6]. As shown in the inset to Figure 2A, there is a sudden change from the normal domain switching to a slow relaxation regime. This suggests the possibility that domain switching occurs initially through typical nucleation and growth, followed by dipolar glass like behavior.

For the pulse applied in the poling direction (Figure 2B), a long relaxation tail is absent. Comparison of switching for the 2 polarities (Figures 2A and 2B) suggests that random fields can be coupled to the disordering field more effectively than to the ordering fields. Random fields are believed to originate from randomly distributed defects, and can lead to relaxor behavior. The evidence for random fields in PMN-PT ceramics was obtained from polarization switching experiments [7].

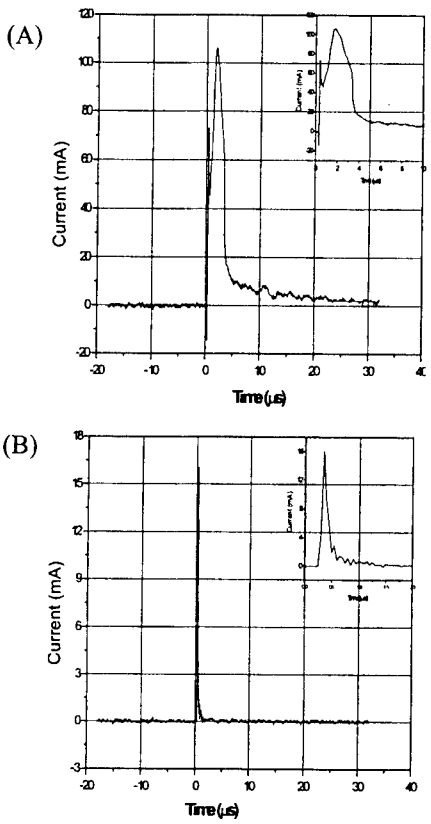

Figure 2. The switching currents for PZN-4.5%PT <001> crystal. (A) reverse switching current, (B) unswitching current.

The relationship between the maximum switching current vs. the applied field was described with two previously developed empirical models:

$$J_{max} = b(\frac{E}{a})e^{-\frac{a}{E}} \quad (1)$$

and

$$J_{max} = ce^{-\frac{d}{E}} \quad (2)$$

where J_{max} is the maximum switching current, a and d are the activation energies, E is applied electric field, and b and c are constants.

Equation (1) was used by Wieder to fit colemanite [8], and Equation (2) by Merz to fit barium titanate [9]. The advantage of using the first equation is that it may fit both the low field nucleation controlled regime (where the exponential term dominates) and high field domain growth controlled regime (where the linear term, (E/a), dominates).

The two models fitted the experimental data equally well. An example of the fitting of switching current using Wieder's model is shown in Figure 3.

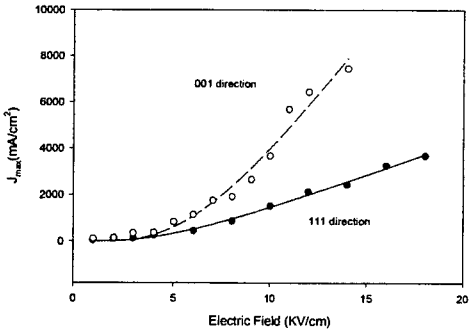

Figure 3. Maximum current for 001 and 111 oriented PZN-4.5%PT crystals. Symbols = experimental data, Line = model.

For all compositions the larger current and shorter switching times were observed for the 001 oriented crystals as compared to the 111. The fitting parameters for equation 1 and 2 are shown in Tables 1 and 2, respectively.

Table 1. Fitting parameters for Equation 1.

Composition PZN-x%PT	Orien-tation	Fitting parameters		
		b	a	b/a
0	001	11502	14.0	819
	111	976	7.7	128
4.5	001	15840	12.0	1320
	111	2594	8.0	324
8	001	7505	8.7	867
	111	312	3.3	94

Note: a is in units of kV/cm

The activation field parameter, a, and the total pre-exponential term, b/a, are always larger for the 001 oriented crystals. A higher activation field in the 001 direction suggests that the domain nucleation is more difficult in this orientation. The mobility of nucleated domains in 001 oriented crystals is higher, however, than in 111 crystals. Activation fields are controlled more by proximity to the MPB than by the amount of PT in the crystal.

Essentially the same conclusion is obtained from the fitting parameters listed in Table 2. However, the activation field, c, is significantly higher for all samples compared to the activation field, a.

Table 2. Fitting parameters for Equation 2.

Composition (PZN-x% PT)	Orien-tation	Fitting parameters	
		c	d
0	001	23410	24.3
	111	4554	20.0
4.5	001	38370	22.4
	111	11220	20.3
8	001	20960	17.3
	111	2019	10.8

Note: d is in units of kV/cm

Merz's and Wieder's Models fit the experimental J_{max} equally well for the field range used in this study. However, as shown in Figure 4, at fields larger than the experimental range (up to 12kV/cm), modeling results diverged considerably.

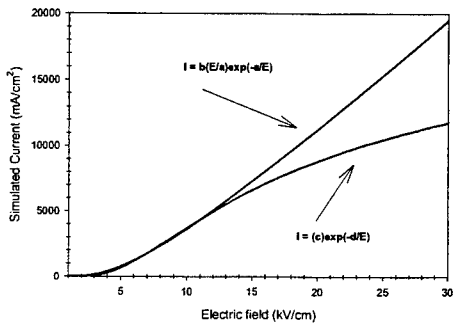

Figure 4. Modeled currents for PZN-8%PT 001 crystals.

Because both models fit the experimental data equally well, it is impossible to tell from the J_{max} vs. E plots alone if the nucleation controlled or domain growth controlled regime predominates in the nearly linear region above 10 kV/cm in Figure 3. However, microstructural observations

of domain structures show that domain growth takes place at high fields [3].

The morphology of the domains on the surface of crystals is dependent on composition, field history, mechanical stress, and cooling rate [3,4]. Unusual dendritic domain structure on the surface of these crystals was observed for a variety of sample histories and for crystals of all compositions and orientations. AFM of a typical domain structure on an etched crystal is shown in Figure 5.

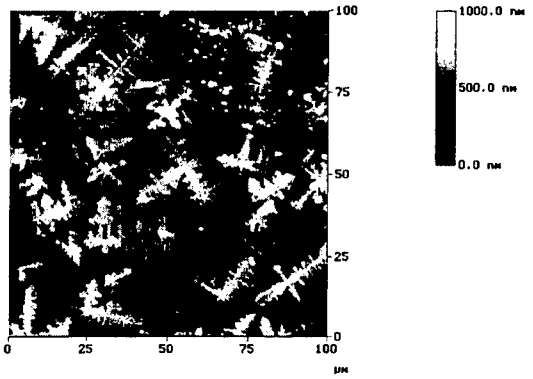

Figure 5. AFM domain growth on PZN-4.5%PT 001 crystal at E=10kV/cm for 10μs×100 pulses.

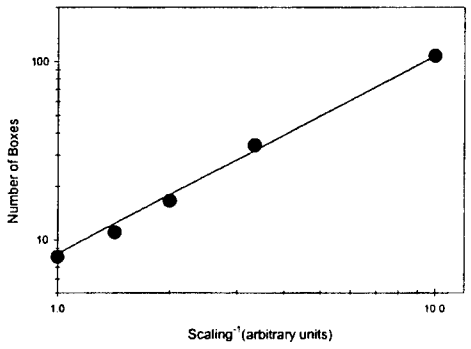

Figure 6. Box counting fractal fitting of the dendritic domain labeled "1" in Figure 5.

The observed dendritic domains are randomly oriented and their length is on the same scale as normal ferroelectric domains. The random non-crystallographic orientation of the domains again supports the importance of random fields for these materials. Only a material with low domain wall energy and low anisotropy can have such microstructure. While the specifics of crystal growth influences the initial random field, the observation of changing density and size of the dendrites with the applied field indicates that the observed features correlate with actual ferroelectric domains.

The self similarity of dendrites on different scales prompted a study of their fractal dimensionality. The Box Counting method [10] was used to estimate the length of the perimeter for the fractal labeled "1" in Figure 5.

As is shown in Figure 6, the straight line through the data indicates that this region behaves as a fractal, giving a Housdorf fractal dimension, d_f, of 1.11 which is a fairly low dimension for a fractal object.

CONCLUSIONS

The domain study of PZN-PT crystals shows a mixture of behavior, some expected for the classical ferroelectrics: J_{max} vs. field, for example, while other properties are indicative of random field dipolar glass: a long tail in switching current, fractal and randomly oriented domains. PZN-PT crystals are balanced between the competing long-range ordering leading to ferroelectricity and frustrated interactions leading to the dipolar glass behavior.

REFERENCES

[1] S.-E. Park and T. R. Shrout, *J. Appl. Phys.*, 82 (4), 1804-1811 (1997).

[2] L. E. Cross and P. Hana, The 9th US-Japan Seminar on Dielectric & Piezoelectric Ceramics, 15-18 (1999).

[3] H. Yu, V. Gopalan, J. Sindel, and C. A. Randall, *J. Appl. Phys.*, 89, 561-567 (2001).

[4] H. Yu and C. A. Randall, *J. Appl. Phys.*, 86, 5733-5738 (1999).

[5] S. F. Liu, S. E. Park, T. R. Shrout, and L. E. Cross, *J. Appl. Phys.*, 85, 2810 (1999).

[6] D. Viehland, PiezoCrystals Workshop, Washington, D. C., 2001.

[7] D. Viehland and Y-H. Chen, *J. Appl. Phys.*, 88, 6696-6707 (2000).

[8] H. H. Wieder, *J. Appl. Phys.*, 31, 180 – 187 (1960).

[9] W. J. Merz, *J. Appl. Phys.*, 27, 938 – 943 (1956).

[10] R. H. Landau and M. J. Paez, "Computational Physics: Problem Solving with Computers," J. Wiley & Sons, New York (1997) pp. 334-335.

Poling Field Dependence of Ferroelectric Properties in $Pb(Zn_{1/3}Nb_{2/3})_{0.91}Ti_{0.09}O_3$ Single Crystal

Toshio Ogawa, Mitsuyoshi Matsushita *, Yoshihito Tachi * and Kazuhiko Echizenya **

Shizuoka Institute of Science and Technology, 2200-2, Toyosawa, Fukuroi 437-8555, Japan
FAX: +81-538-45-0154, E-mail: ogawa@ee.sist.ac.jp
* Kawatetsu Mining Co., Ltd., 1, Niihama-cho, Chuo-ku, Chiba 260-0826, Japan
** Kawasaki Steel Co., Ltd., 1, Kawasaki-cho, Chuo-ku, Chiba, 260-0826, Japan

Big size piezoelectric single crystals of $Pb(Zn_{1/3}Nb_{2/3})_{0.91}Ti_{0.09}O_3$ (abbreviated as PZNT) fabricated by Bridgman method were investigated regarding the material constants, and the temperature and poling field dependences of their ferroelectric properties. The single crystals possessed high piezoelectric constants such as g_{33}, g_{31} and d_{31} as well as high dielectric constant (ε_r), electromechanical coupling factor (k_{33}) and d_{33} for use of sensors and actuators with high performance. From the temperature dependence, sharp discontinuity of the ε_r and frequency constant (fc) was observed at M.P.B. caused by the phase transition between rhombohedral and tetragonal. From the poling field (E) dependence, the minimum k_{33}, d_{33} and ε_r and the maximum fc were observed at E of ± 300 V/mm. The E corresponds to the coercive field (Ec) and the E of 180° domain clamping. The origin of high piezoelectricity in PZNT single crystal was thought that there were the relatively large gaps of the dielectric and elastic constants between rhombohedral and tetragonal phases at M.P.B., and mechanical softness in rhombohedral phase with eight polarization axes in comparison with the ones in tetragonal phase with six polarization axes.

1. INTRODUCTION

The effects of poling fields on ferroelectric properties in lead zirconate titanate (PZT) [1], lead titanate (PT) [2] and barium titanate (BT) [3] ceramics were investigated to clarify their ferroelectric domain structures.

Recently, ferroelectric single crystals such as $Pb(Zn_{1/3}Nb_{2/3})_{0.91}Ti_{0.09}O_3$ (PZNT) have been attracting considerable attention, because of the high electromechanical coupling factor of k_{33} over 92 %[4]. Since big sizes of the crystal were necessary to develop devices such as transducers for medical use[5], we have succeeded in fabricating the PZNT single crystals with large dimensions[6].

Therefore, dielectric, piezoelectric and elastic constants were measured at room temperature to clarify the basic properties of the big size single crystals. Furthermore, the temperature dependence of material constants was evaluated utilizing the crystals. In addition, the poling field dependence of ferroelectric properties was studied to understand the origin of high piezoelectricity.

2. EXPERIMENTAL

The single crystals evaluated were grown by one batch solution Bridgman method with a Pt crucible supported at the bottom by a corn-type insulator stand. The crystals without Pt contamination from the crucible have dimensions: 50 mm (2 inches) diameter and 35 mm high, and the weight of 325 g [6].

The single crystal samples with various dimensions such as $4.2^W x 4.2^L x 12^T$mm for k_{33}, d_{33}; $4.0^W x 13^L x 0.36^T$mm for k_{31}, k_t, d_{31}; $1.8^W x 2.0^L x 0.36^T$ mm for k_{15}, d_{15} were prepared to evaluate the material constants. Poling was conducted at 40℃ for 10 min to obtain the resonators with various vibration modes. After measuring the basic properties, the temperature dependence of material constants were evaluated between -40℃ and 130℃. For poling field dependence of ferroelectric properties, the sample plates ($5.0^W x 5.0^L x 0.28^T$mm) were DC poled at 40℃ for 10 min while varying the poling field (E) from 0 → +100 → --- →+1000 → 0 →-1000 → 0 to +1000 V/mm. P-E hysteresis was measured by a high voltage test system (Radiant: RT6000HVS). Further, piezoelectric d_{33} was directly measured by a d_{33} meter (Academia Sinica: ZJ-3D) to compare with the calculated values of d_{33}.

3. RESULTS AND DISCUSSION

3.1 Material Constants of PZNT Single Crystal

Table I shows the dielectric, piezoelectric and elastic constants of PZNT single crystal at room temperature. High k_{33} over 95% and high d_{33} nearly 2,500 pC/N were obtained regarding the big size crystals. Moreover, it was found that the crystals can be applied to sensors and actuators with high performance because of relatively high g_{33}, g_{31} and d_{31}.

Table I Material constants of PZNT single crystal in comparison with PZT ceramics.

	PZNT	PZT*
ρ [g/cm^3]	8.36	7.87
$\varepsilon^T/\varepsilon_o$ [-]	2575	897
$\varepsilon_{11}^T/\varepsilon_o$	8209	1330
$\varepsilon_{11}^S/\varepsilon_o$	6456	872
$\varepsilon_{33}^T/\varepsilon_o$	4604	1221
$\varepsilon_{33}^S/\varepsilon_o$	-	764
tanδ [%]	0.90	0.54
k_{33} [%]	95.3	58.7
k_{31}	80.8	29.1
k_{15}	46.2	58.6
k_t	56.8	-
Qm_{33} [-]	114	352
Qm_{31}	69	1096
Qm_{15}	12	196
Qm_t	6	-
fc_{33} [Hz·m]	1393	1945
fc_{31}	522	1676
fc_{15}	1513	1176
fc_t	2087	-
d_{33} [10^{-12}C/N]	2498(2440)**	218
d_{31}	-1701	-102
d_{15}	512	374

	PZNT	PZT*
g_{33} [10^{-3}Vm/N]	61.3	20.2
g_{31}	-43.0	-9.44
g_{15}	7.04	31.8
h_{33} [10^8V/m]	-	19.5
h_{31}	-	-8.46
h_{15}	5.30	14.0
e_{33} [C/m^2]	-	13.2
e_{31}	-	-5.72
e_{15}	30.3	10.8
s_{11}^E [10^{-12}m^2/N]	112	11.3
s_{33}^E	169	12.7
s_{44}^E	16.9	34.5
s_{33}^D	15.4	8.32
s_{11}^D	38.9	10.3
s_{44}^D	13.3	22.6
c_{11}^E [10^{10}N/m^2]	-	14.2
c_{33}^E	9.47	13.1
c_{44}^E	5.92	2.90
c_{11}^D	-	14.7
c_{33}^D	14.2	15.7
c_{44}^D	7.53	4.42

* PZT ceramics: 0.05Pb(Sn1/2Sb1/2)O3 - 0.50PbTiO3 - 0.45PbZrO3 + 0.4wt%MnO2.
** d33 value measured by d33 meter.

3.2 Temperature Dependence

Figures 1(a)~(d) show the temperature dependence of the dielectric and piezoelectric constants of PZNT single crystals. The dielectric constant ε r ($\varepsilon_{33}^T/\varepsilon_0$) after poling increased up to 80℃ with temperature, and suddenly reduced over 80℃ in comparison with ε r before poling. Furthermore, the ε r showed the frequency dependence (Fig. 1(a)). The relaxor behavior was confirmed at the M.P.B between the rhombohedral and tetragonal phases. Although the k33 gradually decreased around 80℃ with increasing the temperature, the k31 decreased sharply as shown in Fig. 1(b). While both the d33 and d31 increased up to 80℃ due to the increase of the ε r and little change in k33, k31, the d33 and d31 decreased abruptly in the tetragonal phase (Fig. 1(c)). The frequency constant fc33 and fc31 in the rhombohedral phase were smaller than the ones in the tetragonal. (Fig. 1(d)). We believe one of the reasons to obtain high k33, k31 and d33, d31 in the rhombohedral phase was due to the mechanical softness for easy deformation by E in comparison with the tetragonal phase.

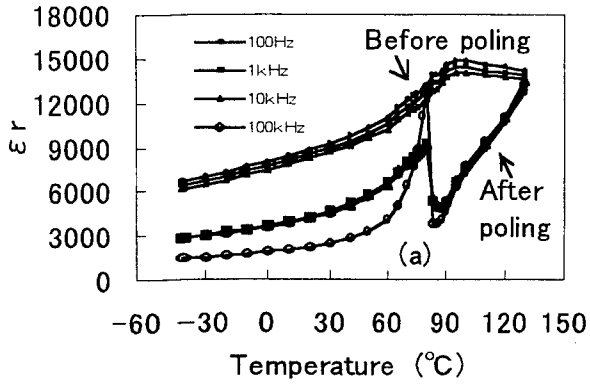

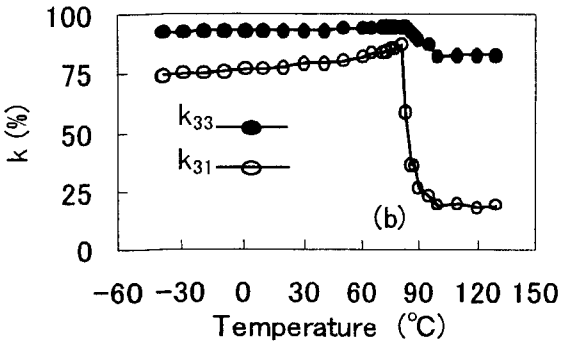

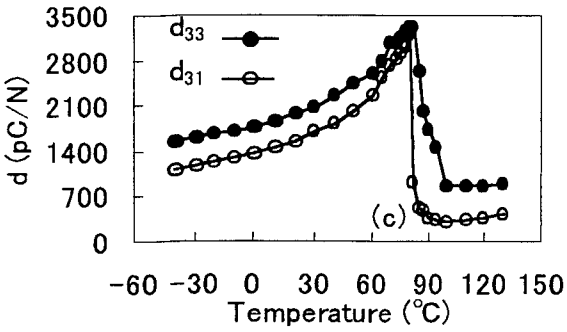

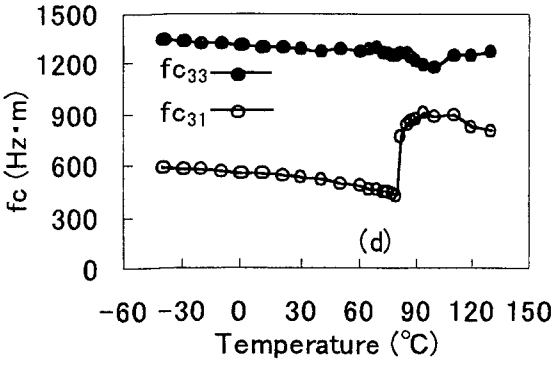

Fig. 1 Temperature dependence of (a) ε r before and after poling, (b) k33, k31, (c) d33, d31 and (d) fc33, fc31.

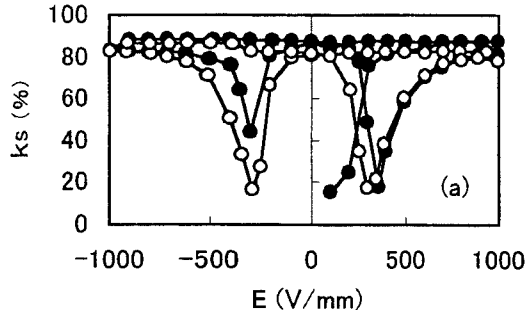

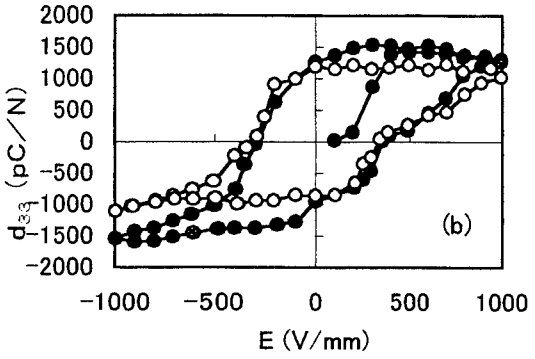

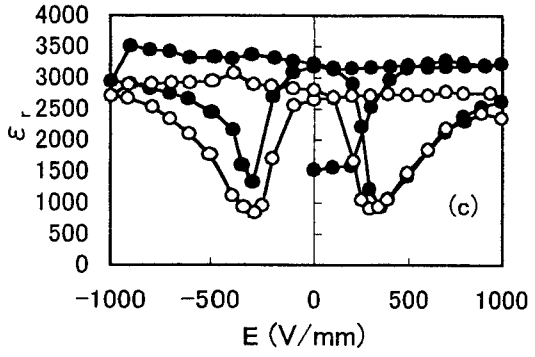

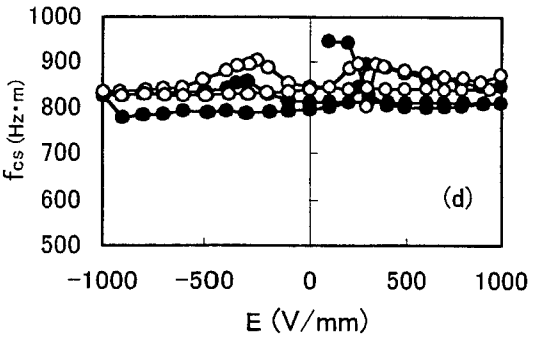

Fig. 2 Poling field (E) dependence of (a) ks, (b) d33, (c) ε r and (d) fcs.

3.3 Poling Field Dependence

From the E vs. ks (counter extensional mode), d33, ε_r and fcs as shown in Figs. 2(a) ~(d), the minimum ks, d33 and ε_r and the maximum fc were observed at E of ± 300 V/mm. The E corresponds to the coercive field (Ec) determined by the poling field dependence and the E of 180° domain clamping. The Ec (± 300V/mm) in PZNT single crystals took the middle values between PZT, PT ceramics (Ec=± 1500 ~± 2000V/mm) [1,2] and BT ceramics (Ec =± 100V/mm) [3]. When poling once again (-○-), the ks, d33 and ε_r slightly decreased in comparison with the ones of the first poling (-●-). It was thought that the deterioration in ferroelectric properties by the second poling (-○-) were due to the domain motions in the crystal.

Figure 3 shows the P-E hysteresis loop of the PZNT crystal (dimensions: 5.0^{W}x5.0^{L}x0.28^{T}mm) measured at 80℃ and an applying field of 5.0kV/mm. The remanent polarization (Pr) and coercive field were 20.0 μC/cm^2 and 590V/mm, this value of which is larger than 300V/mm obtained by the poling field dependence.

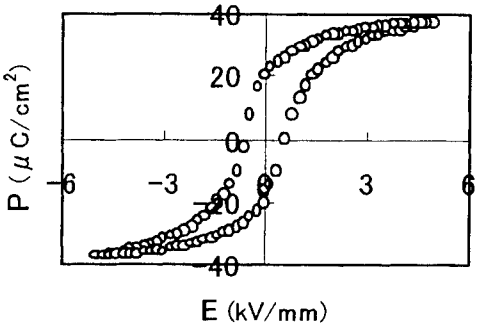

Fig. 3 P-E hysteresis loop of PZNT single crystal measured at 80℃.

From the data above mentioned, the origin of high piezoelectricity in PZNT single crystal was thought as follows;

① high crystal orientation by poling field because of single crystal,

② low coercive field accompanied with low Cure temperature,

③ relatively large gaps of dielectric and elastic constants (Fig. 4) between rhombohedral and tetragonal phases at M.P.B.,

and ④ mechanical softness in rhombohedral phase with eight polarization axes in comparison with the ones in tetragonal phase with six polarization axes. In addition, we believe the items ③ and ④ are more essential factors to appear high k33 in PZNT single crystal and related relaxor single crystals.

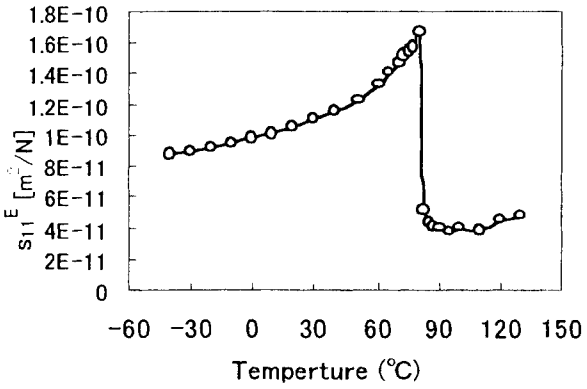

Fig. 4 Temperature dependence of elastic compliance (s_{11}^E) in PZNT single crystal.

4. SUMMARY

Big size PZNT single crystals were evaluated regarding the material constants, and the temperature and poling field dependences of their ferroelectric properties. From the evaluation, the origin of high piezoelectricity in PZNT single crystal was clarified.

ACKNOWLEDGEMENTS

This work was partly supported by a Grant-in-Aid for Scientific Research (C) (No.12650327) from the Japanese Ministry of Education, Culture, Sports, Science and Technology and the Research Foundation between Academy and Industry of Fukuroi City.

REFERENCES

1. T. Ogawa and K. Nakamura, *Jpn. J. Appl. Phys.*, 38, 5465-5469 (1999).
2. T. Ogawa, Jpn. *J. Appl. Phys.*, 39, 5538-5541 (2000).
3. T. Ogawa, To be published in *Jpn. J. Appl .Phys.*, (Sept. 2001).
4. J. Kuwata, K. Uchino and S. Nomura, *Jpn. J. Appl. Phys.*, 21, 1298-1302 (1982).
5. S. Saitoh, T. Takeuchi, T. Kobayashi, K. Harada, S. Shimanuki and Y. Yamashita, *Jpn. J. Appl. Phys.*, 38, 3380-3384 (1999).
6. M. Matsushita et al., Abstract book of Am. Ceram. Soc., 103rd Annual Meeting, p.247 (2001).

Piezoelectric Properties of $KNbO_3$ Single Crystals with Various Crystallographic Orientations

Satoshi Wada, Akira Seike, Hirofumi Kakemoto and Takaaki Tsurumi

Department of Metallurgy and Ceramics Science, Graduate School of Science and Engineering,
Tokyo Institute of Technology, 2-12-1 Ookayama, Meguro-ku, Tokyo 152-8552, Japan
FAX: +81-3-5734-2514, Email: swada@ceram.titech.ac.jp

Piezoelectric properties of $KNbO_3$ single crystals were investigated as a function of crystallographic orientations, *i.e.*, $[110]_c$ of polar direction and $[001]_c$ of non-polar direction. Prior to piezoelectric measurements, the optimum conditions for a conventional poling method were investigated. Though the optimum conditions for a conventional poling method was found, fully poled $KNbO_3$ crystals were not obtained. Thus, to achieve fully poled $KNbO_3$ crystals, a new 2-step poling method was proposed. Using the 2-step poling method, $KNbO_3$ crystals were successfully poled, and then, their piezoelectric properties of k_{31} modes were measured using a resonance method. The $[110]_c$ poled $KNbO_3$ crystals exhibited electromechanical coupling factor k_{31} of 28.9 % and piezoelectric constant d_{31} of 18.4 pC/N while the $[001]_c$ poled $KNbO_3$ crystals exhibited k_{31} of 31.2 % and d_{31} of 51.7 pC/N. The piezoelectric constant d_{31} along non-polar $[001]_c$ direction was 2.8 times higher than that along polar $[110]_c$ direction.

1. INTRODUCTION

In orthorhombic (=monoclinic) $BaTiO_3$ single crystals, when an electric-field was applied along $[001]_c$ of non-polar direction, the higher piezoelectric activities were found by Park *et al.*[1] with d_{33} over 500 pC/N and k_{33} over 85 %. These improved piezoelectric properties along $[001]_c$ in monoclinic $BaTiO_3$ are originated from an engineered domain configuration[2-4]. However, monoclinic phase of $BaTiO_3$ is stable below 5 °C, and this excellent piezoelectric performance cannot be used at room temperature. Thus, monoclinic ferroelectric single crystals at room temperature are expected as new piezoelectric materials with high piezoelectric activity.

$KNbO_3$ single crystal is one of materials satisfying the above request. Ferroelectricity of $KNbO_3$ was first found by Matthias[5], and up to date, a lot of studies on $KNbO_3$ have been reported[6-10]. However, there have been just a few reports about piezoelectricity of $KNbO_3$ single crystals[11-13]. There are two reasons why the reports on the piezoelectricity of $KNbO_3$ crystals were so limited. One is the difficulty in the crystal growth of $KNbO_3$ single crystals with enough electrical resistance to measure piezoelectric property due to high volatility of potassium during the growth process. The other is the difficulty in the poling treatment, *i.e.*, reconstruction of domain configuration. Because of these two reasons, not all piezoelectric properties of $KNbO_3$ crystals were determined even at present. Recently, Yamanouchi *et al.* reported that the electromechanical coupling coefficient (k^2) of the surface acoustic wave (SAW) was 0.53 for $KNbO_3$ crystals with Y-cut plane[14]. Nakamura *et al.* also reported that k_t of the thickness mode was 0.69 for X-cut $KNbO_3$ crystals rotated by 49.5° along Y-axis[15]. Now, $KNbO_3$ crystal is one of the attractive materials for piezoelectric applications. Therefore, it is very important to determine all of piezoelectric properties of $KNbO_3$ crystals. For this objective, the effective poling method must be established for $KNbO_3$ crystals.

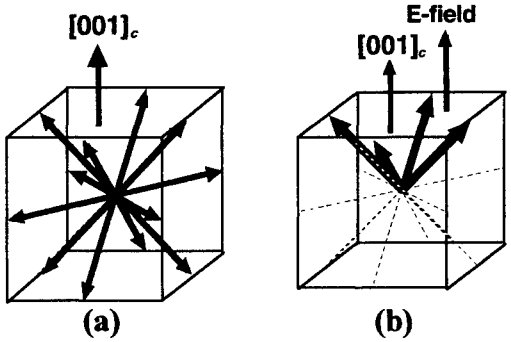

Fig. 1 Schematic domain configuration for $[001]_c$ oriented monoclinic $KNbO_3$ single crystal; (a) before poling and (b) after poling along $[001]_c$ direction.

In this study, using $KNbO_3$ crystals, we establish a new poling method, and its optimum poling conditions. Moreover, using the poled $KNbO_3$ crystals, their piezoelectric properties are investigated as a function of crystallographic orientation, such as $[110]_c$ of polar direction and $[001]_c$ directions of a special direction. The $[001]_c$ direction was chosen to induce the engineered domain configuration (Fig. 1). By inducing this domain configuration, the enhanced piezoelectric property is expected.

2. EXPERIMENTAL

$KNbO_3$ crystals were prepared by a top-seeded solution growth (TSSG) method at Asahi Techno Glass, Ltd. The TSSG-grown $KNbO_3$ crystals were perfectly transparent and colorless. The details of preparation of $KNbO_3$ crystals and the characterization were described elsewhere.[16-18] These crystals were oriented along $[110]_c$ and $[001]_c$ directions.

To investigate the quality of $KNbO_3$ single crystals, dielectric properties were measured from -100 °C to 500 °C using an impedance analyzer (Hewlett- Packard 4192A). In this measurement, heating and cooling rates were fixed at 1 °C/min to avoid cracking due to phase transitions.

Prior to piezoelectric measurements, the poling treatment of $KNbO_3$ crystals were performed. $KNbO_3$ crystals were shaped to a rectangular bar with a size of 4.0x1.2x0.4 mm^3. The degree of poling was judged by a

piezoelectric resonance measurement with k_{31} mode. All poling treatment was done under atmosphere. In a conventional poling process, the following parameters were changed here; (1) temperature, (2) soaking time, (3) heating and cooling rates, (4) DC bias field, and (5) poling current. In some cases, to reveal the degree of poling, the domain wall motion during poling process was directly observed using a polarizing microscope.

Piezoelectric properties of the poled $KNbO_3$ crystals were measured by a resonance method. The length extensional mode, k_{31} mode, was chosen as piezoelectric properties. Impedance (|Z|) and phase (θ) were measured as a function of frequency to determine the resonance frequency (f_r) and the antiresonance frequency (f_p). These values were substituted in an exact formula solution listed in EMAS-6100[19], and finally, d_{31}, k_{31}, elastic compliance coefficient s_{11}^E and mechanical quality factor Q_m were calculated.

3. RESULTS AND DISCUSSION

3.1 Temperature dependence of dielectric property

Figure 2 shows temperature dependence of dielectric permittivity of $[001]_c$ oriented $KNbO_3$ crystals measured at 100 kHz in the cooling process. Three dielectric peaks were clearly observed, and each peak was assigned to a phase transition behavior, *i.e.*, (1) $m\bar{3}m$ -> *4mm* at 436 °C, (2) *4mm* -> *mm2* at 208 °C, and (3) *mm2* -> *3m* at -60 °C. On the other hand, in the heating process, three dielectric peaks were also observed, but these peaks shifted to higher temperatures, *i.e.*, (1) *3m* -> *mm2* at -19 °C, (2) *mm2* -> *4mm* at 230 °C, and (3) *4mm* -> $m\bar{3}m$ at 450 °C. These temperatures well agreed to the reports by Nunes *et al.*[20] It should be noted that tanδ was below 10 % in the wide temperature range from -100 °C to 500 °C. These results indicated that $KNbO_3$ crystals used in this study had enough quality for poling and piezoelectric measurements.

3.2 Poling of $KNbO_3$ single crystals using a conventional poling method

The optimum condition for a conventional poling method was investigated using $[110]_c$ oriented $KNbO_3$ crystals. In general, the poling treatment of PZT ceramics is performed around 120 °C. Thus, the poling of $KNbO_3$ crystals was first tried at 120 °C. In this case, the poling conditions were fixed as follows; temperature (T_p) of 120 °C, soaking time (t_p) of 10 min, heating and cooling rates (ΔT) of 10 °C/min, and poling current (I_p) below 1 mA. The DC bias field (E_p) was changed from 10 to 600 V/mm. Figure 3 shows frequency dependence of |Z| and θ measured at 25 °C for the poled $KNbO_3$ crystals. If the ideal poling state is obtained, the phase angle θ approaches to 90° in the frequency range between f_r and f_p.[21] In Fig. 3, the phase angle θ increased with increasing E_p from 200 to 400 V/mm, but at 400 V/mm, the phase angle θ was limited to around 25°. This means that E_p below 400 V/mm was not enough to reach the full poling state. However, all crystals were cracked when E_p was above 400 V/mm. It is considered that the crack was caused by non-180° domain switching with spontaneous strain.

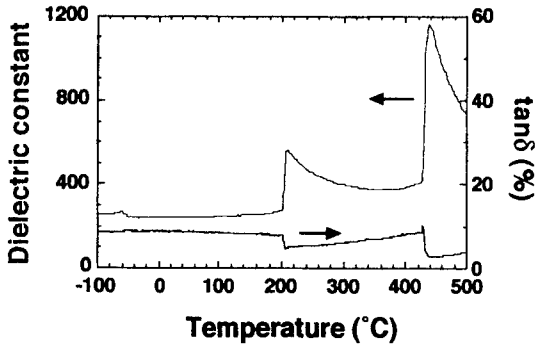

Fig. 2 Temperature dependence of dielectric property for $[001]_c$ oriented $KNbO_3$ single crystal measured at 100 kHz and the cooling process.

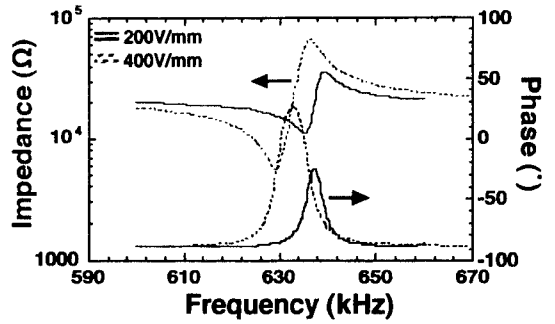

Fig. 3 Frequency dependence of |Z| and θ measured at 25 °C for $[110]_c$ oriented $KNbO_3$ crystals poled with the following conditions; T_p of 120 °C, t_p of 10 min, ΔT of 10 °C/min, E_p from 200 to 400 V/mm, and I_p below 1 mA.

To reduce the effect of the spontaneous strain in the non-180° domain switching, T_p was changed to 200 °C just below phase transition between *mm2* and *4mm*. In this case, even if very low E_p was applied, a large I_p over 1 mA was always detected, and the measured θ was limited below -80°. The observation of the poled crystals revealed that a lot of microcrack were formed in the crystals. The origin of the microcrack seems to be a thermal shock accompanied with rapid heating rate of 10 °C/min. Finally, it was confirmed that in $KNbO_3$ crystals poled using ΔT below 1 °C/min, there was no microcrack.

The effect of poling current I_p was also investigated.

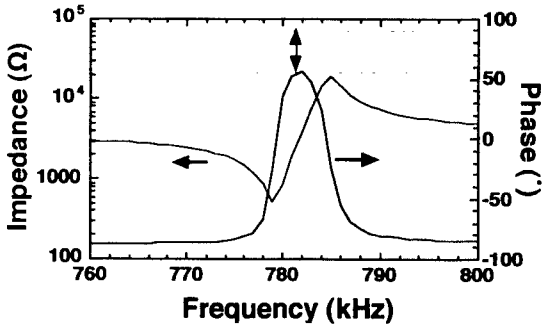

Fig. 4 Frequency dependence of |Z| and θ measured at 25 °C for $[110]_c$ oriented $KNbO_3$ crystals poled with the following conditions; T_p of 200 °C, t_p of 60 min, ΔT of 1 °C/min, E_p of 70 V/mm, and I_p of 1 μA.

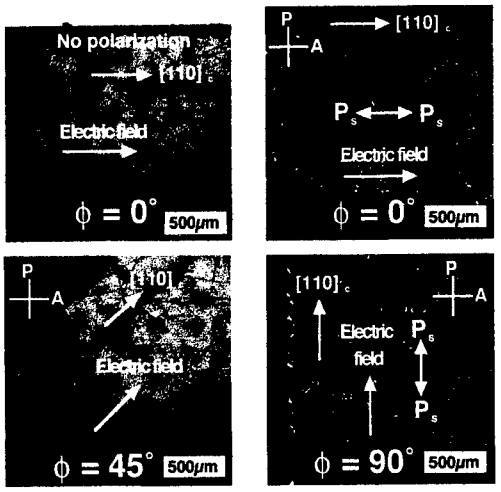

Fig. 5 Domain observation of $[110]_c$ poled $KNbO_3$ crystal at various rotation angles (ϕ).

The phase angle θ increased with decreasing I_p, and the phase angle θ became to around 40° at I_p of 10 μA. Moreover, *in situ* domain observation during the poling using I_p of 10 μA indicated that it took around 60 min until all domain walls disappeared. Finally, the highest θ of 55° was obtained for $KNbO_3$ crystals poled using the following conditions (T_p of 200 °C, t_p of 60 min, ΔT of 1 °C/min, E_p of 70 V/mm and I_p of 1 μA) as shown in Fig. 4, but was still far away from 90°. The above results were revealed that the conventional poling method was not effective to make a full poling state for $[110]_c$ oriented $KNbO_3$ crystals.

3.3 Poling of $KNbO_3$ single crystals using a new 2-step poling method

To investigate the poling state of $[110]_c$ poled $KNbO_3$ crystal in Fig. 4, the domain configuration was observed using the polarizing microscope. Figure 5 shows its domain state under crossed nicols. There was no domain wall over the crystal. When $[110]_c$ direction of the crystal was adjusted to the analyzer direction (an angle between analyzer and $[110]_c$ direction, ϕ, of 0°), the whole crystal became to dark at the same time. This means that at ϕ of 0°, the whole crystal was in an extinction position.[21] Successively, when the crystal was rotated by 45° (ϕ of 45°), the whole crystal was in a diagonal position,[21] and then, at ϕ of 90°, the whole crystal moved to the extinction position, again. Under crossed nicols, the observation of no domain wall means that there was no domain assigned to non-180° domains. Moreover, the simultaneous extinction of the whole crystal suggested that the crystal looked like single domain state. However, the phase angle θ of 55° in Fig. 4 was too low on the assumption that this $KNbO_3$ crystal is the single domain state. Therefore, the above discussion indicated that $[110]_c$ poled oriented $KNbO_3$ crystal in Fig. 4 was composed of only 180° domain structure.

In general, the reorientation of 180° domain requires much larger DC bias field than those of non-180° domains. However, in the poling of $KNbO_3$ crystals at 200 °C, a large DC bias field cannot be applied because of large poling current I_p. To apply large E_p to $KNbO_3$ crystals, temperature must be decreased to around 120 °C. Thus, we proposed a new poling method on the basis of the above discussion. This poling method is composed of 2 poling stages. At the 1st stage, low DC bias field is applied to $KNbO_3$ crystals at higher temperature around 200 °C for the purpose of reorientation of all non-180° domains. Successively, at the 2nd stage, high DC bias field is applied to $KNbO_3$ crystals at lower temperature around 120 °C for the purpose of reorientation of 180° domain. We named the new poling method a 2-step poling method.

Figure 6 shows frequency dependence of |Z| and θ for $[110]_c$ oriented $KNbO_3$ crystal poled using the 2-step poling method. The phase angle θ approached to around 88°, which means that the the poling was significantly improved using the 2-step poling method. The resonance frequency f_s and the antiresonance frequency f_p estimated from Fig. 6 was 785.5 Hz and 813.5 Hz, respectively. Similar investigation was performed for the $[001]_c$ oriented $KNbO_3$ crystals. Figure 7 shows frequency dependence of |Z| and θ for $[001]_c$ oriented $KNbO_3$ crystal poled using the 2-step poling method. In Fig. 7, θ reversed from -90° to around 86°, which means that the the poling was significantly improved. The resonance frequency f_s and the antiresonance frequency f_p was

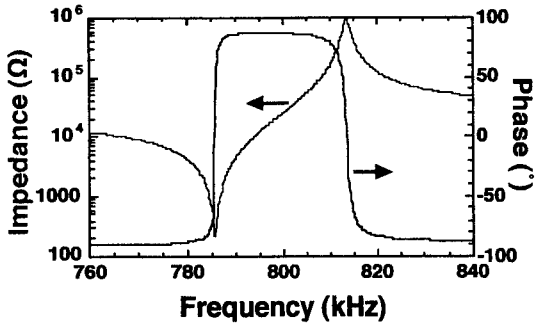

Fig. 6 Frequency dependence of |Z| and θ measured at 25 °C for $[110]_c$ oriented $KNbO_3$ crystals poled using the optimum conditions.

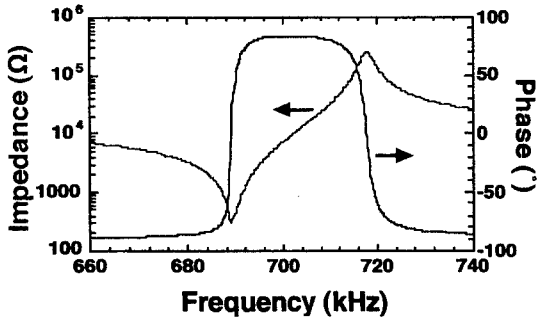

Fig. 7 Frequency dependence of |Z| and θ measured at 25 °C for $[001]_c$ oriented $KNbO_3$ crystals poled using the optimum conditions.

688.8 Hz and 717.7 Hz, respectively.

3.4 Piezoelectric properties of $KNbO_3$ single crystals

Table I shows piezoelectric properties of $KNbO_3$ crystals poled along $[110]_c$ and $[001]_c$ directions. As the reference data, piezoelectric property of $KNbO_3$ single crystal reported by Zgonik *et al.*[13] was also listed. The piezoelectric properties for $[110]_c$ poled $KNbO_3$ crystal showed much higher values than those by Zgonik *et al.*[13] The electromechanical coupling factor k_{31} calculated on the basis of Zgonik's values ($\varepsilon_{33}^T/\varepsilon_0$, s_{11}^E and d_{31}) is estimated at 0.251 while k_{31} value measured in this study is 0.289. It seems that the difference between our k_{31} and Zgonik's k_{31} is caused by the difference of the poling state. Now, we believe that on the basis of this difference, $[110]_c$ poled $KNbO_3$ crystal in this study is more closed to the single domain state than Zgonik's poled crystal. However, there is still one question about dielectric constant. This is because our $\varepsilon_{33}^T/\varepsilon_0$ of 82.9 is twice higher than Zgonik's $\varepsilon_{33}^T/\varepsilon_0$ of 44. This may suggest that $[110]_c$ poled $KNbO_3$ crystal in this study is still far from the full poling state, and if the full poling state is achieved, much higher piezoelectric property and lower dielectric constant may be expected.

In this study, two crystallographic directions were chosen for a comparison of piezoelectric property, *i.e.*, polar direction of $[110]_c$ and engineered domain direction of $[001]_c$. Experimentally, the poling state of $[001]_c$ poled $KNbO_3$ crystal was less sufficient than that of $[110]_c$ poled $KNbO_3$ crystal. However, piezoelectric property of $[001]_c$ poled $KNbO_3$ crystal was much higher than that of $[001]_c$ poled $KNbO_3$ crystal. Especially, d_{31} value along $[001]_c$ direction was 2.8 times higher than that along $[110]_c$ polar direction. Therefore, if the poling state along $[001]_c$ direction is more improved, much higher piezoelectric property can be expected.

It should be also noted that Q_m along $[110]_c$ polar direction was a high value of 1,571 while Q_m along $[001]_c$ direction was a smaller one of 538. It is known that domain wall motion tends to decrease Q_m value. Therefore, this difference of Q_m between $[110]_c$ and $[001]_c$ directions may be attributed to the existence of domain walls. Now, we believe that if the full poling state is achieved along both directions, much higher Q_m can be obtained. $KNbO_3$ single crystal still exhibits a lot of unknown properties, and it is very important to continue the investigation on various piezoelectric properties of $KNbO_3$ single crystals.

Table I Piezoelectric properties of monoclinic $KNbO_3$ single crystals poled along $[110]_c$ and $[001]_c$ directions.

Crystallographic direction / Piezoelectric property	$[110]_c$ direction[a]	$[110]_c$ direction[c]	$[110]_c$ direction[c]
$\varepsilon_{33}^T/\varepsilon_0$	44±2	82.9	446.9
s_{11}^E	3.92±0.05 pm²/N	5.57 pm²/N	6.93 pm²/N
d_{31}	9.8±0.7 pC/N	18.4 pC/N	51.7 pC/N
k_{31}	0.251[b]	0.289	0.312
Q_m	---	1,571	538

a) piezoelectric properties of $[110]_c$ poled $KNbO_3$ single crystal measured by Zgonik *et al.*[13]

b) k_{31} calculated on the basis of Zgonik's values ($\varepsilon_{33}^T/\varepsilon_0$, s_{11}^E and d_{31})

c) piezoelectric properties of the poled $KNbO_3$ single crystals measured in this study

4. CONCLUSIONS

Piezoelectric properties of $KNbO_3$ crystals were investigated along $[110]_c$ of polar direction and $[001]_c$ of engineered domain direction. Prior to piezoelectric measurements, the optimum conditions for the conventional poling method were investigated. However, even if the conventional poling method using these optimum conditions were applied, the poling state of $KNbO_3$ crystals was far from a full poling state. Therefore, we tried to establish a new innovative poling method for $KNbO_3$ crystals. Finally, for poling of $KNbO_3$ crystals, a new 2-step poling method was proposed. Using this 2-step poling method, $KNbO_3$ crystals were poled enough to measure piezoelectric property. Piezoelectric properties with k_{31} modes were measured using a conventional resonance method. $[110]_c$ poled $KNbO_3$ crystals exhibited k_{31} of 28.9 % and d_{31} of 18.4 pC/N while $[001]_c$ poled $KNbO_3$ crystals exhibited k_{31} of 31.2 % and d_{31} of 51.7 pC/N. d_{31} along non-polar $[001]_c$ direction was 2.8 times higher value than d_{31} along polar $[110]_c$ direction. On the basis of the above results, we confirm that $KNbO_3$ crystal is one of the promising materials for piezoelectric application.

ACKNOWLEDGEMENTS

The authors would like to thank Mr. H. Kumagai of Asahi Techno Glass, Ltd. for preparing TSSG-grown $KNbO_3$ single crystals with excellent quality. This study was partially supported by (1) Research Development Program of University-Industry Alliance - A Matching Funds Approach from Japan Society for the Promotion of Science (JSPS), (2) a Grant-in-Aid for Scientific Research (**11555164** and **11555233**) from the Ministry of Education, Science, Sports and Culture, Japan, and (3) TEPCO Research Foundation.

REFERENCES

1. S.-E. Park, S. Wada, L.E. Cross and T.R. Shrout: J. Appl. Phys. **86** 2746 (1999).
2. S.-E. Park and T. R. Shrout: J. Appl. Phys. **82** 1804 (1997).
3. S. Wada, S.-E. Park, L. E. Cross and T. R. Shrout: J. Korean Phys. Soc. **32** S1290 (1998).
4. S. Wada, S.-E. Park, L. E. Cross and T. R. Shrout: Ferroelectrics **221** 147 (1999).
5. B. T. Matthias: Phys. Rev. **75** 1771 (1949).
6. B. T. Matthias and J. P. Remeika: Phys. Rev. **82** 727 (1951).
7. E. A. Wood: Acta Cryst. **4** 353 (1951).
8. G. Shirane, H. Danner, A. Pavlovic and R. Pepinsky: Phys. Rev. **93** 672 (1954).
9. G. Shirane, R. Newnham and R. Pepinsky: Phys. Rev. **93** 672 (1954).
10. S. Triebwasser: Phys. Rev. **101** 993 (1956).
11. E. Wiesendanger: Ferroelectrics **6** 263 (1974).
12. P. Gunter: Jpn. J. Appl. Phys. **16** 1727 (1977).
13. M. Zgonik, R. Schlesser, I. Biaggio, E. Voit, J. Tscherry and P. Gunter: J. Appl. Phys. **74** 1287 (1993).
14. K. Yamanouchi, H. Odagawa, T. Kojima and T. Matsumura: Elect. Lett. **33** 193 (1997).
15. K. Nakamura, T. Tokiwa and Y. Kawamura: Proceedings of the 2000 12th IEEE International Symposium on Applications of Ferroelectrics, Vol. II, Hawaii, 717 (2000).
16. H. Kumagai, K. Murata, Y. Tanabe and T. Fukuda: Denshidenkitsuushinngakkai, **QQE88-43**, 43 (1988).
17. K. Murata, H. Kumagai, N. Kito and Y. Tanabe: Reports Res. Lab. Asahi Glass,. Ltd., **39** 65 (1989).
18. K. Murata, H. Kumagai, N. Kito and Y. Tanabe, T. Fukuda: Kougaku, **18** 148 (1989).
19. EMAS-6100: Standard of Electronic Materials Manufacturers Association of Japan (1993).
20. A.C. Nunes, J.D. Axe and G. Shirane: Ferroelectrics **2** 291 (1971).
21. E. E. Wahlstrom: *Optical Crystallography* (John Wiley and Sons, New York, 1979) 5th ed., Chap. 10.

The Study of Fatigue Anisotropy in $Pb(Zn_{1/3}Nb_{2/3})O_3$-$PbTiO_3$ Ferroelectric Single Crystals

Metin Ozgul*, Koichi Takemura, Susan Trolier-McKinstry, and Clive A. Randall**

Center for Dielectric Studies, Materials Research Institute, The Pennsylvania State University, University Park, PA 16802-4800, U.S.A.

*Fax: 1-814-8652326, email: mxo158@psu.edu

**Present address: ULSI Device Development Division, NEC Electron Devices, NEC Corporation, 1120 Shimokuzawa, Sagamihara 229-1198, Japan.

Polarization fatigue anisotropy has been studied in $Pb(Zn_{1/3}Nb_{2/3})O_3$–$PbTiO_3$ (PZN-PT) single crystal ferroelectrics. It was recently found that ferroelectrics with the rhombohedral phase in the PZN-PT solid solution have essentially no polarization fatigue in the $[001]_C$ directions (orientations will be given in terms of the prototype cubic (m3m) axes and denoted by the subscript C). In this study, we expand upon this observation to correlate fatigue rates more completely with respect to composition, orientation, temperature, and electric field strength. It is inferred that an engineered domain state in a relaxor based ferroelectric crystals with the spontaneous polarization inclined to the normal of the electrode is associated with negligible or no fatigue at room temperature. However, if thermal history, temperature, or field strength induces a phase transition that produces a polarization parallel to the normal of electrode, these orientations fatigue. In summary, this article gives information on the polarization states and orientations that control fatigue in ferroelectric crystals with a relaxor end member.

1.INTRODUCTION

Ferroelectric fatigue is the systematic decrease of switchable polarization in a ferroelectric material undergoing bipolar drive. This phenomenon has received a great deal of investigation over the past ten years to aid the development of thin film ferroelectric random access memories. Fatigue is generally believed to be due, at least in part charge injection and the accumulation of space charge that pins domain walls or retards the nucleation of reversed domains.[1-4]

There have been a number of strategies used to improve fatigue resistance in ferroelectrics; these include:

(i) Doping the ferroelectric with donor dopants, e.g., La or Nb in $Pb(Zr,Ti)O_3$ (PZT).[5,6]

(ii) Using oxide electrodes such as RuO_2,[7] IrO_2,[8] $SrRuO_3$,[9] and $(La,Sr)CoO_3$,[10] for PZT thin film ferroelectrics.

(iii) Employing nonfatiguing ferroelectrics with Pt electrodes, e.g., $SrBi_2Ta_2O_9$ or $SrBi_2Nb_2O_9$.[11, 12]

Our recent studies have explored a fourth possible method to control fatigue, namely, the use of domain engineering and crystal anisotropy.[13-16] In this case, the spontaneous polarization vectors are inclined relative to the normal of the electrode plane. The objective of this article is to build upon the previous studies, which were confined to room temperature fatigue rates, and field levels that did not induce ferroelectric-ferroelectric phase switching. Here we are concerned with the influence of temperature and phase transitions on fatigue rates in crystals measured in different directions and with different compositions.

2. EXPERIMENTAL PROCEDURE

The ferroelectric system selected for this study is the $Pb(Zn_{1/3}Nb_{2/3})O_3$–$PbTiO_3$ (PZN-PT) perovskite type solid solution. PZN-PT single crystals are of interest owing to their extraordinary piezoelectric properties, (piezoelectric coefficients $d_{33} \approx 2500$ pC/N and electromechanical coupling coefficients $K_p^2 \geq 90\%$ in the $[001]_C$ direction in the rhombohedral ferroelectric phase).[17]

Crystals of (1-x)PZN-xPT (x=0.00, 0.045, 0.080, 0.10, and 0.12) were grown using the high temperature flux technique.[17] As shown in Fig. 1, at room temperature and weak field levels, PZN and PZN-4.5PT crystals are rhombohedral (pseudocubic), PZN-8PT is near the morphotropic phase boundary (MPB) (still rhombohedral), and PZT-12 PT is tetragonal. All the crystals were oriented within $\pm 2^0$ along the

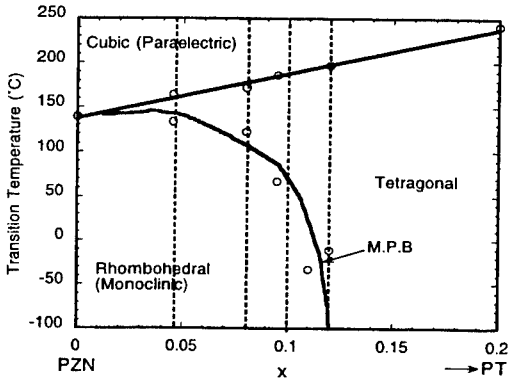

Fig. 1 Phase diagram of the $Pb(Zn_{1/3}Nb_{2/3})O_3$-$PbTiO_3$ system near the MPB (from Ref. 18).

$[111]_C$, $[110]_C$, or $[001]_C$ axes by the back-reflection Laue method. Plate-shaped samples were polished with silicon carbide and alumina powders (down to ~1 μm) to achieve flat and parallel surfaces onto which silver paste electrodes were applied. Silver paste electrodes were preferred due to the fact that they can be removed easily by washing with acetone without changing the nature of the crystal/electrode interface after the experiments. Similar results are obtained with Pt electrodes.[15] The thickness of samples used in this study ranged from 200 μm to 1 mm.

High field measurements including polarization and strain hysteresis utilized a modified Sawyer-Tower circuit and linear variable differential transducer driven by a lock-in amplifier (Stanford Research Systems, Model SR830). Electric fields (E) with a triangle bipolar waveform were applied using a high voltage dc amplifier (Trek Model 609C-6). The frequency of the alternating field was 10 Hz for polarization measurements as well as switching during fatigue measurements, and 0.2 Hz for strain measurements. During measurements, the samples were submerged in Fluorinert, an insulating liquid, to prevent arcing. To study the influence of temperature on fatigue, the Fluorinert liquid was heated or cooled using an oven and liquid nitrogen cryostat, respectively.

The remanent polarizations (P_r) and the coercive fields (E_c) were computed from the recorded hysteresis loops. Fatigue is defined as the change in remanent polarization as a function of the number of switching cycles. All the changes are given as normalized values represented as percentages of the initial remanent polarization or coercive field.

3. RESULTS AND DISCUSSION

3.1 Temperature dependence of fatigue

Figure 2 shows the temperature dependence of fatigue rates in $[111]_C$ oriented PZN-4.5PT crystals for temperatures ranging from 23 (RT) to 100 °C. Fatigue is observed at room and 75 °C temperature within the first 10^5 cycles for a triangular ac field of amplitude 20 kV/cm and frequency 10 Hz. In the $[111]_C$ rhombohedral crystals the fatigue rate is reduced at higher temperatures, as shown in Fig. 2. At temperatures ≥85 °C, fatigue is eliminated. Here, the higher temperatures enable domain switching to overcome the pinning forces. Also at high temperatures, the probability of nucleation (or activating more preexisting nuclei) increases, which also may enable polarization switching to occur throughout the ferroelectric crystals. Collectively, at these higher temperatures the spontaneous polarization does not fatigue as fast as at lower temperatures.

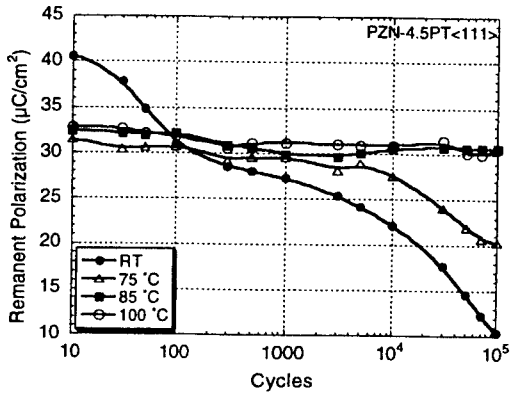

Fig. 2 Fatigue rates as a function of temperature and the number of switching cycles.

3.2 Field induced phase transitions and their impact on fatigue rates

In the rhombohedral phase region the $[111]_C$ oriented crystals fatigue regardless of the applied electric field strength.[15] In this case, the $[111]_C$ oriented crystals have a polarization vector parallel to the electric field and switching is presumably dominated by 180° domain walls. If an electric field is applied along the $[001]_C$ and $[110]_C$ direction, the rhombohedral crystals do not show fatigue at low field strengths. In this case the electric field develops an engineered domain structure with polarization vectors

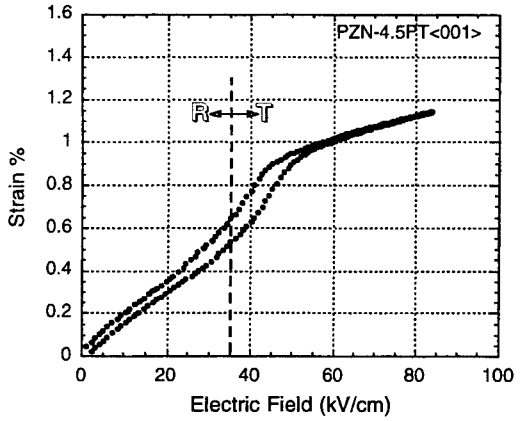

Fig. 3 High field strain vs unipolar electric field behavior in PZN-4.5PT<001>$_C$ single crystals

inclined with respect to the normal vector of the electrode plane.

However, it is known from the work of Park and co-workers[17] that under sufficiently high fields in specific directions, the rhombohedral ferroelectric phase can undergo field forced phase transitions. This can change the nature of the engineered domain state; for example in the $[001]_C$ direction it is possible to induce a tetragonal phase at room temperature with unipolar electric field strengths of >~30 kV/cm. High field strain versus unipolar electric field behavior is given in Fig. 3 for PZN-4.5PT<001>$_C$ crystals indicating the evidence for this phase transformation. PZN-4.5PT<001>$_C$ crystals normally do not fatigue under small electric fields but show remarkable remanent polarization loss when driven at relatively higher fields as illustrated in Fig. 4. Similar experiments

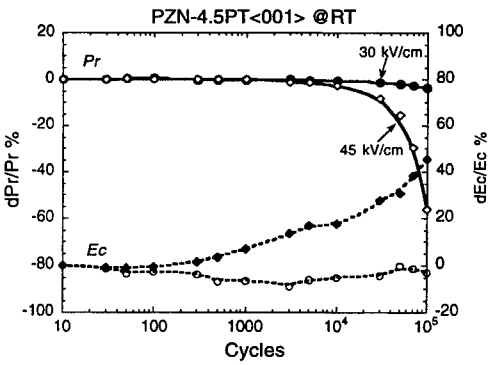

Fig. 4 Fatigue behavior change in PZN-4.5PT<001>$_C$ crystal due to phase switching at higher electric fields; (a) 30 kV/cm (no fatigue) and (b) 45 kV/cm (fatigue).

were performed in $[110]_C$ oriented PZN-4.5PT crystals. Even though rhombohedral PZN-4.5PT <110>$_C$ crystals do not fatigue at low fields, very pronounced fatigue occurred under electric field levels sufficiently high to induce another phase, i.e., the orthorhombic phase. In the case of unipolar drive, different strain-field slopes are noted with a hysteretic transition between the rhombohedral and field induced phase. The field levels for the transformation under unipolar conditions is higher than under ac conditions. Hysteresis losses may locally heat to enable lower temperature transitions. The transition from a ferroelectric rhombohedral to ferroelectric tetragonal (or orthorhombic) phase eventually leads to fatiguing of the crystals.

All of the above results suggest that in these crystals an engineered domain state with the polarization inclined to the electrode is necessary to minimize or eliminate fatigue. This now has been confirmed at a variety of temperatures, compositions, and in both single crystal[15,16] and epitaxial thin film form.[14] The mechanism by which these engineered domain states limit fatigue is not understood. One possibility is that the inclined polarization states redistribute the space charge accumulation and thereby reduce the fatigue rate at a given temperature and composition.

3.3 Influence of fatigue history

The curved morphotropic phase boundary of the PZN-PT system permits fatigue to be studied in single crystals at different temperatures and ferroelectric phases. $[001]_C$ PZN-8PT crystals were induced into the tetragonal phase at 125 °C and cycled with amplitude 20 kV/cm at 10 Hz. After 10^5 cycles, the crystal was substantially (~35%) fatigued. Then, these samples were cooled into the rhombohedral phase at room temperature and again driven under bipolar drive. The samples continued to fatigue as shown in Fig. 5 (in comparison with the crystal cycled only at room temperature). The fatigue at higher temperatures stabilizes local tetragonal regions, which are then retained on cooling into the rhombohedral phase field. The above experiments demonstrate that there are exceptions to high temperature retardation of fatigue rates. This is the case when domain engineered crystals undergo a phase transition to produce polarization vectors parallel to the electric field. Further, the thermal history can also influence the fatigue. If a crystal can undergo a field that induces a domain state that

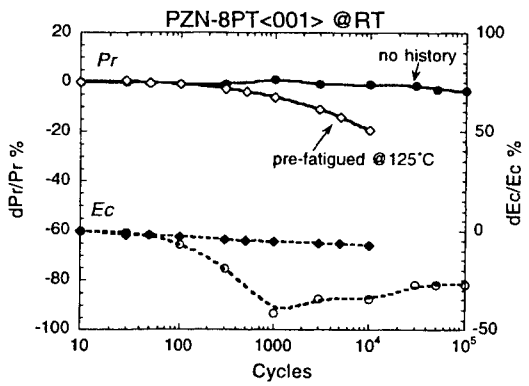

Fig. 5 Comparison of room temperature fatigue behavior of PZN-8PT<001>$_C$ crystals (20 kV/cm, 10 Hz) indicating the influence of fatigue history; (a) cycled only at room temperature and (b) crystals pre-fatigued at 125 °C.

fatigues, this ultimately controls the fatigue process, acting as a nucleation site for pinned domains in the whole crystal.

4. CONCLUSIONS

All of the above illustrates the role of fatigue anisotropy and domain engineering in $Pb(Zn_{1/31}Nb_{2/3})O_3$–$PbTiO_3$ crystals. Fatigue is induced if a polarization vector is normal to the electrode plane and is parallel to the electric field vector. Fatigue rates are suppressed in some directions, provided the thermal energy can overcome pinning effects or alter active nucleation probability. In the compositions close to the MPB, alternating electric fields can induce a ferroelectric phase with polarization parallel to the electric field direction, e.g. a rhombohedral to tetragonal phase transition in a $[001]_C$ crystal. This then can give rise to polarization fatigue. It is hypothesized that if a ferroelectric crystal with a relaxor end member has engineered domains with polarization inclined to the electrode normal, charge injection is either reduced and/or charge is redistributed, and/or domain switching mobility is enhanced, thereby limiting fatigue.

ACKNOWLEDGMENTS

The authors would like to thank Professor T.R. Shrout and Dr. S.-E. Park for their helpful suggestions, and H. Lei and P. Wu for supplying single crystals. This work was achieved with the financial support of The Ministry of Turkish National Education and of DARPA (Grant No. N00014-98-1-0527).

REFERENCES

[1] E. Fatuzzo and W. J. Merz, *Ferroelectricity* (Wiley, New York, 1967).
[2] J. F. Scott and C. A. Pas de Araujo, Science **246**, 140 (1989).
[3] W. L. Warren, D. Dimos, B. A. Tuttle, R. D. Nasby, and G. E. Pike, Appl. Phys. Lett. **65**, 1018 (1994).
[4] J. F. Scott, J. Phys. Chem. Solids **57**, 1439 (1996).
[5] K. Amanuma, T. Hase, and Y. Miyasaka, Jpn. J. Appl. Phys., Part 1 **33**, 5211 (1994).
[6] I. K. Yoo, S. B. Desu, and J. Xing, in *Ferroelectric Thin Films III*, MRS Symp. Proc. Vol. 310, edited by B. A. Tuttle, E. R. Myers, S. B. Desu, and P. K. Larsen (Materials Research Society, Pittsburgh, PA,1993), p.165.
[7] D. P. Vijay and S. B. Desu, J. Electrochem. Soc. **140**, 2640 (1993).
[8] K. Kushida-Abdelghafar, M. Hiratani, and Y. Fujisaki, J. Appl. Phys. **85**, 1069 (1999).
[9] S. Aggarwal, I. G. Jenkins, B. Nagaraj, C. J. Kerr, C. Canedy, R. Ramesh, G. Valasquez, L. Boyer, and J. T. Evans, Jr., Appl. Phys. Lett. **75**, 1787 (1999). 518.
[10] J. Yin, T. Zhu, Z. G. Liu, and T. Yu, Appl. Phys. Lett. **75**, 3698 (1999).
[11] R. Dat, J. K. Lee, O. Auciello, and A. I. Kingon, Appl. Phys. Lett. **67**, 572 (1995).
[12] C. A. Pas de Araujo, J. D. Cuchiaro, L. D. McMillan, M. C. Scott and J. F. Scott, Nature (London) **374**, 627 (1995).
[13] K. Takemura, M. Ozgul, V. Bornand, S. Trolier-McKinstry, and C. A. Randall, Proceedings of the 9th US-Japan Workshop on Dielectric and Piezoelectric Ceramics, Okinawa, Japan, 1999.
[14] V. Bornand, S. Trolier McKinstry, K. Takemura, and C. A. Randall, J. Appl. Phys. **87**, 3965 (2000).
[15] K. Takemura, M. Ozgul, V. Bornand, S. Trolier-McKinstry, and C. A. Randall, J. Appl. Phys. **88**, 7272 (2000).
[16] M. Ozgul, K. Takemura, S. Trolier-McKinstry, and C. A. Randall, J. Appl. Phys. **89**, 5100 (2001).
[17] S.-F. Liu, S.-E. Park, T. R Shrout, and L. E. Cross, J. Appl. Phys. **85**, 2810 (1999)..
[18] J. Kuwata, K. Uchino, and S. Nomura, Ferroelectrics **37**, 579 (1981).

Phase Transitional Behavior of the Morphotropic Phases in PZN-PT and PMN-PT Single Crystals

Yu Lu, D.-Y. Jeong, Z.-Y. Cheng, and Q. M. Zhang

Department of Electrical Engineering and Materials Research Institute, The Pennsylvania State University

University Park, PA 16802, USA

FAX: 814-863-7846, Email: QXZ1@PSU.EDU

Abstract: We report on the observation of an orthorhombic ferroelectric (FE_o) phase in PZN-PT and PMN-PT single crystals, whose polarization is along <011> direction and stability can be altered by poling conditions. By measuring the dielectric behaviors of PZN-PT single crystals with different PT content, a new diagram, which also includes the different orientations, is developed.

INTRODUCTION

Recent discoveries in mixed B-site cation ferroelectric perovskites, such as $Pb(Mg_{1/3}Nb_{2/3})O_3$-$PbTiO_3$ (PMN-PT) and $Pb(Zn_{1/3}Nb_{2/3})O_3$-$PbTiO_3$ (PZN-PT) single crystals, have stimulated significant research activities.[1-4] In these single crystals, an electromechanical coupling factor of greater than 0.9 has been reported for compositions close to the morphotropic phase boundary (MPB) between rhombohedral ferroelectric (FE_r) and tetragonal ferroelectric (FE_t) phases, especially in the FE_r phase near the MPB for specimens poled along <001>.[1-3] Similar enhancements in the electromechanical properties were also reported when crystals were poled at finite angles with respect to the spontaneous polarization direction, although the coupling factors of these finite miss-oriented crystals were lower (~0.8).[5-7]

Naturally, a question to ask is what is unique about the PZN-PT and PMN-PT crystalline solutions and the role of the MPB. In 0.92PZN-0.08PT crystals (which at T=25°C is in the FE_r phase and near an MPB), recent investigations have demonstrated the presence of monoclinic domains, and orthorhombic ferroelectric (FE_o) and monoclinic ferroelectric (FE_m) states.[8-10] This opens an interesting possibility that those states, even meta-stable, may be regarded as intermediate states and responsible for the high piezoelectric and electromechanical responses in PZN-PT and PMN-PT single crystals near the MPB.

In $Pb(Zr_{1-x}Ti_x)O_3$ (PZT), which is another related ferroelectric perovskite material, high electromechanical properties have been widely studied over many years for compositions close to the MPB between FE_r and FE_t phases.[11] Much effort has been expended in determining the mechanism responsible for these significant enhancements. Recently, a FE_m state has been reported over a very narrow composition range near MPB. In this FE_m state, the polarization was confined to the <hhk> plane, which is one of the planes that can "bridge" the tetragonal <001> and rhombohedral <111> directions.[4,12] It was suggested that this "bridging" effect, via the FE_m state, is responsible for the enhanced electromechanical properties.[12]

This investigation reports the phase transition behavior in 0.67PMN-0.33PT, 0.955PZN-0.045PT, 0.92PZN-0.08PT and 0.9PZN-0.1PT single crystals, which are close to the MPB. Dielectric measurements have been used to study crystals with various poling histories and orientations. We have observed, by dielectric and optical microscopy techniques, an intermediate FE_o state whose phase stability depends upon its poling history and mechanical condition. Based on the dielectric and optical data, the phase diagram for the PZN-PT single crystal near MPB is redrawn to include an orthorhombic phase.

0.67PMN-0.33PT single crystals were grown by the Bridgman method,[13] and all the PZN-PT single crystals studied here with different PT content (4.5%, 8% and 10%) were grown by the high temperature flux method.[14] Various crystals were oriented along the <001>, <110> and <111> directions. Typical specimen dimensions were 2×2×2 mm^3. Crystals were poled at room temperature, while the domain patterns were characterized by a Zeiss Axioskop

cross-polarized optical microscope (100× amplification). Dielectric characterization (at 1 kHz) was carried out using a standard LCR meter (HP4284A) equipped with a temperature chamber (Delta 9023).

The optical observation revealed that for the crystals in the FE_r phase near the MPB (0.67PMN-0.33PT and 0.92PZN-0.08PT), <011> orientated specimen could be poled to a <111> twined multidomain or a <011> monodomain conditions depending on the poling condition. The domain configurations for both cases are schematically illustrated in Fig.1, where the dashed arrows indicate the remanent polarization direction and the coordinate systems for both prototype <001> and <011> orientations are pointed out.

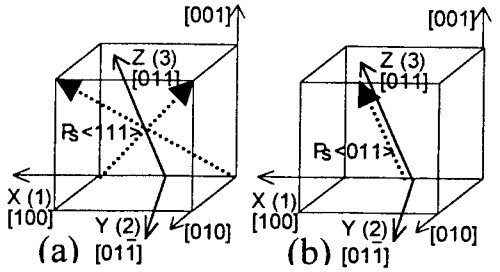

Fig. 1 Schematic drawings of possible domain configurations for [011] poled crystals in (a) twined crystals and (b) mono-domain crystals

This new orthorhombic phase was further confirmed by the dielectric study. Fig. 2(a)-(d) show the dielectric constant and loss as functions of temperature for poled <111>, <011> (E_{poling} >5 kV/cm), <011> (E_{poling} = 4 kV/cm), and <001> oriented 0.67PMN-0.33PT crystals, respectively. Each dielectric curve exhibited a transition at 145°C which is the FE_t to cubic transformation[15,16], and a second dielectric anomaly at ~80°C. For <111> and <011> (E_{poling}<4 kV/cm) orientations, an additional third anomaly was found at ~100°C. It is important to emphasize that the differences between Fig. 2(b) and (c) (which are both for <011> orientations) is only the poling field (E_{poling}). According to the previous optical study, they are referred to the <011> monodomain and <111> twined multidomain configurations. The differences in the dielectric responses of the <011> crystals due to the various poling conditions can be explained based on proposed domain configurations. For E_{poling}<4 kV/cm (Fig. 2(c)), the FE_r state is stable at room temperature. Upon heating to ~80°C, a transition occurs to a FE_o state. On further

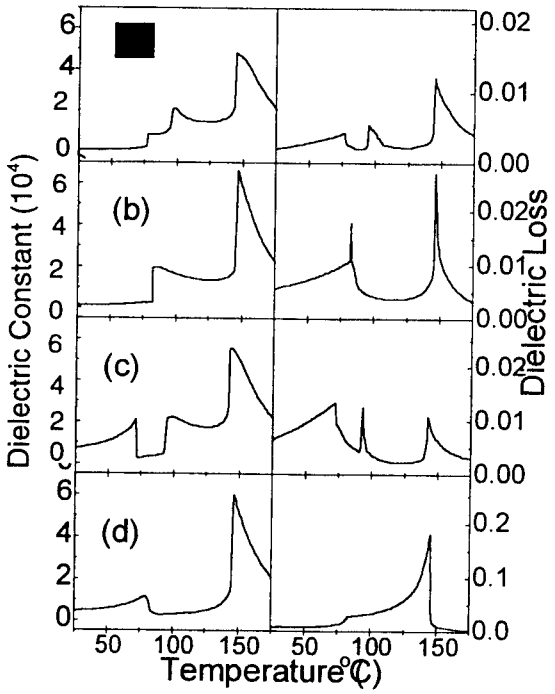

Fig. 2 Dielectric behaviors of 0.67PMN-0.33PT single crystal at different orientations and poling conditions

increase of temperature to ~100°C, a secondary transformation to a FE_t state occurred. In contrast, for E_{poling}>5 kV/cm (Fig. 2(b)), a monodomain FE_o state can be induced at room temperature. Upon heating to 80°C, a transition occurs to a FE_t state. Interestingly, the FE_o-FE_t transition temperature in the monodomain condition was significantly lower (80°C) than in the polydomain condition (100°C).

It should be mentioned that even small variations in the PT content resulted in deviations from this monodomain condition and the disappearance of the FE_o state at room temperature, demonstrating that this state only exists over a narrow composition range near the MPB. Accordingly, at room temperature most of the crystals poled along <011> were polydomain and FE_r. Clearly, the phase transformational pathway is altered by whether the specimen is elastically constrained (polydomain) or free to deform (monodomain).[9]

The dielectric constant for the poled <111> crystals (Fig. 2(a)) exhibited a similar transition sequence as the polydomain <011> (Fig. 2(c)). In both cases, the FE_r to FE_t transition proceeded through an intermediate FE_o state, with the FE_o state being present for ~80<T<100°C. The dielectric constant for poled <001> crystals was shown in Fig. 2(d). Only one FE-FE transition was observed, which occurred at 80°C. This

transition temperature is close to that of the FE_o-FE_t along the <011> (E_{poling}>5 kV/cm, monodomain), and with that of the FE_r-FE_o along the <111> and <011> (E_{poling}<4 kV/cm, polydomain).

The results in Fig. 2 demonstrate a complex transformation sequence that is dependent upon orientation and electrical history. Both the Fig. 2(a) and (c) show that between the FE_r and FE_t, a new FE_o state does exist. Fig. 2(b) also shows that such FE_o phase can be even stabilized at room temperature and directly transit to FE_t phase when increasing temperature. However, the dielectric results also suggest that the phase in the temperature interval between 80 °C and 100 °C may not be a simple FE_o phase but rather contain FE_r component. In viewing of the high degree of defects in the material which could change the local energy balance between different structures and phases, the trapping of FE_r component in the transition to FE_o should be quite likely, resulting in a mixed phase of FE_r component in a FE_o matrix. This mixed phase could also lead to an averaged monoclinic state (for example, P_1 ? P_2=P_3, where P_i is the polarization component along the ith-direction of the prototype cubic cell) if this mixing is on the meso-scale. In this sense, the averaged structure of this "phase" will also depend on the poling level (the amount of FE_r mixed in FE_o matrix) and indeed, the experimental data from <011> oriented crystals poled at different level (E_{poling} <10 kV/cm) show that the observed FE_r-FE_o temperature shifts upwards and FE_o-FE_t shifts downwards by several degrees with the poling field (<10 kV/cm). Therefore, in this paper, we refer this phase as to a modified FE_o phase (FE_o').

The optical and dielectric behaviors of 0.92PZN-0.08PT are similar to those of 0.67PMN-0.33PT, which a FE_o' phase is also found between the FE_r and FE_t phases.

We now discuss the data acquired from 0.9PZT-0.1PT single crystals, which is in the FE_t phase near the MPB at room temperature.[1,2] Therefore, as poled along <001> direction, there is only one dielectric transition FE_t-Cubic phase at 185°C (Fig. 3(a)). However, when oriented and poled along <011> direction (E_{poling} > 5 kV/cm), the optical observation indicates that the crystal is in FE_o phase. As the temperature increases, the dielectric data exhibits a FE_o-FE_t transition at 55°C, followed by the transition to the cubic phase at 188°C (Fig. 3(b)). For crystals oriented and poled along <111>, optical observation shows no sign of monodomain state

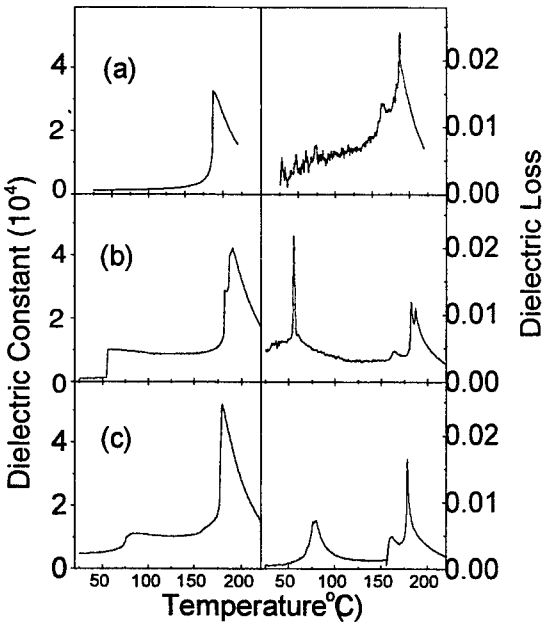

Fig. 3 Dielectric behaviors of 0.9PZN-0.1PT single crystal at different orientations

for crystals under DC poling field to more than 10 kV/cm. However, the dielectric data of poled crystals display a transition at 78°C which we interpret as the transition of FE_o'-FE_t (Fig. 3(c)) and the crystal is in a FE_o' phase at room temperature.

The dielectric constant data and optical observation for crystals at composition 4.5%PT were also carried out as a comparison. Fig. 4 shows the dielectric constant of the single crystal poled along different directions, (a) <111>, (b) <100>, and (c) <110>. All the data indicate that at room temperature, the crystals are in FE_r phase for all the orientations under poling fields up to 10 kV/cm. The transition to FE_t phase is at 115°C.

Based on the dielectric and optical data, the phase diagrams of PZN-PT single crystals at near MPB are redrawn to include FE_o phase and FE_o' phase and the effects of the mechanical and electric conditions and sample history (Fig. 5). The boundaries marked by the solid lines are from the data on crystals poled along <001> which are the same as that reported early.[1] However, when oriented and poled along other crystal orientations, a FE_o or FE_o' can exist at both the rhombohedral and tetragonal sides of MPB. The experimental results indicate that because of the proximity in the free energy between different phases near MPB, what is the experimentally observable phase really depends crucially on the electric and mechanical

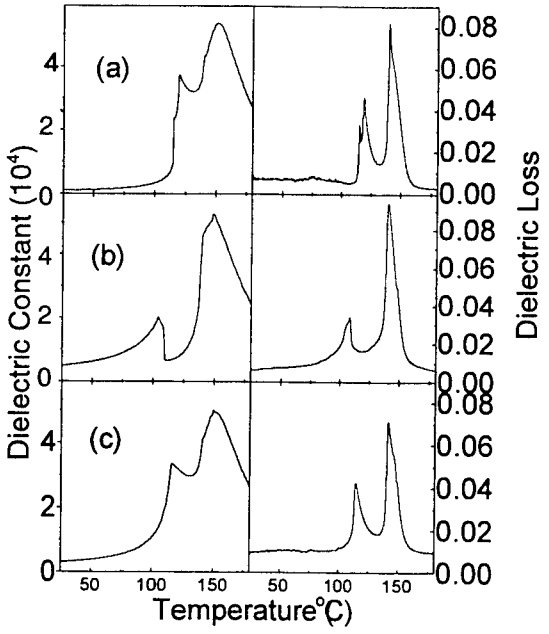

Fig. 4 Dielectric behaviors of 0.955PZN-0.045 PT single crystal at different orientations

boundary conditions, and sample history. In other words, the mechanical and electric boundary conditions can greatly influence the experimentally observed phases near MPB for this crystal system, which may explain the very compliant (high) electromechanical responses in this crystal.

This work was supported by the Office of Naval Research.

References:

[1]J. Kuwata, K. Uchino, S. Nomura, Jpn. J. Appl. Phys. 21, 1298 (1982).

[2]S. Park and T. R. Shrout, J. Appl. Phys. 82, 1804 (1997).

[3]S. Park and T. Shrout, IEEE Trans. Ultrason. Ferro. Freq. Control 44, 1140 (1997).

[4]B. Noheda, D. E. Cox, G. Shirane, J. Gonzalo, L. Cross, and S. Park, Appl. Phys. Lett. 74, 2059 (1999).

[5]K. Nakamura and Y. Kawamura, in 1999 IEEE Ultrasonics Symposium Proceedings, edited by S. C. Schneider, M. Levy, and B. R. McAvoy (New York, IEEE, 1999), pp. 1013-1018.

[6]S. Park, S. Wada, L. Cross, T. Shrout, J. Appl. Phys. 86, 2746 (1999).

[7]X-h Du, J. Zheng, U. Belegundu, and K, Uchino, Appl. Phys. Lett. 72, 2421 (1998).

[8]M. K. Durbin, J. C. Hicks, S. Park, and T. Shrout. J. Appl. Phys. 87, 8159 (2000).

[9]D. Viehland, J. Appl. Phys. 88, 4794 (2000).

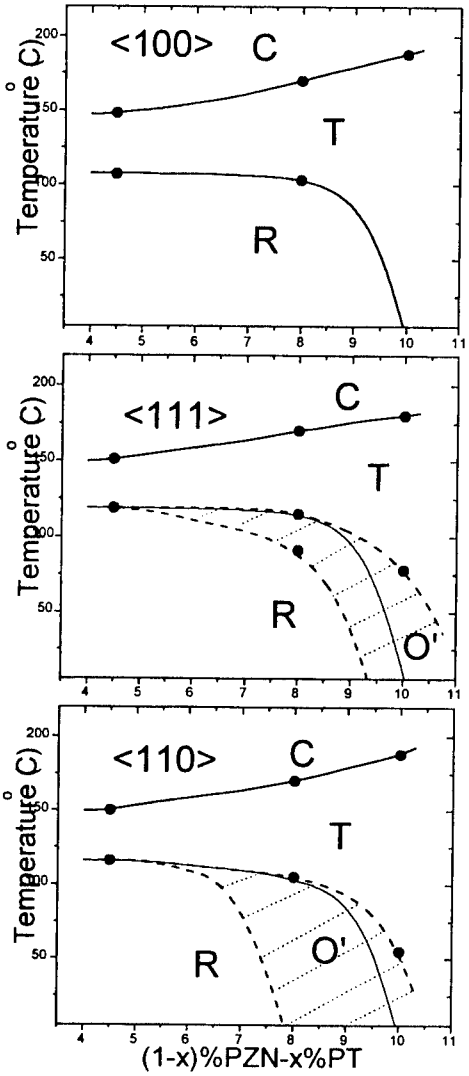

Fig. 5 Phase diagrams for PZN-PT single crystal

[10]B. Noheda, D. Cox, G. Shirane, S. Park, L.E. Cross, and Z. Zhong, unpublished.

[11]B. Jaffe, W. Cook, Jr., and H. Jaffe, Piezoelectric Ceramics (Academic Press Limited, New York, 1971), chapter 7.

[12]R. Guo, L. Cross, S. Park, B. Noheda, D. Cox, and G. Shirane, Phys. Rev. Lett. 84, 5423 (2000).

[13]Z. Yin, H. Luo, P. Wang, and G. Xu, Ferroelectrics 229, 207 (1999).

[14]S. –E. Park and T. R. Shrout, J. Appl. Phys. 82, 1804 (1997).

[15]S. W. Choi, T. Shrout, S. Jang, and A. Bhalla. Ferroelectrics 100, 29 (1989).

[16]O. Noblanc, P. Gaucher, and G. Calvarin, J. Appl. Phys. 79, 4291 (1996).

Electrical Properties of Morphotropic Phase Boundary in $(Bi_{1/2}Na_{1/2})TiO_3$ - $KNbO_3$ Solid Solution System

Tadashi TAKENAKA, Hajime NAGATA and Hideki ISHII
Faculty of Science and Technology, Science University of Tokyo,
Noda, Chiba-ken, 278-8510 Japan
E-mail: tadashi@takenaka.ee.noda.sut.ac.jp

A morphotropic phase boundary (MPB) between (Bi1/2Na1/2)TiO3 (rhombohedral system) and KNbO3 (orthorhombic system) was determined by using an X-ray diffraction and dielectric measurements. A solid solution, (1-x)(Bi1/2Na1/2)TiO3-xKNbO3 [BNTK-100x], shows a rhombohedral symmetry and an orthorhombic symmetry at the composition around of $0 \leqq x \leqq 0.95$ and $0.96 \leqq x \leqq 1.00$, respectively. A dielectric constant, ε_s, at Curie temperature, T_c, was the largest value on the BNTK-96. From these results, the MPB of BNTK system seems to be existed around BNTK-96. The BNTK ceramics were confirmed to be ferroelectric by observing their hysteresis loops. Resistivities, ρ, of BNTK-100x ($0.94 \leqq x \leqq 0.98$) are $10^9 \sim 10^{12}$ Ω·cm. An electromechanical coupling factor, k_{33}, of the BNTK-96 is 0.161 which is unsaturated value.

KEYWORDS: ferroelectrics , $(Bi_{1/2}Na_{1/2})TiO_3$, $KNbO_3$, MPB, lead-free, piezoelectrics, dielectric properties

1. INTRODUCTION

The piezoelectric property is an important function for the electric materials. Most widely used piezoelectric materials are PbTiO3-PbZrO3 three-component ceramics (PZT system). However, it is desired that lead-free materials should be used for environmental protection. Consequently, it is necessary to search for lead-free piezoelectric materials that have excellent properties such as the PZT system.[1-3] (Bi1/2Na1/2)TiO3 and KNbO3 are well known as the lead-free piezoelectric materials with perovskite structures.

Bismuth sodium titanate, (Bi1/2Na1/2)TiO3 (BNT) was discovered by Smolensky as a perovskite-type ferroelectric.[4] BNT is well known as having a rhombohedral symmetry (a = 3.891 Å, a = 89°36') at room temperature. The Curie temperature, T_c, is 320 °C and the second phase transition from ferroelectric to antiferroelectric exists near 200 °C.[5] The remanent polarization, P_r, is 38 μC/cm^2 and the coercive field, E_c, is 73 kV/cm which is a very high coercive field.

Potasium niobate, KNbO3 (KN) has an orthorhombic symmetry at room temperature, and has the phase transition at −10 °C, 225 °C and 425 °C for rhombohedral to orthorhombic to tetragonal to cubic, respectively.[6] KN single crystals were known to have very high piezoelectric activities. So KN single crystals were investigated the orientation dependence on electromechanical coupling factors to explore some optimum cuts for ultrasonic transducers and piezoelectric resonant devices.[7] However the KN single crystal is too expensive to use for lead-free piezoelectric materials in usual commercial products.

The solid solution of BNT and KN seems to have a morphotropic phase boundary (MPB) between rhombohedral and orthorhombic. It is well known that large piezoelectric properties were expected on the MPB composition.[8] However, it is unclear the existence of the MPB for the BNT-KN system because the system is difficult to prepare the densed ceramic sample. In this study, the solid solution (1-x) (Bi1/2Na1/2)TiO3-xKNbO3 [BNTK-100x] ceramics were prepared by using the hot-pressing method and the conventional ceramic technique to investigate their electrical properties near the MPB composition.

2. EXPERIMENTAL

The BNTK-100x ceramics were prepared by using the hot-pressing (HP) method[9,10] and the conventional ceramic technique (the ordinary firing (OF) method). Stoichiometric mixtures of regent grade Bi2O3, Na2CO3, TiO2, K2CO3 and Nb2O5 were mixed by ball-milling for 10 h with zirconia media and ethyl alcohol. Mixed powders were calcinated at 800 °C for 2 h in an alumina crucible and was ground and mixed by ball-milling at 100 h. The milled powders were sintered by HP and OF methods. After setting the sample in the HP apparatus, the sample was kept at 1060 ~ 1090 °C for 1 h without pressure. Finally, the pressure of 200 kg/cm^2 was applied for 1 h, and annealed for 1 h without pressure. On the other hand, the time of ball-milling after the calcinating in the OF method was determined to the optimizing condition with high density of the ceramics. Sintering temperatures were selected at 1060 ~ 1090 °C for 2 h.

The crystal structure of the solid solution was investigated by using an X-ray diffraction with CuKα radiation through a Ni filter at a scanning speed

of 1 °/min.

For the measurement of electrical properties, the fire-on Ag paste was used as the electrodes. The dielectric constants, ε s, and loss tangent, tanδ, were measured by using an LCR meter (YHP 4275A). The D-E hysteresis loops were observed by a standard Sawyer-Tower circuit at 50 Hz at room temperature. Resistivities, ρ, were measured at room temperature by using a high resistance meter (YHP 4339B). Specimens for piezoelectric measurements were poled at room temperature in a stirred silicone oil bath by applying a dc electric field of 7 kV/mm for 10 min. Piezoelectric properties were measured by means of the resonance-antiresonance method on the basis of IEEE standards using an impedance analyzer (YHP 4294A). Electromechanical coupling factors, $k33$, were calculated from the resonance and the antiresonance frequencies using Onoe's formula.

3. RESULTS AND DISCUSSION

3.1 Estimation of the MPB by the HP method

Figure 1 shows X-ray powder diffraction patterns of BNTK-94 to BNTK-100 (KN) solid solution prepared by the HP method. These patterns show a single phase of a perovskite structure with a rhombohedral or an orthorhombic symmetry. The crystal phase changed from orthorhombic to rhombohedral symmetries with increasing the amount of modified BNT (x). The difference of both structures can be remarkably appeared from the X-ray diffraction patterns at the 2θ range of 40° to 50°. [11,12] Figure 2 shows the X-ray diffraction patterns of BNTK-94 ~ BNTK-100 (KN) at the 2θ range of 40° to 50°. The BNTK-100 (KN) shows a splitting (200) reflection of (200), (020) and (002) with the orthorhombic symmetry. The BNTK-94 shows a single reflection (200) with the rhombohedral symmetry. These results confirm that the MPB composition exists between BNTK-94 and BNTK-100.

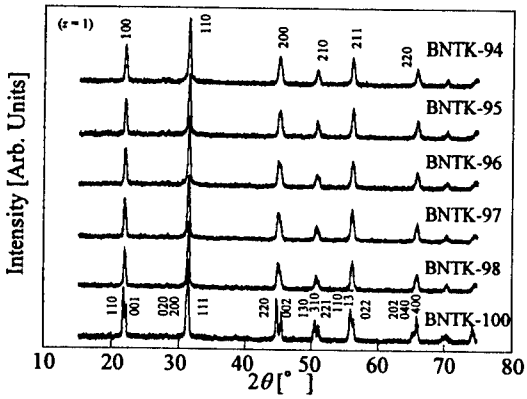

Fig.1 X-ray powder diffraction patterns of BNTK-100x ($0.94 \leqq x \leqq 1.00$).

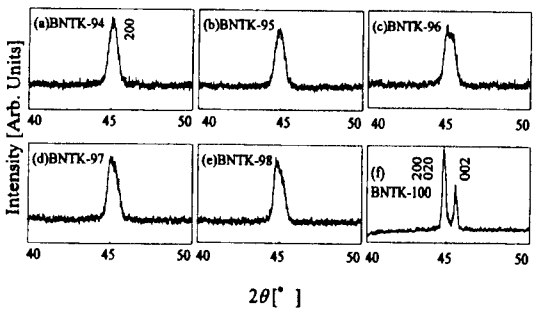

Fig.2 X-ray diffraction patterns at the 2θ range from 40° to 50°.

Figures 3 and 4 show the lattice constants and the volumes of BNTK system as a function of the amount (x) of modified KN, respectively. The lattice constants of all compositions were calculated as the rhombohedral or orthorhombic symmetry. The lattice constants were discontinued around the BNTK-96 composition in case of both symmetries. The MPB composition seems to be existed around the BNTK-96 from the results of the X-ray diffraction. The BNTK ceramics prepared by the HP method have high density ratios of over 90 % to calculated theoretical densities.

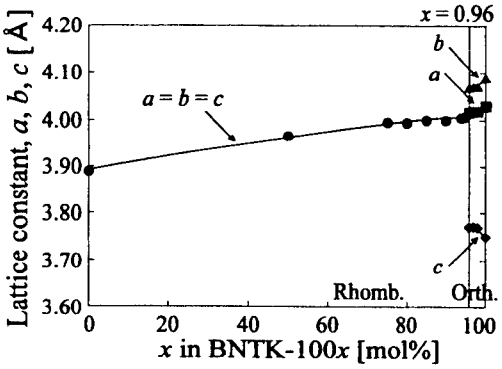

Fig.3 Lattice constants of the BNTK-100x system.

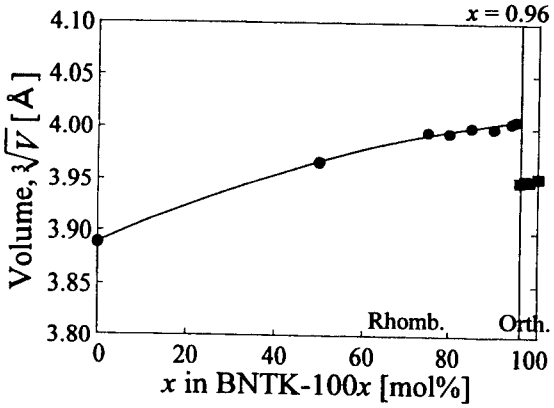

Fig.4 Volumes of the BNTK-100x system.

The densed BNTK ceramics can be prepared by using the OF method. Figure 5 shows the sintering

temperature dependence of the measured density ratio to the theoretical density. The density ratios of BNTK-96 with powders of 20 h and 100 h ball-milling time were 79 % and 97 % sintered at 1085 °C, respectively. It was thought that the particle size of the powder seems to depend on the ball-milling time before the sintering and to be very small by the long time. Bismuth ions in the KN display an effect of promoting to sinter the BNTK ceramics.

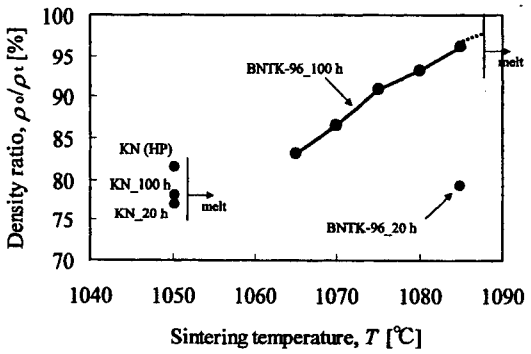

Fig. 5 Density ratio, ρo/ρt, of ordinary fired (OF) BNTK ceramics.

3.2 Electrical properties

Figure 6 shows the temperature dependence of dielectric constants, ε s, and loss tangents, tanδ, of the HP BNTK-100x ceramics measured at 1 MHz. It was confirmed the existence of two phase transitions which are the Curie temperature, T_c, and the secondary phase transition from orthorhombic to tetragonal symmetries, respectively. The ε s at T_c of the BNTK-96 was the largest value. It is considered that the BNTK-96 seems to be the MPB composition from the dielectric measurements, because the crystal structure of the MPB composition is usually very unstable and can be expected to show the high polarization and the high dielectric constants.

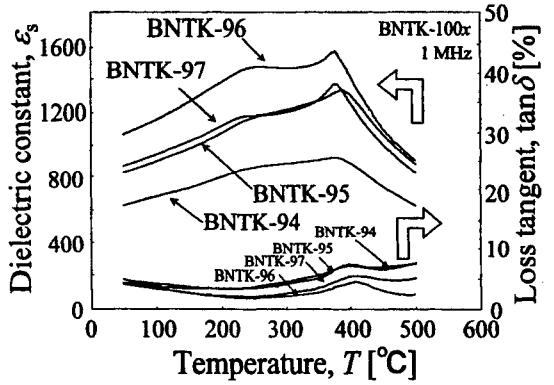

Fig.6 Temperature dependences of dielectric constant ε s, and loss tangent, tanδ, for BNTK-100x ($0.94 \leqq x \leqq 0.97$).

Figure 7 shows the phase diagram of the BNTK-100x system determined from the results of the X-ray diffraction and the dielectric measurements. The crystal phase of (a) the BNT-rich side was a ferroelectric rhombohedral symmetry at room temperature and an antiferroelectric rhombohedral symmetry at higher temperatures than the secondary phase transition. On the other hand, the crystal phase of (b) the KN-rich side was a ferroelectric orthorhombic symmetry at room temperature and a ferroelectric tetragonal symmetry at higher temperatures than the secondary phase transition. The result of the X-ray diffraction shows that the MPB composition is the BNTK-96, however, the results of the dielectric measurements seems to be existed the MPB between BNTK-94 and BNTK-98.

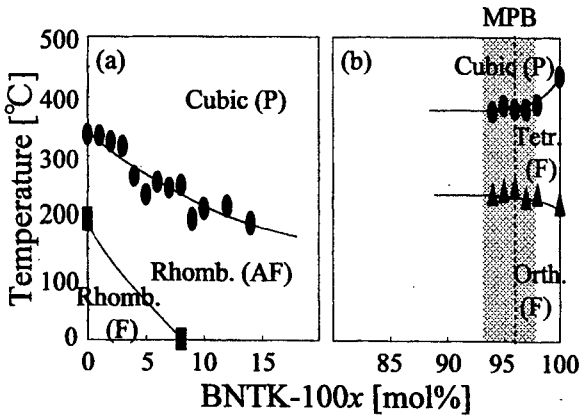

Fig.7 A phase diagram of the BNTK-100x system of near (a) BNT and (b) KN sides, respectively.

Electrical properties such as the D-E hysteresis loops and the piezoelectricities can not be measured on HP BNTK ceramics. A leakage current occurred to HP samples by applying a high electric field because of many cracks in the sample. The resistivities of the OF samples are $10^9 \sim 10^{12}$ Ω·cm and are not high enough to be fully poled by applying high voltages.

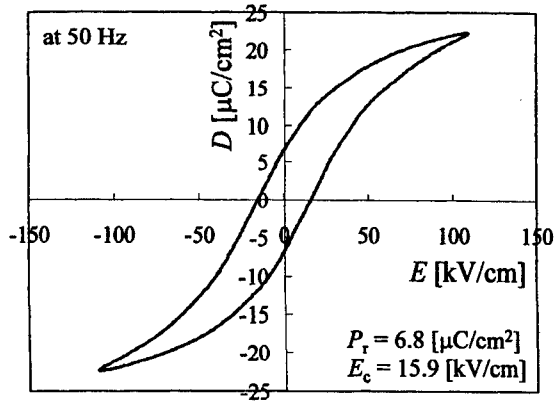

Fig.8 A D-E hysteresis loop of the BNTK-98 ceramic.

The D-E hysteresis loops of the dense samples by the OF method could be observed. Figure 8 shows a D-E hysteresis loop without full-saturation of the OF BNTK-98 ceramic. The BNTK-98 ceramic shows a ferroelectricity. Figure 9 shows a remanent polarization, P_r, for an applied voltage, E_a, of the BNTK-98 ceramic. The P_r gradually increases as the E_a increases up to 110 kV/cm with no saturation.

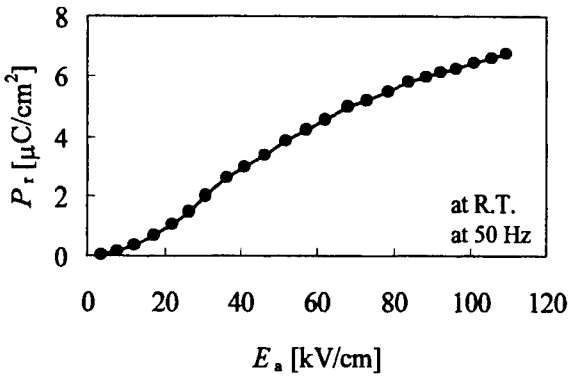

Fig. 9 Remanent polarization, P_r, of BNTK-98 ceramic as a function of the applied voltage Ea.

Figure 10 shows a frequency dependence of an impedance of the BNTK-96. The poling condition is E_p= 7 kV/mm of the applied voltage for 7 min at room temperature. An electromechanical coupling factor, k_{33}, is 0.161 which is not saturated.

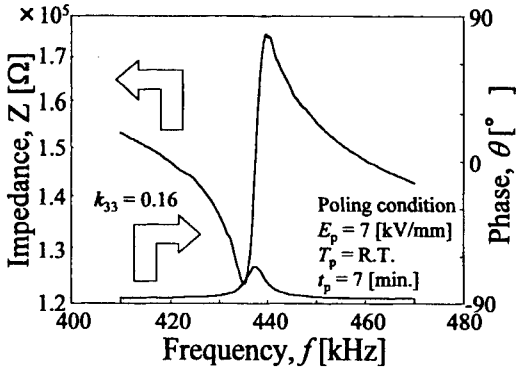

Fig.10 Frequency dependence of an impedance (magnitude and phase) of the BNTK-96 (E_p; a poling field, T_p; a poling temperature, t_p; a poling time).

4. CONCLUSIONS

(1-x)(Bi1/2Na1/2)TiO3-xKNbO3 [BNTK-100x] solid solution ceramics were prepared by using the hot-pressing (HP) method and the conventional ceramic technique (OF). The HP samples were studied by the X-ray diffraction and the dielectric measurements. From these results, the MPB composition of the BNTK-100x system seems to be existed around the BNTK-96. The HP samples could not be measured for applying a high voltage such as the observation of the D-E hysteresis loops and the piezoelectric properties because of many cracks. The dense ceramics were prepared by optimizing the process of the conventional (OF) ceramic technique. The D-E hysteresis loop was observed at BNTK-98 without saturation. The electromechanical coupling factor, k_{33}, of the OF BNTK-96 was 0.16. In future work, it should be enhanced the resistivities to be fully poled the OF ceramic samples by some dopants.

Acknowledgment

This work was partially supported by a Grant-in-Aid for Scientific Research (B) (No. 11555168) from the Japan Society for the Promotion of Science.

References

(1) T. Takenaka and H. Nagata: *Electroceramics in Japan I (Proceedings of the 17th Electronics Division Meeting of the Ceramic Society of Japan)*, pp.57~63 (1998).

(2) T. Takenaka: *Ferroelectrics* **230** (1999) 87.

(3) H. Nagata and T. Takenaka: *Proc. the 12th IEEE International Symposium on the Applications of Ferroelectrics (ISAF XII 2000)* (IEEE Catalog No.00CH37076) pp. 45~51 (2001).

(4) G. A. Smolensky, V. A. Isupov, A. I. Agranovskaya and N. N. Krainik: *Sov. Phys.-Solid State* **2** (1961) 2651.

(5) K. Sakata and Y. Masuda: *Ferroelectrics* **95** (1974) 347.

(6) G. Shirane, R. Newnham and R. Pepinsky: *Phys. Rev.* **96** (1954) 581.

(7) K. Nakamura and Y. Kawamura: *IEEE Trans. Ultrason. & Ferroelectrics & Freq. Control* **47** (3) (2000) 750.

(8) T. Takenaka. K. Maruyama and K. Sakata: *Jpn. J. Appl. Phys.* **30** (9B) (1991) 2236.

(9) R. E. Jaeger and L. Egerton: *J. Am. Ceram. Soc.* **45** (1962) 209.

(10) G. H. Haertling: *J. Am. Ceram. Soc.* **50** (1967) 329.

(11) S. E. Park and K. S. Hong: *J. Appl. Phys.* **79** (1) (1995) 383.

(12) J. K. Lee, H. J. Youn and K. S. Hong: *J. Mater. Res.* **14** (1999) 83.

Shaped Growth of Oriented Single Crystal Rods and Fibers in the $(Bi_{1/2}Na_{1/2})_{1-x}Ba_xZr_yTi_{1-y}O_3$ (BNBZT) System

B.P. Nunes, J. Shen, A.N. Soukhojak and Y.-M. Chiang
Massachusetts Institute of Technology
Room 13-4086, 77 Mass. Ave., Cambridge, MA 02139
FAX 617-253-6201
Email: ychiang@mit.edu

ABSTRACT

Electrostrictive and piezoelectric single crystals of defined cross-sectional shape and orientation can be used in various transducer, sensor, and actuator technologies to take advantage of unique orientation-dependent electromechanical properties. Here we have used the Stepanov technique (ST) and Edge-defined Film-fed Growth (EFG) to grow oriented single crystal rods and fibers of the perovskite solid solution $(Bi_{1/2}Na_{1/2})_{1-x}Ba_xZr_yTi_{1-y}O_3$ (BNBZT). Electrostrictive and piezoelectric compositions of <001> and <111> orientations have been grown. Growth rates range from 3-5 mm/hr in the ST method to 15->200 mm/hr for EFG fibers. Structural, compositional, and electromechanical characterization of the resulting crystals are presented.

INTRODUCTION

The technologies that can benefit from incorporation of high performance oriented single crystal perovskites also require scalable and economical processing methods. In this work we have used two shaped crystal growth methods, the Stepanov technique (ST) and Edge-defined Film-fed Growth (EFG), to grow oriented single crystal rods and fibers in the congruently melting perovskite system $(Bi_{1/2}Na_{1/2})_{1-x}Ba_xZr_yTi_{1-y}O_3$ (BNBZT). These methods are capable of continuous growth of net-shape cross-sections. Recent studies of $(Bi_{1/2}Na_{1/2})_{1-x}Ba_xTi_1O_3$ (BNBT) single crystals[1-3] have shown that low-hysteresis <001> (pseudocubic indices are used unless otherwise specified) actuation occurs in the rhombohedral ferroelectric phase, mechanistically identical to the behavior of rhombohedral phase PMNT and PZNT single crystals.[4] Actuation along <111> in the tetragonal ferroelectric phase is likewise expected to yield low hysteresis. The BNBZT system exhibits rhombohedral and tetragonal phase fields which at room temperature exhibit ferroelectric or macroscopically paraelectric behavior. In the paraelectric phase fields, unusually high electrostrictive actuation has recently been reported.[5,6] As we show, the BNBZT compositions of interest can be crystallized directly from the melt (i.e., they are congruently melting or nearly so), and have moderate melting points of 1230-1250°C. Thus the BNBZT system is a good candidate system for shaped crystal growth, in addition to being a lead-free system of reduced toxicity and volatility compared to lead perovskites.

EXPERIMENTAL PROCEDURE

A conventional rf-heated Czochralski crystal puller was adapted for ST growth, while a custom-designed grower with a resistance-heated furnace was constructed for EFG growth (Advanced Crystal Products). The furnace and die designs of the two approaches are shown in Fig. 1. Stepanov growth utilizes a floating shaper, while EFG utilizes a capillary shaper; both were constructed from platinum. The ST apparatus was used to grow rods of 1-3mm diameter, at growth rates of typically 3-5 mm/h. The EFG apparatus was used to grow 250-700 μm fibers at 15 to >200 mm/hr rates. $SrTiO_3$ (STO) single crystals of <001> and <111> orientation were used. BNBZT powders prepared by solid-state reaction were used as charge material. The resulting crystals were cut and polished for EPMA analysis of composition variations along and across the fiber axis, x-ray diffraction (θ-2θ scan and pole figures), and fabricated into 1:3 composites. Electromechanical tests were conducted on sections of single crystal rods and on the 1:3 composites.

RESULTS AND DISCUSSION

Figure 2 shows a cross-section cut from a typical ST crystal grown at 3 mm/h rate using a

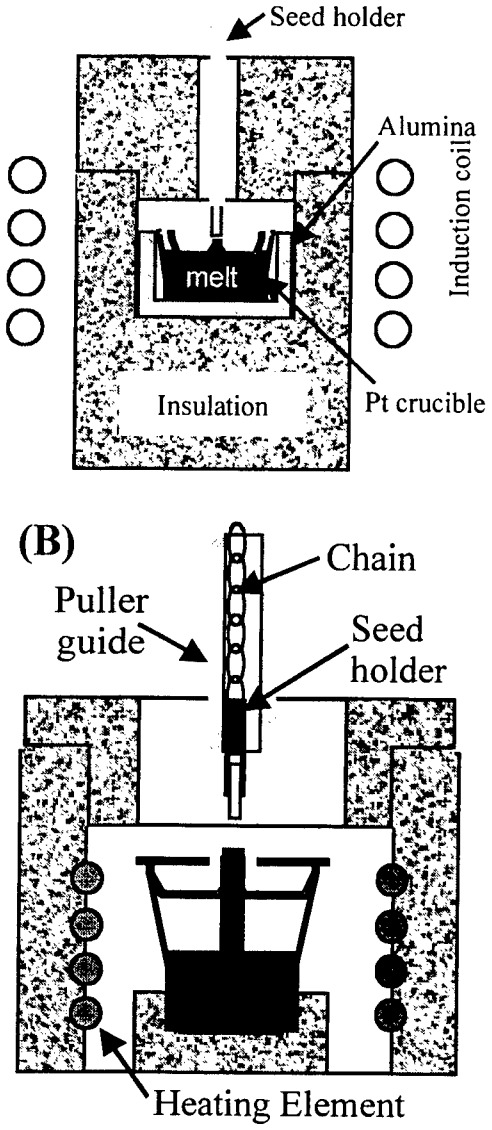

Figure 1. Schematic illustration of (A) Stepanov growth, and (B) EFG growth.

<111> oriented seed. The corresponding θ-2θ scan and pole figure shows that a single crystal oriented to within ~1° of the desired <111> axis has been obtained.

The two crystal growth methods differed considerably in the level of composition control. Stepanov growth allows the growing crystal to equilibrate to a greater extent with the melt source, whereas in EFG the melt source is effectively limited to a small volume within the capillary tube. EPMA analysis showed that the ST crystals incorporated less Ba than the nominal charge composition, and also had a significant degree of grown-in B-site cation deficiency resulting in A/B = 1.05-1.10. We believe that the B-site deficiency, which does not occur in flux-grown crystals, systematically shifts the phase stability diagram for BNBZT with the vacancy acting as an effective ion of larger radius than Ti^{4+}. Consistent with this interpretation was the observation of electrostrictive actuation at doping levels which, in stoichiometric compositions, should have been ferroelectric. Higher Ba doping was introduced to compensate for this effect. Figure 3 shows an example of unipolar and bipolar actuation strain vs. electric field for a disc cut from a <111> oriented single crystal rod.

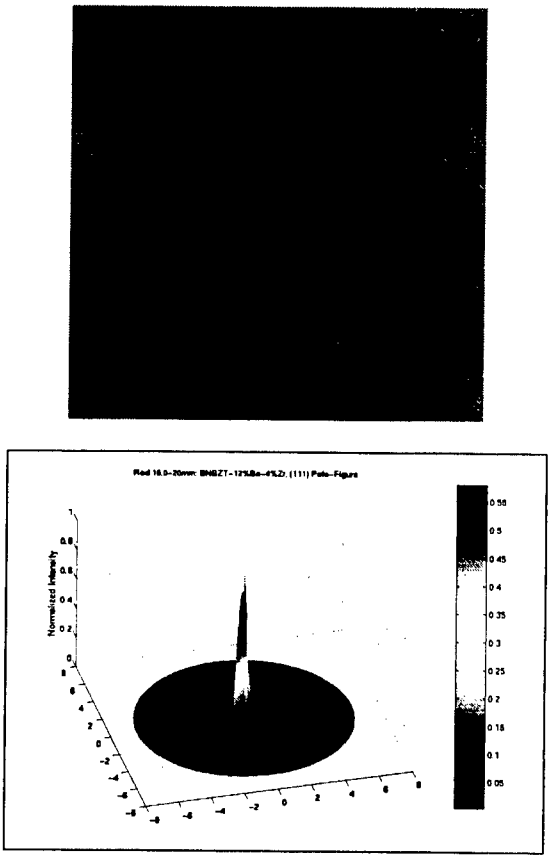

Figure 2. Cross-section of <111> oriented BNBZT rod grown by the Stepanov technique, and its x-ray pole figure.

Greater volatilization of melt components occurred in ST growth than in EFG due to the slower growth rate and differences in crucible sealing. The most volatile species from BNBZT melts is bismuth oxide, condensation of which could be detected within the furnaces after long growth times. Upon sufficient Bi loss from the melt, Bi-deficient secondary phases could be

detected in some of the ST crystals. However, despite clear evidence of Bi loss, EPMA analysis of ST-grown crystals still showed B-site cation deficiency resulting in A/B > 1. This suggests that the congruently melting composition of BNBZT is B-site deficient.

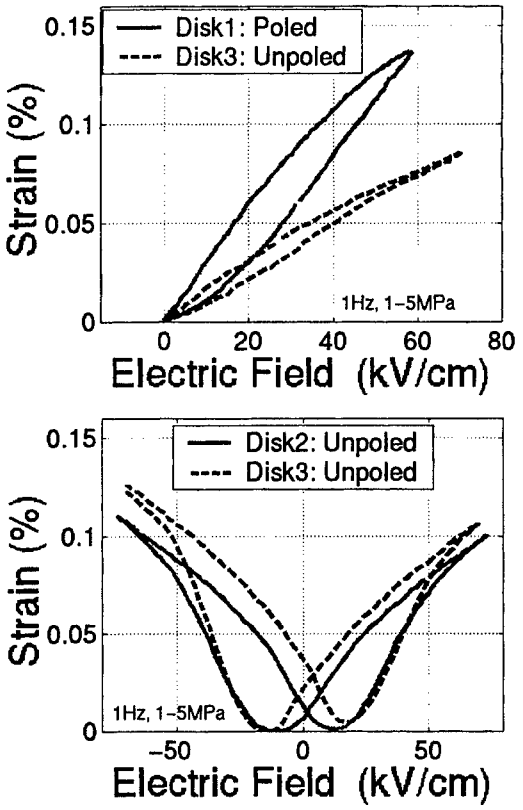

Figure 3. Unipolar and bipolar actuation in ST-grown BNBZT single crystal of <111> orientation and x=0.152, y=0.028 composition, lying within tetragonal ferroelectric phase field.

EFG growth, on the other hand, resulted in compositions that were close to the starting material composition in both doping level (within 0.5% in all constituents) and A/B stoichiometry (1 < A/B < 1.04). This is attributed to the much higher growth, decreasing the exposure time for the liquid meniscus between the growing crystal and the die tip. Ba segregation into the melt is also decreased as the growth rate increases.

Figure 4 shows <111> oriented EFG fibers of 700 μm diameter. When grown at rates of 15 mm/hr, a hexagonal cross-section results, whereas at 30-60 mm/hr, a cross-section with 3-fold symmetry results. It is also seen that the slower rate results in a rougher, microfacetted surface. Fibers as fine as 250 μm diameter, the desired diameter for active-fiber composites (AFCs), were readily grown to lengths >60 cm before growth was terminated. Figure 5 shows <001> oriented fibers, with approximately square cross-section exposing {001} faces, grown in a single run in which the rate was varied from 30 to 160 mm/hr.

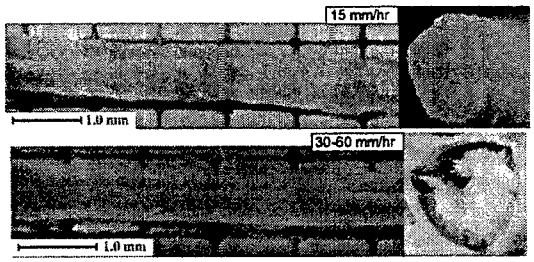

Figure 4. EFG single crystal fibers of <111> orientation and 700 μm diameter.

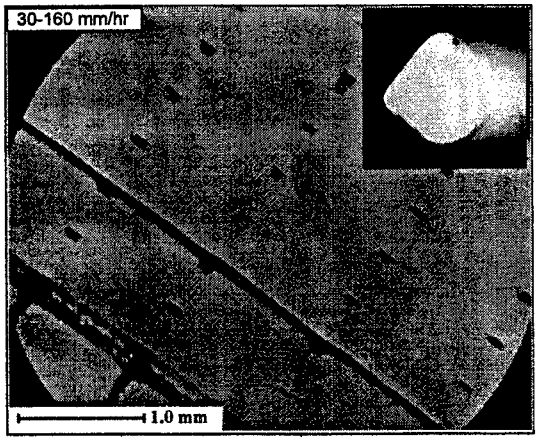

Figure 5. 250 μm diameter EFG fibers of <001> orientation, grown to >60 cm total length.

Figure 6 shows 1:3 composites fabricated from <111> and <001> oriented EFG fibers of ~500 μm diameter. These two fibers were grown from the same charge, and have a composition, x=0.14, y=0.03, which lies within the tetragonal ferroelectric phase field.[5,6] Figure 7 shows unipolar and bipolar strain vs. field measurements of these composites. It is seen that the <001> oriented composite exhibits higher actuation strain but with substantial hysteresis, as expected from domain switching in this orientation. The <111> orientation shows lower hysteresis, but also lower actuation for this particular composition.

These results demonstrate that the continuous growth of single crystal active fibers

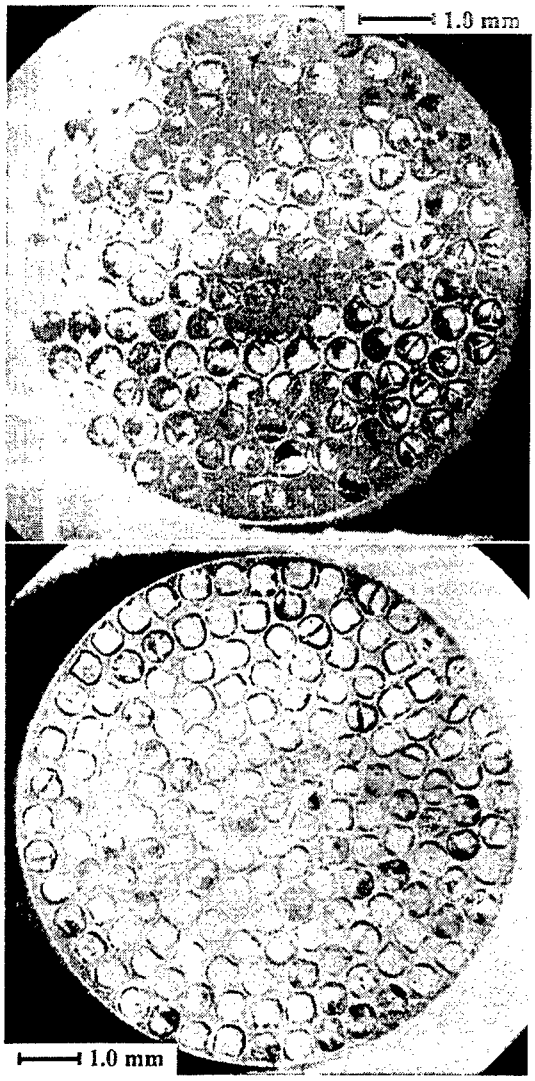

Figure 6. 1-3 composites fabricated from EFG grown <111> fiber (top) and <001> fiber (bottom).

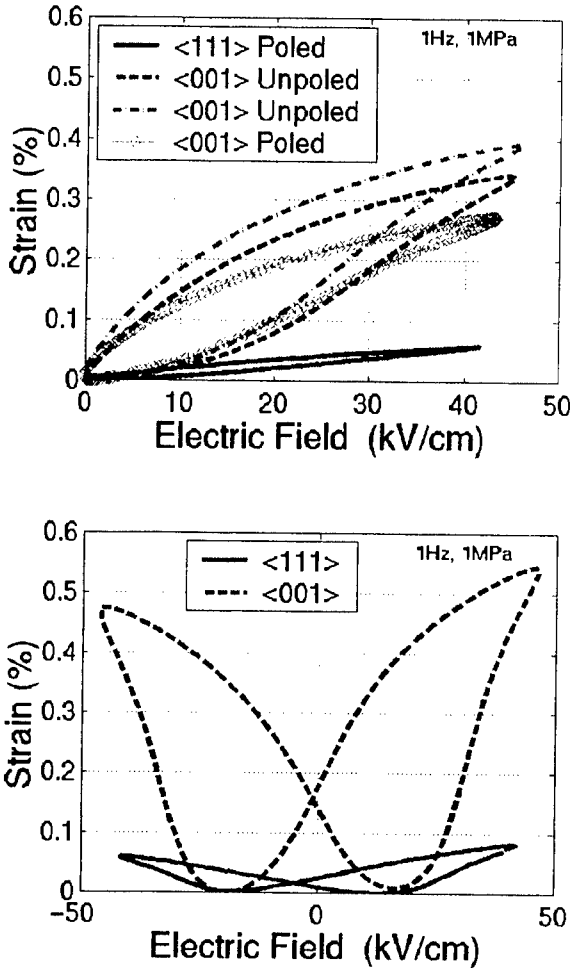

Figure 7. Strain vs. electric field for the 1-3 composites shown in Fig. 6.

with precise control of crystallographic orientation, and at technologically relevant rates, is possible using EFG. Additional work is necessary to further improve composition control and crystal quality. Growth of additional compositions, such as those which in flux-grown single crystals have shown unusually high electrostrictive actuation,[5] or of rhombohedral phase ferroelectric compositions which in <001> orientation are expected to show low hysteresis actuation with higher d_{33} than the <111> oriented samples shown here, is underway.

This work was supported by ONR Grants N00014-97-0989 and N00014-00-1-0424, and AFOSR/DARPA Grant No. F49620-99-2-0332.

References

1. Y.-M. Chiang, G.W. Farrey, and A.N. Soukhojak, *Appl. Phys. Lett.*, **73** [25] 3683 (1998).
2. Y.-M. Chiang, G.W. Farrey, A.N. Soukhojak, S.A. Sheets, "Growth and Characterization of Alkaline Bismuth Titanate Single Crystal Piezoelectrics," 9th US-Japan Seminar on Dielectric and Piezoelectric Ceramics, Nov. 3-5, 1999, Okinawa, Japan.
3. A.N. Soukhojak and Y.-M. Chiang, "Electrorheological Model of High-Strain Active Materials," *Proc.of the 2000 12th IEEE Intl. Symp. on Appl. of Ferroelectrics*, pp. 557-560 (2001).
4. S.-E. Park and T. R. Shrout, *J. Appl. Phys.*, **84** [4] 1804-11 (1997).
5. S.A. Sheets, A.N. Soukhojak, N. Ohashi, and Y.-M. Chiang, *J. Appl. Phys.*, in press.
6. S.A. Sheets, A.N. Soukhojak, N. Ohashi, and Y.-M. Chiang, these proceedings.

High Electrostrictive Strain Relaxors Based on Sodium Bismuth Titanate

S.A. Sheets, A.N. Soukhojak, N. Ohashi, and Y.-M. Chiang
Massachusetts Institute of Technology
Room 13-4006, 77 Mass. Ave., Cambridge, MA 02139
FAX 617-253-6201
Email: ansou@mit.edu

ABSTRACT

Single crystals have been grown in the $(Bi_{1/2}Na_{1/2})_{1-x}Ba_xZr_yTi_{1-y}O_3$ (BNBZT) perovskite system by a self-flux method over the range of compositions y = 0.04 and x = 0.06-0.012. While rhombohedral ($x \leq 0.08$) and tetragonal phase ($x \geq 0.09$) crystals have been obtained, none show polarization or field-induced strain hysteresis characteristic of a ferroelectric. However, frequency-dispersive dielectric response characteristic of a relaxor ferroelectric, and predominantly electrostrictive actuation, is observed across the range of compositions tested, with Q_{11} = 2.8-3.3 x 10^{-2} m^4/C^2. Due to induced polarizations that do not saturate at fields beyond 50 kV/cm, high electrostrictive strains are obtained. Rhombohedral phase crystals exhibit d_{33} up to 1180 pC/N and strains of S_3 = 0.3% before electrical breakdown, while tetragonal phase crystals exhibit d_{33} up to 2000 pC/N and S_3 up to 0.45% strain. These crystals show the highest electrostrictive strains yet reported for an inorganic compound. The unusually high electrostriction is attributed to peculiarities of the energy landscape that allow ferroelastic and ferroelectric distortions to be simultaneously accessible.

INTRODUCTION

Alkaline bismuth titanates with mixed A-site cations based on the prototype $(Na_{1/2}Bi_{1/2})TiO_3$[1] (BNT) exhibit complex and interesting phase behavior including ferroelastic, ferroelectric and relaxor-ferroelectric transitions, often occurring nearly simultaneously. Compared to lead perovskites exhibiting high piezoelectric or electrostrictive response such as PZT and PMN, commercially used in transducers, sensors, and actuators for over 30 years, these compounds are of interest due to their reduced toxicity, ease of processing, higher elastic moduli, lower density, higher strength, and higher fracture toughness. These physical properties improve mechanical reliability or certain weight-based figures of merit (e.g. actuation authority or energy density). Recent studies of $(Bi_{1/2}Na_{1/2})_{1-x}Ba_xTi_1O_3$ (BNBT) single crystals[2-5] have shown that a variety of electromechanical actuation characteristics can be obtained depending on the composition and phase of the crystal. Low-hysteresis [001] (pseudocubic indices are used unless otherwise specified) actuation has been observed in the rhombohedral ferroelectric phase, mechanistically identical to the behavior of PMNT and PZNT single crystals[6] oriented to have domain polarization vectors symmetrically oriented about the actuation field vector. Grown-in cation nonstoichiometry has been correlated with high d_{33} in the BNBT crystals,[4] with the rhombohedral phase showing d_{33} up to 650 pC/N and k_t up to 0.57. Unusual electromechanical behavior has also been observed in tetragonal phase BNBT crystals. Bipolar actuation strain up to 0.85% was observed in a [001] oriented, highly nonstoichiometric tetragonal phase BNBT crystal,[2,4] but while the strain vs. field loop of this material showed a "butterfly" shape suggesting domain switching, the corresponding polarization vs. field relationship was found to be much less hysteretic.[5] Electrorheological modeling[7] indicated that the electromechanical response of this and other doped BNTs contains a significant electrostrictive component, and an unusual decoupling of polarization and strain in the time domain.

Here we show that by simultaneously doping on the A and B sites, the Curie temperature can be suppressed in BNT solid solutions, resulting in rhombohedral and tetragonal phases that are macroscopically nonferroelectric at room temperature, but which exhibit relaxor characteristics. By doping simultaneously on the A-site with Ba and the B-site with Zr, we stabilized the paraelectric phase (which is antiferroelectric for certain compositions[2,8]) to below room temperature. We present the results of characterization of a series of BNBZT single crystals, containing 4% Zr and

6-12% Ba, that exhibited unusually high electrostriction.

EXPERIMENTAL PROCEDURE

The crystals were grown from a flux containing only constituents of the desired perovskite composition (self-flux method). Table I lists the nominal compositions and conditions for flux growths (numbered 1-5) that produced crystals of sufficient size and quality for testing. The lowercase letters following the batch number represent individual samples that were prepared from that growth.

Table I. Nominal Batch Compositions and Growth Schedules for BNBZT Single Crystals

$(Na_{1/2}Bi_{1/2})_{1-x}Ba_x(Ti_{1-y}Zr_y)O_3$

Batch	mole fraction Ba^{2+} (x)	mole fraction Zr^{4+} (y)	Self-Flux Growth Temperature Schedule
1	0.08	0.03	R.T. ♦ 1350°C @ 100°/h, hold 5 h; 1350°C ♦ 800°C @ 5°/h; 800°C ♦ R.T. @ 50°/h.
2	0.08	0.03	R.T. ♦ 1350°C @ 100°/h, hold 5 h; 1350°C ♦ 1260°C @ 100°/h, hold 1 h; 1260°C ♦ 1000°C @ 1.5°/h; 1000°C ♦ R.T. @ 50°/h
3	0.06	0.03	
4	0.10	0.03	
5	0.10	0.03	

The details of the sample preparation are reported elsewhere[9]. X-ray diffraction of single crystals and of powder ground from single crystals confirmed that they were of perovskite structure, and allowed the macrosymmetry (rhombohedral or tetragonal phase) to be determined.

Polarized-light optical microscopy was used to observe microdomain patterns or the absence thereof. High resolution electron microscopy (HREM) was conducted to observe nanometer-scale domains, using a JEOL 2010 instrument equipped with a double-tilt stage.

Compositional analysis was performed using a JEOL JXA-733 Electron Probe Microanalyzer (EPMA)[9]. Dielectric measurements were made using a Hewlett Packard 4192A impedance analyzer. Due to permittivity maxima overlap, the temperature of the dielectric maximum T_m was determined for each frequency from the minimum in second derivative of the smoothed data. The frequency (f) dispersion of the permittivity maxima was analyzed with the Vogel-Fulcher relation.

For electromechanical measurements, poling was first attempted by cooling from 200°C to room temperature at a constant field between 20 – 25 kV/cm. High-field induced strain and polarization were then measured simultaneously, at 0.05, 1, and 20 Hz frequency, using a laser interferometer apparatus with automated data collection software (Trek Model 10/40 high voltage amplifier with a Philips digital function generator). The differential piezoelectric strain coefficient d_{33} was measured directly from the slope of the strain vs. field curves.

RESULTS AND DISCUSSION

Crystal Growth and Characterization

As-grown crystals of both phases often showed no visible domains by optical microscopy.

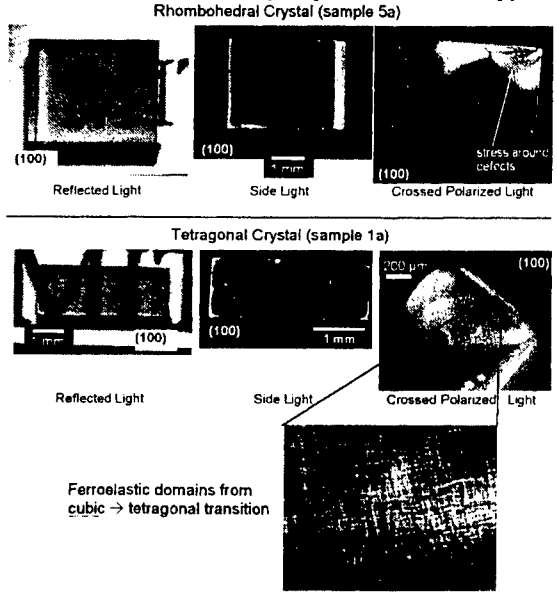

Fig. 1. Optical microfeatures of oriented and polished BNBZT single crystals.

The rhombohedral phase crystal in Fig. 1 is one such example. In contrast, the tetragonal phase crystal in Fig. 1 is an example of a crystal that did exhibit a microdomain structure, here oriented along [110]. Some crystals showed regions of visible microdomains coexisting with clear featureless regions, suggesting that the appearance of optically detectable microdomains is highly sensitive to sample composition or thermal history. While the appearance of 90° misoriented microdomains in tetragonal phase crystals is expected due to the transformation from the high-temperature cubic phase upon cooling, the absence of microdomains in samples that have undergone the cubic-tetragonal or cubic-rhombohedral phase transition is more

unusual. Note that even when microdomains were present, no significant change in the low-field dielectric constant indicative of poling was observed for fields applied along [001]. This suggests that the microdomains, where present, are ferroelastic but not ferroelectric.

HREM was conducted on a representative crystal containing 4% Zr and 11% Ba, and revealed domains of several nanometers scale, as shown in Fig. 2. Since undoped BNT and BNBT crystals have also exhibited domains of similar size scale in HREM, it is likely that nanodomain structures are widespread in many doped BNTs. We believe these to be the nanopolar domains responsible for relaxor properties.

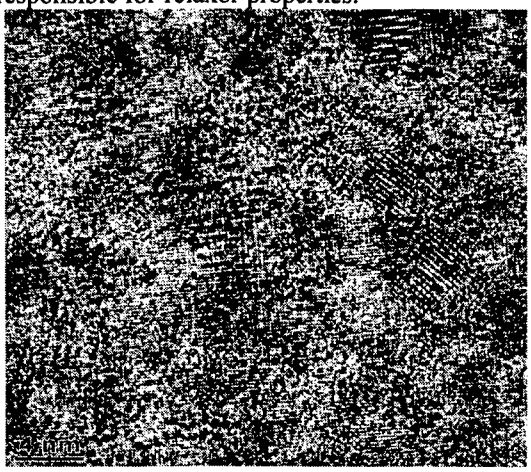

Fig. 2. [001] HREM of BNBZT (4% Zr, 11% Ba)

EPMA analyses of the single crystals (Table II) showed that less Ba was generally incorporated than the nominal composition at the 1.5°C/hr cooling rate (growths 2, 4, 5). From the EPMA analysis, all of the crystals are nearly stoichiometric in cation composition.

Table II. Composition (EPMA) and Phase (XRD) for BNBZT Single Crystals.

		compositions given in mole fraction (normalized to unity on B-site except where indicated by *)							
Sample	Nominal (Ba/Zr)	Na	Bi	Ba	Ti	Zr	O	(Na+Bi+Ba)/ (Ti+Zr)	Macro-symmetry
1a	8/3	0.45	0.43	0.12	0.91	0.04	2.88	1.05	T
1b	8/3	0.47	0.43	0.10	0.90	0.04	2.86	1.06	T
2a	8/3	0.50	0.45	0.05	0.94	0.04	2.94	1.02	R
2b	8/3	0.49	0.46	0.05	0.96	0.04	2.97	0.99*	R
2c	8/3	0.49	0.45	0.06	0.95	0.04	2.94	1.01	R
4b	10/3	0.49	0.43	0.09	0.96	0.04	2.97	1.00	T
4c	10/3	0.50	0.45	0.06	0.96	0.04	2.97	1.00	R
4d	10/3	0.49	0.44	0.07	0.94	0.04	2.94	1.02	R
5a	10/3	0.49	0.46	0.06	0.96	0.04	2.97	1.00	R
5b	10/3	0.50	0.44	0.06	0.89	0.04	2.80	1.08	R

* composition was normalized to unity on the A-site
R = rhombohedral, T = tetragonal

X-ray diffraction (θ-2θ scans) of single crystals and ground powders confirmed that the samples were single-phase perovskites, and allowed the macrosymmetry of the perovskite phase to be determined. Table II shows that at 4% Zr doping, the morphotropic phase boundary (MPB) between rhombohedral and tetragonal macrosymmetry phases lies between 7% and 9% Ba.

Phase Diagram Based On Low-Field Permittivity Measurements

We have used the two overlapping characteristic permittivity maxima (see Fig. 3) to construct a "phase diagram" for doped BNTs as shown in Figure 4. The detailed interpretation of the phase boundaries is given elsewhere[9].

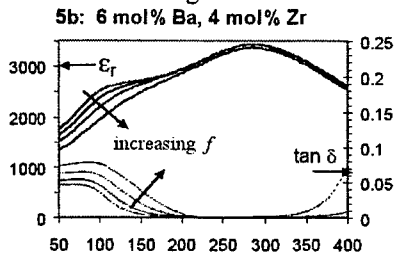

Fig. 3. Typical for BNBZT permittivity/loss temperature and frequency (1-1000 kHz) dependence.

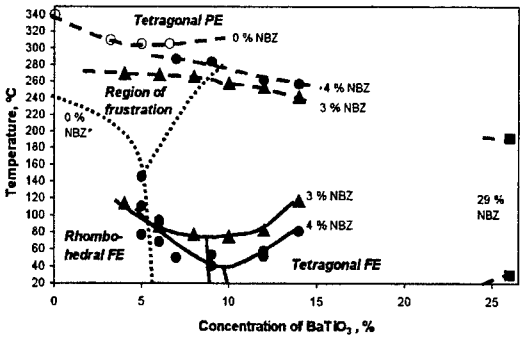

* T Takenaka et al Jap J Appl Phys 30 2236-9 (1991)

Fig. 4. Phase diagram for doped BNTs (FE – ferroelectric, PE – paraelectric).

The main point illustrated by Fig. 4 is expansion of the region of frustration between competing lattice distortions due to doping with Zr. We believe a crystal in the distortionally frustrated state in general has higher sensitivity to external fields and higher actuation strain in particular. Noting the absence of optically-detectable microdomains in many of the crystals, but the presence of nanodomains (Fig. 2), we suggest that multiple shallow energy minima exist for ferroelastic and ferroelectric distortions

at the atomic scale, and contribute to the high electrostrictive strain.

High-Field Measurements

None of the single crystals in this study exhibited noticeable changes in capacitance after the poling procedure. The absence of remnant polarization was also evident in the high-field polarization data: all crystals showed nearly linear and low-hysteresis polarization loops, with permittivities of 5000-7000.

Fig. 5 shows actuation strain of both rhombohedral and tetragonal single crystals (data for polycrystalline samples of same compositions[10] are included for comparison). The values of electrostrictive coefficient Q_{11} range from 2.8 to 3.3 m^4/C^2 for BNBZT single crystals as well as polycrystals. In the case of BNBZT, the fact that the polarization does not saturate until much higher fields, in excess of 50 kV/cm, also contributes to higher electrostrictive strain. We observed differential d_{33} up to 1180 pC/N in the rhombohedral phase, and up to 2000 pC/N in the tetragonal phase. These exceed the highest values previously reported (~1100 pC/N, PMNT system) for any inorganic electrostrictive compound, although it must be recognized that the fields necessary to access such actuation are greater than desired in many practical applications.

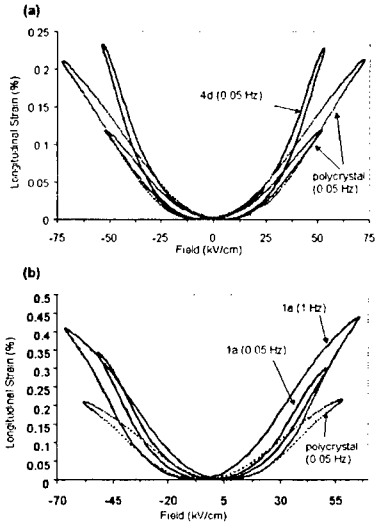

Fig. 5. Field-induced strain in [001] single crystals and polycrystalline electrostrictors of same composition. (a) rhombohedral phase; (b) tetragonal phase.

To our knowledge, BNBZT exhibits not only the highest ultimate electrostrictive strains of any lead-free perovskite reported, but of any inorganic compound to date.

Highly electrostrictive single crystals represent a different approach to increased electromechanical actuation than "domain engineering" whereby ferroelectric crystals are oriented along axes with symmetrically distributed polarization vectors. In the absence of micropolar ferroelectric domains, selective orientation for this purpose is obviously unnecessary. Poling is also unnecessary for electrostrictive single crystals, nor is stress-depoling a concern. Finally, since the electrostrictive single crystals are not actuated near a first-order phase transition temperature, the temperature stability of electrostriction should be quite good.

This work was supported by ONR Grant No. N00014-97-0989 and AFOSR/DARPA Grant No. F49620-99-2-0332.

References

1. G.A. Smolenskii, V.A. Isupov, A.I. Agranovskaya and N.N. Krainik, *Sov. Phys. - Solid State*, **2** [11], 2651 (1961).
2. Y.-M. Chiang, G.W. Farrey, and A.N. Soukhojak, "Lead-Free High Strain Single Crystal Piezoelectrics," *Appl. Phys. Lett.*, **73** [25] 3683 (1998).
3. G.W. Farrey, A.N. Soukhojak, S. Sheets, and Y.-M. Chiang, "Growth and Characterization of $Na_{1/2}Bi_{1/2}TiO_3$-$K_{1/2}Bi_{1/2}TiO_3$-$BaTiO_3$ Single Crystal Piezoelectrics," *IEEE Intl. Symp.on Appl. of Ferroelectrics*, 24-27 Aug. 1998, Montreux, Switzerland, June 1999, pp. 551-554.
4. Y.-M. Chiang, G.W. Farrey, A.N. Soukhojak, S.A. Sheets, "Growth and Characterization of Alkaline Bismuth Titanate Single Crystal Piezoelectrics," Proceedings of the 9th US-Japan Seminar on Dielectric and Piezoelectric Ceramics, Nov. 3-5, 1999, Okinawa, Japan, in press.
5. A.N. Soukhojak and Y.-M. Chiang, "Electrorheological Model of High-Strain Active Materials," *Proc.of the 2000 12th IEEE Intl. Symp. on Appl. of Ferroelectrics*, pp. 557-560 (2001)
6. S.-E. Park and T. R. Shrout, *J. Appl. Phys.*, **84** [4] 1804-11 (1997).
7. A.N. Soukhojak and Y.-M. Chiang, "Generalized Rheology of Active Materials," *J. Appl. Phys.*, **88** [11] 6902 (2000).
8. T. Takenaka,, K. Murayama and K. Sakata, "$(Bi_{1/2}Na_{1/2})TiO_3$-$BaTiO_3$ System for Lead-Free Piezoelectric Ceramics", *Jpn. J. Appl. Phys.* **30** [9B] 2236 (1991).
9. S.A. Sheets, A.N. Soukhojak, N. Ohashi, and Y.-M. Chiang, submitted to *J. Appl. Phys.*(2001).
10. S.A. Sheets, M.S. Thesis, MIT (2000).

Weak-Field Permittivity and High-Field Electromechanical Characterization of Ferroelectric Ceramics at Cryogenic Temperatures

C.J. Pagoda[1], M.L. Mulvihill[2], and S.M. Pilgrim[1]

[1]Laboratory for Electronic Ceramics
School of Ceramic Engineering and Materials Science
New York State College of Ceramics at Alfred University
2 Pine Street, Alfred, New York, 14802
[2]Xinetics Inc.
37 MacArthur Ave., Devens, MA 01432-4443
FAX: 607 871-3469
Email: pilgrim@alfred.edu

ABSTRACT

The weak-field relative permittivity and high-field polarization and longitudinal strain of several ferroelectrics compositionally modified for use at low temperatures were measured from room temperature to ~17 K in order to evaluate their performance as cryogenic actuators. The samples were provided by Xinetics Inc. and tested in the Laboratory for Electronic Ceramics at the New York State College of Ceramics at Alfred University. These samples are some of the first to be characterized in the newly modified cryogenic testing chamber.

INTRODUCTION

Background

Recent advancements in the space program have increased the need for electromechanical actuators that can operate at cryogenic temperatures (30 - 70 K). Projects like the Next Generation Space Telescope (NGST) rely on electromechanical actuators that must be able to operate at low temperatures in order to manipulate deformable mirrors.

Large electrostrictive strain observed in relaxor ferroelectrics such as PMN near T_{max} are of interest for transducer applications because of reduced hysteresis and improved response time over piezoelectric actuators.[1] Electrostrictive strain is proportional to the square of the polarization induced in the material by an applied electric field. Being able to take advantage of large electrostrictive responses at low temperatures, requires a low temperature T_{max} and large polarization. Although a number of materials show promise at cryogenic temperatures,[2, 3] none are fully suitable.

Weak-field characterization provides a method of estimating electromechanical performance evaluation at low temperatures. High-field polarization and strain measurements, however, are the only true characterization techniques that can be used to understand a material's electromechanical response.

Testing Chamber

Samples were characterized using the newly modified cryogenic high-vacuum (CHV) testing chamber. High-field polarization and longitudinal strain measurement capabilities with applied voltages up to 5 kV have recently been added to the improved weak-field characterization apparatus. High-vacuum, high-field electrical and equipment feedthrough flanges were custom designed with MDC Vacuum Products Inc. Samples were cooled using a Model DE-202 He-Displex® from Advanced Research Systems and a Scientific Instruments Series 5500 temperature controller. Sample temperature was measured with a silicon diode temperature sensor placed near the sample. Vacuum levels as low as 5E-8 Torr were achieved with a Varian M 6 diffusion pump.

EXPERIMENTAL PROCEDURE

The XiCryo-1 samples tested were obtained from Xinetics Inc. These are mixed A-site perovskites $A_{1-y}X_yBO_3$. Three samples with compositions y= 0.15, 0.20, 0.25, and 0.30 and 2 samples with y=0.02 were provided. Samples typically measured 0.9 mm in thickness and 10.4 mm in diameter. Weak-field measurements were performed on all samples. High-field measurements were performed on the two flattest samples of each composition capable of withstanding 2 MV/m drive fields.

Weak-Field Dielectric Measurements

Weak-field relative permittivity were measured using a Solartron SI 1260 Impedance/Gain Phase Analyzer. Samples were tested at 0.1, 1, 10, 100, and 1000 kHz using a four-point testing configuration and shielded cables to minimize parasitics from the complex wiring setup. Samples were cooled at 2 K/min from room temperature to ~17 K, held for 10 minutes to allow thermal equilibration, and then heated back to room temperature at 2 K/min. Data were collected using LabVIEW™.

High-Field Electromechanical Measurements

High-field measurements were performed by applying a 1 Hz AC signal to the sample with a maximum amplitude of 2 MV/m. The applied waveform was generated from a Stanford Research Systems DS 345 function generator and amplified with a Trek model 609-3 high voltage amplifier. Polarization measurements were performed using a modified Sawyer Tower circuit[4] with the integrating capacitor set to 10 μF. Longitudinal strain was measured with a custom, high-vacuum, low temperature Fotonic™ sensor model 2047R and MTI 2000 module manufactured by MTI Instruments. High–field data were collected using LabVIEW™.

Polarization measurements were performed on both cooling and heating. Samples were cooled at 2 K/min and the polarization was measured every 25 K after allowing five minutes for thermal equilibration. Heating measurements were performed at 2 K/min without thermal equilibration. Longitudinal strain could only be measured on heating due to sensitivity of the Fotonic™ sensor to large mechanical vibrations introduced when the He-Displex® is running.

Harmonic analysis of the applied electric field and high-field response were performed using a Diffuse Fourier Transform in Autosignal™ Select Version 1.0 (©1999 AISN Software Inc.). Filtering was performed on the frequency domain of the both the electric field and response waveform. 2000 data points were collected at a sampling frequency of 500 Hz resulting in a frequency resolution of 0.25 Hz over 4 complete cycles of the applied signal.

RESULTS AND DISCUSSION

Weak-Field Dielectric Response

Table I summarizes the 1 kHz κ'_{max} and T_{max} data for 15, 20, 25, and 30at% X samples. No T_{max} or κ'_{max} is included for 2at%X samples, which showed a continual increase in relative permittivity to near 6000 when cooled to ~17 K. κ'_{max} was typically 5% lower for all samples on heating. This drop is attributed to aging as concluded from several time dependent tests.[5] The difference in T_{max} on heating is attributed to both aging and a temperature lag. The κ'_{max} decreased for all samples with increasing frequency, while T_{max} increased slightly with frequency.

Table I Summary of 1 kHz κ'_{max} and T_{max} data for 15, 20, 25, and 25%X samples

		Cooling		Heating		% Change from Cooling	
		κ'_{max}	T_{max}	κ'_{max}	T_{max}	κ'_{max}	T_{max}
15%X	average	6888	94	6610	96	-4.0	2.5
	stdev	146	3	125	2	0.3	1.3
20%X	average	7003	112	6628	115	-5.3	2.7
	stdev	673	1	636	1	0.5	1.6
25%X	average	4178	129	3947	133	-5.5	2.9
	stdev	29	2	29	1	0.1	1.2
30%X	average	4102	146	3890	151	-5.1	3.5
	stdev	378	2	346	1	0.3	1.9

Figure 1 shows typical relative permittivity trends as a function of temperature for each of the compositions tested at 1 kHz. Samples with 20%X and lower exhibited larger κ'_{max} values than samples with 25 and 30%X addition. Diffuseness also increased with dopant concentration as expected from increased compositional heterogeneity.[6]

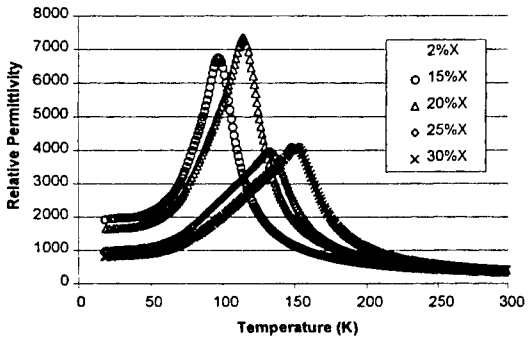

Fig. 1 Typical relative permittivity trends at 1 kHz measured during heating at 2 K/min.

High-Field Polarization

Figure 2 shows the average maximum polarization as a function of temperature for each of the five compositions tested. Due to high-field measurement problems, results for the 2%X composition are reported for one sample tested at 1 MV/m.

Maximum polarization (P_{max}) values increased to temperatures ~25 K below T_{max} for each of the compositions tested. The P_{max} then remained relatively constant for 15 and 20%

doping, while it decreased slightly for the 25 and 30% doping levels down to ~17 K. All 2%X samples exhibited a linear polarization response down to 25 K and therefore 2 MV/m data can be estimated at twice the magnitudes obtained from the 1 MV/m data. The 20%X samples exhibited the largest polarization responses below 100 K at more than 80 mC/m^2.

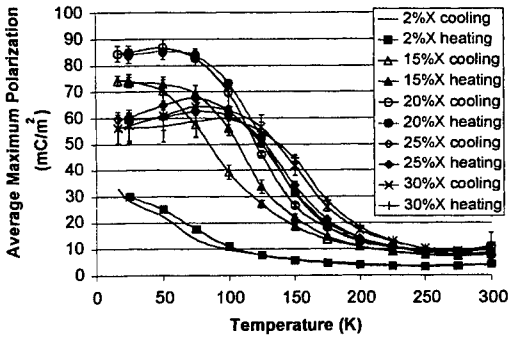

Fig. 2 Average maximum polarization as a function of temperature. (2%X sample tested at 1 MV/m, 15, 20, 25, and 30%X samples tested at 2 MV/m)

Figure 3 shows typical polarization curves for a 25%X sample from room temperature to ~17 K measured on both cooling and heating. Note the onset of saturation and hysteresis as T approaches T_{max} from the weak-field results. Similar polarization curve trends were observed for all compositions. All samples exhibited constriction in the P-E curves at low temperature (~17 K) near zero field. Constriction was more pronounced in 15 and 20at% samples and attributed to aging of the sample as determined from both weak-field and high-field time-based aging tests.[5]

High-Field Longitudinal Strain

All samples exhibited a primarily electrostrictive strain response above and below T_{max}, noted by the large fundamental response amplitude at 2 Hz (twice the drive frequency of 1 Hz) observed during the harmonic filtering procedure.[7] A typical strain response is shown in Figure 4. Maximum μstrain is reported for samples after harmonically filtering the response to include only even-order harmonics of the applied 1 Hz drive signal (i.e. 2, 4, 6 Hz etc). The maximum μstrain for 15, 20, 25, and 30%X samples are presented in Figures 5-8. The 2%X sample tested at 1 MV/m showed measurable strain of ~30 μstrain at 25, 50 and 75 K.

Mechanical noise within the system, to which the Fotonic™ sensor is highly sensitive, increased the measurement error of longitudinal strain data. This error was more evident in odd order harmonics of the response as determined after spectral analysis, which was another reason why only even order harmonics were maintained during the harmonic filtering procedure at this point. The longitudinal strain results do however provide some correlation to the polarization data as noted by the largest measured microstrain for the 20%X samples.

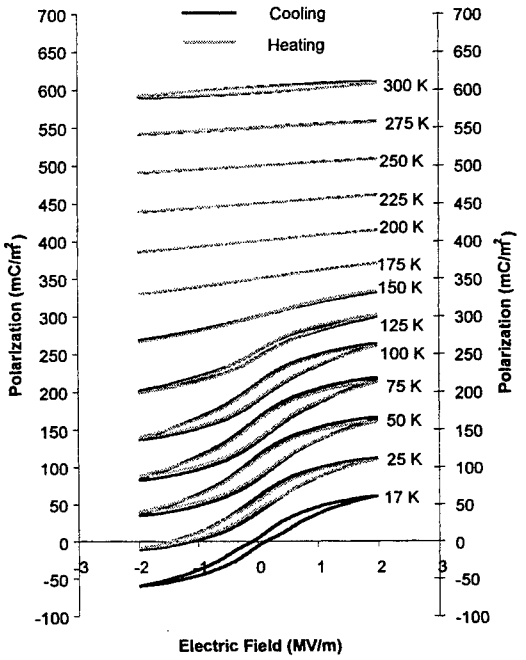

Fig. 3 Typical polarization curves as a function of temperature for a 25%X sample. (curves artificially offset 50 mC/m^2)

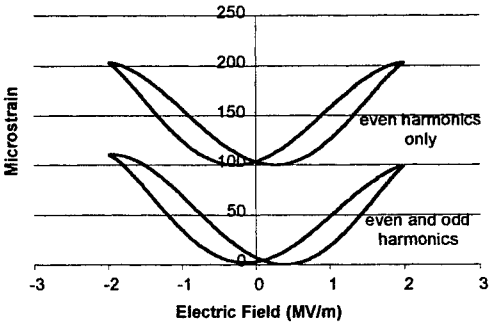

Fig. 4 Typical longitudinal strain response after harmonic filtering. Sample is a 30%X composition tested at 50 K.

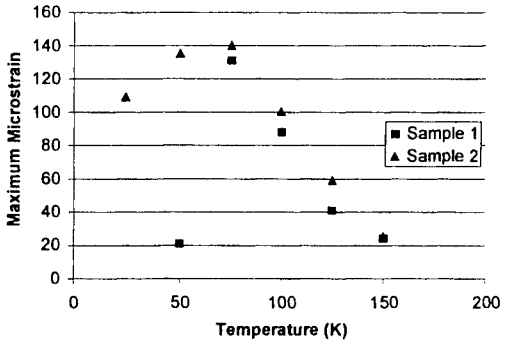

Fig. 5 Maximum microstrain for 15%X samples measured at 2 MV/m during heating at 2 K/min.

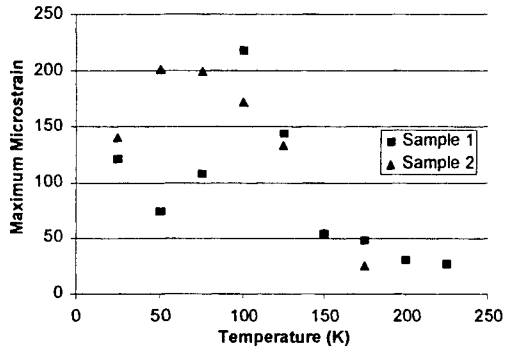

Fig. 6 Maximum microstrain for 20%X samples measured at 2 MV/m during heating at 2 K/min.

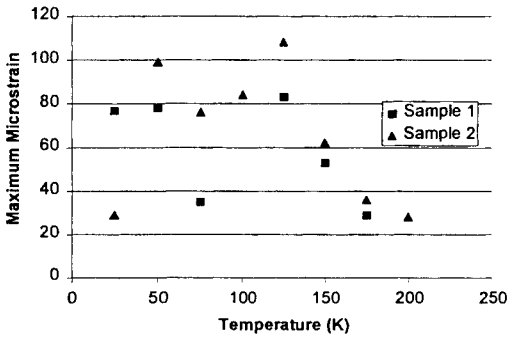

Fig. 7 Maximum microstrain for 25%X samples measured at 2 MV/m during heating at 2 K/min.

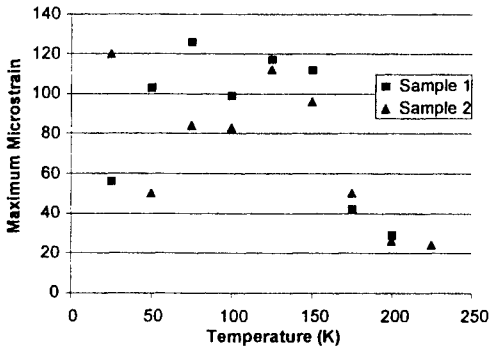

Fig. 8 Maximum microstrain for 30%X samples measured at 2 MV/m during heating at 2 K/min.

CONCLUSION

Although in its initial stages of use, the cryogenic characterization chamber shows great promise in evaluating the electromechanical response of ferroelectrics at low temperatures. Equipment modifications to reduce mechanical vibrations and measurement error in the longitudinal strain measurements are currently in progress. The groundwork has also been established for harmonic analysis of high-field data at low temperatures. Support of Xinetics is greatly appreciated for providing samples suitable to make this study possible.

REFERENCES

1. K. Uchino and S. Nomura, *J. Mater. Sci.*, 16, 569-578 (1981).
2. K. Toyoda, Ferroelectrics. Landolt-Börnstein, New Series, Group III, Volume 3. Springer-Verlag, Berlin, 1970.
3. F.S. Galasso, Perovskites and High Tc Superconductors; Gordon and Breach Science Publishers, NY (1990).
4. C. B. Sawyer and C. H. Tower, *Physical Review*, 35, 269-272 (1930).
5. W. A. Schulze and K. Ogino, *Ferroelectrics*, 87, 361-377 (1988).
6. G. A. Smolensky, *J. Phys. Soc. Jpn.*, 28, 26-37 (1970).
7. C. B. DiAntonio, "Harmonic Analysis of the Electromechanical Response of $Pb(Mg_{1/3}Nb_{1/3})O_3$-Based Compositions"; Ph.D. Thesis. New York State College of Ceramics at Alfred University, Alfred, 2001.

Cryogenic Characterization of Perovskite $Pb(Mg_{0.8}Ni_{0.2})_{1/3}Ta_{2/3}O_3$ and Tetragonal Tungsten Bronze $Ba_6FeNb_9O_{30}$ and $Ba_6CoNb_9O_{30}$ Relaxor Ferroelectrics

C.J. Pagoda and S.M. Pilgrim

Laboratory for Electronic Ceramics
School of Ceramic Engineering and Materials Science
New York State College of Ceramics at Alfred University
2 Pine Street, Alfred, Alfred, New York, 14802
FAX: 607 871-3469
Email: pilgrim@alfred.edu

ABSTRACT

In this work, the $Pb(Mg_{1-x}Ni_x)_{1/3}Ta_{2/3}O_3$ (PMNiT) relaxor-based ferroelectric system was compositionally modified with 20at%Ni to lower T_{max} and improve low temperature electromechanical response. Tetragonal tungsten bronze (TTB) compositions $Ba_6FeNb_9O_{30}$ (BFN) and $Ba_6CoNb_9O_{30}$ (BCN) were also characterized at cryogenic temperatures to further investigate reported ferroelectric behavior. Weak-field dielectric response and high-field electromechanical characterization were performed from 300 K to ~17 K.

INTRODUCTION

$Pb(Mg_{1-x}Ni_x)_{1/3}Ta_{2/3}O_3$ (PMNiT)

Large electrostrictive strain observed in Pb-based relaxor ferroelectrics such as PMN near T_{max} are of interest over piezoelectric transducers because of large electrostrictive strains comparable to the best piezoelectric ceramics, excellent positional reproducibility, no poling, and very low thermal expansion coefficients.[1]

Few studies have been performed on Pb-based relaxor ferroelectrics that exhibit a low T_{max}. Bokov and Myl'nikova report several Pb-based relaxors with a T_{max} below 200 K.[2] The most notable were single crystal $PbMg_{1/3}Ta_{2/3}O_3$ (T_{max}=175 K, κ'_{max}=7000) and $PbNi_{1/3}Ta_{2/3}O_3$ (T_{max}=93 K, κ'_{max}=2400). Nickel additions to $PbMg_{1/3}Ta_{2/3}O_3$ have been shown to lower T_{max}, but have also resulted in increased pyrochlore.[3]

$Pb(Mg_{0.8}Ni_{0.2})_{1/3}Ta_{2/3}O_3$ samples were therefore investigated to increase the perovskite yield and complete electromechanical characterization from room temperature to ~17K.

$Ba_6FeNb_9O_{30}$ (BFN) and $Ba_6CoNb_9O_{30}$ (BCN)

TTB ferroelectrics are an interesting class of ferroelectrics because of the large number of solid solutions possible that allow control of dielectric properties like κ'_{max} and T_{max}.[4] Reported dielectric anomalies in TTB $Ba_6FeNb_9O_{30}$ near 135 K[5, 6] and 583 K[7] along with slight hysteresis observed at room temperature[7] make this composition an interesting subject for cryogenic characterization down to ~17 K in order to better understand its ferroelectric behavior. A similar composition $Ba_6CoNb_9O_{30}$ will also be investigated. Both BFN[8] and BCN[9] are reported in space group *P4bm* at room temperature.

Testing Chamber

Samples were characterized using the cryogenic high-vacuum (CHV) testing chamber. Samples were cooled on a custom sample holder mounted to a Model DE-202 He-Displex® from Advanced Research Systems. Sample temperature was measured with a Scientific Instruments Series 5500 temperature controller and silicon diode temperature sensor placed near the sample. Vacuum levels as low as 5E-8 Torr were achieved with a Varian M 6 diffusion pump.

EXPERIMENTAL PROCEDURES

Sample Preparation

PMNiT: $Pb(Mg_{0.8}Ni_{0.2})_{1/3}Ta_{2/3}O_3$ was processed based on a modified Columbite precursor method[10] from high purity (99.9%) PbO, $MgCO_3$, $NiCO_3$ and Ta_2O_5 raw materials. $NiCO_3$, $MgCO_3$ and Ta_2O_5 powders were stoichiometrically batched to form the precursor $Mg_{0.8}Ni_{0.2}Ta_2O_6$ and ball-milled in methanol for 24 hours. They were then calcined at 1100°C for 4 hours, ground, and then calcined for an

additional 8 hours at 1100°C. PbO was then stoichiometrically added to the precursor and precalcined at 800°C for 4 hours. Pellets were dry-pressed at 112 MPa then buried in sacrificial powder of the same composition and fired at 1225°C for 1 hr in a covered alumina crucible

BFN and BCN: Both TTB compositions were prepared using typical solid-state reaction techniques with high purity (99.9%) $BaCO_3$, FeC_2O_4-$2H_2O$, CoC_2O_4-$2H_2O$, and Nb_2O_5 raw materials. Powders were stoichiometrically batched to form the final composition, wet-ball milled for 24 hrs, and then calcined at 1250°C for 4 hours. Pellets from the calcined BFN and BCN powders were pressed at 225 MPa and fired to 1325°C and 1312°C respectively for 24 hours and held for 6 hours at 500°C on cooling.

Phase identification was performed by x-ray diffraction (XRD) after finely grinding pellets of each composition. Patterns were collected using a Philips diffractometer (Cu K_α, 40 kV, 30mA), and phase identification was performed using Jade 5.0 (© 1991-1999 Materials Data Inc.). Remaining samples were polished and electroded with a fire on electrode paste (Du Pont 7095 65%Ag/35%Pd) for electrical measurements.

Weak-Field Dielectric Measurements

Weak-field relative permittivity and loss tangent were measured using a Solartron SI 1260 Impedance/Gain Phase Analyzer. Samples were tested at 0.1, 1, 10, 100, and 1000 kHz using a four-point testing configuration and shielded cables to minimize parasitics from the complex wiring setup. Samples were cooled at 2 K/min from room temperature to ~17 K, held for 10 minutes and then heated back to room temperature at 2 K/min. Data were collected using LabVIEW™.

High-Field Electromechanical Measurements

High-field measurements were performed by applying a 1 Hz AC signal to the sample with a maximum amplitude of 1 MV/m. The applied waveform was generated from a Stanford Research Systems DS 345 function generator and amplified with a Trek model 609-3 high voltage amplifier. Polarization measurements were performed using a modified Sawyer Tower circuit.[5,11] Longitudinal strain was measured with a custom, high-vacuum, low temperature Fotonic™ sensor model 2047R and MTI 2000 module manufactured by MTI Instruments. High–field data were collected using LabVIEW™.

Polarization measurements were performed on both cooling and heating. Samples were cooled at 2 K/min and the polarization was measured every 25 K after five minutes of thermal equilibration. Heating measurements were performed at 2 K/min without thermal equilibration. Longitudinal strain could only be measured on heating due to sensitivity of the Fotonic™ sensor to large mechanical vibrations introduced when the He-Displex® is running.

Harmonic analysis of the applied electric field and high-field response were performed using a Diffuse Fourier Transform in Autosignal™ Select Version 1.0 (©1999 AISN Software Inc.). 2000 data points were collected at a sampling frequency of 500 Hz resulting in a frequency resolution of 0.25 Hz over 4 complete cycles of the applied signal.[11]

RESULTS AND DISCUSSION

Sample Preparation

PMNiT: Figure 1 shows the pyrochlore free XRD pattern for PMNiT. The measured density was 8.76 g/cm^3 (90% theoretical).

BFN and BCN: Figure 2 shows the XRD pattern for the BFN and BCN samples. Also included is the PDF Card #77-2433 from the ICDD database for a calculated $Ba_6FeNb_9O_{30}$ pattern. The BFN experimental pattern shows good correlation to the calculated pattern. The BCN pattern shows the presence of high intensity peaks not permitted in P4bm. No PDF card is published to date for $Ba_6CoNb_9O_{30}$. BFN samples had a density of 5.02 g/cm^3 (87% theoretical[8]) and BCN samples had a density of 5.28 g/cm^3 (92% theoretical[9]).

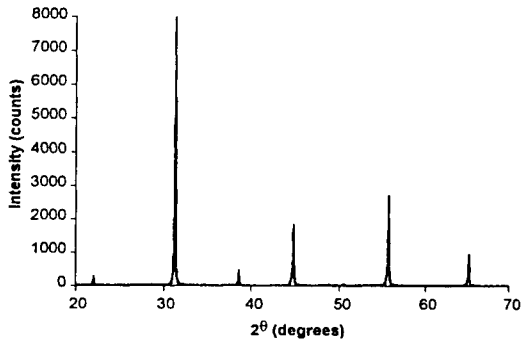

Fig. 1 X-ray diffraction pattern of a PMNiT sample after firing at 1225°C for 1 hour.

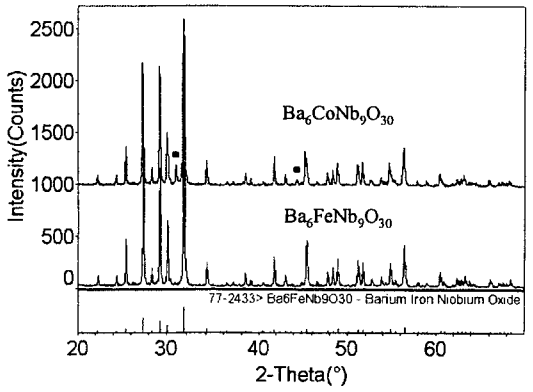

Fig. 2 XRD pattern of BFN and BCN after firing at 1325°C and 1312°C respectively for 24 hours. Highlighted peaks not permitted in *P4bm*.

Weak-Field Dielectric Measurements

PMNiT: Weak-field relative permittivity and loss tangent for a typical PMNiT sample is shown in Figure 3. The curves indicate a diffuse phase transition in agreement with previous studies of similar systems.[2, 3]

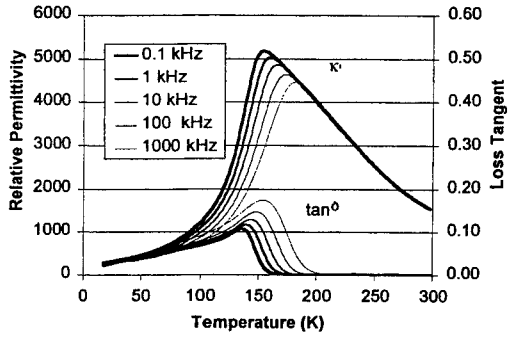

Fig. 3 Typical dielectric response for a PMNiT sample. (heating @ 2 K/min)

BFN and BCN: Weak-field relative permittivity and loss tangent as a function of temperature for a typical BFN sample is shown in Figure 4. BFN samples exhibited large relaxation loss peaks above 125°C, increasing the permittivity to as high as 10,000 near room temperature. Typical relaxor behavior is evident at higher frequencies. T_{max} of the permittivity anomaly at high frequencies is close to reported values.[5,6]

Weak-field relative permittivity and loss tangent as a function of temperature for a typical BCN sample is shown in Figure 5. A diffuse permittivity anomaly was observed between 150 and 300 K.

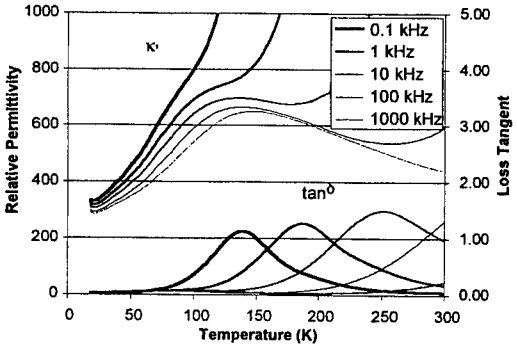

Fig. 4 Typical dielectric response for a BFN sample. (heating @ 2 K/min)

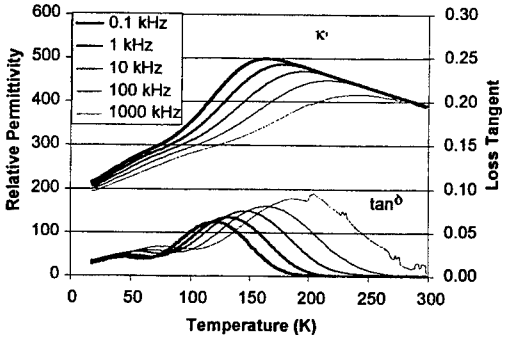

Fig. 5 Typical dielectric response for a BCN sample. (heating @ 2 K/min)

High-Field Electromechanical Measurements

PMNiT: The average maximum polarization (P_{max}) as a function of temperature for the PMNiT samples is shown in Figure 6. Samples exhibited linear response down to 150 K, with maximum hysteresis occurring at 100 K.

Longitudinal strain values were only measurable between 125 and 200 K with maximum longitudinal strain ranging between 20 and 30 μstrain. The strain response was primarily electrostrictive in nature.

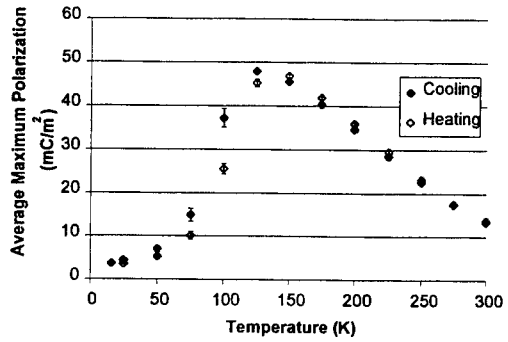

Fig. 6 Average maximum polarization as a function of temperature for PMNiT samples.

BFN and BCN: The large losses in BFN contributed to huge hysteresis in the polarization curves above 100 K (i.e. P_{max}=200 mC/m^2 @ 0.1MV/m at 300 K). The BCN samples, however exhibited a linear polarization response down to 150 K, below which slight hysteresis was observed. The maximum polarization as a function of temperature for the BCN samples are shown in Figure 7. Figure 8 shows the onset of hysteresis at 125 K for the BCN samples indicating a possible ferroelectric transition. Also included in Figure 8 is the polarization response of a BFN sample measured at 17 K, where loss was not a major problem. The magnitude of P_{max} and slight hysteresis indicate possible ferroelectricity. Longitudinal strain was not measurable in any of the BFN or BCN samples tested at 1 MV/m.

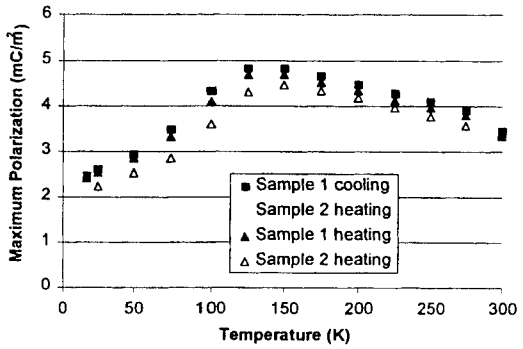

Fig. 7 Maximum polarization as a function of electric field for BCN samples.

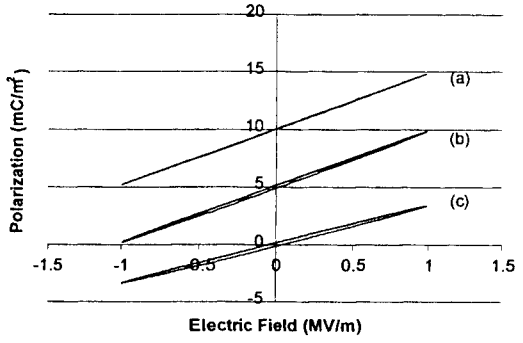

Fig. 8 Polarization curves for BFN and BCN samples at select temperatures (a) BCN at 150 K, (b) BCN at 125 K, (c) BFN at 17 K after 5 minute hold.

CONCLUSIONS

Pyrochlore free $Pb(Mg_{0.8}Ni_{0.2})_{1/3}Ta_{2/3}O_3$ was successfully prepared and characterized down to ~17 K providing groundwork for more in depth electromechanical characterization of Pb-based relaxor ferroelectrics at low temperatures. Both $Ba_6FeNb_9O_{30}$ and $Ba_6CoNb_9O_{30}$ compositions showed possible diffuse ferroelectric transitions at low temperatures. Large losses at elevated temperatures in BFN and the presence of a possible second phase in BCN need to be addressed before further characterization is performed. Low permittivity values and electromechanical response coupled with difficult processing do not make these TTB compositions practical.

REFERENCES

1. S. Nomura and K. Uchino *Ferroelectrics,* **41** 117-32 (1982).
2. V. A. Bokov and I. E. Myl'nikova, *Soviet Physics Solid State,* **2,** 2428-32 (1961).
3. P. Leidinger, "Processing and Dielectric Measurements on $Pb((MgNi)_{1/3}Ta_{2/3})O_3$ as a Cryogenic Smart Ceramic"; B.S. Thesis. NYSCC at Alfred University, Alfred, 1995.
4. T. Ikeda, K. Uno, K. Oyamada, A. Sagara, Jun-ichiKato, S. Takano, and H. Sato, *Jpn. J. Appl. Phys.,* **17** [2], 341-8 (1978).
5. P. H. Fang, R. S. Roth, and H. Johnson, *Journal of Applied Physical Supplements,* **13,** 169 (1960).
6. N. N. Krainik, V. A. Isupov, M. F. Bryzhina, and A.I.Agranovskaya, *Soviet Physics Chrystallography,* **9** [9], 281-5 (1964).
7. M. C. Foster, G. R. Brown, R. M. Nielson, and S. C. Abrahams, *J. Appl. Cryst.,* **30,** 495-501 (1997).
8. R. Brandt and H. Müller-Buschbaum, *Monatshefte für Chemie,* **117,** 1239-44 (1986).
9. V. U. Lehmann and H. Müller-Buschbaum, *Z. Anorg. Allg. Chem.,* **481,** 7-12 (1981).
10. S. L. Swartz and T. R. Shrout, *Mater. Res. Bull.,* **17,** 1245-50 (1982).
11. C. B. DiAntonio, "Harmonic Analysis of the Electromechanical Response of $Pb(Mg_{1/3}Nb_{2/3})O_3$-Based Compositions"; Ph.D Thesis. New York State College of Ceramics at Alfred University, Alfred, 2001.

Piezoelectric Properties of Transparent $Pb(Ni_{1/3}Nb_{2/3})_{1-x-y}Zr_xTi_yO_3$ Ceramics.

E.F. Alberta and A.S. Bhalla
Materials Research Laboratory, The Pennsylvania State University, University Park, PA, 16802 USA
FAX: 814-863-7846
E-Mail: abhalla@psu.edu

ABSTRACT

The dielectric, piezoelectric and optical properties of transparent $Pb(Ni_{1/3}Nb_{2/3})_{1-x-y}Zr_xTi_yO_3$ (PNNZT) ceramics have been investigated. Hot isostatic pressing was used to achieve uniformly transparent ceramics with densities > 99%. For unpoled samples, the room temperature dielectric constant and loss were 4200 and 0.025, respectively. Large electromechanical coupling factors, k_p = 69%, k_{31} = 43%, k_t = 56%, and k_{33} ~ 80%, as well as large piezoelectric strains ~0.3% were observed. The maximum polarization, P_{sat}, was found to be ~43 $\mu C/cm^2$ at room temperature. Transparent PNNZT ceramics are promising candidates for many applications ranging from electrooptics and pyroelectrics to electromechanical transducers and sensors.

INTRODUCTION

There is an ever-increasing need for high performance piezoelectric and electrooptic materials. Many relaxor-ferroelectric based piezoelectric solid solution systems have been developed to fill this demand [1]. The $Pb(Ni_{1/3}Nb_{2/3})_{1-x-y}Zr_xTi_yO_3$ system has been found to have some of the largest piezoelectric and pyroelectric coefficients known [2-4]. The location of the morphotropic phase boundary (x = 0.155 PT, y = 0.345 PZ) was refined by Kondo *et al.* [5].

In this paper we have used hot isostatic pressing to fabricate transparent $Pb(Ni_{1/3}Nb_{2/3})_{0.500}Zr_{0.155}Ti_{0.345}O_3$. The dielectric and piezoelectric properties of these ceramics are presented.

EXPERIMENTAL PROCEDURE

Ceramics of $Pb(Ni_{1/3}Nb_{2/3})_{1-x-y}Zr_xTi_yO_3$ with x = 0.155 and y = 0.345 [PNNZT(0.50/0.155/0.345] were fabricated by the columbite precursor method. Stoichiometric amounts of PbO, ZrO_2, and TiO_2 were added to the $NiNb_2O_6$ precursor and the mixture was calcined at 850°C for 4hours. The calcined powder was vibratory milled for 24 hours and then pressed into pellets. The pellets were sintered at temperatures ranging from 800°C to 1300°C. The sintering atmosphere was maintained using a $PbO/PbZrO_3$ source powder placed within the crucible. The sintered ceramics were then hot isostatically pressed at 3kpsi for 2 hours at a temperature of 1100°C.

Optical transmission measurements were made using a Cary Model-2300 optical spectrophotometer. Ceramics were optically polished to a 0.3μm finish. The transmittance was measured while canning the wavelength from the near-IR to ultraviolet (1500 to 200nm).

Dielectric constant and loss measurements were made using and automated measurement system consisting of an HP-4284 LCR meter, Delta Design DD-9023 oven, and desktop computer. The temperature was varied between −150°C and 200°C at a rate of ± 4°C/min.

Dielectric hysteresis loop measurements were made with a modified Sawyer-Tower circuit. A fluorinated hydrocarbon fluid (Fluorinert FC-77) was used to prevent electric breakdown. Simultaneous strain measurements were made during hysteresis measurements using an LVDT and a lock-in amplifier (Stanford Research, SR-850).

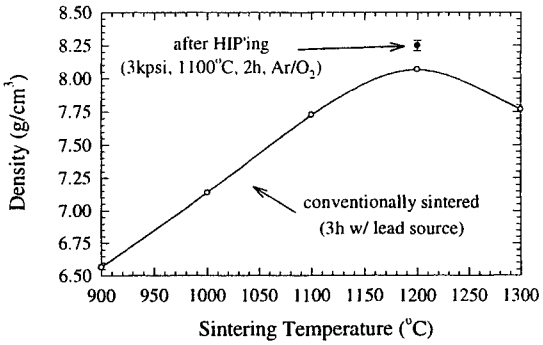

Figure 1. Density of sintered PNNZT ceramics.

Piezoelectric measurements were made using an HP-4194 impedance analyzer after poling the samples with a field of 60kV/cm for 30min. The temperature was maintained with a Delta Design DD-9023 oven. The temperature was increased from 0°C to 160°C in 5-10°C steps allowing approximately 15min at each set-point for the temperature to equilibrate.

RESULTS AND DISCUSSION

Figure 1 shows the measured density obtained at various sintering temperatures. The maximum density and dielectric constant were achieved after sintering for 3 hours at 1200°C. After conventional sintering the ceramics were further densified by hot isostatic pressing. After hot pressing, the ceramics were 100% perovskite (figure 2) and highly dense (8.25 g/cm^3) with a grain size of 3.1μm (figure 3).

The hot isostatically pressed ceramics were translucent at thicknesses less than ~2mm. After thinning to less than ~1mm, the ceramics became increasingly transparent. Figure 4 illustrates the transparency of PNNZT ceramics of various thicknesses. The optical transmittance spectra for poled and unpoled samples 0.32 mm thick is shown in figure 5. Two absorption bands can be observed. These are believed to be due to crystal-field splitting in the nickel ions.

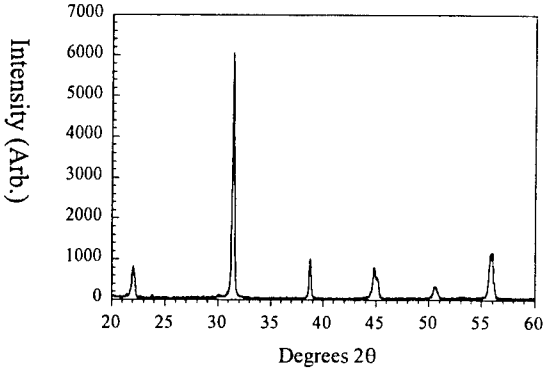

Figure 2. X-ray diffraction pattern of PNNZT.

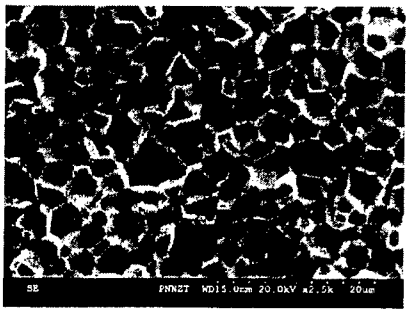

Figure 3. Microstructure of PNNZT ceramics (grain size ~2.6μm).

The transmittance of poled samples was found to be slightly lower than unpoled samples.

Figure 6 shows the temperature dependence of the dielectric constant and loss for PNNZT ceramics. The room temperature dielectric constant for unpoled ceramics (measured at 1kHz) was 4200, after poling this increased to 5940 with a loss tangent of 0.0184. The dielectric constant at the Curie temperature (141°C) was found to be 31503. Hysteresis between heating and cooling cycles was less than 2°C.

Dielectric hysteresis loop for PNNZT is shown in figure 7. At a field of ± 75kV/cm, PNNZT ceramics have well-saturated hysteresis loops with a coercive field of 5.46kV/cm, a maximum polarization of 43.0μC/cm^2, and a remanent polarization of 33.3μC/cm^2. The dielectric breakdown field was found to be in excess of 80kV/cm.

The PNNZT ceramics were poled at room temperature by applying a field of 60kV/cm for 30 minutes. Due to the low coercive field (~5kV/cm) the samples could be fully poled after a single unipolar dielectric hysteresis loop measurement using a maximum applied field of 80 kV/cm at a frequency of

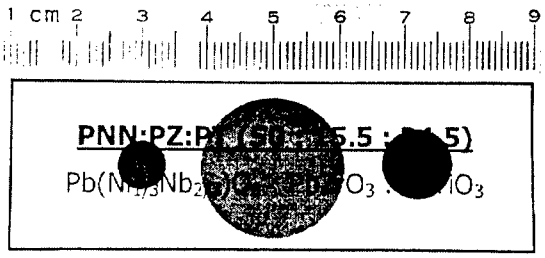

Figure 4. Transparency of HIP'd PNNZT ceramics (disks from left to right are 0.32mm, 0.41 mm, and 0.50 thick).

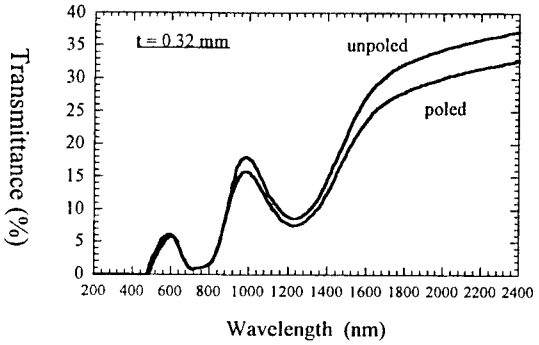

Figure 5. Optical transmittance versus wavelength for PNNZT ceramics.

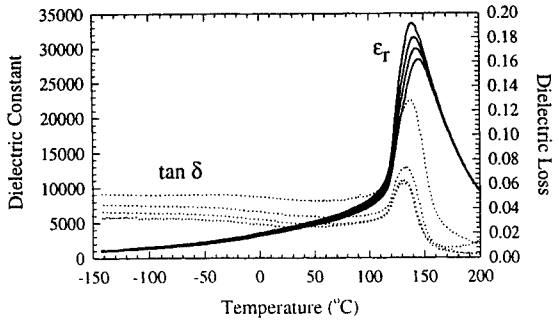

Figure 6. Temperature dependence of the dielectric constant and loss for PNNZT ceramics (measured cooling 4°C/min, with 0.1,1,10,100 kHz).

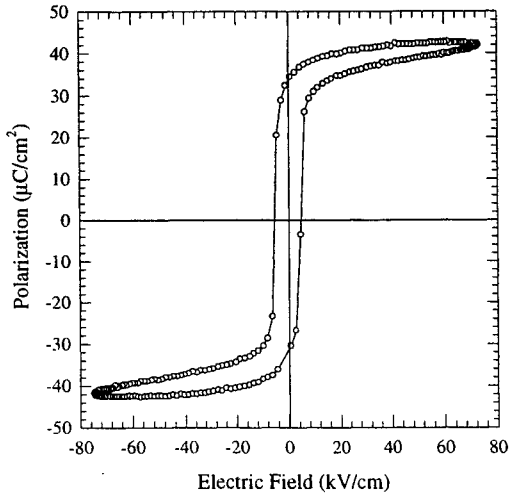

Figure 7. Room temperature dielectric hysteresis loop for PNNZT ceramics. (E_c=5.46kV/cm, P_r=33.3μC/cm^2).

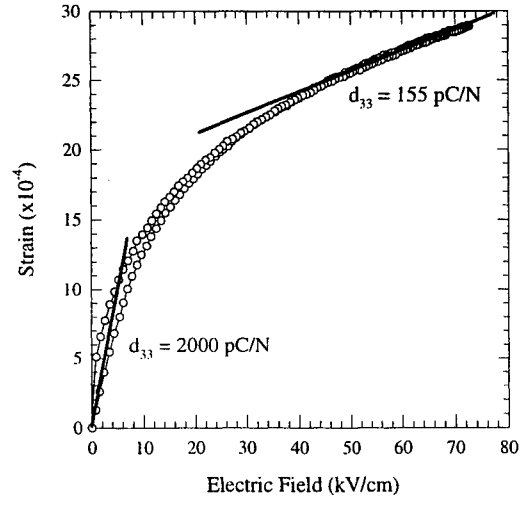

Figure 8. Unipolar strain behavior for PNNZT ceramics (max. strain 0.29%).

0.10 Hz. The room temperature measured piezoelectric coefficients are listed in Table I. The electromechanical coupling coefficients are among the largest values known for relaxor ferroelectric based materials with k_p = 69%, k_{31} = 43%, k_t = 56%, and k_{33} ~ 80%. The electromechanical quality factor, Q_m, for the radial resonance mode of a thin disk was less than 2 while Q_m for the thickness resonance mode was approximately 28.

The piezoelectric coefficient, d_{33}, was determined to be 810 pC/N using a Berlincourt meter. However, from unipolar strain measurements (figure 8) the d_{33} coefficient was observed to be as high as 2000 pC/N at an applied field of 5kV/cm.

Table I. Electromechanical properties of PNNZT ceramics.

Property:	PNNZT
Piezoelectric constants:	
d_{33}	810 pC/N
d_{31}	-378 pC/N
$d_h^{(calc.)}$	55 pC/N
g_{33}	14.7 x10^{-2} Vm/N
g_{31}	-6.8 x10^{-2} Vm/N
$g_h^{(calc.)}$	1.0 x10^{-2} Vm/N
Electromechanical coupling factors:	
k_p	69 %
k_{31}	43 %
k_t	56 %
$k_{33}^{(est.)}$	80 %
Elastic properties:	
velocity	3015 m/s
Poisson's ratio	0.2414
s_{11}^E	14.3 x10^{-12} m^2/N
s_{12}^E	-3.4 x10^{-12} m^2/N
Frequency constants:	
radial mode	1930 kHz cm
thickness mode	2020 kHz cm
Mechanical quality factors:	
radial mode	1
thickness mode	28

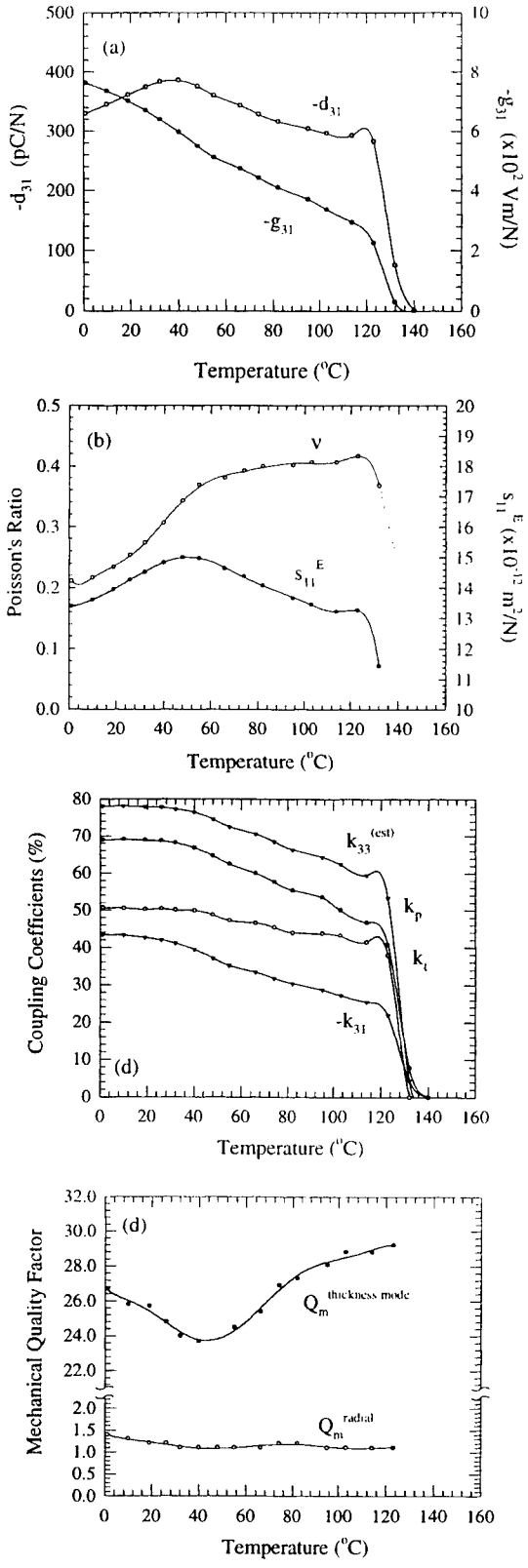

Figure 5(a-d). Temperature dependence of the piezoelectric properties of PNNZT ceramics.

The temperature dependencies of the piezoelectric coefficients are shown in figures 9(a-d). As expected from the dielectric and pyroelectric data, the piezoelectric coefficients show an anomaly at 40°C and rapidly fall to zero between 120°C and 140°C. The piezoelectric coefficient $-d_{31}$ reached a maximum value of 386 pC/N before decreasing to ~0 pC/N at 140°C. The other piezoelectric coefficients showed similar behavior. Electromechanical coupling coefficients, k_{ij}, were relatively temperature independent below 40°C. Above 40°C, the electromechanical coupling coefficients decreased between 5 and 25% near 120°C then rapidly decayed to 0% by 140°C.

CONCLUSIONS

Transparent PNNZT(0.50 / 0.155 / 0.345) ceramics were prepared by hot isostatic pressing. Approximately 98% theoretical density was achieved by sintering the ceramics at 1200°C for 3h. Hot isostatic pressing at 1100°C for 2 hours increased the density to more than 99%. Poled ceramics were found to have an optical transmittance of more than 5% at 633nm and dielectric constant of 5940. The electromechanical coupling coefficients are among the largest values known for relaxor ferroelectric based materials with k_p = 69%, k_{31} = 43%, k_t = 56%, and k_{33} ~ 80%. The piezoelectric coefficient, d_{33}, was determined to be 850pC/N using a Berlincourt-type meter and ~2500pC/N from strain measurements.

REFERENCES

[1] E.F. Alberta, R. Guo, and A.S. Bhalla, *Accepted for publication in Ferroelectrics Review* (2001).

[2] E.A. Buyanova, P.L. Strelets, I.A. Serova, and V.A. Isupov, *Bull. Acad. Sci. USSR Phys. Ser.*, 29, 1877 (1965).

[3] D. Luff, R. Lane, K.R. Brown and H.J. Marshallsay, *Trans. J. Brit. Ceram. Soc.*, 73, 1877 (1965).

[4] E.F. Alberta and A.S. Bhalla, *Submitted to Int'l J. Inorg. Mat.* (2001).

[5] M. Kondo, M. Hida, M. Tsukada, M. Kutami, and N. Kamachara, *Proceedings of the 11th ISAF*, 311 (1998).

LOW-TEMPERATURE SINTERING OF PZT WITH $LiBiO_2$ AS A SINTERING AID

Takashi HAYASHI, Jun TOMIZAWA
Dept. of Materials Science, Shonan Institute of Technology.
1-1-25, Tsujido- nishikaigan, Fujisawa, kanagawa 251-8511, japan.
E-mail : hayashi@mate.shonan-it.ac.jp(Takashi Hayashi)

Low-temperature sintering of PZT was investigated using $LiBiO_2$ (LBiO) as a sintering aid. LBiO-added PZT powders could be densified at 750°C for 2h to sintered bodies with 95% relative density. An addition of the sintering aid was effective for improving the sinterability of PZT powders and piezoelectric / ferroelectric properties of PZT ceramics. 1 mass% LBiO-added PZT bodies sintered at 750°C exhibited an electromechanical coupling factor, kp, of about 61%.

1. INTRODUCTION

Lead zirconate titanate (PZT) ceramics are used in application such as piezoelectric actuators, piezoelectric transformers and ultrasonic motors. Recently, piezoelectric multilayer ceramic actuators have been developed and used for the precise control of small displacements and it's high response speed. It is well known that the sintering temperature of PZT ceramics is above 1200°C. However, the high-temperature processing of PZT ceramics often brings about serious problems such as the reaction between ceramics and electrodes, compositional change and environmental pollution due to the volatility of lead oxide during sintering. These problems can be solved by low-temperature sintering processing of PZT ceramics using low-melting point additives as sintering aids. Several sintering aids for PZT have been reported [1-5] .

In previous work [6-7], we have reported that PZT powders coated with $Pb_5Ge_3O_{11}$ (PGO) prepared from a precursor solution of Ge(OiPr)4 and Pb(NO3)2 by sol-gel method could be densified at a lower temperature and PGO-added PZT ceramics fabricated at 850°C exhibited an electromechanical coupling factor, kp, of about 65%.

In this work, low-temperature sintering of PZT powder was investigated using Li-Bi-oxide additive which is expected to be effective as a sintering aid because of the low melting point. The dielectric, ferroelectric and piezoelectric properties of these PZT ceramics with the sintering aid are also described.

2. EXPERIMENTAL PROCEDURE

PZT ($Pb(Zr_{0.52}Ti_{0.48})O_3$) powder was synthesized by solid state reaction between PbO powder and $(Zr_{0.52}Ti_{0.48})O_2$ powder prepared by chemical process. The mixed oxide powders were ball-milled in ethanol for 24h, pressed and then calcined at 700°C for 2h. After grinding, the calcination was repeated twice to prepare homogeneous PZT powder as a single phase. The particle size of PZT is about 150 nm. 0.3 mol%-Nb_2O_5 was added to PZT powder to improve electric properties. Sintering aids of Li-Bi-O system were added to PZT powder by two addition processes : 1) conventional oxide mixing process (abbreviated as LBiO-added) and 2) chemical coating process using a precursor solution of $Li(O^iPr)$ and $Bi(O^tAm)_3$ (abbreviated as LBiO-coated). The mixtures of PZT powder and a sintering aid were ball-milled in ethanol for 24h, pressed and then sintered at 700-1000°C for 2h. After sintered disc samples were polished to approximately 0.5 mm thickness, fired-on silverpaste was applied to both surfaces of the samples as electrodes. The samples were poled at 120°C for 1h under an electric field of 40 kV/cm

in silicone oil. The microstructure of the sintered bodies was observed using a field-emission scanning electron microscope (FE-SEM). The dielectric constant was measured at 1kHz and electromechanical coupling factor, kp, was calculated by the resonant-antiresonance method using an impedance analyzer (HP4192A). The polarization - electric field (P-E) hysteresis loops were measured by a Sawyer-Tower circuit at 50 Hz at room temperature.

3. RESULTS AND DISCUSSION

3.1 Physical Properties and Microstructure

Figure 1 shows the relative density of PZT sintered bodies with additon of LBiO as a function of sintering temperature. The addition of sintering aids using conventional mixing and chmical coating processes improved the sinterability of PZT powders with a reduction of sintering temperature by approximately 50°C. PZT sintered bodies could be densified to 97% density at a low-temperature of 750°C by LBiO-coating process.

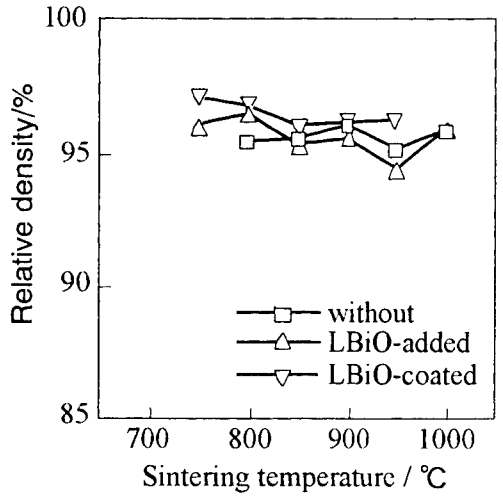

Fig. 1 Relative density of sintering aids-added PZT sintered bodies as a function of sintering temperature.

Figure 2 shows typical FE-SEM micrographs of PZT sintered bodies without and with sintering aid. The grain size of LBiO-coated PZT ceramics is much larger than that of PZT without a sintering aid.The grain growth of PZT was considerably promoted with an addition of sintering aid, as shown in figure 3. This may be attributable to the formation of liquid phase during sintering. Secondary phase formed with liquid phase sintering can be seen to exist along with the grain boundaries of PZT.

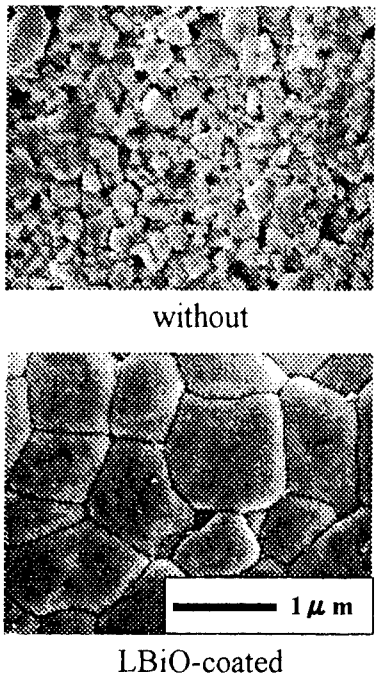

Fig. 2 FE-SEM micrographs of PZT sintered bodies at 800 ℃ without and with LBiO sintering aid.

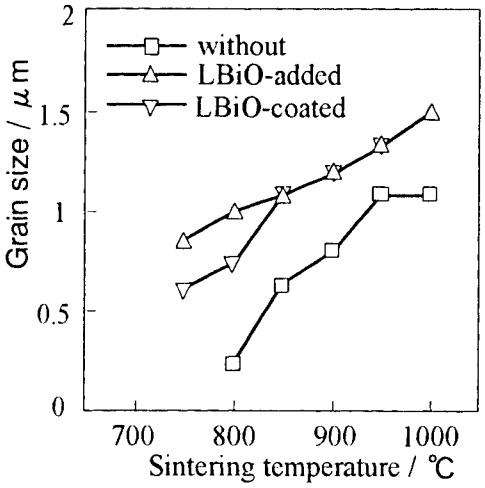

Fig. 3 Grain size of sintering aids-added PZT sintered bodies as a function of sintering temperature.

3.2 Dielectric, Ferroelectric and Piezoelectric Properties

Figure 4 shows dielectric constants of PZT sintered bodies with addition of LBiO as a function of sintering temperature. The dielectric constants of sitering aids-added PZT ceramics were 1400–1600, indicating much higher than that of PZT ceramics without the sintering aid. The increase of the dielectric constants may be due to the grain growth of PZT with addition of the sintering aids.

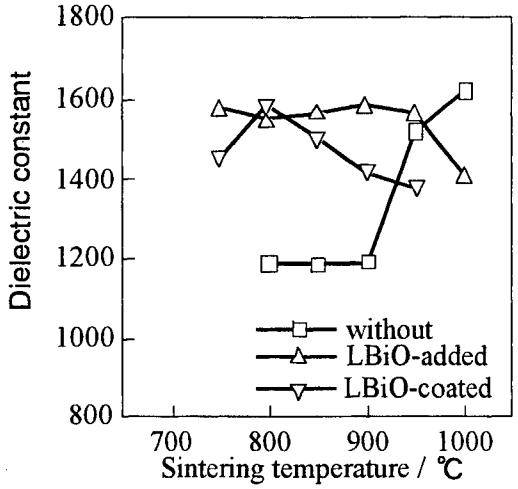

Fig. 4 Dielectric constant of sitering aids-added PZT sintered bodies as a function of sintering temperature.

Figure 5 shows the electromechanical coupling factor, kp, of PZT sintered bodies with addition of LBiO as a function of sintering temperature. Sintering aids-added PZT ceramics showed a much higher kp value than PZT ceramics without sintering aid. LBiO-coated PZT bodies sintered at 750°C showed the kp value of approximately 58%. On the other hand, LBiO-added PZT bodies sintered at 750°C exhibited the kp value of approximately 61%. This sintering temperature is lower by 100°C than that used to fabricate PGO-added PZT ceramics with the same value of kp.

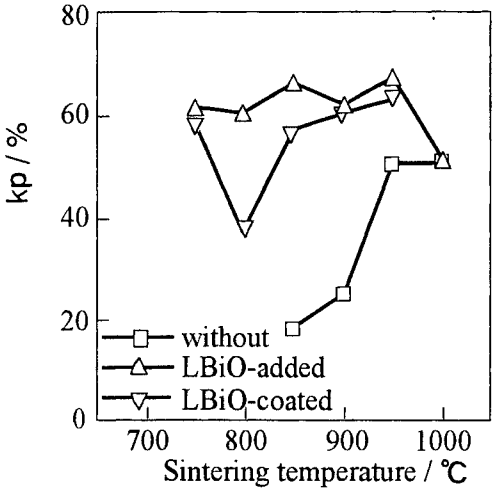

Fig. 5 Electomechanical coupling factor, kp, of sintering aids-added PZT sintered bodies as a function of sintering temperature.

Figure 6 shows P-E hysteresis loops of sintering aid-added PZT bodies sintered at 750°C. The sintering aid-added PZT sintered bodies exhibited the well-saturated hysteresis loop. The values of remanent polarization, Pr, and coercive field, Ec, were 30 $\mu C/cm^2$ and 18 kV/cm, respectively. The increase of ferroelectric properties may be due to the grain growth of PZT with addition of sintering aids.

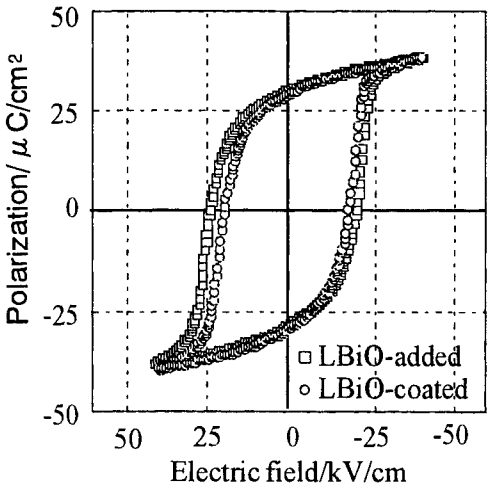

Fig. 6 P-E histeresis loops of sintering aids-added PZT sintered bodies at 750℃.

4. CONCLUSIONS

Low-temperature sintering , microstructure and piezoelectric / ferroelectric properties of aids-added PZT ceramics were investigated. The addition of sintering aids improved the sinterability of PZT powders. The sintering aids seem to exist along the grain boundaries of PZT ceramics. In addition, the addition of LBiO improved dielectric, piezoelectric and ferroelectric properties of PZT ceramics at low sintering temperatures from 750°C to 850°C. The best piezoelectric properties were found for LBiO-added PZT bodies sintered at 750°C. The value of kp is approximately 61%.

A low- temperature sintering was achieved for PZT ceramics to which LBiO has been added.

REFERENCES

[1] M. Adachi , N. Nishide , T. Shiosaki and A. Kawadata : Jpn. J. Appl. Phys. **22** (1983) Suppl. 2, 77.

[2] T. Ogawa , A. Sano , A. Senda and K. Wakino : Jpn. J. Appl. Phys. **28** (1983) Suppl. 2, 91.

[3] K. Murakami , D. Mabuchi , T. Kurita , Y. Niwa and S. Kaneko : Jpn. J. Appl. Phys. **35** (1996) 5188.

[4] S. Kaneko , D. Dong and K. Murakami : J. Am. Ceram. soc. **81** (1998) 1013.

[5] T. Hayashi , T. Inoue and Y. Akiyama : Jpn. J. Appl. Phys. **38** (1999) 5549.

[6] T. Hayashi , T. Inoue and Y. Akiyama : J. Euro. Ceram. Soc. **19** (1999) 999.

[7] T. Hayashi , T. Inoue and T. Shibusawa : Proc. of 9th US-Japan Seminar on Dielectric and Piezoelectric ceramics Okinawa, JAPAN, Nov. 2-5, (1999) p 429.

Fracture Behavior of Ferroelectric Ceramics

C. S. Lynch

The George W. Woodruff School of Mechanical Engineering
The Georgia Institute of Technology
Atlanta, GA 30332-0405
FAX: 404-894-0186
E-Mail: chris.lynch@me.gatech.edu

ABSTRACT

Fracture toughness is a measure of the ability of a material to resist crack propagation. In ferroelectric ceramic materials the fracture toughness increases as a crack propagates. The fracture toughness as a function of crack growth is defined as an R-curve. R-curves were measured for ferroelectric ceramic lead zirconate titanate (PZT) using the surface crack in flexure technique (SCF) for specimens with two different grain sizes. The larger grain size resulted in a higher plateau value of the R-curve. This was consistent with the larger amount of ferroelastic switching observed from the stress/strain curve. The domain structure in the vicinity of the crack tip was revealed by etching. Domain reorientation is apparent. Hysteresis in the domain reorientation is the dissipative mechanism that gives rise to the R-curve behavior.

INTRODUCTION

The plane strain fracture toughness is a material parameter that is used to characterize the ability of a material to resist crack growth. In some materials, the resistance to crack growth is a function of the amount a crack has grown. This is due to the material modified by the crack tip stress field moving into the wake of the crack. Meschke et al. (1997)[1] measured R-curves for $BaTiO_3$ using compact tension (CT) specimens, and found that the toughness increased from initial values of 0.5-0.7 MPa-$m^{1/2}$ to peak values of 0.7-1.2 MPa-$m^{1/2}$, depending on grain size. Munz et al. (1998)[2] and Lucato et al. (2000)[3] performed similar tests on PZT and found that their material displayed similar R-curve behavior. In this work, the surface crack in flexure technique was used to measure the effect of grain size on the R-curve behavior. The analysis technique proposed by Fett al. (2000)[4] was used to determine the stress-strain behavior and the equations of Newman and Raju (1981)[5] were used in the data analysis.

EXPERIMENTAL PROCEDURE

Specimens were prepared from a commercial composition of PZT, TRS600[6]. The composition lies at the morphotropic boundary and the material is donor doped. At room temperature this composition is below the Curie temperature and is both ferroelectric and ferroelastic. The material is translucent but not transparent. The specimens came from two different batches with average grain sizes of 1.4μm and 5μm respectively. Specimens were cut into bars 3x4x25mm^3. The specimens were then prepared as described in detail by Stech and Rödel (1996)[7]. The bars were polished to a 1μm finish on the 4x25mm^2 surfaces. All specimens were unpoled.

A 4-point bend device with inner and outer spans of 10mm and 20mm was used. The fixture is shown in Figure 1. The load was applied using a piezoelectric stack actuator and monitored by a load cell. The fixture was designed to fit into either an optical or scanning electron microscope.

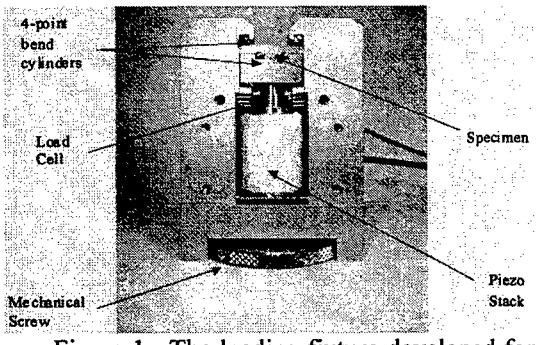

Figure 1. The loading fixture developed for R-curve measurements. A piezoelectric stack actuator is used to provide displacement control.

To measure tensile and compressive stress-strain behavior, strain gages were mounted on the top and bottom surfaces of the specimen and

a non-linear analysis performed as described by Fett and Munz (1999).

To obtain the R-curves, a Knoop indentation was placed in the tensile surface and viewed during loading so that crack growth could be monitored as a function of the applied load. The crack velocity was maintained below 1μm/s. The crack length and load data were used to calculate the applied stress intensity factor, K_I.

In a separate set of experiments, polarized specimens were subjected to Vicker's indentations and then etched to reveal the domain morphology. This clearly showed the domain reorientation in the vicinity of the crack tip.

RESULTS

The non-linear analysis results in the stress - strain curves shown in Figure 2. The curve for the coarse grained material has more non-linearity. This is indicative of a greater amount of ferroelastic switching.

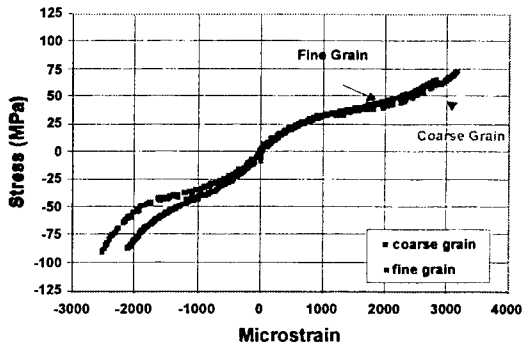

Figure 2. Stress-Strain curves for coarse and fine grain compositions of TRS600 PZT.

The R-curve of the coarser grained specimen has a higher plateau. The rising R-curve is attributed to irreversibly deformed material moving into the wake of the crack as the crack grows. This reduces the crack tip stress intensity factor. The larger observed ferroelastic switching in stress/strain curve of the coarse grained material is consistent with the higher R-curve plateau observed in Figure 3.

Micrographs of the etched domain structure in a region remote from the crack (Figure 4) and near the crack tip (Figure 5) give a direct connection between the domain morphology and the crack tip stress field. uniaxial stress driven ferroelastic switching is the area under the stress/strain curve.

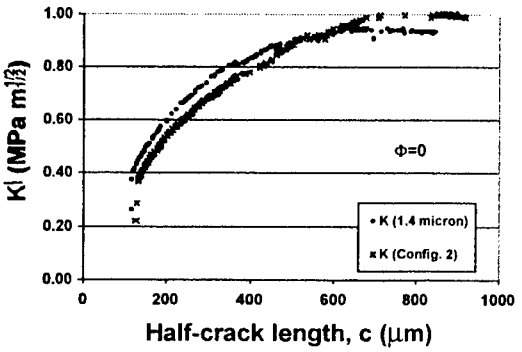

Figure 3. R-Curves obtained from specimens of coarse and fine grained TRS600 PZT.

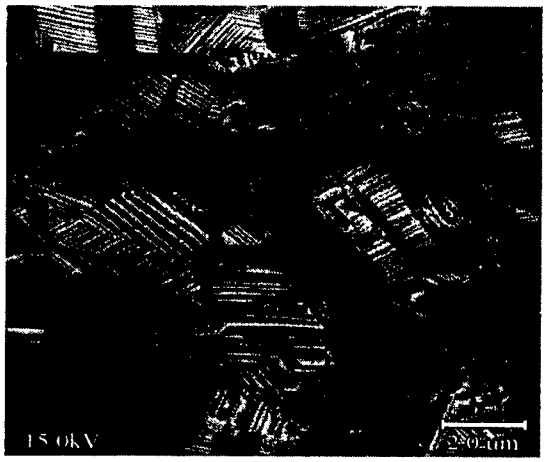

Figure 4. Domain structure of the poled material at a location remote from the crack tip. Poling is in the vertical direction. Domains lie predominantly in the horizontal direction.

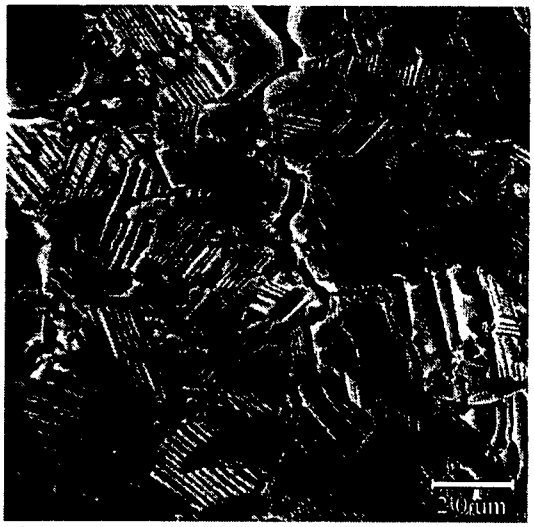

Figure 5. The domain structure in the vicinity of the crack tip lies predominantly parallel to the crack (vertical and center).

The elastic crack tip stress field has a $1/\sqrt{r}$ singularity. This gives rise to a region about the crack tip where the stresses are sufficiently large that ferroelastic switching occurs. The energy density dissipated during switching gives rise to the R-curve behavior. With some additional work, the volume of the switching zone could be directly measured. This would involve sectioning and polishing specimens and observing the frozen in domain structure. Comparisons need to be made between the domain structure at the surface and the domain structure within specimens to separate the plane stress and the plane strain response.

ACKNOWLEDGEMENTS

The author would like to acknowledge the support of TRS Ceramics and DARPA for this work.

REFERENCES

1. Meschke, F., A. Kolleck, and G. A. Schneider, "R-curve behavior of BiTiO3 due to stress-induced ferroelastic domain switching", J. European Ceram. Soc. 17, pp. 1143-1149, 1997.
2. Munz, D., T. Fett, S. Muller, and G. Thun, "Deformation and Strength Behavior of a Soft PZT Ceramic", SPIE, Vol. 3323, 84-95, 1998.Chen, W., D. Lupascu, J. Roedel, and C. S. Lynch, "A comparison of the Short Crack in Flexure R-curve Behavior of Unpoled Ferroelectric 8/65/35 and Quadratic Electrostrictor 9.5/65/35 PLZT", submitted to J. Am. Ceram. Soc., 2000.
3. Lucato, S. L. dos Santos e , D.C. Lupascu, and J. Roedel, "Effect of Poling Direction on R-Curve Behavior in Lead Zircontae Titanate", *J. Am. Ceram. Soc* 83 [2], 424-426, 2000.
4. Fett, T., D. Munz, and G. Thun, "Nonsymmetric deformation behavior of lead zirconate titanate determined in bend tests", J. Am. Ceram. Soc. 81 [1], 269-272, 1998.
5. Newman, J. C., and I. S. Raju, "An empirical stress-intensity factor equation for the surface crack", Engineering Fracture Mechanics 15, pp. 185-192, 1981.
6. TRS Ceramics, State College, PA, USA
7. Stech, M. and J. Rödel, "Method for measuring short-crack R-curves without calibration parameters: case study on Alumina/Aluminum composites", J. Am. Ceram. Soc , 79, pp. 291-297, 1996.

SESSION IV. PROCESSING

Plenary Lectures – Novel Processing

PIV.1 Texture Engineering and Enhanced Properties of Piezoelectric and Dielectric Bulk Ceramics, Toshihiko Tani, Toyota Central R & D Laboratories, Inc., Japan. 293

PIV.2 Micropen Direct Write Fabrication of Integrated Electroceramic Devices, Duane Dimos, P. G. Clem, N. S. Bell, K. VanHeusden°, R. Parkhill*, and K. Church*, Sandia National Laboratories, USA, °Superior Micropowders, USA, *Sciperio, Inc., USA. 301

Piezoelectric Devices

IV.71 Cymbal and BB Underwater Transducers and Arrays, R. E. Newnham, J. Zhang, S. Alkoy, R. Meyer, W. J. Hughes, A. C. Hladky-Herrion, J. Cochran, and D. Markey, Penn State University, USA. 305

IV.72 Design and Modeling of Porous FGM Piezoelectric Actuators, A. Almajid, M. Taya, K. Takagi*, J.-F. Li*, R. Watanabe*, *Tohoku University, Japan, University of Washington, USA. 309

IV.73 Piezoelectric Ceramic Transducers for Miniaturized Applications, A. I. Kingon, A. Gruverman, J. F. Mulling, D. J. Kim, J-P. Maria, J.A. Palmer, E. Grant, and P. Franzon, North Carolina State University, USA. 313

IV.74 Advanced Sonar Technologies for 21st Century Torpedoes, J. G. Kelly, G. T. Stevens, and F. Nussbaum*, Naval Undersea Warfare Center, USA, *ANTEON, USA. 317

IV.75 Active and Passive Structural Vibration Control using Piezoelectric Ceramics, S. Yoshikawa, and M. Giovanardi, Active Control eXperts, Inc., A Division of Cymer, USA. 319

IV.76 Large Displacement Piezoelectric Actuators Using Shear, M. T. Strauss, HME, USA. 323

Textured Piezoelectrics

IV.77 Templated Grain Growth of Textured Piezoelectric Ceramics, S. T. Kwon, E. M Sabolsky, G. L. Messing, and S. Trolier-McKinstry, Penn State University, USA. 327

IV.78 Single Crystal Ferroelectrics from Polycrystalline Precursors, A. M. Scotch, E. P. Gorzkowski, P. T. King, and D. J. Rockosi, S. Wu, M. P. Harmer, and H. M. Chan, Lehigh University, USA. 331

IV.79 Grain Orientation in BNKT-PZT Solid Solutions Made by RTGG Method, T. Kimura, and Y. Abe, Keio University, Japan. 335

IV.80 Processing and Application of Solid State Converted High Strain Undersea Transmitting Materials, K. McNeal, R. Gentilman, K. Ostreicher, and D. Fiore, Materials Systems, Inc., USA. 339

IV.81 Templated Grain Growth of Textured PMN-PT Utilizing Phase Compatible Seed Materials, P. W. Rehrig°, W. S. Hackenberger°, J. H. Adair, and T. R Shrout, Penn State University, USA, °TRS Ceramics, Inc., USA. 343

IV.82 Extruded Electroactive "Single Crystal" Fibers, M. R. Pascucci, H. B. Strock, and P. Bystricky, CeraNova Corporation, USA. 347

IV.83 Textured Piezoelectric Materials Fabricated by Templated Grain Growth, M.M. Seabaugh, G. L. Cheney, K. Hasinska, A. M. Azad, S. L. Swartz, and W. J. Dawson, NexTech Materials, Ltd., USA. 351

Powders and Consolidation

IV.84 Preparation of nm-sized $BaTiO_3$ Fine Particles Using a New 2-step Thermal Decomposition of Barium Titanyl Oxalates, S. Wada, M. Narahara, and H. Kakemoto, and T. Tsurumi, Tokyo Institute of Technology, Japan. 355

IV.85 A Highly Distorted Perovskite Phase in a PMN-PT Powder Synthesized via the Modified Columbite Method, H. Yamada, Cerone, Inc., USA. 359

IV.86 The Formation of PLZT from Oxides During Calcination, J. P. Dougherty, E. Breval, M. Klimkiewicz, and J. D. Weigner°, Penn State University, USA, °Lockheed Martin, USA. 363

IV.87 Synthesis of Nanosized $Pb(Zr_{0.7},Ti_{0.3})O_3$ Particles via Mechanical Activation, X. Liu and R. E. Riman, Rutgers University, USA. 367

Net Shape Forming

IV.88 Layered Manufacturing for Prototyping of Net Shape Grain Oriented Piezoelectric Materials, M. Allahverdi, K. Nonaka, and A. Safari, Rutgers University, USA. 371

IV.89 Robocast 3-3 PZT-5H – Polymer Composites, B. A Tuttle, J. E. Smay, J. Cesarano, III, M.F. Bourbina, E. L. Venturini, D. H. Zeuch, W. R. Olson, J. S. Wheeler, and J. A. Voigt, Sandia National Laboratories, USA. 375

Conductors

IV.91 Microstructure and Grain Boundary Effects on the High-field Electrical Properties of PTCR Barium Titanate, D. Cann, C. T. Chao, and R. B. Gall, Iowa State University, USA. 379

Texture Engineering and Enhanced Properties of Piezoelectric and Dielectric Bulk Ceramics

Toshihiko Tani

Toyota Central R&D Labs., Inc., Nagakute, Aichi, 480-1192, Japan.
Fax: +81-561-63-6498
E-mail: toshit@mosk.tytlabs.co.jp.

ABSTRACT

The design and fabrication of textured polycrystals have been one of the key issues for more than twenty years in the effort to extract intrinsic properties of ferroelectric materials through powder processing. There are two major processing methods to prepare textured ceramics: hot-working and sintering of aligned particles with anisotropic shapes. The latter processing route would have higher productivity for textured ceramics than the hot-working. The reactive templated grain growth (RTGG) is the processing method in which reactive template particles are mixed with complementary reactants and aligned by a shear stress, and during heat-treatment a product material is *in-situ* formed with the preserved orientation of the template. The applicability of the RTGG processing depends on the design of *in-situ* reaction and the synthesis of plate-like particles for the template. Examples are given on the textured perovskite and layered perovskite with enhanced piezoelectric and dielectric properties. Discussions are made on the design strategies and processing techniques in the RTGG method.

INTRODUCTION

There have been two types of strategies to develop high-performance materials; one is to find new systems or compositions, and the other is to tailor ideal microstructures for compounds with known compositions. The control of texture is a typical approach in the latter strategy since material properties can be enhanced by a grain orientation without any changes in the composition. Piezoelectric properties are especially dependent on the direction of an applied field relative to the unique polar axis of a material and thus a grain orientation is effective for the improvement of the performance. Recent reports [1,2] on the excellent properties of regular perovskite-type single crystals have also urged the development of fabrication technology for textured bulk piezoelectrics through inexpensive powder processing.

For ceramic processing, however, texture control is more difficult than for metals or polymers that are given texture mainly by plastic forming. The following two predominant methods are known for preparing textured ceramics; one is hot-working [3,4] and the other is sintering of aligned particles with anisotropic shapes.[5,6] The latter method has advantages in terms of productivity and uniformity in both texture and density, when compared to the former method. Plate- or needle-like particles used in the latter method were prepared by anisotropic grain growth in molten salt, and thus the template materials must have anisotropic crystal structures, such as bismuth layer-structured and tungsten bronze-type ferroelectrics. Highly textured bismuth titanate (BiT) ceramics were prepared by tape-casting and pressureless-sintering of BiT platelets.[6] Furthermore, textured BiT ceramics with improved densities were fabricated by the templated grain growth (TGG), in which the amount of BiT platelets for template was reduced to 5 % and fine particles were used for the rest.[7] The piezoelectric d_{33} constant parallel to the casting plane of the TGG-processed BiT ceramics reached 77 % of the single-crystal value.[8] For regular perovskite-type ferroelectrics, however, the TGG processing would require regular perovskite-type template that is in (pseudo)cubic crystal structure and difficult to grow in an anisotropic shape. Heteroepitaxial templated growth on $BaTiO_3$ and $SrTiO_3$ were recently reported to produce <001> textured $Pb(Mg_{1/3}Nb_{2/3})O_3$-$PbTiO_3$ and $(Bi_{1/2}Na_{1/2})TiO_3$-$BaTiO_3$ ceramics, respectively, with enhanced piezoelectric properties.[9,10]

Hexagonal $BaTiO_3$ platelets were also used as a template for <111> textured regular perovskite.[11] However, undesirable diffusion between template and matrix during sintering could limit the composition of the material to be textured.

We have proposed the reactive templated grain growth (RTGG) method in which reactive template particles are mixed with complementary reactants and aligned by a shear stress, and during heat-treatment a product material is *in-situ* formed with the preserved orientation of the template.[12] This type of processing was first established by Kugimiya, et al.[13] on textured Mn-Zn ferrite polycrystals for magnetic head. The RTGG method enables the fabrication of textured ceramics; (i) with an isotropic crystal structure by the use of a template with an anisotropic crystal structure, and (ii) with complex compositions that would not be realized in a single crystal form. For the use of the method, however, the following conditions must be satisfied:

(1) Thermodynamically favorable *in-situ* reaction is designed so that the final product contains atomic compositions of the reactive template.
(2) The product and the template have a two- or three-dimensional lattice matching.
(3) The overall reaction does not have intermediate phases that disturb the lattice matching.
(4) The template particles can be synthesized in an anisotropic shape.

We fabricated different types of textured ceramics, including regular perovskite-type ferroelectrics and BLSF with enhanced piezoelectric properties. The RTGG method has been extended even to layer-structured conducting oxides.

TEXTURED REGULAR PEROVSKITE

Plate-like BiT particles were prepared by molten salt synthesis [14] and used as a reactive template for a lead-free piezoelectric, $Bi_{0.5}(Na_{0.85}K_{0.15})_{0.5}TiO_3$ (BNKT). The processing and texture design are schematically shown in Figure 1. The BiT platelets were wet-mixed with the complementary ingredient materials (Bi_2O_3, Na_2CO_3, K_2CO_3, TiO_2) at the total atomic ratio of Bi:(Na+K):Ti=1:1:2, according to the reaction design for the perovskite-type BNKT. The amount of BiT was set to provide 20 % of titanium in the total composition. After binder and plasticizer were added, the slurries were tape-cast with the BiT platelets aligned parallel to the sheet surface. The sheets were stacked and then roll-pressed to form ~1 mm-thick plate specimens. Plate specimens containing submicron-sized BNKT particles were also prepared in order to increase the density of the final BNKT ceramics by decreasing the expansion that accompanies the *in-situ* reaction. After the first heat-treatment at 600-700 °C for 2 h for the binder removal and nucleation of BNKT, the specimens were pressureless-sintered

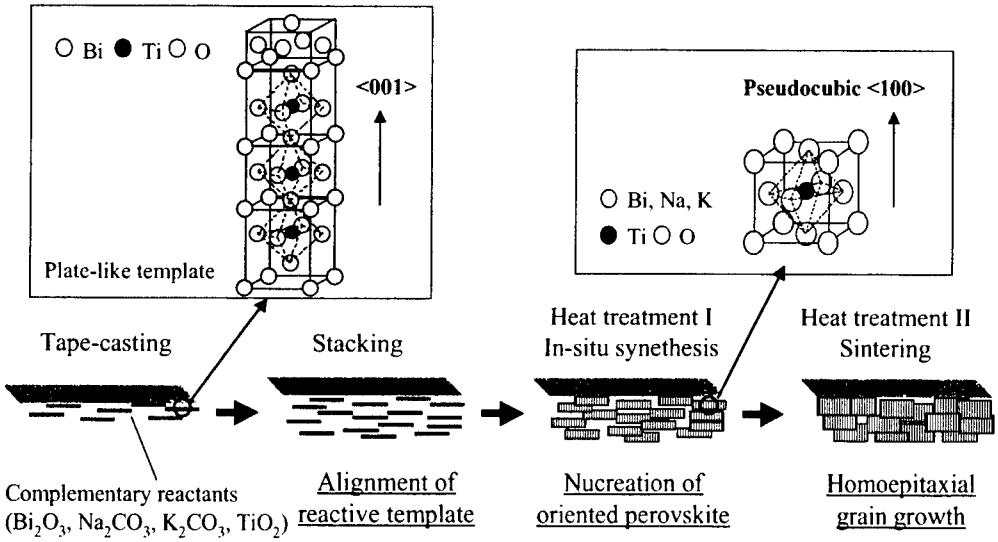

Figure 1 A schematic diagram of RTGG method with the texture and reaction design for textured BNKT.

at 1150-1200 °C for 10 h.

Figure 2 gives X-ray diffraction (XRD) pattern of stacked tape containing BiT platelets with the other reactive ingredients for textured perovskite with comparison to the pattern of equiaxed BiT powder.[12] The BiT template particles were uniaxially aligned with the <001> plane parallel to the casting plane. High-temperature XRD analysis (Figure 3) indicates that the BiT template was converted into regular perovskite during heating at

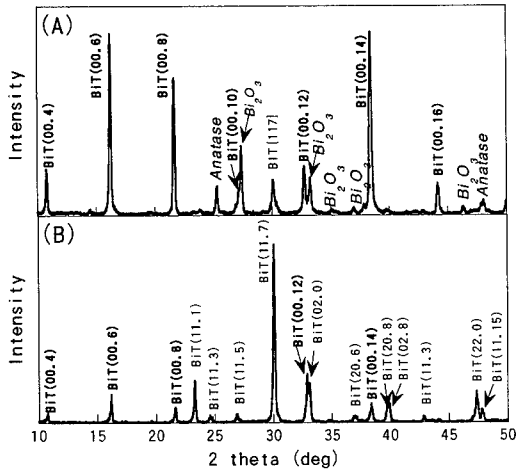

Figure 2 XRD patterns of (A) stacked tape containing plate-like $Bi_4Ti_3O_{12}$ (BiT) with the other reaction ingredients for textured perovskite, and (B) fine BiT powder.

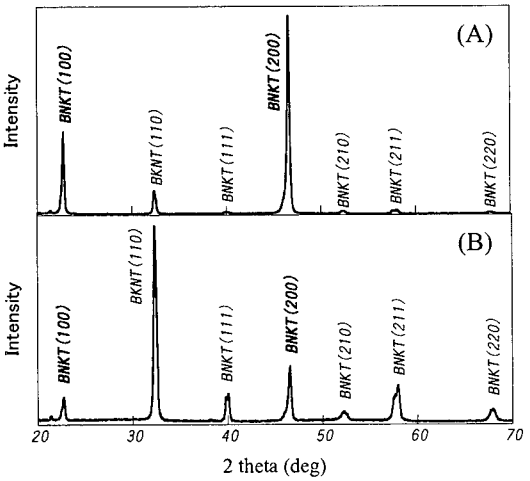

Figure 4 XRD patterns of (A) RTGG-processed $Bi_{0.5}(Na,K)_{0.5}TiO_3$ (BNKT) ceramics, and (B) fine BNKT powder.

600-800 °C and that the development of texture was remarkable above 1000 °C. Transmission electron microscopy (TEM) analysis revealed that the *in-situ* reaction from a layered perovskite BiT to a regular perovskite BNKT started at the vicinity of the BiT surface and proceeded with heat-treatment time toward the inner part of the BiT with the uniaxial orientation preserved.[15] Figure 4 compares XRD pattern of an RTGG-processed BNKT ceramic with that of equiaxed BNKT powder. It is evident that highly textured and single-phase polycrystalline ceramics were prepared with a preferred <001> orientation. Lotgering's orientation factor for <001> texture reached higher than 0.8. Figure 5B gives a typical fracture surface perpendicular to the casting plane, for the RTGG-processed BNKT.[16] It showed a brick-wall-like microstructure and no trace of original plate-like BiT particles was observed. The diameter of BNKT grains was in good accordance with that of the template BiT (Figure 5A), whereas thickness of the grains corresponded to the vertical distance between the original BiT particles.

The textured BNKT ceramics with 97-99 % in relative density were electroded and poled for the piezoelectric and dielectric

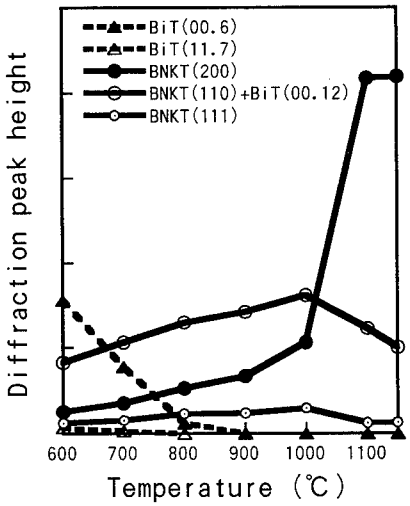

Figure 3 Diffraction peak intensities for representative crystallographic planes of BiT template and *in-situ* formed BNKT, obtained by high-temperature XRD analysis.

measurement. Figure 6 and 7 give electromechanical coupling coefficients and piezoelectric coefficients, respectively, as a function of Lotgering's orientation factor, for the RTGG- and conventionally-processed BNKT. The texture displays remarkable effects on the properties: the electromechanical coupling factor K_p increased by 30-40 % and piezoelectric d_{31} and g_{31} constants increased by 50-60 % by the given texture.[16] The dielectric loss was reduced by 20-40 % by the texture whereas the dielectric constant remains the similar value. The results support the texture engineering of perovskite polycrystals by the RTGG method to be an effective way for the enhancement of performances.

The processing was extended to other combination systems of reactive templates and textured perovskite than BiT and BNKT.[17] Other than BiT, Ruddlesden-Popper-type materials such as $Sr_3Ti_2O_7$ and $Ca_3Ti_2O_7$ were used as a reactive template for {100} textured regular perovskite. Besides, pyroniobate-type materials such as $Sr_2Nb_2O_7$ and $Nd_2Ti_2O_7$ were used as a reactive template for {110} textured regular perovskite. Figure 8 gives the crystallographic

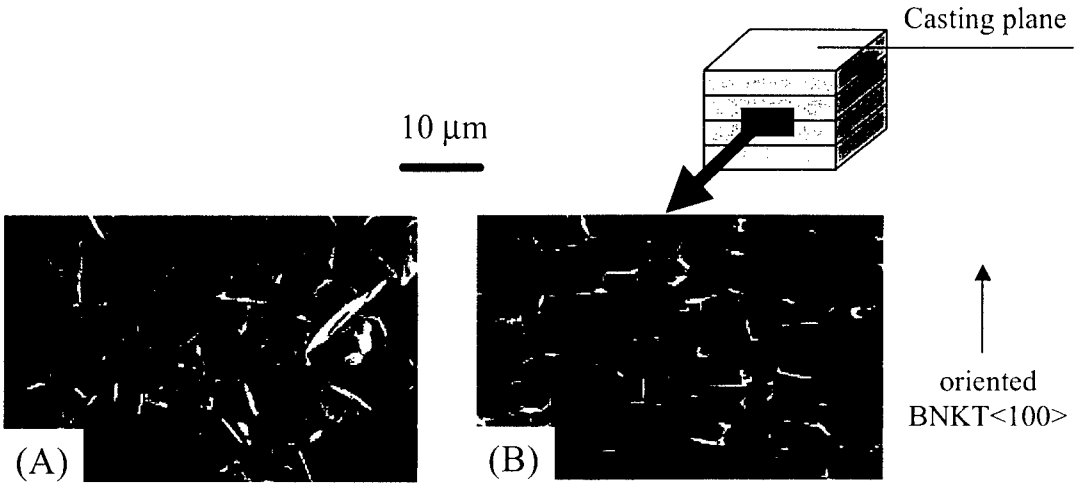

Figure 5 SEM images of (A) BiT reactive template particles and (B) a perpendicular fracture surface to tape-casting plane of a textured BNKT ceramic.

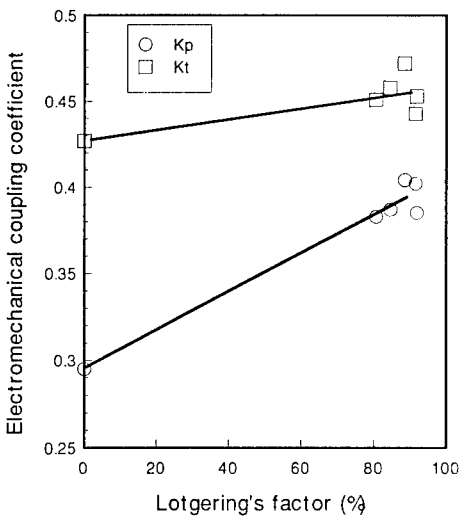

Figure 6 Electromechanical coupling coefficients of textured and randomly oriented BNKT ceramics.

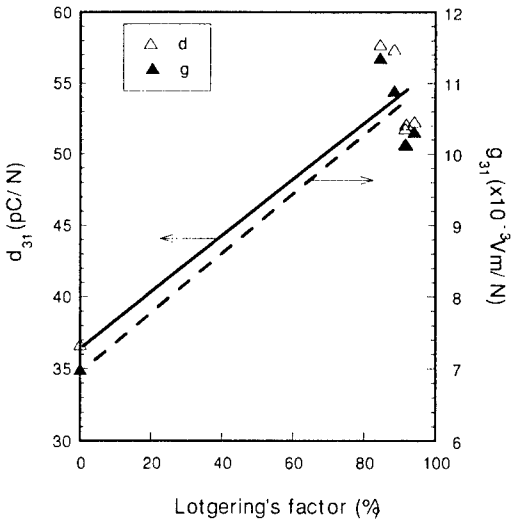

Figure 7 Piezoelectric d and g coefficients of textured and randomly oriented BNKT ceramics.

relationships between those candidate templates and regular perovskite unit cell. And recently, Sugawara et al. succeeded in the fabrication of {111} textured $BaTiO_3$ with the use of $Ba_6Ti_{17}O_{40}$ that has a two-dimensional lattice matching with a regular perovskite although it is not a layered perovskite.[18]

TEXTURED BLSF

Fabrication of textured BLSF ceramics by the use of the other BLSF with a simpler composition is easier than the fabrication of textured regular perovskite if the designed product is thermodynamically more stable than the template at the presence of the complementary reactants. We fabricated three types of four-layered BLSF, Ca-doped $Na_{0.5}Bi_{4.5}Ti_4O_{15}$ (NCBT), $CaBi_4Ti_4O_{15}$ (CBT) and $SrBi_4Ti_4O_{15}$ (SBT) ceramics with a preferred <001> orientation with the use of BiT platelets as a reactive template. The processing and evaluation for CBT ceramics is schematically shown in Figure 9. Fully dense and single-phase ceramics were obtained for NCBT and CBT with high degrees of <001> orientation (>0.9).[19] Figure 10 gives SEM images of the microstructure of a textured CBT ceramic in which plate-like grains are aligned parallel to the original casting plane.

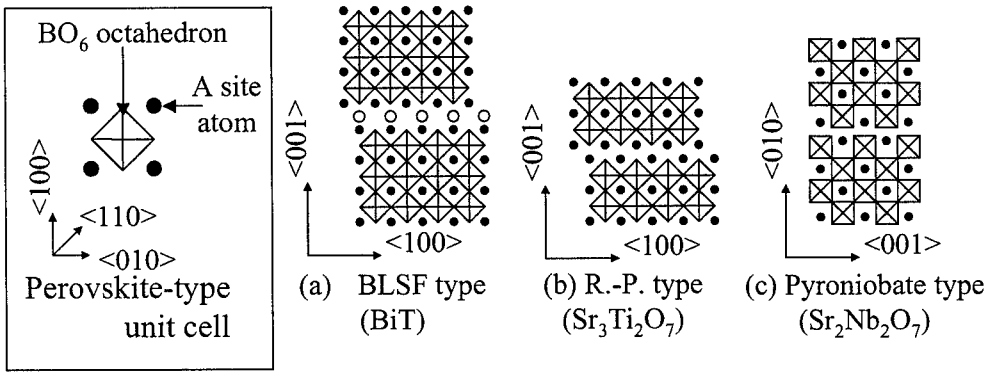

Figure 8 Schematic crystal structures of reactive template materials for regular perovskite-type textured ceramics.

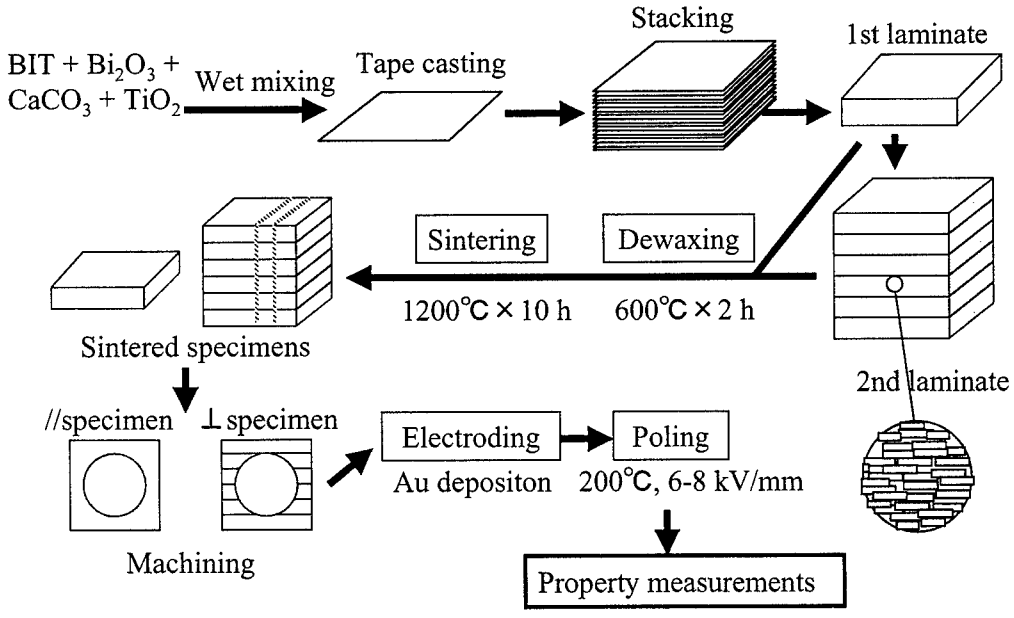

Figure 9 Schematic diagram of preparation method for textured BLSF ceramics by RTGG method.

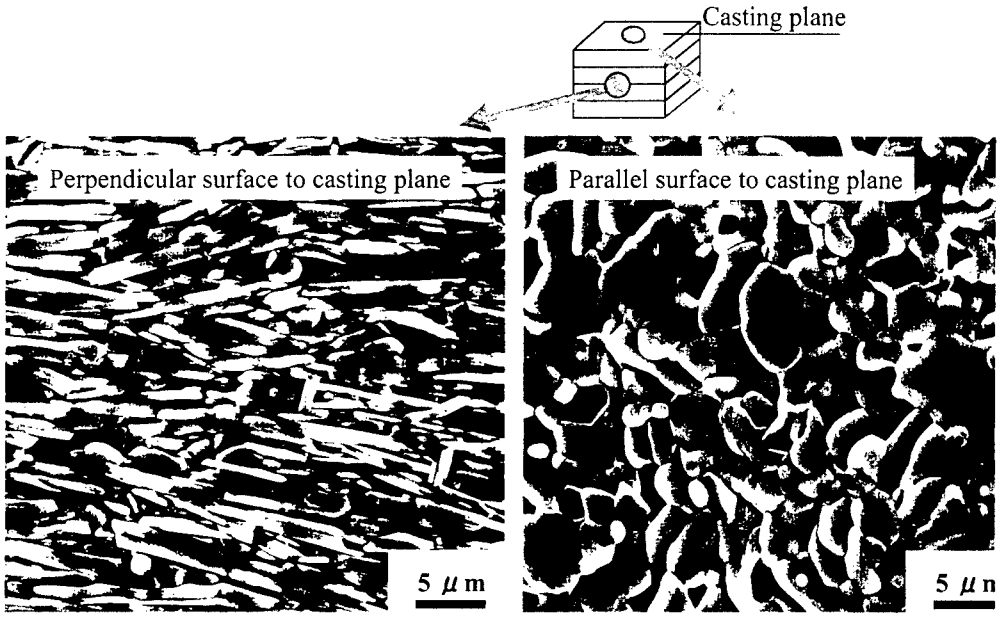

Figure 10 SEM images of polished and etched surfaces of RTGG-processed CBT ceramics by RTGG method.

Figure 11 SEM image of fracture surface of a textured BNT-NBT composite perpendicular to the casting plane.

Table 1 gives the piezoelectric and dielectric properties of the textured CBT ceramics prepared by the RTGG method and of randomly-oriented CBT prepared by a conventional method. Electromechanical k_t and k_{33} coefficients of the RTGG-processed specimen exhibited more than three times as high as those of the randomly oriented specimen.[19] This is the first to obtain a BLSF ceramic with more than 50 % in the k_{33} value. The piezoelectric d_{33} and g_{33} constants of the textured BLSF were also remarkably higher than the randomly oriented ceramics.[19] Besides, unidirectionally textured CBT ceramics were prepared by an extrusion in the RTGG method and enhanced piezoelectric properties were observed when compared to the randomly oriented.[20]

Table 1. Piezoelectric and dielectric properties of textured and randomly-oriented $CaBi_4Ti_4O_{15}$ (CBT) ceramics

	RTGG (•)	RTGG (//)	Random orientation
$\varepsilon_{33}^T/\varepsilon_0$	139	153	149
Tanδ (%)	0.09	0.04	0.13
k_p (%)	4.8	1.4	4.7
k_{31} (%)	3.2	0.9	2.9
k_t (%)	53.4	16.2	16.2
k_{33} (%)	53.5	16.2	16.9
d_{31} (x10^{-12} C/N)	2.8	0.9	2.8
d_{33} (x10^{-12} C/N)	45	17	15
g_{31} (x10^{-3} Vm/N)	2.3	0.6	2.1
g_{33} (x10^{-3} Vm/N)	36.5	12.5	11.4

TEXTURED COMPOSITES

Bi_2O_3, Na_2CO_3, and TiO_2 powders were mixed with the BiT platelets at the ratio of Bi_2O_3:Na_2CO_3:TiO_2:BiT = 3:3:12:1, i.e., the compositional scheme was originally designed to produce stoichiometric $Bi_{0.5}Na_{0.5}TiO_3$ (BNT) for a matrix and BiT for a template at the ratio of

BNT:BiT = 12:1. The powder mixture was processed by the standard RTGG processing at the sintering temperature of 1100 °C. The obtained specimen was a dense and textured composite of plate-like $Na_{0.5}Bi_{4.5}Ti_4O_{15}$ (NBT) grains in the BNT matrix, since NBT is thermodynamically more stable than BiT.[16] The NBT was <001> textured and the matrix BNT was pseudocubic <100> textured. Figure 11 gives a microstructure of the textured composite. The high-temperature XRD analysis suggests that the BiT was converted into NBT topotaxially and the grain growth of heteroepitaxially nucleated BNT filled the matrix. The unique microstructure of layered perovskite/regular perovskite textured composites might offer unique properties.

TEXTURED NON-DIELECTRICS

The proposed RTGG method was extended to conducting thermoelectric materials with electrical anisotropy. P-type $NaCo_2O_4$ polycrystals with a preferred <001> orientation and n-type $(ZnO)_mIn_2O_3$ polycrystals with a preferred <001> orientation were fabricated by *in-situ* reaction of reactive template materials with complementary ingredient materials.[21,22] The RTGG processing have also potential for the design and fabrication of other non-dielectric material system with anisotropic properties.

CONCLUSIONS

A variety of dense and highly textured ceramics were fabricated, including regular-perovskite and non-perovskite. Pseudocubic <100> textured $Bi_{0.5}(Na,K)_{0.5}TiO_3$ (BNKT) bulk ceramics were prepared by the *in-situ* reaction of a template, $Bi_4Ti_3O_{12}$ (BiT) with the complementary ingredient materials and successive grain growth. The preferential orientation of BiT was preserved and the textured BNKT gave a unique brick-wall-like microstructure. Textured bismuth layer-structured ferroelectric (BLSF) ceramics were also prepared with the use of the BiT platelets. The textured polycrystals exhibited enhanced piezoelectric properties and reduced dielectric loss when compared to randomly oriented counterparts with the same compositions. The processing was extended to textured composites and even non-dielectrics. The RTGG processing is an effective method for the texture engineering of materials with anisotropic properties.

ACKNOWLEDGEMENTS

The author is grateful to Professor T. Kimura of Keio University for his invaluable suggestions and comments on this work. The author also acknowledges that the series of work was conducted with Mr. T. Takeuchi, Mr. Y. Saito and Dr. Seno of Toyota CRDL.

REFERENCES

1. S.-E. Park, and T. Shrout, *J. Appl. Phys.*, **82**, 1804-11 (1997).
2. Kobayashi, T., et al., *Jpn. J. Appl. Phys.* **36**, 6035-38 (1997).
3. H. Igarashi, et al., *Am. Ceram. Soc. Bull.*, **57**, 815-17 (1978).
4. T. Takenaka and K. Sakata, *Jpn. J. Appl. Phys.*, **19**, 31-39 (1980).
5. T. Kimura, et al., *J. Am. Ceram. Soc.*, **65**, 223-26 (1982).
6. Y. Inoue, et al., *Am. Ceram. Soc. Bull.*, **62**, 704-08 (1983).
7. J. A. Horn, et al., *J. Am. Ceram. Soc.*, **82**, 921-26 (1999).
8. S.-H. Hong, et al., *J. Am. Ceram. Soc.*, **83**, 113-18, (2000).
9. E. M. Sabolsky, et al., *Appl. Phys. Lett.*, **78**, 2551-53, (2001).
10. H. Yilmaz, et al., *Proc. of ISAF2000*, 405-08 (2001).
11. M. M. Seabaugh, et al., *Proc. of ISAF2000*, 377-80 (2001).
12. T. Tani, *J. Korean Phys. Soc.*, **32**, S1217-20, (1998).
13. K. Kugimiya, et al., *IEEE Trans. Mag.* **MAG-10** , 907-09, (1974).
14. T. Kimura and T. Yamaguchi, *Ceram. Int'l.*, **9**, 13-17, (1983).
15. Y. Seno and T. Tani, *Ferroelectrics*, **224**, 365-72, (1999).
16. T. Tani, et al., *Ceram. Trans.*, **104**, 267-74, (2000).
17. T. Takeuchi and T. Tani, *Electroceramics in Japan IV*, in press.
18. T. Sugawara, et al., *J. Ceram. Soc. Japan*, submitted.
19. T. Takeuchi, et al., *Jpn. J. Appl. Phys.*, **38**, 5553-56, (1999).
20. T. Takeuchi, et al., *Jpn. J. Appl. Phys.*, **39**, 5577-80, (1999).
21. S. Tajima, et al., *Mater. Sci. Eng. B*, in press.
22. T. Tani, et al., *J. Mater. Chem.*, in press.

Micropen Direct Write Fabrication of Integrated Electroceramic Devices

Duane Dimos*, Paul G. Clem*, Nelson S. Bell*, Karel VanHeusden#, Robert Parkhill^, Kenneth H. Church^

*Sandia National Laboratories, Albuquerque, NM; # Superior Micropowders, Albuquerque, NM, ^ Sciperio, Inc. Stillwater, OK.
FAX: 505-284-3093
Email: dbdimos@sandia.gov

INTRODUCTION

High reliability passive components (i.e., capacitors, resistors, and inductors) and packaging substrates are commonly made using multilayer ceramic constructions. However, the desire to achieve further miniaturization, greater functionality, and enhanced reliability in advanced electronic and microelectromechanical systems is driving the development of more highly integrated components based on combining different functional ceramics together into complex 3-D architectures. Currently there are numerous examples achieved by electronic ceramic manufacturers, in which various materials have been combined to produce monolithic, multilayer ceramics with sophisticated functionality, such as filters [1,2] and solid-state dc-dc converters [3]. Similarly, significant work is being done to permit embedding of passive components into low-temperature cofireable ceramic (LTCC) packages [4]. This trend towards higher level integration, which is the passive component analog of an integrated circuit, places increasing demands on fabrication processes and manufacturers.

Multilayer, multi-material, integrated ceramics are typically manufactured by cofiring of laminates made from green tape layers with screen-printed features, such as conductor traces. This manufacturing method has been refined over decades of development, driven by the needs for low cost and high production volumes. While this approach works well for simple parts, such as multilayer capacitors, fabricating multifunctional components with complex geometries is significantly more challenging. Furthermore, commercial development of sophisticated integrated ceramics has emphasized an empirical approach, which has made the technology inaccessible for low-volume, specialty components.

To overcome this limitation, we have been developing a direct fabrication approach that simplifies the processing and provides greater flexibility than would be possible by tape-casting or screen-printing. The goal is to provide a rapid prototyping and agile manufacturing approach to fabricating multifunctional, multimaterial integrated ceramic components (MMICCs). This work was originally based on the use of a commercial micropen system [5,6,7] for depositing electronic-grade slurries in precise patterns. More recently, through the DARPA program on Mesoscopic Integrated Conformal Electronics (MICE), a new system has been developed by Sciperio, Inc.

A critical feature of this work, which was an important goal of the DARPA MICE program, was the ability to fabricate integrated components at low processing temperatures. Achieving processing temperatures (< 400°C) for all materials of interest (conductors, dielectrics, resistors, etc.), will enable fabrication on a wide range of substrate materials.

DIRECT WRITE PRINTING

The Micropen system (Ohmcraft, Inc.) is a computer automated device for precision printing of ceramic slurries [5], as illustrated in Fig. 1. The system uses a computer driven x-y stage for printing, where the print pattern is defined by a CAD instruction file. The CAD file can be easily modified, which permits on-line design changes, in contrast to screen printing where a new screen is required for a pattern change. The cross-sectional area of the printed feature is determined by the nozzle dimensions. The Micropen can use a wide range of nozzle sizes to optimize different print geometries. The finest nozzle for high-definition patterns has an inner diameter of 1 mil and an outer diameter of 2 mil. The slurry is delivered to the print head by a pump block, which uses two internal chambers to provide smooth, continuous delivery of slurry. Slurries are easily loaded into a syringe which screws into the pump block assembly. A key to getting uniform and reproducible processing is elimination of air bubbles in the slurry, which is accomplished by centrifuging the syringe and bleeding the pump block.

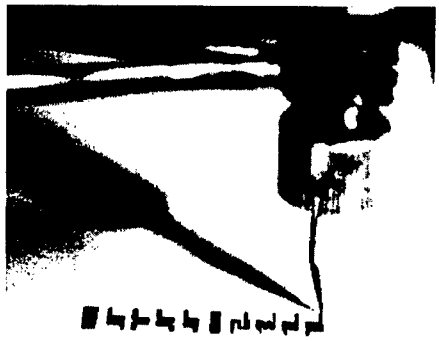

Figure 1. Photograph of the Micropen print head during a printing operation. Adapted from Ref. 5.

The Micropen also uses force feedback control on the pen tip to stabilize the printing conditions. This control leads both to excellent control of the print thickness and the ability to print over variations in the topography (i.e., height) of the workpiece. The system is also inherently capable of laying down multiple materials in a single layer, which cannot be done with conventional tape casting techniques. However, since the workpiece needs to support the force of the pen, any underlying slurry layer must be dried before printing on top of it. Therefore, the system is not suitable for continuous processing of structures, but it is ideally suited for step and repeat procedures, which are appropriate for multilayer, multimaterial electronic components.

MATERIAL FORMULATION

The direct-write (Micropen) approach can use any thick-film paste that is appropriate for screen printing. Although optimal print parameters do not vary greatly for different thick-film formulations, tailoring the slurry viscosity at low shear rates is critical for optimizing materials for either high definition patterns or for smooth filled regions. Specifically, viscous slurries lead to more sharply defined traces (ideal for conductors), whereas more fluid pastes flow together during settling to give a relatively smooth surface for filled areas (typical for dielectrics).

For conductor materials, our approach to achieving high-conductivity materials that can be direct written and processed at low temperatures is to incorporate chemical precursors that achieve low-temperature conversion within a dispersion of silver particles. By achieving high silver particle content in the slurry, silver lines are printed with low shrinkage and high interconnectivity. The reduction of the silver precursor at particle contacts creates conductive networks at low processing temperatures.

In developing these slurries, it was critical to control the rheology (or flow) by tailoring the interactions between particles such that printing is possible using the fine tips of the Micropen and the written lines retain their profile through the conversion process. Dispersion of silver metal particles was successful, which allowed us to achieve a solid volume content of 60% with a highly fluid response. Dispersion chemistries were developed and optimized for different solvent/molecular precursor combinations. Polymeric thickening agents have also been used to tailor the rheology to improve printing. The optimized silver paste can be written with 100 micron orifices, and converts to a bulk resistivity value of 5 times that of bulk Ag at a temperature of 250°C.

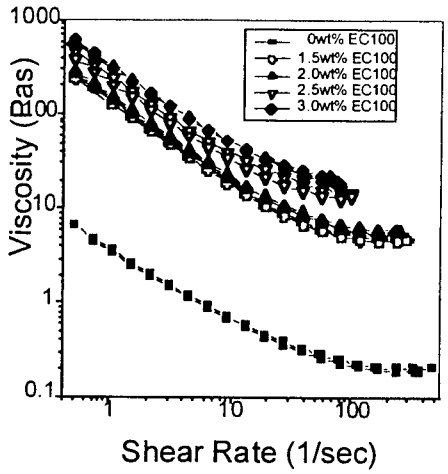

Fig 2. Viscosity of 55 vol. % silver pastes with varying concentration of an ethyl cellulose (EC) thickening agent. The pastes are shear thinning for good printing and have a yield stress to maintain written definition.

DIELECTRICS

A major challenge is the development of high density and high Q (low dielectric loss) materials that can be processed at low temperatures. Both the attainment of density by sintering and the removal of contaminant species that decrease Q are difficult at temperatures compatible with polymer substrates (< 400°C). The use of molecular precursor approaches is well known to be capable of depositing dense ceramics at 700°C, but achieving significantly

lower temperatures and higher Q values has not been demonstrated to date.

Studies of microwave dielectrics generally appreciate that the presence of mobile species such as OH, residual organics, and other defects enable mobile charge hopping, soft vibrational (absorption) modes, and other effects. Attaining dense, hydroxyl-free materials is the approach generally taken for these materials, typically requiring sintering near 1600°C. Dielectric properties can be correlated with thermodynamic predictions of oxide/hydroxide stability, and with chemical spectroscopy of deposited films. In particular, the correlation of low [OH] concentration with high Q was monitored.

Using a simple comparison of energy stability for metal oxides and hydroxides, an indication of metal hydroxide (in)stability was generated for several candidate materials:

$M + 1/2\ O_2 \rightarrow MO$	ΔH(oxide)	ΔH(hydroxide)
ZnO	-83	-153
MgO	-143	-221
TiO_2	-218	-207
ZrO_2	-258	-411
Al_2O_3	-399	-304
Nb_2O_5	-463	small
Ta_2O_5	-499	small

The relative free energies suggested niobates and tantalates as potential alternatives to traditional titanates and zirconates. Infrared spectroscopy of barium titanate (Superior MicroPowders – not shown) and lead tantalate ($Pb_2Ta_2O_7$ – Fig 3.) compounds confirm this behavior. The IR results indicate removal of hydroxides at 400°C for the pyrochlores, while many hydroxyl OH bonds and organic CH bonds remain in barium titanate compounds at the same temperatures.

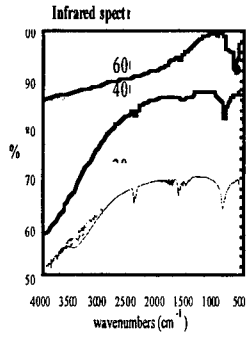

Fig. 3. Infrared spectrum of $Pb_2Ta_2O_7$ indicates that hydroxyl impurities are almost eliminated at 400°C and significantly reduced at 300°C.

To date excellent dielectric properties have been achieved with composites with $Pb_2Ta_2O_7$ as the matrix and barium neodynium titanate (SMP) as the powder phase. With an anneal at only 400°C for 10 min., the dielectric properties of this composite are: K~120, and Q>500. A typical microstructure of this material is shown in Fig. 4.

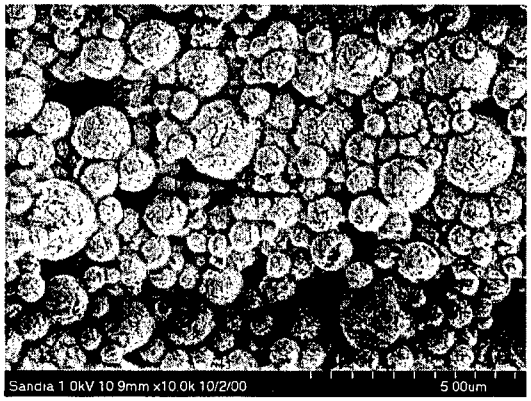

Fig. 4. Micrograph showing composite dielectric with pyrochlore matrix and $BaNd_2Ti_5O_{14}$ powder.

COMPONENTS

Capacitor test structures consist of single layer capacitors with Ag top and bottom electrodes printed on polyimide substrates. The capacitors are heat treated at 300° or 400°C. These low-temperature capacitors (Fig. 5) are fully compatible with the polymer substrate, although some warping of the substrate can occur due to stresses developed during the heat treatment.

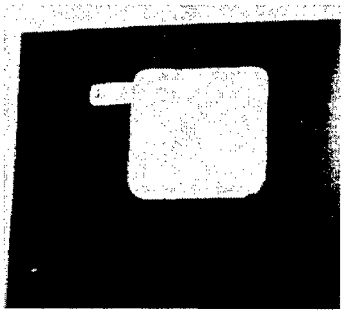

Fig. 5. Single layer direct write capacitor fabricated on a polyimide substrate.

The capability of the Micropen to accommodate various topographies has also been utilized to build a variety of device structures, such as a multi-turn voltage transformer and a wound solenoid inductor, as shown in Fig. 6.

This solenoid inductor was built by writing the bottom windings, then adding several layers of ferrite based material and finally connecting the windings across the top. This structure clearly demonstrates the ability to pattern features with complicated topography.

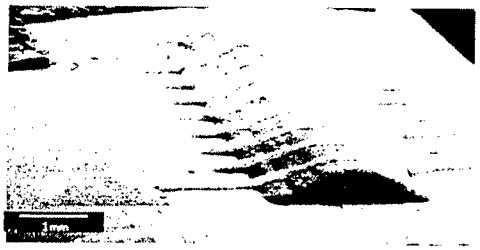

Fig. 6. Direct-write solenoid inductor.

CONCLUSIONS

A direct-write approach for fabricating highly integrated, multilayer components using a micropen to deposit slurries in precise patterns. With this technique, components are constructed layer by layer, simplifying fabrication. The quality of print features depends on slurry viscosity; however, the micropen can accommodate a wide range of slurry viscosities corresponding to most commercial thick-film pastes. The direct-write approach provides the ability to fabricate multifunctional, multimaterial integrated ceramic components in an agile way with rapid turnaround, and has been used to fabricate devices such integrated RC filters, multilayer voltage transformers, and other passive components. In addition, new thick-film formulations have been developed to enable low-temperature processing of dielectrics, conductors and resistors to allow integrated components to be fabricated on polymer (low-cost) substrates.

ACKNOWLEDGMENTS

The authors would like to acknowledge the Defense Advanced Research Projects Agency and Dr. William Warren as the program manager for the Mesoscopic Integrated Conformal Electronics (MICE) program. Sandia is a multiprogram laboratory operated by the Sandia Corporation, a Lockheed Martin Company, for the United States Department of Energy under Contract DE-AC04-94AL85000.

REFERENCES

1. H. Hayashi, T. Ikeda, and S. Nishigaki, ISHM '91 Proceedings, 508-512 (1991).
2. H. Mandai, K. Wakino, H. Okamura, and J.P. Canner, Ceram. Trans., 15 (Mater. Processes Microelectron. Syst.), 391-404 (1990).
3. T. Minoru, Y. Mochizuki, A. Nakano, and H. Kobuke, ISHM '92 Proceedings, 269-274 (1992).
4. R.L. Brown and A.A. Shapiro, Proceedings of the International Conference and Exhibition on Multichip Modules, April 14-16, 1993, 287-294 (1993).
5. Micropen, Inc., Pittsford, NY.
6. C.E. Drumheller, ISHM '82 Proceedings (1982).
7. A. Dziedzic, J. Nijs, and J. Szlufcik, Hybrid Circuits, 30, 18-22 (1993).

Cymbal and BB Underwater Transducers and Arrays

R.E. Newnham, J. Zhang, S. Alkoy, R. Meyer, W.J. Hughes, A.C. Hladky-Hennion, J. Cochran, and D. Markley

Materials Research Laboratory, Penn State University
University Park, PA 16802 USA
Fax: (814) 865-2326
Email: bobnewnham@psu.edu

ABSTRACT

The cymbal is a miniaturized class V flextensional transducer that was developed for use as a shallow water sound projector and receiver. Single elements are characterized by high Q, low efficiency, and medium power output capability. Its low cost and thin profile allow the transducer to be assembled into large flexible arrays. Efforts were made to model both single elements and arrays using the ATILA code and the integral equation formulation (EQI).

Millimeter size microprobe hydrophones (BBs) have been designed and fabricated from miniature piezoelectric hollow ceramic spheres for underwater applications such as mapping acoustic fields of projectors, and flow noise sensors for complex underwater structures. Green spheres are prepared from soft lead zirconate titanate powders using a coaxial nozzle slurry process. A compact hydrophone with a radially-poled sphere is investigated using inside and outside electrodes. Characterization of these hydrophones is done through measurement of hydrostatic piezoelectric charge coefficients, free field voltage sensitivities and directivity beam patterns.

CYMBAL TRANSDUCERS

The cymbal transducer is a small Class V flextensional transducer that originated from the commercially successful "moonie" patent. It consists of a PZT disk sandwiched between two "cymbal" shaped metal end caps that provide the name. First proposed as an actuator, whose performance fills the gap between the multilayer and bimorph actuator, the cymbal was later developed as an underwater transducer. In this report we describe the design, characterization, modeling and optimization of cymbal transducers and arrays.

The underwater behavior of the cymbal transducer was modeled using the finite element analysis code ATILA. It was found that the underwater response is strongly affected by the boundary conditions imposed by the testing fixtures. The PC boards used in the initial experiments partially clamp the motion of the transducer, leading to distorted beam patterns and spurious peaks in the measured TVR curve. Excellent agreement between the calculated and experimentally measured transmitting voltage response and directivity patterns was later obtained with a potting technique in which "free" mechanical boundary condition was maintained for the transducer. The effect of PZT cap material and geometry on the underwater response of cymbal was investigated using ATILA. In general, individual cymbal transducers have a high Q_m and low electrical acoustic efficiency because of poor radiation efficiency, but much more promising results were obtained with cymbal arrays.

The previously used array assembling technique, the PC board technique, was found to have an anisotropic clamping effect on the transducers. A potting technique, which allows the transducers vibrate freely, was proposed and tested. It gives a higher and flatter TVR than the PC board technique. The resulting beam patterns are symmetric and in good agreement with a simple point source model. Two other mounting techniques using pressure release materials around the ceramic ring were also tested. Of the four techniques, the potting method appears to be the most successful. Therefore, a prototype 5x20 array was built by potting the cymbals in polyurethane. The array has a thin profile and low weight, making it superior to the 1-3 composites and tonpilz transducers for certain applications (Fig. 1).

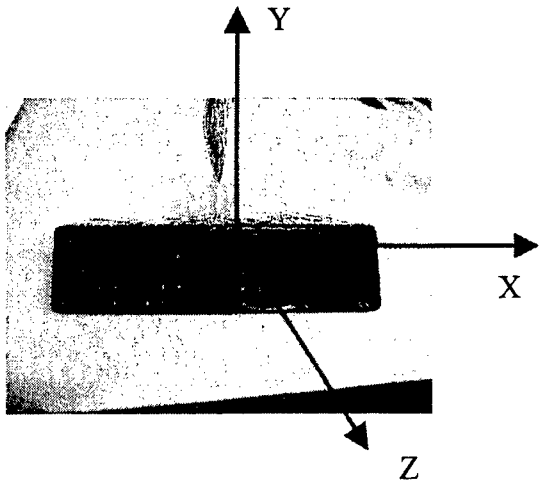

Fig.1 The potted 5x20 rectangular array with electrical connections

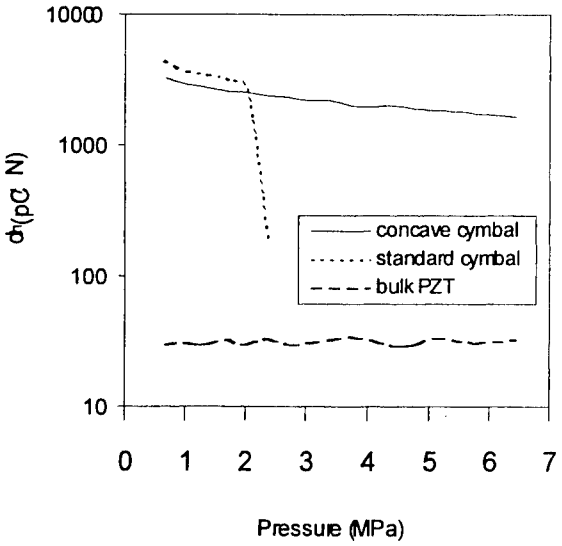

Fig. 2 Pressure dependence of the effective d_h coefficients for the standard and convex cymbal transducers.

Two methods were used to analyze the acoustic loading effect in the array. The equivalent circuit model is straightforward and can provide a qualitative understanding of the array interactions. By coupling finite element analysis to the well developed boundary element method, a more accurate and quantitative prediction of the acoustic loading effect can be achieved. Even though the transducers in the array are driven with the same voltage and phase, they behave differently because of mutual interactions. In a 3x3 array, the central transducer has twice as big displacement as the surrounding transducers. In addition to the displacement difference, the vibration velocities of the transducers lead to significant phase difference. As a consequence, the resonance is strongly damped, resulting in a broader bandwidth.

This study has resulted in two new designs: the double-dipper and the double-driver. The double-dipper consists of a ceramic ring bonded between two inverted cap shaped caps, making it a class VI "concave cymbal". The double-dipper significantly increases the pressure tolerance of the cymbal-type transducer while maintaining a high sensitivity (Fig.2). The use of a ceramic ring allows several poling configurations of the double-dipper which were investigated using ATILA. The double-driver consists of two ceramic disks glued back to back. The two disks are sandwiched between two metal end caps and are driven with different amplitudes and phase. While most small flextensional transducers have an omnidirectional beam pattern, a cardioid beam pattern can be obtained from a double-driver by exciting the driving elements in two different modes.

BB HOLLOW SPHERES

We have also been studying the design, fabrication, modeling and device characteristics of ultrasound transducers made from millimeter-size piezoelectric ceramic hollow spheres. Green ceramic hollow spheres were produced using a coaxial nozzle slurry process and a sacrificial core coating process in the size range of 1-6 mm in diameter and 12-200 μm in wall thickness. Ceramic powders with the morphotropic phase boundary compositions of lead zirconate titanate solid solution known as PZT-4 and PZT-5A, and a modified lead titanate composition were used in these two processes.

After sintering, the desired shapes were obtained by drilling, grinding, or polishing. Sphere surfaces were then coated with an electrode material in desired shapes and area of coverage. Two main poling configurations were studied: a radial poling configuration with inside and outside electrodes, and a tangential poling with top and bottom outside electrodes with several different electrode patterns. Dielectric, piezoelectric and ferroelectric properties of these transducers were measured. Vibration modes were determined using the ATILA finite element analysis (FEA) code, and associated resonant frequencies were measured and compared to the calculated values. The effect of sphere dimensions, materials and electrode configurations were analyzed using FEA. It was determined from the finite elements analysis of the structure that wall thickness variations do not have a pronounced affect on the

vibrations of the structure at lower frequencies (from kHz to low MHz).

Omnidirectional miniature hydrophones (Fig.3) were prepared from radially poled hollow spheres. Underwater sonar performance was evaluated by measuring free field voltage sensitivity (FFVS), transmit voltage response (TVR), source level and directivity beam patterns of these hydrophones. FFVS of –218 dB re 1V/μPa with a frequency independent response up to 500 kHz, and TVR of 150 dB @1m re 1μPa/V at 500 kHz were obtained from these transducers. These results were compared to those calculated by finite element analysis.

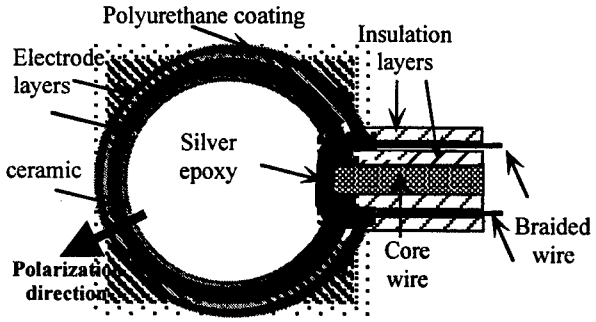

Fig.3 The modified piezoelectric hollow sphere hydrophone design

Hollow spheres were also placed into multielement arrays with individual spheres electrically connected to one another in parallel, series or a mix of both (Fig.4). Superior TVR, FFVS and directional beam patterns were obtained from these arrays.

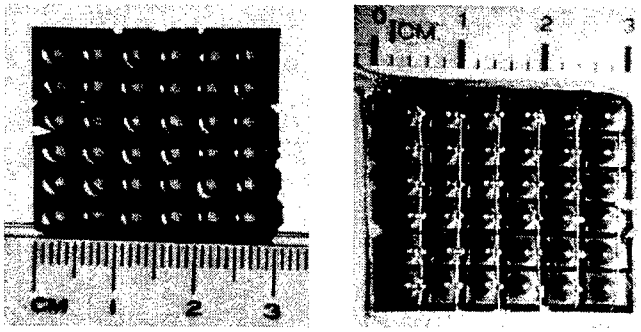

(a) spheres fixed in an epoxy layer (b) final device

Fig. 4 Top-view of a 6x6 array of spheres

Focused transducers were prepared for biomedical ultrasound imaging from dish-shape shell sections of the hollow spheres. Pulse-echo characteristics such as insertion loss, waveform and bandwidth were measured. These transducers were also modeled using FEA. Transducer operation frequencies of up to 50 MHz were achieved with *f*-numbers down to 1.

REFERENCES

J. Zhang, W.J. Hughes, A.C. Hladky-Hennion, and R.E. Newnham, *Materials Research Innovations*, 2, 252-255 (1999).

S. Alkoy, R.E. Newnham, A.C. Hladky-Hennion, A. Dogan, and J.K. Cochran, Jr., *Ferroelectrics*, 226, 11-25 (1999).

J. Zhang, W.J. Hughes, R.J. Meyer, K. Uchino, and R.E. Newnham, *Ultrasonics*, 37, 523-529 (2000).

R.J. Meyer, and R.E. Newnham, *Journal of Intelligent Materials Systems and Structures*, 11, 199-205 (2001).

R.J. Meyer, S. Alkoy, J. Cochran, T. Ritter, and R.E. Newnham, *IEEE UFFC*, 48, 488-493 (2001).

J. Zhang, A.C. Hladky-Hennion, W.J. Hughes, and R.E. Newnham, *IEEE UFFC*, 48, 560-568 (2001).

J. Zhang, A.C. Hladky-Hennion, W.J. Hughes, and R.E. Newnham, *Ultrasonics*, 39, 91-95 (2001).

R.E. Newnham and A. Dogan, *Metal-Electroactive Ceramic Composite Transducer*, 5,729,077, USA, March 17, 1998.

R.E. Newnham, J.K. Cochran, and S. Alkoy, *Hollow Sphere Transducers*, US 6,215,231 B1, USA, April 10, 2001.

Design and modeling of porous FGM piezoelectric actuators

Abdulhakim A. Almajid, Minoru Taya*

Center for Intelligent Materials and Systems, Department of Mechanical Engineering,
University of Washington, Seattle, Washington 98195, U.S.A
Tel:(206)-685-2850, Fax:(206)-685-8047, *E-mail:tayam@u.washington.edu

Kenta Takagi, Jing-Feng Li, Ryuzo Watanabe

Department of Materials Processing, School of Engineering, Tohoku University, Sendai, JAPAN

ABSTRACT

The mechanical behavior of a piezoelectric actuator was studied using classical lamination theory (CLT). The CLT accounts for piezoelectric coupling terms. CLT is capable of predicting the stress field and out of plane displacement of laminated piezoelectric layers. Piezoelectric functionally graded microstructure (FGM) materials were analyzed using CLT. The FGM is of porous graded piezoelectric materials. The porosity of the FGM porous piezoelectric material varies through the thickness of the laminate. Three layer FGM porous unimorph is investigated. Porous FGM unimorphs is fabricated. Different FGM thickness exponent are fabricated to optimize the displacement of the actuator. The analytical results are verified against the experimental ones resulting in a good agreement.

INTRODUCTION

Piezoelectric composites (PC) have been used in the development of intelligent materials. The use of PC-based sensors and actuators in structural systems lead to a better vibration control of such systems. Tzou and Garde(1989) used a thin laminate coupled with piezoelectric shell actuator for vibration control. The control of the vibrations of a flexible beam by utilizing piezoelectric actuator is studied by Baz and Poh(1988). Zhou and Tiersten (1994) used a variational method of elementary flexure and extension of composite plates to analyze a thin piezoelectric film incorporated in a structural system.

The conventional unimorph and monomorph actuators consist of piezoelectric plates and metal shims that are bonded together by an organic agent (usually epoxy resin). The inherent defect of such actuators is the cause of the deterioration of the bonding after a long period of use. The concept of functionally graded materials (FGM) is expected to be a good solution for such a problem (Almajid et. al. (2001)). Recently, the development of FGM piezoelectric actuators has attracted increasing attention. Zhu and Meng (1995) have developed an FGM actuator with a compositional gradient from high piezoelectric-low dielectric material to low piezoelectric-high dielectric material. Wu *et al.* (1996) fabricated a piezoelectric monomorph actuator that has graded electrical resistances through the plate thickness due to the controlled diffusion of zinc borate (ZnB).

The present work is focused on the development of another type of FGM piezoelectric actuators where PC has porosity gradients across the plate thickness. The porosity gradient was *in-situ* formed by sintering layer-stacked PZT powder compacts with stepwise varied contents of stearic acid as pyrolyzable pore-forming agent (PFA), which is burned out during sintering. The resultant ceramic plates with the graded porosity behave like a monolithic piezoelectric bender producing bending displacement when applied to an electric field in the thickness direction. The piezoelectric and elastic properties are gradually reduced through the plate thickness with increased porosity introduced by the pyrolysis of PFA. In the present study, monolithic piezoelectric ceramics with different porosities were prepared and their piezoelectric properties were investigated as a function of porosity, and the electric-field-induced bending displacement

characteristics of the porosity-graded samples were evaluated and analyzed based on a modified classical lamination theory.

CLASSICAL LAMINATION THEORY (CLT)

The classical lamination theory (CLT) model is applied to a thin piezoelectric plate under the assumption of plane stress along the plate thickness (z-axis) direction, i.e. $\sigma_z = \tau_{xz} = \tau_{yz} = 0$. The constitutive equations of a piezoelectric material in the absence of temperature effect are given by

$$\sigma_{ij} = C_{ijkl}\varepsilon_{kl} - e_{mij}E_m \qquad (1)$$

where σ_{ij}, ε_{kl} are stress and strain tensor components, E_m is electric field vector component, and C_{ijkl} is the elastic stiffness, e_{mij} is the piezoelectric coefficients. The classical lamination theory (CLT), as in any composite text book such as Gibson (1994) assume a state of plane stress along the z-axis, $\sigma_z = \tau_{xz} = \tau_{yz} = 0$. The CLT can be extended to account for piezoelectric laminate and the constitutive equations, of each piezoelectric lamina are given by,

$$\begin{Bmatrix}\sigma_x\\ \sigma_y\\ \sigma_{xy}\end{Bmatrix} = \begin{bmatrix}\overline{Q}_{11} & \overline{Q}_{12} & 0\\ \overline{Q}_{21} & \overline{Q}_{22} & 0\\ 0 & 0 & Q_{66}\end{bmatrix}_i \begin{Bmatrix}\varepsilon_x^\circ + z\kappa_x\\ \varepsilon_y^\circ + z\kappa_y\\ \gamma_{xy}^\circ + z\kappa_{xy}\end{Bmatrix} - \begin{bmatrix}0 & 0 & \overline{e}_{31}\\ 0 & 0 & \overline{e}_{32}\\ 0 & 0 & 0\end{bmatrix}_i \begin{Bmatrix}0\\ 0\\ E_z\end{Bmatrix}_i \qquad (2)$$

where

$$\overline{Q}_{ij} = C_{ij} - \frac{C_{i3}}{C_{33}}C_{j3}$$
$$\overline{e}_{ij} = \frac{C_{j3}}{C_{33}}e_{33} - e_{ij} \qquad (3)$$

and where subscript i in the square bracket in Equation (2) denotes the i^{th} lamina. It is noted here that $\overline{Q}_{ij}$, $\overline{e}_{ij}$ are the reduced elastic stiffness constants and reduced piezoelectric constants that are modified by the assumption of plane stress along the z-axis axis. $\varepsilon_x^\circ, \varepsilon_y^\circ$, and ε_{xy}° are the in-plane strain components at mid-plane, z = 0, κ_x, κ_y, and κ_{xy} are the curvatures of the plate. The electric field of the i^{th} layer is computed by using a multilayer capacitor model. Each piezoelectric lamina is considered a capacitor with dielectric constant. The electric field in each lamina of multi layer FGM piezoelectric can be obtained by considering the multi layers piezoelectric FGM laminate as a series of condensers. The relationship between the electric capacity and the voltage is given as

$$C_t = \frac{Q}{V_t} \qquad (4)$$

where C_t is the capacitance, Q is the charge, and V_t is the total voltage. The total capacitance in a series of capacitance is found as

$$\frac{1}{C_t} = \sum_{i=1}^{n}\frac{1}{C_i} = \sum_{i=1}^{n}\frac{d_i}{\varepsilon_i} \qquad (5)$$

where d_i and ε_i are the thickness and the dielectric constant for each lamina. The electric capacity in each lamina will then be

$$C_i = \frac{Q}{V_i} = \frac{\varepsilon_i}{d_i} \qquad (6)$$

Substituting Equation (4) and (5) into Equation (6) results in

$$V_i = Q\frac{d_i}{\varepsilon_i} = V_t\frac{d_i}{\varepsilon_i\sum_{l=1}^{n}\frac{d_l}{\varepsilon_l}} \qquad (7)$$

The electric field in each layer can then be

$$E_i = \frac{V_i}{d_i} = V_t\frac{1}{\varepsilon_i\sum_{l=1}^{n}\frac{h_l - h_{l-1}}{\varepsilon_l}} \qquad (8)$$

The resultant in-plane forces and bending moments are defined as follows

$$\{N, M\} = \sum_{i=1}^{n}\int_{h_{i-1}}^{h_i}\{\sigma\}(dz, zdz) \qquad (9)$$

By carrying out the integration through the plate thickness of h, the resultant forces and bending moments can be written as

$$\begin{bmatrix}N\\ M\end{bmatrix} = \begin{bmatrix}A & B\\ B & D\end{bmatrix}\begin{Bmatrix}\varepsilon^\circ\\ \kappa\end{Bmatrix} - \begin{bmatrix}N^E\\ M^E\end{bmatrix} \qquad (10)$$

where

$$[A, B, D] = \sum_{i=1}^{n}\int_{h_{i-1}}^{h}[\overline{Q}]_i(dz, zdz, z^2dz) \qquad (10a)$$

$$[N, M]^E = \sum_{i=1}^{n}\int_{h_{i-1}}^{h_i}[\overline{e}]_i\{E\}_i(dz, zdz) \qquad (10b)$$

and where h_{k-1} and h_k are the distance from the bottom of the plate to the bottom and top interfaces of the k^{th} laminae with k = 1,2, ... n, hence the thickness of the k^{th} laminae is h_k-h_{k-1}. Under the applied electric field in z-direction only, and in absence of external mechanical

loading, i.e. M and $N = 0$, in Equation (10) the in-plane strain and curvature can be solved as

$$\begin{bmatrix} \varepsilon^{\circ} \\ \kappa \end{bmatrix} = \begin{bmatrix} a & b \\ b & d \end{bmatrix} \begin{bmatrix} N^{E} \\ M^{E} \end{bmatrix} \tag{11}$$

where

$$\begin{bmatrix} a & b \\ b & d \end{bmatrix} = \begin{bmatrix} A & B \\ B & D \end{bmatrix}^{-1} \tag{12}$$

Under a given voltage difference throughout the laminate, one can then predict the stress and displacement field of each layer as well as the out-of-plane displacement of the composite plate.

RESULTS AND DISCUSSION

The concept of FGM (functionally graded material) was originally launched by Japanese materials scientists in late 1980 with the aim of designing stronger and more durable high temperature materials where a ceramic plate is bonded to metal plate with its interface being FGM microstructure. The FGM interface between the ceramic and the metal is to diffuse the otherwise high thermal stress induced by the mismatch of the coefficients of thermal expansion. The idea of the FGM is explored here to investigate whether FGM can reduce the stresses generated by the piezoelectric actuation while maintaining a high level of displacement. Three layers FGM is processed, Fig. 2. The FGM ranges from dense PZT to porous PZT. The top most layer is a dense PZT while the second and third layers towards the bottom are 10 and 20% porous, respectively. The thickness of each layer is predicted by the following equation,

$$\frac{h_i - \sum_{l=1}^{i} h_{l-1}}{h_t} = \left(\frac{i}{n}\right)^{\frac{1}{m}} \tag{13}$$

where h_i and h_t are the thickness of the i^{th} layer and the total thickness of the laminate, n is the number of layers in the laminate, m is the FGM thickness exponent.

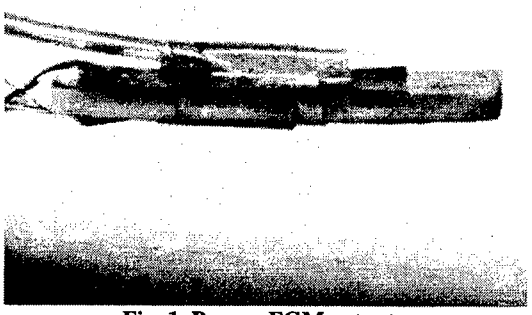

Fig. 1 Porous FGM actuator

The curvature can be evaluated from the strain measurement using the following equation,

$$\kappa = \frac{1}{\rho} = \frac{1}{t}\left(1 - \frac{1+\varepsilon_1}{1+\varepsilon_2}\right) \tag{14}$$

where t is the total thickness of the laminate and, ε_1 and ε_2 are the strain at the top and bottom locations, respectively. The comparison of the analytical to experimental data for the FGM actuator with FGM exponent, m=1, is shown in Fig. 2. The analytical agreed very well with the experimental results.

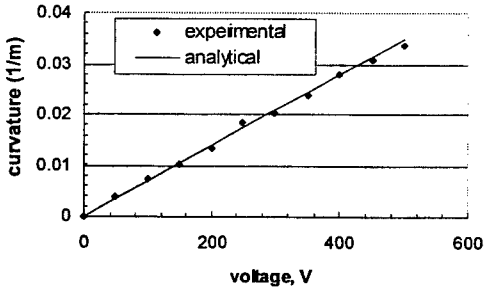

Fig. 2 Curvature versus voltage for FGM actuator

The effect of the thickness of each layer in the overall performance of the actuator is studied. The microstructural views of the porous FGM for different FGM exponent are shown in Fig. 3 where the porosity increases from the dense side to the porous one. The analytical and experimental values are presented in Fig. 4. The FGM exponent of one gave the highest curvature.

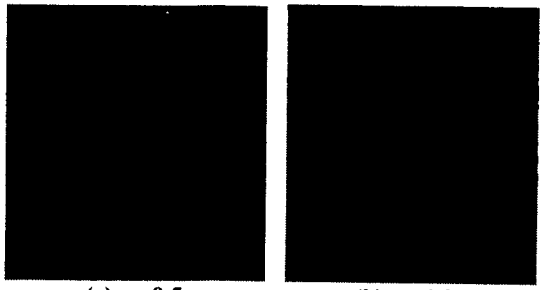

(a) m=0.5 (b) m=1.0

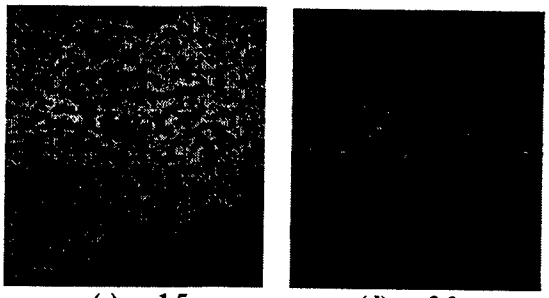

(c) m=1.5 (d) m=2.0

Fig. 3. Microstructural view of 3 layers porous FGM

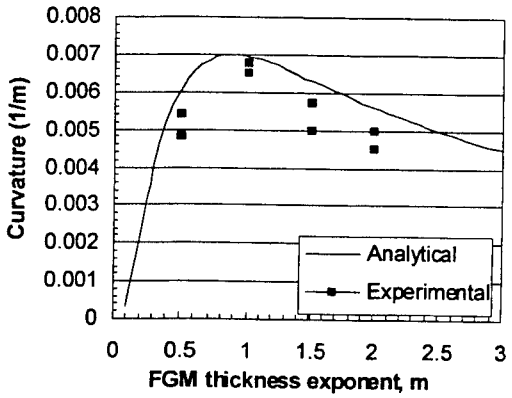

Fig. 4 The curvature as a function of FGM exponent.

CONCLUSION

The CLT results coincide well with the experimental results. The FGM exponent, m=1, gave the maximum curvature of the actuator.

ACKNOWLEDGMENT

The present work was supported in part by a grant from Air Force to the University of Washington (F49620-96-0158) and NEDO project on intelligent materials and structures.

REFRENCES

Alamjid, A., Taya, M., and Hudnut, S. 2001. "Analysis of Out-of-plane displacement and stress field in a piezocomposite plate with functionally graded microstructure," *Intl. J. Solids Structures,* 38:3377-3391

Baz, A., Poh, S. 1988. "Performance of an active control system with piezoelectric Actuators," *J. Sound Vib.*, 126:327-343

Gibson, R. F. 1994. "Principles of Composite materials and Mechanics," McGraw Hill

Tzou, H. S. and Garde, M. 1989. "Theoretical Analysis of a Multi-Layered Thin Shell Coupled with Piezoelectric Shell Actuators for Distributed Vibration Controls," *J. Sounds and Vibration*, 132:433-450

X. Zhu, Z. Meng Sensors and Actuators, A48 (1995), 169.

Wu, C. C., Khan, M., and Moy, W., 1996. "Piezoelectric Ceramics with Functional Gradient: A New Application in Material Design," *J. Am. Ceram. Soc.*, 79:809-812

Zhou, Y. S. and Tiersten, H. F. 1994. "An elastic analysis of laminated composite plates in cylindrical bending due to piezoelectric actuators," *Smart Mater. Struct.*, 3:255-2

Piezoelectric Ceramic Transducers for Miniaturized Applications

Angus I. Kingon, A. Gruverman, J.F. Mulling, D.J. Kim, and J-P. Maria, J.A. Palmer*, E.Grant* and P. Franzon*

Department of Materials Science and Engineering, North Carolina State University, Raleigh. NC 27695-7919
Fax: (919) 515 3419,
*Department of Electrical and Computer Engineering, North Carolina State University, Raleigh NC 27695
Email: angus_kingon@ncsu.edu

This paper describes the use of two types of piezoelectric actuators in small, high torque or high load linear and rotary motors. The first type is that of the low cost, flexural mode, stressed unimorphs (tradenamed "Thunder"). We show that the compliance of these actuators must be carefully considered when used under loaded conditions. The second actuator types is the stack operating in length mode resonance, with mechanical couplers to achieve the necessary longitudinal and torsional components of stator displacement.

1. INTRODUCTION

Piezoelectric ceramic actuators have been used to power a number of different types of linear and rotary motors [1]. A particular interest is in miniaturized motors, where scaling issues limit the efficiency and power density of electomagnetic motors. However, for more widespread application of piezoelectric motors to be achieved, several important issues need to be resolved. Among these are the well-known issues of motor wear, and efficient power supplies, as well as that of achieving high load-bearing capability, or torque density. This paper addresses the design of linear and rotary motors using two types of actuators, while paying special attention to the issue of load and torque.

2. LINEAR MOTORS BASED ON STRESSED UNIMORPHS

2.1 Characterization of Stressed Unimorph Actuators

The stressed unimorph actuators utilized in the present work, also known as "Thunder" actuators, are of interest due to the large displacements which can be achieved, and are produced by bonding PZT ceramic and substrate at elevated temperature [2, 3]. The thermal expansion mismatch results in the ceramic being under compressive stress at room temperature, this stress being only partly relieved by bowing of the unimorph. The stressed unimorphs are closely related to the "Rainbow" actuators [4], which achieve compressive stress in the piezoelectric ceramic by reduction of one side of the PZT to Pb metal. While there has been some debate regarding the mechanistic origins, both the Thunder and Rainbow actuators have been shown to achieve large displacements, significantly larger than what is typically achieved in a standard unimorph or bimorph configuration [5-7]. We have concentrated on the Thunder type, due to their greater ruggedness, and more reliable fabrication process.

A typical Thunder actuator is shown in Figure 1a, with the corresponding field-displacement "butterfly loops" shown in Fig 1b. Asymmetry in the loop is clearly observed. We can simply attribute the large displacement capability of the Thunder element to this asymmetry; it allows the transducer to be driven at high fields in one direction, without failure of the ceramic by the usual tensile fracture. It should be noted that driving the actuator in the large loop direction corresponds to "flattening" of the actuator, which increases the average compressive stress in the PZT. If the actuator is operated with a static load applied, maximum performance is achieved if the displacement direction is in the same direction as the static load. In other words, the method of operation is to consider the actuator as a spring. Applying a field displaces the spring in the direction of increasing spring tension, and removal of the field allows the spring to do work against the load, displacing back into its zero field position.

As can be deduced from the above discussion, the actuator is a **compliant** structure, and special care must be taken if one is to achieve large displacements under loaded conditions. Working with a compliant actuator under loaded conditions, implies that particular consideration must be given to the following: (a) the load displacement (strain of the actuator versus stress) in conjunction with the piezoelectric displacement; and (b) the mounting

conditions. We make a few points regarding these issues.

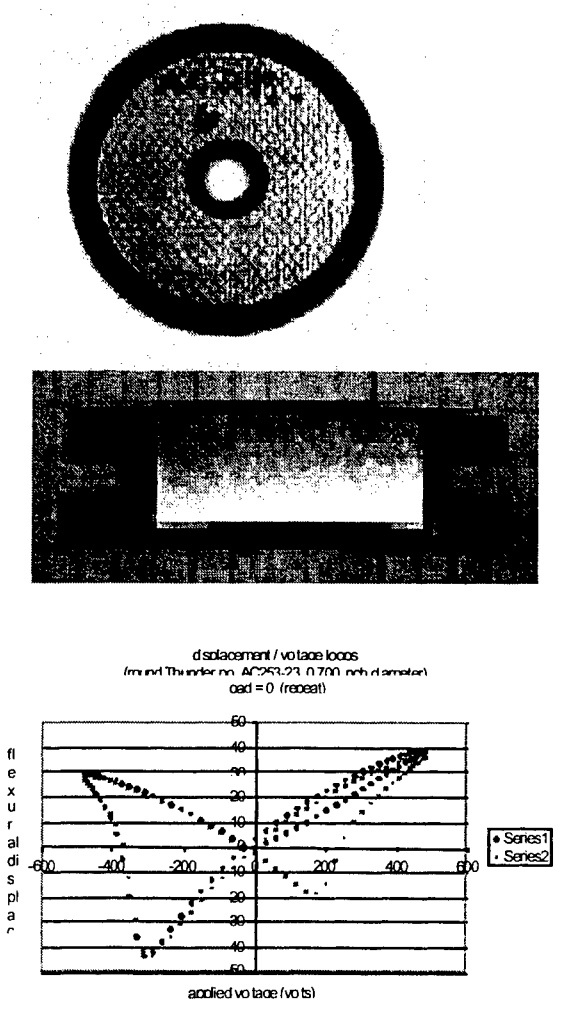

Figure 1: (a) Typical "Thunder" actuators; (b) typical asymmetric butterfly displacement-voltage loop.

Figure 2 shows a set of displacement curves for a typical Thunder actuator at drive voltages up to 480V, and under superimposed static loads of 10N. The data implies that the achievable displacement decreases with increasing load, as expected. The end conditions are such that rotation and translation of the ends are allowed. However, Figure 3 shows data corresponding to that in Figure 2, but plotted such that there is a single displacement reference. It can be seen that in this case, the displacement due to the 10N load is considerably larger than the piezoelectric displacements (at each load). In theory, the actuator can be used up to loads at which the two curves intersect, ie that static load at which no further piezoelectric displacement is observed. The practical load limit however, is usually lower, and is strongly influenced by the overall device design. For example, large field-driven displacements (many millimeters) can be achieved if the Thunder actuator is designed into the mechanical system as a spring, and the system is operated at resonance. This is consistent with observations that Colla has made regarding the use of unimorphs for vibration control systems [8].

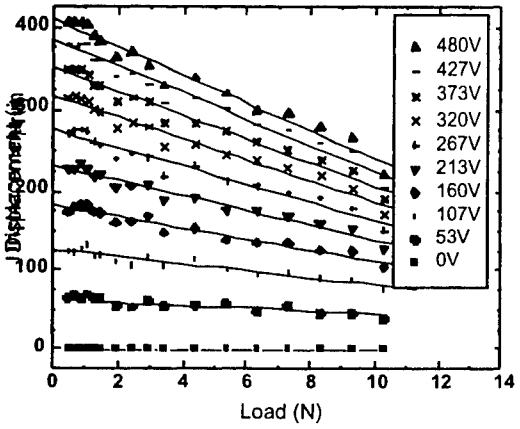

Figure 2: Displacement versus load curves for a typical Thunder element at various drive voltages. The displacement is referenced to zero voltage at each applied load.

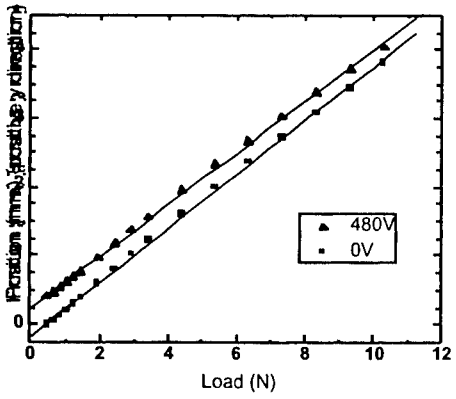

Figure 3: Displacement data corresponding to 0 and 480 V from Fig 2, but with a displacement referenced to the starting value.

The second point is that the displacement-field-load curves for these compliant Thunder actuators are strongly dependent upon the mounting (or end) conditions. This has been discussed in detail in a recent paper [9], but the summary is that constraining the end conditions with respect to translation and/or rotation, reduces the piezoelectric displacements, but increases the actuator stiffness. This makes the actuator less sensitive to static loads. In some cases larger displacements can be achieved at high load.

2.2 Use of Stressed Unimorph Actuators in Linear Motors

The designs studied were influenced by piezoelectric linear inchworm motors. The motivation for the present work was based upon the need for high tolerance slides in standard inchworm designs, particularly as these are scaled to smaller sizes. We therefore wanted to explore the use of Thunder-type actuators, which displayed some promise based upon the combination of large displacement, reasonable load-bearing capability, and low cost. Our design brief was for a low-cost linear motor could load an actuation spring to values of 10-20 N. In this paper we describe our "Thunderworm" concept, which consists of a single Thunder actuator elements (or several connected mechanically in series), along with two passive latches. The use of passive latches contrasts with the active latches more conventionally used in inchworm motors. The latches allow one-way motion along the track. The device therefore functions by the actuator pushing one clamp ahead, while anchoring itself using the second, followed by anchoring itself using the first, and pulling the second along as during the actuator depowering cycle. A motor of this type is shown in Figure 4.

While the design is novel, and forces of up to 18 N could be achieved at linear speeds of 400 mm/sec, the concept did not quite achieve the force performance which we expected. The design turns out to be strongly limited by the passive clamps. An extensive effort was put into modelling and optimizing the clamp designs. The important feature is the "backlash" inherent in the clamp. The backlash clearly needs to be significantly smaller than the actuator displacement. However, as the displacement reduces with increasing load (for example the spring being loaded), the ultimate force the can be achieved is that load at which the piezoelectric displacement reduces to the latch backlash (at the same load). The optimized latches require appropriate design as well as appropriate choice of materials to minimize material elasticity effects.

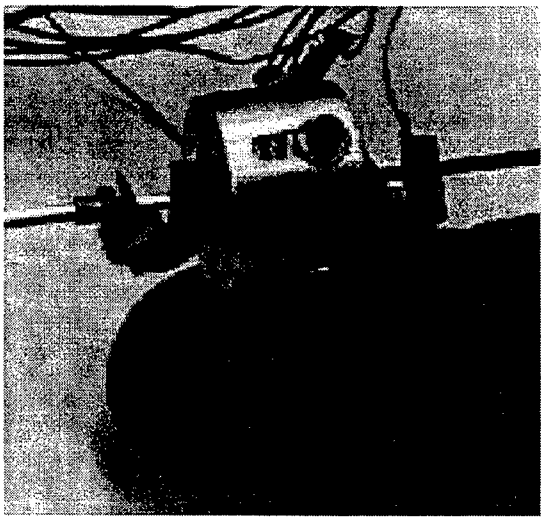

Figure 4: Example of a miniature "Thunderworm". The stressed unimorphs are circular, and the two passive latches can be seen on either side of the actuator housing.

The concept is therefore applicable to low-cost linear motors with intermediate force requirements.

3. ROTARY ULTRASONIC MOTORS

This section of work that will be described has the objective of developing small size, low cost rotary solid state motors which are optimized for torque. The need for only one rotation direction, coupled with lax speed control requirements, allowed us to explore the "Kumada" –style motors. These are characterized by using an ultrasonic stack with a single length-mode resonance, and converting this into an ultrasonic wave with coupled longitudinal and transverse components. Kumada achieved this by use of a simple "torsional coupler", although there are a number of different approaches to achieving the coupled resonances.

The work has focused upon optimizing the torsional coupler by use of finite element analyses, coupled with an experimental characterization of the displacements of the torsional couplers using optical techniques. Figure 5 shows the output of a typical FEM analysis of a torsional coupler, with the longitudinal and torsional components clearly shown. Figure 6 shows a picture of a small-scale ultrasonic motor that operates at about 60 kHz, and can rotate masses of several kg.

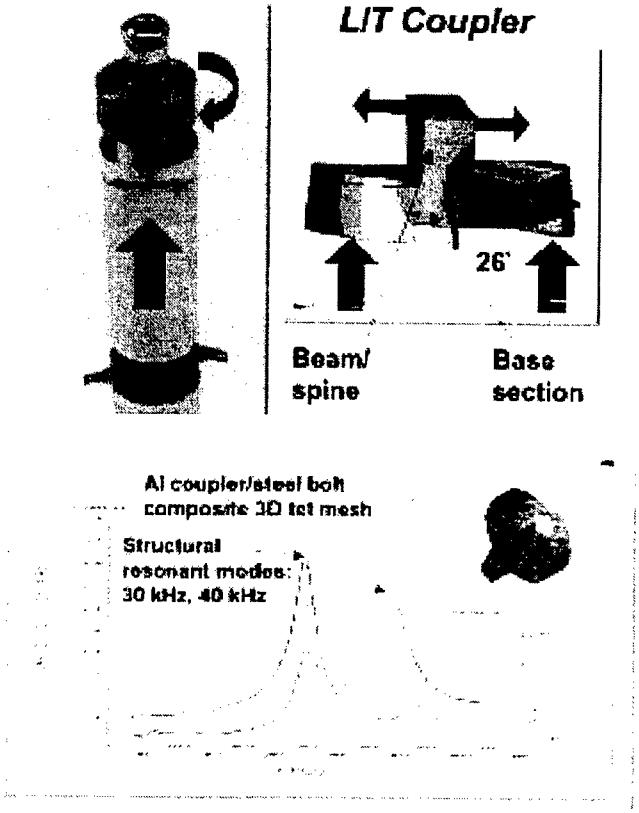

Figure 5: (a) High torque rotary ultrasonic motor showing a Langevin-type driver, torsional coupler, and rotor. The FEM static displacement analysis on the right is of the torsional coupler. (b) Dynamic analysis of the resonances, including both longitudinal and torsional components.

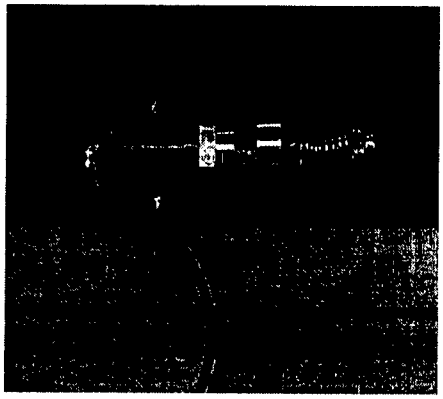

Figure 6: Example of a miniature Kumada-style motor driven by a PZT stack (under orange cover.he motor weighs less than 10g.

4. CONCLUSIONS

Piezoelectric ceramics have been used to demonstrate a new concept in linear solid state motors (section 2), and to optimize an old design for a rotary ultrasonic motor in miniaturized form (section 3). More understanding of scaling is required to achieve a combination of small size and high torque in the case of the miniature rotary motors.

ACKNOWLEDGMENTS:

Research supported by DARPA under contract 39998–98-C-3566

REFERENCES

1. K. Uchino, *Piezoelectric Actuators and Ultrasonic Motors,* Kluwer Academic Publishers, Boston/Dordrecht/London, 1997.
2. *R. F. Hellbaum, R. G. Bryant and R. L. Fox, Thin layer composite unimorph ferroelectric driver and sensor, US patent number 5632841 (1997).*
3. *"Thunder" is trademark of Face International; Norfolk, Virginia, USA (www.faceco.com)*
4. *G. H. Haertling, Rainbow Ceramics- A New Type of Ultra-High-Displacement Actuator, Bull. Am. Ceram. Soc. , 73, (1994) 93-96.*
5. *Y Sugawara, K. Onitsuka, S. Yoshikawa, Q. C. Xu, R. E. Newnham and K. Uchino, Metal-ceramic composite actuators, J. Amer. Ceram. Soc. 75, (1992) 996-998.*
6. *K. M. Mossi, G.V. Selby, and R.G. Rryant, Thin-layer composite unimorph ferroelectric driver and sensor properties, Materials Letters 35, (1998) 39-49.*
7. *S. A. Wise, Displacement properties of RAINBOW and THUNDER piezoelectric actuators, Sensors and Actuators A 69, (1998) 33-38.*
8. *E.L. Colla, E.S. Thiele, D. Damjonvic and N. Setter, Proceedings of the 2000 12th International Symposium on the Applications of Ferroelectrics, ed S.K Streiffer, B.J. Gibbons and T. Tsurumi, publisehd by IEEE, p317-320 (2001).*
9. *J. F. Mulling, T. Usher, B. Dessent, J. A. Palmer, . Franzon, E. Grant and A. I. Kingon, accepted for publication in Sensors and Actuators A 3090 (200*

Advanced Sonar Technologies For 21st Century Torpedoes

James G. Kelly and Gerald T. Stevens
Naval Undersea Warfare Center Division Newport
Fax 401 832 1122
Fred Nussbaum
ANTEON
nussbaumf@npt.nuwc.navy.mil

The US Navy needs to develop advanced sonar technology for torpedoes and UUV's in order to conduct effective ASW operations in littoral waters, which are defended by increasingly sophisticated platforms, weapons and countermeasures. To deal with these challenges, torpedo sonars must provide more acoustic resolution than was formerly required for open ocean ASW. This will drive designs of advanced torpedo sonars to differ markedly from the torpedo sonars currently in use. For example, to double acoustic resolution, the number of sensors in a torpedo sonar will quadruple. To address the technical issues associated with higher sensor counts, consideration is given to separating acoustic transmit and receive hardware functions. Processing hundreds of sensor signals in real time poses technical (and cost) challenges. Ongoing development at NUWC of advanced sonar transducer and array technology and development of advanced signal conditioning and processing hardware technology is the subject of this paper.

DISCUSSION

Prior to the last decade the US Navy's ASW mission was to prosecute threat submarines in open ocean. Today and for the foreseeable future the most likely engagement sites are in the littoral, but current fleet torpedoes which were introduced in the 1970's and 1980's are optimized to detect and home on targets in deep water. Although current torpedoes can operate effectively in some benign shallow water environments they do not match their deep-water performance effectiveness when operating in the harsh acoustic environments found at many potential littoral conflict sites. This, coupled with proliferation of quiet air independent powered submarines, advanced torpedoes and sophisticated weapon countermeasures provides impetus to develop advanced torpedoes that can operate in both littoral and in open ocean environments.

Environmental conditions that make operating in littoral sites so challenging (for an acoustic homing torpedo) include reverberation from surface and bottom boundaries and sound velocity profiles that exhibit large (frequently unpredictable) depth/horizontal gradients over short ranges. Echo returns from relatively nearby targets (and false targets) arrive via multiple paths having varying angles of arrival and exhibiting a range of time delays. Small changes in relative position of a torpedo and target can cause target echo returns to fade abruptly at one frequency and appear abruptly at a different frequency. To obtain accurate target range and bearing estimates in such acoustic environments requires that the receive angles of target echo returns be measured accurately and the only way to do that is with sonar receivers that provide considerably more angular resolution (narrower beams) than is provided by current fleet torpedo sonars. Since physical aperture on the nose of a torpedo is more or less fixed, this will require torpedo sonars to employ higher operating frequencies in the littoral compared with homing frequencies used for open ocean operations. Additionally, wider bandwidth capability is also needed (at the high frequencies) to avoid data starvation in situations where frequency dependent fading occurs.

The reason that current torpedo sonars don't provide the angular resolution needed for effective shallow water operation is that

their design was subject to a trade-off to maximize detection ranges in deep water while maintaining just enough bearing resolution to home effectively. That was accomplished by minimizing the operating frequency, which reduced acoustic aperture, which in turn reduced angular resolution. There are only two ways to increase acoustic resolution; one is to increase physical aperture and the other is to operate at higher frequencies.

Increasing the physical aperture is not feasible because current torpedo sonars already use most of the real estate available on the nose, so increasing the sonar operating frequency is the only way to increase angular resolution and improve torpedo performance in littoral environments. However, a redesigned torpedo sonar must also retain ability to operate at the current lower frequencies if it is to be capable of open ocean operation at current levels of effectiveness.

To highlight technologies that need to be developed to satisfy this need, this paper will focus on a notional torpedo sonar that can operate over a wide band of frequencies, up to 50kHz at the high end of the band. The high end of a sonar's operating band dictates its sensor spacing and sensor count. To function effectively at 50 kHz the notional sonar will be populated by 300-350 sensors that are spaced little more than one half wavelength apart (at 50 kHz). If sensor spacing is appreciably greater than one half wavelength, the sonar will generate grating lobes and spatial discrimination will be degraded. This is a fundamental fact of life for any sonar array and cannot be disregarded.

The sensor count of the notional sonar could be reduced and still maintain proper spacing. An example would be a depleted sensor array of 100-150 sensors. The drawback of such an arrangement is that it greatly reduces sidelobe control, resulting in sidelobe levels that cannot be brought below ~25 dB. Actual sidelobe levels would most likely be considerably higher. Since low sidelobes are of great value in reducing reverberation returns (which are particularly problematical in littoral environments), the notional sonar will contain a fully populated sensor array.

To employ higher frequencies in active mode for target detection in shallow water, the notional sonar will be designed to project a wide beam (but to receive echo returns on many narrow beams). This mode of operation is required to maximize volume search rates.

Transducer hardware employed in the notional sonar will be functionally discrete. That is, one transducer group will be used exclusively to transmit acoustic signals and the other transducer group will be used exclusively to receive them. To allow both transducer groups to use the entire available physical aperture, they will be stacked one above the other. The active transducers will be the base layer and the receive hydrophones will be the top layer.

Foregoing remarks regarding sensor spacing and sensor count apply to the top layer array of receive hydrophones. The number of transducers required to project active signals will be far fewer.

There are a number of unique engineering challenges that must be addressed to implement this approach.

a) Mounting an acoustic hydrophone array over a high power projector array
b) Channeling hundreds of individual sensor signals from the array to the interior of the torpedo
c) Processing hundreds of signal outputs in real time

The paper to be presented addresses these challenges.

Active and Passive Structural Vibration Control using Piezoelectric Ceramics

S. Yoshikawa and M. Giovanardi
Active Control eXperts, Inc. (ACX), A Division of Cymer, 215 First Street, Cambridge, MA 02142
Fax: 617-577-0656
e-mail: syoshikawa@cymer.com

ABSTRACT

A new type of composite damper, a hybrid active and passive damping system, was designed and built which is capable of attenuating sound radiation due to structural vibration in a wider frequency range. This hybrid damper combines the broadband higher frequency control capability of constrained-layer viscoelastics with the narrowband lower frequency capabilities of active control using piezoelectric ceramic actuators and sensors.

Another example of vibration/motion control was shown in the application of second stage meso-scale actuators for hard disk drive read/write head precision control using piezoceramic single crystal. A significant improvement was shown both in the reduction of radiated sound and in the settling time of the disk drive head.

INTRODUCTION

Piezoelectric ceramics have been applied to control vibration and motion of various structures, including aircraft fuselages and precision positioning equipment. A passive shunt with piezoceramic actuators for sports equipment [(1)], and buffet flutter suppression on and F-18 twin tail through active control[(2)] have been discussed previously.

In this extended abstract, the use of piezoceramic actuators for active-passive hybrid damping of sound radiated by plates for noise suppression in aircraft cabins and hard disk drive head motion/vibration control through second stage actuators are discussed.

ACTIVE-PASSIVE HYBRID DAMPING

Active damping of sound radiation has in the past not been able to find its market in production applications despite its proven effectiveness for specific applications. One of the main reasons is that broadband control very quickly reaches its limits in terms of variability allowed to the structure. While it is possible to design an excellent broadband control law for a controlled environment, it is also nearly impossible to do so for a variable environment or for structures with high modal density, such as thin plates. However, single mode control laws can be sufficiently stable to the environmental changes a structure undergoes during its lifetime, but can only do so in low frequency or low modal density applications. Conversely, passive methods for broadband sound reduction have been successful in the past, however only in high frequency, high modal density applications. This leads to the conclusion that if it were possible to combine the positive aspects of the two approaches, an optimal control system would be found.

While the concept of combining active and passive materials is not new and has been explored elsewhere[(3,4)], most of these studies concentrate on improving the damping characteristics of the passive material by adding a layer of active materials, such as a piezoceramic plate, as a constraining layer and increasing the shear in the passive layer through activation of the active layer (a method called ACLD, or Active Constrained Layer Damping). Although ACLD increases the performance of the passive layer, it does not make full use of the active layer, because of the soft viscoelastic layer residing between active layer and the structure.

The concept presented in this work performed under a NASA SBIR Phase I program uses a piezoceramic actuator for active control in its optimum condition, i.e. directly bonded to the structure, while a constrained-layer damper is placed on top to add optimal passive damping. Figure 1 shows the cross section of such a system.

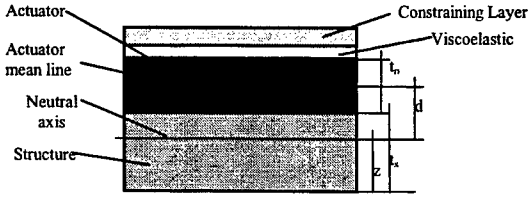

Figure 1: Cross section of hybrid damper

First, the behavior of viscoelastic material was modeled through a macroscopic approach called standard nonlinear model, then in order to optimize the thickness of each layer, an analysis was performed based on the simple model shown in Figure 1. A survey of constrained-layer viscoelastic materials was done to find a material suited for the kind of application desired. Based on the modeling and analysis, the "Damping Foil 2552"(3M) was selected. It consists of a 0.127 mm thick viscoelastic layer with adhesive on one side, and a 0.254mm thick aluminum foil on the other side.

The actuators used to demonstrate the concept were ACX QuickPack actuators, Type QP40W. The constrained-layer viscoelastic was cut out to fit the size of the actuator, and bonded directly on top. Figure 2 shows the prototype hybrid actuator.

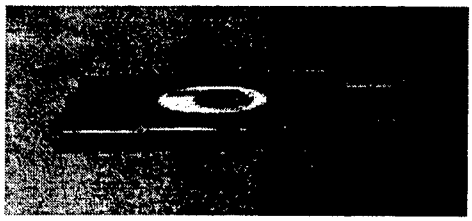

Figure 2: Prototype hybrid actuator with ACX QP40W actuator and 3M Damping Foil 2552.

An aluminum plate of the approximate dimension of a fuselage bay between struts (25x36cm, with a thickness of 1mm) was chosen as a test structure and set up in a transmission loss facility. The plate was bolted into an anechoic wall, excited from one side through a speaker signal and the sound and vibration were measured on the opposite side of the wall. Fifteen accelerometers, mounted to the back of the plate, and one microphone in the front of the plate on the anechoic side were used to measure the sound radiation. A random signal between 0-800 Hz was fed into the speaker, with the sound levels reaching 100 dB on the speaker side. Figure 3 shows the test set-up.

To obtain a good comparison between the three different types of control approaches; purely passive, purely active, and hybrid, tests were performed with viscoelastic on and off, and with the active control turned on and off. Figure 4 shows the layout of actuators and viscoelastic constrained layer strips used for this test. The patches 1 and 2 are piezoelectric actuators with viscoelastic constrained-layer, i.e. hybrid dampers, and patches 3-6 are viscoelastic constrained layer patches that were subsequently removed for the tests without passive damping. Additional tests showed that patches 3-6 added only a marginal amount of damping because of their non-ideal location, while patches 1-2 were the most effective.

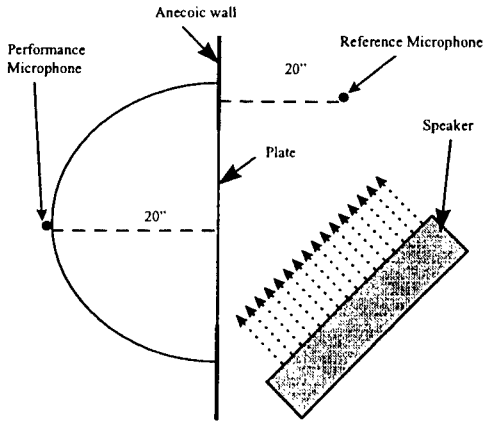

Figure 3: Test set-up of hybrid damper

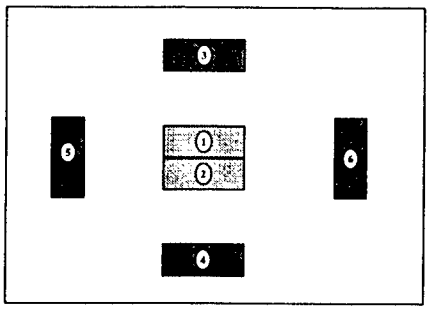

Figure 4: Hybrid damper layout on the panel

One of the advantages of a hybrid actuator over a pure active broadband control is the fact that the control design is simpler, since only a limited number of modes is targeted. In this study, the (1,1) and (1,3) modes were targeted since they were the lowest two radiating modes, isolated from the rest. A positive position feedback or PPF control approach was used in this case. The transfer function from actuators to sensors was collected and a model fit to it with ACX SmartID™ software. Based on this model description of the plate, the closed loop response was simulated to determine the optimal values for the control parameters.

The optimal control was then implemented and results collected with only passive, only active and active-passive hybrid control strategies. Figure 5 shows the performance of the hybrid system; due to space limitations not the all data can be shown, but the results show that the first two modes were reduced by active control, and peaks above 450Hz influenced by the passive dampers.

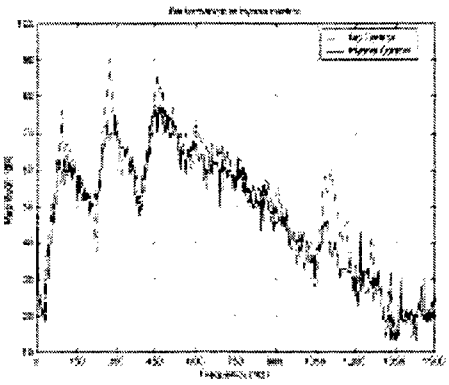

Figure 5: Performance of the hybrid damper

SECOND STAGE ACTUATION FOR DISK-DRIVE SUSPENSION

As hard disk drive areal densities increase at a compound annual growth rate of 60%, disk drives must position the head over increasingly small areas while moving more rapidly to reach the desired position. This results in an increase in vibration disturbance. To meet this demand, many hard disk drive manufactures have created prototype dual-stage actuators employing piezoelectric ceramics for the second stage. The terms micro-actuators and micro-positioning are used in this context since either very small (millimeter or meso-scale) actuators at the base of the standard suspension, or actual microactuators (micrometers scale) with MEMS technology at the tip of the suspension close to the read-write heads (co-located)[5] are used.

Under the AXIS (Advanced Crystal Integrated Systems) Consortium program funded by DARPA, the application of PZN-PT single crystal piezoceramic as a second stage disk drive actuator was studied[6], based on the fact that the single crystal materials provides larger stroke than its traditional PZT counterparts.

First, the 3-1 direction of the free stain of single crystal PZN-PT cut to the size of second stage mesoactuators was measured using a laser interferometer, and compared that of PZT-5H ceramics. At the maximum field tested (up to 8 kV/cm), the single crystal material showed twice the displacements of PZT-5H. Each material was then placed in the suspension as shown in Figure 6.

The test set-up is shown in Figure 7. From the displacement data of the second stage actuator placed in the suspension, an attempt was made to construct the force-displacement curve for both materials, since the higher compliance value of the single crystal was a concern. While the force calculation for the single crystal indicated still nearly two times higher displacements at the same force as those of PZT-5H, repeated tests showed another problem. Regardless of which materials were used, the strain concentration in the bonding area is such that fatigue cracks eventually formed. This needs to be investigated separately, and hinged actuator system will have to be introduced to solve this problem.

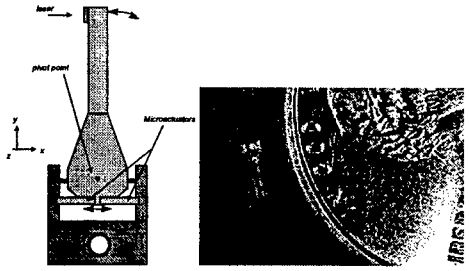

Figure 6: Suspension with mesoactuator location and actual size compared to that of a penny coin.

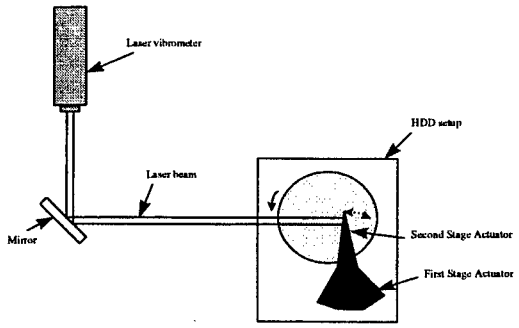

Figure 7: Test setup

A classical linear quadratic gaussian (LQG) control approach was used for servoing of the first and second stage actuators, with the laser vibrometer output as feedback signal. A digital electronics board was built for the laser vibrometer to overcome the difficulty of reading large motions with high resolution with a single sensor. While the first stage actuator has much larger motion, it also needs much less resolution, and the second stage has a small range of motion, but requires much higher resolution.

The simulated voltages for the voicecoil (above) and the piezo actuator (below) during a step response are displayed in Figure 8 and Figure 9, showing the significant improvement in the use of PZN-PT single crystal as the second stage actuator as compared to the use of PZT-5H.

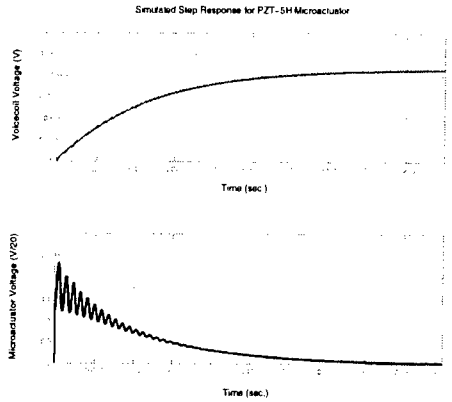

Figure 8: Step response voltages with polycristalline actuator

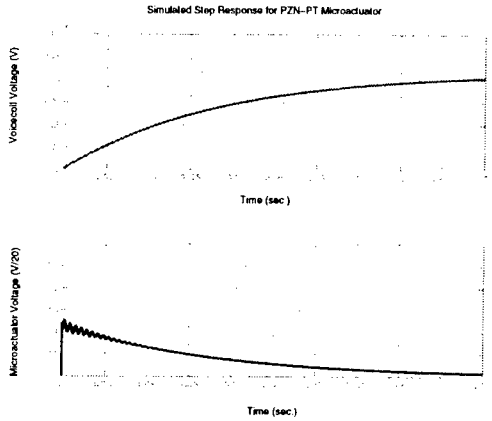

Figure 9: Step response voltages with single crystal actuator

Further investigation brought a detailed performance metric for the dual stage system. Most conventional Hard Disk Drives (HDD's) have a recording density of 1 Gb/in^2, a track density of 5 kTPI (kilo tracks per inch) and a servo bandwidth of 500-600 Hz. In the near future, the recording densities will reach 10 Gb/in^2, the track densities 25 kTPI and the servo bandwidths 2kHz or more. This requires a 1μm track width and a ±0.1 μm tracking accuracy. Limits of ±0.05 μm and 2kHz should therefore be used as performance targets. These numbers also show why a single crystal actuator is needed, since the maximum stroke recorded with PZT-5H second stage actuator is in the range of only 2 μm.

SUMMARY

Piezoelectric ceramics have been shown to provide effective vibration damping of low and well-defined frequency peaks for panel-like structures. However, in order to control larger bandwidths the control design becomes extremely complex. It was shown that the use of piezoelectric ceramics in combination with viscoelastic constrained layer damping gives good performance for acoustic noise control over a broad bandwidth for aeronautical applications.

A second stage mini-actuator for disk drive suspensions was introduced as another example of the use of piezoelectric materials for precision motion and vibration control. Both PZN-PT single crystal and PZT-5H ceramics were tested as second stage actuators in motion ranges where single stage actuation alone cannot meet the future requirements. The single crystal material showed superior performance over PZT-5H. A significant contribution was also made to developing better sensing methods and the servo control theory involved in such an application.

ACKNOWLEDGMENTS

A portion of this effort was funded under a NASA SBIR phase I, and also under the AXIS consortium lead by TRS Ceramics, which was funded by DARPA/NAVSEA.

REFERENCES

1. S.Yoshikawa, A.Bogue, B.Degon, "Commercial Application of Passive and Active Piezoelectric Vibration Control" Proceedings, International Symposium on application of Ferroelectrics XI, Montreux, Switzerland, Aug 24-27, 1998. IEEE #98CH36245, pp293-294
2. M.Hopkins, R.Moses, D.Zimcik, D.Henderson, T.Ryall and R.Spangler, " Active Vibration Suppression Systems Applied to Twin Tail Buffeting," Industrial and Commercial Applications of Smart Structures Technologies, SPIE vol. 3326, 1998, pp27-33
3. W.H.Liao, and K.W. Wang, "A new active constrained layer configuration with enhanced boundary conditions," Smart Materials and Structures, Vol.5, 1996 pp. 638-648
4. I.Y. Shen, "Hybrid damping through intelligent constrained layer treatments," ASME Journal of Vibrations and Acoustics, 116, 1994, pp. 341-349
5. B. McInerney, "Surveying micro-positioning technology for advanced disk drives" DATA STORAGE, Aug 2000 pp.24-27
6. M. Giovanardi, K. McKenney, J. Rule, S. Yoshikawa, "Single crystal disk drive mini actuators", Proceedings 8th International Symposium on Smart Structures and materials, Newport Beach, CA, March 4-8, 2001.

Large Displacement Piezoelectric Actuators Using Shear

Michael T. Strauss
HME, 56 Federal Street, Newburyport, MA 01950
PHONE: 978-462-0102 (P), FAX:508-462-0102
EMAIL: mstrauss@alum.mit.edu

ABSTRACT

Piezoelectric shear coefficients, d_{15}, are 200% to 400% greater than d_{31} (used in benders and flextensors) and 20% -70% greater than the piezo-coefficients d_{33} (used in stacks and multilayers) for most materials. Even taking into account the lower modulus for shear, the strain energy density for a given electric field is as high or higher for shear strain than d_{33} and much higher than d_{31} actuation. An actuator that can convert a shear strain into a linear displacement would therefore have a very high actuation authority per unit mass of piezoelectric material. This is particularly important for applications where size and weight are critical.

Shear is piezoelectrically induced directly using d_{15}. The geometry of the actuator converts the shear into a linear displacement, much like a normal spring, where a small amount of shear is transformed into a large linear displacement.

INTRODUCTION

Small forces cause large displacements in coils and spirals, because the material is under shear and bend instead of stretching under a uniaxial stress. Coils and spirals undergo continuous bending. Direct actuation requires actuating the shear mode (d_{15}). This is an advantage because the shear mode generally has the largest piezoelectric coefficients, storing greater amounts of energy per unit of electric field. Shear piezo-coefficients for shear, d_{15} and g_{15}, are 200% to 400% greater than d_{31} (used in benders and flextensors) and 20% -70% greater than the piezo-coefficients d_{33} and g_{33} (used in stacks and multilayers). Analysis shows piezoelectric coils and spirals have displacements centimeters and larger, with significant forces. Actual coils that HME has machined from brittle ceramics show that ceramics can be made into coils and can be stretched like a slinky.

ANALYSIS

Helical and spiral coils can generate very large displacements, not just microns but centimeters and larger, from small amounts of shear stress shown in figure 1. Helical coils have large displacements along their main axis. Spiral coils have large displacements normal to the spiral plane. An unextended spiral can be very thin, having a large extension out of the plane.

Extension in a coil or spiral cause a bending moment in the spring wire, causing a shear stress in the wire cross section[1]. However, the shear needed is $\tau_{\theta z}$. Instead, an applied electric field causes a shear stress in the wire cross section. The shear creates an unbalanced force on the inner and outer surfaces of the wire, leading to an axial force. The axial force creates a bending moment, causing shear stress, $\tau_{\theta z}$. Figure 2 shows the wire cross section shear stress. Figure 3 shows how shear stress becomes an axial force along the coil main axis or normal to a spiral plane. The inner diameter area is smaller than the outer diameter, leading to the axial force:

$$F = 2\pi RH\tau_{xy} - 2\pi(R-W)H\tau_{xy} = 2\pi WH\tau_{xy} = 2\pi WH\, e_{15}(\Delta V/H) = 2\pi W d_{15}(\Delta V)/\, s_{44}^{E}$$

Where:
R = outer radius of the coil or spiral,
H = height of the coil or spiral cross section and distance between the actuation electrodes,
τ_{xy} = induced shear stress,
W = width of the coil or spiral cross section distance between the poling electrodes,
ΔV = actuation voltage,
e_{15} = piezoelectric shear block force constant,
d_{15} = piezoelectric strain constant,
s_{44}^{E} = shear compliance in short circuit (reciprocal of shear modulus).

[1] Crandall, S. H., Dahl, N. C., and Lardner, T. J. "An Introduction to the Mechanics of Solids," McGraw-Hill, New York, Second edition, (1972).

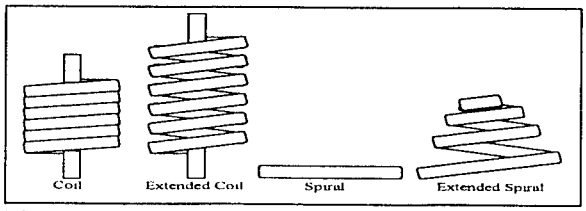

Fig. 1. Coils and spirals can generate large displacements.

The block force constant, e_{15}, is the strain constant, d_{15}, by divided by the shear compliance[2]. The compliances and ds are usually reported, while the block force constant is not. The actuation electrodes must be across the dimension H, while the poling parallel to W (By switching the poling and actuation, the radial electric field varies with 1/R, canceling the stress difference, resulting in zero net axial force). The axial force, F, creates a bending moment in the coil or spiral wire cross section, shown in figure 4. The bending moment, M, is:

$$M = F \times R - W/2$$

For spirals, vector addition shows it does not matter where the contact point is on the circumference:

$$\vec{M} = \vec{F} \times ((R - W/2) - \vec{r}) + \vec{F} \times \vec{r} = \vec{F} \times (R - W/2)$$

This relationship is valid for any point on the spiral. For equilibrium, the bending moment is balanced by a shear stress distribution in the plane of the cross section of the wire:

$$M = \int_A \tau_{\theta z} \cdot r dA$$

Where:

$\tau_{\theta z}$ = shear stress distribution in the plane of the cross section of the wire,

r = radius from the center of the cross section,

A = the area of the cross section of the wire.

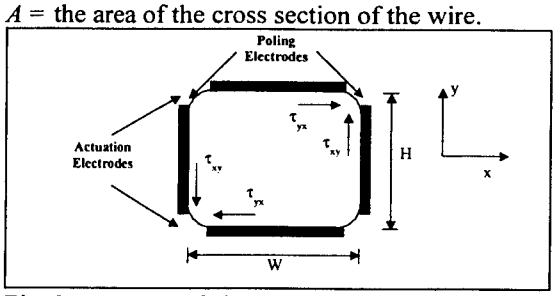

Fig. 2. Two sets of electrodes are needed to induce a piezoelectric shear. One set poles the material, the other actuates or senses. The actuation electric field is perpendicular to the poling direction, causing a shear stress.

[2] Standards on Piezoelectric Crystals, 1949, Proceedings of the IRE.

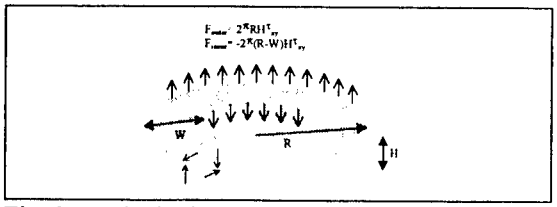

Fig. 3. A single ring of a coil or spiral in shear generates an unbalanced axial force due to the difference in the inner and outer surface areas. The net force is: $F = 2\pi WH\tau_{xy}$.

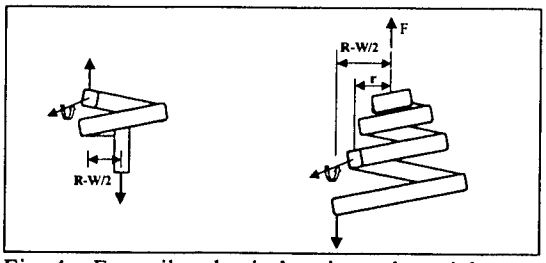

Fig. 4. For coil and spiral springs, the axial force times the radius of the spring, FxR, is the bending moment. For spirals, vector addition shows it does not matter where the contact point is on the circumference.

Figure 5 shows the cross section and the shear stress. This shear stress, $\tau_{\theta z}$, is different from, but is a response to the piezoelectrically induced shear stress, τ_{xy}.

The strain energy due to torsion in the coil or spiral is:

$$U = \frac{1}{2}\int s_{44}^E \left(\frac{Mr}{I_z}\right)^2 dv = \frac{1}{2}\int s_{44}^E \frac{M^2}{AI_z^2}(Adz)\int r^2 dA$$

$$= \frac{s_{44}^E M^2 v}{2AI_z} = \frac{s_{44}^E F^2 (R - \frac{W}{2})^2 v}{2WHI_z}$$

Where:

U = the elastic energy in the system,

v = the volume of the coil or spiral,

I_z = the moment of inertia of the cross section = $\int r^2 dA$.

z = the wire length of the coil or spiral

The volume integral becomes the material volume because M is constant in the spring. The spring displacement, δ, is:

$$\delta = \frac{\partial U}{\partial F} = \frac{s_{44}^E F(R - \frac{W}{2})^2 v}{WHI_z} = \frac{2\pi(R - \frac{W}{2})^2 d_{15}(\Delta V)v}{HI_z}$$

For the rectangular cross section used here, the moment of inertia is:

$$I_z = \frac{WH}{6}(W^2 + H^2)$$

The displacement becomes:

$$\delta = \frac{12\pi(R - \frac{W}{2})^2 d_{15}(\Delta V)v}{WH^2(W^2 + H^2)}$$

For a coil spring, the volume is like the volume of a cylinder:

$v_{coil} = 2\pi(R-W/2)WL\beta$

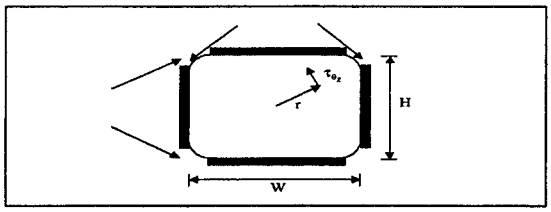

Fig. 5 The total moment in the cross section is the integral of the product of the shear stress, $\tau_{\theta z}$, and the radius, r, over the area.

where:

L = length of the coil, and

β = dimensionless constant between 0 and 1, denoting how tightly wrapped the coil or spiral is. If the coil is tightly wrapped then β is 1, if there is space between the coils then it is less than 1.

For a coil the displacement becomes:

$$\delta_{coil} = \frac{24\pi^2(R - \frac{W}{2})^3 L\beta d_{15}(\Delta V)}{H^2(W^2 + H^2)}$$

For a spiral spring, the volume is that of a disk:

$v_{spiral} = \pi R^2 H\beta$

For a spiral the displacement becomes:

$$\delta_{spiral} = \frac{12\pi^2 R^2(R - \frac{W}{2})^2 \beta d_{15}(\Delta V)}{WH(W^2 + H^2)}$$

The following table summarizes the force and displacement equations for both coils and spirals. Included are the pressures exerted, assuming the force is exerted over an area formed by a square around the coil or spiral. The square has a side length of $2R$, and an area of $4R^2$.

	Coil	Spiral
Force, $F(d)$	$2\pi W d_{15}(\Delta V)/ s_{44}^E$	$2\pi W d_{15}(\Delta V)/ s_{44}^E$
Pressure	$\pi W d_{15}(\Delta V)/(2R^2 s_{44}^E)$	$\pi W d_{15}(\Delta V)/(2R^2 s_{44}^E)$
Displacement δ	$\frac{24\pi^2(R - \frac{W}{2})^3 L\beta d_{15}(\Delta V)}{H^2(W^2 + H^2)}$	$\frac{12\pi^2 R^2(R - \frac{W}{2})^2 \beta d_{15}(\Delta V)}{WH(W^2 + H^2)}$

EXAMPLES

A 10cm long coil, radius 10mm, cross section 1mm by 1mm, produces significant force and displacement. Using $d_{15} = 5.84 \times 10^{-12}$ Meters/Volt, $s_{44} = 47.5 \times 10^{-12}$ Meters^2/Newton, for PZT-5H, activating at 10Volts, a block force of 0.8 Newtons (3 ounces) and extension of 40 mm (1.6 inches) are generated. This is a huge extension, not microns, but inches!

Coils and spirals have added flexibility in applications, with extra parameters (radius, cross section dimensions, and length). Displacements increase with radius (squared for coils and cubed for spirals) and decreasing cross section (cubed). Coil displacement increases linearly with length, while block force remains the same. Doubling length doubles displacement.

An array of smaller radii coils or spirals increases the block force over a constrained area, shown in figure 6. A smaller spiral exerts twice the force of a larger spiral (half the radius). The total force is 8 times a single spiral. For a constant area, the force of n spirals or coils is $F(n) = n^{3/2}F(1)$. Hexagonal close packing can also boost the force.

A spiral made out of a bimorph wafer has a greater displacement. The tip displacement of a bimorph used as a cantilever is:

$$\delta_{bimorph} = 3d_{31}\Delta V\frac{L^2}{t^2}$$

Where:

t = the combined thickness of the two wafers and

L = the length of the bimorph.

A single wafer ($R = L/2$) can be made into a spiral with a square cross section, then:

$$\frac{\delta_{spiral}}{\delta_{bimorph}} = \frac{\pi\beta}{(24)(0.38)}\left(\frac{L}{t}\right)\left(\frac{d_{15}}{d_{31}}\right) = 0.34\beta\left(\frac{L}{t}\right)\left(\frac{d_{15}}{d_{31}}\right)$$

Assuming half the material was removed to make the spiral ($\beta = 0.5$), a square wafer 2.54 cm on a side and 0.5mm thick, and made out of PZT-5H ($d_{15}/d_{31} = 2.7$), then:

$$\frac{\delta_{spiral}}{\delta_{bimorph}} = 23.3$$

The spiral has a displacement over 20 times that of the bimorph. Activating with 100 Volts, the bimorph has a tip displacement of 0.2mm, while the spiral has a displacement of 5mm.

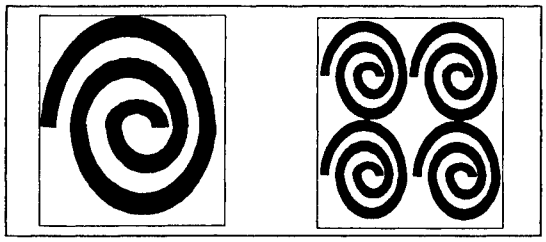

Fig. 6. Four spirals exert 8 times the force of a single spiral of the same coil thickness and width filling the same area. Four spirals each exert twice the force of the larger spiral.

USING BIMORPHS OR MONOMORPHS

Helical and spiral coil springs produced from bimorphs and monomorphs do not actuate the shear mode. Different expansion or contraction of neighboring material produces bending. Bimorphs and monomorphs act as cantilever beams: displacement goes as beam length squared [3]. A spiral cut monomorph or bimorph has a much larger displacement. This alternative is in case unforeseen problems arise with shear based actuators. A spiral cut bimorph, length L, width W, has effective length L_s, and width W_s,. Cutting a 1inch spiral with a width of 0.1 inch, 50% material removal, the spiral length, L_s, is 5 inches. Since displacement goes as the length squared, the spiral displacement is 25 times that of the bimorph or monomorph.

Bimorphs and monomorphs coils have very long displacements due to long beam length. Coils increase displacement by increasing the number of wraps. A coil with a one-inch diameter and 0.1 width, has about a 3-inch circumference or length. Each wrap gives 9 times the displacement of a 1x1 inch bimorph or monomorph. A coil with ten wraps has a displacement 90 times that of a single bimorph or monomorph. These devices can produce these large displacements without circular or curved geometries. Some possibilities are shown in figure 7.

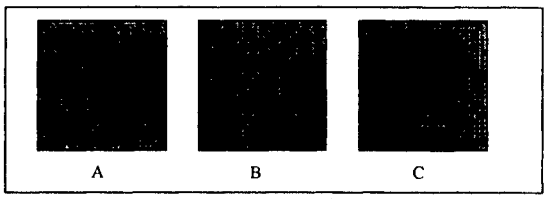

Fig. 7. The effective length of a bimorph or monomorph increases many times, increasing the displacement. A shows the original uncut device, an accordion-like fold is made by simple straight line cuts as shown in B, and a rectilinear spiral is shown in C.

MACHINING COILS FROM CERAMICS

One important issue is the ability to actually create coils out of ceramic materials. HME has already developed technology to machine coils from tubes of brittle ceramics. In particular, HME has successfully machined coils from two brittle ceramics, YBCO (yttrium barium copper oxide) and BSCCO (bismuth strontium calcium copper oxide) for an NIH SBIR to create high temperature superconducting coil magnets. Even though these are brittle ceramics they can be stretched like a slinky when machined into a coil, because the internal stresses are very low even with displacements measured in inches.

[3] Uchino, K. "Piezoelectric Actuators and Ultrasonic Motors," Kluwer Academic Publishers, Norwell Massachusetts, (1997).

Templated Grain Growth of Textured Piezoelectric Ceramics

S. Kwon, E. M. Sabolsky, G. L. Messing*, S. Trolier-McKinstry
Materials Research Institute, The Pennsylvania State University, University Park, PA USA 16802
FAX: 814-865-2917
Email: messing@ems.psu.edu

ABSTRACT

Fiber textured 0.68PMN-0.32PT was fabricated using the Templated Grain Growth (TGG) process. Isostructural $SrTiO_3$ templates were [001] oriented in a fine matrix during tape casting. A high degree of [001] texture (Lotgering factor > 0.8) was a result of heat treatment which allowed heteroepitaxial growth of oriented single crystal PMN-PT from template particles. The effect of matrix chemistry, time, and temperature on the degree of texturing was investigated for both a reactive matrix and a perovskite powder matrix. A reactive matrix system results in substantially better growth and crystal quality. [001] textured PMN-PT has a piezoelectric coefficient of 1200 pC/N up to 10 kV/cm and 0.32% strain at 50 kV/cm.

INTRODUCTION

Texturing PMN-PT ceramics with a composition slightly on the rhombohedral side of morphotropic phase boundary (MPB) is attractive because of the potential for taking advantage of the extremely high piezoelectric d_{33} coefficients >2000 pC/N and longitudinal electromechnical coupling coefficients (k_{33}) >0.9 of [001] oriented cuts of piezoelectric single crystals.[1,2]

Lead-based ferroelectric crystals are grown by a high-temperature flux process, but the control of size and crystallographic direction of the grown crystal is difficult to control. A more refined method for producing relatively large lead-based single crystals is the Bridgman method,[3,4] but compositional heterogeneity becomes an issue in this process. Solid state conversion is also another method for growing single crystals.[5] All of the above methods require a considerable amount of excess PbO, which can limit the properties or result in processing difficulties.[6]

Templated grain growth (TGG) is an alternative approach for obtaining textured ceramics.[7-10] In this process, nucleation and growth of matrix on the oriented, isostructural single crystal templates results in an increased fraction of oriented material after heating. There are several important requirements for successful TGG. The single crystal templates should possess anisotropic morphology so they can be aligned during the forming process, such as tape casting, extrusion, or uniaxial press. The single crystal templates also must have the desired crystallographic orientation and a similar lattice parameter to the crystal to be grown. The chemical and thermodynamic stability of templates is also important until at least the nucleation step. A fine grain, dense matrix is favored since this process is driven by the difference in surface free energies between the advancing crystal plane and the matrix grains during thermal processing.

A fundamental understanding of the heteroepitaxial nucleation and growth of the single crystal PMN-PT from the oriented template crystal is useful for understanding the factors affecting TGG of textured ceramics. Rehrig *et al.*[11,12] showed that $BaTiO_3$ and $(Ba,Zr)TiO_3$ crystals of various orientations could be grown using either a $BaTiO_3$ or $SrTiO_3$ template crystal. This process was shown to follow cubic growth kinetics, and thus, it was proposed to be controlled by diffusion. Similar information would be useful for the design of solid state processes for the growth of single crystal or textured ceramics of PMN-PT and other relaxor-PT systems.

Reactive templated grain growth uses a reactive precursor as the matrix and has been found to be very effective in texturing several ceramics including mullite,[13] alumina,[14] $(SrBa)Nb_2O_6$,[9] and $CaB_4Ti_4O_{15}$.[15] The effect of reactive templated grain growth compared to normal templated grain growth was well evidenced in the case of alumina.[14] It has been reported that fast transformation of a precursor mixture and a fined-grained, dense microstructure were achieved by reactive sintering of PMN-PT without using excess PbO. The reactive matrix also was shown to have high probability for successful TGG.[16] This presentation reports the development of fully

dense, textured PMN-32.5PT ceramics by TGG using $SrTiO_3$ as template particles in a reactive matrix. The processing parameters such as sintering time, use of excess PbO, and type of matrix are correlated with the texture development and the results are compared to those of textured PMN-32.5PT templated on $BaTiO_3$ particles.[17]

EXPERIMENTAL PROCEDURE

A precursor mixture was prepared with $(PbCO_3)_2$ $Pb(OH)_2$ (Aldrich, mean particle size 3.7 μm), $MgNb_2O_3$ (H. C. Starck, mean particle size 0.4 μm), and fumed TiO_2 (Degussa, mean particle size 0.03 μm). The chemical composition of the mixture was fixed at 0.675PMN-0.325PT, and excess PbO was not added, but one batch with 3% excess PbO was prepared for comparison.

The slurry was mixed with $SrTiO_3$ templates after balling using a magnetic stir bar. The $SrTiO_3$ tabular particles were synthesized by a two step molten salt process[18] using KCl as a flux. The partilce size was 5-15 μm with an aspect ratio > 5 as shown in Figure 1.

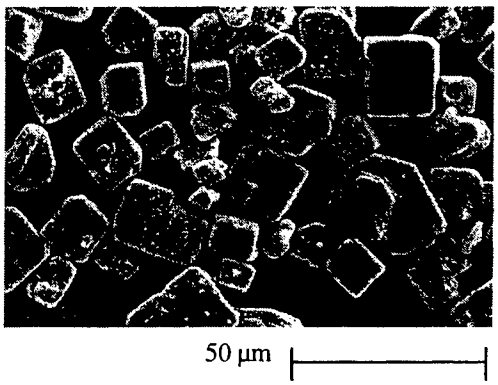

Figure 1. Tabular $SrTiO_3$ particles synthesized by molten salt method

Samples were sintered in flowing oxygen using a tube furnace. For sintering, samples were first encapsulated in platinum foil and then embedded in a powder of the same composition as the samples in an alumina boat.

RESULTS AND DISCUSSIONS

X-ray diffraction was used to estimate the texture fraction. The main peak in random PMN-PT is (110), but the surface of the textured PMN-PT, which corresponds to the <001> of templates, has a diffraction pattern with significantly increased (100) and (200) peaks and whereas other peaks are suppressed including the (110) peak relative to the untextured case. There was no substantial difference in the diffraction pattern between textured samples with and without excess PbO.

Figure 2 shows a fracture surface of a sample with ST templates and no excess PbO. When the temperature reaches 1150°C, there is very little growth from the templates as shown in Fig. 2 (a). After 1 h at 1150°C, there is a significant amount of growth from the templates and the templates seem to react with PMN-PT leaving a porous region inside of each large, grown grains. The cubic symmetry of the perovskite structure resulted in uniform growth from all surfaces and a decrease in the aspect ratio of grown grains compared to the initial templates.

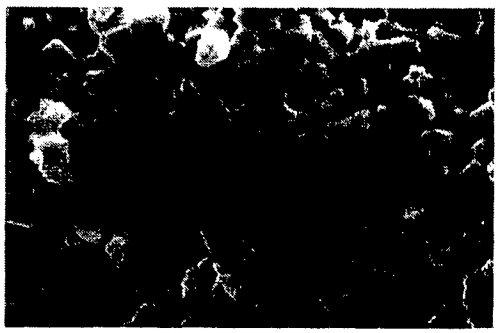

(a)

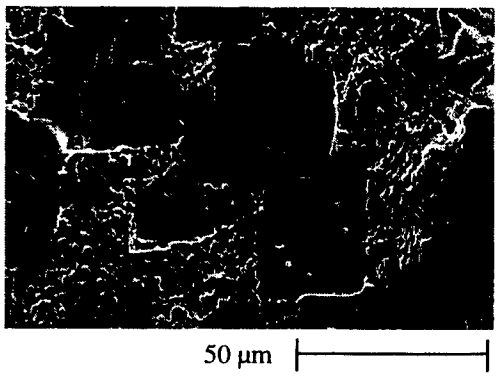

(b)

Figure 2. Side view of fractured samples heat treated at 1150°C (a) for 0 min and (b) for 1 h

Microstructures of polished and thermally etched surfaces of textured samples sintered at 1150°C for 10 and 50 h are shown in Figure 3. The large blocky grains are ≈ 30 μm in scale and aligned along the tape casting

direction. After 10 h sintering, the sample showed 56% texturing by Lotgering factor and 67% texturing after 50 h sintering. It should be noted that there was no significant increase in the fraction of textured material after 50 h. Considering the limited growth after 50 h, it is apparent that texture development is saturated.

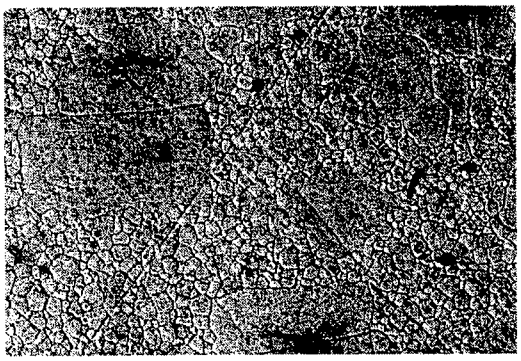

(a)

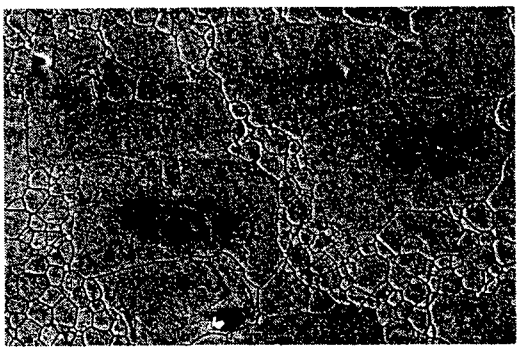

(b)

Figure 3. Polished surface of textured samples sintered at 1150°C (a) for 10 h and (b) for 50 h

There can be several reasons for the retardation or the cessation of growth: growth of matrix grains and reduction of driving force, impurity drag along the grain boundary and impingement of grown large grains. Figure 3 shows the increase in the size of matrix grains after 50 h sintering compared to 10 h sintering, but the difference is not sufficient to explain the saturation in template growth. It should also be noted that the interface between the matrix grains and large grains still retains curvature thus having a driving force for grain growth in the 50 h sintered sample (Figure 3 (b)). The textured samples are translucent, which implies clean grain boundaries and high density. Thus, neither the excessive growth of matrix grains or impurity drag explains growth retardation. As the templates are randomly dispersed in the matrix, it is natural that the impingement of the large grains occurs after certain texturing degree as evidenced in the microstructure. The overall loss of matrix-crystal interface when crystals impinge results in a substantial loss of growth surfaces and thus plays a major role in overall growth saturation.

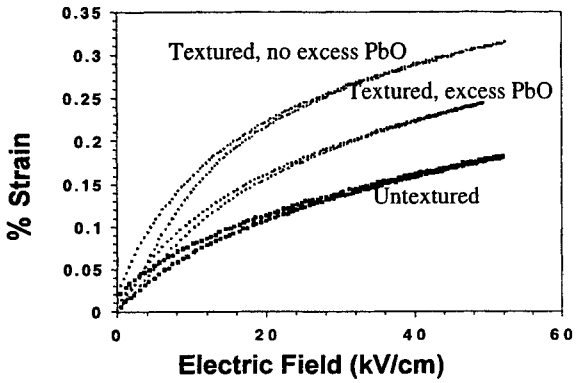

Figure 4. Effect of texture and excess PbO on the piezoelectric behavior of textured PMN-0.325PT

The strain field curves of textured and random samples are shown in Figure 4. The maximum levels of strain achievable in the materials seem to be dependent on the grain orientation and existence of excess PbO. The textured sample without PbO showed ~0.3% strain at an electric field of 40kV/cm, which is approximately twice that of the strain of a random sample. The textured sample with excess PbO has strain in between them, in spite of the higher degree of texturing. The hysteresis for the textured sample and the random samples were ~ 0.03% and ~0.02%, respectively. The piezoelectric coefficient for each sample was determined from the slope of the strain vs E field curves, since this gives a direct estimate of the d_{33} of a specimen. The slopes were determined in the low field region between 0-10 kV/cm. For the random sample d_{33} was found to be 580 pC/N and for the textured samples, it was 1200 pC/N when no excess PbO was used and 990pC/N for when excess PbO was used.

The piezoelectric response of the textured sample is comparable to the textured PMN-PT templated on $BaTiO_3$ (BT) templates.[17] The amount of strain and the piezoelectric coefficient are similar to the BT templated PMN-PT.

CONCLUSIONS

Dense, [001] textured PMN-0.325PT ceramics can be fabricated by tape casting and using $SrTiO_3$ as template particles. The piezoelectric property of the textured sample are twice the value of random ceramics.

References

1. S.-E. Park and T.R. Shrout, *IEEE Trans. on Ultrasonics, Ferroelectrics, and Frequency Control*, **44** [5] 1140-47 (1997).

2. S-E. Park and T.R. Shrout, *J. Appl. Phys.*, **82** [4] 1804-11 (1997).

3 K. Harada, S. Shimanuki, T. Kobayashi, S. Saitoh, and Y. Yamashita, *J. Am. Ceram. Soc.*, **81** [11] 2785-88 (1998).

4 S.G. Lee, R.G. Monteiro, R.S. Feigelson, H.S. Lee, M. Lee, and S.E. Park, *Appl. Phys. Lett.*, **74** [7] 1030-32 (1999).

5 T. Li, A.M. Scotch, H.M. Chan, and M.P. Harmer, *J. Am.. Ceram. Soc.*, **81** [1] 244-48 (1998).

6 Y. Yamashda, K. Harada, Y. Hosono, and Zuo-Guang Ye, 2001 U.S. Navy Workshop on Acoustic Transduction Materials and Devices, Baltimore, MD, 2001

7 B. Brahmaroutu, G. L. Messing, S. Trolier-McKinstry, and U. Selvaraj, pp. 883-86, Vol. 2, *Proceedings of the Tenth International Symposium on the Applications of Ferroelectrics*. Edited by B. Kuwicki, A. Amin, and A. Safari. IEEE, East Brunswick, NJ, 1996.

8 B. Brahmaroutu, *Templated Grain Growth of Textured Strontium Niobate Ceramics*, Ph.D. Thesis, Pennsylvania State University, University Park, PA (1999).

9 C. Duran, S. Trolier-McKinstry, and G. L. Messing, *J. Am. Ceram. Soc.*, **83** [9] 2203-13 (2000).

10 J. A. Horn, S.C. Zhang, U. Selvaraj, G. L. Messing, and S. Trolier-McKinstry, *J. Am. Ceram. Soc.*, **82** [4] 921-26 (1999).

11 P. W. Rehrig, S.E. Park, S. Trolier-McKinstry, G. L. Messing, B. Jones, and T.R. Shrout, *J. Appl. Phys.*, **86** [3] 1657-61 (1999).

12 P. W. Rehrig, G.L. Messing, and S. Trolier-McKinstry, *J. Am. Ceram. Soc.*, **83** [11] 2654-60 (2000).

13 S.-H. Hong, W. Cermignani, and G. L. Messing, *J. Euro. Ceram. Soc.*, **16** 133-41 (1996).

14 M. M. Seabaugh, I. H. Kerscht, and G. L. Messing, *J. Am. Ceram. Soc.*, **80** [5] 1181-88 (1997).

15 T. Takeuchi, T. Tani, and Y. Saito, *Jpn. J. Appl. Phys.*, **38** 5553-56 (1999).

16 S. Kwon, E. M. Sabolsky, G. L. Messing, *J. Am. Ceram. Soc.*, **84** [3], 648-50 (2001).

17 E. M. Sabolsky, A. R. James, S. Kwon, S. Trolier-McKinstry, and G. L. Messing, *Appl. Phys. Lett.*, **78** [17], 2551-53 (2001).

18 K Watari, B. Brahmaroutu, G. L. Messing, S. Trolier-McKinstry and S. C. Cheng, *J. Mater. Res.*, **15**, 846-849 (2000)

Single Crystal Ferroelectrics from Polycrystalline Precursors

A. M. Scotch, E. P. Gorzkowski, P. T. King, D. J. Rockosi, S. Wu, M. P. Harmer, and H. M. Chan

Materials Research Center, Lehigh University
5 E. Packer Ave., Bethlehem, PA 18015
Fax: 610-758-3526
Email: mph2@lehigh.edu

Relaxor-based ferroelectric single crystals of $Pb(Mg_{1/3}Nb_{2/3})$-$PbTiO_3$ [PMN-PT] have been produced via the Seeded Polycrystal Conversion [SPC] technique. Polycrystalline precursors of PMN-PT are converted to single crystals by inducing the boundary of a seed crystal to migrate through a polycrystalline matrix at the expense of the smaller matrix grains. Successful implementation of the SPC process requires understanding of the factors that control the single crystal growth rate and microstructure. These include the chemistry and volume fraction of second phase, degree of porosity, and evolution of the matrix microstructure. This paper will offer an overview of the SPC process and the factors that influence single crystal growth.

INTRODUCTION

Conventional techniques for forming ferroelectric single crystals are based on high temperature solution growth from fluxes. Though suitable for growing bulk single crystals, these methods are not readily transferable to large-scale manufacturing, especially for the fabrication of complex shapes. Furthermore, these methods often have difficulty in achieving chemically homogeneous crystals.

The group at Lehigh University has implemented the successful application of seeded polycrystal conversion (SPC) to ferroelectric materials. In the SPC technique, a seed crystal is brought into intimate contact with a polycrystalline ceramic matrix, and single crystal conversion takes place by inducing the crystal boundary to migrate at the expense of the smaller matrix grains.

Initial work at Lehigh established the feasibility of using the SPC process to grow single crystals of the relaxor-based ferroelectric $Pb(Mg_{1/3}Nb_{2/3})O_3$-35mol%$PbTiO_3$ (PMN-35PT) from seed crystals of the same composition.[1] A subsequent study showed that a PbO-based liquid second phase at the single-crystal/polycrystal interface was a critical requirement for PMN-35PT single crystal growth. Although the grown single crystals contained trapped PbO-based inclusions, they nonetheless exhibited impressive strain vs. electric field properties, e.g., strain values up to 0.68% under an electric field of 30 kV/cm.[1,2]

EFFECT OF SINTERING ATMOSPHERE

Ceramic powder consisting of PMN-35PT and excess PbO was pressed into compacts, cold isostatically pressed, and sintered at temperatures from 1000-1200°C for 0-12 hours under (i) air and (ii) oxygen atmospheres. The microstructures of the samples fired in air (Fig. 1(a)) varied markedly

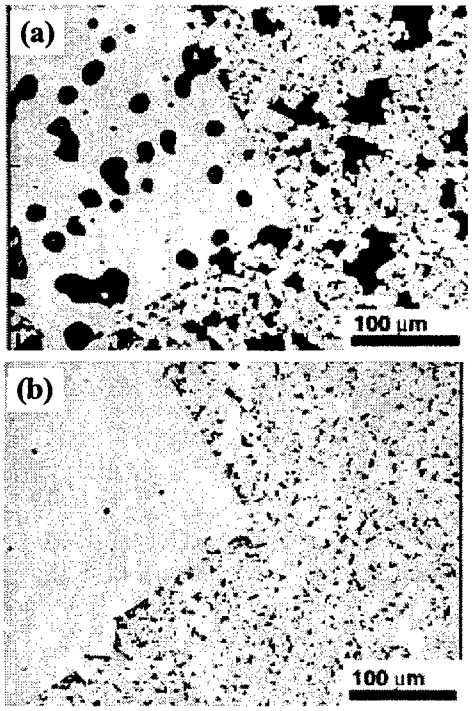

Fig. 1. PMN-35PT + 5v%PbO sintered in (a) air, and (b) oxygen; 1150°C 4hr.

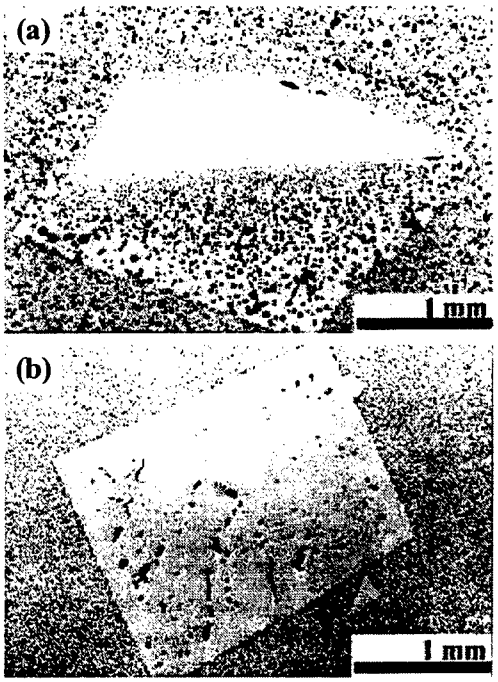

Fig. 2. PMN-35PT single crystals grown by SPC from (111) PMN-35PT plates at 1150°C for 4 hrs. in (a) air and (b) oxygen; 5v% PbO in the precursor.

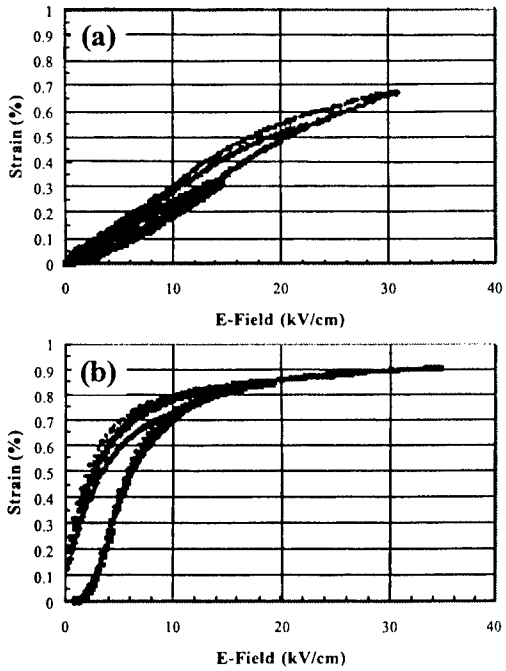

Fig. 3. Strain behavior of PMN-35PT single crystals grown by SPC in (a) air and (b) oxygen; 5v% PbO in the precursor.

from those of the samples fired in oxygen (Fig. 1(b)). The samples fired in oxygen consisted of nearly fully dense microstructures with large, pore-free abnormal grains. The samples fired in air, however, were less dense and contained large abnormal grains with trapped porosity.

To examine the effect of atmosphere on single crystal growth via SPC, single crystal (111) plates of PMN-35PT were embedded into powder compacts consisting of PMN-35PT and excess PbO. The compacts were subsequently sintered in both air and oxygen atmospheres. Fig. 2(a) and 2(b) show the SPC single crystals that were grown in air and oxygen, respectively. The single crystals grown in air atmospheres exhibited significantly more trapped porosity and second phase than the single crystals grown in oxygen.

The electric-field induced strain properties of the PMN-PT crystals grown in air and oxygen are shown in Fig. 3(a) and 3(b), respectively. Note the difference in strain behaviors. The shape of the hysteresis loop for the oxygen-grown crystal resembles that of a crystal on the tetragonal side of the morphotropic phase boundary. The tetragonal structure was confirmed by x-ray diffraction.

Samples of PMN-35PT + 5v%PbO were sintered in oxygen at 1150°C from the green state and subsequently annealed in both oxygen and air atmospheres at 1150°C for 4hrs. The oxygen sintered material maintained its >99% density when annealed in oxygen. However, annealing in air yielded a drop in density that correlated with the generation of internal porosity. These results are shown in Fig. 4(a-c).

Polycrystalline compacts were also hot pressed at 900°C and subsequently annealed at 1150°C in oxygen and air atmospheres. After annealing, these samples also exhibited a drop in density associated with the formation of internal porosity.

Though the source of the porosity has not been positively identified, possibilities include the entrapment of insoluble gases, the burn-out of organic materials, and the decomposition of lead oxide. Work is underway to distinguish between these processes.

It is important to note that pore formation is not observed in samples of PMN-PT with zero additions of PbO and fired under identical conditions as those of Fig. 4. This is significant because it suggests the source of the bloating to be linked to the PbO second phase.

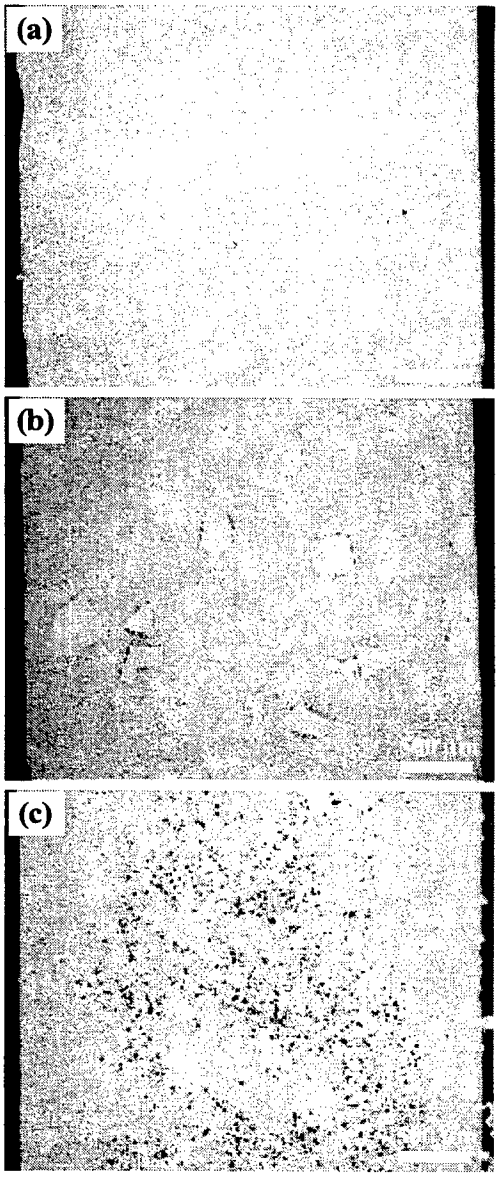

Figure 4. PMN-35PT + 5v%PbO (a) sintered in oxygen then (b) annealed in oxygen, (c) annealed in air.

It is suspected that much of the pore formation stems from the decomposition of lead oxide. Conventionally, the decomposition reaction of PbO is written as,

$$PbO(s,l) \leftrightarrow PbO(g) \leftrightarrow Pb(g) + \tfrac{1}{2} O_2(g)$$

In an oxidizing atmosphere, this reaction is not likely to take place to the extent of yielding Pb(g) and $O_2(g)$ as final products.[3] Several authors[4,5] have examined the vapors over PbO using mass spectrometry and found the predominent species to be PbO and its polymers Pb_2O_2, Pb_3O_3, and Pb_4O_4. Another type of reaction is proposed here. A thorough evaluation of the PbO literature revealed that PbO readily oxidizes to higher oxides such as Pb_3O_4, $Pb_{12}O_{17}$, and $Pb_{12}O_{19}$.[6] It is suggested that PbO was oxidized during preparation of the ceramic specimens and then the excess oxygen was subsequently liberated at high temperatures. As for the difference between oxygen and air atmospheres, it is assumed that the higher lead oxides are more stable in pure oxygen than air.

EFFECT OF LIQUID PHASE CHEMISTRY

Previous results suggest that the amount of liquid phase present at the firing temperature has a dramatic effect on the grain growth and single crystal growth kinetics in PMN-PT. It is suspected that the observed change in kinetics is largely due to an increase in the boundary mobility with the presence of a liquid. Thus, it may be possible to control the boundary mobility and growth kinetics by adjusting the composition of the liquid phase.

Conventionally, PbO is used as a liquid phase additive for PMN-PT to promote sintering, grain growth, and single crystal growth. However, the high volatility of PbO makes it difficult to contain it in the sample. A promising alternative to PbO is a eutectic composition of lead aluminate, $Pb_2Al_2O_5$ (P_2A), and PbO, as shown on the PbO-Al_2O_3 phase diagram (Fig. 5).

Powder of the P_2A-PbO eutectic composition was mechanically add-mixed to PMN-35PT powder and then pressed into pellets and fired at 1150°C. Preliminary results indicated that very large grain sizes could be obtained using the P_2A eutectic, as seen in Fig. 6. The grain sizes obtained from this liquid phase composition are larger than any previously reported by the authors. However, slightly higher Al contents suppresses grain growth, as shown in Fig. 7.

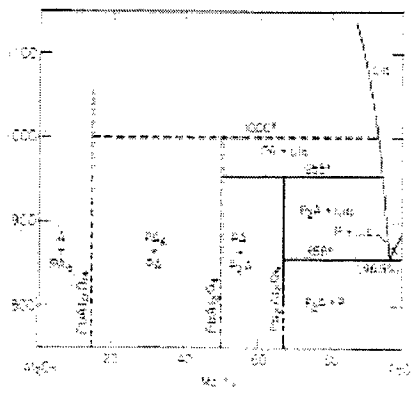

Fig. 5. PbO-Al_2O_3 Phase Diagram[7]; note the eutectic composition listed in Ref. 7 is incorrectly printed; according to Ref. 8, the composition should be at 96.5 mol% PbO.

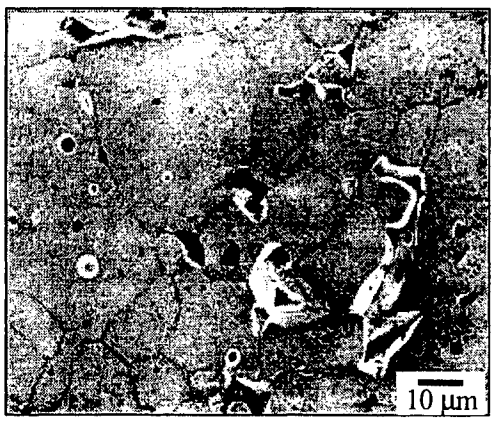

Fig. 6. PMN-35PT + 5 vol% P_2A-PbO eutectic composition; sintered at 1150°C for 1 hr in air.

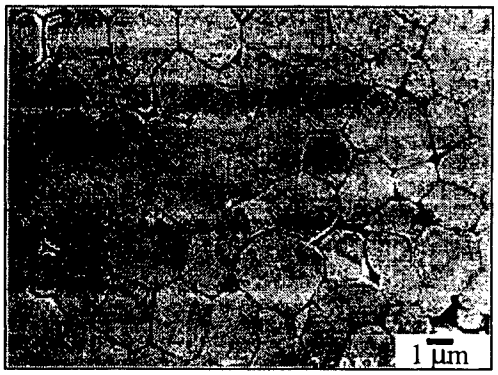

Fig. 7. PMN-35PT + 5 vol% P_2A + PbO mixture with twice the Al content as that of Fig. 6.; sintered at 1150°C for 1 hr in air.

This suggests that the liquid phase chemistry plays a vital role in influencing growth kinetics and consequently producing single crystals of PMN-35PT.

EFFECT OF STARTING PARTICLE SIZE

In an effort to deduce the effect of grain coarsening on polycrystalline conversion, single crystals of PMN-PT were grown into matrices of different starting grain sizes. Powders of different mean particle sizes were prepared by precoarsening PMN-PT powders and subsequently milling to the desired mean size.

The powders were cold isostatically pressed into bilayer specimens which were seeded with (100) PMN-35PT single crystal seed plates. The seeded, layered compacts were then sintered at 1150°C for 4 hours in oxygen atmosphere. Microstructures of the grown regions are shown in Fig. 8(a-b). Matrix grain growth and single crystal growth of both coarse (1.8 μm) and fine-grained (0.6 μm) layers were comparable.

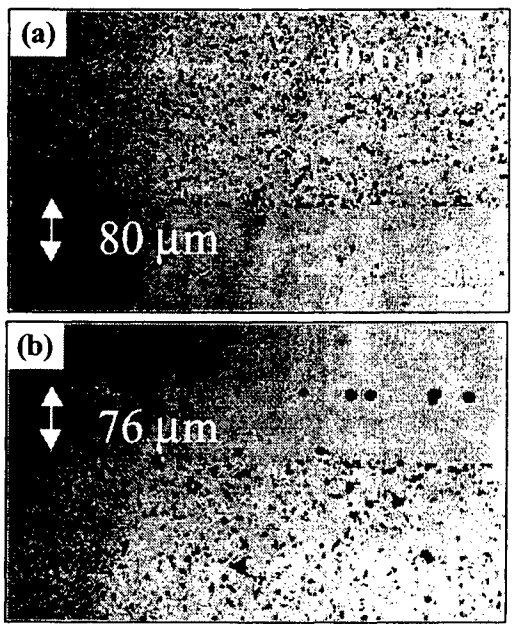

Fig. 8. SPC single crystal growth of PMN-35PT into (a) fine-grained layer (0.6 μm) and (b) coarse-grained layer (1.8 μm); sintered at 1150°C for 4 hr in oxygen.

ACKNOWLEDGMENTS

This work was sponsored by the Air Force Office of Scientific Research under contract number F49620-99-1-0340 and by the Office of Naval Research contract number N00014-98-C-0200.

The authors would like to thank K. McNeal and R. Gentilman at Materials Systems, Inc. for their invaluable discussions.

REFERENCES

1. T. Li, A. M. Scotch, H. M. Chan, M. P. Harmer, S-E. Park, T. R. Shrout and J. R. Michael, *J. Am. Ceram. Soc.*, **81**[1], 244 (1998).
2. A. Khan, F. A. Meschke, A. M. Scotch, T. Li, H. M. Chan, and M. P. Harmer, *J. Am. Ceram. Soc.*, **82**[11], 2958 (1999).
3. R. H. Lamoreaux and D. L. Hildenbrand, *J. Phys. Chem. Ref. Data*, **16**[3], 419 (1987).
4. J. Drowart, R. Colin, and G. Exsteen, *Trans. Faraday Soc.*, **61**[511], Pt. 7, 1376 (1965).
5. E. K. Kazenas and A. A. Petrov, *Russian Metallurgy*, [4], 17 (1996).
6. D. Risold, *J. Phase Equil.*, **19**[3] 213 (1998).
7. "Phase Diagrams for Ceramists-Vol. IV", Ed. G. Smith, The Amer. Ceram. Soc., Columbus, Ohio (1981) p. 105.
8. U. Kuxmann and P. Fischer, *Erzmetall*, **27**[11], 533 (1974).

Grain Orientation in BNKT-PZT Solid Solutions Made by RTGG Method

Toshio Kimura and Yuichi Abe

Department of Materials Science, Graduate School of Science and Technology, Keio University
3-14-1 Hiyoshi, Kohoku-ku, Yokohama 223-8522 Japan
FAX: 814-45-566-1551
Email: kimura@applc.keio.ac.jp

ABSTRACT

Grain oriented $Bi_{0.5}(Na_{0.85}K_{0.15})_{0.5}TiO_3$-$Pb(Zr_{0.5}Ti_{0.5})O_3$ (BNKT - PZT) ceramics were prepared by the reactive templated grain growth method using plate-like $Bi_4Ti_3O_{12}$ particles. Factors determining the degree of orientation were examined. Prereacted PZT gave a larger degree of orientation than PZT raw materials (PbO, ZrO_2, and TiO_2) in the 75BNKT-25PZT system. An increase in the PZT concentration reduced the degree of orientation.

INTRODUCTION

Piezoelectric property is closely related to the poling direction with respect to the crystal axis. Therefore, the piezoelectric property of a polycrystalline ceramic is smaller than that of a single crystal. Grain orientation is an effective method to enhance the piezoelectric property of a polycrystalline ceramic. Successful results have been reported for the grain oriented ceramics with anisotropic crystal structures such as bismuth layer-structured ferroelectrics and tungsten bronze niobates.[1-4]

Recently, Tani proposed the fabrication method of grain-oriented ceramics with the perovskite structure and prepared $Bi_{0.5}(Na_{0.85}K_{0.15})_{0.5}TiO_3$ (BNKT) with the large degree of orientation.[5] He named this method the reactive templated grain growth (RTGG) method. In this method, plate-like $Bi_4Ti_3O_{12}$ (BIT) was used as one of the starting materials, and BNKT was formed by *in situ* reaction between BIT and other starting materials.

The RTGG method has two advantages; this method can introduce grain orientation to compounds with isotropic crystal structures, and has the possibility of application to solid solutions with complex compositions. This work is related to the latter advantage. The purpose of this work is to examine the possibility of obtaining grain-oriented BNKT-PZT solid solutions. This paper deals with the effects of (1) PZT formation reaction and (2) PZT concentration on the grain orientation. PZT used in this experiment was $Pb(Zr_{0.5}Ti_{0.5})O_3$.

EXPERIMENTAL PROCEDURE

Chemically pure Bi_2O_3, Na_2CO_3, K_2CO_3, TiO_2, ZrO_2, and PbO were used as raw materials. Plate-like BIT particles were prepared by molten salt synthesis using NaCl-KCl (at 1150°C for 1 h),[6] and had an average diameter of about 10 μm and thickness of 0.5 μm. The plate-like BIT particles were mixed with the raw materials for BNKT. The amount of BIT particles was designed so that all Bi was supplied from BIT. In the first experiment to examine the effect of PZT formation reaction, overall composition was selected to be 75BNKT-25PZT and prereacted PZT or PZT raw materials (PbO, ZrO_2, and TiO_2) were mixed with the mixture of BIT, Na_2CO_3, K_2CO_3, and TiO_2. In the second experiment to examine the effect of PZT concentration, prereacted PZT was mixed with the mixture of BIT, Na_2CO_3, K_2CO_3, and TiO_2 to form the overall composition of xBNKT-(100-x)PZT with various x values.

The powder mixtures were mixed with a solvent in a centrifugal ball mill for 30 min, and then binder and plasticizer were added and mixed for 1 h. The slurry was tape-cast to form a sheet with a thickness of about 0.07 mm. In the sheet, plate-like BIT particles were aligned with their plate face parallel to the sheet surface. The sheet was cut, stacked, and pressed at 80°C and 50 MPa for 10 min to form green compacts with a thickness of about 1.5 mm.

The green compacts were heated at 650°C for 4 h for binder burn-out and calcination. The calcined compacts were sintered at temperature

between 900° and 1200°C for 1 h.

Crystalline phases and the degree of orientation were determined by X-ray diffraction analysis (XRD) using CuKα radiation on the major surface of the compacts. The degree of orientation was calculated by the Lotgering method.[7] Microstructure of sintered compacts was observed with a scanning electron microscope (SEM) on polished and etched side surface of the compacts.

RESULTS AND DISCUSSION

Effect of PZT Formation Reaction

Prereacted PZT and PZT raw materials (PbO, ZrO_2, and TiO_2) were used in this experiment. The specimens using prereacted PZT and PZT raw materials were designated as 75BNKT-25PZT and 75BNKT-25P+Z+T, respectively.

Figures 1 and 2 show the XRD patterns of 75BNKT-25PZT and 75BNKT-25P+Z+T, respectively, sintered between 900° and 1200°C for 1 h. Relative intensity of (h00) and (00l) peaks increased as the sintering temperature increased, indicating that these specimens had <100> grain orientation. The degree of orientation increased as the sintering temperature increased (Fig. 3). The degree of orientation was dependent on the supplying method of PZT. The specimens containing prereacted PZT (75BNKT-25PZT) had the larger degree of orientation than those containing PZT raw materials (75BNKT-25P+Z+T).

Figure 4 shows the microstructure of polished and thermally etched sections of the specimens sintered at 1200°C for 1 h. 75BNKT-PZT was mainly composed of plate-like grains, whereas 75BNKT-25P+Z+T was mainly composed of equiaxed grains.

The reaction sequence from powder mixture to solid solution was different for 75BNKT-25PZT and 75BNKT-25P+Z+T (Figs. 5 and 6, respectively). In BNKT-25PZT, the formation of BNKT was completed by heating at

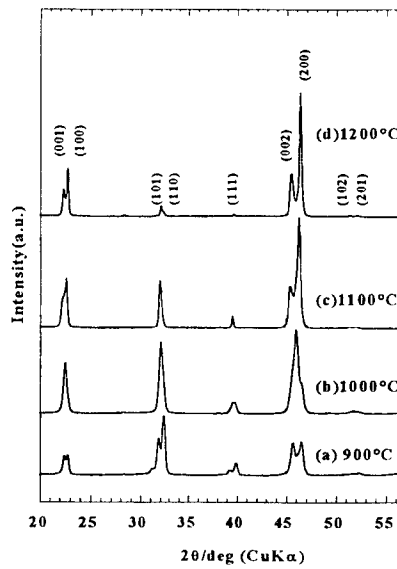

Fig. 1 XRD patterns of 75BNKT-25PZT sintered at various temperatures for 1h.

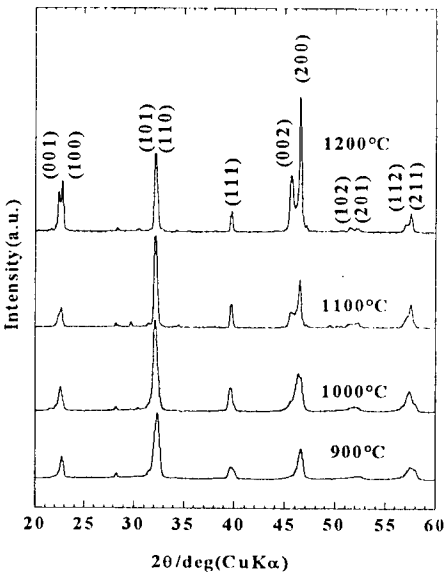

Fig. 2 XRD patterns of 75BNKT-25P+Z+T sintered at various temperatures for 1h.

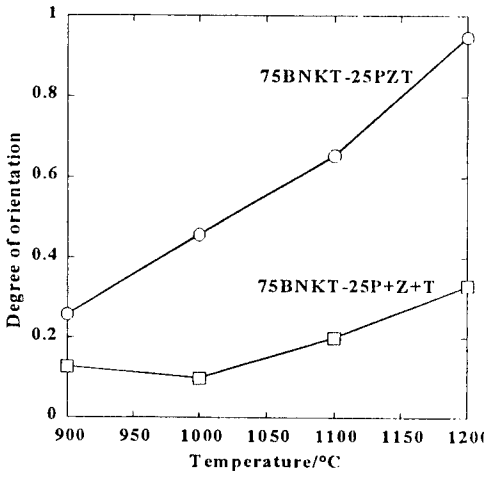

Fig. 3 Effect of sintering temperature on the degree of orientation

900°C for 1 h. At this stage, BNKT and PZT were present as different phases. The solid solution between BNKT and PZT formed at 1100°C by 1 h-heating. In 75BNKT-25P+Z+T, on the other hand, BNKT-PZT solid solution formed at 700°C.

The microstructure observation and phase analysis explain the difference in grain orientation behavior between 75BNKT-25PZT and 75BNKT-25P+Z+T. In 75BNKT-25PZT, the presence of PZT does not influence the BNKT formation from BIT, Na_2CO_3, K_2CO_3, and TiO_2. Thus, plate-like BNKT particles form at about 900°C, and the compact is composed of <100> oriented BNKT and randomly oriented PZT. The BNKT-PZT solid solution forms between 900° and 1100°C. At this stage, the components of PZT diffuse into BNKT particles, resulting in the <100> oriented BNKT-PZT solid solution. In 75BNKT-25P+Z+T, on the other hand, solid solution forms by the reaction between BIT, Na_2CO_3, K_2CO_3, PbO, TiO_2, and ZrO_2 at about 700°C. At this stage, major part of the solid solution forms out of BIT particles, and equiaxed and randomly oriented BNKT-PZT grains form. Therefore, the volume fraction of <100> oriented grains is small.

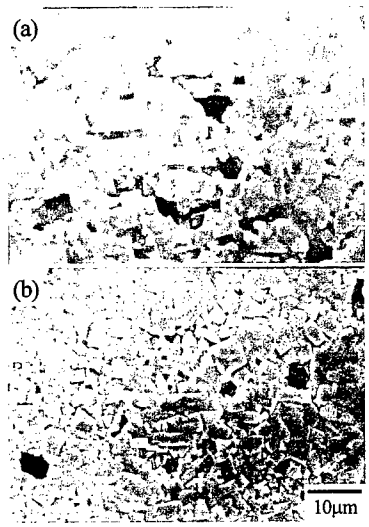

Fig. 4 Microstructures of (a) 75BNKT-25PZT and (b) 75BNKT-25P+Z+T specimens sintered at 1200°C for 1h.

Effect of PZT Concentration

The effect of PZT concentration in the solid solutions was examined in the xBNKT-(100-x)PZT system. Prereacted PZT was employed in this experiment. Figure 7 shows the effect of PZT concentration on the degree of orientation of specimens sintered at 1200°C for 1 h. The sintered compacts with the large degree of orientation were obtained for the BNKT-PZT solid solutions with $x \geqq 75$.

Figure 8 shows the microstructure of polished and chemically etched section of the

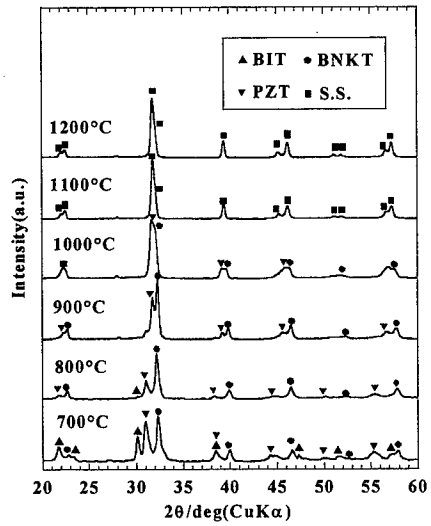

Fig. 5 XRD patterns of 75BNKT-25PZT powder mixture heated at various temperatures for 1h.

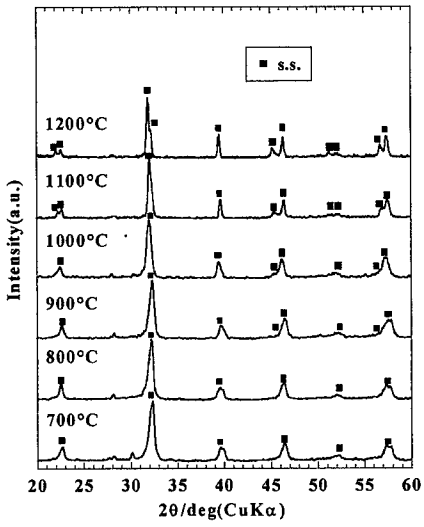

Fig. 6 XRD patterns of 75BNKT-25P+Z+T powder mixture heated at various temperatures for 1h.

50BNKT-50PZT (x=50) specimen sintered at 1200°C for 1h. As compared to Fig. 4(a), no plate-like grains were observed.

The effect of PZT concentration on the degree of orientation is explained as follows. In this experiment, the amount of plate-like BIT particles is dependent on the overall composition; an increase in the PZT concentration reduces the amount of BIT. The grain orientation is caused by the presence of aligned BIT particles. Therefore, an increase in the PZT concentration reduces the degree of orientation.

The above explanation cannot be fully applicable to the reduction in the degree of orientation in the PZT-rich specimens. In the preparation of grain-oriented BNKT, 20% of Ti was originated from plate-like BIT and 80% were supplied from equiaxed particles.[5] The calcined compact was composed of plate-like and equiaxed BNKT particles. Therefore, a small amount of plate-like BNKT contributed to the large degree of orientation.

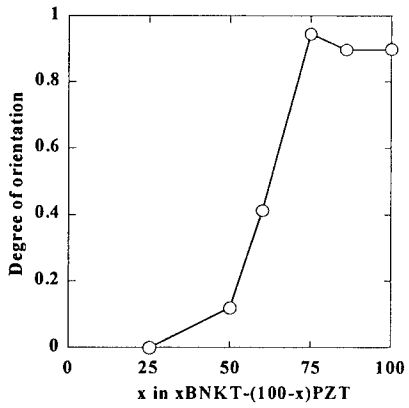

Fig. 7 Effect of PZT concentration on the degree of orientation.

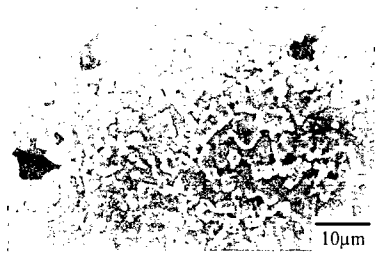

Fig. 8 Microstructure of 50BNKT-50PZT sintered at 1200°C for 1 h.

Another possible explanation is based on the direction of diffusion during the formation of solid solutions. In the BNKT-rich specimens, the final solid solution has a similar composition to that of BNKT. Thus, PZT diffuses into plate-like BNKT, resulting in the large degree of orientation. In the PZT-rich specimens, on the other hand, the situation is reversed, and BNKT diffuses into PZT, resulting in the disappearance of template grains.

CONCLUSIONS

This work exemplifies that the RTGG method is applicable to give grain orientation in the BNKT-PZT system. <100> Oriented BNKT forms from BIT, Na_2CO_3, K_2CO_3, and TiO_2 and acts as a template for the solid solutions. However, when the PZT raw materials are used as a PZT source, the BNKT-PZT solid solution, instead of BNKT, forms at the expense of BIT, resulting in the small degree of orientation. The PZT concentration is also a decisive factor on the grain orientation; the BNKT-PZT solid solutions with the large degree of orientation are only obtained in the BNKT-rich compositions.

REFERENCES

1. H. Igarashi, K. Matsunaga, T. Taniai, and K. Okazaki, *Am. Ceram. Soc. Bull.*, **57**, 815-17 (1978).
2. T. Takenaka and K. Sakata, *Jpn. J. Appl. Phys.*, **19**, 31-39 (1980).
3. S. –H. Hong, S. Trolier-McKinstry, and G. L. Messing, *J. Am. Ceram. Soc.*, **83**, 1130-18 (2000).
4. C, Duran, S. Trolier-McKinstry, and G. L. Messing, *J. Am. Ceram. Soc.*, **83**, 2203-13 (2000).
5. T. Tani, *J. Korean Phys. Soc.*, **32**, S1217-20 (1998).
6. T. Kimura and T. Yamaguchi, *Ceram. Int'l.*, **9**, 13-17 (1983).
7. F. K. Lotgering, *J. Inorg. Nucl. Chem.*, **9**, 113-23 (1959).

Processing and Application of Solid State Converted High Strain Undersea Transmitting Materials

K. McNeal, R. Gentilman, K. Ostreicher, and D. Fiore
Materials Systems Inc., 521 Great Road Littleton, MA 01460
FAX: 978-486-0706
Email: mcneal@matsysinc.com

ABSTRACT

Single crystal relaxor ferroelectrics have been found to exhibit significant electroacoustic property enhancements in comparison to their polycrystalline counterparts. This property enhancement combined with the manufacturability advantages offered by injection molding or tape casting and solid state conversion (SSC) has the potential of producing single crystal actuators at an affordable production viable rate.

Two actuator configurations are being evaluated: 1-3 piezocomposites and multilayers. 1–3 piezocomposite production requires the integration of acicular <001> seeds into PMN-PT feedstock. The seeded feedstock is then injection molded into 1–3 preforms. The seeds become aligned during injection molding. The approach for SSC of polycrystalline layers uses oriented single crystal platelet seeds. Individual layers are produced using both tape casting and injection molding processes. SSC of the seeded materials occurs during heat treatment under controlled conditions.

Feasibility of the SSC process has been demonstrated in the PMN-PT system. Strain measurements have been made by the Naval Undersea Warfare Center, Newport, RI (NUWC) on several SSC materials exhibiting 70% orientation in the <001> direction. At 10 kV/cm, a typical electric field for Navy applications, SSC materials exhibited up to 80% the strain of flux grown PMN-PT single crystals.

INTRODUCTION

The overall goal is to achieve the high performance characteristics of piezo single crystals at the low cost of traditional polycrystalline piezo ceramics. The desirable single crystal crystal performance characteristics include higher coupling coefficients (k_{33} > 90%, k_t > 63%) dielectric constants from 1000 to 5000 with loss values < 1%, and higher piezoelectric coefficients (d_{33} > 2000 pC/N).

BACKGROUND

MSI injection molding, and tape casting technologies provide a ceramic process route for producing oriented SSC preforms or sheets. Feasibility of the recrystallization process has already been demonstrated by placing seed single crystals in contact with dense ceramic relaxor samples and heating to temperatures from 950°C-1200°C.[1,2,3] SSC PMN-PT plates have been fabricated using $BaTiO_3$ platelet seeds in a tape casting process achieving up to 79% <001> preferred orientation.[4]

The prime requirements for successful solid state conversion of a polycrystalline ceramic into a single crystal are (1) high propensity for growth front migration from the seed into the matrix, (2) absence of grain boundary pinning, and (3) the presence of grain growth promoting species at the grain boundaries.[5,6,7] To achieve this conversion while exploiting low cost manufacturing techniques two methods are being evaluated: injection molding and tape casting. The integrated seed approach to SSC involves the addition of oriented acicular or platelet single crystal seeds to the matrix material.

In injection molding PMN-PT ceramic, wax, and seeds are combined, as shown in Figure 1. The mixture is then heated and injection molded into a cold mold. The acicular seeds used are oriented with the <001> direction along the length of the seed, as shown in Figure 2. The seed alignment during processing occurs due to thermoplastic flow of the feedstock material during molding. This process orients the acicular seeds with respect to the 1-3 preform rod direction.

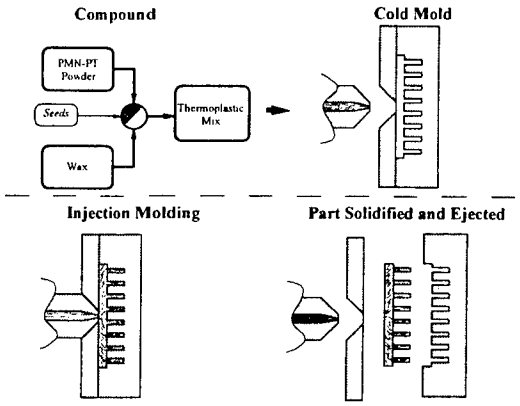

Fig. 1 Injection molding of 1-3 preforms with integrated seeds.

PMN-PT seeds as well as other isostructural seeds have been used in processing SSC materials. The key issues with respect to the seeds are stability in a lead rich system, structural similarity to the matrix material, and a reasonable lattice match to the matrix material.

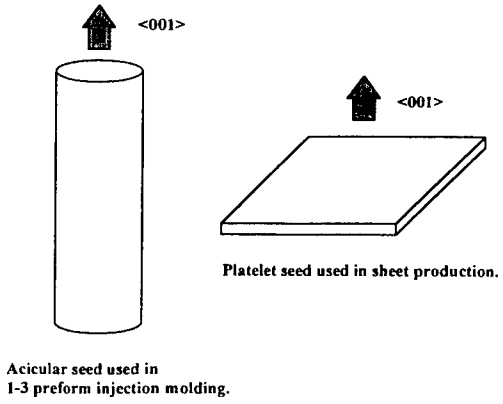

Fig. 2 Seed orientations used in processing.

After injection molding the preforms go through a series of controlled processing steps to initiate SSC. For the injection molding process columbite processed PMN-PT is used as a matrix material with excess lead. Samples are sintered in a lead rich environment at 1150°C from 2 to 20 hours. The seeds initiate solid state conversion within the 1-3 preform. Figure 3 illustrates the steps in this process and resultant microstructure.

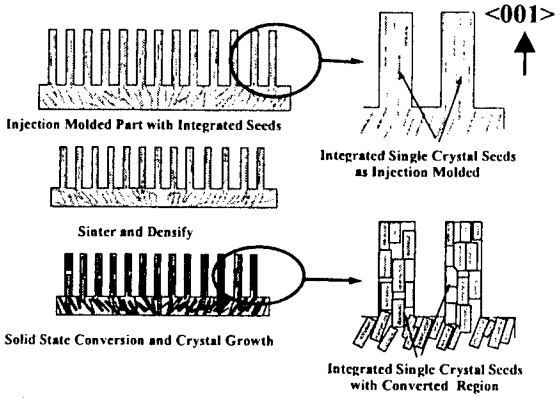

Fig. 3 Solid state conversion process using integrated seeds.

The second manufacturing method being explored is tape casting. This method also employs integrated shaped seeds. The seeds used in tape casting are platelet seeds with the <001> direction perpendicular to the platelet face, Figure 2. This technique is demonstrated in Figure 4. Platelet seeds are added to the tape cast slurry and through shear forming during casting the platelets align in the proper orientation.

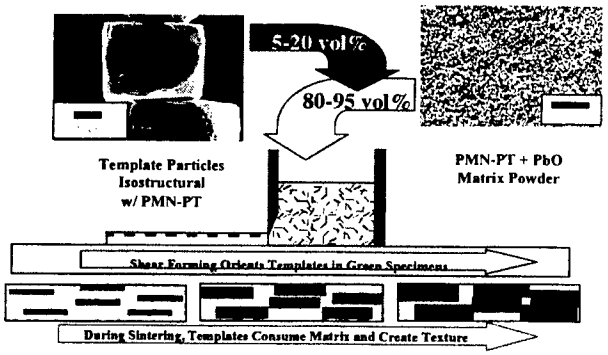

Fig. 4 Tape casting process with integrated seeds for SSC.

In the tape casting process a reactive matrix powder has been developed that can be fully densified at ~1000°C without the need for excess lead. The elimination of excess lead and reduction in the processing temperature allows for a fine grain PMN-PT matrix, reduces lead vaporization, and enhances the driving force for SSC.[8] SSC from templated grains has been demonstrated using $BaTiO_3$, $SrTiO_3$, and $(Ba, Sr)TiO_3$ (BST) seeds,[9] as shown in Figure 5.

Injection molding is also used to produce seeded plate material. The technology used is similar to that demonstrated in Figure 1.

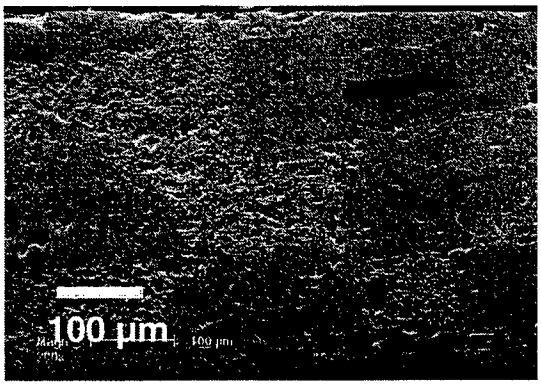

Fig 5 SSC from $BaTiO_3$ template grains in a reactive PMN-PT matrix.

RESULTS

To confirm the properties of solid state converted materials several samples were fabricated for evaluation. These samples were processed by embedding properly oriented, flux grown platelet seeds in pellets. Processing conditions were then employed to initiate SSC. Figure 6 shows a cross-section of a typical sample used for property evaluation. The dark regions are the embedded single crystals with the SSC area surrounding them in a ceramic matrix. Samples were processed with 25 to 70% oriented material.

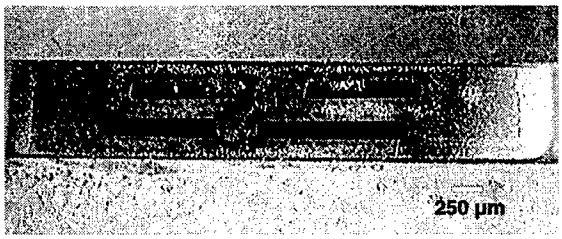

Fig. 6 Sample with embedded PMN-PT seeds used for strain measurements. (~30% oriented material)

Strain vs. electric field was measured for several samples with varying amounts of oriented material. Ceramic, and flux grown single crystals were measured as well as samples with 25 to 70% oriented material. As shown in Figure 7, the strain for a 70% oriented material sample was 80% the strain of a melt grown single crystal material at 10kV/cm. As previously mentioned 10 kV/cm is of interest because it represents a typical Navy operating voltage.

Figure 8 shows the field dependent behavior of several SSC samples from 0 to 30 kV/cm.

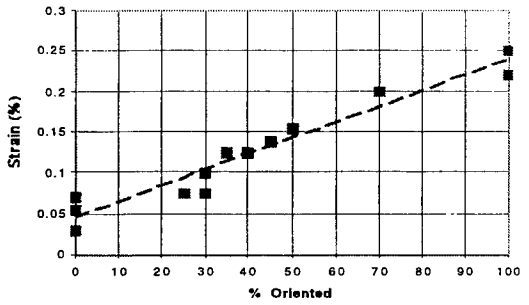

Fig. 7 Strain vs. % oriented material for SSC , ceramic, and single crystal samples at 10 kV/cm.

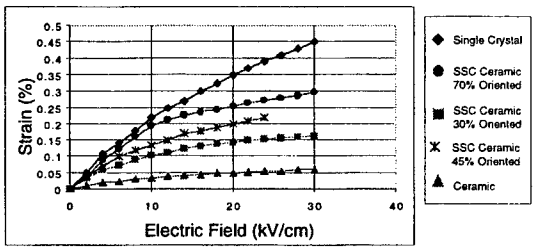

Fig. 8 Strain vs. Electric Field for SSC, ceramic, and flux grown single crystal samples.

CONCLUSIONS AND FUTURE WORK

SSC has been accomplished using template grains using both PMN-PT with excess lead as well as a reactive PMN-PT. PMN-PT, $BaTiO_3$, and $SrTiO_3$ have all worked successfully as seeds in the SSC process. Shaped seed alignment and conversion have been demonstrated in both injection molding and tape casting. Processing parameters have also been established. Optimal processing temperature is 1150°C for 2 to 20 hours in an oxygen atmosphere.

Strain measurements confirm a linear relationship between the % oriented material in a sample and the % strain achieved. Samples with 70 % <001> preferred orientation exhibit 80% the strain of PMN-PT single crystals.

Additional electromechanical characterization of SSC materials is necessary. 1-3 preforms as well as sheet materials are currently being processed. When complete these materials will be assembled into actuators and tested.

ACKNOWLEDGMENTS

This work was supported by the Office of Naval Research and the Defense Advanced Research Projects Agency.

REFERENCES

1. M.P. Harmer, H.M. Chan, T. Li, A. M. Scotch and H. Lee, ONR Piezoelectric Crystal Planning Workshop, 1997.

2. T. M. Li, H. M. Scotch, H.M. Chan, M.P. Harmer, S.E. Park, T.R. Shrout and J.R. Michael, J.Am. Ceram.Soc., 81 [2], 244-48 (1998)

3. M.P. Harmer, H.M. Chan, T. Li, F. Meschke and A. Scotch, "Relaxor Single Crystals from Polycrystalline Precursors," Proceedings of the Eighth US-Japan Seminar on Dielectric and Piezoelectric Ceramics, October 15-19, 1997.

4. E. Sabolsky, A. R. James, S. Kwon, S. Troiler-McKinstry, and G. L. Messing, "Piezoelectric Properties of <001> Textured $Pb(Mg_{1/3}Nb_{2/3})O_3$-$PbTiO_3$ Ceramics," App. Phys. Lett., 78 [17],1-3 (2001).

5. T.R. Shrout and S.E. Park, "Relaxor Based Ferroelectric Single Crystals for Electro-Mechanical Actuators," Materials Research Innovations, 1, pp. 20-25, 1997.

6. N. Yamamoto and S. Matsuzawa, Fine Ceramics, ed. S. Saito, Elsevier Publication, NY, 39-44, 1988.

7. S. Matsuzawa and S. Mace, US Patent 4,339,301, 1982.

8. S-T. Kwon, E. Sablosky, and G. Messing, "Low-Temperature Reactive Sintering of 0.65PMN-0.35PT," J. Am. Ceram. Soc., 84 [3], 648-50 (2001).

9. M. Seabaugh, "Development of a Templated Grain Growth System for Texturing Piezoelectric Ceramics," Presented at 2001 U.S. Navy Workshop on Acoustic Transduction Materials and Devices, May 2001.

Templated Grain Growth of Textured PMN-PT Utilizing Phase Compatible Seed Materials

Paul W. Rehrig and Wesley S. Hackenberger,
TRS Ceramics, Inc., 2820 East College Ave., Suite J, State College, PA 16801
Phone: 814-238-7485 Fax: 814-238-7539

James H. Adair and Thomas R. Shrout
Department of Materials Science and Engineering, The Pennsylvania State University
Materials Research Laboratory, University Park, PA 16802

Email: pwr@trsceramics.com

Textured $Pb(Mg_{1/3}Nb_{2/3})O_3$-$PbTiO_3$ (PMN-PT) ceramics were fabricated by templated grain growth (TGG) utilizing phase compatible seed materials. TGG involves orienting anisotropic seed particles in a matrix of ceramic powder by tape casting and then heating the assemblage to a temperature that promotes grain growth nucleated by the template seed particles throughout the matrix. This results in a grain-textured polycrystalline ceramic. Hydrothermally synthesized lead titanate, $PbTiO_3$, template particles were aligned by tape casting in combination with PMN-PT powder. The resulting ceramics possessed strong texture along the [001] axis of the PMN-PT. The properties of highly textured ceramics grown by TGG were examined. A dielectric constant, K_{33}^T, of 2355 and piezoelectric coefficient of d_{33} ~ 900 pC/N was achieved for a sample that has a Lotgering Factor of ~0.65 and a T_C of 189°C. From the Curie temperature the composition was 0.625PMN-0.375PT, which is on the tetragonal side of the morphotropic phase boundary (MPB). The tetragonality was confirmed by X-ray diffraction, but future compositional tuning suggests the ability to achieve a textured rhombohedral phase with potentially much higher properties. These results show that TGG utilizing phase compatible seed materials is possible and a method for improving the properties, by approaching the single crystal values, in polycrystalline ceramics.

INTRODUCTION

Single crystal relaxor ferroelectrics (PZN:PT and PMN:PT) have been found to exhibit order of magnitude improvements in strain over conventional piezoelectric ceramics. In this research, templated grain growth in PMN-PT was investigated as a means of producing grain oriented ceramics with piezoelectric properties approaching those of single crystals. The resulting materials technology has the potential to dramatically advance the performance of actuators in the form of higher strains, generated forces, and energy efficiency while utilizing existing low-cost manufacturing methods such as tape casting and screen printing. Unique to this work was the use of PT platelet seeds developed at The Pennsylvania State University to provide the necessary crystallographic orientation in the TGG crystals. The current results are discussed below.

RESULTS AND DISCUSSION

The requirements for producing grain textured ceramics by TGG are anisotropic seed materials, compatible seed material compositions, and a ceramic powder with the proper TGG characteristics. In this research $PbTiO_3$ (PT) was chosen as the seed material for its chemical compatibility with the host ceramic material. The approach was to use hydrothermally derived tabular PT particles (Figure 1) as seeds in a matrix of fine grain PMN-PT powder. To orient the seeds, a slurry consisting of fine grain powder, seeds and organic binder was tape cast into thin sheets.

Figure 1: Hydrothermally derived platelets.

Several sheets were then laminated and fired. During the sintering process the seeds promoted the growth of large cubical grains (Figure 2) oriented along the <001> crystallographic axis.

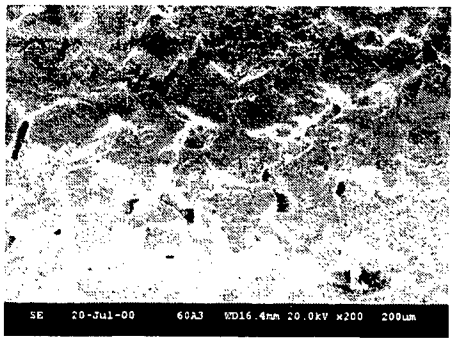

Figure 2: Cubical PMN-PT grains on the surface of tape cast, sintered ceramic. The grains were templated by PT seed platelets.

X-ray analysis indicated that roughly 60-65% of the grains in the ceramic was oriented (Figure 3) resulting in significant strain increases (Figure 4) compared to untextured ceramic of similar composition.

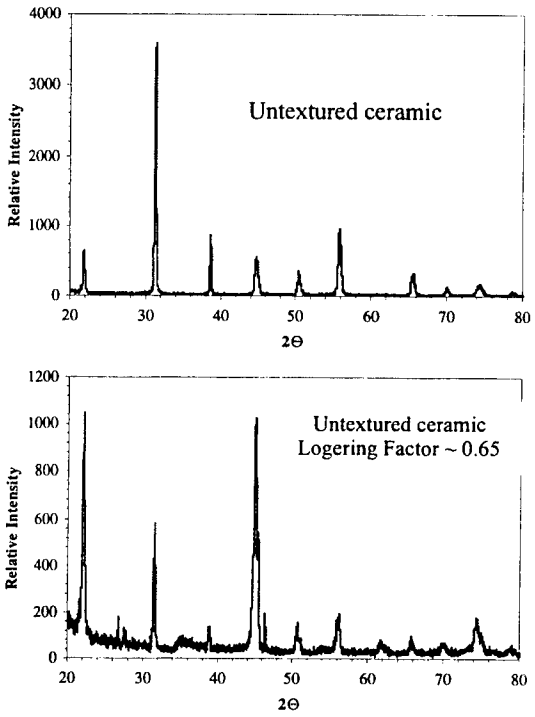

Figure 3: X-ray diffraction patterns of *a)* untextured and *b)* textured PMN-PT ceramic after firing. The seeded ceramic exhibits ~ 65% texturing along the <001> direction as determined by Lotgering factor.

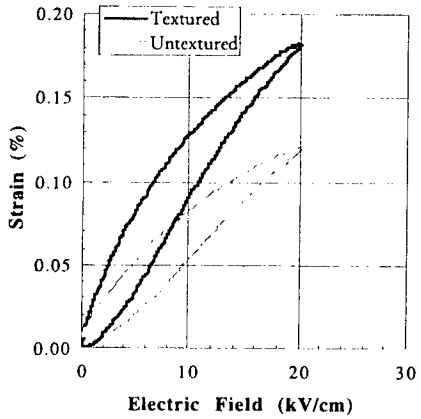

Figure 4. Comparison of piezoelectric coefficient of textured and untextured PMN-PT.

The most successful results to date have been obtained with tetragonal PMN-PT due to the addition of PT platelets to the 0.675PMN-0.325PT powder which was already close to the morphotropic phase boundary (~35% PT). Templated grain growth has been demonstrated in the rhombohedral PMN-PT (Figure 5), although orientation optimization to obtain a fully textured sample is still in progress.

Figure 5: Large cubical templated grain in rhombohedral PMN-PT.

The main advantages of the above approach are 1) a nearly chemically homogeneous ceramic and 2) no reduction in the Curie temperature. This is not the case with seed particles such as $SrTiO_3$ and $BaTiO_3$ being investigated by other researchers. For both these types of seeds, residual seed material remains at the center of the templated grains, and dissolution of the seed material into the PMN-PT results in reduced Curie temperature. Production of oriented ceramic from PT is, therefore, a major breakthrough in the development of textured PMN-PT ceramics. However, the seed quality is an issue that need to be addressed.

The main issue with seed quality has been the tendency for overgrowth, which results in cubical rather than plate-like particles (see Figure 6) that are difficult to align. In addition seed production is currently done by a lab-scale process with a yield of only a 5 grams per hydrothermal growth run (600 mL). This will need to be scaled up considerably (perhaps 100's to 1000's of grams) to make templated grain growth an economically viable process. These topics will be discussed.

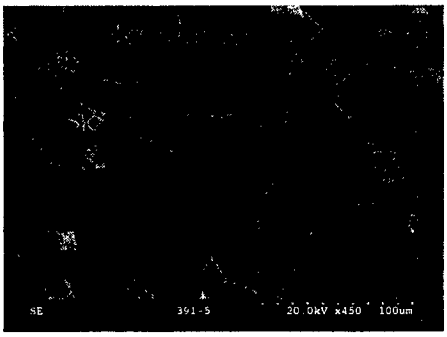

Figure 6: $PbTiO_3$ seed platelets exhibiting overgrowth.

CONCLUSION

Templated grain growth of grain oriented tetragonal PMN-PT ceramics from hydrothermally grown $PbTiO_3$ platelets has been demonstrated for the first time. This produces a chemically homogeneous microstructure and has the potential to be applied to large scale, low cost ceramic manufacturing techniques. Initial compositional tuning experiments have begun to produce a textured rhombohedral PMN-PT ceramic with limited success. The focus of the research has shifted to producing higher quality PT platelets.

Extruded Electroactive "Single Crystal" Fibers

Marina R. Pascucci, Harold B. Strock, and Pavel Bystricky
CeraNova Corporation, 101 Constitution Blvd. Suite D, Franklin, MA 02038
Phone: 508-520-7600 Fax: 508-520-7637
www.ceranova.com

Through a DARPA/AFOSR funded program, CeraNova is extending the expertise gained in the production of polycrystalline piezoelectric fibers to the development of "single crystal" fibers. Various recrystallization approaches are under investigation, including seeded solid state conversion and self-seeded texturing. Experiments have been performed with PMN-31PT and with compositions in the BNBZT system under development by Chiang at MIT. Textured fiber microstructures containing large (>50μm) grains have been achieved. Recrystallization results and analyses of fiber composition, microstructure and fiber quality/performance will be presented.

INTRODUCTION

Polycrystalline piezoelectric fibers are manufactured by CeraNova Corporation using a proprietary extrusion and sintering process. Significant performance improvements for current applications would be realized, and new applications could be addressed, if the advantages of single crystal properties could be achieved in fibers. CeraNova's goal is to develop a practicable production process to cost-effectively manufacture single crystal fibers.

Through a DARPA/AFOSR funded program, CeraNova is extending the expertise gained in the production of polycrystalline piezoelectric fibers to the development of "single crystal" piezoelectric and electrostrictive fibers. As an interim step, various recrystallization approaches are under investigation, including seeded solid state conversion and self-seeded texturing. Experiments to-date have been performed with PMN-31PT, and with piezoelectric compositions in the BNBZT system. This latter system is under development by Chiang at MIT, and is a sodium bismuth titanate (NBT) co-doped with various amounts of barium and zirconium (BZ). Textured fiber microstructures containing large (>50μm) grains have been achieved. Since fiber diameters are small (100-500 μm), grain growth is required over relatively small distances. Times required to achieve recrystallization under non-equilibrium thermal conditions are two orders of magnitude shorter than solid state conversion approaches reported by others.

SAMPLE PREPARATION

Powder Synthesis, Mix Formulation, Seeding

Matrix powders of PMN-31PT and BNBZT, approximately 1 kg per batch, were synthesized at CeraNova in a Union Process attritor mill using reagent grade oxide and carbonate powders. High-energy milling produced a stable slurry of creamy consistency with high solids loading. The slurry was dried to a friable cake, calcined and remilled. In addition to calcined powder, quantities of "reactive matrix" / "precursor" powders (i.e., uncalcined) were retained for separate processing. The calcined stoichiometric BNBZT powder showed only perovskite phase by x-ray diffractometer powder analysis. XRD powder analysis of stoichiometric perovskite PMN-31PT showed minimal evidence of the pyrochlore phase.

Extrudable mixes were made using standard mix formulations and procedures. Calcination and composition, however, both significantly affected mix formulation and viscosity.

Seeds were provided by NexTech Materials Ltd. (Columbus, OH). Initially, $PbNbO_6$ seeds were provided for functional evaluation, i.e., to demonstrate the ability of CeraNova's extrusion process to align shaped seed crystals along a preferred crystallographic axis (Figure 1). Since these seeds were known to be incompatible with a PMN matrix at expected growth temperatures, no sintering experiments were performed in this system. However, the aligned $PbNbO_6$ prismatic columns shown in Figure 1 illustrate the high degree of alignment possible by extrusion. Fiber drawing does not qualitatively improve the degree of orientation observed.

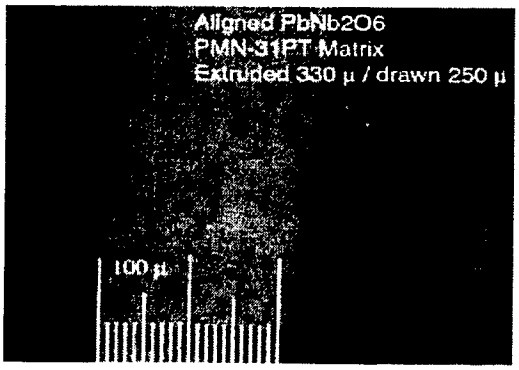

Figure 1 Extruded PMN-31PT fiber showing aligned $PbNbO_6$ crystals.

Stronium titanate ($SrTiO_3$) and barium strontium titanate (BST-20) seeds provided for sintering experiments were mostly cuboidal or tetragonal prism and sharply faceted, with occasional tabular and irregular morphologies (Figure 2). One or more faces generally showed a deeply layered structure. Aspect ratios were estimated as less than 2:1.

Figure 2 – Barium strontium titanate, BST-20, seeds from NexTech Materials. Marker = 20 μm.

Seeds were blended into small batches of extrusion mix to provide a uniform dispersion (volumetric seed loading) or, alternatively, were dispersed on the surface of extruded fiber (surface seeding). Samples were prepared at 1:1, 2.5, 5, 7.3 and 10 percent by weight seeding levels. During extrusion the (100) faces of the tetragonal prism shaped seed crystals are aligned parallel to ribbon or fiber surfaces

Sintering – Static and Dynamic

Extruded fibers and ribbons were fired in a DelTech furnace for binder burnout and presintering (750 - 1000°C in air for 4 hours).

Presintered fibers were transferred to a vertical sintering furnace and fired in air under either "static" or "dynamic" conditions. Under static conditions (i.e., stationary fiber) the furnace temperature gradient results in a range of sintering temperatures along the fiber length. The processing temperature along the fiber axis is determined by correlating sample location with a previously measured furnace temperature profile. Thus, a range of sintering temperatures can be probed in a single static sintering experiment. Process temperatures so defined can then be tested dynamically by moving a fiber through the furnace at varying rates.

RESULTS

BNBZT System

Sintering experiments with BNBZT, without seeds, showed no exaggerated grain growth, with rapid faceting of matrix grains above 1100°C.

Significant seeded growth was observed in a matrix of BNBZT, using both $SrTiO_3$ (ST) and BST-20 seed crystals. For both seed types, sintering times as short as 15 minutes at 1200°C, in air, yielded 5μm growth layers that are highly perfect in appearance (Figure 3). No strontium was observed in the growth layer (SEM-EDX analysis) indicating minimal diffusion of seed components into the matrix. Growth layers are transparent and contain no obvious porosity. Matrix morphology beyond the growth boundary is not effected - the matrix NBT grains do not coarsen beyond 5 micrometers in size.

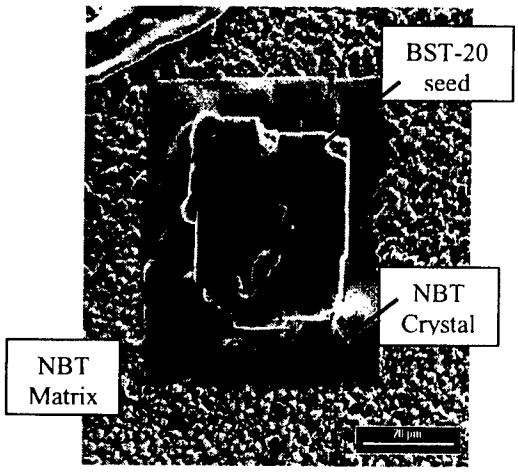

Figure 3 – BST-20 seed crystal in NBT matrix showing growth of NBT material around seed. Fiber surface. (Marker = 20 μm)

Thermal history and bismuth stoichiometry appear to affect seeded growth rate. Various surface crystals were observed along the fiber axis as a function of the thermal profile and local atmosphere in the sintering furnace. Bismuth deficient phases form readily above 1050°C, particularly below the hot zone suggesting vertical transport of vapor-phase bismuth species. The Bi-deficient crystals have a platelet morphology and can become quite large (Fig. 4). Small, feather-like Bi-rich crystals were observed above the hot zone in the vicinity of 900°C (Figure 5). Bismuth deficiency or excess was confirmed by SEM analysis.

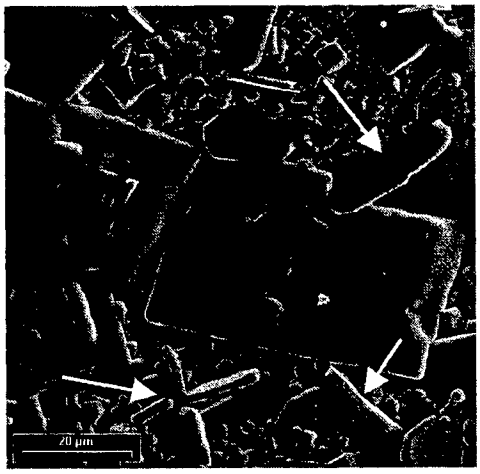

Figure 4: Bismuth deficient platelet phases (white arrows). Marker = 20 µm.

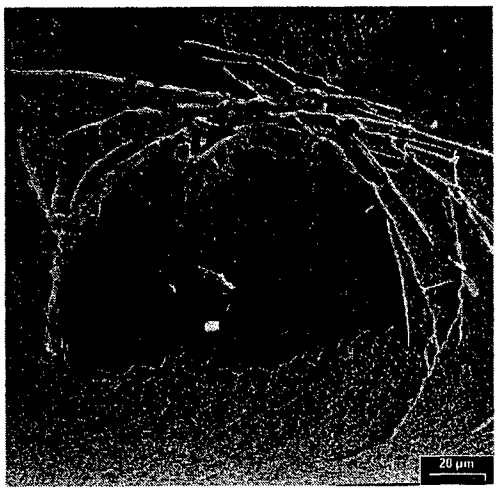

Figure 5 - Bismuth rich feather-like crystals. Marker = 20 µm.

Seeded growth has been observed to cover ~80% or more of a ribbon surface after sintering for 4 hours at 1150°C. Seed growth exceeded the original seed dimension with recrystallized zones of 100 µm or more frequently observed. Such extensive growth may be a surface phenomenon as well as a function of bismuth deficiency. Work is underway to determine if seed and matrix growth are proportional to bismuth deficiency, i.e., directly related to it, or merely co-existing phenomena.

BNBZT Seeded Growth Experiments

Ribbons containing BST-20 and ST seeds at various loading levels were sintered simultaneously to assure equal processing time, temperature and atmosphere. Ribbon sections representing particular time and temperature conditions were mounted, polished and examined in cross-section using optical microscopy. A limited set of seed growth versus time and temperature data was collected. Data from four process times (15-120 min), and four soak temperatures (1125°C-1200°C), were analyzed. Data for BNBZT matrix with BST-20 seeds is presented in Figure 6. (BNBZT matrix with ST seeds showed similar results.) Ten to twenty individual seed measurements were averaged to obtain a single data point. Limits to growth are being explored and the growth mechanism investigated. Quantitative analysis to determine activation energy for growth and boundary mobility is in progress.

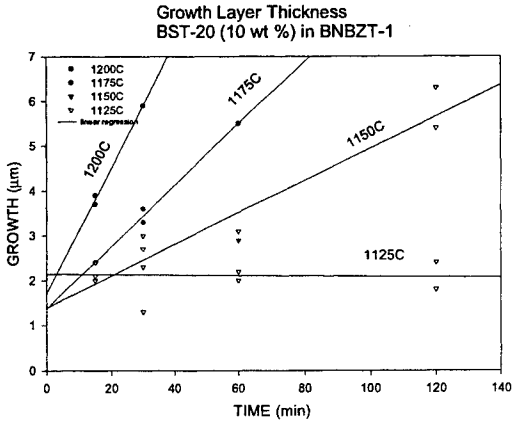

Figure 6 - Seeded growth versus time and temperature. BNBZT matrix with BST-20 seeds (10 wt%).

General observations for both seed systems:

- Seed growth appears to be a linear function of time, at least up to 2 hrs.
- Seed growth rate increases with temperature; it is 3x faster at 1200°C than 1150°C ($2x10^{-7}$ cm/s vs $6x10^{-8}$cm/s) and minimal at 1125°C.
- There is no obvious incubation or "nucleation" period. (However, incubation could have occurred during presintering.)
- Overgrowth material is transparent and appears to be pore free.
- There is no obvious rejection of solute or porosity at the growth / matrix interface.

BNBZT Electric Characterization

Procedures for single fiber P-E hysteresis loop tests were modified in order to achieve the higher fields required for the BNBZT system. Tests on unseeded BNBZT fibers sintered at various temperatures showed good piezoelectric behavior. P-E loop and AFC actuator pack displacement measurements are planned for seeded and highly recrystallized material.

PMN-31PT System

Dynamic sintering conditions were identified for a self-seeded process in PMN-31PT which lead to the formation of perovskite macrocrystals (50-100μm) over 10cm sample lengths (Fig. 7). "Over-sintering" resulted in excessive lead loss, porosity development and pyrochlore formation. Oxygen atmosphere accelerated lead transport relative to rates observed in air.

Figure 7 – Cross-section of sintered PMN-31PT ribbon showing self-seeded macrocrystal development. Ribbon width is 220 μm.

Surface-seeding experiments with BST-30 seeds (provided by NexTech) did not result in seed growth or adverse matrix reaction in both air and oxygen atmospheres. Volumetric seeding experiments with ST seeds are in progress.

PMN-31PT macrocrystalline fibers showed good P-E loop characteristics (Fig. 8). Remanent polarization was about half and coercive field was approximately double when compared with values for a single crystal PMN-PT "fiber" cut from a Bridgeman boule (Crystal Associates).

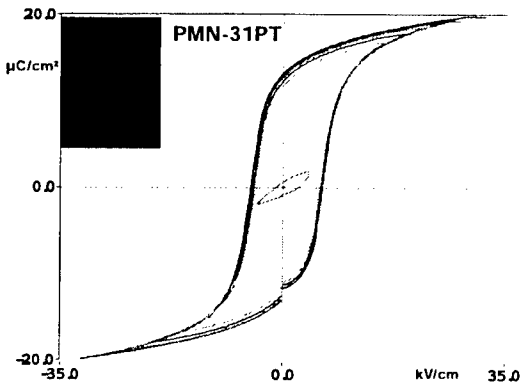

Figure 8 - P-E hysteresis loop behavior for a single fiber of macrocrystalline PMN-31PT.

Macrocrystalline PMN-PT fibers 4cm long were submitted to Continuum Control for AFC pack fabrication and evaluation. Actuators made with these fibers had very good performance – 1600με and d_{33} ~600 pm/V. These results are comparable to production PZT-fiber-containing AFC packs of the same electrode geometry.

SUMMARY

Macrocrystalline growth in seeded BNBZT and self-seeded PMN-PT has been demonstrated. Work continues with newly developed seed crystals and matrix compositions. Experiments to maximize yield of recrystallized material, to elucidate growth mechanisms, and to characterize composition and orientation are in progress. Production of larger quantities of macrocrystalline fibers for actuator fabrication and evaluation is a near term objective.

ACKNOWLEDGEMENTS

Prof. Katherine Zeisler-Mashl (Worcester Polytechnic Institute) provided SEM photos and XRD data. Karen Staples, CeraNova laboratory assistant, prepared optical microscopy samples and performed growth measurements. This work was supported by DARPA/AFOSR Contract F49620-99-2-0332.

Textured Piezoelectric Materials Fabricated by Templated Grain Growth

M. M. Seabaugh, G. L. Cheney, K. Hasinska, A.-M. Azad, S. L. Swartz and W. J. Dawson
NexTech Materials, Ltd
Worthington, OH 43085
FAX: (614) 842-6607
seabaugh@nextechmaterials.com

ABSTRACT:

Textured polycrystalline piezoelectric materials provide improved properties compared to untextured ceramics, and have low processing costs compared to single crystals. NexTech Materials is developing such materials using templated grain growth (TGG), a processing route that produces textured materials using conventional ceramic forming techniques. In TGG, anisotropic template particles are oriented in a fine particle matrix during forming. The matrix grows epitaxially on the templates during heat treatment, consuming the surrounding matrix and creating a textured polycrystal. TGG is being pursued in two systems, $Na_{0.5}Bi_{0.5}TiO_3$ and $Pb(Mg_{1/3},Nb_{2/3})O_3$-$PbTiO_3$.

Good templates are anisotropic, to allow convenient orientation, and crystallographically isostructural with the matrix, to lower the energy barrier to epitaxial growth from template surfaces. PMN and $BaTiO_3$ crystallites are excellent templates, but are difficult to manufacture in quantity with high aspect ratios. $Ba_{1-x}Sr_xTiO_3$ plates can be synthesized with an aspect ratio of ~3, major axis dimensions of 20-50 μm, and Ba contents of 5-45 mol%, using relatively inexpensive and high-yield processes.

Template growth controls texture development, and growth strongly depends on the thermodynamic driving force supplied by the matrix. Matrices of piezoelectric powders and powder precursors are being evaluated.

INTRODUCTION:

Greatly improved properties have been reported for single crystals of piezoelectric $Pb(Mg_{1/3}Nb_{2/3})O_3$-$PbTiO_3$ (PMN-PT), $Pb(Zn_{1/3}Nb_{2/3})O_3$ (PZN), and $(Na_{1/2}Bi_{1/2})TiO_3$ (NBT)[1-2]. A number of research groups are attempting to lower the costs these crystal materials. Flux grown crystals are giving way to crystals grown using Bridgeman techniques, which offer improved control of crystal size, shape and composition[3] However, the costs of these methods remain high, and the geometries that can be obtained are limited to simple shapes. Machining single crystals remains costly and technically challenging.

Recently, highly textured PMN-PT[4,5] and NBT[6,7] ceramics have been fabricated by templated grain growth (TGG) and reactive templated grain growth (RTGG). These materials have piezoelectric properties similar to those of single crystals in the oriented direction. TGG offers an opportunity to further reduce the cost of single-crystal-like materials and uses high-volume, low-cost conventional ceramic forming processes to produce simple and complex parts. NexTech Materials is currently participating in two projects to commercialize TGG ceramic piezoelectric monoliths and fibers[8,9].

One challenge to commercialization of TGG-derived materials is the difficulty of producing the template particles, the anisotropic seeds that control texture development, in large quantities with controlled aspect ratio and particle size. A second challenge is that piezoelectric matrix powder--the source material for template growth--can be difficult to synthesize with high phase purity and reactivity. Both PMN-PT, and the lead-free NBT system are being considered for pilot scale production.

EXPERIMENTAL:

Template Synthesis:

Templates serve as nucleation sites for epitaxial growth of the matrix phase, and must therefore be crystallographically isostructural (though not necessarily chemically identical) with the matrix. The templates must also have a high aspect ratio to increase their orientability during forming. Finally, the templates must be sufficiently larger than the matrix to assure growth, but be small enough to have a high ratio of surface area to volume. Figure 2 shows that high surface area templates require less growth from their surface to completely texture a TGG specimen. This simple geometric calculation shows that with equivalent volumes of templates perfectly dispersed in the matrix (five volume percent) and templates that grow equivalently in

all directions, much less growth is required from the surface of small, high aspect ratio templates.

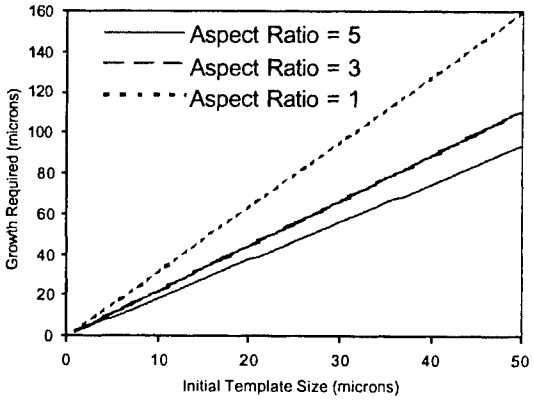

Figure 2. Effect of template size and aspect ratio on growth required for complete texture.

Many experiments have been conducted to obtain template particles, using molten salt synthesis, hydrothermal synthesis, and sol-gel processing, as well as hybrid, multi-step methods. Platelets of hexagonal $BaTiO_3$, and acicular particles of $SrNb_2O_6$, $Sr_2Nb_2O_7$, $PbNb_2O_6$, and $(Sr,Ba)Nb_2O_6$ have all been evaluated and found to be unsatisfactory for PMN-PT. Hydrothermal processing has been used to make $PbTiO_3$ in needle and platelet forms, but these templates dissolved before texture developed in PMN-PT. Cubic $BaTiO_3$[4], $SrTiO_3$[4,7], and $PbTiO_3$[10] have been demonstrated as viable template particles for PMN-PT and NBT, but the routes used to produce templates are expensive and low yield.

$SrTiO_3$ and $(Ba,Sr)TiO_3$ templates have been investigated as commercially-viable template particles. $SrTiO_3$ platelet particles with <100> facets can be synthesized from $Sr_3Ti_2O_7$ in molten salt or hydrothermal solutions[11,12]. The $Sr_3Ti_2O_7$ particles provide the anisotropic template shape; the highly anisotropic crystal structure of the layered perovskite predisposes the material to crystallize in small high aspect ratio plates, similar to those shown in Figure 3.

To obtain $SrTiO_3$ platelets, $Sr_3Ti_2O_7$ particles are reacted in a molten salt flux or hydrothermal solution with TiO_2. During heating, the $Sr_3Ti_2O_7$ reacts with the TiO_2 and forms $SrTiO_3$ platelets (Fig. 4). The size and shape of the $Sr_3Ti_2O_7$ particles control the same characteristics of the $SrTiO_3$ particles, emphasizing the importance of controlling the shape of the precursor $Sr_3Ti_2O_7$. To reduce the cost and increase the yield of $SrTiO_3$ templates, it is essential to optimize the yield of the precursor $Sr_3Ti_2O_7$. If processing temperatures for making $Sr_3Ti_2O_7$ are increased, the yield of platy particles increases, as shown in Figure 5. Longer processing holds also result in an increased yield, but this increase is due to the template thickening. Together, these studies suggest crystal growth takes place at the hold temperature, where particles nucleate and grow by a process akin to Ostwald ripening.

Figure 3. $Sr_3Ti_2O_7$ platelet particles synthesized at 1250°C, 1 hour. (bar = 50 µm)

Figure 4. $SrTiO_3$ platelet particles produced by molten-salt synthesis. (bar = 50 µm)

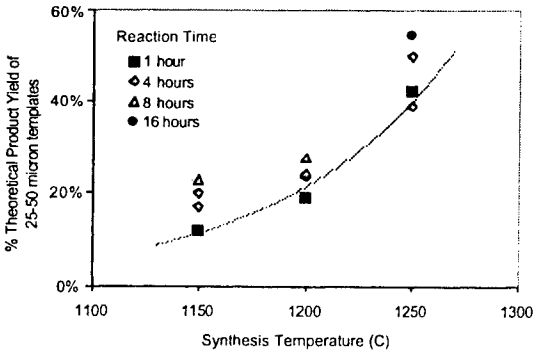

Figure 5. $Sr_3Ti_2O_7$ platelet particle yield as a function of processing conditions.

Barium titanate template particles are very stable in PMN-PT matrices, but are very difficult to synthesize as plates with <100> facets. Strontium titanate templates can be grown as<100> plates, but eventually dissolve in the PMN-PT matrix—the templates foster texture

development, but the dissolution of Sr into the matrix may be detrimental to properties. $(Ba,Sr)TiO_3$ templates may provide an intermediate composition that shares the advantages of its two end members.

To obtain $(Ba,Sr)TiO_3$ templates, $Sr_3Ti_2O_7$ plates are added to a molten salt mixture. $BaCl_2$ in the melt releases Ba^{2+} to react with the $Sr_3Ti_2O_7$ plates, substituting for Sr^{2+} sites on the plates. Simultaneously, excess SrO is leached from the platelets, leaving platelets with a slight (~10 mol%) Ba content and a perovskite structure. Figure 6 is an example of the type of template particles formed by this process.

Figure 6. $(Ba,Sr)TiO_3$ (10% Ba) platelet particles produced by molten-salt synthesis. (bar = 20 μm)

As shown in Figure 7, the Ba content of the template particles is strongly related to the concentration of oxides in the molten salt and additions of $BaTiO_3$ precursors to the molten salt mixture. A linear relationship exists between the targeted Ba content and that measured in the product, but it appears that as the oxide content of the melt is increased, a smaller amount of Ba is incorporated into the templates. This effect is likely a result of the higher concentration of Ba and Ti containing reactants, which dissolve easily into the melt, and then homogeneously nucleate as $BaTiO_3$ crystallites.

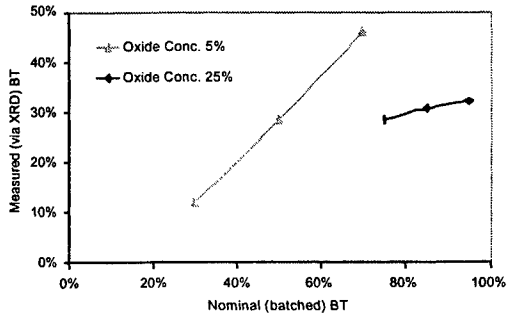

Figure 7. $BaTiO_3$ incorporation in $(Ba,Sr)TiO_3$ at as a function of composition and oxide contents.

As the Ba content of the templates increases, lower aspect ratios are obtained in the $(Ba,Sr)TiO_3$ templates, as shown in Figure 8. This is an important consideration in balancing the chemical stability the Ba content provides with the aspect ratio, which controls the degree of orientation that can be obtained during forming.

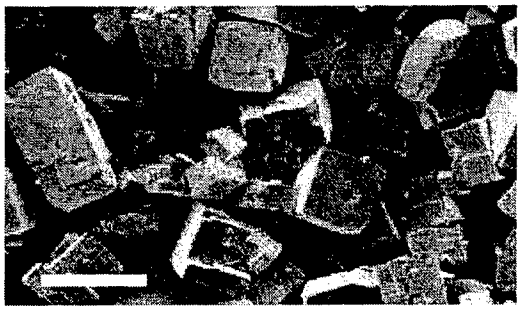

Figure 8. $(Ba,Sr)TiO_3$ (45% Ba) platelet particles produced by molten-salt synthesis. (bar = 50 μm)

Matrix Materials:

An important question to address in TGG processing is how to maximize the free energy available for growth of the template particle, and how to balance this free energy between densification and grain growth. For complex matrices, two routes are available. The first is to begin with fine powder of the desired phase. The high surface area of the powder provides the driving force for both densification and growth. For this approach, PMN-PT was synthesized by calcining mixed oxides of PbO, $MgNb_2O_6$, and TiO_2, and attrition milling the resulting powder until it has a surface area of approximately 6 m^2/g. Similar routes were used to produce NBT with a surface area greater than 5 m^2/g. The second approach to matrix production is to make a fine powder of the precursor materials and take advantage of the additional free energy given up during crystallization of the product phase. This approach is complicated in the PMN-PT system by the difficulty of forming perovskite PMN-PT without crystallizing the undesirable pyrochlore phase. A reactive matrix precursor system has been demonstrated for both the PMN-PT and NBT systems[6,13,14], and similar routes have been used in the experiments detailed below.

Tape Casting Experiments:

Matrix powders were ball milled in an organic solvent to deagglomerate the powders. Platelets of $(Ba,Sr)TiO_3$ were added to the NBT powders; ST platelets were added to the PMN-PT. The volume ratio of matrix precursor to template particles 95:5 for the PMN-PT, while a 90:10 ratio was used for the NBT. The slurry was slowly stirred to incorporate the templates,

then tape cast at 20 cm/min at a blade height of 250μm. The resulting tape was cut and laminated in stacks of several layers to form a green body 1 mm thick.

The green body was heated to remove the binder, then sintered. XRD was used to measure the crystallographic texture of the specimen.

RESULTS

Figure 9 shows two XRD patterns for PMN-PT. The bottom pattern is for randomly oriented PMN-PT matrix material, tape cast and sintered in a manner very similar to the templated material. The top pattern is the XRD pattern for material containing <100> $SrTiO_3$ platelet templates. The <100> peak intensities much greater in the templated sample compared to the matrix material, indicating that significant template growth has resulted in a strong <100> texture of the material.

Figure 10 is the XRD pattern for a <100> textured NBT-$(Ba,Sr)TiO_3$ material tape cast and sintered under similar conditions. This pattern also shows increased intensity of the [100] and [200] peaks, indicating the $(Ba,Sr)TiO_3$ templates have successfully textured the NBT.

CONCLUSIONS AND FUTURE WORK

Template particles for TGG in PMN-PT have been synthesized by a number of routes. The templates have been successfully integrated into a tape casting process, and PMN-PT tapes with <100> textures have been produced. Future work will be directed toward synthesizing new template compositions and geometries, particularly acicular particles. In addition, sintering studies will be implemented to increase the degree of <100> texture in the perovskite-templated materials and improve densification during sintering. Scale-up of synthesis processes will also be implemented.

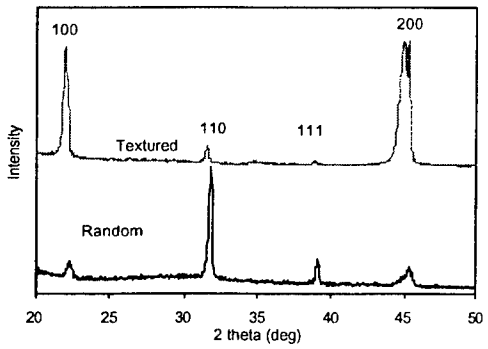

Figure 9. XRD patterns for texturedand untextured PMN-PT materials

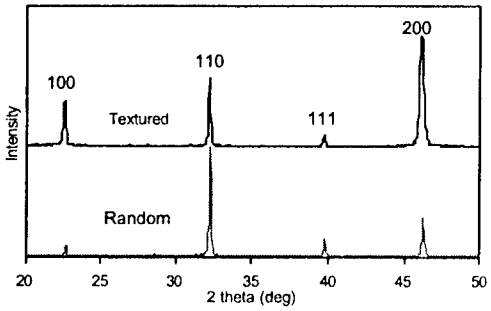

Figure 10. XRD patterns for textured and untextured NBT materials

ACKNOWLDEGEMENTS

NexTech Materials gratefully acknowledges the support of DARPA, AFOSR, and ONR under ONR Contract No. N66604-99-C-4622 and AFOSR Contract No. F49620-99-2-0332. We also thank Drs. Messing and Kwon for their cooperation in the PMN-PT experiments described above.

REFERENCES

[1] Park, S-E. and Shrout T.R., *J. of Appl. Phys.* 82, 1804-1811,, 1997.

[2] Chiang, Y.M., Farrey, G.W., Soukhojak, A.N., *Appl. Phys. Letters* 73, 3683-5, 1998.

[3] Bridenbaugh P.M., Costa L., Paper I.17, *Abstracts of the 2001 U.S. Navy Meeting on Acoustic Transduction Materials and Devices*, Baltimore, MD May 14-16, 2001.

[4] Sabolsky, E.M., James, A.R., Kwon, S., Trolier-McKinstry, S., Messing, G.L., *Appl Phys. Letters*, 78, 2551-2553, 2001.

[5] James, A., Kwon, S., Messing, G.L., Trolier-McKinstry, S. Yilmaz, H, Paper ELEC2E-06-2001-O, *Abstr. of 103rd Annual Meeting and Exposition of the American Ceramic Society*, Indianapolis, IN April 22-25, 2001.

[6] Tani, T., 1998 *J. Kor. Phys. Soc.* **32**, S1217.

[7] Trolier McKinstry, S.E., Yilmaz, H., Messing G.L., Paper ELEC2E-07-2001-O, *Abstracts of 103rd Annual Meeting and Exposition of the American Ceramic Society*, Indianapolis, IN April 22-25, 2001.

[8] ONR Contract No. N66604-99-C-4622

[9] AFOSR Contract No. F49620-99-2-0332

[10] Rehrig, P.W., Hackenberger, W.S., Adair, J.H., Shrout, T.R., Paper V.2, *Abstracts of the 2001 U.S. Navy Meeting on Acoustic Transduction Materials and Devices*, Baltimore, MD May 14-16, 2001.

[11] Watari K, Brahmaroutu B, Messing GL, Trolier-McKinstry S, Cheng SC, *J. of Mat. Res.*, 15, 846-849.

[12] Takeuchi, T., Tani, T., Satoh, T., *Solid State Ionics*, 108, 67-71.

[13] H. Yilmaz, G.L. Messing, and S. Trolier-McKinstry, "Textured Sodium Bismuth Titanate Ceramics by Templated Grain Growth," Proceedings of the 2000 12th IEEE International Symposium on Application of Ferroelectrics, Ed. S.K. Streiffer, et al., IEEE, (2001) pp. 405-408.

[14] E.M. Sabolsky, S. Kwon, A.R. James, G.L. Messing, and S. Trolier-McKinstry, "Dielectric and Electromechanical Properties of <001>-Textured $(0.68)Pb(Mg_{1/3}Nb_{2/3})$-$(0.32)PbTiO_3$," Proceedings of the 2000 12th IEEE International Symposium on Application of Ferroelectrics, Ed. S.K. Streiffer, et al., IEEE, (2001) pp. 405-408.

Preparation of nm-sized $BaTiO_3$ Fine Particles Using a New 2-step Thermal Decomposition of Barium Titanyl Oxalates

Satoshi Wada, Miho Narahara, Hirofumi Kakemoto and Takaaki Tsurumi

Department of Metallurgy and Ceramics Science, Graduate School of Science and Engineering,
Tokyo Institute of Technology, 2-12-1 Ookayama, Meguro-ku, Tokyo 152-8552, Japan
FAX: +81-3-5734-2514, Email: swada@ceram.titech.ac.jp

To obtain inpurity-free and nm-sized barium titanate ($BaTiO_3$) particles, a new 2-step thermal decomposition method from barium titanyl oxalates ($BaTiO(C_2O_4)_2 \cdot 4H_2O$) was proposed. At the 1st step, $BaTiO(C_2O_4)_2 \cdot 4H_2O$ was annealed at 400 °C for 1 h in the O_2 flow. The annealing temperature of 400 °C was chosen for the following reasons; (1) no formation of $BaCO_3$ and TiO_2 and (2) the complete removal of H_2O and other carbon species. This compound obtained at 400 °C was amorphous phase, but its chemical composition was $BaCO_3$-TiO_2. When this compound was annealed in air at higher temperatures, the large $BaTiO_3$ particles were prepared with by-products such as $BaCO_3$. Thus, to prevent the crystal growth and the formation of $BaCO_3$, this compound was annealed in vacuum. Finally, the $BaTiO_3$ single crystals with a size below 20 nm were prepared around 620 °C. These $BaTiO_3$ fine particles were characterized using various methods to investigate defects and impurities in the particles.

1. INTRODUCTION

Ferroelectric $BaTiO_3$ fine particles have been used as raw materials for electronic devices such as multilayered ceramic capacitors (MLCC). Recently, with the miniaturization of electronic devices, the down-sizing of MLCC has been developed and accelerated. As a result, it is expected that the thickness of dielectric layers in MLCC will become less than 1μm in the future. Consequently, $BaTiO_3$ raw materials with particle size from a few hundred nm to a few ten nm are required. However, in ferroelectric fine particles, it was well-known that ferroelectricity decreases with decreasing particle and grain sizes, and disappears below certain critical sizes; this is called the "size effect" in ferroelectrics.[1-9] Therefore, the size effect in ferroelectrics such as $BaTiO_3$ is one of the most important phenomena for an interest of the industry and science. To date, some researchers have estimated the critical size to be around 10~20 nm in $BaTiO_3$ fine particles.[9-12] This critical size is just an estimated value, and there is no experimental evidence on the critical size. Thus, it is very important to prepare $BaTiO_3$ ferroelectric crystals with sizes below the estimated critical size, and investigate their size effect. However, it is very difficult to prepare impurity-free and nm-sized $BaTiO_3$ crystallites using the conventional wet processes such as the sol-gel[13], hydrothermal[14] and low temperature direct synthesis (LTDS) methods[15-16]. Especially, the existence of the lattice hydroxyl group was so negative for the ferroelectricity. This means that the lattice hydroxyl group was a common problem for the wet-process derived $BaTiO_3$ fine particles.[13-16] Therefore, to prepare impurity-free and nm-sized $BaTiO_3$ crystals below 10 nm, a new innovative preparation method, except for all of the solution methods, is required.

Normally, a thermal decomposition of $BaTiO(C_2O_4)_2 \cdot 4H_2O$ leads to a formation of large $BaTiO_3$ particles over 1 μm, via the intermediate compounds such as $BaCO_3$ and TiO_2.[17-19] However, there is a significant advantage that a Ba/Ti atomic ratio of the prepared $BaTiO_3$ is completely 1.000 because of the Ba/Ti atomic ratio of 1.000 in $BaTiO(C_2O_4)_2 \cdot 4H_2O$. If nm-sized $BaTiO_3$ particles are prepared from $BaTiO(C_2O_4)_2 \cdot 4H_2O$, it is possible to obtain the inpurity-free, defect-free and nm-sized $BaTiO_3$ particles. The large particle sizes of $BaTiO_3$ particles derived from $BaTiO(C_2O_4)_2 \cdot 4H_2O$ is caused by the formation of $BaTiO_3$ via a reaction between $BaCO_3$ and TiO_2 at higher temperatures over 850 °C. Thus, it is very important to prevent the formation of these intermediate compounds. For this purpose, the optimum condition for the thermal decomposition of $BaTiO(C_2O_4)_2 \cdot 4H_2O$ must be refined to obtain impurity-free and nm-sized $BaTiO_3$ crystallites, *i.e.*, atmosphere, heating and cooling rate, temperature and soaking time.

In this study, we try to prepare impurity-free and nm-sized $BaTiO_3$ crystallites from $BaTiO(C_2O_4)_2 \cdot 4H_2O$. For this objective, we propose a new thermal decomposition method of $BaTiO(C_2O_4)_2 \cdot 4H_2O$ using the both atmosphere of the O_2 flow and vacuum.

2. EXPERIMENTAL

Barium titanyl oxalates ($BaTiO(C_2O_4)_2 \cdot 4H_2O$) were prepared at Fuji Titanium Co., Ltd.[20] The Ba/Ti atomic ratio of this compound was 1.000 and the amount of the impurity was less than 0.02 %.[20] Figure 1 shows the TG-DTA curve of this $BaTiO(C_2O_4)_2 \cdot 4H_2O$ measured at a heating rate of 10 °C/min in air. Over 710 °C, no weight loss was observed, which suggests the formation of $BaTiO_3$ particles. Normally, to prepare $BaTiO_3$ particles from $BaTiO(C_2O_4)_2 \cdot 4H_2O$, the higher temperatures over 1000 °C were used in air, but in this case, the larger $BaTiO_3$ particles with sizes around 1 μm were obtained.

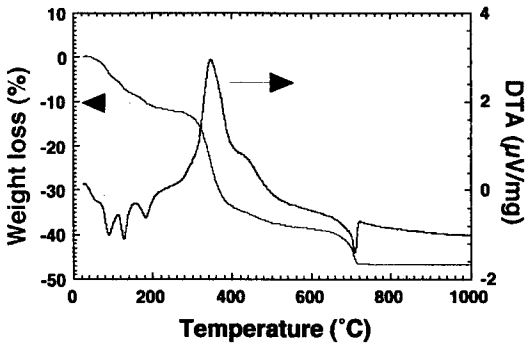

Fig. 1. The TG-DTA curve of $BaTiO(C_2O_4)_2 \cdot 4H_2O$.

Hence, if the calcination temperature can decrease down to 710 °C, the formation of the smaller $BaTiO_3$ particles with sizes below 100 nm is expected. Thus, the conditions of the normal thermal decomposition in air were optimized using (1) temperatures and (2) the soaking times.

On the other hand, to investigate the effect of the atmosphere, the vacuum and the O_2 flow atmosphere were used. This is because (a) the decrease of the decomposition temperature of $BaCO_3$ in vacuum and (b) the easy removal of the carbon species from $BaTiO(C_2O_4)_2 \cdot 4H_2O$ can be expected. In this study, the special designed quartz reactor chamber was used for the ease change from the O_2 flow to the vacuum. Temperature was changed from 100 °C to 1000 °C, and the soaking time was changed from 0 h to 5 h.

The crystal structure of the products was investigated at 25 °C using a powder X-ray diffractometer (XRD) (RINT2000, Rigaku, Cu-kα, 50 kV, 30 mA) and a laser Raman scattering spectrometer (Raman) (NRS-2100, Jusco, 514 nm, 100 mW). The average particle sizes and crystallite sizes were estimated using a transmission electron microscope (TEM) (CM300, Philips, 300 kV) and XRD. The impurity in the products was analyzed using a Fourier transform infrared spectrometer (FT-IR) (SYSTEM 2000 FT-IR, Perkin Elmer) and by differential thermal analysis with thermogravimetry (TG-DTA) (TG-DTA2000, Mac Science).

3. RESULTS AND DISCUSSION

3.1 The conventional thermal decomposition process in air

Normally, the thermal decomposition of $BaTiO(C_2O_4)_2 \cdot 4H_2O$ over 1000 °C leads to the formation of the large $BaTiO_3$ particles over 1 μm.[17-19] Recently, Kajita and Nishido reported that the thermal decomposition at 850 °C leads to the formation of the $BaTiO_3$ particles with sizes of 150 nm.[20] This means that if the conditions for the conventional thermal decomposition are optimized, it is expected to prepare the smaller $BaTiO_3$ particles below 100 nm. Figure 2 shows a XRD pattern of the products prepared at 700 °C for 1 h. As a main product, the formation of the cubic $BaTiO_3$ particles was confirmed while as a by-product, a slight amount of $BaCO_3$ was also found. The crystallite size D_{111} was calculated from a FWHM of (111) plane around 39° using the Scherrer's equation. It should be noted that $SrTiO_3$ crystal as a external standard materials for the correction of FWHM. As a result, D_{111} was estimated at around 50 nm. On the other hand, TEM observation also revealed that two kinds of particles were observed, and the average $BaTiO_3$ particle size was around 45 nm. When the temperatures below 700 °C was used for the thermal decomposition, no $BaTiO_3$ particle was prepared. When the temperatures above 700 °C was used, the average $BaTiO_3$ particle size increased. These results revealed that it was very difficult to prepare the impurity-free and nm-sized $BaTiO_3$ crystallites using the conventional thermal decomposition process in air.

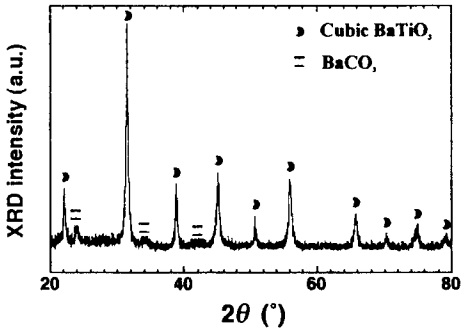

Fig. 2. A XRD pattern of the products prepared at 700 °C for 1 h in air.

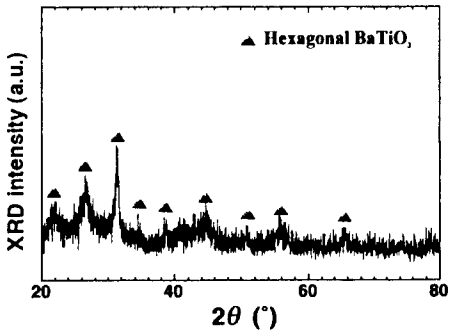

Fig. 3. A XRD pattern of the products prepared at 620 °C for 1 h in vacuum.

3.2 The unusual thermal decomposition process in vacuum

In vacuum, it is possible to prepare the impurity-free and nm-sized $BaTiO_3$ fine particles below 50 nm. This is because it is expected that the vacuum atmosphere can make the decomposition temperature of $BaCO_3$ lower than that in air. Thus, the unusual thermal decomposition of $BaTiO(C_2O_4)_2 \cdot 4H_2O$ in vacuum was performed at various temperatures from 500 °C to 750 °C for 1 h. Figure 3 shows a XRD pattern of the products prepared at 620 °C for 1 h in vacuum of 2.3×10^{-2} torr. The FWHM of all peaks were broadened, which suggests that their crystallite size was extremely small below 10 nm. However, all of XRD peaks in Fig. 3 were assigned to the hexagonal $BaTiO_3$. Moreover, the color of these particles was completely black. This means that in the hexagonal $BaTiO_3$ particles, there was the residual carbon, *i.e.*, the hexagonal $BaTiO_3$ was prepared under the reduced atmosphere. Some researchers reported that the reduced atmosphere caused the formation of the hexagonal $BaTiO_3$ because of the oxygen deficiency.[21-23] For our objective, the hexagonal $BaTiO_3$ is a undesirable phase, and the oxygen deficiency leads to the defect structure such as the oxygen vacancies into the $BaTiO_3$ lattice. Thus, to remove the residual carbon and oxygen vacancies, these hexagonal $BaTiO_3$ particles were treated at 400 °C for 15 h in the O_2 flow. This oxidizable treatment made the color of the particles gray, which means that the residual carbon was still remained. And, its XRD pattern was the completely same as Fig. 3. These results revealed that it was very difficult to prepare the impurity-free $BaTiO_3$ crystallites using the unusual thermal decomposition process in vacuum.

3.3 A proposal of a new 2-step thermal decomposition process

The above two process had some merits and demerits. The thermal decomposition in air can

produce the cubic $BaTiO_3$ crystallites, but its problems are the larger crystallite sizes and the formation of $BaCO_3$. On the other hand, the thermal decomposition process in vacuum can produce the nm-sized $BaTiO_3$ crystallites, but its problems are the hexagonal phase and the residual carbon. Therefore, if we can well combine these two processes, it is possible to prepare the impurity-free and nm-sized $BaTiO_3$ crystallites.

In the former process, the $BaTiO_3$ particles were prepared via intermediates such as $BaCO_3$ and TiO_2. Thus, the decomposition reaction of $BaCO_3$ was the rate-determining stage in the $BaTiO_3$ formation, and its decomposition temperature was over 700 °C. At the high temperature around 700 °C, as the growth rate of $BaTiO_3$ is so fast, the larger $BaTiO_3$ crystallites can be obtained easily. Therefore, to reduce the temperature of the $BaTiO_3$ formation, it is important to prevent the formation of $BaCO_3$ phase as the intermediate.

In the latter process, the nm-sized $BaTiO_3$ particles were prepared as the hexagonal phase with the residual carbon. As the above mentioned, this hexagonal phase with the residual carbon was caused by the reduced atmosphere originated from the low temperature decomposition of $BaTiO(C_2O_4)_2 \cdot 4H_2O$ in vacuum. Thus, if the decomposition of $BaTiO(C_2O_4)_2 \cdot 4H_2O$ into $BaCO_3$ and TiO_2 is performed in the O_2 flow, we can expect that there is no oxygen deficiency at this stage. After this stage, even if the $BaTiO_3$ formation from $BaCO_3$ and TiO_2 is done in vacuum, there is no reduced atmosphere. Moreover, the lowering decomposition temperature of $BaCO_3$ can be expected in vacuum. Therefore, to prepare the impurity-free and nm-sized $BaTiO_3$ crystallites from $BaTiO(C_2O_4)_2 \cdot 4H_2O$, it is important to combine two processes, *i.e.*, (I) the low temperature decomposition of $BaTiO(C_2O_4)_2 \cdot 4H_2O$ in the O_2 flow and (II) the $BaTiO_3$ formation from $BaCO_3$ and TiO_2 in vacuum. Moreover, as the intermediate compounds in the reaction (II), the best way is no formation of $BaCO_3$ and TiO_2 phase, but the formation of an amorphous phase with a chemical composition of $BaCO_3$-TiO_2. We named this new method a 2-step thermal decomposition method.

3.4 The preparation of nm-sized $BaTiO_3$ crystallites and their characterization

At the 1st step, $BaTiO(C_2O_4)_2 \cdot 4H_2O$ was annealed at various temperatures from 100 °C to 450 °C for 1 h in the O_2 flow. As a result, below 400 °C, it was confirmed that there was no complete decomposition of $BaTiO(C_2O_4)_2 \cdot 4H_2O$, while above 400 °C, a slight formation of $BaCO_3$ phase was also detected. Figures 4 and 5 show a XRD pattern and a Raman scattering spectrum of the products annealed at 400 °C for 1 h in the O_2 flow, respectively. In Fig. 4, though several unknown broad peaks were observed, the most of the products were assigned to the amorphous phase. If $BaTiO(C_2O_4)_2 \cdot 4H_2O$ is completely decomposed into $BaCO_3$ and TiO_2 phase, the weight loss can be calculated at 38.3 %. The experimental weight loss at 400 °C was almost similar to this one. Therefore, this result suggests that the prepared amorphous phase in Fig. 4 can have the chemical composition of $BaCO_3$-TiO_2. The Raman spectrum in Fig. 5 indicated one significant broad peak. Though this peak was composed of the overlapping of the several broad

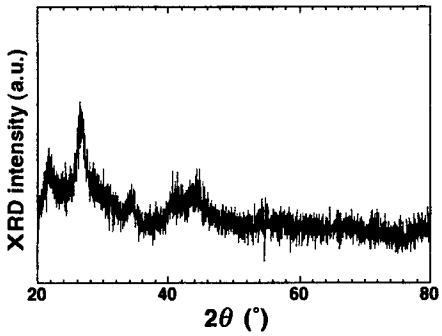

Fig. 4. A XRD pattern of the products annealed at 400 °C for 1 h in the O_2 flow.

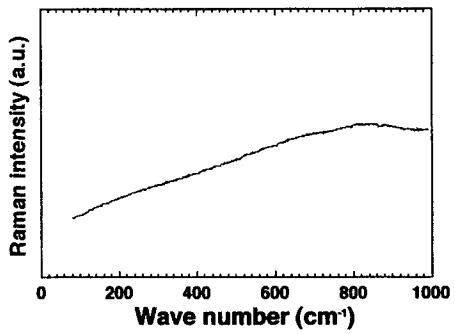

Fig. 5. A Raman scattering spectrum of the products annealed at 400 °C for 1 h in the O_2 flow.

peaks, we cannot separate the peak into the several peaks. However, this means that there was the disordered lattice vibration like a molecule. Now, we believe that the local structure of the amorphous compounds is closed to the structure with a random network of the $BaCO_3$ and the TiO_2 molecules.

At the 2nd step, the amorphous intermediate compounds were annealed at various temperatures from 550 °C to 750 °C for 0.5 h in vacuum. As a result, above 600 °C, the $BaTiO_3$ formation was confirmed. Figures 6 and 7 show a XRD pattern and a Raman scattering spectrum of the products annealed at 620 °C for 0.5 h in vacuum, respectively. In Fig. 6, the most of clear peaks were assigned to the cubic $BaTiO_3$ phase. However, two very weak and broad peaks were observed around 27 ° and 42.4 °, and these peaks were assigned to the hexagonal $BaTiO_3$ phase. Moreover, the Raman spectrum in Fig. 7 indicated that the most of peaks were assigned to the tetragonal $BaTiO_3$ phase while a peak at 640 cm^{-1} was assigned to the hexagonal $BaTiO_3$ phase.[24-25] However, we must take care of the hexagonal $BaTiO_3$

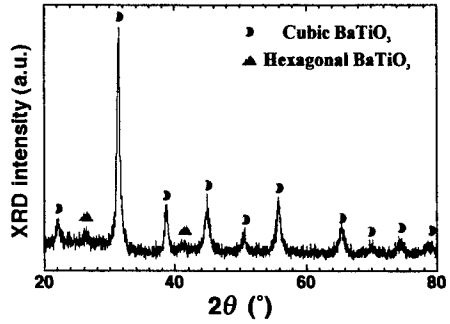

Fig. 6. A XRD pattern of the products annealed at 620 °C for 0.5 h in vacuum.

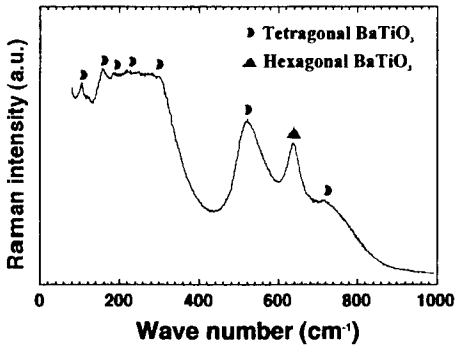

Fig. 7. A Raman scattering spectrum of the products annealed at 620 °C for 0.5 h in vacuum.

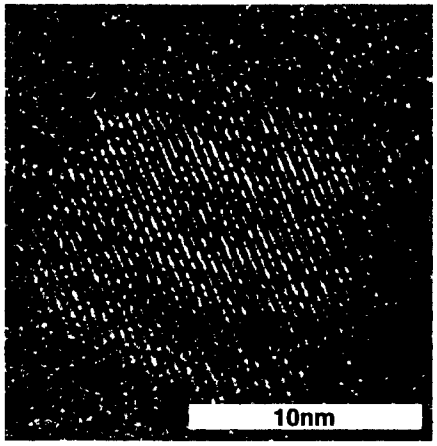

Fig. 8. A TEM bright-field image of the products annealed at 620 °C for 0.5 h in vacuum.

phase. Recently, Cho *et.al.* reported that the cubic $BaTiO_3$ fine crystallites with nanotwins of (111) plane were assigned to the hexagonal phase using XRD and Raman.[26-29] Therefore, now we do not consider about the hexagonal $BaTiO_3$ phase.

The crystallite size D_{111} was calculated from a FWHM of (111) plane using the Scherrer's equation. As a result, D_{111} was estimated at around 17 nm. TEM observation revealed that the average $BaTiO_3$ particle size was around 16.5 nm as shown in Fig. 8. Figure 8 indicates that one particle was a single crystal, and there is no twinning structure. Moreover, its selected area electron diffraction (SAED) pattern revealed that its crystal structure was assigned to the cubic phase.

To investigate the impurity in the $BaTiO_3$ crystallites, TG-DTA and FT-IR measurements were performed. As a result, on the surface of the $BaTiO_3$ crystallites, there were two adsorbed species of OH^- and CO_3^- groups, and in the $BaTiO_3$ lattice, there was no detectable lattice OH^- group. At present, we do not confirm whether the Ba/Ti atomic ratio is 1.000 or not. Therefore, about the impurity and defect structure, more investigation is required.

4. CONCLUSIONS

In this study, the new 2-step thermal decomposition method using $BaTiO(C_2O_4)_2 \cdot 4H_2O$ was proposed to obtain inpurity-free and defect-free nm-sized $BaTiO_3$ particles. At the 1st step, $BaTiO(C_2O_4)_2 \cdot 4H_2O$ was annealed at 400 °C for 1 h in the O_2 flow. The annealing temperature of 400 °C was chosen for the following reasons; (1) no formation of $BaCO_3$ and TiO_2 and (2) the complete removal of H_2O and other carbon species. This compound obtained at 400 °C was amorphous phase, but its chemical composition was $BaCO_3$-TiO_2. At the 2nd step, the amorphous compound was annealed under vacuum. Finally, $BaTiO_3$ single crystals with a size below 20 nm were prepared around 620 °C. Their characterization was also done using various methods, and especially, the impurity in these $BaTiO_3$ crystallites was investigated. As a result, as the impurities, the surface adsorbed hydroxyl group and the surface adsorbed carbonate were detected, but no lattice hydroxyl group was detected using IR. This suggests that the $BaTiO_3$ crystallites have less impurity in their lattice.

ACKNOWLEDGEMENTS

The authors would like to thank Mr. M. Nishido of Fuji Titanium Co., Ltd. for preparing high purity barium titanyl oxalates. This study was partially supported by (1) Research Development Program of University-Industry Alliance - A Matching Funds Approach from JSPS) (2) a Grant-in-Aid for Scientific Research (**12450267**) from the Ministry of Education, Science, Sports and Culture, Japan, and (3) Takayanagi Foundation for Electronics, Science and Technology.

REFERENCES

1. K. Kinoshita and A. Yamaji: J. Appl. Phys. **45** 371 (1976).
2. G. Arlt, D. Hennings and G. De With: J. Appl. Phys. **58** 1619 (1985).
3. K. Ishikawa, K. Yoshikawa and N. Okada: Phys. Rev. B **37** 5852 (1988).
4. K. Uchino, E. Sadanaga and T. Hirose: J. Am. Ceram. Soc. **72** 1555 (1989).
5. H. Ikawa: in "Dielectric Ceramics; Ceramic Transactions, Vol. 32" (Am. Ceram. Soc., 1993) p. 19.
6. M. H. Frey and D. A. Payne: Phys. Rev. B **54** 3158 (1996).
7. S. Wada, T. Suzuki and T. Noma: J. Ceram. Soc. Jpn. **104** 383 (1996).
8. K. Ishikawa, T. Nomura, N. Okada and K. Takada: Jpn. J. Appl. Phys. **35** 5196 (1996).
9. D. McCauley, R. E. Newnham and C. A. Randall: J. Am. Ceram. Soc. **81** 979 (1998).
10. M. Tanaka and Y. Makino: Ferroelectric Lett. **24** 13 (1998).
11. M. R. Srinivasan, M. S. Multani, P. Ayyub and R. Vuayaraghavan: Ferroelectrics **51** 137 (1983).
12. A. J. Bell, A. J. Moulson and L. E. Cross: Ferroelectrics **54** 147 (1984).
13. H. Matsuda, M. Kuwabara, K. Yamada, H. Shimooka, and S. Takahashi: J. Am. Ceram. Soc. **81** 3010 (1998).
14. S. Wada, T. Suzuki and T. Noma: J. Ceram. Soc. Jpn. **103** 1220 (1995).
15. S. Wada, H. Chikamori, T. Noma and T. Suzuki: J. Mater. Sci. **35** 4857 (2000).
16. S. Wada, H. Chikamori, T. Noma, T. Suzuki and T. Tsurumi: J. Ceram. Soc. Jpn. **108** 728 (2000).
17. K. Iizumi, K. Sobata and K. Kudaka: J. Ceram. Soc. Jpn. **92** 4 (1984).
18. T. Isshiki, K. Nishio, M. Shiojiri, H. Noguchi, Y. Deguchi and H. Yamamoto: Elect. Techno. **31** 202 (1998).
19. J. Xu, S. Tsutai, S. Hayashi, M. Sugi and Z. Nakagawa: J. Ceram. Soc. Jpn. **107** 27 (1999).
20. T. Kajita and M. Nishido: Ext. Abst. the 9th US-Japan Seminar Dielect. Piezoelect. Ceram. Okinawa (1999) p.425.
21. R. M. Glaister and H. F. Kay: Proc. Phys. Soc. **76** 763 (1960).
22. M. Wakamatsu, N. Takeuchi, G.-C. Lai and S. Ishida: J. Ceram. Soc. Jpn. **95** 1181 (1987).
23. N. Takeuchi, H. Tanaka, M. Wakamatsu, Y. Sakabe and K. Wakino: J. Ceram. Soc. Jpn. **98** 836 (1990).Raman
24. N. G. Eror, T. M. Loehr and B. C. Cornilsen: Ferroelectrics **28** 321 (1980).
25. Y. Akishige, K. Kamishina, J. Nakahara and E. Sawaguchi: Ferroelectrics **152** 225 (1994).
26. W.-S. Cho, E. Hamada and K. Takayanagi: J. Appl. Phys. **81** 3000 (1997).
27. W.-S. Cho: J. Phys. Chem. Solids **59** 659 (1998).
28. E. Hamada, W.-S. Cho and K. Takayanagi: Phil. Mag. A. **77** 1301 (1998).

A Highly Distorted Perovskite Phase in a PMN-PT Powder Synthesized via the Modified Columbite Method*

Hisao Yamada
Cerone, Inc.
8100 Bainbrook Drive
Bainbridge, OH 44023-4883
Voice: 216-533-1176
Fax: 440-708-1258
Email: ceroneinc@yahoo.com

Abstract

A highly distorted perovskite phase is observed in the PMN-PT solid solution powder synthesized via the modified columbite method at temperatures as low as 650°C. The crystallographic symmetry of the powder cannot be determined uniquely by using the X-ray powder diffraction method, but it is most likely to be triclinic. The powder gradually loses its distortion with increasing calcination temperature. At temperatures higher than 950°C the powder exhibits a cubic symmetry. The powder is highly sinterable due to its fine particle size and highly distorted crystal structure.

INTRODUCTION

In order to consistently produce high-purity, high-reactivity powder of solid solutions between lead magnesium niobate and lead titanate, we investigated modifications to the columbite method. By synthesizing highly reactive columbite powder via the modified mixed oxide method, we succeeded in synthesizing phase-pure perovskite powder at temperatures as low as 650°C. However, the powder possesses a highly distorted crystal structure, most likely to be triclinic. In this paper we discuss the transformation of the distorted phase into a cubic structure during calcination at higher temperatures.

EXPERIMENTAL

Highly reactive columbite powder was synthesized via the modified mixed oxide method. Then, the synthesized columbite powder was mixed with PbO and TiO_2 to formulate a 68PMN-32PT solid solution. The resulting mixture was calcined in air at temperatures between 500°C and 900°C for five hours. The mixture was also calcined at 1,000°C for 20 hours. The calcined PMN-PT powders were examined via XRD and high-resolution SEM. For the quantitative determination of lattice parameters, columbite was chosen as an internal standard. Prior to XRD runs, the calcined powders were mixed with 10 weight percent of the columbite powder.

RESULTS and DISCUSSIONS

Fig. 1 shows XRD curves of the powder mixture calcined at various temperatures. The figure shows that a distorted perovskite phase begins forming at a temperature slightly lower than 500°C. The powder mixture is completely converted to the perovskite phase when calcined at 650°C for five hours. The distorted perovskite phase converts to a cubic perovskite phase when calcined at a temperature between 950°C and 1,000°C. In order to determine a precise crystallographic symmetry of the distorted phase, the XRD curve of the distorted perovskite phase is compared critically with that of the cubic perovskite phase. Since (i00) peaks of the cubic perovskite phase are split into three peaks in the distorted perovskite phase, the distorted perovskite phase is orthorhombic, monoclinic, or triclinic. However, it has not been possible to uniquely determine its crystallographic symmetry due to missing of higher order peaks.

The transformation of the distorted perovskite phase to the cubic perovskite phase is not reversible during cooling. Thus, the distorted perovskite phase is metastable and is present only in PMN-PT powder synthesized at low temperatures.

The transformation of the distorted perovskite phase into the cubic perovskite phase has been investigated by carefully determining

*work supported by U.S. Defense Advanced Research Project Agency (DARPA)

three lattice parameters of the distorted perovskite phase of the powder mixture calcined at 700°C, 800°C and 900°C for five hours. In order to precisely determine lattice parameters, the

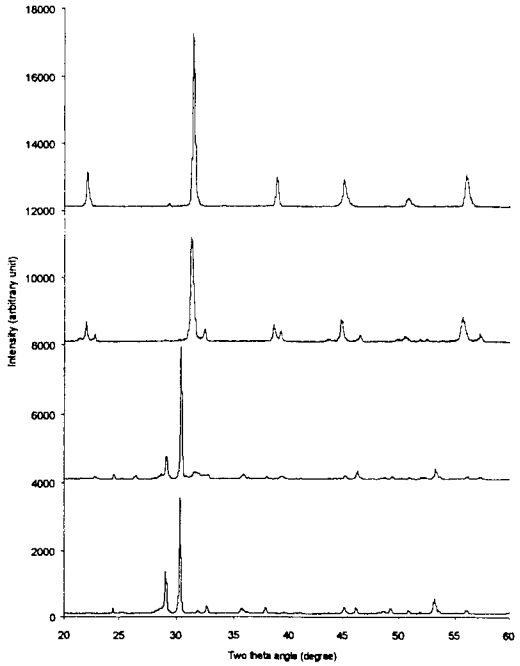

Fig. 1 XRD of 68PMN-32PT. Three curves from top are for the powder calcined at 1,000°C, 650°C, and 500°C. The bottom curve is for as-formulated powder mixture.

calcined powders were mixed with 10 weight percent of columbite powder as an internal standard. Furthermore, Sintag X-ray powder diffractometer was step-scanned at a significantly slower rate. The resulting (100) peaks were deconvoluted into three separate peaks by using a least-square curve fitting routine. The results are shown in Fig. 2 and 3.

The figures show the following. Two of the lattice constants of the distorted perovskite phase are larger than that of the cubic perovskite phase (4.024A). Both lattice constants decrease slightly with increasing calcination temperature. On the other hand, the third lattice constant of the distorted perovskite phase is shorter than that of the cubic perovskite phase and increases slightly with increasing calcination temperature.

Normalized X-ray intensities of the peaks with the longest and shortest lattice constants decrease with increasing calcination temperature. Because the intensity of the peak with the shortest lattice constant is so weak for the powder calcined at 900°C, the shortest lattice constant cannot be determined precisely at the temperature. The normalized X-ray intensity of the peak with a lattice constant close to that of the cubic perovskite phase increases with increasing calcination temperature.

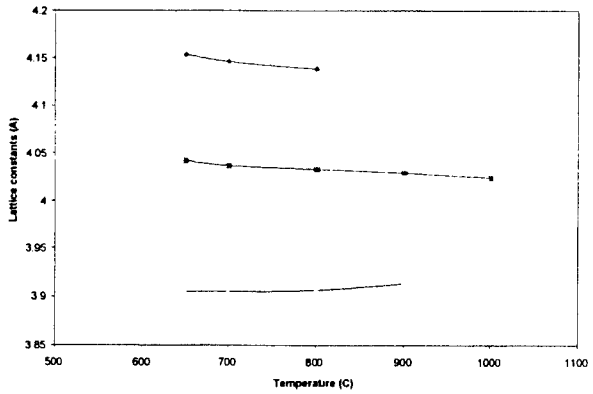

Fig. 2 Lattice constants of the distorted perovskite phase of the powder calcined at temperatures between 650°C and 1,000°C

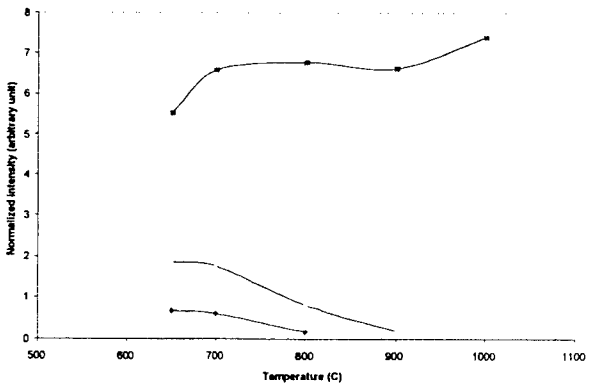

Fig. 3 Normalized intensity of three (001) Group peaks of the powder calcined at temperatures between 650°C and 1,000°C

Fig. 4 shows the SEM micrograph of the PMN-PT powder calcined at 650°C for five hours. The powder consists of weakly agglomerated submicron-sized particles. The powder is highly sinterable and can be sintered to a relative density higher than 95% by heating at a temperature as low as 950°C. The sinterability of the powder is comparable to that of nano-sized PMN-PT powder synthesized via the aqueous solution method. The sintering of the powder will be discussed in detail in a forthcoming paper.

* work supported by U.S. Defense Advanced Research Project Agency (DARPA)

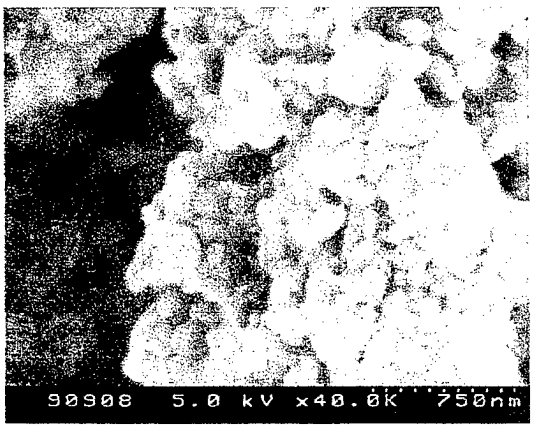

Fig. 4 SEM micrograph of the PMN-PT powder calcined at 650°C for five hours.

CONCLUSION

PMN-PT powder is synthesized via the modified columbite method at a temperature as low as 650°C. The powder possesses the crystal structure of a distorted perovskite phase which is metastable and transforms into a cubic perovskite phase when heated above 950°C. The powder is highly sinterable due to its weakly agglomerated, submicron-sized particles and highly distorted crystal structure.

ACKNOWLEDGEMENT

This work was carried out as part of Phase II SBIR program supported by U.S. Defense Advanced Research Project Agency (DARPA).

*work supported by U.S. Defense Advanced Research Project Agency (DARPA)

The Formation of PLZT from Oxides During Calcination

J. P. Dougherty*, E. Breval*, M. Klimkiewicz*, and J. D. Weigner°

Materials Research Institute, Penn State University, University Park, PA 16802, FAX: 814-865-2326, Email: joedoc@psu.edu
° Lockheed Martin, PO Box 4840:EPS-H20. Syracuse, NY 13221-4840.

INTRODUCTION

PLZT is a well-known material, capable of storing and releasing large amounts of electrical energy (1,2). Multilayer capacitors made from compositions in the antiferroelectric L/Z/T phase for L < 8, and T < 7.5 are well suited for this application. In this paper the orthorhombic antiferroelectric phase 5.5/97.5/2.5 PLZT was studied. The purpose of the paper was twofold: 1) to investigate the kinetics during calcination of PLZT from oxides as a function of calcination temperature, and soak time, and 2) to study the sinterability and features of sintered parts as a function of the oxygen pressure during calcination.

EXPERIMENTAL

Raw Materials.

See Table I and Figs 1 to 4. The amounts were weighed off for the PLZT "A-Site Vacancy" composition $(Pb,La)_{0.9175}La_{0.055}Zr_{0.975}Ti_{0.025}O_3$ with 2.5w% extra PbO. The high loss on ignition of La_2O_3 results in a weight loss for the entire powder of 0.5w%.
In addition, NH_4OH (technical grade, 25% in water) was used to control pH for optimum dispersion. Darvan 821A (Vanderbilt Company, Inc, CT) was used as the dispersant for optimum particle dispersion and viscosity control. Optimum mixing occurs at low viscosity but drying requires high viscosity to prevent sedimentation. To minimize sedimentation, Acetic acid glacial was used in small amounts during drying to adjust pH for maximum gelation to prevent sedimentation.

Calcination

5 grams of raw mix was calcined in air for different time periods (3 to 24 hours) at different soak temperatures (400 to 1050°C) in crucibles with a well fitting, but not sealed lid. The temperature ramp-up varied from 7 to 8°C/minute. The weight loss was determined.

Table I. Raw materials for synthesis of PLZT 5.5/97.5/2.5. Loss on Ignition was made at 700°C for PbO and 1000°C for La_2O_3, ZrO_2, and TiO_2.

Raw Material	Company	Grade	Loss on Ignition	Amount in raw mix	
			w%	w%	Vol %
PbO	Hammond Lead	Litharg electr. grade	0.00	61.4	53.8
ZrO_2	SEPR		0.68	34.8	41.5
La_2O_3	American Rarox	99.99 %	14.99	3.3	3.6
TiO_2	Baker	Anatase	0.27	0.6	1.1

Sintering of calcined powder.

Selected powders were crushed in a mortar, 4±1 w% binder was added and it was sieved through a 100 mesh screen. A pellet of 0.5 inch diameter was pressed at a pressure of $20N/m^2$. Binder-burn-out was carried out in air with a ramp of RT to 350°C in 150 minutes, held 350°C for 120 minutes, ramp of 350 to 550°C in 120 minutes, and held at 550°C for 60 minutes. The sintering was carried out in covered crucibles in air at 1270°C or 1300°C for 2 hours at a ramp-up of 10°C/min. A protective PbO atmosphere was established by the presence of ZrO_2 +PbO powder in a boat inside the crucible.

Characterization

Powder X-ray diffractometry was used for phase distribution determinations and calculation of PLZT lattice parameters and unit cell volume. SEM/EDS techniques were used for the morphology and elemental distribution. The capacitance, and dielectric loss of sintered pellets were measured on an HP 4284A Precision LCR Meter, as a function of the temperature up to 275°C.

Fig. 1: SEM image of PbO raw material

Fig. 3: SEM image of La_2O_3 raw material.

Fig. 2: SEM image of ZrO_2 raw material

Fig. 4: SEM image of TiO_2 raw material

RESULTS AND DISCUSSION

Calcination temperature and time as parameter

The results are seen in Table II, which show the X-ray phases of the raw mix and calcined material together with weight loss and the PLZT unit cell volume.

Though the amount of the ZrO_2 is ~ 42 V% as compared to the amount of the PbO (~54 V%) in the raw uncalcined material (Table 1) the maximum peak of the ZrO_2 is less than a quarter of that of the PbO (massicot). This is due to 1) the lower atomic scattering factors for the atoms in the ZrO_2 unit cell as compared to those in the PbO unit cell 2) the nm particle size of ZrO_2, a feature that is often connected with lower crystallinity and thereby also lower, broader X-ray peaks. This is also why it is often possible to find remnant ZrO_2 in calcined powder using the SEM technique even if it does not show up in the X-ray diffraction pattern. Fig. 5 shows an example of such calcined X-ray phase pure powder. The PLZT grains are roundish and appear most frequently, but it is common to find unreacted ZrO_2 as shown here as µm-sized aggregates consisting of nm sized ZrO_2 particles as identified by the EDS.

Fig. 5: Example of ZrO_2 aggregate consisting of nm sized particles (center) shown by SEM in a calcined PLZT powder that does not show the presence of ZrO_2 in the X-ray diffraction pattern.

Table II. Weight loss and X-ray results for raw PLZT 5.5/97.5/2.5 calcined in air 1) Temperature series, 2) soak time series: The intensity of each X-ray phase is given as the strongest peak of this phase in percentage of the strongest peak in the entire spectrum (i%). PbOL is litharge, PbOM is massicot. The unit cell of PLZT was calculated from the PLZT hkl reflections.

Calci-nation	Weight Loss	X-ray Results									
		Phases									PLZT
T/soak		ZrO_2	PbOL	PbOM	La_2O_3	$La(OH)_3$	TiO_2	PLZT	$PbO_{1.5}$	$La_2Zr_2O_7$	unit cell
°C/hr	w%	i%	i%	i%	i%	i%	i%	i%	i%	i%	Å^3
Uncal.	0	23.01	16.48	100	3.80	1.09	trace	0	0	0	-
400/3	1.06	20.65	20.11	100	3.80	0	trace	0	0	0	-
500/3	1.08	16.13	18	100	3.80	0	trace	0	0	0	-
600/3	1.34	12.77	28	100	3.26	0	trace	0	0	0	-
650/3	1.38	12.23	0	100	3.26	0	0	0	1.06	0	-
700/3	1.64	0	0	0	0	0	0	100	4.79	0	71.631
750/3	1.65	0	0	0	0	0	0	100	3.61	0	71.544
800/3	1.71	0	0	0	0	0	0	100	3.11	0	71.535
850/3	1.71	0	0	0	0	0	0	100	1.79	0	71.557
900/3	1.73	0	0	0	0	0	0	100	0.62	0	71.519
950/3	1.72	0	0	0	0	0	0	100	0	0	70.907
1000/3	1.81	0	0	0	0	0	0	100	0	0	71.126
1050/3	1.93	0	0	0	0	0	0	100	0	0	71.033
Uncal.	0	23.01	16.48	100	3.80	1.09	trace	0	0	0	-
900/3	1.73	0	0	0	0	0	0	100	0.62	0	71.519
900/6	1.76	0	0	0	0	0	0	100	0.10	0	70.899
900/12	1.77	0	0	0	0	0	0	100	0	0	71.044
900/24	1.85	0	0	0	0	0	0	100	0	0	70.977
950/3	1.73	0	0	0	0	0	0	100	0	0	70.907
950/6	1.76	0	0	0	0	0	0	100	0	0	70.971
950/12	1.86	0	0	0	0	0	0	100	0	0	71.043
950/24	1.87	0	0	0	0	0	0	100	0	0	71.371
1000/3	1.81	0	0	0	0	0	0	100	0	0	71.126
1000/6	1.87	0	0	0	0	0	0	100	0	0	70.944
1000/12	2.05	0	0	0	0	0	0	100	0	0	70.936
1000/24	2.56	1.78	0	0	0	0	0	100	0	0	71.283
1050/3	1.93	0	0	0	0	0	0	100	0	0	71.033
1050/6	2.46	2.14	0	0	0	0	0	100	0	0	71.383

Calcination atmosphere as parameter

The influence of the oxygen in the atmosphere is seen in Table III, which shows properties of both the calcined powder and the sintered parts when made from powder calcined at different oxygen partial pressure. Calcination at 1000°C for more than ~2 hours or at 1050°C for more than ~3 can lead to evaporation of PbO resulting in appearance of enough ZrO_2 to show up in the X-ray diffraction pattern. This happens even though the total weight loss is less than the sum of the 0.5w% from the weight loss of La_2O_3 and the extra 2.5w% PbO added. This indicates that some of the extra PbO may go into the PLZT lattice leaving unreacted La_2O_3. Calcination at 1050°C for more than ~6 hours results in two events: 1) the powder has a weight loss higher than expected from the La_2O_3 plus the extra PbO, and 2) the stronger thermal exposure causes the ZrO_2 to react with still free La_2O_3 to form $La_2Zr_2O_7$. The unit cell volume of the PLZT does not change much with either calcination temperature or with calcination time.

Table III. Properties of selected powders calcined in nitrogen, air or oxygen at 1000°C/3h and of air-sintered pellets made from these powders. Sinterability (loss, density, and shrinkage), PLZT unit cell volume, and RT dielectric properties. A recording of the dielectric constant as a function of the temperature from RT up to 800 °C gives the maximum dielectric constant Kmax at the Curie temperature (Tmax).

Atmosphere		calcined in nitrogen			calcined in air			calcined in oxygen		
O_2 partial pressure		0			0.2			1		
		powder	sintered		powder	sintered		powder	sintered	
Sinter temp. /time	°C/h	-	1270/2	1300/2	-	1270/2	1300/2	-	1270/2	1300/2
sinter loss	w%	-	4.46	5.16	-	4.61	5.75	-	4.93	5.16
sinter density	g/cc	-	6.79	7.10	-	7.24	7.43	-	7.39	7.45
shrinkage	%	-	15.77	17.51	-	17.35	18.52	-	17.64	18.04
V(PLZT)	$Å^3$	71.098	70.404	70.366	71.126	70.455	70.395	70.676	70.395	70.473
RT tan∂		-	0.0093	0.0043	-	0.0055	0.0045	-	0.0045	0.0040
RT dielectric const.		-	269.6	292.5	-	287.6	298.7	-	281.8	291.1
RT Capacity	pF	-	343.4	365.3	-	380.0	353.7	-	329.1	343.2
Kmax, 100kHz		-	589.2	618.6	-	704.6	685.5	-	763.7	769.5
Tmax 100kHz	°C	-	228.1	225.3	-	231.0	226.0	-	234.7	231.9

With increasing oxygen partial pressure during calcination the sinterability improved as both the sintered density and the shrinkage increased, even though the weight loss during sintering was unchanged. The volume of the unit cell value decreased with increasing oxygen pressure during calcination indicating the ability to larger energy storage (1,2). The RT dielectric properties do not show a special trend, but the increase of Kmax and Tmax, with increasing oxygen pressure during calcination is a sign of good incorporation of Ti and La into the PLZT lattice.

CONCLUSIONS

PLZT 5.5/97.5/2.5 is formed between 650 and 700°C during calcination from oxides.

The PLZT 5.5/97.5/2.5 unit-cell volume is independent of calcination temperature and time.

Between 950 and 1050°C PLZT 5.5/97.5/2.5 is phase pure in X-ray diffraction, but unreacted ZrO_2, detected by SEM/EDS, is still present.

Calcination temperatures up to 1050°C and calcination times up to 12 to 24 hours are not sufficient to incorporate the full amount of La into the PLZT (5.5/97.5/2.5) lattice.

Long calcination times and high temperatures result in the formation of X-ray detectable free ZrO_2 and at still longer times and higher calcination temperatures $La_2Zr_2O_7$ due to PbO loss.

Higher oxygen partial pressure during calcination increases the sinterability of the calcined powder.

Higher oxygen partial pressure during calcination eases incorporation of La and Ti into the PLZT lattice during sintering and thereby decreases the PLZT unit cell volume of the sintered part.

REFERENCES

1. Gene H. Haertling, "Piezoelectric and Electrooptic Ceramics", pp139-225 in "Ceramic Materials for Electronics, Processing, Properties and Applications" in the series "Electrical Engineering and Electronics" edited by, Relva C. Buchanan, Marcel Dekker, Inc, New York, Basel, 1986.

2. I. Burn, The American Ceramic Society Bulletin, vol. 50, no.5, p.501, 1971

ACKNOWLEDGEMENT

This work was supported by Medtronic Promeon Division.

SYNTHESIS OF NANOSIZED $Pb(Zr_{0.7}Ti_{0.3})O_3$ PARTICLES VIA MECHANICAL ACTIVATION

X. Liu and R.E. Riman
Department of Ceramic and Materials Engineering,
Rutgers, the State University of New Jersey,
607 Taylor Road, Piscataway, NJ 08854
FAX: 732-445-6264
Email: xyliu@rci.rutgers.edu

ABSTRACT

Mechanical activation was successfully used to synthesize phase pure $Pb(Zr_{0.7}Ti_{0.3})O_3$ (PZT) particles of 50-150 nm in size. Lead zirconium-titanium (Pb, Zr-Ti) hydrous oxide precursor, which can be obtained from chemical co-precipitation, was mechanically activated by using a Spex 8000 Mixer/Mill. To control the degree of particle agglomeration and obtain well-dispersed PZT particles of nanocrystallinity, mechanical activation was carried out in NaCl matrix. The synthesized PZT particles were characterized by using X-ray Diffractometer (XRD), Field Emission Scanning Microscope (FESEM) and Dynamic Light Scattering particle size analyzer (DLS). The best reaction conditions were corresponded to mechanical activating Pb, Zr-Ti hydrous oxide precursor in NaCl matrix with a NaCl/precursor weight ratio of 4/1 for 8 h and gave phase pure PZT with a mass weighted particle size distribution of 105±54 nm. In contrast, a conventional calcination of the Pb, Zr-Ti hydrous oxide precursor at 750 °C for 2 h yielded PZT powder with a mass weighted particle size distribution of 1257±573 nm, which was much bigger than what was achieved via mechanical activation.

INTRODUCTION

It is well-known that properties of sintered electrical ceramics are strongly influenced by the grain size and bulk density[1], which are dependent on the initial powder characteristics and processing route. Because of the unique application in grain growth from seeds, fine-grained ceramics are of special interest for scientists[2]. An ideal PZT powder for the fabrication of a fine-grained dense PZT ceramic materials should have a small particle size with a narrow particle size distribution, spherical morphology, an absence of hard aggregates, high chemical and phase homogeneity as well as purity.

Many processing techniques, such as sol-gel[3], microemulsion[4] and ultrasonic spray pyrolysis[5], have been successfully used for PZT nanopowder synthesis. As a relatively new processing route for material synthesis, mechanical activation is able to deliver ceramic powders of nanosized particles and nanocrystallinity[6]. The objective of this work is to develop a mechanical activation processing route for nanosized PZT particle synthesis. This is accomplished through mechanical activation of a co-precipitated Pb, Zr-Ti hydrous oxide precursor in NaCl matrix.

EXPERIMENTAL PROCEDURE

The starting materials used included Zr-tetra-n-propoxide, Ti-tetra-iso-propoxide, Pb-acetate, ammonium hydroxide solution (28-30%), sodium chloride and deionized water. The various steps involved in processing route are shown in Fig. 1. Pb, Zr-Ti hydrous oxide precursor was prepared by co-precipitation[7]. The freeze-dried precursor was divided into three different portions and then treated in the following different manners:

(i) Conventional calcination at 750 °C for 2 h.
(ii) Mechanical activation in NaCl with NaCl/precursor weight ratio ($m_{NaCl/precursor}$)=4/1 for 2, 4, 6, and 8 h by using a Spex 8000 Mixer/Mill.
(iii) Mechanical activation for 8 h in NaCl with $m_{NaCl/precursor}$ of 1/1, 2/1 and 4/1 by using a Spex 8000 Mixer/Mill.

Phases present in the Pb, Zr-Ti hydrous oxide precursor, the powder conventional calcined at 750 °C for 2 h and the powder subjected to mechanical activation for 8 h with

$m_{NaCl/precursor}$=4/1 were analyzed by using a XRD. FESEM was employed to examine particle characteristics of the powder mechanical activated for 8 h with $m_{NaCl/precursor}$ of 1/1, 2/1 and 4/1. The particle size and size distribution of prepared PZT powders were measured by using DLS.

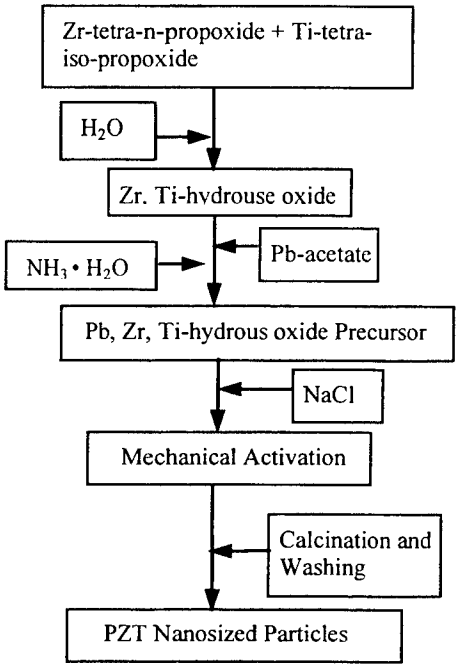

Fig. 1. A flow chart showing the mechanical activation route for nanosized PZT particles.

RESULTS AND DISCUSSION

Fig. 2(a, b, c) show the X-ray diffraction pattern of the as-dried Pb, Zr-Ti hydrous oxide precursor, the precursor calcined at 750 °C for 2 h without mechanical activation and the precursor mechanically activated for 8 h in sodium chloride matrix and then calcined at 750 °C for 2 h. The as-dried precursor exhibits a broadened peak over the range of 24-34°, indicating that the hydrous oxide precursor is considerably low in crystallinity. It may therefore be considered amorphous in nature. Peak locations and relative intensity shown in Fig. 2 (b) indicate that phase pure PZT can be obtained by conventional calcination of the precursor at 750 °C for 2 h. When the precursor is mechanically activated in NaCl for 8 h and then calcined at 750 °C for 2 hours, slightly broadened peaks that have the same location with those shown in Fig.2(b) can be observed (Fig 2 (c)). This indicates the occurrence of crystalline PZT with reduced crystallite size in the mechanically activated powder.

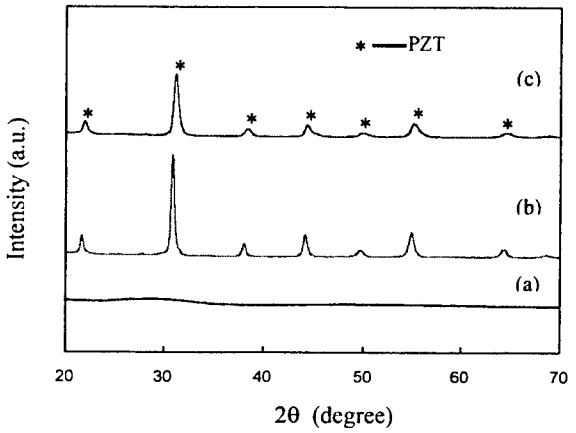

Fig. 2. XRD patterns of (a) the as-dried hydrous oxide precursor, (b) the powder calcined at 750 °C for 2 h and (c) the powder mechanically activated in NaCl ($m_{NaCl/precursor}$=4/1) for 8 h and then calcined at 750 °C for 2 h.

Fig. 3(a, b, c) show the FESEM micrographs for the powder synthesized by mechanical activation route with $m_{NaCl/precursor}$ of 1:1, 2:1 and 4:1, respectively. The DLS particle size measurement results for the powders synthesized with different $m_{NaCl/precursor}$ are shown in Fig. 4. The average particle size of synthesized PZT powder decreases with increasing the $m_{NaCl/precursor}$. When mechanically activated for 8 h in NaCl with $m_{NaCl/precursor}$=4/1, the synthesized powder consists of PZT particles of 105 nm in size, which are rather well dispersed and spherical in morphology.

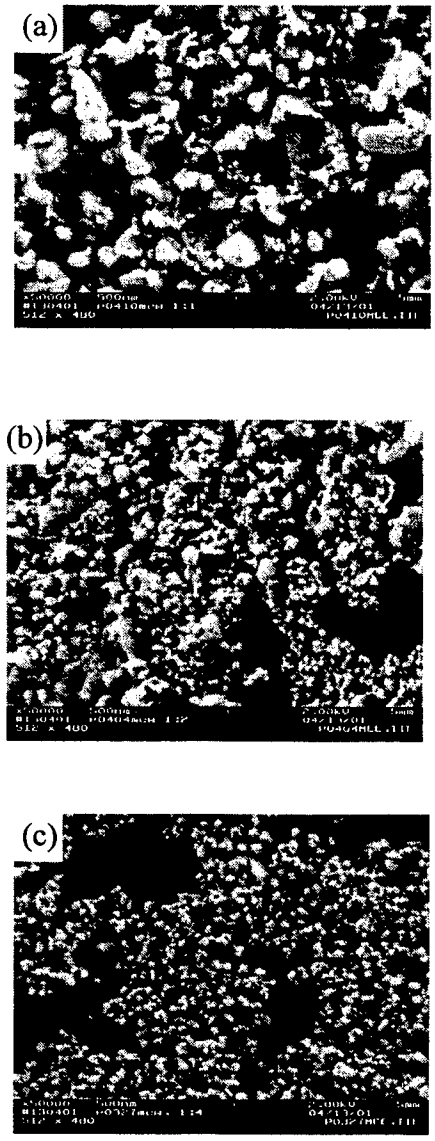

Fig. 3(a, b, c). FESEM micrographs of powder mechanically activated in NaCl for 8 h with $m_{NaCl/precursor}$ of (a) 1/1, (b) 2/1 and (c) 4/1

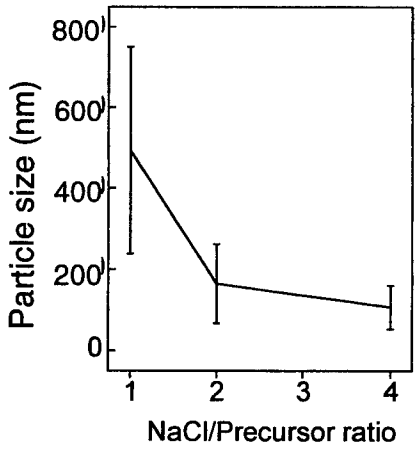

Fig. 4. The effect of $m_{NaCl/precursor}$ on particle size of PZT powders mechanically activated for 8 h.

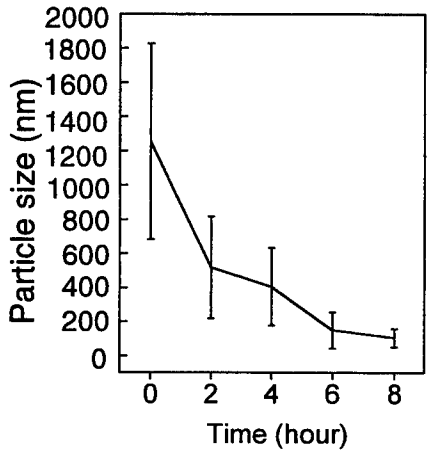

Fig. 5. The effect of mechanical activation duration on the particle size of synthesized PZT nanopowder ($m_{NaCl/precursor}$=4/1).

Mechanical activation duration is another important processing parameter that can affect the physical characteristics of synthesized PZT powders. DLS results (Fig. 5) show that when the activation duration extends from 2 to 8 h, the particle size decreased steadily from 518 to 105 nm. During this processing route, Particle sizes of NaCl matrix and Pb, Zr-Ti hydrous oxide precursor are reduced under mechanical activation condition and at the same time, the precursor particles are dispersed in NaCl matrix.

A longer activation duration results in a better dispersed system, and so a smaller particle size for PZT powder.

To further demonstrate the effectiveness in reducing the particle size of co-precipitation derived Pb, Zr-Ti hydrous oxide precursor by carrying out mechanical activation in NaCl matrix, fig. 6 (a, b) show the DLS particle size and size distribution measurement results for the powder calcined at 750 °C for 2 hour and the powder mechanically activated for 8 h in NaCl matrix ($m_{NaCl/precursor}$=4/1) followed by further calcination at 750 °C for 2 h, respectively. The PZT nanoparticles synthesized by mechanical activation are well dispersed and exhibit an average particle size of 105 nm, which is contrasted to the very high degree of particle coarsening and agglomeration (an average particle size of 1257 nm) observed in the precursor synthesized via conventional calcination at 750 °C for 2 hours. It is obvious that sodium chloride acted as an effective dispersing matrix, which avoided the formation of particle aggregates and the occurrence of significant particle coarsening during mechanical activation and subsequent calcination at 750 °C.

CONCLUSIONS

Phase pure PZT nanopowder with narrow particle size distribution and good dispersibility, which cannot be achieved by conventional calcination method, have been successfully synthesized via the developed mechanical activation processing route. Physical characters of the synthesized PZT powders can be controlled with the weight ratio of NaCl/Pb, Zr-Ti hydrous oxide precursor or the mechanical activation duration.

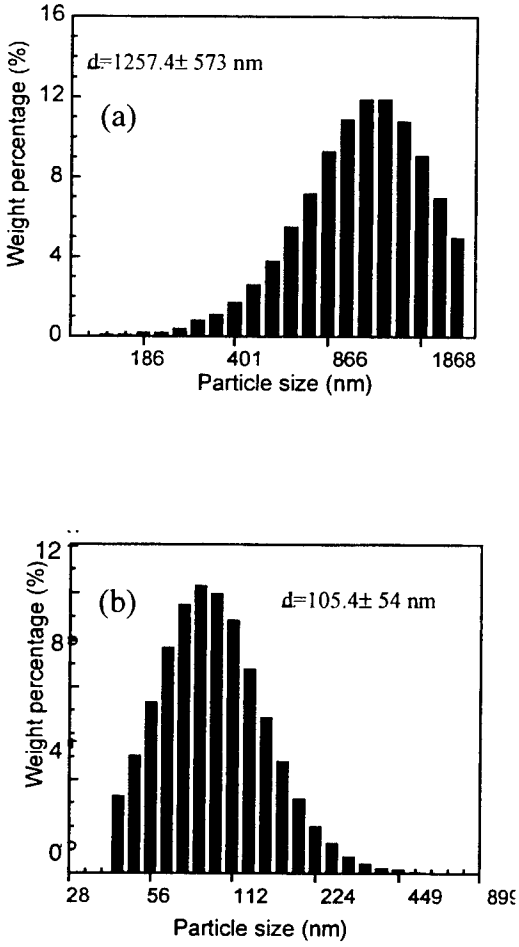

Fig. 6(a, b). DLS particle size and size distribution measurement result for: (a) the powder calcined at 750 °C for 2 hour and (b) the powder mechanically activated in NaCl matrix ($m_{NaCl/precursor}$=4/1) followed by calcinations at 750 °C for 2 hour.

REFERENCES

[1] G. Binning, H. Rohrer, C. Gerger and E. Weibel, Phys. Rev. Lett., 49, 57 (1982).

[2] T. Yamamoto and T. Sakuma, J. Am. Ceram. Soc., 77 [4], 1107 (1994).

[3] H. Hirashima and J. Boy, J. Non-Cryst. Solids, 121, 404 (1990).

[4] L.S. Ee, J. Wang, S.C. Ng and L.M. Gan, Mater. Res. Bull., 33(7), 1045 (1998).

[5] H. Kim, J. Lee and S.J. Park, J. Mater. Sci., 6, 84 (1995).

[6] X. Liu, J. Ding and J. Wang, J. Mater. Res., 14(8), 3355 (1999).

[7] X. Liu and R.E. Riman, to be submitted.

Layered Manufacturing for Prototyping of Net Shape Grain Oriented Piezoelectric Materials

M. Allahverdi, K. Nonaka, and A. Safari
Department of Ceramic and Materials Engineering, Rutgers University
607 Taylor Road, Piscataway, NJ 08854 USA
Fax: 732-445-5577; Email: safari@rci.rutgers.edu

ABSTRACT

The feasibility of Fused Deposition of Ceramics (FDC) to fabricate grain oriented ceramic components was investigated in piezoelectric systems of bismuth titanate ($Bi_4Ti_3O_{12}$; BiT) and lead metaniobate ($PbNb_2O_6$; PN). Platelet seeds of BiT and needle-shaped seeds of PN were prepared by molten salt synthesis at 1100 and 1150°C, respectively. Several FDC feedstocks with 5 wt% seeds were prepared. SEM analyses showed that the seeds survived harsh compounding during filament preparation without major damage. The needle-like seeds were aligned in the extrusion direction whereas the platelet seeds were almost randomly oriented within the bulk of filament. In the prototyped and sintered FDC components, highly oriented microstructures were observed in the PN system, as opposed to partial orientation in the sintered BiT samples.

FUSED DEPOSITION OF CERAMICS

Fused Deposition of Ceramics (FDC), a unique Layered Manufacturing technique developed at Rutgers University [1], is based on FDM™ technology where ceramic loaded polymer filaments are used for the fabrication of green ceramic components. The FDC process allows rapid manufacturing of new designs and facilitates frequent alteration of design / dimensions.

Over the past few years, significant technical success has been achieved with a number of ceramics including lead-zirconate-titanate (PZT), and lead magnesium niobate (PMN) among others [2,3]. Piezoelectric ceramics and ceramic / polymer composites with novel designs have been fabricated for various sensor / actuator applications. [3,4]

. Piezoelectric actuators including tube, bellows, spiral, dome, and telescoping were made with different dimensions and their electromechanical properties were measured. Among the actuators, spirals showed giant displacement (up to 7 mm at a resonance frequency of 40 Hz) with moderate blocking force (1 N).[5] Multi-material components such as piezoelectric/electrostrictive benders have also been made to obtain improved field-induced displacements.

The prototyped electromechanical components were all polycrystalline with random granular microstructures. Recently, we started fabrication of piezoelectric components with grain orientation. In this article, we discuss the processing technology for fabricating such materials in bismuth titanate (BiT) and lead metaniobate (PN) systems.

GRAIN ORINETED CERAMICS BY FDC

A novel technique referred to as templated grain growth (TGG) has been implemented to create oriented grain structures in a variety of ceramics.[6,7] Grain oriented microstructures are beneficial since improved electrical and/or mechanical properties can be obtained as a result of crystal anisotropy.

Our objective was to combine the method of templated grain growth with the FDC process to fabricate net shape electromechanical components with superior properties. In order to achieve primary orientation in the TGG process, small percentage of anisometric (i.e., needle or platelet) seed particles must be initially incorporated and oriented within the fine powder matrix. Thus, a fabrication method with shear mechanism is required. Tape casting has been normally employed, where the slurry including 5-15 vol.% seeds is sheared to align the seeds in the casting direction.

In the FDC process, the material to deposit is sheared both during filament fabrication and deposition of material through fine nozzles. We have explored the possibility of grain oriented structures in BiT and PN systems using the manufacturing process of FDC.

NET SHAPE BISMUTH TITANATE (BIT) CERAMICS

In the bismuth titanate system, fine BiT powder (~0.5 μm) and platelet seeds (10-30 μm in diameter and <0.5μm thick) were fabricated

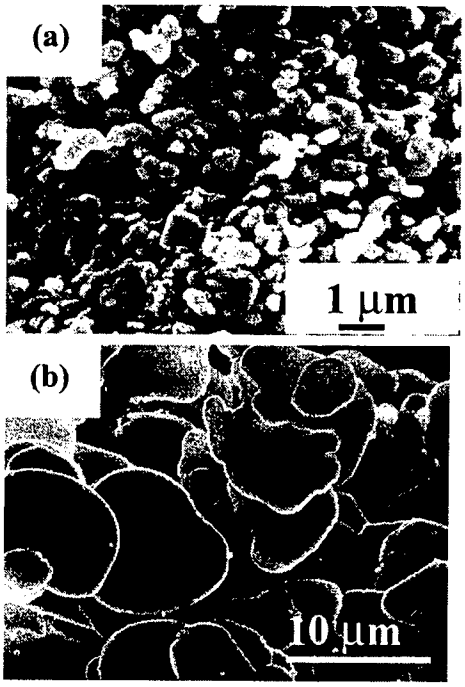

Fig. 1. SEM micrographs of BiT (a) matrix powder and (b) platelet seeds.

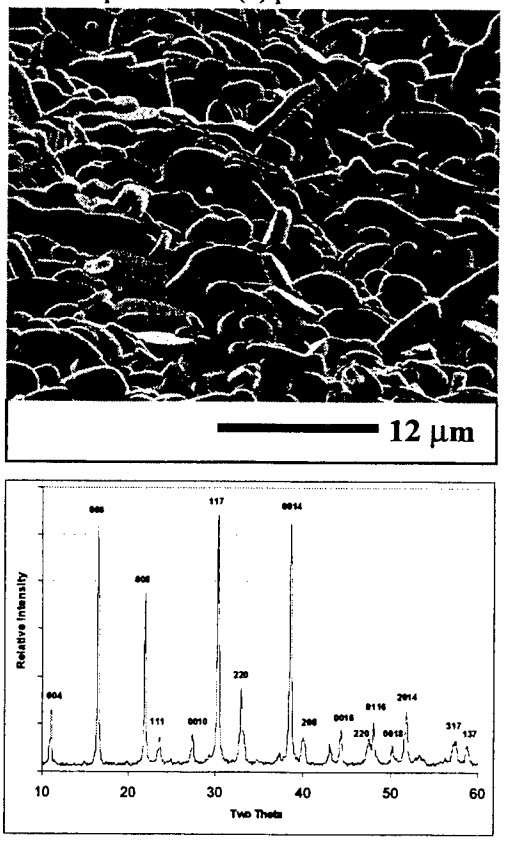

Fig 2- A typical microstructure of the sintered surface of bismuth titanate and the corresponding X-ray, illustrating partial orientation.

using molten salt synthesis and dissolution-precipitation methods, respectively (Figure 1).[8] FDC feedstocks were prepared by mixing fine powder, 5 wt% seeds and a suitable FDC binder (ECG9), and then extruded into 1.78 mm filaments. SEM observation showed that on the surface of the BiT filaments, seeds were all aligned in the extrusion direction, whereas in the bulk of the filament, the platelet seeds were almost randomly oriented. However, due to extra-shearing of the material during fused deposition, seeds were partially aligned in the deposition direction/plane.

Green FDC samples were heated to remove the organic and then sintered at 1100°C/1hr to induce grain growth and orientation. The X-ray diffraction and microstructure of the sintered samples illustrated partial orientation (Figure 2). The calculated Lotgering factor [9] was 0.46 for the sintered BiT samples. These results manifested the potential of FDC technique for development of textured microstructures.

It is evident that the orientation of the seeds during extrusion depends strongly upon the morphology / size of the seeds. For example, it is expected that a proper grain alignment can be obtained if needle-shaped particles with high aspect ratios are used.

NET SHAPE LEAD METANIOABTE (PN) CERAMICS

Lead metaniobate ceramics are desirable due to their electro-acoustic applications (hydrophones) where a higher d_{33}/d_{31} ratio and hence a higher k_t/k_p ratio is beneficial.[10] In a polycrystalline samples, high d_{33}/d_{31} ratio can be obtained when the microstructure shows strong grain orientation (as opposed to a random granular structure). Hence, if PN samples can be fabricated with grain-orientated microstructures, improved electro-acoustic properties are expected.

As the second system, net shape grain orientation was examined in lead metaniobate (PN) ceramics. It is known that needle-shaped PN particles can be synthesized via molten salt technique.[11] Hot pressing[12] and tape casting[13] of powder and slurry containing needle like PN seeds showed improved piezoelectric properties in the grain oriented pellets and tapes.

PN Seed and Powder Preparation

Seeds: Needle-shaped particles of PN were synthesized as templates by molten salt method at 1150 °C for 1h (Figure 3-b). The major aspect ratio of the seeds is estimated to be about 10.

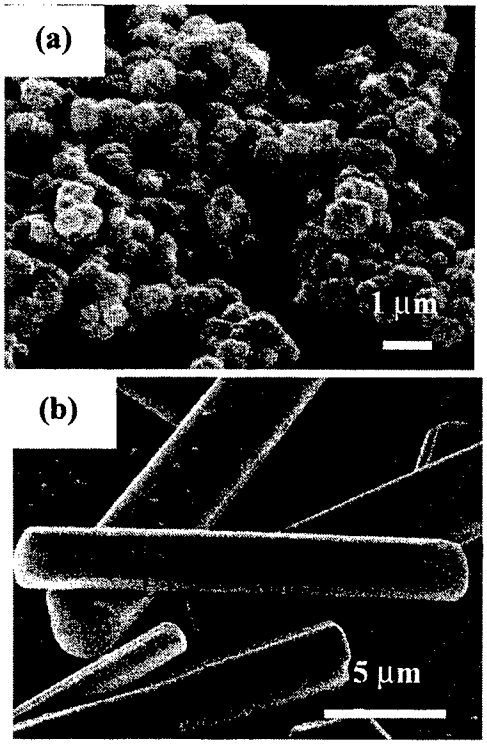

Fig. 3. SEM micrographs of PN (a) matrix powder and (b) needle-shaped seeds.

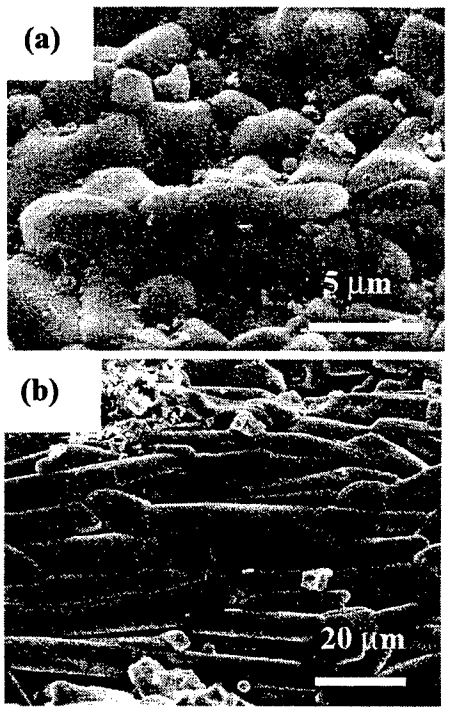

Fig. 4. SEM micrographs of the surface of FDC components upon sintering at (a), 1200 °C, and (b) 1250 °C for 1h.

Matrix Powder: Fine, equiaxed particles of PN were prepared by conventional solid-state reaction process between PbO and Nb_2O_5 at 800°C for 1 h. (Figure 3-a). The matrix powder had an average particle size of 0.3 μm in diameter. The XRD measurements showed that the matrix powder was rhombohedral (non-ferroelectric phase) whereas the crystal structure of the seeds was orthorhombic (ferroelectric phase).

To make PN filament, fine powder, 5 wt% needle-like seeds, and ECG9 binder were initially mixed in a compounding bowl and then extruded into filaments of 1.78 mm-diameter using a Rheometer. Simple geometry components were prototyped using the seeded filaments. SEM observation of the filaments and green FDC parts revealed that the seed particles were mainly oriented parallel to the deposition direction both on the surface and within the bulk of the samples. This indicates that primary seed alignment can be obtained when need-like seeds are used.

Microstructure Development

PN samples were sintered at 1100-1300°C for 1 hour. Observation of the samples showed that the seeds initially started to sinter to the surrounding fine matrix grains at low temperature (1100°C). Densification reaction proceeds rapidly in a narrow temperature range between 1100 °C and 1200 °C where the theoretical density increased from ~60% to ~90%. The microstructure developed at 1200 °C consisted of matrix grains of mostly equi-axed shape (Figure 4-a). When the sintering temperature increased to 1250 °C, a remarkable change in the microstructure was observed. All of the grains had grown into elongated grains with large aspect ratios, and mainly oriented parallel to the deposition direction (Fig 4-b).

XRD Phase Analysis

XRD data suggest that to retain the ferroelectric phase upon cooling to room temperature, the samples must be sintered at temperatures higher than 1250 °C.[10] A single ferroelectric phase with orthorhombic structure was obtained by sintering at 1300 °C. Only the diffractions peaks of (hk0) planes appeared in the as-sintered sample, suggesting that the needle-like grains are largely orientated in a plane parallel to the deposition layer.

Sintered PN samples were poled under an electrical field of 20-40 kV/cm at 140°C. The measured d_{33} coefficients for such samples were

moderate (~38 pC/N) due to poor poling caused by the microcracks formed upon sintering at 1300°C.

SUMMARY

The feasibility of developing grain-oriented microstructure was investigated in BiT and PN ceramic components using FDC and templated grain growth techniques.

We summarize our results as follows:

1. Needle-like PN seeds can be successfully aligned in the filament and net shape FDC components. However, platelet BiT seeds can be only slightly aligned during fused deposition process.
2. The proper orientation of the PN seeds in the green FDC samples led to strong grain orientation upon sintering/TGG. On the other hand, the poor orientation of the platelets only produced partial orientation in the sintered BiT samples.
3. During sintering at temperatures higher than 1250 °C, the PN matrix particles grew rapidly into elongated grains with high aspect ratios.
4. Ferroelectric (orthorhombic) phase of PN was obtained by sintering at 1300°C for 1h.
5. XRD patterns collected from the surface of the PN samples sintered at 1300 °C correlates well with SEM observations, indicating orientation of the crystal c-axis in a plane parallel to the FDC deposition layer.

ACKNOWLEDGEMENT

The authors wish to acknowledge ONR for funding of the project under contract numbers of N00014-00-1-0626 and N00014-96-1-0959.

REFERENCES

1. S.C. Danforth, M.K. Agarwala, A. Bandyopadhyay, N. Langrana, V.R. Jamalabad, A. Safari and R. van Weeren, "Solid Freeform Fabrication Methods", U.S. Pat. No. 5 738 817, Apr. 1998.

2. A. Bandyopadhyay, R. K. Panda, V.F. Janas, M.K. Agarwala, R. van Weeren, S.C. Danforth and A. Safari, "Processing of Piezocomposites by Fused Deposition Technique"; pp.999-1002 in *Proceedings of the Tenth IEEE International Symposium on Applications of Ferroelectrics (ISAF) '96*, Part vol.2, Edited by B.M. Kulwicki, A. Amin and A. Safari. IEEE, East Brunswick, 1996.

3. A. Safari, S.C. Danforth, "Development of Novel Piezoelectric Ceramics and Composites for Sensors and Actuators By Solid Freeform Fabrication", *Proceedings of the 11th IEEE International Sym. on Application of Ferroelectrics*, pp. 229-234, 1998.

4. A. Safari, "Development of Piezoelectric Composites for Transducers", *J. Phys. III*, France 4, p. 1129, 1994.

5. F. Mohammadi, A.L. Kholkine, B. Jadidian, and A. Safari, "High-Displacement Spiral Piezoelectric Actuators", *Applied Physics Letters*, vol. 75, No. 16, pp. 2488-90, 1999.

6. Seabaugh, M. M., Kerscht, I. H., and Messing, G. L., "Texture Development Templated Grain Growth in Liquid-Phase-Sintered α-Alumina," *J. Am. Ceram. Soc.*, 1997, **80** (5) 1181–88.

7. Horn, J. A., Zhang, S. C., Selvaraj, U., Messing, G. L., Trolier-McKinstry, S., and Yokoyama, M. "Fabrication of Textured $Bi_4Ti_3O_{12}$ by Templated Grain Growth"; *J. Am. Ceram. Soc.*, 1999, **82** (4) 921–26.

8. M. Allahverdi, B. Jadidian, Y. Ito and A. Safari, "Fabrication of Bismuth Titanate Components with Oriented Microstructures via FDC and TGG", in *Proceedings of the 12thIEEE International Symposium on Applications of Ferroelectrics (ISAF) 2000- 00CH37076,* Edited by S.K. Streiffer, B.J. Gibbons, and A. Tsurumi, Vol.I, pp385-388.

9. Lotgering, F.K., "Topotactical Reactions with Ferrimagnetic Oxides Having Hexagonal Crystal Structures-I", *J. Appl. Phys.*, **39** [5] 2268-2274 (1968).

10. P. Eyraud, L. Eyraud, P. Gonnard, D. Noterman and M. Troccaz, "Electromechanical Properties of $PbNb_2O_6$ and $PbTiO_3$ Modified Ceramics Elaborated by a Coprecipitation Process"; pp.410-13 in *Proceedings of the Sixth IEEE International Symposium on Applications of Ferroelectrics*, IEEE, New York, 1986.

11. T. Kimura, T. Yamaguchi and R.E. Newnham, "Phase and Morphology of $PbNb_2O_6$ Obtained by Molten Salt Synthesis", *Particulate Science and Technology*, **1** 357-64 (1983).

12. K. Nagata and K. Okazaki, "One-Directional Grain-Oriented Lead Metaniobate Ceramics", *Japanese Journal of Applied Physics*, **24** [7] 812-14 (1985).

13. M. Granahan, M. Holmes, W.A. Schulze and R.E. Newnham, "Grain-Oriented $PbNb_2O_6$ Ceramics", *Journal of the American Ceramic Society*, **64** C-68-9 (1981).

Robocast 3-3 PZT-5H – Polymer Composites

B. A. Tuttle, J. E. Smay, J.Cesarano, III, M. F. Bourbina, E. L. Venturini, D. H. Zeuch, W.R. Olson, J.S. Wheeler and J.A. Voigt
Sandia National Laboratories, Albuquerque, NM 87185
Fax: 505 844-9781, email: batuttl@sandia.gov
J. A. Lewis,
University of Illinois, Urbana, IL 61801

ABSTRACT

Robocasting, a computer controlled slurry deposition technique that utilizes highly concentrated colloidal slurries with low organic content (< 1 wt%), was used to construct periodic 3-dimensional lattice structures for use in forming 3-3 PZT-polymer composites. Materials for this study were PZT-5H and Spurrs Epoxy. The robocast lattices consisted of layers of aligned 160 μm diameter PZT rods stacked with 90° rotation between layers. The rods flowed together slightly at their intersections creating high integrity interfaces. The volume fraction of PZT in 3-3 composites was systematically varied by controlling the spacing of the PZT rods in each layer. Measured dielectric and elastic properties were in very good agreement with calculations using the unit cell model. Robocasting promises to be an attractive technique for rapid manufacturing of complex, multiphase assemblage devices, such as, piezoelectric ceramic- polymer composites, photonic band gap lattices, and high frequency ultrasound elements.

1. INTRODUCTION

Direct fabrication techniques, such as, fused deposition [1], three-dimensional printing [2] and robocasting [3] have recently attracted much interest for agile manufacturing. Robocasting, which is the green body formation technique used in this study, has been developed by Cesarano and Calvert [4] and is based on the computer controlled deposition of highly concentrated colloidal slurries. For robocasting, the desired structure is developed using a computer aided design package. The slurry is then deposited through precision nozzles onto an X-Y stage manipulated by computer controlled servo motors. Typical slurry bead diameters range from 200 to 800 μm and diameters as small as 80 μm have been achieved. Slurry rheology is controlled to shear thinning behavior to aid in flow through fine diameter nozzles and to substantial yield stress at rest to maintain dimensional stability. Thus, complex 3-dimensional ceramic structures with spanning features can be fabricated without support materials by simply controlling colloidal forces. High quality robocast PZT monolithic ceramics can also be fabricated using slightly lower yield stress slurries which permit some flow after deposition to fill space between beads. High quality microstructures result from robocasting, as recently demonstrated by robocast PZT 95/5 monoliths and composites, for which high field electrical and hydrostatic pressure induced transformation properties were proven equivalent to ceramics formed by 200 MPa cold isostatically pressing (CIP). [5]

PZT-polymer composites were developed by Newnham and coworkers [6] and shown to have far greater hydrostatic sensitivities than bulk ceramics. An excellent review of PZT-polymer composite work was comprised by Tressler [7] in 1997. Previous work on PZT-polymer composites for hydrophone sensors has focussed on 1-3 composites because of the difficulty of fabricating 3-3 composites using traditional bulk materials. We demonstrate that for low thickness (1 mm) transducers that specimens fabricated by robocasting have 10 times the hydrostatic figure of merit ($d_h g_h$) as bulk piezoelectrics.

2. EXPERIMENTAL PROCEDURE

PZT-5H powders (Morgan Matroc, Bedford, OH) were chosen for fabrication of PZT-polymer composites because of their larger hydrostatic response compared to PZT-5A materials. First, PZT-5H skeletons were robocast using an extrusion rate of 8 mm/sec and a 200 μm diameter nozzle. The z spacing was set at 85% (170 μm) of the bead diameter

to promote good knitting between the layers. Lattices consisting of 10 layers and systematically varied lattice spacing in the x and y directions were fabricated. The lattice spacing varied from 300 to 1200 μm to achieve a wide range of PZT volume fraction (ϕ_{PZT}) in the final 3-3 composites. Densification of the green bodies was achieved by bisque firing at 700°C for 1 hour and then sintering at 1275°C for 2h. The PZT skeletons were then vacuum infiltrated with Spurrs epoxy (Polysciences, Inc. Warrington, PA) and cured at 70°C for 12 hours to form the final composites. In addition to PZT lattices, monoliths containing no epoxy were formed by both robocasting and 200 MPa CIP. Densities were measured for both lattices and the monoliths using the Archimedes technique.

All samples were poled at 20 kV/cm for 30 minutes at 25°C. Dielectric hysteresis measurements were made at 2 Hz using a ferroelectric tester (Model RT6000-HVS, Radiant Technologies). Impedance measurements using an HP4284A precision LCR meter and a HP4294A impedance analyzer were used to characterize monolith and composite properties. Elastic, dielectric and piezoelectric properties were determined from high frequency resonance data consistent with standard practice.[8] Hydrostatic measurements were made using a low oscillating pressure technique to minimize domain wall contributions and thus obtain static rather than dynamic hydrostatic response. Specifically, specimens were taken to 0.76 MPa (110 psi) using a pressure transfer fluid (Isopar H) and then cycled from 0.76 MPa to 0.62 MPa (90 psi) at a rate of 0.2 Hz.

3. RESULTS AND DISCUSSION

The dielectric hysteresis loop of a robocast PZT-5H sample, shown in Fig. 1, was essentially identical to that for a 30 ksi CIP PZT-5H sample. Remanent polarizations of 31.8 μC/cm^2 and 31.5 μC/cm^2 were obtained for the robocast and CIP sample, respectively. The robocast sample was formed using a spiral deposition pattern with 200 μm diameter beads. Densities of 7.48 g/cm^3 and 7.52 g/cm^3 were measured for the robocast and iso-pressed samples, respectively. The robocast sample exhibited good high temperature dielectric integrity as it could be poled at 70°C for 30 minutes. Low loss behavior was also observed during 30 kV/cm hysteretic field cycling.

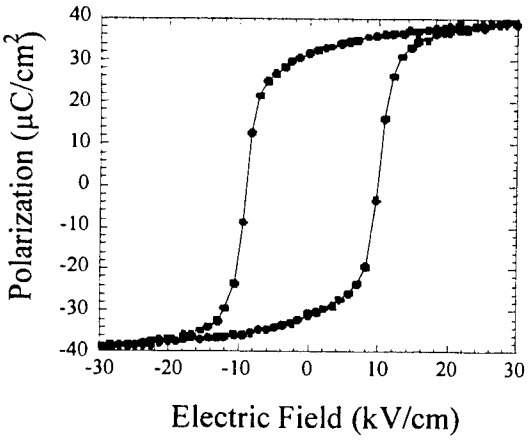

Fig.1. Dielectric hysteresis characteristics of spiral pattern robocast PZT-5H Ceramic.

Dielectric and electromechanical property data is shown in Table 1 for three PZT-5H samples: (1) Morgan Matroc (MM), (2) SNL CIP (CIP) and (3) SNL robocast (Robocast). The Morgan Matroc data is taken from a MM product catalog. There is reasonable agreement among all three samples with all properties listed being within 7% of one another. The transverse piezoelectric constant and planar electromechanical coupling coefficients were derived from high frequency resonance data and the d_{33} values were obtained by direct measurement using a 100 Hz, 0.2 N force. Calculated hydrostatic piezoelectric coefficients (d_h) were 45, 63 and 66 pC/N for the MM, CIP and robocast samples, respectively.

Table 1. Properties of PZT-5H Monoliths

Property	MM	CIP	Robocast
K_{33}	3400	3280	3250
d_{33}	593	573	604
k_p	-.65	-.645	-.670
k_{31}	-.388	-.382	-.391
d_{31}	-274	-255	-269

Robocast PZT – polymer composites were fabricated using a range of lattice spacing to optimize hydrostatic response. The lattice spacing is defined as the center-to-center distance between adjacent rods. The sintered PZT-5H material in the skeletons had measured densities of 98.5% similar to the density of the robocast monolith described

earlier. The PZT rod diameter was 160 μm such that a pitch of 230 μm results in a fired volume fraction of PZT of 70%; whereas, the 230 μm pitch sample results in PZT volume fractions of 17%. An example of an intermediate composite with 535 μm pitch (volume fraction of PZT of 30%), is shown in Figure 2. Two cuts were made to obtain this cross section: one perpendicular to the rods in the top layer and the second at 45°. The 45° cut reveals the PZT columns formed by the intersection of the lattice rods.

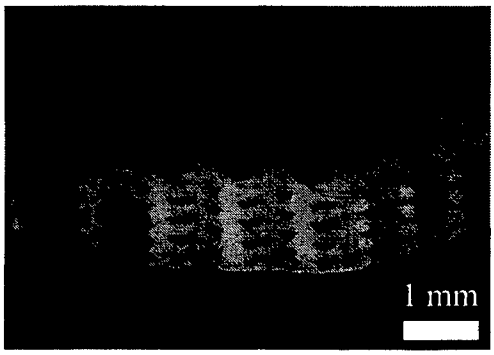

Figure 2. Cross section of a PZT polymer composite with $\phi_{PZT} = 30\%$

The unit cell approach developed by Rittenmeyer [9] and Banno [10] has been used to analyze dielectric and piezoelectric response of the composites. A unit cell containing the intersection of two lattice rods is dissected into 4 types of elements for which the dielectric and piezoelectric properties can be approximated using series and parallel mixing rules. The responses of all 4 elements are then combined to provide the total response of the composite. For the 3-3 composites of PZT-5H and epoxy the elastic compliance, s_{33}, is given by the following equation:

$$s_{33,comp} = (s_{33,poly} + s_{11,PZT})\, s_{33,poly}s_{33,PZT})) / (\phi^2_{poly}s_{33,PZT}(s_{33,poly} + s_{11,PZT}) + \phi^2_{PZT}s_{33,poly}(s_{33,poly} + s_{11,PZT}) + 4\,(\phi_{PZT}\phi_{poly})\, s_{33,poly}\, s_{33,PZT}) \quad (1)$$

where the comp, poly and PZT subscripts correspond to the composite, polymer, and PZT properties, respectively. ϕ_{PZT} and ϕ_{poly} are the volume fractions of the PZT and the polymer in the composite, respectively. The composite dielectric constant, $K_{3,comp}$ is given by:

$$K_{3,comp} = \phi^2_{poly}K_{3,poly} + \phi^2_{PZT}K_{3,PZT} + 4\,(\phi_{PZT}\phi_{poly})\,((K_{1,PZT}K_{3,poly}) / (K_{1,PZT} + K_{3,poly})) \quad (2)$$

The longitudinal piezoelectric coefficient of the composite ($d_{33,comp}$) site is given by:

$$d_{33,comp} = d_{33,PZT}\,\phi^2_{PZT}\,(s_{33,comp}/s_{33,PZT}) \quad (3)$$

If one has an infinitely compliant polymer matrix, then the longitudinal piezoelectric constant, d_{33}, of the composite equals the d_{33} of the PZT and the transverse dielectric constant of the composite, $d_{31,comp}$ is given by

$$d_{31,comp} = 0.5\phi_{PZT}d_{31,PZT} \quad (4)$$

The change in s_{33} and K_3 of the composites with ϕ_{PZT} is shown in Figure 3. There is a very good correlation of s_{33} with pulse–echo acoustic velocity measurements and the unit cell model analysis. As expected, the composite becomes less compliant as the ϕ_{PZT} increases. The dielectric constant K_3 decreases monotonically with decreasing ϕ_{PZT}. These results confirm that minimal deformation of the PZT rods over considerable span distance and good knitting at the intersections has been achieved. Proper tailoring of slurry rheology, specifically in the low shear yield stress, are critical to forming these ideal periodic structures without molds or support structures.

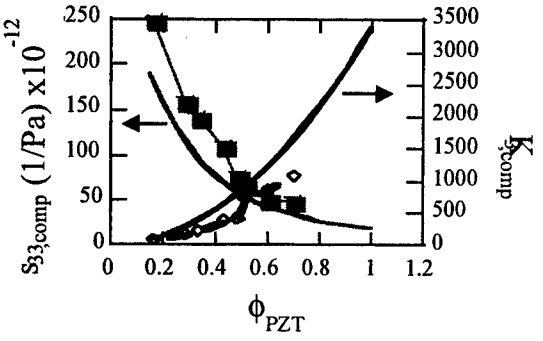

Figure 3. Theoretical and experimental behavior of elastic compliance ($s_{33,comp}$) and dielectric constant ($K_{3,comp}$) versus ϕ_{PZT}.

The hydrostatic figure of merit (FOM) for the composites as a function of ϕ_{PZT} is shown in Figure 4. The unit cell model predicts the FOM to be maximized for

intermediate ϕ_{PZT} and this general trend is reflected in the experimental data.

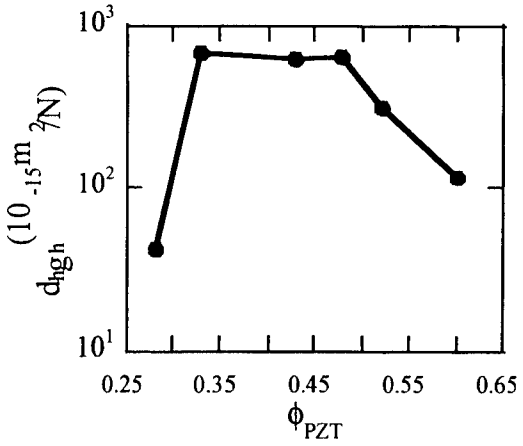

Figure 4. Plot of $d_h g_h$ as a function of ϕ_{PZT}

The FOM depends on the ratio of the hydrostatic piezoelectric coefficient divided by the dielectric constant. The ϕ_{PZT} = 0.43 composite has more than ten times greater FOM than bulk PZT-5H ($d_h g_h$ = $70x10^{-15}$). While the qualitative trend is reasonable, the quantitative correlation with the unit cell model is not as good as there is with the compliance and dielectric constant shown in Figure 3, being 100 times less than expected.

This over prediction by the unit cell model is due to its assumption of uniform surface deflections across exposed polymer and PZT faces. Similar effects have been observed and the phenomena described by Cao[11] for 1-3 composites. This effect is particularly strong in thin composites (less than 2 mm) like the ones in this study. The non-uniform strains result in a diminished d_{33} value for the composite while d_{31} remains near theoretical and therefore reduces hydrostatic response. For 1-3 composites this effect has been reduced by using brass endcaps [12]. Ideally, a direct write procedure could result in as good performance and would substantially facilitate manufacturing. We are presently working on a direct write design that will eliminate non-uniform surface stress and undesirable lateral stress that result in detrimental d_{31} contributions. [13]

4. SUMMARY

We have shown that robocasting can be used to fabricate PZT 5H ceramics with equivalent ferroelectric, piezoelectric and dielectric properties to PZT-5H ceramics that have been formed by cold isostatic pressing at 200 MPa. Further a series of robocast PZT – polymer composites have been fabricated with PZT volume fractions that varied from 17% to 70%. The best of these composites had a hydrostatic figure of merit ($d_h g_h$) that was 10 times better than bulk PZT-5H,. However, the hydrostatic response was still 2 orders of magnitude less than that projected. This was partly attributed to less than expected d_{33} behavior because of non-uniform surface displacement. Techniques and designs to produce low profile, highly volumetric efficient sensors with near theoretical sensitivities are in progress.

Acknowledgments: The authors acknowledge enlightening discussions with Don Berlincourt, Jim, Tressler, Amar Bhalla, John Gieske and George Samara. Outstanding technical support was provided by J. Mark Grazier, Jill Wheeler, Diana Sipola, Gary Zender and Bonnie McKenzie. Sandia is a multiprogram laboratory operated by Sandia Corporation, a Lockheed Martin Company, for the United States Department of Energy under contract DE-ACO4-94AL85000.

References

1. T.F. McNulty, D.J. Shanefield, D.J. Danforth and A. Safari, *J. Amer. Ceram. Soc.*, **82**, 1757-60 (1999)
2. U. A. Uhland, R. K. Holman, M. J. Cima, E. Sachs, Y. Enokido, *Mater. Res. Soc. Symp. Proc.*, **542**, 153-58, (1999)
3. J. Cesarano III, R. Segalman, and P. Calvert, "Robocasting Provides Moldless Fabrication from Slurry Deposition," *Ceramic Industry*, Vol. 148, No. 4, pp 94-102, April (1998)
4. J. Cesarano III, P. Calvert, "Freeforming Objects with Low-Binder Slurry," U.S. Patent Number 6,027,326
5. B.A. Tuttle, J.E. Smay, J. Cesarano, J.A. Voigt, T.W. Scofield, W.R. Olson, and J. A. Lewis, *J Amer. Ceram. Soc.*, **84** , (4) 872-4 (2001).
6. R.E. Newnham, R.E., Bowen, L.J., Klicker, K.A., and Cross, L.E., *Materials in Engineering*, 1980, 2 93-106.
7. J.F. Tressler, S. Alkpu, A. Dogan,and R.E. Newnham, *Composites Part A (Applied Science and Manufacturing)*, 1999, 30A [4], 477-82.
8. IEEE Standard on Piezoelectrics (1987).
9. K. Rittenmeyer, T, Shrout, W.A. Schulze, and R.E. Newnham, *Ferroelectrics*, 41 [1-4], 189-95.
10. Banno, H., *Japanese Journal of Applied Physics Part 1*, 1994, 33 [9B], 5518-20.
11. W. Cao, Q.M. Zhang, L.E. Cross, *J. Appl.. Phys.*, 1992, 72 [12], 5814-5821
12. N.M. Shorrocks, M.E. Brown, R.W. Whatmore, F.W. Ainger, *Ferroelectrics*, 1984, 54, 215-218.
13. J.E. Smay, J. Cesarano, B.A. Tuttle and J.A. Lewis, *J. Appl. Phys.* (submitted) (2001). .

Microstructure and Grain Boundary Effects on the High-Field Electrical Properties of PTCR Barium Titanate

David P. Cann, Charles T. Chao, and R. Bruce Gall
Materials Science and Engineering Department, Iowa State University, Ames, IA 50010
FAX: 515-294-5444
Email: dcann@iastate.edu

ABSTRACT

In this work, the interrelationship between the microstructure, the grain boundary structure, and the high field electrical properties of positive temperature coefficient of resistivity (PTCR) $BaTiO_3$ ceramic thermistors was explored. At high temperatures, the resistance of the material is strongly dependent on the field strength. This is an intrinsic feature of the double Schottky barrier structure present at the grain boundaries. For PTCR devices designed to operate under high fields, the resistance must be maximized to prevent thermal runaway into the NTC regime.

Low resistivity thermistors ($\sigma \approx$ 10-100 Ω-cm) were prepared by standard ceramic processing routes. Low-field properties show a large resistivity jump starting at temperatures above 130°C. High-field electrical properties were measured in the insulating state at elevated temperatures (180 < T < 220°C). It was observed that the combination of grain boundary dopants (e.g. Mn) and doping levels beyond the resistivity minimum (X_{La}, X_{Nb} > 0.3 mol %) were found to significantly improve the high-field resistance. In addition to grain size effects, this behavior was also attributed to the presence of deep-level grain boundary states.

BACKGROUND

Barium titanate-based positive temperature coefficient of resistance (PTCR) devices have found use in wide ranging applications including self-regulating heaters, current limiters, temperature sensors, and degaussers. A number of researchers have been successful at fabricating multilayer PTCR devices with the aim of reducing the overall device resistance[1-4]. Multilayer-based PTCR devices have also been found to have an enhanced temperature sensitivity due to the small thermal mass[3]. The use of PTCR thermistors for high power applications has also been proposed for current limiting devices and mechanical relays[5]. The use of barium titanate-based materials for these new applications is limited by the weakening of the PTCR effect at high fields ($E \geq 10$ V/mm).

For multilayer PTCR devices with thick film thermistor layers, relatively high fields are attained under moderate voltages which are sufficient to minimize the PTCR effect. For high power applications, it is difficult to compromise between maintaining a low device resistance to allow a high current rating (e.g. 30 A) and yet maintain a sufficient device thickness that prevents high electric fields which suppress the PTCR effect.

The mechanism behind the PTCR effect, as described by Heywang[6] and later by Daniels[7], arises from the temperature dependence of the potential barrier height ϕ_0 of double Schottky barriers located at the grain boundaries. Under low fields, the resistivity is described by:

$$\rho \propto \exp\left(\frac{q\phi_0}{kT}\right) \qquad (1)$$

where q is the electron charge. The potential barrier ϕ_0 can be described by the equation[6]:

$$\phi_0 = \frac{qN_S^2}{2\varepsilon_0 \varepsilon N_D^2} \qquad (2)$$

where N_S is the surface state density, N_D is the donor density, and ε is the permittivity.

As the field is increased, the potential barrier height is decreased according to[8]:

$$\phi = \phi_0\left(1 - \frac{V}{4\phi_0}\right)^2 \qquad (3)$$

where V is the potential drop across the individual grain boundary. As the PTCR effect is suppressed at high fields, the ultimate voltage withstanding of the device is limited if the device temperature goes beyond the resistivity maximum and into thermal runaway.

In this work, the microstructure and grain

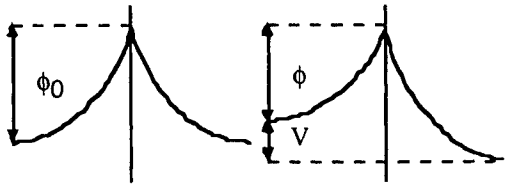

Fig. 1. Schematic of double Schottky barrier structure with potential barrier ϕ at a grain boundary under no potential (top) and under a potential V (bottom).

boundary structure of La-doped $BaTiO_3$ will be related to the high field PTCR properties. The effects of grain size and dopants will be related to the PTCR effects under high E-fields.

EXPERIMENTAL

Semiconducting $BaTiO_3$ was prepared by conventional ceramic processing techniques. The binary oxides La_2O_3 (0.2 to 0.4 mol %) and MnO_2 (0.03 to 0.09 mol %) were added to stoichiometric $BaTiO_3$. To aid in grain growth and sintering, 1 mol % excess TiO_2 and 2 mol % SiO_2 was added. Powders were milled in ethanol and calcined in air at 1100°C for 2 hours.

The calcined powder was mixed with 5 weight percent binder, pressed into 12.5 mm diameter discs, and fired in flowing nitrogen ($pO_2 \approx 0.0001$ atm) at 1350°C for 2 hours. Following sintering, the samples were annealed in air at 1200°C for varying times.

To facilitate the electrical measurements, In-Ga electrodes were utilized because of their low contact resistance[9]. Low voltage resistivity versus temperature measurements were performed with an electrometer and an environmental chamber. High voltage measurements were conducted with a 2.8 kW power supply at temperatures ranging from 180 to 220°C. Utilizing a LabView interface, the current was measured after a voltage pulse on the order of 1 ms was applied to the sample. Impedance spectroscopy measurements were conducted with an HP-4194A impedance analyzer over a frequency range from 100 Hz to 4 MHz.

RESULTS AND DISCUSSION

Fig. 2 illustrates the suppression of the PTCR effect at high electric fields over the temperature range 180 to 220°C. From inspection of Eqs. 2 and 3, it is noted that the resistance versus E-field behavior should be

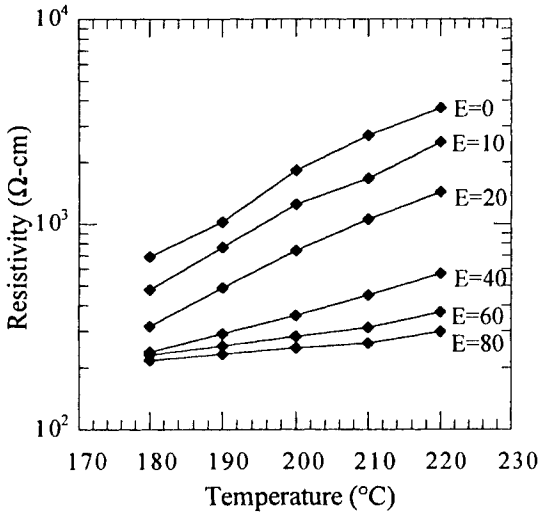

Fig 2. Resistivity versus temperature at fields ranging from 0 to 80 V/mm for a 0.3 mol % La-doped sample.

sensitive to grain size and the potential barrier ϕ_0. The addition of Mn in concentrations on the order of 0.03 to 0.09 mol % caused a decrease in the grain size and an increase in ϕ_0 since Mn is known to occupy deep acceptor states within the grain boundary[10].

Fig. 3 below shows the enhanced PTCR effect due to varying levels of Mn additions. For example, the 0.09 mol % Mn sample exhibited an increase in resistivity of over 5 orders of magnitude. Impedance spectroscopy measurements on the grain and grain boundary resistances are shown in Table I below.

From the impedance spectroscopy data, it is apparent that the Mn-dopants were distributed in both the grain and grain boundary. Further

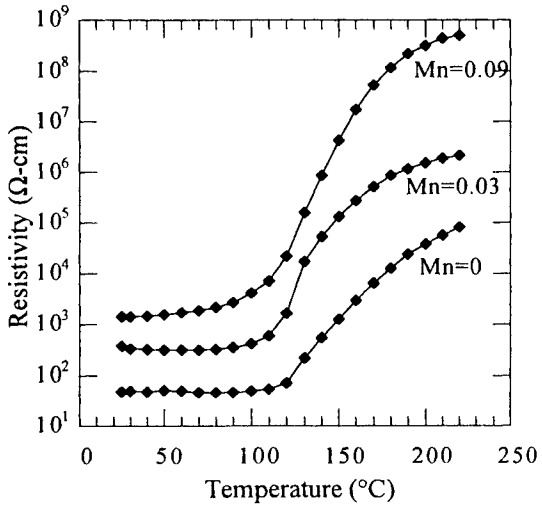

Fig 3. Resistivity versus temperature for PTCR samples with varying Mn concentrations.

Table I. Grain and grain boundary resistances measured via impedance spectroscopy for 0.35 mol % La-doped $BaTiO_3$.

	Mn = 0	Mn = 0.03	Mn = 0.09
R_{grain}	1.5 Ω	8.0 Ω	31 Ω
$R_{grain\ boundary}$	3.6 Ω	60 Ω	230 Ω

Table II. Room temperature resistivities for La- and Mn-doped PTCR ceramics.

La	Mn (mol %)			
mol%	0	0.03	0.06	0.09
0.25	37 Ω-cm	220	1400	19000
0.30	61	170	320	1700
0.35	150	380	160	1400

confirmation of this was evidenced by the shift in the room temperature resistivity minimum with increased Mn-concentrations (e.g. Table II).

The shift of the room temperature resistivity follows the model of Chen *et al*[11] where the donor density is partially compensated by Mn^{2+} and Mn^{3+} within the grain via the relationship:

$$N_D \approx [La] - \tfrac{5}{3}[Mn] \qquad (4)$$

Measurements of the average grain size revealed a significant decrease in grain size as Mn was added. For example, for a 0.35 mol % La-doped sample without Mn the average grain size was 15 μm. However, the grain size decreased to 8.8 μm when 0.09 mol% Mn was added.

The effects of Mn-additions at high fields at 180 and at 220°C is shown in Figs. 4 and 5, respectively. For samples with no Mn-additions, the resistivity versus voltage curve showed an initial quasi-linear decrease followed by a voltage independent region at higher fields. All of the data has been normalized to the parameter voltage per grain boundary so that grain size effects can be minimized. As shown in the data, as the Mn-concentration increased, the slope d(logρ)/dV decreased and the quasi-linearity extended to higher fields. Similar experimental results were obtained for La dopant concentrations of 0.3 and 0.25 mol %.

Plotted in Fig. 6 is the calculated resistivity versus voltage for various values of ϕ_0 assuming the voltage dependence derived from equation 3. The plot shows that for values of ϕ_0 on the order of 1.0 eV, the resistivity at high fields becomes relatively voltage independent. Whereas for larger values of ϕ_0, the quasi-linear regime extends to higher fields.

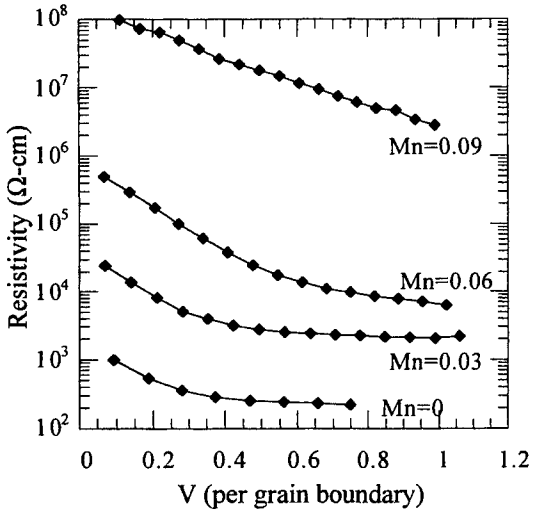

Fig. 4. Resistivity versus voltage per grain boundary for 0.35 mol% La-doped samples at 180°C.

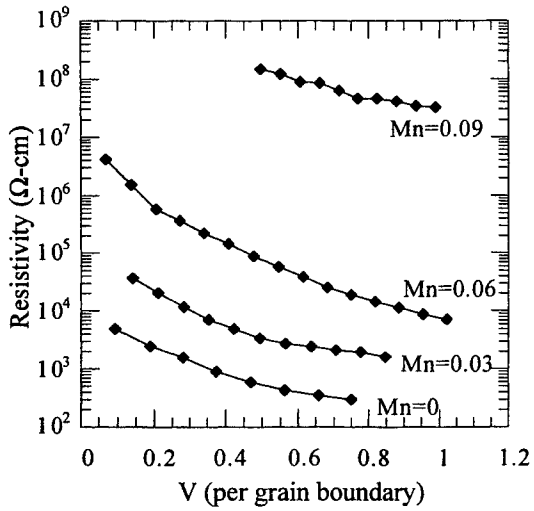

Fig. 5. Resistivity versus voltage per grain boundary for 0.35 mol% La-doped samples at 220°C.

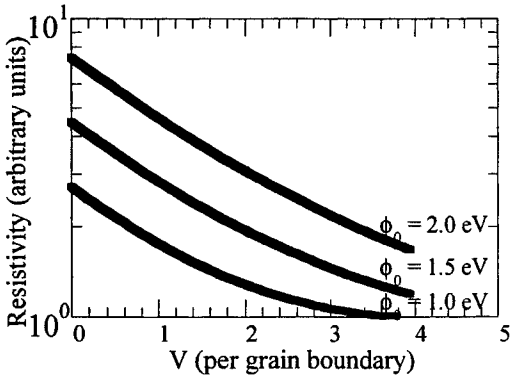

Fig. 6. Calculated resistivity versus voltage assuming the voltage dependence of equation 3.

The similarities between these curves and the high field data in Figs. 4 and 5 supports the idea that the addition of Mn increased the grain boundary potential barrier[12]. However, the voltage independent region appears at much lower voltages than predicted from the calculations. This may be the result of a non-uniform field distribution across the sample. While detailed measurements on the grain size distributions were not conducted in this study, there is evidence to suggest that hot spots can occur due to microstructural effects[13]. There is also an abundance of evidence of microstructural effects in the conduction mechanisms in ZnO varistors[14].

In addition to Mn-additives, the potential barrier ϕ_0 is also sensitive to annealing conditions. Fig. 7 illustrates the effects of annealing on the high field properties. The t = 0 and t = 10 min anneal samples exhibited behavior similar to that found in the samples with small or no Mn doping in Figs. 4 and 5. After a 100 minute anneal, however, the log ρ versus voltage curves resemble the data found for the 0.09 mol% Mn-doped samples. According to the Daniels model[7], during the annealing stage the surface state density N_S increases as acceptor defects are created in the grain boundary (and diffuse in towards the grains). The increased N_S would increase ϕ_0 in a similar manner as for Mn-doping.

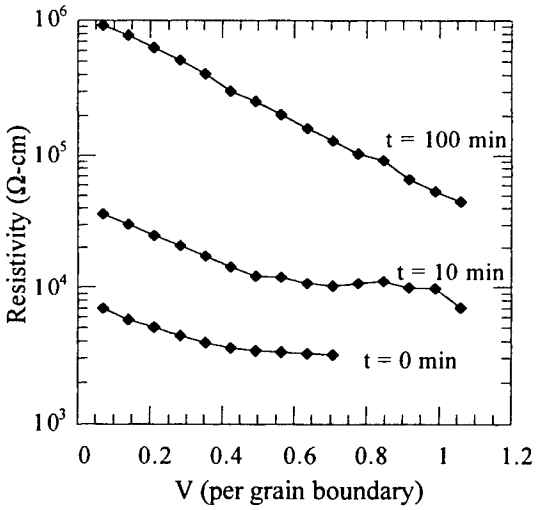

Fig. 7. Resistivity versus voltage per grain boundary for samples annealed from 0 to 100 min.

CONCLUSIONS

The PTCR effect in $BaTiO_3$ ceramics under high fields exhibits a strong voltage dependence due to the double Schottky barrier structure at the grain boundaries. In this work, the high field properties of La-doped $BaTiO_3$ was studied by relating the resistance versus voltage properties at high fields to the grain size and grain boundary structure. The addition of Mn was found to significantly improve the PTCR properties at high fields. The Mn additives were found to decrease the grain size of the material. This resulted in a lowering of the net voltage across each grain boundary. However, after normalizing the high field data to voltage per grain boundary it was observed that the improved PTCR effect could be attributed to a higher grain boundary potential barrier ϕ_0. This behavior was shown to be consistent with known models for the voltage dependence of ϕ_0 in double Schottky barriers.

ACKNOWLEDGEMENTS

The authors would like to thank William Chen of Square D Company, Cedar Rapids, Iowa, for his insightful comments throughout the progress of this work. The authors would also like to thank Nathan Ashmore for his assistance with the grain size measurements.

REFERENCES

[1]S. Tashiro, A. Osonoi, and H. Igarashi, *J. Ceram. Soc. Jpn.*,107, 15-20 (1999).
[2]W. Lingling, L. Juan, S. Liyang, and Z. Zhigang, *Piezoelectrics and Acoustooptics*, 17, 37-39 (1985).
[3]S. Chatterjee, K. Sengupta, H.S. Maiti, *Sensors and Actuators B*, 60, 155-160 (1999).
[4]K. Sasaki and H. Niimi, Multilayer positive temperature coefficient thermistor device, 5,493,266, United States Patent, (1996).
[5]W. Chen, *44th IEEE Holm Conference on Electrical Contacts*, 87-90 (1989).
[6]W. Heywang, *J. Mat. Sci.*, 6, 1214-1224 (1971).
[7]J. Daniels and R. Wernicke, *Philips Res. Repts*, 31 544-559 (1976).
[8]K. Mukae, *Key Engineering Mat.*, 125-126, 317-320 (1997).
[9]D. Cann and C. Randall, *J. Appl. Phys.*, 80 [3] 1628-1632 (1996).
[10]H. Ihrig, *J. Am. Ceram. Soc.*, 64, 617-620 (1981).
[11]Y.C. Chen, G.M. Lo, and M.Y. Su, *Jpn. J. Appl. Phys.*, 35, 2745-1748 (1996).
[12]F. Zeng and Z. Cao, *J. Appl. Phys.*, 79 (5), 2487-2490 (1996).
[13]G. Mader, H. Meixner, and P. Kleinschmidt, *J. Appl. Phys.*, 56, 2832-36 (1984).
[14]F. Modine, L. Boatner, M. Bartkowiak, G. Mahan, H. Wang,, and R. Dinwiddie, *Ceram. Trans.*, 100, 469-491 (1999).

SESSION V

PV.1 Integrated Passive Device Thin Film, Thick Film and Disruptive Technology for Wireless and High Speed Signal Processing Applications, Robert H. Heistand, II, J. L. Galvagni, A. P. Ritter, R. M. Kennedy III, and G. Korony, AVX Corporation, USA. 383

PV.2 Micromachined Capacitor Ultrasonic Transducers, B. T. Khuri-Yakub, M. Karaman, C.-H. Cheng, S. Ergun, G. Yaralioglu, B. Bayram, U. Demerci, S. Hansen, M. Badi, and O. Oralkan, Stanford University, USA. 391

PV.3 Recent Developments in Dielectrics and Piezoelectrics in Europe, Andrew J. Bell, Leeds University, UK. 401

PV.4 Three-Dimensional Analysis of Inverted Domain Structures in $LiNbO_3$ by SHG Interference Microscope, Y. Uesu, H. Shibata, and Y. Shindoh, Waseda University, Japan. 409

Integrated Passive Device Thin Film, Thick Film and Disruptive Technology for Wireless and High Speed Signal Processing Applications

R. H. Heistand II, J. L. Galvagni, A. P. Ritter, R. M. Kennedy III and G. Korony
AVX Corporation
Advanced Products and Technology Center
2200 AVX Drive
P.O. Box 867
Myrtle Beach, SC 29578-0867
FAX: (843) 448 2106
Email: heistand@avxus.com

After decades of research in integrated passive devices, applications now exist in the wireless and high speed signal processing markets. Passive devices may finally take the leap that transistors did with the advent of the IC. Examples of thin film technology for RC networks and filters are presented based upon a K1100, spin coatable sol-gel dielectric PNZT with a specific capacitance up to 2500 nF/cm^2. Alternatively, the incorporation of traditional hybrid circuit and LTCC material systems using resistor electrodes in a standard multi-layer ceramic capacitor fabrication process also yields RC arrays, networks and filters. On the horizon are technologies incorporating passive devices into printed wiring board processing. The infrastructure issues surrounding the commercialization of these IPD technologies is also discussed.

INTRODUCTION

Passive component trends can be summarized as more performance in less space for less cost. Standard component costs have been driven by market forces to a fraction of the assembly costs, which leads to the conclusion that integrated passives should provide the ultimate density, cost, and performance benefit. This paper reviews the state of passive integration in several technologies and discusses the current trends and issues from both a technology and infrastructure perspective. Table 1 shows the trend in personal computers we have been tracking for the last ten years, which reveals more than an order of magnitude increase in the number of elements on the motherboard from the 486 through the Pentium® III [1,2]. It also demonstrates the introduction of simple resistor arrays in the 1993 time frame, followed by capacitor arrays in 1997.

Table I: Passives in Evolving Desktops

Board:	486	Pentium 120	Pentium 200 MMX	Pentium II 333MHz	Pentium III
Released:	**1989**	**1993**	**1997**	**1998**	**1999**
Leaded MLC	58	0	0	0	0
SMT MLC	0	151	190	300	600
Cap Arrays (x4)	0	0	32	140	200
Leaded Tantalum	15	1	0	0	0
SMT Tantalum	0	0	0	37	80
Aluminum	0	7	32	11	15
Feed-through	0	0	3	0	0
Disks	0	0	0	4	0
Leaded Resistors	92	0	0	0	0
SMT Resistors	0	146	188	635	1000
Resistor Arrays (x2)	0	0	0	10	0
Resist Arrays (x4)	0	64	148	336	300
Total	**165**	**369**	**593**	**1,473**	**2,195**

The wireless sector has also fueled the use of passive components with around 500 in the most recent cell phones [2]. It is interesting to look at the distribution of capacitor values and the dielectric technologies that fit these ranges (Fig. 1). The component counts were taken from seven cell phones produced from 1997 to 2000, a global positioning satellite (GPS) device and a BlueTooth PMCIA card. Unlike the 10 uF-to-1500 mF power plane decoupling capacitors on a current P4 motherboard, these capacitor values are very small; from a few tenths of a pF to 100 nF for the RF and base band circuits. This allows many alternative dielectric materials to be used in place of the standard ceramic bodies, thus opening the potential for thin film

Figure 1: Capacitance Value Spectrum in Hand Held RF Systems and the Relevant Technologies

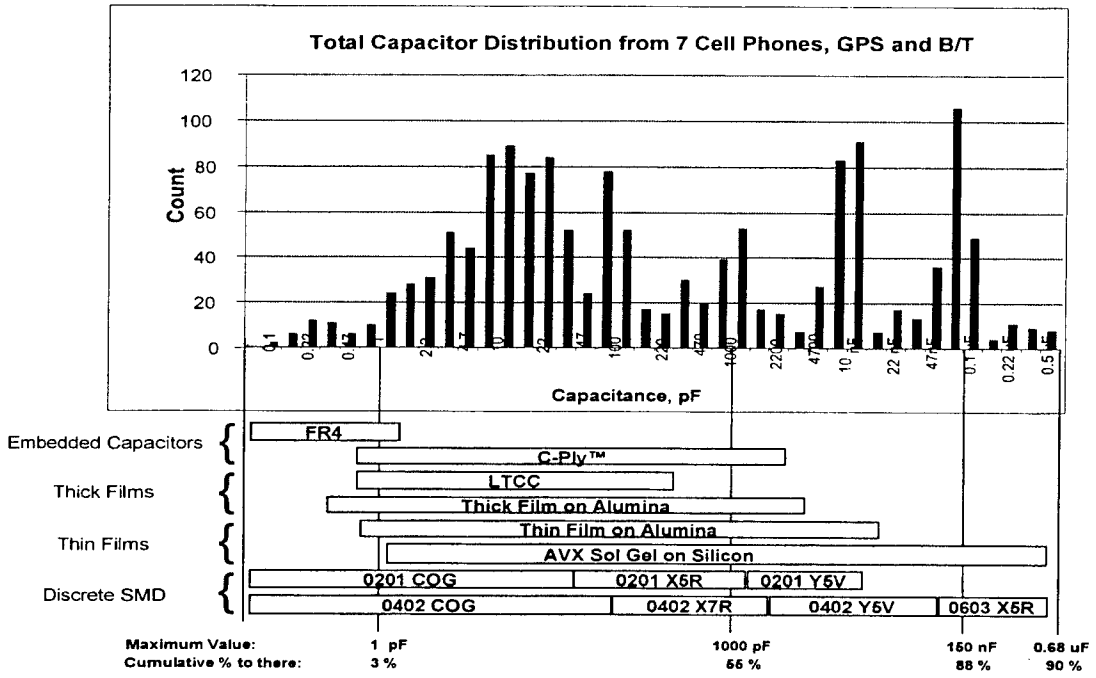

and PWB embedded technologies. The technology ranges for a given dielectric are bounded on the low end by a 20% capacitance tolerance based on the production control tolerance for the smallest feature size, and are bounded on the upper end when the part geometry would exceed 0.5 cm_. Not only are the component values small, but so are the part sizes. On an average, 86% of the passives in 2000-01 model year phones are 0402 size. Thus it is useful to look at the actual passive component density (per square centimeter) of a recent cell phone (Fig. 2). Clearly some circuit sections are dense enough for passive integration.

Figure 2: Passives Density in a 2000 cell phone

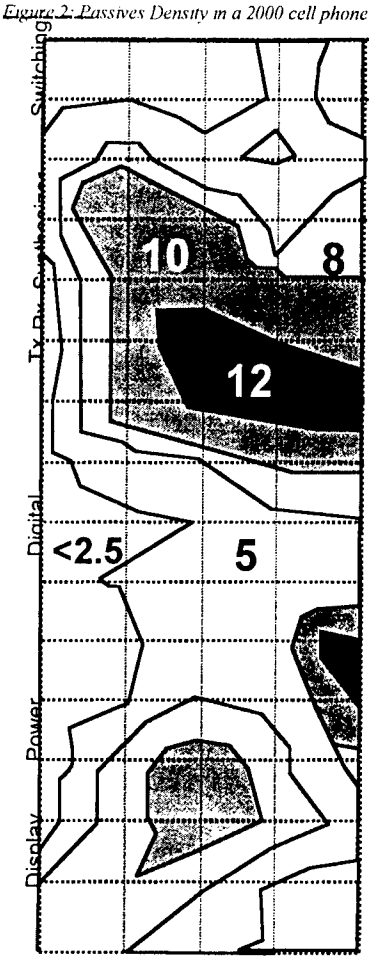

NEMI [2] has been developing road-maps every two years for the electronic technologies needed in several market sectors. Some relevant sectors or platforms are hand held wireless, high performance workstations, cost performance PC's and automotive applications. Table II is a ten-year projection for board size, routing density (critical for I/O or termination density), passive component count and average component density counting both sides of the board. Hand held is the density leader while high performance is the component count leader. Both density and bill of material reductions can be drivers for integration.

To make optimum use of the board real estate, the components I/O or SMD terminations

Table II: Selected NEMI 2000 Projections

		2001	2003	2005	2010
Board Size cm?	Hand Held	30	28	26	20
	High Perf	400	300	200	100
	Cost Perf	600	400	300	200
Lines & Spaces microns	Hand Held	60	35	30	20
	High Perf	55/75	55/75	50/70	35/55
	Cost Perf	125	100	75	75
Passives Count	Hand Held	465	560	598	600
	High Perf	3500	4375	5700	8500
	Cost Perf	3000	3500	4375	5700
Avg Component Density Parts/cm?	Hand Held	15.5	20	23	30
	High Perf	2.0	2.8	3.6	5.9
	Cost Perf	1.7	2.1	2.4	2.8

should match the wiring pitch, and the projections for the hand held sector drive this down to 60 μm or almost 2 mil in the next five years. Again, this can best be solved with an IPD.

|Z| CHIP ® TECHNOLOGY

|Z| Chip® technology creates integrated passive resistor-capacitor (RC) devices using LTCC glass/alumina dielectric materials with multilayer cofired ruthenium oxide resistor electrodes in the architecture of a standard multilayer capacitor [3-6]. The device resistance

Figure 3: The Evolution of Integrating Passives

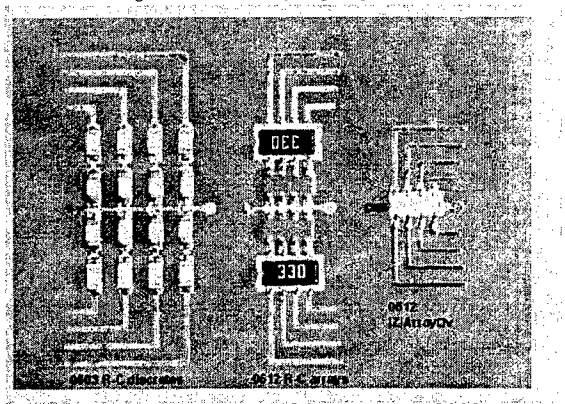

stems from the parallel resistance of the individual layers by AC coupling and the device capacitance arises from capacitive coupling of the planar resistor elements. In this general structure, the resistor layers themselves form the electrodes of a parallel plate capacitor. Although the structure is simple, the device is electrically complex because the capacitance and resistance are physically distributed throughout the entire device.

Figure 3 demonstrates the power of integration that is achievable in the |Z| Chip® technology, so named for its series RC impedance matching capability. Three identical circuits of 8 parallel RC traces with a common ground are presented in 0603 discrete SMD components, in four-up 0612 capacitor and resistor arrays, and in one single 0612 |Z| Chip®. The latter achieves a seven fold increase in density over the discrete solution and eliminates 22 solder joints for both the discrete and four-up array solution. It also eliminates 15 components and 15 assembly operations over the

Figure 4: Comparative RC Circuits

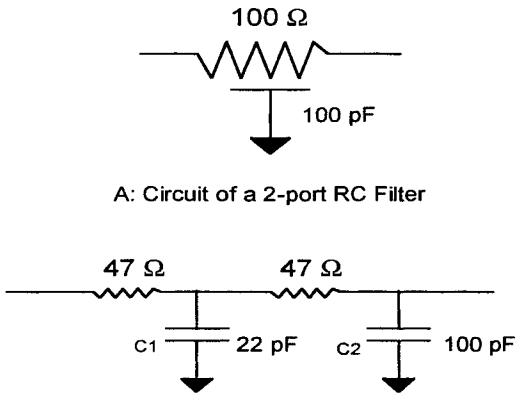

discrete embodiment.

The technology is very flexible since standard conducting electrodes can also be cofired in this device. This creates the opportunity to make more complex networks such as filters [4]. A simple, 2-port T-filter (Fig. 4 A) can be constructed with resistor electrodes between ports 1 and 2, which are capacitively coupled to a transverse conducting electrode ground plane. The function of the more complex two-cell filter equivalent circuit (Figure 4B) can be achieved with a fabricated structure consisting of five parallel resistor

Figure 5: 0603 Discrete 2-Cell Filter on a Penny

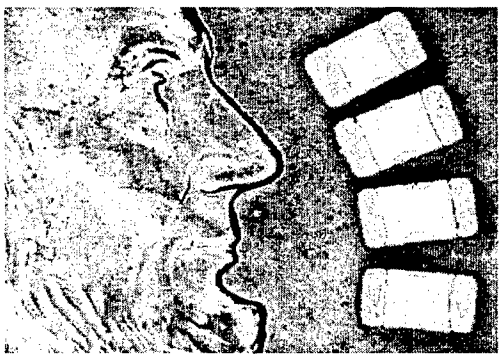

layers, a 22 pF integral resistor to ground plane capacitor, and a twenty-two layer, 100pf capacitor. (Figure 6) This also incorporates shielded internal electrodes all in an 0603 package size (Fig 5) .

A cross section shows the compatibility of the LTCC dielectric, the RuO_2 resistive

Figure 6: Cross-section of the Filter

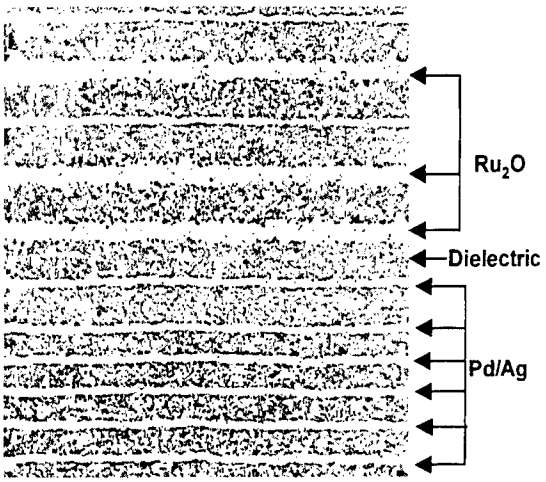

electrodes and the Ag/Pd conductive electrodes all constructed to current MLC feature dimensions of 10 micron thick dielectric between the Ag/Pd electrodes (Fig 6). The electrical performance is presented in Figure 7 as S21 transmission losses in comparison with the simple T-filter from this technology. An additional 10dB of filtering performance is obtained in the 2-cell circuit. This single 0603

Figure 7: Electrical Performance of Filter

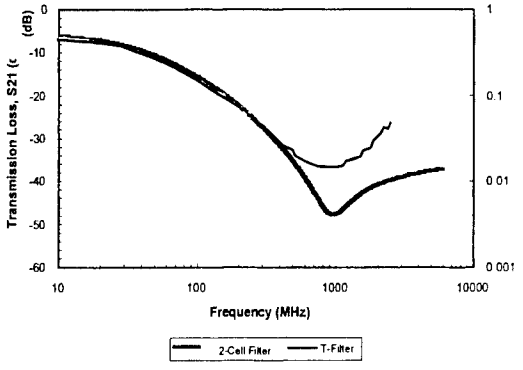

component replaces four 0402 discrete devices.

THIN FILM SOL-GEL BASED TECHNOLOGY

Much research has been invested globally in developing low cost, high K, thin film dielectric processes. One route was the sol-gel or chemical solution deposition systems; however, an impediment to practical manufacturing implementation was the ability to achieve only 100 nm layers per coat. This

Figure 8: Capacivity and DF as function of Thickness

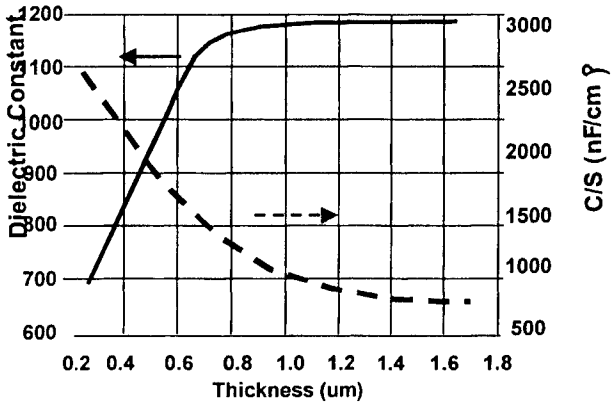

created two serious issues: 1) cracking of the film over the metallization steps, and 2) high processing costs when 5 to 10 coats are required to make a moderately thick, reliable dielectric layer. AVX Corporation has developed a sol-gel precursor for niobium doped PZT that can be coated up to 1 _m fired thickness in a single coat [7,8]. This provides good continuous step coverage and crack free, fired dielectric films. On Pt substrates a pure perovskite phase is formed with 66% (111) orientation using a 600°C crystallization step [7]. The dielectric

Figure 9: CAP/DF for the HiFLT™ Sol-Gel Dielectric Device

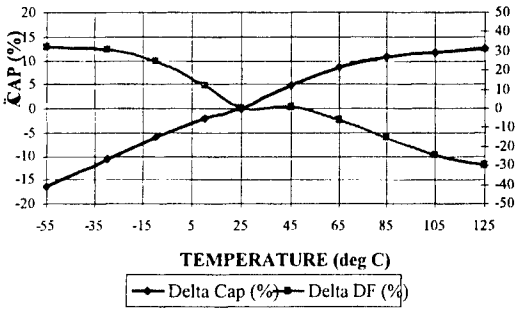

constant and specific capacitance are plotted in Figure 8 and the TCC and dissipation factor in Figure 9. Thus a specific capacitance of 2500 nF/cm^2 is achieved in a thin film X7R body.

Figure 10: 9-Channel Thin-Film T-Filter Array

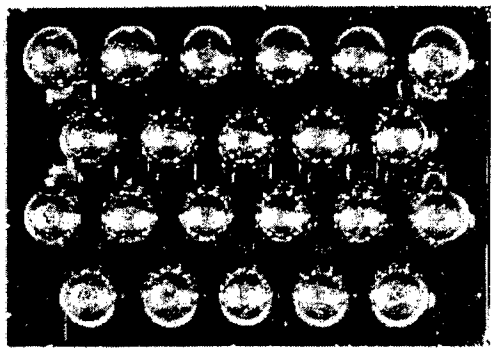

Coupling this technology with thin film TaN resistors, very dense IPD's can be constructed [1]. Figure 10 shows a 9-channel 220 pF, 33 ohm T-filter array in a 1208 package. This would replace 27 discrete components. The chip size is completely dictated by the BGA pitch since in this array the capacitors only utilize 8% of the chip area and the resistors cover 4%. The voltage transfer function (1 M_ load impedance), including temperature dependence, is shown in Figure 11.

Figure 11: Voltage Transfer Response (at 1 MΩ output impedance) for the T-Filter at various Temperatures

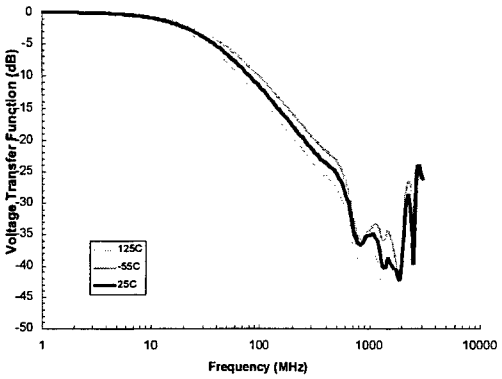

Figure 13: S21 of a Twin-T Filter

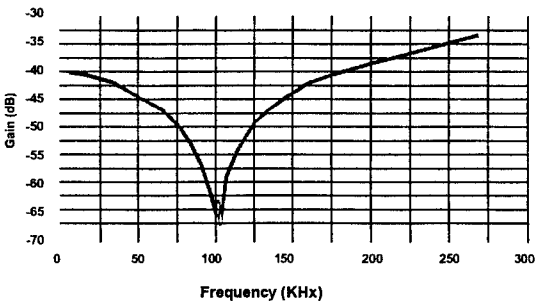

Another embodiment of this technology is shown in Figure 12 for a 0404 twin T-filter whose circuit is found in Figure 12 and S21 curve for a 50 ohm impedance environment in Figure 13. This single 0404 IPD replaces six 0402 discrete components. Without a dielectric material whose capacitance value is an order of magnitude greater than the standard thin film SiO_2 or Si_3N_4, this would not be possible in such a small case size.

Figure 12: Twin T Filter

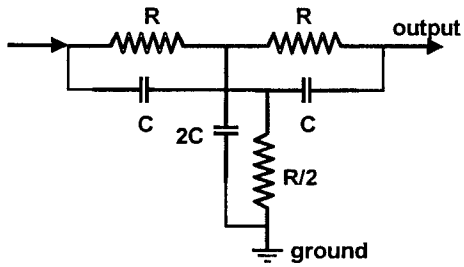

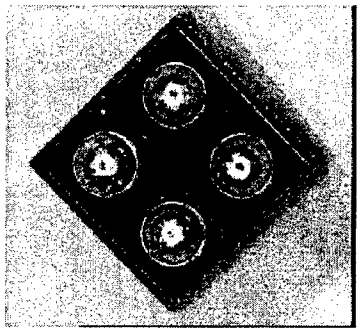

HIGH SPEED DECOUPLING

The thin film, high K-X7R dielectric also fits high speed decoupling applications. It is generally recognized that low inductance capacitive decoupling is a gating issue for continued advances in higher speed central processor units. Several strategies are being practiced to minimize this inductance, but generally they can be summarized by the concept of mounting the capacitors as close as possible to the IC [9]. In Figure 14, two such strategies are depicted. Both of these require thin, low inductance capacitors. A high I/O, BGA, thin film capacitor meets this need. Utilizing the sol-gel dielectric, a high frequency low inductance (HiFLI™) capacitor family from 100 nF to 270 nF with only a 0.35 mm height mounted on the PWB has been developed. The 100 nF capacitor has a resonance at 108 MHz, only 25 pH of ESL

and 2 to 4 mΩ of ESR in a 2.1 x 4.1 mm die with thirty-two 250 _m balls on a 500 _m pitch (Figure 15).

Figure 14: Decoupling Strategies for High Speed Processors

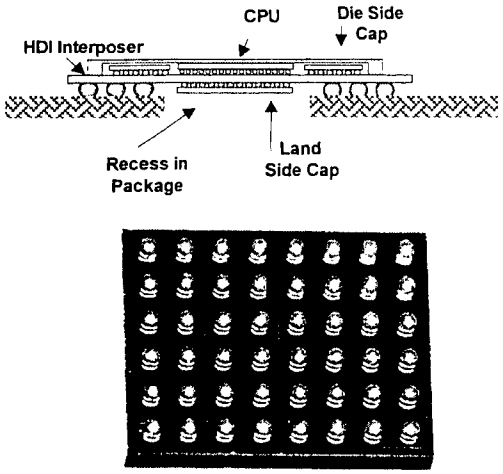

For comparison, a 100 nF 0603 MLC has an ESL of 800 pH, and an ESR of 200 mΩ with a mounted height of 0.95 mm. The die size, I/O,

Figure 15: S21 Parameters for HiFLI™ Capacitors

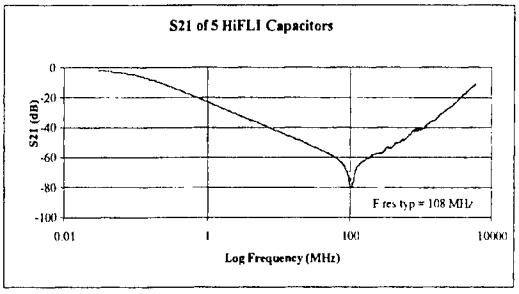

capacitance value and dielectric thickness is provided for this family in Table III. Thin film clearly offers a radical solution for advanced decoupling.

Table III: Current Parameters of HiFLI™

Capacitance	Size (mm)	I/O
100 nF	2.1 x 4.1	32
220 nF	3.1 x 4.1	48
270 nF	4.1 x 4.1	64

MODULES and SYSTEMS in a PACKAGE

The next level of integration after an IPD is a fully functional module such as a power amplifier circuit, a voltage control oscillator (VCO) or even a complete BlueTooth or global positioning satellite (GPS) module. Module is herein defined as a surface mountable package, which has all of the necessary circuitry, passive components and IC's either embedded in the substrate or mounted on the substrate. Sometimes this is referred to as a system in a package (SiP). Three examples of VCO modules are shown in Figure 16 demonstrating the use of LTCC, PWB and thin film technologies. The metal packaging lid has been removed from the LTCC and PWB modules which are mounted face up, whereas the thin film on glass is solder bumped to be mounted face down. The LTCC and PWB versions, which

Figure 16: Recent Examples of VCO Modules (bottom picture courtesy of Intarsia)

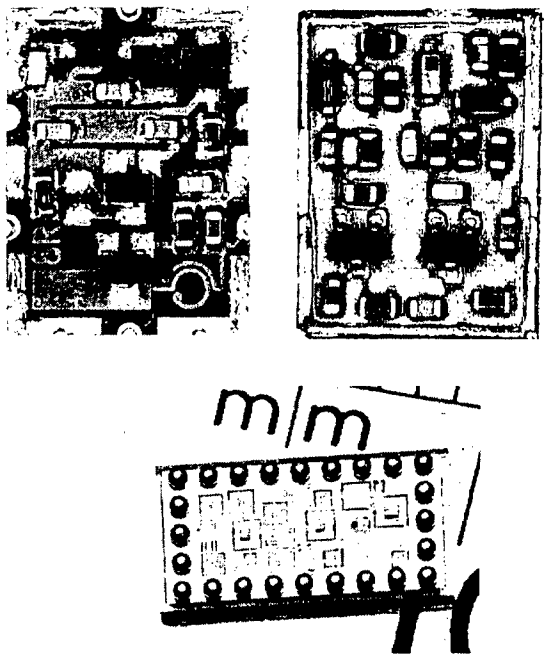

were made to be interchangeable, have a die area of 63 mm_, while the thin film variant is smaller as expected at 30 mm_.

Each of these variants contains roughly 30 passive resistor, capacitor and/or inductor elements. Both LTCC and PWB can embed some R,C, & L components within the substrate. However, it is still difficult to co-fire a high dielectric constant capacitor in LTCC and trim buried resistors. This is an area of intensive development. Two US government-funded consortia have worked on embedding capacitors into the PWB. Solutions for up to approximately 100 pF capacitors are available by use of

polymer or ceramic filled polymer materials. However, there are no commercial materials for embedding high value capacitors in the PWB. Research is ongoing to make a ceramic equivalent of the resin-coated copper foil used as the fundamental building block for PWB. One way is to screen print standard low fire, thick film dielectric materials on the foil [10] and the other is to calcine a standard PLZT ceramic dielectric from a chemical solution deposition directly on a nickel coated copper foil [11].

The fact is that none of these technologies is perfect for integrating the full range of desired components: LTCC has difficulty trimming buried resistors, difficulty cofiring high K dielectrics, and difficulty with precision inductors; PWB has difficulty with high capacitance and requires infrastructure change for embedding technology; and thin film can require too much expensive real estate. It would make sense to partition the module into the technologies that deliver the cost "sweet spot" for that section of the circuit instead of using a single *tour de force* technology. Thus wide tolerance resistors and low value/wide tolerance capacitors could be embedded in the PWB, thick film technology such as the |Z| Chip® IPD could handle the mid-tolerance and mid-value R 's & C's, and thin film IPD's would make the tight tolerance, matching network R,C &L's. This should create the lowest cost, optimum integration for the module/package within the current existing commercial infrastructure.

MARKET FORCES and DISRUPTIVE TECHNOLGY

What are the real market forces behind integration of passive components? The standard litany is space savings, part count reduction, higher reliability (fewer solder joints), lower assembly cost (less placements) and system performance yield. So why has it not happened to a greater extent? The answer is that the only true market driver (lower cost) has yet to be universally delivered. Few applications must have the space savings; nobody pays for the higher reliability of fewer solder joints; and most IPD's cost more than the sum of the discrete components. This leaves lower assembly costs and system yield. The latter is the driver for the SiP's. If each of the precision circuit blocks in a cell phone could be obtained as a fully tested module, then the end-of-line system yield would increase dramatically. This has a real cost impact and will probably make the module/SiP the next technology wave of microelectronics.

There is another impediment to passive integration, namely the current supply chain. It is now a misnomer to refer to this as a chain, as it is truly a spider's web (Figure 17). Most OEM's have shed their manufacturing responsibilities to a contract manufacturer. Who has design responsibility? Who will do value engineering? Who is the real purchasing agent? This supply network, versus the old vertically integrated company, has greatly increased the difficulty of adopting IPD's.

Finally, we must recognize that within this integration ferment there is the potential for a disruptive technology to the current passive component supply business. Clayton Christensen defines the attributes of a disruptive technology as typically cheaper, simpler, smaller and more convenient to use. Generally the technology initially under performs in the mainstream market, but offers a few customers a new value from a different perspective than that which the mainstream market values [12]. Examples are the transistor, the personal computer and the Winchester® disc drive. The system in a package could be such a technology for the passives industry. Already there are the alliances of packaging houses/contract assemblers/OEM such as Amkor/Flextronics/ Ericsson. What will be the product format for R, C &L's in the future? Who will own this business within the supply chain? These are the issues before us.

Figure 17: Fragmented Supply Web of Microelectronics Industry

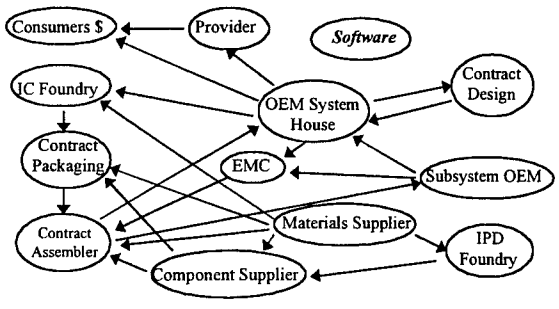

REFERENCES

1) R.H.Heistand II, J.Hock, R. M. Kennedy III, G.Korony, D.Liu & A.P.Ritter, *Proceedings of 36th IMAPS Nordic Conference*, Helsinki, Sept. 19-22, 41-46 (1999).

2) *National Electronics Manufacturing Technology Roadmaps-2000*, National Electronics Manufacturing Initiative, Inc., 2214 Rock Hill Road, Herdon, VA 22070-4005

3) A. Ritter, M. Strawhorne, B. Smith, A. Templteton, and R. Heistand, *Int. J. of Microelectronics and Electronic Packaging*, Vol. 21, No.4, 334-340 (1998).

4) A.Ritter, B. Smith, R.H.Heistand II, *Proc. 99' International Symposium on Microelectronics*, Chicago IL, Oct 26-28 (1999)

5) A. Ritter, and J. Galvagni, *Multilayer RC Device*, U.S. Patent 5,889,445.

6) J.R. Rellick and A. Ritter, *Proc. 99' International Conference on HDP and MCM's*, Denver CO, April 6-9, 420-424 (1999)

7) D. Liu and J. Mevissen, *Integrated Ferroelctrics*, 18, 263-274 (1997).

8) D. Liu, R.M.Kennedy, G. Korony, S.Makl, J.P.Mevissen, J.M.Hock, R.H.Heistand II, *Proc. 99' International Conference on HDP and MCM's,* Denver CO, April 6-9, 431-437 (1999)

9) G. Korony, A.Ritter, C. Gonzalez-titman, J. Hock, J. Galvagni, R. Heistand II, *Proc. 01' International Symposium on Microelectronics*, Baltimore MD, Oct 9-11 (2001).

10) A. I. Kingon, J-P. Maria, TY Kim, *Proc. 01' International Symposium on Microelectronics*, Baltimore MD, Oct 9-11 (2001)

11) W.Borland and J.J.Felten, *Proc. 01' International Symposium on Microelectronics*, Baltimore MD, Oct 9-11 (2001)

12) C.M.Christensen, "The Innovator's Dilemma," Ed. by M.L.Tushman and A.H. Van de Ven, Harvard Business School Press, Boston p xv.

Micromachined Capacitor Ultrasonic Transducers

Butrus T. Khuri-Yakub, Mustafa Karaman, Ching-Hsiang Cheng, Sanli Ergun, Goksenin Yaralioglu, Baris Bayram, Utkan Demerci, Sean Hansen, Mohammad Badi, and Omer Oralkan

Edward L. Ginzton Laboratory
Stanford University
Stanford, CA 94305-4085
USA
FAX: 650.725.2533
Email: Khuri-yakub@stanford.edu

This paper will review the use of capacitor micromachined ultrasonic transducers for the generation of longitudinal waves in gases and liquids, Lamb waves in plates, and surface waves on half spaces. Such transducers have the advantage of being fully made by surface silicon micromachining, thus enabling any type of transducer geometry by photolithography, and the possibility of electronic integration. We will present a theory that predicts the performance of the capacitor as a transducer of various modes of propagation. Next, we will present a silicon micromachining technology for making the transducers. Finally, we will present experimental results showing the performance of capacitor transducers in air (single element), water (single element, one-dimensional array, and two-dimensional arrays), and as a Lamb wave transducer on a silicon substrate. In all these applications, we will demonstrate that the capacitor transducer is a viable alternative to piezoelectric transducers. In air applications, the capacitor has a dynamic range of over 100 dBs in 100 kHz bandwidth, while in water it has over 140 dB dynamic range in 1 Hz bandwidth. For the first time, we will also show efficient excitation of A0 Lamb waves and surface waves on silicon plates.

INTRODUCTION

Capacitors have long been used as ultrasound transducers [1]. Conventional designs have relatively large gaps, 50-100 μm, and use the air in the gap as the restoring force of the vibrating electrode. These transducers thus suffer from low efficiency because of the relatively large gap height, and low DC electric field in the gap of the capacitor. We propose a design where silicon micromachining is used to define the capacitors. The gaps are made to be as small as 500 Å, and the restoring force of the vibrating electrode is the stiffness of the electrode itself, and electric fields in the 10^9 V/m are attained. This approach makes possible the fabrication of very efficient transducers. Indeed, it makes possible transducers that compete with piezoelectric transducers in terms of efficiency and bandwidth [2,3]. One advantage of these transducers is that they allow integration of electronics components on the same silicon wafer. Another is the potential for fabricating one-dimensional, two-dimensional, and annular arrays of transducers using simple photolithography. Finally, the micromachined capacitors can be used as transducers for plate modes, that is Lamb and surface waves.

ELECTRICAL EQUIVALENT CIRCUIT MODEL OF THE TRANSDUCER

We use Mason's model to represent the capacitor transducer [4]. A schematic of the transducer and its equivalent circuit is shown in Fig. 1. A metal-coated silicon nitride membrane is used as the vibrating electrode of the capacitor. Standard integrated manufacturing processes are used to define the dimensions

of the capacitor. Residual stress in the membrane is controlled via the process of chemical vapor deposition and is held at around 100 MPas [5].

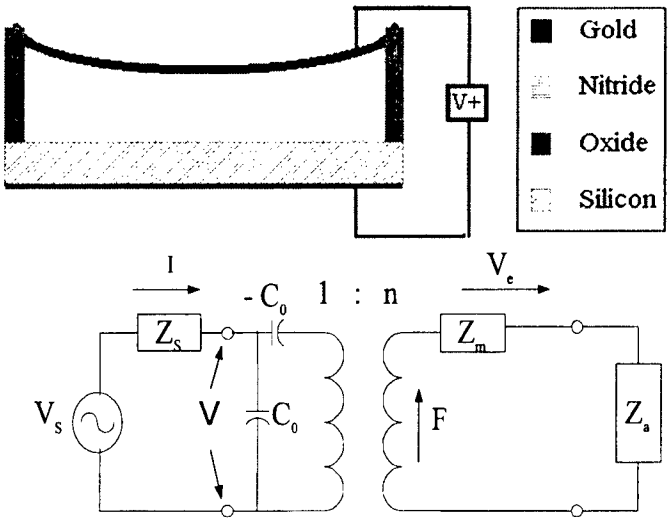

Fig. 1 Schematic diagram of a capacitor transducer and its electrical equivalent circuit.

In the equivalent circuit, C_0 is the capacitance of the device, Z_s is the impedance of the source, Z_a is the impedance of the medium (air or water), and Z_m is the mechanical impedance of the circular membrane of radius 'a" which is given by:

$$Z_m = j\omega\rho l_t\left[\frac{ak_1k_2\left(k_2J_0(k_1a)J_1(k_2a)+k_1J_1(k_1a)J_0(k_2a)\right)}{ak_1k_2\left(k_2J_0(k_1a)J_1(k_2a)+k_1J_1(k_1a)J_0(k_2a)\right)-2\left(k_1^2+k_2^2\right)J_1(k_1a)J_1(k_2a)}\right] \quad (1)$$

where ω is the radian frequency, ρ is the density of the membrane, l_t is the thickness of the membrane, J_0 and J_1 are the zeroth and first-order Bessel functions of the first kind and k_1 and k_2 are given by:

$$k_1 = \sqrt{\frac{\sqrt{d^2+4c\omega^2}-d}{2c}}, \quad k_2 = \sqrt{\frac{\sqrt{d^2+4c\omega^2}+d}{2c}}, \quad c = \frac{\left(Y_0+T\right)l_t^2}{12\left(1-\sigma^2\right)} \quad \text{and} \quad d = \frac{T}{\rho}, \quad (2)$$

where Y_0 is Young's modulus, T is the residual stress and σ is the Poisson's ratio of the membrane material. The impedance of the membrane can be represented by a series resistance-inductance-capacitance (RLC) circuit with a resistance corresponding to the loss in the membrane.

The transformer ratio in the equivalent circuit is given by:

$$n = V_{dc}\frac{\varepsilon_0\varepsilon^2 S}{\left(\varepsilon_0 l_t+\varepsilon l_a\right)^2}, \quad (3)$$

where V_{dc} is the dc bias on the electrode, ε_0 is the dielectric constant of the free space, ε is the dielectric constant of the membrane material, S is the area of the transducer and l_a is the thickness of the air gap.

The importance of the approach we propose lies in the fact that the transformer ratio can be made very large. The capacitance of the capacitor can be 10 s of pFs, and the electric field can be as high as 10^9 V/m. This high electric field is achieved because the gap of the capacitor can be made to be as small as 500 Å. It is easy to see why the sensitivity of these capacitors is markedly higher than that of the earlier designs. The gap being several orders of magnitude smaller results in a relative change in capacitance that is the same number of orders of magnitude higher.

In a typical capacitor, each membrane is in the range of 20-100 microns in diameter. Thus, to fabricate a transducer, a very large number of membranes are electrically connected in parallel using a lithography step. This use of lithography allows the manufacture of single elements, or array elements side by side on the same wafer and in one step.

In an air transducer, the impedance of the membrane at resonance is zero and comparable in value to the impedance of air over the bandwidth. The transducer exhibits a characteristic RLC resonant behavior. Without dc bias, the real part of the input impedance is zero and the imaginary part is that of a capacitor. As the dc bias is applied, the resonant membrane introduces a real resistance resonant peak that represents real power coupled into the sound, and the imaginary part shows the characteristic acoustic "N" corresponding to potential and kinetic energy storage.

In immersion transducers the impedance of the membrane is smaller than the impedance of water and can be ignored. Thus, the input impedance of an immersion transducer has no resonance and consists only of an RC circuit in series (or parallel) [6]. Thus, impedance matching of the electronics to the RC circuit determines the bandwidth and efficiency of the transducer.

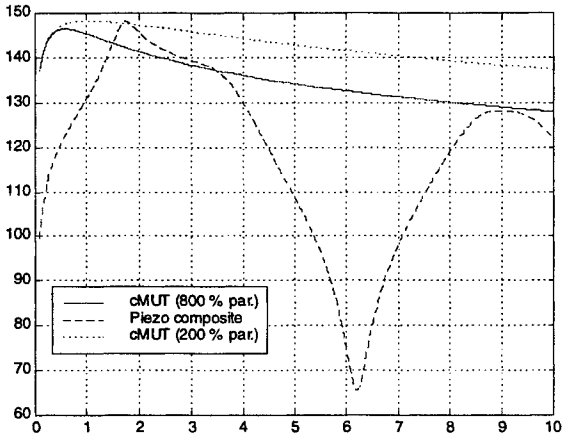

Fig. 2 Comparison of the dynamic ranges of a cMUT and a piezoelectric transducer.

The performance of a cMUT and a piezoelectric transducer are compared. For comparison, we use a square element with a side of 0.4 mm as the subject of our research program. The design calls for a center frequency of operation of 3 MHz with a bandwidth enabling operation at 0.75 MHz. The KLM model is used to represent the piezoelectric transducer, and the Mason model outlined above is used to represent the

cMUT. For the piezoelectric transducer, we use PZT 5H for the piezoelectric material and assume a perfect match into water using one matching layer. The cMUT has an air gap of 1500 Å, a silicon nitride membrane thickness of 8000 Å, a cell radius of 18 μm, and operates at a dc voltage of 100 V.

The performance of each device as a transmitter is determined by calculating the pressure at the face of the transducer that is generated by applying 1 V at its input terminals. The receiver sensitivity is calculated by evaluating the signal-to-noise level of the received voltage for an input pressure of 1 Pa at the face of the transducer. This signal-to-noise is calculated assuming an amplifier with an input resistance of 300 kΩ and capacitance of 0.3 pF. The total dynamic range of the system is calculated by adding together the transmitter and the receiver sensitivities for each transducer. Figure 2 shows the results of this comparison.

It is seen from Fig. 2 that the cMUT can have as good a dynamic range as a piezoelectric transducer over a much larger bandwidth. The minimum insertion loss and bandwidth are determined by electrical matching considerations of the transducer to the electronic circuit.

TRANSDUCER FABRICATION

Standard integrated circuit fabrication processes are used to fabricate the cMUT. Figure 3 shows the process presently used for fabricating transducers. First, the silicon wafer receives a high-doping-density ion implantation for formation of the back contact of the capacitor. Then, a layer of insulating silicon nitride is deposited to protect the back contact and as an etch stop. An amorphous silicon sacrificial layer is deposited over the wafer. The sacrificial layer is defined by photolithography. The amorphous silicon is left in regions that are to become vacuum gaps. Another silicon nitride layer is deposited over the amorphous silicon. Holes are defined at the edges of the amorphous silicon which are then removed by wet etching. Silicon nitride is again deposited and used to plug the holes through which the etching fluid was introduced. Finally, an aluminum layer is deposited over the wafer to define the top electrode of the capacitor. An optical image of a finished device is shown in Fig. 4.

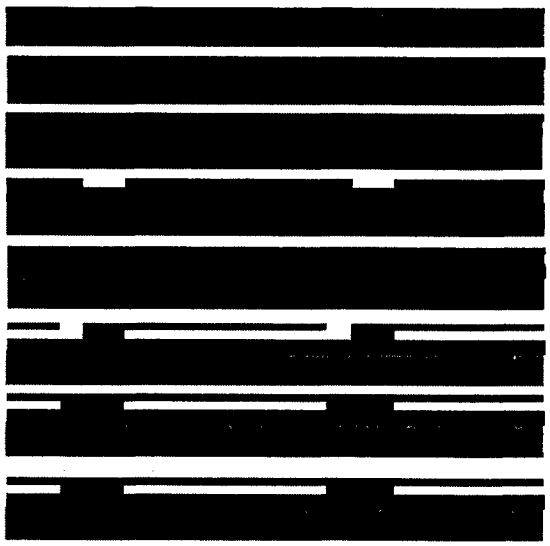

Fig. 3 Schematic of the processing schedule for fabricating cMUTs.

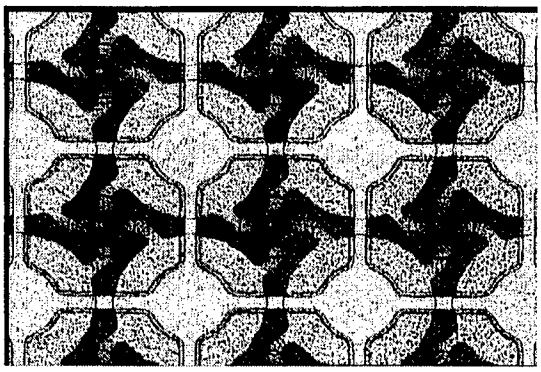

Fig. 4 A finished cMUT.

The individual cells are connected electrically in parallel using aluminum metal. The metal over each cell is clearly seen to be one half of the diameter of each cell. The size of the electrode is decreased to reduce the capacitance of the device without reducing the displacement at the surface of the membrane.

EXPERIMENTAL RESULTS

Immersion and air transducers are evaluated via measurements of their electrical input impedance, input response and bandwidth, beam profile and insertion loss. In order to fit the measured impedance of a transducer to the theoretically predicted value, a loss term has to be added to account for the insertion loss of the transducer, and a parasitic capacitance term has to be included to accurately predict the imaginary part of the impedance.

The impulse response of an immersion transducer is shown in Fig. 5. The impulse response of the transducer shows the large bandwidth that is characteristic of cMUTs. The measured fractional bandwidth is over 100%, which is limited by the electronics and not the transducer. Measurement of the insertion loss of the device shows that there is a one-way loss of 5 dB that is due to coupling into the propagation modes of the wafer.

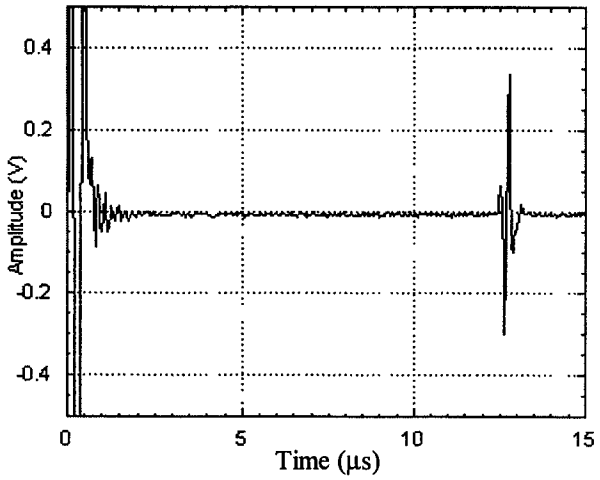

Fig. 5 Impulse response of an immersion cMUT transducer.

One of the main features of the cMUT technology is that it allows the use of photolithography to define one-dimensional or two-dimensional arrays. Another feature of cMUT arrays is that they have a thin profile, equal to the thickness of the silicon wafer. Thus, arrays can be made small to fit in tight spaces. Electronic circuits can be integrated on the same wafer as the transducers. Or, the transducer wafer can be flip-chip bonded to an electronics wafer without a significant increase in the profile of the array.

Figure 6 shows a 64-element 1-D array. The elements of the 1-D array are on 0.4 mm centers and are each 5.6 mm long. Each element consists of a number of cells that are connected in parallel in the same fashion as in single-element transducers.

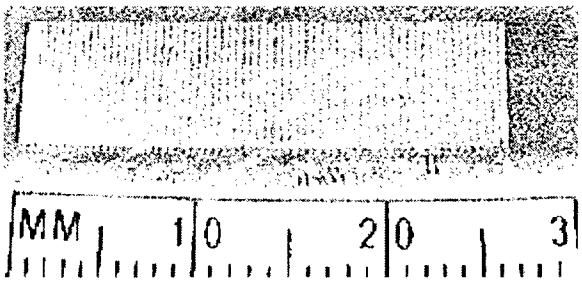

Fig. 6 A 1-D array of transducers.

The 64-element 1-D array was used to image a 0.4 mm x 0.4 mm (active area of 0.28 mm x 0.28 mm) transmitter which is placed 5 cm away in the plane perpendicular to the center of the array. The point source is excited with a pulse and all 64 elements in the array are used to receive the signal from the transmitter. Each received signal has a time delay associated with the distance between the transmitter and receiver. Typical medical imaging reconstruction algorithms are used to image a six-wires phantom as shown in Fig. 7.

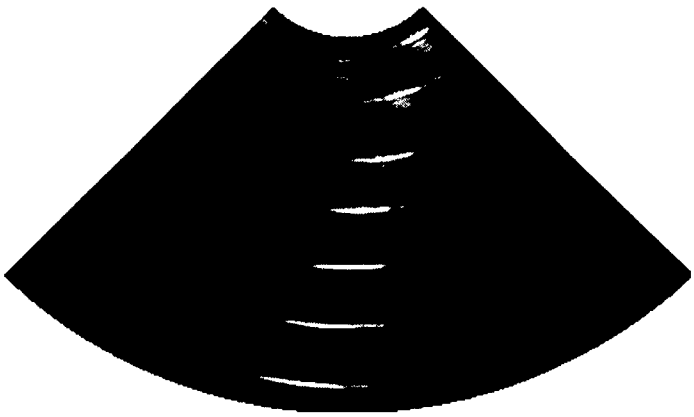

Fig. 7 Reconstructed image of a six-wires phantom at 30 dB signal-to-noise ratio.

The elements of the 1-D array excite Lamb waves in the silicon wafer. This energy leaks back into the fluid and introduces ripples in the beam profile of an array element. Another source of cross talk between elements is the interface wave that propagates at the silicon water interface. These sources of cross talk and ripple in the impulse response of the transducer and its beam profile are subject of ongoing research.

Two-dimensional arrays can also be made using the same process as described above. However, there needs to be some means to connect each individual element. One method for establishing electrical connection to each element in the 2-D array is with filled through-wafer vias as shown in Fig. 8. Again, each element of the 2-D array is constructed by connecting in parallel a number of individual cells.

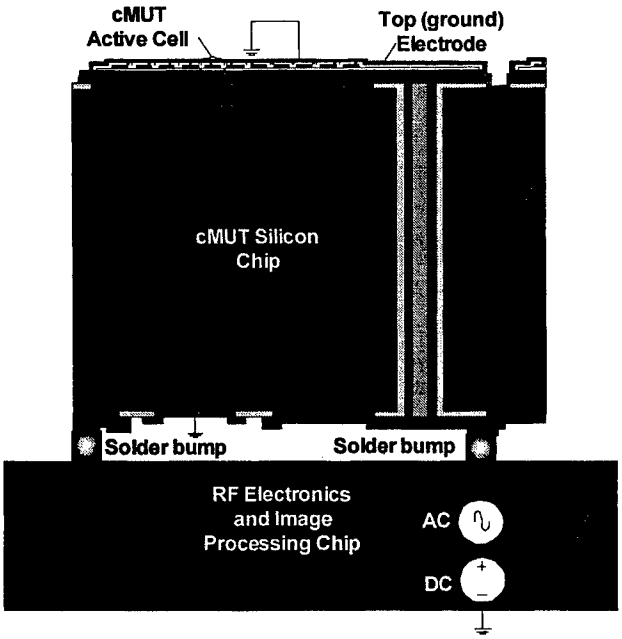

Fig. 8 Schematic diagram of a 2-D array element with a through-wafer via.

The measured acceptance angle of a 2D array element is in excellent agreement with theoretical predictions, as shown in Fig. 9. There is a slight ripple in the acceptance angle at 12° and 22° where the lowest-order antisymmetric and symmetric Lamb waves are excited at 4 MHz in a 0.5-mm-thick silicon wafer.

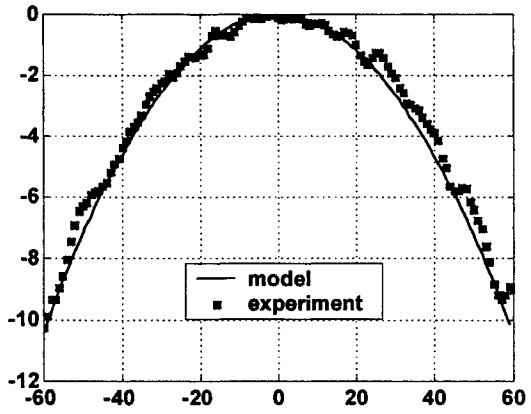

Fig. 9 Beam profile of a 0.4 mm x 0.4 mm element of a 2-D array at a frequency of 3 MHz.

The dynamic range of a 2-D element in the array is measured using a calibrated hydrophone (Specialty Engineering Associates model # PZT-Z44-0400). The output pressure at the face of the transducer, for an input voltage of 1 V, is about 20 kPa with a flat frequency response from 1 MHz to 10 MHz over the range of calibration of the hydrophone. The receiver signal-to-noise ratio is 45 dB/Pa/Hz. As seen from Fig. 10, the total dynamic range is then found to be about 130 dB/Volt/Hz. This dynamic range can be further increased by 10 dB using an amplifier with a better noise figure and by reducing the parasitic capacitance of the device. The minimum detectable pressure was measured to be 5 mPa/$\sqrt{Hz}$, which corresponds to a detectable displacement of 2.5×10^{-16} m/$\sqrt{Hz}$. Again, this minimum detectable noise floor can be further reduced by using a lower noise amplifier and a transducer element with a lower parasitic capacitance. The dynamic range plot shows a ripple around 1.5 MHz, which is further evidence of the coupling into Lamb waves that can be reduced.

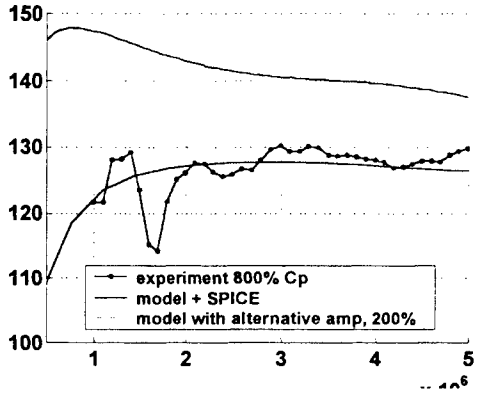

Fig. 10 Measured dynamic range of a 0.4 mm x 0.4 mm element of a 2-D array element.

As the vibrating elements are anchored into the silicon wafer, they couple energy into the substrate through their anchors. Through this means, it is possible to design transducers to couple Lamb waves and surface waves into the silicon. We calculate that at low frequencies the coupling is mostly into the lowest order Lamb waves, whereas at high frequencies, the coupling is dominated by the surface waves. Fig. 11 shows a design for a transducer for coupling the lowest order Lamb wave into the silicon wafer.

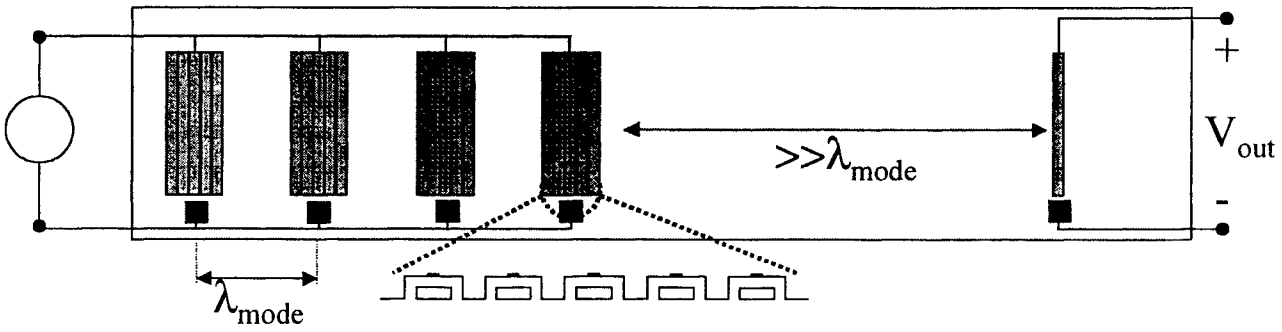

Fig. 11 Schematic diagram of a delay line using capacitor inter-digital transducer for the excitation and detection the lowest order anti-symmetric Lamb wave.

The transducer of Fig. 11 was designed to operate around 1 MHz, and the result of a through transmission experiment with this delay line is shown in Fig. 12.

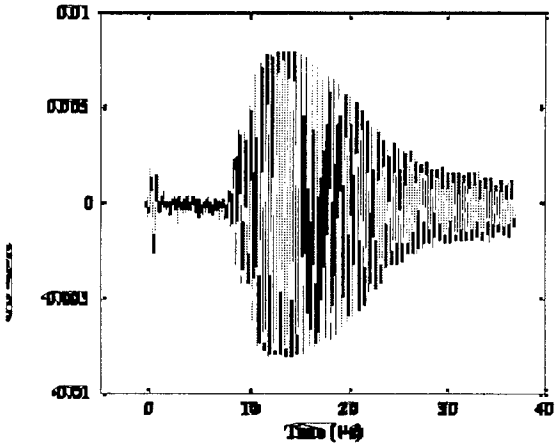

Fig. 12 Transmission through a Lamb wave delay line using capacitor interdigital transducers.

More work is needed to improve the performance of the interdigital transducers, however this experiment proves that it is possible to use cMUT structures to transmit and receive Lamb waves.

CONCLUSIONS

Silicon micromachining can be used to fabricate capacitive ultrasonic transducers that can compete with piezoelectric transducers in terms of efficiency and bandwidth. The main reason for the promise of cMUTs is the fact that the electric field in the gap of the capacitors can be made as high as 10^9 V/m. Researchers in the field have recognized this fact for almost 100 years now. Only the advent of silicon micromachining has enabled this capability and brought cMUTs to the competitive edge they now demonstrate. Theory predicts the performance, and only manufacturing and characterization issues remain to be solved. Besides performance, silicon micromachining also adds the promise of ease of manufacture of one-dimensional and two-dimensional arrays and of integration with electronic circuitry.

ACKNOWLEDGMENTS

We are grateful for the support of the Defense Advanced Research Agency, the Air Force Office of Scientific Research, and the Office of Naval Research.

REFERENCES

1. W. Khul, G.R. Schodder, and F.K. Schodder," *Acustica,* 4, 520 (1954).
2. M. I. Haller and B. T. Khuri-Yakub, *IEEE Trans. UFFC*, 43, 1 (1996.
3. I. Ladabaum, T. Soh, X.C. Jin, A. Atalar and B. T. Khuri-Yakub, *IEEE Trans. UFFC*, 45, 698 (1998).
4. W. P. Mason: *Electromechanical Transducers and Wave Filters*, 2nd ed (1948).
5. X. C. Jin, I. Ladabaum, and B. T. Khuri-Yakub, *IEEE/ASME J. Micro-Eelectro-Mechanical Syst.,* 7, 295 (1998).
6. X. C. Jin, I. Ladabaum, and B. T. Khuri-Yakub, *Proc. IEEE Workshop on Microelectromechanical Systems,* 649 (1998).
7. X. C. Jin, F. L. Degertekin, S. Calmes, X. J. Zhang, I. Ladabaum, and B.T. Khuri-Yakub, *Proc. IEEE Ultrasonic Symp.,* 1877 (1998).

Recent Developments in Dielectrics and Piezoelectrics in Europe

Andrew J. Bell
University of Leeds, Department of Materials, Leeds, LS2 9JT, UK
FAX: +44-131-242-2531
E-mail: a.j.bell@leeds.ac.uk

ABSTRACT

Recent activity in Europe in the field of dielectric and piezoelectric ceramics is reviewed. Details are given relating to dielectrics and piezoelectrics both in bulk ceramic and thin-film forms, with some attention given to the increasing activity on piezoelectric single crystals. Material relating to basic science, materials processing and properties, and device fabrication and characterization is presented. In addition to highlighting the prominent laboratories and significant advances in the field, attention is given to recent measures taken to promote collaboration within Europe. In this context, a number of the major EU funded collaborative projects are also examined.

INTRODUCTION

Research on piezoelectric and dielectric ceramics is flourishing in Europe. Although, due to increasing globalization, larger companies are perhaps carrying out less fundamental work, and perhaps undertaking fewer, but better targeted development programs, work within universities and nationally funded laboratories in this field continues to increase.

This paper identifies the key laboratories contributing to the growth in work in this field, by reviewing the more significant contributions over the last 18 months. The environment that both the EU and national governments are creating to help this growth is examined. In this context a number of collaborative projects befitting from EU funding are covered in detail.

SOCIO-ECONOMIC MEASURES

The EU's Framework V is a program of industrially led research and development, benefiting from €15 billion. As funding to industry is provided at a rate of 50% of eligible costs, the total program is worth over €25 billion. To qualify for support, projects must have participants from at least 2 different EU member states, but partners from Associated States (including most of Eastern Europe) may also participate. For the first time recently, jointly funded projects with the US National Science Foundation were also made possible. Mainstream research and development projects may typically have 8 partners, the majority being industrial, but with a number of universities or other RTOs in support. Most projects last 3 years, with a total budget of €3 to €5 million. The projects are inclined towards "problem solving" which in the context of electronic materials means "product development", with little significance given to major programs of fundamental or basic research. Hence materials research tends to be carried out under the umbrella of device or systems development.

In addition to the funding of major development projects, Framework V also provides a number of measures to stimulate cross-border collaboration. One such measure is known as a Thematic Network and provides funding for a wide range of laboratories to participate in activities intended to result in a greater exchange of information and opportunities to identify new partners for collaboration.

This year saw the launch of a major new Thematic Network, known as POLECER, covering the field of dielectric and piezoelectric ceramics. Coordinated by Ferroperm Piezoceramics A/S of Denmark, POLECER brings together 43 different laboratories including 5 from each of Germany, France and UK, 3 from each of Spain, Italy, Norway and Romania and 2 from each of Sweden, Denmark, Poland and the Czech Republic. Other representatives are from Ireland, Portugal, Latvia, Lithuania, Finland, Israel, Slovenia and Switzerland. Approximately one third of the members are industrial laboratories, whilst universities account for over half the partners, the rest being national laboratories or research institutes. Activities undertaken within POLECER include workshops, summer schools, database compilation exchange programs and dissemination, with key areas including thick-film piezoelectrics, particularly for ultrasonic

motors, thin piezoelectric plates, high frequency applications, environmental aspects and next generation materials. The total EU funding is approximately €2.2 million, mostly for travel, but some labor costs for co-ordination of the Network and its workgroups.

Similar activities are also promoted at the national level. For example, the UK's Engineering and Physical Sciences Research Council (EPSRC) have this year approved funding of €100,000 for a Ferroelectric Materials Network, coordinated from the University of Leeds. This will help the 22 UK academic groups and approximately 15 industrial partners coordinate their activities, including an annual national conference.

EU FUNDED PROJECTS

There are at present approximately 20 projects on the European Commission's database with dielectric, capacitor or piezoelectric as keywords, most of the projects involve piezoelectric materials development, indicating both the growth in new piezo-devices and applications and the renaissance in materials development sparked by (i) the impending environmental legislation and (ii) the discovery of new piezoelectric materials. The following are examples of the key projects, funded under the EU's Framework V Program, with significant content in the field of piezoelectrics:

Piramid

The full project title is "High sensitivity novel piezoceramics for advanced applications – textured, thick films and multilayer structures". The partners are Ultrasons (F), Thomson-CSF (F), Bruel & Kjaer (DK), Thomson Marconi Sonar (F), EPFL (CH), Institute of Materials Science, Madrid (E), Xaarjet AB (S), Medizintechnik Basler (CH), Ferroperm Piezoceramics (DK), Nanomotion Ltd (Is), Vermon SA (F), Norwegian Institute of Technology (N), Josef Stefan Institute (SL).

The program focuses on the development of relaxor-ferroelectric solid solutions, employing sol-gel synthesis and texturing by casting and hot-forging. Two demonstration applications are a sonar transducer and inkjet print-head.

Leaf

The LEAF program focuses on "Lead-free piezoelectric ceramics based on alkaline niobates", with partners including Ferroperm Piezoceramics (DK), Josef Stefan Institute (SL), Forschungzentrum Juelich (D), Ultrasons (F), Simrad (N), Ceram AB (S), EPFL (CH), Institute of Materials Science, Madrid (E) and Karl Deutsch (D). As the title suggests the aims are to develop lead-free materials around (Na, K)NbO_3 compositions. Advanced ceramic processing techniques are proposed to circumvent the normally poor densification of these materials.

Doris

The DORIS program is aimed at the growth and application of single crystal perovskites for medical imaging. The consortium, consisting of Veron SA (F), Institut fur Kristallzuchtung, Berlin (D), EPFL (CH), Forschungsinstitut fur Edelsteine und Edelmetalle (D), CEA, Grenoble (F) and Mateck (D), aim to grow both "conventional" lead based and lead-free crystals. The program continues until the start of 2003, but at present no data is being made available.

Pads

The objective of the PADS project is to develop long-travel, low-cost, small, high efficiency, high speed actuators for applications in digital loudspeakers and phase array antennas. The consortium consists of 1...Ltd (GB), Marconi Caswell (GB), University of Birmingham (UK), Laboratoire Ondes et Acoustique (F), UMIST (UK) and the University of Erlangen (D). The actuators are based upon helical piezoelectric ceramic bimorph structures with embedded electrodes, a lightweight core and a gas bearing (Fig. 1). The ceramic processing route relies heavily upon the viscous plastic processing route originally developed by ICI in the UK and now exploited by the University of Birmingham. The route is proving exceptionally useful where near-net shaping is required, e.g. curved or complex shapes.

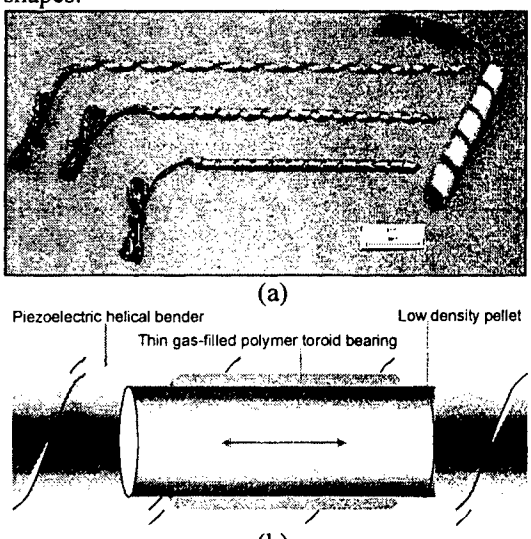

Fig 1. (a) Helical piezoelectric ceramic bimorphs and (b) the principle of the "PADS" project actuator.

Parmenide

The full title of the project is "Piezoelectric Array for Medical Imaging and Non Destructive Control using Integrated Micro Electro Mechanical Devices" and involves partners from Thomson CSF and Microsonics (F), Fraunhofer Institute for Biomedical Technology (D), Service Ultrasound Microsystems (D), EPFL (CH), Cranfield University (GB) and Protavic (F).

The project objective is to develop cheaper and better ultrasonic transducers using piezoelectric films and micro-machined silicon. To reach this objective two structures are to be designed and manufactured :

- ultrasonic arrays in the 3-10 MHz band, to be applied in the real-time trans-thorasic imaging
- air transducers for non destructive industrial testing

The actuation principle is the unimorph piezoelectric bender. In this basic example, the piezoelectric film actuates a silicon membrane made by bulk micro-machining (Fig. 2).

The PZT is deposited on a SOI (Silicon On Insulator) wafer, which is micro-machined on the back-side. Through chip interconnects and bonding techniques are being developed with the aid of deep reactive ion etching to achieve a final array structure.

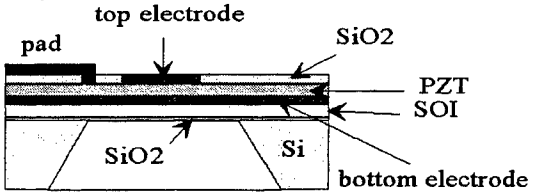

Fig. 2. Structure of a simple PZT on silicon unimorph element

The PZT is being deposited by a conventional sol gel process for films between 0.2 and 1 μm. Two additional processes are being investigated: direct photo-patterning of the gel precursor and composite powder gel-precursors to minimize shrinkage during the processing of thicker films

ANSYS and ATTILA finite element methods are being used for modeling the unimorph characteristics.

Medcom

The slightly misleading acronym represents "Microwave electroacoustic devices for mobile and land based communications", a project with partners from Uppsala University (S), EPFL (CH), Balzers (LN), Thomson Microsonics (F), Phillips Semiconductors (D), Ericsson Microwave Systems (S). As the title suggests, the partners predict that the next generation of microwave acoustic devices for communications will be based on piezo-thin films on various substrates such as silicon, glass and polycrystalline diamond. The piezoelectric materials being studied include PVD deposited PZT and AlN. The demonstrator devices will include both SAW and BAW prototypes in the 2 to 7 GHz band to be built.

MAJOR PLAYERS

The above highlights of the EU program may be somewhat misleading, as the projects cited appear to be dominated by a rather small number of university laboratories and industrial players. The true picture is one in which there is far wider representation. However, it is probably true to say that in recent years, two groups have been particularly prolific, that of the Laboratoire de Ceramique at EPFL in Lausanne, Switzerland and the joint efforts of the Technische Hochschule, Aachen and Forschungszentrum, Juelich. During the preparation of this paper, both Professor Setter (Lausanne) and Professor Waser (Aachen) were asked to identify the most significant contributions of their groups in the last two years.

The lists are reproduced here, edited only to moderate the number of superlatives.

Lausanne:

- Understanding the nucleation and growth kinetics of oriented PZT ([111] and [100]) on various electrodes
- PZT thin films with excellent electromechanical properties (e_{31}).
- PMN thin films with high permittivity and relaxor behavior ($\varepsilon_{max} = 7500$).
- Theory/modeling to show that stresses induce rounding of the dielectric maximum in thin films.
- A model of fatigue and size effects in ferroelectric films; modification of the films to practically to eliminate fatigue
- Ferroelectric film response to nanosecond driving signals: physical aspects of switching and polarization losses.
- Direct observation of polarization inversion as a function of depth in thin films.
- Piezoelectric filters (BAW devices) integrated onto silicon.
- Polar, epitaxial AlN on Si.
- Proof of presence of Pb on the B site of sputtered PZT.
- Screen-printed PZT, PMN and PMN-Pt on Si with excellent properties.

- A new type of simple/cheap high-force high-displacement actuator.
- Theory/modeling to predict level of losses in paraelectrics at GHz; differentiation intrinsic and extrinsic effects.
- Demonstration, analysis and modeling of Maxwell-Wagner piezoelectric relaxation in ferroelectric heterostructures.
- Preisach modeling of non-linearity in piezoelectric ceramics.

Aachen/Juelich:
- MOCVD of BST films, smooth over 6".
- Understanding imprint of FE films.
- Understanding the switching kinetics of FE films.
- Understanding the relaxation, leakage & degradation of BST films.
- Understanding the defect chemistry of grain boundaries in acceptor doped titanates.
- Microstructure control of titanate films by CSD.
- In-plane AFM piezo-response analysis of FE films.
- Nanosized single FE grains on wafers.

The emphasis on thin films in both the Lausanne and Aachen portfolios perhaps redresses the balance in the lack of attention in the EU sponsored programs.

GENERAL SURVEY

It would be wrong to over-focus attention on two laboratories alone. As suggested above, there is a very wide range of activities in laboratories throughout Europe. The following sections highlight only a few of the current activities, with apologies to those who have been overlooked.

Basic Science

IR Studies: Petzelt, Kamba and co-workers at the Institute of Physics, Academy of Sciences of Czech Republic continue to exploit their expertise in FTIR reflectivity and Raman and micro-Raman spectroscopies, but with the addition of novel techniques unique in the field of dielectrics. These include:
- Time-resolved THz spectroscopy based on pulsed femtosecond Ti-sapphire lasers (complex transmittance in spectral range 3-80 cm^{-1});
- Monochromatic coherent source spectroscopy based on tunable backward-wave-oscillator sources (complex transmittance and reflectivity in spectral range 3-40 cm^{-1} in collaboration with University of Stuttgart and General Physics Institute RAS Moscow).

Recent achievements include:
- Ferroelectric soft-mode studies in thin films (PZT, PLZT, BST, SBT); evidence of over-damped soft mode in most of the films; under-damped soft mode seen in PTO and STO; Most interesting – saturation of the low temperature mode softening in STO films as the main reason for the much lower permittivity compared with bulk materials.[1]
- Detailed spectroscopic evidence of polar grain boundaries in nominally pure STO ceramics.[2]
- Incipient soft mode behavior in CTO crystals and ceramics.
- Detailed FIR study of the antiferroelectric phase transition dynamics in PZO ceramics and crystals; evidence of strong anharmonicity and central-mode phenomena.[3]
- Phase transition dynamics in $Cd_2Nb_2O_7$ pyrochlore crystals – evidence of strong anharmonicity and mode-coupling.[4]
- Wide-frequency study of the dielectric dispersion in relaxor PLZT ceramics (including microwave and IR range) – evidence of essential contribution from polar cluster walls dynamics.[5]
- Study of sub-mm losses in many microwave ceramics – possibility to extrapolate down to the microwave range and estimate the intrinsic losses.[6]

Aurivillius Phases: Crystallographic studies at the University of St. Andrews (Hervoches & Lightfoot) has thrown new light on the phase transitions on the Sr-Bi-Ti series:
- $Bi_4Ti_3O_{12}$ - The ferroelectric distortion is shown to be driven by the coordination requirements of Bi in the perovskite A-site.
- $Sr_{0.85}Bi_{2.1}Ta_2O_9$ - The transition at T_c is unambiguously shown to be $A2_1am$ to Amam. The transition to the parent tetragonal phase occurs at a much higher temperature. This supports previous suggestions based on electron diffraction.
- $SrBi_4Ti_4O_{1\ 5}$. The room-temperature structure is confirmed as $A2_1am$, in agreement with previous suggestions for an all "even-layered" structures. The intermediate Amam phase was not seen

Microwave Materials

Many of the IR studies in Prague have been in collaboration with other workers in Europe on either dielectric resonator or thin film varactor

materials. There is activity on new compositions in a number of groups throughout Europe. For example, work at the University of Sheffield, UK (Reaney et al) is currently focusing on layer structures (e.g. $SrTiO_3$-$SrNb_2O_6$) in which the layer ratio may be used as a means of tuning the temperature coefficient of resonant frequency.

At South Bank University in the UK, Alford and co-workers have made excellent use of low temperature microwave measurements on resonators to elucidate loss mechanisms as a function of dopant in TiO_2 ceramics. This has aided the in the development of a composite approach to a temperature stable ultra-high Q resonator (Q.f = 300,000, τ_f = 0 MK^{-1}) for satellite applications (Fig. 3).

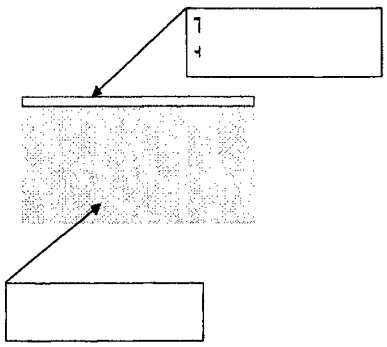

(a)

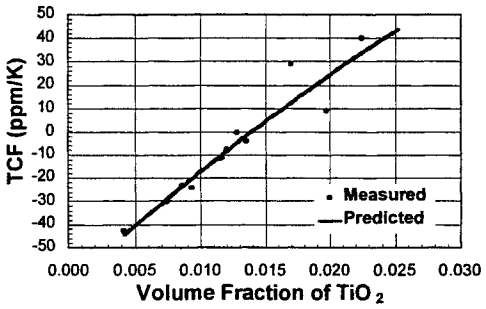

(b)

Fig 3. (a) Concept of composite resonator and (b) comparison of model and experimental data for τ_f as a function of TiO_2 volume fraction.

Piezoelectric Ceramics

In addition to work on various aspects of the processing and properties of PZT, more "topical" issues are being addressed by a number of groups. The search for lead-free dielectrics is progressing outside the EU LEAF program. $(Na,Bi)TiO_3$-based materials attract much attention with interest in most countries of the EU, even those not previously associated with a high level of activity in this field (e.g. Italy[7]).

The development of thick-films is also a key theme, with processes having been developed at the Jo_ef Stefan Institute in Slovenia, EPFL in Switzerland, and Cranfield in the UK. Much of the thick-film work is directed towards MEMS type actuators, where thin films do not provide sufficient force. Other MEMS oriented developments focus on methods of complex shape-forming. Ink-jet printing is being developed both at the Manchester Materials Science Centre and Queen Mary College in the UK.

Excellent structures have also been obtained in Sweden by replication process from photolithographically defined moulds, (Fig. 4).

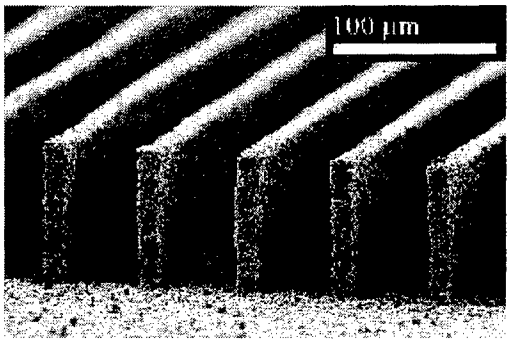

Fig. 4. SEM of replicated PZT micro-ridges (Rosqvist and Johannsson, University of Uppsala, Sweden).

Thin Films

As evidenced by the output from Lausanne and Aachen, thin film research is still very much a hot-topic. Much of the work in Universities is dominated by sol-gel techniques. Progress on new chemical routes has been made in Slovenia, and at Cranfield (UK), Leeds (UK), EPFL (CH), Aachen (D), etc. (It would seem that few European laboratories in this field, can meet the costs associated with MOCVD techniques, Aachen being an exception). Novel device work is less common. Cranfield have used sol-gel deposited PZT to produce prototype bulk acoustic wave resonators, with some success (Fig. 5).

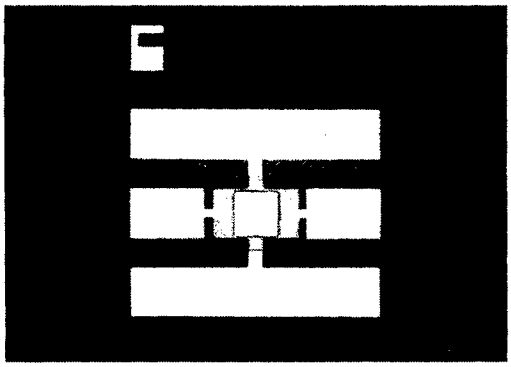

(a)

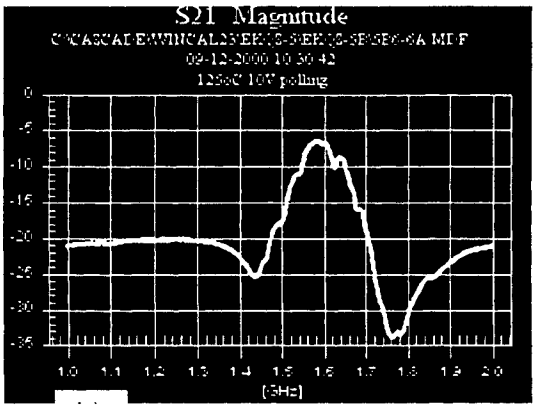

(b)

Fig. 5. (a) PZT FBAR resonator and (b) insertion loss as a function of frequency.

Pulsed laser deposition is gaining favor for complex materials or for carrying out model experiments. Workers at Queen's University, Belfast have been fabricating ferroelectric and relaxor superlattices. The example in Fig.6 is of a PMN/PZN-BT heterostructures, which undergoes coupled polar melting when the superlattice distance is less than 20 nm, as indicated by the increase in permittivity without corresponding increases in loss.

Single Crystals

Experimental work on single crystals in Europe has been slow to get off the ground. As referred to above, one EU funded project is underway, but no reports are yet available from the project partners.

In the UK an EPSRC-funded program (Leeds U., Strathclyde U., TCC Ltd, Morgan Electroceramics) concerning crystal growth has just begun, focusing on the use of multiple (12) zone furnaces to control thermal gradients and so improve compositional uniformity in device quality crystals (50 mm x 25 mm). Various device fabrication methods, particularly for ultrasonic imaging transducers, will be explored.

Interest in the mechanism of the high piezoelectric coefficients and the origin of apparently related monoclinic phase in PZT, have motivated the author's own work on thermodynamic models. A full exploration of the field-temperature phase diagrams was carried out for $BaTiO_3$, revealing some interesting agreement and discrepancies with the

(a)

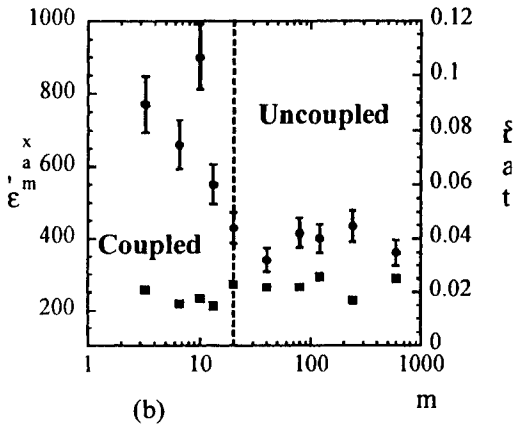

(b)

Fig 6. (a) PMN / PZN-BT superlattice and (b) the dielectric properties as a function of superlattice spacing.

experimental work in which fields are applied along the low index axes[8]. A new approach to a thermodynamic model for PZT, in which the free energy is expressed as a function of the coupled polar displacements of the end-members. The model accurately predicts the composition of the morphotropic phase boundary and describes a monoclinic phase similar to that seen

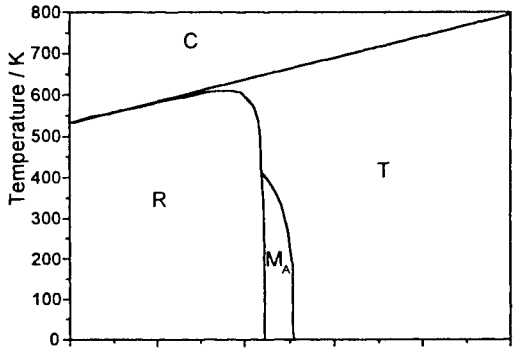

Fig. 7. PZT phase diagram produced from the couple order parameter model.

experimentally (Fig. 7).

CONCULSIONS

A review of some of the recent and current activities in Europe has been carried out, including a survey of current EU sponsored programs on piezoelectrics, details of significant contributions from two of the most prolific European laboratories and some highlights from work in other laboratories in Europe in the fields of basic science, piezoelectric ceramics, ferroelectric thin-films and ferroelectric single crystals.

REFERENCES

[1] Petzelt et al., Integr. Ferroel. **32**, 11 (2001), Ferroelectrics **239**, 117 (2000)

[2] Petzelt et al. J. Europ. Cer. Soc., in press; submitted. to Phys. Rev. B

[3] Ostapchuk et al. J. Phys. Cond. Matter **13**, 2677 (2001), Ferroelectrics **239**, 109 (2000)

[4] Buixaderas et al., Eur. Phys. J. B **19**, 9 (2001)

[5] Kamba et al. J. Phys. Cond. Matter **12**, 497 (2000)

[6] Kamba et al., J. Appl. Phys. **89**, 3900 (2001), Petzelt and Kamba, inv. paper on APMC 2001, Taiwan, Dec. 2001

[7] A. Sanson, C. Galassi, A.L. Costa, U. Russo, Proc. Ferroelectrics UK 2001 (11-12 April 2001)

[8] A. J. Bell, J. Appl. Phys. **89** 3907 (2001)

Three-Dimensional Analysis of Inverted Domain Structures in $LiNbO_3$ by SHG Interference Microscope,

Y.Uesu*, H.Shibata and Y.Shindoh
Department of Physics, Waseda University;
3-4-1 Okubo, Shinjuku-ku, Tokyo 169-8555, Japan

The SHG interference microscope was applied to the observation of ferroelectric 180° domain structures along the axial direction in a y-cut MgO:$LiNbO_3$. By using four different second harmonic (SH) interference images with phase difference of 0, π, $+\pi/2$, and $-\pi/2$ between SH waves from a specimen and a standard SH-generating plate, the characteristic functions of the SHG intensities were calculated in the "η-plane", from which the 3D-domain structure was successfully reproduced. The form of inverted domain was found to be wedge-shaped along the axial direction as well as along the lateral direction.

1.INTRODUCTION

Using the SHG interference microscope, we have already succeeded in observing domain reversal process in MgO:$LiNbO_3$ under the pulsed-electric field [1]. However, the observation was limited to the two-dimensional one. Similar restriction exists in other conventional methods such as linear optical and scanning-type microscopes. The 3D-analysis of domain structure is important especially in characterizing quasi phase matching (QPM) devices. The present paper reports the principle of the method and its application to the observation of reversed domain structure of MgO:$LiNbO_3$.

2.PRINCIPLE

2.1 The principle of the SHG interference microscope

SHG interference microscope is a nonlinear optical system for nondestructive observation of ferroelectric 180° structure [1-3]. The SHG tensor is the third rank tensor and has opposite sign in up and down domains [4]. Therefore, they produce optical second harmonic waves with same amplitude but opposite phase. When an SHG standard plate (consisting of MgO:$LiNbO_3$ in the present experiment) is inserted in front of the specimen in order to generate homogeneous SH-wave, the interference between two SH waves from the specimen and the standard plate discloses the domain structure as the intensity contrast.

To get the maximum contrast, the phase and amplitude should be controlled. For this purpose, the standard plate is rotated to adjust the amplitude of the additional SH-wave by using the Maker Fringe technique. We also insert a glass plate between the specimen and the standard plate, and the glass plate is rotated to adjust the phase of the additional SH-wave by changing optical path length. The principle is illustrated in Figure 1.

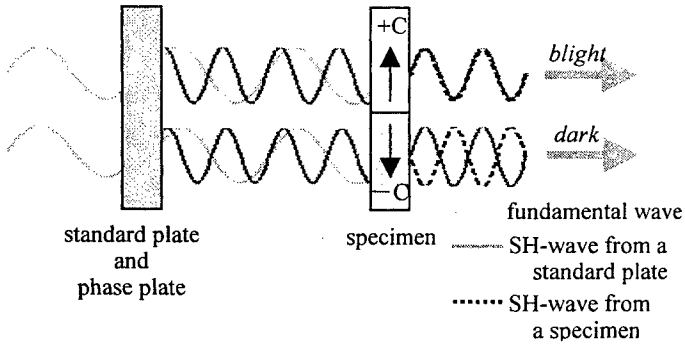

Figure 1: The principle of the SHG interference microscope

2.2 Dependence of the SHG intensity on the depth of reversal domain

SHG intensity $I^{(2\omega)}$ from a specimen with the width L is expressed as,

$$I^{(2\omega)} \propto (\varepsilon_0 d_{ijj})^2 \left\{E_j^{(\omega)}\right\}^4 \times L \cdot \left[\frac{\sin(\Delta kL/2)}{(\Delta kL/2)}\right]^2 \qquad (1)$$

Here d_{ijj} is an SHG tensor component of a specimen, $E_j^{(\omega)}$ an electric field component of the fundamental wave, Δk the mismatch of wave-numbers between the fundamental and SHG waves. The term in the square brackets comes from the interference of SH waves produced in the specimen. When $\Delta k \neq 0$, it oscillates with the period termed the coherence length Lc

$$Lc = \frac{\lambda}{4\left(n^{(2\omega)} - n^{(\omega)}\right)} \tag{2}$$

where $n^{(\omega)}$ and $n^{(2\omega)}$ are refractive indices of the fundamental and SH waves, respectively. Here a function G(x) is introduced for the convenience.

$$G(x) \equiv x \times \sin(\Delta kx/2)/(\Delta kx/2) \tag{3}$$

If a reversed domain exists in the specimen with a small depth x from the bottom (Figure 2), the SHG intensity is

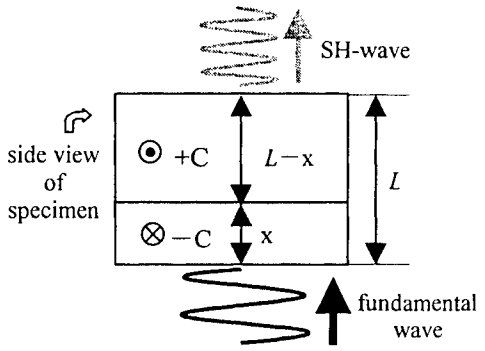

Figure 2: The side view of a specimen containing an inversed domain

expressed as

$$I^{(2\omega)} \propto (\varepsilon_0 d_{ijj})^2 \left\{E_j^{(\omega)}\right\}^2 \left\{2(G^2(x)+G^2(L-x))-G^2(L)\right\} \tag{4}$$

When the SH-wave from the standard plate enters the specimen, the intensity of mixed SH-wave is calculated as

$$I^0 \propto (\varepsilon_0 d_{ijj})^2 \left\{E_j^{(\omega)}\right\}^2 4G^2(L-x), \quad I^{\pi} \propto (\varepsilon_0 d_{ijj})^2 \left\{E_j^{(\omega)}\right\}^2 4G^2(x)$$
$$I^{\pm\pi/2} \propto (\varepsilon_0 d_{ijj})^2 \left\{E_j^{(\omega)}\right\}^2 2\left[G^2(x)+G^2(L-x) \pm \Delta kG(L)G(x)G(L-x)\right] \tag{5}$$

Here the upper-subscript means the phase difference between SH-wave from the non-reversed domain of the specimen and standard plate. These four intensities change as the function of x and they provide information on the depth of the reversed domain. However, these four functions are periodic with the period of 2Lc. So we must limit the case where the depth is less than twice of Lc. However, this limit is enough to analyze the depth of reversed domains, when we make use of d_{31} component of $MgO:LiNbO_3$, as Lc of d_{31} is not less than 51 μm at the wavelength of the fundamental wave (λ=1.06μm).

2.3 η -plane and domain structure

Here, we introduce two functions $\eta 1$ and $\eta 2$ which are expressed by $I^0, I^{\pm\pi/2}$ and I^{π}. They enable to calculate the depth of reversed domain. The definition is as follows.

$$\eta 1 = \frac{I^{\pi} - I^0}{I^{\pi} + I^0}, \quad \eta 2 = \frac{I^{+\pi/2} - I^{-\pi/2}}{I^{+\pi/2} + I^{-\pi/2}} \tag{6}$$

The ηs represent " contrast ratios", as η becomes 0 when there is no difference between two intensities, and η becomes maximum when the difference is maximum. The functions

$\eta 1$ and $\eta 2$ form a space when they are expressed as the horizontal and vertical axes of the space, respectively. This new plane is termed " η -plane" . This plane indicates the domain structure, as will be explained in following.

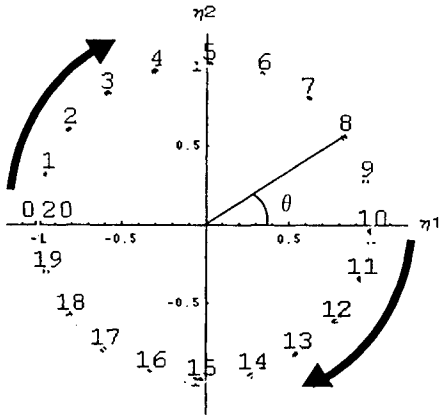

Figure 3: η -plane (L=465 μ m)

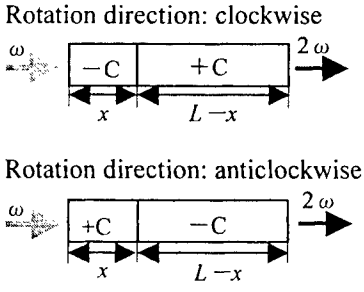

Figure 4: The relation between the rotation direction and the domain structure

Figure 3 shows the η -plane in the case of L=465 μ m. The gray line is a continuous function of x, and, black points on the gray line are plotted at every 10 μ m of reversed domain depth with number of order. Judging from

it, a point in the η -plane corresponds to a depth of reversed domain. The point rotates in the clockwise direction on the η -plane with x. If the rotation direction is opposite, the domain structure is opposite as shown in Figure 4. In order to indicate a point on η -plane, the argument of the point is used. The relation between this argument and reversal domain depth is expressed as follows.

when looking at I^{π} carefully, we notice that the center of reversal domain becomes dark, again. This is because the depth of reversed domain changes depending on the place of the specimen, since the growth of reversed domain is three-dimensional. We also took SH images with I^{0}, $I^{+\pi/2}$ and $I^{-\pi/2}$.

In our SHG interference microscope, the intensity of SH-

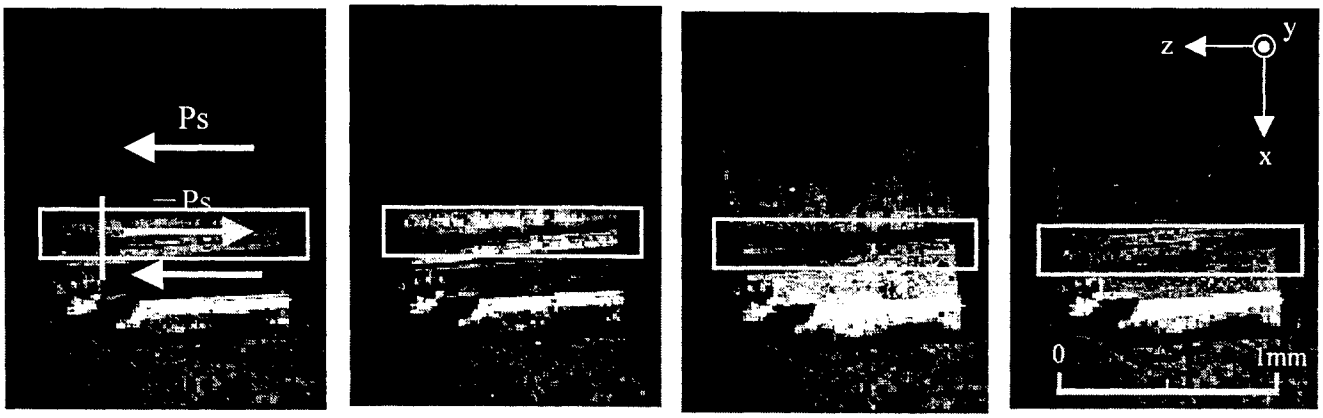

Figure 5: SH-image of I^{0}, I^{π}, $I^{+\pi/2}$ and $I^{-\pi/2}$

i) If $2n \cdot 2\mathrm{Lc} < L < (2n+1) \cdot 2\mathrm{Lc}$ then,

$$x = \frac{L}{2} - 2nLc + \frac{1}{\Delta k}\left[-\theta + \arccos\left\{\cos\theta \cos\left(\frac{1}{2}\Delta kL\right)\right\}\right] \tag{7}$$

ii) If $(2n+1) \cdot 2\mathrm{Lc} < L < (2n+2) \cdot 2\mathrm{Lc}$ then,

$$x = \frac{L}{2} - 2nLc + \frac{1}{\Delta k}\left[-\theta - \arccos\left\{\cos\theta \cos\left(\frac{1}{2}\Delta kL\right)\right\}\right] \tag{8}$$

Here x denotes a depth of reversed domain, θ , an argument on the η -plane and n, an integer (>0).

Therefore the argument in the η -plane indicates the depth of reversed domain, and the rotation direction of η -plane indicates the direction of polarization. From equations (7) and (8), we can calculate the depth of reversal domain in the specimen.

3.EXPERIMENTAL RESULTS

Applying an pulsed electric field of 6kV/mm between both sides of the specimen of MgO:$LiNbO_3$, we made a reversed domain in the specimen and took an SH image of I^{π}. This image is observed as a blight region in Figure 5. However wave from the specimen can be quantitatively obtained. From these four intensity distributions data, $\eta 1$ and $\eta 2$ were calculated according to the formula (5) and the corresponding η -plane was obtained. The argument θ of each point in this η -plane is expressed as

$$\theta = \arctan\left(\frac{\eta 2}{\eta 1}\right) \tag{8}$$

According to formula (6) and θ obtained using the above-formula, the depth of reversal domain was calculated. Three-dimensional distribution of the reversal domain in the region surrounded by a rectangle in Figure 5 is shown in Figure 6.

In Figure 6, a valley corresponds to the boundary plane of domains with Ps directed along the +C and −C . From this figure, it is turned out that the shape of reversal domain formed by applying electric field is a wedge along the axial direction.

Observation direction

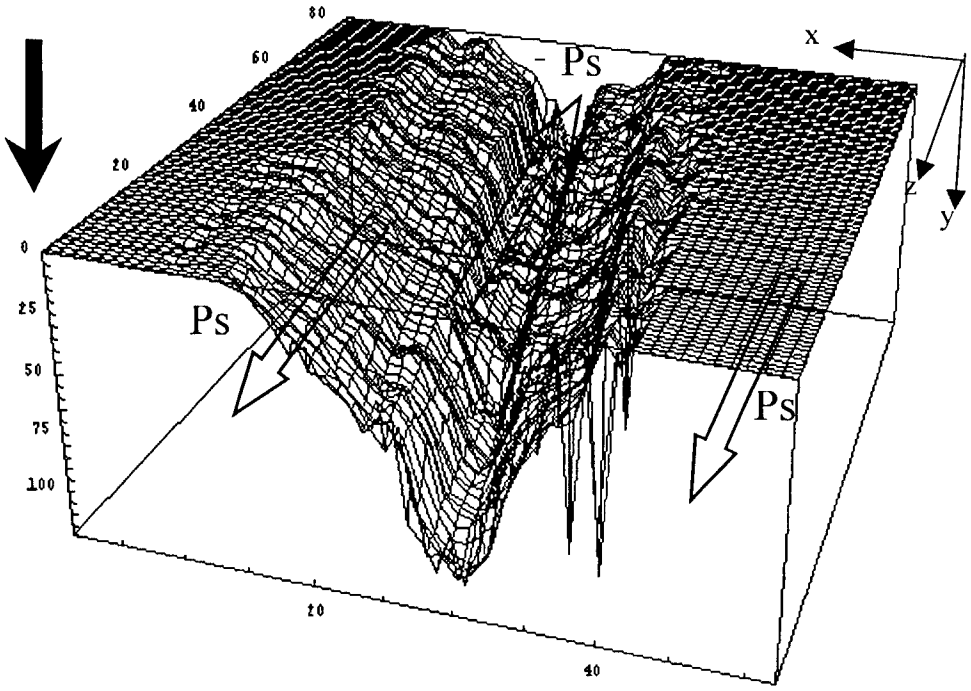

Figure 9: 3D-structure of domain in the specimen

ACKNOWLEDGMENTS

We are grateful to Dr. N.Kato, Waseda University, and Dr.S.Kurimura, Laser Research Center, Institute for Molecule and Science, for helpful discussions.

REFERENCES

* uesu93@mn.waseda.ac.jp

1. Y.Uesu, H.Mohri, Y.Shindoh, S.Kurimura, "SHG mictoscope as a tool of nondestructive observation of ferroelectric 180° domain structure and its kinetics under electric fields" *Ferroelectrics*, **253**,115,2001.

2. Y.Uesu, S.Kurmura, Y.Yamamoto, "Optical second harmonic images of 90° domain structure in $BaTiO_3$ and periodically inverted antiparallel domains in $LiTaO_3$", *Appl.Phys.Lett.*, **66**, 2165, 1995

3. S.Kurimura, Y.Uesu "Application of the second harmonic generation microscope to nondestructive observation of periodically poled ferroelectric domains in quasi-phase-matched wavelength converters", *J.Appl.Phys.* **81,** 369, 1997

4. R.C.Miller, "Optical Harmonic Generation in Single Crystal $BaTiO_3$", *Phys.Rev.* **134,** A1313, 1964

10th US-Japan Seminar on Dielectric and Piezoelectric Ceramics
September 26–29, 2001

Participant List (Japan)

Masatoshi Adachi
Toyama Prefectural University
5180 Kurokawa
Kosugimachi
Toyama , 939-0398 Japan
Phone: 81- 0766-56-7500
Fax: 81- 0766-56-8023
e-mail: adachi@pu-toyama.ac.jp

Yuji Akimoto
Shoei Chemical Inc.
Aza-wakazakura
Fujiki-cho, 5-3
Saga , 841-0048 Japan
Phone: 81- 942-82-6661
Fax: 81- 942-82-6667
e-mail: y-akimoto@shoeichem.co.jp

Hiroshi Funakubo
Tokyo Institute of Technology
Dept. Innov. Eng. Mater.
GI-405, 4529
Nagatsuta-cho, Midori-ku
Yokohama , 226-8502 Japan
Phone: 81- 45-924-5446
Fax: 81- 45-924-5446
e-mail: funakubo@iem.titech.ac.jp

Takashi Hayashi
Shonan Institute of Technology
Dept. of Materials Science
1-1-25 Tsujido-Nishikaigan
Fujisawa
Kanagawa , 251-8511 Japan
Phone: 81- 466-30-0224-
Fax: 81- 466-30-0224
e-mail: hayashi@mate.shonan-it.ac.jp

Noburu Ichinose
Waseda University School of Science and Engineering
3-4-1 Ohkuba Shinjuku-ku
Tokyo , 169-8555 Japan
Phone: 81- 3-5286-3307
Fax: 81- 3-3200-2567
e-mail: ichinose@mn.waseda.ac.jp

Takashi Iijima
AIST
Smart Structures Research Center
Tsukuba Central 2
1-1-1 Umezono
Tsukuba , 305-8568 Japan
Phone: 81- 298-61-3073
Fax: 81- 298-61-3126
e-mail: iijima-t@aist.go.jp

Jun-ichi Itoh
Mitsui Mining & Smelting Co. Ltd.
1-1 Namiki
Ibaraki , 305-0044 Japan
Phone: 81- 298-58-5643
Fax: 81- 298-55-1196
e-mail: ito.junichi@nims.go.jp

Nobuo Kamehara
Fujitsu Laboratories Ltd.
10-1 Morinosato-Wakamiya
Atsugi , 243-0197 Japan
Phone: 81- 46-250-8827
Fax: 81- 46-248-8812
e-mail:

Kazumi Kato
National Institute of Advanced Industrial Science and Technology
1 Hirate-cho
Kita-ku
Nagoya , 462-8510 Japan
Phone: 81- 052-911-2179
Fax: 81- 052-916-6992
e-mail: kzm.kato@aist.go.jp

Toshio Kimura
Keio University
3-14-1 Hiyoshi
Kohoku-ku
Yokohama , 223-8522 Japan
Phone: 81- 45-566-1565
Fax: 81- 45-566-1551
e-mail: kimura@applc.keio.ac.jp

10th US-Japan Seminar on Dielectric and Piezoelectric Ceramics
September 26–29, 2001

Participant List (Japan)

Hiroshi Kishi
Taiyo Yuden Co., Ltd.
5607-2 Nakamuroda
Haruna-machi
Gunma-gun , Gunma 370-3347 Japan
Phone: 81- 27-360-8307
Fax: 81- 27-370-3347
e-mail: hkishi@jty.yuden.co.jp

Youichi Mizuno
Taiyo Yuden Co., Ltd.
5607-2 Nakamuroda
Haruna-Machi
Gunma-gun , Gunma 370-3345 Japan
Phone: 81- 27-360-8307
Fax: 81- 27-360-8315
e-mail: ymizuno@jty.yuden.co.jp

Tsuyushi Kobayashi
Toshiba Co.
Corporate R&D Center
1 Komukai Toshiba-cho
Saiwai-ku
Kawasaki , Kanagawa 212-8582 Japan
Phone: 81- 44-549-2134
Fax: 81- 44-520-1286
e-mail: tuyosi.kobayashi@toshiba.co.jp

Kazuro Nagashima
Shoei Chemical Inc.
Aza-wakazakura
Fujiki-cho, 5-3
Saga , 841-0048 Japan
Phone: 81- 942-82-6661
Fax: 81- 942-82-6667
e-mail: k-nagashima@shoeichem.co.jp

Hiroshi Maiwa
Shonan Institute of Technology
1-1-25 Tsujido-Nishikaigan
1-1-25 Tsujido-Nishikaigan
Fujisawa , Kanagawa 251-8511 Japan
Phone: 81- 466-30-0236
Fax: 81- 466-36-1594
e-mail: maiwa@mate.shonan-it.ac.jp

Toshio Ogawa
Shizuoka Institute of Science and Technology
2200-2, Toyosawa
Shikuoka , 437-8555 Japan
Phone: 81- 538-45-0149
Fax: 81- 538-45-0154
e-mail: ogawa@ee.sist.ac.jp

Yoichiro Masuda
Hachinohe Institute of Technology
88-1 Obiraki Jyo Hachinohe
Aomori , 031-8501 Japan
Phone: 81- 178-25-8047
Fax: 81- 178-25-1430
e-mail: ymasuda@hi-tech.ac.jp

Soichiro Okamura
Nara Institute of Science and Technology
8916-5 Takayama-cho
Nara , 630-0101 Japan
Phone: 81- 743-72-6061
Fax: 81- 743-72-6069
e-mail: okamura@ms.aist-nara.ac.jp

Mitsuyoshi Matsushita
Kawatetsu Mining Company Ltd.
1 Niihama-cho, Chuo-ku
Chiba , 260-0826 Japan
Phone: 81- 43-262-2176
Fax: 81- 43-262-4259
e-mail: mi-matsushita@kawako.kawatetsu.ne.jp

Hirotake (Okino) Niori
National Defense Academy
1-10-20 Hashirimizu
Kanagawa , 239-8686 Japan
Phone: 81- 468-41-3810 (3330)
Fax: 81- 468-44-591
e-mail: hokino@nda.ac.jp

10th US-Japan Seminar on Dielectric and Piezoelectric Ceramics
September 26–29, 2001

Participant List (Japan)

Yukio Sakabe
Murata Manufacturing Co. Ltd.
Shiga-ken Yasu-gun
Yasu-cho , 520-2393 Japan
Phone: 81- 077-586-8275
Fax: 81- 077-587-1923
e-mail: sakabe@murata.co.jp

Hiroshi Tamura
Murata Manufacturing Co., Ltd.
Yasu Plant
Yasu-gun
Shiga , 520-2393 Japan
Phone: 81- 77-586-8523
Fax: 81- 77-587-1923
e-mail: tamura@murata.co.jp

Isao Sakaguchi
National Institute for Materials Science
1-1 Namiki
Ibaraki , 305-0044 Japan
Phone: 81- 298-51-3354 (655)
Fax: 81- 298-52-7449
e-mail: sakaguchi.isao@nims.go.jp

Toshihiko Tani
Toyota Central Research and Development Labs, Inc.
41-1 Yokomichi
Nagakute
Aichi , 480-1192 Japan
Phone: 81- 561-63-6196
Fax: 81- 561-63-6498
e-mail: toshit@mosk.tytlabs.co.jp

Tadashi Shiosaki
Nara Institute of Science and Technology
8916-5 Takayama-cho
Nara , 630-0101 Japan
Phone: 81- 743-72-6060
Fax: 81- 743-72-6069
e-mail: shiosaki@ms.aist-nara.ac.jp

Daichi Togawa
Shonan Institute of Technology
1-1-25 Tsujido-Nishikaigan
Kanagawa , 251-8511 Japan
Phone: 81- 466-30-0224
Fax: 81- 466-30-0224
e-mail: hayashi@mate.shonan-it.ac.jp

Sunao Sugihara
Shonan Institute of Technology
1-1-25 Tsujido Nishikaigan
Fujisawa
Kanagawa , 251-8511 Japan
Phone: 81- 0466-30-0227
Fax: 81- 0466-36-1594
e-mail: sugihara@mate.shonan-it.ac.jp

Takaaki Tsurumi
Tokyo Institute of Technology
2-12-1 Ookayama
Maguro-ku
Tokyo , 152-8552 Japan
Phone: 81- 3-5734-2517
Fax: 81- 3-5734-2514
e-mail: ttsurumi@ceram.titech.ac.jp

Tadashi Takenaka
Science University of Tokyo
Yamazaki 2641
Noda
Chiba-ken , 278-8510 Japan
Phone: 81- 471-24-1501
Fax: 81- 471-23-0856
e-mail: tadashi@takenaka.ee.noda.sut.ac.jp

Yoshiaki Uesu
Waseda University
3-4-1 Okubo, Shinjuku-ku
Tokyo , 169-8555 Japan
Phone: 81- 3-5286-3446
Fax: 81- 3-3202-4962
e-mail: uesu93@mn.waseda.ac.jp

10th US-Japan Seminar on Dielectric and Piezoelectric Ceramics
September 26–29, 2001

Participant List (Japan)

Satoshi Wada
Tokyo Institute of Technology
2-12-1 Ookayama
Meguro-city
Tokyo , 152-8552 Japan
Phone: 81- 3-5734-2520
Fax: 81- 3-5734-2514
e-mail: swada@ceram.titech.ac.jp

Sakamoto Wataru
Nagoya University
Graduate School of Engineering
Furo-cho, Chikusa-ku
Nagoya , Aichi 464-8603 Japan
Phone: 81- 52-789-3345
Fax: 81- 52-789-3182
e-mail: sakamoto@apchem.nagoya-u.ac.jp

Takashi Yamamoto
National Defense Academy
1-10-20 Hashirimizu
Kanagawa , 239-8686 Japan
Phone: 81- 468-41-3810 (3330)
Fax: 81- 468-44-591
e-mail: ytakashi@nda.ac.jp

10th US-Japan Seminar on Dielectric and Piezoelectric Ceramics
September 26–29, 2001

Participant List (U.S.)

Knuth Albertsen
DMC-2 Electronic Materials B.V.
Electronic Materials Division
Front Straat 2
Uden, 5405PB The Netherlands
Phone: 37- 473-283286
Fax: 37- 473-283369
e-mail: knuth.albertsen@dmc-2.nl

Andrew J. Bell
University of Leeds
Dept. of Materials
Leeds, L32 9JT United Kingdom
Phone: 44- 113-233-2370
Fax: 44- 113-242-2531
e-mail: a.j.bell@leeds.ac.uk

Joanne Aller
Conference Coordinator
Penn State University
169 Materials Research Laboratory
University Park, PA 16802 USA
Phone: 1- 814-865-2896
Fax: 1- 814-865-8126
e-mail: joannealler@psu.edu

Amar S. Bhalla
Penn State Univ.
Materials Research Institute
187 Mat. Res.Lab. Bldg.
University Park, PA 16802-4800 USA
Phone: 1- 814-865-9232
Fax: 1- 814-863-7847
e-mail: abhalla@psu.edu

Abdulhakim Almajid
University of Washington
10501 8th Avenue #405
Seattle, WA 98125 USA
Phone: 1- 206-616-9117
Fax: 1- 206-616-4088
e-mail: almajid@u.washington.edu

Mike Biegalski
Penn State University
A7 Materials Research Lab
University Park, PA 16802 USA
Phone: 1- 814-865-2434
Fax: 1- 814-865-2326
e-mail: mdb210@psu.edu

Ahmed Amin
Naval Undersea Warfare Center
Office of Naval Research
Code 2132, Bldg. 1170
1176 Howell St.
Newport, RI 02841-1708 USA
Phone: 1- 401-832-3304
Fax: 1- 401-832-6401
e-mail: aminah@npt.nuwc.navy.mil

Ian Burn
DMC^2
3900 South Clinton Ave.
South Plainfield , NJ 07080 USA
Phone: 1- 908-226-2161 x2015
Fax: 1- 908-757-0411
e-mail: ian.burn@dmc-2.com

James Beeson
Kemet Electronics Corp.
201 Fairview St. Ext.
P. O. Box 847
Fountain Inn, SC 29644 USA
Phone: 1- 864-409-5615
Fax: 1- 864-409-5665
e-mail: jimbeeson@kemet.com

Pavel Bystricky
CeraNova Corporation
101 Constitution Blvd., Suite D
Franklin, MA 02038-2587 USA
Phone: 1- 508-520-7600
Fax: 1- 508-520-7637
e-mail: pavel@ceranova.com

10th US-Japan Seminar on Dielectric and Piezoelectric Ceramics
September 26–29, 2001

Participant List (U.S.)

David Cann
Iowa State Univ.
3053 Gilman Hall
MSE Dept.
Ames, IA 50010 USA
Phone: 1- 515-294-3202
Fax: 1- 515-294-5444
e-mail: dcann@iastate.edu

Zhongyang Cheng
Penn State University
Materials Research Institute
187 Mat. Res. Lab. Bldg.
University Park, PA 16802 USA
Phone: 1- 814-865-0146
Fax: 1- 814-863-7846
e-mail: zxc7@psu.edu

Yet-Ming Chiang
Massachusetts Institute of Technology
Room 13-4086
77 Massachusetts Ave.
Cambridge, MA 02139 USA
Phone: 1- 617-253-6471
Fax: 1- 617-253-6201
e-mail: ychiang@mit.edu

L. Eric Cross
Pennsylvania State Univ.
Materials Research Institute
187 Mat. Res. Lab. Bldg.
University Park , PA 16802 USA
Phone: 1- 814-865-1181
Fax: 1- 814-863-7846
e-mail: lec3@psu.edu

Steve Xunhu Dai
Motorola Inc.
7700 South River Parkway
Tempe, AZ 85284 USA
Phone: 1- 480-755-6004
Fax: 1- 480-755-5350
e-mail: steve.dai@motorola.com

Duane Dimos
Sandia National Laboratories
MS 0885
P.O. Box 5800
Albuquerque , NM 87185-0885 USA
Phone: 1- 505-844-6385
Fax: 1- 505-284-3093
e-mail: dbdimos@sandia.gov

Joseph Dougherty
Penn State Univ.
Materials Research Institute
167 Mat. Res. Lab. Bldg.
University Park, PA 16802 USA
Phone: 1- 814-865-1638
Fax: 1- 814-865-2326
e-mail: joedoc@psu.edu

Roberta Dowling
DMC-2/
Ferro Electronic Materials
Reception Coordinator
3900 South Clinton Avenue
South Plainfield, NJ 07080 USA
Phone: 1- 908-561-1100 x2025
Fax: 1- 908-668-7896
e-mail: bobbie_dowling@dmc-2.com

Lynn Ewart
Naval Undersea Warfare Center
1176 Howell Street
Attn: C2132 Bldg. 1170
Newport, RI 02841-1708 USA
Phone: 1- 401-832-5093
Fax: 1- 401-832-6401
e-mail: ewartlm@npt.nuwc.navy.mil

Brian Foster
Ferro Electronic Materials
1789 Transelco Drive
Penn Yan, NY 14527 USA
Phone: 1- 315-536-3357
Fax: 1- 315-536-0376
e-mail: fosterb@Ferro.com

10th US-Japan Seminar on Dielectric and Piezoelectric Ceramics
September 26–29, 2001

Participant List (U.S.)

Glen Fox
Ramtron International Corp.
1850 Ramtron Drive
Colorado Springs, CO 80921 USA
Phone: 1- 719-481-7225
Fax: 1- 719-481-9170
e-mail: glen.fox@ramtron.com

Robert Heistand
AVX Corporation
2200 AVX Drive
P. O. Box 867
Myrtle Beach, SC 29578-0867 USA
Phone: 1- 843-444-2886
Fax: 1- 843-448-2106
e-mail: heistand@avxus.com

Eugene Furman
Materials Research Institute
Penn State University
152 Mat. Res. Lab.
University Park, PA 16802 USA
Phone: 1- 814-865-5361
Fax: 1- 814-865-2326
e-mail: euf1@psu.edu

B. Pierre Khuri-Yakub
Stanford University
Dept. of Electrical Eng.
Ginzton Lab., Room 11
Stanford, CA 94305-4085 USA
Phone: 1- 650-723-0718
Fax: 1- 650-725-2533
e-mail: khuri-ya@ee.stanford.edu

Ruyan Guo
Penn State University
Materials Research Institute
187 Mat. Res. Lab.
University Park, PA 16802-4800 USA
Phone: 1- 814-863-7847
Fax: 1- 814-863-7846
e-mail: ryguo@psu.edu

Angus Kingon
North Carolina State Univ.
Dept. Mat. Sci. & Eng.
Box 7919
Raleigh, NC 27695-7919 USA
Phone: 1- 919-515-8636
Fax: 1- 919-515-3419
e-mail: Angus_Kingon@ncsu.edu

Wesley Hackenberger
TRS Ceramics, Inc.
2820 East College Avenue
State College, PA 16801 USA
Phone: 1- 814-238-7485
Fax: 1- 814-238-7539
e-mail: wsh@trsceramics.com

Jung-Kun Lee
Seoul National University
Materials Science and Engineering
Shilim-dong, Kwanak-Gu
Seoul, 151-742 Korea
Phone: 82- 2-880-8316
Fax: 82- 2-886-4156
e-mail: ljk3703@plaza1.snu.ac.kr

Martin Harmer
Lehigh Univ.
Materials Res. Center
5 East Packer Ave.
Bethlehem, PA 18015 USA
Phone: 1- 610-758-4227
Fax: 1- 610-758-3526
e-mail: mph2@lehigh.edu

Xiangyuan Liu
Rutgers University
Dept.of Cer. & Mat. Eng.
607 Taylor Road
Piscataway, NJ 08854 USA
Phone: 1- 732-445-5754
Fax: 1- 732-445-6264
e-mail: liu_xiangyuan@yahoo.com

10th US-Japan Seminar on Dielectric and Piezoelectric Ceramics
September 26–29, 2001

Participant List (U.S.)

Christopher Lynch
The Georgia Inst. of Technology
The G.W.W. School of
Mechanical Engineering
Atlanta , GA 30332-0405 USA
Phone: 1- 404-894-6871
Fax: 1- 404-894-0186
e-mail: chris.lynch@me.gatech.edu

Galeb Maher
MRA Laboratories
96 Marshall Street
North Adams, MA 01247 USA
Phone: 1- 413-664-4524
Fax: 1- 413-663-5535
e-mail: mralabs@sover.net

Larry Mann
Kemet Electronics Corp.
P. O. Box 849
201 Fairview St. Ext.
Fountain Inn, SC 29644-0849 USA
Phone: 1- 864-409-5746
Fax: 1- 864-409-5665
e-mail: larrymann@kemet.com

Jon-Paul Maria
North Carolina State Univ.
Dept. of Mat. Sci. & Eng.
1010 Main Campus Dr., Office 223-D
Raleigh, NC 27695-7920 USA
Phone: 1- 919-513-2843
Fax: 1- 919-515-3027
e-mail: jpmaria@unity.ncsu.edu

Elizabeth McLaughlin
NUWC
Code 2131, B-1170
1176 Howell Street
Newport, RI 02841-1708 USA
Phone: 1- 401-832-5103
Fax: 1- 401-832-6401
e-mail: mclaughlinea@npt.nuwc.navy.mil

Kelley McNeal
Materials Systems, Inc.
521 Great Road
Littleton, MA 01460 USA
Phone: 1- 978-486-0404
Fax: 1- 978-486-0706
e-mail: mcneal@matsysinc.com

G. Messing
Penn State Univ.
Materials Research Institute
121 Steidle Bldg.
University Park , PA 16802 USA
Phone: 1- 814-865-2262
Fax: 1- 814-865-2917
e-mail: messing@mrl.psu.edu

R. Newnham
Penn State Univ.
Materials Research Institute
251A Mat. Res. Lab. Bldg.
University Park , PA 16802 USA
Phone: 1- 814-865-1612
Fax: 1- 814-865-2326
e-mail: bobnewnham@psu.edu

Craig Nies
AVX Corporation
P. O. Box 867
2200 AVX Drue
Myrtle Beach, SC 29577 USA
Phone: 1- 843-946-0517
Fax: 1- 843-626-9632
e-mail: cnies@avxus.com

Juan C. Nino
Penn State University
Materials Research Institute
A2 Materials Research Lab Bldg.
University Park, PA 16802 USA
Phone: 1- (814) 865-2434
Fax: 1- (814) 865-8126
e-mail: jcn125@psu.edu

10th US-Japan Seminar on Dielectric and Piezoelectric Ceramics
September 26–29, 2001

Participant List (U.S.)

Fred Nussbaum
Naval Undersea Warfare Center
ANTEON
1176 Howell Street
Bldg. 679
Newport, RI 02841-1708 USA
Phone: 1- 401-832-3188
Fax: 1- 401-832-2146
e-mail: nussbaumf@npt.nuwc.navy.mil

S. E. (Eagle) Park
Fraunhofer-IBMT Technology Center Hialeah (FTeCH)
601 W. 20th St.
Hialeah, FL 33010 USA
Phone: 1- 305-925-1261
Fax: 1- 305-925-1262
e-mail: epark@ftech.org

Takayuki Ohba
DMC-2 Electronic Materials
Front Straat 2
Uden, 5405PB The Netherlands
Phone: 31- 413-283-319
Fax: 31- 413-283-369
e-mail: takayuki.ohba@dmc-2.nl

Marina Pascucci
CeraNova Corporation
101 Constitution Blvd., Suite D
Franklin, MA 02038-2587 USA
Phone: 1- 508-520-7600
Fax: 1- 508-520-7637
e-mail: mpascucci@ceranova.com

Ming-Jen Pan
Naval Research Laboratory
Code 6351
Washington, DC 20375-5343 USA
Phone: 1- 202-404-1534
Fax: 1-
e-mail: pan@anvil.nrl.navy.mil

Dharmesh P. Patel
Naval Research Laboratory
Code 5317
4555 Overlook Ave., S.W.
Code 5317
Washington, DC 20375 USA
Phone: 1- 202-767-3355
Fax: 1- 202-767-2986
e-mail: patel@radar.nrl.navy.mil

Rajesh K. Panda
Agilent Technologies Inc.
3000 Minuteman Road
MS 0095
Andover, MA 01810 USA
Phone: 1- 978-659-3370
Fax: 1- 978-687-7265
e-mail: rajesh_panda@hsgmed.com

Steven M. Pilgrim
Alfred University
New York State College of Ceramics
2 Pine St.
Alfred , NY 14802 USA
Phone: 1- 607-871-2431
Fax: 1- 607-871-3469
e-mail: pilgrim@alfred.edu

Hyun Park
Ferro Electronic Materials
1789 Transelco Dr.
Penn Yan, NY 14527 USA
Phone: 1- 315-536-3357
Fax: 1- 315-536-0376
e-mail: parkh@ferro.com

Pascal G. Pinceloup
DMC-2
3900 South Clinton Avenue
South Plainfield, NJ 07080 USA
Phone: 1- (908) 226-2160
Fax: 1- (908) 757-0411
e-mail: Pascal_Pinceloup@Degussa-Huls.com

10th US-Japan Seminar on Dielectric and Piezoelectric Ceramics
September 26–29, 2001

Participant List (U.S.)

Philip Pruna
Ferro Corporation
1789 Transelco Drive
Penn Yan, NY 14527 USA
Phone: 1- 315-536-3357 x5262
Fax: 1- 315-536-8091
e-mail: prunap@ferro.com

A. Safari
Rutgers Univ.
Dept of Cer. and Mat. Eng
607 Taylor Rd.
Piscataway , NJ 08854-8065 USA
Phone: 1- 732-445-4367
Fax: 1- 732-445-5577
e-mail: safari@rci.rutgers.edu

Clive Randall
Penn State Univ.
Materials Research Institute
Mat. Res. Lab. Bldg.
University Park, PA 16802 USA
Phone: 1- 814-863-1328
Fax: 1- 814-865-8126
e-mail: car4@psu.edu

Hitoshi Saita
Penn State University
Materials Research Institute
161 Materials Research Laboratory
University Park, PA 16802 USA
Phone: 1- 814-863-3231
Fax: 1- 814-865-2326
e-mail: his2@psu.edu

Michael Randall
Kemet Electronics
201 Fairview Street Ext.
P.O. Box 849
Fountain Inn, SC 29644-0849 USA
Phone: 1- 864-409-5617
Fax: 1- 864-409-5665
e-mail: mikerandall@kemet.com

Steven Santoro
DMC-2
L.P.
3900 South Clinton Avenue
South Plainfield, NJ 07080 USA
Phone: 1- 908-226-2011
Fax: 1- 908-668-7896
e-mail: steve_santoro@dmc-2.com

Paul W. Rehrig
TRS Ceramics, Inc.
2820 East College Ave., Suite J
State College, PA 16801 USA
Phone: 1- 814-238-7485
Fax: 1- 814-238-7539
e-mail: pwr@trsceramics.com

Walter Schulze
Alfred University
New York State College of Ceramics
2 Pine Street
Alfred, NY 14802 USA
Phone: 1- 607-871-2471
Fax: 1- 607-871-2354
e-mail: schulze@alfred.edu

John Roelofsma
DMC-2 Electronic Materials B.V.
Electronic Materials Division
Front Straat 2
Uden, 5405PB The Netherlands
Phone: 37- 314-328-3269
Fax: 37- 314-328-3369
e-mail: john.roelofsma@dmc-2.nl

Matthew M. Seabaugh
NexTech Materials, Ltd.
720-1 Lakeview Plaza Boulevard
Worthington, OH 43085 USA
Phone: 1- 614-842-6606
Fax: 1- 614-842-6607
e-mail: seabaugh@nextechmaterials.com

10th US-Japan Seminar on Dielectric and Piezoelectric Ceramics
September 26–29, 2001

Participant List (U.S.)

Deb Shay
Assistant Coordinator
Penn State University
165 Applied Research Lab
University Park, PA 16802 USA
Phone: 1- 814-863-8005
Fax: 1- 814-863-0679
e-mail: debshay@psu.edu

Harold Strock
CeraNova Corporation
101 Constitution Blvd., Suite D
Franklin, MA 02038-2587 USA
Phone: 1- 508-520-7600
Fax: 1- 508-520-7637
e-mail: hstrock@ceranova.com

Wallace A. Smith
Office of Naval Research
DARPA Defense Sciences Office
3701 North Fairfax Drive
Arlington, VA 22203-1714 USA
Phone: 1- 703-696-0091
Fax: 1- 703-696-3999
e-mail: wsmith@darpa.mil

Susan Trolier-McKinstry
Penn State Univ.
Materials Research Institute
151 Mat. Res. Lab. Bldg.
University Park , PA 16802 USA
Phone: 1- 814-863-8348
Fax: 1- 814-865-2326
e-mail: stmckinstry@psu.edu

A. N. Soukhojak
Massachusetts Institute of Technology
Room 13-4006
77 Massachusetts Ave.
Cambridge, MA 02139 USA
Phone: 1- 617-253-6886
Fax: 1- 617-253-6201
e-mail: ansou@mit.edu

Bang-Hung Tsao
University of Dayton
Research Inst.
300 College Park
Dayton, OH 45469-0179 USA
Phone: 1- 973-255-6016
Fax: 1- 973-255-3211
e-mail: bang.tsao@wpafb.af.mil

Michael T. Strauss
HME
56 Federal Street
Newburyport, MA 01950-2821 USA
Phone: 1- 978-462-0102
Fax: 1- 508-4623-0393
e-mail: mstrauss@alum.mit.edu

Bruce Tuttle
Sandia National Laboratories
Electronic Ceramics Dept.
P.O. Box 5800 MS 1411
Albuquerque , NM 87185-1411 USA
Phone: 1- 505-845-8026
Fax: 1- 505-844-9781
e-mail: Batuttl@sandia.gov

Stephen K. Streiffer
Argonne National Lab.
Materials Science Div.
9700 S. Cass Ave
Argonne , IL 60439 USA
Phone: 1- 630-252-5832
Fax: 1- 630-252-4289
e-mail: streiffer@anl.gov

Sridhar Venigalla
Cabot Corporation
P. O. Box 1608,
County Line Road
Boyertown, PA 19512-1608 USA
Phone: 1- 610-369-8246
Fax: 1- 610-369-8552
e-mail: Sridhar_Venigalla@cabot-corp.com

10th US-Japan Seminar on Dielectric and Piezoelectric Ceramics
September 26–29, 2001

Participant List (U.S.)

D. Viehland
Naval Undersea Warfare Center
Office of Naval Research
Bldg. 1170, 1176 Howell St.
Newport, RI 02841-1708 USA
Phone: 1- 401-832-5107
Fax: 1- 401-832-6401
e-mail: Ddviehland@aol.com

Koto White
US Air Force Office of Scientific Research
404 North Fairfax Drive
Arlington, VA 2203 USA
Phone: 1- 703-696-7319
Fax: 1- 703-696-7320
e-mail: koto.white@afosr.af.mil

David L. Wilcox
Motorola, Inc.
Ceramic Tech Research Lab.
7700 S. River Pkwy
Tempe, AZ 85284 USA
Phone: 1- 480-755-6016
Fax: 1- 480-755-5531
e-mail: cdw024@email.mot.com

Carl Wu
Office of Naval Research
800 North Quincy Steret
Arlington, VA 22217-5660 USA
Phone: 1- 703-696-0689
Fax: 1- 703-696-0934
e-mail: wucarlc@onr.navy.mil

Hisao Yamada
Cerone, Incorporated
8100 Bainbrook Drive
Bainbridge, OH 44023 USA
Phone: 1- 216-533-1176
Fax: 1- 440-708-1258
e-mail: ceroneinc@yahoo.com

Shoko Yoshikawa
Active Control eXperts
A division of Cymer
215 First Street
Cambridge, MA 02142-1227 USA
Phone: 1- 617-577-0700 x 282
Fax: 1- 617-577-0656
e-mail: Shoko_Yoshikawa@cymer.com

Takeshi Yoshimura
Penn State University
Materials Research Institute
152 Materials Res. Lab. Bldg.
University Park, PA 16802 USA
Phone: 1- 814-865-5361
Fax: 1- 814-865-2326
e-mail: txy7@psu.edu

Fengyan Zhang
Sharp Laboratories of America
5700 N. W. Pacific Rim Blvd.
Camas, WA 98683 USA
Phone: 1- 360-834-8654
Fax: 1- 360-834-8689
e-mail: Fzhang@Sharplabs.com

Author Index

A

Abe, Y. 335
Adachi, M. 99
Adair, J.H. 343
Alberta, E.F. 169, 281
Albertsen, K. 15
Alkoy, S. 305
Allahverdi, M. 371
Almajid, A. 309
Amin, A. 213
Aratani, M. 131
Auciello, O. 75
Ayguavives, F. 91
Azad, A-M. 351

B

Badi, M. 391
Bailey, R. 103
Baker, A. 59
Bayram, B. 391
Beck, H. 233
Beeson, J.J. 39
Bell, A.J. 401
Bell, N.S. 301
Bhalla, A. 281
Bonistall, J. 31
Bourbina, M.F. 375
Breval, E. 363
Burn, I. 15
Burton, J. 31
Bystricky, P. 347

C

Cann, D. 379
Cesarano, J. 375
Chan, H.M. 331
Chao, C.T. 379
Chazono, H. 35, 43
Chen, J. 233
Cheney, G.L. 351
Cheng, C-H. 391
Cheng, Z-Y. 257
Chiang, Y-M. 265, 269
Chino, M. 87
Chu, F. 103
Chu, M. 23
Church, K. 301
Clem, P.G. 301
Cochran, J. 305
Creedon, M. 31
Cross, L.E. 169, 189

D

Dai, S. 1
Davenport, T. 103
Davis, E. 23, 31
Davis, R.J. 147
Dawson, W.J. 351
Demerci, U. 391
Deng, K. 147
Deyneka, E. 79
DiAntonio, C.B. 173, 177, 221
Dimos, D. 301
Dougherty, J.P. 363
Dougherty, T.K. 95

E

Ebihara, H. 181
Echizenya, K. 209, 245
Egami, T. 159
Eitel, R. 201
Erck, R. 75
Ergun, S. 391
Ewart, L. 225

F

Feng, C. 221
Fiore, D. 339
Foster, B. 31
Fox, G.R. 103
Franzon, P. 313
Fujita, S. 185
Funakubo, H. 131
Furman, E. 241

G

Gall, R.B. 379
Galvagni, J.L. 383
Gentilman, R. 339
Giovanardi, M. 319
Gorzkowski, E.P. 331
Grant, E. 313
Gruverman, A. 313
Guo, R. 169
Gururaja, R. 233

H

Hackenberger, W. 201, 343
Hagiwara, T. 35
Haneda, H. 47, 51
Hansen, S. 391
Harada, K. 229
Harigai, T. 71
Harmer, M.P. 331
Hasinska, K. 351
Hayashi, T. 119, 285
Heidger, S. 67
Heistand, R.H. 383
Hirano, S. 139
Hishita, S. 51
Hladky-Herrion, A.C. 305

Hong, K.S. 237
Horie, Y. 139
Hosono, Y. 217
229
Hsu, S.T. 127
Hughes, W.J. 305

I

Ichikawa, T. 71
Ichinose, N. 143
217
Ida, T. 181
Iijima, T. 155
Im, J. 75
Ishii, H. 261
Ishizuka, C. 83
Itoh, J. 47
Itsumi, K. 229
Izumi, M. 229

J

Jeong, D-Y. 257
Jha, M.K. 165
Jones, B.A. 169

K

Kakemoto, H. 249
355
Kakimoto, K. 185
Kamehara, N. 135
Karaki, T. 99
Karaman, M. 391
Kato, K. 123
Kaufman, D.Y. 75
Kawashima, T. 83
Kelly, J.G. 317
Kennedy, R.M. 383
Kerchner, J.A. 19
Khuri-Yakub, B.T. 391
Kim, D.J. 313
Kimura, N. 83
Kimura, T. 335
King, P.T. 331
Kingon, A.I. 91
313
Kishi, H. 35
43
Klimkiewicz, M. 363
Kobayashi, M. 87
Kobayashi, T. 115
229
Kohzu, N. 43
Korony, G. 383
Kraus, B. 103
Kunii, K. 155
Kurasawa, M. 135
Kurihara, K. 135
Kwon, S.T. 327

L

Lanagan, M.T. 55
59, 79
Lee, J.K. 237
Li, J-F. 309
Lim, L.C. 213
Liu, X. 367
Lu, Y. 257
Lynch, C.S. 289

M

Ma, W. 189
Maher, G.H. 27
Maher, S.C. 27
Maiwa, H. 143
Mann, L.A. 39
Maria, J-P. 91
313
Markey, D. 305
Masuda, Y. 185
Matsushita, M. 209
245
McCauley, D. 23
McLaughlin, E.A. 225
McNeal, K. 339
Megherhi, M. 23
Messing, G.L. 327
Meyer, R. 305
Miki, T. 123
Mizuno, Y. 35
Moffat, A. 95
Mortazawi, A. 91
Mulling, J.F. 313
Mulvihill, M.L. 273

N

Nagata, H. 261
Nagata, S. 209
Narahara, M. 355
Newnham, R.E. 305
Nies, C. 79
Nino, J.C. 55
59
Niori (Okino), H. 87
181
Nishizawa, K. 123
Nonaka, K. 371
Nunes, B.P. 265
Nussbaum, F. 317

O

Ogawa, T. 245
Ogiso, Y. 63
Ohashi, N. 47
51, 269
Ohba, T. 15
Ohsato, H. 43
Oikawa, T. 131
Okamura, S. 109
115
(Okino) Niori, H. 87
181
Okuda, T. 43
Olson, W.R. 375
Oralkan, O. 391
Ostreicher, K. 339
Ozgul, M. 253

P

Pagoda, C.J. 273, 277
Palmer, J.A. 313
Panda, R. 233
Park, H. 23
Park, P.K. 95
Park, S-E. 201, 237
Parker, C.B. 91
Parkhill, R. 301
Pascucci, M.R. 347
Patel, D.P. 95
Paulsen, J.L. 39
Pilgrim, S.M. 173, 177, 221, 273, 277
Pinceloup, P. 15
Pruna, P. 31

R

Ramotowski, T.S. 213
Randall, C.A. 55, 59, 201, 241, 253
Randall, M.S. 39
Rao, J.B.L. 95
Reaney, I.M. 55, 59
Reed, E.K. 39
Rehrig, P.W. 201, 343
Riman, R.E. 367
Ritter, A.P. 383
Rockosi, D.J. 331
Roelofsma, J. 15

S

Sabolsky, E.M. 327
Safari, A. 371
Saha, S. 75
Saigo, Y. 217
Saito, K. 131
Saitoh, M. 87
Sakabe, Y. 63
Sakaguchi, I. 47, 51
Sakamoto, W. 139
Schultz, D.L. 19
Schulze, W.A. 165, 221
Scotch, A.M. 331
Seabaugh, M.M. 351
Seike, A. 249
Sekita, M. 51
Sengupta, L.C. 95
Sheets, S.A. 269
Shen, J. 265
Shibata, H. 409
Shindoh, Y. 409
Shiosaki, T. 109, 115
Shrout, T. 59, 201, 343
Smay, J.E. 375
Sogabe, H. 59
Soukhojak, A.N. 265, 269
Stauf, G. 91
Stevens, G.T. 317
Strauss, M.T. 323
Streiffer, S.K. 75
Strock, H.B. 347
Sugihara, S. 83
Sugino, J. 43
Sun, S. 103
Suzuki, K. 115, 123
Swartz, S.L. 351
Symes, W. 31

T

Tachi, Y. 209, 245
Takagi, K. 309
Takeda, T. 63
Takemura, K. 253
Takenaka, T. 261
Tamura, H. 9
Tanaka, J. 47
Tani, T. 293
Taya, M. 309
Thomas, A. 169
Togawa, D. 119
Tombak, A. 91
Tomizawa, J. 285
Trolier-McKinstry, S. 147, 151, 253, 327
Tsao, B-H. 67
Tsu, K. 99
Tsurumi, T. 71, 193, 249, 355
Tuttle, B.A. 375

U

Uesu, Y. 409

V

Van Heusden, K. 301
Venigalla, S. 19
Venturini, E.L. 375
Viehland, D. 161
Voigt, J.A. 375

W

Wada, N. 63
Wada, S. 71, 193, 249, 355
Wang, L.P. 147
Wang, Y. 147
Watanabe, K. 185
Watanabe, R. 309
Weigner, J.D. 363
Weimer, J.A. 67
Wheeler, J.S. 375
Wilcox, D.L. 1
Williams, F.A. 173, 177, 211
Witter, S. 31
Wlodkowski, P. 147
Wolf, R. 147

Wu, S. 331

Y

Yamada, H. 359
Yamamoto, T. 87
181
Yamashita, Y. 217
229
Yaralioglu, G. 391
Yashima, I. 47
Yin, Z. 221
Yogo, T. 139
Yoshikawa, S. 319
Yoshimura, T. 151
Youn, H-J. 59
Yu, H. 241

Z

Zelik, J.A. 95
Zeuch, D.H. 375
Zhang, B-P. 155
Zhang, F. 127
Zhang, J. 305
Zhang, Q.M. 257
Zou, L. 147